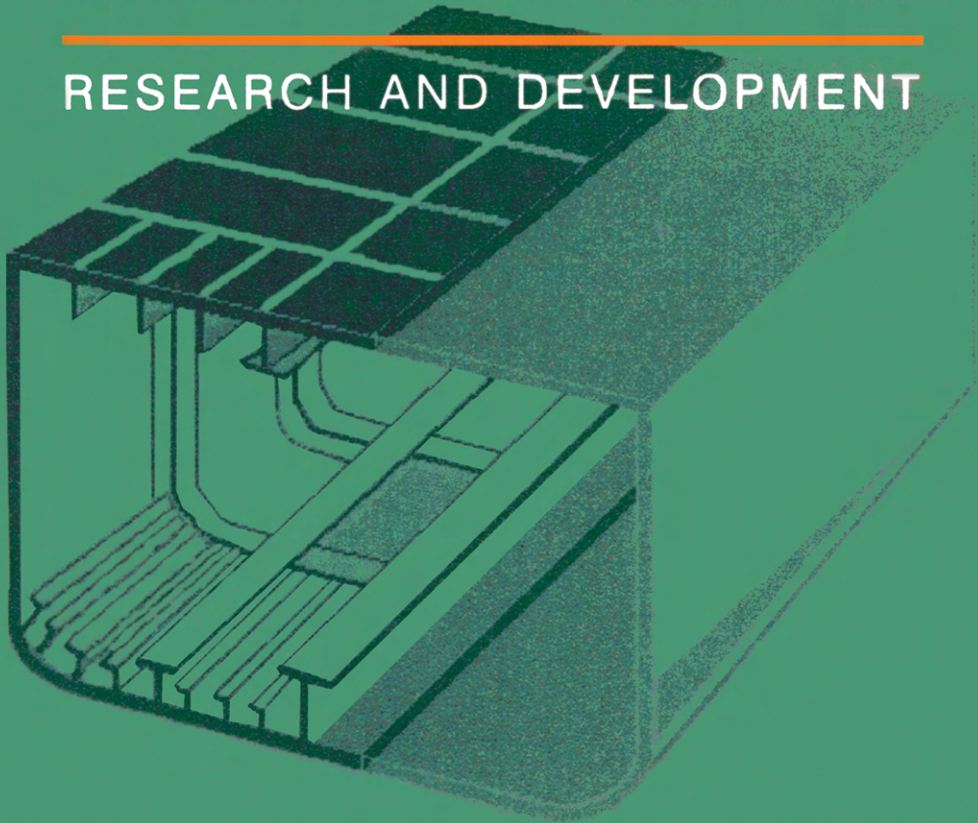

THIN-WALLED STRUCTURES

RESEARCH AND DEVELOPMENT



Edited by

N. E. Shanmugam

J. Y. Richard Liew

V. Thevendran

ELSEVIER

THIN-WALLED STRUCTURES

RESEARCH AND DEVELOPMENT

Elsevier Science Internet Homepage

<http://www.elsevier.nl> (Europe)
<http://www.elsevier.com> (America)
<http://www.elsevier.co.jp> (Asia)

Consult the Elsevier homepage for full catalogue information on all books, journals and electronic products and services.

Elsevier Titles of Related Interest

SRIVASTAVA

Structural Engineering World Wide 1998 (CD-ROM
Proceedings with Printed Abstracts Volume, 702 papers)
ISBN: 008-042845-2

OWENS

Steel in Construction (CD-ROM Proceedings with Printed
Abstracts Volume, 268 papers)
ISBN: 008-042997-1

GODOY

Thin-Walled Structures with Structural Imperfections:
Analysis and Behavior
ISBN: 008-042266-7

FUKUMOTO

Structural Stability Design
ISBN: 008-042263-2

USAMI & ITOH

Stability and Ductility of Steel Structures
ISBN: 008-043320-0

GUEDES-SOARES

Advances in Safety and Reliability (3 Volume Set)
ISBN: 008-042835-5

BJORHOVDE, COLSON & ZANDONINI

Connections in Steel Structures III
ISBN: 008-042821-5

CHAN & TENG

ICASS '96, Advances in Steel Structures (2 Volume Set)
ISBN: 008-042830-4

FRANGOPOL, COROTIS & RACKWITZ

Reliability and Optimization of Structural Systems
ISBN: 008-042826-6

Related Journals

*Free specimen copy gladly sent on request: Elsevier Science Ltd, The Boulevard, Langford Lane,
Kidlington, Oxford, OX5 1GB, UK*

Advances in Engineering Software
CAD

Cement and Concrete Composites

Composite Structures

Composites B: Engineering

Computer Methods in Applied Mechanics & Engineering

Computers and Structures

Construction and Building Materials

Engineering Failure Analysis

Engineering Fracture Mechanics

Engineering Analysis with Boundary Elements

Engineering Structures

Finite Elements in Analysis and Design

International Journal of Solids and Structures

International Journal of Fatigue

Journal of Wind Engineering & Industrial Aerodynamics

Journal of Constructional Steel Research

NDT & E International

Structural Safety

Thin-Walled Structures

To Contact the Publisher

Elsevier Science welcomes enquiries concerning publishing proposals: books, journal special issues, conference proceedings, etc. All formats and media can be considered. Should you have a publishing proposal you wish to discuss, please contact, without obligation, the publisher responsible for Elsevier's civil and structural engineering publishing programme:

Dr James Milne

Senior Publishing Editor

Engineering and Technology

Elsevier Science Ltd

The Boulevard, Langford Lane

Kidlington, Oxford

OX3 7LR, UK

Phone: +44 1865 843891

Fax: +44 1865 843920

E.mail: j.milne@elsevier.co.uk

General enquiries, including placing orders, should be directed to Elsevier's Regional Sales Offices - please access the Elsevier homepage for full contact details (homepage details at top of this page).

THIN-WALLED STRUCTURES

RESEARCH AND DEVELOPMENT

Second International Conference on Thin-Walled Structures

Edited by

N.E. Shanmugam

J.Y. Richard Liew

V. Thevendran

*Department of Civil Engineering
National University of Singapore
Singapore*



1998

ELSEVIER

Amsterdam - Lausanne - New York - Oxford - Shannon - Singapore - Tokyo

ELSEVIER SCIENCE Ltd
The Boulevard, Langford Lane
Kidlington, Oxford OX5 1GB, UK

© 1998 Elsevier Science Ltd. All rights reserved.

This work and the individual contributions contained in it are protected under copyright by Elsevier Science Ltd, and the following terms and conditions apply to its use:

Photocopying

Single photocopies of single chapters may be made for personal use as allowed by national copyright laws. Permission of the publisher and payment of a fee is required for all other photocopying, including multiple or systematic copying, copying for advertising or promotional purposes, resale, and all forms of document delivery. Special rates are available for educational institutions that wish to make photocopies for non-profit educational classroom use.

Permissions may be sought directly from Elsevier Science Rights & Permissions Department, PO Box 800, Oxford OX5 1DX, UK; phone: (+44) 1865 843830, fax: (+44) 1865 853333, e-mail: permissions@elsevier.co.uk. You may also contact Rights & Permissions directly through Elsevier's home page (<http://www.elsevier.nl>), selecting first 'Customer Support', then 'General Information', then 'Permissions Query Form'.

In the USA, users may clear permissions and make payments through the Copyright Clearance Center, Inc., 222 Rosewood Drive, Danvers, MA 01923, USA; phone: (978) 7508400, fax: (978) 7504744, and in the UK through the Copyright Licensing Agency Rapid Clearance Service (CLARCS), 90 Tottenham Court Road, London W1P 0LP, UK; phone: (+44) 171 436 5931; fax: (+44) 171 436 3986. Other countries may have a local reprographic rights agency for payments.

Derivative Works

Subscribers may reproduce tables of contents for internal circulation within their institutions. Permission of the publisher is required for resale or distribution of such material outside the institution.

Permission of the publisher is required for all other derivative works, including compilations and translations.

Electronic Storage or Usage

Permission of the publisher is required to store or use electronically any material contained in this work, including any chapter or part of a chapter. Contact the publisher at the address indicated.

Except as outlined above, no part of this work may be reproduced, stored in a retrieval system or transmitted in any form or by any means, electronic, mechanical, photocopying, recording or otherwise, without prior written permission of the publisher.

Address permissions requests to: Elsevier Science Rights & Permissions Department, at the mail, fax and e-mail addresses noted above.

Notice

No responsibility is assumed by the Publisher for any injury and/or damage to persons or property as a matter of products liability, negligence or otherwise, or from any use or operation of any methods, products, instructions or ideas contained in the material herein. Because of rapid advances in the medical sciences, in particular, independent verification of diagnoses and drug dosages should be made.

First edition 1998

Library of Congress Cataloging in Publication Data

A catalog record from the Library of Congress has been applied for.

British Library Cataloguing in Publication Data

A catalogue record from the British Library has been applied for.

ISBN: 0-08-043003-1

∞ The paper used in this publication meets the requirements of ANSI/NISO Z39.48-1992 (Permanence of Paper).

Transferred to digital printing 2006

Printed and bound by Antony Rowe Ltd, Eastbourne

PREFACE

Thin-plated structures are used extensively in building construction, automobile, aircraft, shipbuilding and other industries because of a number of favourable factors such as high strength-weight ratio, development of new materials and process and the availability of efficient analytical methods. This class of structure is made by joining thin plates together at their edges and they rely for their rigidity and strength upon the tremendous stiffness and load-carrying capacity of the flat plates from which they are made. Many of the problems encountered in these structures arise because of the effects of local buckling. The knowledge of various facets of this phenomenon has increased dramatically since the 1960s. Problem areas which were hitherto either too complex for rigorous analysis or whose subtleties were not fully realized have in these years been subjected to intensive study. Great advances have been made in the areas of inelastic buckling. The growth in use of lightweight strong materials, such as fibre-reinforced plastics has also been a contributory factor towards the need for advances in the knowledge of the far post-buckling range. This conference is expected to serve as an international forum for academics, researchers and practising engineers to exchange ideas and experiences, and to promote better understanding through technological co-operation. The conference is a sequel to the international conference organised by the University of Strathclyde in December 1996 and, this international gathering will provide the opportunity for discussion of recent developments and trends in design of thin-walled structures.

There are 93 papers of which five are Keynote papers. The remaining 88 papers are grouped under nine separate topics which include Aluminium Structures, Cold-Formed and Light Gauge Steel Structures, Composite and Ferrocement Structures, Compression Members, Analysis and Design, Perforated Members, Shells and Pressure Vessels, Shear and Bending and Tubular Members and Bridge Piers.

There are many individuals who have extended their help in one way or another in the preparation of this volume and the support of such individuals is gratefully acknowledged. Thanks are due to all the contributors for their careful preparation of the manuscript and to the Members of the international Advisory Committee for their co-operation and advice. The support of Professor K Y Yong, the Head of the Department of Civil Engineering, National University of Singapore and the Members of the Publication Committee who reviewed the final manuscripts is deeply appreciated.

The conference is organised by the Structural Steel Research Group (SSRG), Centre for Construction Materials and Technology, Department of Civil Engineering, National University of Singapore (NUS) with the support by the Mechanical and Production Engineering, NUS in collaboration with University of Strathclyde, UK and National Science Foundation, USA. Centre for Advanced Construction Studies, NTU, Singapore, Construction Industry Development Board, Singapore, Institution of Engineers, Singapore, Singapore Structural Steel Society, Singapore Technologies Aerospace, Centre for Advanced Structural Engineering, University of Sydney and Centre for Cold-Formed Steel Structures, University of Missouri-Rolla are the other supporting organisations.

N.E. Shanmugam
J.Y. Richard Liew
V. Thevendran

ORGANIZING COMMITTEE

Chairman: N E Shanmugam
Co-Chairmen: J Rhodes
K P Chong
Secretary: Richard J Y Liew
Treasurer: V Thevendran
Members: W A M Alwis
K K Ang
Y S Choo
K H Lee
M A Mansur
C J Tay
S L Toh
C M Wang
C H Yu

INTERNATIONAL SCIENTIFIC COMMITTEE

S L Chan	Hong Kong	D A Nethercot	UK
S F Chen	P R China	P Paramasivam	Singapore
W F Chen	USA	T Pekoz	USA
Y K Cheung	Hong Kong	S Rajasekaran	India
W Z Chien	P R China	J Rondal	Belgium
C K Choi	Korea	C K Soh	Singapore
J M Davies	UK	J Spence	UK
P J Dowling	UK	J W B Stark	The Netherlands
H R Evans	UK	A S Tooth	UK
W C Fok	Singapore	John J Tracy	USA
Y Fukumoto	Japan	N S Trahair	Australia
N K Gupta	India	V Tvergaard	Denmark
G J Hancock	Australia	S Ujihashi	Japan
J E Harding	UK	T Usami	Japan
T Hoglund	Sweden	Reza Vaziri	Canada
N Jones	UK	A C Walker	UK
S Kitipornchai	Australia	S T Wang	USA
N S Lee	Singapore	Y B Yang	Taiwan
S L Lee	Singapore	Y C Yip	Singapore
J Loughlan	UK	W W Yu	USA
R. Narayanan	India	J Zaras	Poland

Contents

Preface	v
KEYNOTE PAPERS	
Smart Thin-Walled Structures <i>KP Chong and BK Wada</i>	3
Light Gauge Steel Framing for House Construction <i>J Michael Davies</i>	17
Ferrocement: A Cementitious Thin Wall Structural Elements - Research to Practice <i>P Paramasivam</i>	29
Design of Steel Arches <i>NS Trahair, Y-L Pi and JP Papangelis</i>	41
Finite Strip Analysis of Shear Walls and Thin Plates with Abrupt Changes of Thickness by Using Modified Beam Vibration Modes <i>YK Cheung, FTK Au and DY Zheng</i>	53
GENERAL SESSION PAPERS	
Section I: Aluminium	
Buckling of Aluminium Plates <i>M Langseth, OS Hopperstad and L Hanssen</i>	67
Shear Strength of Welded Aluminium Plate Girders <i>A Bhogal and AW Davies</i>	77
Strength of Aluminium Extrusions under Compression and Bending <i>OS Hopperstad, M Langseth and L Moen</i>	85
Ultimate Strength of Stiffened Aluminium Plates <i>A Aalberg, M Langseth, OS Hopperstad and KA Malo</i>	93
Section II: Cold-Formed and Light Gauge Steel Structures	
A Comparison Between British and European Design Codes for Cold-Formed Thin-Gauged Structures <i>DB Moore and YC Wang</i>	103
Behaviour of Cold-Formed Steel Wall Frame Systems Lined with Plasterboard <i>Yaip Telue and Mahen Mahendran</i>	111

Buckling, Torsion and Biaxial Bending of Cold-Formed Steel Beams <i>NS Trahair, YL Pi and BM Put</i>	121
Design of Slotted Light Gauge Studs <i>Torsten Höglund</i>	129
Direct Strength Prediction of Cold-Formed Steel Members Using Numerical Elastic Buckling Solutions <i>BW Schafer and T Peköz</i>	137
Ductile and Connection Behaviour of Thin G550 Sheet Steels <i>CA Rogers and GJ Hancock</i>	145
Effect of Cold Forming on Compressed Carbon and Stainless Steel Struts <i>M Macdonald, J Rhodes and GT Taylor</i>	153
Local Buckling of Partially Stiffened Type 3CR12 Stainless Steel Compression Elements in Beam Flanges <i>GJ van den Berg</i>	161
Effects of Spot-Weld Spacing on the Axial Crushing of Closed-Hat Section Members <i>HF Wong, J Rhodes, J Zaras and S Ujihashi</i>	173
Flexural Strength of Cold-Formed Steel Panels Using High-Strength, Low-Ductility Steel <i>Shaojie Wu, Wei-Wen Yu and Roger A LaBoube</i>	181
Flexural-Torsional Stability of Thin-Walled Orthotropic Channel Section Beams <i>Mohammad Z Kabir</i>	189
Inelastic Behaviour of Cold-Formed Channel Sections in Bending <i>V Enjily, RG Beale and MHR Godley</i>	197
Inelastic Lateral Buckling of Cold-Formed Channel and Z-Section Beams <i>Yong-Lin Pi, Bogdan M Put and Nicholas S Trahair</i>	205
Loading Capacity of Cold-Formed RHS Members Used in Multi-Story Buildings <i>ZY Shen, YY Chen, SJ Pan, GY Wang and Y Tang</i>	213
Local Failures in Trapezoidal Steel Claddings <i>M Mahendran and RB Tang</i>	221
Performance of Cold Formed Steel Angles under Fatigue Loading <i>S Kandasamy, GM Samuel Knight and Nagabhushana Rao</i>	229
Quasi-Static Axial Crushing of Top-Hat and Double-Hat Thin-Walled Sections <i>Norman Jones and MD White</i>	237
Structural Performance of Bolted Moment Connections Between Cold-Formed Steel Members <i>K F Chung and Y J Shi</i>	245

Stability Design of Thin-Walled Members Including Local Buckling <i>F Werner, P Osterrieder and H Lehmkuhl</i>	253
 Section III: Composite and Ferrocement	
Axial Crushing of Foam Filled Composite Conical Shells <i>NK Gupta and R Velmurugan</i>	263
Buckling Failure of Titanium-Steel Composite Chimney Liner <i>RHR Tide and MH Darr</i>	271
Influence of Geometric Imperfections and Lamination Defects on the Buckling Behaviour of Composite Cylinders <i>N Panzeri and C Poggi</i>	279
Influence of Shear Deformation on Geometrically Non-linear Deflections of Composite Laminated Plates <i>TS Lok and QH Cheng</i>	289
Post-Buckling and First-Ply Failure of Thin-Walled Frames and Columns Made of Composite Materials <i>Luis A Godoy, Leonel I Almanzar and Ever J Barbero</i>	297
Progressive Damage Analysis of GRP Panels under Extreme Transverse Pressure Loading <i>SSJ Moy, RA Sheno, HG Allen, Z-N Feng and GS Pahdi</i>	305
Snap-Through Buckling of Plastic-Glassy Sheeting <i>SL Chan, AKW So and SW Yuen</i>	313
Behaviour of Thin Walled Composite Beams and Columns <i>KMA Hossain, L Mol and HD Wright</i>	321
Development of the 'Slimdek' System Using Deep Composite Decking <i>RM Lawson and DL Mullett</i>	329
Geometric and Material Nonlinear Behaviour of Steel Plates in Thin-Walled Concrete Filled Box Columns <i>QQ Liang and B Uy</i>	339
Lateral-Distortional Buckling of Composite Cantilevers <i>MA Bradford</i>	347
Lightweight Thin Walled Profiled Steel Sheeting/Dryboard (PSSDB) Composite Floor System <i>WH Wan Badaruzzaman and HD Wright</i>	355
Local Buckling of Cold Formed Steel Sections Filled with Concrete <i>B Uy, HD Wright and AA Diedricks</i>	367
The Dynamic Response of Filled Thin-Walled Steel Sections <i>HD Wright and A W Mohamed</i>	375

A Study of Thin-Walled Ferrocement Elements for Prefabricated Housing <i>MA Mansur, KL Tan, AE Naaman and P Paramasivam</i>	383
Long-Term Deformation Analysis of Thin-Walled Open-Profile RC Beams <i>WAM Alwis</i>	391
 Section IV: Compression Members	
Design Procedures for Stub-Columns <i>KY Teo and SM Chou</i>	401
Inelastic Bifurcation Analysis of Locally Buckled Channel Columns <i>B Young and KJR Rasmussen</i>	409
Stability and Bracing of Thin-Walled Columns <i>Pratyoosh Gupta, ST Wang and George E Blandford</i>	417
Influences of Welding Imperfections on Buckling/Ultimate Strength of Ship Bottom Plating Subjected to Combined Bi-axial Thrust & Lateral Pressure <i>Tetsuya Yao, Masahiko Fujikubo, Daisuke Yanagihara, Balu Varghese and Osamu Niho</i>	425
Post-Ultimate Behaviour of Stiffened Panels Subjected to Axial Compression <i>SR Cho, B-W Choi and I-C Song</i>	433
Strength and Ductility of Steel Stiffened Plates under Cyclic Loading <i>HB Ge, T Usami and T Watanabe</i>	441
Thin Plates Subjected to Uniformly Varying Edge-Displacements <i>NE Shanmugam and R Narayanan</i>	449
 Section V: Analysis and Design	
Geometric Nonlinear Analysis of Diaphragm-Braced C-Purlins <i>YJ Zhu, YC Zhang and XL Liu</i>	461
A Rectangular Plate Element for Ultimate Strength Analysis <i>Koji Masaoka, Hiroo Okada and Yukio Ueda</i>	469
General Solution for C-Shaped Bellows Overall-Bending Problems <i>WP Zhu, Q Huang, P Guo and WZ Chien</i>	477
Advanced Inelastic Analysis of Thin-Walled Core-Braced Frames <i>JY Richard Liew, H Chen, CH Yu and NE Shanmugam</i>	485
Investigation of Collapsed Rack Storage Systems <i>RHR Tide and FA Calabrese</i>	493
Natural Frequencies and Mode Shapes of Thin-Walled Members under In-Plane Forces <i>M Ohga, K Nishimoto, T Shigematsu and T Hara</i>	501

Non-linear Dynamic Analysis of Thin-Walled Tapered Towers with Concentrated Masses <i>GT Michaltsos and TG Konstandakopoulos</i>	509
Optimal Design of Piecewise-Constant Thickness Circular Plates for Minimax Axisymmetric Deflection <i>CM Wang and KK Ang</i>	517
Analysis with Non-Orthogonal Functions for Anisotropic Shells <i>Kai-Yu Xu, Zhe-Wei Zhou and Wei-Zhang Chien</i>	527
Transformations of Displacement and Force Quantities Between Systems of Axes and Generic Points of Rigid Open Cross-Sections <i>Risto Koivula</i>	535
Numerical Modelling of Extended Endplate and Composite Flush Endplate Connections <i>S Troup, RY Xiao and SSJ Moy</i>	543
A Simple Nonlinear Frame Element and its Application to Postbuckling Analysis <i>YB Yang, SR Kuo, and SC Yang</i>	553
Section VI: Perforated Members	
Design of Perforated Plates under In-Plane Compression <i>V Thevendran, NE Shanmugam and YH Tan</i>	563
Study on the Effect of Symmetrical Openings on the Ultimate Capacity of Lipped Channels <i>Y Pu, MHR Godley, RG Beale and J Wallace</i>	571
Tension Buckling of Plates Having a Hole under Combined Loadings <i>S Shimizu and H Nishimura</i>	579
Ultimate Strength of Cylindrical Tubular Columns with Circular Perforation <i>S Murakami, N Nishimura, S Takeuchi, H Inoguchi and K Jikuya</i>	587
Section VII: Shells and Pressure Vessels	
The Buckling Behaviour of Horizontal Storage Vessels - Experiments and Codes <i>AS Tooth, J Spence and GCM Chan</i>	597
Buckling Strength of T-Section Transition Ringbeams in Elevated Steel Silos and Tanks <i>JG Teng and F Chan</i>	605
Cylindrical Shells Subjected to Vertical Edge Deformation and Internal Pressure <i>M Jonaidi, M Chaaya and P Ansourian</i>	613
Inelastic Buckling of a Layered Conical Shell <i>J Zielnica</i>	621

Modelling Methodologies with Beam Finite Elements for Collapse Analysis of Tubular Members/Cylindrical Shells <i>B Skallerud and J Amdahl</i>	629
Nonlinear Vibration and Dynamic Instability of Thin Shallow Conical Shells <i>YE Zhiming</i>	639
Evaluation of the Principal Stresses in a Deaerator Vessel of a Thermoelectric Power Plant <i>NS Maia, EB Medeiros and TR Mansur</i>	647
Strength of Reticulated Shells Designed by Second-Order Elastic Analysis <i>S Kato, I Mutoh and Y Matsunaga</i>	655
Stresses in Elastic Cylindrical Shells under Wind Load <i>Martin Pircher, Werner Guggenberger, Richard Greiner and Russell Bridge</i>	663
The Influence of Weld-Induced Residual Stresses on the Buckling of Cylindrical Thin-Walled Shells <i>Martin Pircher, Martin O'Shea and Russell Bridge</i>	671
Bending Effects on Instabilities of Internally Pressurised Tubes Modelled by a Nonlocal Membrane Theory <i>Lars Pilgaard Mikkelsen and Viggo Tvergaard</i>	679
 Section VIII: Shear and Bending	
An Experimental Study of Viscoplasticity-Creep Interaction of Thin-Walled Tubes under Pure Bending <i>WF Pan and CM Hsu</i>	689
Dynamic Equilibriums of Nonprismatic Thin-Walled Beams Considering the Effects of Transverse Shear Deformations Defined on an Arbitrary Coordinate System <i>CN Chen</i>	697
Lateral Buckling Capacities of Thin-Walled Monosymmetric I-Beams <i>M Kubo and H Kitahori</i>	705
Post Buckling Deformations of Rectangular Hollow Sections in Bending <i>Frode Paulsen and Torgeir Welø</i>	713
A Unified Method for Calculating Shear Stresses in Thin-Walled Sections <i>Ali H Khan and Mark J Sharrock</i>	723
Influence of Shear Buckling on the Ductility of Steel Members <i>Ioannis Vayas</i>	733
Qualities and Use of Beams with Expanded Metal <i>M Hellsten</i>	741

Section IX: Tubular Members and Bridge Piers

Blast Loading of Offshore Structural Members Using Novel Experimental Techniques <i>SS Hsu, MD White and GK Schleyer</i>	753
Lateral (Diametral) Crushing of Steel Circular Cylindrical Tubes, Welded to the Platens <i>SV Khonsari and SMH Parvinnia</i>	761
Quasi-Static Axial Compression of Thin-Walled Circular Metal Tubes Including Effects of Foam Filling <i>SR Guillow and G Lu</i>	771
Cyclic Loading Test of Steel Octagonal Section Pier Models <i>M Suzuki and T Aoki</i>	779
Elasto-Plastic Behavior of Steel-Pipe Pier Models under Lateral Cyclic Loading <i>H Koeda, S Ono, N Kishi and Y Goto</i>	787
Experimental Study on Elasto-Plastic Dynamic Behavior of Steel-Pipe Pier Models <i>N Kishi, H Koeda, M Komuro and KG Matsuoka</i>	795
On Plasticity Models for Analysis of Bridge Box Pier with Round Corners under Cyclic Loading <i>E Yamaguchi, Y Goto, Norimitsu Kishi, M Komuro and K Abe</i>	803
Elasto-Plastic Instability of Steel Compression Tubular Members Subjected to Cyclically Applied Bi-Directional Horizontal Loads <i>Eiichi Watanabe, Kunitomo Sugiura and Walter O Oyawa</i>	809
Author Index	817
Keyword Index	821

This Page Intentionally Left Blank

KEYNOTE PAPERS

This Page Intentionally Left Blank

SMART THIN-WALLED STRUCTURES

K.P. Chong¹ and B. K. Wada²

¹National Science Foundation
4201 Wilson Blvd., Arlington, VA 22230, U.S.A.

²Jet Propulsion Laboratory, California Institute of Technology
4800 Oak Grove Dr., Pasadena, CA 91109, U.S.A.

ABSTRACT

Research and development in smart thin-walled structures and materials have shown great potential for enhancing the functionality, serviceability and increased life span of the aerospace, civil and mechanical infrastructure systems and as a result, could contribute significantly to the improvement of every nation's productivity and quality of life. The intelligent renewal of aging and deteriorating aerospace, civil and mechanical infrastructure systems as well as the manufacturing or construction of new ones, includes efficient and innovative use of high performance sensors, actuators, materials, mechanical and structural systems. In this paper some examples of NSF funded projects and NASA projects, as well as some research needs are presented.

KEYWORDS

thin-walled structures, smart structures, structural control, solid mechanics, smart materials, composites, adaptive structures, space structures, inflatable structures.

INTRODUCTION

Spacecraft enhances opportunity to observe earth, planets and solar system and to provide communication from various locations on earth to other locations. Various types of observations and communications are limited by the size and precision of very large structures. The size of structure may range upwards of 100 meters with submicron precision requirements. Other demands on the structure include a very efficient lightweight system with the capability of being stowed under a launch vehicle shroud and the deployed/erected to its final dimensions in space. Thin walled structures are essential to space programs. Beginning in the early 1980's, Smart Structures technology focused on simpler approaches to add damping to large precision space structures to attenuate the small vibrations of these large space structures by using new developments in actuators and sensors. Smart Structures is a multidisciplinary activity that integrates materials, actuators, sensors, controls, composites, structures, concepts and dynamics. One of many definitions is "a

structural system whose geometric and inherent structural characteristics can be beneficially changed to meet mission requirements either through remote commands or automatically in response to adverse external stimulation" [Wada, 1990]. The approach provides solutions to a broad range of space structures challenges including: ground validation tests, on-orbit deployment, system identification, static adjustment and reliability. It results in a *robust* structure [Wada, 1994]; a robust structure meets the mission requirements by reducing the influence of uncontrollable, uncertain or costly design parameters and processes. ***The full benefits of smart structures are the realization that it enables many of the future space missions and can reduce overall mission cost while increasing overall reliability.***

Thin-walled composites have been candidates for use in high tech applications for some time (Chong, et al, 1994). However, for use in the civil infrastructure systems and construction type applications, in the clean car and even in civilian aircraft, substantial total lifetime *cost* improvements must be realized. Thus the durability and lifecycle performance as well as maintenance and repair are very important considerations. Study on the collapse of highway bridges in the January 1994 Northridge Earthquake indicates that the massive inertia due to the heavy reinforced concrete in earlier designs is a major cause. A composite thin-walled bridge should be about 3 to 5 times lighter. In the next section a futuristic smart composite bridge will be presented.

In recent years, researchers from diverse disciplines have been drawn into vigorous efforts to develop smart or intelligent structures that can monitor their own condition, detect impending failure, control damage, and adapt to changing environments (Rogers and Rogers, 1992; Chong, 1998). The applications of such smart materials/systems are abundant -- ranging from design of smart aircraft skin embedded with fiber optic sensors to detect structural flaws; thin-walled bridges with sensing/actuating elements to counter violent vibrations; flying micro-electrical-mechanical systems (MEMS) with remote control for surveying and rescue missions; and stealth submarine vehicles with swimming muscles made of special polymers. Often times these structures are thin-walled structures due to structural efficiency and/or payload constraints. Such a multidisciplinary research front (Chong, et al, 1993), represented by material scientists, physicists, chemists, biologists, and engineers of diverse fields--mechanical, electrical, civil, control, computer, aeronautical, etc.--has collectively created a new entity defined by the interface of these research elements. Smart structures/materials are generally created through synthesis by combining sensing, processing, and actuating elements integrated with conventional structural materials such as steel, aluminum, concrete, or composites. Some of these structures/materials currently being researched or in use are (Chong, et al, 1994; Liu et al, 1994):

- piezoelectric composites, which convert electric current to (or from) mechanical forces;
- shape memory alloys, which can generate force through changing the temperature across a transition state;
- electro-rheological (ER) fluids, which can change from liquid to solid (or the reverse) in an electric field, altering basic material properties dramatically. Since ER fluids are really suspended solutions, the settlement of solids under long-term inactivity is a problem.

Current research activities aim at understanding, synthesizing, and processing material systems, which behave like biological systems. Smart structures/materials basically possess their own sensors (nervous system), processor (brain system), and actuators (muscular systems)--thus mimicking biological systems (Rogers and Rogers, 1992). Sensors used in smart structures/materials include optical fibers, corrosion sensors, and other environmental sensors and sensing particles. Examples of actuators include shape memory alloys that would return to their original shape when heated, hydraulic systems, and piezoelectric ceramic polymer composites. The processor or control aspects of smart structures/materials are based on microchip, computer software and hardware systems. In the past, engineers and material scientists have been involved extensively with the characterization

of given materials. With the availability of advanced computing and new developments in material sciences, researchers can now characterize processes, design and manufacture materials with desirable performance and properties. One of the challenges is to model short-term micro-scale material behavior, through meso-scale and, macro-scale behavior into long term structural systems performance (cf. Fig. 1). Accelerated tests (Chong et al, 1998) to simulate various environmental forces and impacts are needed. Supercomputers and/or workstations used in parallel are useful tools to solve this scaling problem by taking into account the large number of variables and unknowns to project micro-behavior into infrastructure systems performance, and to model or extrapolate short term test results into long term lifecycle behavior.

RESEARCH NEEDS IN SMART STRUCTURES AND MATERIALS

Recent developments in precision actuators, sensors, and miniature electronics with frequency response from static to kilo-hertz capable of direct integration into the structure itself to sense and actuate structural strains enables Smart Structures. Fortunately, the availability of commercial piezoelectric materials for actuators suitable (space compatible and low load carrying requirements) for spacecraft applications allowed rapid transition from laboratory experiments to space applications. The traditional approach to the design of structures is to increase the wall thickness as necessary to carry the loads generated by external loads or to maintain the necessary geometric shape. *For smart structures, a thin wall structure is preferable to provide transfer of strain from the smart material to the structure with smaller forces. The strain induced by the smart materials will then be used to reduce the loads in the structure and to provide the desired geometric shape.* Until recently, space structures were not capable of changing its initial characteristics. The capability to design structures with changing characteristics during its operational life excites many engineers by providing many more options and opportunities. To date, the rapid worldwide growth in research and applications in Smart Structures is almost exponential.

One of the challenges is to achieve optimal performance of the total system rather than just in the individual components. Among the topics requiring study is energy - absorbing and variable dampening properties as well as those having a stiffness that varies with changes in stress, temperature or acceleration. The National Materials Advisory Board (NAS, 1993) has published a good perspective on the materials problems associated with a high performance car and a civilian aircraft which develops the "values" associated with these applications. Among the characteristics sought in smart structures/materials are self healing when cracks develop and in-situ repair of damage to structures such as bridges and water systems in order that their useful life can be significantly extended. There is the associated problem of simply being able to detect (predict) when repair is needed and when it has been satisfactorily accomplished. The use of smart materials as sensors may make future improvements possible in this area. The concept of adaptive behavior has been an underlying theme of active control of structures that are subjected to earthquake and other environmental type loads. Through feedback control and using the measured structural response, the structure adapts its dynamic characteristics for performance instantaneously.

Fig. 1 is a sketch of a futuristic smart composite bridge system, illustrating some new concepts: including advanced composite materials with protective coating to mitigate ultraviolet damage, wireless sensors, optical fiber sensors, data acquisition and processing systems, advanced composite materials, structural controls, dampers, and geothermal energy bridge deck de-icing. Since a composite bridge is very much lighter (up to five times lighter) than a conventional concrete or steel bridge, excessive vibration/deformation as well as stability and the resulting fatigue damages can be minimized and durability maximized by elaborate structural control systems (Liu, Chong and Singh, 1994; Rogers and Rogers, 1992). An artist rendition of this bridge appeared in *USA Today*, 3/3/97.

The recent research activities in infrastructure (Chong, et al, 1993) for example call for efforts in:

- deterioration science
- assessment technologies
- renewal engineering
- institutional effectiveness and productivity at the system level.

These are in addition to the implied needs in:

- Stability, large deformation and buckling
- Reliable accelerated tests for long term durability behavior
- improved computers, microprocessors and networking
- more accurate/complete modeling of lifetime predictions
- new sensors and control systems; NDT; new materials
- electro-rheological fluids (e.g. settlement of solids over time in the suspended solution)
- shape memory alloys, etc.
- understanding corrosion better at the detail level
- life-cycle performance and costs.

This list is meant to illustrate rather than be complete.

SOME BASIC PRINCIPLES

Traditional Approach: External Force Control

The basic fundamental principles using Smart Structures is almost the direct opposite to the historically traditional approach of forcing the distorted shape to the desired accuracy by applying a set of external vector forces to cancel the distortion. The application of external vector forces becomes more difficult in space because a “ground” does not exist to react the forces. Fig. 3 illustrates a conceptual structure in space using the traditional approach to change the shape of the structure. Challenges with the external force control approach are:

- The external vector forces F_e are applied by expelling mass or by proof-mass actuators (PM) that applies forces through reaction against a mass.
- The magnitude, phase and direction of F_e must be accurately coordinated with the distortions of the structure. This requires very accurate knowledge of the structural distortion through a multitude of inertial sensors. Thus the actuators and sensors are at locations of maximum distortion. To visualize the problem, imagine trying to push a balloon inwards with thrusters. No matter in how many places you push, it seems impossible to make the sphere shrink uniformly and prevent rigid body motion.
- Without precision control and positioning of F_e , the rigid body motions (u_r) the structure will be excited along with the elastic motions (u_e). The inertia sensors must filter the rigid body motions to establish the elastic motion for control.
- The external vector force approach is not realistic for long term static shape control.
- The characteristics of the PM introduces additional undesired dynamics and is difficult to use low frequency PMs in the presence of gravity.
- The system is not robust because any failure of the actuator or sensors in external vector force control would probably result in instabilities.

Smart Structure: Internal Force Control

Smart Structure uses internal force control or strain energy to control and adjust the distortion of structures. Unlike external vector forces, the strain energy is algebraic and can thus be combined. This feature is very important since it allows redundancies by using several local active elements to either introduce damping or provide forces. If a few active elements fail, then the others can be used to extract energy or provide the necessary force. As shown in Fig. 4, the actuator sensors are at locations of maximum strain energy, often these locations are not at the locations of maximum displacement. The structure itself provides communication between sensors and the actuators by its ability to transmit force information. The features of Smart Structures are:

- Active members are placed at locations of high strain energy. Each is capable of dissipating strain energy from the system without applying external forces to the structure. Since strain energy is an algebraic quantity, multiple active members provide redundancy to the system.
- Integrating actuators into the structure results in high stiffness designs with high internal resonance, no additional dynamics are introduced.
- The control algorithms are significantly less sensitive to structural uncertainties including non-linearities.
- The actuators as exciters for on-orbit system identification and controls only excite the elastic deformations. They apply equal and opposite forces to the structure.
- Static shape changes are easily made.

SPACE CHALLENGES

Although the initial motivation of Smart Structures was to provide damping to attenuate the vibration motion of large space structures, it provides solution options to many other space structure system challenges. The benefits are frequently to the overall system, not just a technological improvement. From a systems perspective, the large precision space structure must be capable of deployment or space assembly because the finite flight configuration is larger than the interior diameter of the launch vehicle shroud. The structure requires ground testing to validate its design, survive the launch environments, deploy, retain its shape during the mission with the other constraints such as lightweight, inexpensive and very reliable. The various challenges will be described along with current status of development or application. Fig. 5 illustrates a graphite epoxy sandwich plate with honeycomb cores using PZT actuator to change or control the shape of the plate.

Robust Design

The most significant benefit of Smart Structures to space application is the ability to help develop robust spacecraft designs, resulting in enabling specific missions, reducing overall cost, while significantly improving its reliability. The conventional approach to the design, fabrication and test of large precision structures is not *robust* because it depends upon precisely controlling many parameters and processes. Problems with a lack of controls result in spacecraft failure. In all spacecraft, the total system cannot be ground tested in its intended environment.

The first operational use of Smart Structures in space was for the Articulating Fold Mirror (AFM) [Fanson and Ealey, 1993] for the replacement Wide Field Planetary Camera (WFPC) used to correct the aberration of the Hubble Space Telescope. The initial hardware required extensive efforts in stable composites; characterization of the materials for space effects; extensive analysis, test and correlation; extensive inspection; post-fabrication treatment and handling; and environment testing. The hardware was not *robust* because the final position of a fold mirror was dependent upon the accuracy and control of the many parameters and processes mentioned. Within one year of the

flight, a new design including the use of electro-strictive materials capable of adjusting the angular position of the critical fold-mirror was completed and flown.

Ground Testing

Ground validation tests on spacecraft is the only opportunity to experimentally establish the design will meet the requirements. Mostly likely, structural concepts that cannot be validate by ground tests are not acceptable to program managers. For large precision structures, the displacements and strain energy resulting from earth's gravitational force are possibly 3-5 orders of magnitude larger than the values important to mission success in space. Thus ground testing are not able to detect errors sources significant to the operation of the spacecraft because the large strain energy or forces due to gravity masks important deficiencies. Smart structures [Wada, 1992] provides a solution option by alleviate (by 3 orders of magnitude) the necessity of precision measurements on the ground by making the precision adjustments in space. The ground tests are to assure the range and fidelity of the actuators, sensors and controllers are adequate to encompass the uncertainties.

Deployment and Space Construction

Deployment reliability continues to be a problem on many space missions. The problem seems to be attributable to "binding" of joints and mechanisms due to thermal expansion or other error sources, creating unexpected internal strain energy that cannot be overcome by the work from the deployment mechanism. A solution option [Wada, 1992], is to incorporate active members that controls the amount of strain energy in predetermined locations in the structure. The amount of strain energy allowable is controllable from ground or automatically in response to the deployment. The feasibility of the approach has been demonstrated in the laboratory on a very simple structure.

Linearization of the Structure

Precision structures with x-displacement requirements are not feasible if the structure itself has x-displacement gaps. Gaps in joints manifest themselves as a non-linear structure whose geometric position is not determinable nor controllable. Structures with gaps tend to respond "chaotically"; the dynamic response is random when subject to deterministic inputs. Some gap in select joints are necessary to design deployable structures. However the difficulty is the gaps in the joints are not detectable during ground testing because the gravity field preloads all the joints.

The combination of Smart Structures and structural configuration allows a design where the members of the structure can be preloaded by activating active members. By preloading the members the joints are preloaded and the gaps are eliminated. Laboratory experiments show that gaps in joints are detectable using active members by measuring the load distribution pattern in the structure and then eliminated [Bruno, et al, 1994].

System Identification

Once the spacecraft is in its operational configuration in space, the dynamics are important because they often affect the precision of structures. Accurate measure of its modal parameters is important. In traditional approaches, vibration shakers that are attached to the structure are used to excite the structure. On a free-free system in space, a proof mass actuator (PMA) is a likely candidate since "ground" does not exist to hold the shakers. Unfortunately these approaches require additional weight, power, and complications.

Smart Structures provides an ideal and possibly a more accurate approach to identify the system dynamic characteristics. The active members located at the areas of maximum strain energy for the modes of interest are also ideal to provide the excitation force for system identification. The actuators provide input forces in the direction of the force distribution of the modes of vibration and the force levels are comparable to the motion levels of interest. Laboratory demonstration [Chen, et al, 1989 and Kuo, et al, 1990] verifies that the active members in the structure for other functions, such as active damping, are excellent sources of force for system identification.

Static Adjustment

Establishing, changing and maintaining the static position or shape is often more difficult than measuring the controlling the dynamic motion. Static adjustments require a knowledge and control of the overall system, whereas dynamics are controllable through local energy dissipation. Laboratory experiments show that errors in static displacement of two dimensional parabolic surface formed by a truss structure can be reduced by up 80% by adjusting the lengths of 10% of the total members using active members [Bruno, et al 1992]. Mirror surfaces achieving 0.035 micron rms wavefront accuracy over a 3.75 meter diameter with a 70 kg/m² net area density was achieved using lightweight Ultra Low Expansion glass mounted on active electrostrictive actuators spaced 9.2 meter separation on a triangular grid.

Vibration Attenuation

The initial objective of Smart Structures to attenuate vibration is successful. Success exists in adding active local damping by placing actuator/sensor/controllers at locations of maximum strain energy of structures with a wide range and size of structures from mm to 12 meters in dimension. Active members up to 5 meters in length exist. Both force and a combination of force and relative displacement feedback are successfully in use. The use of multiple active members at a location of maximum strain energy provides redundancy and is successful for poorly modeled structures that includes nonlinearities. Flight experiments on a 12 meter long truss [Lawrence, et al 1990] and CASTOR experiment [Bousquet, et al , 1995] on the MIR station demonstrated the maturity of the technology.

Vibration Isolation, Suppression and Steering (VISS)

The capability to stabilize and precisely move observational instruments on a spacecraft with a variety of vibration sources provides the capability to integrate instruments on a variety of potential flights. The approach is to develop a platform consisting of six active members. The platform will provide the interface of the instrument with the spacecraft. Through the active members, the six degrees of freedom of the instrument are controllable. A flight experiment referred to as VISS [Rahmen, 1997] will be launched as part of the STRV-2 spacecraft within the next 6 months. The goal is to achieve 20 db isolation of vibrations from the spacecraft above 2 Hz, 15 db vibration suppression of disturbances at 60 and 120 Hz on the instrument, and plus/minus 0.3 degree steering at 2 and 4Hz. or an instrument weighing about 40 pounds. A cryocooler vibration suppression experiment [Glaser, et al 1995] demonstrating the ability to suppress the motions of the first five harmonics of 60 Hz. by over a factor of 80 flew on the STRV-1b spacecraft in 1994.

Inflatable Structures

The use of very thin walled inflatable structures is creating excitement since the recent Shuttle Inflatable Antenna Experiment [Freeland, et al 1997] where a antenna packaged in a 7x3x1.5 foot box inflated into a 50 foot diameter offset parabolic surface with three 92 foot long struts to its

focal point. The weight of the inflatable part of the system with the pressurant Nitrogen gas weighed 132 pounds and the goal was to achieve a surface accuracy of around one to two mm rms. The antenna was successfully deployed but the desired pressurization was not achieved. The antenna surface was .00025 inch thick Mylar and the struts and doughnut-shaped frame are made of .010-.012 inch thick coated fabric. The excitement is that this thin walled structure potentially provides a very inexpensive, lightweight, and efficiently packaged structure for space application. Challenges for the future includes the technology to develop structural elements for the struts and doughnut-shaped frame providing the boundaries for the antenna membrane that are flexible during deployment but rigidizes in space and to develop the capability to reliably inflate and maintain the membrane to the desired shape accuracy for the many year life of the missions. Approaches to adjust the rigidizeable frames and the membrane surface to the design dimensions during its mission using smart structures technology will provide the necessary confidence to its successful implementation.

EXAMPLES OF SMART STRUCTURES AND MATERIALS

Smart structures and materials may heal themselves when cracked. NSF grantees have been developing self-healing concrete. One idea is to place hollow fibers filled with crack-sealing material into concrete, which if cracked would break the fiber releasing the sealant, according to Surendra Shah, Director of the NSF Science and Technology (S&T) Center at Northwestern. Lehigh researchers at ATLSS, an NSF Engineering Research Center, are looking into smart paints, which will release red dye (contained in capsules) when cracked. Optical fibers, which change in light transmission due to stress, are useful sensors. They can be embedded in concrete or attached to existing thin-walled and other structures. NSF-supported researchers at Rutgers University studied optical fiber sensor systems for on-line and real-time monitoring of critical components of structural systems (such as bridges) for detection and warning of imminent structural systems failure. NSF grantees at Brown University and the University of Rhode Island investigated the fundamentals and dynamics of embedded optical fibers in concrete. Japanese researchers recently developed glass and carbon fiber reinforced concrete, which provides the stress data by measuring the changes in electrical resistance in carbon fibers. Under an NSF Small Grants for Exploratory Research Programs, researchers at the University of California-Berkeley recently completed a study of the application of electro-rheological (ER) fluids for the vibration control of structures. ER fluids stiffen up very rapidly (changing elastic and damping properties) in an electric field. Other NSF supported researchers are studying shape memory alloys (University of Texas, Virginia Tech, and MIT); surface superelastic microalloying as sensors and microactuators (Michigan State); and magnetostrictive active vibration control (Iowa State, Virginia Tech); etc. Photoelastic experiments at Virginia Tech demonstrated that NiTiNOL shape memory alloy (SMA) wires could be used to decrease the stress intensity factor by generating a compressive force at a crack tip. SMA thin-walled tubes, which will enlarge under body temperature, have been used to mitigate the effects of enlarged prostates in men. Other examples in the following include innovations in thin-walled structures with or without intelligence.

- Fiber-optic Sensors in Bridges, R. Idriss, New Mexico State University.

Fiberoptic cables are etched by laser with 5-mm long internal gauges, spaced about 2 m apart. These cables, strung under the bridge with epoxy, will be able to detect the stresses by sending light beams down the cable at regular intervals and by measuring the bending of the light beams. These gauges can also be used to monitor general traffic patterns. The sensors serve as a data collector as well as a wireless transmitter.

- Intelligent Structures and Materials, C.A. Rogers, University of S. Carolina.

Specifically, this Presidential Young Investigator (PYI) project (Rogers and Rogers, 1992) includes: distributed sensing and health monitoring of civil engineering structures, active buckling control structures and active damage control of composites. Micron size magnetostrictive particles are mixed with the composite for health monitoring. Proof-of concept experiments have demonstrated that delaminations could be located using active magnetostrictive tagging. Low velocity impact damage resistance of composites can be improved by hybridizing them with shape memory alloy material (SMA). The graphite epoxy specimen has significantly more fiber breakage compared to the hybrid specimen and is completely perforated at the impact site.

- Energy Absorbing Flexurally Loaded Pultruded Tubes, L. Bank, University of Wisconsin – Madison, WI.

This project will study the energy-absorption capacity of composite material tubes when loaded in bending. In a composite material tubular beam, energy is absorbed in a stable manner by progressive "tearing failure" at the tube corners, and that this provides the beam with a behavior analogous to that of an elasto-plastic beam. Such a phenomenon has recently been reported but an in-depth study has not been conducted. This research will investigate the phenomenon in-depth, by use of experimentation and numerical modeling, and provide recommendations for design.

- Innovative System of Continuous Prestressed Composite Bridges for the 21st Century, N. F. Grace, Lawrence Tech. University, MI.

This research presents a new concept dealing with the development of a multi-span continuously prestressed concrete bridge system that requires no shoring or forms and has superior characteristics compared to conventional continuous bridge systems. The non-corrosive bridge system will be built of: (i) modified precast pretensioned, with internal carbon fiber reinforced plastic (CFRP) strands, Double-T (DT) girders, (ii) cast-in-place continuous deck, reinforced with glass carbon fiber reinforced plastic (GFRP or CFRP) rebars, connected to the DT through CFRP or GFRP shear connectors, and (iii) externally draped continuous CFRP post-tension strands. An analytical and experimental study will be conducted to examine the static, dynamic, fatigue and ultimate load characteristics of the multi-span continuously prestressed new bridge system.

- NDE of Debonding in Fibrous Composites, C.T. Herakovich and M.J. Pindera, University of Virginia (Lissenden, et al, 1994).

The objective is to determine the feasibility of a method for nondestructive evaluation of debonding in fibrous composite materials. It is based upon micromechanical predictions which indicate that damage in the form of debonding in unidirectional metal matrix composites has no influence on the axial modulus in the fiber direction, whether it has an appreciable influence on the shear modulus for loading by pure longitudinal composites subjected to combined stress states remains an open question. It turns out the shear stiffness, at the high axial stress levels, shows modest degradation until the very highest axial stress levels where significant shear stiffness degradation and energy dissipation is observed.

- Smart Reinforcement Strength and Nondestructive Evaluation with Hybrid Composites, A. E. Nanni, Pennsylvania State University (Nanni et al, 1992).

This project investigated the feasibility of using several different types of fibers to increase the ductility of the group acting as prestressing strands for use in concrete construction. The carbon

fiber may also be used as a monitor for permanent damage in the concrete. Fibers considered are: carbon, aramid, and poly-vinyl-alcohol, because they are stable in the alkaline environment of the concrete.

- Micromechanics of Composites, J.-W. Ju, University of California, Los Angeles, (J.W. Ju and T.M. Chen, 1993a; 1993b)

This PYI award investigated several topics on the micromechanics of both brittle and ductile composites. Some of the research, for example, is for metal matrix composites in the case where the matrix is visco-plastic and the particles are elastic. Other parts examine the role of particulate shape changes. In the industrial matching aspect, the work is extended to develop microstructure-based macroscopic constitutive behavior for fiber-reinforced cement based composites.

- Failure in Anisotropic Curved Layered Structure, F.G. Yuan, North Carolina State University, (F.G. Yuan, 1993a; 1993b)

The primary objective is to establish an analytical and experimental program to understand and to predict the failure mechanics and mechanisms of curved layered composites.

- Damage Evolution Based on Distributed and Localized Changes in Microstructure, D. Lagoudas, Texas A & M.

PI developed a continuum theory of damage based on the gauge principle, investigated the interrelation between global instability and local compressive failure as well as conducted compressive tests on composite cylinders.

- TiNi Shape Memory Alloy Fibers and Reinforcements in Aluminum and Epoxy Matrix Composites, M. Taya, Univ. of Washington, Seattle

The use of a shape memory alloy for a fiber reinforcement can result in the production of compressive residual stresses in the matrix phase of the composite. This can result in increases in flow stress and toughness of the composite compared to these properties in the same composites when the TiNi was not treated to produce a shape memory effect in the composite. The induced compressive stress in the matrix as a result of the shape memory alloy treatment of TiNi is responsible for the enhancement of the tensile properties and toughness of the composite. The concept of enhancing the mechanical properties of composites by inducing desirable stress states via shape memory reinforcements is innovative.

- New Test Methods to Measure the Poisson's Ratio and the Fracture Toughness of Microelectromechanical Systems (MEMS), Sharpe and Hemker, Johns Hopkins University.

While engineers today are able to design MEMS and predict their overall response, they cannot yet optimize the design to predict the allowable load and life of a component because the mechanical properties of the material are not available. This research is attempting to measure and provide such data. Further, they are performing comprehensive microstructural studies of MEMS materials, which, together with the mechanical testing, will enable a fundamental understanding of the micromechanical response of these materials. There is currently a trend toward thicker materials (of the order of hundreds of micrometers) in MEMS because a larger aspect ratio is needed for a mechanical device to be able to transmit usable forces and torques. The mechanical testing techniques are being extended for such applications also. MEMS have great potential in smart structures.

- Synthesis of Smart Material Actuator Systems for Low and High Frequency Macro Motion: An Analytical and Experimental Investigation, G. Naganathan, University of Toledo.

This project is to demonstrate that motions of a few centimeters can be performed by smart material actuator system. A program that combines theoretical investigations and experimental demonstrations will be conducted. Potential configurations made of piezoceramic and electrostrictive materials will be evaluated for providing larger motions at reasonable force levels for applications.

SUMMARY AND CONCLUSIONS

An overview of the state of the art and NSF engineering research in smart structures and materials are presented. The authors hope that this paper will act as a catalyst, sparking interest and further research in these areas. This paper reflects the personal views of the authors, not necessarily those of the NSF or NASA.

ACKNOWLEDGMENTS

The first author would like to acknowledge the input and additions by his NSF grantees and colleagues, including Drs. C.S. Hartley, S. Saigal, S.C. Liu, O.W. Dillon, and C. A. Rogers.

REFERENCES

- Bousquet, P.W., Guay, P. and Mercier, F., 1995, "Evaluation of Active Damping Performances in Orbit," Proc. of the 5th International Conference on Adaptive Structures, Technomic, Lancaster, PA, Key West, FL.
- Bruno, R., 1994, "Identification of Nonlinear Joints in a Truss Structure," AIAA-94-1776-CP AIAA/ASME Adaptive Structures Forum, Hilton Head, SC.
- Bruno, R., Salama, M.A. and Garba, J. A., 1992, "Actuator Placement for Static Shape Control on Nonlinear Truss Structure," Proc. of the 3rd International Conference on Adaptive Structures, San Diego, CA, Technomic, Lancaster, PA.
- Chen, J.C. and Fanson, J.L., 1989, "System Identification Test Using Active Members," AIAA 89-1290, Proc. Of the 30th AIAA Structures, Structural Dynamics, Materials Conference, Mobile, AL.
- Chong, K. P. (1998), Smart Structures Research in the U. S., *Keynote Paper, Proc. of NATO Adv. Research Workshop on Smart Structures*, Pultusk, Poland.
- Chong, K. P., et al, (1993), *Civil Infrastructure Systems Research: Strategic Issues*, NSF 93-5, 54 pp., National Science Foundation (NSF), Arlington, VA.
- Chong, K. P., et al, (1998), *Long Term Durability of Materials and Structures: Modeling and Accelerated Techniques*, NSF 98-42, NSF, Arlington, VA.

Chong, O.W. Dillon, J.B. Scalzi and W. A. Spitzig (1994), Engineering Research in Composite and Smart Structures, *Composites Engineering*, 4(8), 829-852.
Composite Structures, Vol. 26, Nos. 1 & 2, pp. 63-75

Fanson, J. and Ealey, M., 1993, "Articulating Fold Mirror for the Wide-Field Planetary Camera II," SPIE 1920-37, Active and Adaptive Optical Components and Systems II, Albuquerque, NM.

Freeland, R. E., Bilyeu, G. D., and Veal, G.R, 1997, "Large Inflatable Deployable Antenna Flight Experiment Results," IAF Paper 97-1.3.01, 48th Congress of the International Astronautical Federation, Turin, Italy, October 6-10, 1997.

Glaser, R., Garba, J. and Obal, M., 1995, "STRV-1b Cryo-cooler Vibration Suppression," AIAA 95-1122, Proc. of the 36th AIAA Structures, Structural Dynamics and Materials Conference, New Orleans, LA.

Ju, J.W. and Chen, T.M. (1993), Micromechanics and Effective Moduli of Elastic Composites Containing Randomly Dispersed Ellipsoidal Inhomogeneities, *Acta Mechanica*.

Kuo, C.P., Chen, G-S, Pham, P., and Wada, B.K., 1990, "On-Orbit System Identification Using Active Members," AIAA 90-1129, Proc. of the 31st AIAA Structures, Structural Dynamics and Materials Conference, Long Beach, CA.

Lawrence, C.R., Lurie, B.J., Chen, G-S, and Swanson, A, 1990, "Active Member Vibration Control Experiment in a KC-135 Reduced Gravity Environment," Proc. Of the First Joint US/Japan Conference on Adaptive Structures, Technomic Publishing Co, Lancaster, PA.

Lissenden, C. J., Herakovich, C.T., & Pindera, M-J. (1994), Damage Induced Room Temperature Creep of TMC, *Damage Mechanics in Composites*, ASME-AMD Vol. (Allen & Ju, Eds),

Liu, S. C., Chong, K. P. and Singh M. P. (1994), Civil Infrastructure Systems Research Hazard Mitigation and Intelligent Material Systems, *Smart Mater. Struct.* 3, A169-A174.

Nanni, A., Okamoto, T., Tanigaki, M., and Henneke, A., (1992), Hybrid (FRP & Steel) Reinforcement for Concrete Structures, *Proc. Materials Eng. Congress*, ASCE, Atlanta, GA, Aug. 10-12, pp 655-665.

National Academy of Sciences, (1993), *Materials Research Agenda for the Automotive and Aircraft Industries*, NMAB-468.

Rogers, C.A., and Rogers R.C., eds. (1992), Recent Advances in Adaptive and Sensory Materials and Their Applications, Technomic Publishing, Lancaster, PA

Yuan, F. G., (1993a) Thermal Stresses in Thick Laminated Composite Shells, *Composite Structures*, vol 26, no. 1 and 2, pp. 63-75.

Yuan, F.G., (1993b) Bending of Filament Wound Composite Laminated Cylindrical Shells, *Composite Engineering*, Vol. 3, No. 9, pp. 835-849.

BIBLIOGRAPHY

Chong, K. P., et al, eds (1990) *Intelligent Structures*, Elsevier, London.

Boresi, A.P. and Chong, K. P., (1987), *Elasticity in Engineering Mechanics*, Elsevier, New York; Chinese edition published by Science Publishers (1995).

Tzou, H. S. and Anderson, G. L., eds (1992) *Intelligent Structural Systems*, Kluwer Academic Publ.

Materials	Structures	Infrastructure
<i>Micro-level</i> Atomic scale	<i>meso-level</i> Microns	<i>macro-level</i> Meters
~micro-mechanics ~nanotechnology	~meso-mechanics ~interfacial	~shells ~plates
<i>smart materials</i>	<i>smart structures</i>	<i>smart t-w systems</i>
systems integration Up to km scale		~bridge systems ~lifelines

Fig. 1. Scales in Materials and Structural Systems (NB: t-w = thin-walled)

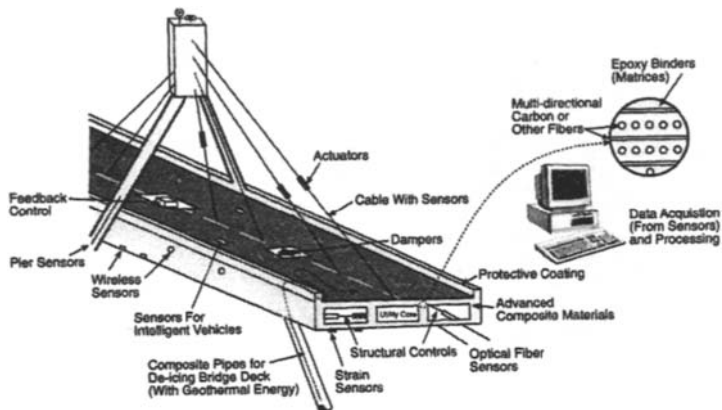


Fig. 2. A Futuristic Smart Bridge System with Thin-Walled Advanced Composite Box Girders

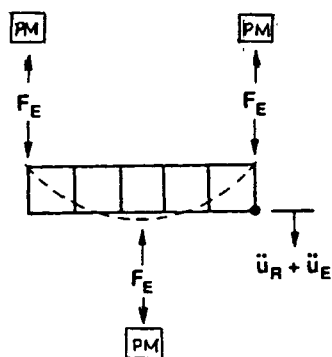


Fig. 3. A Space Structure with Traditional Approach for Shape Change

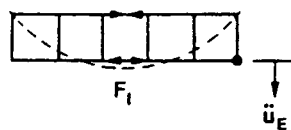


Fig. 4. Location of Actuator Sensors

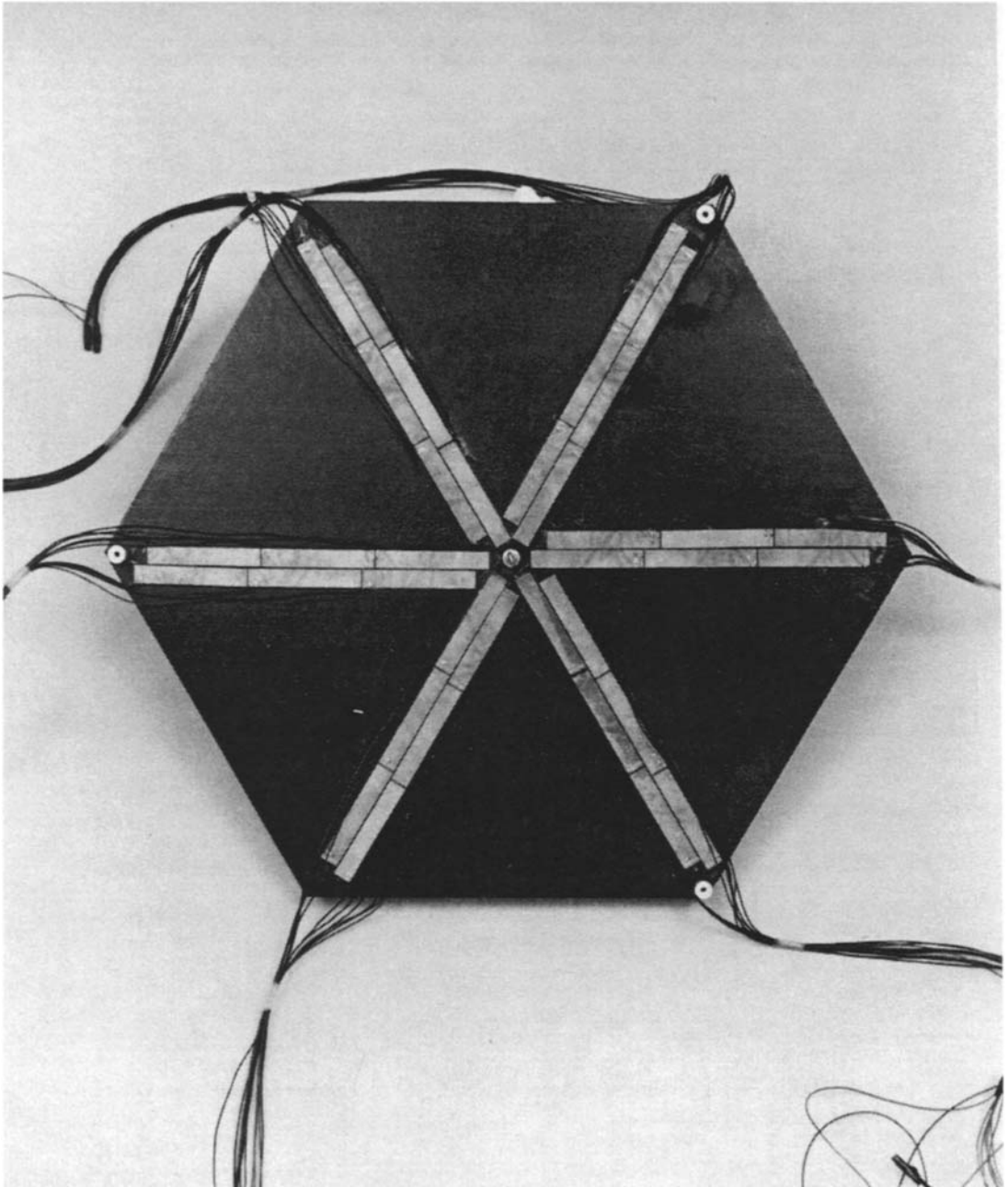


Fig. 5. PZT Actuator on Sandwich Plate

LIGHT GAUGE STEEL FRAMING FOR HOUSE CONSTRUCTION

J. Michael Davies

Manchester School of Engineering, University of Manchester
Manchester M13 9PL, UK

ABSTRACT

Steel framed house construction is an immature art and the next evolutionary stage is probably overdue. This paper considers the current methods of construction and also how they may advantageously develop. After highlighting some potential problems with steel stud wall construction, it is shown that cassette wall construction may have significant advantages. Other possible improvements to current practice are also proposed. However, the full potential of steel framed construction will not be achieved until current prejudices are set aside and the design of a 'modern' house approached with an open mind. This requires the collaboration from the outset of the full design team including the architect, structural engineer, materials supplier and builder.

KEYWORDS

Cassette, cold-formed steel, house, steel frame, stressed skin, wall stud,

INTRODUCTION

All over the industrialised world, the use of light gauge steel framing for house and other low-rise construction is increasing rapidly. In some countries, such as the UK, this is from a small base. In others, such as the USA and Canada, there is a well-developed industry with well-established practices. The reasons for this increase have been expounded elsewhere, Farach and Grupe (1994) and the trend is clearly set to continue for the foreseeable future. This is encouraging news for those of us who are interested in light gauge steel construction.

This raises the fundamental question of what the steel framed house of the future will look like for we are clearly in a period of transition. The history of the present generation of steel framed construction for the middle market is from traditional construction to timber frame to steel frame without any significant change in either the architecture or the interior and exterior finishing materials. It appears that steel-framed houses must not look or 'feel' any different!

Thus, the early timber framed designs simply involved placing a framing system based on 4 inch x 2 inch timber members at 18 inch centres behind the same facades. In many current steel frame designs, the timber has merely become 100 mm x 50 mm cold formed steel channel sections at 450

mm (or possible 600 mm) centres. This is disappointing because a facade designed for construction in (say) load-bearing brickwork is unlikely to be optimal for construction based on steel framing.

However, this is changing and indeed it has to change. Traditional construction designed to conceal a steel frame is not the way forward into the 21st Century. This paper does not attempt to answer the question of what the house of the future will look like, this is more a task for an architect and the author is a structural engineer. It does attempt to consider what the structural solutions behind the architecture will look like. It is implicit in this discussion that the steel structures will not remain concealed for ever. The time will surely come when house owners will be proud to own their steel framing.

It may be noted here that one of the driving forces towards steel framed construction is the increasing shortage of suitable timber for timber-framed construction. Ecological pressures are reducing the amount of good quality timber that can be felled and rapidly grown softwood is susceptible to shrinkage, warping and twisting which make it difficult to maintain the dimensional accuracy necessary for modern construction. A surprisingly large number of trees are required in order to construct a single timber-framed house so that steel framing which is 100% recyclable may be clearly seen as the 'greener' option.

PRIMARY FEATURES OF STEEL FRAMED CONSTRUCTION

There are a number of features that make steel framed construction essentially different from traditional construction. Different authors may place these in a different order of priority. However, the list which follows is what the author of this paper considers should be the distinctive features.

It is clear that the primary feature ought to be factory-based prefabrication. In every other walk of life, (eg cars, TV sets, computers) the trend has been to dramatically reduce the number of components in the final installation. The construction industry has been amazingly slow to follow this trend. However, sooner rather than later, this has to happen with house construction too. The economic driving forces for this change are speed of construction linked to levels of quality control that are only possible under factory conditions. Another important factor is the increasing shortage of skilled tradesmen on site.

The next important parameter has to be dry construction. The dirt, dust, shrinkage and general lack of precision associated with hand-laid masonry, in-situ concrete and wet plaster should be unacceptable in modern construction.

The architect of the future will have to accept a stricter modular discipline. This will primarily affect the dimensions and locations of openings such as doors and windows. Rational steel frame designs will only be obtained when the engineer works side by side with the architect to realise a modular frame design with members on a regular grid and sensible paths to ground for both vertical and wind loads.

This requirement leads naturally to the related requirement for simplified engineering design. The engineering design of a complete light gauge steel framed house from basic code of practice principles is unacceptably labour intensive. This may be possible for architect-designed individual houses at the expensive end of the market. In the current economic climate, it may also be justified if a large number of identical houses are to be built, but this is not what the consumer wants. Modular discipline does not demand tedious repetition, it should enable precisely the opposite to be achieved. However, this will require that more attention is given to prescriptive methods of design so that,

ultimately, a steel framed solution will require no more engineering input than the timber-framed or load bearing masonry competition.

Simpler engineering has logically to be associated with simpler detailing of connections. In particular, this entails taking a long look at how wind forces are transmitted through the structure to the foundations. Many of the rather "fussy" details which tend to characterise current designs are concerned with this aspect of design whereas the vertical load bearing structure is relatively simple.

Ideally, the steel frame should be fully integrated with both the external and internal wall panel systems so that they are mutually supporting. A special case of this, which is considered in more detail later, is to use a steel cassette wall system with the wide flange outwards in "cold frame" construction. The steel cassette is thus both the frame and the outer cladding combined and just needs a suitable external finish to complete the wall construction.

Current wisdom is that the designers of light gauge steel frames should make strenuous efforts to demonstrate that their product can do everything that the competitive products can do, and more. Thus, it must be possible to design a steel frame to fit behind and support any facade, however many door and window openings it may contain. This may be a necessary marketing ploy in the present climate but it is hardly the way forward into the future.

Somewhat reluctantly, therefore, the author concedes that a necessary alternative is that the steel frame should be capable of being designed to be independent of the external cladding system. Another reason for this is that an external cladding system which is not integrated but merely applied externally to "warm frame" construction may only make a minimal structural contribution and it is more versatile to neglect this completely, thus allowing the customer complete freedom as to how his or her home might be clad. It also allows a brick facade, connected to the steel frame by stainless steel brick ties, to be offered, thus emphasising the often overlooked point that an outer brick skin makes no useful contribution to the stability of the basic structure of a house!

Similarly, conventional dry lining, such as plasterboard, makes only a modest contribution to the stability of the steel studs and can also be neglected.

Finally, but by no means least in economic importance, the construction should provide a usable roof space. This is not logically essential. However, the point is that a habitable roof area can be provided at little additional cost. When this is done, it can be the single factor that makes steel framed construction significantly cheaper than the alternatives.

ANATOMY OF THE FRAME

The transmission of vertical load to the foundations usually poses few problems and it is merely necessary to ensure that the floor beams and roof trusses coincide with the wall studs which carry essentially axial loads.

However, the provision of resistance to the in-plane forces arising as a result of horizontal (wind) loads on the building is more problematic. In order to consider how the stability requirements might be met in the light of the above discussion, consider the schematic diagram in Fig. 1. This shows how wind forces are carried and it should be immediately obvious that stressed skin (diaphragm) action provides the key to the solution. There are two components of the problem:

- The floor and roof planes must be able to act as diaphragms in plan to transmit wind forces on the windward and leeward elevations back to the walls parallel to the direction of the wind.

- The walls themselves must be able to transmit the in-plane forces from the floor and roof planes down to the foundations. It is then found that significant uplift forces may arise at the leeward end of the wind-frames. Providing an adequate tie to adequate foundations is another aspect of this problem.

Both of these requirements can be problematical and the critical importance of diaphragm action in the first floor should be particularly noticed. Most structural systems place a high reliance on this element.

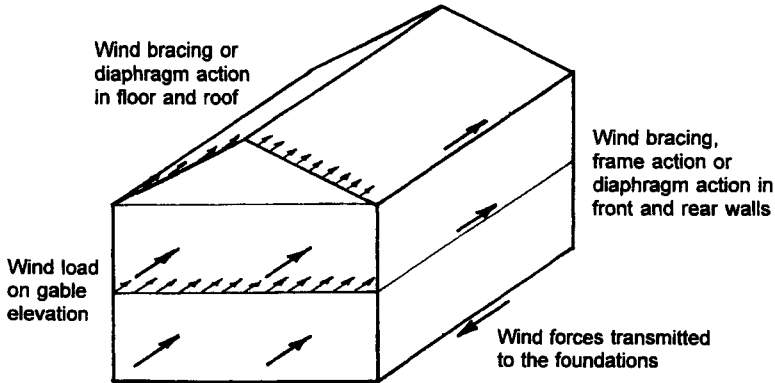


Fig. 1: Resistance to horizontal wind loads in house construction

Floor construction often takes the form of a timber-based product supported by steel joists as shown in Fig. 2. It is sometimes assumed that this form of construction can provide the necessary diaphragm action without formal calculations. This is a highly dangerous assumption! Diaphragm action in the floor is fundamental to the stability of the structure and the in-plane forces can be very significant. The situation is not helped by the presence of a stair well. The diaphragm action of the floor must always be properly calculated when it will be found that the main problem is in providing the required shear connection to the primary structure at the same time bearing in mind the absence of any 'seam strength' between the individual sheets of floor material. More details of the procedures for this calculation may be found in the literature on timber construction!

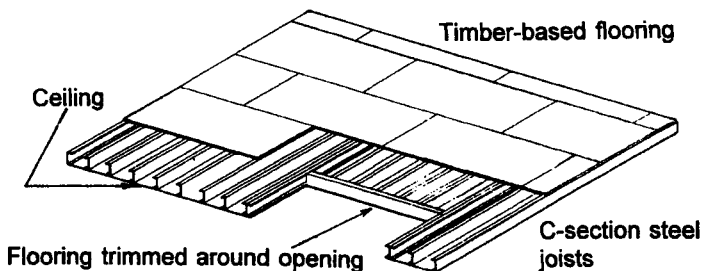


Fig. 2: Lightweight steel floor construction

With light steel framing, a more reliable solution is to provide a light gauge steel floor deck. This

allows the formal calculation procedures of stressed skin design, Davies and Bryan (1981) and ECCS (1995), to be used. When these procedures are properly used, it is found that the required shear strength can be readily achieved, helped by the provision of seam fasteners. The demands made on the relatively reliable metal to metal fasteners in this form of construction highlight the potential difficulties with timber floors.

It is necessary to make similar provision at the roof level and, here, designers have tended to be more circumspect and often provide a wind girder as shown in Fig. 3. However, if, as is readily possible with light gauge steel framing, it is intended to utilise the roof space, an alternative and advantageous solution is to take advantage of the diaphragm action of the roof space floor deck. The considerations then become similar to those discussed above.

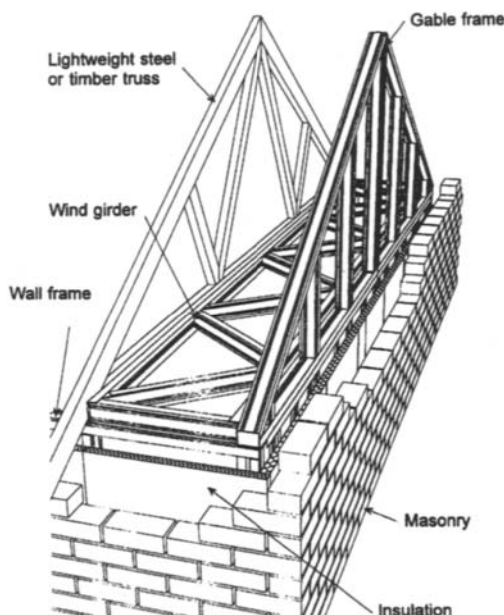


Fig. 3: Wind girder at eaves level, Grubb and Lawson (1997)

There are several methods available for providing in-plane stability in vertical walls:

- The most common method is the use of X-bracing whereby crossed flat straps of thin steel pass over the external faces of the studs, as shown in Fig. 4. These straps act only in tension so that only one is active at any given time. They are usually nominally fixed to the studs in order to reduce their tendency to sag. They must, of course, be properly anchored at their ends in order to transfer the calculated tensile force to the primary structure.
- An alternative system is K-bracing which takes the form of C-sections fixed within the depth of the stud walls as shown in Fig. 5. These members act in either tension or compression and, together with the adjacent studs, form a vertical truss. They again require appropriate connections at their ends. The additional compressive stresses in the leeward member of this truss may require that the adjacent studs have a larger section than the norm.

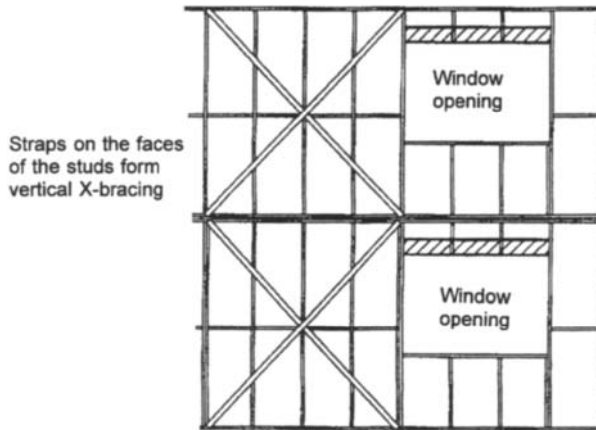


Fig. 4: Elevation of a building with vertical 'X' bracing, Grubb and Lawson (1997)

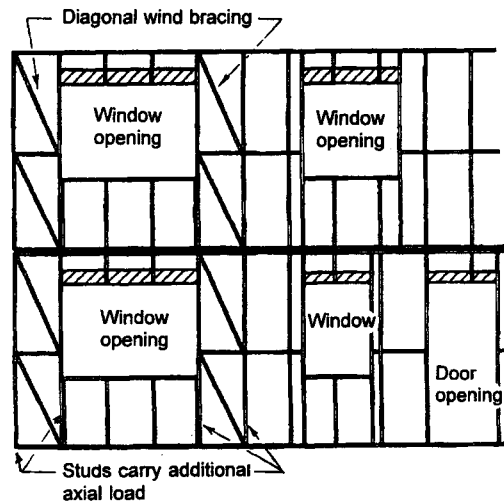


Fig. 5: Elevation of a building with vertical 'K' bracing, Grubb and Lawson (1997)

As a practical point, it is important to detail either form of diagonal bracing system to avoid significant eccentricities at the connections.

Evidently, X-bracing should be used wherever possible and current practice is to use this method for the party walls of semi-detached and terraced houses and for other gable walls where there are sufficiently few door and window openings. However, the currently popular building style results in front and rear elevations which contain much more opening than solid wall. In such cases, X-bracing of the type shown in Fig. 4 may not be possible.

- The wall structure can act as a 'rigid-jointed' plane frame. It is important to appreciate here that bolted joints in light-gauge steel construction are by no means rigid to the extent that a

convention rigid-jointed plane frame analysis is unlikely to be valid. It is essential to estimate the flexibility of the connections and to include these in a semi-rigid analysis.

- The wall structure can, of course, also act as a diaphragm. With conventional stud walling, it is sometimes claimed that it is possible to take advantage of suitable board materials when they are properly fixed to the supporting members. However, before using the diaphragm action of conventional walling, it is necessary to justify it by test or calculation in the light of the actual forces present.
- It is possible to use conventional diaphragm action with either a flat or trapezoidally profiled sheet metal lining although this may not always be economically practical. However, the author does know of one example where a flat sheet metal outer skin has proved to be successful in the construction of modular hotel room units.
- However, what is clearly practical is to use conventional diaphragm action in cassette wall construction. The next section will address this possibility in more detail.

With all of the wall systems discussed above, it is expedient to space the holding down points as far apart as possible in order to reduce the shear forces in the wall and, at the same time, reduce the holding down forces into the foundations. This has implications for the architectural design so that early interaction between the Architect and the Engineer is required. The design of the holding down detail itself is another critical point in the structural design.

CASSETTE WALL CONSTRUCTION

The cassette wall system has been pioneered in France by the company 'Produits Acier Batiment' (PAB) under the name 'CIBBAP'. The basic arrangement of a cassette wall is shown in Fig. 6. Lipped C-shaped cassettes span vertically between top and bottom tracks. Cassette construction may be viewed as stud construction integrally combined with a metal lining sheet to provide a metal frame together with a flat steel wall. This flat steel wall may be external and provide the watertight skin of the building or it may be internal with insulation and the weather proof skin provided externally. These options are often referred to as cold-frame and warm frame respectively and are also available with other forms of steel framed construction.

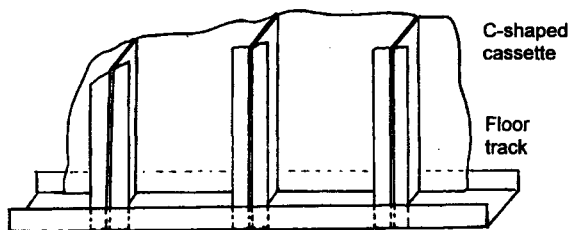


Fig. 6: Cassette wall construction

Light gauge steel cassettes do not readily lend themselves to stick construction, in which individual members are assembled piecemeal on site, so that it is usual to prefabricate complete sub-frames comprising the cassettes and their top and bottom tracks in the factory. A particular advantageous possibility is the use of press-joined connections to form the seams between individual cassettes. Press-joining is quick, cheap and does not destroy the galvanising. The structural details tend to be

simpler than those with stud construction so that erection is rapid.

The main advantages of cassette construction in comparison with the use of wall studs may be summarised as follows:

- Simple details and rapid modular construction
- The wall structure is immediately water-tight
- The stability problems of thin slender studs are avoided
- A rational provision for wind shear can be made without additional bracing members

The last bullet point is particularly important and is worthy of more detailed discussion. As shown in Fig. 7, a cassette wall is subject to a rather comprehensive system of loads. The design for vertical load and bending is reasonably straightforward and is covered in some detail in Part 1.3 of Eurocode 3, CEN (1996). However, a cassette sub-assembly is also a ready-made shear panel or 'diaphragm' for stressed skin construction, Davies and Bryan (1981). Stressed skin design is explicitly allowed in Eurocode 3 and appropriate enabling clauses are included in section 9. Eurocode 3 also includes somewhat rudimentary provisions for cassettes acting as shear panels. These make it clear that the behaviour of a cassette wall panel in shear is not significantly different from that of a conventional shear panel comprising trapezoidal steel sheeting framed by appropriate edge members.

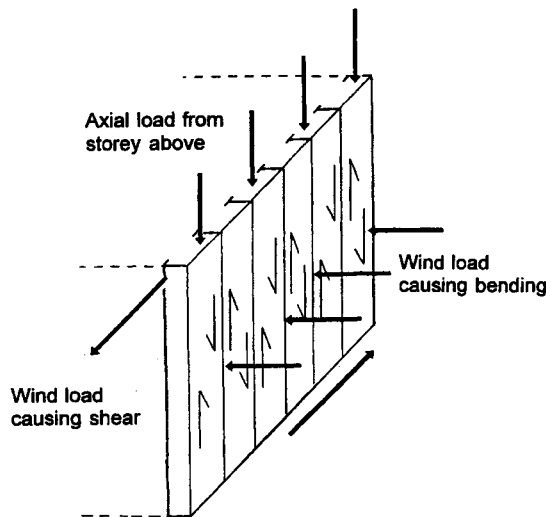


Fig. 7: Load system in a cassette wall

Cassette wall panels can, therefore, be readily designed on the basis of Eurocode 3 together with the established procedures for stressed skin design and it is found that, for most low-rise construction, a standard panel and fastener specification suffices to carry the wind shear without any special provision other than for holding down forces at the leeward ends of the diaphragms.

Fig. 8 shows an elevation of a cassette wall as used in a typical house facade. The lines x-x show the division into prefabricated sub-panels for factory construction. The wind-shear diaphragms are indicated by cross-hatching.

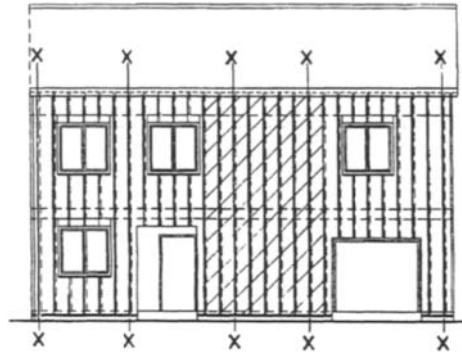


Fig. 8: Typical cassette wall in house construction

INTERNAL AND EXTERNAL LINING MATERIALS FOR WALL CONSTRUCTION

If steel frame house construction is to advance, the choice of the internal and external lining materials is crucial. In the rare occasions when steel framed construction has given rise to problems in use, it has been nothing to do with structural engineering. Some early designs did not pay sufficient attention to thermal insulation and thermal bridges with the result that there was unacceptable condensation. Other failures occurred because of insufficient attention to moisture penetration. It is also necessary to give due attention to acoustic insulation.

These are all matters of building physics and, although this is a paper for structural engineers, it has to be admitted that the building physics aspects of house construction, and wall construction in particular, are often more important than the structural aspects. Thus, typical "warm frame" wall construction for domestic buildings is shown in Fig. 9. For most climates, the first essential is a high level of thermal insulation and this generally involves the provision of a suitable thickness of insulation material as well as a cavity. The insulation material is generally mineral wool although a wide variety of suitable alternatives is available.

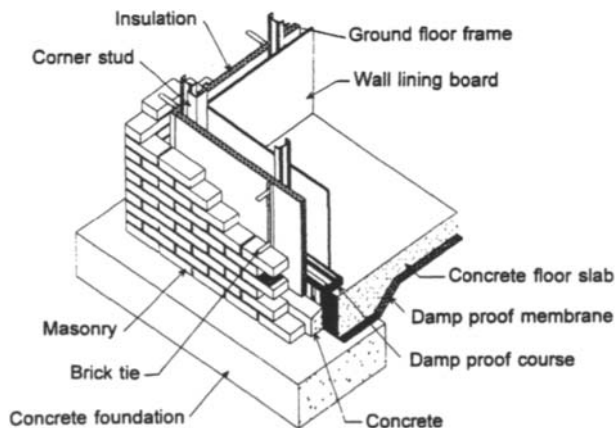


Fig. 9: Typical wall construction for domestic buildings, Grubb and Lawson (1997)

At one time, the author thought that it was the external cladding that was inhibiting progress and, in particular, the desire to accommodate all of the features commonly associated with the brick-clad facades of 20 years ago. However, this is not the only factor. For many reasons, external load bearing steel walls usually need to be lined and insulated internally and equally restrictive is the necessity of accommodating traditional dry lining materials such as plasterboard. Evidently, it is the limiting spanning capabilities of dry lining materials which have forced designers to adopt solutions with C-shaped metal studs at 450 or 600 mm centres.

Evidently, steel stud solutions would be more efficient if the studs could be more widely spaced. This is only possible if stronger dry lining materials are used. Suitable materials are available which can meet all of the functional requirements such as a smooth internal surface, spanning capability, adequate fire resistance, adequate resistance to sound transmission etc. It is up to the designers to use these in the most efficient way possible. Consideration should be given to sandwich solutions internally as well as externally as these may ultimately provide the most efficient way of meeting all of the performance requirements.

External cladding is less problematic as most of the candidate materials have better spanning capabilities than dry lining. The following materials are among those that have been used:

- Brickwork connected to the steel frame with stainless steel brick ties
- Timber ship lap. This is the usual North American choice
- Rendered exterior grade sheathing with or without an intermediate layer of insulation. This is the solution used in "Browne's County Villa", SCI (1997) which uses the Browne-EIFS framing system. Of particular interest in this context is the system used in a social housing project at Garnant, Wales, The Forge Company (1996). This was the result of collaborative design between a research and design consultant, a cold-formed steel supplier and a materials producer. The exterior sheathing was a breathable, water-resistant material manufactured from wood waste products to which were cemented mineral wool lamellas. These were then rendered to provide the external weatherproof finish.

The interest in this latter project lies not only in the solution but also in the way that it was attained. Collaboration of this nature is essential if optimum steel framed solutions are to be achieved.

- Panelled metal cladding. This is often used in the Scandinavian countries.
- Sandwich Panels. This is the logical solution and viable panels may be produced with a variety of face materials. There are also several alternative core materials such as polyurethane, foam expanded or extruded, polystyrene, phenolic foam, mineral wool etc.

OTHER CONSIDERATIONS IN FLOOR CONSTRUCTION

In houses with light steel framing, the floor construction is logically lightweight and dry. However, there are circumstances where heavier construction is specified, usually to meet requirements for fire and/or sound insulation. There are, therefore, three generic systems for floor construction:

- Steel joists (usually C- or Z-section) with a timber-based deck as shown in Fig. 2. The joists are usually on a module which coincides with studs on the supporting elevations.
- Trapezoidally profiled steel deck supported on steel primary beams and carrying a timber-

based walking surface.

- Composite (steel-concrete) deck supported on steel primary beams.

Superficially, the structural engineering design is conventional and elementary. However, joist designs are rarely based on the bending resistance of the cross-section. Normally, the serviceability criteria of deflection and vibration control the design. Suspended floors can sometimes resonate with the vibrations induced by human footsteps and, although this does not usually lead to failure, it can be a source of discomfort. This problem tends to become more acute when lightweight construction is used. In light gauge steel construction, it is usual to use a rather rudimentary approach to this problem based on an estimate of the natural frequency.

Engel (1998) discusses the advantages of dry floor construction and shows how the requirements of building physics may be achieved. He offers the scheme shown in Fig. 10 as providing a tried and tested means of providing a performance which meets all of the criteria of strength, stiffness, serviceability (vibration), acoustic and thermal insulation. It also has the advantage of providing an effective stressed skin diaphragm.

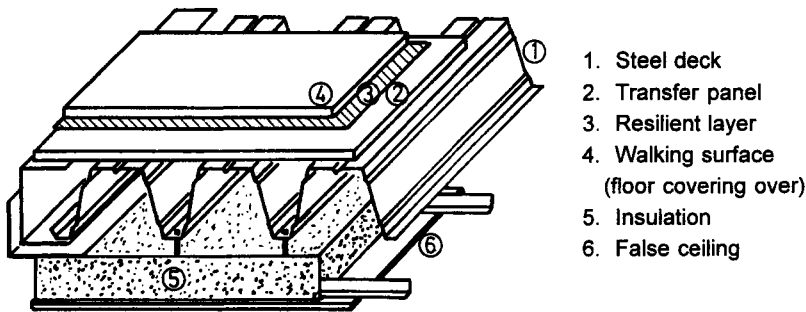


Fig. 10: Typical internal structure of a dry floor on a steel deck, Engel (1998)

HOUSES AT CHAMPFLEURY

The nearest solution to the ideals expressed in this paper has been realised in a group of five houses at Champfleury, near Reims in France. These were designed by architect Paul Depondt in association with a comprehensive research and development team headed by the French steel company PAB (Produits Acier Batiment). They were designed for the upper end of the market with no inhibitions regarding traditional appearance. They were in all-steel construction with cassette wall construction, steel deck dry floors and a two-skin built-up steel roof. Fig. 11 shows an artists impression and cross-section. Fig. 8 is one of the less interesting elevations.

The steel cassettes were expressed externally and finished with an architectural coating applied directly to the steel face of the cassettes. These were insulated and dry lined on their inside faces but, otherwise, the steel structure of the houses were clearly expressed internally. The occupants are very pleased with the result.

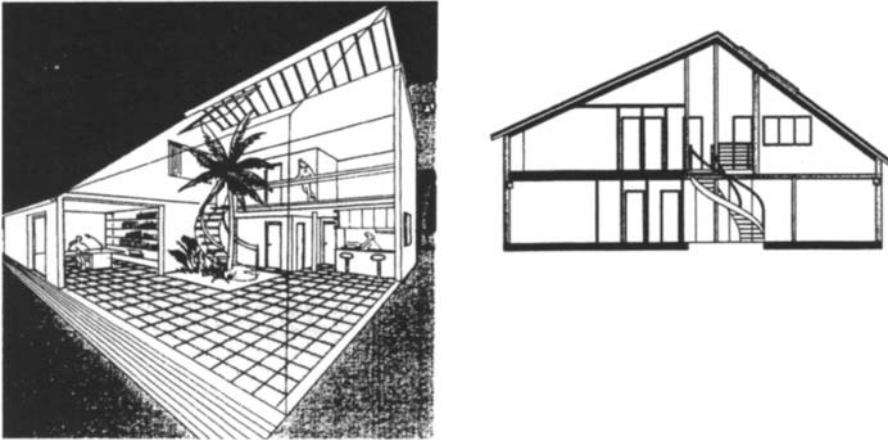


Fig. 11: House at Champfleury, artists impression and cross-section

CONCLUSIONS

As the design of steel framed houses develops and matures, it will be necessary to progress from the current situation, where they are often indistinguishable from their traditional counterparts, to a distinctive steel-framed architecture. The optimum designs will only be achieved when the full design team collaborates from the outset without any preconceived ideas regarding the outcome. This will require enlightened architects!

REFERENCES

- Davies J M and Bryan E R (1981) *Manual of stressed skin diaphragm design*, Granada.
- ECCS (1995) European recommendations for the application of metal sheeting acting as a diaphragm, European Convention for Constructional Steelwork, Publication No. 88.
- Engel P (1998) Recent developments in dry floors using light gauge steel and composite components. Paper No. 62, *2nd World Conference on Steel in Construction*, San Sebastian.
- Farach G and Grupe RC (1994) Light gauge engineering in today's marketplace - The challenges. *12th International Speciality Conference on Cold-Formed Steel Structures*, St Louis, USA, October 18-19, 725-734.
- Grubb P J and Lawson R M (1997) Building design using cold formed steel sections: Construction detailing and practice. *SCI Publication P165*, Steel Construction Institute.
- SCI (1997) Case Study 12, Case studies on light steel framing, *SCI Publication 176*, Steel Construction Institute.
- The Forge Company (1996) "Low energy steel frame housing", London and New York.
- CEN (1996) Eurocode 3: Design of Steel Structures: Part 1.3: General Rules: Supplementary rules for cold formed thin gauge members and sheeting. *European Committee for Standardisation*, ENV 1993-1-3.

FERROCEMENT: A CEMENTITIOUS THIN WALL STRUCTURAL ELEMENTS - RESEARCH TO PRACTICE

P. Paramasivam

Department of Civil Engineering, The National University of Singapore,
Singapore

ABSTRACT

Ferrocement is a type of cementitious thin-wall reinforced concrete construction of cement mortar reinforced with closely spaced layers of relatively small diameter wire mesh. The mesh may be made of metallic or other suitable materials. It is usually suited for thin wall structural elements as the uniform distribution and dispersion of reinforcement provide better cracking resistance, higher tensile strength to weight ratio, ductility and impact resistance. Considerable research has been carried out at the National University of Singapore, since early 1970's. The R&D works have resulted in several applications such as sunscreens, secondary roofing slabs, water tanks and repair material in the building industries. The salient features of the design, construction and performance of some of these applications of ferrocement structural elements are highlighted in this paper.

KEYWORDS

Ferrocement cementitious thin wall structures, impact resistance, sunscreens, secondary roofing slabs, water tanks.

INTRODUCTION

The concept of reinforced mortar by closely spaced fine wire mesh was used for boat building construction by Lambot in 1849. Subsequently in 1940's, Nervi promoted the use of ferrocement in civil engineering structures. Since then the ferrocement has been studied extensively by various research groups and gained wide acceptance only in 1960's. There has been wide spread use of ferrocement applications in agriculture and housing throughout the world including North and South America, East European and Asia-Pacific countries.

Ferrocement is a cementitious thin-wall composite structural material comprising a cement mortar matrix uniformly distributed throughout its cross section. The uniform distribution and dispersion of reinforcement in the ferrocement composite provide better cracking characteristics, higher tensile strength, ductility and impact resistance. Ferrocement has a high tensile strength to weight ratio and

superior cracking behaviour in comparison to conventional reinforced concrete. Hence it is an attractive material for construction of thin wall structures.

Ferrocement construction in the early seventies was labour intensive and particularly suitable for rural applications in developing countries. This does not require heavy plants or machinery and being a low-level technology, the construction skills can be acquired fairly quickly. Accordingly, considerable research effort was directed towards the use of ferrocement in low-cost rural housing and agriculture compatible with indigenous traditions and materials. Since then the material has been shown to have many potential applications in urban areas as well. In this case, to alleviate the shortage and high cost of skilled labour, more so in developed countries, mechanised production and proper choice of reinforcement are used to ensure cost competitiveness and speed of construction.

A team of researchers at the Department of Civil Engineering, National University of Singapore, has since early 1970's made effort to popularise ferrocement as a construction material through research and development. Extensive investigations were carried out on its mechanical properties and several prototype structural elements were built to demonstrate construction technique and to evaluate their performance in service [1 - 10]. From the experience gained in these studies, considerable progress has been made in the use of ferrocement in public housing in Singapore as well as neighbouring countries. Ferrocement structural elements have gained gradual acceptance by building authorities through research and development even though ferrocement design has not been regulated by a formal code of practice. ACI publications [11, 12] also provide useful guidelines and information of technical know-how. Several case studies involving the adaptation and successful implementation of the research results into economical and beneficial applications of ferrocement. The salient features of the design, construction and performance of these ferrocement structural elements are discussed briefly in this paper.

MATERIAL, DESIGN AND CONSTRUCTION

The properties and types of constituent materials used in ferrocement construction are shown in Table 1. Although meshes of glass and vegetable fibres have been used, the most common form involves steel and it is this type that is described in this paper. The cement mortar matrix should be designed for appropriate strength and maximum denseness and impermeability, with sufficient workability to minimise voids. The use of sharp fine grade sand as aggregate together with ordinary Portland cement is generally adequate, despite the low covers employed. This is due to the comparatively high cement content in the mortar matrix.

The strength of the ferrocement composite made with varying steel content, types of mesh, wire size, mesh size and number of layers have been investigated and reported previously (1-10). Design guidelines, adequate for most applications, have been published (12). These include recommendations concerning surface area per unit volume of mesh reinforcement, cover, ultimate strength in flexure and serviceability requirements of cracking. However no particular deflection limitations are recommended as most ferrocement members and structures are thin and very flexible and their design is very likely to be controlled by design criteria rather than deflection. Stresses in flexural members may also be checked at service loads.

Several means are used in the construction of ferrocement but all methods seek to achieve the complete infiltration of several layers of reinforcing mesh by a well compacted mortar matrix with a minimum of entrapped air. The choice of the most appropriate construction technique depends on the nature of the particular ferrocement application, the availability of mixing, handling and placing machinery, and the skill and cost of available labour. After compaction, proper curing is essential to develop the desired properties of the mortar matrix.

TABLE 1
 PROPERTIES AND TYPES OF CONSTITUENTS MATERIALS USED IN FERROCEMENT CONSTRUCTION

Materials	Range
<u>Wire Mesh:</u>	
Diameter of wire (ϕ)	$0.5 \leq \phi \leq 1.5$ mm
Type of mesh	Chicken wire or square woven or welded galvanised mesh or expanded metal
Size of mesh opening (S)	$6 \leq S \leq 25$ mm
Volume fraction (V_R) of reinforcement in both directions	$2\% \leq V_R \leq 8\%$
Specific surface (S_R) of reinforcement in both directions	$0.1 \leq S_R \leq 0.4$ mm ² /mm ³
Elastic Modulus (E_R)	140 - 200 N/mm ²
Yield strength (σ_{Ry})	250 - 460 N/mm ²
Ultimate tensile strength (σ_{Ru})	400 - 600 N/mm ²
<u>Skeletal Steel:</u>	
Type	Welded mesh, steel bars, strands
Diameter (d)	$3 \text{ mm} \leq d \leq 10$ mm
Grid size (G)	$50 \text{ mm} \leq G \leq 200$ mm
Yield strength	250 - 460 N/mm ²
Ultimate tensile strength	400 - 600 N/mm ²
<u>Mortar Composition:</u>	
Cement	Any type of Portland cement (depending on application)
Sand to cement ratio (s/c)	$1 \leq s/c \leq 3$ by weight
Water cement ratio (w/c)	$0.35 \leq w/c \leq 0.65$ by weight
Gradation of sand	5 mm to dust with not more than 10%* passing 150 μ m BS test sieve
Compressive strength (cube)	30 - 50 N/mm ²

* For crushed stone sands may be increased to 20%.

SUNSCREENS

In Singapore, the housing developments consist of multistorey apartment blocks. All the west-facing blocks were, in general, provided with cast-in-situ reinforced concrete sunscreens to prevent direct exposure to sunlight in the living rooms. In one occasion, three building estates were completed without sunscreens in some of the blocks. The existing design of reinforced concrete sunscreens was too bulky and heavy for long spans more than 3 m and also cumbersome connection details for the precast construction. A number of alternative designs using light weight materials such as glass fibre reinforcement concrete, aluminium and ferrocement were carefully assessed and compared with conventional reinforced concrete. Considerations in terms of the ease of handling and erection, architectural requirements, durability and overall cost led to the choice of ferrocement as the most suitable alternative material in this application.

Inverted L-shape sunscreen modules of length 2.7 m were proposed with bolted connections. In the design of these sunscreens, due considerations were given to the aesthetic and functional requirements. The top face of the flange was provided with a backward slope to flush out, by rain, the accumulation dust without staining the front face to reduce the cost of maintenance. The design service load consisted of a concentrated live load of 5 kN applied either vertically or horizontally at mid-span and a

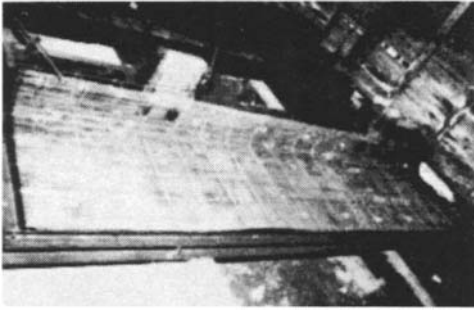


Figure 1: Reinforcement layout in steel mould



Figure 2: Sunscreens after installation

wind load of 0.6 Pa in addition to self-weight. A thickness of 25 mm was found to be sufficient for the design loadings. The reinforcement consisted of two layers of fine welded galvanised wire mesh, 1.2 mm in diameter with a 12.5 mm square grid, separated by a layer of coarser welded wire mesh of diameter of 3.3 mm and a square grid of 150 mm (Figure 1). For the mortar matrix, the mix proportions of cement:sand:water by weight was 1:2:0.5. The sunscreens were cast in steel moulds in a precast factory. After the necessary curing, they were painted and transported to the site. A special lifting device was used during erection.

Three stainless steel bolts were used to connect the sunscreens to the existing structures at each support; one 16 mm in diameter at the rear and two 12 mm in diameter at the front. A total of 500 sunscreens were installed on the 11-storey apartment blocks in three different estates. A typical block after installation is shown in Figure 2. It can be seen that the slender design achieved by using a ferrocement imparts a graceful appearance to the buildings.

Another type of ferrocement sunscreens was installed in several partially completed apartment blocks. The design should be flexible enough for the long spans ranging from 3 m to 5 m, with the ends supported on two 200 mm thick short cantilever beams of depth 600 mm attached through the facade to reinforced concrete walls. The sunscreens comprised a flat panel 0.6 m x 4.0 m with a thickness of 40 mm except for a 90 mm x 90 mm edge beam at the top. The design loads were the same as in previous case. Two layers of galvanised fine wire mesh of 12.5 mm square grid and 1.2 mm wire diameter separated by a layer of skeletal steel of 100 mm square grid and 6 mm diameter were used as reinforcements. The mortar strength was 35 MPa and the mix proportions of the cement, sand and water in the ratio of 1:1.5:0.4 by weight was used. The cracking strengths of the ferrocement composite in flexure and direct tension were 7.9 MPa and 3.1 MPa, respectively. These strengths were checked against the stresses due to dead load, wind load and accidental live loads with the appropriate factors of safety. The panels were also checked for deflection and natural frequency because of its slenderness.

The front panel of the sunscreens was cast in steel moulds in a precast factory as shown in Figure 3 with the projecting steel bars for continuity of reinforcements with the supporting cantilever. After the necessary curing, the sunscreens were transported to the site. Prefabricated steel trusses were attached onto the reinforced concrete walls and bolted to the facade by a proprietary bolting system. The sunscreens were lifted into position and the continuity steel bars spot-welded onto the steel trusses. Additional galvanised fine wire meshes were assembled around the steel trusses and the supporting beams cast-in-situ against precast permanent formwork.

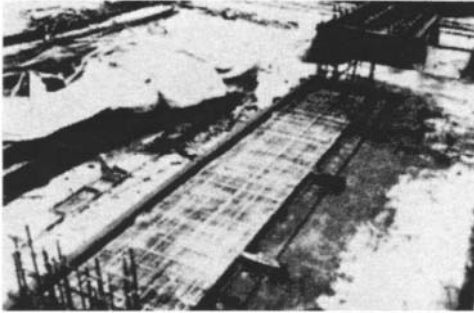


Figure 3: Casting of sunscreen



Figure 4: View of installed sunscreens

The ferrocement sunscreens were much thinner and significantly lighter than the existing reinforced concrete ones of similar design. The slender design of the ferrocement sunscreens gives them a more elegant and aesthetically appealing appearance. A typical block of apartment with the sunscreens installed is shown in Figure 4. The building authorities have now accepted without any reservation the use of ferrocement in sunscreens and facades.

SECONDARY ROOFING SLABS

In tropical countries, secondary roofing slabs are installed on the roof top of the buildings to insulate against intense heat. In Singapore these slabs consist typically of 1500 mm x 600 mm x 50 mm precast cellular concrete slabs containing a centrally placed layer of galvanised welded wire mesh of 50 mm square grid and 3.25 mm diameter. The slabs were assembled side by side, each being supported on 150 mm x 150 mm x 225 mm precast hollow blocks placed on the top of the structural roof to provide an air gap of 225 mm. The cellular concrete mix has a sand:cement ratio of 2.2 with a density of about 1500 kg/m³. These slabs pose a problem of severe cracking even before they are transported and erected in place. Although the presence of cracks may not be critical with respect to strength requirements, they are undesirable from a durability point of view. Consequently there is a need to replace such slabs at least once every 10 years.

A study was carried out at National University of Singapore to examine the current design with the intention of improving durability of the slabs. A ferrocement design of 30 mm thickness with two layers of galvanised fine wire mesh of 25 mm square grid and 1.6 mm wire diameter separated by a layer of skeletal steel of galvanised welded wire mesh of 150 mm square grid and 3.3 mm diameter, as shown in Figure 5, was found to be adequate. Because of the reduced thickness, the dead weight of the ferrocement slabs remains approximately the same as that of the cellular concrete slabs.

The functionality of such slabs was investigated by carrying out flexural tests, patch load tests and shrinkage measurements on specimens. It was found that the slabs could be subjected to design service load of 1.8 kN patch load, two days after casting without cracking. The slabs also registered low long term shrinkage of about 400 microns.

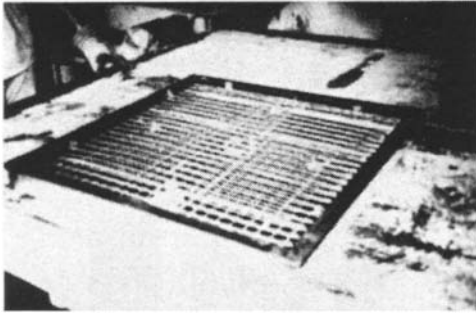


Figure 5: Reinforcement details of ferrocement secondary roofing slabs

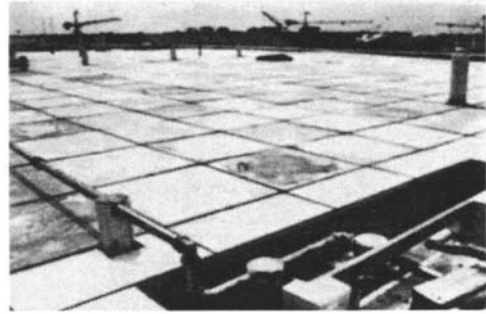


Figure 6: View of installed ferrocement secondary roofing slabs

The effects of weathering and thermal fluctuations were also studied. Slabs subjected to alternate wetting and drying test do not show any deterioration in first crack or ultimate strengths. Cyclic compression test to simulate the effect of thermal stresses due to heating in the day and cooling at night did not affect the strength significantly. Comparison in terms of production costs shows the ferrocement slabs to be slightly more expensive than the cellular slabs. However, it is expected that with ferrocement slabs the frequency of replacements will be reduced. The cost can be reduced through increasing productivity by demoulding them in the shortest possible time, minimising the controlled curing period and installation on site at the earliest time with less number of spoils during transportation and erection. The recent experimental study using reliability analysis [13] shows that the ferrocement slabs can develop up to 87 and 90 percent of their mean 28-day first crack and ultimate strengths, respectively, three days after casting. The reliability study indicates that the ferrocement slabs used were safe against ultimate failure one day after casting when subjected to both dead and live loads and in the case of first cracks with respect to dead load alone. In another study [14] the durability of the ferrocement secondary roofing slabs was investigated with respect to service life-cycle in relation to the actual load range that a typical slab would experience. The results show that the slabs have good fatigue properties within the stress range considered. Figure 6 shows the ferrocement secondary roofing slabs already installed on the structural roof of some housing estates.

WATER TANKS

Rural applications

In rural areas of many developing countries, there is a scarcity of water for drinking and washing. Traditionally rain water was collected for such usage. Therefore there is a need to provide simple and economical storage facilities that can be constructed with unskilled labour. Although steel tanks have been used commonly for this purpose, they have disadvantages such as high cost, rusting and consequent maintenance and limited life-span due to corrosion. The use of reinforced concrete water tanks poses problems of a different nature being heavier and more massive with construction requiring complicated formworks. Ferrocement construction, on the other hand, being of low level technology but labour intensive, is ideally suitable for water tanks in rural areas of developing countries. A study [15] was conducted to propose simple, economical and durable ferrocement water tanks for potable water in the rural areas of Capiz island, Philippines, which can be constructed by means of locally available construction skills and building materials. Funded by the International Development Research Centre, Canada, two prototypes of 5 m³ and 16 m³ capacities were analysed, constructed and tested in Singapore.

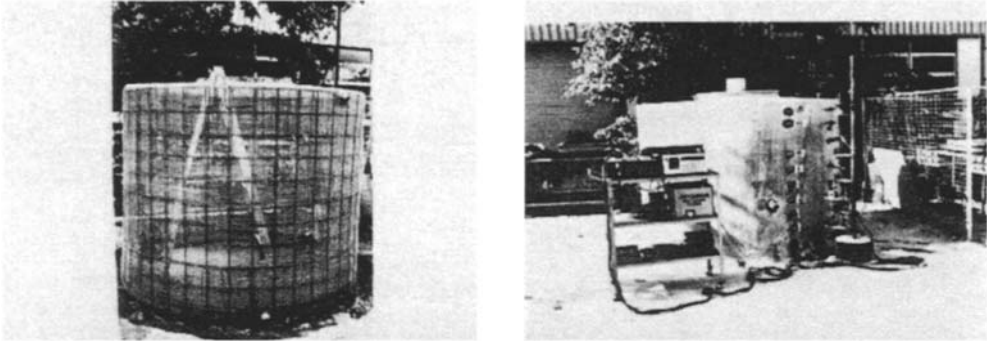


Figure 7: Reinforcement details and completed tank (5m³) capacity

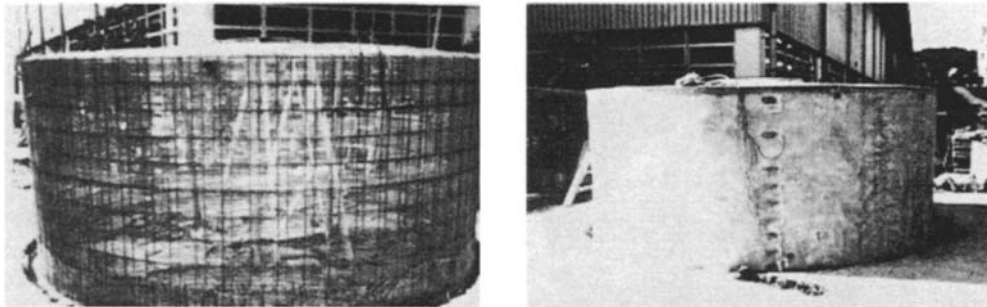


Figure 8: Reinforcement details and completed tank (16m³) capacity

The adapted water tank design consists of cylindrical wall rigidly connected to a circular base plate as the bottom and covered by a truncated conical roof on the top. The tanks were analysed using linear elastic theory of shells and designed to be uncracked under service conditions. Each of these tanks has a wall height of 1.8 m, the internal diameters were 2 m and 3.6 m with a wall thickness of 35 mm and 50 mm for the small and big prototype tanks respectively. In both cases, the roofs had a thickness of 25 mm and a slope of 1:3 with an opening of 0.8 m diameter at the centre as a service requirement. The reinforcement details and completed water tanks, 5 m³ and 16 m³ capacities, are shown in Figures 7 and 8, respectively. Their successful performance confirms the viability of using ferrocement water tanks, of the proposed design and attendant construction technique, for rural applications. Such water tanks can be easily fabricated as a community project in the rural areas of developing countries. At present more than 5000 such tanks have been constructed in the province of Capiz in the Philippines.

Urban applications

For an urban environment like Singapore, mechanised methods must be used to alleviate the acute shortage and high cost of skilled labour to expedite the construction. A pilot study [16] was carried out to propose a suitable and durable precast ferrocement cylindrical water tank for use in high rise buildings by adapting available mechanised production methods, example, spinning technique and the proper choice of reinforcement to ensure cost competitiveness.

The adapted water tank design consists of a cylindrical wall rigidly connected to a ring beam with a domed base as shown in Figure 9. The tank had a height of 2.25 m with a diameter of 3.6 m at the base. From the strength as well as practical view point, a thickness of 35 mm is recommended for the

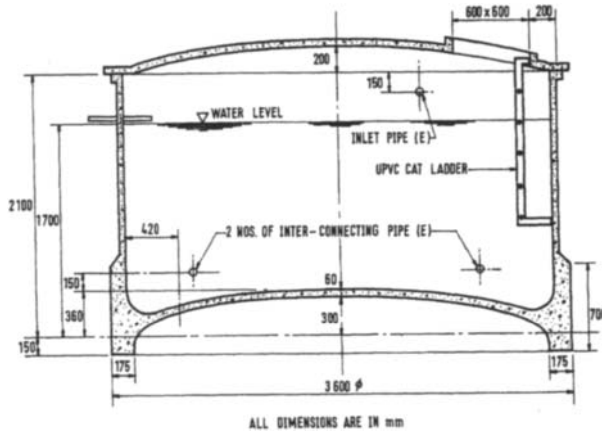


Figure 9: Sectional elevation of precast water tank

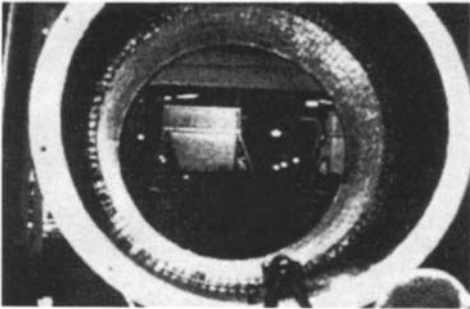


Figure 10: Spinning of the ferrocement water tank wall during casting

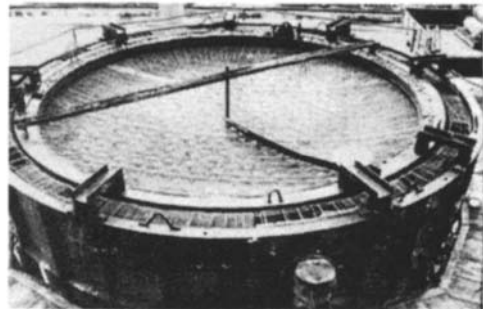


Figure 11: Casting the base of the water tank



Figure 12: Erection of the completed tank



Figure 13: View of the tanks after installation

roof and 40 mm-100 mm for the cylindrical wall. The thickness of the base should be slightly larger and a value of 60 mm-120 mm was recommended. The designs of the base, wall and roof were determined by checking the strength of each component against the maximum stress resultants acting on it. The reinforcement for wall consists of two layers of fine galvanised wire mesh of 1.2 mm wire diameter with a square grid of 12.5 mm. The meshes were separated by two layers of coarser galvanised wire mesh of 5.4 mm diameter with square grid of 150 mm. The cement mortar is designed

for a strength of 35-40 N/mm² to provide a low permeability with sufficient workability to minimise voids. A water cement ratio of 0.35-0.45 combined with a sand:cement ratio of 1.5:1 is generally used. The spinning technique was used for the walls (Figure 10) while the bases were cast-in-situ in the factory as shown in Figure 11. The erection and installation of the tanks are shown in Figures 12 and 13, respectively. The ferrocement tanks weigh only six tonnes compared to the conventional reinforced concrete tank weighing 14 tonnes. Although the present production cost is 20 percent more than that for reinforced concrete tanks of similar design, the ferrocement tanks can be easily installed onto the roof tops using lower tonnage cranes and with further reduction in the cost of supporting structures on the roof. It will be more economical in the long run to use ferrocement water tanks in view of their performance and durability with possible lower production costs with more tanks being manufactured.

STRENGTHENING OF RC BEAMS USING FERROCEMENT LAMINATES

The need to repair and strengthen concrete structural elements are commonly reported due to overloading, structural alterations, poor workmanship and non-compliances of standards. Several practical applications such as epoxy resin injections, externally bonded steel plates and encased additional reinforcing bars have been accepted as possible remedial techniques. The use of ferrocement in repair is relatively new. The material is ideally suitable due to its ability to arrest crack and high tensile strength-to-weight ratio.

Rectangular and T beams were tested failure under concentrated loads. A 20 mm thick ferrocement laminate was attached onto the tension face of the beams with different types of shear connectors (Figure 14). The reinforcement in the laminate consisted of two plain steel bars of 6 or 8 mm diameter sandwiched between two layers of galvanised wire mesh of diameter 1.2 mm and square grid 12.5 mm. The study [17] focused on the different types of shear connectors using Ramset nails, Hilti bolts, dowel bars and epoxy resin adhesive. The effects of the volume fraction of reinforcements of the ferrocement laminate and the level of damage of the beams were also studied. The performance of the strengthened beams were compared to the control beams with respect to cracking, deflection and ultimate strength. The results show that all the strengthened beams exhibited higher ultimate strength, greater stiffness and reduced crack width and spacing. Studies are currently under progress on shear strengthening using prefabricated reinforcement (Figure 15). Tests are also being conducted to generate information on the performance and durability of such beams under cyclic loading. Deterioration was quantified in terms of the reduction in flexural rigidity after 100,000 cycles of cyclic loading at different stress levels. The performance can be estimated using the probabilistic evaluation of the experimental results.

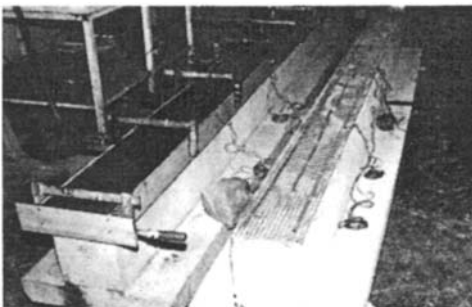


Figure 14: Reinforcement details for flexural strengthening

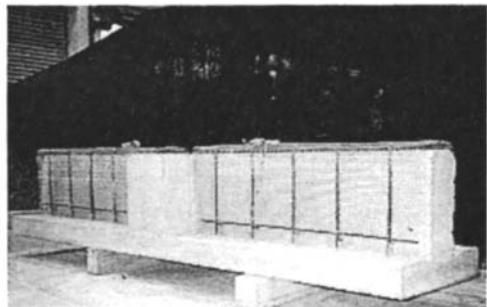


Figure 15: Reinforcement details for shear strengthening

CONCLUSIONS

This paper presents some of case studies of cementitious thin walled ferrocement applications based on the research and development work carried out at National University of Singapore. These have demonstrated that quality and economy can be achieved using modern construction techniques. Basic considerations of the materials used, fine galvanised wire mesh and cement rich mortar coupled with good crack controlling characteristics; indicate that ferrocement can provide better durability, easy maintenance and lower life-cycle cost compared to conventional reinforced concrete. Experience at National University of Singapore with ferrocement structures built and in use for more than a decade shows that durability has not been a problem with proper construction techniques and regular maintenance.

ACKNOWLEDGMENTS

The author acknowledges the contributions of his colleagues involved in the research team and engineers in the Housing and Development Board for their collaboration. The author also extends his thanks to International Development Research Centre, Canada, Daewoo Corporation, Construction Technology Pte. Ltd., and Hong Leong Manufacturing Industries Pte. Ltd. for their support in some of these works. The basic research was partly supported by RDAS research grants, C/81/01 and ST/88/04, provided by the Ministry of Trade and Industries and NUS research grants, RP880623 and RP900616.

REFERENCES

1. Nathan, G.K. and Paramasivam, P., (1974). Mechanical Properties of Ferrocement. *Proc. First Australian Conference on Engineering Materials*, Sydney, 309-331.
2. Paramasivam, P. and Lee, S.L. (1981). Ferrocement Structural Elements. *Proc. RILEM International Symposium on Ferrocement*, Bergamo, 3/37-3/46.
3. Paramasivam, P. and Nathan, G.K. (1981). Ferrocement Sunshade. *Journal of Ferrocement* **11:1**, 47-54.
4. Paramasivam, P. and Nathan, G.K. (1984). A Prefabricated Ferrocement Water Tank. *ACI Journal* **81:45**, 582-586.
5. Lee, S.L., Tam, C.T., Paramasivam, P., Das Gupta, N.C., Sri Ravindrarajah, R. and Mansur, M.A. (1988). Ferrocement: Ideas Tested at the University of Singapore. *Concrete International: Design and Construction* **5:11**, 12-14.
6. Paramasivam, P., Ong, K.C.G., and Lee, S.L. (1988). Ferrocement Structures and Structural Elements. *Steel-Concrete Composites Structures*. ed. R. Narayanan, Elsevier Applied Science, London, 289-330.
7. Paramasivam, P. and Sri Ravindrarajah, R. (1988) Effects of Arrangements of Reinforcements on Mechanical Properties of Ferrocement. *ACI Structural Journal* **85:1**, 3-11.
8. Mansur, M.A., Paramasivam, P. and Lee, S.L. (1987). Ferrocement Sunscreens on High rise Buildings, *Concrete International: Design and Construction* **9:11**, 19-23.
9. Lee, S.L., Paramasivam, P., Tam, C.T., Ong, K.C.G. and Tan, K.H. (1990). Ferrocement: Alternative Materials for Secondary Roofing Elements. *ACI Materials Journal* **87:4**, 378-386.
10. Paramasivam, P., Ong, K.C.G., Tan, K.H., Swaddiwudhipong, S., and Lee, S.L. (1990). Long-span Precast Ferrocement Sunscreens in Public Housing. *Concrete International: Design and Construction* **12:9**, 33-36.
11. ACI committee 549. (1982). *State-of-the-Art Report on Ferrocement*, ACI, Detroit, ACI549-R82.
12. ACI Committee 549. (1988). *Guide for the Design, Construction and Repair of Ferrocement*, ACI, Detroit, ACI549-IR88.

13. Quek, S.T., On, S.H., Paramasivam, P. and Lee, S.L. (1991). Early-age Reliability of Ferrocement Slabs. *ACI Material Journal* **88:6**, 644-649.
14. Quek, S.T., On, S.H., Paramasivam, P. and Lee, S.L. (1991). Fatigue Reliability of Ferrocement Slabs. *ACI Structural Journal* **88:1**, 78-83.
15. Paramasivam, P., Ong, K.C.G., Tan, K.H. and Lee, S.L. (1990). Rainwater Storage using Ferrocement Tanks in Developing Countries. *Journal of Ferrocement* **20:4**, 377-384.
16. Lee, S.L., Paramasivam, P. and Ong, K.C.G. (1992). Precast and In-situ Ferrocement Structural Elements. *Proc. International Conference on The Concrete Future*, C.I. Premier, Kuala Lumpur, Malaysia, 79-84.
17. Ong, K.C.G., Paramasivam, P. and Lim, C.T.E. (1992). Flexural Strengthening of Reinforced Concrete Beams Using Ferrocement Laminates. *Journal of Ferrocement* **22:4**, 331-342.

This Page Intentionally Left Blank

DESIGN OF STEEL ARCHES

N.S. Trahair, Y.-L. Pi, and J.P. Papangelis

Department of Civil Engineering, University of Sydney
Sydney, NSW, 2006, Australia

ABSTRACT

Few steel structures design codes provide procedures for designing steel arches against in-plane or out-of-plane failure, despite the increasing amount of research that has been carried out over the past 20 years.

This paper uses recent and current research carried out at the University of Sydney on pin-ended circular arches of I-section with the web in the plane of the arch to develop tentative design procedures that are consistent with the Australian limit states design code AS4100.

The methods of analysis which might be used to determine the distribution of the in-plane design bending moments and axial forces in the arch are discussed, and then recommendations are made for the nominal section and in-plane and out-of-plane member capacities.

KEYWORDS

Analysis, Arches, Buckling, Design, In-plane strength, Lateral buckling, Out-of-plane strength, Section strength, Steel structures, Structural engineering.

INTRODUCTION

Few steel structures design codes provide procedures for designing steel arches against in-plane or out-of-plane failure [1], probably because of a lack of authoritative theoretical and experimental information on their behaviour. However, there has been an increasing amount of research on arches carried out over the past 20 years, particularly on pin-ended circular arches (Fig. 1) of I-section with the web in the plane of the arch (arch research carried at the University of Sydney is listed in References [2-16, 19, 21-24]). It therefore now seems appropriate to attempt to set out tentative design procedures

which are consistent with those of modern limit states codes [17] for the design of steel structures composed of straight members.

This paper provides such an attempt. It first discusses the methods of analysis which might be used to determine the distribution of the design in-plane actions S^* (moments and axial forces) to be used in design.

It then proposes methods of determining the nominal capacities R_u (section capacity, in-plane member capacity, and out-of-plane member capacity) which can be used in the limit state design inequality

$$S^* \leq \phi R_u \quad (1)$$

in which $\phi = 0.9$ is suggested as a suitable capacity factor. The design of steel arches will rarely be governed by their section capacities, and it is more likely that the design of laterally braced arches will be governed by their in-plane capacities, and unbraced arches by their out-of-plane capacities.

The paper also anticipates the use of the method of design by advanced analysis which is now a focus of attention for the design of structures composed of straight members.

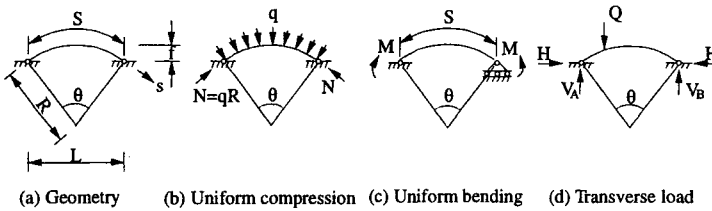


Figure 1. Pin-ended circular arches and loading.

ANALYSIS

Elastic Analysis

The distribution around an arch of the design in-plane moments M_x^* and axial forces N^* should be determined by carrying out either a second-order elastic analysis of the arch under the design loads, or by amplifying the results of a first-order elastic analysis. These methods of elastic analysis are discussed briefly in the following sub-sections.

First-Order Elastic Analysis

An approximate first-order elastic analysis of the bending of an arch under transverse loads may be made by hand by using a traditional method. A pin-ended arch has one redundancy, and so this is comparatively simple.

Alternatively, a more accurate first-order elastic analysis of the bending and compression of an arch may be made by using a suitable computer program. Although strictly speaking such a program should be based on the use of curved elements, it has been found [23] that sufficiently accurate results can be obtained by using a sufficient number of straight elements. While the number of elements required can be determined by examining the rate of convergence, it is suggested that sufficiently accurate results may be obtained when the angle between adjacent elements does not exceed 5° .

Amplified First-Order Elastic Analysis

The design moments M_x^* may be approximated by amplifying the first-order elastic moments M according to

$$M_x^* = M / (1 - N^* / N_{oma}) \tag{2}$$

in which N^* is the maximum first-order axial compression in the arch and N_{oma} is the lesser of the antisymmetric elastic buckling load (Fig. 2a) approximated by

$$N_{oma} = 4\pi^2 EI_x / S^2 \tag{3}$$

in which EI_x is the in-plane flexural rigidity and S is the developed length of the pin-ended arch, and the symmetric snap-buckling load (Fig. 2b) approximated by

$$N_{oms} = (0.15 + 0.006 \lambda_s^2) N_{oma} \tag{4}$$

in which
$$\lambda_s = (S / 2r_x) \theta / 2 \tag{5}$$

in which r_x is the in-plane radius of gyration and θ (in degrees) is the included angle of the arch.

Usually, $N_{oma} < N_{oms}$, except for very shallow arches with $\lambda_s < 11.9$. The strengths of very shallow arches are very sensitive to changes in the curvature, require large horizontal reactions to be developed at the supports, and are very sensitive to horizontal displacement at the supports. For these reasons, it is sensible to avoid the use of shallow arches.

Alternatively, and less conservatively, N_{oma} may be determined by an elastic bifurcation buckling analysis, and N_{oms} by a second-order elastic analysis. Such analyses will generally require the use of a suitable computer program. Again, sufficiently accurate results may be obtained by using a sufficient number of straight elements.

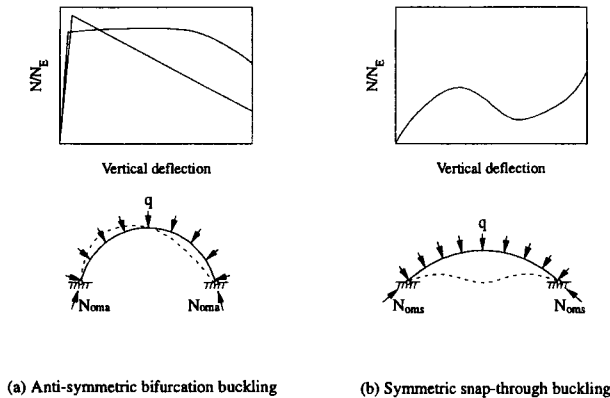


Figure 2. Elastic buckling modes.

Second-Order Elastic Analysis

The design in-plane moments M_x^* may be determined more accurately by using a second-order elastic analysis based on a suitable computer program. Sufficiently accurate results may be obtained by using a sufficient number of straight elements.

Plastic Analysis

Arches may be designed using plastic analysis (Fig. 3), provided that their cross-sections are compact so that there are no local buckling effects, provided that there is sufficient bracing to prevent lateral buckling, and provided the in-plane buckling effects are so small that

$$\lambda_c \geq 5 \quad (6)$$

in which λ_c is the load factor by which the design loads must be multiplied to cause elastic buckling. The arch is then satisfactory when the first-order plastic collapse load factor λ_p [23] satisfies

$$1 \leq \phi \lambda_p / (1 - 1/\lambda_c) \quad (7)$$

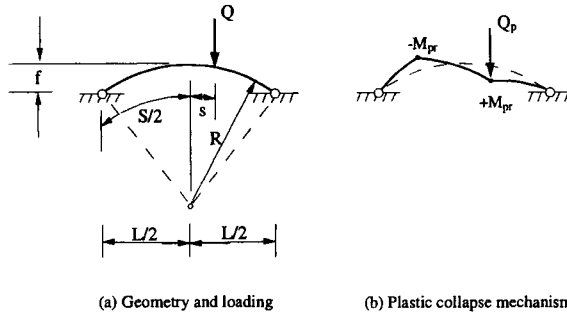


Figure 3. Plastic collapse of a pin-ended arch.

Advanced Analysis

Design by advanced analysis is permitted by the Australian limit states design code AS4100 [17] for the in-plane design of plane structures composed of straight compact members. For this method, the effects of residual stresses and initial curvature are included and an inelastic non-linear in-plane analysis is made of the structure. The structure is satisfactory if it can reach an equilibrium position under the design loads, increased by multiplying them by $1/\phi$.

This method of design may also be used for the in-plane design of arches. There seems no reason why advanced analysis computer programs which are based on straight elements should not be used for this purpose, provided a sufficient number of elements is used. Advanced analyses based on curved elements [12, 16] have been made of the in-plane behaviour of arches, and may be used as bench mark problems.

Advanced analyses based on curved elements [14, 15] have also been made of the out-of-plane behaviour of arches. These may be used as bench mark problems when generalised out-of-plane analysis programs are developed. It is anticipated that it will be found that straight elements are usually unsatisfactory for the out-of-plane behaviour of arches.

SECTION CAPACITY

The section capacity rules of limit states design codes [17] for straight steel members are intended to ensure that the design axial forces and bending moments at a cross-section do not cause failure at that cross-section by yielding and/or local buckling [20].

These section capacity rules can also be used for steel I-section arches. Thus the section capacity is satisfactory when

$$M_x^* \leq 1.18\phi M_{sx}(1 - N^*/\phi N_s) \leq \phi M_{sx} \tag{8}$$

for compact I-sections, and when

$$M_x^* \leq \phi M_{sx}(1 - N^*/\phi N_s) \tag{9}$$

otherwise, in which M_x^* and N^* are the design actions at the section and M_{sx} and N_s are the nominal section moment and axial force capacities [17].

IN-PLANE MEMBER CAPACITY

Arches in Uniform Compression

Arches in uniform compression may fail by antisymmetric buckling (Fig. 2a), or by symmetric snap-through buckling (Fig. 2b). The variation of the ratio of the elastic buckling load N_{om} [13] to the antisymmetric buckling load N_{oma} given by Eqn. 3 with the subtended angle θ of the arch is shown in Fig. 4. For high values of θ (medium-deep arches with $\theta > 60^\circ$), the elastic buckling load N_o is reasonably close to the linear prediction of N_{oma} , but is much lower for low values of θ (especially for shallow arches with $\theta < 30^\circ$).

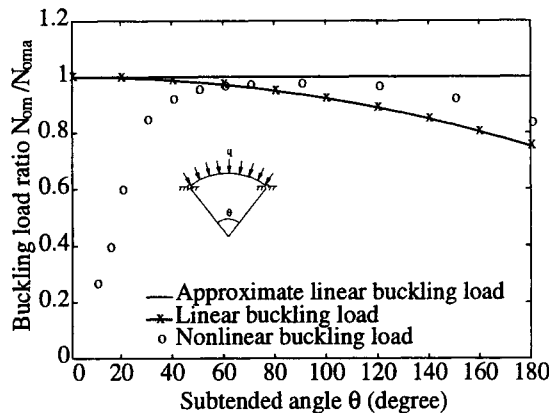


Figure 4. Elastic in-plane buckling of pin-ended arches.

For a medium-deep arch in uniform compression (Fig. 1b), it seems probable that its in-plane member-capacity will be satisfactory when

$$N^* \leq \phi N_{cax} \quad (10)$$

in which N^* is the design uniform compression, and N_{cax} is the in-plane compression capacity given by

$$N_{cax} = \alpha_{cax} N_s \quad (11)$$

in which α_{cax} is an arch compression slenderness reduction factor. It seems probable that the functional relationship

$$\alpha_{cax} = f_c(\lambda_x) \quad (12)$$

used for the design of a straight compression member [17] of modified slenderness

$$\lambda_x = (L / r_x) \sqrt{(f_y / 250)} \quad (13)$$

in which L is the member length, r_x the in-plane radius of gyration, and f_y the yield stress in MPa, can be used for arches as

$$\alpha_{cax} = f_c(\lambda_{xa}) \quad (14)$$

in which $\lambda_{xa} = (S / 2r_x) \sqrt{(f_y / 250)} \quad (15)$

in which S is the developed length of the arch. This proposal is currently being evaluated [16].

The in-plane member capacities of shallow arches are currently being studied. However, the strengths of very shallow arches, which develop large compressions, are very sensitive to changes in arch curvature and horizontal displacement of the supports, and it seems sensible to avoid the use of shallow arches.

Arches in Uniform Bending

The in-plane member capacity of an arch in uniform bending (Fig. 1c) will be satisfactory when

$$M_x^* \leq \phi M_{sx} \quad (16)$$

in which M_x^* is the design uniform moment.

Arches Under Transverse Loads

Arches are rarely in uniform compression or uniform bending, as transverse loads (Fig. 1d) cause both bending and compression actions. It seems probable that the in-plane member capacity of an arch will be satisfactory when

$$\frac{N^*}{N_{cax}} + \frac{M_x^*}{M_{sx}} \leq \phi \quad (17)$$

in which N^* and M_x^* are the maximum design actions in the arch.

It is likely that this linear interaction equation will be very conservative for three reasons. First of all, the elastic in-plane buckling loads of arches under transverse loads are likely to be significantly greater than the uniform compression antisymmetric buckling load N_{oma} used in the determination of the uniform compression nominal in-plane member capacity N_{cax} .

Secondly, it is known that the in-plane member capacity of a straight beam-column is significantly affected by the bending moment distribution, and that a linear interaction equation is only appropriate for uniform bending [20].

Thirdly, the use of the maximum design actions M_x^* and N^* determined by elastic analysis ignores the favourable redistributions that take place in redundant arches after the first plastic hinge forms. Arches with compact cross-sections and bracing that prevents lateral buckling may be designed plastically when the in-plane buckling effects are small, as discussed earlier.

The in-plane member capacities of arches with transverse load are currently being studied [16].

OUT-OF-PLANE MEMBER CAPACITY

Arches in Uniform Compression

The out-of-plane capacity of an unbraced simply supported steel arch in uniform compression (Fig. 1b) will be satisfactory when

$$N^* \leq \phi N_{cay} \quad (18)$$

in which N^* is the design uniform compression and N_{cay} is the arch nominal out-of-plane compression capacity given by

$$N_{cay} = \alpha_{cay} N_s \quad (19)$$

in which α_{cay} is an arch compression slenderness reduction factor. It has been found [14] that the functional relationship

$$\alpha_{cy} = f_c (\lambda_y) \quad (20)$$

used for the design of a straight compression member [17] of modified slenderness

$$\lambda_y = (L / r_y) \sqrt{f_y / 250} \quad (21)$$

in which L is the member length, r_y the minor axis radius of gyration, and f_y the yield stress in MPa, can be modified for arches to

$$\alpha_{cay} = f_c (\lambda_{ya}) \quad (22)$$

in which

$$\lambda_{ya} = (S / r_y) \sqrt{(1 / k_{ya})} \sqrt{f_y / 250} \quad (23)$$

is the modified arch slenderness, in which S is the developed length of the pin-ended arch and k_{ya} relates the arch elastic flexural buckling load N_{ya} to the corresponding straight member elastic buckling load N_y through

$$N_{ya} = k_{ya} N_y \tag{24}$$

An expression for k_{ya} is given in [14] and [15].

The predictions of Eqns 18-24 (with $\phi = 1$) shown in Fig. 5 compare very favourably with the numerical results obtained from advanced analyses [14].

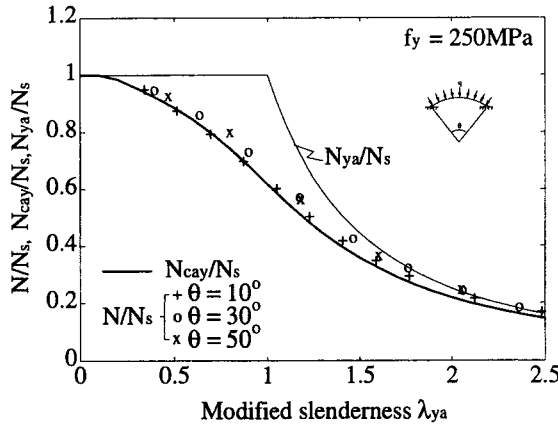


Figure 5. Out-of-plane strengths of arches in uniform compression.

Arches in Uniform Bending

The out-of-plane capacity of a simply supported arch in uniform bending (Fig. 1b) will be satisfactory when

$$M_x^* \leq \phi M_{abx} \tag{25}$$

in which M^* is the design uniform moment and M_{abx} is the arch nominal out-of-plane member moment capacity given by

$$M_{abx} = \alpha_{sa} M_{sx} \tag{26}$$

in which α_{sa} is an arch slenderness reduction factor. It has been found [14] that the functional relationship

$$\alpha_s = f_b (\lambda_b) \tag{27}$$

used for the design of a straight beam [17] of modified slenderness

$$\lambda_b = \sqrt{(M_{sx} / M_{yz})} \tag{28}$$

in which M_{yz} is the elastic flexural-torsional buckling moment of a straight beam in uniform bending [18, 20] can be modified for arches to

$$\alpha_{sa} = f_b (\lambda_{ba}) \tag{29}$$

in which

$$\lambda_{ba} = \sqrt{(M_{sx} / k_{yza} M_{yz})} \tag{30}$$

is the modified arch slenderness, in which k_{yza} relates the arch elastic flexural-torsional buckling moment M_{yza} to the corresponding straight member elastic buckling moment M_{yz} through

$$M_{yza} = k_{yza} M_{yz} \tag{31}$$

An expression for k_{yza} is given in [14] and [15].

The predictions of Eqns 25-31 (with $\phi = 1$) shown in Fig. 6 compare favourably with the numerical results obtained from advanced analyses [14].

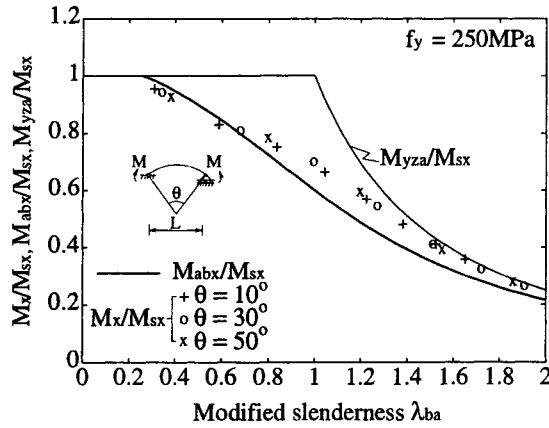


Figure 6. Out-of-plane strengths of arches in uniform bending.

Arches Under Transverse Loads

Arches are rarely in uniform compression or uniform bending, as transverse loads (Fig. 1d) cause both bending and compression actions. It has been found [15] that the out-of-plane capacities of arches under transverse loads are satisfactory when

$$\frac{N^*}{\alpha_{an} N_{cay}} + \frac{M_x^*}{\alpha_{am} M_{abx}} \leq \phi \tag{32}$$

in which N^* and M_x^* are the maximum design actions in the arch and α_{an} and α_{am} are modification factors which account approximately for the variations of the axial compressions and moments along the arch. The approximate values of α_{an} and α_{am} suggested in [15] are shown in Fig. 7.

The predictions of Eqn. 32 for arches with concentrated loads shown in Fig. 8 compare favourably with the lower bounds of the numerical results obtained from advanced analyses [15].

Arch						
α_{an}	1.0	1.1	1.4	1.4	2.7	—
α_{am}	—	1.1	1.1	1.2	1.2	1.0

Figure 7. Factors α_{am} and α_{an} for arches.

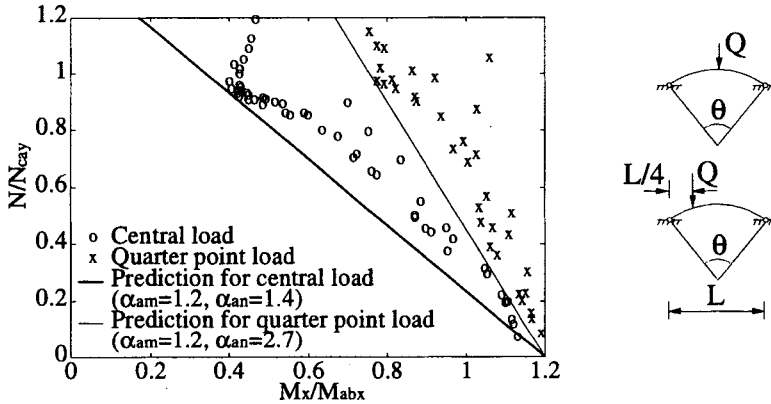


Figure 8. Strengths of arches with concentrated load.

CONCLUSIONS

This paper uses recent and current research at the University of Sydney on pin-ended circular I-section steel arches to develop tentative design procedures that are consistent with those of the Australian limit states steel design code AS4100.

It discusses the methods of elastic analysis that might be used to determine the distributions of the in-plane bending moments and axial forces in arches, and then provides formulations for the design section, in-plane, and out-of-plane capacities.

The formulations for the in-plane capacities of medium-high rise arches are tentative and likely to be conservative in many cases, while low rise arches are sensitive to curvature changes and horizontal support displacements. Current research studies are intended to provide evidence on which more accurate formulations can be based.

The methods of plastic design and design by advanced analysis are also discussed.

REFERENCES

- [1] Beedle, LS (editor). (1991). *Stability of Metal Structures. A World View*, 2nd ed., Structural Stability Research Council, Bethlehem, Pa.
- [2] Papangelis, JP, and Trahair, NS. (1986). In-Plane Finite Element Analysis of Arches. *Proceedings, Pacific Structural Steel Conference*, Auckland, 4, 333-350.
- [3] Papangelis, JP, and Trahair, NS. (1987). Finite Element Analysis of Arch Lateral Buckling. *Civil Engineering Transactions*, Institution of Engineers, Australia, CE29:1, 34-39.
- [4] Papangelis, JP, and Trahair, NS. (1986). Flexural-Torsional Buckling of Arches. *Journal of Structural Engineering*, ASCE, 113:4, 889-906.
- [5] Papangelis, JP, and Trahair, NS. (1987). Flexural-Torsional Buckling Tests on Arches. *Journal of Structural Engineering*, ASCE, 113:7, 1433-1443.
- [6] Papangelis, JP, and Trahair, NS. (1988). Buckling of Monosymmetric Arches Under Point Loads. *Engineering Structures*, 10:4, 257-264.
- [7] Papangelis, JP, and Trahair, NS. (1991). Flexural-Torsional Buckling of Arches Using Curved Finite Elements. *Proceedings*, 6th International Conference in Australia on Finite Element Methods, Sydney, Australia, 323-331.
- [8] Papangelis, JP, and Trahair, NS. (1993). Design of Steel Arches Against In- and Out-of-Plane Buckling. *Proceedings*, 12th Australasian Conference on the Mechanics of Structures and Materials, Wollongong, 665-672.
- [9] Pi, Y-L, Papangelis, JP, and Trahair, NS. (1995). Prebuckling Deformations and Flexural-Torsional Buckling of Arches. *Journal of Structural Engineering*, ASCE, 121:9, 1313-22.
- [10] Pi, Y-L, and Trahair, NS. (1995). Nonlinear Inelastic Analysis of Arches. *Proceedings*, International Conference on Structural Stability and Design, Sydney, 113-118.
- [11] Pi, Y-L, and Trahair, NS. (1996). Three Dimensional Nonlinear Analysis of Elastic Arches. *Engineering Structures*, 18:1, 49-63.
- [12] Pi, Y-L, and Trahair, NS. (1996). In-Plane Inelastic Buckling and Strengths of Steel Arches. *Journal of Structural Engineering*, ASCE, 122:7, 734-747.
- [13] Pi, Y-L, and Trahair, NS. (1998). Non-linear Buckling and Post-buckling of Elastic Arches. *Engineering Structures*, 20:7, 571-579.
- [14] Pi, Y-L, and Trahair, NS. (1998). Out-of-Plane Inelastic Buckling and Strengths of Steel Arches. *Journal of Structural Engineering*, ASCE, 124:2, 174-183.
- [15] Pi, Y-L, and Trahair, NS. (1997). Inelastic Lateral Buckling Strengths and Design of Steel Arches. *Research Report R764*, Department of Civil Engineering, University of Sydney.
- [16] Pi, Y-L, and Trahair, NS. (1998). In-Plane Buckling and the Design of Steel Arches. *Research Report*, Department of Civil Engineering, University of Sydney.
- [17] SA. (1990). *AS4100 Steel Structures*. Standards Australia, Sydney.
- [18] Trahair, NS. (1993). *Flexural-Torsional Buckling of Structures*, E & FN Spon, London.
- [19] Trahair, NS. (1995). Stability and Design of Steel Beams and Arches. *Proceedings*, International Conference on Structural Stability and Design, Sydney, 3-12.
- [20] Trahair, NS, and Bradford, MA. (1998) *The Behaviour and Design of Steel Structures to AS4100*, 3rd Edition, E & FN Spon, London.
- [21] Trahair, NS, and Papangelis, JP. (1987). Flexural-Torsional Buckling of Monosymmetric Arches. *Journal of Structural Engineering*, ASCE, 113:10, 2271-2288.
- [22] Trahair, NS, Papangelis, JP, and Pi, Y-L. (1997). Recent Australian Research on the Strengths of Steel Arches. *Research Report R753*, Department of Civil Engineering, University of Sydney.
- [23] Trahair, NS, Pi, Y-L, Clarke, MJ, and Papangelis, JP. (1997). Plastic Design of Arches. *Advances in Structural Engineering*, 1:1, 1-9.
- [24] Vacharajittiphan, P, and Trahair NS. (1975). Flexural-Torsional Buckling of Curved Members. *Journal of the Structural Division*, ASCE, 101:ST6, 1223-1238.

This Page Intentionally Left Blank

FINITE STRIP ANALYSIS OF SHEAR WALLS AND THIN PLATES WITH ABRUPT CHANGES OF THICKNESS BY USING MODIFIED BEAM VIBRATION MODES

Y. K. Cheung, F. T. K. Au and D. Y. Zheng

Department of Civil Engineering
The University of Hong Kong, Pokfulam Road
Hong Kong, China

ABSTRACT

In Rayleigh-Ritz types of structural analysis, the choice of the trial displacement functions is of utmost importance. This paper presents a new finite strip method for the analysis of deep beams, shear walls and thin plates with abrupt changes of thickness. The essence of the method lies in the adoption of displacement functions possessing the right amount of continuity at the ends as well as at locations of abrupt changes of thickness. The equilibrium conditions at locations of abrupt changes of thickness are taken into account by the incorporation of piecewise continuous correction functions. As these displacement functions are built up from beam vibration modes with appropriate corrections, they possess both the advantages of fast convergence of harmonic functions as well as the appropriate order of continuity. Numerical results also show that the method is versatile, efficient and accurate.

KEYWORDS

Finite strip, deep beam, shear wall, thin plate, harmonics, beam vibration modes

INTRODUCTION

In structural analysis using the semi-analytical finite strip method (Cheung, 1977), the interpolation functions have to satisfy *a priori* the boundary conditions in the longitudinal direction, and they are normally the eigen-functions of vibration or stability of an Euler beam. In the spline finite strip method for plate bending analysis (Fan, 1982), C^2 -continuous B_3 -spline functions are chosen instead. However these methods are not capable of dealing with problems involving abruptly changes of thickness because of the excessive continuity inherent in the longitudinal interpolation functions. This paper describes the use of interpolation functions obtained by combining the normal eigen-functions of vibration and piecewise continuous augmenting functions which take care of the required continuity at locations of abrupt changes of thickness. In plane stress problems, the augmenting functions are

piecewise linear to achieve C^0 -continuity at locations of abrupt changes of thickness, whereas in plate bending problems, the augmenting functions are piecewise cubic polynomials to achieve C^1 -continuity. The application of this approach to vibration and buckling analysis of beams with abrupt changes of cross sections has been rather successful (Au *et al.*, to appear).

The chosen interpolation functions therefore possess both the advantages of fast convergence of eigenfunctions and the appropriate order of continuity at the locations of abrupt changes of sectional properties. The method allows extensive use of matrix notations and programming is rather straightforward. The present method can cope with strips with abrupt changes of rigidity as well as rectangular domains with re-entrant corners. A few numerical examples are given to demonstrate the versatility, efficiency and accuracy of the method.

ANALYSIS OF DEEP BEAMS AND SHEAR WALL BY C^0 MODIFIED DISPLACEMENT FUNCTIONS

An arbitrary function $f(y)$ continuous over the interval $[0, l]$ may be written in the terms of the basic trigonometric functions as

$$f(y) = \frac{a_0}{2} + \sum_{n=1}^{\infty} \left[a_n \cos \frac{n\pi y}{l} + b_n \sin \frac{n\pi y}{l} \right] \quad (1)$$

in which periodic extension is implicit (Liu *et al.*, 1995). This form of periodic extension is superior to the normal form of half-range expansions involving either odd or even components, as the function and its derivatives are well defined at the end points of the interval. In the analysis of cantilever deep beams and shear walls, it is often more convenient to adopt an equivalent set of displacement functions $\{\bar{Y}_i(y), i = 1, 2, \dots$ with zero values at the base, i.e.

$$\bar{Y}_{2n-1}(y) = 1 - \left[\cos \frac{n\pi y}{l} + \sin \frac{n\pi y}{l} \right] \quad n = 1, 2, \dots, r/2 \quad (2)$$

$$\bar{Y}_{2n}(y) = 1 - \left[\cos \frac{n\pi y}{l} - \sin \frac{n\pi y}{l} \right] \quad n = 1, 2, \dots, r/2 \quad (3)$$

This set of functions is a complete set to describe an arbitrary function $f(y)$ in which $f(0) = 0$. It is important to note that, unlike vibration functions obtained from cantilever beams, the slope of the resulting displacement function may be non-zero at the starting point. This is essential to structures in which shear effect is significant. A shear wall can be sub-divided into finite strips extending from the base to the top. Figure 1 shows a typical strip of width b comprising s segments of different thickness $t = t_1, t_2, \dots, t_s$ with step change of thickness at locations $y = y_2, y_3, \dots, y_s$. The displacements u and v in x and y directions respectively at an arbitrary point (x, y) within the strip can be written in series form as

$$u(x, y) = \sum_{i=1}^r Y_{iu}(y) \mathbf{M}(x) \mathbf{u}_i, \quad v(x, y) = \sum_{i=1}^r Y_{iv}(y) \mathbf{M}(x) \mathbf{v}_i \quad (4,5)$$

where $Y_{iu}(y)$ and $Y_{iv}(y)$ are i -th terms of the series part of the displacement function, $\mathbf{M}(x)$ is a row vector containing the shape functions, and \mathbf{u}_i and \mathbf{v}_i are vectors containing the corresponding displacement parameters associated with the nodal lines. They are further elaborated below in equations (6) to (10).

$$Y_{iu}(y) = \bar{Y}_i(y), \quad Y_{iv}(y) = \bar{Y}_i(y) + \tilde{Y}_i(y) \quad (6,7)$$

$$\mathbf{M}(x) = \begin{bmatrix} 1 - \frac{x}{b} & \frac{x}{b} \end{bmatrix} \quad (8)$$

$$\mathbf{u}_i = [u_1 \quad u_2]^T, \quad \mathbf{v}_i = [v_1 \quad v_2]^T \quad (9,10)$$

The functions $Y_{iu}(y)$ for displacements in x direction can be simply taken as the functions $\bar{Y}_i(y)$ defined in equations (2) and (3). However the functions $Y_{iv}(y)$ used to describe displacements in y direction should be capable of satisfying the equilibrium conditions at step change of thickness, and hence piecewise linear augmenting functions $\tilde{Y}_i(y)$ are incorporated to satisfy C^0 -continuity conditions at locations $y = y_2, y_3, \dots, y_s$. In a plane stress problem, the equilibrium condition at a step change of thickness can be written as

$$Y_i'(y)|_{y=y_j-0} = \frac{t_j}{t_{j-1}} Y_i'(y)|_{y=y_j+0} \quad (j=2, 3, \dots, s) \quad (11)$$

where the zero denotes an infinitesimal quantity. The properties of the augmenting function $\tilde{Y}_i(y)$ can be obtained from equations (7) and (11), i.e.

$$\tilde{Y}_i'(y)|_{y=y_j-0} = \frac{t_j}{t_{j-1}} \tilde{Y}_i'(y)|_{y=y_j+0} + \left(\frac{t_j}{t_{j-1}} - 1 \right) \bar{Y}_i'(y)|_{y=y_j} \quad (j=2, 3, \dots, s) \quad (12)$$

If we set $f_j = \tilde{Y}_i'(y)|_{y=y_j}$ and $h_k = y_{k+1} - y_k$, then the augmenting function $\tilde{Y}_i(y)$ can be written as:

$$\tilde{Y}_i(y) = \sum_{j=1}^{s+1} f_j l_j(y) \quad (13)$$

where

$$l_j(y) = \begin{cases} \frac{y - y_{j-1}}{y_j - y_{j-1}} & y_{j-1} \leq y \leq y_j \quad (\text{omitted if } j = 1) \\ \frac{y - y_{j+1}}{y_j - y_{j+1}} & y_j \leq y \leq y_{j+1} \quad (\text{omitted if } j = s + 1) \\ 0 & y \notin [y_{j-1}, y_{j+1}] \end{cases} \quad (14)$$

Introducing the parameters ξ_j and η_j defined as follows

$$\xi_j = \frac{t_j}{t_{j-1}}, \quad \eta_j = (\xi_j - 1) \bar{Y}_i'(y)|_{y=y_j} \quad (j = 2, 3, \dots, s) \quad (15,16)$$

equation (12) can be written as

$$-h_j f_{j-1} + [h_j + h_{j-1} \xi_j] f_j - h_{j-1} \xi_j f_{j+1} = h_{j-1} h_j \eta_j \quad (j = 2, 3, \dots, s) \quad (17)$$

The augmenting function is also prescribed to be zero at the two ends, i.e.

$$f_1 = f_{s+1} = 0 \quad (18)$$

Equations (17) and (18) represent $(s+1)$ conditions whereby the augmenting function $\tilde{Y}_i(y)$ can be uniquely determined. Once the C^0 interpolation functions have been determined, the standard procedure of finite strip formulation can be followed for the solution.

ANALYSIS OF BI-DIRECTIONALLY STEPPED PLATE BY C^1 MODIFIED DISPLACEMENT FUNCTIONS

In the finite strip analysis of a bi-directionally stepped plate (Figure 2) supported by Winkler elastic foundation of stiffness $k(x, y)$, the plate is first of all sub-divided into longitudinal strips each of which has transverse cross sections of constant thickness. The deflection of point (x, y) of the plate at time t is denoted by $w(x, y, t)$.

Formation of C^1 Longitudinal Interpolation Functions

The longitudinal displacement functions $Y_i(y)$ are made up of functions from two families, i.e.

$$Y_i(y) = \bar{Y}_i(y) + \tilde{Y}_i(y) \quad (19)$$

The first family of functions $\{\bar{Y}_i(y), i = 1, 2, \dots, n$ comprises the vibration modes of a hypothetical prismatic beam of total length l with the same end supports but with neither the intermediate supports nor the abrupt changes of cross-section. The family of augmenting functions $\{\tilde{Y}_i(y), i = 1, 2, \dots, n$ comprises piecewise C^1 -continuous cubic polynomials which are so chosen that each $Y_i(y)$ satisfies the boundary conditions at the two ends, the zero deflection conditions at the intermediate point supports (if any) and the continuity conditions at locations of abrupt changes of cross-section. For a beam with simple end supports, the vibration modes $\bar{Y}_i(y)$ are Fourier sine series. Those for other end conditions are given by Cheung (1977).

Each category of strips has to be analyzed as a beam to obtain the augmenting functions. Figure 3 shows such a beam made up of Q segments with abrupt changes of cross-section. The beam may be supported at any junctions. If we introduce the following undetermined coefficients for the j -th junction point at y_j ,

$$z_y = \tilde{Y}_i(y_j), \quad \phi_y = \tilde{Y}_i'(y_j) \quad i = 1, 2, \dots, n; \quad j = 1, 2, \dots, (Q+1) \quad (20,21)$$

the augmenting function $\tilde{Y}_i(y)$ at the j -th segment can be written as

$$\tilde{Y}_i(y) = H_{1j}(\xi_j) z_y + H_{2j}(\xi_j) \phi_y + H_{3j}(\xi_j) z_{i(j+1)} + H_{4j}(\xi_j) \phi_{i(j+1)} \\ y \in [y_j, y_{j+1}]; \quad j = 1, 2, \dots, Q \quad (22)$$

where

$$H_{1j}(\xi_j) = 1 - 3\xi_j^2 + 2\xi_j^3, \quad H_{2j}(\xi_j) = l_j \xi_j (1 - \xi_j)^2 \quad (23,24)$$

$$H_{3j}(\xi_j) = 3\xi_j^2 - 2\xi_j^3, \quad H_{4j}(\xi_j) = l_j \xi_j^2 (\xi_j - 1) \quad (25,26)$$

$$\xi_j = (y - y_j) / l_j, \quad l_j = y_{j+1} - y_j \quad j = 1, 2, \dots, Q \quad (27,28)$$

Continuity of bending moment at the $(j+1)$ -th junction gives

$$EI_j Y_i''(y_{j+1} - 0) = EI_{j+1} Y_i''(y_{j+1} + 0) \quad j = 1, 2, \dots, (Q-1) \quad (29)$$

where the zero denotes an infinitesimal quantity, I_j stands for the moment of inertia of the j -th segment, I_{j+1} stands for the moment of inertia of the $(j+1)$ -th segment and E is the modulus of elasticity. Hence it follows from equation (29) that

$$\widetilde{Y}_i''(y_{j+1} - 0) = \eta_{j+1} \widetilde{Y}_i''(y_{j+1} + 0) + (\eta_{j+1} - 1) \overline{Y}_i''(y_{j+1}) \quad j = 1, 2, \dots, (Q-1) \quad (30)$$

where

$$\eta_{j+1} = I_{j+1} / I_j \quad j = 1, 2, \dots, (Q-1) \quad (31)$$

A junction may or may not be provided with a point support. If the beam is supported at the junction and hence deflection there is zero, equation (19) gives

$$z_{i(j+1)} = -\overline{Y}_i(y_{j+1}) \quad j = 1, 2, \dots, (Q-1) \quad (32)$$

If the beam is not supported at this junction, the shear force is continuous across the junction and therefore

$$\left\{ \frac{d}{dy} [EI_j Y_i''(y)] \right\} \Big|_{y=y_{j+1}-0} = \left\{ \frac{d}{dy} [EI_{j+1} Y_i''(y)] \right\} \Big|_{y=y_{j+1}+0} \quad j = 1, 2, \dots, (Q-1) \quad (33)$$

We can easily obtain from Equation (19)

$$\widetilde{Y}_i''(y_{j+1} - 0) = \eta_{j+1} \widetilde{Y}_i''(y_{j+1} + 0) + (\eta_{j+1} - 1) \overline{Y}_i''(y_{j+1}) \quad j = 1, 2, \dots, (Q-1) \quad (34)$$

Using the undetermined coefficients introduced in equations (20) and (21), equations (30) and (34) can be written respectively as

$$\begin{aligned} \frac{6}{l_j^2} z_{ij} + \frac{2}{l_j} \phi_{ij} + \left[-\frac{6}{l_j^2} + \eta_{j+1} \frac{6}{l_{j+1}^2} \right] z_{i(j+1)} + \left[\frac{4}{l_j} + \eta_{j+1} \frac{4}{l_{j+1}} \right] \phi_{i(j+1)} - \eta_{j+1} \frac{6}{l_{j+1}^2} z_{i(j+2)} + \\ \eta_{j+1} \frac{2}{l_{j+1}} \phi_{i(j+2)} = (\eta_{j+1} - 1) \overline{Y}_i''(y_{j+1}) \quad j = 1, 2, \dots, (Q-1) \quad (36) \end{aligned}$$

$$\begin{aligned} \frac{12}{l_j^3} z_y + \frac{6}{l_j^2} \phi_y + \left[-\frac{12}{l_j^3} - \eta_{j+1} \frac{12}{l_{j+1}^3} \right] z_{i(j+1)} + \left[\frac{6}{l_j^2} - \eta_{j+1} \frac{6}{l_{j+1}^2} \right] \phi_{i(j+1)} + \left[\eta_{j+1} \frac{12}{l_{j+1}^3} \right] z_{i(j+2)} + \\ \left[-\eta_{j+1} \frac{6}{l_{j+1}^2} \right] \phi_{i(j+2)} = (\eta_{j+1} - 1) \bar{Y}_i''(y_{j+1}) \quad j = 1, 2, \dots, (Q-1) \end{aligned} \quad (37)$$

The introduction of boundary conditions at the end supports is straightforward and details can be found in the work by Au *et al.* Using these boundary conditions and equation (36), together with equation (32) or (37) as appropriate, the coefficients of the augmenting functions can be easily solved.

Formulation of Finite Strip

The strain energy U stored in a typical strip of width b between nodal lines i and $i+1$ can be written in terms of the displacement w , the generalized stress vector σ and strain vector ϵ as

$$U = \frac{1}{2} \iint_{Area} k(x, y) w^2(x, y, t) dx dy + \frac{1}{2} \iint_{Area} \sigma^T \epsilon dx dy \quad (38)$$

The kinetic energy V of the strip can similarly be written as

$$V = \frac{1}{2} \iint_{Area} \rho h(x, y) \dot{w}^2(x, y, t) dx dy \quad (39)$$

in which ρ is the mass density of the plate, $h(x, y)$ denotes the thickness of the plate and the dot denotes differentiation with respect to time t . In line with the normal finite strip approach, the displacement w can be expressed in terms of the shape function matrix $C(x)$, the nodal displacement vector δ_m and the displacement functions $Y_m(y)$ as

$$w(x, y, t) = \sum_{m=1}^r C(x) \delta_m(t) Y_m(y) \quad (40)$$

where

$$C(x) = \left[\left(\frac{2x}{b} + 1 \right) \left(1 - \frac{x}{b} \right)^2 \quad x \left(1 - \frac{x}{b} \right)^2 \quad \left(-\frac{2x}{b} + 3 \right) \left(\frac{x}{b} \right)^2 \quad (x - b) \left(\frac{x}{b} \right)^2 \right] \quad (41)$$

$$Y_m(y) = \bar{Y}_m(y) + \tilde{Y}_m(y) \quad (42)$$

$$\delta_m(t) = \left[w_i^{(m)}(t) \quad \theta_i^{(m)}(t) \quad w_{i+1}^{(m)}(t) \quad \theta_{i+1}^{(m)}(t) \right]^T \quad (43)$$

Notice that $\bar{Y}_m(y)$ is the usual vibration mode of a hypothetical prismatic beam with appropriate boundary conditions, and $\tilde{Y}_m(y)$ is the augmenting C^1 -continuous piecewise cubic polynomials to take care of the abrupt changes of plate thickness. Substituting equation (40) into equations (38) and (39), the strain energy U and the kinetic energy V of the strip can be expressed in matrix form as

$$U = \frac{1}{2} \sum_{m=1}^r \sum_{n=1}^r \delta_m^T K_{mn} \delta_n, \quad V = \frac{1}{2} \sum_{m=1}^r \sum_{n=1}^r \delta_m^T M_{mn} \dot{\delta}_n \quad (44,45)$$

where the stiffness sub-matrix K_{mn} and the mass sub-matrix M_{mn} are given by

$$K_{mn} = \iint_{Area} \mathbf{B}_m^T(x, y) \mathbf{D}(x, y) \mathbf{B}_n(x, y) dx dy + \iint_{Area} k(x, y) Y_m(y) Y_n(y) \mathbf{C}^T(x) \mathbf{C}(x) dx dy \quad (46)$$

$$M_{mn} = \iint_{Area} \rho(x, y) h(x, y) Y_m(y) Y_n(y) \mathbf{C}^T(x) \mathbf{C}(x) dx dy \quad (47)$$

in which the strain matrix \mathbf{B}_m and the rigidity matrix \mathbf{D} are given by Cheung (1977). Applying the Lagrangian equation, the equation of motion for free vibration can be written as

$$\sum_{n=1}^r M_{mn} \ddot{\delta}_n(t) + \sum_{n=1}^r K_{mn} \delta_n(t) = 0 \quad (48)$$

Use of Mixed Strips

The above derivation applies to one particular type of strips strictly speaking. When one strip adjoins another strip of a different type, there is a potential problem of incompatibility as the two adjoining strips have different sets of displacement functions. To overcome this problem, a mixed strip is required and details can be found in the work by Cheung (1977).

NUMERICAL EXAMPLES

A number of numerical examples are given to demonstrate the versatility of the present method. Results obtained by the present method are compared to solutions published before if available or solutions obtained by finite element method. As some of the examples published before were presented using imperial units, these units are omitted altogether for simplicity.

Example 1: Asymmetrical Coupled Shear Wall with Step Change in Thickness

Figure 4(a) shows an asymmetrical coupled shear wall with step change in thickness previously studied by higher order finite elements (Chan and Cheung, 1979). The wall is subjected to a unit horizontal uniformly distributed load at the left side. The wall is assumed to be made of isotropic material having Young's modulus E of 463000 and Poisson's ratio μ of 0.0. In the analysis of coupled shear walls, the spandrel beams and openings between the coupled shear walls are very often represented by an orthotropic continuum with equivalent elastic properties. Referring to Figure 4(b), the equivalent Young's moduli of the continuum in the x and y direction, as well as the equivalent shear rigidity of the continuum are given respectively by

$$E_x = \frac{d}{h} E, \quad E_y = 0, \quad G = \frac{d}{h} \cdot \frac{E}{\left(\frac{c'}{d}\right)^2 + 2.4}$$

where $c' = c + d$ is the effective span length of the spandrel beam. The adjustment to the span length of the spandrel beam is to allow for the fact that the rigid-end condition could not possibly occur immediately at the junction of the wall and beam. The equivalent properties of the continuum are therefore calculated as $E_x=115750$, $E_y=0$ and $G=2251.9$. In the analysis by the present method, the shear wall was first discretized into 14 strips of equal widths. In addition, a very coarse mesh comprising only three strips (one for the equivalent continuum and two for the walls) was tried. The

number of terms used in the analysis ranges from 12 to 20. The problem was also solved using 1512 QM6 incompatible finite elements (Lashkari, 1992). Table 1 shows the convergence of the deflection at the top right corner of the shear wall as compared with the finite element results. The horizontal deflection of the right side of the wall is shown in Figure 5. The vertical stresses at the horizontal cross section at $y=3.375$ are plotted in Figure 6. The vertical stresses along the centre line of the rightmost strip (i.e. at $x=6.75$) are shown in Figure 7. It is observed that results from the present method agree very well with those obtained by finite element method and the higher order finite elements (Chan and Cheung, 1979). The accuracy of the deflections obtained from the very coarse mesh is also striking.

TABLE 1
COUPLED SHEAR WALL
DEFLECTION AT TOP RIGHT CORNER

Scheme used in the present method	Deflection at $x=7, y=21$
3 strips, 12 terms	9.6485×10^{-3}
3 strips, 14 terms	9.6489×10^{-3}
3 strips, 16 terms	9.6492×10^{-3}
3 strips, 18 terms	9.6494×10^{-3}
3 strips, 20 terms	9.6495×10^{-3}
14 strips, 12 terms	9.6887×10^{-3}
14 strips, 14 terms	9.6909×10^{-3}
14 strips, 16 terms	9.6922×10^{-3}
14 strips, 18 terms	9.6928×10^{-3}
14 strips, 20 terms	9.6936×10^{-3}
Finite element method	9.6974×10^{-3}

TABLE 2
STEPPED SQUARE PLATE
FREQUENCY COEFFICIENTS β_1

h_2/h_1	Scheme used in the present method		Ju et al. (1995)	Bambil et al. (1991)
	3 strips, 1 term	8 strips, 3 terms		
0.70	15.560	15.477	15.586	15.619
0.75	16.309	16.189	16.394	16.412
0.80	17.024	16.917	17.012	17.121
0.85	17.715	17.635	17.665	17.789
0.90	18.410	18.361	18.307	18.507
0.95	19.091	19.051	18.964	19.102

Example 2: Bi-directional Stepped Square Plate with All Edges Simply Supported

Figure 8 shows a bi-directionally stepped square plate which is simply supported on all edges. Two schemes have been used. Scheme 1 comprises only three strips, i.e. one central strip through the thickened section and two side strips of constant thickness. The two side strips are of the mixed type so that the influence of the central stepped section is gradually reduced. Only one term has been used in the evaluation of the fundamental frequencies. In Scheme 2, the plate is divided into 8 strips of equal widths, with the two strips adjacent to the thickened section being of the mixed type. Three terms have been used but the second term, itself being anti-symmetrical, in fact does not contribute to the fundamental mode. The thickness ratio h_2/h_1 is varied to study its effect on convergence and accuracy. The fundamental angular frequency ω_1 can be expressed in terms of a dimensionless coefficient β_1 and the flexural rigidity D_1 of the thinner portion as

$$\omega_1 = \frac{\beta_1}{4a^2} \sqrt{\frac{D_1}{\rho h_1}} \quad \text{where } D_1 = \frac{Eh_1^3}{12(1-\nu^2)}$$

The present results are tabulated in Table 2 and compared with results obtained by Bambil et al. (1991) and Ju et al. (1995). Good agreement is observed in spite of the coarseness of the meshes.

Example 3: A Uniform Square Plate on Non-homogeneous Elastic Foundation

A uniform square plate of size $2a \times 2a$ supported on non-homogeneous elastic foundation is shown in Figure 9. The plate is supported on elastic foundation of modulus k_2 within the central square region of

size $1.2a \times 1.2a$, while elsewhere it is supported on elastic foundation of modulus k_1 . The plate itself may be clamped or simply supported on all four sides. Two schemes have been used. In Scheme 1, the plate is divided into three strips with the middle strip going through the central square, and only one term has been used. In Scheme 2, the plate is divided into 10 strips of equal widths and 5 terms are used. The fundamental angular frequency ω_1 is similarly expressed in terms of a dimensionless coefficient β_1 and the flexural rigidity D as

$$\omega_1 = \frac{\beta_1}{4a^2} \sqrt{\frac{D}{\rho h}} \quad \text{where } D = \frac{Eh^3}{12(1-\nu^2)}$$

Table 3 compares the present results with those due to Laura and Gutierrez (1985) and Ju *et al.* (1995) and good agreement is demonstrated.

TABLE 3
UNIFORM SQUARE PLATE ON NON-HOMOGENEOUS ELASTIC FOUNDATION
FUNDAMENTAL FREQUENCY COEFFICIENTS β_1

$\frac{k_1 a^4}{D}$	$\frac{k_2 a^4}{D}$	All sides clamped				All sides simply supported			
		3 strips, 1 term	10 strips, 5 terms	Ju <i>et al.</i> (1995)	Laura & Gutierrez (1985)	3 strips, 1 term	10 strips, 5 terms	Ju <i>et al.</i> (1995)	Laura & Gutierrez (1985)
0	20	40.54	39.88	39.26	39.89	25.52	25.49	25.04	25.48
0	50	45.66	45.09	44.51	45.10	32.24	32.19	31.80	32.23
0	100	53.09	52.61	52.40	52.66	41.02	40.87	40.52	41.09
20	0	37.08	36.33	35.66	36.33	21.25	21.17	20.68	21.21
50	0	37.59	36.82	36.15	36.84	23.24	23.08	22.63	23.25
100	0	38.43	37.60	36.93	37.66	26.18	25.80	25.41	26.29
20	50	45.94	45.37	44.75	45.37	33.18	33.15	32.78	33.15
20	100	53.34	52.86	52.33	52.89	41.78	41.70	41.35	41.81
50	20	41.33	40.64	39.98	40.65	28.31	28.22	27.84	28.29
100	20	42.09	41.36	40.74	41.40	30.79	30.55	30.21	30.83

CONCLUSIONS

A new finite strip method has been developed for the analysis of deep beams, shear walls and thin plates. The use of piecewise linear or cubic augmenting functions in conjunction with the basic harmonic functions and beam modes results in displacement functions with the appropriate order of continuity at the locations of abrupt changes of sectional properties. It therefore allows the use of continuous finite strips with step changes in thickness. The present method can also cope with rectangular domains with re-entrant corners. A few numerical examples have been given to demonstrate the versatility, efficiency and accuracy of the method.

REFERENCES

Au F.T.K., Zheng D.Y. and Cheung Y.K. Vibration and Stability of Non-Uniform Beams with Abrupt Changes of Cross-Section by Using C^1 Modified Beam Vibration Functions. *Applied Mathematical Modeling* (accepted for publication).

Bambil D.V., Laura P.A.A., Bergmann A. and Carnicer R. (1991). Fundamental Frequency of Transverse Vibration of Symmetrically Stepped Simply Supported Rectangular Plates. *Journal of Sound and Vibration* **150**, 167-169.

Chan H.C. and Cheung Y.K. (1979). Analysis of Shear Walls using Higher Order Finite Elements, *Building and Environment*, **14**, 217-224.

Cheung Y.K. (1977). *Finite Strip Method in Structural Analysis*, Pergamon Press, Oxford, UK.

Fan S.C. (1982). *Spline Finite Strip in Structural Analysis*, Ph.D. thesis, The University of Hong Kong, Hong Kong.

Ju F., Lee H.P. and Lee K.H.(1995). Free Vibration of Plates with Stepped Variations in Thickness on Non-Homogeneous Elastic Foundations. *Journal of Sound and Vibration* **183:3**, 533-545.

Lashkari M. (1992). *COSMOS/M User Guide, 7th Edition*. Structural Research and Analysis Corporation.

Laura P.A.A. and Gutierrez R.H. (1985). Transverse Vibrations of Rectangular Plates on Inhomogeneous Foundation, Part I: Rayleigh-Ritz Method. *Journal of Sound and Vibration* **101**, 307-315.

Liu J.Y., Zheng D.Y. and Mei Z.J. (1995). *Practical Integral Transforms in Engineering*, Huazhong University of Science and Technology Press.

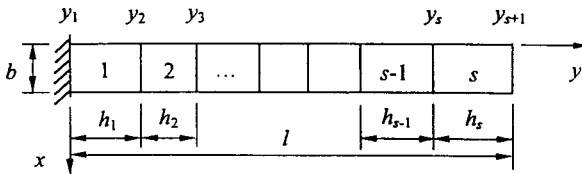


Figure 1: A cantilever strip comprising s segments of thicknesses t_1, t_2, \dots, t_s and with step changes in thickness at locations y_2, y_3, \dots, y_s .

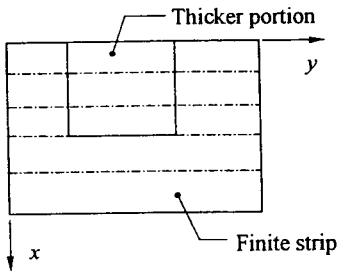


Figure 2: A typical bi-directionally stepped plate divided into finite strips.

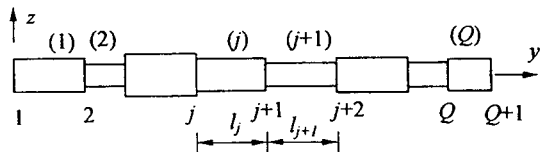


Figure 3: A general stepped beam with abrupt cross-section changes at points $2, 3, \dots, Q$.

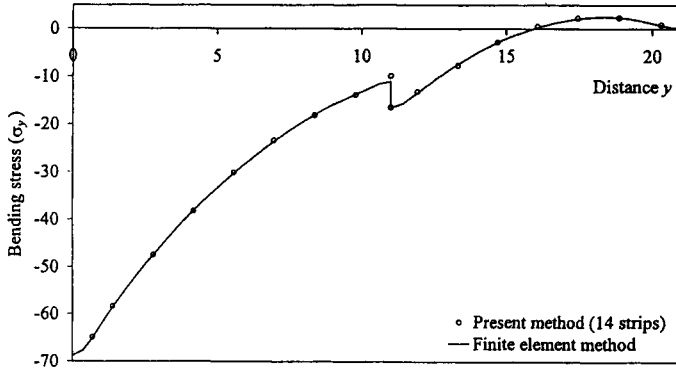


Figure 7. Coupled shear wall with step change in thickness, bending stresses (σ_y) along vertical line at $x=6.75$.

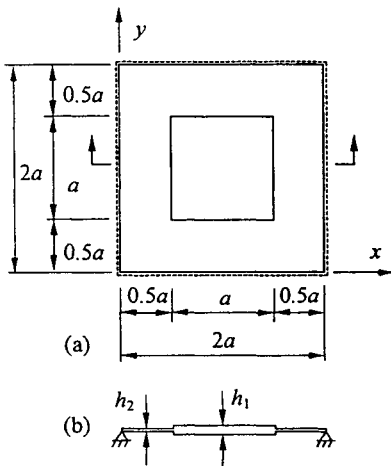


Figure 8: Bi-directionally stepped square plate with all edges simply supported (a) Plan; (b) Section.

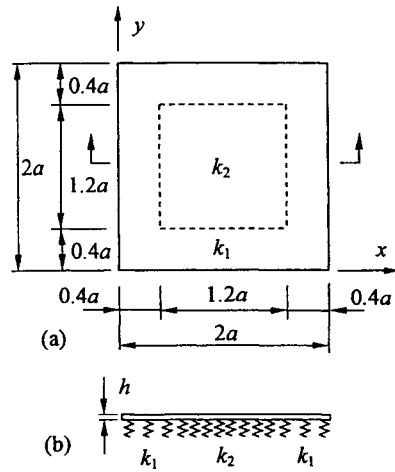


Figure 9: Square plate on non-homogeneous elastic foundation (a) Plan; (b) Section.

Section I

ALUMINIUM

This Page Intentionally Left Blank

BUCKLING OF ALUMINIUM PLATES

M. Langseth¹, O.S. Hopperstad¹ and L. Hanssen²

¹Department of Structural Engineering, Norwegian University of Science and Technology

²SINTEF Materials Technology
N-7034 Trondheim, NORWAY

ABSTRACT

Numerical simulations were carried out to study the behaviour of simply supported internal plate aluminium elements in alloy AA6082 tempers T4 and T6 that were subjected to a combination of axial compression and bending. In the analyses, geometrical imperfections, residual stresses and heat-affected zones due to welding were modelled. It was found that the main effect of welding for temper T6 was related to the softening of the material properties in the heat-affected zone and not the residual stresses set up as a result of welding. Furthermore, the ultimate strength of the plates subjected to combined in-plan loading can be conservatively calculated using linear interaction. A comparison was also made between non-welded plates in tempers T4 and T6 as well as between the present numerical analyses for temper T6 plates, EC9 and BS8118.

KEYWORDS

Aluminium, plate buckling, numerical analyses, design codes.

INTRODUCTION

A common approach in modern design codes for predicting the local buckling strength of thin-walled sections in compression involves the summation of the strength of the individual plate elements using for instance the effective width or the effective thickness approach. There are two generic classes of plate elements in thin-walled sections, namely internal elements supported on both unloaded edges and outstand elements supported on one edge only.

The local buckling strength of such elements in aluminium alloys is related to several factors such as the shape of the stress-strain curve, heat-affected zones and residual stresses due to welding and initial geometrical imperfections. In the new European design code for aluminium structures, EC9 [CEN (1997)], as well as in the British design code, BS8118 [British Standard (1991)], the strength of a plate element is taken care of by an effective thickness approach. Three different design curves are used to capture the different types of behaviour of welded and non-welded heat-treated and non heat-treated

aluminium plates in EC9, while two curves are used in BS8118. In both codes, however, the reduced strength of the material in the heat-affected zones due to welding is taken care of by a separate thickness reduction of the plate element.

In order to assess the European design approaches for internal elements, a non-linear finite element study is presented in this paper. Firstly, a parametric study will be shown where the effect of temper and welding is considered. Secondly, a comparison is made between the present numerical simulations and the design codes. In the simulations, the plates are subjected to a combination of axial compression and bending, and the results are shown for a relative slenderness, λ , in the range 0.5-2.5. The relative slenderness is here defined as the square root of the ratio between the 0.2% proof stress of the material and the elastic buckling stress.

NUMERICAL MODELLING AND VALIDATION

Numerical Modelling

The non-linear finite element simulations were carried out using the general purpose code ABAQUS [Hibbit, Karlsson & Soerensen (1994)].

Figure 1 shows the geometry, loading and support conditions and the finite element mesh of the chosen internal element. Due to symmetry only one half of the plate was modelled using four node shell elements (element S4R5 in ABAQUS) with five integration points through the thickness and one point in the plane of the elements. Several simulations were carried out in order to optimise the number of elements to be used. It was found that 20 elements in the x-direction and 16 elements in the y-direction were sufficient.

A geometric imperfection field was introduced as seven half sine waves in the x-direction of the plate, while a one half sine wave was used in the y-direction. The amplitude was kept constant for all simulations and equal to $\delta_0/b_s = 0.005\text{mm}$. Based on investigations carried out by Mofflin and Dwight (1983), this value was assumed to be an upper bound for geometric imperfections in a welded aluminium plate. The wavelength of the initial geometric imperfections in the x-direction was based on a value, which minimised the ultimate strength of the plates in the whole slenderness range studied. Axial compression gave a value of the wave length parameter, μ , in the range 0.55-0.7, while the corresponding value for pure bending was 0.5. In order to have only one value of the wave length parameter in the simulations, μ was chosen equal to 0.6. It should be mentioned that the corresponding values for the pure elastic buckling of a plate subjected to axial compression and bending are 1.0 and 0.7, respectively.

Table 1 shows the load combinations used in this study. In addition to pure bending and pure axial compression, three combinations of bending and axial compression were investigated. The relative slenderness, λ , was given values in the range 0.5-2.5 for each combination as shown in the table. The buckling factor, k_σ , used to calculate the relative slenderness, λ , is based on the values given in Eurocode 3: Design of steel structures-Part 1-1 [CEN (1992)]. The load was applied by specifying an in-plane displacement of the transverse edges. The longitudinal edges were simply supported and free to pull-in, whereas the transverse edges were simply supported.

The analyses were carried out using material data for AA6082, tempers T4 and T6. The parent material for both tempers was modelled with the Ramberg-Osgood formula with $E = 70000\text{N/mm}^2$. For temper

T4 the $\sigma_{0.2}$ stress and the hardening parameter n was chosen equal to 125 N/mm² and 12.5, respectively. The corresponding values for temper T6 were 250 N/mm² and 25.

The effect of welding was studied for temper T6 only. In the simulations a residual stress field and heat-affected zones were introduced as indicated in Figure 2, using the same width of the tension block as the width of the heat-affected zone. The width of this zone was based on BS8118, as shown in Figure 2, when assuming that the internal plate element was to be the web plate of an aluminium plate girder.

In the heat-affected zones, reduced values of the yield stress and the hardening exponent were defined as $\sigma_{0.2}^* = 125 \text{ N/mm}^2$ and $n^* = 12.5$, i.e. the same as the temper T4 condition. Furthermore, the residual stresses in the tension block were estimated to $\sigma_t^* = 0.75\sigma_{0.2}^*$, which is approximately equal to the proportionality limit of the material in the heat-affected zone. The magnitude of the stresses in the compression block, σ_c^- , was then calculated to give self-equilibrating residual stress fields.

Validation

Numerical simulations are important to assess the behaviour of statically and dynamically loaded structures. Thus, numerical simulations can be used to evaluate new design and materials without extensive testing. However, an essential ingredient in the development and use of numerical models is the validation of the codes by comparison with experimental data.

The non-linear finite element model used in the present study was validated by Hopperstad, Langseth and Hanssen (1998) against tests carried out on outstand and internal elements. The tested outstand elements were of alloy AA6082, tempers T4 and T6 with b_s/t_s -ratios from 10.5 to 30.5 [Hopperstad, Langseth and Tryland (1997)]. The internal elements were validated using tests carried out by Mofflin and Dwight (1983) on alloy 5083 M and 6082 TF with controlled initial out-of-flatness and residual stresses and with b_s/t_s -ratios in the range 20-85.

The investigation showed that the overall correlation between experimental and predicted ultimate compressive strengths for aluminium outstands and internal elements was satisfactory for engineering purposes and within ± 10 -15% both for welded and non-welded plates.

PARAMETRIC STUDY

The results from the parametric study are shown in Figures 3-6. The data in Figures 3-5 is presented as non-dimensional buckling curves where the x- and y-axes represent the relative slenderness (λ) and the non-dimensional stress ($\sigma_{cr}/\sigma_{0.2}$), respectively. The stress σ_{cr} in the figures represents the maximum stress in the plate at ultimate load, and is defined as:

$$\sigma_{cr} = N/A + M/W \quad (1)$$

where

$$N = \int_A \sigma dA, \quad M = \int_A \sigma z dA, \quad A = b_s t_s, \quad W = \frac{1}{6} b_s^2 t_s \quad (2)$$

Here, N and M are defined as stress resultants over the height of the plate.

Figure 3 shows a comparison between a non-welded plate in tempers T4 and T6 subjected to axial compression and bending. In the slenderness range studied the ratio between the non-dimensional stresses for a temper T6 and a temper T4 plate is in the range 1.09-1.12 with the highest value occurring for a relative slenderness equal to 1.0. The corresponding values for pure bending are less and lie in the range 1.02-1.08.

The difference between the curves shown in Figure 3 is related to how the dimensionless axes are chosen. Although in practice this form of non-dimensionalisation is most suitable, it lacks theoretical justification due to the definition of $\sigma_{0.2}$. Complete similarity means that the temper T4 and T6 curves should plot as one curve when they are non-dimensionalised with respect to $\sigma_{0.2}$. As long as this is not the case, no coincidence between T4 and T6 can be expected.

The results shown in Figure 3 for axial compression is coincident with the curves given in EC9. Here the ratio between curve A (non-welded, heat-treated) and curve B (non-welded, non heat-treated) is approximately 1.10 in the whole slenderness range. It should be noted, however, that BS8118 gives only one curve that is independent of the heat treatment of the alloy.

Figure 4 shows a comparison between a welded and a non-welded plate in temper T6. For the welded plates residual stresses and heat-affected zones are included. The welding implies a reduction of the ultimate strength of the plate of 10-15% in the slenderness range studied. The results in Figure 4 do not give the effect of the residual stresses only, which in EC9 and in BS8118 is taken care of by a separate design curve given a 10% reduction compared with a non-welded plate. Figure 5 gives the effect of the residual stresses for a plate with constant axial compression and bending, respectively. The analyses show that for constant axial compression the effect is negligible owing to the fact that the magnitude of the residual stresses is related to the proportionality limit in the heat-affected zone. This means that the compressive stresses are less than 10% of the proof stress of the parent material. Looking at bending, the residual stresses have a positive effect on the ultimate strength of the plate, which is caused by the tensile residual stresses at the outer part of the compression zone. It should be noted that the simulations were carried out with the same initial geometrical imperfection field and amplitude. This might not be strictly correct as a non-welded plate may have imperfections that are different from a welded one. This effect has not been studied separately, and general conclusions therefore cannot be given regarding the effect the residual stresses have on the buckling strength for heat-treated alloys. For non heat-treated alloys such as temper T4, it is believed that the residual stresses will play a more significant role than with heat-treatment, as no material softening is present.

Figure 6 shows typical interaction curves for a simply supported non-welded internal element subjected to a combination of bending and axial compression. The curves are obtained by separating the applied stress field into axial compression (σ_N) and bending (σ_M). The stresses $(\sigma_\sigma)_N$ and $(\sigma_{cr})_M$ in the figure represent the ultimate stress of the plate when subjected to pure axial compression and bending, respectively. For the slenderness range studied, the interaction curves are slightly convex and linear interaction will therefore give a good, conservative estimate of the strength of the plate when subjected to combined in-plan loading. The same result was obtained when introducing welding for the temper T6 plates.

The regulations given in BS8118 are supported by the present findings as a linear interaction formula is given for a plate subjected to axial force and bending. EC9 does not specifically give such recommendations, but handles the plate when it is subjected to a transverse stress gradient with a subsequent thickness reduction in the compression part of the element.

COMPARISON WITH DESIGN CODES

For plates in temper T6 a comparison will be given between the numerical analyses carried out, EC9 and BS8118. As the simulations are a function of the chosen model parameters, they will be used as reference only, and not as measure of the accuracy of the design codes. However, based on the validation studies carried out, representative values of the buckling strength of the plates should be obtained.

Figure 7 shows that the design curves in EC9 and BS8118 for non-welded plates subjected to axial compression give the same ultimate strength in the whole slenderness range. However, compared with the numerical simulations, the design codes overestimate the capacity for compact plates by approximately 10%.

Figure 8 shows the comparison for non-welded plates in bending only. The buckling stress is calculated using Eq. (1), where the moment capacity $M = W_e \sigma_{0.2}$ is obtained by reducing the plate thickness in the compression zone only. Here, W_e is the effective elastic modulus of the section. As can be seen, the BS8118 gives excellent agreement with the simulations except for compact plates. The buckling curves given in EC9 and BS8118 are identical and the difference shown in the figure is related to how the slenderness is defined. In BS8118 the slenderness, β/ϵ , for pure bending of a plate with $\sigma_{0.2} = 250 \text{ N/mm}^2$ is defined as $0.35b_s/t_s$. The corresponding value in EC9 is $0.4b_s/t_s$, which implies a difference between these two design codes of a maximum of 10% in the slenderness range studied.

Figures 9 and 10 give the comparison for welded internal elements. For axial compression only, EC9 overestimates the numerical simulations. The difference between EC9 and BS8118 for compact plates is related to a different extent of the heat-affected zone as well as a different value of the softening factor. Be aware that the properties of the heat-affected zone in the simulations are taken from BS8118. For bending only, the design codes give conservative values of the ultimate strength compared with the numerical simulations. Here, the difference between the design codes is not only related to the heat-affected zone, but also is a function of how the plate slenderness is defined.

CONCLUSIONS

Numerical simulations were carried out to study the behaviour of welded and non-welded aluminium plates in alloy AA6082, tempers T4 and T6. Furthermore, a comparison was made between the numerical simulations, EC9 and BS8118. The following main conclusions can be made based on this study:

- Based on the same geometrical imperfection field, it was found that the main effect of welding on the buckling strength for temper T6 was related to softening of the material properties in the heat-affected zone and not the residual stresses set up as a result of welding. This is in contrast to BS8118 and EC9 where the two design curves are given only to take residual stresses into account. The softening of the material in these design codes is then taken care of by a separate thickness reduction in the heat-affected zone.
- The ultimate strength of internal elements subjected to a combination of axial compression and bending can be found by using linear interaction.
- In general, EC9 and BS8118 give a good estimate of the ultimate strength of a plate in temper T6 compared with the numerical simulations. Of the two design codes considered in this study, the

most conservative one due to bending is EC9. This is caused by a different definition of the plate slenderness in EC9 and BS8118 when subjected to a stress gradient.

- The difference found in the simulations between the ultimate strength of non-welded temper T4 and T6 plates was the same as that given in the design codes.

Acknowledgements

The authors would like to thank Hydro Aluminium a.s. for their generous support of the research project that forms the basis for the present work.

References

British Standard (1991). Structural use of aluminium. Part 1. Code of practice for design.

CEN (1992). Eurocode 3: Design of steel structures. Part 1-1.

CEN (1997). Eurocode 9: Design of aluminium structures. Part 1-1.

Hibbit, Karlsson & Soerensen (1994). ABAQUS Ver. 5.4

Hopperstad O.S., Langseth M. and Tryland T. (1997). Ultimate Strength of Aluminium Alloy Outstands in Compression: Experiments and Simplified Analyses. Accepted for publication in the *Journal of Thin-Walled Structures*.

Hopperstad O.S., Langseth M. and Hanssen L. (1998). Ultimate Compressive Strength of Plate Elements in Aluminium: Correlation of Finite Element Analyses and Tests. Accepted for publication in the *Journal of Thin-Walled Structures*.

Mofflin D.S. and Dwight J.B. (1983). Tests on Individual Aluminium Plates Under In-Plane Compression. Univ. of Cambridge, Tech. Rep. No. CUED/D-Struct/TR. 100.

TABLE 1
LOAD COMBINATIONS

Load combinations	$\psi = \sigma_2 / \sigma_1$	k_ψ	λ
Axial compression	1.000	4.0	} 0.50 0.75 1.00 1.25 1.50 1.75 2.00 2.25 2.50
Axial compression and bending	-0.143	6.8	
" "	-0.200	9.3	
" "	-0.385	11.5	
Bending	-1.000	23.9	
$\lambda = 1.04 \frac{b_s}{t_s} \frac{1}{\sqrt{k_\psi}} \sqrt{\frac{\sigma_{0.2}}{E}}$		$k_\psi = \begin{cases} 8.4 / (\psi + 1.1) & 0 < \psi < -1 \\ 7.63 - 6.27\psi + 10\psi^2 & -1 < \psi < 0 \end{cases}$	

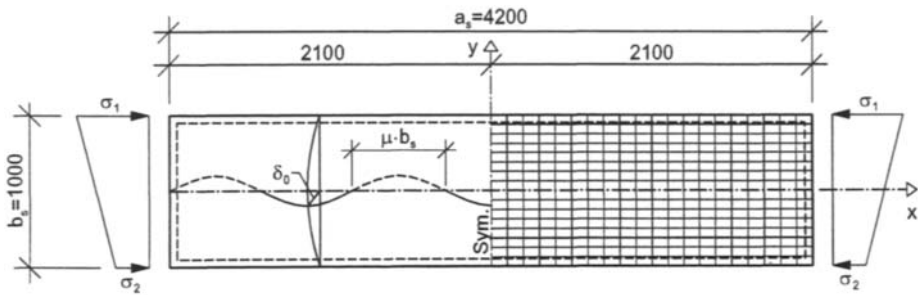


Figure 1: Geometry, loading and support conditions and finite element mesh

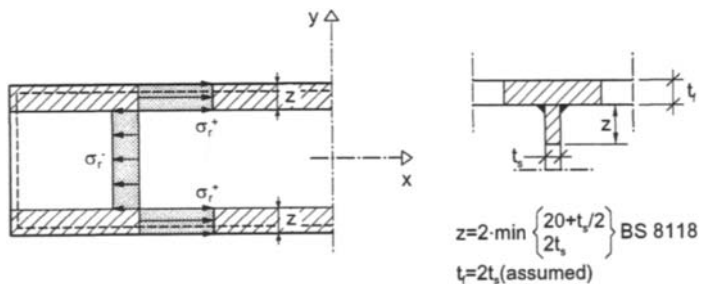


Figure 2: Heat-affected zone and residual stresses

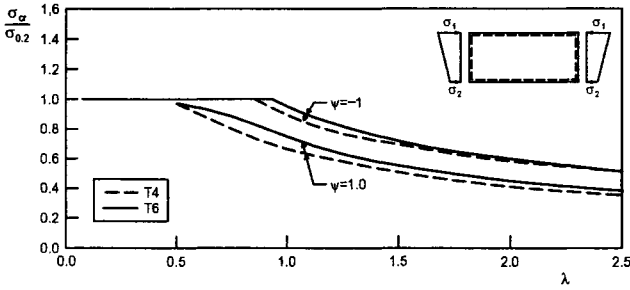


Figure 3: Comparison between a temper T4 and a temper T6 plate.

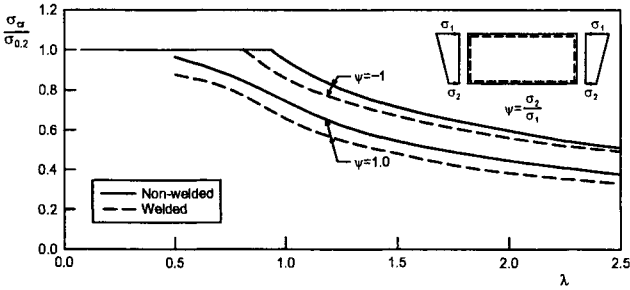


Figure 4: Comparison between welded and non-welded plate. Temper T6.

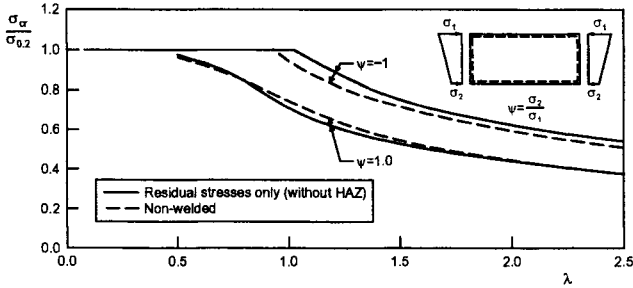


Figure 5: Effect of residual stresses. Temper T6.

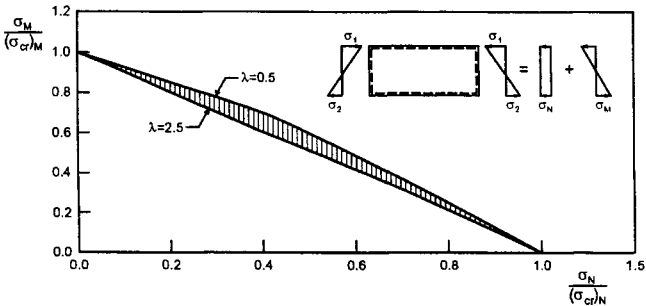


Figure 6: Interaction between axial compression and bending, non-welded. Tempers T4 and T6.

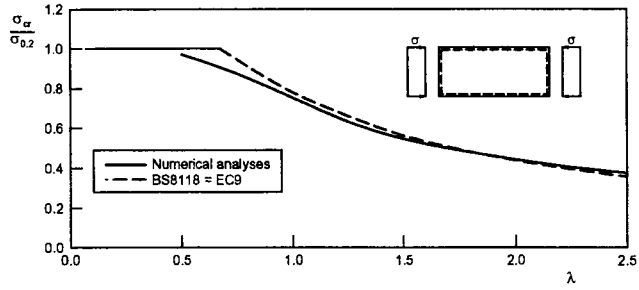


Figure 7: Axial compression, non-welded.

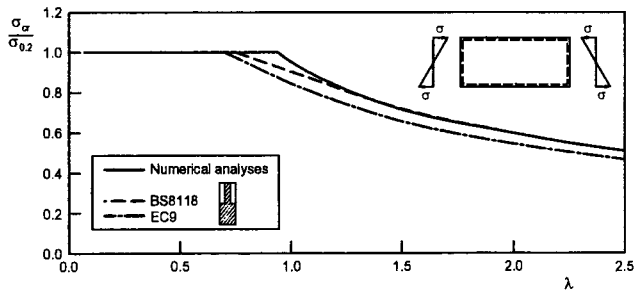


Figure 8: Bending, non-welded.

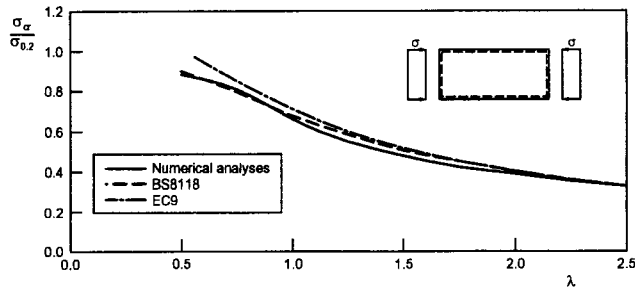


Figure 9: Axial compression, welded.

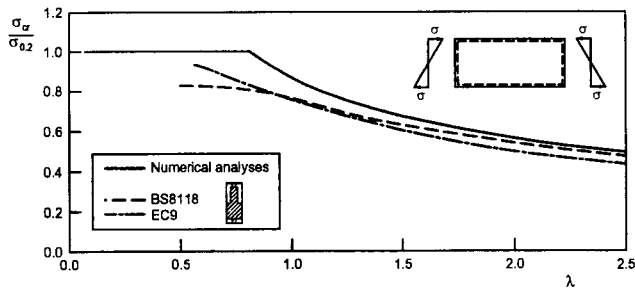


Figure 10: Bending, welded.

This Page Intentionally Left Blank

SHEAR STRENGTH OF WELDED ALUMINIUM PLATE GIRDERS

A. Bhogal and A. W. Davies

Cardiff School of Engineering, University of Wales Cardiff,
P O Box 686, CF2 3TB, Cardiff, UK

ABSTRACT

Experimental studies of the ultimate shear resistance of welded aluminium alloy plate girders have indicated that at failure, the girders exhibit shear sway characteristics, diagonal buckling of the web and development of plastic hinges within the flanges. Failure generally occurs due to rupture of the heat affected web boundary, during the development of a typical shear failure mechanism. Theoretical procedures for predicting ultimate shear resistance, based on tension-field theory and including material strength reduction factors to allow for welding, are now incorporated in BS8118, Part 1, Structural use of aluminium. However, when compared with available test data, theoretical predictions in accordance with BS8118 appear unduly conservative. Available test results for the ultimate shear resistance of welded aluminium alloy plate girders are reviewed and discussed. An improved theoretical procedure for predicting ultimate shear resistance, similar to that incorporated in BS8118 but retain the rigour of the original tension-field theory, is presented which shows consistent and significantly improved correlation with the test data.

KEYWORDS

Welded aluminium girders, Codes of practice and standards, Design methods and aids, Shear strength

INTRODUCTION

Aluminium alloys are used in a variety of structural engineering applications due to their high strength to weight ratio. These characteristics are of particular significance in the design of lightweight and transportable bridges, for which ease and speed of construction, low maintenance and long service life are important considerations (Swan 1997).¹ However, the heat of welding reduces the strength of aluminium alloys in the vicinity of the weld. The heat affected zone (HAZ) extends, within the parent metal, approximately 25mm in all directions from the weld.

The ultimate shear resistance of steel plate girders has been studied extensively, both experimentally and theoretically, resulting in the development of the now well established Cardiff tension-field theory (Porter *et al* 1975). Experimental studies of the ultimate shear resistance of welded aluminium alloy plate girder by Rockey and Evans (1980), Evans and Burt (1990) and Lee (1994) have indicated that at failure, the girders exhibit shear sway characteristics, diagonal buckling of the web and development of plastic hinges within the flanges. Failure occurs due to fracture within the

heat affected weld boundary during the formation of a typical shear sway mechanism (Evans and Lee, 1995).

To allow for the reduction in material strength due to welding, Evans and Burt (1990) and Lee (1994) incorporated a material softening factor k_z in the Cardiff tension-field theory to predict the ultimate shear resistance of aluminium alloy plate girders. It was argued that since the tension-field must pass through the welded web boundary to anchor onto the boundary members, the material softening factor should be applied to all components of shear resistance i.e. web and flange components, except the buckling resistance. This recommendation was subsequently incorporated in BS8118, Part 1, Structural use of aluminium (1991). BS8118 also recommends that the allowable yield stress in the HAZ be taken as $k_z \sigma_y$, where σ_y is the yield stress of the parent material and k_z is equal to 0.5 and 0.6 respectively for 6000 and 7000 series aluminium alloys.

ULTIMATE SHEAR RESISTANCE OF ALUMINUM ALLOY PLATE GIRDERS

Original Cardiff tension-field theory

Theoretical predictions of the ultimate shear resistance of slender plate steel girders can be made using the well established Cardiff tension-field theory (Porter *et al* 1975). The steel theory is based on an assumed equilibrium stress field (tension-field) in the girder, which satisfies the theoretical conditions for a lower bound strength prediction, provided the material possesses sufficient ductility for the stress field to develop. For the assumed failure mechanism, the ultimate shear resistance V_S of a transversely stiffened girder can be expressed as

$$V_S = \tau_{cr} dt + \sigma_t^y t \sin^2 \theta \left(d \cot \theta - b + \frac{c_c}{2} + \frac{c_t}{2} \right) + \frac{2M_{pfc}}{c_c} + \frac{2M_{pft}}{c_t} \quad (1)$$

τ_{cr} is the critical or buckling shear stress of the web panel, σ_t^y is the web tension-field stress developed in the post-buckling stage, d is the depth of the web and t is the web thickness. M_{pfc} and M_{pft} are the plastic moments of the compression and tension flanges and c_c and c_t are the distances at which plastic hinges form in the flanges. The buckling shear stress τ_{cr} is given by

$$\tau_{cr} = k_b \frac{\pi^2 E}{12(1 - \nu^2)} \left(\frac{t}{d} \right)^2 \quad (2)$$

where k_b is the buckling coefficient for a simply supported plate given by

$$k_b = 5.35 + 4(d/b)^2 \quad (\text{for } b/d \geq 1) \quad (3)$$

$$k_b = 5.35(d/b)^2 + 4 \quad (\text{for } b/d < 1) \quad (4)$$

Other terms in Eqn. 1 are given by

$$\sigma_t^y = \frac{-3}{2} \tau_{cr} \sin 2\theta + \sqrt{\left\{ \sigma_{yw}^2 + \tau_{cr} \left[\left(\frac{3}{2} \sin 2\theta \right)^2 - 3 \right] \right\}} \quad (5)$$

$$c_c = \frac{2}{\sin \theta} \sqrt{\frac{M_{pfc}}{\sigma_t^y t}} \quad (6)$$

$$c_t = \frac{2}{\sin \theta} \sqrt{\frac{M_{pft}}{\sigma_t^y t}} \quad (7)$$

σ_{yw} is the yield strength of the web material and θ is the angle of inclination of the web tension field σ_t^y which can be determined by iteration to give the maximum value of V_S or approximated as

$$\theta = \frac{2}{3} \tan^{-1} \left(\frac{d}{b} \right) \quad (8)$$

Modified Cardiff tension-field theory for aluminium girders – Evans and Burt

During the fabrication of aluminium alloy plate girders heat from the welding process reduces the material strength in the vicinity of the welds. Evans and Burt (1990) and Lee (1994) modified the Cardiff tension-field theory by incorporating a material softening factor k_z to compensate for this reduction in strength. Since buckling resistance depends on the stiffness of the web plate, it was argued that the web buckling resistance would not be affected by the reduction in material strength along the web boundary. The ultimate shear resistance V_{EB} proposed by Evans and Burt can be expressed as

$$V_{EB} = \tau_{cr} dt + \left\{ \sigma_t^y t \sin^2 \theta \left(d \cot \theta - b + \frac{c_c}{2} + \frac{c_t}{2} \right) + \frac{2M_{pfc}}{c_c} + \frac{2M_{pft}}{c_t} \right\} k_z \quad (9)$$

in which k_z is defined as

$$k_z = \frac{\sigma_{0.2w}^r}{\sigma_{0.2w}} \quad (10)$$

where $\sigma_{0.2w}^r$ and $\sigma_{0.2w}$ are the 0.2% proof stresses of the web material in the HAZ and the parent material respectively. The design procedure incorporated BS8118 (1991) is based on the modification of the Cardiff tension-field theory proposed by Evans and Burt (1990). The code also introduces a partial material safety factor $\gamma_m=1.2$ in the calculation of the ultimate shear resistance V_{RS} , which is expressed as

$$V_{RS} = \frac{V_{EB}}{\gamma_m} \quad (11)$$

Proposed design method

The proposed design method differs from the modified Cardiff tension-field theory proposed by Evans and Burt (1990), in that the influence of the reduction in material strength due to welding is not taken as having a uniform effect on the post-buckling shear resistance provided by the web and flanges. The HAZ is limited to a small region in the vicinity of welds, the extent of which can be determined according to the recommendations of BS8118. Since the assumed web tension-field stress σ_t^y has to pass through these regions, σ_t^y is now calculated using the reduced material strength in the HAZ equal to $k_z \sigma_{0.2w}$. Eqn. (5) may then be rewritten as

$$\sigma_t^{yF} = \frac{-3}{2} \tau_{cr} \sin 2\theta + \sqrt{\left\{ \left(k_z \sigma_{0.2w} \right)^2 + \tau_{cr} \left[\left(\frac{3}{2} \sin 2\theta \right)^2 - 3 \right] \right\}} \quad (12)$$

where σ_t^{yF} is the reduced web tension-field stress required to produce yielding in the HAZ. The ultimate shear resistance of an aluminium alloy plate girder V_A can be obtained from Eqn. (1) by substituting σ_t^y in Eqn. (5) by σ_t^{yF} in Eqn. (12)

EXPERIMENTAL RESULTS

Extensive experimental studies have been conducted in Cardiff on the ultimate shear resistance of aluminium alloy plate girders, a summary of which has been presented by Evans and Lee (1995). Tests were conducted on girders fabricated from 6082 and 7019 aluminium alloys, having both transverse and longitudinal stiffeners. A summary of the tests conducted on transversely stiffened 6000 and 7000 series aluminium alloy plate girders, subjected to predominantly shear loading, is presented in Tables 1 and 2.

TABLE 1
DETAILS OF 6000 SERIES ALUMINIUM ALLOY TEST GIRDERS AND TEST RESULTS

Test	Girder/test reference	b (mm)	d (mm)	t _w (mm)	b _f (mm)	t _f (mm)	M _{pf} (Nmm)	E (kN/mm ²)	σ _{yw} (N/mm ²)	σ _{yf} (N/mm ²)	V _{exp} (kN)
1	AG1	669	455	1.60	101	9.6	698112	69.5	283	300	56.3
2	AG2	671	455	1.21	101	9.6	700439	69.3	260	301	41.4
3	AG3	672	456	1.21	102	6.5	307052	68.1	259	285	33.9
4	AG4	669	455	1.64	101	6.5	305108	67.8	285	286	52.3
5	AG5	667	457	1.61	101	12.6	1182564	67.5	287	295	69.3
6	AGS1-T1	442	454	1.20	102	6.3	241891	71.5	279	239	47.0
7	AGS2-T1	218	456	1.20	104	6.3	246634	71.5	252	239	62.0
8	AGS2-T2	218	456	1.20	104	6.3	246634	71.5	252	239	63.5
9	AGS3-T2	218	456	1.20	103	6.3	244262	71.5	252	239	59.0
10	AGS4-T1	218	456	1.20	104	6.3	246634	71.5	252	239	60.5
11	AGS5-T1	144	455	1.20	102	6.3	241891	71.5	245	239	62.0
12	AGS5-T2	143	455	1.20	102	6.3	241891	71.5	245	239	68.5
13	AGCS1-T1	219	455	1.20	102	6.4	289321	71.5	268	277	57.7
14	AGCS1-T2	215	455	1.20	102	6.4	289321	67.5	268	277	59.7
15	AGCS2-T1	218	454	1.20	102	6.4	289321	67.5	268	277	61.7
16	AGCS2-T2	216	454	1.20	102	6.4	289321	67.5	268	277	61.8
17	AGCS3-T1	219	455	1.20	103	6.4	292157	67.5	268	277	56.7
18	AGCS3-T2	216	455	1.20	103	6.4	292157	67.5	268	277	60.6
19	A6G72s-2	444	898	3.20	174	12.7	2182012	68.4	287	311	330.0
20	TAG1	900	900	3.02	175	12.8	2190530	70.0	303	308	277.5

1-5 (Rockey and Evans,1980), 6-12 (Hamoodi 1983), 13-19 (Seah 1984), 20 (Newark 1997)

TABLE 2
DETAILS OF 7000 SERIES ALUMINIUM ALLOY TEST GIRDERS AND TEST RESULTS

Test	Girder/test reference	b (mm)	d (mm)	t _w (mm)	b _f (mm)	t _f (mm)	M _{pf} (Nmm)	E (kN/mm ²)	σ _{yw} (N/mm ²)	σ _{yf} (N/mm ²)	V _{exp} (kN)
1	A7G1	943	602	3.20	115	12.9	1469255	75.2	344	307	185.3
2	A7G2	624	602	3.20	105	10.1	822341	75.2	344	307	234.2
3	A7G3	478	601	3.20	209	9.5	1448149	75.2	344	307	285.9
4	A7G4	304	601	3.20	125	12.9	1597016	75.2	344	307	454.9
5	A7G5	201	602	3.20	90	15.9	1746854	75.2	344	307	447.9
6	A7G6	302	317	3.20	138	6.1	394238	75.2	344	307	192.3
7	A7G7	885	894	3.20	175	12.9	2235822	75.2	344	307	298.9
8	A7G8	1039	1052	3.20	222	16	4379654	75.2	344	307	360.7
9	A7G9	624	603	3.20	130	9.6	919826	75.2	344	307	236.2
10	A7G10	626	602	3.20	116	15.9	2251501	75.2	344	307	236.2
11	A7G11	624	602	3.20	165	18.7	4429829	75.2	344	307	254.2
12	Lee	662	885	6.17	*	*	55321000†	67.9	325	374	1186.0
13	Bhogal	1280	885	6.17	*	*	53398000†	66.6	359	361	934.0
14	AG7/1-T2	899	898	3.20	175	12.8	2637824	71.7	383	368	334.0

1-11 (Burt 1987), 12 (Lee and Davies 1995), 13 (Bhogal *et al* 1997), 14 (Evans and Lee 1995)

* non-rectangular flanges

† compression flange plastic moment

COMPARISON OF EXPERIMENTAL AND THEORETICAL RESULTS

Theoretical predictions of ultimate shear resistance are compared with experimental values in Tables 3 and 4 and in Figures 1 and 2. Theoretical predictions were determined in accordance with:

- original tension-field theory with no allowance for material softening (V_S)
- modified tension-field theory with the allowance for material softening proposed by Evans and Burt (V_{EB})
- the proposed design method (V_A)

All the theoretical predictions are based on measured material properties with k_z assumed equal to 0.5 and 0.6 respectively for 6000 and 7000 series aluminium alloys. The modified tension-field theory of Evans and Burt (V_{EB}) corresponds to the BS8118 design procedure (V_{RS}) when the partial material safety factor in Eqn. 11, $\gamma_m = 1.0$.

In general the original tension-field theory (V_S) with no allowance for material softening overestimates the shear resistance of aluminium alloy plate girders, with many values of V_{exp}/V_S , below unity. Mean values of V_{exp}/V_S are 0.91 and 1.09, with corresponding standard deviations of 0.07 and 0.12 respectively for the 6000 series and 7000 series alloys. The modified tension-field theory proposed by Evans and Burt (V_{EB}) provides inconsistent and unduly conservative predictions of the ultimate shear resistance, with several values of V_{exp}/V_{EB} greater than two. The mean values for the 6000 and 7000 series aluminium alloys are 1.97 and 1.92 respectively with corresponding standard deviations of 0.26 and 0.27.

Results for the proposed design method (V_A) are more consistent and less conservative. Mean values of the ratio V_{exp}/V_A are 1.53 and 1.55 respectively for the 6000 and 7000 series aluminium alloy girders, with corresponding standard deviations of 0.11 and 0.17. These values indicate a lower bound characteristics strength prediction ratio V_{exp}/V_A (mean minus two standard deviations) of

approximately 1.2, which in view of the sudden and catastrophic mode of failure (rupture of the heat affected zone) is considered satisfactory for the purpose of design.

TABLE 3
COMPARISON OF EXPERIMENTAL AND THEORETICAL RESULTS FOR 6000 SERIES ALUMINIUM ALLOY
PLATE GIRDERS

Test	Girder/test reference	V_{exp} (kN)	V_{exp}/V_S	V_{exp}/V_{EB}	V_{exp}/V_A
1	AG1	56.3	0.95	2.23	1.53
2	AG2	41.4	0.94	2.38	1.50
3	AG3	33.9	0.94	2.17	1.56
4	AG4	52.3	1.01	2.17	1.68
5	AG5	69.3	1.01	2.50	1.58
6	AGS1-T1	47.0	0.96	2.16	1.63
7	AGS2-T1	62.0	0.94	1.96	1.60
8	AGS2-T2	63.5	0.96	2.00	1.64
9	AGS3-T2	59.0	0.89	1.86	1.53
10	AGS4-T1	60.5	0.91	1.91	1.56
11	AGS5-T1	62.0	0.82	1.56	1.41
12	AGS5-T2	68.5	0.91	1.71	1.56
13	AGCS1-T1	57.7	0.82	1.74	1.39
14	AGCS1-T2	59.7	0.84	1.78	1.43
15	AGCS2-T1	61.7	0.87	1.86	1.49
16	AGCS2-T2	61.8	0.87	1.85	1.48
17	AGCS3-T1	56.7	0.80	1.71	1.36
18	AGCS3-T2	60.6	0.85	1.81	1.45
19	A6G72s-2	330.0	0.86	1.66	1.46
20	TAG1	277.5	1.08	2.33	1.83
Mean			0.91	1.97	1.53
Standard Deviation			0.07	0.26	0.11

TABLE 4
COMPARISON OF EXPERIMENTAL AND THEORETICAL RESULTS FOR 7000 SERIES ALUMINIUM ALLOY
PLATE GIRDERS

Test	Girder/test reference	V_{exp} (kN)	V_{exp}/V_S	V_{exp}/V_{EB}	V_{exp}/V_A
1	A7G1	185.3	1.10	1.92	1.55
2	A7G2	234.2	1.13	1.89	1.64
3	A7G3	285.9	1.08	4.84	1.56
4	A7G4	454.9	1.33	2.09	1.93
5	A7G5	447.9	1.08	1.47	1.54
6	A7G6	192.3	1.21	1.67	1.60
7	A7G7	298.9	0.98	1.78	1.46
8	A7G8	360.7	0.97	1.84	1.43
9	A7G9	236.2	1.12	1.89	1.63
10	A7G10	236.2	0.98	1.78	1.40
11	A7G11	254.2	1.28	2.48	1.79
12	Lee	1186.0	0.94	1.92	1.28
13	Bhogal	934.0	1.04	2.46	1.34
14	AG7/1-T2	334.0	0.99	1.82	1.48
Mean			1.09	1.92	1.55
Standard Deviation			0.12	0.27	0.17

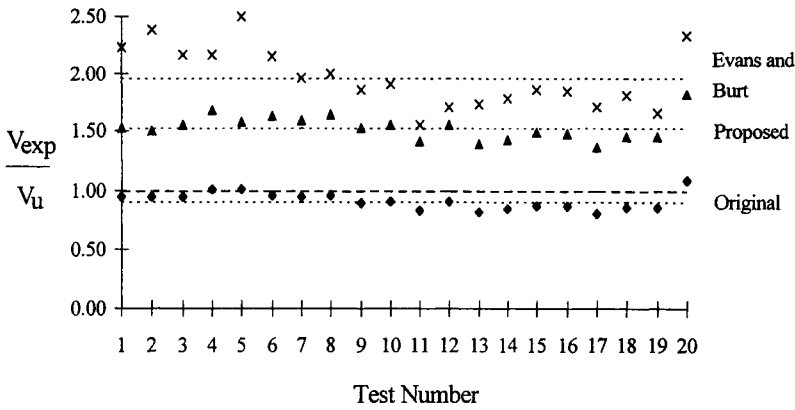


Figure 1: Comparison of experimental and theoretical results for the 6000 series girders

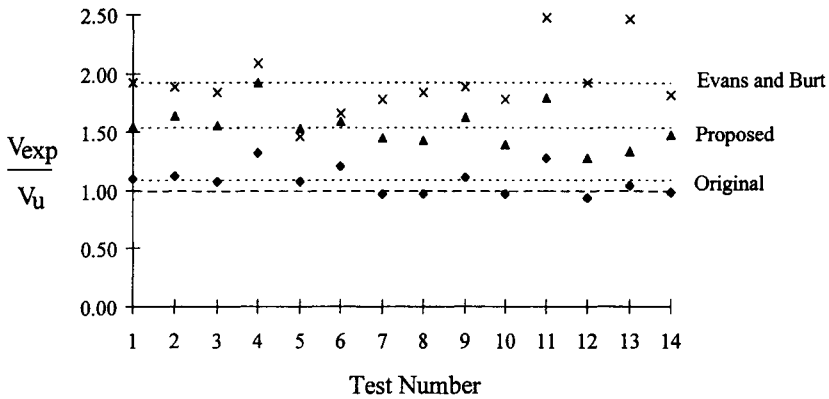


Figure 2: Comparison of experimental and theoretical results for the 7000 series girders

SUMMARY AND CONCLUSIONS

Aluminium alloy plate girders subjected to predominantly shear loading have indicated that at failure, the girders exhibit shear sway characteristics, diagonal buckling of the web and development of plastic hinges within the flanges. Failure occurs due to rupture of the heat affected zone during the formation of a typical shear failure mechanism.

Theoretical predictions of shear resistance based on the original tension-field theory, with no allowance for material softening, are generally unsafe. Theoretical predictions based on the modified tension-field theory proposed by Evans and Burt, which forms the basis of the design procedure in

BS8118, are inconsistent and unduly conservative. Theoretical predictions based on the proposed design method are more consistent and far less conservative. The proposed method will enable the design of more efficient and economical aluminium alloy plate girders while still maintaining a reasonable level of safety.

ACKNOWLEDGEMENTS

The studies reported were supported by the Defence Research Agency, Chertsey, UK. Thanks are extended to Dr T.M. Roberts for his helpful advice.

REFERENCES

Bhogal A., Davies A.W. and Roberts T.M. (1997). Performance testing of full size transportable bridge girders. Research report, Research agreement CB/CEN/94/2072/079-amendment 3, University of Wales, Cardiff.

BS8118 (1991). Part 1, Structural use of aluminium. British Standards Institute.

Burt C.A. (1987). The ultimate strength of aluminium plate girders. University of Wales College of Cardiff, PhD thesis.

Evans H.R. and Burt C.A. (1990). Ultimate load determination for welded aluminium plate girders. Aluminium structures: Advances Design and Construction. Elsevier applied science, London, 70-80.

Evans H.R. and Lee A.Y.N. (1995). An appraisal, by comparison with experimental data, of new design procedures for aluminium plate girders. *Proc. Instn. Civ. Engrs, Structures and Buildings*, **110, Feb**, 34-49.

Hamoodi M.J. (1983). The behaviour of reinforced aluminium plate girders in shear loading. University of Wales College of Cardiff, MSc thesis.

Lee A.Y.N. (1994). Collapse behaviour of aluminium girders. University of Wales Cardiff, PhD Thesis.

Lee A.Y.N. and Davies A.W. (1995). Shear strength of an AL-Zn-Mg (7019) aluminium alloy girder panel. Research report CAR/DRA/TEST3, Research agreement CB/CEN/94/2072/079, University of Wales Cardiff.

Newark A.C.B. (1997). Strength of tapered web aluminium plate girders under shear and patch loading. University of Wales college of Cardiff, PhD thesis.

Porter D.M., Rockey K.C. and Evans H.R. (1975). The collapse behaviour of plate girders loaded in shear. *The Structural Engineer*, **August**, 313-326.

Rockey K.C. and Evans H.R. (1980). An experimental study of the ultimate load capacity of welded aluminium plate girders loaded in shear. Research report, University of Wales College of Cardiff.

Seah M.H. (1984). The behaviour of welded aluminium alloy plate girders reinforced with carbon fibre reinforced plastic. University of Wales College of Cardiff, MSc thesis.

Swan R. (1997). The light touch. *Bridge design and engineering No. 8*, 57-59.

STRENGTH OF ALUMINIUM EXTRUSIONS UNDER COMPRESSION AND BENDING

O.S. Hopperstad, M. Langseth & L. Moen

Department of Structural Engineering, Norwegian University of Science
and Technology, N-7034 Trondheim, NORWAY

ABSTRACT

The ultimate strength of thin-walled aluminium alloy sections subjected to uniform compression and moment-gradient loading is investigated experimentally. Square and rectangular hollow sections and I-sections of alloy 6082 in tempers T4 and T6 and alloy 7108 in temper T7 are tested. The results from 32 different tests are presented, varying cross sectional geometry, alloy and temper, and loading conditions. Since extruded aluminium alloys have mechanical anisotropy owing to the manufacturing process, results from uniaxial tensile tests carried out to determine the variation of the flow stress and the R-value with respect to the tensile direction are also presented. The experimental compressive and bending strengths of the sections are compared with the specifications in EC9. In general, good correlation between test results and EC9 is obtained.

KEYWORDS

Aluminium alloys, extrusions, experiments, plastic anisotropy, compressive strength, bending strength

INTRODUCTION

The failure mode of an extrusion subjected to compression and bending actions is governed by the slenderness of the cross sectional parts and the ductility of the material. For a compact extrusion the ultimate capacity is limited by ductility requirements, while for an extrusion with a slender cross section local buckling determines the capacity. In the new European design code for aluminium structures, EC9 (CEN, 1997), a cross section is classified into one of four classes according to the slenderness of the compressed parts and the 0.2 % proof stress of the alloy.

This method has proved an efficient way of classifying steel beams, which are characterised by a yield plateau and high material ductility. When adopting this method for aluminium beams, two questions should first be addressed. First, is the material ductility always sufficient to avoid premature tensile failure? Second, how do the different mechanical properties of extruded aluminium beams, e.g. strain hardening and plastic anisotropy, affect the response of thin-walled sections in compression?

In this study, the ultimate strength of aluminium extrusions in compression and bending is obtained from laboratory experiments, and the experimental results are compared with the design rules provided in EC9. Different alloys, tempers and cross sections were tested, and for each combination of these parameters the mechanical properties were determined from uniaxial tensile tests. In some cases, also the anisotropy of the mechanical properties was investigated.

EXPERIMENTAL DETAILS

The experimental programme consists of compression and bending tests of square hollow sections (SHS), rectangular hollow sections (RHS) and I-sections. The test programme is compiled in Table 1, giving test number, alloy and temper, loading conditions and measured dimensions of the specimens.

Figure 1a shows the static systems of the compression and bending tests, while the measured dimensions of the cross sections are defined in Figure 1b. The experiments were performed in quasi-static loading conditions and at room temperature, measuring load and displacement at the loading point. In the bending tests, also the support rotations were measured. It is referred to Dolven and Drage (1997) and Moen et al (1998) for detailed reports on the compression and bending tests, respectively.

MECHANICAL PROPERTIES

Extruded aluminium sections may have relatively strong mechanical anisotropy due to the manufacturing process. Prior studies have shown that the flow stress and the R-value, i.e. the ratio of the width to thickness plastic strain, may vary significantly in uniaxial tensile tests in different directions with respect to the extrusion direction, Lademo et al (1998). Tensile test results obtained for the alloys 7108 T1 and T5 and 6063 T1 are shown in Figure 2. The proportional limit stress Y (stress at 0.01 % offset strain) and the R-value vary significantly for both alloys, but the variation is completely different for 7108 and 6063, respectively. This is due to texture differences in the two alloys. Tempers T1 and T5 of alloy 7108 exhibit similar directional variations, but the anisotropy effect is stronger for temper T1 than for temper T5, e.g. the ratio Y_{45}/Y_0 is 0.73 for 7108-T1 and 0.84 for 7108-T5.

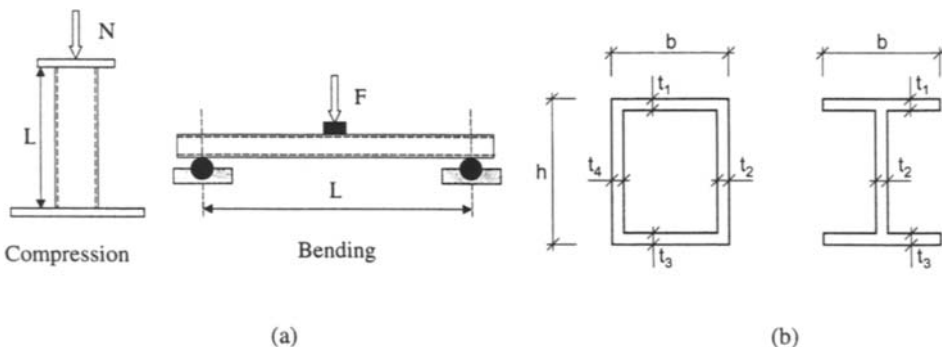


Figure 1: Experimental details. (a) Schematic set-up for compression and bending tests. (b) Geometry of SHS, RHS and I-sections in Table 1.

TABLE 1
SECTION DESIGNATIONS AND GEOMETRICAL DATA

Section	Alloy & Temper	Loading	Measured Cross Sectional Dimensions (mm)						
			t ₁	t ₂	t ₃	t ₄	h	b	L
SHS-01-C	6082-T6	Comp.	5.95	5.99	5.91	5.90	100.4	99.3	376.3
SHS-02-C	6082-T4	"	5.93	5.98	5.90	5.86	100.4	99.1	376.9
SHS-03-C	7108-T7	"	5.89	5.91	5.94	6.04	100.1	99.9	376.0
SHS-04-C	7108-T7	"	3.76	3.63	3.91	3.62	102.3	102.6	383.8
SHS-05-C	6082-T6	"	2.84	2.87	2.80	2.86	99.5	99.5	387.7
SHS-06-C	6082-T4	"	2.78	2.85	2.82	2.84	98.9	99.9	388.0
SHS-07-C	6082-T6	"	1.91	1.95	1.95	1.96	99.5	99.5	392.0
SHS-08-C	6082-T4	"	1.98	1.90	1.98	1.96	99.6	99.6	392.2
SHS-09-C	6082-T4	"	1.45	1.48	1.44	1.42	100.4	100.4	393.8
SHS-10-C	6082-T4	"	2.46	2.46	2.48	2.50	80.1	80.1	310.0
SHS-11-C	6082-T4	"	2.05	2.02	2.06	2.05	80.3	80.2	310.1
RHS-01-C	6082-T6	"	2.11	2.60	2.89	2.30	119.5	60.8	470.5
RHS-02-C	6082-T6	"	2.93	2.99	3.03	2.89	99.1	61.0	387.9
I-01-C	6082-T6	"	7.96	5.08	7.94	—	119.8	119.9	447.3
I-02-C	6082-T6	"	4.97	4.97	4.96	—	79.9	69.8	260.0
SHS-01-B	6082-T6	Bending	5.94	5.88	5.94	5.89	100.3	99.6	L
SHS-02-B	6082-T4	"	5.95	5.86	5.95	5.89	100.0	100.0	L
SHS-03-B	6082-T4	"	2.90	2.85	2.88	2.81	99.7	100.0	L
SHS-04-B	7108-T7	"	5.94	6.03	5.94	5.93	100.0	100.1	L
RHS-01-B	6082-T6	"	2.55	2.89	2.03	2.27	119.4	60.0	L
RHS-02-B	6082-T6	"	2.97	3.01	2.91	2.86	100.0	60.1	L
I-01-B	6082-T6	"	7.98	5.09	7.93	—	120.2	119.9	L
I-02-B	6082-T6	"	4.95	4.97	4.93	—	80.35	70.0	L

Notes: Measured dimensions refer to Figure 1b.
L is equal to 1000 mm, 2000 mm and 3000 mm in bending tests

In order to determine the stress-strain behaviour of the sections tested in compression and bending, uniaxial tensile tests in the extrusion direction were performed for all sections. Typical engineering stress vs. displacement curves and true stress-strain curves for the alloys are shown in Figure 3. It is evident that the alloys 6082-T4, 6082-T6 and 7108-T7 have different mechanical properties with respect to strength and ductility. Alloy 6082-T4 has low yield strength, but exhibits strong strain hardening and high ductility. Alloys 6082-T6 and 7108-T7 have high strength, but are significantly less ductile than 6082-T4.

The mechanical characteristics of the SHS, RHS and I-sections are given in Table 2 in terms of elastic modulus E , yield strength f_{02} and ultimate strength f_u and strain at ultimate strength ϵ_u . For some of the sections the true stress vs. true plastic strain curve was fitted to the relation

$$\sigma = Y_0 + \sum_{k=1}^2 Q_k (1 - \exp(-C_k \epsilon_p)) \quad (1)$$

where σ is the true stress, ϵ_p is the true plastic strain, Y_0 is the proportional limit stress, and Q_k and C_k are model constants. The results are given in Table 3. The model gives a good fit to the experimental behaviour, and is useful as input in numerical simulations.

The mechanical anisotropy of the extrusions tested in three-point bending was studied by conducting uniaxial tensile tests with different angles between the tensile and extrusion directions, Moen et al (1998). The location and geometry of the tensile test specimens are illustrated in Figure 4. The angle α between the tensile axis of the specimens and the extrusion direction is 0° , 45° and 90° , respectively. The test results are compiled in Table 4. The R-values were calculated based on the specimen width and thickness as measured in a uniform section before loading and after fracture. The alloys display significant anisotropy in the proportional limit stress Y_α , but the effect is more severe for the R-value. In the extrusion direction, the R-value is 0.3-0.4 and thus significantly less than one, which is expected for an isotropic material.

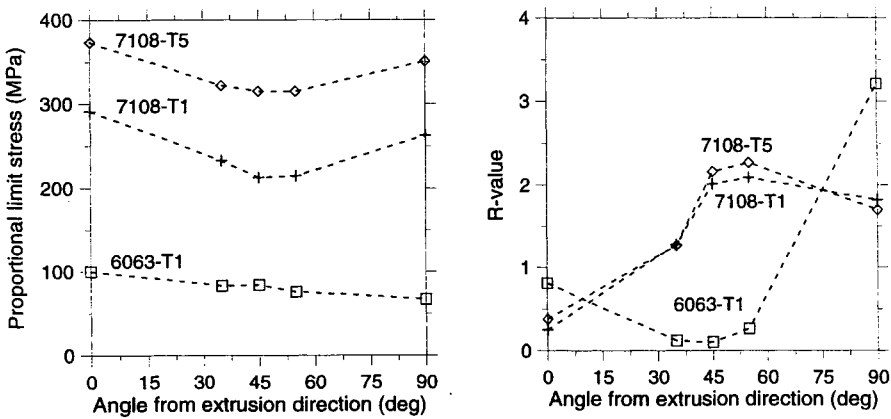


Figure 2: Proportional limit stress and R-value for various tensile directions with respect to the extrusion direction, Lademo et al (1998)

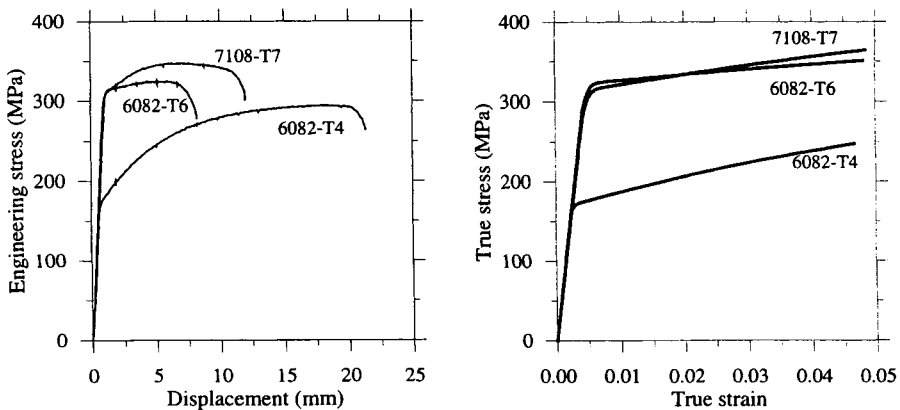


Figure 3: Typical uniaxial tensile behaviour of the investigated alloys, Moen et al (1998)

TABLE 2
UNIAXIAL MATERIAL PROPERTIES

Section	Alloy & Temper	E (MPa)	f_{02} (MPa)	f_u (MPa)	ϵ_u (%)
SHS-01-C	6082-T6	70129	312.1	325.2	—
SHS-02-C	6082-T4	72944	178.7	292.7	—
SHS-03-C	7108-T7	68155	311.2	352.1	—
SHS-04-C	7108-T7	70534	306.6	349.4	—
SHS-05-C	6082-T6	69013	197.9	240.1	—
SHS-06-C	6082-T4	71323	168.3	282.5	—
SHS-07-C	6082-T6	68325	252.3	281.4	—
SHS-08-C	6082-T4	72484	135.7	242.6	—
SHS-09-C	6082-T4	70609	139.3	263.3	—
SHS-10-C	6082-T4	74765	111.4	226.2	—
SHS-11-C	6082-T4	69083	138.5	259.1	—
RHS-01-C	6082-T6	68296	245.2	282.8	—
RHS-02-C	6082-T6	65648	283.2	290.2	—
I-01-C	6082-T6	65549	309.6	316.8	—
I-02-C	6082-T6	68649	287.4	311.8	—
SHS-01-B	6082-T6	68886	314.9	323.5	6.3
SHS-02-B	6082-T4	66868	176.2	283.4	19.7
SHS-03-B	6082-T4	66853	119.9	221.0	19.8
SHS-04-B	7108-T7	66880	313.4	333.4	10.6
RHS-01-B	6082-T6	66577	287.9	302.3	4.2
RHS-02-B	6082-T6	66225	280.8	290.4	5.8
I-01-B	6082-T6	66716	311.6	324.2	6.9
I-02-B	6082-T6	66874	278.8	300.7	6.9

Note: E, f_{02} and f_u are mean values from 2–4 tests, ϵ_u is from one test

TABLE 3
PARAMETRIC TRUE STRESS-STRAIN CURVES IN THE EXTRUSION DIRECTION

Section	Alloy & Temper	Y_0 (MPa)	Q_1 (MPa)	C_1	Q_2 (MPa)	C_2
SHS-01-B	6082-T6	288.5	27.9	2303	78.7	8.10
SHS-02-B	6082-T4	162.5	8.8	4065	171	13.8
SHS-03-B	6082-T4	109.8	4.3	4064	137	18.7
SHS-04-B	7108-T7	278.2	35.2	2303	170	8.13
RHS-01-B	6082-T6	265.3	24.8	1256	49.1	13.0
RHS-02-B	6082-T6	250.2	32.6	1818	43.6	14.7
I-01-B	6082-T6	283.1	31.2	2559	143	5.32
I-02-B	6082-T6	252.9	27.4	2094	55.9	13.8

Note: Y_0 , Q_k and C_k are mean values from 4 tests.

TABLE 4
ANISOTROPY OF PROPORTIONAL LIMIT STRESS AND R-VALUE

Section	Alloy & Temper	Y ₀ (MPa)	Y ₄₅ (MPa)	Y ₉₀ (MPa)	R ₀	R ₄₅	R ₉₀
SHS-01-B	6082-T6	288.5	250.7	277.3	0.36	1.77	0.97
SHS-02-B	6082-T4	162.5	118.7	165.6	0.40	1.50	1.13
SHS-03-B	6082-T4	109.8	81.4	114.0	0.39	1.52	0.72
SHS-04-B	7108-T7	278.2	249.1	274.0	0.39	1.15	1.29
RHS-01-B	6082-T6	265.3	238.6	254.5	0.31	1.40	0.74
RHS-02-B	6082-T6	250.2	252.7	243.2	0.41	1.89	0.86
I-01-B	6082-T6	283.1	246.5	243.2	0.31	0.92	0.86
I-02-B	6082-T6	252.9	205.4	234.6	0.44	1.17	1.18

Note: Y₀ is mean value from 4 tests, other data are from one test.

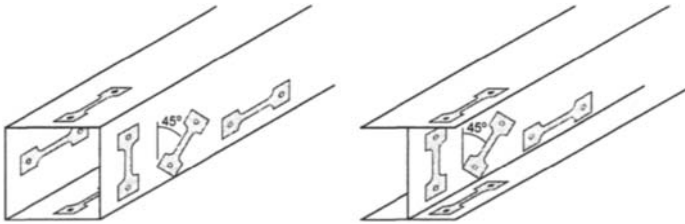


Figure 4: Position and geometry of uniaxial tensile specimens, Moen et al (1998)

EXPERIMENTAL RESULTS AND COMPARISON WITH EC9

The experimental results are compiled in Table 5 for the compression and bending tests in terms of the ultimate force N_u and ultimate bending moment M_u , respectively. It is seen that the experiments cover extrusions in classes 2, 3 and 4 according to Eurocode 9.

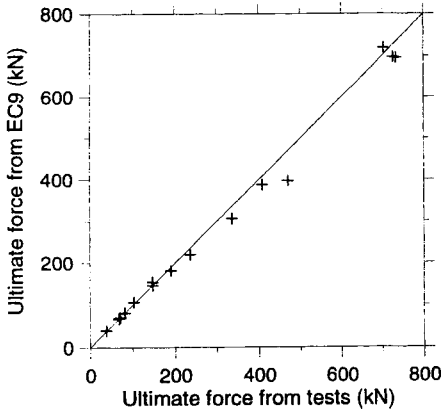
From Table 5 it is evident that the span of the simply supported beam in the bending tests (cf. Figure 1a) is of little importance for the strength in bending. However, the rotational capacity was found to increase significantly as the span was reduced, Moen et al (1998).

The average ultimate strengths in compression and bending obtained experimentally for each section are compared with EC9 in Table 5. The measured section geometry and uniaxial mechanical properties obtained from tensile testing were used in the calculations. All partial factors were taken equal to unity. The refined method for calculation of the ultimate bending moment resistance proposed in EC9 was used for class 3 extrusions. The table also provides the ratios κ_N and κ_M between the experimental and predicted strengths in compression and bending, respectively. Figure 5 shows correlation plots for the ultimate strengths in compression and bending as determined experimentally and calculated using EC9. In general, the predicted strengths correlate well with the experimental ones in both compression and bending. Since strain hardening is not accounted for in EC9, the design rules are conservative for sections of 6082-T4 in class 2.

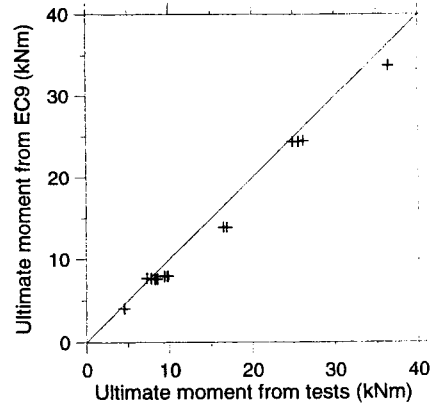
TABLE 5
EXPERIMENTAL RESULTS AND COMPARISON WITH EC9

Compression tests					Bending tests					
Section	Class	$N_{u,exp}$ (kN)	$N_{u,EC9}$ (kN)	κ_N	Section	Class	L (mm)	$M_{u,exp}$ (kNm)	$M_{u,EC9}$ (kNm)	κ_M
SHS-01-C	3	726.2	697.3	1.04	SHS-01-B	3	1000	25.6	24.4	1.05
SHS-02-C	2	470.1	397.0	1.18	"	3	2000	24.9	24.4	1.02
SHS-03-C	3	733.6	695.6	1.05	SHS-02-B	2	1000	16.9	13.9	1.22
SHS-04-C	4	408.2	387.5	1.05	"	2	2000	16.5	13.9	1.19
SHS-05-C	4	190.4	181.4	1.05	SHS-03-B	4	1000	4.55	4.02	1.13
SHS-06-C	4	147.3	146.2	1.01	"	4	2000	4.57	4.02	1.14
SHS-07-C	4	102.8	106.3	0.97	SHS-04-B	3	2000	26.2	24.5	1.07
SHS-08-C	4	67.6	67.3	1.00	RHS-01-B	4	1000	7.84	7.67	1.02
SHS-09-C	4	38.2	39.4	0.97	"	4	2000	7.84	7.67	1.02
SHS-10-C	4	81.9	80.9	1.01	"	4	3000	7.34	7.67	0.96
SHS-11-C	4	70.4	70.2	1.00	RHS-02-B	3	1000	8.27	7.61	1.09
RHS-01-C	4	146.8	153.8	0.95	"	3	2000	8.35	7.61	1.10
RHS-02-C	4	236.3	219.8	1.08	"	3	3000	8.59	7.61	1.13
I-01-C	4	703.4	719.3	0.98	I-01-B	4	2000	36.5	33.8	1.08
I-02-C	3	335.9	305.9	1.10	I-02-B	3	1000	9.88	7.95	1.24
—	—	—	—	—	"	3	2000	9.80	7.95	1.23
—	—	—	—	—	"	3	3000	9.44	7.95	1.19

Note: $N_{u,exp}$ is mean value from 3 tests, while $M_{u,exp}$ is mean value from 1-3 tests



(a) Compression tests



(b) Bending tests

Figure 5: Comparison of experiments and EC9

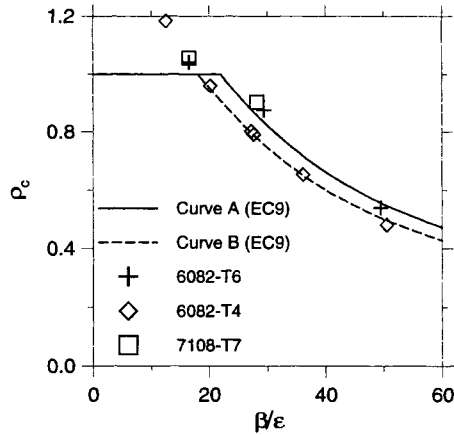


Figure 6: Comparison between compression tests on square hollow sections and local buckling curves A and B in EC9, where $\rho_c = N_u/f_{0.2}A$ and β/ϵ is a slenderness parameter, Eurocode 9 (CEN, 1997).

In Figure 6, the experimental data for the square hollow sections are plotted together with the local buckling curves A and B of EC9, assuming each section to consist of four internal elements. Curves A and B are used for unwelded, heat-treated elements and unwelded, non heat-treated elements, respectively. The experimental results for 6082-T4 (non heat-treated) extrusions in class 4 are in close agreement with curve B. Similarly, the experimental data points for heat-treated extrusions (6082-T6 and 7108-T7) in class 4 are well represented by curve A in EC9.

CONCLUSIONS

The following main conclusions can be made based on this study. The aluminium alloys 6082 and 7108 exhibit significant anisotropy with regards to proportional limit stress and R-values. EC9 gives, in general, good estimates of the experimental ultimate strength in compression and bending for extrusions with different cross sectional geometry and mechanical properties.

ACKNOWLEDGEMENTS

The authors gratefully acknowledge the financial support of Hydro Aluminium to this study.

REFERENCES

- [1] CEN (1997) Eurocode 9: Design of Aluminium Structures. Part 1-1.
- [2] Dolven A. and Drage P. (1997). Load and Deformation Capacity of Aluminium Profiles (in Norwegian). Master thesis, Department of Structural Engineering, Norwegian University of Science and Technology
- [3] Moen L., Hopperstad O.S. and Langseth M. (1998). Rotational Capacity of Aluminium Beams Subjected to Non-Uniform Bending – Part I: Experiments. In preparation.
- [4] Lademo O.G., Hopperstad O.S. and Langseth M. (1998). An Evaluation of Yield Criteria and Flow Rules for Extruded Aluminium Alloys. Accepted for publication in Int. J. Plasticity.

ULTIMATE STRENGTH OF STIFFENED ALUMINIUM PLATES

A. Aalberg, M. Langseth, O. S. Hopperstad and K. A. Malo

Department of Structural Engineering, Norwegian University of Science and Technology
7034 Trondheim, Norway

ABSTRACT

An experimental and numerical investigation is carried out to study the buckling behaviour of aluminium plates with longitudinal stiffeners subjected to axial compression. The test specimens, 2000 mm long, are built up with extruded aluminium profiles connected with welding. Two types of stiffened plates are investigated; one with open section (L shape) stiffeners and the other with closed stiffeners, both in aluminium alloy AA6082 temper T6. The experimental programme comprises tests on plates supported along all four edges, and as a special case plates supported at two edges only ("column behaviour"). All details, such as cross-sectional geometry, material properties and measured initial imperfections, are given, and the experimental results are shown by means of response curves. Numerical simulations of the tests are carried out using the finite element code ABAQUS. It is found that the finite element simulations predict quite accurately the behaviour and the resistance of the stiffened aluminium plates, both for the observed global buckling and the stiffener tripping (for the L shaped stiffeners only). The experimental results are also compared with the resistance calculated from the design rules in ENV 1999-1-1 (EC 9) for aluminium structures. In all experiments the measured maximum load exceeds the EC 9 design resistance.

KEYWORDS

Aluminium, stiffened plates, axial loading, numerical simulations, imperfections, design code.

INTRODUCTION

Stiffened panels in aluminium are structural elements used in a variety of structures such as high speed boats, marine vessels, bridges, helicopter landing decks, offshore modules and containers. Under normal conditions these panels are required to resist axial compressive forces and out-of-plane loads. However, as aluminium is a quite new structural material compared to steel, the existing design recommendations for such panels are mainly based on experience with steel structures. This means that effects such as the heat treatment of the material, heat-affected zones and the effect of new fabrication methods on the initial geometrical imperfections are not adequately taken into account in the design recommendations.

Many investigators have carried out testing of stiffened steel plate panels. Reference is made to recent papers by Grondin et al. (1997) and Paik & Thayamballi (1997) for a survey of the literature on the subject of axial compressed plates. The available literature on tests on stiffened aluminium panels is very limited. One of the few contributions here is given by Clarke (1985), who carried out buckling tests on aluminium AA5083 multi-span stiffened plates for ship structures.

When testing stiffened plates, i.e. plate panels with multiple longitudinal stiffeners, the loading and boundary conditions should ideally be such that the behaviour of the panel in the complete structure is reproduced. Due to the difficulty of (and costs of) carrying out such tests, most studies are concerned with the behaviour of single panels (or parts of single panels). The actual continuous boundary conditions for the panel are in most cases simplified, and the longitudinal edges of the panel are considered either free, pinned (simply supported) or fixed.

The present paper presents some of the data from an extensive experimental and numerical investigation of aluminium plate panels with multiple stiffeners. The objective of the full study is to obtain reliable data for plates subjected to axial loading as well as axial loading combined with other actions. The purpose of the experimental programme is to perform precision laboratory tests on such panels in order to validate numerical models for typical panel geometries. The validated models will later be used for parametric studies in order to verify and extend the existing aluminium design recommendations such as EC 9 [CEN (1997)]. For such validation studies it is imperative that the loading and boundary conditions are well defined, and are easily accounted for in the numerical model.

Results are given for plates with closed and L shape stiffeners subjected to axial compression, and for some selected nonlinear finite element simulations of the tests.

TEST SPECIMENS AND TEST RIG

Tests on eight specimens are reported in this paper, all subjected to axial compression in the direction of the stiffeners. The test specimens are built up from extruded aluminium profiles in alloy AA6082 temper T6, joined together with welding. Each extrusion has one central stiffener.

Two types of extrusions are used for the specimens, one with an open section (L shape) stiffener and the other with a closed section (box) stiffener. Tests are carried out on specimens consisting of five extruded profiles, supported along all four edges, and on specimens consisting of three extruded profiles, supported only at the two loaded ends. In the following the former tests are referred to as *plate* tests and the latter as *column* tests. Two plate tests and two column tests are carried out for both types of extrusions. The cross-sectional geometry of the extruded profiles and the cross-section of the plate specimens (five extrusions) are shown in Figure 1. As shown, the nominal width of the extruded profile with the open stiffener is 252.5 mm, while the width is 280 mm for the profile with closed stiffener. The total width of the specimens for the plate tests (five extrusions) is hence 1262.5 mm for the plate with open stiffeners and 1400 mm for the plate with closed stiffeners. The column specimens consist of three extrusions, having total widths of 757.5 mm and 840 mm for the specimens with open and closed stiffeners, respectively.

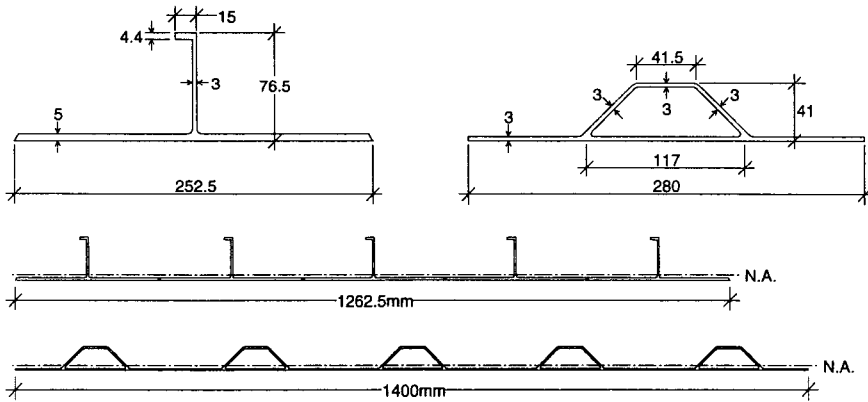


Figure 1: Cross-sectional geometry of extruded profiles and cross-section of specimens for plate tests.

The test panels were fabricated by Hydro Aluminium Maritime a.s. using their common fabrication procedures. The panels with closed section stiffeners were welded by means of friction stir butt welding, while the panels with L shaped stiffeners were joined by MIG welding. Both types of panels were taken from the production line for high-speed ferries (catamarans), and were fabricated in units 12 meter long. The panels are intended for use as the floor for passenger decks. The ends of the 2000 mm long specimens were machined carefully to give plane ends.

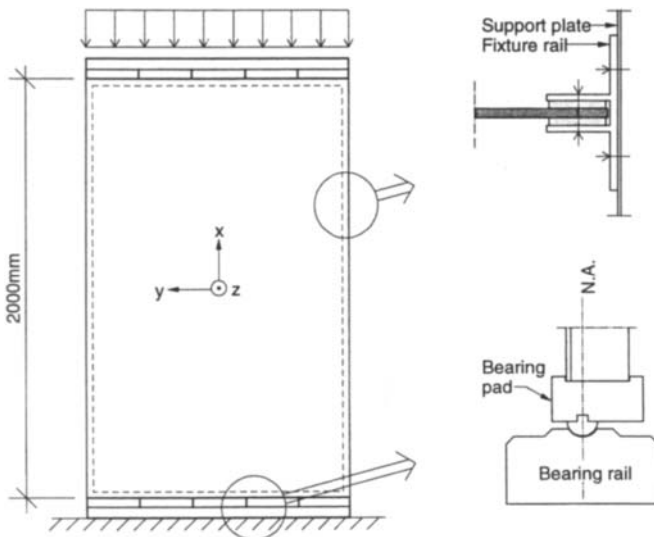


Figure 2: Test set-up, schematic view of simply supported plate specimen in test rig, detail of support arrangement at longitudinal edges (vertical) and detail of cylindrical bearings at loaded ends.

The test rig is based on a standard vertical loading frame consisting of two supporting columns, two stiff transverse beams and a hydraulic actuator with a capacity of 2500 kN. The test specimen is

mounted in a vertical position, the axial compressive loading is applied at the upper end of the specimen through a stiff loading beam, while the reaction force is carried at the lower end. Figure 2 shows a schematic view of the test set-up for the *plate* tests, i.e. specimens consisting of five extrusions and supported (pinned) along all four edges. The figure also shows the cross-section details of the support arrangement at the unloaded longitudinal edges and the bearing arrangement at the upper and lower ends of the specimen. As shown (cross-section of the bearing), the bearing arrangement is designed to allow the axial loading to be applied through the neutral axis (N.A.) of the cross-section at the specimen ends. The end of each extruded profile is inserted into a seat in a bearing pad that covers one profile width. Each bearing pad can rotate individually (about the y-axis) due to a 20 mm diameter half cylinder steel bearing. Negligible friction is ensured by using a 0.2 mm Teflon sheet between the bearing faces. The loading beam has a pinned connection to the actuator, which allows a small rotation about the z-axis.

The “simply supported” boundary conditions along the two unloaded plate edges are provided by specially designed fixtures as shown in Figure 2. The fixture consists of an aluminium support rail in which the outstand edge of the specimen is inserted into and bolted to. Strips of Teflon linings are used between the test specimen and the fixture rail, and longitudinal slotted holes are used for the bolts. The flanges of the fixture rail are bolted to a 1.0 mm steel support plate (in the xz-plane) which is fixed to a support frame. The dimensions of the support plate are 1500 mm (z-axis direction) times 2000 mm (x-axis direction). The support plate provides stiff restraints (fixture) to displacements in the xz-plane, while at the same time allows the longitudinal edges of the test specimen to contract when buckling deformations occur. Freedom of rotation about the x-axis is provided partly by the flexibility of the support plate and partly by deformations in the thin walled aluminium fixture rail.

For the *column* tests the same end bearing arrangement is used (using only three bearing pads at each end) while no restraints is imposed on the longitudinal edges (i.e. free edges).

In the tests the axial loading is applied by imposing a displacement of the actuator of approximately 1.0 mm per minute. The axial load is measured with a load cell placed between the actuator and the loading beam. Axial shortening of the specimen is measured at the loading beam, not directly on the specimen. Out of plane displacements (z-axis direction) at the midpoint of the specimen is measured by means of a laser. A rotation meter mounted on the loading beam registers any rotation of the beam that may occur. All test data are continuously logged to a PC. Prior to the testing, with the specimen mounted in the test rig, the initial geometrical imperfections of each specimen were measured.

TEST RESULTS

A section classification is carried out according to the rules in Eurocode 9 [CEN 1997]. For the plate with open stiffeners both the “main plate” (i.e. the 5.0 mm thick plate) and the outstand L shaped stiffeners are of cross-sectional class 4 and hence expected to be affected by local buckling. For the plate with closed stiffeners the main plate is in class 4, both for the part between each stiffener and the part that belongs to the closed section. The stiffener walls are in class 3. Based on the column buckling approach of Eurocode 9, where the axial resistance of a simply supported plate with multiple longitudinal stiffeners is obtained from inelastic flexural buckling of a column sub-unit (i.e. stiffener with adjacent plate parts), a component slenderness parameter of $\bar{\lambda} = 1.86$ is found for the plate with closed stiffeners [Aalberg et al. (1997)]. The corresponding value is $\bar{\lambda} = 1.83$ for the plate with open stiffeners. Due to the large relative slenderness, global flexural buckling is expected for both plates.

Material tests are carried out for all specimens. The mean values of the strength properties (longitudinal direction) for the plate with closed stiffeners are $f_{02} = 265$ MPa and $f_u = 290$ MPa, and correspondingly $f_{02} = 258$ MPa and $f_u = 290$ MPa for the plate with open stiffeners. The variation in

strength within each extruded section is insignificant. Tests on the material taken from longitudinal welds (i.e. between the extrusions) show a f_{02} value approximately 170 MPa for both MIG welded and friction stir welded specimens. The measured cross-sectional dimensions for the extrusions are close to their nominal values (see Figure 1).

The results from the column tests are presented in Figure 3, showing recorded axial load vs. applied axial displacement (i.e. the axial shortening of the specimen). For the two test specimens with open stiffeners (Specimen 1 and 2) failure is caused by sudden stiffener tripping (cripling), followed by column buckling displacements in direction of the plate (negative z-direction) combined with an overall panel twist at midspan. Inelastic stiffener tripping occurs for the stiffener near one of the edges and the stiffener in the middle (failure is accompanied by loading beam rotations). Both specimens had initial out-of-straightness less than +3.0 mm (towards the stiffener side, i.e. in positive z-direction) while the straightness deviation at the tip of the stiffeners was less than 1.0 mm (in y-direction). For the specimens with closed stiffener extrusions initial out-of-straightness deviations of about +0.6 mm (Specimen 3) and +1.8 mm (Specimen 4) were found. For these specimens failure took place in a regular flexural buckling mode with displacements in direction towards the stiffener side. No local buckles were observed. For Specimen 3, the total width was reduced to 730 mm (to avoid local buckling of free out-standing parts, which did not occur) and this is the main reason for the difference between the results.

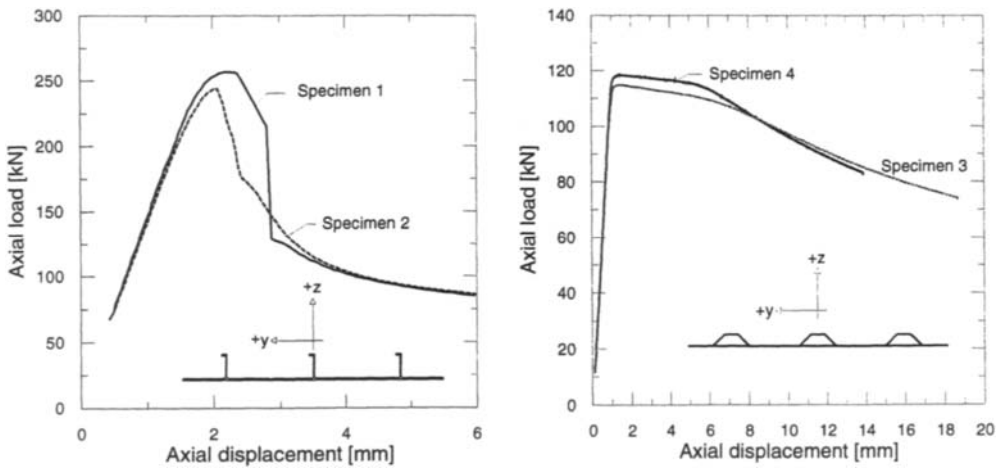


Figure 3: Column tests. Tests on specimens with open stiffeners and closed stiffeners.

Figure 4 depicts the response curves from the plate tests, i.e. the tests on the simply supported plate specimens. All tests resulted in flexural buckling with a single large buckle. In the tests on the specimens with open stiffeners (Specimen 5 and 6) the buckling took place with displacements in the direction of the stiffeners (positive z-direction). Specimens 7 and 8 with closed stiffeners buckled in the opposite direction (i.e. negative z-direction). It should be added that for a test specimen similar to Specimens 7 and 8 buckling actually occurred in direction of the stiffeners, and gave a response curve similar to that of Specimen 7. The initial midspan imperfections (in z-direction) were measured, and the mean values were +2.1 mm, +2.7 mm, +0.3 mm and ± 0.0 mm for specimens 5 to 8 respectively. Even though the mean value for Specimen 7 and 8 was quite small, the actual imperfection field had the form of three half waves in the transverse direction (one wave was measured for Specimen 5 and 6). The difference in the initial imperfections, one half wave vs. three half waves, explains the sudden onset of non-linearity of Specimen 7 and 8. The drop in the response curves after the peak load has

been reached is due to local failure (buckling) at the highly stressed longitudinal edges. This is inevitable for the type of boundary conditions that are chosen for these edges.

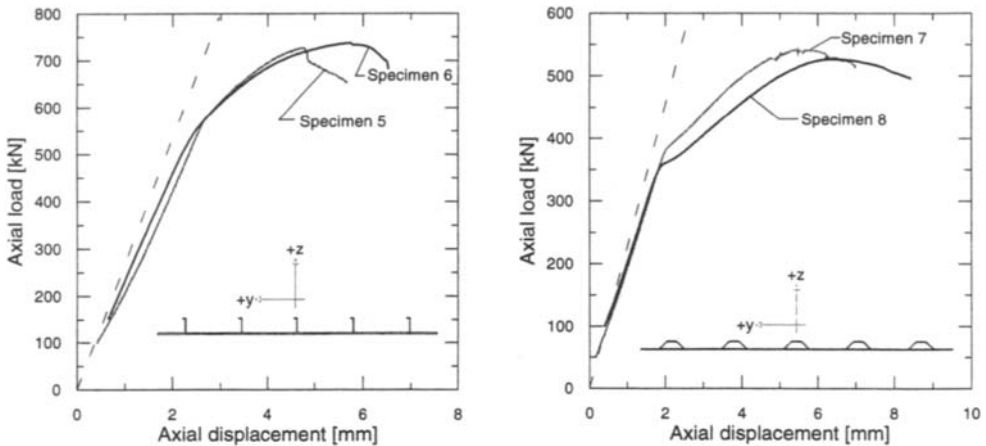


Figure 4: Plate tests. Tests on plates simply supported along all four edges. Specimens with open and closed longitudinal stiffeners.

NUMERICAL SIMULATIONS AND COMPARISON WITH EC 9

Numerical simulations of the tests are carried out using the finite element code ABAQUS [Hibbitt, Karlsson & Soerensen (1996)]. The full test specimens are modelled using four-node shell elements (S4R5 in ABAQUS). An extensive presentation of the models for all specimens is given by Aalberg et al. (1997). In the present paper, only the model for the plate specimen with closed stiffeners is shown.

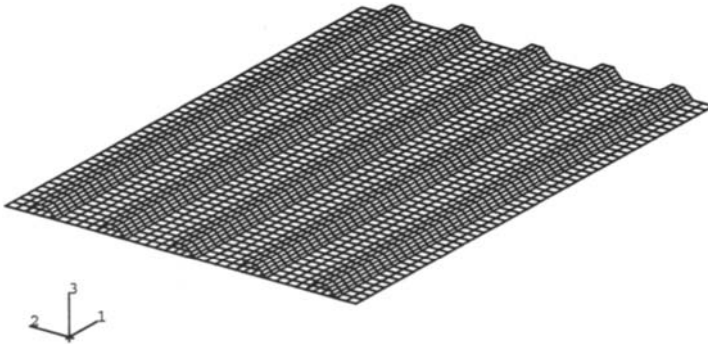


Figure 5: Shell model of plate specimen with five closed stiffeners, length 2000 mm, width 1400 mm.

As shown in Figure 5 the specimen is modelled with 50 elements in the length direction, 40 elements in the width direction for the plating, while each stiffener web is modelled using 4 elements over the height and 2 elements across the flange plate. The material properties of AA6082 T6 are modelled using a piece-wise linear fit to the measured stress-strain curve of the material. In ABAQUS, a standard von Mises yield surface with isotropic hardening is used. Five integration points are used through the shell thickness.

The axial compression of the specimen is analysed by applying an incremental axial displacement in the longitudinal direction (1-direction, see Figure 5) at one end of the plate, and restraining the same displacements at the opposite end. The axial displacement is applied at the theoretical initial neutral axis (N.A.) of the specimen (see Figure 1) to produce axial loading only. The correct loading position is achieved by adjusting the element mesh in the stiffener webs to give nodes located at the intersection with the neutral axis, and then applying the displacement at these nodes only. For the plate with closed stiffeners (Figure 5) this gives a node set containing 10 nodes at the end where the displacement is applied and 10 nodes at the opposite end where the displacement is restrained. For the model in Figure 5 the neutral axis is located 8.39 mm from the midplane of the “main” plate.

A uniform displacement field along the loaded end-sections of the stiffened plates, as in the tests, is provided by using linear multipoint constraints (i.e. identical displacements) for the loaded nodes in the stiffeners. As the rotations about the 2-axis are not restrained by the loading, the “simple support” condition is maintained for the stiffened plate at the ends. To allow this kind of concentrated loading without severe local yielding close to the loaded nodes, stiff beam elements are added to the model at the end sections (covering the stiffener webs). At the unloaded longitudinal edges, the nodes are fixed in the direction of the 3-axis.

An initial geometrical imperfection field for the specimens is constructed from the first elastic buckling mode found with ABAQUS, and applied in the inelastic analyses with an amplitude equal to the measured initial imperfections.

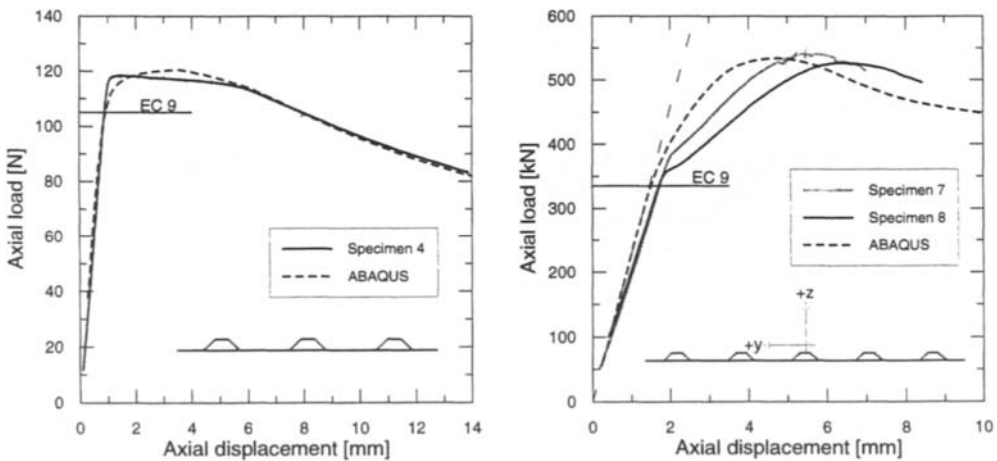


Figure 6: Numerical simulation of column test and plate test and comparison with design resistance.

Figure 6 compares the response curves from the numerical simulations with the experimental curves. The numerical response agrees quite well with the experimental one, both for the shape of the curves and the predicted maximum loads. In the simulation of the plate specimens (the graph to the right in Figure 6) the initial imperfection field with one wave is used, while the actual shape as mentioned had three waves. The resulting deviation is hence to be expected. For the specimens with open section stiffeners the agreement between the curves from simulations and experiments is also quite good.

The design resistance found using the design formulae in EC 9 is also shown in Figure 6 (taking all partial factors equal to unity, and the effect of HAZ into account). The EC 9 resistance is very close to the experimental maximum load for the column test, while it is about 65 % of the experimental value

for the tests on the plate specimens. Here it should be noted that if the plate specimens had buckled in the opposite direction, a slightly lower top load would be reached (seen in numerical simulations). Numerical simulations show that the buckling direction (+z or -z direction) strongly influences the maximum load and the shape of the response curve for the plate specimens with open stiffeners.

CONCLUSIONS

Experience has shown that the test rig is well suited for buckling studies of the stiffened aluminium plates. Tests are carried out on specimens with open and with closed stiffeners. For the specimens tested as columns (i.e. free longitudinal edges) the failure modes were stiffener tripping (for the L shaped stiffeners) and flexural buckling. For the specimens simply supported along all four edges the failure was flexural buckling with one large buckle. In all experiments the measured maximum load exceeded the EC 9 design resistance. Numerical simulations are shown to predict quite accurately the behaviour and the resistance of the stiffened plates, both for the observed global buckling and the stiffener tripping. Numerical simulations can hence be used in further studies to supplement extensive tests.

ACKNOWLEDGEMENTS

The authors gratefully acknowledge the financial support of Hydro Aluminium a.s. and the Norwegian Defence Construction Service to this study.

REFERENCES

- Aalberg A., Langseth M., Hopperstad O. S. and Malo K. A. (1997). *Stiffened plates in aluminium under uniform compression : Numerical investigation and comparison with design resistance according to Eurocode 9*. Report No R-45-97, Department of Structural Engineering, Norwegian University of Science and Technology.
- CEN (1997). *Eurocode 9 : Design of aluminium structures. Part 1.1 (ENV 1999-1-1)*.
- Clarke J. D. (1987). Buckling of Aluminium Alloy Stiffened Plate Ship Structure. *Aluminium Structures - Advances, Design and Construction*. Edited by R. Narayanan, Elsevier 1987.
- Gronin G. Y., Chen Q., Elwi A. E. and Cheng J. J. (1998). Stiffened Steel Plates Under Compression and Bending. *Journal of Constructional Steel Research* **45:2**, 125-148.
- Hibbitt, Karlsson & Soerensen (1996). ABAQUS Version 5.6.
- Paik J. K. and Thayamballi A. K. (1997). An Empirical Formulation for Predicting the Ultimate Compressive Strength of Stiffened Panels. *Proceedings of the Seventh International Offshore and Polar Engineering Conference, Honolulu, USA 1997*.

Section II

**COLD-FORMED AND
LIGHT GAUGE
STEEL STRUCTURES**

This Page Intentionally Left Blank

A COMPARISON BETWEEN BRITISH AND EUROPEAN DESIGN CODES FOR COLD-FORMED THIN-GAUGED STRUCTURES

D.B. Moore¹ and Y C Wang²

¹ Centre for Steel Construction, Building Research Establishment, UK
² Structures Research Group, The Manchester School of Engineering, UK

ABSTRACT

This paper presents the results of a comparative study between BS5950 and the ENV (prestandard) version of Eurocode 3 Part 1.3 for the design of cold-formed thin-gauged steel structures. Both documents deal with most subjects in a similar fashion and where there is a difference in their treatments, the final results are generally in close agreement. However, the results of the comparative study also revealed a number of discrepancies between these two codes. These are described in detail in this paper.

KEYWORDS: British standards, Eurocode, National Application Document, Code calibration

INTRODUCTION

As part of the introduction and acceptance of the Eurocodes into the UK, the Building Research Establishment (BRE) recently conducted an assessment of the ENV (prestandard) version of Eurocode 3 Part 1.3 for the design of cold formed thin gauged steel members and sheeting. Based on the results of this assessment, BRE developed the UK's National Applications Document (NAD) to enable Eurocode 3 Part 1.3 to be used for the design and construction of buildings in the UK. The assessment of a Eurocode aims to translate the experience obtained with the existing (old) UK code into the new code by appraising the differences and by deriving numerical values for the partial safety factors while at the same time making allowances for new research data. The method of assessment is based on a comparison of the capacities of structural elements designed to the new and old codes and the partial factors are chosen such that the new code gives the same member size for the same loading condition as the old code.

Design for cold formed thin gauged structures are dealt with in various parts of BS 5950 (Parts 5, 6 and 9, to be collectively referred to as BS 5950 in this paper) for different types of structural system, and are covered entirely in Eurocode 3 Part 1.3 (to be referred to as EC3 in this paper). Due to the specialist nature of this subject, many parts of both codes are based on the same research data. Therefore, both codes deal with many topics in a similar fashion. Even when some topics are treated differently, the final results from both codes are generally in close agreement. However, the results of the comparative study also revealed a number of areas of discrepancy between these two codes. This paper describes these differences in some detail and also presents the recommendations given in the UK's NAD on these topics.

The use of both the British Standards and the Eurocode is not restricted to construction in the UK, thus the introduction of the Eurocode will have a much wider implication. This paper explains the background to the UK's NAD and helps to introduce the Eurocode to a wider audience.

GENERAL COMPARISON

Before describing the major differences between the two codes, it is useful to list the contents of EC3 to enable designers to become familiar with its scope, and to make a general comparison between the two codes so that later discussions on their major differences are put into perspective.

EC3 Chapters	General remarks on comparison with BS5950
1. General	Very similar
2. Basis of design	Very similar; each adopts its parent code clauses.
3. Properties of materials and cross-sections	Broadly similar. BS 5950 gives variable enhanced yield stress as a function of the degree of effectiveness and EC3 does not.
4. Local buckling	Broadly similar, but there are a number of differences.
5. Resistance of cross-sections	Similar, but with a number of minor differences.
6. Buckling resistance:	
6.2 Axial compression	BS 5950 uses only one column buckling curve and EC3 uses three.
6.3 L-T buckling	Very similar
6.4 Distorsional buckling	Not dealt with in BS 5950 but EC3 guidance is very descriptive.
6.5 Bending and axial compression	Similar results for combined axial compression and uniform bending, but large differences for double curvature bending +axial compression.
7. Serviceability limit states	Very similar
8. Joints and connections	Broadly similar with a number of minor differences.
9. Design assisted by testing	Very similar
10. Particular applications	BS 5950 does not deal with liner trays. Others are similar.
Annex A. Testing procedures	Broadly similar but both are still under development.

MAJOR DIFFERENCES AND THE UK NAD'S MODIFICATIONS TO EC3

The differences are described according to the Eurocode clause numbering system.

Cl. 3.1.2(3)P Average yield strength

Cold forming may increase the average yield strength of steel. Although both codes recognise this behaviour and have used the same equation for calculating this increase, EC3 only allows the average yield strength to be increased if the cross-section is fully effective. BS 5950 does not have this restriction, therefore, non-fully effective cross-sections may also benefit from the increase in the average yield strength due to cold-forming. Figure 1 clearly illustrates the difference between EC3 and BS 5950. The UK's NAD recommends the use of the BS 5950 method.

Cl. 3.1.3(3)P & Cl. 3.1.3(4) Thickness tolerances

A small reduction in the material thickness of a thin element will result in a large reduction in its loadbearing capacity. To account for the effect of thickness tolerances, the UK's NAD has introduced a multiplication factor (k) to reduce the nominal core material thickness t_{cor} (excluding coating) to give the design thickness t , i.e. $t = k t_{cor}$. For the same thickness tolerance, the value of k decreases when thinner steel is used.

Cl. 4.2 Plane elements without stiffeners

When determining the effective width of a plate element in a section, BS5950 allows for the beneficial restraining effect of adjacent plate elements. This beneficial effect is not included in EC3. In BS 5950, this effect is represented by the K factor. Figure 2 compares the effective width of a plate supported on both edges and subject to uniform compressive stress, calculated using BS5950 for different values of K with EC3. As the differences between the EC3 value and the various BS5950 values are small, the UK's NAD has taken the view of not recommending any change to EC3.

Table 4.2 Outstand compression elements

While in most cases, the results given by the different equations in EC3 and BS 5950 are quite similar, the equations in EC3 may lead to a significant overestimation of the effective width for an unstiffened plate under both bending and axial compression which cause compression on the unsupported edge. This is clearly illustrated by the example in figure 3. However, the UK's NAD has not recommended any modification because the format of the EC3 method is radically different from that of BS 5950 and in most cases, both EC3 and BS 5950 produce results that are in close agreement.

Cl. 4.2(9) Effective width using the iteration method

When determining the effective width of an element subjected to stress gradient, EC3 allows two methods: (1) the stress gradient is evaluated using the gross cross-section; (2) the stress gradient is evaluated using the effective cross-section after successive iterations. However, in many cases, the successive iteration process may give results for the effective width which is only a small fraction of the value based on the gross cross-section. Figure 4, which shows Rhodes' [Rhodes 1997] comparison with some test results, clearly indicates that the effective width without iteration gives better correlation with test results. Thus it is not necessary and indeed it is misleading to adopt the iteration method in EC3. The UK's NAD therefore recommends that the iterative method not be used.

Cl. 5.4.2 Plastic behaviour

EC3 is very restrictive on the use of the plastic capacity for cold-formed thin gauged structures. Firstly, EC3 does not allow any moment distribution unless demonstrated by tests. Secondly, partial plastic behaviour is allowed only when the member is subject to bending moment about one principal axis. In comparison, BS 5950 is more flexible. In BS 5950, moment distribution is allowed provided the section is plastic. For other types of section, although moment distribution is not allowed, the section may develop plastic behaviour and the enhanced moment capacity may be used, either for bending alone or for combined bending and axial load. The UK's NAD suggests that moment distribution should be allowed by calculation for plastic sections. However, for the general case of plastic behaviour, accepting the BS 5950 method would require modifying all the relevant EC3 clauses where the section moment capacity appears. Thus, the UK's NAD recommends the use of the BS 5950 method to calculate the section moment capacity, but subject to the EC3 restriction of bending moment about only one principal axis.

Cl. 5.8 Shear force

When calculating the values of the web shear resistance, EC3 distinguishes between a web with stiffening at the supports and a web without stiffening. In BS 5950, there is no such distinction. Figure 5 compares the predicted values of shear resistance (assuming a steel yield stress of 275 N/mm²) using the EC3 equation for webs without stiffening at the supports, with BS5950 and with EC3 for webs with stiffening at the supports. Figure 6 gives the ratios of the predicted shear resistance using the EC3 equations divided by those using the BS5950 equation. It shows that for webs with stiffening at the supports, EC3 can give

much higher shear resistance than BS 5950. While stiffening at the supports can increase the local web shear buckling resistance, it may be reasoned that for the part of the web away from the supports, it should be treated as unstiffened. Since the location where the support stiffening effect becomes negligible is not given in EC3, it may be argued that the whole web should be treated as unstiffened. The UK's NAD has therefore taken this view and ignores the support stiffening effect.

Cl. 5.11 Combined bending moment and local load or support reaction

While the bending resistance (from Cl. 5.4) calculated using EC3 is very similar to that calculated using BS 5950 (although the calculating procedure in BS 5950 is much simpler to use), and the calculation for local load capacity is identical in both codes, the design procedure for the combined actions is slightly different. BS 5950 distinguishes between single thickness webs and double thickness webs while EC3 makes no distinction. The interaction equation is also slightly different. However, figure 7 suggests that the differences between single and double thickness webs, and between EC3 and BS 5950 values are small. Therefore, the UK's NAD does not recommend any modification to the EC3 clause.

Cl. 6.2.1 & Cl. 6.2.2 axial compression - flexural buckling

EC3 adopts the approach in its parent document for hot-rolled sections and uses different column buckling curves depending on the type of cross-section and axis of buckling, however, this method is not adopted in BS 5950 for thin-gauged sections. Close examination of the equation in BS 5950 reveals that the column buckling curve resembles column buckling curve "a", but reducing slightly for less effective cross-sections. In general, if flexural buckling controls (e.g. symmetrical sections), either column buckling curve "a" or "b" would be used in EC3, and as indicated in figures 8 and 9, the difference between EC3 and BS5950 is small. If torsional flexural buckling is more likely to govern, predictions from EC3 and BS 5950 are close. Therefore, the UK's NAD does not recommend any change to the EC3 clause.

Cl. 6.5 Bending and axial compression

For columns under combined axial compression and non-uniform bending, EC3 and BS 5950 predict quite different results, the difference being particularly high for slender columns under high axial compression. For example, figure 10 compares the axial load - bending moment interaction curves used in EC3 with those in BS 5950, assuming a steel yield stress of 280 N/mm² and using column buckling curve "b" in EC3 calculations. However, since there is no experimental result to resolve this problem, the UK's NAD has taken the conservative approach and recommends using the BS 5950 approach.

Table 8.4 Design resistance for bolts in shear

EC3 and BS 5950 are different in the important clause of bolt resistance. The EC3 bolt resistance for thin-gauged steel is identical to that given in its parent document for hot-rolled thick steel. However, BS 5950 takes the view that because the bearing failure in thin-gauged steel plates is more complex than in hot-rolled thick steel plates, different calculating procedures should be used for the resistance of bolts, depending on the thickness of the connected plate. As indicated in figure 11, EC3 is more conservative when the plate thickness is higher than 2mm, but less safe at a lower plate thickness. However, the UK's NAD has not recommended any modification as this EC3 clause was written after considerable debate by the code drafters.

In addition, BS 5950 reduces the bolt design resistance by 25% if no washer or only 1 washer is used, and EC3 does not distinguish between the number of washers used. The UK's NAD therefore specifies that 2 or more washers should be used.

Cl. 10.1 Beams restrained by sheeting

This section in EC3 is outside the scope of BS 5950. In particular, a calculation method is included in EC3 to determine the resistance of purlins subject to wind uplift. Leach [Leach 1993] examined the EC3 calculation method for purlins restrained by sheeting and subject to wind uplift and found that the calculation method gave design resistance about 20-25% less than the manufacturers' test results. Since these test results are already a lower bound, this implies that the EC3 calculation method may be refined further. As BS 5950 does not have any provision on this topic and EC3 gives conservative results, the UK's NAD recommends the use of the EC3 calculation method.

PARTIAL SAFETY FACTORS

Both BS 5950 and EC3 are limit state design codes and use partial safety factors. Although EC3 gives a set of values for the partial safety factors, these values may be changed to suit the practice of the particular country where EC3 is used. The partial safety factors may be easily identified in EC3 as the boxed value. The UK's NAD have chosen the alternative values such that the new code (EC3) gives the same member size for the same loading condition as the old code (BS5950). Thus, the designer should replace the values of the partial safety factors in EC3 with those in the UK's NAD for buildings constructed in the UK.

CONCLUSIONS

This paper gives a brief account of a detailed comparative study between British and European codes for the design of cold-formed, thin-gauged structures, which has been carried out during the development of the UK's National Application Document (NAD) for Eurocode 3: Part 1.3. This paper describes in some detail the major differences between these two codes and presents the background reasoning for the UK's NAD. The authors hope that this paper will help designers to use the Eurocode to gain valuable experience during the conversion from British Standards to Eurocodes.

REFERENCES

Davies J M and Leach P (1997), "Calibration of EC3: Part 1.3, Chapters 1,2,3,5,7,8 & 10", final report to the Building Research Establishment

Leach P (1993), "The behaviour of purlins subject to uplift, an assessment of Eurocode 3: Part 1.3", *The Structural Engineer*, Vol. 71, No. 14

Rhodes J (1997), "Calibration of Eurocode 3: Part 1.3, Chapters 4,5,6,9 + Annex A", final report to the Building Research Establishment

ACKNOWLEDGEMENTS

The NAD has been prepared under the direction of the UK's Civil Engineering and Technical Sector Board for Building and Civil Engineering.

The authors wish to acknowledge the contributions of Professor J. M. Davies at the University of Manchester, Professor J. Rhodes at Strathclyde University and Dr. P. Leach at Salford University who undertook the detailed comparative studies.

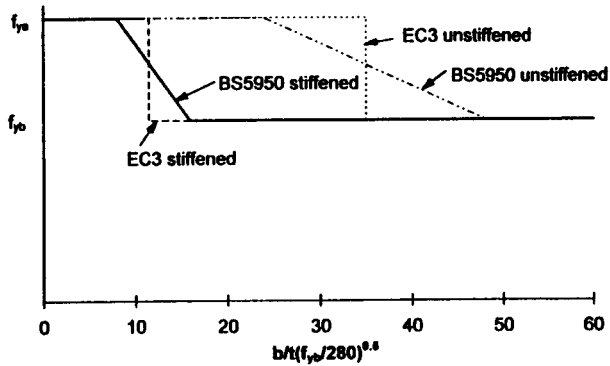


Fig. 1: Comparison for effective steel yield stress

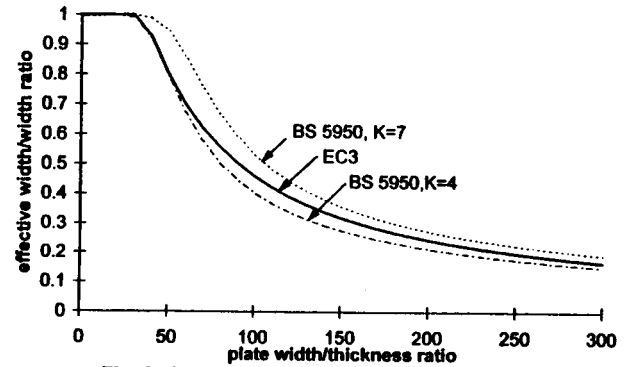


Fig. 2: Comparison for effective width, doubly supported compression elements

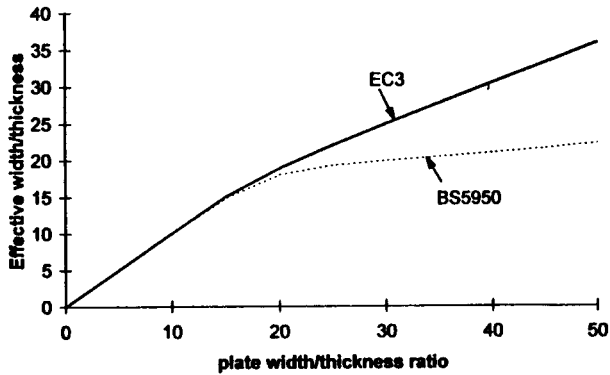


Fig. 3: Comparison for effective width

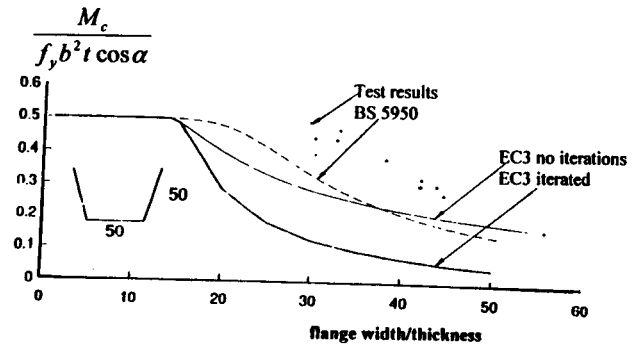


Fig. 4: Comparison for effective width

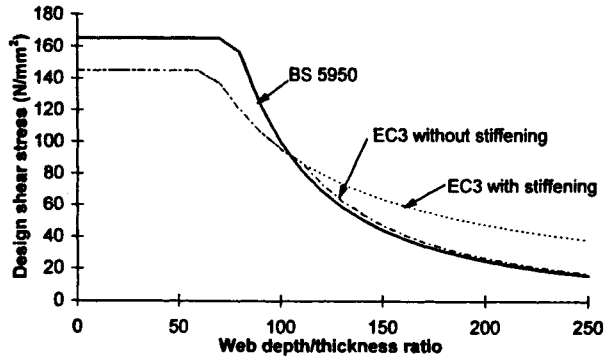


Fig. 5: Comparison for shear resistance of webs

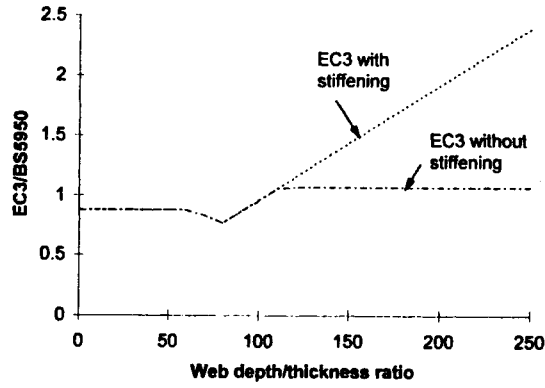


Fig. 6: Comparison for web shear resistance

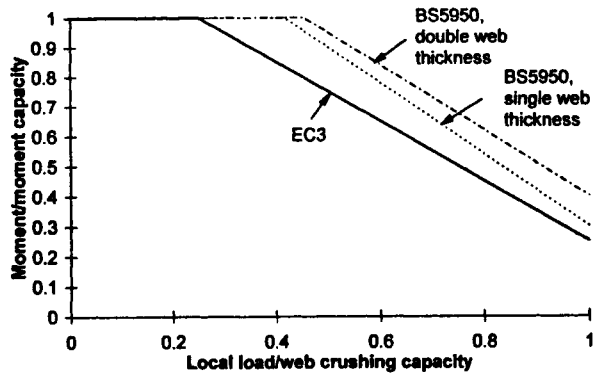


Fig. 7: Comparison for bending and web crushing

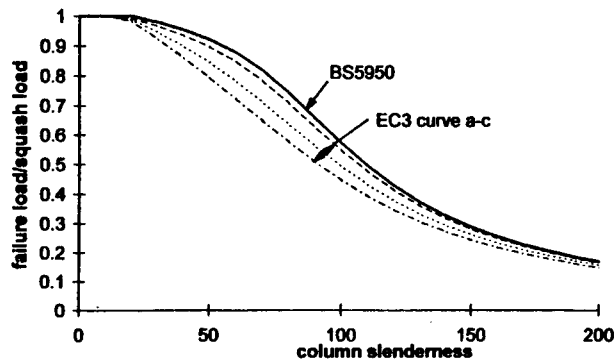


Fig. 8: Comparison for flexural buckling resistance, fully effective cross-section

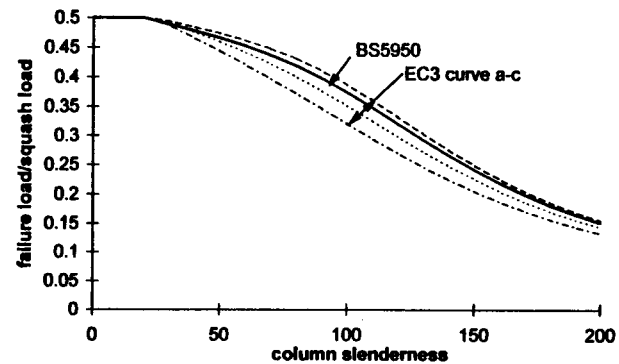


Fig. 9: Comparison for flexural buckling resistance, 50% effective cross-section

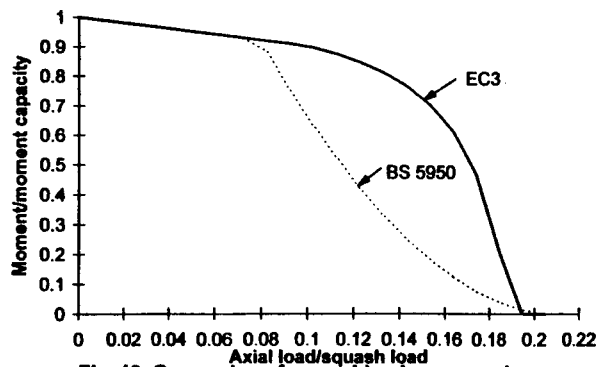


Fig. 10: Comparison for combined compression and double curvature flexural bending, $L/r=180$

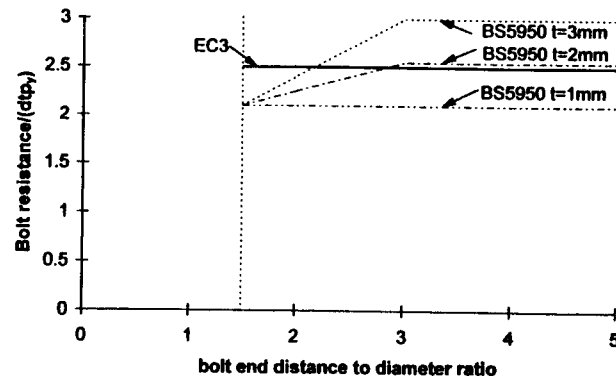


Fig. 11: Comparison for bolt design resistance

BEHAVIOUR OF COLD-FORMED STEEL WALL FRAME SYSTEMS LINED WITH PLASTERBOARD

Yaip Telue and Mahen Mahendran

Physical Infrastructure Centre, School of Civil Engineering,
Queensland University of Technology,
Brisbane Qld 4000, Australia

ABSTRACT

Gypsum plasterboard is a common lining material for steel wall frame systems. It is used in combination with cold-formed steel studs (C or lipped C-sections) for both the load bearing and non-load bearing walls in the residential and commercial building construction. This type of construction is common in Australia and the USA. However, the design of these wall frames does not utilise the full strengthening effects of the plasterboard in carrying axial loads. Therefore an experimental investigation was conducted using a total of 20 full-scale wall frame tests including unlined, both sides lined and one-side lined wall frames. Test results were compared with predictions from the Australian standard AS 4600-1996 and the American specification AISI-1996. This paper presents the details of the experimental study, the results, and comparisons with design code predictions.

KEYWORDS

Buckling of studs, Plasterboard lining, Cold-formed Steel wall frames, Full scale wall frame tests.

INTRODUCTION

Gypsum sheeting (plasterboard) is a common lining material used in combination with cold-formed steel studs (C or lipped C sections) for both the load bearing and non-load bearing walls in the residential and commercial building construction in Australia and the USA. In the design of load bearing walls, the support provided by the plasterboard in carrying the axial load is not considered. This is because the plasterboard is not considered to be a structural material. The current Australian Standard for Cold-formed Steel Structures AS 4600 (AS, 1996) only considers the lining material to provide lateral and rotational supports to the stud in the plane of the wall. However, the American Specification (AISI, 1996) includes checking for column buckling between wallboard fasteners, overall

buckling (flexural, torsional and flexural-torsional) and for shear failure of the plasterboard. Design equations for lined studs were derived from the work of Simaan and Pekoz (1976) based on the shear diaphragm model.

Miller and Pekoz (1994) have studied the behaviour of gypsum plasterboard lined stud walls under axial compression from experiments and have concluded that the results contradict the shear diaphragm model assumed by the American specification AISI (1986). Contrary to the shear diaphragm model, the strength of plasterboard lined stud was observed to be insensitive to stud spacing. The deformations of the panels in tension were also observed to be localised at the fasteners and not distributed throughout the panel as in a shear diaphragm (Miller and Pekoz, 1994). The failure loads of lined walls were much higher than those predicted by the AISI (1986). All these imply that the behaviour of lined stud walls is not accurately modelled by the American Specification. An experimental study was therefore carried out to address these problems. This paper presents the details of this experimental study and the results. Experimental results were compared with predictions based on AS 4600 (SA, 1996) and the AISI (1996), based on which appropriate conclusions and recommendations have been made.

EXPERIMENTAL INVESTIGATION

In order to investigate the behaviour of plasterboard lined steel stud walls under axial compression using full-scale tests, it is important that key parameters are chosen carefully in the design of test frames. These key parameters are plasterboard lining (thickness and type, no lining vs one side lining vs both sides lining), geometry of the stud section, stud thickness and grade, number of studs and their spacing in the frame. To investigate the effects of these parameters, a total of twenty full-scale wall frames consisting of three studs with studs spaced at 600 and 300 mm were chosen. All the frames consisted of three studs as shown in Figure 1. This configuration was adopted as it represents a typical stud wall in a building with two external studs and a middle stud. Miller and Pekoz (1994) have shown in their tests that the failure loads of each of the studs in a three-stud wall system were the same. The height of the frames was set at 2.4 metres to represent a typical wall in a building. Four frames were unlined. Eight frames were lined on one side while the remaining eight had lining on both sides. For the lined frames, the more commonly used 10 mm plasterboard was used as the lining material. The unlined wall frames had only one stud spacing (600 mm), as the strength of the studs in the unlined condition is independent of the stud spacing. The studs were made from two unflipped C-sections. The dimensions and details of these sections are as shown in Figure 2 and were fabricated from two grades of steel, a mild steel grade G2 (minimum yield stress = 175 MPa) and a high tensile steel grade G500 (minimum yield stress = 500 MPa).

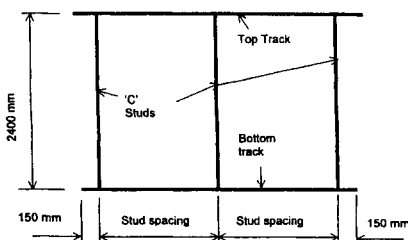


Figure 1: Layout and Dimensions of Frames

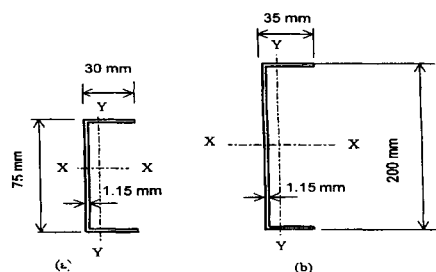


Figure 2: Dimensions of C-section Studs
a) 75mm Stud. b) 200mm Stud

Test frames were made by attaching the studs to the top and bottom tracks made of C-sections using a single 8-18 gauge 12 mm long wafer head screw at each joint. The C-sections used as tracks were chosen to fit the stud sections chosen for this study. Plasterboard lining was fixed to the lined frames in the horizontal position. The horizontal butt joints in the plasterboard were joined together in accordance with Plasterboard Manufacturer's Installation Manual (CSR, 1990). Type S 8-18 gauge x 30 mm long plasterboard screws were used to fix the plasterboard to the studs. The screws were spaced at 220 mm centres along the length of the studs. This is within the maximum spacing of 300 mm recommended by the industry (RBS, 1993). The first screw was located 75mm from the edge of the tracks at both ends and is within a maximum distance of 100 mm recommended by RBS (1993). Table 1 presents the details of test frames under the three groups of unlined, one side lined and both sides lined walls.

Table 1: Details of Test Frames

Frame Number	Stud (mm)	Steel Grade	Frame Number	Stud (mm)	Steel Grade	Stud Spacing (mm)	Lining Condition
1	75	G2	3	200	G2	600	Unlined
2	75	G500	4	200	G500		
5	75	G2	7	200	G2	600	Lined one side
6	75	G500	8	200	G500		
9	75	G2	11	200	G2	300	
10	75	G500	12	200	G500		
13	75	G2	15	200	G2	600	Lined both sides
14	75	G500	16	200	G500		
17	75	G2	19	200	G2	300	
18	75	G500	20	200	G500		

TEST SET-UP AND PROCEDURE

The test set-up for the full-scale tests is shown in Figure 3. The test frame was placed in a vertical position within the support frame and adequately restrained. The bottom track of the frame was fixed to the steel universal beam support at both ends. At the top of the frames, timber blocks were used as restraints at each end of the frame to stop in-plane movement. Timber restraints were also used to prevent the frames from moving out of plane. These restraints were fixed between the studs such that they prevented out of plane movement of the studs, but allowed shortening of the studs to occur freely. Figure 4 shows the timber restraints at the top of the frames. Three hydraulic jacks were suspended off the top horizontal beam and were placed directly over each stud in order to apply a concentric load. They were connected to separate manual hydraulic pumps. A load cell attached to each jack enabled the load to be monitored during the tests. Loading plates were placed on the top of the track directly under the jacks to enable uniform load distribution to the entire stud cross-section. (see Figure 5). Any gaps between the stud and the tracks were packed with steel shims to ensure direct load transfer to studs from the loading plate.

During each test, the axial compression load on each stud was increased until failure. When one stud failed, loading was continued for the remaining studs until they also failed one after the other. In this manner, three stud failure loads were obtained for each wall frame. This approach was used because the aim of this study was to investigate the behaviour of the studs and determine their failure loads as members of the wall assembly. It was not the intention to determine the failure load of the wall frame. For each test, axial shortening of the studs and the relevant in-plane and out-of-plane deflections along the studs were monitored continuously and recorded.

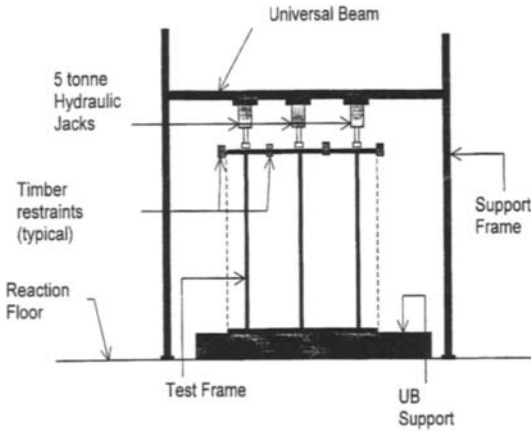


Figure 3: Test Set-up



Figure 4: Timber Restraints at the Top of Studs



Figure 5: Loading Plates

RESULTS AND DISCUSSION

Unlined Frames

The failure loads from the tests are given in Table 2 for the four unlined frames. Predicted failure loads based on the Australian Standard, AS 4600 (SA, 1996) are also included. It must be noted that predictions based on the American Specification (AISI, 1996) and AS 4600 (SA, 1996) are identical for the unlined frames. The failure loads from tests are generally higher than those predicted by the code. The predicted failure loads were first computed taking the effective length factors K_x , K_y and K_t as 1.0, (where K_x and K_y are the effective length factors for the buckling about the x and y-axes, respectively, and K_t is the effective length factor for torsion). It should be pointed out that AS 4600 (SA, 1996) does not have any procedures to determine these factors. The AISI Specification (1996) states that these values can be determined using a rational method but shall not be less than the actual unbraced length. In these tests, timber restraints were used to prevent sway of the frames during the tests; therefore the effective length factor can not be greater than unity. The predicted failure loads based on an effective length factor of 1.0 were found to be conservative as the top and bottom tracks would provide some restraints to buckling about the x, y and z-axes (see Table 2). Hence various effective length factors were investigated. When a value of 0.75 was used for K_x , K_y and K_t the predicted loads agreed well with experimental results. This is similar to Miller and Pekoz's (1993) recommendation of 0.65 based on their tests on lipped C-sections.

The observed and predicted failure modes are also given in Table 2. In the computation of the failure loads the lowest load was selected based on the three possible failure modes. These were the elastic flexural buckling (FB), torsional and flexural-torsional buckling failures (FTB). In general, the codes accurately predicted the failure mode. For the 200 mm studs, the code predicted a flexural buckling failure however, some twisting of the studs was also observed at failure due to the slender web. Miller and Pekoz (1993) considered the need to allow for loading eccentricity caused by local buckling. However, it was not considered here as global buckling failures preceded local buckling in the wall frames considered.

Table 2: Ultimate Failure Loads of Unlined Frames.

Frame Number	Stud	Expt. Failure Load (kN)	Expt. Failure Mode	Section Capacity (N_s) (kN)	$K_x = K_y = K_t = 1.0$		$K_x = K_y = K_t = 0.75$	
					Pred. Failure Mode	Expt./Pred. Load	Pred. Failure Mode	Expt./Pred. Load
1	1	5.6	FB	19.5	FB	1.43	FB	0.81
	2	5.3	FB			1.32		0.77
	3	4.3*	FTB			-		-
2	1	7.8	FB	38.3	FB	1.95	FB	1.11
	2	7.2	FB			1.80		1.03
	3	6.6	FTB			1.69		0.94
3	1	5.3*	FTB	21.7	FB	-	FB	-
	2	8.3	FB			1.36		0.89
	3	10.7	FTB			1.75		1.15
4	1	10.8	FTB	40.6	FB	1.74	FB	1.15
	2	10.8	FTB			1.74		1.15
	3	10.4	FTB			1.68		1.11

* Denotes values that were ignored in the subsequent computations and discussions.

FB: - denotes flexural buckling; FTB: - denotes flexural-torsional buckling.

Frames with Plasterboard Lining on both sides

All the frames with plasterboard lining on both sides except 2 studs in Frame 18, failed by buckling between the fasteners at the top of the stud with the screws pulling through the plasterboard. As the load approached failure, the buckling between the two fasteners at the top of the stud (or the top screw and the track) increased causing the load to be eccentric. As the load increased further, it resulted in the screw pulling through the plasterboard. Once this occurred, the stud alone had reduced strength at this location and a sudden failure occurred. Figure 6 shows a typical failure of the studs while Figure 7 shows the buckling between the fasteners. The failure of the plasterboard was observed to be localised and not distributed throughout. Similar behaviour was also observed by Miller and Pekoz (1994).



Figure 6: Typical Failure of the Stud between the Top Screw Fasteners.

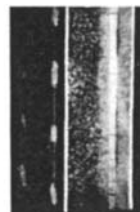


Figure 7: Buckling between the Fasteners.

Experimental failure loads of the studs are summarised and compared with those predicted by AS 4600 (SA, 1996) in Table 3. AS 4600 (SA, 1996) requires that the ultimate strength of the studs under axial compression be computed by: (i) ignoring the lining material or (ii) considering the lateral and rotational supports in the plane of the wall. There are specific conditions the wall assembly must meet before the lateral and rotational supports are considered.

In the tests, the studs were connected to the tracks at both ends and therefore the rotation about the longitudinal stud axis and the horizontal displacements in the x and y axes at both ends were restrained. The studs, however, were free to rotate about x and y axes at both ends. In these tests the

lining material was not fixed to the top and bottom tracks as required by AS 4600. The lining material was connected to the studs with fasteners located along the studs with the first screw located at 75 mm from each end of the stud. This is the normal practice adopted by the industry, provided the last fastener is located within 100 mm of stud end (RBS, 1993). This aspect will be further investigated in the finite element analysis of this study. For the purposes of utilising the rotational and lateral supports, the frames in these tests can be considered to comply with the wall stud provisions of AS 4600. However, AS 4600 falls short in stating what level of lateral or rotational support can be used. Various combinations of the effective length factors were therefore investigated and the predicted failure loads are given in Table 3. In computing the predicted loads, the effective length factors for the studs K_y (in-plane buckling), K_x (out of plane buckling) and K_t (torsional buckling) were initially taken as 0.75. This was based on the restraints used at the end of the studs as discussed earlier for the unlined frames. In the latter computations an effective length factor of 0.75 was maintained for K_x while a value of 0.1 was investigated for K_y and K_t . This is because the flexural buckling of the studs in the plane of the wall and twisting of the studs were expected to improve by lining the wall. Experimental failure modes are also given in Table 3. If the effect of lining material is ignored, the predicted loads would be as presented in Table 2 for the unlined frames.

Table 3: Ultimate Failure Loads of Both Sides Lined Frames to AS 4600 (SA, 1996)

Frame Number	Expt. Failure Load (kN)	Expt. Failure Mode	Section Capacity (N_s) (kN)	Expt. Load/ N_s	Case 1	Case 2
					Expt./Pred. Load	Expt./ Pred. Load
13	21.3	a	19.5	1.09	3.09	1.20
14	35.8	a	38.3	0.93	5.11	1.22
15	22.0	a	21.7	1.01	2.37	1.03
16	41.7	a	40.6	1.03	4.44	1.07
17	19.0	a	19.5	0.97	2.75	1.07
18	36.6	a & c	38.3	0.96	5.23	1.25
19	22.3	a	21.7	1.03	2.40	1.04
20	38.2	a	40.6	0.94	4.06	0.98

Case 1: $K_x = K_y = K_t = 0.75$; Case 2: $K_x = 0.75$, $K_y = K_t = 0.1$

The AS 4600 method underestimated the ultimate failure loads of the studs lined on both sides when an effective length factor of 0.75 was applied to the overall height of the studs. (see Table 3). Predicted loads based on AS 4600 are therefore conservative and inadequate for both sides lined wall frames. However, a good correlation of experimental and predicted failure loads was obtained when the effective length factors, K_y and K_t were reduced to 0.1. An effective length factor of 0.1 corresponds to an effective length equal to the fastener spacing used in the lined frames. These results support the observation of buckling of the studs between the fasteners during the tests (see Figure 7). The section capacities of the studs were also compared with the experimental failure loads and the two results were in good agreement (see Table 3). This result implies that the studs must fail by local buckling and/or yielding which was not the case during the tests, as all (except 2) studs failed by buckling between the top screws. Since only one screw spacing was adopted in the tests, it is difficult to conclude whether the failure loads of the studs with lining on both sides can be predicted by the section capacity. Finite element analyses to investigate the effect of the screw spacing will be used to confirm this result. The results based on assuming the appropriate effective length factors discussed above agreed reasonably well with the actual failure loads and the manner in which the studs failed. It is therefore reasonable to conclude that the failure load predictions of AS 4600 can be improved by using the effective length factors $K_x = 0.75$, $K_y = K_t = 0.1$ for the type of wall frames considered in this study.

In the AISI Method (1996), the studs were checked for three failure modes and the lowest load was

taken as the predicted failure load. These were the failure between the fasteners (mode (a)), failure by overall column buckling (mode (b)) and the shear failure of the lining material (mode (c)). Failure mode (a) requires the studs to be checked for buckling between the fasteners. An effective length factor K_f of 2 is used with the fastener spacing to allow for a defective adjacent fastener (AISI, 1996). In failure mode (b), the total length of the stud is considered. In this study using AISI rules, the same effective length factors used earlier ($K_x = 0.75$, $K_y = K_t = 0.1$) were adopted to check failure mode (b). For failure mode (a), $K_f=2$ was used whereas for failure mode (c) plasterboard was checked to ensure that the allowable shear strain of 0.008 (AISI, 1996) was not exceeded. The predicted failure loads and modes based on the AISI method are given in Table 4. Although reasonable estimates of the failure loads can be achieved when the effective length factors K_y and K_t were reduced to 0.1, the actual failure modes can only be predicted in 50 percent of the cases. There was no improvement in the results when the effective length factor for failure mode (a), K_f was reduced to one. It only resulted in an increase in the failure load for mode (a) which made mode (b) to govern. The AISI method therefore requires further improvement to ensure that both the failure loads and modes are accurately predicted.

Table 4: Ultimate Failure Loads of Both Sides Lined Frames to AISI 1996

Frame Number	Expt. Failure Load (kN)	Expt. Failure Mode	Section Capacity (N_s) (kN)	Expt. Load/ N_s	Case 1		Case 2	
					Pred. Failure Mode	Expt./ Pred Load	Pred. Failure Mode	Expt./ Pred. Load
13	21.3	a	19.5	1.09	b	1.21	b	1.20
14	35.8	a	38.3	0.93	c	1.27	b	1.21
15	22.0	a	21.7	1.01	b	1.10	a	1.07
16	41.7	a	40.6	1.03	c	1.67	a	1.19
17	19.0	a	19.5	0.97	b	1.06	b	1.04
18	36.6	a & c	38.3	0.96	c	1.28	b	1.23
19	22.3	a	21.7	1.03	b	1.11	a	1.07
20	38.2	a	40.6	0.94	c	1.53	a	1.09

Case 1: $K_x = K_y = K_t = 0.75$, $K_f = 2$; Case 2: $K_x = 0.75$, $K_y = K_t = 0.1$, $K_f = 2$

Experimental results showed that there was little difference in the failure loads for the stud spacings (300 mm and 600 mm) and that the failure mode was independent of the stud spacing. Even though the stud spacing has been removed from the AISI (1996) the results imply that the shear diaphragm model assumed by AISI is not applicable to wall frames lined with gypsum plasterboard. Miller and Pekoz (1994) also made similar observations. Further research using tests and finite elements analyses are needed to study the effect of the fastener spacing and the location of the last screw on the studs.

Frames with Plasterboard Lining on one side

The failure of the studs in this group was by flexural-torsional buckling (mode (b)) with the screws pulling through the lining at failure. Twisting of the web was observed and was more noticeable in the 200mm studs. As expected the unlined flanges of the studs were severely twisted. The lined flange was observed to deform/buckle between the fasteners. At failure there was no crushing or tearing of the plasterboard.

When the effect of the plasterboard was ignored for frames with lining on one side as recommended by AS 4600, the predicted loads would be the same as those of unlined frames with $K_x = K_y = K_t = 1.0$ (see Table 2). When the lateral and rotational supports were considered, the same approach taken in predicting the failure loads for frames with lining on both sides was adopted. Since the lining material

did not provide any restraints in the buckling of the studs out of plane, the effective length factor K_x was maintained at 0.75 (as in the unlined frames and both sides lined frames). However, the other effective length factors K_y and K_t were reduced to 0.1 and 0.2, respectively, in predicting the failure loads. Table 5 presents these results. Good correlation of the predicted and experimental loads was achieved for the 75mm studs (web $b/t < 70$). However, the predicted failure loads were overestimated for the 200 mm studs. Since the lining was on one side only, the unlined flange was prone to twisting, and in the case of the slender 200mm studs the twisting was more severe, resulting in premature failures. All the studs failed well below their predicted section capacity confirming that the failure was not by yielding but by flexural-torsional buckling. From these observations it can be concluded that slender C-sections should not be used in frames with plasterboard lining on one side only. For the C sections (web b/t less than 70), the AS 4600 predicted failure loads can be improved if the following effective length factors: $K_x = 0.75$, $K_y = 0.1$ and $K_t = 0.2$ are used.

Table 5: Ultimate Failure Loads of One Side Lined Frames to AS 4600-1996

Frame Number	Expt. Failure Load (kN)	Expt. Failure Mode	Section Capacity (N_s) (kN)	Expt. Load / N_s	Case 1	Case 2
					Expt./pred. Load	Expt./Pred. Load
5	16.7	b	19.5	0.86	2.42	0.97
6	28.3	b	38.3	0.74	4.04	1.05
7	15.0	b	21.7	0.69	1.61	0.72
8	18.2	b	40.6	0.45	1.94	0.51
9	18.5	b	19.5	0.95	2.68	1.08
10	26.6	b	38.3	0.69	3.80	0.99
11	14.4	b	21.7	0.66	1.55	0.69
12	19.4	b	40.6	0.48	2.06	0.54

Case 1: $K_x = K_y = K_t = 0.75$; Case 2: $K_x = 0.75$, $K_y = 0.1$, $K_t = 0.2$

Failure mode (b) denotes flexural-torsional buckling failure with the screw pulling through.

Since AISI (1996) does not include any provisions for one side lined walls, the failure loads and modes were predicted using AISI (1986) (see Table 6). The same procedures in checking the studs for frames with both sides lining were adopted for the studs in this group. When the effective length factors for K_y and K_t were reduced, the failure loads were overestimated. The predicted failure modes changed from mode (b) to (a) for all the frames except one. When the effective length for failure mode (a), K_t was reduced from two to one there was an increase in the predicted failure load, but the failure mode was unchanged. Therefore the AISI specification cannot accurately predict the failure loads or the failure modes of studs lined on one side. This explains why the AISI (1996) does not include any design provisions for this case.

Table 6: Ultimate Failure Loads of One Side Lined Frames to AISI 1986

Frame Number	Expt. Failure Load (kN)	Expt. Failure Mode	Section Capacity (N_s) (kN)	Expt. Load / N_s	Case 1		Case 2	
					Pred. Failure Mode	Expt./Pred. Load	Pred. Failure Mode	Expt./Pred. Load
5	16.7	b	19.5	0.86	b	1.88	a	0.89
6	28.3	b	38.3	0.74	b	3.14	c	0.90
7	15.0	b	21.7	0.69	b	1.33	a	0.71
8	18.2	b	40.6	0.45	b	1.58	a	0.50
9	18.5	b	19.5	0.95	b	2.08	a	0.98
10	26.6	b	38.3	0.69	b	2.96	c	0.77
11	14.4	b	21.7	0.66	b	1.27	a	0.68
12	19.4	b	40.6	0.48	b	1.69	a	0.53

Case 1: $K_x = K_y = K_t = 0.75$, $K_r = 2$; Case 2: $K_x = 0.75$, $K_y = 0.1$, $K_t = 0.2$, $K_r = 1.0$

CONCLUSIONS

An experimental investigation into the behaviour of the cold-formed steel wall frame systems lined with plasterboard under axial compression has been described in this paper. Twenty full-scale tests on wall frames without lining and with one and both sides lining were conducted. Following conclusions can be made from these tests.

- The failure loads of the studs in an unlined wall frame can be approximately predicted by the AS 4600 and AISI methods using effective length factors of $K_x = K_y = K_t = 0.75$.
- Both the AS 4600 and AISI methods can predict the failure loads of studs lined on both sides if the effective length factors K_x , K_y and K_t are taken as 0.75, 0.1 and 0.1, respectively. However, the AISI method is unable to predict the failure mode of some studs. Experimental results contradict the shear diaphragm model assumed by the AISI method.
- The design methods are inadequate in predicting the failure loads of the studs lined on one side, in particular studs with slender web. Further investigations using finite element analysis and testing are needed to develop improved behavioural models for wall studs with one or both sides lining.

ACKNOWLEDGEMENT

The authors wish to thank AusAid for providing a scholarship to the first author, Mr Ross Morris from CSR for donating the lining material and QUT's Physical Infrastructure Centre and School of Civil Engineering for providing other materials and test facilities.

REFERENCES

- American Iron and Steel Institute. (1996). *Specification for the Design of Cold-formed Steel Structural Members*, Washington, USA
- American Iron and Steel Institute. (1986). *Specification for the Design of Cold-formed Steel Structural Members*, Washington, USA
- CSR Plasterboard. (1990). *Do it yourself Gyprock Plasterboard Installation Manual*, Sydney
- Miller, T.H. and Pekoz, T.A (1993) Behaviour of Cold-formed Steel Wall Stud Assemblies. *Journal of Structural Engineering ASCE* **119:2**, 641-651
- Miller, T.H. and Pekoz, T.A. (1994). Behaviour of Gypsum Sheathed Cold-formed Steel Wall Studs. *Journal of Structural Engineering ASCE* **120:5**, 1644-1650.
- Rondo Building Systems (RBS). (1993). *Design Manual for Steel studs systems in non-cyclonic areas*.
- Simaan, A. and Pekoz, T.A. (1976). Diaphragm Braced Members and Design of Wall Studs. *Journal of Structural Division, ASCE Proceedings* **102:1**, 77-93.
- Standards Australia (SA). (1996). *AS 4600, Cold-formed Steel Structures*, Sydney
- Telue, Y.K. and Mahendran, M. (1997). *Behaviour and Design of Plasterboard Lined Cold-formed Steel Stud Walls under Axial Compression*, Research Monograph No.97-4, QUT, Brisbane

This Page Intentionally Left Blank

BUCKLING, TORSION, AND BIAXIAL BENDING OF COLD-FORMED STEEL BEAMS

N.S. Trahair, Y.-L. Pi, and B.M. Put

Centre for Advanced Structural Engineering
University of Sydney, NSW, 2006, AUSTRALIA

ABSTRACT

Codes for the design of cold-formed steel beams against lateral buckling are often inappropriately based on studies of hot-rolled I-beams, while there is little appropriate guidance on how to design cold-formed channels for torsion effects and zed beams for biaxial bending resulting from loading in the plane of the web. This paper summarises some of the recent research carried out at the University of Sydney on the lateral buckling strengths of cold-formed steel beams, and on the development of appropriate rules for designing channel and zed beams for torsion and biaxial bending.

KEYWORDS

Biaxial bending, buckling, channel beams, cold-formed, hollow flange beams, rectangular hollow beams, steel beams, structural engineering, torsion, zed beams.

INTRODUCTION

Code clauses for designing cold-formed steel beams against lateral buckling have often been based on studies of hot-rolled I-section columns (Trahair, 1994). However, cold-formed beams have very different cross-sectional shapes, residual stress distributions, and geometrical imperfections.

Cold-formed rectangular hollow section beams (Fig. 1b) have comparatively higher strengths than I-section beams (Fig. 1a), even when allowance is made for the very high torsional and flexural rigidities of hollow sections. Theoretical studies have shown that this is primarily due to the presence of two webs spaced apart, which delay the significant reductions in the inelastic flexural rigidity which occur in single web I-beams. Experimental studies have confirmed these increased strengths.

On the other hand, the strengths of cold-formed hollow-flange beams (Fig. 1c) are lower than might be expected from studies of hot-rolled I-beams, as a result of significant web distortion, which markedly reduces the apparently high torsional stiffnesses of the hollow flanges.

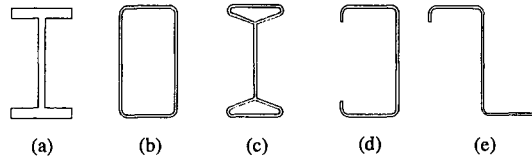


Fig. 1 Cross-section types

Theoretical studies of the lateral buckling of cold-formed lipped channel beams (Fig. 1d) loaded through the shear centre have shown that their strengths are lower when the initial imperfections increase the compressive stresses in the compression flange lip, and higher when they decrease these stresses. Experimental studies have confirmed this finding.

Channel beams are more usually loaded through the web than through the shear centre, so that the beam is under combined bending and torsion. Theoretical studies have predicted and experiments have confirmed that the maximum beam strength is available when the loading acts between the shear centre and the web.

Theoretical studies of cold-formed lipped zed beams (Fig. 1e) loaded in the stiffer principal plane have shown that the effective section rotates after yielding, and predict that the fully plastic moment may not be able to be reached unless the beam is fully braced laterally. The strengths of unbraced beams are lower when the initial imperfections increase the compressive stresses in the compression flange lip.

Zed beams are often loaded in the plane of the web, instead of in a principal plane, in which case the beam is under biaxial bending. Theoretical and experimental studies of the lateral buckling and biaxial bending of zed beams will be reported.

This paper summarises some of the recent research carried out at the University of Sydney on the lateral buckling strengths of cold-formed beams, including the development of appropriate rules for designing these beams against lateral buckling and biaxial bending and torsion.

LATERAL BUCKLING STRENGTHS

Rectangular Hollow Section Beams (RHSs)

Design rules for the lateral buckling of cold-formed rectangular hollow section (RHS) beams are given by Standards Australia (1990), but these are based on data for hot-rolled I-beams, which have a very different cross-section, stress-strain curve, and residual stress distribution. The lateral buckling strengths of RHS beams have been studied theoretically by Pi and Trahair (1995) and experimentally by Zhao *et al* (1995). These studies showed that the inelastic buckling resistances of RHS beams are superior to those of I-section beams because yielding in the two webs of an RHS is less rapid than in the flanges of an I-section. The increased theoretical and experimental strengths are shown in Fig. 2, together with the design strengths of AS4100, and a proposal to increase these design strengths.

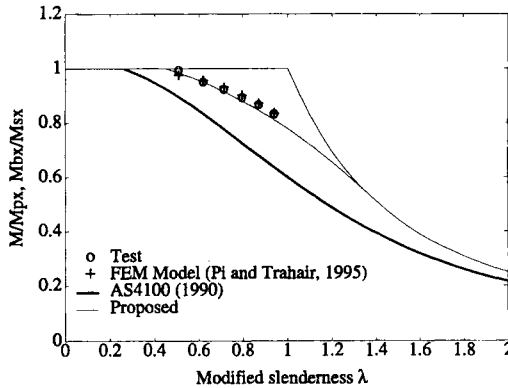


Fig. 2 Proposed design rule for RHS beams

Hollow Flange Beams (HFBs)

Research on the flexural-torsional buckling of beams (Trahair 1993, Trahair and Bradford 1998) usually assumes that the cross-section of the beam remains undistorted while the beam buckles by deflecting laterally and twisting. Hollow flange beams (HFB) appear to have quite high resistances to flexural-torsional buckling because the hollow flanges have high torsional stiffness. However, distortion of the comparatively flexible web (Fig. 3a) allows lateral displacement of the critical flange with only small rotations of the flanges, so that their high torsional stiffness is not fully mobilised during lateral buckling, and the resistance to elastic buckling is reduced (Fig. 3b). Pi and Trahair (1997) developed a simple method of allowing for the effects of web distortion on the elastic lateral-distortional buckling of HFBs, and showed that design rules developed for hot-rolled I-beams (Standards Australia, 1990) could be adapted for HFBs by replacing the elastic flexural-torsional buckling resistance by the elastic lateral-distortional buckling resistance.

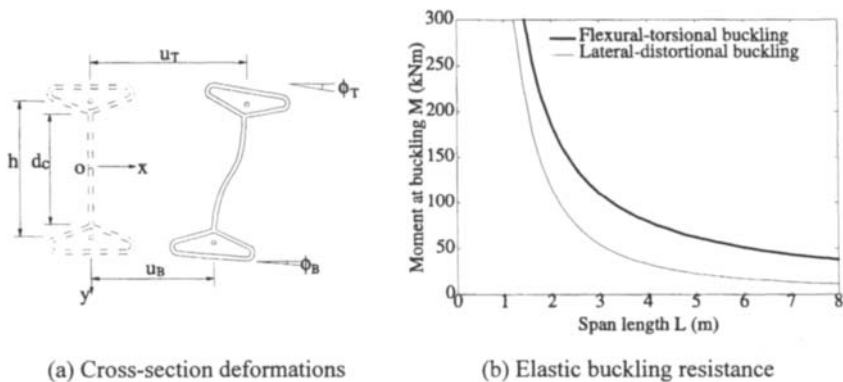


Fig. 3 Lateral-distortional buckling of a hollow flange beam

Cold-Formed Channel Beams (CFCs)

There is a lack of data on the lateral buckling strengths of cold-formed channel section beams (CFCs) loaded through their shear centres (Trahair, 1994). The monosymmetry of a channel section is a characteristic that is not possessed by an I-section. Monosymmetry causes the effective section to become asymmetrical after the initiation of yielding, and the effective shear centre moves towards the web, so that an elastic shear centre load exerts a torque which causes the beam to twist and deflect laterally (Pi et al, 1997). The strengths of beams with initial crookedness and twist depend on the direction of failure, which is strongly influenced by the senses of the initial crookedness and twist, and the strengths of lipped CFCs that fail by increasing the compression at the lip of the compression flange are lower than those that fail by decreasing the compression at the compression flange lip, as hown in Fig. 4. This effect is increased by local buckling of the compression lip (Put et al, 1998).

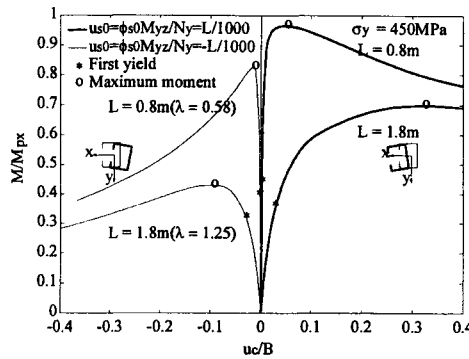


Fig 4 Effects of the direction of initial crookedness and twist

Cold-Formed Zed Beams (CFZs)

Design rules (Standards Australia, 1996) for the strengths of cold-formed zed beams (CFZs) do not distinguish between the very different loading conditions of principal plane loading, free web plane loading, and constrained web plane loading shown in Fig. 5. Theoretical solutions for elastic lateral buckling apply only to the principal plane loading shown in Fig. 5a, for which pre-buckling in-plane deflections v are followed by orthogonal out-of-plane buckling deflections u and twist rotations ϕ .

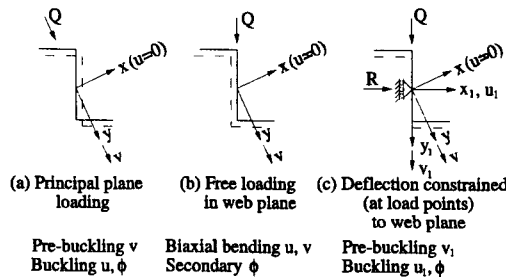


Fig. 5 Loading conditions for CFZ beams

On the other hand free web plane loading of CFCs causes primary biaxial bending about both principal axes, and non-linear behaviour (rather than bifurcation buckling) is caused by torsion actions generated by the eccentricity of the free load which displaces horizontally with the beam. Quite different behaviour occurs when lateral deflection is prevented at all points where loads or reactions act in the web plane. In this case, the primary action is deflection only in the plane of the web. It seems likely that flexural-torsional buckling may occur subsequently by horizontal deflections and twist rotations.

The lateral buckling strengths of CFZs under principal plane loading have been investigated theoretically by Pi *et al* (1997b), who showed that the effective cross-section rotates after yielding, and that the buckling strengths are decreased when the senses of the initial crookedness and twist cause increases in the compression of the compression flange lip. At the time of writing, a series of tests on the lateral buckling strengths of CFZs has just been completed (Put *et al*, 1998c).

Computer Design of Cold-Formed Purlins

Cold-formed C- and Z-section purlins are frequently used in building construction to support roof and wall sheeting, but most design standards for cold-formed purlins have design rules which are too complex for design engineers to use easily in hand calculation. In particular, the calculation of the effective section properties can be very tedious and time consuming. Design aids such as computer programs are essential for the efficient use of these design standards. Papangelis *et al* (1998) have described a user-friendly computer program PRFELB for the design of cold-formed C- and Z-purlins according to the Australian/New Zealand Standard for Cold-Formed Steel Structures, AS/NZS 4600 (SA, 1996). The program first performs a flexural-torsional buckling analysis of the purlin, which can be subjected to any type of loading. The program can also take account of the height of the load, and of the restraining effects caused by bracing and roof sheeting. The results of the buckling analysis are then used to design the purlin.

BENDING AND TORSION OF CHANNEL BEAMS

Channel section beams are often loaded in the plane of the web, so that the loads induce primary torsion actions about the shear centre, in addition to the primary major axis bending actions. The behaviour of such beams is non-linear, as the coupling of the twist rotations with the major axis moments induces minor axis bending actions.

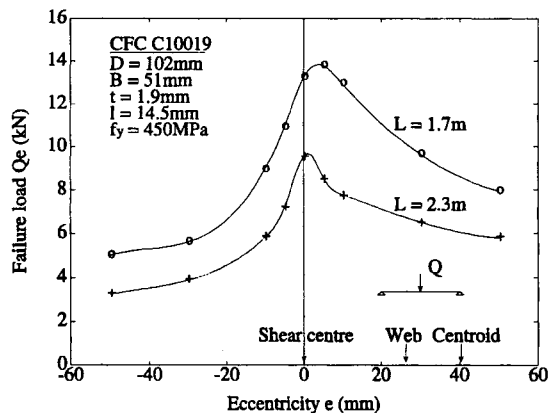


Fig. 6 Strengths of eccentrically loaded CFC beams

Experimental studies of eccentrically loaded channel section beams have been summarised by Put *et al* (1998b), who found that there is a lack of information on how the strengths vary with the eccentricity of loading, and on how this is related to the lateral buckling strengths of concentrically loaded channels. Recent experiments (Put *et al*, 1998b) have shown that the strength depends on the sense of the eccentricity, as indicated in Fig. 6, as well as on the magnitude. These have confirmed the theoretical predictions of Pi *et al* (1997a) that yielding causes the effective shear centre to move towards the web, so that the optimum loading position lies between the web and the shear centre. Figure 6 indicates that the strength is greater when the load acts on the web side of the shear centre, than when it acts on the side away from the web.

BIAXIAL BENDING OF ZED BEAMS

The biaxial bending of cold-formed zed beams whose loading plane is inclined to the principal planes has rarely been studied. At the time of writing, a series of biaxial bending tests (Put *et al*, 1998d) is nearing completion.

CONCLUSIONS

Code rules for beam design are often derived from studies of doubly symmetric hot-rolled I-beams, but cold-formed beams have very different cross-sections, stress-strain curves, and residual stresses. This paper summarises some recent theoretical and experimental research on the lateral buckling of strengths of cold-formed beams.

These studies have shown that rectangular hollow sections have higher strengths than equivalent hot-rolled I-beams, while hollow flange beams have lower strengths because of web distortion effects. Experimental studies of the lateral buckling strengths of cold-formed channel and zed beams will provide data for assessing and improving existing design rules.

This paper also reports on the bending and torsion strengths of cold-formed channel beams loaded eccentrically to the shear centre, and on the biaxial bending strengths of cold-formed zed beams loaded in a plane inclined to the principal planes.

References

- Hancock G.J. and Trahair N.S. (1997). Distortional Buckling of Single Web Steel Members. *Proceedings*, Theodore V. Galambos Symposium, Structural Stability Research Council, 85-96.
- Papangelis J.P., Hancock G.J. and Trahair N.S. (1998). Computer Design of Cold-Formed C- and Z-Section Purlins. *Proceedings*, Second World Conference on Steel In Construction, San Sebastian, Spain, Steel Construction Institute, Ascot.
- Pi Y.-L. and Trahair N.S. (1995). Lateral Buckling Strengths of Cold-Formed Rectangular Hollow Sections. *Thin-Walled Structures* **22:2**, 71-95.
- Pi Y.-L. and Trahair N.S. (1997). Lateral-Distortional Buckling of Hollow Flange Beams. *Journal of Structural Engineering*, ASCE **123:6**, 695-702.

- Pi Y.-L., Put B.M., and Trahair N.S. (1997a). Lateral Buckling Strengths of Cold-Formed Channel Section Beams. *Research Report R748*, Department of Civil Engineering, University of Sydney.
- Pi Y.-L., Put, B.M., and Trahair N.S. (1997b). Lateral Buckling Strengths of Cold-Formed Z-Section Beams. *Research Report R752*, Department of Civil Engineering, University of Sydney.
- Put B.M., Pi Y.-L., and Trahair N.S. (1998a). Lateral Buckling Tests on Cold-Formed Channel Beams. *Research Report R767*, Department of Civil Engineering, University of Sydney.
- Put B.M., Pi Y.-L., and Trahair N.S. (1998b). Bending and Torsion Tests on Cold-Formed Channel Beams. *Research Report*, Department of Civil Engineering, University of Sydney (in preparation).
- Put B.M., Pi Y.-L., and Trahair N.S. (1998c). Lateral Buckling Tests on Cold-Formed Zed Beams. *Research Report*, Department of Civil Engineering, University of Sydney (in preparation).
- Put B.M., Pi Y.-L., and Trahair N.S. (1998d). Biaxial Bending Tests on Cold-Formed Zed Beams. *Research Report*, Department of Civil Engineering, University of Sydney (in preparation).
- Standards Australia. (1990). *AS4100 Steel Structures*. Standards Australia, Sydney, Australia.
- Standards Australia. (1996). *AS/NZS 4600 Cold-Formed Steel Structures*. Standards Australia, Sydney, Australia.
- Trahair N.S. (1993). *Flexural-Torsional Buckling of Structures*, E & FN Spon, London.
- Trahair N.S. (1994). Lateral Buckling Strengths of Unsheeted Cold-Formed Beams. *Engineering Structures* **16:5**, 324-331.
- Trahair N.S. (1997). Multiple Design Curves for Beam Lateral Buckling, *Proceedings*, 5th International Colloquium on Stability and Ductility of Steel Structures, Nagoya, 33-44.
- Zhao X.-L., Hancock G.J., and Trahair N.S. (1995). Lateral Buckling Tests of Cold-Formed RHS Beams. *Journal of Structural Engineering*, ASCE **121:11**, 1565-1573.
- Zhao X.-L., Hancock G.J., Trahair N.S., and Pi Y.L. (1995). Lateral Buckling of Cold-Formed RHS Beams, *Proceedings*, International Conference on Structural Stability and Design, Sydney, 55-60.

This Page Intentionally Left Blank

DESIGN OF SLOTTED LIGHT GAUGE STUDS

Torsten Höglund

Department of Structural Engineering, Royal Institute of Technology,
SE-100 44 Stockholm, Sweden

ABSTRACT

The strength of slotted light-gauge steel studs loaded in bending and compression depends on the stiffness and strength of the perforated web. Shear deformations of the slotted web increase the stresses in the flanges, thus reducing the axial and bending resistance. A design method of simple supported and continuous studs is presented taking into account deformation of the web, deformation of fasteners in plasterboard, local buckling of flanges and webs. One or both flanges may be supported by plasterboard.

KEYWORDS

Steel, stud, slots, design, cold-formed, resistance, thin-walled, shear deformation, shear resistance.

GENERAL

Light-gauge steel framing

Walls made of slotted C sections of steel in interaction with plasterboard have the same good thermal properties as e.g. timber stud walls and are suitable for prefabrication. Lightweight construction using slotted steel studs has therefore become a competitive alternative to traditional construction. The system even has a certain advantage as regards recycling of materials and efficiency in production.

Owing to slotting, however, the stiffness and resistance of the web are radically altered. The usual design methods are not applicable, and other types of failure must be considered in design. So far, design has been mainly based on tests. This report describes analytical models, which are in good agreement with tests so far performed.

The slotted light-gauge stud

Several fabricators of lightweight constructions now have slotted studs in their range, intended for loadbearing external walls in single family houses and for infill walls in blocks of flats. The slots

normally form a pattern as shown in Figure 1c). The slots are normally about 70 mm in length, and the distance between them in the longitudinal direction is 20-25 mm. The transverse distance is 6-9 mm.

The slots can be punched out and then have a width of about 3 mm. They can also be 'cut' out in which case an opening of one mm or two is formed. The edges are folded inwards and form edge stiffeners which increase resistance, but at the same time make it difficult for the insulation boards to make close contact with the web. In order to increase resistance further, the web is sometimes folded or given a longitudinal groove in the centre. In most cases the web has two panels with five rows of slots between them, as shown in Figure 1c), while in smaller sections there are fewer rows of slots.

Slotted C sections are used as vertical studs, connected at top and bottom to slotted channels, rails. The studs are clad on both sides with one or more sheets of plasterboard. The sheets of plasterboard are screwed to the C studs. Screw spacing is mostly 300 mm in the centre stud and 200 mm along the sides when the sheets of plasterboard are 1200 mm wide. The plasterboard provides lateral bracing against buckling. In order to increase resistance, screw spacing in the centre stud is sometimes reduced to 200 mm.

Types of failure

The slotted light-gauge stud is thus a cold formed C section or channel with staggered oblong longitudinal holes (slots) in part of the web. See Fig. 1a) and c). The slotted part may be divided into two panels with unslotted material or a web fold between them. The term b_{slot} in Figure 1a) then refers to the sum of the slotted parts. The symbols for the cross section are given in Figure 1a). The thickness of the sheet is $t = t_o = t_u$

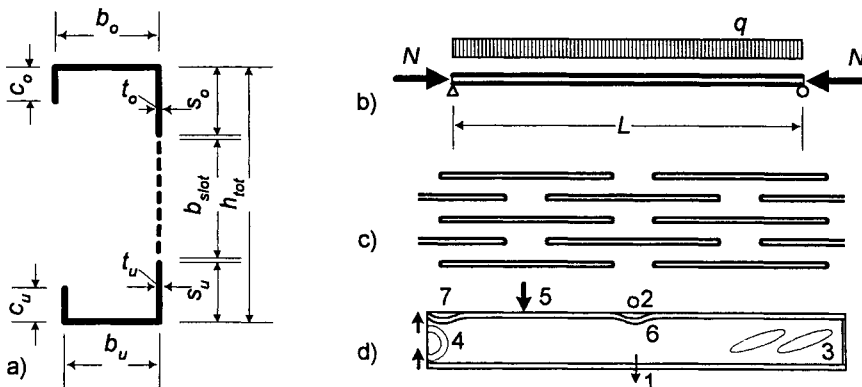


Figure 1: Slotted stud. a) cross section, b) loading, c) slots, d) failure modes.

The load is an axial load which may be applied eccentrically, and a transverse load which is either uniformly distributed or may be concentrated at some points. See Figure 1b). Several types of failure may occur. See Figure 1d).

1. Buckling in the plane of the web.
2. Lateral buckling of flanges in compression.
3. Shear failure in the slotted web.
4. Failure due to support reactions.

5. Failure under concentrated forces.
6. Buckling of the edges of the flanges in the span.
7. Buckling of the edges of the flanges at the supports.

In all cases, resistance is affected by the shear deformation of the slotted web and by the reduced transverse bending stiffness of the web. The calculation methods are based on Swedish Code for Light Gauge Metal Structures 79 (StBK-N5 and formulae for beams in two parts connected by elements which can be deformed in shear, Norlin (1995).

CALCULATION WITH RESPECT TO LOCAL AND OVERALL BUCKLING

Calculation steps

Calculation is performed in several steps.

- Calculation of the gross and effective cross section for both flange parts (upper part = $c_o + b_o + s_o$ and the lower part = $c_u + b_u + s_u$). The effective cross section for bending moment is different from that for axial force.
- The effect of the modulus of elastic shear support in the slotted part of the web. This modulus can be determined by testing or FE calculation, and is expressed in the form of a reduced shear modulus G_{red} for the web.
- Calculation of moments and normal force in the two parts of the beam, due to the transverse force on its own and the eccentric axial force on its own.
- Calculation of the stresses in the flanges and in the web section between the flanges and the slotted part of the web.
- Calculation of the reduction factors for lateral buckling of the flanges. These are assumed to be braced laterally by the sheets of plasterboard, which are assumed to act as elastic supports. The normal force is assumed to act in such a way that the sheets of plasterboard are not loaded at the ends of the beam.
- Calculation of resistance with respect to overall buckling in the plane of the web. The effect of the modulus of elastic shear support is taken into consideration.
- If the flange in tension is not braced, the additional stress and additional deflection due to lateral deflection of the flange in tension are calculated.

Gross cross section and effective cross section

For the gross cross section, the cross sectional areas A_o and A_u , the position of the centroid, the edge distance and second moments of area I_{xo} , I_{yo} and I_{xu} , I_{yu} about the x and y axes are calculated for the upper (o) and lower (u) part of the beam comprising edge folds c_o and c_u if any, flanges b_o and b_u , and web panels s_o and s_u outside the slotted part of the web.

The effective cross-section is based on the effective thickness concept.

Shear deformations of the web

Shear deformations give rise to longitudinal displacement of the flanges. This causes bending of both remaining panels of the web, with increased stress at the extreme fibres and reduced stress in the web where it joins the slotted part.

The shear deformation Δ in Figure 2 consists of the sum of the shear deformations and in the slotted part b_{slot} in the non-slotted panels e_{io} and e_{iu} of the web.

$$\Delta = \frac{\tau}{G}(h_t - b_{slot}) + \frac{\tau}{G_{red}}b_{slot}$$

where G_{red} is an effective shear modulus for the slotted part b_{slot} . A mean value G_{ck} of the shear modulus for the whole web can be determined by putting $\Delta = \tau h_t / G_{ck}$, which gives

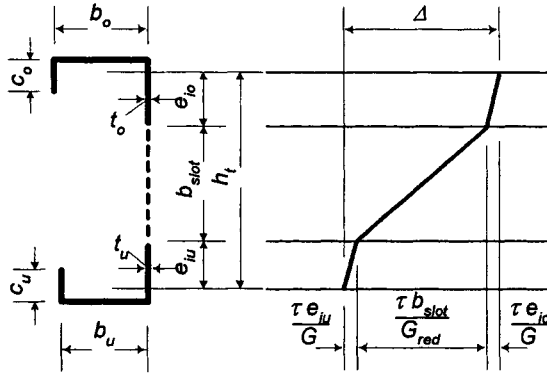


Figure 2: Shear deformations of the web

$$G_{ck} = \frac{G}{1 - \frac{b_{slot}}{h_t} + \frac{G}{G_{red}} \cdot \frac{b_{slot}}{h_t}}$$

Forces and deformations

The axial forces N_{ep} in the flange parts and the shear force between the flanges and the slotted part of the web N'_{ep} are calculated taking shear deformations in the slotted web into account. Furthermore the deflection w_q and the bending moments M_{fo} and M_{fu} in the flange parts are calculated for distributed load and eccentric axial force separately.

Buckling in the plane of the web

Consideration to shear deformations in the slotted part of the web is given through the well-known expression

$$N_{crit} = \frac{1}{\frac{1}{N_E} + \frac{1}{GA}}$$

where $N_E = \frac{\pi^2 EI_x}{L^2}$ and $GA = G_{ck} h_t t$. However, N_{crit} is not smaller than $N_{Esep} = \frac{\pi^2 (EI_o + EI_u)}{L^2}$

In calculating the resistance, the effective cross section and the reduction factor according to Eurocode 3, Curve a, are used for the compressive force, i.e. $N_{xcr} = \chi A_{ef} f_{yk}$.

Lateral buckling

If a flange is braced laterally by sheets of plasterboard, the buckling load is in most cases dependent on the shear stiffness of the fasteners. This stiffness determined by tests.

The buckling load N_{cryo} for the top flange is dependent on $L_{c1} = \pi^4 \sqrt{EI_{yo} / c_{screwo}}$ and may be given by

$$N_{cryo} = 2\sqrt{c_{screwo}EI_{yo}} \quad \text{if } L \geq L_{c1} \text{ (one or more buckling waves)}$$

$$N_{cryo} = \frac{\pi^2 EI_{yo}}{L^2} + \frac{L^2 c_{screwo}}{\pi^2} \quad \text{if } L < L_{c1} \text{ (one buckling wave)}$$

where c_{screwo} is the modulus of elastic support from the screws in top flange.

The resistance of the top flange is $N_{Rdyo} = \chi_o A_{ef} f_{yko}$ where χ_o is determined in accordance with Eurocode 3, Curve a. The resistance N_{Rdyu} of the bottom flange is determined in the same way.

The total resistance is given by

$$N_{Ryd} = 2N_{Rdmin} \quad \text{for a central axial force}$$

$$N_{Ryd} = N_{Rdyo} \quad \text{for a load on the top flange}$$

Where $N_{Rdmin} = \min(N_{Rdyo}, N_{Rdyu})$ i.e. it is assumed that the resistance is exhausted when the flange of the least resistance buckles laterally. The force in the other flange is then of the same magnitude since the axial force acts centrally in the cross section.

It is assumed that a groove in the web does not contribute to the resistance since it has little support from the adjoining slotted parts of the web.

Unbraced flange

Owing to the asymmetry of the unbraced flange, a distributed load gives rise to a distributed lateral load $k_n q$. See Figure 3 and StBK-N5 (1979). This force gives rise to lateral deflection which increases the tensile stress at the junction between web and flange, and increases deflection with the amount of σ_{1add} and w_{add} respectively.

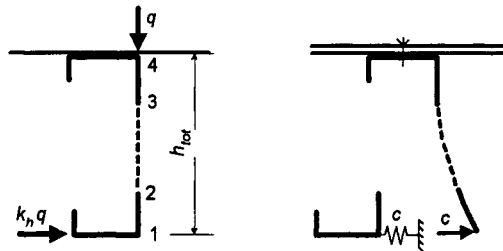


Figure 3: Lateral force on flange in tension and bracing provided by web

The slots steeply reduce the bending stiffness of the web in the lateral direction. An unbraced flange in compression therefore has very little lateral support even when twisting of the other flange is

restrained. But the unbraced flange is very slender, so that even a small elastic support from the web gives rise to an increase in buckling load. Calculations show that the elastic lateral support is approximately 10% of that which is provided if the web acts as a series of cantilevers fixed in the braced flange. See Figure 3.

Lateral buckling check

Stresses in points 1 to 4 in Figure 3 are calculated. The stress σ_4 in the upper flange is compared to $\chi_o f_y / \gamma_{M1}$ where χ_o is the reduction factor for lateral buckling and the stress $\sigma_1 + \sigma_{1add}$ in the bottom flange is compared to f_y / γ_{M1}

SHEAR STRENGTH

The shear force in the slotted part of the web is $V_s = N'_{ep} h_t$ where N'_{ep} is determined as above. Normally, N'_{ep} is highest at the supports, i.e. for $x = 0$ or $x = L$, but in some cases e.g. eccentric axial force the shear force is highest some distance from the supports, due to shear deformations.

The shear resistance τ_{wk} of the slotted parts is determined by calculation, e.g. according to Höglund (1997), or by testing. Owing to the shear deformations, the shear force V_s in the web is almost always smaller than the transverse force V . The difference is taken up by the cross sections of the two flange parts.

In the case of punched slots, ultimate shear failure occurs in the form of buckling or lateral-torsional buckling of the strips of sheeting between the slots. See Figure 4. Every other of these strips along the stud is acted upon by compressive force and bending moment and every other by tensile force and bending moment. After buckling, tensile failure may occur in the latter sheeting strip. Tensile failure can also occur at stress concentrations when slots are not punched. The details of the calculation method for punched slots are set out in Höglund (1997).

When slots are punched and there are no longitudinal web stiffeners, shear failure occurs after extensive global shear buckling in the web. The slots considerably reduce buckling stress, due to the fact that bending stiffness, especially across the web, is steeply reduced. An estimate of the shear buckling strength is given in Höglund (1997). Since the shear buckling stress is low, the post-buckling range is large.

In the case of cut slots, see to the right in Figure 4, the cross section of the sheeting strips between the slots is channel shaped, except at the ends where it is angle shaped. The stiffness of these strips is so high that buckling does not occur. However, at the ends of the slots the channel shaped section changes into an angle shaped section, which has smaller moment resistance and axial force resistance than the channel section. Here, resistance is governed by yield. The ends of the slots may have a sharp corner which initiate yield. To a very local extent, buckling at the ends of the slots may even give rise to redistribution of stresses and accelerate yield. A calculation example for cut slots is given in Höglund (1997).

The shape of the end stiffeners is significant for the lateral force resistance at the supports. In the case of punched slots these end stiffeners can tightly surround the web end. Local lateral buckling of free sheeting strips between slots is prevented.

In the case of cut slots, contact at the edges of the sheet can be less good. If there is a longitudinal

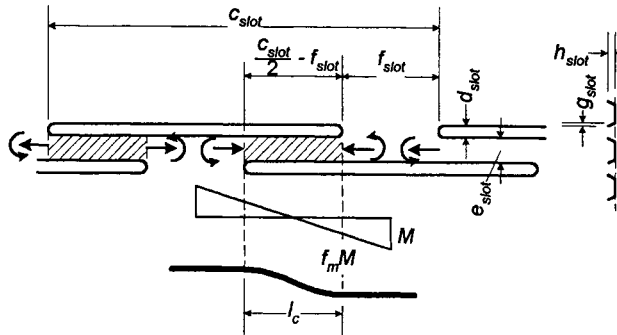


Figure 4: Forces which act upon the sheeting strips (crosshatched) between the slots. To the right, cross section with cut slots.

groove in the web between rows of slots, a channel shaped end stiffener in which the width of the bottom of the channel is equal to the depth of the groove cannot stiffen the ends of the sheeting strips, and consequently the shear force resistance (or actually the crippling strength) is reduced.

In finished walls with sheets of plasterboard on both sides, the sheets make some contribution to shear force resistance. But the influence of the plasterboard depends on the pull-out resistance of the screw connections, which is dependent on workmanship. The contribution due to the plasterboard should not therefore be taken into consideration.

CONCENTRATED FORCE

A concentrated force in the span can also cause local failure unless transverse stiffeners are used. What happens is that the loaded flange deflects inwards towards the slotted part of the web, which has little ability to resist forces transverse to the web. This inward deflection result in a positive curvature at point 1 in Figure 5 and increases compressive stresses in the loaded flange below the concentrated load, but it also results in negative curvature at point 2 some distance from the point of application of the load.

Compressive forces in the sheets of plasterboard may cause loss of attachment between the sheets and the stud; the flange loses its lateral support with immediate failure as the result.

Resistance is governed by the combination of the concentrated load and the compressive force in the plasterboard. Even if no consideration is given to the fact that the sheets of plasterboard can resist some axial compressive and tensile force, the sheets will be axially loaded, and the negative curvature near the concentrated load may therefore give rise to tensile failure in the screw attachments. Moment resistance is thus reduced when a concentrated load is applied.

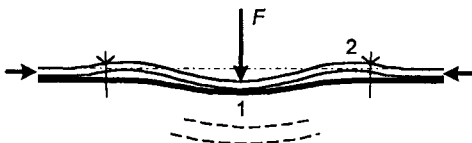


Figure 5: Bending of flange (thick line) and plasterboard (two lines) due to a concentrated load. Positive curvature at point 1 and negative curvature at point 2.

In Höglund (1997), a calculation model is used which estimates the additional stresses due to local bending under point 1 in Figure 5.

BUCKLING OF THE FLANGE EDGE STIFFENERS

The web has very little flexural stiffness in the transverse direction. The restraint provided by the web when the flange undergoes torsion is therefore negligible. Buckling of the flange stiffener is therefore mainly prevented by the screws in the plasterboard.

If the screw attachments, and also the sheets of plasterboard, were completely rigid the effective length of the flange stiffener would be half the distance between the screws. Owing to flexibility, chiefly slip in the screw attachments, the effective length is greater. The approximate effective length given by tests is $l_c = 0,72 c_{screw}$ where c_{screw} is the spacing of screws. See Figure 6.

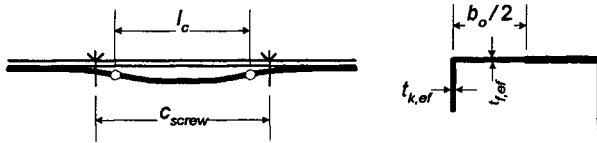


Figure 6: Effective length and effective cross section of flange edge stiffener.

TESTS

Tests on slotted studs with plasterboard have been carried out by e.g. the Norwegian Building Research Institute, Hallquist et al (1981) and (1982) and Ramstad (1983), the Danish Technological Institute, Fredriksen and Spange (1992) and the Department of Structural Engineering, Steel Structures, Royal Institute of Technology, Stockholm, Höglund (1997). These tests are in good agreement with calculations using the computer program SVE, Höglund (1996), based on the above principles.

References

- Frederiksen, I. O. and Spange, H. (1992). *Danogips steel construction system. Investigation of resistance of lightweight external walls.* (In Danish). Institute of Building Technology, Hørsholm.
- Hallquist, Å. et al (1981). *Light gauge sections in walls. Preliminary project.* (In Norwegian). Norwegian Building Institute (NBI), Oslo.
- Hallquist, Å. et al (1982). *Tests on wall elements with light gauge steel studs.* (In Norwegian). NBI, Oslo.
- Höglund, T. (1996). *SVE - A computer program for the analysis of beams of two parts and an elastic shear medium.* (In Swedish). Department of Structural Engineering, Steel Structures, Royal Institute of Technology, Stockholm.
- Höglund, T. (1997). *Calculation of slotted steel studs.* Report 42, Department of Structural Engineering, Steel Structures, Royal Institute of Technology, Stockholm.
- Norlin, B. (1995). *Incomplete interaction in laminated timber beams.* (In Swedish). Part of Compendium in Lightweight Construction. Department of Structural Engineering, Steel Structures, Royal Institute of Technology.
- Ramstad, T. O. (1983). *Tests on light gauge steel sections in external walls.* (In Norwegian). NBI, Oslo.
- StBK-N5 (1979). Swedish Code for Light Gauge Metal Structures 79. Svensk Byggtjänst. Stockholm.

DIRECT STRENGTH PREDICTION OF COLD-FORMED STEEL MEMBERS USING NUMERICAL ELASTIC BUCKLING SOLUTIONS

B.W. Schafer¹ and T. Peköz²

^{1,2} School of Civil and Environmental Engineering,
Cornell University, Ithaca, NY 14853, USA

ABSTRACT

Current design of cold-formed steel members is unduly complicated. Part of this complication arises from the need to perform elastic buckling calculations by hand. Also, complications occur in determining the effective width and resulting effective properties of members. Further, as cross-sections become more optimized (e.g., through the introduction of longitudinal stiffeners) both the elastic buckling and effective width calculations become markedly more complex. In order to investigate alternatives to current design a large amount of experimental data on flexural members of varying geometry is collected. The use of numerical elastic buckling solutions for the entire member, is investigated as an alternative to current practice. Employing strength curves on the entire member, similar to the effective width strength curves for an element, it is found that a “direct strength” approach is a reliable alternative to current design. Such an approach leads to complete flexibility in cross-section geometry, thus greatly increasing the ability to optimize cold-formed steel members. Conservative limitations of the direct strength approach are also addressed.

KEYWORDS

cold-formed steel, direct strength, elastic buckling, finite strip, AISI

INTRODUCTION

The thin-walled nature of typical cold-formed steel members makes stability a primary concern. Most modern design specifications (e.g., AISI (1996)) account for stability issues by using an effective width approach. The expression for empirical determination of the effective width includes the elastic buckling stress of an element and the applied compressive stress on the element. For simple cross-sections (e.g., a hat with no intermediate stiffeners) this approach is relatively straightforward. However, for more modern, optimized, cross-sections the calculation of the elastic buckling stress and

the calculation of the effective properties can become complicated. A simple design method that avoids the complexity of current methods, yet is general enough to be applicable to modern optimized cross-sections is needed.

ELASTIC BUCKLING SOLUTIONS

A necessary first step in cold-formed steel member design is calculation of the elastic buckling solution. Design specifications typically use idealized plate buckling solutions. For example, the $k = 4$ solution for a simply supported plate in pure compression, is employed for local buckling of the compression flange. These simple solutions ignore interaction amongst elements, also unusual member geometry, such as the addition of longitudinal stiffeners, is difficult to incorporate. Further, new buckling modes that arise with more complex member geometry (e.g., distortional buckling) are difficult to predict using these simple, classical methods.

The result of these complications is that existing design specifications actively hamper the development of more optimized member geometry. Reliance on hand methods insures that in the few cases in which design rules are developed for more optimized cross-sections, the resulting guidelines are even more complicated. The hand calculation of elastic buckling requires a great deal of effort and complication, even though reliable computational methods now exist. Modern computational methods: finite element (example programs: ABAQUS, ANSYS, STAGS), finite strip (example programs THIN-WALL, CUFSM) may all be used to determine the elastic buckling solution. In this work, the "semi-analytical" finite strip method, as implemented in CUFSM, is employed.

COLLECTED EXPERIMENTAL DATA

Experimental data is collected from 17 researchers for a total of 574 flexural members. The member types investigated include laterally braced channels and zees, as well as hats and trapezoidal decks. The members include different types, locations, and numbers of longitudinal stiffeners. The geometry of the collected members is summarized in Table 1. Finite strip analysis is completed on every member to determine the elastic buckling solution. The slenderness of each member is determined from the minimum critical buckling moment (M_{cr}) and the yield moment (M_y). In Figure 1, the slenderness is plotted versus the experimental bending strength (M_{test}) normalized by M_y . Despite the vastly differing member geometry clear trends exist.

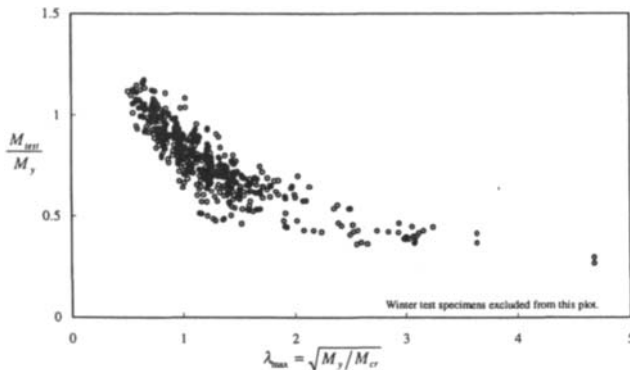


Figure 1: Slenderness vs. strength for the experimental data

TABLE 1
DESCRIPTION OF THE EXPERIMENTAL DATABASE FOR FLEXURAL MEMBERS

Researcher	Lapped C	Unlapped C	Sloping Lip C	Lapped C + Web Stiffener	Hat	Hat + 1 Intern. Stiffener	Hat + 2 Intern. Stiffener	Hat + 3 Intern. Stiffener	Hat + 4 Intern. Stiffener	Trapezoidal Deck	Trap. + 1 Int. Stiffener	Trap. + 1 Int. St. + 1 Web St.	Trap. + 1 Int. St. + 2 Web St.	Trap. + 2 Int. St. + 2 Web St.	Z	Z with unstopped lips	Grand Total
Acharya (1997)							30	32	32								94
Bernard (1993)										6	12						18
Cohen (1987)	14		22														36
Desmond (1977)						22											22
Ellifritt et. al. (1997)	5														5		10
Hoglund (1980)										6	53	16	4	19			98
Konig (1978)					4	15	13										32
LaBoube and Yu (1978)	32																32
Moreyra (1993)	9																9
Papazian (1994)						2	6	6	6								20
Phung and Yu (1978)	6			42													48
Rogers (1995)	50	9															59
Schardt and Schrade (1982)															8	29	37
Schuster (1992)	5																5
Shan (1994)	29																29
Willis and Wallace (1990)	4														6		10
Winter (1946)					15												15
Grand Total	154	9	22	42	19	39	49	38	38	12	65	16	4	19	19	29	574

PREDICTION METHODS

Based on the trend shown in Figure 1, three new prediction methods are introduced. The methods are also compared to the current AISI Specification (1996) approach. The AISI Specification for a cold-formed steel flexural member is based on the unified effective width approach of Peköz (1987). For members that do not undergo lateral-torsional buckling the nominal bending strength (M_n) is calculated as:

$$(M_n)_{AISI} = S_{eff} f_y \tag{1}$$

The effective section modulus (S_{eff}) is determined by finding the effective moment of inertia and effective neutral axis location. These are determined once the effective width (b_e) of the component elements is calculated, via:

$$b_e = \rho b, \rho = (1 - 0.22/\lambda)/\lambda, \lambda = \sqrt{f_y/f_{cr}} \text{ and } \lambda > 0.673 \text{ or } \rho = 1 \tag{2}$$

Three “direct strength” methods are investigated as alternatives to the “effective width” approach. The first alternative method employs the same reduction factor, ρ , as in Eqn. 2, but applies ρ to the entire section, such that:

$$(M_n)_1 = \rho M_y = (\rho S_x) f_y = S_x (\rho f_y) \tag{3}$$

Though ρ in Eqn. 3 is applied directly to M_y , in some cases it may be simpler to think of ρ as providing a reduced section modulus, or a reduced stress. To determine ρ in Eqn. 3, λ , (see Eqn. 2) applies to the

entire cross-section. If $\lambda < 0.673$ then $M_n = M_y$. For cases in which $\lambda > 0.673$, Eqn. 3 may be rewritten to give the direct strength prediction:

$$(M_n)_1 = \sqrt{\frac{M_{cr}}{M_y}} \left(1 - 0.22 \sqrt{\frac{M_{cr}}{M_y}} \right) M_y \quad (4)$$

The second prediction method provides an additional reduction for failures in the distortional mode. Hancock (1995) and Schafer (1997) observed decreased post-buckling capacity in distortional failures. Further, the distortional mode may control failure even when elastic buckling predicts otherwise. Therefore, a correction can be made in determining M_{cr} . The selected approach based on Schafer (1997) is:

$$(M_n)_2 = \sqrt{\frac{M_{cr}^*}{M_y}} \left(1 - 0.22 \sqrt{\frac{M_{cr}^*}{M_y}} \right) M_y \quad (5)$$

$$M_{cr}^* = \min \left((M_{cr})_{local}, R_d (M_{cr})_{dist} \right) \quad (6)$$

$$R_d = \frac{1.17}{\lambda_d + 1} + 0.3 \text{ for } \lambda_d > 0.673, \text{ where } \lambda_d = \sqrt{M_y / (M_{cr})_{dist}} \quad (7)$$

The third, and final, direct strength prediction method is based on the form of Eqn. 4, modified to better agree with the available experimental data. If $\lambda < 0.776$ then $M_n = M_y$. For cases in which $\lambda > 0.776$ then:

$$(M_n)_3 = \left(\frac{M_{cr}}{M_y} \right)^{0.4} \left(1 - 0.15 \left(\frac{M_{cr}}{M_y} \right)^{0.4} \right) M_y \quad (8)$$

PERFORMANCE OF PREDICTION METHODS

The strength curves for the direct strength method: M_1 (Eqn. 4), M_2 (Eqn. 5), and M_3 (Eqn. 8) are shown in Figure 2. M_2 only differs from M_1 in cases where distortional buckling controls. For these cases the reduced strength curve for M_2 is plotted in Figure 2. Direct comparison of the adequacy of the proposed approaches as well as the existing AISI Specification is provided in Figure 3 and Table 2.

On average the AISI Specification performance is reasonable. However, the variation is high (i.e., wide scatter in the test to predicted ratio plot of Figure 3). The results by researcher indicate consistently unconservative strength predictions for certain classes of channels and zees. Also, the prediction of members with multiple intermediate stiffeners in the compression flange is quite poor. The AISI Specification has no design rules for members with web stiffeners. Therefore, no AISI data is reported for the work of Hoglund, or Phung and Yu.

The first direct strength approach, M_1 , appears relatively conservative for all the members tested. The variation in the predictions is lower than the AISI Specification. Figure 3 shows that the prediction becomes progressively more conservative as slenderness increases. Use of the standard reduction factor (ρ) on the whole member works reasonably well on a wide class of members. The M_2 approach is

poorer than the M_1 approach. The method is based on the observation that distortional buckling has a lower post-buckling capacity than local buckling. This conclusion is not borne out by this experimental data. The M_3 approach performs well, excepting the conservative predictions for the Winter (1946) data. The method is markedly more accurate and reliable than the other direct strength approaches and even better than the AISI Specification. A simple direct strength approach is viable for this class of cold-formed steel flexural members.

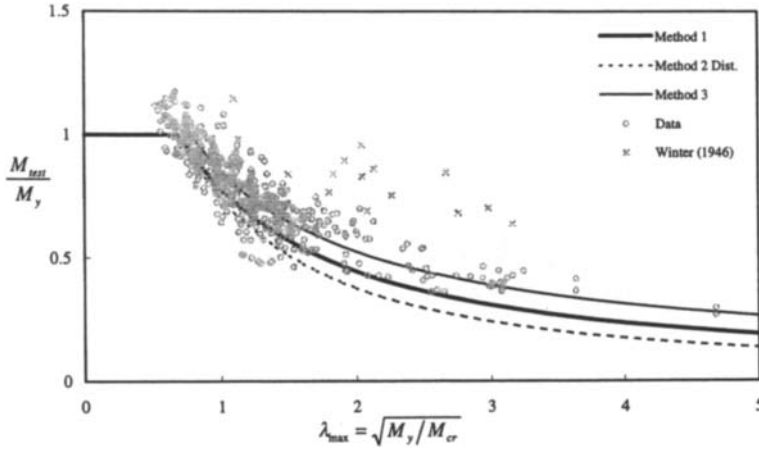


Figure 2: Strength curves and experimental data

TABLE 2
TEST TO PREDICTED RATIOS OF DIFFERENT PREDICTION METHODS

	average of test to predicted ratio				standard dev. of test to predicted ratio				count
	$\frac{M_{test}}{M_{AISI}}$	$\frac{M_{test}}{M_1}$	$\frac{M_{test}}{M_2}$	$\frac{M_{test}}{M_3}$	$\frac{M_{test}}{M_{AISI}}$	$\frac{M_{test}}{M_1}$	$\frac{M_{test}}{M_2}$	$\frac{M_{test}}{M_3}$	
	Acharya (1997)	1.03	1.15	1.24	1.04	0.32	0.16	0.22	
Bernard (1993)	1.04	1.22	1.33	1.01	0.12	0.19	0.26	0.11	18
Cohen (1987)	1.14	1.12	1.15	1.02	0.09	0.12	0.13	0.10	36
Desmond (1977)	1.07	1.06	1.11	0.94	0.07	0.07	0.08	0.07	22
Ellifritt et. al. (1997)	0.78	0.89	0.97	0.81	0.10	0.11	0.13	0.10	10
Hoglund (1980)		1.06	1.06	0.99		0.13	0.12	0.09	98
Konig (1978)	1.01	1.18	1.26	0.96	0.23	0.33	0.35	0.18	32
LaBoube and Yu (1978)	1.02	1.14	1.14	1.04	0.08	0.12	0.13	0.10	32
Moreyra (1993)	0.82	0.96	0.96	0.88	0.09	0.10	0.10	0.09	9
Papazian (1994)	0.90	1.11	1.15	1.03	0.17	0.12	0.13	0.11	20
Phung and Yu (1978)		1.15	1.21	1.03		0.10	0.12	0.07	48
Rogers (1995)	1.01	1.15	1.22	1.05	0.12	0.11	0.17	0.08	59
Schardt and Schrade (1982)	1.05	1.15	1.17	1.03	0.10	0.07	0.09	0.07	37
Schuster (1992)	0.82	1.03	1.03	0.94	0.04	0.04	0.04	0.04	5
Shan (1994)	0.97	1.08	1.12	0.99	0.13	0.12	0.16	0.10	29
Willis and Wallace (1990)	1.00	1.07	1.08	0.98	0.07	0.07	0.07	0.07	10
Winter (1946)	1.10	1.84	1.84	1.54	0.08	0.32	0.32	0.21	15
Grand Total	1.02	1.14	1.18	1.02	0.16	0.14	0.16	0.10	574

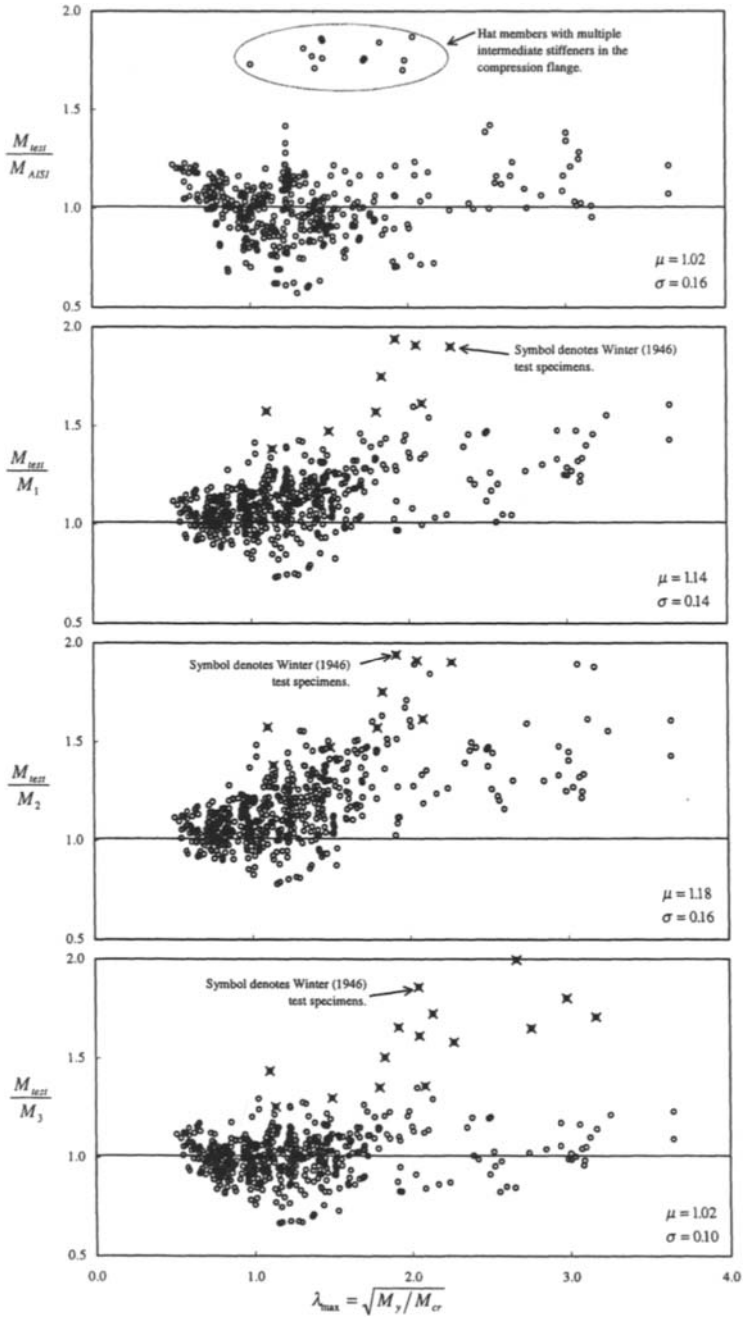


Figure 3: Test to predicted ratios for AISI and direct strength methods

LIMITATIONS OF DIRECT STRENGTH METHODS

Multiple Minima in the Elastic Buckling Solution

When determining the elastic buckling solution numerically many different modes will exist. One philosophy is to simply take the minimum buckling moment (stress) and use that to determine the slenderness of the member. This seemingly rational decision has some rather serious ramifications. First, it assumes that the strength and failure mode are governed by the mode of behavior consistent with the minimum elastic buckling moment (stress). Experimental data shows that when two buckling modes compete the final failure mode may not be consistent with the elastic minimum. Second, this encourages an optimum design in which several different modes occur at the same elastic buckling moment (stress). Experimental evidence shows this is a poor optimum, due to strength considerations and that it invites problems with coupled instabilities. The M_2 method is an attempt to alleviate these concerns. However, the approximations made for this approach appear to be excessively conservative.

Effective Width vs. Direct Strength

One obvious limitation to the direct strength method is the conservative predictions for the Winter test specimens. The basic geometry of these specimens is shown in Figure 4. These hat sections illustrate an important conceptual difference between the direct strength approach and the effective width approach. Consider that as the flange becomes more slender the results for the two methods approach Figures 4b and 4c. For the effective width approach the elimination of the compression flange as ρ goes to zero causes a large neutral axis shift and the resulting section is left to carry the load. For the direct strength approach as ρ goes to zero so goes the entire strength. A parametric study of hats similar to those of Figure 4 shows that the difference between these two methods is particularly pronounced in specimens similar to those Winter tested. Specimens with low height to flange width (h/b) ratios, and low tension flange width to compression flange width (c/b) ratios, and low reduction factors (ρ) are predicted quite conservatively using a direct strength approach. However, as h/b , or c/b or ρ increase the two prediction methods become similar again. For more typical sections the adequacy of the direct strength approach is evidenced by the fine correlation with existing data.

CONCLUSIONS

Current design methods for cold-formed steel members are unduly complicated and as a result hamper innovation in cross-section design. A significant amount of this complication is due to the need to calculate elastic buckling solutions by hand. Today, these solutions may be completed numerically with great reliability and ease. Further, using numerical methods for the elastic buckling solution the whole member may be treated consistently, rather than just the component elements. A secondary complication of current design methods is the determination of the effective section. Comparison to a large experimental database of flexural members of varying geometry shows that accurate knowledge of the member buckling solution (member slenderness) provides a direct way to get at the member capacity. The current AISI Specification and three alternative direct strength approaches are compared with the large experimental database. It is shown that a direct strength method can provide the same overall average predictive capabilities and lower variation than the existing AISI Specification. The direct strength approach is not however without its limitations, for some specific cross-sections (low h/b , and c/b and ρ) it may become too conservative.

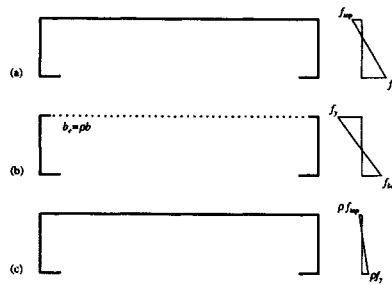


Figure 4: Difference in effective width vs. direct strength methods (a) gross section (b) effective section as ρ approaches 0 (c) direct strength approach as ρ approaches 0.

REFERENCES

- American Iron and Steel Institute (1996). *Cold-Formed Steel Design Manual*. American Iron and Steel Institute.
- Bernard, E.S. (1993). Flexural Behavior of Cold-Formed Profiled Steel Decking. Ph.D. Thesis, U. of Sydney, Australia.
- Desmond, T.P. (1977). The Behavior and Design of Thin-Walled Compression Elements with Longitudinal Stiffeners. Ph.D. Thesis, Cornell University, Ithaca, New York.
- Ellifritt, D., Glover, B., Hren, J. (1997). Distortional Buckling of Channels and Zees Not Attached to Sheathing. *Report for the American Iron and Steel Institute*.
- Haaijer, G. (1957). Plate Buckling in the Strain-Hardening Range. *Transactions, ASCE*. 124.
- Hancock, G.J., Kwon, Y.B., Bernard, E.S. (1994) Strength Design Curves for Thin-Walled Sections Undergoing Distortional Buckling. *J. of Constructional Steel Research* 31:2-3, 169-186.
- Höglund, T. (1980). Design of Trapezoidal Sheeting Provided with Stiffeners in the Flanges and Webs. *Swedish Council for Building Research D28:1980*.
- König, J. (1978). Transversally Loaded Thin-Walled C-Shaped Panels With Intermediate Stiffeners. *Swedish Council for Building Research D7:1978*.
- LaBoube, R.A., Yu, W. (1978). Structural Behavior of Beam Webs Subjected to Bending Stress. *Civil Engineering Study Structural Series, 78-1*, Department of Civil Engineering, University of Missouri-Rolla, Rolla, Missouri.
- Moreyra, M.E. (1993). The Behavior of Cold-Formed Lipped Channels under Bending. M.S. Thesis, Cornell University.
- Papazian, R.P., Schuster, R.M., and Sommerstein, M. (1994). Multiple Stiffened Deck Profiles. *Twelfth International Specialty Conference on Cold-Formed Steel Structures*, University of Missouri-Rolla.
- Peköz, T. (1987). *Development of a Unified Approach to the Design of Cold-Formed Steel Members*. American Iron and Steel Institute Research Report CF 87-1.
- Phung, N., Yu, W.W. (1978). Structural Behavior of Longitudinally Reinforced Beam Webs. *Civil Engineering Study Structural Series, 78:6*, Department of Civil Engineering, University of Missouri-Rolla, Rolla, Missouri.
- Rogers, C.A., Schuster, R.M. (1995) Interaction Buckling of Flange, Edge Stiffener and Web of C-Sections in Bending. *Research Into Cold Formed Steel, Final Report of CSSBI/IRAP Project*, Department of Civil Engineering, University of Waterloo, Waterloo, Ontario.
- Schafer, B.W. (19957). Cold-Formed Steel Behavior and Design: Analytical and Numerical Modeling of Elements and Members with Longitudinal Stiffeners. Ph.D. Thesis, Cornell University, Ithaca, New York.
- Schardt, R. Schrade, W. (1982). Kaltprofil-Pfetten. Institut Für Statik, Technische Hochschule Darmstadt, Bericht Nr. 1, Darmstadt.
- Schuster, R.M. (1992). Testing of Perforated C-Stud Sections in Bending. Report for the Canadian Sheet Steel Building Institute, University of Waterloo, Waterloo Ontario.
- Shan, M., LaBoube, R.A., Yu, W. (1994). Behavior of Web Elements with Openings Subjected to Bending, Shear and the Combination of Bending and Shear. *Civil Engineering Study Structural Series, 94:2*, Department of Civil Engineering, University of Missouri-Rolla, Rolla, Missouri.
- Willis, C.T., Wallace, B. (1990). Behavior of Cold-Formed Steel Purlins under Gravity Loading. *J. of Structural Engineering, ASCE*. 116:8.
- Winter, G. (1946). Tests on Light Beams of Cold-Formed Steel. Forty-fifth Progress Report, Cornell University. (Unpublished)

DUCTILE AND CONNECTION BEHAVIOUR OF THIN G550 SHEET STEELS

C.A. Rogers and G.J. Hancock

Department of Civil Engineering, University of Sydney,
Sydney, NSW 2006, Australia

ABSTRACT

This paper summarises the findings of a research project into the ductility and connection behaviour of G550 sheet steels, which are manufactured by cold-reduction. Specimens ranging in base metal thickness from 0.40-0.60mm were tested as tensile coupons. Measurements of local and uniform elongation were completed using a fine gauge length grid marked on the surface of the steel. Test results indicate that the ability of the material to undergo deformation is dependent on the direction of load within the material. In addition, the measured elongations of the G550 sheet steels do not meet the Dhalla and Winter requirements. Also included is a summary of results detailing the shear behaviour of bolted and screwed connections composed of 0.42-1.0mm G550, and 0.60-0.80mm G300 sheet steels. Various modes of failure were observed including end pull-out, bearing, tilting and net section fracture. Recommendations concerning the adequacy of current design standards with respect to the design of thin sheet steel connections are made.

KEYWORDS

G550, Sheet Steel, Ductility, Bolt, Screw, Connection, Net Section Fracture, Bearing, Tilting

INTRODUCTION

Cold formed structural members are fabricated from sheet steels which must meet the various material requirements prescribed in applicable national design standards. The Australian / New Zealand AS/NZS 4600 (SA/SNZ, 1996) and North American (CSA, 1994; AISI, 1997) design standards allow for the use of thin ($t < 0.90\text{mm}$) high strength ($f_y = 550\text{MPa}$) sheet steels in members which primarily undergo bending, *i.e.*, purlins, girts, and decks. However, in design the engineer must use a yield stress and ultimate strength reduced to 75% of the minimum specified values. A reduced yield stress and ultimate strength are required because of the lack of ductility exhibited by sheet steels which are cold-reduced to thickness. The ductility criterion specified in the Australian / New Zealand and North American design standards is based on an investigation of sheet steels by Dhalla and Winter (1974*a,b*). High strength G550 sheet steels (SA 1397, 1993) currently used in construction were not included in the formulation of this adequate ductility criterion for cold formed steel sections. G300 sheet steels have tensile and elongation properties which are similar to normal mild steels and are often formed by annealing G550 cold-reduced sheet steels.

DUCTILITY OF THIN G550 SHEET STEELS

Various G300 and G550 sheet steels were tested and used as a basis for comparison with the current material property requirements specified in the Australian / New Zealand and North American design standards. All steels were cold-reduced to thickness, with an aluminum/zinc alloy, or zinc coating and obtained from standard coils during normal rolling operations. Triplicates of all coupons were cut from different locations in the sheet to avoid localised material properties. Detailed information regarding this ductility study can be found in Rogers and Hancock (1996, 1997a).

Basic Material Properties

Material properties for both static and dynamic conditions were calculated using the base metal thickness (see Table 1). The material properties for the 0.42mm and 0.60mm G550 sheet steels are dependent on the direction from which the coupons were obtained. Yield stress and ultimate strength values are significantly higher for specimens from the transverse direction in comparison to specimens from the longitudinal and diagonal directions. The material properties of the G300 sheet steel are not dependent on direction. All of the G550 sheet steels tested for this report yielded gradually with minimal strain hardening, whereas the G300 sheet steel displayed a sharp yield point, followed by a yield elongation plateau and then a strain hardening region. The G550 sheet steels do not meet the Dhalla and Winter or current design standard requirements for ultimate strength to yield stress ratio, $f_u / f_y \geq 1.08$. The yield stress and ultimate strength values for the G550 sheet steels are significantly above the minimum specified 550MPa. This is most evident for specimens obtained from the transverse direction where dynamic yield stresses are as high as 785MPa. Dynamic yield stress results for specimens cut from the longitudinal and diagonal directions range from 668 to 707MPa.

TABLE 1
MATERIAL PROPERTIES OF SHEET STEELS (MEAN VALUES)

Specimen Type	Direction	t_b (mm)	f_y^1 (MPa)	f_u^1 (MPa)	f_u / f_y^1	E (MPa)
0.42mm G550	Longitudinal	0.41	681/658	681/658	1.00/1.00	219000
	Transverse	0.41	768/745	768/745	1.00/1.00	252000
	Diagonal Right	0.41	668/645	668/645	1.00/1.00	192000
	Diagonal Left	0.41	673/650	673/650	1.00/1.00	193000
0.60mm G550	Longitudinal	0.59	703/686	703/686	1.00/1.00	214000
	Transverse	0.59	785/767	785/767	1.00/1.00	236000
	Diagonal	0.59	707/690	707/690	1.00/1.00	203000
0.60mm G300	Longitudinal	0.58	368/348	431/411	1.17/1.18	202000
	Transverse	0.58	381/360	428/408	1.12/1.13	210000
	Diagonal	0.58	376/356	437/417	1.16/1.17	218000

Note: Material properties calculated using base metal thickness, t_b . ¹ Dynamic/Static values given.

Distribution of 2.5mm Gauge Length Elongation

The percent elongation of each 2.5mm gauge (see Figure 1) was calculated based on its original measured length and then graphed to show the extent and location of elongation over the constant width section of the coupon. Four representative elongation distribution graphs for the 0.42mm G550 and 0.60mm G300 sheet steels are provided in Figure 2. In general, the G550 longitudinal specimens have constant uniform elongation for each 2.5mm gauge with an increase in percent elongation at the gauge in which fracture occurs. The transverse G550 specimens show almost no uniform elongation, but do have limited elongation in the fracture zone. The results obtained from the diagonal G550 specimens indicate that uniform elongation is limited outside of a 12.5mm zone around the fracture, while local elongation occurs in the fracture gauge, as well as in the adjoining gauges. These results show that the distribution of gauge elongation for thin G550 sheet steels is dependent on the direction from which the tensile coupons are obtained, however, the thickness of the material does not significantly affect the distribution of elongation for the range of thicknesses tested. In contrast, the

G300 sheet steel tensile specimens have an elongation distribution which is independent of the direction from which the coupons are cut. Uniform elongation occurs in each 2.5mm gauge length with a more gradual increase in elongation for gauges close to the fracture.

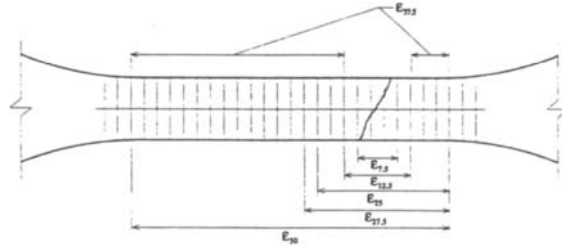


Figure 1: Gauge Length Measurements

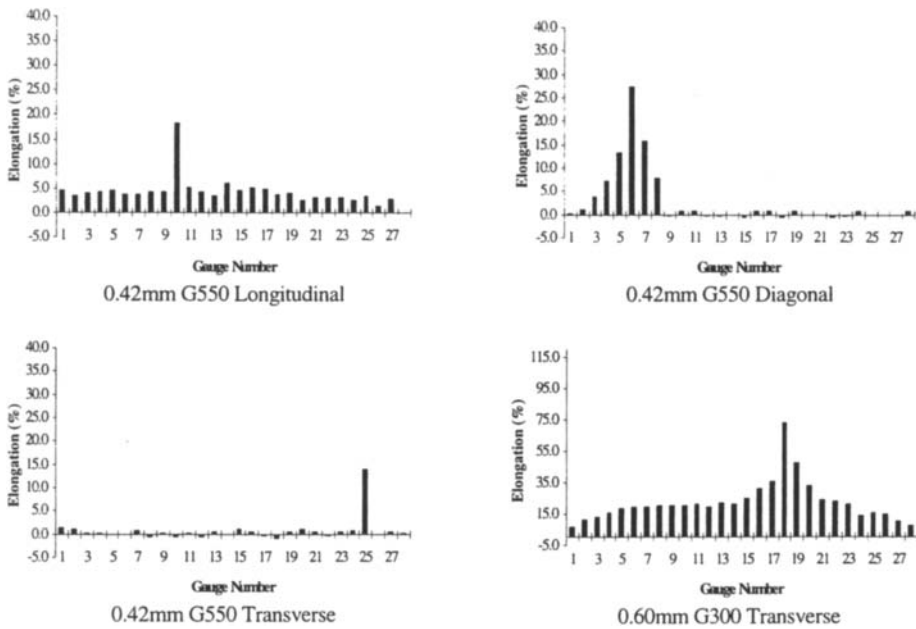


Figure 2: 2.5mm Gauge Length Elongation Distribution

Gauge Length Elongation

Dhalla and Winter recommended that sheet steels must possess adequate uniform ductility, $\epsilon_U \geq 3\%$, to fully plastify the net section and to distribute stress over the net area at perforations or other stress raisers. A minimum local elongation capability, $\epsilon_L \geq 20\%$, over a $1/2''$ (12.7mm) gauge length was suggested to ensure ductile failure. These recommendations are incorporated into the specifications of many cold formed steel design standards in existence today, in lieu of the standard 50mm overall elongation requirement, $\epsilon_{50} \geq 10\%$. Individual 2.5mm gauge length measurements were used to determine the standard 50mm gauge length elongation, ϵ_{50} , along with the Dhalla and Winter recommended local (12.5mm length across the fracture zone, $\epsilon_{12.5}$) and uniform (37.5mm length excluding the fracture zone, $\epsilon_{37.5}$) gauge length elongation.

The coated G550 sheet steels tested as part of this investigation do not have adequate ductility to meet the overall elongation requirement, $\epsilon_{50} \geq 10\%$, specified by the current design standards (see Table 2). However, the fully annealed G300 test specimens possess adequate ductility according to the same design standards. The elongation capability of the G300 sheet steel is not dependent on direction, in contrast to the G550 sheet steels which have limited ductility when tested in the transverse direction. The longitudinal G550 sheet steel specimens provide the greatest amount of ductility compared to both the diagonal and transverse test specimens. It is also noted that elongation capability increases with an increase in thickness for most sheet steel types. Similarly, the G550 sheet steels do not meet the Dhalla and Winter local elongation requirements, $\epsilon_L \geq 20\%$, whereas the G300 sheet steels have sufficient ductility. Again the G550 test specimens taken from the transverse direction have the lowest measured elongation, with the elongation in the diagonal and longitudinal directions significantly higher. The G550 sheet steels obtained from the longitudinal direction have a greater ability to elongate uniformly along the entire gauge length. The 0.42mm and 0.60mm G550 test specimens exceed the uniform elongation requirement, $\epsilon_U \geq 3\%$, as do the G300 test specimens. The transverse and diagonal G550 test specimens do not have adequate ductility to meet the uniform elongation requirements.

TABLE 2
COATED GAUGE LENGTH ELONGATION MEASUREMENTS (MEAN VALUES)

<i>Specimen Type</i>	<i>Direction</i>	ϵ_{50} (%)	$\epsilon_{12.5}$ (%)	$\epsilon_{37.5}$ (%)
0.42mm G550	<i>Longitudinal</i>	4.61	7.04	3.75
	<i>Transverse</i>	0.82	3.03	0.18
	<i>Diagonal Right</i>	3.54	12.5	0.94
	<i>Diagonal Left</i>	4.05	14.8	0.49
0.60mm G550	<i>Longitudinal</i>	5.59	10.5	3.93
	<i>Transverse</i>	1.78	5.71	0.47
	<i>Diagonal</i>	3.56	11.7	0.82
0.60mm G300	<i>Longitudinal</i>	24.3	38.5	19.5
	<i>Transverse</i>	27.4	46.0	21.3
	<i>Diagonal</i>	24.2	35.9	20.3

BEHAVIOUR OF BOLTED CONNECTIONS

A total of 158 single lap bolted shear connections fabricated from G550 and G300 sheet steels which range in base metal thickness from 0.42-0.60mm were tested. The specimen size and shape, as well as the type and number of bolts, were varied to cause three distinct modes of failure; end pull-out, bearing, and net section fracture. Information obtained from the tensile testing and elongation measurements of G550 and G300 sheet steels was used to aid in the evaluation of the connection resistance equations for use in limit states design. A detailed description of the results summarised in this paper can be found in Rogers and Hancock (1997b).

Connection Elongation and Ultimate Load Comparison

Previous research by Rogers and Hancock (1996, 1997a) concluded that G300 sheet steels possess a greater ability to elongate compared with G550 sheet steels. The distribution of elongation varies not only between the two types of material, but between directions in the plane of the sheet for G550 sheet steels. A comparison of the relative displacement of connections, nominally identical except for the type of sheet steel used was completed using the 0.60mm G550 and 0.60mm G300 materials for each type of test specimen. Bolted connections composed of G550 sheet steels displayed an ability to elongate which was at worse 90% (mean value) of that measured for the nominally identical G300 test specimens. The single bolt specimens were capable of displacing from 94 to 98% of the distances measured for the G300 sheet steels. The G550 double bolt specimens were able to elongate to a larger degree than their G300 counterparts. These results give evidence that the limited elongation capability exhibited by the G550 sheet steels in coupon tests does not

translate to a small displacement capability for failures by end pull-out and bearing. Lower displacement ratios were observed for the triple bolt specimens due to failure by net section fracture, a similar mode to that found for the tensile coupons tested. No significant variation in elongation between the longitudinal, transverse and diagonal test specimens was observed for any failure type.

Comparison of Ultimate Test-to-Failure Criterion Predicted Loads

The bolted connections included in this paper were divided into separate categories according to the failure mode recorded during testing, *i.e.*, end pull-out, bearing, and net section fracture. Thus, the predicted connection resistance used in comparison with the ultimate tensile load of a bolted connection was calculated using the design equation developed for that failure mode with the full value of the material properties, *e.g.*, all specimens which failed by bearing were compared with the predicted bearing resistance calculated using f_u . This type of failure based criterion comparison reveals the accuracy of each individual design equation by eliminating the influence of the remaining bolted connection design provisions.

The AS/NZS 4600 and AISI design standards can both be used to conservatively predict the net section failure loads of bolted connections. Calculated end pull-out loads are unconservative, especially for transverse specimens where mean test-to-predicted ratios of 0.795 and 0.729 occur for the 0.42mm G550 and 0.60mm G550 sheet steel specimens, respectively. The resistance of the 0.60mm G300 test specimens which failed by end pull-out is more accurately predicted using these design standards. The connection resistance of bolted specimens which failed in bearing is inaccurately modelled by the existing AS/NZS 4600 and AISI design provisions. The resulting mean test-to-predicted ratios are significantly unconservative, ranging from 0.591 in the transverse direction to 0.661 in the longitudinal direction for the 0.42mm G550 sheet steel specimens and from 0.798 in the longitudinal direction to 0.842 in the diagonal direction for the 0.60mm G300 sheet steel specimens.

The CSA-S136 design standard provides overly conservative predictions of the end pull-out resistance for both the G550 and G300 sheet steels tested. Mean test-to-predicted values range from 1.060 for the transverse 0.60mm G550 test specimens to 1.467 for the diagonal 0.60mm G300 test specimens. Net section fracture connection resistance can be modelled accurately using the net cross-sectional area and the ultimate material strength without a stress reduction factor. Mean test-to-predicted ratios range from 0.977-1.088 for the G550 sheet steels and from 0.963-0.986 for the 0.60mm G300 test specimens. A dramatic improvement in the ability to predict the ultimate bearing resistance of the sheet steels tested for this paper occurs with the use of the CSA-S136 design standard. Mean test-to-predicted ratios for the 0.42mm G550 test specimens range from 0.887-0.991, for the 0.60mm G550 test specimens from 0.954-1.077 and for the 0.60mm G300 test specimens from 1.197-1.264. The variation in mean test-to-predicted ratios for the G550 and G300 test specimens which failed in bearing exhibits the need for a bearing formulation which is dependent on material properties, as well as thickness. However, the consistently unconservative mean test-to-predicted ratios for the bearing failure of the 0.42mm G550 sheet steels indicate that a bearing coefficient of less than the current $C = 2$ for $d/t \geq 15$ may be necessary.

Ultimate Failure Stress Ratios

The cross-section stress at ultimate load for each specimen which failed by either end pull-out or bearing or a combination of end pull-out and bearing is plotted in Figure 3. The nominal ratio of ultimate cross-section stress, f_{bu} , to dynamic base metal ultimate material strength, f_u , (without the 0.75 reduction factor) is compared with the ratio of edge distance, e , to bolt diameter, d . The resulting graph for the 0.42mm G550 sheet steel bolted specimens shows that the ultimate bearing stress reaches a maximum of approximately 1.5-2.0 times the ultimate material strength. The design formulation for the bearing resistance of sheet steels with single shear bolted connections with washers is three times the ultimate material strength for the AS/NZS 4600 and AISI design standards and twice the ultimate material strength for the CSA-S136 design standard, when the ratio of $d/t \geq 15$, as found for the thin steels tested for this paper. The ultimate cross-section stress of the

specimens which failed by end pull-out is less than that observed for specimens which failed by bearing, and lies near the expected end pull-out stress if the CSA-S136 design formulation is followed. The bearing coefficient clearly needs to be reduced in the AS/NZS 4600 and AISI design standards for thin sheet steels.

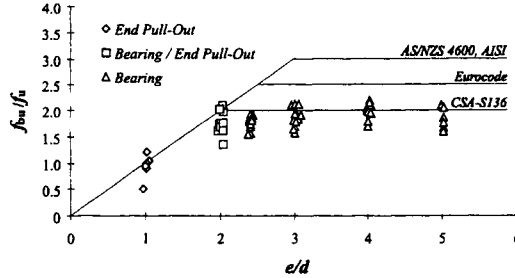


Figure 3: 0.42 mm G550 End Pull-Out and Bearing Failure Stress vs. Ultimate Strength Ratios

The cross-section stress at ultimate load for each specimen where net section failure occurred is plotted in Figure 4. The ratio of net section fracture stress at ultimate, f_{net} , to dynamic base metal ultimate material strength, f_u , (without the 0.75 reduction factor) versus the ratio of bolt diameter, d , to specimen width, s , is given, along with the predicted ratio of f_{net}/f_u determined using the AS/NZS 4600 and AISI design standards. Test specimens joined with a single bolt did not fail by net section fracture due to the thinness of the material used, therefore, only a limited amount of data is available for the double and triple bolt connections. In most instances the ratio of net section fracture stress at ultimate to ultimate material strength is approximately unity, which indicates that the use of a stress reduction factor, which is dependent on r and the ratio of d/s , is overly conservative for the design of thin G550 and G300 sheet steels. The stress reduction formulation used in the AS/NZS 4600 and AISI design standards is not present in the CSA-S136 design standard, where the net section fracture stress at a hole or at a connection are considered equal. The CSA-S136 design standard can be used to predict the tensile resistance of a bolted connection which has failed in the net section fracture mode.

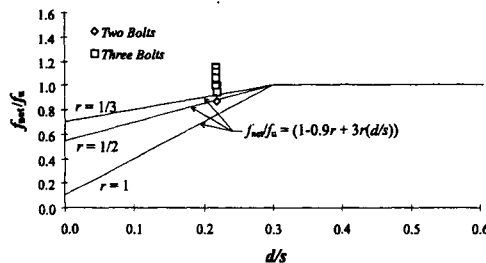


Figure 4: 0.42 mm G550 Net Section Failure Stress vs. Ultimate Strength Ratios

BEHAVIOUR OF SCREWED CONNECTIONS

A total of 150 single overlap screwed connections concentrically loaded in shear, and fabricated with multiple point fasteners using five different G550 and G300 sheet steels, which range in base metal thickness from 0.42-1.00mm were tested. The type, number and placement of screws were varied to observe the behaviour of connections which are subjected to shear load. The main objective of this experimental testing phase was to evaluate the existing design provisions for screwed connections fabricated from thin G550 sheet steels. A more detailed description of the results summarised in this paper can be found in Rogers and Hancock (1997c).

Possible Modes of Failure

Various modes of failure can occur in a single overlap screwed sheet steel connection including; gross cross-section yielding, net cross-section fracture, end pull-out, bearing, tilting, combined bearing/tilting and screw shear. All connections tested were designed such that screw shear did not occur, hence, only failure of the sheet steel was considered. Specimens were dimensioned and screws were positioned, such that only bearing, tilting and combined bearing/tilting failures were possible.

Comparison of Ultimate Test-to-Failure Criterion Predicted Loads

The predicted ultimate connection capacity, P_{up} , used in comparison with the ultimate, P_{ut} , load of each screwed connection were calculated using the design equation developed for the bearing/tilting failure mode. The AS/NZS 4600 and AISI design standards can be used to conservatively estimate the load carrying capacity of the longitudinal and diagonal 042/042-G550 connections, the longitudinal 060/060-G550 connections and the 055/055-G300 connections, where e.g. 042/060-G550 refers to a connection constructed with a 0.42mm G550 sheet steel adjacent to the screw head and a 0.60mm G550 sheet steel below. In all other cases the test-to-predicted ratios were found to be less than unity. Screw connections composed of the 042/060-G550 and 042/100-G550 sheet steels have the most unconservative test-to-predicted ratios with P_{ut} / P_{up} values as low as 0.766, as shown in Table 3. For the design case where two different thickness sheet steels are connected with screws, and the thinner sheet steel is placed adjacent to the screw head, the capacity of the connection becomes increasingly dependent on the bearing provisions as the relative difference in thickness increases. It appears that the bearing formulation specified for screwed connections is unconservative, due to a decrease in the ability to accurately predict the failure loads of the 042/060-G550 and 042/100-G550 connections with the AS/NZS 4600 and AISI design standards. This is similar to the bearing behaviour observed for the bolted connection tests of thin G550 and G300 sheet steels, as described above.

The CSA-S136 design standard provides conservative predictions of the bearing/tilting capacity of screwed connections for the longitudinal 042/042-G550, longitudinal 042/060-G550 and all of the G300 sheet steels tested. Test specimens fabricated using the transverse and diagonal 042/042-G550, 060/060-G550 and 042/100-G550 sheet steels all provide mean test-to-predicted ratios which range between 0.90 and 1.0.

TABLE 3
FAILURE BASED CRITERION (BEARING/TILTING) TEST-TO-PREDICTED STATISTICAL DATA, P_{ut} / P_{up}

Stat. Info.	042/042-G550 Longitudinal	042/042-G550 Transverse	042/042-G550 Diagonal	042/060-G550 Longitudinal	042/100-G550 Longitudinal
AS/NZS 4600 & AISI					
Mean	1.065	0.943	1.046	0.766	0.790
No.	32	32	14	12	12
S.D.	0.204	0.142	0.196	0.097	0.154
C.o.V.	0.198	0.156	0.204	0.139	0.215
CSA-S136					
Mean	1.032	0.915	0.973	1.128	0.976
No.	32	32	14	12	12
S.D.	0.181	0.127	0.182	0.149	0.168
C.o.V.	0.181	0.144	0.204	0.147	0.190

CONCLUSIONS

Test results indicate that the ability of G550 sheet steels to undergo deformation is dependent on the direction of load within the material, with the transverse specimens exhibiting the least amount of overall, local and uniform elongation. The G550 sheet steels do not meet the Dhalla and Winter material requirements, except for uniform elongation in longitudinal test specimens.

The current connection provisions set out in the AS/NZS 4600 and AISI design standards cannot be used to accurately predict the failure mode of bolted connections fabricated from thin G550 and G300 sheet steels if the full value of f_u is used in the calculation. Furthermore, these design standards cannot be used to accurately determine the bearing resistance of bolted specimens based on a failure criterion for predicted loads. It is necessary to incorporate a variable bearing resistance equation which is dependent on the thickness of the connected material, similar to that found in the CSA-S136 design standard. In addition, the ultimate bearing failure stress-to-ultimate material strength ratios show that a bearing equation coefficient of less than two may be appropriate for G550 sheet steels where $d/t \geq 15$. The net section fracture resistance of a bolted connection calculated following the CSA-S136 design standard procedure, where the net cross-sectional area and the ultimate material strength are used without a stress reduction factor, is adequate. Bolted connections composed of G550 sheet steels were able to elongate to at least 90% of the distance measured for the nominally identical G300 test specimens. The limited elongation ability exhibited by the G550 sheet steels in coupon tests did not translate into a small displacement capacity for bolted connection failures by end pull-out and bearing.

The current connection provisions set out in the CSA-S136 design standard can be used to predict the failure mode of screwed connections fabricated from thin G550 and G300 sheet steels. The AS/NZS 4600, CSA-S136 and AISI design standards provide accurate load predictions when the two connected sheet steels are of similar thickness and the full value of f_u is used in the calculation. However, when two different thickness sheet steels are connected with screws, failure will more likely result from bearing distress in the thinner of the connected elements. The accuracy of the AS/NZS 4600, CSA-S136 and AISI design standards when used to estimate the bearing resistance of screwed connections diminishes as the relative difference in thickness between the two connected elements increases, and the connection is forced to fail in a bearing mode rather than a combined bearing/tilting mode. Hence, it is necessary that the coefficient used in the bearing formulations for screwed connections be reduced to limit the existing unconservative nature of these design standards. Once these adjustments to the bearing formulae have been made, it will not be necessary to use the $0.75f_u$ reduction for the design of bolted and screwed connections.

Acknowledgements

The authors would like to thank the Australian Research Council and BHP Steel Research for their financial support, as well as ITW Buildex® - A Division of W.A. Deutscher Pty. Ltd. for the supply of screw fasteners. The first author is supported by a joint Commonwealth of Australia and Centre for Advanced Structural Engineering Scholarship.

References

- American Iron and Steel Institute. (1997). "1996 Edition of the Specification for the Design of Cold-Formed Steel Structural Members", Washington, DC, USA.
- Canadian Standards Association, S136. (1994). "Cold Formed Steel Structural Members", Etobicoke, Ont., Canada.
- Dhalla, A. K., Winter, G. (1974a). "Steel Ductility Measurements", *J. Struct. Div., ASCE*, 100(2), 427-444.
- Dhalla, A. K., Winter, G. (1974b). "Suggested Steel Ductility Requirements", *J. Struct. Div., ASCE*, 100(2), 445-462.
- Rogers, C.A., Hancock, G.J. (1996). "Ductility of G550 Sheet Steels in Tension - Elongation Measurements and Perforated Tests", Research Report No. R735, Centre for Advanced Structural Engineering, University of Sydney, Sydney, NSW, Australia.
- Rogers, C.A., Hancock, G.J. (1997a). "Ductility of G550 Sheet Steels in Tension", *J. Struct. Engrg., ASCE*, 123(12), 1586-1594.
- Rogers, C.A., Hancock, G.J. (1997b). "Bolted Connection Tests of Thin G550 and G300 Sheet Steels", Research Report No. R749, Centre for Advanced Structural Engineering, University of Sydney, Sydney, NSW, Australia.
- Rogers, C.A., Hancock, G.J. (1997c). "Screwed Connection Tests of Thin G550 and G300 Sheet Steels", Research Report No. R761, Centre for Advanced Structural Engineering, University of Sydney, Sydney, NSW, Australia.
- Standards Australia. (1993). "Steel sheet and strip - Hot-dipped zinc-coated or aluminium/zinc coated - AS 1397", Sydney, NSW, Australia.
- Standards Australia / Standards New Zealand. (1996). "Cold-formed steel structures - AS/NZS 4600", Sydney, NSW, Australia.

EFFECT OF COLD FORMING ON COMPRESSED CARBON AND STAINLESS STEEL STRUTS

M.Macdonald¹, J.Rhodes² and G.T.Taylor³

1.Department of Engineering, Glasgow Caledonian University, Glasgow.

2.Department of Mechanical Engineering, University of Strathclyde, Glasgow.

3.Department of Energy and Environmental Technology, Glasgow Caledonian University, Glasgow.

ABSTRACT

The effects of cold forming on both carbon steel and stainless steel structural members has been the subject of extensive research since the early 1940's. Design codes for carbon steel members have been published in many countries around the world, including BS5950, Part 5 in the UK (Ref. 1), the AISI code in the USA (Ref. 2), and the new Eurocode 3: Part 1.3 (Ref. 3). For stainless steel members there are fewer design codes available, and those that are available, which include the ANSI/ASCE in the USA (Ref. 4) and the new Eurocode 3: Part 1.4 (Ref. 5), do not give such detailed design recommendations as the carbon steel codes. This paper describes the results obtained from a series of axial compression tests performed on short strut members of plain channel cross section cold formed from carbon steel and Type 304 stainless steel. The corner radius and the material thickness are varied to examine the effects of cold forming on the load capacity of the channels in compression and the results are compared to those obtained from the relevant design codes. Conclusions are drawn on the basis of the comparisons.

KEYWORDS

Stainless steel, carbon steel, cold forming, channels, compression, corner radii, load capacity.

NOTATION

A = full, unreduced cross-sectional area (ANSI/ASCE-8-90)
A_e = effective cross-sectional area (AISI; ANSI/ASCE-8-90)
A_{eff} = effective cross-sectional area (BS5950; ENV 1993-1-3; ENV 1993-1-4)
A_g = gross cross-sectional area (BS5950; ENV 1993-1-3; ENV 1993-1-4)

E	=	modulus of elasticity (BS5950; ENV 1993-1-3)
E_o	=	initial modulus of elasticity (ANSI/ASCE-8-90)
E_t	=	tangent modulus (ANSI/ASCE-8-90)
E_s	=	secant modulus (ANSI/ASCE-8-90)
F_{cr}	=	critical buckling stress (ANSI/ASCE-8-90)
F_y, f_y, f_c	=	virgin yield strength (AISI; ENV 1993-1-4; ANSI/ASCE-8-90; BS5950)
$N_{b,Rd}$	=	design buckling resistance (ENV 1993-1-3; ENV 1993-1-4)
P_a	=	axial load (AISI)
P_{cs}	=	short strut capacity (BS5950)
P_n	=	design axial strength (ANSI/ASCE-8-90)
r	=	inside bend or corner radius
t	=	material thickness
Y_s	=	virgin yield strength (BS5950)
β_A	=	A_{eff}/A_g (ENV 1993-1-3; ENV 1993-1-4)
χ	=	reduction factor (ENV 1993-1-3; ENV 1993-1-4)

INTRODUCTION

Cold formed sections are widely used for building structures, storage racking and domestic equipment. This is due to various characteristics such as their high strength to weight ratio, their ease of manufacture and the fact that a wide range of cross-sections can be formed from many different materials.

An advantage gained from cold forming structural members is the increase in yield strength gained due to cold working. Such cold working causes strain hardening of the material which affects its mechanical properties, and consequently the material properties of a formed section may be markedly different from those of the virgin sheet material from which it was formed. In general, this strain hardening increases both the yield strength and the ultimate tensile strength. This is certainly true for carbon steel as reported by Karren [Ref. 6] and Karren and Winter [Ref. 7]. However, for a material such as stainless steel, these increases may not be the same as for carbon steel. Karren and Winter demonstrated with their tensile test approach on carbon steel that the effect that cold forming has on structural sections is generally confined to the areas of formed bends and it is in these areas that increases in yield and ultimate strength are located. Further research by Macdonald et al [Refs. 8 and 9] using a hardness test approach, confirmed this type of behaviour for carbon steel and also examined similar behaviour for stainless steel cold formed members.

The localised effect of cold forming is now investigated further by examining its consequence on the axial compression behaviour of short struts with plain channel cross sections manufactured from carbon steel and stainless steel sheet with relatively small bend radius/material thickness (r/t) ratios.

Three widely used design codes in the field of cold forming of carbon steel structural sections are BS 5950, Part 5 [Ref. 1], AISI [Ref. 2] and the Eurocode 3: Part 1.3 [Ref. 3]. For stainless steel members, no UK design code exists, but two widely used codes are the ANSI/ASCE specification [Ref. 4] and

the Eurocode 3: Part 1.4 [Ref. 5]. These codes give many design recommendations which include methods on how to compute the load capacity of short structural members subjected to axial compressive loading, often known as "stub columns".

DESIGN CODE RECOMMENDATIONS

In the formation of a profiled section, the cold working occurs in localised areas, with the material at the bends being strain hardened to a much greater degree than that in the flat elements. Therefore the properties of the material vary throughout the cross-section where at the formed bends, a higher yield strength will exist. The effect that the areas of high strength have on the load capacity of short struts of plain channel cross-section is considered here for two materials - carbon steel and Type 304 stainless steel. The plain channel cross-section struts have constant flange width, web depth and length. To vary the amount of cold forming, the corners were manufactured with various sizes of inside bend radius and also, the two materials were of three different thicknesses hence providing a range of r/t ratios. The r/t ratios were kept small varying from approximately 2.5 to 8.5. The design codes make the assumption that cold formed bends with $r/t \leq 5$ can be treated as sharp corners. Hence one of the aims of this investigation was to determine if an increase in load capacity in compression could be gained for plain channel sections with variation in r/t .

The lengths of the struts were kept short so that failure by Euler type buckling would be eliminated and that failure would occur due to local buckling effects only. Further details of the experimental investigation are described later.

The load capacity for short struts subjected to axial compression loading for carbon steel and stainless steel cold formed members according to the relevant design codes are calculated as follows:

Carbon Steel: **BS5950, Part 5; Section 6:**
Short Strut Capacity, $P_{CS} = A_{eff}Y_s$ (N) (1)

Eurocode 3, Part 1.3; Section 6:
Design Buckling Resistance, $N_{b,Rd} = \chi\beta_A A_g f_y$ (N) (2)

AISI; Section C4:
Axial Load, $P_a = A_e F_y$ (N) (3)

Stainless Steel: **ANSI/ASCE-8-90; Section 3.4:**
Design Axial Strength, $P_n = A_e f_y$ (N) (4)

Eurocode 3, Part 1.4: Section 5:
Design Buckling Resistance, $N_{b,Rd} = \chi\beta_A A_g f_y$ (N) (5)

For the stainless steel struts, the effective area calculated in both design codes is based on the effective widths of the elements which are directly related to the initial elastic modulus, and do not take any account of the degradation of E as loading progresses.

The results obtained from the above equations are used to compare with the results obtained from the axial compression tests described later.

EXPERIMENTAL INVESTIGATION

A total of 29 plain channel section short strut specimens were manufactured from carbon steel sheet of three different thicknesses - nominally 0.8mm, 1mm and 1.2mm. The inside radius of the corner bends of the plain channels were varied with sizes of 3mm, 5mm and 6mm to give a small range of r/t ratio. The cross-section dimensions were kept constant with the flange being of nominal width 30mm and the web being of nominal depth 60mm. The length of the short strut specimens was also kept constant at a nominal 180mm. Three specimens were manufactured for each specimen of a given thickness and bend radius so that an average load capacity could be used for comparison to design code predictions.

A further set of 29 plain channel section short strut specimens were manufactured from Type 304 stainless steel sheet of three different thicknesses - nominally 0.7mm, 0.9mm and 1.2mm. All other dimensions (i.e. flange width, web depth, length and bend radius) were the same as the carbon steel specimens.

For both materials, one specimen was manufactured for each thickness with sharp corners to give a radius as close as possible to zero so that the load capacity for sections with formed corners could be compared to that obtained for no formed corners.

Figure 1 shows a plain channel section short strut column with all dimensions shown being nominal. The ends of the specimens were ground to ensure flatness and the specimens were compressed uniformly to failure between flat plattens in a Tinius Olsen Electro-mechanical testing machine, with the load-end compressive displacement path being recorded.

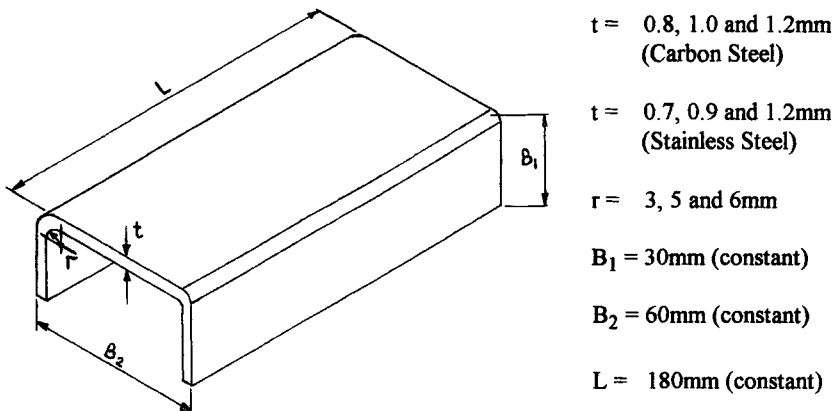


Figure 1 - Cold Formed Plain Channel Section Nominal Dimensions.

RESULTS

The specimen details and the experimental and design specification predictions for the axial compressive load capacity of the carbon steel and stainless steel short struts are shown in Tables 1 and 2 respectively. The tables show a comparison of the experimental load capacities obtained with the load capacities obtained from the design codes. Figure 2 shows the variation of A_{eff}/t^2 at failure with variation in r/t ratio for the three different material thicknesses of carbon steel. Figure 3 shows the variation of A_{eff}/t^2 at failure with variation in r/t ratio for the three different material thicknesses stainless steel.

OBSERVATIONS

Figure 2 shows the variation in the ratio of total effective area to thickness squared at failure for the carbon steel stub columns tested, and plots the results against r/t for each of the different thicknesses investigated. The design code predictions are very similar and have been incorporated in the figure mainly as a control to ensure that any variations in individual specimen dimensions or properties which could have significantly affected the results would be seen. As may be observed this quantity (i.e. $\sum b_{\text{eff}} \cdot t / t^2$) is approximately 90 for all specimens regardless of the r/t ratio, being slightly greater (90-100) for the thinner specimens, and slightly less (approximately 78-95) for the thicker specimens. The quantity is actually the sum of b_{eff}/t taken over a complete section, and with one stiffened element and two unstiffened elements the sum of effective widths should be approximately 90 at failure. The tests back up the carbon steel design code predictions in this respect. It is, however, obvious from the test results that the corners do not have any significant influence on the strength, and that evaluation of the properties, particularly the local buckling properties, on the basis of mid-line dimensions assuming square corners gives a good approximation to the test results.

Figure 3 shows the variation in the ratio of total effective area to thickness squared at failure for the stainless steel stub columns tested, and again plots the results against r/t for each of the different thicknesses investigated. The design code predictions are, as in Figure 2, very similar and again have been incorporated in the figure mainly as a control to ensure that any variations in individual specimen dimensions or properties which could have significantly affected the results would be seen. As may be observed this quantity (i.e. $\sum b_{\text{eff}} \cdot t / t^2$) is approximately 70 for all specimens regardless of the r/t ratio, being slightly greater (71-75) for the thinner specimens, and slightly less (approximately 68) for the thicker specimens. The sum of effective widths for the stainless steel struts should be approximately 70 at failure. The tests back up the stainless steel design code predictions in this respect. As was the case with the carbon steel struts, the corners do not have any significant influence on the strength, and that evaluation of the properties, particularly the local buckling properties, on the basis of mid-line dimensions assuming square corners gives a good approximation to the test results.

CONCLUSIONS

The main conclusion from the investigation is that for carbon steel members, the BS5950, Part 5, Eurocode 3: Part 1.3 and AISI design codes give accurate predictions of the load capacity of stub columns with plain channel cross-sections.

For stainless steel members, the Eurocode 3: Part 1.4 and the ANSI/ASCE design codes, give accurate predictions of the stub column strength of plain channel sections. The neglect of the changes in E as loading progresses does not seem to have resulted in any substantial errors in the evaluation of axial load capacity.

For both materials, the variation in capacity with the variation in corner radii is small, and inconsistent, and for members with corner r/t ratios as examined here the assumption of mid-line dimensions and square corners is perfectly satisfactory.

REFERENCES

1. BS 5950, "Structural Use of Steelwork in Building" - Part 5: "Code of Practice for the Design of Cold Formed Sections". 1990.
2. AISI, "Specification for the Design of Cold-Formed Steel Structural Members". 1986.
3. ENV 1993-1-3, Eurocode 3: Design of Steel Structures; Part 1.3: General Rules - Supplementary Rules for Cold Forming Thin Gauge Members and Sheeting. February 1996. (Edited Draft).
4. ANSI/ASCE-8-90, "Specification for the Design of Cold-Formed Stainless Steel Structural Members". 1991.
5. ENV 1993-1-3, Eurocode 3: Design of Steel Structures; Part 1.4: General Rules - Supplementary Rules for Stainless Steel. July 1996.
6. Karren, K. W. (1967) Corner Properties of Cold-Formed Steel Shapes. *Proc. ASCE J. Struct. Div., Vol. 93(ST1)*.
7. Karren, K. W. and Winter, G. (1967). Effects of Cold-Forming on Light-Gage Steel Members. *Proc. ASCE J. Struct. Div., Vol. 93(ST1)*.
8. Macdonald, M., Rhodes, J., Crawford, M. and Taylor, G. T. (1996). A Study of the Effect of Cold-Forming on the Yield Strength of Stainless Steel Type 304 - Hardness Test Approach. *Proc. 13th International Specialty Conference in Cold-Formed Steel Design and Construction. St. Louis, USA*.
9. Macdonald, M., Rhodes, J. and Taylor, G. T. (1996). The Effects of Cold-Forming on the Yield Strength of Thin-Gauge Steel - Hardness Test Approach. *Proc. Thin-Walled Structures Bicentenary Conference, University of Strathclyde, Glasgow*.

Table 1
Compression Test Results: Mild Steel Plain Channel Section Short Struts
 (Nominal Dimensions: Flange-30mm; Web-60mm; Length-180mm)

Specimen Ref.	Bend Radius, r (mm)	Thickness t (mm)	r/t	Whole C.S.A., A (mm ²)	Virgin 0.2% P.S. (N/mm ²)	Exp. Load Capacity (Ave) P _{cm} (kN)	BS5950 (Ave) P _c (kN)	Eurocode 1.3 (Ave) N _{b,Rd} (kN)	AISI (Ave) P _n (kN)
Sharp Corner Specimens:									
CTMSSC1	N/A	0.760	N/A	97.02	178.00	9.31	10.22	10.10	9.28
CTMSSC2	N/A	0.970	N/A	125.00	221.70	15.86	18.27	17.76	16.50
CTMSSC3	N/A	1.220	N/A	156.68	210.60	29.17	26.88	25.54	23.92
Formed Corner Radius Specimens:									
CTMS1	3.00	0.772	3.886	98.78	178.00	10.03	10.63	10.57	9.74
CTMS2	5.00	0.772	6.477	97.27	178.00	9.78	10.50	10.44	9.61
CTMS3	6.00	0.772	7.772	97.07	178.00	9.74	10.57	10.46	9.61
CTMS4	3.00	0.960	3.125	121.54	221.70	17.13	17.89	17.46	16.25
CTMS5	5.00	0.960	5.208	121.46	221.70	17.45	17.92	17.51	16.28
CTMS6	6.00	0.970	6.186	122.25	221.70	17.66	18.24	17.76	16.49
CTMS7	3.00	1.244	2.412	158.86	210.60	20.02	27.86	26.56	24.92
CTMS8	5.00	1.250	4.000	158.33	210.60	31.68	28.15	26.83	25.15
CTMS9	6.00	1.244	4.823	157.75	210.60	30.01	28.05	26.68	24.94

Table 2
Compression Test Results: Stainless Steel Plain Channel Section Short Struts
 (Nominal Dimensions: Flange-30mm; Web-60mm; Length-180mm)

Specimen Ref.	Bend Radius, r (mm)	Thickness t (mm)	r/t	Whole C.S.A., A (mm ²)	Virgin 0.2% P.S. (N/mm ²)	Exp. Load Capacity (Ave) P _{cm} (kN)	Eurocode 1.4 (Ave) N _{b,Rd} (kN)	ANSI/ASCE (Ave) P _n (kN)
Sharp Corner Specimens:								
CTSSSC1	N/A	0.69	N/A	89.89	304.50	11.05	10.79	10.66
CTSSSC2	N/A	0.84	N/A	109.41	319.10	15.81	16.04	15.85
CTSSSC3	N/A	1.13	N/A	146.63	304.10	28.13	26.85	26.55
Formed Corner Radius Specimens:								
CTSS1	3.00	0.70	4.290	90.88	304.50	10.70	11.09	10.96
CTSS2	5.00	0.69	7.250	88.65	304.50	11.04	10.79	10.66
CTSS3	6.00	0.70	8.570	90.19	304.50	10.84	11.92	11.77
CTSS4	3.00	0.95	3.160	123.79	319.10	18.73	19.44	19.39
CTSS5	5.00	0.93	5.380	121.02	319.10	18.70	19.23	19.01
CTSS6	6.00	0.93	6.450	130.68	319.10	18.53	19.27	19.04
CTSS7	3.00	1.19	2.520	156.97	304.10	28.02	29.63	29.31
CTSS8	5.00	1.19	4.200	156.17	304.10	27.91	29.63	29.31
CTSS9	6.00	1.22	4.920	162.78	304.10	28.03	30.92	30.59

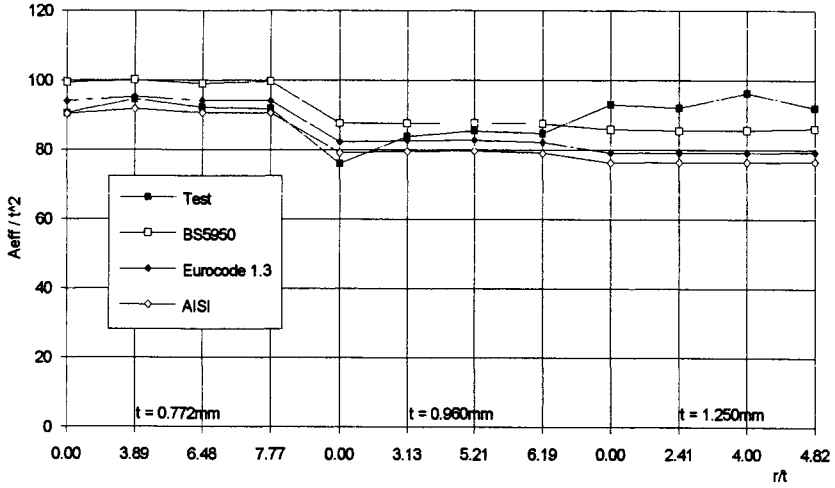


Figure 2 - Variation of A_{eff}/t^2 with r/t ratio for carbon steel short struts of all thicknesses.

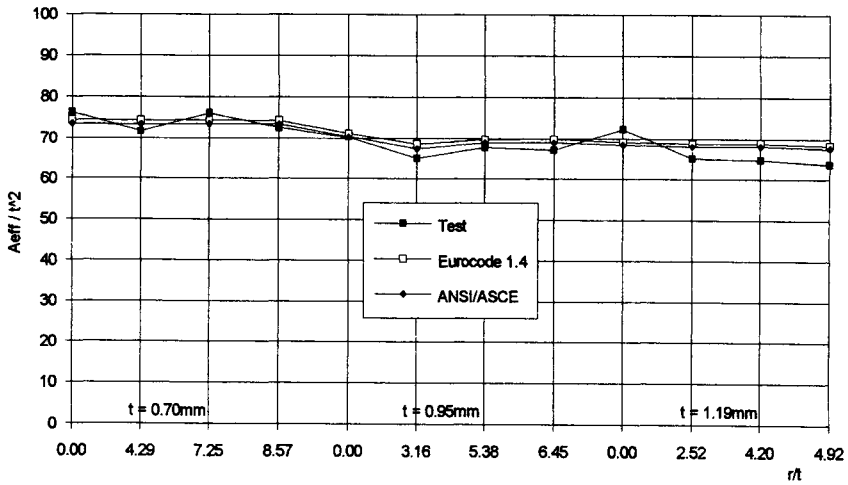


Figure 3 - Variation of A_{eff}/t^2 with r/t ratio for stainless steel short struts of all thicknesses.

LOCAL BUCKLING OF PARTIALLY STIFFENED TYPE 3CR12 STAINLESS STEEL COMPRESSION ELEMENTS IN BEAM FLANGES

GJ van den Berg

Department of Civil Engineering, Faculty of Engineering
Rand Afrikaans University, Johannesburg, South Africa.

ABSTRACT

This study is the final report of a series of tests on partially stiffened compression elements in beam flanges. Partially stiffened compression flanges with varying widths and varying lip lengths were studied. The effect of the non-linear behaviour of stainless steels on the local buckling and ultimate strength of partially stiffened compression elements in beam flanges were studied. The steel under investigation is Type 3CR12 stainless steel. Lipped channels were placed back to back to form a doubly symmetric lipped I-section. The different plasticity reduction factors suggested in the ASCE³ and South African¹³ stainless steel design specifications for stiffened and unstiffened compression elements are used to compare experimental results with theoretical predictions.

It is concluded that the ASCE³ and South African¹³ stainless steel design specifications overestimate the local buckling stress in the beam flanges as well as the ultimate strength of partially stiffened stainless steel beams. The experimental results compare well with the theoretical predictions when the two plasticity reduction factors are used.

KEYWORDS

Stainless steel, local buckling, distortional buckling, partially stiffened, tangent modulus, secant modulus, lipped channel

General Remarks

In contrast to carbon steels, stainless steels yield gradually under load. Due to the non-linear stress-strain relationship of stainless steels the design specifications for carbon and low alloy steels cannot be used. It is thus necessary to develop separate design criteria for stainless steels. For the overall stability of members the ASCE³ and South African¹³ stainless steel design specifications make use of plasticity reduction factors for design in the inelastic stress range. For overall stability the initial elastic modulus is replaced by the tangent modulus.

Johnson⁹ and Wang¹⁶ investigated the stability of stainless steel stiffened and unstiffened compression elements. Based on their work the ASCE³ design specification for stainless steel structural members recommended that certain plasticity reduction factors could be used but that the effective width of these elements could be determined without using any plasticity reduction factors. It was found that this was in good agreement with experimental results.

No work was done at that stage on the stability of partially stiffened stainless steel compression elements. In this study the effect of the non-linear behaviour of stainless steels on the stability of partially stiffened compression elements in beam flanges is studied. The plasticity reduction factors recommended by Johnson⁹ and Wang¹⁶ will be used to determine the validity of their application to determine the effective width of partially stiffened compression elements. In this study it was decided to test doubly symmetric I-section beams.

THEORETICAL MODEL

Mechanical Properties

The average stress-strain curves can be drawn by using the Ramberg-Osgood¹⁰ equation as revised by Hill⁸. A detailed discussion of the Ramberg-Osgood¹⁰ equation is given in Reference 14 and 15. The revised equation is given by Equation 1.

$$\varepsilon = \frac{f}{E_o} + 0.002 \left(\frac{f}{f_y} \right)^n \quad \text{Eq 1}$$

where

$$n = \frac{\log(\varepsilon_y / \varepsilon_p)}{\log(f_y / f_p)} \quad \text{Eq 2}$$

ε	strain
f	stress
E_o	initial elastic modulus
f_y	yield strength
f_p	proportional limit
n	constant

The tangent modulus, E_t , is defined as the slope of the stress-strain curve at each value of stress. It is obtained as the inverse of the first derivative with respect to strain and can be computed by using Equation 3.

$$E_t = \frac{f_y E_o}{f_y + 0.002 n E_o \left(f / f_y \right)^{n-1}} \quad \text{Eq 3}$$

The secant modulus, E_s , is defined as the stress to strain ratio at each value of stress and can be computed by using Equation 4.

$$E_s = \frac{E_o}{1 + 0.002 E_o \frac{f^{n-1}}{f_y^n}} \quad \text{Eq 4}$$

Critical Local Buckling

The small deflection theory for the equilibrium of plates can be used to calculate the critical local buckling stress of a stiffened, unstiffened or partially stiffened compression element. Many researchers have suggested different approximate or more exact theories to calculate the critical local buckling stress in the inelastic stress range. Equation 5 can be used to calculate the critical local buckling stress for an isotropic plate in the inelastic stress range.

$$f_{cr} = \frac{\eta k \pi^2 E_o}{12(1 - \nu^2) \left(\frac{w}{t}\right)^2} \quad \text{Eq 5}$$

where

f_{cr}	critical local buckling stress
η	plasticity reduction factor
k	buckling coefficient
E_o	initial elastic modulus
ν	Poisson's ratio
w	flat width of the element
t	thickness of the element

The buckling coefficient k depends upon the edge rotational restraint, the type of loading and the aspect ratio of the plate. The buckling coefficients for the different plate elements under consideration can be summarised as follows.

$k = 0.425$	for unstiffened compression elements
$k = 4$	for stiffened compression elements
$0.425 < k < 4$	for partially stiffened compression elements

Several theories have been developed for the determination of the plasticity reduction factors for different types of compression elements. Johnson⁹ and Wang¹⁶ showed the validity of the following plasticity reduction factors for the determination of the critical local buckling stress for stainless steel structural members.

$\eta = 1$	for elastic buckling for carbon steel compression members
$\eta = E_S / E_o$	for buckling of unstiffened compression elements
$\eta = \sqrt{E_t / E_o}$	for buckling of stiffened compression elements

The above three plasticity reduction factors will be used in this study to compare the theoretical predictions with the experimental critical local buckling stresses.

Post Buckling

For the theoretical calculation of the post buckling strength of partially stiffened compression elements the model suggested by the Canadian⁶ and South African¹² carbon steel cold-formed design specifications, which is similar to the ASCE³ stainless steel specification, will be used. The proposed South African¹³ stainless steel design specification is similar. The equations in the above specifications will be revised to take into account the non-linear behaviour of stainless steels in the inelastic stress range by introducing plasticity reduction factors. The procedures described in the

South African¹² and Canadian⁶ carbon steel cold-formed design specifications and the proposed South African¹³ stainless steel design specification will be followed.

The design procedure to calculate the effective width of partially stiffened compression elements is divided into three categories. Case 1 deals with compression flanges that are fully effective, even if it has no lip and it is an unstiffened compression element. For this case it is not necessary to add a stiffener lip to the one side of the compression flange. The effective area of the compression flange is thus equal to the full unreduced area of the compression element. Only the stiffener lip has to be checked for local buckling. Figure 1 gives a general layout of partially stiffened compression elements.

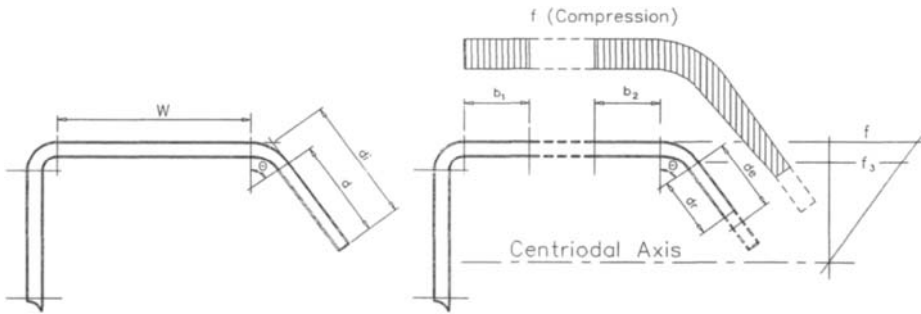


Figure 1 Typical Partially Stiffened Compression Element

The following equations are used in all the cases.

$$W_{lim1} = 0.644 \sqrt{\frac{\eta k E_o}{f}} \quad \text{with } k = 0.425 \quad \text{Eq 6}$$

$$W_{lim2} = 0.644 \sqrt{\frac{\eta k E_o}{f}} \quad \text{with } k = 4 \quad \text{Eq 7}$$

$$B = 0.95 \sqrt{\frac{\eta k E_o}{f}} \left(1 - \frac{0.208}{W} \sqrt{\frac{\eta k E_o}{f}} \right) \quad \text{Eq 8}$$

Case 1: $W \leq W_{lim1}$

$$B = W$$

$$d_r = d_e$$

Case 2 $W_{lim1} < W \leq W_{lim2}$

$$I_s = \frac{1}{12} t d^3 \sin^2 \theta \quad \text{Eq 9}$$

$$I_a = 400t^4 \left[\frac{W}{W_{lim2}} - \sqrt{\frac{0.425}{4}} \right]^3 \tag{Eq 10}$$

$$I_r = \frac{I_s}{I_a} \tag{Eq 11}$$

$$d_r = d_e I_r \leq d_e \tag{Eq 12}$$

Case 3 $W > W_{lim2}$

$$I_a = t^4 \left[115 \frac{W}{W_{lim2}} + 5 \right] \tag{Eq 13}$$

For Cases 1 to 3 the value of the buckling coefficient k is calculated from the equations given in Table 1. The value for n is recommended by Schuster⁷.

Where

- W_{lim1} the limit for the flat width ratio above which an unstiffened compression element will buckle
- W_{lim2} the limit for the flat width ratio above which a stiffened compression element will buckle
- η plasticity reduction factor
- k buckling coefficient for different types of compression elements
- E_o initial elastic modulus
- f maximum stress in the compression element
- B effective width ratio b/t for compression elements
- W flat width ratio w/t for compression elements
- b effective width for compression elements
- w flat width of compression elements
- t thickness of the steel
- d_e effective width of the stiffener
- d_r reduced effective width of the stiffener

**TABLE 1
VALUES FOR BUCKLING COEFFICIENT K**

Case	I_r	$d/w \leq 0.25$	$0.25 < d/w \leq 0.8$
1		$k = 4$	$k = 4$
2 and 3	$I_r \geq 1$	$k = 4$	$k = 5.25 - 5d_j / w$
	$I_r < 1$	$k = 3.57I_r^n + 0.43$	$k = [4.82 - 5d_j / w] I_r^n + 0.43$
Note: $d/t \leq 14$		$n = \frac{25}{43} - \frac{37W}{192} \sqrt{\frac{f}{\eta E_o}}$	$n \geq \frac{1}{3}$

EXPERIMENTAL PROCEDURE

Mechanical Properties

Uniaxial compression tests were carried out on specimens taken from the steel in the longitudinal directions. The tensile tests were carried out in accordance with the procedures outlined by the ASTM Standard A370-77².

Beam Tests

In this study the local and post buckling behaviour of lipped-I-sections were investigated. The different profiles were formed through a press brake process. Short beams were tested to exclude the effect of lateral torsional buckling interaction. The beams are loaded statically and readings were taken every two seconds. The test is continued past the forming of local buckling waves until ultimate failure is reached when the load applied starts to decrease.

The specimen cross-sections were proportioned in such a way to observe all the local buckling modes. In order to cover the whole range of variables governing element behaviour, the flat widths of the flanges were varied. The thickness of the sheet was 1.6 mm and the inside radius was 3 mm. The location of the strain gauges is shown in Figure 2. The placement of the strain gauges enables the detection of all the local buckling modes. The strain gauges mounted on the stiffener are used to indicate the presence of the local plate buckling mode. The strain gauges mounted on the flange are used to detect the flange stiffener buckling mode. The strain gauges mounted on the flange-stiffener junction are used to detect distortional buckling, which refers to the out-of-plane movement of the junction.

The beams are tested in a four point loading set-up arrangement as shown in Figure 2. The load is applied at a rate of less than 2 mm/minute movement of the crosshead of the Instron universal testing machine

DISCUSSION OF RESULTS

Mechanical Properties

Type 3CR12 steel yields gradually under load. This is in contrast to carbon and low alloy steels for which the transition to yielding is clearly noticeable. The mechanical properties of the stainless steel in longitudinal compression are.

$$E_o = 198 \text{ GPa} \quad F_y = 326 \text{ MPa} \quad F_p = 232 \text{ MPa}$$

Beam Tests

The experimental results and theoretical predictions using the three plasticity reduction factors for the critical local buckling stresses and the ultimate strengths for the beams are given in Tables 2 and in Figures 3 and 4. The strain reversal method was used to determine the experimental critical local buckling stress. The experimental critical local buckling stresses are compared with the theoretical predicted local buckling stresses by using the plasticity reduction factors mentioned before.

Figure 3 shows that the theoretical prediction using no plasticity reduction factor as recommended by the AISI¹, South African¹² and Canadian⁶ carbon steel as well as the ASCE³ and South African¹³

stainless steel design specifications overestimates the critical local buckling stresses. The theoretical predictions using the other two plasticity reduction factors compare well with the experimental results. The following symbols apply in Table 2.

- f_e experimental critical local buckling stress
- f_{cr} theoretical critical local buckling stress using no plasticity reduction factor
- f_s theoretical critical local buckling stress using the secant modulus plasticity reduction factor approach
- f_t theoretical critical local buckling stress using the tangent modulus plasticity reduction factor approach

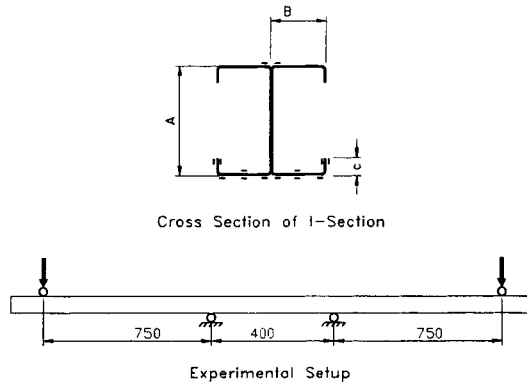


Figure 2 Dimensions and Detail of I-Sections

The experimental results and theoretical prediction for the ultimate capacities of the beams are given in Table 2 and in Figure 4. From Table 2 it can be seen that the theoretical predictions using the secant and tangent modulus approach plasticity reduction factors are generally more conservative and in better agreement with the experimental results. In a study by Buitendag^{4,5} and Reyneke¹¹ on the strength of partially stiffened stainless steel compression members similar results were obtained. The following symbols apply in Table 2.

- M_{exp} experimental ultimate failure moment
- M_e elastic failure moment
- M_s theoretical moment using the secant modulus approach plasticity reduction factor
- M_t theoretical moment using the tangent modulus approach plasticity reduction factor

CONCLUSIONS

It is concluded in this study that the ASCE³ and South African¹³ stainless steel design specifications overestimate the local buckling stress as well as the ultimate strength of partially stiffened stainless steel compression elements. The experimental results compare well with the theoretical predictions when the two plasticity reduction factors are used. For the same width to thickness ratio of the compression flanges the experimental critical local buckling stress increases when the lip size is increased.

From the limited number of tests carried out in this study it can be concluded that there is a general tendency for the elastic theory to slightly overestimate the ultimate capacity of a section for large lip

length to flat width ratios of the compression flange. This is when the width to thickness ratios of the compression flanges are small and when the critical local buckling stresses are large and in the inelastic stress range. For determining the ultimate capacity of a partially stiffened beam section the plasticity reduction factor using the secant modulus approach are in better agreement with the experimental results than the tangent modulus approach.

REFERENCES

1. American Iron and Steel Institute. Cold-Formed Steel Design Manual. 1986.
2. American Society for Testing and Materials. A370-77. Standard Methods and Definitions for Mechanical Testing of Steel Products. Annual Book of ASTM Standards. 1981.
3. American Society of Civil Engineers. Specification for the Design of Cold-Formed Stainless Steel Structural Members. ANSI/ASCE-8-90. 1991.
4. Buitendag, Y. The Strength of Partially Stiffened Stainless Steel Compression Members. M.Eng Dissertation. Rand Afrikaans University. Johannesburg. South Africa. 1995.
5. Buitendag, Y, Van den Berg, GJ. The Strength of Partially Stiffened Stainless Steel Compression Members. Twelfth Specialty Conference on Cold-Formed Steel Structures. St Louis. Missouri. 1994.
6. Canadian Standard Association. Cold-Formed Steel Structural Members. CSA Standard Can3-S-136 1984.
7. Dinovitzer, AS, Sohrabpour, M, Schuster, RM. Observation and Comments Pertaining to CAN/CSA-s136-M89. Eleventh Specialty Conference on Cold-Formed Steel Structures. St Louis. Missouri. 1992.
8. Hill, BN. Determination of Stress-Strain Relationships from Offset Strength Values. NACA Technical Note No 927. Feb 1944.
9. Johnson, AL. The Structural Performance of Austenitic Stainless Steel Members. Report No. 327. Cornell University. Ithaca. New York. November 1966.
10. Ramberg, W, Osgood, WR. Description of Stress-Strain Curves by Three Parameters. NACA Technical Note No 902. July 1942.
11. Reyneke, W. The Strength of Partially Stiffened Stainless Steel Compression Flanges. M.Eng Dissertation. Rand Afrikaans University. Johannesburg. South Africa. 1996. (In Preparation).
12. South African Bureau of Standards. SABS 0162-2:1993. Code of Practice. The Structural Use of Steel. Limit-States Design of Cold-Formed Steelwork. 1994.
13. South African Bureau of Standards. SABS 0162-4:1996. Draft Code of Practice. The Structural Use of Steel. Limit-States Design of Cold-Formed Stainless Steel Members. 1996.
14. Van den Berg, GJ. The Torsional Flexural Buckling Strength of Cold-Formed Stainless Steel Columns. D.Eng. Thesis. Rand Afrikaans University. Johannesburg. South Africa. 1988.
15. Van der Merwe, P. Development of Design Criteria for Ferritic Stainless Steel Cold-Formed Structural Members and Connections. Ph.D. Thesis. University of Missouri-Rolla. 1987.
16. Wang, ST. Cold-Rolled Austenitic Stainless Steel. Report No. 334. Cornell University. Ithaca. New York. July 1969.

TABLE 2
EXPERIMENTAL AND THEORETICAL CRITICAL LOCAL BUCKLING RESULTS

Beam			Critical Local Buckling							Ultimate Strength						
AxBxC	w/t	d/w	f_c MPa	f_{cr} MPa	f_r MPa	f_t MPa	f_o/f_{cr}	f_o/f_r	f_o/f_t	M_{exp} kNm	M_e kNm	M_s kNm	M_t kNm	M_{exp}/M_e	M_{exp}/M_s	M_{exp}/M_t
No			Exper	Elastic	Secant	Tangent				Exper	Elastic	Secant	Tangent			
120x30x8	14.8	0.339	313 (304)	1117	351	294	0.28	0.89	1.06	7.1	6.6	6.2	5.8	1.07	1.07	1.08
120x40x8	21.0	0.238		590	313	262	0.00	0.00	0.00	0.0	7.5	6.5	6.1	0.00	1.16	1.07
120x50x8	27.3	0.183	228 (202)	350	271	231	0.65	0.84	0.99	7.8	7.8	6.8	6.3	1.00	1.16	1.08
120x60x8	33.5	0.149		232	220	194	0.00	0.00	0.00	8.0	8.1	6.9	6.4	0.99	1.16	1.08
120x70x8	39.8	0.126	103 (99)	165	164	147	0.62	0.63	0.70	8.4	8.3	7.1	6.6	1.01	1.17	1.08
120x80x8	46.0	0.109	146 (119)	123	123	107	1.19	1.19	1.36	8.6	8.5	7.2	6.7	1.02	1.17	1.08
120x90x8	52.3	0.096	125 (109)	95	95	81	1.32	1.32	1.54	8.6	8.6	7.3	6.8	1.00	1.18	1.08
120x30x10	14.8	0.424	246 (275)	1257	358	298	0.20	0.69	0.83	7.1	6.8	6.5	5.9	1.04	1.10	1.19
120x40x10	21.0	0.298	240 (269)	695	324	269	0.35	0.74	0.89	8.0	7.7	6.7	6.3	1.04	1.19	1.28
120x50x10	27.3	0.229	182 (237)	429	290	242	0.42	0.63	0.75	8.7	8.3	7.1	6.5	1.05	1.23	1.33
120x60x10	33.5	0.187	276 (205)	284	287	215	0.97	0.96	1.28	8.7	8.5	7.3	6.7	1.03	1.20	1.30
120x70x10	39.8	0.157	221 (241)	202	197	179	1.09	1.12	1.23	9.4	8.7	7.4	6.8	1.08	1.27	1.38
120x80x10	46.0	0.136	195 (262)	151	150	136	1.29	1.30	1.43	9.8	8.9	7.5	6.9	1.10	1.31	1.42
120x90x10	52.3	0.120	162 (91)	117	117	103	1.38	1.38	1.57	9.6	9.1	7.6	7.0	1.06	1.25	1.36
120x30x15	14.8	0.636	266 (353)	1312	360	297	0.20	0.74	0.90	6.8	7.2	7.2	6.4	0.94	0.94	1.06
120x40x15	21.0	0.446	287 (235)	847	336	277	0.34	0.85	1.04	7.2	8.4	7.3	6.7	0.85	0.99	1.07
120x50x15	27.3	0.344	277 (230)	572	311	256	0.48	0.89	1.08	8.0	9.3	7.7	7.0	0.87	1.05	1.14
120x60x15	33.5	0.280	294 (180)	407	285	239	0.72	1.03	1.23	8.7	9.4	8.0	7.3	0.93	1.09	1.20
120x70x15	39.8	0.236	288 (127)	298	254	219	0.97	1.13	1.32	9.3	9.7	8.2	7.4	0.96	1.14	1.25
120x80x15	46.0	0.204	263 (105)	223	213	191	1.18	1.23	1.38	10.1	9.9	8.3	7.5	1.01	1.22	1.34
120x90x15	52.3	0.179	233 (74)	172	171	156	1.35	1.36	1.49	10.5	10.1	8.4	7.6	1.04	1.25	1.38
120x30x20	14.8	0.847	277 (285)	833	335	271	0.33	0.83	1.02	7.1	7.5	6.9	6.5	0.94	1.03	1.10
120x40x20	21.0	0.595	291 (282)	855	336	275	0.34	0.87	1.06	8.7	8.7	7.9	7.1	1.00	1.11	1.23
120x50x20	27.3	0.459	- (296)	638	319	261				9.8	10.0	8.3	7.5	0.98	1.18	1.31
120x60x20	33.5	0.373	247 (275)	474	298	247	0.52	0.83	1.00	10.0	10.4	8.6	7.7	0.96	1.16	1.29
120x70x20	39.8	0.314	281 (279)	362	275	232	0.78	1.02	1.21	10.3	10.8	8.8	7.9	0.95	1.17	1.30
120x80x20	46.0	0.272	258 (258)	283	248	215	0.91	1.04	1.20	10.2	11.1	9.0	8.1	0.92	1.13	1.26
120x90x20	52.3	0.239	239 (244)	225	215	192	1.06	1.11	1.24	10.6	11.3	9.1	8.2	0.94	1.16	1.30

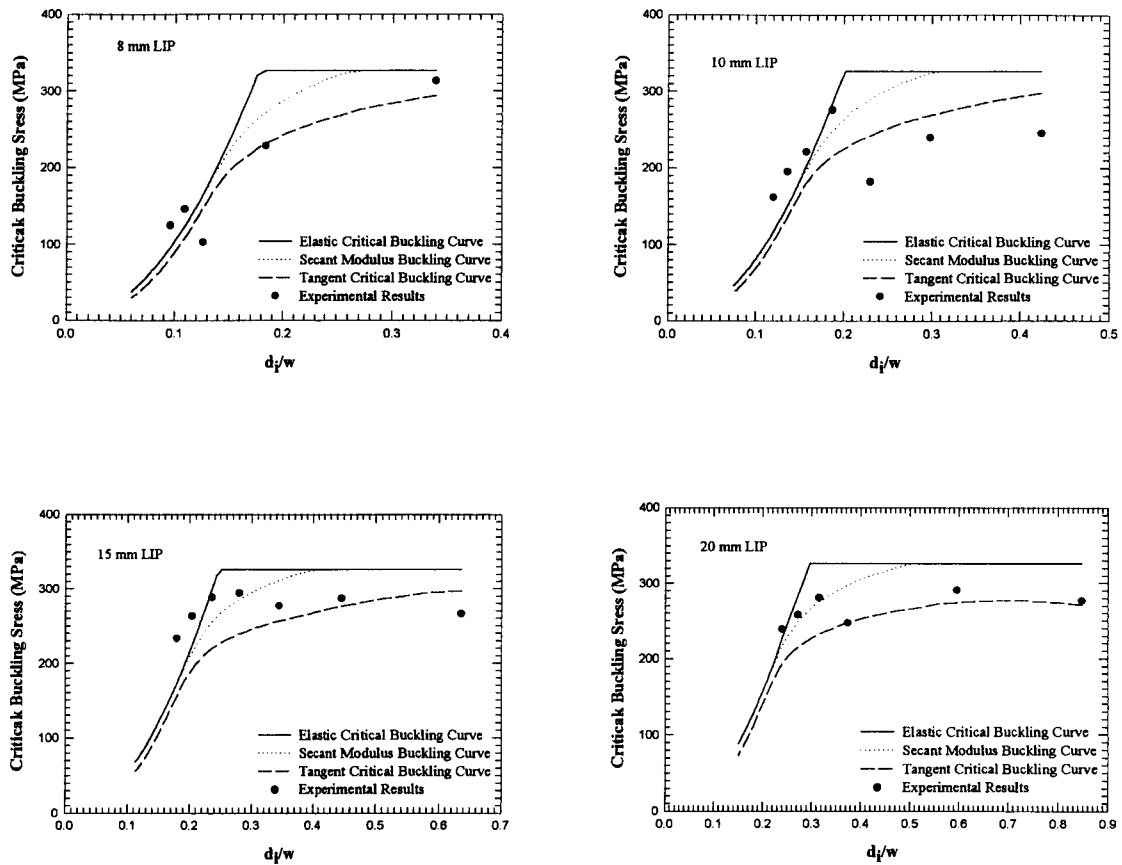


Figure 3 Critical Local Buckling Strength of Sections

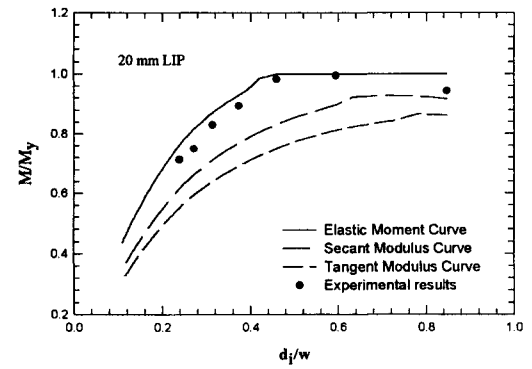
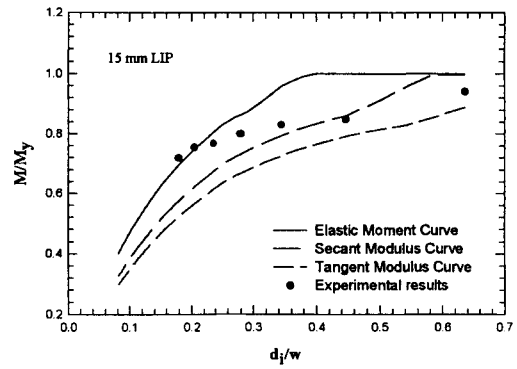
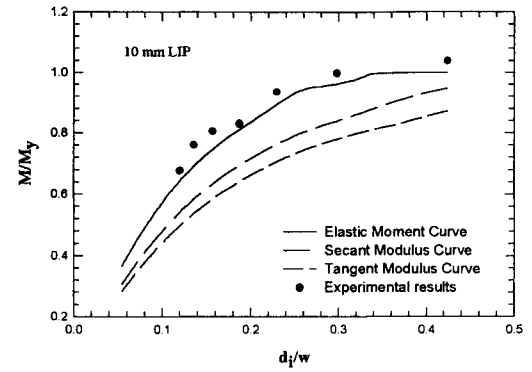
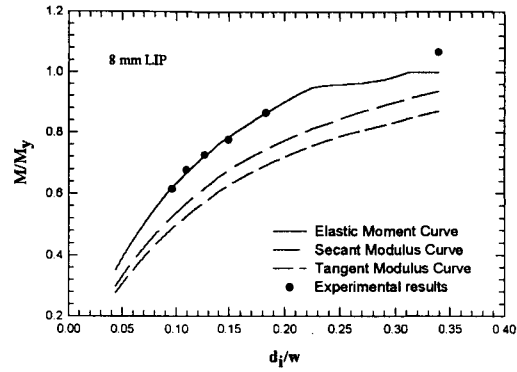


Figure 4 Ultimate Strength of Sections

This Page Intentionally Left Blank

EFFECTS OF SPOT-WELD SPACING ON THE AXIAL CRUSHING OF CLOSED-HAT SECTION MEMBERS

H. F. Wong¹, J. Rhodes¹, J. Zaras² and S. Ujihashi³

¹ Department of Mechanical Engineering, University of Strathclyde,
75 Montrose Street, Glasgow G1 1XJ, U.K.

² Institute of Applied Mechanics, Technical University of Lodz,
ul. Stefanowskiego 1/15, 90-924 Lodz, Poland.

³ Faculty of Engineering, Tokyo Institute of Technology, 2-12-1
Oh-okayama Meguro-ku, Tokyo 152, Japan.

ABSTRACT

This paper describes an experimental investigation into the effects of the spacing of spot welds on the collapse behaviour of axially crushed cold formed steel closed-hat section members. Suitable spacing requirements for spot welds to ensure stable collapse procedures are examined and proposals are made for minimum spacing distances. The effects of spot weld spacing on the collapse loads and subsequent crushing behaviour are examined.

KEYWORDS

Crushing, energy absorption, cold formed steel, spot welds, columns, plates, closed hat section.

INTRODUCTION

With the increasing demand for smaller automobiles the task of ensuring passenger safety is ever more important. For small cars the crushable space in head-on collision is limited and crash energy must be absorbed by the deformation of the vehicle's front-end only. The members which provide energy absorption capabilities are generally made of cold-rolled sheet steel and are structured as thin-walled components having closed-hat cross section. In order to achieve maximum energy absorption these members have to collapse in a stable regular accordion-like fashion. A large test programme was carried out to investigate the static and dynamic crushing behaviour of this type of member, and one aspect of this investigation was an examination of the effects of the spacing of spot welds joining the hat sections to the backing plates. This aspect is discussed here.

TEST SPECIMENS

A total of 21 specimens, of hat section shape with spot welded backing plate as shown in Figure 1, were tested. Much care and preparation went into the making of test specimens. All the dimensions of the specimens were documented and are shown in Appendix I. Of the 21 specimens tested, three nominal thicknesses of mild steel sheets were used. These were 0.6mm, 0.7mm, and 0.95mm.

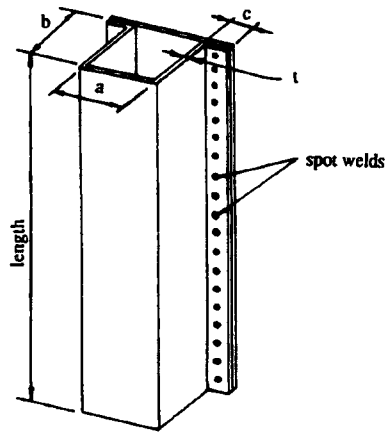


Fig.1 Closed-hat section member

Tensile tests were to evaluate the properties of the materials used in the static crushing tests with much care and following closely BS 18; 1987 for tensile testing of thin steel specimens.

The specimens were taken from the sheets of 0.6mm, 0.7mm and 0.95mm thick plate of BS1449CR4 steel. Six coupons were taken from each cold rolled steel sheet. Three were cut along and the rest perpendicular to the rolling process. The tests were carried out in the Mayse Testing Machine which has a closed-loop hydraulic with computer control and extensometer feedback ensuring a constant strain rate. The average values of the results obtained from the tensile tests were as follows:-

Material Thickness (mm)	Yield stress N/mm ²	Ultimate stress N/mm ²
0.622	167	313
0.745	137	284
0.974	188	329

STATIC TEST RIG

The test rig was designed for use in conjunction with a Tinius Olsen Electro-Mechanical Testing Machine. A sectional view of the static test rig is shown in Figure 2.

Uniform axial loading on the specimen under test was applied via a specially designed Extended Loading Head. This Loading Head was designed to adapt onto the Tinius Olsen Testing Machine's Crosshead, such that they formed an integral unit. The presence of the extended loading head allowed sufficient room underneath the crosshead so that an A3 size X-Y plotter could be placed without being damaged as the specimen was progressively crushed. This provided instant correlation between the crushing process and its Load-Displacement behaviour.

In order that uniform compression of the specimens could be obtained, their ends had to be parallel. A universal table was used to ensure that any deviation from the desired parallel condition was accommodated. The universal table was used in conjunction with a supporting plate and four screw jacks (see Figure 2). The purpose of the supporting plate was to provide a base on which the

specimen could be placed and against which the four jacks could ensure that the ends of the specimen were uniformly loaded. The four jacks were to ensure that once the gap between the ends of the specimen and its supporting elements was eliminated (by the use of the universal table), the supporting plate on which it sat was prevented from any axial movement.

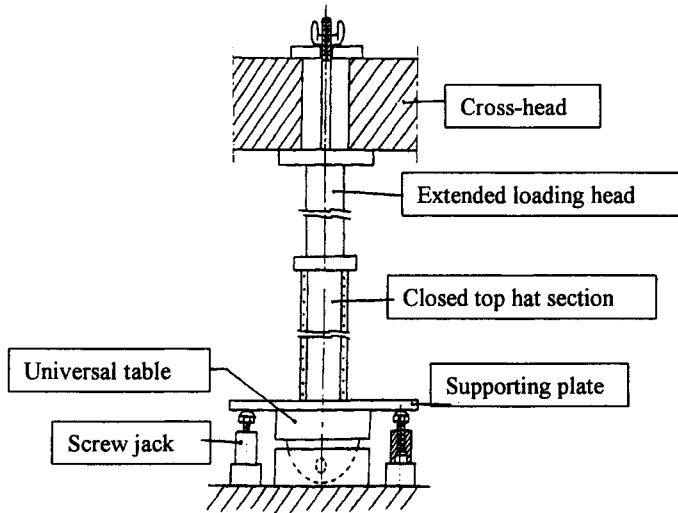


Fig. 2. Sectional view of static test rig

During the tests, load-displacement behaviour was continuously monitored using the Tinius Olsen measuring devices together with external displacement transducers.

TEST PROCEDURE

The twenty one tests discussed here are from a complete program of 250 static and 250 dynamic impact tests, and a consistent procedure was used for all tests of each type (Static or dynamic). A standard procedure was used to set up the specimen initially and ensure that the specimen was seated perfectly before locking the levelling jacks and beginning the test proper. In the test the specimen was compressed axially inducing progressive set-up and collapse of progressive buckles until its length had been reduced to around a quarter of its initial length. A photograph of a test nearing the final stage is shown in figure 3.

SPOT WELD SPACING – ANALYTICAL CONSIDERATIONS

For members which have plate elements connected by spot welds, such as a top-hat section with backing plate, as illustrated in Figure 1, if the spacing of the spot welds is substantial then column type buckling can occur between spot welds. If this happens the ultimate strength of the member will be reduced.

It was noted by Bulson (1) that for a plate with intermittent supports, if the intermittent supports were close together, the buckling modes were similar to those for a continuously supported plate. He also observed that rivets heads offered some fixity to a strip of plates between them and the

critical stress could be given by

$$\sigma_{CR} = \frac{K_R \pi^2 E}{12(1-\nu^2)} \left(\frac{t}{l}\right)^2 \quad (1)$$

where K_R is a fixity coefficient. For spotwelds, $K_R = 3.5$, a value which he extracted from the Engineering Science Data Sheet, Aeronautical series, Structures Sub-series, 02.01.08.

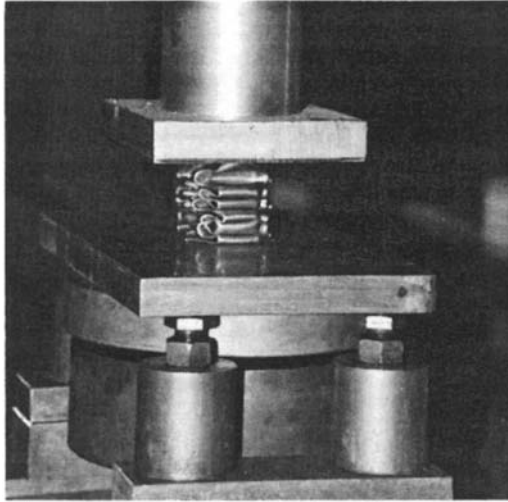


Fig. 3. Crushing test in progress, close to final condition

In the examination of a suitable "critical gap" between supports, Norris [2] noted from typical specifications for carbon steel members that this gap should not exceed 16 times the thickness, t , of the thinner plate joined. For a long plate supported intermittently on both edges and uniformly compressed at the ends, Norris found that if the gap between the supports was less than half the width of the plate, b , then this plate behaved as if continuously supported along the edges, and

$$\sigma_{CR} = \frac{4 \pi^2 E}{12(1-\nu^2)} \left(\frac{t}{b}\right)^2 \quad (2)$$

at spacing greater than $b/2$, the plate behaved as a flat strip buckling in Euler manner between supports, and

$$\sigma_{CR} = \frac{\pi^2 E}{12(1-\nu^2)} \left(\frac{t}{l}\right)^2 \quad (3)$$

A simple way to assess the clear spacing between the spot welds is to consider the connected backing plate as a column of unsupported span equal to the spacing of the spot welds. It could be argued that the ends of the column are restrained from rotation by the connected plate element, as illustrated in Figure 4, but the degree of restraint is not complete as the connected plate tends to deflect with the backing plate, as illustrated in the figure. It may be considered that the most realistic evaluation will result if the column between spot welds is considered as having end conditions somewhere between fixed and simply supported.

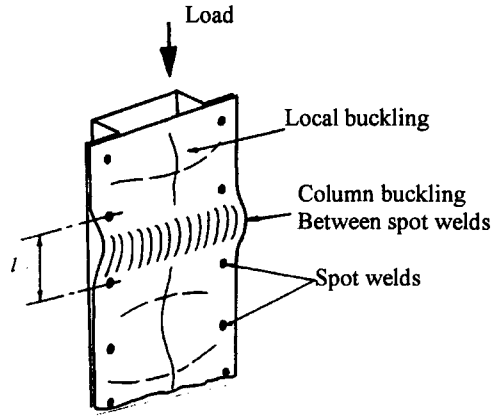


Figure 4. Buckling between spot welds

Assuming that the end conditions are such that the column buckling stress is twice that of a simply supported column, we have:

$$\sigma_E = \frac{2 \pi^2 E}{(l/r)^2} = \frac{\pi^2 E t^2}{6l^2} \quad (4)$$

Buckling between the spot welds and yielding of the cross section will occur simultaneously if

$$\sigma_E = \sigma_y \quad \text{i.e.} \quad \frac{\pi^2 E t^2}{6l^2} = \sigma_y \quad \text{whence} \quad l = \sqrt{\frac{\pi^2 E t^2}{6\sigma_y}} = 1.28 t \sqrt{\frac{E}{\sigma_y}} \quad (5)$$

In the case of steel with a yield strength of 164 N/mm², which is the approximate average value for the members tested, this gives a spot weld spacing of about 45 times the material thickness. It should be mentioned here that the 1980 AISI cold formed steel code [3] gave a minimum spacing slightly greater than this, about 53t for the same steel and conditions. This was based on the consideration that at the design stress, equal to 0.6 times the yield stress, buckling between spot welds, with effective column length equal to 0.6 times the spot weld spacing, should not occur.

The distances obtained from the formulae used to evaluate the minimum spacing between spot welds to avoid buckling between the welds given in different publications for material of 164 N/mm² are shown in the following table:-

Source	Max. spacing to avoid buckling between welds
Bulson (1)	60t
AISI (3)	53t
Norris (2)	32t
Authors	45t

EFFECTS OF SPOT WELD SPACING

The maximum spacing distances specified in the table above only give an indication of the spacings above which buckling of the backing plate independently of the top hat can be observed. No sudden or dramatic change in behaviour occurs for members with spot weld spacings on each side of the

specified values. An indication of the effect of spot weld spacing on the maximum load and the mean crushing load can be obtained by considering the backing plate as a series of columns between the spot welds. Using the British cold formed steel specification (4) for example, the column buckling load for the backing plate may be evaluated on the basis of equation (4), the short strut squash load for this plate can be derived using the effective width approach of the British Standard, and the Perry-Robertson interaction formula of BS 5950:Part 5 then used to give the ultimate load for the backing plate. The top hat ultimate load can then be added to furnish the final load capacity of the member. This decreases gradually as the spot weld spacing increases, due to the column action in the backing plate.

The variation in ultimate load with variation in spot weld spacing is shown in the Appendix for all specimens of this series. Figures 5, 6 and 7 show this variation for each different material thickness individually. Also shown in these figures are the results obtained by analysis to BS 5950:Part 5 using the approach described above. As may be observed, analysis as described results in fairly accurate, and on the whole slightly conservative approximations to the experimental loads. The actual dimensions of each specimen were used in the analyses. It is noticeable that the differences in capacity between members with closely spaced spot welds and those with widely spaced spot welds are not extremely large within the range of spacings examined, being within 20% with one exception.

The table in the Appendix notes the experiments in which buckling of the backing plate could be clearly observed. These include one member with spot weld spacing of approximately 35t and another 5 members all with spot weld spacings above 41t. This suggests that the approach postulated to determine this spacing gives realistic predictions, but the relatively small change in the ultimate load indicates that the use of slightly greater spacing, while detrimental, is not calamitous.

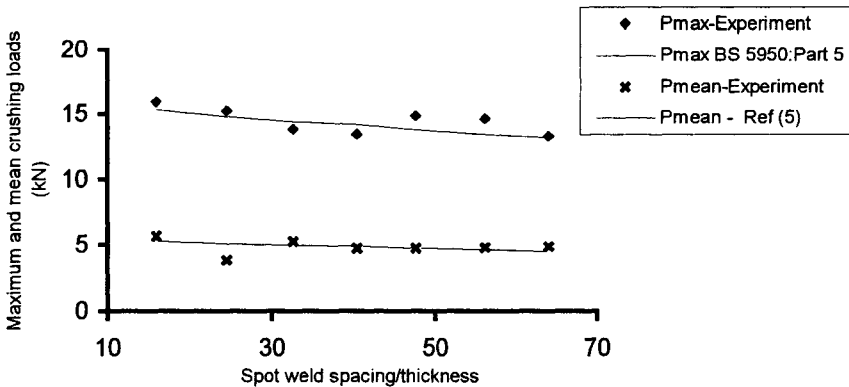


Figure 5. Variation of Maximum and mean crushing load with spot weld spacing – t=0.6mm

Of perhaps greater importance in dealing with axial crushing is the mean crushing load. While the member is undergoing crushing local buckles are progressively set up and collapsed with consequent variation in the load being carried. The mean load carried during this behaviour specifies the energy absorption capacity of the member, and is thus a very important quantity. In an examination of this load in Ref (5) the authors suggested that the mean crushing load for this type of member was given consistently by dividing the maximum capacity by 2.9. The value thus derived is shown in Figures 5, 6 and 7 in comparison with the mean crushing load values obtained experimentally. As may be observed there is reasonably good and consistent agreement with the experimental loads.

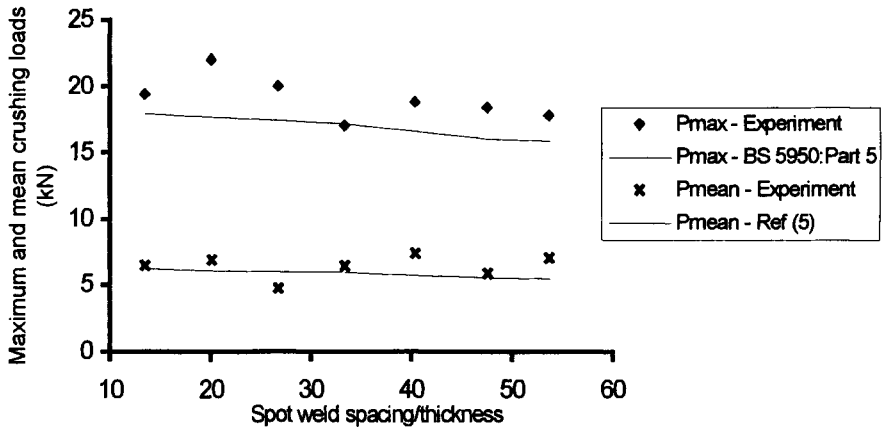


Figure 6 Variation of maximum and mean crushing load with spot weld spacing – $t=0.7\text{mm}$

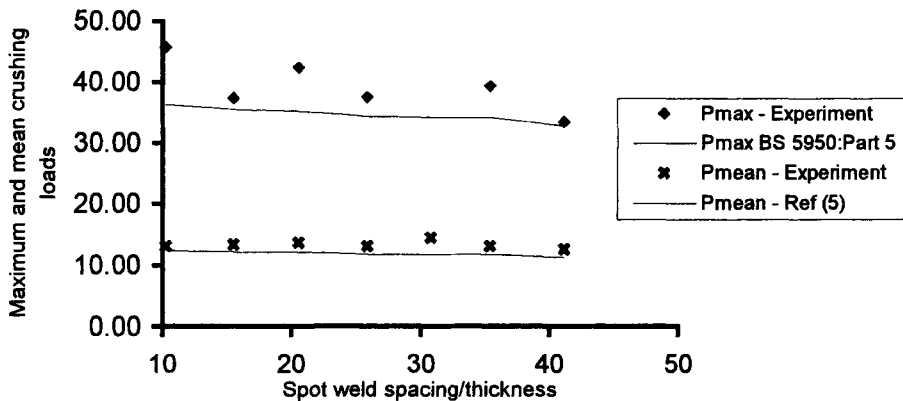


Figure 7 Variation of maximum and mean crushing load with spot weld spacing – $t=0.95\text{mm}$

CONCLUSIONS

The peak load and mean crushing load of the closed hat sections examined here are both affected by the spot-weld spacing, but within the range of spacing distances examined the effects, while noticeable, are not extremely substantial. The simple analysis presented has been shown to provide a good estimate of the effect of spot weld spacing on both maximum load and mean crushing load.

ACKNOWLEDGEMENTS

The financial support given by the Division of Mechanics of Materials, University of Strathclyde for the construction of the Impact Testing Machine is gratefully acknowledged, as is the assistance

with measuring equipment from Tokyo Institute of Technology. The first author was supported by two grants; one from the Committee of Vice-Chancellors and Principals of the Universities of the United Kingdom and the other from the Carnegie Trust for the Universities of Scotland in the course of his Ph.D. study. The third author was the recipient of research grants from the Lady Curran Endowment, and from the Faculty of Engineering, University of Strathclyde, to enable his contribution to the research program.

REFERENCES

1. Bulson P.S., The stability of flat plates. Chatto and Windus, (1970) 116-119
2. Norris C.H. and Polychrone D.A., Buckling of intermittently supported rectangular plates. *Welding Journal*, Vol.30, Nov (1951) 5465-5565
3. American Iron and Steel Institute, Specification for the design of cold-formed steel structural members. Section 4.4, Sep (1980)
4. British Standards Institution. BS 5950:Part 5. Code of Practice for the design of cold formed steel sections. 1987
5. H. F. Wong, J. Rhodes, J. Zaras and S. Ujihashi. Experimental investigation of static progressive crushing of closed hat section members. *IMPLAST '96*. New Delhi, India, December 1996.

APPENDIX. Table of section dimensions and test results

Specimen No.	Corner Radius (mm)	a (mm)	b (mm)	c (mm)	t (mm)	l (mm)	back plate buckle?	P _{max} (kN)	P _{mean} (kN)
SF1	3.5	34.30	34.25	15.26	0.628	10	N	15.90	5.62
SF2	3.5	34.46	35.26	15.65	0.614	15	N	15.20	3.84
SF3	3.5	34.40	35.24	15.18	0.613	20	N	13.80	5.26
SF4	3.5	34.48	34.96	15.51	0.619	25	N	13.40	4.75
SF5	3.5	33.48	33.83	14.94	0.630	30	Y	14.80	4.74
SF6	3.5	34.65	34.90	15.34	0.622	35	Y	14.60	4.77
SF7	3.5	34.57	35.05	15.49	0.625	40	Y	13.20	4.85
SF8	2.5	38.41	40.61	19.97	0.745	0	N	19.40	6.49
SF9	2.5	38.40	40.86	19.81	0.745	15	N	22.00	6.89
SF10	2.5	38.23	40.47	20.20	0.748	20	N	20.00	4.76
SF11	2.5	38.23	40.64	20.02	0.750	25	N	17.00	6.39
SF12	2.5	38.88	40.26	20.20	0.743	30	N	18.80	7.40
SF13	2.5	38.41	40.44	20.44	0.736	35	Y	18.40	5.84
SF14	2.5	38.31	40.65	19.90	0.745	40	Y	17.80	7.06
SF15	3.0	44.56	45.41	20.23	0.977	0	N	45.80	13.12
SF16	3.0	44.40	45.32	20.52	0.969	15	N	37.40	13.45
SF17	3.0	44.78	45.25	20.12	0.974	20	N	42.50	13.62
SF18	3.0	44.35	45.49	20.11	0.966	25	N	37.50	13.18
SF19	3.0	44.22	45.20	20.53	0.975	30	N	-	14.50
SF20	3.0	44.01	45.81	20.10	0.988	35	Y	39.40	13.15
SF21	3.0	44.30	45.52	20.34	0.972	40	Y	33.40	12.62

FLEXURAL STRENGTH OF COLD-FORMED STEEL PANELS USING HIGH-STRENGTH, LOW-DUCTILITY STEEL

Shaojie Wu¹, Wei-Wen Yu², and Roger A. LaBoube²

¹Sargent & Lundy, Chicago, IL 60603

²Department of Civil Engineering, University of Missouri-Rolla, Rolla, MO 65409, U.S.A.

ABSTRACT

Ninety-three cold-formed deck panel specimens were tested using the Structural Grade 80 of ASTM A653 steel (formerly ASTM A446 Grade E steel) to evaluate the flexural strength of the deck panels and their performance as affected by high-strength and low-ductility of the steel. The panels were tested in both two-point and one-point loading conditions. The test results indicated that for the panel specimens with small w/t ratios, the tested yield moments were reached and are compared reasonably well with the calculated effective yield moments. However, for the panel specimens with large w/t ratios, the tested ultimate moments are lower than the calculated effective yield moments, but much larger than the calculated moments using the specified value of 60 ksi (414 MPa). A modified yield strength reduction factor was developed for the design of flexural strength of members with yield strength exceeding 80 ksi (552 MPa).

KEYWORDS

Flexural Strength, High-Strength Low-Ductility Steel, Cold-Formed Steel, Yield Strength Reduction Factor, Decks, Panels

INTRODUCTION

Cold-formed steel decks made of Structural Grade 80 of ASTM A653 steel (formerly ASTM A446 Grade E steel) have been widely used in the United States. The unique property of the Structural Grade 80 steel, as compared to the conventional steels used for cold-formed members, is that it has high specified yield strength $F_y=80$ ksi (552 MPa) and a low tensile-to-yield strength ratio ($F_u/F_y=1.03$). The ductility of the steel is unspecified (ASTM A446) and was reported to be smaller than the ductility requirements for the conventional steels (Dhalla and Winter 1971).

Due to the lack of ductility and the low tensile-to-yield strength ratio of the Structural Grade 80 steel and consideration of the required ductility for adequate structural performance, Section A3.3.2 of the *Specification for the Design of Cold-Formed Steel Structural Members* (AISI 1996) permits the use of the steel for particular configurations provided that (1) the yield strength, F_y , used for the design of elements, members, and structural assemblies, is taken as 75% of the specified minimum yield point or 60 ksi (414 MPa), whichever is less, and (2) the tensile strength, F_u , used for the design of connections and joints, is taken as 75% of the specified minimum tensile strength or 62 ksi (428 MPa), whichever is less.

In the past, the strength and performance of structural components made of the Structural Grade 80 steel had not been fully studied (Wu, Yu, and LaBoube 1995). The reduction of the specified material properties by 25% for design purposes is based on the fact that the structural performance of cold-formed members and connections made of such a steel had not been fully investigated and understood. Therefore, a research project involving a test program was carried out at the University of Missouri-Rolla to further study the strength and performance of flexural members using Structural Grade 80 of A653 steel. This paper presents the results of the study.

TEST PROGRAM

Material tests

A total of seventy-six tensile coupon tests were conducted to determine the ductility and material properties of the Structural Grade 80 steel sheet used to fabricate the test specimens. These properties were used for evaluating the results of panel tests (Wu, Yu, and LaBoube 1995). The tensile coupons were made from 22, 24, 26, and 28 gage steel sheets and cut both parallel and perpendicular to the rolling direction of the sheets. Only 22, 26, and 28 gage sheets were used for the panel tests with actual thickness of sheet varying from 0.015 to 0.029 inches (0.381 to 0.736 mm) and actual yield strength of the sheet steels varying from 103.9 to 112.5 ksi (716 to 776 MPa).

Panel specimens

Deck panel specimens consisted of single and multiple hat-shaped ribs in their cross sections. A total of twenty-four typical hat-shaped sections were used for the panel study. The section parameters include: thickness of panel sheet, flange flat-width-to-thickness ratio (w/t), web flat-width-to-thickness ratio (h/t), and first yielding condition in a section represented by extreme fiber tension-to-compression stress ratio (f_t/f_c). Three yielding conditions were considered in the design of the panels, namely, (1) first yielding in compression flange only, (2) yielding in both the compression and tension flanges simultaneously, and (3) yielding in the tension flange only, with the f_t/f_c ratio being equal to 0.8, 1.0, and 1.2, respectively. The shape of panel specimens is shown in Figure 1.

For all panel specimens, the actual w/t ratios ranged from 17.18 to 189.95 and the actual h/t ratios ranged from 16.35 to 104.89. Actual angle between planes of the web and bearing surface varied from 59.06 to 62.21 degrees. Actual inside bend radius, R , was 1/32 inches (0.79 mm).

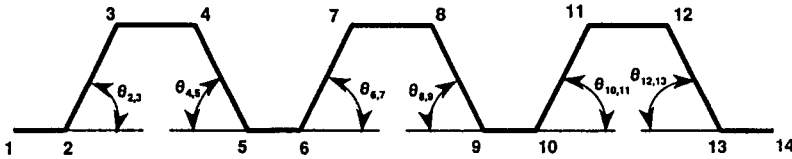


Figure 1: Cross section of panel specimens

Test set-up and instrumentation

Each panel specimen was placed on two simple supports (one was a roller condition and the other was a pin condition) which were fastened on a wide flange support beam. The support beam was firmly connected to the platen of the MTS 880 loading frame located at the Engineering Research Laboratory at the University of Missouri-Rolla. A cross beam was used to establish a two-point loading condition, with one pin and one roller at each end of the beam. Load was applied to the center of the cross beam. Bracing was attached to the tension flanges of panel specimens using C-clamps at several locations along the entire length of all specimens to prevent the section from changing its shape.

LVDTs were used to record the displacements of the panel specimen. An LVDT was located on each side of the test specimen. Six to eighteen strain gages were used for each panel to record extreme tensile and compressive fiber strains. As a result, the tested yield moment could be determined. All LVDT and strain gage data were simultaneously recorded through a CMAC data acquisition system. After a specimen had failed, the displacement control mode was terminated while the data recording continues until applied load was completely released from the specimen.

Panel test

A total of ninety-three panels were tested with simple supports. Of the ninety-three panels, seventy-two panels were tested in two-point loading condition. Five panels were tested with screws penetrating through tension flanges. Test results indicated that for the two-point loading condition, only six panels with the w/t ratio of 118.64 or larger experienced yielding, while yielding occurred in forty-two panels with the w/t ratio of 103.52 or less. The number of panels that underwent yielding tended to decrease with increases in the w/t ratios. Ultimate strains prior to failure of the panels were much larger than the yield strains in the majority of the panels with the w/t ratio of 103.52 or less, but less than the percent elongation in a 2-inch gage length of the steel. The magnitude of the ultimate strains decreased with increases in the w/t ratios. All the panels except the 22 gage panels with smallest w/t ratios failed when a local failure mechanism formed due to crushing of the corners between the flange and web in compression. The panels without flange local buckling showed sufficient ductility. Fracture in tension was not observed in the tested panel specimens.

Fifteen panels with w/t ratios ranging from 17.93 to 189.95 and tested in one-point loading condition experienced yielding in section based on recorded strain gage reading. The ultimate strains prior to failure were much larger than yield strains but still less than the percent elongation in 2-inch gage length of the

steel. Panels tested in one-point loading condition tended to develop higher ultimate strains near concentrated load as compared to the panels tested in two-point loading condition. However prior to failure, the panels with smaller w/t ratios and two-point loading condition demonstrated a plateau in the load vs. central deflection curve, while this plateau usually was not developed in the panels with one-point loading condition. Fracture in tension was also not observed in the panels. All the panels in one-point loading condition failed due to a formation of a local failure mechanism near one edge of the central bearing plate. The local failure mechanism was also initiated by crushing of the corners between the flange and webs in compression, but the process of forming the complete mechanism was more gradual in the panels with one-point loading condition than in the panels with two-point loading condition.

EVALUATION OF TEST RESULTS

Flexural strength of members in two-point loading condition

Per AISI Specification (1996), the effective moment of a section using Structural Grade 80 steel should be determined based on a minimum yield strength of 60 ksi (414 MPa). Using this provision as a basis, the effective moments of the panels tested in two-point loading condition were calculated with actual dimensions and compared to the tested ultimate moments for all the panels. The moment ratios tend to decrease with increases in the w/t ratios. The predicted flexural strength of the panels using the specified 60 ksi stress proves to be conservative.

As observed in the tests, most of the test panels experienced yielding in the section prior to final failure, especially for the panels with small w/t ratios (17.93 to 61.07). The tested ultimate moments are compared with the effective yield moments calculated using the actual yield strength of the steel and actual dimensions. The ratio of the tested ultimate moment to the calculated effective yield moment using the actual yield strength decreases from 1.25 to about 0.80 with the w/t ratio increasing from 17.93 to 189.95. Most moment ratios are larger than 1.0 for the w/t ratios of 61.07 or less, and less than 1.0 for the w/t ratios of 102.86 or larger, with a tendency to converge to 0.85 at larger w/t ratios (120 to 190).

Flexural strength of members in one-point loading condition

The effective moments of the sixteen panels tested in one-point loading condition were calculated using the specified stress of 60 ksi and actual dimensions and are compared to the tested ultimate moments of the panels. For all panels, the ratio of the tested ultimate moment to the calculated effective moment using the 60 ksi is larger than 1.4. The moment ratio decreases from 2.71 to 1.42 with the w/t ratio increasing from 17.93 to 189.95. The calculated effective moment using the AISI specified 60 ksi stress underestimates the actual flexural strength of the panels.

For all sixteen panels, the tested ultimate moments were also compared with the effective yield moments calculated using the actual yield strength of the steel and actual dimensions. The ratio of the tested ultimate moment to the calculated effective yield moment using the actual yield strength decreases from 1.59 to 0.85 with increases in the w/t ratios. The moment ratios are larger than 1.0 for the w/t ratios of 31.65 or less and less than 1.0 for the w/t ratios of 118.64 or larger, with a tendency to converge to 0.85 at larger w/t ratios (120 to 190).

Comparison of test results between two loading conditions

The test results from two-point loading condition and those from one-point loading condition were compared with calculated effective moments. The moment ratios are all larger than 1.0 and tend to decrease from 1.37 to 1.00 with the w/t ratio increasing from 17.93 to 189.95. The panels using the one-point loading condition were designed so as to avoid the large effect of concentrated load on the flexural strength. As a result, the moment gradient caused by the one-point loading setup tends to increase the ultimate moment capacity of the panels.

Flexural strength of members with screws through tension flanges

The concern for structural performance of the panels with screws through the tension flange is the effect of stress concentration and the reduction in tension flange area on the strength and deformation of the panels.

The tested yield and ultimate moments of the panels with screws are compared with those of the panels without screws. The tested yield and ultimate moments of the panels with screws are close to and tend to be slightly larger than those of the panels without screws. The holes in the tension flanges created by the screws did not appear to have a significant effect on the ultimate strength and failure mode of the panels studied in this program. This may be because, for the panels that failed due to a formation of a local failure mechanism and were designed for first yielding in compression flanges, the recorded tensile strains in the tension flanges were lower than their yield strains at the time of failure. This was especially true for the panels with larger w/t ratios, since at failure, the yield strength of the steel could not usually be reached in these panels designed for first yielding in either the compression or tension flange. Even for the panels with smaller w/t ratios and designed for first yielding in compression flange, the recorded tensile strains were still lower than their yield strains after the ultimate load was reached. As a result, the stress concentration near the holes at the screw locations would not be raised to a level that could cause tensile fracture in the tension flanges before compression flanges were crushed to form a local failure mechanism.

DEVELOPMENT OF MODIFIED YIELD STRENGTH REDUCTION FACTOR

The test results demonstrated a need for better prediction of flexural strength of sections using the Structural Grade 80 steel. One approach for improvement is to use a more realistic maximum stress in the section to determine the effective section modulus and the effective moment of the section.

According to the AISI Specification (AISI 1996), the nominal section strength of flexural members that are made of the Structural Grade 80 of ASTM A653 steel (former ASTM A446 Grade E steel) should be determined by Procedure I in Section C3.1.1 of the Specification, that is, the nominal section strength equals to a design stress, F_y , times the elastic section modulus of the effective section, S_e , calculated at the extreme compression or tension fiber. For most of the conventional cold-formed sheet steels listed in Sections A3.1 and A3.2 of the Specification, this design stress is usually taken as the specified minimum yield strength of the steel. For calculating the elastic section modulus of the effective section, S_e , the effective width equations as specified in Section B of the Specification should be used for the elements subjected to compressive stress. The effective width formulas were developed based on the sheet steels whose yield strength did not usually exceed 60 ksi. However, the tests conducted in this program prove that the use of the higher yield strength of the Structural Grade 80 steel can overestimate the effective moment capacity of sections with larger w/t ratios in the compression flange. On the other hand, for sections with small w/t ratios, the use of the required 75% of the specified yield strength of the steel underestimates the effective moment capacity of the sections. Therefore a yield strength reduction factor

is needed to better estimate of design stress.

An earlier study by Pan (1987) on the effective design width of high strength cold-formed steel members found that a correlation exists between a yield strength reduction factor and a factor of $(w/t)(F_y/E)$. This yield strength reduction factor was modified to incorporate the new test data and the findings obtained from this research program (Wu, Yu, and LaBoube, 1996).

A four-step procedure was used to develop a modified yield strength reduction factor. (1) Develop the theoretical stress-strain relationship for the three different steel sheets used in this study, namely 22, 26, and 28 gage steel sheets, and compare the theoretical stress-strain curves with all coupon test data. (2) For each panel specimen tested in the two-point loading condition, obtain the average compressive edge strains and the average tensile strains recorded at the failure of each panel. Then determine the corresponding tested ultimate stresses, f_{max} , based on the average compressive and tensile strains at the failure and the theoretical stress-strain relationships; and calculate the ratio of the tested ultimate stress to the yield strength of the steel, f_{max}/F_y , for each panel. (3) Examine the effect of w/t and F_y/E ratios on the f_{max}/F_y ratio, based on the plots of the f_{max}/F_y ratio vs. w/t ratio and the f_{max}/F_y ratio vs. F_y/E ratio for the panels tested in this study and those members with stiffened flanges tested by Pan (1987). (4) Construct the relationship between f_{max}/F_y ratio and the parameter $(w/t)(F_y/E)$, based on the plot of the f_{max}/F_y ratio vs. $(w/t)(F_y/E)$ for all the specimens used in step (3). The modified yield strength reduction factor, R_b , is equal to f_{max}/F_y . Detailed discussion for developing the reduction factor can be found elsewhere (Wu, Yu, and LaBoube, 1996).

Based on the test data from this study and those from Pan (1987), a modified yield strength reduction factor was developed to relate the f_{max}/F_y ratio (the yield strength reduction factor) with the parameter $(w/t)(F_y/E)$. The test results come from the specimens with the yield strength of steels ranging from 84.3 to 153.3 ksi (581 to 1057 MPa) and the w/t ratio ranging from 17.7 to 189.95. The reduction factor is written as follows:

$$R_b = \frac{f_{max}}{F_y} = 1 - 0.26 \left(\frac{w}{t} \frac{F_y}{E} - C \right)^{0.4} \leq 1.0$$

Where w/t is the flat-width-to-thickness ratio of the compression flange; F_y is the yield strength of the steel; E is the modulus of elasticity and equal to 29,500 ksi (203403 MPa); and C represents the limit for the steels with yield strength of 80 ksi, and is equal to:

$$C = \left(\frac{219.76}{\sqrt{F_y}} \times \frac{F_y}{E} \right)_{F_y = 80 \text{ ksi}} = \frac{219.76}{\sqrt{80}} \times \frac{80}{29500} = \frac{1}{15}$$

When $(w/t)(F_y/E)$ is equal to C , $R_b=1.0$, meaning that no reduction in yield strength of steel is needed in the design of flexural strength of members.

Corresponding to the above range of yield strength (84.3 to 153.3 ksi) and w/t ratio (17.7 to 189.95), the reduction factor varies from 1.00 to 0.75. In predicting the flexural strength of a section, the yield strength, F_y , is multiplied by the reduction factor, R_b , to obtain a reduced yield strength, $R_b \times F_y$, that replaces F_y in the calculation of the effective design width and the moninal moment.

The tested ultimate moments are compared with the predicted moments using the modified yield strength

reduction factor. The ratios of tested ultimate moment to predicted moment are plotted in Figure 2. This approach is conservative for the members with small w/t ratios, for which an inelastic strength reserve exists in these members as observed in the tests.

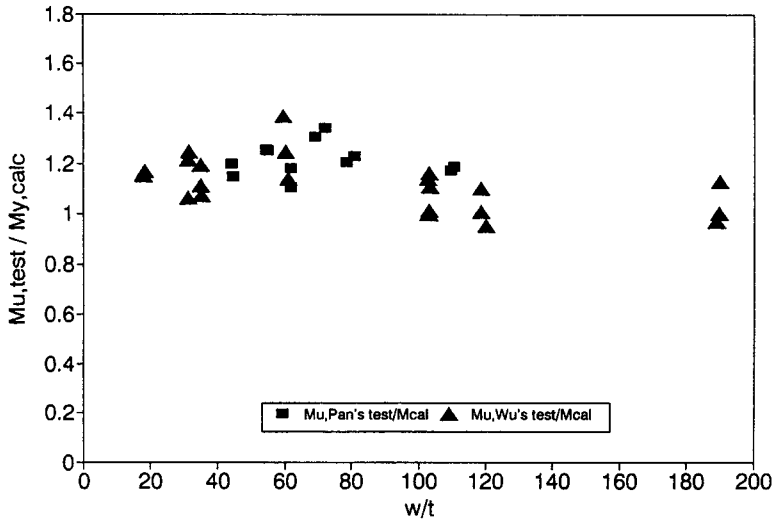


Figure 2: Comparison of tested ultimate moment and calculated effective moment using modified yield strength reduction factor

SUMMARY

A total of ninety-three deck panels were tested to study the flexural strength of panels fabricated using the high-strength low-ductility Structural Grade 80 of ASTM A653 steel. The panels were tested in both two-point and one-point loading conditions. The tested panels involved twenty-four different hat-shaped sections and all the panels were made of 28, 26, and 22 gage sheet steels. Major research findings are summarized as follows.

The current design practice for determining flexural strength of the panels using 75% of the specified minimum yield strength of the steel is conservative, especially for the panels with small w/t ratios (less than 60). A modified yield strength reduction factor was developed to be used for the design of flexural strength of the panels with yield strengths of 80 to 150 ksi (552 to 1034 MPa) and w/t ratios not exceeding 190. For panels with a $(w/t)(F_y/E)$ ratio of 1/15 or less, the actual yield strength of the steel sheet can be used in determining flexural strength of the panels. Reasonable agreements are reached between tested moments and predicted moments using the modified yield strength reduction factor.

The tested ultimate moment capacity of the panels with a one-point loading condition tended to be larger than the tested ultimate moment capacity of the panels with a two-point loading condition. The moment ratio ranged from 1.37 to 1.00 and tended to decrease with increasing the w/t ratios from 17.93 to 189.95.

Panel specimens which were designed for first yielding in the tension flange developed a higher ratio of the tested ultimate moment, or yield moment, to the calculated effective yield moment as compared to the

panels designed for first yielding in both compression and tension flanges and in the compression flange only. The low tensile-to-yield strength ratio of the Structural Grade 80 steel ($F_u/F_y=1.03$) did not show negative effect on flexural strength based on the tests of this study.

The flexural strength of the panels with screw holes in the tension flange are similar to those of the panels without screw holes, based on the reduction of area in the tension flange ranging from 13% to 27%. One 22 gage panel with the smallest w/t ratio and designed for first yielding in tension flanges developed a tensile fracture and necking near the holes at all screw locations. This panel failed after it entered a plateau on its load-deflection curve. Fracture failure was not observed in all the panels without screws.

ACKNOWLEDGEMENTS

The research work reported herein was sponsored by the American Iron and Steel Institute. The technical guidance provided by Subcommittee 24(J.N. Nunnery, Chairman) of the AISI Committee on Specifications and the AISI staff are gratefully acknowledged. All of the steel sheet materials used for the panel tests were kindly donated by Wheeling Corrugating Company, Wheeling, West Virginia.

REFERENCES

American Iron and Steel Institute (AISI) (1996), *Specification for the Design of Cold-Formed Steel Structural Members*, Washington, D.C.

ASTM A446, *Standard Specification for Steel Sheet, Zinc-Coated (Galvanized) by the Hot-Dip Process, Physical (Structural Quality)*, Annual Book of ASTM Standards.

Dhalla, A.K. and Winter, G. (1971), "Influence of Ductility on the Structural Behavior of Cold-Formed Steel Members," Report No. 336, Cornell University.

Pan, L.C. (1987), "Effective Design Widths of High Strength Cold-Formed Steel Members," thesis presented to the University of Missouri-Rolla, in partial fulfillment of the requirements for the degree of Doctor of Philosophy.

Wu, S., Yu, W.W., and LaBoube, R.A. (1995), "Strength of Flexural Members Using Structural Grade 80 of A653 and Grade E of A611 of Steels," First Progress Report, Civil Engineering Study 95-5, University of Missouri-Rolla.

Wu, S., Yu, W.W., LaBoube, R.A. (1996), "Strength of Flexural Members Using Structural Grade 80 of A653 and Grade E of A611 of Steels, Second Progress Report," Civil Engineering Study 96-4, University of Missouri-Rolla.

FLEXURAL-TORSIONAL STABILITY OF THIN-WALLED ORTHOTROPIC CHANNEL SECTION BEAMS

Mohammad Z. Kabir

Department of Civil Engineering, AmirKabir University of Technology
Tehran, Iran, P. O. Box 15375

ABSTRACT

This paper presents an analytical solution for predicting the lateral buckling capacity of laminated channel beams, including the influences of load form and lamination architecture. A detailed parametric study demonstrates that an improved design can be suggested which shows superior performance for optimal fibre orientation in both flanges and web in comparison with the traditional unidirectional pultrusion process.

KEYWORDS

Composite, Pultruded, Flexural, Torsional, Stability, Laminate

INTRODUCTION

This study outlines an attempt to determine the effect of non-coincident centroid and centre of rotation on the values of the lateral buckling loads. An asymmetric fibre composite channel section with mid-plane symmetric laminate is chosen for this investigation. To show the effect of single symmetry on the lateral failure mode, the transverse loads are at first assumed to act at the top. Virtual work is used to facilitate the determination of the load potential. An element of the unbuckled beam is represented by a length, dz , along the centroid line, Figure. 1a. The displacement field characterizing buckling produces rigid body motion for element, dz , curvature, $V + \phi$, of the centroid line about the \bar{s} axis, and twist angle, ϕ , about a longitudinal axis through P, Figure. 1b. The vertical deflection due to section rotation is

$$e_T - d [\cos \psi - \cos (\psi - \phi)] \quad (1)$$

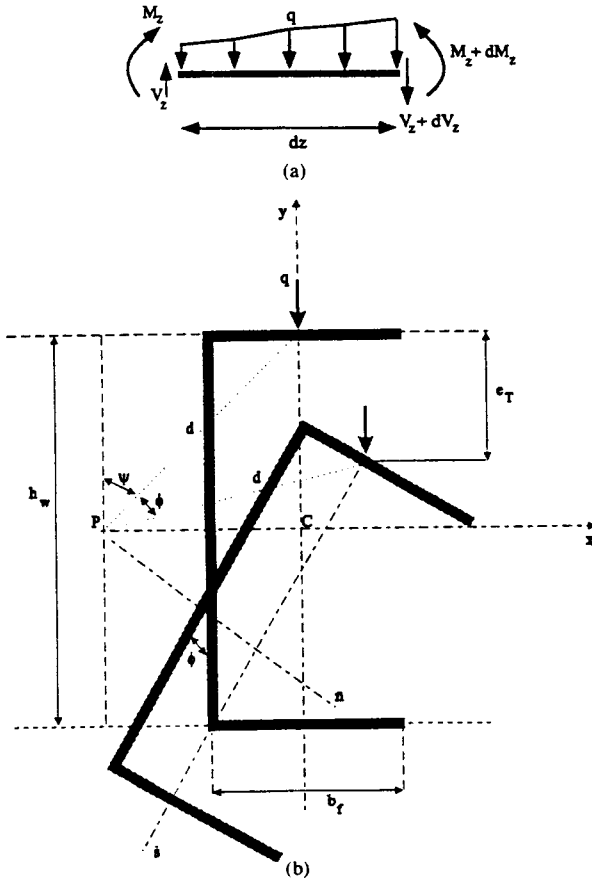


Figure 1: Coordinates of Channel Beam in Lateral Stability

For small ϕ , after some algebra, it can be simplified as

$$e_T = d(\phi \sin \psi + \frac{1}{2} \phi^2 \cos \psi) \tag{2}$$

From the virtual work theorem, the work of the forces and moments of Figure 1a, in

consequence of the buckling displacements, is equal to the work of the end moments and transverse loads of the entire member for the same displacement. Referring to the constitutive relations for beam stress and displacement, which have been defined previously, (Bauld and Tzeng 1984), the internal strain energy, in terms of active bar forces and bar displacements in the principal coordinates is

$$\Pi_s = \frac{1}{2} \int (NW' \cdot M_y U'' - M_x V'' \cdot M_w \phi'' \cdot T_s \phi') dz \tag{3}$$

in which (·) denotes differentiation with respect to z, N is the axial force, M_x and M_y are the bending moments acting about the x and y axes respectively, M_w is the warping moment and T_s is the Saint Venant torsion or free warping. Forces, V_y , and its corresponding displacement, V, do not contribute to lateral virtual work; therefore, the work of the loads due to the uniform distributed load q is

$$\Pi_w = - \int_0^L (M_w \phi U'' + q e_T) dz \tag{4}$$

Following the classical expression for total energy and using the calculus of variation, the differential equations for the single symmetric cross-section with respect to the x axis, at the equilibrium stage, are expressed as

$$\begin{aligned} I_{yy} U'' - M_w \phi &= 0 \\ I_{\omega\omega} \phi''' - (JG - M_x K_x) \phi'' - M_w U'' - q d \cos(\psi) - q d \sin(\psi) \end{aligned} \tag{5}$$

where K_x is a geometrical characteristic of the section with dimension of length defined by Bauld and Tzeng (1984). Since the channel section has one axis of symmetry and the moments act in the plane perpendicular to that axis, it is found that $K_x = 0$, Timoshenko and Gere (1961). Eliminating the lateral displacement, U, between the two coupled equilibrium equations (5), the final expression for lateral stability of the channel section is obtained as

$$I_{\omega\omega} \phi''' - JG \phi'' - \left(\frac{M_w^2}{I_{yy}} + q d \cos \psi \right) \phi - q d \sin \psi \tag{6}$$

The presence of the non-homogeneity term on the right hand side of relation (6) obviates the standard eigen value problem. The equation differs considerably in terms of buckling behaviour of the channel section from what obtained earlier for the doubly-symmetric I-section, Pandey *et al* (1995). To illustrate the effect of non-coincidency of centroid and pole on the lateral failure load, equation (6) is solved for the simply-supported channel beam under Uniform Distributed Load (UDL). The displacement function, ϕ , is selected as

$$\phi = \sum_{m=1}^M \alpha_m \sin \frac{m \pi z}{L} \quad \text{for: UDL} \quad 0 \leq z \leq L \tag{7}$$

Substituting the relations (7) in (6) leads eventually to the following identity for the UDL

$$\frac{L}{2} a_n [I_{\omega\omega} (\frac{n\pi}{L})^4 + JG (\frac{n\pi}{L})^2 - qd \cos \psi] - \frac{q^2}{4I_{yy}^{m-1}} \sum a_m \int_0^L [z^2(L-z)^2 \sin \frac{m\pi z}{L} - \sin \frac{n\pi z}{L}] dz - qd \sin(\psi) \frac{2L}{n\pi}, \quad n - \text{odd} \quad (8)$$

By taking $n=1$, the closed form relation for maximum (amplitude) twist angle of the section is obtained as

$$\phi_{\max} = \frac{4 \frac{d}{\pi} \sin \psi}{I_{\phi} - d \cos \psi q - \frac{q^2 L^4}{82.1 I_{yy}}}, \quad I_{\phi} = \frac{\pi^2}{L^2} [I_{\omega\omega} (\frac{\pi}{L})^2 + JG] \quad (9)$$

If the load is applied at the centroid, C , $d=e_p$ and $\psi=90^\circ$ and relation (9) is simplified as follows

$$\phi_{\max} = \frac{104.51 e_p I_{yy} q}{82.1 I_{yy} I_{\phi} - q^2 L^4} \quad (10)$$

By taking more terms in equation (7) for UDL and calculating the corresponding value of a_m , the maximum twist angle is calculated as

$$\phi_{\max} = a_1 + a_3 + a_5 + \dots \quad (11)$$

The accuracy of the results obtained by numerical analysis in taking 5 terms, ($M=5$), compared with using only the first term, ($M=1$), is about a 0.1% error. The torsional-flexural rigidities of channel section beams including warping constant, $I_{\omega\omega}$, torsion constant, GJ , and flexural terms, I_{xx} , I_{yy} are calculated in previous work, Kabir & Sherbourne (1998).

NUMERICAL RESULTS

Buckling Solution

For a Glass/Polyester pultruded channel beam, with the depicted geometry in Figure 2 and material properties introduced as follows, numerical results are obtained for the simply-supported beam: Elastic Modulus: $E_f=68.9E+9$ N/m², $E_m=3.45E+9$ N/m², Poisson Ratio: $\nu_f=0.2$, $\nu_m=0.3$ and Fibre Volume Fraction: 50%. The results obtained for three aspect ratios are shown in Figures. 3. For this type of loading it should be noted that the asymmetric channel section converts the lateral stability problem into the load-deflection mode. When the load is applied at the pole, however, no lateral movement occurs until the critical level, q_{cr} , is reached. Loads placed at the centroid, being eccentric to the centre of rotation, eventually cause failure by reaching the yield limit of the material at large twist angle. The results also show less imperfection sensitivity for longer beams, $L/H \geq 12$.

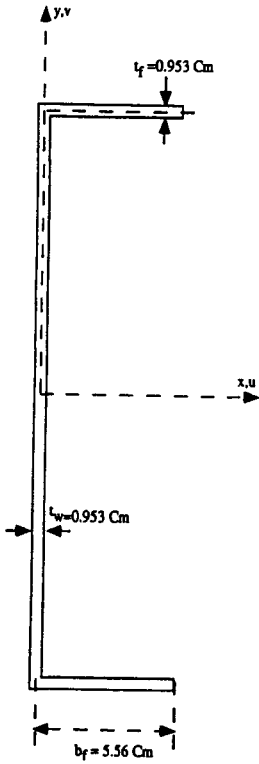


Figure 2 Channel Section

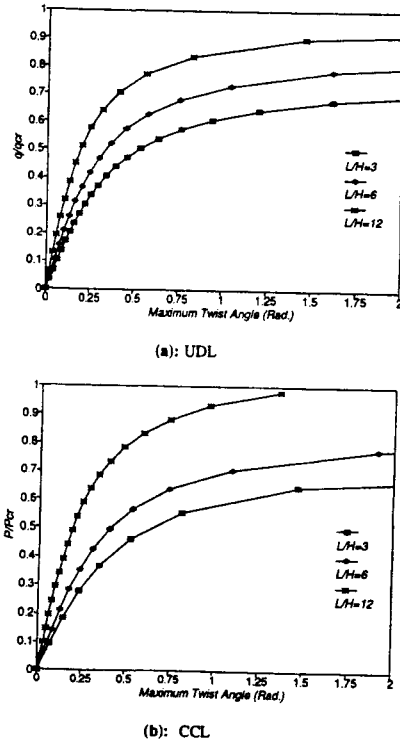


Figure 3 Load vs Channel section twist angle

Optimal Solution

Load applied at the Centroid

The variation of web fibre orientation with cross-section rotation for unidirectional flange fibre, $\theta=0^\circ$, is presented in Figures 4 (under $q=1$ kN/m). For short beams $L/H \leq 6$ the unidirectional pultrusion process gives the minimum twist angle. However, as the beam lengthens, by placing the web fibres at near $\pm 45^\circ$, the twist angle would be reduced about 27% for both loading systems with respect to its value at 0° .

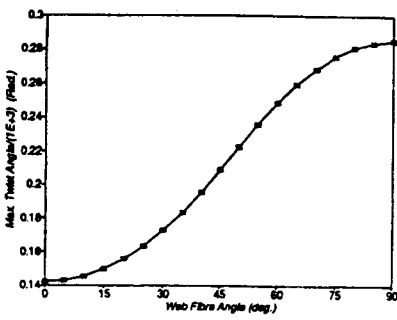
Load applied at the Pole

In this case, lateral movement is triggered by increasing the applied loads to their critical values

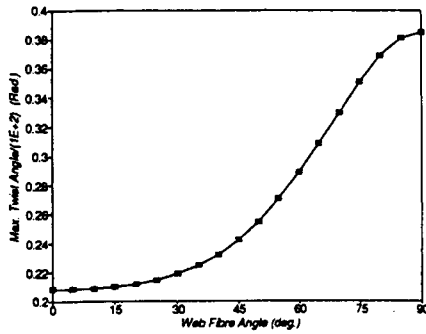
at the bifurcation point; the channel beam has similar behaviour with the doubly-symmetric I-section beam when the load is applied at the pole.

$$q_{cr} = \frac{28.46}{L^3} \sqrt{\frac{JG}{y}} \sqrt{1 + \frac{\pi^2 I_{\omega\omega}}{L^2 JG}} \tag{12}$$

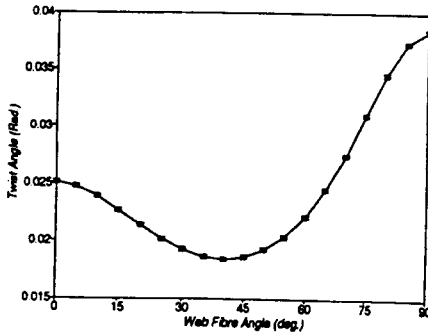
The sensitivity of the web fibre orientation to the buckling load is depicted in Figures 5. It is seen that the predominantly uni-directional fibre-orientation in the pultruded section is optimal for shorter beams, $L/H \leq 6$. However to improve the failure load in longer beams, the web fibre angle should be directed at $\pm 35^\circ$ for $L/H=12$, which increases the buckling load about 12.3%. This angle increases toward $\pm 45^\circ$ for $L/H > 12$ to obtain an optimal design.



(a): L/H=3

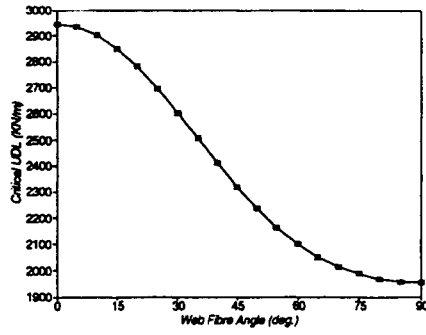


(b): L/H=6

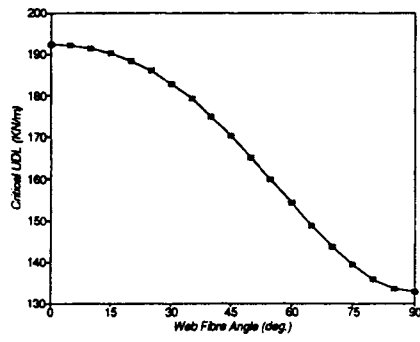


(c): L/H=12

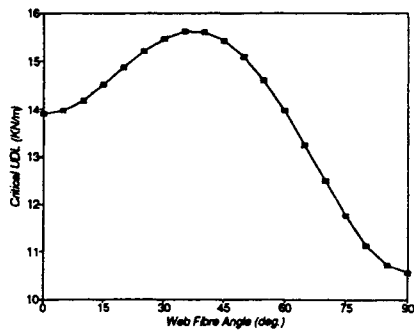
Figure 4 Variation of Channel section rotation with web fibre angle under $q=1$ kN/m



(a): L/H=3



(b): L/H=6



(c): L/H=12

Figure 5 Sensitivity of failure load with web fibre angle (UDL)

CONCLUSION

The present investigation is an explicit analytical solution of the elastic, lateral-torsional buckling of a composite, single layered pultruded channel section, with the purpose of optimizing fibre orientation in the lateral stability of such members.

Extended parametric studies reveal that the web fibre angle has an important influence on improving the lateral buckling load as the beam span becomes longer. However, in short beam, $L/H \leq 6$, the predominantly unidirectional flange and web fibre orientation represent optimal designs under transverse loads. It is also concluded that lateral buckling behaviour of the asymmetric channel section is markedly different from the I-section when transverse loads are applied at the centroid.

REFERENCES

- Bauld, N.R. and Tzeng, L. (1984). "A Vlasov theory for fibre-reinforced beams with thin-walled open cross section", *Int. J. Solids. Structures*, 20(3), pp. 277-297.
- Kabir, M.Z. & Sherbourne A.N. (1998) " Optimal Fibre Orientation in lateral stability of laminated channel section beams", *Composites part B* 29B, pp 81-87
- Pandey, M.D., Kabir, M.Z. and Sherbourne, A.N. (1995). " Flexural-Torsional stability of thin-walled composite I-section beams", *Composite Engineering*, 5(3), pp. 321-342
- Timoshenko, S.P. and Gere, J.M. (1961), *Theory of Elastic Stability*, Mc-Graw Hill, New York, 1961

Inelastic Behaviour of Cold-Formed Channel Sections in Bending

By V Enjily¹, R G Beale², M H R Godley²

¹Building Research Establishment Ltd., Watford, WD2 7JR, UK

²School of Construction & Earth Sciences, Oxford Brookes University, Oxford, OX3 0BP, UK

ABSTRACT

Cold-formed channel sections were tested in four point bending with both stiffened and unstiffened elements in compression. Theories have been derived using yield line mechanisms considering both simply-supported and partially fixed boundaries to predict ultimate moment capacity and resulting midspan deflections. These theories clearly show the effects of different boundary conditions on the post-buckling behaviour. Good correspondence was observed between theory and experiment.

KEYWORDS

Inelastic, cold-formed, bending, post-buckling, channels, yield-line

INTRODUCTION

Considerable research has been carried out into the inelastic behaviour of channel sections in compression, for example, Rhodes and Harvey (1976), Stowell (1951), Murray (1984) and Little (1982) but little research has been reported into the behaviour under bending, Rhodes (1982, 1985). The objective of this research was to produce a post-elastic theory of plain channels and to correlate it with experiments.

In this paper experimental work using four point bending tests on sections using 500mm and 1000mm spans with both their stiffened and unstiffened elements in compression are described.

The yield line mechanism pioneered by Murray (1973) and Davies, Kemp and Walker (1975) was extended to the post-buckling of cold-formed sections in bending with a view to determining moment-curvature relationships. Most yield-line mechanisms for plates consider simply-supported conditions at their supports. However, as far as sections are concerned, boundary conditions of plate elements are either free or partially fixed to the adjoining component. Post-buckling theories have been developed which consider both simply-supported and partially fixed boundaries. These theories clearly identify the effects of different boundary conditions on the post-buckling behaviour of sections in bending. The effect of movement of the neutral axis is incorporated into the elastic and post-buckling deformations of the beams. The theories predict both ultimate moment capacity and the resulting midspan deflections.

EXPERIMENTAL TECHNIQUES

Specimens were manufactured from mild steel sheet 1.6mm thick by cold-forming. The internal radius of all bends was 1.6mm. Plates were welded to the ends of the section to provide a means of support and to hold the section into the correct shape.

The beams were tested in four point bending. The end-plates ensured that the beams were simply-supported. The load was applied through a central screw jack and distributed by means of a spreader beam to two rollers. Load cells were placed at each load and support point. The distance between the rollers was 200mm for the 500mm span and 300mm for the 1000mm spans. The deflection at the centre of each beam was measured with a dial gauge. Complete details of the experimental procedure are described in Enjily (1985).

Unstiffened components in compression

26 channels were tested with width to thickness ratios for the unstiffened flanges ranging from 3 to 92. For sections with these ratios less than 15, the beams were able to carry the full plastic moment of the section. Above this value the sections developed local buckles in the flanges which ultimately produced yield lines as shown in figure 1. A typical experimental load deflection curve is given in figure 2 on which are also imposed the results of the theories derived below.

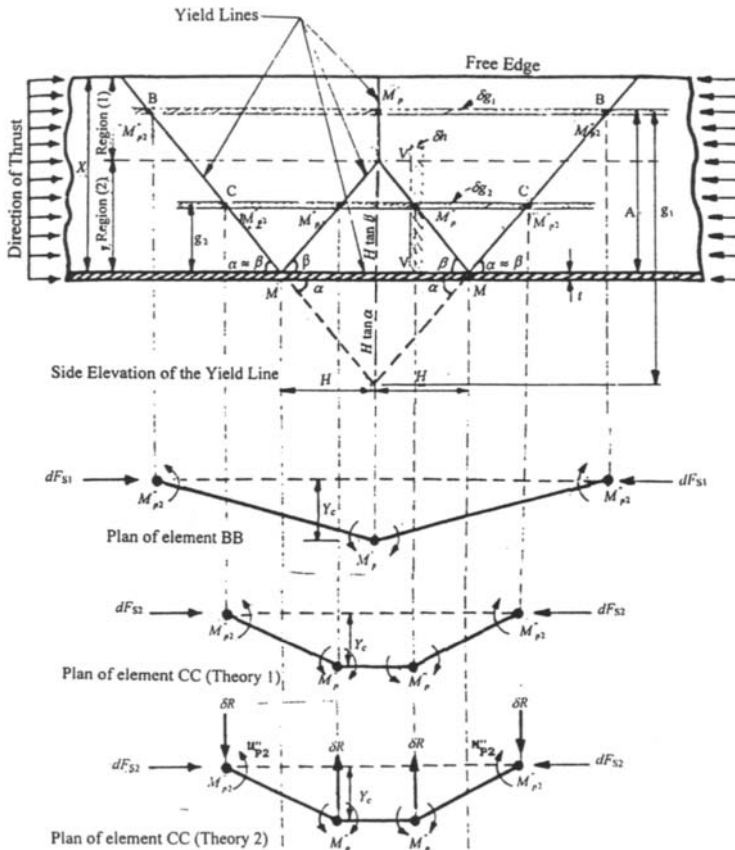


Figure 1: Side elevation of yield line pattern in the region of localised buckling

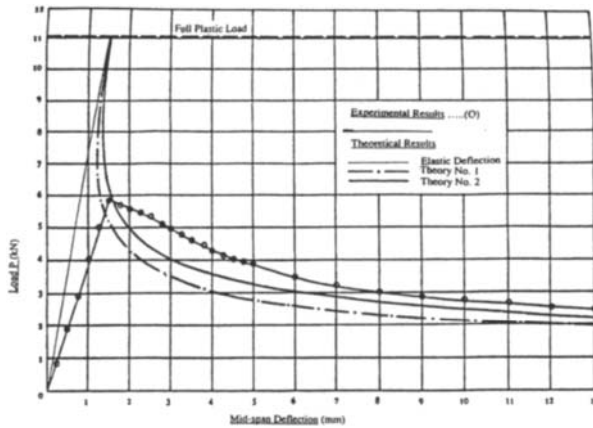


Figure 2: Typical experimental curve for a test with the unstiffened elements in compression

Stiffened elements in compression

Tests were also conducted on 24 beams with webs in compression. The width to thickness ratios of the stiffened webs ranged from 15 to 180. From the results it was found that full plastic theory can be used for sections with a width to thickness ratio less than 60. Some results were affected by a reduction in load carrying capacity due to local crushing and if this is taken into account the sections probably carried a full plastic moment up to width/thickness ratio of 100. The mode of failure was by a series of yield lines forming a hipped-end roof structure as shown in figure 3. A typical test result is given in figure 4. Theoretical results are also superimposed on the load-deflection curves

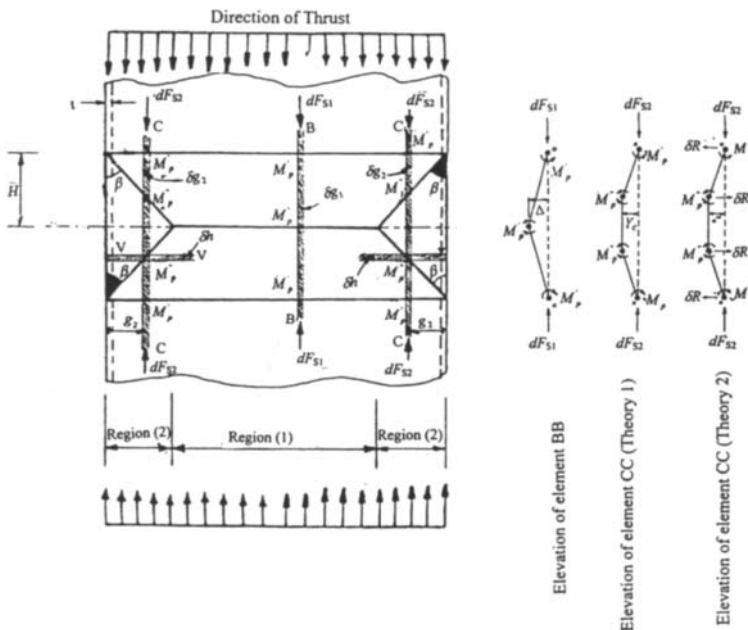


Figure 3: Yield line mechanism for plain channel sections in bending with their stiffened element in compression

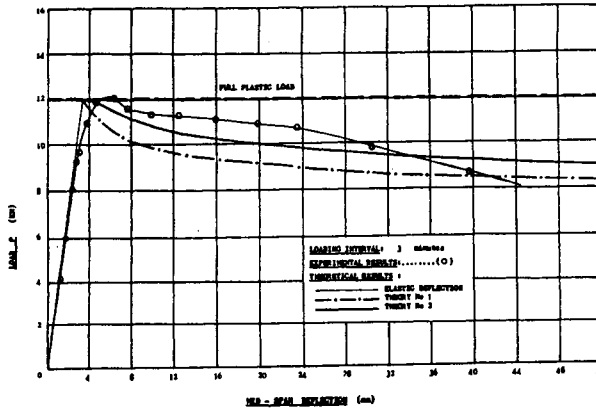


Figure 4: Typical experimental curve for a test with the unstiffened elements in compression

THEORETICAL MODELS

Elastic deformation

The vertical deflection Δ_e due to elastic deformation of the beam at the centre of the beam can be calculated by strain energy to be

$$\Delta_e = \frac{P(L-Q)}{96EI} [3L^2 - (L-Q)^2] \tag{1}$$

where P is the total load on the beam, L , the span of the beam, E , Young’s modulus, I the reduced second moment of area of the beam taking into account local buckling, and Q , the distance between the point loads at the centre of the beam.

Unstiffened elements in compression

Although recent research by Bakker (1990), Zhou and Hancock (1993) has modified the yield line formulation of Murray (1973,1984) his original approach is used in this paper as it enables formulae for inelastic bending of plate elements to be derived. Figure 2 shows the agreement with the theory below and experiment. To determine the inelastic deformation of the beam due to bending the yield line pattern shown in figure 1 was used.

The localised yield pattern is divided into two regions, Region (1) with only three hinges and Region (2) with four hinges. Elemental strips BB and CC in the two regions are considered.

The reduced plastic moment M_p' acting on an element subjected to an axial force dF is given by

$$M_p' = M_p \left(1 - \frac{dF^2}{F_y^2} \right) \tag{2}$$

where M_p is the full plastic moment when no axial force is acting and F_y is the full plastic load when

no moment is acting.

The equilibrium equation of element BB is given by

$$dF_{s1} \cdot Y_c = M_p' + M_{p2}'' \quad (3)$$

where Y_c and dF_{s1} are defined in figure 1.

Murray's formula for the plastic moment, M_{inc} due to an inclined yieldline is

$$M_{inc} = M \sec^2 \gamma \quad (4)$$

where γ is the angle of inclination of the yield line with the perpendicular to the line of action of the force. In the case of Region (1) this implies that

$$M_{p2}'' = M_p' \operatorname{cosec}^2 \alpha \quad (5)$$

where α is the inclination of the yieldline in region (1) to the horizontal.

Substituting
$$dF_{s1} \cdot Y_c = M_p' (1 + \operatorname{cosec}^2 \alpha) \quad (6)$$

Considering the strip CC in Region (2) we can similarly derive

$$dF_{s2} \cdot Y_c = M_p' (\operatorname{cosec}^2 \alpha + \operatorname{cosec}^2 \beta) \quad (7)$$

Experimentally the differences between the inclinations α and β of the two yield lines in figure 1 were less than 5° . For the purposes of the analysis of the section they were therefore taken to be the same and denoted as β .

Substituting for plastic moments ($M_p = f_y \delta g_1 t^2 / 4$) and axial forces ($F_y = f_y t \delta g_1$) in equation 2 where f_y is the yield stress, t the thickness of the plate and δg_1 the elemental strip width we get

$$M_p' = f_y \delta g_1 t^2 / 4 \left(1 - \frac{dF^2}{f_y^2 \delta g_1^2 t^2} \right) \quad (8)$$

Substituting in (6) we get

$$dF_{s1} \cdot Y_c = f_y \delta g_1 t^2 / 4 \left(1 - \frac{dF_{s1}^2}{f_y^2 \delta g_1^2 t^2} \right) (1 + \operatorname{cosec}^2 \beta) \quad (9)$$

Solving

$$dF_{s1} = f_y t \left\{ \sqrt{\frac{4Y_c^2}{J^2 t^2} + 1} - \frac{2Y_c}{Jt} \right\} \delta g_1 \quad (10)$$

where $J = 1 + \operatorname{cosec}^2 \beta$ (11)

Similarly

$$dF_{s2} = f_y t \left\{ \sqrt{\frac{4Y_c^2}{K^2 t^2} + 1} - \frac{2Y_c}{Kt} \right\} \delta g_2 \quad (12)$$

where $K = 2\text{cosec}^2 \beta$ (13)

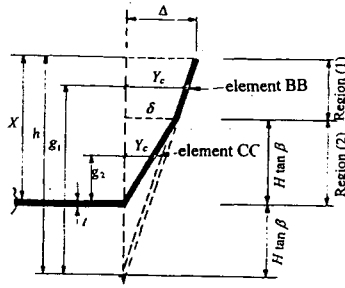


Figure 5: Cross-sectional view, at the centre of the localised buckling, of an unstiffened flange in compression

For Region (1) of the buckled pattern in figure 2, we can write

$$Y_c = \Delta g_1 / h \tag{14}$$

where Δ is the lateral deflection of the top edge of the section as seen in figure 5. The contribution to the moment of resistance of the elements in Region (1) is given by

$$M_{u1} = \int (g_1 - H \tan \beta) dF_{S1} \tag{15}$$

and by substituting for Y_c in equation 10 and replacing dF_{S1} , equation 15 may be integrated with respect to g_1 over the range $g_1 = h-x$ to $g_1 = h$ to obtain an expression for M_{u1} in terms of the lateral displacement Δ .

A similar process has been used in Region (2) of the failure mechanism of figure 1 to obtain an expression M_{u2} for the moment of resistance of the elements in region 2.

The total internal moment in the compression zone of one of the unstiffened webs is given by $M_{u1} + M_{u2}$.

The total moment applied to the section is $2(M_{u1} + M_{u2})$ + moment of the tensile yielded material. The position of the neutral axis was determined from standard beam theory. The standard correction for reduction in plate thickness at the corners given in Eurocode 3 (1996) due to cold forming was included. After buckling the position of the neutral axis changes. However, the inclusion of this change had negligible effects on the resulting moment-curvature curves.

The assumption that the difference in inclinations α and β between the yield lines in regions 1 and 2 is negligible enables us to use Murray's formula (1984) which relates the horizontal displacement of the top of the flange Δ to the inelastic vertical deformation of the beam, Δ_p . It is

$$\Delta_p = \frac{\Delta^2 L}{4b^2 \cot \beta} \tag{16}$$

where b is the flat width of the flange.

Adding the elastic deformation given in equation (1) the total deformation of the beam can be determined.

Typically, as shown in figure 3, curves of moment-central deflection drawn using theory 1 are below the experimental results.

A major assumption employed in theory 1 is that simply-supported conditions exist at the common boundary between the unstiffened webs and flange. The edge strip is not in moment equilibrium along the common intersection axis unless twisting moments exist along the inclined yield lines. The theory ignores the existence of a plastic hinge M_p which rotates about this axis. A second theory including this hinge is now presented.

The effects of the plastic hinge are to cause an additional force δR at each internal hinge in Region (2).

Moment equilibrium gives

$$\delta M = f_y \frac{t^2 \delta h}{4} = \delta R \cdot g_2 \quad (17)$$

But
$$\delta h = \frac{\delta g_2}{\tan \beta} \quad (18)$$

Hence
$$\delta R = f_y \frac{t^2}{4 \tan \beta} \frac{\delta g_2}{g_2} \quad (19)$$

Adding this term in as an additional force in the elemental equation for moment equilibrium in Region (2) and integrating in the same manner as before produces a modified expression for the moment of resistance of the section.

The revised moment-central deflection curves are plotted as theory 2 in figure 3 where it can be clearly seen that the plastic hinge occurring along the web-flange intersection has a major effect.

Stiffened elements in compression

The inelastic analysis of channel sections with the web in compression is analysed using yield lines in a similar manner to the above. The mechanism used is shown in figure 4.

The resulting forces for region (1), F_1 , and region (2), F_2 , are found by integration of elemental strips in the same manner as described above for beams with unstiffened components in compression. Calculations have been made for both theories 1 and 2.

The total force in the web is $F_1 + 2F_2 = F$

The internal moment depends upon the position of the neutral axis and is found by applying plastic theory to the flanges together with the contribution from the total force in the web.

Sample moment-central displacement results for both theories are plotted in figure 5. It can be seen from this sample plot that theory 2 produces a curve which has a smaller reduction in moment capacity

from the full plastic load than that from theory 1. When the formulae were applied to all the sections for which experiments were carried out this result was shown to be always true (see Enjily 1985).

CONCLUSIONS

The paper has presented the results of a theoretical and experimental investigation into the behaviour of thin-walled, cold-formed channel sections under bending. The experimental results show that channels can develop full plastic moment capacity for flange/thickness ratios less than 15 if the unstiffened elements are in compression and for web/thickness ratios less than 60 if the stiffened elements are in compression.

Two theoretical models for the inelastic deformation of channels are developed. These models are in good agreement with experimental results.

REFERENCES

- Bakker M.C. (1990). Yield line analysis of post-collapse behaviour of thin-walled steel members. *Heron*, **35**, 1-50
- Davies, P. Kemp, K.O. & Walker.A.C. (1975). An analysis of the failure mechanism of axially loaded simply-supported steel plates. *Proc. Instn. Civil Engineers*. **59:2**, 645-58.
- Enjily V. (1985). The inelastic post-buckling behaviour of cold-formed sections, *Ph. D. Thesis*, Oxford Brookes University (formerly Oxford Polytechnic).
- Eurocode 3, Part 1.3 (1996): General Rules, Supplementary Rules for Cold Formed Thin Gauge Members and Sheeting, ENV 1993-1-3, European Committee for Standardisation.
- Little G.H. (1982). Complete collapse analysis of steel columns. *Int. J. Mech. Sci.* **24**, 279-98
- Murray N.W. (1973). Buckling of Stiffened Panels Loaded axially and in Bending. *The Structural Engineer* **51:8**, 285-301
- Murray N. W. (1984). Introduction to the theory of thin-walled structures, Clarendon Press, Oxford.
- Rhodes J. and Harvey J. M. (1976). Plain channel section struts in compression and bending beyond the ultimate load. *Int. J Mech Sci.* **18**, 511-519.
- Rhodes J. (1982). The post-buckling behaviour of bending elements. *Proc. Sixth Int. Speciality Conference on Cold-Formed Steel Structures*, St. Louis, 135-155
- Rhodes J. Behaviour of Thin-walled Channel Sections in Bending. *Proc. Dynamics of Structures Congress 87*, Orlando, 336-351
- Stowell E. Z.(1951). Compressive strength of flanges. *NACA Tech Rep. No. 1029*
- Zhao X-L. & Hancock G.J. (1993). Experimental Verification of the Theory of Plastic-Moment Capacity of an Inclined Yield Line under Axial Force, *Thin-Walled Structures*, **15**, 209-33

INELASTIC LATERAL BUCKLING OF COLD-FORMED CHANNEL AND Z-SECTION BEAMS

Yong-Lin Pi, Bogdan M. Put, and Nicholas S. Trahair

Center for Advanced Structural Engineering, Department of Civil Engineering,
University of Sydney, NSW 2006, Australia

ABSTRACT

The monosymmetry of CFC sections and the point symmetry of CFZ sections introduce some characteristics to CFC and CFZ beams that are not encountered in doubly symmetric I-beams. Firstly, after yielding, the effective centroid and the effective shear centre of a CFC beam move toward the web and the effective section of a CFZ beam rotates, so that a CFC or a CFZ beam under in-plane bending in the elastic stage is subjected to bending and torsion (for the CFC beam) or biaxial bending (for the CFZ beam) in the plastic stage. Secondly, the minor axis bending and warping strain distributions of CFC and CFZ beams and therefore their inelastic lateral buckling behaviours are related to the twist rotation and minor axis displacement directions. The stress-strain curves, residual stresses, initial crookednesses and twists, and lipped flanges of CFC and CFZ beams are all different to those of hot-rolled I-beams. This paper uses a nonlinear inelastic finite element model, which accounts for web distortion, the asymmetrical nature of a yielded CFC section, and the effective section rotation of a yielded CFZ section, to investigate the effects of the monosymmetry of CFC beams and point symmetry of CFZ beams on their inelastic bending and lateral buckling behaviours.

KEYWORDS

Beam, Buckling, Channel section, Cold-formed, Distorsional, Inelastic, Lateral, Monosymmetry, Point symmetry, Z-section.

INTRODUCTION

When a CFC beam bends in its stiffer plane $o_s y_s z_s$, or a CFZ beam bends in its stiffer geometrical principal plane $o y z$, it is under in-plane bending, and may buckle laterally out of the plane of bending (Fig. 1). The web may also distort, so that the flanges have different lateral displacements u_t and u_b and twist rotations ϕ_t and ϕ_b . Web distortion may reduce the lateral buckling resistances of CFC and CFZ beams. The monosymmetry of a channel section and the point symmetry of a Z-section introduce some characteristics that are not encountered in doubly symmetric I-beams. Firstly, after yielding, the effective centroid and the effective shear centre of a CFC beam move

toward the web and the effective section of a CFZ beam rotates, so that a CFC or a CFZ beam under in-plane bending in the elastic stage is subjected to bending and torsion (for the CFC beam) or biaxial bending (for the CFZ beam) in the plastic stage. Secondly, the distributions of the bending strains about the minor principal axis and the warping strains are related to the twist rotation and minor axis displacement directions, so that the inelastic lateral buckling behaviour of CFC and CFZ beams is affected not only by the magnitudes of the initial crookedness and twist but also by their directions.

The cold-formed nature of CFC and CFZ beams also introduces some considerations that are not encountered in hot-rolled I-section beams, as the stress-strain curves, residual stresses, initial imperfections and lipped flanges of CFC and CFZ beams are all different from hot-rolled I-beams.

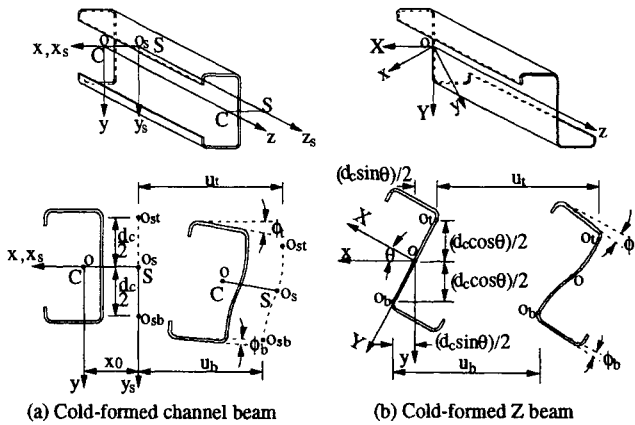


Fig. 1 Axis system and buckling deformations

Most studies of the lateral buckling of CFC and CFZ beams have been concentrated on modifications of formulations for hot-rolled I-beams to allow for elastic local and distortional buckling (Trahair 1994, Hancock 1997, and Rogers and Schuster 1997). The effects of the monosymmetry of CFC sections and point symmetry of CFZ sections on their inelastic lateral buckling have not been studied adequately. This paper uses a nonlinear inelastic finite element model, which accounts for web distortion, the asymmetrical nature of a yielded CFC section, and the effective section rotation of a yielded CFZ section, to investigate the effects of the monosymmetry of CFC beams and point symmetry of CFZ beams on their inelastic bending and lateral buckling behaviours.

NONLINEAR FINITE ELEMENT MODEL

The nonlinear inelastic finite element model used in this paper has been developed on the basis of the following assumptions and considerations (Pi et al 1997a,b): (1) the strains are small. (2) the geometric nonlinearities include the effects of large displacements and twist rotations and load height. (3) The cross-section of each flange maintains its shape during deformation, but the web distorts into a cubic curve (Bradford 1992). (4) Vlasov's theory of torsion (Vlasov 1961) and the Euler-Bernoulli theory of bending are used for the flanges, and the Kirchhoff theory of plate bending is used for the web. (5) The initial crookedness, twist, and distortion vary sinusoidally along the beam. (6) Longitudinal normal residual stresses are induced by the manufacturing process (Fig. 2, Weng and Pekoz 1988). (7) Elastic-plastic-strain hardening and Ramberg-Osgood stress-strain relationships are used for the flats and corners (Fig. 3, Key and Hancock 1988),

respectively. (8) The elastic-plastic incremental stress-strain relationship is derived from the von Mises yield criterion, a strain flow rule, and an isotropic hardening rule.

The nonlinear incremental-iterative equilibrium equations can be obtained using the principle of virtual work (Pi et al. 1997a,b). Full details of the method of solution of the equations are given by Pi and Trahair (1994).

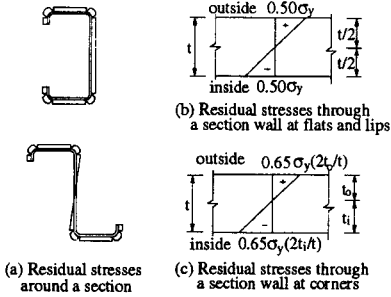


Fig. 2 Residual stresses

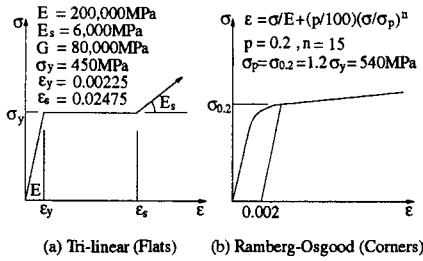


Fig. 3 Stress-strain curves

The finite element model has been used to calculate the ultimate loads of CFC beams with the section of Fig. 4(a) tested by Put et al (1998). The beams were subjected to a central concentrated load at 0.04m below the shear centre in the plane $o_s y_s z_s$. The comparison of finite element results Q_t with the test results Q_e is shown in Table 1. The agreements between them are good.

Table 1 Comparison of Finite Element and Test Results

Beam	L(m)	y_Q (m)	α_w (kNm ³ /rad)	Q_e (kN)	Q_t (kN)	Q_t/Q_e
19L17e0	1.7	0.04	0.00937	13.24	13.08	0.99
19L19e0	1.9	0.04	0.00937	12.11	10.88	0.90
19L21e0	2.1	0.04	0.00937	10.98	10.89	0.99
19L23e0	2.3	0.04	0.00937	9.54	9.30	0.97
19L25e0	2.5	0.04	0.00937	7.79	8.00	1.03

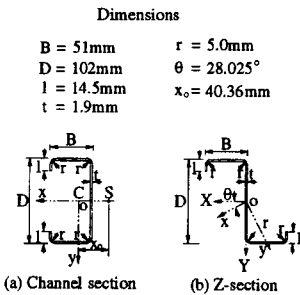


Fig. 4 Cross-sections

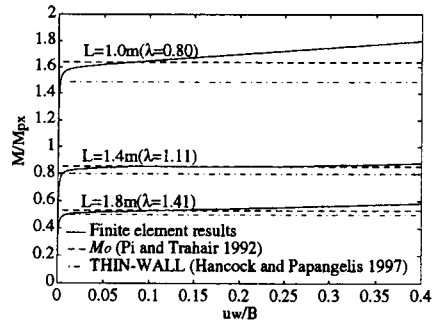


Fig. 5 Elastic lateral-distortional buckling

The finite element model has also been used to investigate the elastic lateral-distortional buckling of CFC and CFZ beams with the sections shown in Fig. 4. These beams are subjected to equal and opposite end moments. The typical results for CFZ beams are compared with those of the computer program THIN-WALL (Hancock and Papangelis 1997) and the flexural-torsional

buckling moments M_o including the effects of the prebuckling deflection effects (Pi and Trahair 1992) in Fig. 5. The lateral-distortional buckling moments are close to those of THIN-WALL and lower than M_o due the effects of web distortion. CFC beams have similar results (Pi et al 1997a).

INELASTIC BENDING

To simplify the illustration of the effects of monosymmetry of CFC beams and the point symmetry of CFZ beams on their in-plane bending, the cross-sections are assumed to be rigid. For in-plane deformations ($u = \phi = 0$), the stress distributions are shown in Fig. 6. In the elastic range, the longitudinal normal stress varies linearly from compression in the upper extreme fibres to tension in the lower extreme fibres until first yield at $\pm\sigma_y$. The stress resultants $M_y = \int_A E^{ep}\epsilon x dA$ and $B = \int_A E^{ep}\epsilon \omega dA$ are zero because $E^{ep} = E$ is a constant, and $\int_A x dA = \int_A xy dA = \int_A \omega dA = \int_A \omega y dA = \int_A \omega(x + x_o) = 0$.

After yielding, the effective centroid and the effective shear centre of a CFC beam move toward the web and the loading becomes eccentric, so that a CFC beam under in-plane bending in the elastic range is subjected to bending and torsion in the plastic range, while the effective principal axes of a CFZ beam rotate clockwise, so that a CFZ beam under in-plane bending in the elastic range is subjected biaxial bending in the plastic range. In addition, the elastic-plastic secant modulus E^{ep} varies around the section so that the stress resultants M_y and B are no longer zero, which causes laterally unbraced CFC and CFZ beams to displace in the negative direction of ox axis and twist in the negative direction of the axis $o_s z_s$ (for CFC beams) or oz (for CFZ beams). Thus, laterally unbraced CFC and CFZ beams under in-plane bending in elastic range fail by biaxial bending and torsion in the plastic range before the full plastic section moment M_{px} is reached.

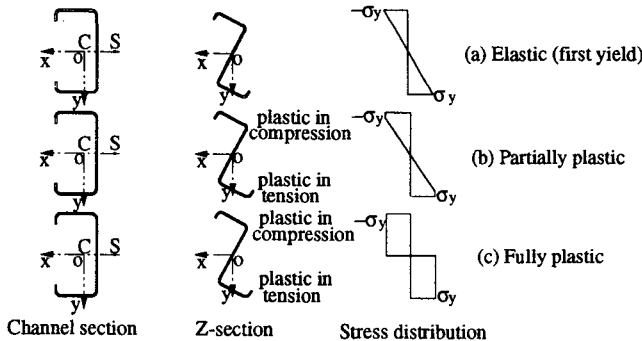


Fig. 6 In-plane bending

In order to understand this better, inelastic thin-walled cross-section analyses have been made for the simple unlippped Z-section shown in Fig. 7(a) which has an elastic-plastic stress-strain relationship. The neutral axis nn is inclined at an angle β to the rectangular axis oX , and at an angle $(\beta - \theta)$ to the geometrical principal axis ox ($\theta = 22.5^\circ$). The longitudinal normal strain and stress distributions are defined by the distance y_n from the neutral axis nn to the point in the Z-section where the longitudinal normal stress σ is equal to the yield stress σ_y . The variations of the dimensionless moments M_X/M_{pX} and M_Y/M_{pY} for different angles β and different distances y_n are shown in Fig. 7(b) where M_X and M_Y are the moments about the rectangular axes oX and oY and M_{pX} and M_{pY} are the plastic moments of the cross-section about the rectangular axes oX and oY . In the calculation of M_X , M_Y , M_{pX} , and M_{pY} , the wall of the cross-section is assumed to be so thin that the neutral axis nn intersects the web only at the centroid and the effects of the second order terms of the wall thickness on these moments can be ignored.

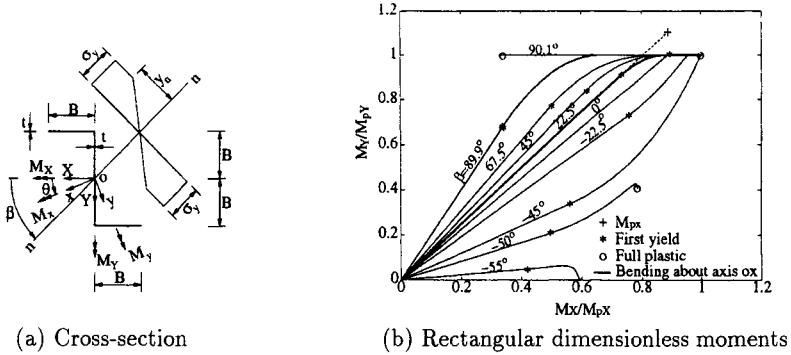
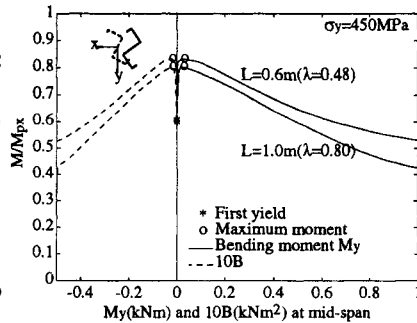
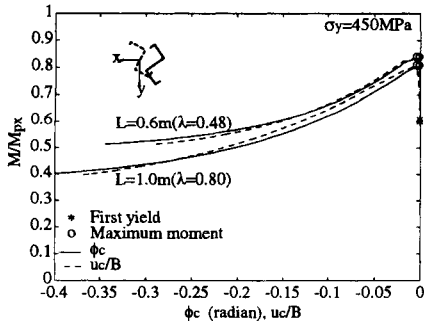


Fig. 7 In-plane bending of a CFZ beam

When the beam is prevented from twisting and deflecting laterally out of a plane of deflection, then that plane defines a fixed value of β at right angles to the plane. For the case where $\beta = \theta$, deflections are confined to the principal yz plane. It can be seen that while the beam remains elastic, the value of M_Y/M_X remains constant and $M_y = 0$. However, when yielding starts, the value of M_Y/M_X decreases towards M_{pY}/M_{pX} , and M_y is no longer zero. The non-zero value of M_y corresponds to the moment exerted by the restraints which prevent lateral deflections u . It can also be seen that M_{pX} and M_{pY} remain constant for $-45^\circ < \beta < 90^\circ$.

When the beam is loaded so that M_y is equal to 0 and M_Y/M_X remains constant, then β is equal to θ while the beam remains elastic. However, when yielding starts, then β starts to increase so as to maintain $M_y = 0$. As M_x increases further, β increases more rapidly, and the limit of $\beta = 90^\circ$ is reached before the full plastic moment M_{px} can be reached.



The finite element model is used to investigate the inelastic behaviour of laterally unbraced perfect beams subjected to in-plane equal and opposite end moments M in the plane $y_s z_s$ for CFC beams or in the plane yz for CFZ beams. The variations of the central twist rotation ϕ_c and dimensionless central lateral displacement u_c/B with the dimensionless end moment M/M_{px} for CFZ beams with $L = 0.6\text{m}$, 1.0m are shown in Fig. 8, and the variations of the minor axis moments M_y and bimoment B at the mid-span with the dimensionless end moment M/M_{px} are shown in Fig. 9. There are no twist rotations and lateral displacements before yielding because $M_y = B = 0$. After yielding, small minor axis moments M_y and bimoments B arise, and each beam displaces laterally in the negative direction of the axis ox and twists about the negative direction of the oz direction

(clockwise). As the dimensionless moment M/M_{px} increases, so do the values of M_y and B . A maximum value of M is reached (which is lower than the plastic moment M_{px} of the cross section about the major geometrical axis), after which the minor axis moment M_y and bimoment B and therefore the twist rotations and lateral displacements increase rapidly, while the capacity of each beam to resist in-plane bending decreases. CFC beams have similar results (Pi et al 1997a).

INELASTIC LATERAL BUCKLING AND POSTBUCKLING

When a CFC or a CFZ beam subjected to equal and opposite end moments M displaces laterally $u = u_c \sin \pi z/L$ and twists $\phi = \phi_c \sin \pi z/L$, the beam is then under bending actions $M_x = M \cos \phi$ about the major axis ox , bending actions $M_y = -M \sin \phi$ about the minor axis oy , and torsion actions $T = -Mu'$ about the longitudinal axis $o_s z_s$ (for CFC beams) or oz (for CFZ beams).

The strain distributions caused by the actions M_x, M_y , and T are shown in Fig. 10 for CFC beams, where the warping strains, Wagner strains, and uniform torsion shear strains correspond to the torsion actions. Strain distributions of CFZ beams under these actions are similar to those of CFC beams (Pi et al 1997b). When twist rotations are about the negative direction of the $o_s z_s$ axis (clockwise) and the lateral displacements are in the negative direction of the ox axis (from left to right), the strains in the top flange lip due to the moments M_x and M_y and the warping bimoment B are all compressive, so that first yield occurs at this top flange lip. This yielding is asymmetrical, and further changes the effective cross section, which rotates in the same sense as the twist rotation ϕ . These changes are in addition to those caused by the yielding due to bending M_x alone, which also causes the effective cross section to rotate clockwise, as discussed above. The combination of these two effects cause the beam to buckle laterally at a lower moment M .

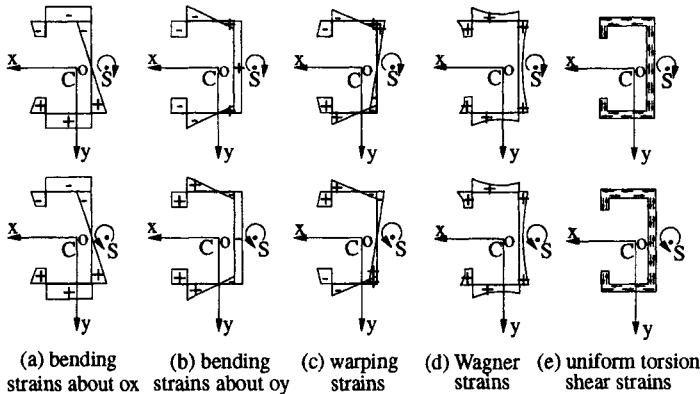


Fig. 10 Strain variations around CFC section

However, when the twist rotations are about the positive direction of the $o_s z_s$ axis (anticlockwise) and the lateral displacements are in the positive direction of the ox axis (from right to left), the strains at the corner between the top flange and web due to the moments M_x and M_y and the warping bimoment B are all compressive, and it is possible that first yield may occur at this corner. The effective cross section then rotates in the same direction as ϕ . This effect opposes that due to yielding caused by M_x alone, and so the beam buckles laterally at a higher moment M . Thus, the inelastic strengths of CFC beams with positive (anticlockwise) twist rotations are higher than those of the beams with negative (clockwise) twist rotations. The direction of the

twist rotations is influenced by both the yielding and the directions of the initial crookedness and twist.

The finite element model is used to investigate the effects of the direction of the lateral displacements and twist rotations on the inelastic lateral buckling and postbuckling behaviour of CFC and CFZ beams subjected to equal and opposite end moments M . The variations of the dimensionless central lateral displacement u_c/B with the dimensionless end moment M/M_{px} are shown in Fig. 11. The beams with negative initial crookedness and twist (clockwise) displace laterally in the negative direction of the axis ox and twist about the negative direction of the axis $o_s z_s$ (for CFC beams) or oz (for CFZ beams) (clockwise), because both the initial crookedness and twist and the yielding cause the negative lateral displacements and twist rotations.

However, positive initial crookedness and twist cause a beam to displace laterally in the positive direction of the ox axis and twist about the positive direction of the axis $o_s z_s$ (for CFC beams) or oz (for CFZ beams) (anticlockwise), while yielding causes the beam to displace laterally in the negative direction of the ox axis and twist about the negative direction of the axis $o_s z_s$ or oz (clockwise). For CFC beams ($L = 0.8m$ and $L = 1.8m$) and the slender CFZ beam ($L = 1.6m$) with positive initial crookedness and twist (anticlockwise), the effects of yielding are less important than those of the initial crookedness and twist, and the beams displace laterally in the positive direction of the axis ox and twists about the positive direction of the axis $o_s z_s$ or oz (anticlockwise). On the other hand, the short CFZ beam ($L = 0.8m$) with positive initial crookedness and twist (anticlockwise) initially displaces laterally in the positive direction of the axis ox and twists about the positive direction of the axis oz (anticlockwise), but then displaces laterally in the negative direction of the axis ox and twists about the negative direction of the axis oz (clockwise) because the effects of yielding, which causes the beam to twist clockwise, are more important. It can also be seen in Fig. 11 that the inelastic lateral buckling moments of the beams with positive initial crookedness and twist are higher than those of the beams with negative initial crookedness and twist.

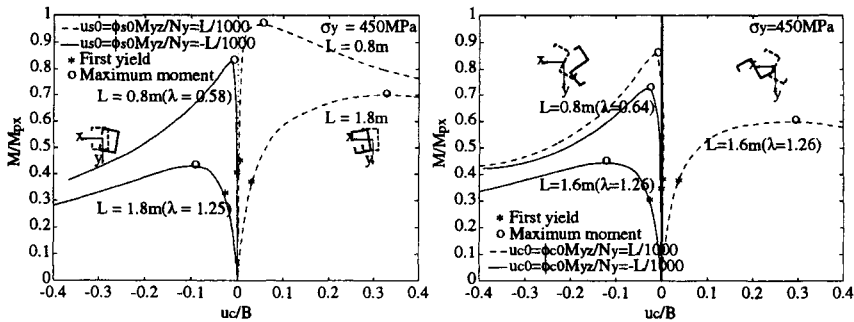


Fig. 11 Effects of lateral displacement and twist rotation directions

CONCLUSIONS

This paper has used a nonlinear inelastic finite element model to investigate the lateral-distortional buckling behaviour of CFC and CFZ beams which consist of two lipped flanges connected by a flexible web plate. The model includes the effects of web distortion, the asymmetrical nature of yielded CFC sections and the rotation nature of the yielded CFZ sections, the prebuckling in-plane deflections, the initial crookedness and twist, the residual stresses, material inelasticity, and the lipped flanges.

It is found that when a perfect CFC or CFZ beam subjected to in-plane bending is unrestrained laterally between the supports, it is liable to displace laterally and to twist after yielding, and the full plastic moment of cross section cannot be reached unless the beam is restrained laterally at frequent intervals.

The directions of the initial crookedness and twist affect the inelastic lateral buckling strengths and postbuckling behaviour of unbraced CFC and CFZ beams. The beams with positive initial crookedness and twist have higher inelastic lateral buckling moments and postbuckling stiffnesses than those with negative initial crookedness and twist.

REFERENCES

- Bradford, M.A. (1992). Lateral-distortional buckling of steel I-section members. *Journal of Constructional Steel Research*, **23:1-3**, 97-116.
- Hancock, G.J. (1997). Design for distortional buckling of flexural members. *Thin-Walled Structures*, **27:1**, 3-12.
- Hancock, G.J. and Papangelis, J.P. (1997). *THIN-WALL User's Manual*. Centre for Advanced Structural Engineering, University of Sydney, Sydney, Australia.
- Key, P.W. and Hancock, G.J. (1993). A theoretical investigation of the column behaviour of cold-formed square hollow sections. *Thin-Walled Structures*, **16:1**, 31-64.
- Pi, Y.-L., Put, B.M., and Trahair, N.S. (1997a). Lateral buckling strengths of cold-formed channel section beams. *Research Report*, No. R748, Department of Civil Engineering, University of Sydney, Sydney, Australia.
- Pi, Y.-L., Put, M.B., and Trahair, N.S. (1997b). Lateral buckling strengths of cold-formed Z-section beams. *Research Report*, No. R752, Centre for Advanced Structural Engineering, Department of Civil Engineering, University of Sydney, Sydney, Australia.
- Pi, Y.-L. and Trahair, N.S. (1992). Prebuckling deflections and lateral buckling - Applications. *Journal of Structural Engineering*, ASCE, **118:11**, 2967-2985.
- Pi, Y.-L. and Trahair, N.S. (1994). Nonlinear inelastic analysis of steel beam-columns. I: Theory. *Journal of Structural Engineering*, ASCE, **120:7**, 2041-2061.
- Put, B.M, Pi, Y.-L., and Trahair, N.S. (1998). Lateral buckling tests on cold-formed channel beams. *Research Report*, No. R767, Centre for Advanced Structural Engineering, Department of Civil Engineering, University of Sydney, Australia.
- Rogers, C.A. and Schuster, R.M. (1997). Flange/web distortional buckling of cold-formed sections in bending. *Thin-Walled Structures*, **27:1**, 13-29.
- Weng, C.C., and Pekoz, T. (1988). Residual stresses in cold-formed steel members. *Journal of Structural Engineering*, ASCE, **116:6**, 1611-1625.
- Vlasov, V.Z., (1961). *Thin-walled elastic beams*. 2nd edn., Israel Program for Scientific Translation, Jerusalem, Israel.
- Trahair, N.S. (1994). Lateral buckling strengths of unsheeted cold-formed beams. *Engineering Structures*, **16:5**, 324-331.

LOADING CAPACITY OF COLD-FORMED RHS MEMBERS USED IN MULTI-STORY BUILDINGS *

Z. Y. Shen¹, Y. Y. Chen¹, S. J. Pan¹, G. Y. Wang², Y. Tang²

¹ Tongji University, Shanghai 200092, China

² Shanghai Institute of Mechanical & Electrical Engineering, Shanghai 200040, China

ABSTRACT

Cold-formed steel rectangular hollow section (RHS) members have good properties in high efficiency to resist loads. This kind of members is being considered to be used in multi-story or middle rise building structures recently in the area where earthquake response is not a predominant factor. However the behaviors of RHS members should be thoroughly studied. A series of loading tests on cold-formed RHS compressive specimens are recently performed. The research parameters are types of steel, including low carbon steel and weatherproof steel, cold-formed hardening effect, eccentricities of compressive loads, slenderness, width-to-thickness ratio of plates as well as the types of ribs.

KEYWORDS

cold-formed members, rectangular hollow section, loading test, ultimate load, deformability, local buckling

INTRODUCTION

There has been a long history for the use of thin-walled cold-formed steel members in the roof systems, the wall systems and the floor systems of industrial and dwelling building structures. Nowadays, however, due to the progress of industrial technology, it has been possible to use thicker plates to form efficient components of relatively heavy loaded building frames by cold-press or cold-formed procedure.

Since the utilization of cold-formed steel members in heavy loaded structures often makes the section of columns having large size and its plate elements having large width-to-thickness ratio, the decreasing of ductility due to elastic local buckling is brought into consideration, which is very important to the steel structures, either in the area where the earthquake action is not a predominant actor, or in the severe zones.

* Project Supported by Shanghai Municipal Construction Commission

Research work carried out in this paper is focused on the thinner but larger section size cold-formed members. The purpose is to study the possibility of using this kind of members into middle-high rise buildings as main bearing components.

TEST OUTLINE

Two types of materials, low carbon steel and weatherproof steel, are adopted for test specimens. Table 1 lists main mechanical properties by tension coupon. Q235 is popular material while 10PCu-Re is newly used for building structures for its good corrosion protective natures and relatively higher strength.

TABLE 1
MATERIAL PROPERTIES

Steel Type	Nominal Thickness (mm)	Yield Stress (MPa)	Strength (MPa)	Prolongation (%)
Q235	3	297	420	40
	5	225	375	43
	7	215	392	41
10PCu-Re	3	362	477	39
	5	330	477	38
	7	277	445	30

Two cold-formed channels with lips are welded together as shown in Figure 1, forming a rectangular section, with the outer size 300x380 mm for all specimens. The curved corner radii of outer surfaces are 5.83, 3.5 or 2.5 times of the plate thicknesses of 3 mm, 5 mm, 7 mm, respectively. In the middle of the two wider edges, vertical ribs of 3 mm thick were welded inside. Besides these ribs, a pair of 3 mm plates were welded as horizontal stiffeners at the mid-height of long column specimens. Table 2 shows specimen codes and their main features.

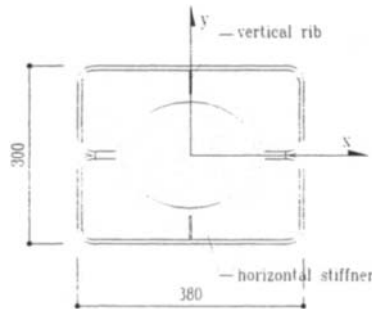


Figure 1: Section of specimens

For the specimen code, the first letter S refers to stub column, L to long column, respectively. The second letter C or E means the centrally or eccentrically compressive load. The third one, Q or R, identifies the steel material Q235 or 10PCu-Re. The thickness in above table is nominal one, while the area and length between end plates are measured results. Width-to-thickness ratios are calculated supposing that the vertical ribs are effective and the corner curves are reduced from the width.

TABLE 2
LIST OF SPECIMEN

Specimen Code	Thickness (mm)	Area (mm ²)	Length (mm)	Width-to-thickness Ratio	Specimen Code	Thickness (mm)	Area (mm ²)	Length (mm)	Width-to-thickness Ratio
SCQ3-1	3	4390	1060	57.5	SCR3-1	3	4239	1052	57.5
SCQ3-2	3	4382	1056	57.5	SCR3-2	3	4231	1052	57.5
SCQ5-1	5	7098	1054	34.5	SCR5-1	5	6831	1053	34.5
SCQ5-2	5	7269	1058	34.5	SCR5-2	5	6849	1052	34.5
SCQ7-1	7	9286	1055	24.6	SCR7-1	7	9575	1052	24.6
SCQ7-2	7	9333	1044	24.6	SCR7-2	7	9544	1052	24.6
LCQ3-1	3	4149	2750	57.5	LCR3-1	3	4561	2748	57.5
LCQ3-2	3	4140	2750	57.5	LCR3-2	3	4392	2750	57.5
LCQ5-1	5	7081	2748	34.5	LCR5-1	5	6815	2750	34.5
LCQ5-2	5	7149	2750	34.5	LCR5-2	5	6713	2752	34.5
LCQ7-1	7	9200	2750	24.6	LCR7-1	7	9628	2750	24.6
LCQ7-2	7	9428	2750	24.6	LCR7-2	7	9595	2749	24.6
LEQ3-1	3	4359	2750	57.5	LER3-1	3	4385	2750	57.5
LEQ3-2	3	4207	2750	57.5	LER5-1	5	6941	2744	57.5
LEQ5-1	5	7016	2749	34.5	LER5-2	5	6672	2748	34.5
LEQ5-2	5	7009	2748	34.5	LER7-1	7	9848	2748	34.5
LEQ7-1	7	9462	2748	24.6	LER7-2	7	9632	2748	24.6
LEQ7-2	7	9400	2750	24.6					

For stub columns, loading and boundary conditions followed CRC stub-column test procedure, Johnston (1976). Strain gages on four sides were used to adjust the loading center until the deviation did not exceed 5 percent of the average value.

In the case of long column specimen, two universal ball bearings were set up on both ends. For axial loading tests, geometrical loading center was carefully fixed. In the eccentric loading tests, the eccentricity was 100 mm from the strong axes. Static compression was applied to each specimen.

STUB COLUMN TESTS

Loading Versus Vertical Deformation Curves

Axial loading versus compressive deformation curves are shown in Figure 2 and Figure 3. Solid lines indicate the loading-deformation curves for ideal elasto-plastic models. Figure 2 and Figure 3 show that the fork points which indicate the loading-deformation curves of stub column specimens deviating from the ideal curves are about the half levels of the yield loads determined by gross section area and average yield stress, which reflects the mingled effects of residual stress and local buckling. Of course, the hardening effect strengthened the specimen capacities somewhat in these cases. These are the reasons why the actual loading capacities can exceed ideal yield forces in some cases.

It can be also observed from Figure 2 and Figure 3 that the curves declined slowly after ultimate loads. Using the points where the resistances decrease to the ninety-five percentages of the maximum loads to investigate the deformability, it can be found that the deformations at these points are two to four times

of the values at the ideal yield points. This fact is very important that thinner walled members possess plastic deformability to some extents.

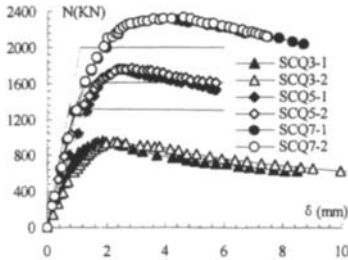


Figure 2: Loading-deformation curves of Q235 steel stub columns

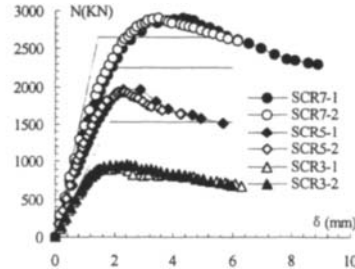


Figure 3: Loading-deformation curves of 10Pcu-Re steel stub columns

Influence of Local Buckling

As examples, the strains measured from the outside and inside gages at the same point of the stub column section are shown in Figure 4 for SCQ3-1 and Figure 5 for SCQ5-1. In 3 mm specimen, the strains coincided each other very well under lower loading level. After the bifurcation, however, strains developed in different way. It reveals that the thin wall flexured badly due to local buckling. In 5 mm specimen, however, though at the beginning, the inside and outside strain data were not equal due to initial imperfection, the two-side strains increased compressively all the way and the ultimate load was not affected distinctly by local buckling.

To 10PCu-Re specimens, the critical width-to-thickness ratio corresponding to local buckling is less. The vertical ribs being 3 mm thick seemed not stiff enough as an intermediate stiffener for the 5 mm plates. Thus the maximum loads were lower than yield loading capacities. This is different from the situation of Q235 members.

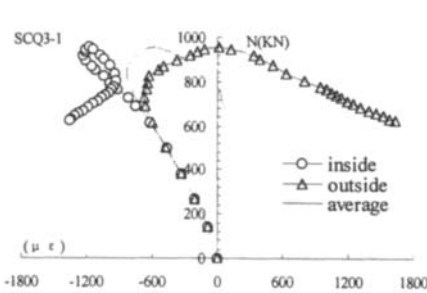


Figure 4: Strain versus loading curve (SCQ3-1)

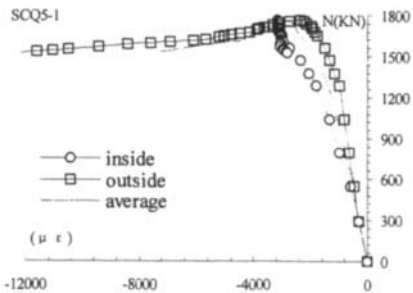


Figure 5: Strain versus loading curve (SCQ5-1)

AXIALLY COMPRESSIVE COLUMN TESTS

Initial Imperfection and Failure Modes

Specimen section has strong and weak axis, and the initial crookedness existed around both axes, with the largest lateral deformation about 0.2 percent of whole length. Initial twist and unflatness of plates

were observed too. Because of these imperfections and the unavoidable eccentricity, loading versus deformation curves behave complexly. When specimens reached their ultimate capacities, some of them changed the direction of lateral displacements.

In the stage near to the ultimate loading, local buckling happened in all of these specimens. The local deformation appeared obviously close to the midheight or one fourth of the height of the columns. In some cases, there were three or four places having concave and convex deformation. Since the slenderness ratios of specimens ranged from 21 to 24 around weak axes, which is considered relatively small to flexural buckling, and the rectangular section is also hardly to torsional buckling, the failure type was mainly local buckling, but the global flexural buckling also decreased the maximum loads to certain extend.

Loading Versus Deformation Curves

Figure 6 shows three typical curves of axially compressive columns, where the horizontal coordinate refers the lateral displacement at the midheight of tested specimens. From the figure it can be seen that the thicker specimen LCQ-7 deteriorates moderately compared with the thinner specimen LCQ-3, which manifests that the former has better plastic deformability.

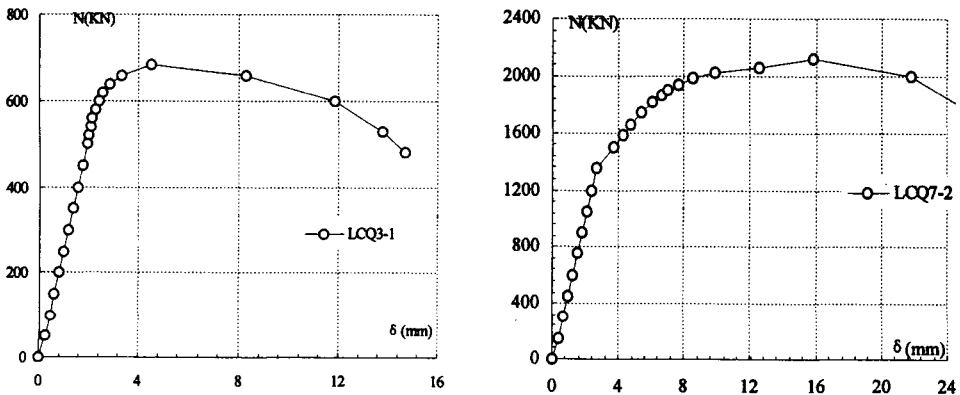


Figure 6: Loading versus lateral displacement curves of axial loaded specimens

Strain Analysis

Nominal strains, which are the quotients of axial loads divided by nominal gross section, versus average measured strains are shown in Figure 7. The fork point of two lines indicates that local buckling makes part of section softening and after then the average measured strain becomes greater than nominal one obviously.

ECCENTRICALLY COMPRESSIVE COLUMN TESTS

Though there existed crookedness around two axes for each specimen, the nominal eccentricities, e_0A/W , however, ranging from 0.6 to 0.8, are quite large, and make the bending deformation around strong axes become predominant. As happened in the axial loading cases, the local buckling is

concomitant.

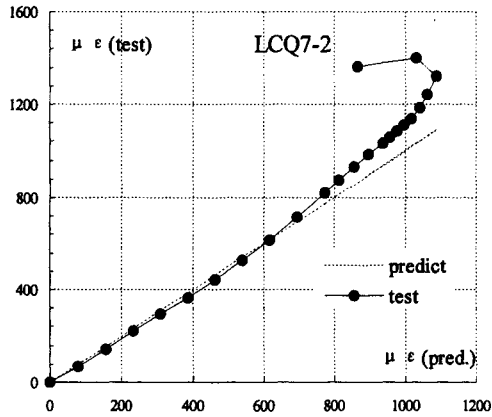


Figure 7: Nominal strain and measured strain

The deviations of ultimate loads in each set of two specimens are small except one of 3 mm thick specimen. At the limit points, the axial force ratios are 0.43, 0.57-0.67, 0.71-0.77 to 3 mm, 5 mm and 7 mm thick specimens respectively. For building structural members, the ratio can be considered great enough.

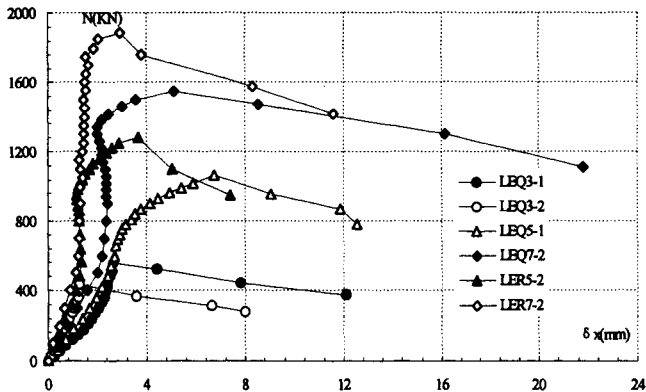


Figure 8: Loading versus lateral displacement curves of eccentrically loaded specimens

Figure 8 shows that before the ultimate point, the plastic deformations are evident except the single case of 3 mm specimen. After that point, deterioration is not severe, that is to say, the loading versus displacement curves do not decline sharply.

In these curves, the original data are used to plot. The sensors, which are connected to the specimen wall surface directly, record lateral displacements at the midheight of specimens as well as the local deformation of the touched points. It generates the inflection of loading-displacement curves even in the stage of 'elastical deformation'.

Define post-ultimate deformability (PUD) as equation 1.

$$PUD = Du/Dy \quad (1)$$

where, Du is the displacement corresponding to the resistance decreasing to ninety-five percent of maximum load, while Dy is the yield displacement described as equation 2.

$$Dy = Myc L^2 / (8EI) \quad (2)$$

Substituting Myc with $My(1-N/Ny)$, and considering $My = (2I/h) fy$, we can get equation 3.

$$Dy = 0.25 fy L^2 (1-N/Ny) / (E h) \quad (3)$$

Where, Ny is the yield axial force, N the maximum load, fy the yield stress, L the length between support points and h the depth of section. Thus we can get PUD from loading-displacement curves. For example, 5 mm and 7 mm thick Q235 specimens have PUD 3.4 and 5.6 respectively, while the 3 mm thick specimen is not satisfied. Considering that the axial force ratio is one of the main factors influencing deformability, it can be deduced that for 3 mm thick specimen, the design load should be controlled in a relatively low level for maintain necessary plastic deformability.

PREDICTION OF LOADING CAPACITIES

Table 3, 4, and 5 list the ultimate loads in tests and the expected values. Nm in all tables represents the maximum load in tests. Ny is the yield force using average yield stress multiplying gross section area. Ncr is the result that Ny times the stability factor of axial compressive members according to Chinese Steel Structural Design Code. Np is the expected maximum load which can be sustained by the eccentrically loaded specimen. When Np being computed, Perry formula is utilized, but the elastic moment is replaced with plastic limit moment, Mp . In this prediction of Ny , Ncr and Np , no local buckling effect is considered. The Chinese design code formulae are employed to compute Nsc , Ncc and Nec , corresponding to stub columns, axially compressive columns and eccentrically compressive columns respectively. Here local buckling is considered by the idea of effective area, Yu (1991). By the following tables, we can see that, for Q235 members with 5 mm and 7 mm plates and 10PCu-Re members with 7 mm plate, where elastic local buckling does not control the failure mode, the simple formulae are enough to predict the loading capacities in good agreement with the test results somewhat. However, for 3 mm plate specimens, local buckling becomes primary factor, more accurate formula is desired. The computation results seem to be errors here mainly due to the relatively larger imperfection existed exceeding to the tolerance of the design code.

TABLE 3
LOADING CAPACITY OF STUB COLUMNS

Specimen Code	Nm (kN)	Nm/Ny	Nm/Nsc	Specimen Code	Nm (kN)	Nm/Ny	Nm/Nsc	Specimen Code	Nm (kN)	Nm/Ny	Nm/Nsc
SCQ3-1	956	0.73	1.01	SCQ5-1	1764	1.09	1.37	SCQ7-1	2323	1.16	1.22
SCQ3-2	951	0.73	1.00	SCQ5-2	1767	1.09	1.37	SCQ7-2	2328	1.16	1.22
SCR3-1	923	0.60	0.81	SCR5-1	1970	0.87	1.19	SCR7-1	2910	1.10	1.21
SCR3-2	951	0.62	0.83	SCR5-2	1932	0.86	1.16	SCR7-2	2896	1.09	1.21

TABLE 4
LOADING CAPACITY OF AXIALLY LOADED COLUMNS

Specimen Code	Nm (kN)	Nm/Ncr	Nm/Ncc	Specimen Code	Nm (kN)	Nm/Ncr	Nm/Ncc	Specimen Code	Nm (kN)	Nm/Ncr	Nm/Ncc
LCQ3-1	686	0.54	0.75	LCQ5-1	1510	0.97	1.24	LCQ7-1	1980	1.03	1.10
LCQ3-2	629	0.50	0.68	LCQ5-2	1550	1.00	1.27	LCQ7-2	2115	1.10	1.17
LCR3-1	942	0.65	0.88	LCR5-1	1835	0.86	1.18	LCR7-1	2645	1.06	1.19
LCR3-2	900	0.62	0.84	LCR5-2	1815	0.85	1.17	LCR7-2	2550	1.03	1.14

TABLE 5
LOADING CAPACITIES OF ECCENTRICALLY LOADED COLUMNS

Specimen Code	Nm (kN)	Nm/Np	Nm/Nec	Specimen Code	Nm (kN)	Nm/Np	Nm/Nec	Specimen Code	Nm (kN)	Nm/Np	Nm/Nec
LEQ3-1	556	0.68	0.84	LEQ5-1	1065	1.10	1.33	LEQ7-1	1500	1.32	1.35
LEQ3-2	432	0.53	0.62	LEQ5-2	1085	1.12	1.36	LEQ7-2	1543	1.36	1.39
LER3-1	659	0.69	0.82	LER5-1	1300	0.97	1.19	LER7-1	1970	1.32	1.41
				LER5-2	1280	0.95	1.17	LER7-2	1887	1.26	1.35

CONCLUSION

Thirty-five pieces of cold-formed welded specimens were tested under static loading conditions in this research work. Test data show that the thin-walled cold-formed rectangular section members have high bearing capacity and deformability. Thus we can consider to use the members in heavy loaded multi-story building systems as main structural members. The study also shows that simple formulae can be used with satisfied accuracy in some extents to predict loading capacities. However, in the case that the width-to-thickness ratio is great, initial imperfection should be control strictly.

References

- Johnston B.G. (1976). Guide to Stability Design Criteria for Metal Structures, John Wiley & Sons, Inc. New York, USA
 Yu W.W. (1991). Cold-formed Steel Design, John Wiley & Sons. Inc. New York, USA

LOCAL FAILURES IN TRAPEZOIDAL STEEL CLADDINGS

M. Mahendran and R.B. Tang

School of Civil Engineering, Queensland University of Technology, Brisbane, Qld. 4000, Australia

ABSTRACT: When crest-fixed thin steel roof claddings are subjected to wind uplift, local pull-through/dimpling failures occur prematurely at their screwed connections because of the large stress concentrations in sheeting under the screw heads combined with lack of steel ductility. During high wind events such as storms and cyclones, these localized failures then lead to severe damage to the buildings and their contents. At present the design of profiled steel claddings is based on testing of two-span cladding systems to eliminate such failures. However, this is a time consuming and expensive exercise. Therefore an investigation was conducted to develop simple tests and design formulae for crest-fixed steel claddings based on detailed experimental and finite element analyses of steel claddings. This paper presents the details of this investigation. It includes a description of the types of local failures and appropriate design formulae.

KEYWORDS: Profiled steel roof claddings, crest-fixed, pull-through/dimpling failures, wind uplift, steel ductility, finite element analysis, design formulae, two-span cladding tests, small scale cladding tests.

1. INTRODUCTION

The profiled steel roof and wall cladding systems in Australia (Fig. 1a, b) are commonly made of very thin high tensile steels, and are crest-fixed with screw fasteners (Fig. 1c) whilst in the USA and Europe the claddings are made of thicker lower strength steels and are valley-fixed. The thin high tensile steels (0.42 mm base metal thickness) have a very high yield stress (G550 – minimum yield strength of 550 MPa) at the expense of reduced ductility (strain at failure < 2 %). During high wind events, these claddings have suffered severely because of local failures of their screwed connections under wind uplift/suction loading. The two common local failures, pull-out and pull-through failures, are shown in Fig. 2. The pull-out failure occurs when the screw fastener pulls out of the batten or purlin whereas the pull-through failure occurs when the screw head pulls through by splitting the steel sheeting due to the presence of large stress concentrations around the fastener holes under wind uplift loading (Mahendran, 1994). In some cases, a localised dimpling failure occurs instead of splitting. The pull-out failure has been investigated in detail and appropriate formulae developed (Mahendran and Tang, 1996). Although the pull-through (splitting and dimpling) failures have been investigated previously (Mahendran, 1990,1994, 1995; Xu, 1994), further research data is needed in order to develop reliable design formulae that can be used in design practice without the need for further testing. Thus an investigation was carried out to study the pull-through failures in profiled steel claddings using both large scale tests of two-span claddings and small scale tests under static wind uplift/suction load conditions. A series of profiled steel claddings, which are commonly used in Australia (Fig. 1), was investigated for a range of screw fasteners and washers. Experimental studies were followed by finite element analyses of the same claddings. The applicability of the USA/Europe design formula for pull-through strength of crest-fixed roof and wall cladding systems was investigated first. Improved formulae were then developed in terms of the thickness and ultimate tensile strength of steel, diameter of screw fasteners, and washers. This paper presents the details of this investigation and its results.

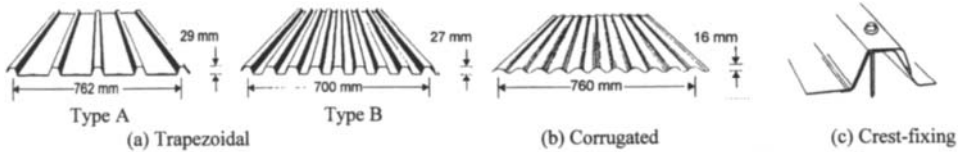


Figure 1. Standard Profiled Steel Cladding Systems Commonly Used in Australia

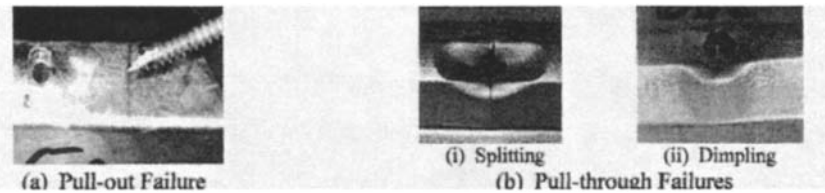


Figure 2. Typical Local Failures

2. CURRENT DESIGN AND TEST METHODS

Currently the American (AISI, 1989) and European (Eurocode, 1992) design provisions recommend detailed design formulae for a range of mechanically fastened connections such as bolts and screws in tension in cold-formed thin-walled steel sheeting and members. The pull-through strength is calculated as follows:

$$\text{AISI (1989)} \quad F_{ov} = 1.5 t d f_u \quad (1a)$$

$$\text{Eurocode 3 (1992)} \quad F_{ov} = 1.1 t d_w f_y \quad (1b)$$

where d = larger value of the screw head or the washer diameter, but limited to 12.7 mm
 t = thickness of the cladding material d_w = the washer diameter
 f_u = ultimate tensile strength of steel f_y = yield stress of steel

In contrast, previous Australian design codes do not recommend any design formula, and the design for the local failures of screwed connections in tension has been entirely based on laboratory experiments. However, Equation 1a has now been included in the new cold-formed steel structures code AS4600 (SA, 1996). This design formula was developed for conventional fasteners and thicker mild steel and therefore there is a need to verify the applicability of this formula for Australian steel cladding systems.

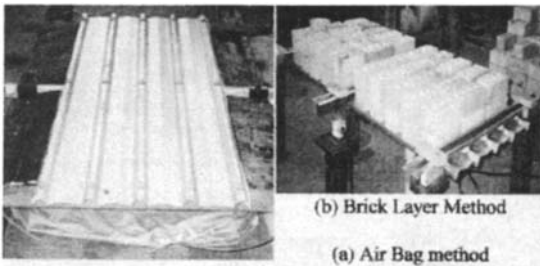


Figure 3. Two-span Test Methods

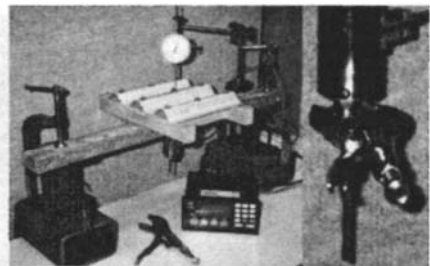


Figure 4. Small Scale Test Method

As an alternative to the design method, the American and European specifications (AISI, 1992, Eurocode, 1992) and the new code AS4600 (SA, 1996) recommend standard test methods using small scale models. They were mainly developed for valley-fixed claddings and cold-formed connections in general. Hence these test methods are not able to predict the pull-through strength of crest-fixed steel cladding systems (Mahendran, 1995). In the absence of suitable simple design and test methods, Australian manufacturers and designers have been using a two-span steel cladding assembly with simply supported ends (Mahendran, 1990). The steel claddings of either one or two sheet width were crest-fastened to battens. They were about 800 mm in width and included five screw fasteners on each batten. The uniform wind uplift pressure was simulated by either using air bags or layers of bricks. The steel sheeting pulled-through the screw heads (or

dimpled) at the central support that had the largest reaction. The central support reaction was used to determine the average failure load per fastener at the critical central support.

Although the two-span cladding test methods using air bags or bricks (Fig.3) were the preferred methods, Mahendran (1994) developed a small scale test method to simulate the pull-through failures in crest-fixed claddings (see Fig. 4) as these failures are highly localized around the screw holes (Fig. 2b). He recommended a small scale cladding specimen of approximately 240 mm × 240 mm bolted to a small wooden frame. The width of the specimen between the bolts in transverse direction was the pitch of the cladding profile including the rib. A long screw fastener with a load cell attached to it is located at the center of the specimen. The specimen is then loaded with a tension force by using a simple hand-tightening procedure. This method models both the longitudinal and transverse membrane and bending deformations around the fastener hole and the tension force in the screw fastener. The tension force in the screw fastener at dimpling/pull-through will be the required failure load. This method is very simple to use and enables a large number of tests to be completed with limited resources in a short period of time. However, the accuracy of results from this method is not known for claddings other than those currently used (Fig.1).

3. EXPERIMENTAL INVESTIGATION

In this investigation the small scale test method was used for trapezoidal steel claddings and screw fasteners, which are commonly used in the Australian building industry. The G550 grade steel trapezoidal claddings with different thicknesses from 0.42 mm to 0.48 mm BMT were tested. The screw fasteners included screw sizes of No. 12 and 14 (both nominal screw head diameters of 12.7 mm). The screw head d_h or washer diameter d_w was varied from 12.7 to 22.0 mm. A larger hole diameter d_o of 9.0 mm was also used in order to simulate a larger screw shaft size. Thus the effects of different screw shaft sizes (d_o from 5.2 mm to 9.0 mm) were also studied in this manner. Tests were conducted for a combination of each type of screw fastener and cladding resulting in a total of 154 tests. Table 1 presents some of the experimental pull-through and dimpling failure loads for trapezoidal (type A) claddings.

Table 1. Experimental Results for Crest-fixed Trapezoidal (Type A) Claddings

G550 Steel, f_y / f_u (MPa)			Screw Diameter		Failure Load (N/f)	Comment
t (mm)	Measured	Specified	d (mm)	d_o (mm)		
0.42	717 / 721	550 / 550	14.5	5.2	1323	Dimpling & Fracture
				9.0	1389	
			20.0	1548	No Fracture	
0.48	717 / 721	550 / 550	14.5	5.2	1798	& Fracture
			20.0		2073	No Fracture

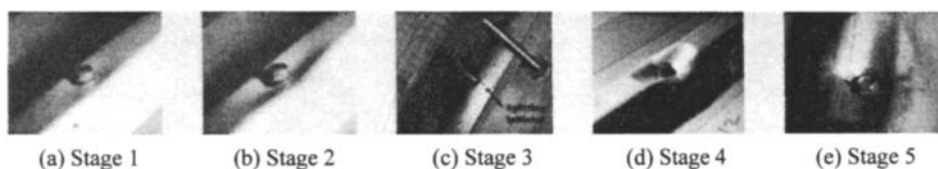


Figure 5. Localized Deformations and Splitting Failures around the Fastener Hole

In this investigation, some two-span cladding tests were also conducted using the air bag method for the sake of completeness. It was observed that the uplift loading caused severe cross-sectional distortions of this profile since the screwed ribs are separated by wide pans. This distortion led to a premature localized failure of the crests. Combined membrane and bending actions in both longitudinal and transverse directions were observed in the region around the fastener holes on two-span and small scale cladding specimens. The membrane stresses appeared to be much more dominant than the bending stresses in the longitudinal direction. At first, the crests slightly dimpled (Fig. 5a), but as the loading was increased, the membrane action developed in the region of the crests, and the small region around fastener hole was yielding at this stage (Fig. 5b). With further loading, tests clearly indicated the presence of high membrane tensile actions in the longitudinal direction for the sheeting around the fastener hole (Fig. 5c). Since the high tensile steel used in the claddings has very limited ductility (about 2% strain at failure), it led to the transverse splitting

(Fig. 5d). The splitting then grew rapidly and led the fasteners to pull-through the sheeting (Fig. 5e). The local pull-through failure at the crests determined the strength of trapezoidal-type A claddings. A local dimpling failure (without any splitting) occurred for corrugated claddings and some trapezoidal claddings (Fig. 2b(ii)). This is because the bending stresses within the sheet were dominant than the longitudinal membrane tensile stresses in this case. Although there was some reserve strength beyond this dimpling failure in the two-span cladding tests, it cannot be included for design purposes. The localized deformations and the splitting failure occurred in most of the tests with different screw head/washer and hole sizes. Experimental results obtained in this investigation were grouped on the basis of cladding profile, thickness, and diameter of the screw head or washer and analysed to develop appropriate design formulae (Section 5.1). However, they are only applicable to claddings made of high tensile steels such as G550.

4. FINITE ELEMENT ANALYSIS

A finite element analysis (FEA) was conducted using ABAQUS on a mini-supercomputer SIRIUS. A range of finite element models of trapezoidal claddings (Fig.6a) were analysed to study the behavior of crest-fixed steel claddings under a uniform wind uplift pressure. The intermittently crest-fixed, thin steel sheeting undergoes very large deformations followed by localised yielding around the fastener holes when subjected to wind uplift/suction loading. Therefore a non-linear static analysis including both geometry and material non-linearities was used in this investigation. Measured material properties were used in the analyses. The higher grade steel used in the experiments (0.42 mm G550) had a high yield stress of 721 MPa, but had only a 2% strain at failure and no strain hardening.

Following the verification of deformation shapes (Fig.6b), the load-deflection curves and pull-through failure loads were compared with corresponding experimental results. Load-deflection curves from FEA agreed well with those from two-span experiments of 0.42 mm BMT trapezoidal-type A cladding (Fig. 7). However, there was concern about the pull-through failure load predicted by the FEA. The FEA predicted a failure load of 1405 Newtons per fastener (N/f) which is in fact the maximum load the cladding could carry provided there was no splitting prior to this. The corresponding pressure was 6.86 kPa. It is possible the true pull-through load caused by splitting is lower than this value as the FEA is not capable of detecting splitting that was observed in the experiments. However, the FEA results (1405 N/f) from the commonly used trapezoidal-type A cladding reasonably agreed with those from two-span and small scale cladding tests (1450 and 1470 N/f). However, this agreement cannot be expected for other trapezoidal profiles.

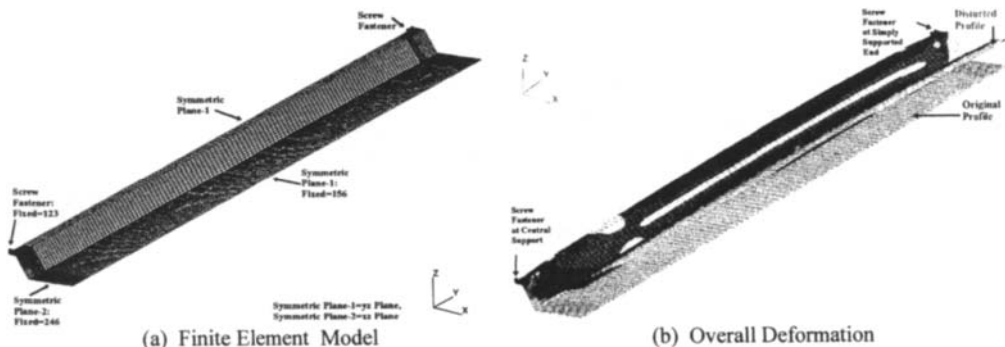


Figure 6. Finite Element Model of Trapezoidal Type A Cladding

For the FEA to predict the splitting around the fastener holes, it is necessary to introduce a failure criterion for splitting. Attempts to model the splitting around the fastener hole by using the measured stress-strain curve with a steep unloading curve to lower stress values were not successful. Therefore a reliable strain criteria is needed. Since the tensile coupons of 0.42 mm G550 steel split at 2% strain level, it was considered that transverse splitting around the fastener hole occurred when the longitudinal membrane tensile strain at the edge of the fastener hole reached 0.02. The FEA clearly showed the presence of large membrane tensile strains in the longitudinal direction at the fastener hole (points 1 and 2 in Fig. 8). This might have initiated the transverse splitting at the hole. Results from a number of FEA were investigated to determine whether

the failure load predicted by FEA coincided with the load at 2% membrane tensile strain. It was found that there was little correlation between these two results. This meant that the longitudinal membrane tensile strains at the edge of fastener holes varied depending on other parameters such as screw head diameter, steel thickness and yield stress, and geometry of profile. This can be explained by the fact that the region around the fastener hole has complicated stress patterns that could vary depending on the parameters mentioned above. Although longitudinal membrane tensile strains dominate and cause the splitting, the strain level at which this splitting will occur is not known under the combined membrane and bending strains in the region. Therefore, the results from the FEA are not applicable to claddings made of high tensile steels such as G550 unless an accurate failure criterion for splitting is developed for these steels under combined membrane tension and bending actions. The use of 2% strain at failure obtained from simple tension tests may not be applicable here. A detailed experimental program using two-span claddings is required to determine a failure strain criterion for splitting. It was therefore decided to use the finite element analyses for steels with greater ductility (strain at failure > 10%). The G250 steel used in Australia readily satisfies this criterion. The pull-through failure caused by splitting will not occur in the claddings made of these steels. Instead the localized dimpling (Fig. 2b (ii)) will occur and the FEA can adequately model this phenomenon. Therefore the FEA results obtained in this investigation were analysed and appropriate design formulae were developed for trapezoidal claddings made of steels of greater ductility (Section 5.2).

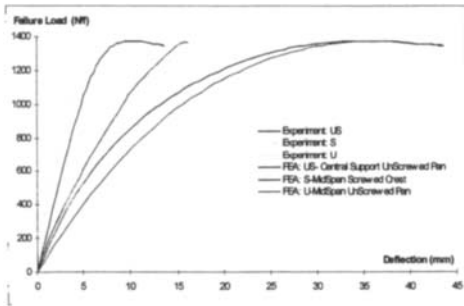


Figure 7. Load-deflection Curves

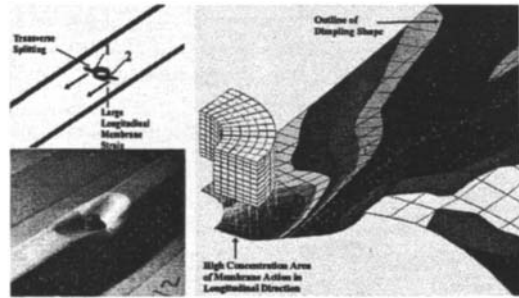


Figure 8. Longitudinal Membrane Tensile Strains

5. RESULTS AND DISCUSSION

5.1 Trapezoidal claddings made of high tensile steel

Experimental results obtained for steel claddings made of 0.42 mm G550 steel are considered in this section. As seen in Table 1, the pull-through strength was very much dependent on the base metal thickness (BMT) t of the steel claddings. When the shaft/hole diameter d_s of screw fasteners was changed (ie. 5.2, 9.0 mm), the strength changed only marginally for all three profiles. However, when the diameter of screw head or washer d was changed from 14.5 to 17.5, 20.0 and 22.0 mm, there was significant increase in the pull-through strength of screwed connections for trapezoidal-type A cladding, and some increase for trapezoidal-type B cladding. Experimental pull-through failure loads were compared with the predictions from the American design formula given by Equation 1a using both the measured and specified (nominal) values for the properties of the steel and screw fasteners (Table 2). In Table 2, 75% of the specified minimum strength of G550 steel (412 MPa) was used for G550 steels of thickness less than 0.9 mm based on AISI (1989) and AS4600 (SA, 1996). Although Equation 1a requires the use of a maximum value of 12.7 mm for d , experimental results did not agree with this. Therefore, actual diameter d was also used in Equation 1a to calculate the loads for comparison with experimental results in Table 2.

As seen in Table 2 results, the mean Test to Predicted value is extremely low (<0.25) for crest-fixed claddings. It reveals the inadequacy of the American design formula in predicting the pull-through failure loads in crest-fixed cladding systems. The use of an upper limit of 12.7 mm for diameter d in Equation 1a does not appear to be correct as test failure loads increased with increasing d beyond 12.7 mm. However, further experimental evidence is needed to confirm this beyond any doubt. The use of specified properties reveal that the mean values have increased but still less than 1.0 for all cases. Therefore the use of 75% of

specified tensile strength for G550 steel less than 0.9 mm in the current design formula is preferred, but is still inadequate for the pull-through strengths of crest-fixed claddings.

Table 2. Test to Predicted Values Based on Current Design Formula

Material Properties	Screw d (mm)	Trapezoidal Type A		Trapezoidal Type B	
		Mean	COV	Mean	COV
Measured	Actual	0.20	0.11	0.17	0.15
	12.7	0.25	0.11	0.23	0.07
Specified	Actual	0.35	0.11	0.31	0.14
	12.7	0.45	0.10	0.40	0.07

Table 3. Test to Predicted Values Based on Mahendran's Design Formula (1994)

Material Property	Trapezoidal Type A		Trapezoidal Type B	
	Mean	COV	Mean	COV
Measured	1.18	0.09	1.19	0.06
Specified	1.34	0.08	1.36	0.06

Note: 1. COV. = Coefficient of Variation
 2. d = larger value of screw head or washer diameter

Mahendran (1994) developed a formula (Eqn. 2) for pull-through strength F_{ov} of crest-fixed steel cladding systems based on limited results from FEA. By using the term $f_u^{1/3}$, this equation eliminates the need for the use of 75% of the specified minimum strength for G550 steels with a thickness less than 0.9 mm.

$$F_{ov} = c t^2 f_u^{1/3} \tag{2}$$

where $c = 0.74$ for Trapezoidal-type A Claddings and 0.66 for Trapezoidal-type B claddings

The experimental pull-through failure load results were compared with the predicted values using Equation 2 (Table 3). The mean Test to Predicted values are greater than 1.0 for all cases of crest-fixed claddings with all groups of screw fasteners. This reveals that Mahendran's design formula may imply high level of conservativeness for profiled steel claddings. However it does not include the effects of screw fastener or washer diameter in predicting the pull-through failure loads. Hence it must be considered inadequate. Therefore a new formula is proposed as follows by including the screw head/washer diameter d.

$$F_{ov} = c d^\alpha t^2 f_u^{1/3} \tag{3a}$$

$$\text{or } F_{ov} = c d^\alpha t^\beta f_u^\chi \tag{3b}$$

where $c, \alpha, \beta, \chi = \text{constants}$ $d = \text{larger value of the screw head or washer diameter}$

Equation 3a was first considered as a simple extension of Mahendran's design formula by including d, but keeping the same t^2 and $f_u^{1/3}$ terms. Subsequently, Equation 3b was developed as a general equation with different power coefficients for t and f_u . Unlike Mahendran's (1994) method, the constants of c, α , β , and χ were determined by considering all the parameters simultaneously. The "Solver" in Microsoft Excel, which is based on the method of least squares, was used to obtain the best equation that fits the test data with minimum errors. These constants are given in Table 4. It is considered unnecessary to impose an upper limit for d as in the current design formula. Hence, only the actual values of diameter d were used in Table 4.

Table 4. Test to Predicted Values Based on Improved Formulae for Crest-fixed claddings

Cladding Profile	Eqn. 3a						Eqn. 3b					
	c	α	β	χ	Mean	COV	c	α	β	χ	Mean	COV
Trapezoidal Type A	0.25	0.45	2.00	1/3	0.99	0.05	0.27	0.15	2.25	0.48	1.00	0.07
Trapezoidal Type B	0.45	0.20	2.00	1/3	1.00	0.05	0.28	0.20	2.00	0.40	1.03	0.05

The local dimpling or pull-through failure loads were predicted well by both Equations 3a and 3b using the measured properties of the steel and screw fasteners (Tab. 4). For both Equations 3a and 3b, the mean test to predicted values are about 1.0 and tend to be more uniform across all the cases of crest-fixed claddings while the coefficients of variation are less than 0.07. However, Equation 3b with constants as shown in Table 4 is recommended because it was obtained by allowing for interaction between all three parameters. Since the pull-through strength depends on the geometry of the cladding profile, this design equation must be further improved to include relevant geometrical parameters if its applicability is to be extended to other profiles.

5.2 Trapezoidal claddings made of ductile steel

The finite element model discussed Section 4 was used to determine the local dimpling load of a range of trapezoidal-type A steel claddings made of steels with greater ductility (strain at failure >10%). The following parameters were varied in this study: BMT of steel t of 0.30, 0.40, 0.42, 0.48, 0.50 and 0.60 mm; steel yield stress f_y of 300, 400, 500, 600 and 690 MPa; diameter of screw head or washer d of 6.5, 8.0, 10.4,

14.5, 17.5, 20.0 and 22.0 mm; and diameter of screw shaft (hole size) d_o of 5.2 and 9.0 mm. Selected results agreed well with previous results obtained by Mahendran (1994) and hence confirm the accuracy of the FEA model used in this study. This section presents and discusses the FEA results. It was found that the screw shaft/hole size d_o did not affect the local dimpling or pull-through strength of crest-fixed steel cladding systems. In the analysis of results, failure loads corresponding to a d_o of 5.2 mm were used.

The following formulae similar to Equations 3a and 3b were proposed to model the local dimpling strength of the profiled steel cladding systems more accurately and appropriate constants were determined using the same procedure used with Equations 3a and 3b.

$$F_{ov} = c d^\alpha t^\beta f_y^{1/3} \tag{4a}$$

$$F_{ov} = c d^\alpha t^\beta f_y^\chi \tag{4b}$$

where c, α, β, χ = coefficients
 and d = larger value of the screw head or washer diameter in mm.
 f_y = yield strength of steel in MPa

In this case, the yield strength of steel f_y is used instead of the ultimate tensile strength f_u as this study deals with claddings made of ductile steels. Table 5 results show that local dimpling failure loads were predicted well by both Equations 4a and 4b using the properties of the steel and screw fasteners used in the FEA. The improved Equation 4b appears to provide more uniform and less conservative mean (ranged from 1.00 to 1.10) and coefficient of variation values (mostly less than 0.10) in all groups than Equation 4a, and is therefore recommended. However, in order to reduce the improved design formulae to a single equation for all groups, the parameters α, β and χ were then forced to be 0.25, 2.30 and 0.65, respectively. These changes were still able to provide uniform mean values (1.03 to 1.05) and COV values (less than 0.10). Therefore Equation 4b is recommended with the following parameters: $c = 0.08, \alpha = 0.25, \beta = 2.30,$ and $\chi = 0.65$. It must be noted that in the above equation, t and d are in mm and f_y in MPa.

Table 5. FEA to Predicted Values Based on Improved Formulae for Trapezoidal-type A Claddings

Steel		Screw	Equation 4a				Equation 4b				Recommended Equation							
f_y (MPa)	t (mm)	d (mm)	c	α	Mean	COV	c	α	β	χ	Mean	COV	c	α	β	χ	Mean	COV
All	All	All	0.40	0.30	1.00	0.13	0.08	0.25	2.30	0.65	1.00	0.07	0.08	0.25	2.30	0.65	1.04	0.07
		≤ 12.7	0.08	1.00	1.09	0.15	0.85	0.45	2.70	0.25	1.05	0.19	0.08	0.25	2.30	0.65	1.05	0.10
		> 12.7	0.25	0.45	1.03	0.13	0.08	0.35	2.35	0.60	1.10	0.04	0.08	0.25	2.30	0.65	1.03	0.05
	≤ 0.45	All	0.55	0.15	1.02	0.09	0.30	0.15	2.40	0.50	1.01	0.04	0.08	0.25	2.30	0.65	1.04	0.07
	> 0.45		0.48	0.45	1.01	0.13	0.05	0.35	2.05	0.65	1.08	0.08	0.08	0.25	2.30	0.65	1.03	0.07

Although Equation 4b provides accurate local dimpling strength values, it does not include the geometrical parameters of the cladding profile. This implies that it is only applicable to profiles that are identical or similar to the commonly used cladding profiles (Fig. 1). As the local dimpling strength of steel cladding systems greatly depends on the geometry of the profile, this investigation considered the effects of five geometrical parameters, the crest width b , crest height H , pitch P , trough width B , and pan height h . The preliminary FEA confirmed that within the small range of pan height values used in practice (4 to 8 mm), the cladding strength changed only marginally. Therefore, it was decided not to include h in further analyses. The remaining four geometrical parameters were varied in this investigation and the results (273 of them) were used to develop a suitable formula in the form of Equation 5 for trapezoidal-type A cladding.

$$F_{ov} = c d^\alpha t^\beta f_y^\chi b^k H^l P^m B^n \tag{5}$$

where $c, \alpha, \beta, \chi, k, l, m,$ and n are constants $d, t,$ and f_y as defined in Equations 4a and 4b

The constants in Equation 5 were determined using the same procedure described earlier for Equation 4b as $\alpha = 0.25, \beta = 2.30, \chi = 0.65,$ and $c = 0.30, k = 0.15, l = 0.55, m = -0.85,$ and $n = 0.20$.

The recommended Equations 3b, 4b and 5 are based on average local dimpling and pull-through strengths from limited number of test data and analyses. The actual pull-through strength of a real connection can be considerably less than the value predicted by these equations because of the expected variations in material, fabrication and loading effects. Therefore a capacity reduction factor commonly used in design codes should be recommended for the pull-through strength predicted by these equations. Tang (1998) has determined these factors using a statistical model recommended by AISI (1989). Based on these calculations, capacity reduction factor of 0.55, 0.60 and 0.60 is recommended for use with Equations 3b, 4b and 5, respectively.

Although steel claddings and screw fasteners used in this investigation were obtained from particular manufacturers, results should be equally applicable to other claddings and screw fasteners provided they comply with the respective specifications for the grades of steels and fasteners used in this investigation.

6. CONCLUSIONS

An investigation into the local failures of screwed connections in crest-fixed trapezoidal steel claddings has been described. It included large number laboratory experiments and finite element analyses. Both types of local pull-through failures (splitting and dimpling) were investigated in detail and reasons for their occurrence given. It was found that the current design formula and the test method are incapable of predicting the strengths of the crest-fixed steel cladding systems. Experimental results from small scale sheeting models were used to develop an accurate design formula for the pull-through strength of crest-fixed steel cladding systems made of high tensile steels such as G550. The improved design formula (Eqn. 3b) appears to provide a greater accuracy in predicting the local dimpling and/or pull-through strength of profiled steel cladding systems. However, the improved design formulae are applicable to only the commonly used profiled steel claddings shown in Figure 1, and are only based on small scale test models.

Finite element analyses were unable to model the splitting type pull-through failures observed in high tensile steel claddings. Therefore until a suitable failure criterion is determined, they cannot be used to improve the accuracy of equations obtained from testing. However, they were used to model the local dimpling failure that occurred for trapezoidal claddings made of ductile steels. A design formula including not only the thickness and yield strength of steel and the diameter of screw fasteners or washers used, but also the geometrical parameters of the profiled cladding has been developed for one of the trapezoidal claddings.

7. REFERENCES

- American Iron and Steel Institute (AISI) (1989), Specification for the Design of Cold-formed Steel Structural Members, 1986 Edition with 1989 Addendum, AISI, Washington, DC.
- American Iron and Steel Institute (AISI) (1992), Test methods for Mechanically Fastened Cold-formed Steel Connections, Report CF92-1, AISI, Washington, DC.
- Eurocode 3 (1992), Design of Steel Structures, Part 1.3 - Cold-formed Thin-gauge Members and Sheeting, Draft document CEN/TC250/SC3 - PT1A, Commission of the European Communities.
- Macindoe, L. and Hanks, P. (1994), Standard Tests for Cold-formed Steel Single Fastener Connections, Proc. of Australasian Structural Engineering Conference, Sydney, pp.253-257
- Mahendran, M. (1990), Static Behaviour of Corrugated Roofing under Simulated Wind Loading, Civil Eng. Trans., I.E.Aust., Vol.32, No.4, pp.211-218
- Mahendran, M. (1994), Behaviour and Design of Crest-fixed Profiled Steel Roof Claddings under High Wind Forces, Engng. Struct., Vol.16, No.5.
- Mahendran, M. (1995), Test Methods for Determination of Pull-through Strength of Screwed Connections in Profiled Steel Claddings, Civil Eng Trans., IEAust., Vol.CE37, No.3, pp.219-227.
- Standards Australia (SAA) (1996), AS4600 Steel Structures Code.
- Mahendran, M. and Tang, R.B. (1996), Pull-out Strength of Steel Roof and Wall Cladding Systems, Research Report No. 96-38 Physical Infrastructure Centre, QUT, Brisbane
- Tang, R.B. (1997), Local Failures of Steel Cladding Systems under Wind Uplift, M.Eng. Thesis, School of Civil Engineering, QUT.
- Xu, Y.L. (1994) Behaviour of Different Profiled Roofing Sheets Subject to Simulated Wind Uplift, Technical Report No. 37, James Cook University Cyclone Testing Station, Townsville.

PERFORMANCE OF COLD FORMED STEEL ANGLES UNDER FATIGUE LOADING

S.Kandasamy, G.M. Samuel Knight and Bh. Nagabhushana Rao.

**Structural Engineering Division, Department of Civil Engineering
Anna University, Chennai - 600 025 , INDIA.**

ABSTRACT

Cold formed steel sections are increasingly used these days in structural applications due their inherent high strength to weight ratio. Further, the cost of transportation ,erection and foundation is enormously reduced due to their light weight characteristics. Most of the codes of practice for the usage of cold formed steel sections in structural applications, deal only with static conditions of loading. Under dynamic situations, cold formed light gauge steel sections experience very low inertia forces as compared to hot rolled sections because of their low mass. Hence the thought of using cold formed steel sections under dynamic loading conditions become attractive. Even though the static behaviour of cold formed elements is well established, fatigue behaviour of these elements under fluctuating loads needs to be investigated. Angle sections are the most common steel structural elements. They are extensively used in Towers, Multi-storeyed Industrial Structures etc. The aim of this investigation is to examine the performance of cold formed steel angle members when subjected to fatigue loading. Tests have been conducted under constant amplitude sinusoidal and stepped loading on single angle specimens using servo hydraulic static-dynamic UTM. Based on the results the influence of fatigue parameters, like Maximum stress, Minimum stress, Stress range and type of loading on fatigue life is studied. An attempt has been made to study the fatigue crack growth rate using Fracture Mechanics principles . Empirical relations to estimate fatigue life and crack growth rate have been developed.

KEY WORDS

Fatigue, Fracture, Cold - formed Steel , Angles, S- N curves , Crack propagation .

INTRODUCTION

Fatigue strength is important for cold formed steel structural members and the probability of failure by fatigue is comparable with that of other Ultimate Limit state modes of failure. The source of fluctuating stress in cold formed steel structures could be machinery vibrations, environmental loads, temperature changes and acceleration forces. Since cold formed members are thin, their behaviour is governed by local buckling, low torsional stiffness, reduced bearing strength and corrosion. Two things become important when these sections are subjected to fatigue loads. Firstly, their low mass coupled with low stiffness makes their response and mode of failure complex; secondly, the reversal of loading makes them highly susceptible to fatigue failure. Even though extensive investigations on the fatigue behaviour of hot rolled steel structural elements particularly bridge members, welded structures and joint details are carried out in the past, the performance of cold formed structural steel members under fatigue loading conditions is still highly uncertain.

Klipstein, K.H(1980) investigated the Fatigue Behaviour of Sheet Steel Fabrication details. Beam specimens consisting of cold formed channels back-to back and I beam with welded and other fabrication details were fatigue tested at constant stress ranges. It was concluded that the existing fatigue design curves used for plate steel fabrication details can also be used conservatively for the design of sheet steel fabrication details. Yeon -Soo-Park et.al., (1996) carried out experimental and analytical investigations for steel angle members under very low cycle loading to identify the seismic damage process leading to cracks and/or rupture. Experimental investigations revealed that regardless of the loading patterns and deflection modes, visible cracks were initiated during the stretching on the concave side due to the buckling deformation induced in the previous load cycles. A Finite Element Analysis was also carried out to predict the local and global elasto- plastic behaviour under severe cyclic deformations in the post buckling range. In the present investigation cold formed lipped angle members are tested to study their performance under Fatigue loading.

EXPERIMENTAL INVESTIGATION.

Material Properties and Test Specimen.

The angle specimens are made from 2mm thick St-34-1079 grade steel sheets conforming to IS-1079-1973. Standard tension test results showed that Modulus of Elasticity, Yield stress and Ultimate stress were 195 GPa, 264 MPa and 346 MPa. The specimens used in this investigation are shown in Figure 1. The size and length of the weld are so proportioned in such a way that the eccentricity in the plane of the gusset plate is eliminated. From the results of the static test on specimens the maximum and minimum loads to be applied on the specimens are planned by selecting five load levels and adopting the stress ratios of 0.11, 0.18, 0.25, 0.33, 0.43, 0.54, 0.67 and 0.82.

Fatigue Testing

The specimens are tested in the 100 kN Dartec Servo Hydraulic Static Dynamic Universal Testing Machine. Constant amplitude Tension- Tension sinusoidal loading is applied and the number of cycles to failure are recorded. Forty specimens are tested at a frequency of 5 Hz. In a second set of experiments thirty six specimens are tested under the condition of sinusoidal and stepped loading at a frequency of 2 Hz. The specimens failed by development of fatigue crack at the root of the angle and propagating in the direction perpendicular to the plane of loading, when the maximum load levels adopted are more than the yield load. Other specimens tested under maximum load levels which are below and nearer to yield load failed by the initiation of fatigue cracks nearer to the weld toe and propagating in an inclined direction towards the lip of the angles. The influence of fatigue loading on these cold formed angles are studied in terms of maximum stress, minimum stress, stress range and stress ratio.

FATIGUE TEST RESULTS

The results of the forty experiments are presented in Table 1.

TABLE 1
FATIGUE TEST RESULTS : FREQUENCY 5HZ

R	S_{max}	282	251	228	142	128
0.11	38	7443	18925	25180	31763	
0.18	1029	10457	23012	41891	100500	
0.25	6625	13678	23387	66910	123378	
0.33	106	37897	45294	69294	126057	
0.43	8395	41641	73573	172178	347749	
0.54	1545	43565	80973	431172	831157	
0.67	774	131352	153015	743267	110326	
0.82	2000000	3000000	-	-	-	

Figure 2 shows the variation of Maximum stress Vs Number of cycles to failure. It is observed that when the maximum stress increases the fatigue life decreases. However the extent and rate of decrease depends on the stress ratio, being higher for lower stress ratios. It is also observed that when the maximum stress is 90% of the ultimate stress its influence on fatigue life is only marginal irrespective of the value of stress ratio. A similar behaviour is observed in the variation of mean stress and minimum stress with number of cycles. Figure 3 shows the variation of Stress range Vs Number of cycles to failure. Linear regression analysis is adopted to fit the fatigue data in the finite life region of the S-N curve. This data is usually approximated by classical Basquin equation of the form

$$N = k S^m \quad (1)$$

where k and m are empirical constants related to material properties, S - Stress range, N - Number of cycles to failure. The following empirical equation is obtained for the cold formed angles tested.

$$N = 3.382 \times 10^{11} S^{-3.23} \quad (2)$$

in which S - in MPa.

Figure 4 shows the variation of Stress ratio with Number of cycles. It is observed that the relationship between stress ratio and fatigue life is linear. The line corresponding to a constant maximum stress $S_{max} = 228$ MPa has a different slope since this stress is close to the yield stress of the specimen. Further regression analysis of the slope and intercept of the other three curves and the maximum stresses is performed which yields a non-linear empirical relation between Maximum stress, Stress ratio and Number of cycles to failure which is as follows.

$$R = 0.275 \log N + 6.6601 \times 10^{-4} S_{max} \log N - 4.5164 \times 10^{-4} S_{max} - 1.4822 \quad (3)$$

for $0 \leq S_{max} \leq 280$ Mpa.

When the above equation is plotted in a three dimensional scale it results in a fatigue failure surface as shown on Figure 5. It is observed that the fatigue failure surface is having a negative curvature. It can be seen that the fatigue life is maximum when the stress ratio and maximum stress are minimum and the fatigue life decreases when the other two parameters are increasing. Table 2 gives the comparison of Number of cycles pertaining to three different stress ratios under sinusoidal and stepped loading. It can be seen that the fatigue life decreases by 10 to 20% in the case of stepped loading condition.

TABLE 2

COMPARISON OF NUMBER OF CYCLES FOR SINUSOIDAL AND STEPPED LOADING: FREQUENCY 2Hz

Stress Ratio	Max. Stress	No. of cycles Sinusoidal load	No. of cycles Stepped load	Percentage reduction
0.54	283	5758	4665	20
0.54	251	19160	15940	17
0.54	228	31700	25106	20
0.54	142	182320	144398	11
0.54	128	812152	643224	20

Fatigue Crack Propagation

During the experiments the fatigue crack growth is measured with the help of a microscope. The principles of Paris equation of Linear Elastic Fracture Mechanics are used to relate the fatigue Crack growth rate with Stress Intensity Factor range. The results are shown in Figure 6. It is observed that even though the stress ratio is same, the crack growth rate increases with increase in stress range. From this investigations on the cold formed lipped angles the following conclusions can be drawn.

CONCLUSIONS

1. Fatigue life of Cold formed angle decreases when the maximum stress increases and the rate of decrease in fatigue life depends on the stress ratio.
2. The empirical equation in the form of Basquin equation can be used to predict the fatigue life of cold formed angles for various ranges.
3. The fatigue failure surface and the empirical non-linear relationship can be used readily to predict the influence of maximum stress and stress ratio on fatigue life.
4. The fatigue crack growth rate increases when the stress range increases for constant stress ratio.
5. The fatigue life decrease about 10 to 20% in the case of stepped loading as compared to sinusoidal loading.

ACKNOWLEDGEMENTS

This experimental investigation has been carried out at the Strength of Materials Laboratory of Structural Engineering Division, Anna University. The authors express their gratitude to the authorities for the facilities provided.

REFERENCES

1. Balamurugan P.K.(1996). Fatigue Behaviour of Cold Formed Lipped Angles in Eccentric Tension, Postgraduate Thesis (Structural Engineering), Dept. of Civil Engineering , Anna University, Chennai, India.
2. Bulson P.S., Walker A.C,(1990) Concepts of Limits State Design. Design of Cold Formed Steel Members Ed. Rhodes, Elsevier Applied Science, London.
3. Ewalds H.L, Wanhil R.J.H.(1984). Fracture Mechanics, Edward Arnold Ltd., Baltimore, USA.
4. Jagan P.(1996). Fatigue Behaviour of Cold Formed Lipped Angles in Eccentric Tension, Post Graduate Thesis(Structural Engineering), Dept. of Civil engineering, Anna University, Chennai, India.
5. Kumar B.R(1995). Fatigue Behaviour of Cold Formed Lipid Angles in Eccentric Tension, Post Graduate Thesis(Structural Engineering), Dept. of Civil Engineering, Anna University, Chennai, India.
6. Klipstein K.H.(1980). Fatigue Behaviour of Sheet Steel Fabrication Details, Proceedings of the Fifth International Speciality Conference on Cold Formed Steel Structures, University of Missouri-Rolla , Missouri, USA, pp.681-701.
7. Yeon-Soo-Park, Satoshi Iwai, Hiroyuki Kameda and Taijiro Nonaka(1996) Very Low Cycle Failure Process of Steel Angle Members, ASCE-Journal of Structural Engg., Volume 122, No2, pp 133-141.

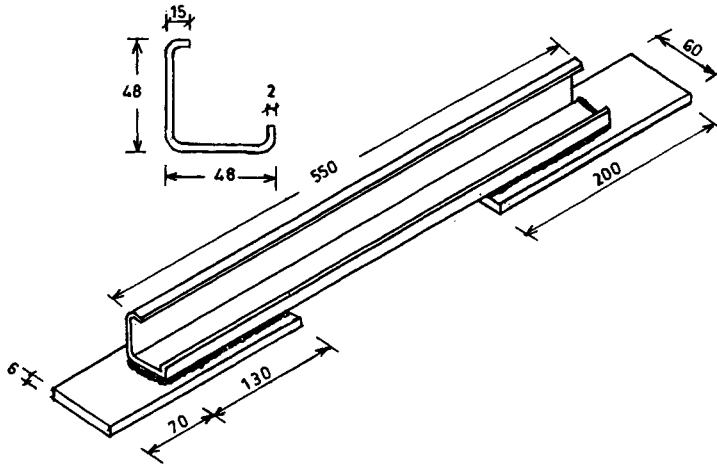


Figure 1 Test Specimen

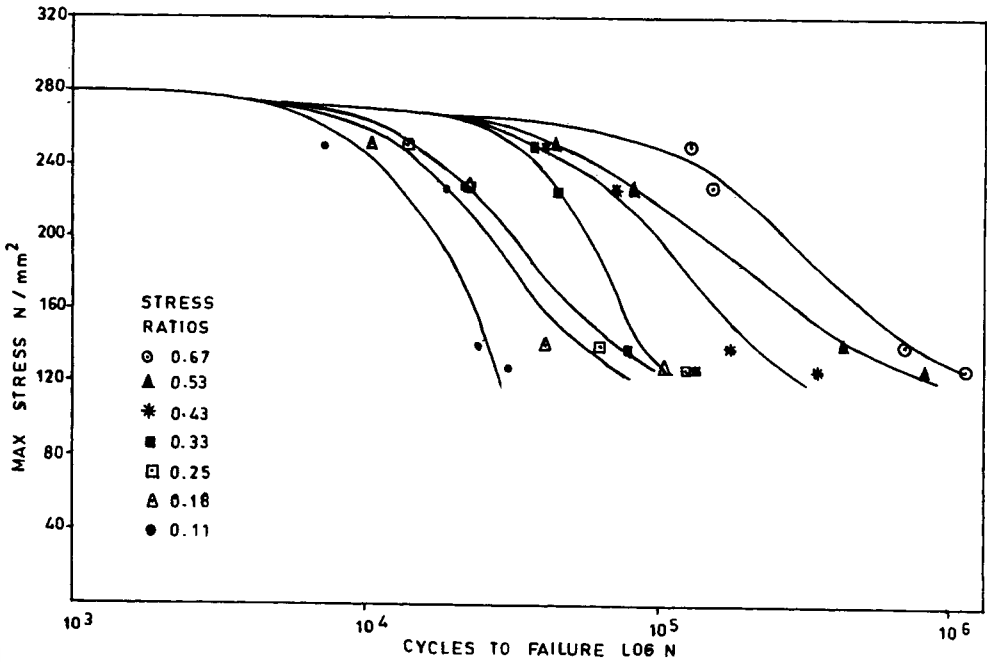


Figure 2 S-N curves with Smax Vs N

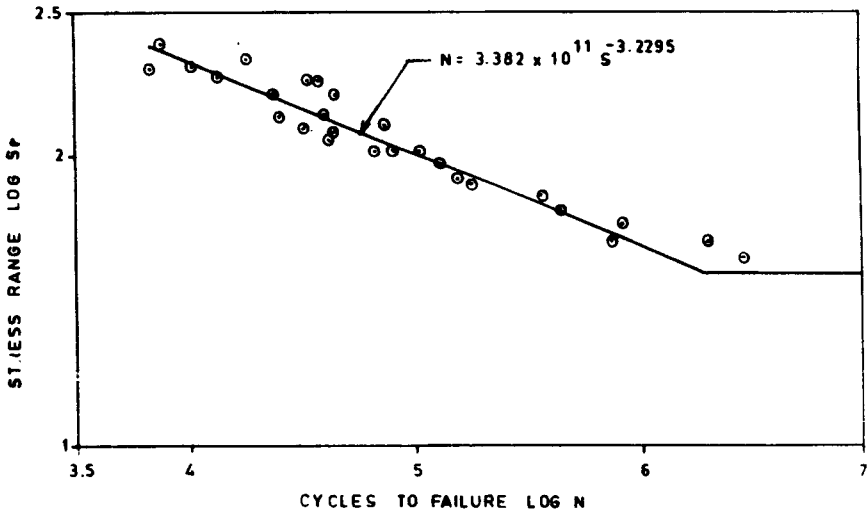


Figure 3 S-N curve for angle specimens

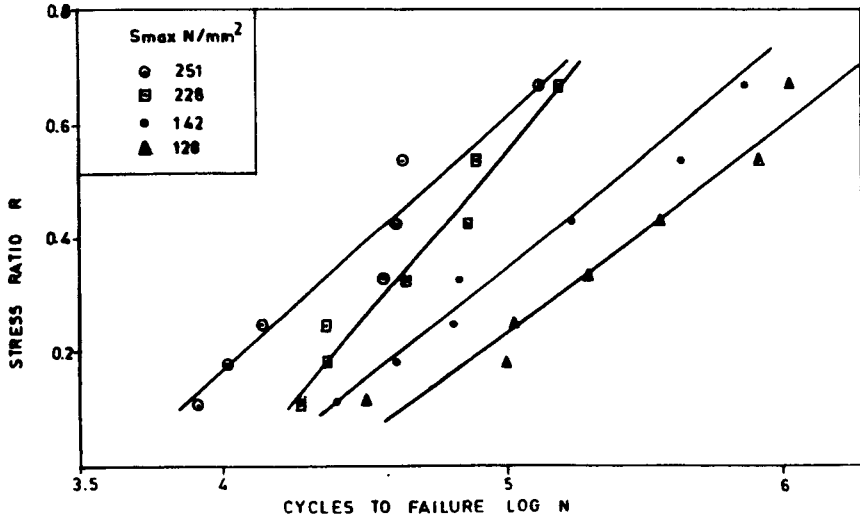


Figure 4 Stress Ratio Vs cycles to failure

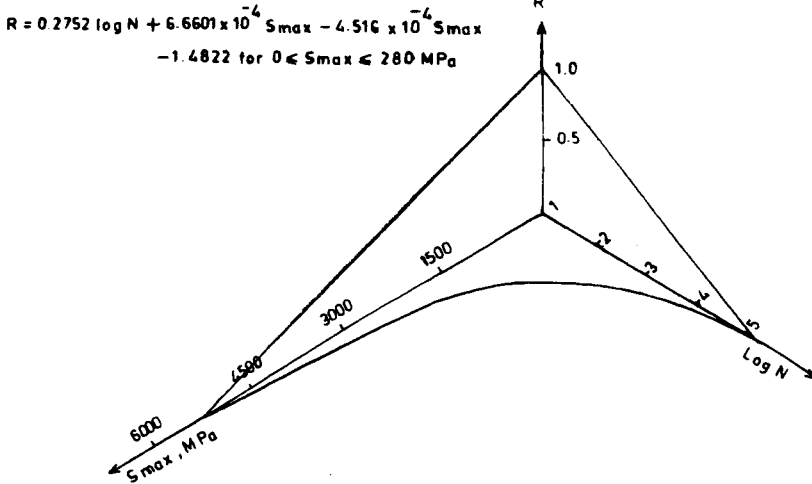


Figure 5 Fatigue Failure Surface

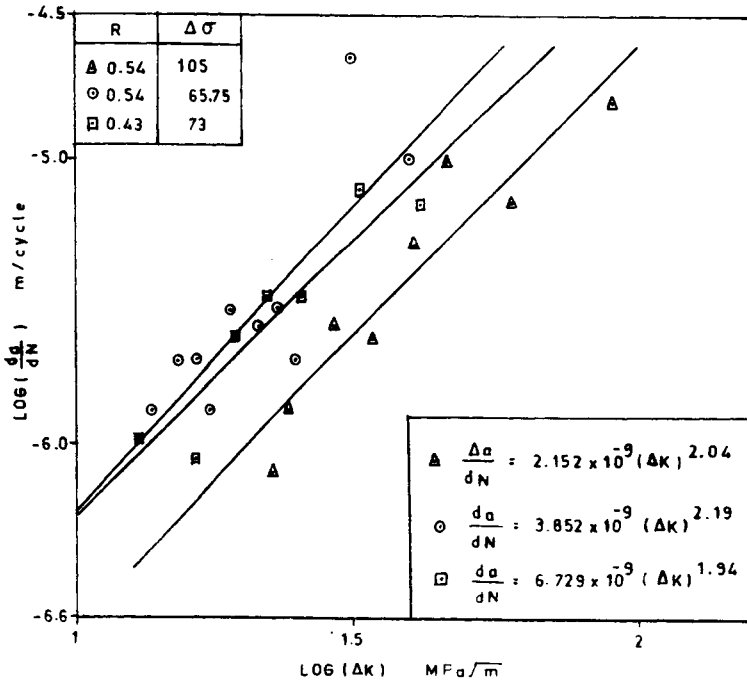


Figure 6 Crack growth Vs Stress Intensity Factor Range

QUASI-STATIC AXIAL CRUSHING OF TOP-HAT AND DOUBLE-HAT THIN-WALLED SECTIONS

Norman Jones and M. D. White

Impact Research Centre, Department of Engineering
The University of Liverpool
Liverpool L69 3GH, U.K.

ABSTRACT

Some recent theoretical predictions and experimental results are reported for thin-walled top-hat and double-hat sections subjected to static axial crushing forces. The phenomenon of progressive crushing is explored using a theoretical procedure which is based on the plastic methods of analysis for superfolding elements. The theoretical predictions are compared with some recent experimental results on thin-walled mild steel sections.

KEYWORDS

Crushing, progressive buckling, top-hat sections, double-hat sections, thin-walled tubes, static, structural crashworthiness, theory, experiments, empirical.

INTRODUCTION

Energy-absorbing systems of various kinds are of considerable interest for many engineering applications and those systems which absorb energy through the inelastic deformation of materials have received widespread attention. In particular, thin-walled tubes with various cross-section shapes have been studied because of their efficient energy-absorbing characteristics under static and dynamic axial loads (Johnson and Reid (1978,1986), Jones (1989, 1997) and Wierzbicki and Abramowicz (1989)).

The static collapse performance of spot-welded top-hat and double-hat structures, which are used extensively in the automobile industry, are examined in the present study. An approximate theoretical analysis, which uses the superfolding elements of Wierzbicki and Abramowicz (1989), has been developed recently (White, Jones and Abramowicz (1997)) and is compared in the present paper with some recent experimental results (White and Jones (1997)) on mild steel specimens having a range of flange widths and axial lengths. The most efficient energy absorbing characteristics of these thin-walled members are associated with axial progressive buckling, which is also known as static axial crushing.

A similar axial progressive buckling develops in thin-walled tubes for axial impact velocities up to about 15 m/s, approximately (Abramowicz and Jones (1986)). Thus, the static crushing behaviour examined in this paper, is of interest for the axial impact loading case and, indeed, the quasi-static approximation (Jones (1995)) is used extensively in structural crashworthiness studies which must, however, cater for any strain rate sensitive properties of the material. Nevertheless, a less efficient energy absorbing behaviour may develop if the specimens are too long and cause the development of global bending (Abramowicz and Jones (1997)), or the impact velocities are too high and produce dynamic plastic buckling (Jones (1989, 1997)).

The next two sections of this paper outline briefly the recent approximate theoretical developments for the static axial crushing of top-hat and double-hat sections. These theoretical predictions are then compared with some experimental results obtained on mild steel sections and some conclusions drawn.

THEORETICAL PREDICTIONS FOR A TOP-HAT SECTION

The cross-section of a top-hat section is illustrated in Figure 1(a), while Figure 1(b) shows the deformation pattern of a single wrinkle after being crushed by a large static axial force. This behaviour is known as the phenomenon of progressive buckling. Generally speaking, a wrinkle is initiated at one end of the section and the deformation remains localised in that vicinity until the wrinkle is fully developed. Another wrinkle then develops in the adjacent tube material and the process is repeated until all of the external energy has been absorbed by a number of wrinkles which form along the tube length, as shown in Figure 2.

If it is assumed that a typical wrinkle can be idealised as shown in Figure 1(b), then each L-shaped element which makes up a single wrinkle, can be described by an improved superfolding element studied by Abramowicz and Wierzbicki (1989). The material is assumed to be isotropic with time-independent properties and is taken as rigid, perfectly plastic, since the strains which are developed in the plastic region are large compared with the maximum elastic strains.

It is shown by White, Jones and Abramowicz (1997) that equating the external work done by a mean axial crushing force, P_m , to the inelastic strain energy consumed by a wrinkle, which includes four elements and a closing plate, and minimising, gives

$$P_m = 32.89 M_o (L/t)^{1/3} , \quad (1)$$

where $M_o = \sigma_o t^2/4$, $L = 2a + 2b + 4f$, σ_o is the uniaxial yield stress and the remaining variables are defined in Figure 1(a).

An expression for the mean crushing force is also obtained for a strain hardening material with the stress, $\sigma(\epsilon)$, at a strain, ϵ , described by the power law

$$\sigma(\epsilon)/\sigma_u = (\epsilon/\epsilon_u)^n , \quad (2)$$

where σ_u and ϵ_u are the ultimate tensile stress and the associated strain, respectively, and where n is a constant for a given material. In this case, it is found that

$$\bar{P}_m = 35.55 M_u (L/t)^{0.29} \quad (3)$$

where $\epsilon_u = 0.3$ and $n = 0.1$ for a typical mild steel and where $M_u = \sigma_u t^2/4$.

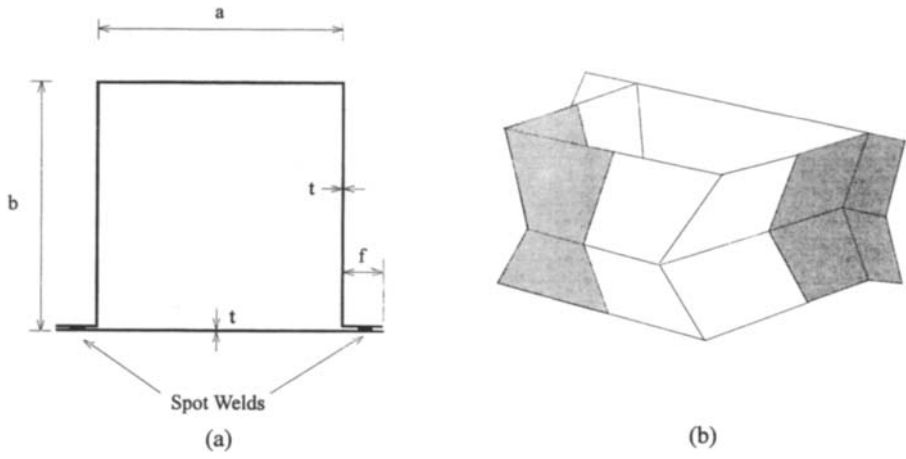


Figure 1. (a): Cross-section of a top-hat specimen, (b): Four asymmetric elements forming a collapse profile

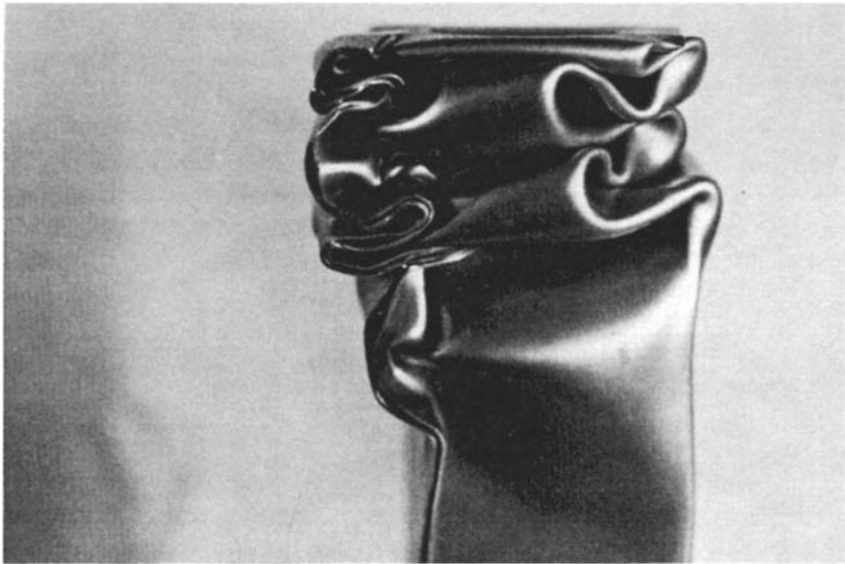


Figure 2: Asymmetric collapse profile for a top-hat structure

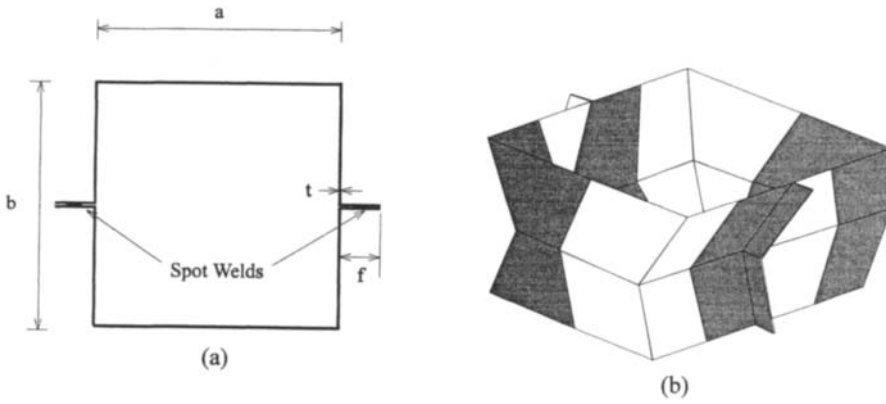


Figure 3. (a): Cross-section of double-hat section, (b): Eight asymmetric elements forming a collapse profile

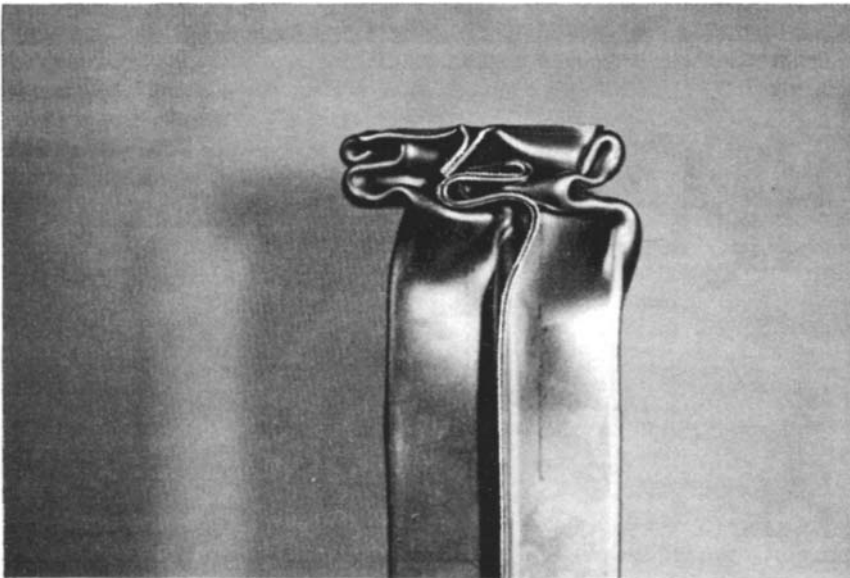


Figure 4: Asymmetric collapse profile for a double-hat structure

THEORETICAL PREDICTIONS FOR A DOUBLE-HAT SECTION

The cross-section of a typical double-hat section is shown in Figure 3(a), while the side view of an axially crushed member is given in Figure 4. This behaviour also may be modelled using improved superfolding elements. The idealised layer in Figure 3(b) consists of eight superfolding elements which White, Jones and Abramowicz (1997) examine and predict the mean crushing forces

$$P_m = 52.20 M_o (L/t)^{1/3} \quad (4)$$

and

$$\bar{P}_m = 58.15 M_u (L/t)^{0.29} \quad (5)$$

for perfectly plastic and strain hardening materials ($\epsilon_u = 0.3$, $n = 0.1$), respectively.

COMPARISON WITH EXPERIMENTAL RESULTS

Some comparisons are made in Figure 5 between the theoretical predictions in the previous two sections and the experimental results obtained by White and Jones (1997) for the static axial crushing of mild steel top-hat and double-hat structures. It is evident that equations (3) and (5), for a strain hardening material, and equations (1) and (4), for a perfectly plastic material, provide upper and lower bounds to the experimental values for the mean crushing forces of top-hat and double-hat sections.

The theoretical predictions of Tani and Funahashi (1978), Ohkubo et al. (1974) and Aya and Takahashi (1976) for top-sections are also shown in Figure 5(a). Tani and Funahashi (1978) used an effective width concept which gives good agreement with the experimental results. However, an empirical factor was introduced into the equation unlike the theoretical developments of White, Jones and Abramowicz (1997). Aya and Takahashi (1976) also used an effective width concept, but the predictions for the mean crushing force are too low despite introducing an empirical factor. The theoretical predictions of Ohkubo et al. (1974) are based on a plastic limit method together with an empirical factor.

It is evident from Figure 5(b) that the theoretical predictions of Tani and Funahashi (1978) lie below the experimental results for the mean crushing forces of double-hat sections, while the theoretical approach of McGregor et al. (1990) lies slightly above equation (4). The theoretical analysis of McGregor et al. (1990) is similar to the method used by White, Jones and Abramowicz (1997) except that McGregor et al. (1990) do not take into account the energy equivalent flow stress and the effective crushing distance.

The theoretical predictions of equations (1) and (3) are compared in Figure 6 with the experimental data obtained by Ohkubo et al. (1974) on top-hat sections. Again, it is observed that the theoretical predictions for perfectly plastic and strain hardening materials provide lower and upper bounds on the mean crushing forces. This degree of agreement is typical of other comparisons which are made with other experimental results by White, Jones and Abramowicz (1997).

The dimensionless variables, structural effectiveness, $\eta = P_m/A\sigma_u$, where $A = Lt$ and σ_u is the ultimate tensile stress for the material, and the solidity ratio, $\phi = Lt/ab$, are used to plot various experimental results, theoretical predictions and empirical equations in Figure 7 for top-hat and double-hat sections. It is apparent that the results in Figure 7 exhibit a fair amount of scatter. It is also evident that the top-hat and double-hat sections in Figure 7 are weaker than square tubes having the same solidity ratio, according to the empirical equations of Thornton (1980) and the theoretical predictions of Abramowicz and Jones (1986).

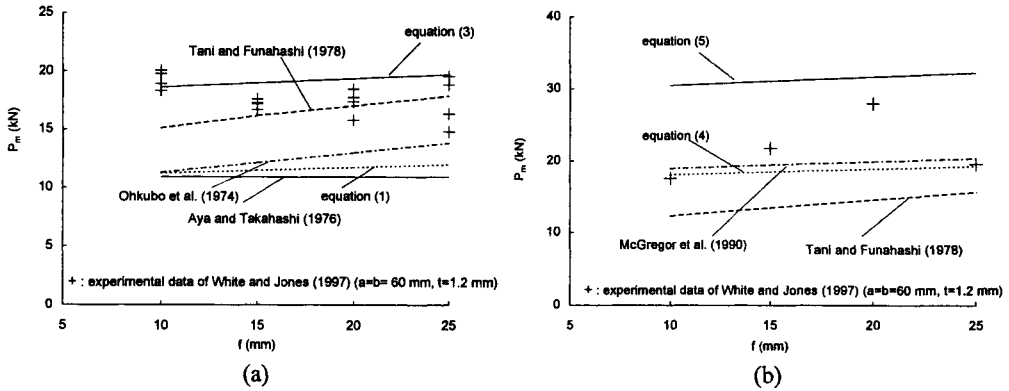


Figure 5: Quasi-static mean crushing load of (a) top-hat sections, (b) double-hat sections

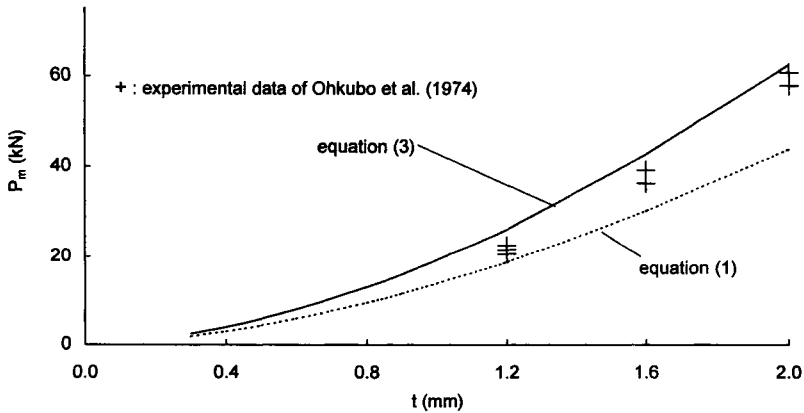


Figure 6: Comparison of current theory with experimental results of Ohkubo et al. (1974) for a 70 x 60 mm top-hat section (1.2, 1.6 and 2.0 mm thick)

The empirical equation

$$\eta = 0.57 \phi^{0.63} \tag{6}$$

is suggested by White and Jones (1997) for the design of top-hat and double-hat structures. An empirical equation of Wong et al. (1997) is also shown in Figure 7 for the static crushing of top-hat

structures which are made from mild steel sheets having thicknesses of 0.6-0.95 mm.

It should be noted that equations (1) to (5), for the same value of ϕ , show that the mean crushing forces of double-hat sections are 59%, and 64% larger than for top-hat sections which are made from the same perfectly plastic and strain hardening materials, respectively. Thus, equation (6) must be regarded as a crude design equation until more experimental data becomes available, particularly for the static crushing of double-hat sections. Moreover, the theoretical predictions of equations (1)-(5) give good agreement with the corresponding experimental data and are no more difficult to use than equation (6).

CONCLUSIONS

Recent theoretical predictions are reported which provide bounds for the static progressive crushing of thin-walled top-hat and double-hat sections. Theoretical analyses, which are based on perfectly plastic and strain hardening materials, predict lower and upper bounds to the experimental values of the mean crushing forces, respectively. It is also observed that the top-hat and double-hat tubes are weaker than square tubes having the same solidity ratio. The double-hat sections appear to have larger mean crushing forces than top-hat sections, though more experimental data is required, particularly for the double-hat sections.

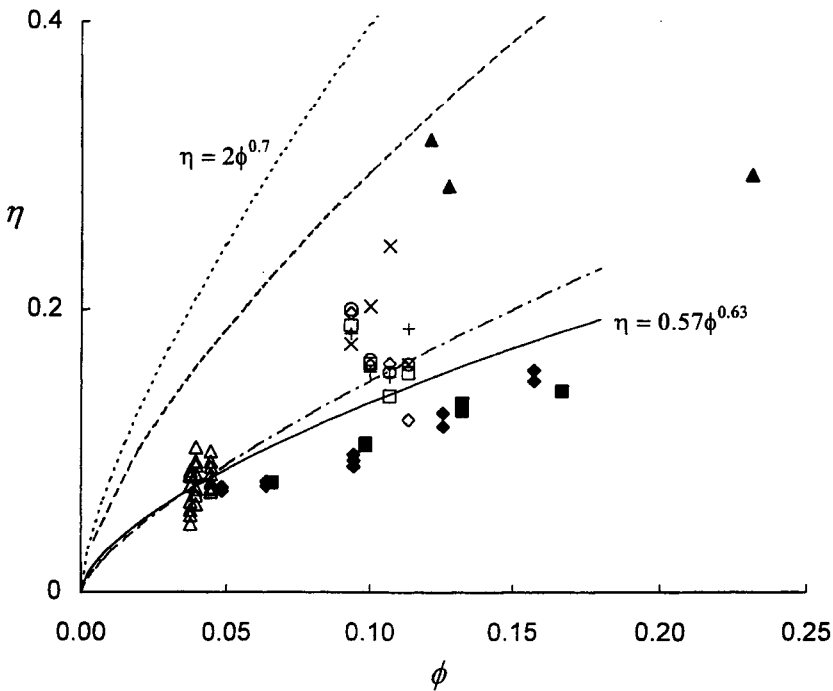


Figure 7: Structural effectiveness, η , versus solidity ratio, ϕ .
 ————— : empirical equation (6); - - - - - : Thornton (1980) square tube;
 - . . . - : Wong et al. (1997); - - - - - : Abramowicz and Jones (1986)
 (see White and Jones (1997) for further details)

REFERENCES

- Abramowicz, W. and Jones, N. (1986). Dynamic Progressive Buckling of Circular and Square Tubes", *International Journal of Impact Engineering*, **4:4**, 243-270
- Abramowicz, W. and Jones, N. (1997). Transition from Initial Global Bending to Progressive Buckling of Tubes Loaded Statically and Dynamically. *International Journal of Impact Engineering*, **19:5/6**, 415-437.
- Abramowicz, W. and Wierzbicki, T. (1989). Axial Crushing of Multi-Corner Sheet Metal Columns. *Journal of Applied Mechanics*, **56**, 113-120.
- Aya, N. and Takahashi, K. (1976). Energy Absorption Characteristics of Vehicle Body Structure. Part 1, *Japanese Society of Automotive Engineers*, Bulletin No. 7, 65-74.
- Johnson, W. and Reid, S. R. (1978). Metallic Energy Dissipating Systems. *Applied Mechanics Reviews*, **31**, 277-288. Update of this article in 1986, **39**, 315-319.
- Jones, N. (1989). *Structural Impact*, Cambridge University Press. Paperback edition, 1997.
- Jones, N. (1995). Quasi-Static Analysis of Structural Impact Damage. *Journal of Constructional Steel Research*, **33:3**, 151-177.
- McGregor, I. J., Seeds, A. D. and Nardini, D. (1990). The Design of Impact Absorbing Members for Aluminium Structural Vehicles. *SAE Technical Paper Series*, Paper No. 900796.
- Ohkubo, Y., Akamatsu, T. and Shirasawa, K. (1974). Mean Crushing Strength of Closed Hat Section Members. *Society of Automotive Engineers*, Paper No. 740040.
- Tani, M. and Funahashi, A. (1978). Energy Absorption by the Plastic Deformation of Body Structural Members. Paper 780368 presented at the *Society of Automotive Engineers Annual Meeting*, Detroit, February.
- Thornton, P. H. (1980). Energy Absorption by the Structural Collapse of Spot-Welded Sheet Metal Sections. *Society of Automotive Engineers*, Paper No. 800372.
- White, M. D., Jones, N. and Abramowicz, W. (1997). A Theoretical Analysis for the Quasi-Static Axial Crushing of Top-Hat and Double-Hat Thin-Walled Sections. Impact Research Centre Report No. IRC/112/94, Department of Engineering, The University of Liverpool.
- White, M. D. and Jones, N. (1997). Experimental Quasi-Static Axial Crushing of Top-Hat and Double-Hat Thin-Walled Sections. Impact Research Centre Report No. IRC/111/95, Department of Engineering, The University of Liverpool.
- Wierzbicki, T. and Abramowicz, W. (1989). The Mechanics of Deep Plastic Collapse of Thin-Walled Structures, *Structural Failure*, Ed. T. Wierzbicki and N. Jones, John Wiley and Sons, 281-329.
- Wong, H. F., Rhodes, J., Zaras, J. and Ujihashi, S. (1997). Experimental Investigation of Static Progressive Crushing of Closed-Hat Section Members. *Plasticity and Impact Mechanics*, Ed. N. K. Gupta, New Age International Publishers (P) Ltd., New Delhi, 250-272.

STRUCTURAL PERFORMANCE OF BOLTED MOMENT CONNECTIONS BETWEEN COLD-FORMED STEEL MEMBERS

K F Chung ¹ and Y J Shi ²

¹Department of Civil and Structural Engineering,
the Hong Kong Polytechnic University, Hong Kong, China

²Department of Civil Engineering, Tsinghua University,
Beijing, China

ABSTRACT

The paper presents findings of an experimental investigation ^[1] on cold-formed steel members with bolted moment connections. A number of connection configurations with gusset plates of both hot rolled steel plates and cold-formed steel strips were tested to investigate the structural performance of bolted moment connections among cold-formed steel members. The investigation aims to quantify the maximum moment resistances of the connections which may be safely mobilised in practical connection configurations, and a total number of 16 component tests and system tests on bolted moment connections between double lipped C sections with interconnections were carried out.

In the proposed connection configurations, only the section webs are connected onto the gusset plates while the section flanges are not connected for ease of installation. Consequently, incomplete load path exists in the connections and the moment resistances of the connections are found to lie between 50% and 85% of the moment resistances of the connected members. It is thus demonstrated that bolted moment connections among cold-formed steel members are feasible and also structurally economical. However, rational design on connection configuration is required to provide effective load path across the connections. Based on the stress distribution of a finite element analysis, a simple design expression is proposed to allow for the partial effectiveness of the section flanges at the connection.

KEYWORDS

• Cold-formed steel members • bolted moment connections • experimental investigation • finite element modelling.

INTRODUCTION

Cold-formed steel members are traditionally used as secondary structural members such as purlins for lightly loaded roofs. Since 1990's, there is a steady trend ^[2] to use cold-formed steel members as

primary structural members in buildings, and low to medium rise houses are built with cold-formed steel beams and columns as structural frames. The most widely used cold-formed steel members are the C sections and Zed sections, and the thickness of these sections ranges typically from 1.2 mm to 3.0 mm. Both steel with yield strength of 280 N/mm² and 350 N/mm² are commonly used. A number of design recommendations^[3-7] on the design of cold-formed steel structures together with worked examples may be found in the literature.

In order to extend the constructability of cold-formed steel members to moment frame structures, it is proposed to use double lipped C sections back to back as primary members. The beam column moment connections are formed by attaching the section webs of the cold-formed steel members onto gusset plates with bolts; the section flanges are not connected for ease of installation. For bolted moment connections, it is necessary to examine the structural adequacy of various components in the connections which are under high local forces and bending moments, such as web cleats and gusset plates, and also connected parts of the cold-formed steel members. In the past, a number of cold-formed steel framing systems were developed by extensive laboratory tests. Application of finite element analysis is also reported in the literature^[8-9] on connections between cold-formed steel members. It should be noted that most of the design recommendations^[3-7] on connections among cold formed steel members concern the load carrying capacities of individual fasteners such as bolts, screws, rivets and spot welds rather than the structural performance of the connections among cold-formed steel members. In general, little information is available for design of bolted moment connections between cold-formed steel members, especially, for generic sections such as lipped C sections.

COMPONENT AND SYSTEM TESTS ON BOLTED MOMENT CONNECTIONS

A total number of three column base connection component tests and six beam column connection component tests were carried out with different connection configurations using both hot rolled steel and cold-formed steel gusset plates. Furthermore, seven system tests with rectangular, L-shaped and haunched gusset plates of both hot rolled steel and cold-formed steel were also tested as portal frame structures. Full details of the test programme and the test results are presented in Reference 1. Among the tests, four failure modes are identified as follows:

- *BF_{csw}* bearing failure in section web around bolt hole
- *LTB_{gp}* lateral torsional buckling of gusset plate,
- *FF_{cs}* flexural failure of connected member, and
- *CB_{col}* combined compression and bending of column member.

It should be noted that most of design recommendations provide design rules to evaluate the load carrying capacity of individual fasteners, which may be used to design connections against the failure mode *BF_{csw}*; the design rules on failure mode *LTB_{gp}* are presented in Reference 10.

This paper aims to examine the structural performance of one of the proposed connection configurations, namely *P8*, which is associated with the flexural failure of connected members, *FF_{cs}*. Haunched gusset plates of either 6 mm thick hot rolled steel or two number 2.5 mm cold-formed steel strips are used with four bolts per member; refer to Figure 1 for details. The dimensions of the C sections are 150 mm section depth, 65 mm flange width, 15 mm lip outstand and 1.6 mm thick; the design yield strength is 450 N/mm². The test results related to the proposed connection configuration *P8* are presented in Table 1. According to *BSS5950: Part 5*, the effective section modulus of the double C section is 39.73 cm³ and the moment resistance is 17.88 kNm at design yield strength of 450 N/mm². The moment resistances of the connections are found to lie between 50% and 85% of the moment resistances of the connected members.

FINITE ELEMENT MODELING

In order to visualise the stress distribution in the connected parts of cold-formed steel members and also the load path across the connections, a finite element analysis is carried out using the general finite element package *SAP91*. The mid-line dimension of cold-formed steel section is used in constructing the finite element meshes with 4 node shell elements; the corners of the C section are assumed to be sharp. It is envisaged that linear elastic analysis is sufficient to provide design information at the presence; advanced material and geometrical non-linear analysis may be carried out as necessary.

Due to symmetry, only a single C section under pure end moment is modelled. Pure end moment is applied as couples to the top and the bottom section flanges and also in the section web at one end of the section away from the connection. It should be noted that in the proposed connection configuration, the moment is transferred from the section web to the gusset plate via the bolts, and ideally, the interaction between the bolts and the connected parts of the section web should be modelled with gap or contact elements^[9]. However, as the present study aims to examine the structural performance of the connection merely for design purpose, a simplistic approach is taken that neither the bolts nor the gusset plate are included in the model. The FE mesh is refined locally in the connection zone to provide four bolt holes. In each of the bolt holes, three nodes are fixed appropriately to provide a simplified support condition. Physically, both the bolts and the gusset plate are thus implied as infinitely rigid, and the simplified model may provide upper bound solution to the structural performance of the connected parts of the cold-formed steel member, in particular, the section web.

Two finite element meshes, namely *C90* and *C240*, were studied where the bolt pitch, p , is taken as 90 mm and 240 mm respectively; the bolt gauge, g , is 90mm in both cases. The FE mesh *C90* consists of 1292 nodes and 1112 elements while the FE mesh *C240* consists of 1712 nodes and 1512 elements. In order to avoid direct interaction between the applied end moment and the reactions around bolt holes, a distance of twice the section depth, i.e. 300 mm is always provided in the FE meshes. The finite element meshes are presented in Figure 2. The applied moment is 9.2 kNm, i.e. about 50% of the design moment resistance of the double C sections.

RESULTS OF FINITE ELEMENT ANALYSIS

The deformed shape and the stress distributions of both the longitudinal direct stress σ_x and the equivalent stress σ_e are shown in Figure 2 for both FE meshes *C90* and *C240*. Figure 3 presents the distribution of σ_x across Sections I, II and III along the section length. By integrating σ_x over a particular cross section, the moment resistance contribution from the section flanges, the section web and also the lips are obtained and summarised in Table 2. It is shown that at Section I, 67% of the applied moment is resisted by the section flanges while 28% of the applied moment is resisted by the section web; the section flanges and the section web are assumed to be fully effective.

However, at Section II, only 53% to 56% of the applied moment is resisted by the section flanges while 41% to 44% of the applied moment is resisted by the section web. Consequently, there is a load transfer from the section flanges via the section web to the supports (the gusset plate). It should also be noted that at Section II, high stress concentration exists in the section web around bolt holes and the longitudinal direct stress σ_x reaches 370 N/mm² and 350 N/mm² in meshes *C90* and *C240* respectively. As σ_x increases significantly at Section II by a factor of about 1.5 from their original values at Section I, local buckling or yielding in the web section is likely to occur.

Furthermore, as the section flanges are not connected to the gusset plate, the section flanges are not fully effective in resisting moment at the connection due to incomplete load path in the section flanges. As shown in Figure 3, the longitudinal direct stress σ_x in the section flanges decreases sharply toward the section end, confirming the partial effectiveness of the section flanges within the connection. It may be assumed conservatively that the lips are ineffective within the connection zone. Examination on the supports reveals that the reaction forces are unequal among the four bolt holes in both meshes C90 and C240, and the reaction forces of the bolt holes at Section II are always higher than those at Section III by a factor of at least two.

PARTIAL EFFECTIVENESS OF SECTION FLANGES

The moment resistance of lipped C sections, M_{xr} , may be expressed as follows:

$$M_{xr} = M_f + M_w + M_l \quad (1)$$

where M_f , M_w and M_l are the moment resistances provided by the section flanges, the section web and the lips respectively. In the proposed connection configuration, as the section web is directly connected to the gusset plate, it is reasonable to assume that M_w is fully mobilised in the connection. However, due to incomplete full path, the section flanges may only be effective when the overlap between the section web and the gusset plate is comparable in length with the section depth. A certain overlap length between the section web and the gusset plate is required to facilitate load transfer from the connected C section (both web and flanges) via the section web to the gusset plate. The contribution of the lips may be neglected conservatively, i.e. $M_l = 0$. Consequently, in order to estimate the partial effectiveness of the section flanges across the connection, a simple linear expression is proposed to evaluate the moment resistance of the connection, M_{con} , as follows:

$$M_{con} = M_w + \alpha M_f \leq 0.85 M_{xr} \quad \text{where} \quad \alpha = p / 5b < 1.0 \quad (2)$$

where α is a measure of the effectiveness of load transfer at the connection, and is defined by the ratio of p , the bolt pitch, and b , the width of section flanges. The maximum value of M_{con} is limited to 85% of M_{xr} , as confirmed with the test results; this restriction may be relaxed when more test data is available.

The above proposed expression is calibrated with the test results given in Table 1 and it is shown in each of the tests that the evaluated resistance is always smaller than the measured value; the average model factor is 1.10 among five test results. Consequently, the proposed approach is shown to be simple, conservative and yet reliable in allowing partial effectiveness of section flanges for the proposed connection configuration. It should be noted that for other connection configurations, the linear expression may be adopted but the definition of α should be revised as appropriate.

CONCLUSIONS

Both the laboratory tests and the finite element analysis have shown that effective bolted moment connections may be achieved between cold formed steel members of double lipped C sections. Only the section webs are connected onto the gusset plates with four bolts per member, the section flanges are not connected for ease of installation. However due to incomplete load path in the section flanges, the section flanges are only partially effective in resisting moment at the connection. In order to establish a rational design approach for bolted moment connections between cold-formed steel members, a simple linear expression is proposed to assess the moment resistance of the proposed connection configuration. It should also be noted that there is a significant increase in longitudinal direct stress in the section web due to load transfer between the section flanges to the section web.

REFERENCES

1. Chung, K. F. and Lau, L. (1998) Experimental investigation on bolted moment connections among cold formed steel members, *Engineering Structures* (accepted for publication).
2. Trebilcock, P. J. (1994) *Building design using cold formed steel sections: an architect's guide*, The Steel Construction Institute, UK.
3. BS5950: *Structural use of steelworks in buildings : Part 5 Code of practice for the design of cold formed sections*, British Standards Institution, London, 1987.
4. Yu, W. W. (1991) *Cold formed steel design*, second edition John Wiley & Sons Inc., New York.
5. Chung, K. F. (1993) *Building design using cold formed steel sections Worked example to BS5950: Part 5: 1987*, The Steel Construction Institute, U.K.
6. Eurocode 3: *Design of steel structures: Part 1.3: General rules – Supplementary rules for cold formed thin gauge members and sheeting*, ENV 1993–1–3(draft February), European Committee for Standardisation, Brussels, 1996.
7. *Cold formed steel structure code AS/NZ 4600: 1996*, Standards Australia / Standards New Zealand, Sydney, 1996.
8. Sivakumaran, K. S. and Abdel-Rahman N. (1996) Finite element computer models for analysis of cold-formed steel members, *Computing in Civil Engineering*, edited by Vanegas J. and Chinowsky P., USA.
9. Choi, C. K., Chung, G. T. and Song, M. K. (1996) Refined three-dimensional finite element model for end-plate connections, *Proceedings of International Conference on Advances in Steel Structures*, edited by Chan S. L. and Teng J. G., Vol. 1, pp 365 – 370, Hong Kong, 1996.
10. Chung, K. F. and Shi, Y. J (1998) Lateral torsional buckling of gusset plates in bolted moment connections among cold formed steel members, *The Second World Congress on Steel in Construction, Spain, 1998*, edited by Owens G.W., *Special issue of Journal of Constructional Steel Research*, Vol. 46, Nos. 1-3, Paper number 418, 1998.

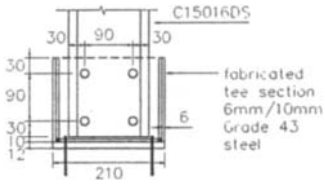
TABLE 1
MOMENT RESISTANCE OF CONNECTIONS

Test	p (mm)	Type of gusset plate	P_y (N/mm ²)	Failure Mode	M_{Test} (kNm)	$\frac{M_{Test}}{M_{xr}}$	M_{con} (kNm)	$\frac{M_{Test}}{M_{con}}$
CB04	90	hot rolled steel	455	FFcs	10.39	0.59	8.42	1.23
HRS-BC-P8	240	hot rolled steel	471	FFcs	15.38	0.82	14.50	1.06
CFS-BC-P8		cold-formed steel	465	FFcs	15.38	0.83	14.31	1.07
HRS-HS01-P8		hot rolled steel	480	CBcol	16.08	0.84	14.78	1.09
CFS-HS03-P8		cold-formed steel	475	CBcol	14.72	0.78	14.62	1.01

TABLE 2
MOMENT RESISTANCE OF SECTION COMPONENTS AT VARIOUS CROSS SECTIONS

Section	Mesh C90			Mesh C240		
	M_f / M	M_w / M	M_l / M	M_f / M	M_w / M	M_l / M
I	67%	28%	5%	67%	28%	5%
II	53%	44%	3%	56%	41%	4%
Ratio of M_f at II to I	0.79	–	–	0.84	–	–
Ratio of M_w at II to I	–	1.57	–	–	1.46	–

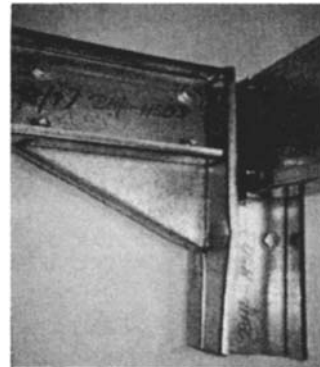
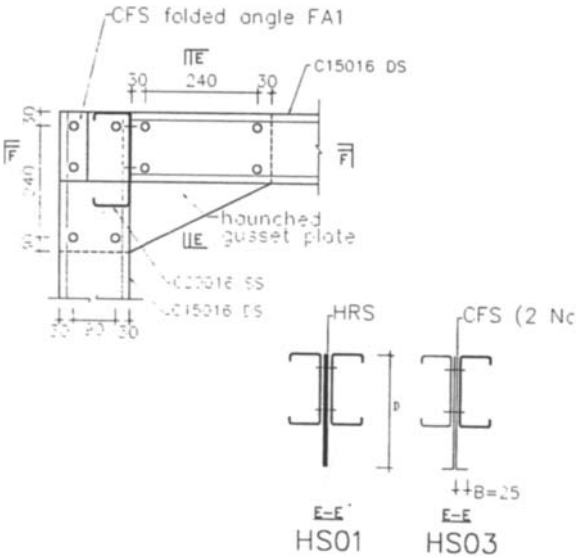
Connection configuration P8
for column base connection component test
(a) CB04



Flexural failure of cross section, $FFCs$,
of connected C section (after test)



Connection configuration, P8
for both component and system tests
(b) HRS-BC-P8, HRS-HS01-P8
(c) CFS-BC-P8, CFS-HS03-P8



2.5mm thick G450
CFS folded angle FA1

Figure 1 Connection details
(a) CB04; (b) HRS-BC-P8, HRS-HS01-P8; (c) CFS-BC-P8, CFS-HS03-P8

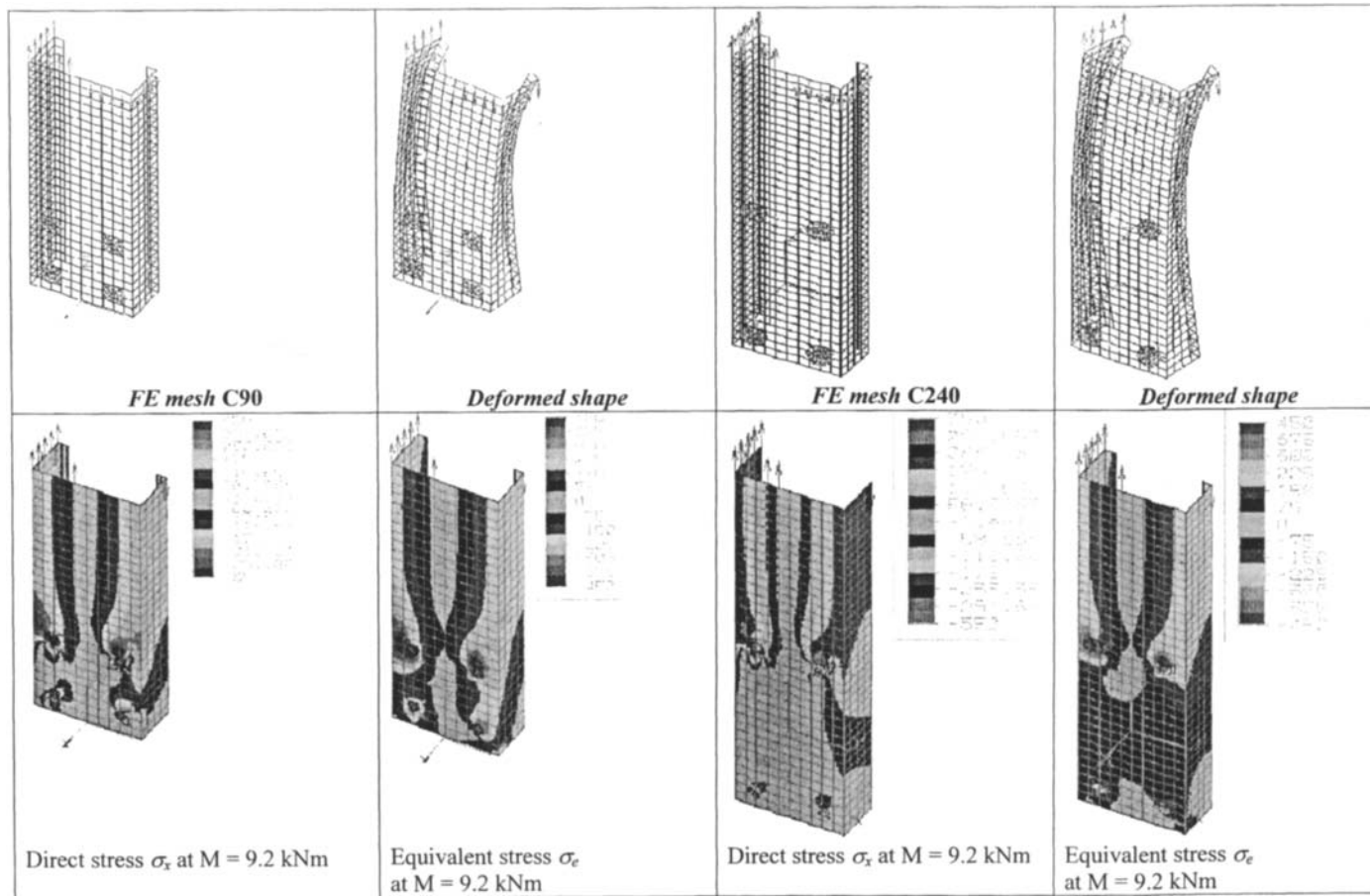


Figure 2 FE meshes, deformed shapes and stress plots for FE meshes C90 and C240

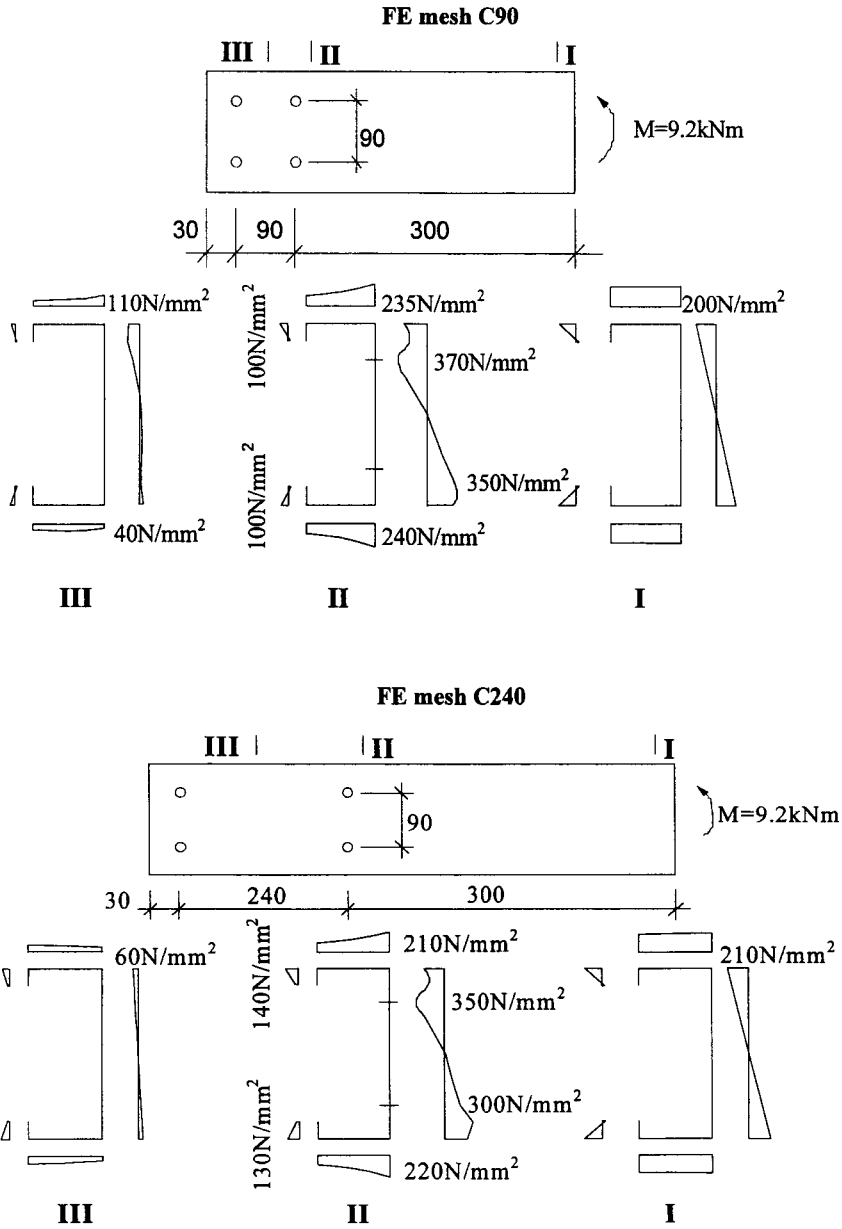


Figure 3: Stress plots of longitudinal direct stress σ_x for FE meshes C90 and C240

STABILITY DESIGN OF THIN-WALLED MEMBERS INCLUDING LOCAL BUCKLING

F. Werner¹; P. Osterrieder² and H. Lehmkuhl¹

¹Department of Civil Engineering, Bauhaus University, Weimar, Germany

²Department of Civil Engineering, University of Brandenburg, Cottbus, Germany

ABSTRACT

In Germany design calculations for thin-walled structural components such as purlins and wall cladding rails are based at present on design specifications in the national code DAST 016 or Eurocode 3. Both provide simplified design equations and procedures, whose application leads to limitations in structural idealisation. However a more economic and safer design is possible by applying computer programs, which allow a second order out-of-plane analysis of any arbitrary structure modelled by finite beam elements. Local instabilities may be considered within this method through effective widths and reduced cross section capacities. In addition analytical solutions and numerical calculations, using shell elements, were carried out to verify the concept.

A FE-based design procedure is presented, which is capable of dealing with most of the practical problems and also may be used to replace otherwise necessary and expensive testing.

KEYWORDS

thin-walled structures, purlins, code, second order analysis, finite beam elements, effective widths

INTRODUCTION

The design of members, subjected to flexural torsion, according to DIN 18800 or EC 3 [2, 3] is based essentially on formulas that either represent the theory very simplified or have a clearly empirical basis. The reason for this is the absence of practicable numerical analysis methods until recently.

The lack of tools which are reliable and able to be used in practice for the design of thin-walled asymmetrical members in accordance with the German Code DAST 016 [1] is particularly obvious.

Torsion moments caused by loading eccentric to the shear centre (inherent torsion moments), lack of symmetry in the cross section and different forms of elastic restraints can not be modelled in a simple practicable way with the help of the codes.

The objective of this paper is to show that the use of analysis systems based on the 2nd order flexural torsional theory could provide valuable extended design opportunities in the future. The statements are verified by comparative calculations with finite shell elements [7]. The results of these investigations

are quite extensive and cannot be given in full, therefore, the presentation has been limited to the essential information only.

BASIS OF DESIGN

General

The design of structural elements consisting of thin-walled cold formed members with open sections based on formulas and methods given in [1, 2] is actually practical only for a limited set of constructional elements. In the following cases, which are common in practice, the design of purlins is quite complicated :

- member systems with unequal spans - difficulties in the determination of M_{cr} ;
- non uniform loading on members or in the spans (snow accumulation, concentrated loads);
- transfer of axial loads (wind and/or stability loads in bracing systems);
- no continuous full lateral restraint or rotational restraint of the flanges (non-restraining cladding);
- existence of discrete horizontal restraints and/or rotational restraints in the span.

According to [1] and [2] a „Numerical determination of the load carrying capacities“ is possible. A design could then be carried out using the following formula for example [1, (414)] :

$$\sigma_{total} = \sigma_N + \sigma_{My} + \sigma_{Mz} + \sigma_w \leq f_{y,d} \quad (1)$$

Such calculation generally requires the use of an analysis program based on the 2nd order flexural torsional theory. The imperfection parameters required are given in the codes.

If such programs use finite beam elements the following aspects should be considered :

- the use of effective cross sections and the respective effective cross section properties;
- the consideration of the effective critical moment for lateral torsional buckling $M_{cr,y,red}$;
- effective direction and application points of the applied loads;
- modelling of structural elements which provide restraining effects.

In principle, two procedures using analysis programs for 2nd order flexural torsional theory, exist:

- 1 limit states on the basis of 2nd order theory
 - determination of effective cross sections according to the codes;
 - analysis of internal forces according to 2nd order flexural torsional theory and stress calculation.
- 2 limit states according to the codes [1] and [2]
 - determination of effective cross sections according to the codes;
 - buckling mode examination for the determination of $M_{cr,y}$ (gross cross section);
 - verification according to the codes using formulas.

It has to be considered that the second procedure should only be used if the member is not subjected to torsion. This assumption is questionable if we recognise that the member cross sections are asymmetrical with load application points on one flange and without any horizontal restraint.

Local instabilities

The real difficulty of a calculation according to 2nd order theory using finite beam elements is the consideration of the local buckling effects in proportion to their practical influence.

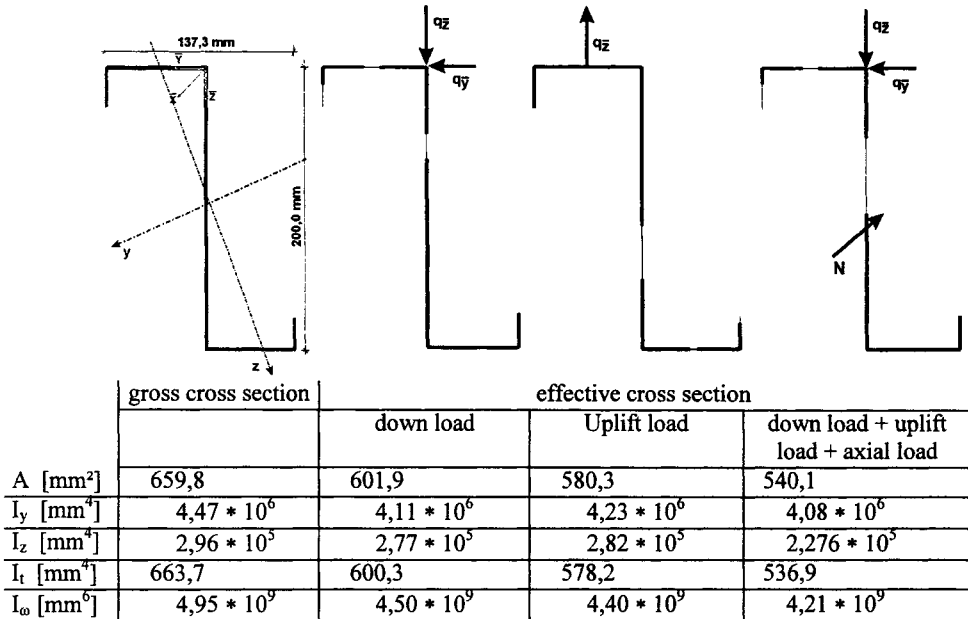


Figure 1 : Reduced (effective) cross sections according to [1] for different loading

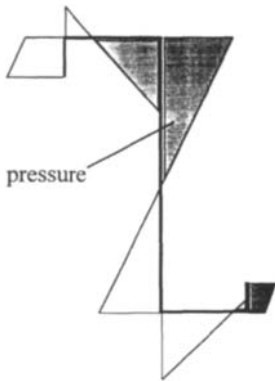


Figure 2: stress distribution for an unrestrained 5m single span purlin

Effective cross sections can be calculated quite simply according to the methods given in the codes [1] and [2]. In Figure 1 the effective cross sections are shown simplified assuming a constant compressive stress (f_y) distribution in one flange. But in theory a more complex stress distribution (Figure 6 and 7) arises generally in the most loaded cross section which would consequently lead to some different reductions of the cross section (Figure 2).

The influence of local instabilities can not be determined in a simple way for all cross section types. For a doubly symmetrical cross section, like an I-Section, the failure zones in the web cannot easily be taken into account by changing the cross section properties for the calculation of $M_{cr,y}$. Therefore a reduced $M_{cr,y}$ is introduced for such profiles considering the local buckling effects [1, (428)]:

$$red M_{\sigma,y} = M_{\sigma,y} \cdot \sqrt{\frac{1}{1 + (M_{\sigma,y} / M_{\sigma,B})^2}} \tag{2}$$

with : $M_{cr,y}$ -elastic critical moment for lateral torsional buckling (see literature)
 $M_{cr,B} = k * \sigma_e * W_g$ where $\sigma_e = 189800 \cdot (t/b)^2$;
 k relevant buckling factor;
 W_g section modulus.

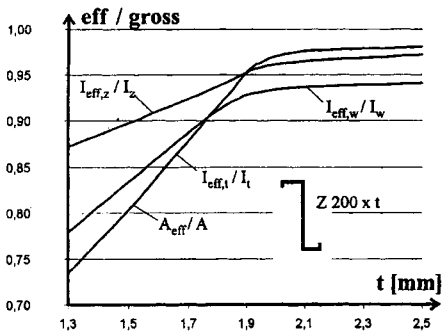


Figure 3 : Change of the section properties due to the reduction of the cross sections

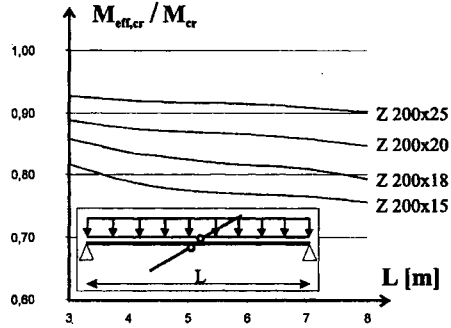


Figure 4 : Change of $M_{cr,y}$ for effective cross section

The reduction of areas in compression of cross section elements of asymmetrical profiles (compression flange and web) directly affects the load carrying capacity - see [4, comments to DIN 18800, P2, (725)] - which is expressed by the considerable reduction of I_z , I_ω and I_t for the effective cross section properties (Figure 1, 3 and 4).

TABLE 1
CALCULATION OF ELASTIC CRITICAL MOMENTS $M_{cr,y}$ ACCORDING TO [1] AND [8]

Profile	$M_{cr,y}$ [kNm] calc.[8] or [1]	$M_{cr,B}$ [kNm] calc.[1]	red. $M_{cr,y}$ [kNm] formula (2)	eff. $M_{cr,y}$ [kNm] calculation [8]
Z 200 * 15	2,47	7,30	2,34	1,70
Z 200 * 25	4,69	39,44	4,66	4,35
Z 240 * 17	3,57	9,53	3,24	2,50
Z 240 * 30	6,94	56,49	6,89	6,47

If the effective cross section has been determined using the calculated stress distribution, the resulting cross section properties are generally more favourable i.e. smaller non-effective zones in compression elements (Figure 2).

The comparisons of the values for $M_{cr,y}$, determined on the basis of the code [1] and by means of the program [8] for gross and effective cross sections, show for practical purposes a sufficient correlation of results (Table 1). In assessing the deviations that do appear, it has to be understood that the differences in the $M_{cr,y}$ - values do not lead to differences in the load carrying capacity in the same proportion. Also, simple examination of parameters also shows that the influence of local instabilities on the limit load should not be over assessed for situations where the slenderness is

$$\bar{\lambda}_{M1} < 1,1 \text{ and } M_{cr,B} > 2 * M_{cr,y} \text{ which is a normal situation.}$$

With the modification of the geometry of asymmetrical cross sections (non-effective zones in cross section, different cross section depths and so on) the location of the gravity centres and shear centres changes. This causes additional stresses which can only be assessed with difficulty particularly if torsion should be considered. For this reason, at present, the analysis program [8] will allow only one cross section definition for the finite beam elements over the complete span length. The use of integrated cross section properties for the most reduced cross section provides internal forces which are on the safe side even if the sign of the stresses changes over the length of a multiple span system.

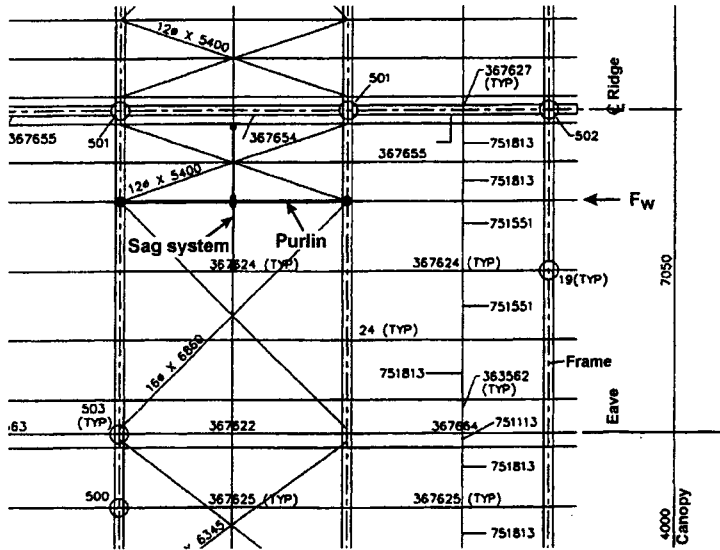


Figure 5 : Roof system

ANALYSIS OF A PURLIN

The practical procedure using 2nd order flexural torsional theory will be demonstrated on an example of a purlin design. The situation was taken from an actual project that has already been constructed (see Figure 5). In order to keep the example brief, a single span system has been considered.

System:

- single span purlin: simplified $L = 5,00$ m
- tributary width: 1,5 m; 1,2 m at the ridge
- cross section: Z-profile; $h = 200$ mm; $t = 1,8$ mm \rightarrow numerical core thickness $t = 1,75$ mm
- material: $f_y = 280$ N/mm²
- roof: profiled sheet connected with clips to the purlin
 \rightarrow does not give a defined horizontal restraint to the purlin flanges
- horizontal restraint and rotational restraint of the purlin in the middle of the span by C-profile

Loading (for a tributary width of 1,5 m):

- Dead Load (roof): $g = 0,225$ kN/m
- Snow Load: $p_s = 1,5 * 0,75 = 1,125$ kN/m
- Wind Load, uplift conditions: $p_{WP} = 1,5 * (-0,6) * 0,5 * 1,25 = -0,563$ kN/m
- axial load from gable wall $F_w = 10,2$ kN

Load combination (according to [2] or [3]):

- 1 Dead Load * 1,35 + Snow Load * 1,5 = 2,0 kN/m
- 2 Dead Load * 1,35 + Snow Load * 1,35 + Wind Load * 1,35 = 1,21 kN/m $\Rightarrow q_x$
- $F_w * 1,35 = 13,8$ kN $\Rightarrow N$
- 3 Dead Load * 1,0 + Wind Load * 1,5 = -0,62 kN/m
- $F_w * 1,5 = 15,3$ kN

For the determination of the load components (q_y and q_z) the slope of the frame rafter (here 1 in 6 \rightarrow $9,5^\circ$) has to be considered if necessary (except wind loads). The load components q_y and q_z refer to the coordinate system \bar{x} , \bar{y} , \bar{z} (see Figure 1) and the axial load N to the x -axis.

The analysis of internal forces is carried out with the analysis program BTII [8]. As an assumption on the safe side the effective cross section shown in figure 1 is used which was determined according to [1, section 3.7] for the most unfavourable loading (load combination2).

Support conditions:

- at the member ends:
 - restraint of the displacements in y - and z -direction
 - torsional restraint about the x -axis
- in the middle of the span:
 - restraint of the displacements in y -direction
 - torsional restraint about the x -axis

The imperfections are applied to the system in shape of two half sine waves in such a way that they approximate to the lowest buckling mode for lateral torsional buckling with a value of v_0 (y -direction).

$v_0 = (L / 2) / 375 \rightarrow$ [1, table 302]; buckling curve b according to [1, table 408], two half waves

$v_0 = (5000 / 2) / 375 = \pm 6,7 \text{ mm} \rightarrow$ simplified $v_0 = \pm 10 \text{ mm}$

The analysis results for internal forces and deformations are represented in Figure 6 for load combination 2. The maximum stress will be determined using Formula (1).

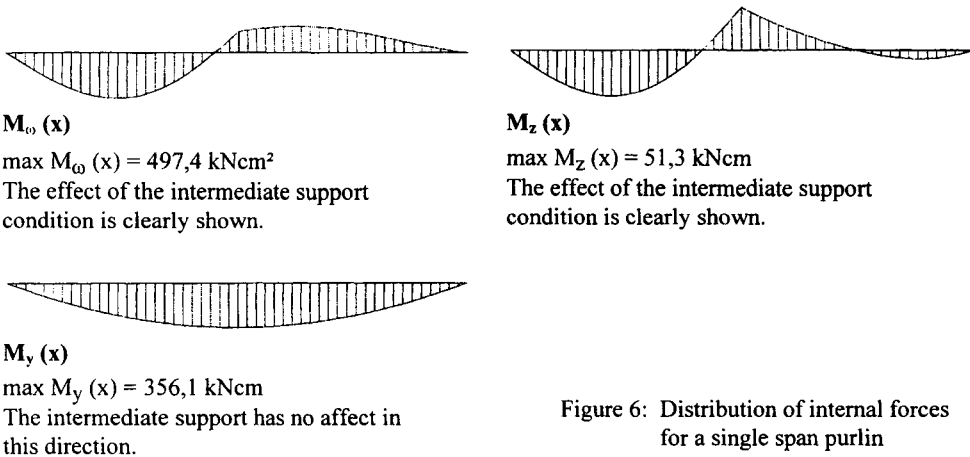


Figure 6: Distribution of internal forces for a single span purlin

For assessing the reliability of statements concerning the load carrying capacity of purlins or similar structural members, it should always be considered that there are reserves in the load carrying capacities due to the neglect of full and elastic (partial) restraint provided by properly fixed cladding systems. In the case of an elastic connection of the profile sheet to the purlins by clips, as used in 'non-restraining' cladding systems, more favourable design results could be achieved even with very small spring stiffness.

A further assumption on the safe side is to use the reduced cross section over the complete member length. This leads to an underestimation of the load carrying capacity, particularly of multi-span systems.

It is also possible to carry out a purlin design that considers trapezoidal sheets ([1] or [2]) if required. An elastic (partial) restraint of the top flange can be modelled either with longitudinal or rotational springs, see also [5 and 6].

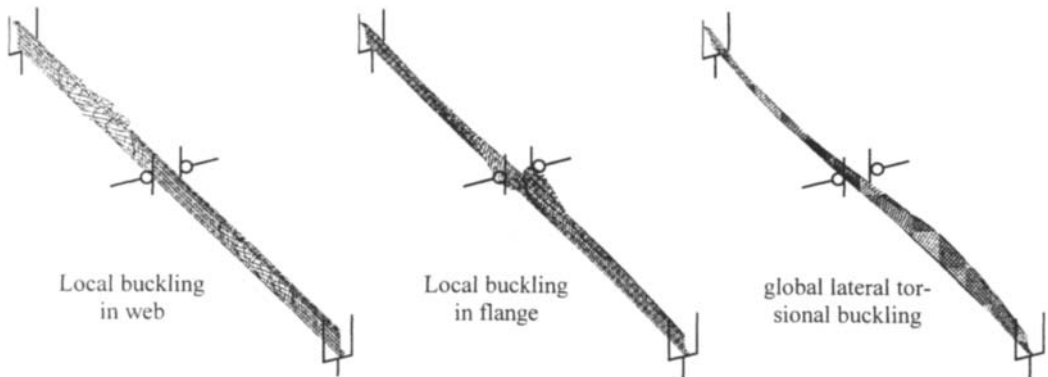


Figure 7: Buckling modes for the examined purlin system

COMPARATIVE CALCULATIONS

Comparative calculations were carried out with the analysis program ANSYS [7] using finite shell elements. The creation of accurate models for this purposes is fairly complex because thin walled profiles exhibit local instabilities that do not correspond to practical relevant failure modes if the profiles are inappropriately modelled.

The generation of the necessary imperfection figures for the global and local failure figures requires an extensive buckling analysis since the required buckling modes for local and global stability failure occur on various load levels. The three essential buckling modes which were also used in the limit load calculations are represented in Figure 7:

- local buckling in web → reduction of the web in the beam model
- local buckling in flange → reduction of the compression flange in the beam model
- global lateral torsional buckling → applying geometrical imperfections to the beam model

Because of the complex applications of imperfections, considerable stress peaks may occur locally. Therefore statements about the load carrying capacity should always be based on a physical and geometrical nonlinear analysis.

In Table 2 the calculation results of the example shown above (system 1), as well as the results of a two span system (system 2) under the same conditions, are represented for the various calculation methods and models.

The geometrical and physical nonlinear analysis with the program ANSYS was carried out taking large deformations into account. The ultimate load factors given in Table 2 are the load factors for the case where the tangent stiffness matrix becomes singular. For the program BTII the limit load is defined as the load under which the limit stress f_y (yield stress) is reached in one cross section fibre. The small differences in the ultimate load factors between both programs show that plastic influences are of little significance even for relatively small span lengths and that the dominating influence is from stability.

CONCLUSIONS

The use of practicable analysis methods on the basis of 2nd order flexural torsional theory is an essential precondition for a realistic design of structural members subjected to flexural torsion. The existing

TABLE 2
RESULTS OF COMPARATIVE CALCULATIONS

System	I		II		III		IV	
	max σ [N/mm ²]		max σ [N/mm ²]		max σ [N/mm ²]		ultimate load factor	
	B	A	B	A	B	A	B	A
1	175	182	187	225	226	243	1,25	1,30
2	126	144	145	163	176	179	1,50	1,70

B: analysis system BTII [8]

A: analysis system ANSYS [7]

1: Single span purlin (figure 6)

2: Two span purlin with same profile and loads like sys.1

Model:

I: 1st order theory; BTII gross cross section

II: 2nd order theory; BTII gross cross section

global horizontal imperfection $v_0 = \pm 10$ mm

III: 2nd order theory; BTII effective cross section

ANSYS: local imperfection: $w_0 = 2$ mm

global horizontal imperfection: $v_0 = \pm 10$ mm

IV: System like III; BTII: elastic limit load

ANSYS: geometrical + physical nonlinear analysis

results show that thin walled profiles can also be analysed and designed on this basis. The influence of local instabilities (local buckling) for asymmetrical cross sections can be described by employing effective cross sections. Hence the much limiting conditions which arise from the use of simplified formulas could be circumvented in many cases in the future.

Since generally the boundary conditions and the internal stress conditions are difficult to model, any examinations should be conducted using the possible most unfavourable assumptions. The use of finite shell element models is generally too complex for use in general practice at the moment.

REFERENCES

- [1] DASt-Richtlinie 016 (1992), *Bemessung und konstruktive Gestaltung von Tragwerken aus dünnwandigen kaltgeformten Bauteilen – Design of cold formed thin gauge members*, Stahlbau-Verlagsgesellschaft, Germany
- [2] EC 3 Part 1.3 (1996), *General rules; Supplementary rules for cold formed thin gauge members and sheeting*, European Committee for Standardisation, Brussels
- [3] DIN 18800, Teil 2 (1990): *Stahlbauten; Stabilitätsfälle, Knicken von Stäben und Stabwerken - Steel structures; stability; buckling of bars and skeletal structures*, Beuth Verlag GmbH, Ernst & Sohn, Berlin, Germany
- [4] Lindner J., Scheer J and Schmidt H. (1993). *Stahlbauten - Erläuterungen zu DIN 18800 Teil 1 bis Teil 4*, Beuth Verlag GmbH, Ernst & Sohn, Berlin, Germany
- [5] Lindner J. (1987). Stabilisierung von Trägern durch Trapezbleche; Stabilisierung von Biegeträgern durch Drehbettung. *Der Stahlbau* 56, 9-15 and 365-373
- [6] Lindner J. (1997). Influence of the Type of Connection on the Torsional Restraint Coefficient. *Proceedings of the 5th International Colloquium on Stability and Ductility of Steel Structures*. Nagoya, Japan
- [7] ANSYS Release 5.3; Swanson Analysis Systems Inc.; Houston, PA; USA 1996
- [8] BTII Version 5/98; Friedrich & Lochner; Stuttgart/Dresden; Germany 1998

Section III

**COMPOSITE AND
FERROCEMENT**

This Page Intentionally Left Blank

AXIAL CRUSHING OF FOAM FILLED COMPOSITE CONICAL SHELLS

N.K.GUPTA¹ and R.VELMURUGAN²

¹DEPT. OF APPLIED MECHANICS, INDIAN INSTITUTE OF TECHNOLOGY
NEW DELHI - 110 016, INDIA

²DEPT. OF CIVIL ENGINEERING, MEPCO SCHLENK ENGINEERING COLLEGE
SIVAKASI - 626 005, INDIA

ABSTRACT

Experiments were performed wherein layered composite conical shells made of short, randomly oriented fiber glass mats with polyester resin were subjected to axial compression. These shells were truncated and their cone angles were varied from 9.5° to 45° . The shells employed in these experiments were both empty and filled in-situ with polyurethane foam. The modes of collapse of the empty and foam filled shells, their load-compression response and energy absorption characteristics were studied. Typical post crushing load-compression curves and failure modes of the shells are presented. Effect of the cone angle as well as that of the in-fill foam on the deformation mechanics, and the energy absorbing characteristics of these shells is discussed. Based on the experimental observations, various failure modes of deformation were identified. A suitable analytical model based on energy considerations is proposed to predict the average crush stress and the crush length in a cycle. The results thus obtained are presented and compared with the experimental values. It is observed that the presence of foam increases the energy absorbing capacity of the shell.

KEY WORDS

Composites, Conical shells, Axial compression, energy absorption, Progressive crushing, Average crush load, Crush length, Foams.

INTRODUCTION

Progressive crushing behaviour of the composite shells has been studied in the past for their application in design for energy absorbing devices. It is important that the composite shells, which are inherently brittle, collapse in a controlled manner. In cylindrical shells, a triggering mechanism becomes important

[1] for proper initiation of the crushing process, whereas in truncated conical shells a progressive crushing process starts from the narrow ends[2].

Experimental studies on the crushing behaviour of conical shells were carried out by Price & Hull [2], Fleming & Vizzini[3] Mamalis et. al [4]. These studies were mostly experimental to study the effect of cone angle and size of the conical shells on their collapse behaviour. The crushing mechanism involved in composite shell is quite complex, and there are not many analytical studies on their collapse behaviour [4,5].

In the present work, experiments were performed to study the crushing characteristics of the composite conical shells. The load compression curves and the crush energy absorption characteristics are presented. The effect of cone angle on the crush energy absorption of the conical shells was also studied, and typical results are presented. The composite conical shells, tested were both empty and filled in-situ with polyurethane foams. The effect of foam on the energy absorption characteristics and the deformation mechanism of conical frusta are discussed.

Analytical expressions were obtained to find the average crush stress and the average crush length in a crush cycle of the shells, by considering all the failure mechanisms involved in the crushing process. The results thus obtained compared well with the experimental results.

EXPERIMENTS

Truncated conical shells made of short, randomly oriented glass fiber mat with polyester resin were subjected to axial compression in the Instron machine at a cross head speed of 2 mm/min. Experiments were carried out on truncated conical shells of semi cone angles 9.5° , 14° , 18.4° , 21° and 45° . Some of these shells were filled in-situ with polyurethane foam and subjected to axial compression. Typical crushing mode and the post collapse load compression curves of the empty and foam filled composite shells are given in Figs. 1- 3.

In the shell of cone angle 9.5° the deformation started from the narrow end. Fig 1(a) shows its typical deformation mode. It is seen that the crush zone is formed as the load in the load-compression curve reaches its first peak. There after the composite layers begin to peel off both inside and outside the shell radius. This is accompanied by a drop in the load-compression curve. The load -compression curve was seen to be oscillatory after the crush zone formation, and the average mean load kept on increasing up to 50 mm of deformation and thereafter it was constant. Conical shells with cone angle $\phi = 14^\circ$ had also similar type of progressive crushing.

In conical shells with cone angle $\phi = 18.4^\circ$ and 21° the deformation started with progressive crushing and then a vertical crack was formed at the bottom end. This reduced the load carrying capacity of the shells leading to their catastrophic failure. In the shell of $\phi = 18.4^\circ$ the vertical crack formation took place after a 40mm deformation and in the shell of $\phi = 21^\circ$ it was after the 12 mm of deformation. In the conical shell of $\phi = 45^\circ$ the vertical crack formed just after the first peak and there was no progressive crushing seen. It was observed that as the cone angle is increased the amount of fiber layers bending inside the shell radius is higher than those bending outside. In shells with $\phi = 0$, the fiber layers bend equally inside and outside the shell radius, in shells with $\phi = 9.5^\circ$, 60% of the fibers bent inside and remaining 40% bent outside the shell radius and in shells of $\phi = 21^\circ$, more than 90% of the shells bent inside the shell radius. Fig. 1(b) shows the deformation of the conical shell in which the progressive crushing, vertical crack formation and the layer bending are clearly seen.

The truncated conical shells of different sizes were filled in-situ with polyurethane foam and subjected to axial compression in the Instron machine. Fig. 3 shows the load-compression curves of the empty and foam filled composite shells. From the figure it can be seen that the presence of foam increases the average crush load and hence the energy absorbing capacity of the shells. But the nature of variation of energy absorbing capacity with the cone angle is same as that of empty shells, i.e., increase in cone angle decreases the energy absorbing capacity and the crushing mode is changed from axial crushing to vertical fracture of the shells. But the presence of foam delays the formation of the vertical crack. Fig. 2(b) shows the top view of the foam filled conical shell of $\phi = 18.4^\circ$.

Based on the experimental observations of the conical shells, an analysis is carried out to find the average crush stress and average crush length in a crush cycle by considering the energy terms due to laminate bending, matrix crack, friction between debris and platen and the hoop strains.

ANALYSIS

Fig.4 Shows the analytical model considered for analysis. As the crushing process initiates, fibers bend both inside and outside the shell radius. The ratio of fibers bending inside to those bending outside varies with variation of cone angle of the shells. Let t_1 and t_2 be the thickness of the fiber layers bending inside and outside the shell radius, and β and α be the corresponding bending angles.

Assuming that the fiber layers are perfectly plastic when they bend, the energy due to the bending is

$$dW_b = \frac{\pi}{2} \sigma_o (t_1^2 \beta + t_2^2 \theta) (R + h \sin \phi) \tag{1}$$

where σ_o is the ultimate stress in uni-axial tension. Assuming that the hoop strain varies linearly between A and C, i.e., 0 at A and maximum at C, the strain energy due to hoop strain is

$$W_h = \pi \sigma_o h^2 [t_1 (\sin(\phi + \beta) - \sin \phi) + t_2 (\sin \phi - \sin(\phi - \theta))] \tag{2}$$

The energy due to the central crack which moves lengthwise for a single crush cycle is given by

$$\begin{aligned} W_m &= \int_0^h \sigma_m \cos \phi \epsilon_m dv = \int \sigma_m \cos \phi \epsilon_{m_i} dv + \int \sigma_m \cos \phi \epsilon_{m_o} dv \\ &= \int_0^h \sigma_m \cos \phi \frac{\delta_1}{h \cos \phi} 2\pi (R + (h-x)\sin \phi) t_1 dx + \int_0^h \sigma_m \cos \phi \frac{\delta_2}{h \cos \phi} (R + (h-x)\sin \phi) t_2 dx \\ &= 2\pi \sigma_m (\delta_1 t_1 + \delta_2 t_2) (R + \frac{h}{2} \sin \phi) \end{aligned} \tag{3}$$

here σ_m is the shear strength of the polyester resin and is equal to 26 Mpa [5].

From the figs.4(b) & (c) the values of δ_1 & δ_2 are given by

$$\begin{aligned} \delta_1 &= h(\sin(\phi + \beta) - \sin \phi) \\ \delta_2 &= h(\sin \phi - \sin(\phi - \theta)) \end{aligned}$$

The frictional energy involved in the crushing process between the platen and the debris is

$$W_f = \mu P \delta_x \tag{4}$$

Where $\mu = 0.35$, is the coefficient of friction between the platen and the debris.

Therefore the total strain energy which is the sum of the energy terms due to bending, hoop strain, central matrix crack and the friction, is given by,

$$W_T = W_b + W_n + W_m + W_f$$

$$= \frac{\pi}{2} (R + h \sin\phi) \sigma_o t^* + \pi \sigma_o h^2 t^{**} \left(R + \frac{h}{2} \sin\phi \right) + \mu P \delta_x \tag{5}$$

Where $t^* = t_1^2 \beta + t_2^2 \theta$ and $t^{**} = \delta_1 t_1 + \delta_2 t_2$

The work done by the applied load is

$$W_p = P \delta \tag{6}$$

where δ is the reduction in length of the shell in a cycle and from Fgi. 4, it is given by

$$\delta = h[\cos\phi - \cos(\phi + \beta)]$$

Equating the total strain energy to the work done by the applied load in a cycle the expression for the crush length and average crush load in a cycle are obtained.

The expression for crush zone length in a crush cycle is obtained by minimising the total potential energy involved in the single crush cycle with respect to the crush zone length. The expression thus obtained is

$$h = \left(\frac{1}{2} \frac{\sigma_o R t^{**}}{(\sigma_o + \sigma_m \sin\phi) t^*} \right)^{1/2} \tag{7}$$

The expression for the average crush load in a crush length is the total energy in the crushing process divided by the corresponding crush length and is given by

$$P_m = \frac{\pi}{\delta - \mu \delta_1} \left(\frac{1}{2} \sigma_o (R + h \sin\phi) t^* + \left(\sigma_o h^2 + 2\sigma_m \left(R + \frac{h}{2} \sin\phi \right) h \right) t^{**} \right) \tag{8}$$

The average crush stress of the conical shell in a single crush cycle is obtained by dividing the average load by the mean area of the crush zone under consideration.

The average crush length, average crush load and the average crush stress are obtained when the value of the bending angles β and θ is $\pi/2$.

The computed values of average crushing load and the crush length for shells of $\phi=9.5^\circ$ to 45° are given in table 1. Corresponding experimental values for the shells along with their dimensions are also given for comparison and these match well.

TABLE 1
MEAN CRUSH LOAD AND CRUSH LENGTH OF THE GFRP CONICAL SHELL (K= 0.6).

S.No	R mm	t mm	ϕ Deg.	P KN		h mm	
				Th.	Ex.	Th.	Ex.
1	9.35	3.15	9.5	24.6	25.5	3.8	6.22
2	14.99	2.9	14	24.8	21.0	4.1	4.63
3	30.97	2.5	11	35	42.0	5.5	8.00
4	34.63	4.0	11	68.8	70.0	7.35	10.27

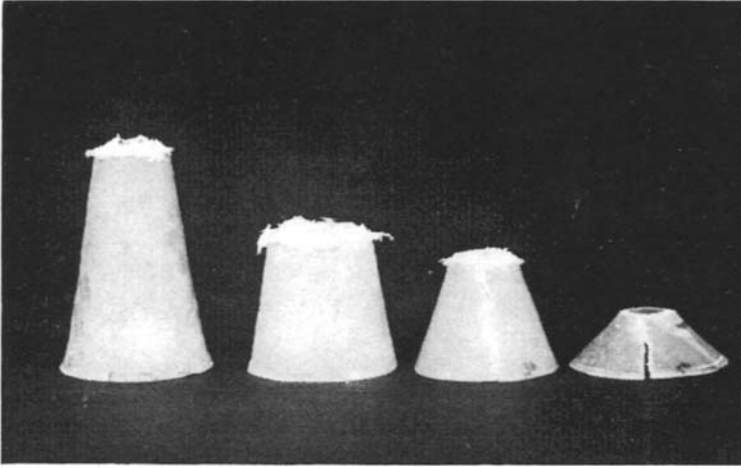
CONCLUSIONS

Analytical expressions are derived for the prediction of the average crush load and average crush length of the composite conical shells that deform in progressive crushing. The results are compared with the experimental results obtained for short randomly oriented glass fiber mats with polyester resin conical shells of different cone angles.

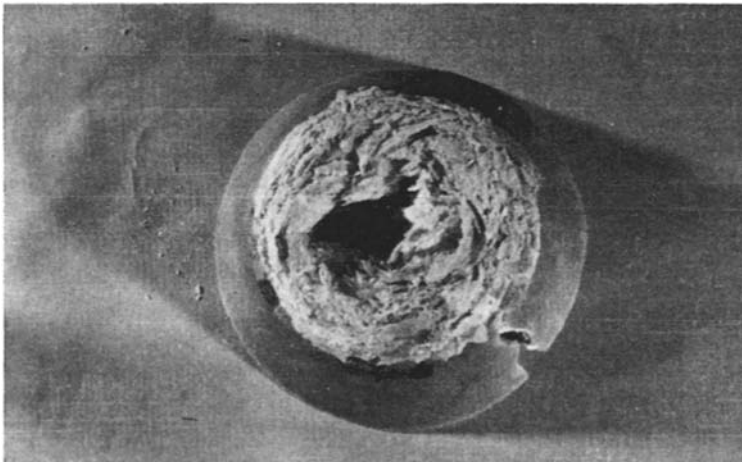
The various failure modes of the composite conical shells were studied experimentally for different sizes and cone angles. It is seen that as the cone angle increases, the progressive crushing is followed by a vertical crack which forms at the bottom end of the cone. This causes the catastrophic failure. Experiments have shown that the presence of foam in the shells delays the formation of this crack and increases the energy absorption capacity of the shell.

REFERENCES

1. Thronton P.H. (1979). Energy absorption in composite structures. *Journal of Composite Materials* 13: 247-263.
2. Price J.N. and Hull D. (1987). Axial crushing of glass fiber-polyester composite cones. *Composite Science and Technology* 28:211-230.
3. Fleming D.C. & Vizzini A.J. (1992). The effect of side loads on the energy absorption of composite structures. *Journal of composite materials* 26:4, 486-499.
4. Mamalis A.G., Manolacos D.E., Demosthenous G.A. and Ioannidis M.B. (1997). Analytical modeling of the static and dynamic axial collapse of thin-walled fiber glass composite conical shells. *Int. J. of Impact Eng.* 477-492.
5. N K Gupta and R Velmurugan, " Experimental and theoretical studies of foam filled composite conical shells "; *J. of Composite Materials*, 1998 (to appear).
6. *Composites-Engineering materials Hand book* (1987). Vol. 1: ASM International.



a) Conical shell of different sizes



b) Conical shell of $D_s = 19.2$ mm, $t = 2.9$ mm and $\phi = 18.4^\circ$

Fig. 1: Typical crushing mode of empty composite conical shells

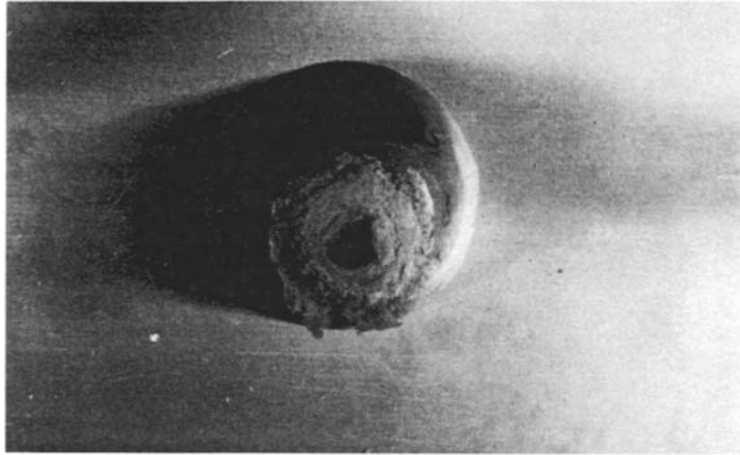


Fig. 2: Deformation pattern of the foam filled composite shell of $D_s = 19.2$ mm, $t = 2.9$ mm and $\phi = 18.4^\circ$

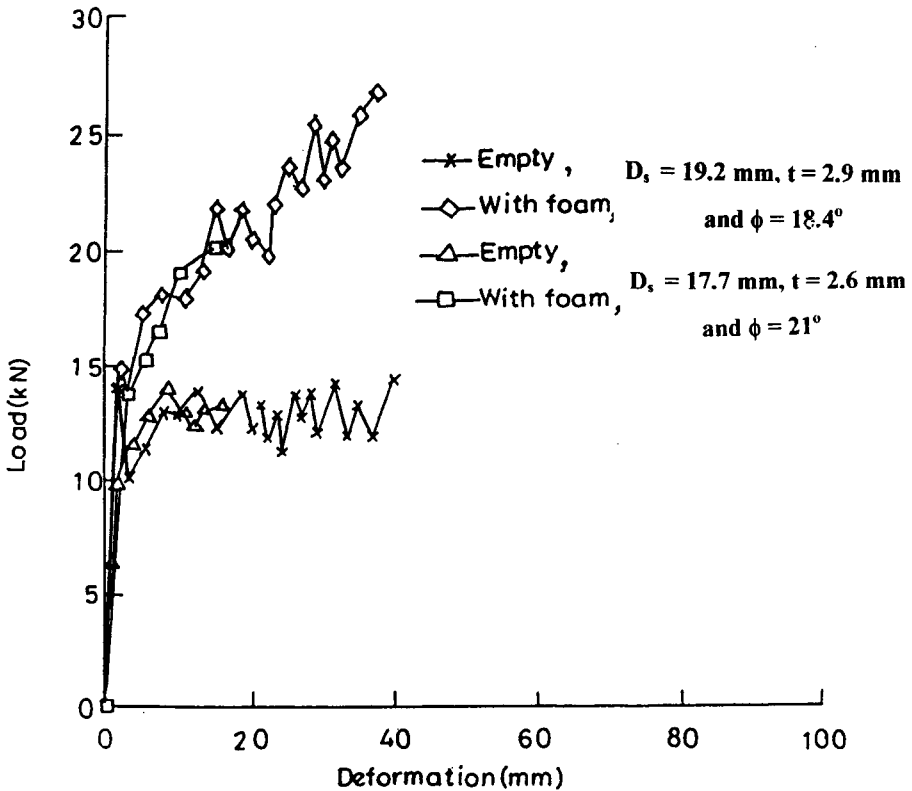
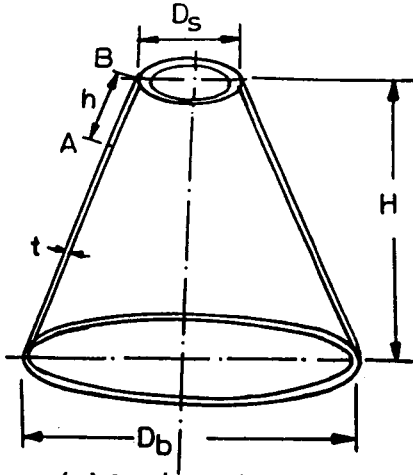
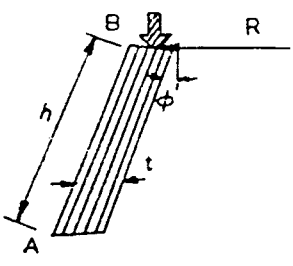


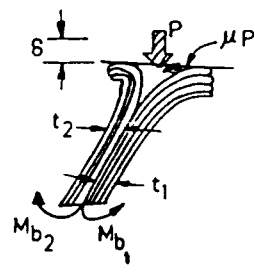
Fig. 3: Load-compression curves of empty and foam filled conical shells



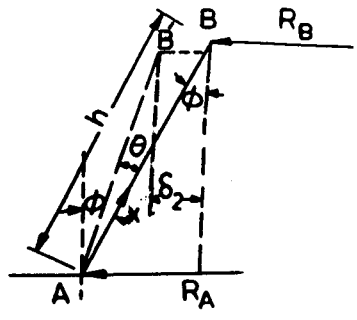
(a) Conical shell



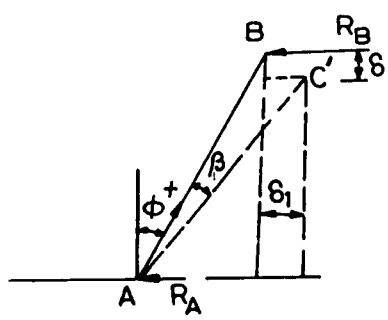
b) Undeformed configuration



c) Deformed configuration



d) Layer bending externally



e) Layer bending internally

Fig. 4: Conical shell model for analysis

BUCKLING FAILURE OF TITANIUM-STEEL COMPOSITE CHIMNEY LINER

R.H.R. Tide and M.H. Darr

WISS, JANNEY, ELSTNER ASSOCIATES, INC.
Northbrook, Illinois, 60062-2095, USA

ABSTRACT

Current chimney design divides the system into two distinct components consisting of a structural frame supporting an independent liner. One economic design solution consists of a circular reinforced concrete structure with a composite titanium-steel liner. The composite liner system provides the strength and stiffness of the relatively inexpensive carbon-steel backing to support the relatively expensive but corrosion-resistant thin titanium sheet overlay. However, problems may arise in this type of system, as illustrated by this case study of two coal-fired power plant chimneys. Within months after the power plant was placed in operation, the titanium sheets began to debond from the carbon-steel backing. The investigation into the cause of the chimney liner failure included physical testing of the titanium-steel composite system and metallographic examination of the fusion bond concept and fracture surfaces. A buckling analysis was also performed to identify the primary cause of the problem. Both two-dimensional and three-dimensional finite element method (FEM) analyses confirmed stress concentrations were present at the tips of the fusion bond.

KEYWORDS

Chimney, liner, titanium, steel, fusion bond, buckling, debonding, fracture, stress concentrations.

INTRODUCTION

Historically, chimney liners were an integral part of masonry chimneys manufactured to withstand the conditions imposed by coal-fired power plants. Later, environmental requirements dictated that chimney heights exceed practical limits of freestanding masonry chimneys. One solution to this problem was to construct a reinforced concrete structure with a corrosion-resistant liner. This paper addresses two chimneys that are approximately 134 m tall and 13.7 m in diameter at the base, tapering 9.8 m at the top. The diameter of the liner is approximately 6.8 m.

To construct these chimney liners, large, rectangular sheets of 1.6 mm thick titanium are placed on 6.4 mm thick carbon-steel sheets that extend a small distance beyond the edges of the titanium sheets. Vertical liner splices are present at the third points of the circumference resulting in steel plates

approximately 7.1 m long 2.3 m high. The vertical liner segment splices are staggered by approximately 3.55 m to avoid a continuous splice condition. The steel side of the composite system is insulated to prevent significant heat loss.

Because titanium cannot be welded directly to steel, the two sheets are fused together using a proprietary system where an electrically charged rotary mandrel applies pressure as it traverses the long direction of the sheets. The 150 mm spacing of the 9 mm wide fusion bond is determined in the design of the liner. To facilitate fusion a fine stainless steel mesh is placed between the titanium and carbon-steel plates. The 50 mm wide stainless steel mesh consists of 0.36 mm diameter wires spaced at 1.14 mm in each direction. When the electrical current from the rotary mandrel passes through the composite system under pressure the stainless steel melts, forming a brazing-like bond between the titanium and the steel sheets. A side effect of the fusion process is that the titanium is systematically deformed and ripples continuously occur between each fusion bond row as shown in Figure 1. The composite system is then rolled to the required liner radius. Individual titanium-steel sheets are interconnected by welding the exposed edges of the carbon-steel sheets together horizontally and vertically at the site to form the liner. The exposed welded carbon-steel bands are then covered with approximately 200 mm wide vertical and 150 mm wide horizontal titanium batten plates that are welded to adjacent titanium sheets using a tungsten inert gas (TIG) process. An example of the batten plates and fusion bond is shown in Figure 2.

The original design specifications indicated that the operating steady state temperature inside the chimney could vary from 50°C to 150°C. During emergency shut-down conditions it was expected that the chimney flue gas temperature could be as high as 370°C for up to 30 minutes. Because of the insulating blanket on the steel side of the liner and the thermal conductivity of titanium and steel, only a small temperature gradient through the titanium-steel system would exist during a steady state operating condition.

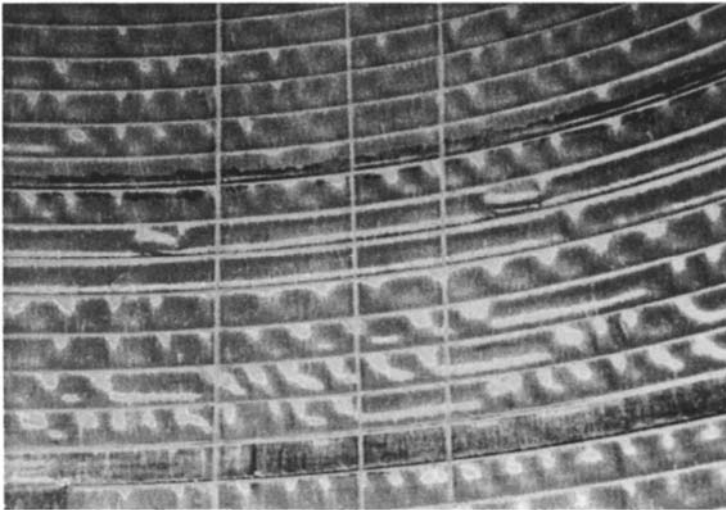


Figure 1 - Buckling of titanium sheets between fusion bond rows

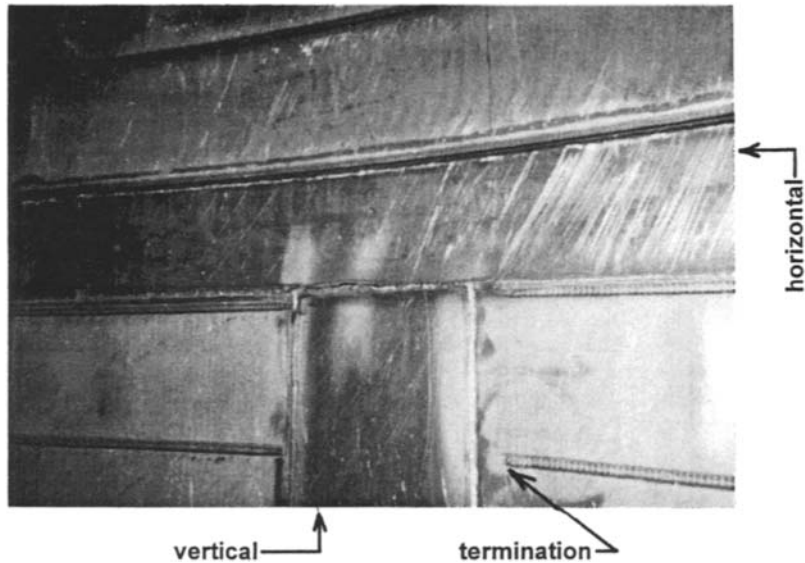


Figure 2 - Intersection of horizontal and vertical batten plates

FAILURE MECHANISMS

Within months after the power plant was placed in operation, the titanium sheets in one chimney began to debond from the carbon-steel backing. The extent of the debonding varied from small, localized blisters about 0.3 m wide to large areas extending several meters both horizontally and vertically. An example of the liner failure is shown in Figure 3. The second chimney, which had been in service for a shorter period of time, exhibited only a few very small blisters. A comparison of the failure locations in the two chimneys suggested that the failure initiation points were located adjacent to the vertical batten plates.

At several locations within the first chimney, heat tinting of the titanium sheets was observed. Several titanium sheets displayed pink, green, straw and purple colors. The heat tinting suggested that the titanium sheets were subjected to elevated temperatures. Power plant records indicated that 150°C flue gas temperatures were frequently measured near the chimney breach. Because all measuring devices were not fully operational during the start-up operations, a complete temperature record was not available.

Observations indicated that failure had occurred by debonding of the titanium-steel composite system. Although titanium batten strip welding had also failed, no significantly defective titanium batten plate fillet welds were observed.

TESTING PROGRAM

Samples of the composite system were removed from both damaged and intact areas for examination and testing. Because of the observed failure mechanisms, a few test coupons were prepared to

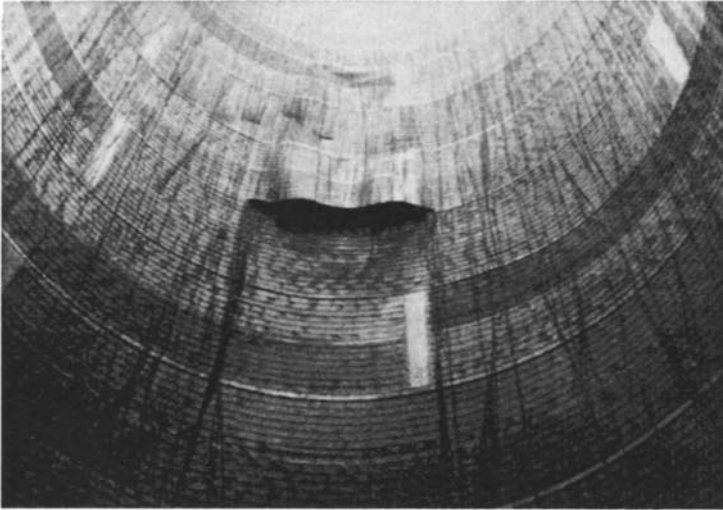


Figure 3 - Representative titanium debonding failure conditions

measure the properties of the steel, titanium and the fusion bond between the two. The chemistry and physical strength of the carbon-steel suggested that it conformed to ASTM A36 with an average yield strength of 336 MPa. Similarly, the titanium conformed to ASTM B265 Grade 2 with an average yield strength of 339 MPa. Fusion bond hardness readings of Rockwell C (Rc) in the 50-55 range were measured, suggesting a tensile strength exceeding 1380 MPa. These over-scale hardness readings indicate a very brittle material with very little ductility. Polished and etched samples taken near the fusion bond termination points and magnified 100X indicated that cracking had occurred in the fusion zone as shown in Figure 4.

Shear and peel-off tests were conducted according to ASTM A263-92. The five shear tests indicated average and minimum shear strengths of 214 MPa and 193 MPa, respectively, which exceed the published shear strength of 172 MPa. The five peel-off tests indicated an average capacity of 67 N/mm or 8.9 MPa and a minimum peel-off force of 54 N/mm or 8.5 MPa. Both the average and minimum peel-off strengths of the chimney samples were less than the manufacturer listed strength of 102 N/mm.

Chimney titanium test samples exposed to temperatures in the range of 370°C to 480°C exhibited blue, purple, various shades of straw and some pink colors when exposed for 1½ to 2 hours. By increasing the temperature range from 540°C to 650°C additional pink areas became visible and green tints were added to the other observed color bands. This suggests that localized areas of the liner were probably exposed to high temperatures for short periods of time so that the high-temperature titanium oxides could form creating the observed tinting.

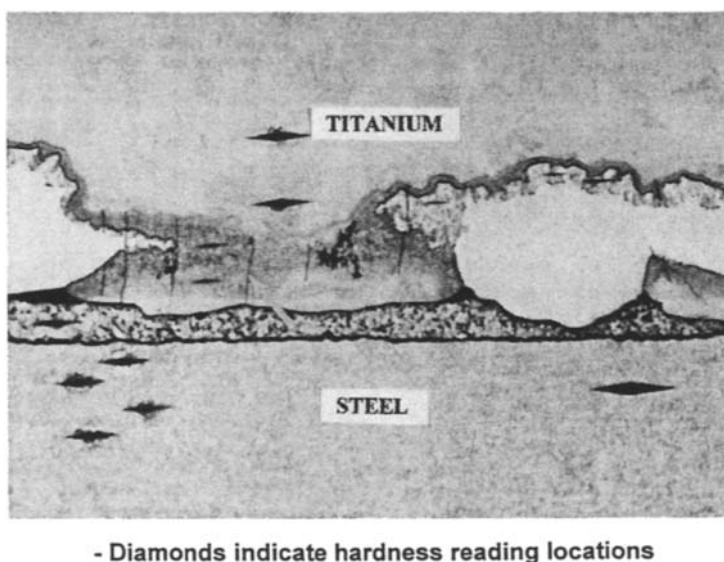


Figure 4 - Composite titanium-steel system (100X)

STRUCTURAL ANALYSIS

General

The physical properties of steel and titanium that most significantly effect the structural performance of the composite liner system are the modulus of elasticity (E) and the coefficient of thermal expansion (α). For steel and titanium E is 200,000 MPa and 103,000 MPa, respectively. The α values for steel and titanium are 11.5×10^{-6} mm/mm/ $^{\circ}$ C and 8.6×10^{-6} mm/mm/ $^{\circ}$ C, respectively. These differences affect the performance of the chimney liner during both elevated steady state temperature operations and during rapid increases or decreases in flue gas temperature.

The observed failure modes and titanium heat tinting suggested possible structural damage associated with the fusion bond terminations and with thermal effects on the titanium-steel composite components due to exposure to the anticipated operating temperatures, as well as possible exposure to unusually high temperatures. To confirm the suspected causes of liner failure, as indicated by the above testing and field observations, structural analyses were performed. The structural analyses of the chimney liner was divided into two parts; basic hand computations to identify critical issues and finite element method (FEM) analyses to clarify and accurately define stress conditions.

Preliminary Analyses

Basic shear stresses at the titanium-steel interface were calculated to be approximately 27.6 MPa when the composite sheets were rolled and plastically deformed to conform to the radius of the chimney liner. However, the shear stress is not defined at the fusion bond termination and transition from the composite to the non-composite system. There are approximately 4000 of these fusion bond

terminations in each chimney. Preliminary calculations suggested that during a normal start-up condition the differential temperature increase would result in titanium batten plate buckling.

Computer Analyses

The hand calculations and physical testing indicated the likelihood of excessive stress conditions at the fusion bond terminations. Both two and three dimensional (2D and 3D) FEM analyses were performed to further investigate these conditions.

The 2D FEM analysis indicated that for a 139°C steady state temperature increase in the overall composite system, the nominal circumferential stress in the steel and titanium would be a non-critical 9.7 MPa compression and 38.6 MPa tension, respectively. These stresses indicate that as the liner temperature increases, steel with a higher E , α and thickness expands circumferentially increasing its radius and that the titanium, although thermally expanding, is further elongated by its attachment to the steel. Additionally, the shear stress was less than 7 MPa in the fusion bond interface away from the terminations. Because the power plant start-up testing occurred during the winter months, liner temperature differentials in some cases were probably greater than the assumed 139°C.

For a 139°C increase in flue gas temperature to approximately 150°C the liner steel plate will initially restrain the vertical 200 mm wide titanium batten plates from expanding and, therefore, exert a horizontal compressive stress of 123 MPa in the batten plates. The fillet weld anchorage of the batten plates results in an eccentricity that magnifies this axial stress. For analysis purposes, the welded batten plate edges may be considered to have a fixed boundary resulting in a column effective length factor (K) equal to 0.5. The column slenderness for a 1.6 mm thick and 25 mm wide strip is equal to 216 indicating a purely elastic Euler buckling condition. A critical buckling stress for a strip of titanium with the assumed boundary conditions is approximately 21.7 MPa, which is considerably less than the 123 MPa determined from FEM analysis. This indicates that the flat vertical batten plates would buckle during an increase in flue gas temperature subjecting the fusion bond terminations to some undefined prying force. In the main body of the liner, the titanium sheets were essentially pre-buckled during the fusion bonding and subsequent rolling process. Any liner differential temperature would subject the fusion bond to a stress concentration in the vertical direction as well.

The 2D FEM sufficiently represented the liner circumference to fully incorporate the radial tension forces between the titanium and steel composite system. The segment of interest was the vertical batten plate attachment, an example of which is shown in Figure 5. A unit width of fusion bond termination and titanium batten strip was considered in the model. When a steady state temperature increase of 139°C was applied to the model, a significant stress concentration developed at the fusion bond termination as shown in Figure 6. The tensile peel-off force at the fusion bond termination for this temperature increase was approximately 35 N/mm, which is less than the minimum test values of 54 N/mm. However, for any temperature change exceeding 200°C, steady state or otherwise, the stresses would exceed the measured peel-off test values and progressive cracking of the fusion bond terminations could be expected based on this 2D model.

A 3D FEM model was constructed to further refine the fusion bond termination conditions. This model included a 150 mm wide batten strip centered on a 9 mm wide fusion bond. When a steady state temperature increase of 139°C was applied, the peel-off stress concentration at the fusion bond termination increased to 81 N/mm, as compared with 35 N/mm in the 2D model. A stress concentration of this magnitude exceeds the minimum and average peel-off test values of 54 N/mm and 67 N/mm, respectively. Increasing the flue gas temperature only briefly to 370°C would certainly result in localized peel-off forces exceeding the published values of 102 N/mm.



Figure 5 - Partial two-dimensional FEM model of composite titanium-steel system

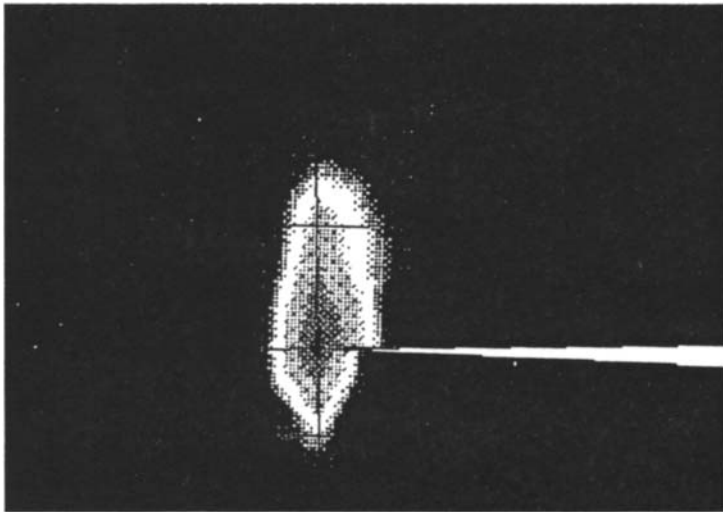


Figure 6 - Stress concentration at tip of titanium-steel fusion bond termination

SUMMARY AND CONCLUSION

An investigation has been conducted into the cause of the debonding of titanium sheets from a titanium-steel composite chimney liner system. The debonding began to occur in the chimneys shortly after the coal-fired power plant began operation. Samples of the liner system were removed for testing to verify the nominal composition and physical properties of the steel and titanium. In addition, interface shear strength and peel-off tests were performed between the steel and titanium and compared with manufacturer published values. Tests were conducted to identify the temperature ranges at which heat tinting would result from various titanium oxide conditions.

Calculations were performed to determine the imposed shear stresses at the composite interface between the steel and titanium. Buckling conditions were identified at various chimney flue gas operating temperatures for the vertical batten plates. Finally, two and three dimensional finite element method (FEM) analyses were performed to determine nominal operation stresses in the liner and stress concentration levels at the fusion bond terminations. The FEM results were compared to published strength values and test results.

The investigation indicated the stress concentrations at the fusion bond terminations were the critical issue in the liner failure. The very brittle interface between the steel and titanium sheets, which was composed of a stainless steel material, probably experienced some cracking at the time of liner rolling, especially at the fusion bond terminations. During the initial start-up and shut-down cycles the design flue gas temperatures induced peel-off stresses which equaled or slightly exceeded the nominal strength. Any random higher flue gas temperature that occurred during emergency or rapid shut-down operations probably resulted in peel-off stresses that exceeded even the most optimistic fusion bond termination capacities. Additional stresses caused by buckling of the vertical titanium batten plate exacerbate a condition that was already critical.

In conclusion, it appears that the composite titanium-steel liner would be expected to randomly fail in some of the 4000 locations adjacent to the vertical batten plates in each chimney due to the properties of the brittle fusion bond system. The available literature indicated that the manufacturer was not aware of this condition.

ACKNOWLEDGEMENT

The authors wish to acknowledge the work done by Dr. Kent L. Johnson of Bodycote Taussig, Inc. for performing the metallurgical testing.

INFLUENCE OF GEOMETRIC IMPERFECTIONS AND LAMINATION DEFECTS ON THE BUCKLING BEHAVIOUR OF COMPOSITE CYLINDERS

N.Panzeri and C.Poggi

Department of Structural Engineering, Politecnico di Milano
I-20133 Milano, Italy

ABSTRACT

The buckling behaviour of composite cylinders is highly influenced by the presence of geometric imperfections and other factors that can cause big discrepancies between experimental loads and analytical values. The influence of the geometric imperfections has been widely analysed in steel shells and only recently it has been tackled also for composite shells. In this work the effects of geometric imperfections and other defects due to the manufacturing process, like the thickness variations or possible misalignments of the fibers from the nominal directions, are analysed with the objective of producing relevant suggestions for the designers. The research is aimed at providing scientific background for a better exploitation of the material properties and defining the influence of the processing conditions on the product performance.

KEYWORDS

Composite cylinders, buckling, postbuckling, perturbation techniques, geometric imperfections, lamination defects.

INTRODUCTION

The design of buckling sensitive shells is usually based on 'knock-down' factors that are applied to the buckling load derived from a linear eigenvalue analysis. In the design of metallic structures these factors are derived from lower bound curves based on test results, ECCS (1988). Even if several research activities have been devoted to this problem, large databases of test results exist only for few basic shell geometries and loading conditions and are referred to models made with different manufacturing techniques and accuracy. As a consequence the knock-down factors defined on this basis can be unduly conservative. For this reason imperfection data-banks for steel cylinders were created collecting homogeneous results, Arbocz (1983). Comparisons were carried out on the basis of statistical

techniques applied to the Fourier coefficients of the imperfection modes for nominally identical specimens. This procedure allows to define characteristic imperfection modes that represent the particular manufacturing method and helps in performing numerical calculations to evaluate the effects of multimode imperfection patterns. Only recently, similar procedures have been applied to composite shells and a statistical analysis on composite cylinders manufactured using 'hand lay-up' has been concluded, Chryssanthopoulos and Poggi (1995). The dimensions of the examined specimens should be comparable to those of real structures to make the recorded geometric imperfections fully representative of the manufacturing process.

It is known that the effect of geometric imperfections is particularly severe in axially compressed cylindrical shells where the presence of almost coincident buckling modes makes these structural elements very sensible to the imperfections. The imperfection sensitivity can be examined either theoretically, using asymptotic analysis based on single or multimode analysis, Budiansky (1974), or through nonlinear analysis of imperfect configurations introducing imperfections of known shape and amplitude, Simitses *et al.* (1985). In this work, an asymptotic method has been used to study the initial post-buckling behaviour of composite cylinders subject to axial load and torsion. The imperfection sensitivity curves obtained for a composite cylinder subject to the combination of these actions are discussed and compared to numerical values produced by means of detailed finite element models. The results are limited to single modes but it is shown how they can be significant even if they are quite different from the real imperfections in the structure.

Other important imperfections influencing the buckling behaviour of composite shells can be produced during the manufacturing process. In hand lay-up cylinders they consist in thickness variations due to the overlapping of successive plies and in possible misalignments of the fibers from the nominal directions. Chryssanthopoulos *et al.* (1995) showed that thickness variations could be thought of as longitudinal stiffeners of low rigidity and, hence, their influence is expected to be noticeable only if their spacing and stiffness induce the cylinder into a buckling mode different from that corresponding to their counterpart of uniform thickness. Misalignments of the fibers from the nominal orientations have been detected both in flat specimens, used for material characterisations, and in real parts. The effects on buckling behaviour are here investigated by means of analytical models varying the angles of misalignment in the range admitted by common manufacturing specifications.

BASIC EQUATIONS

A brief description of the asymptotic method used in the present study is here included. Part of the formulation was presented in Poggi *et al.* (1991). Consider a cylindrical shell of radius R , length L and thickness t as shown in Fig. 1, where the coordinate system is indicated. The displacements of the middle surface are denoted by u and v along the longitudinal and circumferential directions respectively and by w along the normal to the surface (positive outward).

The nonlinear equation of equilibrium and related boundary conditions are derived from the principle of stationarity of the total potential energy and are based on Donnell-type kinematic relations (moderately large rotations). It has been demonstrated that this assumption is adequate for thin shells that tend to buckle with circumferential wave numbers greater than four, Kardomateas (1996), Geier and Singh (1997). The material is supposed to have linearly elastic behaviour. Introducing a stress function F allows to reduce the problem to two nonlinear equations

$$L_1[F] - L_2[w] = -\frac{1}{2} L_{NL}[w, w] \quad (1a)$$

$$L_2[F] + L_3[w] = L_{NL}[F, w]. \quad (1b)$$

The form of the differential operators may be found in Poggi *et al.* (1991).

If the classical buckling load parameter λ_c is assumed to be associated to a single buckling mode w_1 and

the corresponding stress function F_1 , the initial post-buckling behaviour can be investigated expanding the functions w and F in the form

$$\begin{aligned} w &= w_0 + w_1\varepsilon + w_2\varepsilon^2 + \dots \\ F &= F_0 + F_1\varepsilon + F_2\varepsilon^2 + \dots \\ \frac{\lambda}{\lambda_c} &= 1 + a\varepsilon + b\varepsilon^2 + \dots \end{aligned} \quad (2a-c)$$

where ε is the perturbation parameter.

Introducing the prebuckling solution, that is considered to be linearly related to the load parameter λ , into the nonlinear Eqs. (1a-b) generates various sets of linear differential equations that allow to determine w_1 and F_1 . These quantities correspond to the classical buckling mode and stress function.

If the cylinder is subject to axial load and torsion, the radial displacement corresponding to the classical buckling mode for the perfect cylinder assumes the form

$$w_1 = t \sin\left(\frac{m\pi x}{L}\right) \cos\left[\frac{n}{R}(y - \tau x)\right] \quad (3)$$

where m and n are the number of half-waves and full-waves in the longitudinal and circumferential directions respectively while τ generates the coupling between the curvatures k_x and k_y with k_{xy} . This allows to use the model in presence of torsional loads. The expressions of w_2 and F_2 are not reported here for sake of brevity. The initial post-buckling behaviour and the influence of imperfections are investigated on the basis of the asymptotic theory determining the two coefficients normally called "a" and "b", Budiansky (1974).

If the imperfections, \bar{w} , are similar to a buckling mode associated to the critical load λ_c , then the equation relating the load to the buckling deflection in the initial postbuckling regime becomes :

$$\left(1 - \frac{\lambda}{\lambda_c}\right)\varepsilon + b\varepsilon^3 = \frac{\lambda}{\lambda_c} \frac{\bar{w}}{t} \quad (4)$$

The buckling load of the imperfect structure, λ_s , may be obtained maximizing λ which leads to the following well known equation,

$$\left(1 - \frac{\lambda_s}{\lambda_c}\right)^{3/2} = \frac{3\sqrt{3}}{2} \sqrt{-b} \left| \frac{\bar{w}}{t} \right| \frac{\lambda_s}{\lambda_c} \quad (5)$$

BUCKLING AND POSTBUCKLING ANALYSIS

The imperfection sensitivity of two series of cylinders was studied on the basis of the asymptotic theory validated by simulations with finite element models. Two geometries and various laminations were analysed. The specimens indicated with the symbols B, as reported in Tables 1-2, were tested in Braunschweig by Geier, Klein and Zimmermann (1991) while the ones indicated with the symbol M were studied at Politecnico of Milano by Bisagni (1996). The laminations, the geometries and the material characteristics are reported in Table 1 and 2. The layers of specimens B and M2 were made of unidirectional carbon fibers while carbon fabric was used for specimens M1.

TABLE 1
COMPOSITE CYLINDER LAMINATIONS

Cylinder	Lamination (inner → outer)
B1 (optimum)	$\pm 30 \pm 90 \pm 22 \pm 38 \pm 53$
B2 (pessimum)	$\pm 51 \pm 45 \pm 37 \pm 19 \pm 0$
B3 (B2 reversed)	$\pm 0 \pm 19 \pm 37 \pm 45 \pm 51$
M1	0,45,-45,0
M2	(45,-45,45,-45) _s

TABLE 2
CYLINDER GEOMETRIES AND LAYER
CHARACTERISTICS

[N , mm]	B1-B2-B3	M1	M2
Radius	250.6	350	350
Layer thickness	0.125	0.33	0.15
Length	510	534	534
E ₁₁	123550	52000	120000
E ₂₂	8707.9	52000	8000
ν_{12}	0.319	0.302	0.223
G ₁₂	5695	2350	3978

The specimens of group B were designed to maximise or minimise the buckling load. The number of plies n_p was kept constant while the orientation was varied according to a sequence $\pm\theta$. The laminations of the cylinders here examined were respectively the *optimum*, the *pessimum* and the *pessimum* with the laminae oriented in the *reverse* sequence. The optimisation procedure, studied by Zimmermann (1989), is based on mathematical programming and needs a quick tool to evaluate the buckling load of each lamination that cannot be neither a numerical model to solve the governing equations nor a finite element model. Simple analytical solutions should be used even if some simplifying hypothesis must be introduced. In the case of composite cylinders the analytical calculation performed by Zimmermann were based, like in the present work, on the assumptions of a uniform membrane state of stress in the prebuckling region. It is known that in the reality the boundary conditions at the edges of the cylinders prevent the radial expansion of the cylinder and, as a consequence, circumferential membrane stresses are produced. Nevertheless, it has been demonstrated that, for isotropic cylinders, this hypothesis reduces the buckling load of about 15%, see Fischer (1963). The experimental results of the cylinders of Table 1 can be found in Geier and Singh (1997).

The groups of specimens named M1-M2 comprises nominally identical cylinders that were constructed for an experimental project developed at Politecnico of Milano. The specimens were built using the methods of hand lay-up with plies made of carbon fabric for M1 and carbon unidirectional fibres for M2, embedded into epoxy resin. The plies were wrapped around a cylindrical mandrel and each layer was made up of two pieces of fabric of width πR and length L . The overlapping of the pieces causes a thickness variation that can be detected even manually. In order to avoid excessive thickness variations, the successive plies were joined together at different circumferential positions. The cylinders tested in Milano were accurately examined to measure the geometric imperfections and evaluate their main features. In fact in shell structures the assessment of the effects of imperfections can be obtained only from a complete map of the surface. The measurements can be recorded in different ways depending on the level of detail required, Arboz (1983) and Chryssanthopoulos *et al.* (1995).

The buckling analysis of the cylinders of Table 1 was conducted using the analytical procedure presented above. This allowed to determine the buckling loads associated to different modes and to derive the relevant imperfection sensitivity curves. It is known that single mode analyses can suffer of some limitations mainly when the cylinder presents multiple bifurcations. In fact, composite cylinders with some particular laminations and subject to axial compression can present almost coincident

buckling modes in a way similar to isotropic cylinders. A multimode imperfection sensitivity analysis would be desirable but this is not immediate and can be solved mainly numerically. Analytical solutions for bimodal analysis were presented in Poggi *et al.* (1991). Nevertheless a single mode analysis can provide useful information regarding the imperfection sensitivity of the structure under consideration and sometimes a good estimate of the real buckling load, Geier and Singh (1997).

TABLE 3
BUCKLING LOADS FOR AXIAL COMPRESSION

	N_x [N/mm]	P_{tot} [kN]	buckling mode [n,m, τ]	b coeff
B1a	183.51	288.98	6,13,0	-2.76
B1b	175.34	276.21	8,10,-0.81	-1.89
B2	62.35	97.29	13,1,0	-0.011
B3	113.11	178.12	1,7,0	-0.058
M1	108.92	239.53	7,14,0	-2.061
M2	55.52	102.09	13,2,0	-0.090

Fig. 1 : Cylinder geometry

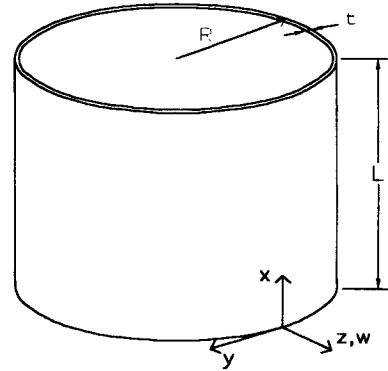


Table 3 reports the buckling loads per unit length obtained for each cylinder. It is important to notice that cylinder B1a presented the so called 'classical boundary conditions' where the torsional rotation of each circumferential edge is prevented while in cylinder B1b the torsional degree of freedom was released. The buckling load of B1a is 4.6% higher and presents 6 axial half-waves and 13 circumferential waves. In what follows, cylinder B1a (optimum lay-up) will be used as reference value. It presents the maximum buckling load while B2 and B3 buckle for loads that are only a fraction of the first one. In particular the critical load of B2 (pessimism lay up) is only equal to 34% of B1 while for B3 (reversed pessimism) the buckling load is twice B2 but still only 61% of B1. The apparent advantage in adopting the optimum lay-up must be verified with an imperfection sensitivity analysis at least for single modes. The adimensional imperfection sensitivity curves of specimens B are reported in Fig. 2 and are referred to single mode analysis assuming that the imperfection mode had the same shape of the buckling mode. The imperfection sensitivity curve of B1b, not reported here, is similar to B1a with a maximum difference comparable with the difference of the buckling loads.

From Figure 2 it is immediate to verify that the optimum lay-up shows the highest imperfection sensitivity. This confirms that an optimisation process can maximise the buckling load but the relevant imperfection sensitivity curves should be considered at least for single modes. The knock-down factor for an imperfection with maximum amplitude equal to 0.5 times the thickness varies from 0.32, for cylinder B1 with the optimum lay-up, to 0.75 for cylinder B2 that presents the 'pessimism' orientation of the layers. Cylinder B3 ('pessimism reversed') has an intermediate behaviour. In conclusion the collapse loads of cylinder B1 for this amplitude of the imperfection is approximately 93 kN against 73 kN of cylinder B2. This confirms how the designer should pay attention in trying to optimise the cylinder laminations in term of buckling load. Design oriented knock-down factors are not available today for composite cylinders but there is a considerable effort to formulate reliable proposals for various loadings and geometries.

The nondimensional imperfection amplitudes were examined up to value of 0.5 that is a reasonable limit of validity of the asymptotic method. In order to verify the accuracy of the method some cases were analysed also using finite element models of the cylinders including the geometric imperfections. The

results for cylinder M2 are reported in Figure 3 that shows the imperfection sensitivity curve compared to the obtained numerical results. The maximum difference is lower than 5% but becomes higher for values of w/t larger than 0.5 confirming the range of validity of the method.

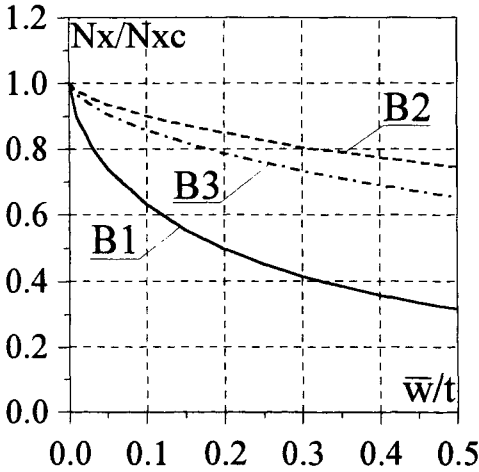


Figure 2: Imperfection sensitivity for axial load

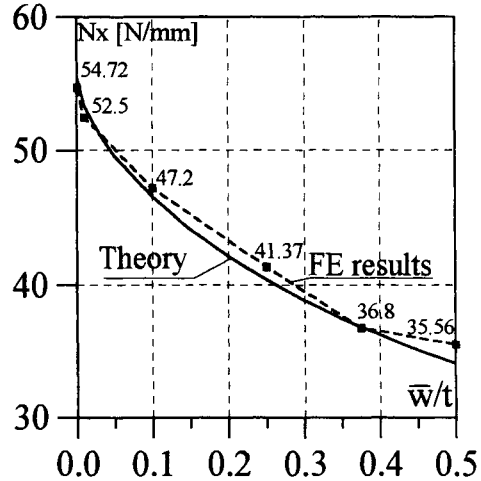


Figure 3 : Theory against finite element

Buckling loads and imperfection sensitivity curves were derived also for the case of torsional forces applied to the cylinder, Figure 4. The results are presented in Table 4 for clockwise and anticlockwise torsional moments. The variation of the results is small for the cylinders of group B and for M1 while the difference in the case of cylinder M2 is significant. This can be explained by the particular lamination and the type of lamina made of unidirectional fibers. Further analyses for different ratios of M_t/N were also conducted and the limit loads were calculated according to the theory presented above. This allowed to produce interaction diagrams that are reported in Figures 5-6 for cylinders B1 and M2 respectively. The behaviour of cylinder B1, Figure 5, is practically symmetric in terms of torsional behaviour with a small difference of about 5% in terms of buckling load. The curves relevant to the cases with geometric imperfections are also reported and show how the domains become smaller but with the same shape of the interaction curve of the perfect cylinder. The decrease of the limit load is evidently higher when the axial load alone is acting on the shell while the intersections of the dominia with the vertical axis are similar in the case of clockwise and anticlockwise moments. Different are the curves reported in Figure 6, where there is an evident asymmetry of the behaviour and the differences of the torsional buckling moments are significant. The imperfection sensitivity is still more pronounced when the axial load alone is present.

LAMINATION DEFECTS

The construction methods of composite cylinders can be the origin of misalignments or deviations of the fibre orientation from the nominal value. In particular, the quality of the method of hand-lay-up depends on the accuracy of the operator that joins together various pieces of fabric. The final product is influenced also by the position of the joints and their thickness that can cause a change in the buckling mode and, as a consequence, in the buckling load. The precision in the orientation of the fibres is frequently insured by the acceptance specifications imposed by the manufacturer but the designer should be aware of the effects of these possible defects in the calculations of the bearing capabilities of the

structure.

TABLE 4
BUCKLING LOADS FOR TORSION

	N_{xy} [N/mm] clockwise	mode [n,m]	N_{xy} [N/mm] anticlock.	mode [n,m]
B1b	41.41	1,10	43.52	1,10
B2	30.98	1,12	34.07	1,10
B3	23.86	1,11	24.61	1,11
M1	31.51	1,11	31.51	1,11
M2	18.32	1,12	24.17	1,10



Fig. 4 : Buckling mode for torsion

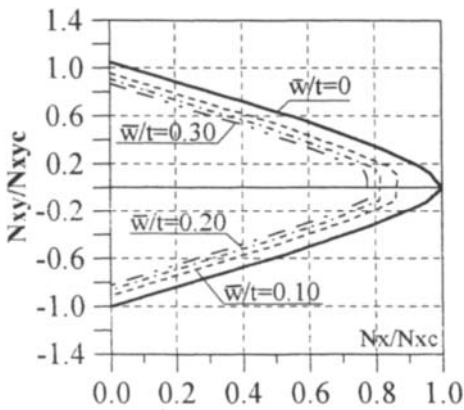


Fig. 5 : Buckling loads for cylinders B1 subject to axial load and torsion

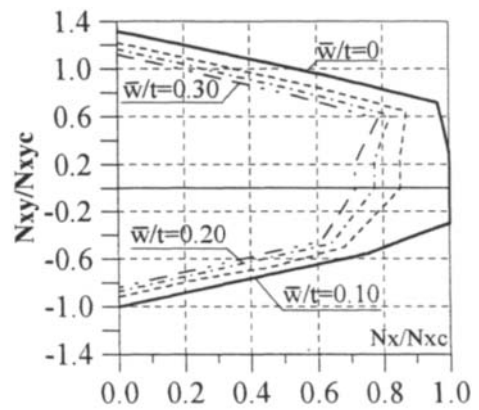
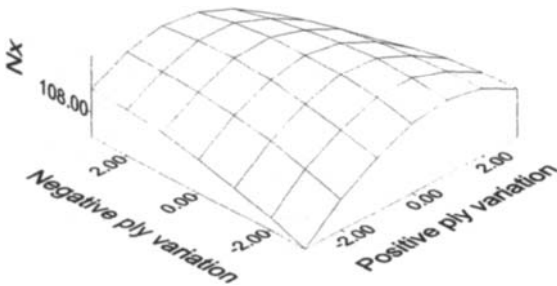


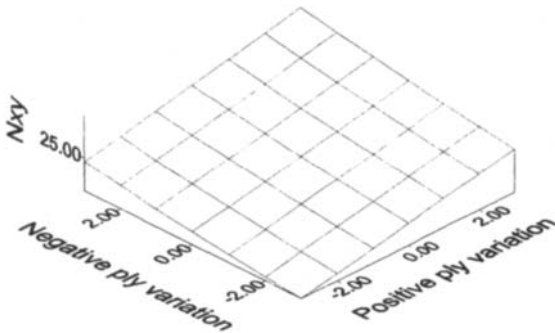
Fig. 6 : Buckling loads for cylinders M2 subject to axial load and torsion

In this work the effects of misalignments of the fibres from the nominal orientation have been analysed in terms of variation of the buckling load of a cylinder. The cylinders B3,M1 and M2 have been examined considering a variation of the fibres within a range of $\pm 3^\circ$. Because of the number of plies of each cylinder, the same orientation defect has been applied simultaneously to all the plies with positive or negative orientation. This allows to plot the surfaces representing the buckling load in terms of the variation of the angles for the 'positive plies' or 'negative plies'. The results showed that the variation of the buckling load for axial compression is usually low and varies within the range of 2-3% on the positive or negative side. For cylinder M1, as reported in Figure 7, the ply orientation defects cause only a decrease of the buckling load limited to 1.5%. The variation of the anticlockwise torsional buckling load is represented in Figure 8. In this case the variation is significant and is included in the range limits -7.4% and +8.9%.



Ply with + angle	Ply with - angle	$N_{\sigma} = 108.92$ (N/mm)
0°	0°	1
0°	-3°	0.998
0°	+3°	0.998
-3°	0°	0.991
+3°	0°	0.991
-3°	-3°	0.985
-3°	+3°	0.994
+3°	+3°	0.985
+3°	-3°	0.994

Figure 7: Axial load for $\pm 3^\circ$ variation of the ply orientation - Cylinder M1



Ply with + angle	Ply with - angle	$N_{\sigma} = 24.17$ (N/mm)
0°	0°	1
0°	-3°	0.974
0°	+3°	1.035
-3°	0°	0.950
+3°	0°	1.051
-3°	-3°	0.926
-3°	+3°	0.982
+3°	+3°	1.089
+3°	-3°	1.023

Figure 8 : Torsional anti-clockwise load for $\pm 3^\circ$ variation of the ply orientation - Cylinder M2

CONCLUSIONS

The problem of buckling and post-buckling of composite cylinders subject to axial load and torsion was examined. The effects of the geometric imperfections were included and the influence of possible defects in the lamination were analysed. The most important conclusions are here summarised:

- Composite cylinders subject to axial compression may be very sensitive to initial imperfections as isotropic geometries.
- The optimisation of the lamination sequence in terms of the buckling load leads to high imperfection sensitive structures while other laminations can be low sensitive.
- Laminated cylinders under torsion are less sensitive to geometric imperfections than under compression
- The buckling torsional load can be significantly different in clockwise or anticlockwise directions.
- The influence of lamination defects can be significant and should be considered in a design procedure according to the adopted manufacturing process.

REFERENCES

- Arbocz J (1983). Shell Stability Analysis: Theory and Practice' in *Collapse: The Buckling of Structures in Theory and in Practice*, J.M.T. Thompson and G.W. Hunt (eds), Cambridge University Press, 43-74.
- Bisagni C. (1996). Buckling and Post-buckling Behaviour of Composite Cylindrical Shells. Proc. of XX ICASS Conference, Sorrento Italy.
- Budiansky B.(1974). Theory of Buckling and Post-Buckling Behaviour of Elastic Structures. *Advances in Applied Mech.*, 14,1-65.
- Chryssanthopoulos M., V.Giavotto, C.Poggi (1995). Characterization of Manufacturing Effects for Buckling-sensitive Composite Cylinders' *Composite manufacturing*, 6, 93-101.
- Chryssanthopoulos M., Poggi C. (1995). Probabilistic Imperfection Sensitivity Analysis of Axially Compressed Composite Cylinders. *Engineering Structures*, 17:6, 398-406.
- European Convention for Constructional Steelwork (1988). *Buckling of Steel Shells* European Recommendations, Fourth Edition,.
- Fischer G.(1963). Uber den Einfluss der gelenkigen Lagerung auf die Stabilitat dunnwandiger Kreiszyinderschalen unter Axiallast und Innendruck. *Zeitschrift fur Flugwissenschaften*, 3, 111-119.
- Geier B., Klein H., Zimmermann R. (1991). Buckling Tests with Axially Compressed Unstiffened Cylindrical Shells Made from CFRP. In *Buckling of Shell Structures on Land, in the Sea and in the Air*. Elsevir Science, London, 498-507.
- Geier B. and Singh G. (1997). Some Simple Solutions for Buckling Loads of Thin and Moderately Thick Cylindrical Shells and Panels Made of laminated Composite Material. *Aerospace Science and Technology*, 1, 47-63.
- Kardomateas G.A. (1996). Benchmark Three-dimensional Elasticity Solutions for the Buckling of Thick Orthotropic Cylindrical Shells. *Composites Part B*, 27B, 569-580.
- Poggi C., Taliercio A., Capsoni A. (1991). Fibre Orientation Effects on the Buckling Behaviour of Imperfect Composite Cylinders. In *Buckling of Shell Structures on Land, in the Sea and in the Air*. Elsevir Science, London, 498-507.
- Simitses G.J., Shaw D., Sheinman I. (1985). Imperfection Sensitivity of Laminated Cylindrical Shells in Torsion and Axial Compression", *Composite Structures*, 4, 335-360.
- Zimmermann R.(1989). Optimization of Axially Compressed Fiber Composite Cylindrical Shells. In *Optimisation: Methods and Applications, Possibilities and Limitations*. ed. H.W. Bergmann, Springer Verlag, Berlin, 63-82.

This Page Intentionally Left Blank

INFLUENCE OF SHEAR DEFORMATION ON GEOMETRICALLY NON-LINEAR DEFLECTIONS OF COMPOSITE LAMINATED PLATES

T. S. Lok and Q. H. Cheng

School of Civil and Structural Engineering
Nanyang Technological University, Nanyang Ave., Singapore 639798

ABSTRACT

Geometrically non-linear deformations including the effects of transverse shear strains of composite laminated plates are investigated using the perturbation finite element method (PFEM). The PFEM is more economic in terms of computational time than conventional finite element iterative procedure. To account for the transverse shear strains, a discrete-layer shear deformation theory is introduced. This approach predicts more accurately the distribution of displacements and stresses through the thickness than single-layer theories. The perturbation finite element solutions are shown to be in good agreement with published experimental and numerical results.

KEYWORDS

Composite laminated plate, finite element method, perturbation method, non-linear flexural behaviour, transverse shear deformation.

NOTATIONS

\underline{u}	$= [u \ v \ w]^T$	vector of displacement; the superscript T denotes the transformation.
$\underline{\phi}$	$= [\phi_x \ \phi_y]^T$	rotation of normal lines in xz and yz planes.
$\underline{\varepsilon}$	$= [\varepsilon_x \ \varepsilon_y \ \varepsilon_{xy}]^T$	vector of in-plane strains.
$\underline{\gamma}$	$= [\gamma_{xz} \ \gamma_{yz}]^T$	vector of transverse shear strains.
$\underline{\kappa}$	$= [\kappa_x \ \kappa_y \ \kappa_{xy}]^T$	bending and twisting curvature.
\underline{N}	$= [N_x \ N_y \ N_{xy}]^T$	resultants of in-plane forces.
\underline{M}	$= [M_x \ M_y \ M_{xy}]^T$	bending and twisting moments.
\underline{Q}	$= [Q_{xz} \ Q_{yz}]^T$	resultants of transverse shear forces.
\underline{q}	$= [q_x \ q_y \ q_{xy}]^T$	external loads distributed on surface.

INTRODUCTION

The inherent properties of composites in terms of strength, stiffness and minimum weight makes the material suitable for lamination as thin-walled plates. For these structures, geometrically non-linear deformation occurs, even at low load application levels. Further, most composite materials possess a high ratio of elastic to shear modulus which, in turn, leads to additional transverse shear deformation.

Generally, there are two theories which can be used to account for the effect of shear deformation. These are:

- a. single layer plate models - first-order and higher-order shear deformation theory can predict accurately the global deformation of the laminate. However, these are insufficiently accurate for predicting the distribution of deformations and stresses through the thickness, and
- b. discrete layer model - in which a plate is divided into several sub-layers through its thickness and the displacement fields are constructed for each sub-layer. This model is preferred because it is more accurate for predicting the response of laminated composites.

Qian (1947) obtained large-deflection solutions of circular plates by the perturbation method although geometrically non-linear deformation of isotropic and anisotropic plates was subsequently investigated by a number of authors (e.g. Stavsky, 1964). In the method by Qian, non-linear equations are converted into linear forms. In this way, the equations can be easily solved. Unfortunately, the method is not applicable to plate structures with irregular shapes and complicated boundaries. For such problems, the finite element method is more appropriate. However, additional problems such as memory storage and computational time further restrict its application especially in a non-linear analysis.

By combining the perturbation method and the finite element method, the perturbation finite element method (PFEM) was developed. This was successfully applied in a geometrically non-linear analysis of axi-symmetric shells (Xie, *et al.*, 1984). The principle is that by introducing perturbation procedures to the non-linear variational formulation, independent linear variational perturbation equations are established which can then be solved using the finite element method.

In this paper, geometrically non-linear deformation of composite laminates is computed using the perturbation finite element method. To account for transverse shear effect, a discrete-layer theory (Xie & Li, 1989) is adopted in which the displacement field of each sub-layer is constructed. Numerical results are obtained and it is shown that the perturbation finite element solutions are in good agreement with exact solution, experimental data and calculated numerical results from other investigators.

FORMULATIONS

Basic Equations

The laminate considered here is made up of a number of thin flat sub-layers. Fig. 1 shows a typical section of a laminate comprising $(N^a + N^b)$ sub-layers. The origin of the global co-ordinate system (x, y, z) is taken in the reference plane with the z -axis perpendicular to the plane. The n^{th} sub-layer is considered as an orthotropic material as shown in Fig. 2; l -axis is oriented in the fibre direction and at an angle θ to the x -axis. The properties of this material is described by elastic moduli E_1 & E_2 , shear moduli G_{13} & G_{23} , and Poisson's ratios ν_{13} & ν_{23} .

Based on the straight-normal hypothesis of the Mindlin theory, the displacement field of the n^{th} sub-layer may be written as (with reference to Fig. 3):

$$\underline{u}_n = \underline{u}_n^0 - \zeta_n \begin{Bmatrix} \phi_{xn} \\ \phi_{yn} \\ 0 \end{Bmatrix} = \underline{u}_n^0 - \zeta_n \begin{Bmatrix} \frac{\partial w_n}{\partial x} - \gamma_{xzn} \\ \frac{\partial w_n}{\partial y} - \gamma_{yzn} \\ 0 \end{Bmatrix} \quad (1)$$

where \underline{u}_n^0 is the displacement vector at the mid-plane of the n^{th} sub-layer where the local co-ordinate ζ_n -axis (which is in the direction of the z -axis) originates. Imposing the continuity conditions of displacement between adjacent sub-layers, the above displacement field becomes:

$$\underline{u}_n = \underline{u}_0 - (z_n + \zeta_n) \begin{Bmatrix} \frac{\partial w_0}{\partial x} - \gamma_{xzn} \\ \frac{\partial w_0}{\partial y} - \gamma_{yzn} \\ 0 \end{Bmatrix} \quad (2)$$

where z_n is the z -axis value of the mid-plane of the n^{th} sub-layer, and \underline{u}_0 is the displacement of the reference plane.

Substituting Eqn. 2 into the Von Karman non-linear strain-displacement relationship, the strain field of the n^{th} sub-layer (ignoring higher-order minors) may be written as:

$$\underline{\varepsilon}_n = \underline{\varepsilon}_n^0 + \zeta_n \underline{k}_n = \underline{\varepsilon}_{n(l)}^0 + \underline{\varepsilon}_{n(n)}^0 + \zeta_n \underline{k}_n \quad (3a)$$

$$\underline{\gamma}_n = [\gamma_{xzn} \quad \gamma_{yzn}]^T \quad (3b)$$

$$\text{where } \underline{k}_n = \begin{Bmatrix} -\frac{\partial^2 w_0}{\partial x^2} + \frac{\partial \gamma_{xzn}}{\partial x} \\ -\frac{\partial^2 w_0}{\partial y^2} + \frac{\partial \gamma_{yzn}}{\partial y} \\ -2\frac{\partial^2 w_0}{\partial x \partial y} + \frac{\partial \gamma_{xzn}}{\partial y} + \frac{\partial \gamma_{yzn}}{\partial x} \end{Bmatrix}, \quad \underline{\varepsilon}_{n(l)}^0 = \begin{Bmatrix} \frac{\partial u_0}{\partial x} - z_n \frac{\partial^2 w_0}{\partial x^2} \\ \frac{\partial v_0}{\partial y} - z_n \frac{\partial^2 w_0}{\partial y^2} \\ \frac{\partial u_0}{\partial y} + \frac{\partial v_0}{\partial x} - 2z_n \frac{\partial^2 w_0}{\partial x \partial y} \end{Bmatrix}, \quad \underline{\varepsilon}_{n(n)}^0 = \begin{Bmatrix} \frac{1}{2} \frac{\partial w_0}{\partial x} \frac{\partial w_0}{\partial x} \\ \frac{1}{2} \frac{\partial w_0}{\partial y} \frac{\partial w_0}{\partial y} \\ \frac{\partial w_0}{\partial x} \frac{\partial w_0}{\partial y} \end{Bmatrix},$$

and the subscripts (l) and (n) denote linear and non-linear normal strains, respectively.

Variational Formulation

The laminate is acted upon by distributed loads q_t on the top face, q_b on the bottom face and several concentrated loads indicated as P_c ($c = 1, 2, \dots$) as shown in Fig. 1. The corresponding generalised displacements are \underline{u}_t , \underline{u}_b and u_c respectively. Thus, the variational formulation of the minimum potential energy principle takes the form:

$$\begin{aligned}
 & \left(\sum_{n=1}^{N'} + \sum_{n=1}^{N^b} \right) \int (\delta \underline{\varepsilon}_n^{0T} \underline{A}_n \underline{\varepsilon}_n^0 + \delta \underline{\kappa}_n^T \underline{D}_n \underline{\kappa}_n + \delta \underline{\gamma}_n^T \underline{G}_n \underline{\gamma}_n) dx dy \\
 & - \int (\delta \underline{u}_i^T \underline{q}_i + \delta \underline{u}_b^T \underline{q}_b) dx dy - \sum_c \delta u_c P_c = 0
 \end{aligned} \tag{4}$$

where \underline{A}_n , \underline{D}_n and \underline{G}_n are extension, bending and shearing stiffness of the n^{th} sub-layer respectively.

Perturbation Method

To apply the perturbation method, all variables involved in the formulation are set non-dimensional by multiplying an appropriate factor to each variable. The non-dimensional maximum deflection of the laminate, $\Delta (= w_{0(max)}/H)$, is selected as the perturbation factor. Thus, the displacement, strains, curvature and load can be expressed respectively as:

$$\underline{u} = \sum_{k=1}^{\infty} \underline{u}^{(k)} \Delta^k \quad \underline{\varepsilon}_n^0 = \sum_{k=1}^{\infty} \underline{\varepsilon}_n^{0(k)} \Delta^k \quad \underline{\gamma}_n = \sum_{k=1}^{\infty} \underline{\gamma}_n^{(k)} \Delta^k \quad \underline{\kappa}_n = \sum_{k=1}^{\infty} \underline{\kappa}_n^{(k)} \Delta^k \quad \alpha = \sum_{k=1}^{\infty} \alpha^{(k)} \Delta^k \tag{5}$$

where α is a constant proportion factor by which all external loads are increased systematically in a step-by-step manner. \underline{q}_i , \underline{q}_b and P_c are now replaced by $\alpha \underline{q}_i$, $\alpha \underline{q}_b$ and αP_c respectively.

It can be shown that the k^{th} -order perturbation variational equation may be written as:

$$\begin{aligned}
 & \sum_n \int_{\Omega_0} (\delta \underline{\varepsilon}_n^{0(k)T} \underline{A}_n \underline{\varepsilon}_n^{0(i)} + \beta^2 \delta \underline{\kappa}_n^{(k)T} \underline{D}_n \underline{\kappa}_n^{(i)} + \frac{G}{E} \frac{1}{e^2} \delta \underline{\gamma}_n^{(k)T} \underline{G}_n \underline{\gamma}_n^{(i)}) dx dy \\
 & + \sum_n \int_{\Omega_0} (\delta \underline{\eta}_1^{(k)} \sum_{j=1}^{i-1} \xi_1^{(j)} \underline{A}_n \underline{\varepsilon}_n^{0(i-j)} + \delta \underline{\eta}_2^{(k)} \sum_{j=1}^{i-1} \xi_2^{(j)} \underline{A}_n \underline{\varepsilon}_n^{0(i-j)}) dx dy \\
 & - \frac{1}{\beta} \int_{\Omega_0} (\delta \underline{u}_i^{(k)T} \underline{q}_i + \delta \underline{u}_b^{(k)T} \underline{q}_b) \alpha^{(i)} dx dy - \frac{1}{\beta} \sum_c \delta u_c^{(k)} P_c \alpha^{(i)} = 0
 \end{aligned} \tag{6}$$

where $e = H/L$, $\beta = h/H$. L is the width and h is the thickest sub-layer of the laminate. E and G are the largest elastic modulus E_1 and shear modulus G_{13} of all the sub-layers respectively. $\underline{\eta}_1$, ξ_1 , $\underline{\eta}_2$ and ξ_2 are derived from non-linear strains and are themselves linear.

Finite Element Solution

A displacement-based three-node triangular element model has been developed. Over each element, displacement interpolation functions are assumed and all variables are derived in relation to the generalised nodal displacement vector:

$$\underline{a} = [\underline{u}_0^T \quad -\frac{\partial w_0}{\partial y} \quad \frac{\partial w_0}{\partial x} \quad \underline{\gamma}_{1'}^T \quad \underline{\gamma}_{2'}^T \quad \cdots \quad \underline{\gamma}_{N'}^T \quad \underline{\gamma}_{1^b}^T \quad \underline{\gamma}_{2^b}^T \quad \cdots \quad \underline{\gamma}_{N^b}^T]^T \tag{7}$$

Substituting the interpolation for all variables into Eqn. 6 and integrating over the element using the Gauss numerical integration procedure, the element stiffness matrix and force vector are derived. Adding the contributions of all elements in the domain, an expression may be obtained as:

$$\underline{K} \underline{a}^{(k)} = \alpha^{(k)} \underline{F}_C - \underline{F}_A^{(k)} - \underline{F}_B^{(k)} \quad (k \geq 1) \tag{8}$$

where \underline{K} is the global stiffness matrix, $\underline{a}^{(k)}$ and $\alpha^{(k)}$ are unknowns and \underline{F}_C is a constant vector in relation to the external loads. $\underline{F}_A^{(k)}$ ($k \geq 2$) and $\underline{F}_B^{(k)}$ ($k \geq 3$) are additional vectors associated with non-linear strains from J^{st} to $(k-1)^{th}$ perturbation steps. These vectors are known at the k^{th} step.

Eqn. 8 can be solved step-by-step from $k=1$ to a certain k^{th} value such that the desired solution accuracy is satisfied; usually five steps is adequate. The solution of the first step, i.e. when $k=1$, is the linear response. Non-linear deformation is obtained for $k>1$. The stiffness matrix \underline{K} remains unchanged at each perturbation step. Therefore, the method requires less computational time than a standard iterative procedure for non-linear analysis.

NUMERICAL RESULTS AND DISCUSSION

To demonstrate the applicability of the method discussed above, several examples with different material properties, ply angles and orientation, boundary conditions and loading types are provided. Computed results with and without the influence of shear deformation are shown. The boundary conditions used in the study are summarised in Table 1.

Solution Without Shear Deformation

To test the accuracy of the perturbation finite element method, linear and non-linear deformations of a simple-supported 4-ply ($0^\circ/90^\circ/90^\circ/0^\circ$) symmetric square plate ($a=b=12$ in., $h=0.096$ in.) subjected to uniform loading q_0 are calculated and plotted in Fig. 4. The material properties are: $E_1=1.8282 \times 10^6$ psi, $E_2=1.8315 \times 10^6$ psi, $G_{12}=G_{13}=G_{23}=0.3125 \times 10^6$ psi, and $\nu=0.23949$.

It is observed for this cross-ply plate that the PFEM linear solution is in good agreement with the higher-order shear deformation plate theory (HSDPT) result of Putchá & Reddy (1986) and the classical plate theory (CPT) finite difference result of Zaghoul & Kennedy (1975). For the non-linear comparisons, the PFEM solution is closer to the classical plate theory (CPT) finite difference result but exhibits slight disparity with experimental results and the higher-order theory solution. The reason, as stated by Zaghoul & Kennedy (1975), is that transverse shear deformations have not been accounted for in their analysis.

Solution With Shear Deformation Included

To account for the effect of transverse shear strain on the deflection of a four-layer ($0^\circ/90^\circ/90^\circ/0^\circ$) symmetric cross-ply plate, an analysis was undertaken for different width (L) to thickness (H) ratios. The plate is subjected to a sinusoidal distributed loading of the form $q=q_0 \sin(\pi x/L + \pi/2) \sin(\pi y/L + \pi/2)$ with $x=0$ and $y=0$ at the centre of the plate. The material properties used are: $E_1/E_2=25$, $G_{12}=G_{13}=0.5E_2$, $G_{23}=0.2E_2$, and $\nu_{12}=\nu_{13}=0.25$.

Results of the linear analysis are plotted in Fig. 5. Computed results are almost identical to the 3-D elasticity solution and the closed-form solution for a range of L/H ratios; the latter two results were derived by Reddy & Chao (1981). When shear deformation is neglected, the result is not surprising; constant response is obtained regardless of the width to thickness ratio.

One measure of the effect of transverse shear is to consider the transverse shear coefficient (r) at the centre of the plate where maximum deflection occurs. Transverse shear coefficients have been computed and are shown in Table 2 for the above four-layer symmetric cross-ply plate. It is seen that as width (L) to thickness (H) ratio decreases, the influence of transverse shear increases rapidly.

Finally, to investigate the influence of transverse shear on the non-linear deformation under different boundary conditions, two square laminated plates are analysed. The plates are subjected to sinusoidal distributed loading of the form $q=q_0\sin(\pi x/L+\pi/2)\sin(\pi y/L+\pi/2)$ with $x=0$ and $y=0$ at the centre of the plate. The material properties are: $E_1/E_2=2.5$, $G_{12}=G_{13}=0.5E_2$, $G_{23}=0.2E_2$, and $\nu_{12}=\nu_{13}=0.25$. Details of the two plates, each comprising four layers, are (a) symmetric cross-ply ($0^\circ/90^\circ/90^\circ/0^\circ$); and (b) anti-symmetric angle-ply ($45^\circ/-45^\circ/45^\circ/-45^\circ$).

Computed transverse shear coefficients (r) are shown in Table 3, and from which the following observations can be summarised:

- the effect of transverse shear strains is less significant on large deflections than on small deflections of laminated plates except for symmetric cross-ply simply-supported (SS) and hinge-supported (HS) plates which change little when deflections become large;
- the effect of shear deformation on SS plates, which is approximately the same as that of HS plates, is less than those of clamped (CC) and fixed (FF) plates. This is because shear deformation is influenced by the rotational restraints at the boundaries; CC and FF plates have high rotational restraints while it is absent on SS and HS plates;
- for linear small deflections, the shear effects on the anti-symmetric angle-ply laminate are larger than those of symmetric cross-ply laminate with SS and HS boundary conditions, but are completely reverse for CC & FF boundary conditions;
- for non-linear large deflections, the shear effects on the anti-symmetric angle-ply laminate are larger than those of symmetric cross-ply laminate regardless of the boundary condition.

CONCLUSIONS

A perturbation finite element model has been presented for the geometrically non-linear analysis of laminated plates. The model is formulated from a discrete-layer shear deformation theory. The advantages of the model are (a) accurate representation of displacements, (b) rapid convergence of the solution and (c) low computation time.

Several examples showing linear and non-linear numerical results of laminated anisotropic square plates including the effects of shear for different laminate orientation, loading and boundary conditions have been presented. Calculated results using the present model are in good agreement with published experimental data, theoretical solution, 3-D solution and closed-form solution. Based on the present model, the perturbation finite element method can also be used for the non-linear analysis of composite thin-walled shells.

REFERENCES

- Putcha, N. S. and Reddy, J. N. (1986). A refined mixed shear flexible finite element for the nonlinear analysis of laminated plates. *Comput. & Struct.*, **22:4**, 529-538.
- Qian, W. C. (1947). Large deflection of a circular clamped plate under uniform pressure. *Chinese J. of Physics, China*, **7**, 102-113.
- Reddy, J. N. and Chao, W. C. (1981). Large-deflection and large-amplitude free vibration of laminated composite material plates. *Comput. & Struct.*, **13:1-3**, 341-347.
- Stavsky, Y. (1964). On the general theory of heterogeneous aerolotropic plates. *Aeronautical Quarterly*, **15**, 29-38.
- Xie, Z. C. and Li, L. F. (1989). A new FEM for the study of composite laminated plates. *Proc. 7th Int. Conference on Composite Materials*, Guangzhou, China, 170-174.

Xie, Z. C., Yang, X. Z., Qian, Z. D., Liu, Y. and Zhang, L. P. (1984). Perturbation finite element method for solving geometrically nonlinear problems of axi-symmetry shells. *App. Math. & Mech, China*, **5:5**, 1679-1691.

Zaghloul, S. A. and Kennedy, J. B. (1975). Nonlinear behavior of symmetrically laminated plates. *J. App. Mech.*, **42:1**, 234-236.

TABLE 1
DEFINITION OF BOUNDARY CONDITIONS

	Simply-supported (SS)	Hinged-supported (HS)	Clamped (CC)	Fixed (FF)
For edges parallel with x-direction	$w_0 = w_{0,x} = 0$	$u_0 = v_0 = w_0 = w_{0,x} = 0$	$w_0 = w_{0,x} = w_{0,y} = 0$	$u_0 = v_0 = w_0 = 0$ $w_{0,x} = w_{0,y} = 0$
For edges parallel with y-direction	$w_0 = w_{0,y} = 0$	$u_0 = v_0 = w_0 = w_{0,x} = 0$	$w_0 = w_{0,x} = w_{0,y} = 0$	$u_0 = v_0 = w_0 = 0$ $w_{0,x} = w_{0,y} = 0$

where $w_{0,x} = \frac{\partial w_0}{\partial x}$, $w_{0,y} = \frac{\partial w_0}{\partial y}$.

TABLE 2
TRANSVERSE SHEAR COEFFICIENTS (r) OF A FOUR-LAYER SYMMETRIC CROSS-PLY PLATE WITH DIFFERENT WIDTH-TO-THICKNESS RATIOS

L/H	100	40	20	10	5
0°/90°/90°/0°	0.76%	4.07%	17.8%	64.0%	207.6%

$r = (\Delta_{0(\max)}^{(s)} - \Delta_{0(\max)}) / \Delta_{0(\max)} \times 100\%$; $\Delta_{0(\max)}$ and $\Delta_{0(\max)}^{(s)}$ are the non-dimensional maximum deflection of the plate, with transverse shear strain neglected and included respectively.

TABLE 3
TRANSVERSE SHEAR COEFFICIENTS (r) OF LINEAR AND NON-LINEAR DEFORMATIONS OF SYMMETRIC CROSS-PLY AND ANTI-SYMMETRIC ANGLE-PLY PLATES FOR DIFFERENT BOUNDARY CONDITIONS

Laminate type/orientation	Boundary conditions	Linear solution	For $\Delta = 0.5$	For $\Delta = 1.0$	For $\Delta = 1.5$	For $\Delta = 2.0$
Symmetric cross-ply laminate (0°/90°/90°/0°)	Simply-supported	11.6%	9.8%	7.6%	7.4%	10.7%
	Hinge-supported	11.6%	10.3%	9.9%	10.0%	10.2%
	Clamped	42.2%	35.0%	25.4%	19.7%	17.8%
	Fixed	41.5%	21.9%	9.6%	4.2%	2.2%
Anti-symmetric angle-ply laminate (45°/-45°/45°/-45°)	Simply-supported	18.3%	14.3%	9.1%	6.4%	5.6%
	Hinge-supported	22.8%	10.3%	4.4%	2.6%	1.6%
	Clamped	30.6%	24.2%	27.4%	5.5%	1.1%
	Fixed	31.8%	21.9%	10.0%	5.1%	3.1%

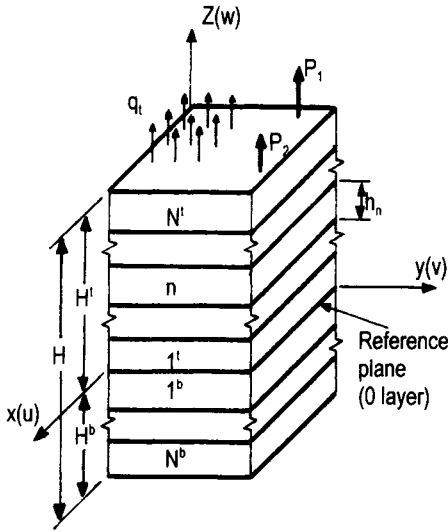
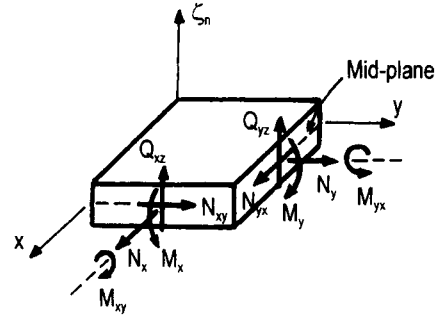


Fig. 1 Geometry of laminate with external loads



(a) Force resultants (subscripts 'n' omitted for all signs)

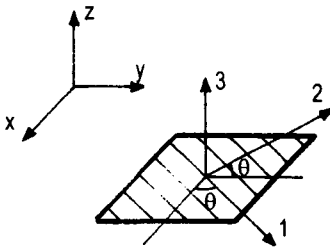
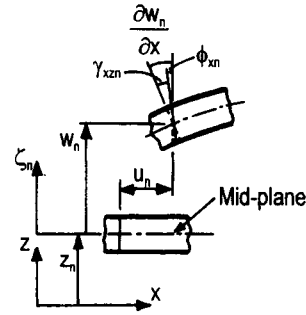


Fig. 2 Material scheme of the n^{th} sub-layer



(b) Deformations in x-z plane

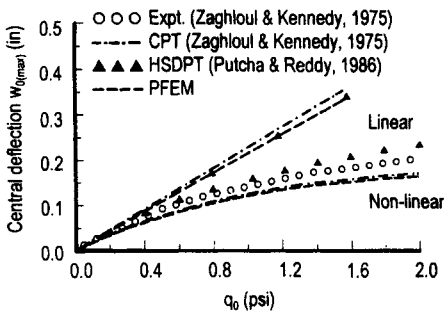


Fig. 4 Fixed-supported cross-ply square plate subjected to uniformly distributed load

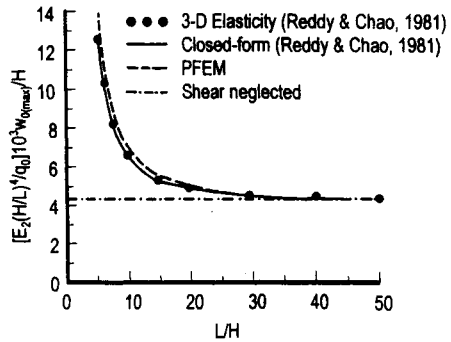


Fig. 5 Transverse shear effect vs width-to-thickness ratio of simply-supported cross-ply laminate

POST-BUCKLING AND FIRST-PLY FAILURE OF THIN-WALLED FRAMES AND COLUMNS MADE OF COMPOSITE MATERIALS

Luis A. Godoy¹, Leonel I. Almanzar¹, and Ever J. Barbero²

¹ Civil Infrastructure Research Center, Civil Engineering Department, University of Puerto Rico, Mayaguez, PR 00681-09041, USA

² Department of Mechanical and Aerospace Engineering, West Virginia University, Morgantown WV 26506-6101, USA

ABSTRACT

First-ply failure (FPF) of composite thin-walled columns and frames is investigated in the buckled structure. Elastic behavior is assumed during the pre-buckling and buckling states, and along part of the post-buckling equilibrium path. The Tsai-Hill criterion is employed to identify failure of one ply at one specific location. The technique of analysis is based on evaluation of the post-buckling elastic path, and using FPF as a constraint in the analysis. The structure is modeled using a few degrees of freedom to include local and/or overall buckling modes. The theoretical results are compared with experimental bounds and show good agreement for local buckling of isolated columns. There are no experimental results for frames in the literature, but theoretical results are presented for a simple case with asymmetric bifurcation.

KEYWORDS

Buckling, Composites materials, Frames, Ply-failure, Post-buckling, Thin-Walled Columns.

INTRODUCTION

This paper is about the post-buckling behavior of columns and frames made with composite materials. The members of the structures considered are formed by pultrusion using high-strength e-glass fibers embedded in a polymer resin. Because of limitations of cost and maximum thickness, all pultruded structural shapes have thin walls and are thus liable to buckling under compression. Most studies on the buckling of composite columns are limited to the critical load itself. Beyond elastic buckling the structure may have a stable post-buckling path and further load can be taken with large deflections. How far is the structure from a maximum load is not given by such eigenvalue calculations. Some mode of failure criterion is needed to compute more realistic maximum loads and thus guide the design and improve material performance.

The structural shapes considered in this paper are wide flange *I*-sections. A number of researchers have addressed the problem of post-buckling behavior of *I*-columns, but consideration of frames made with such shapes is not easily found in the literature, although they are frequently employed in practice.

This paper deals with local and global buckling modes of thin-walled members and frames, constructed using fiber-reinforced polymers. Such members are fabricated by pultrusion and are assembled to build frame structures for industrial purposes. The paper includes theoretical models based on simple analytical and numerical procedures to account for buckling and post-buckling. The formulation uses the total potential energy and the theory of elastic stability, so that an asymptotic solution of the post-buckling path is obtained. Rather than computing the non-linear material behavior along the path, the present approach is to include first-ply failure (FPF) as a material constraint to the elastic buckling process. To achieve that, first ply failure is modeled using Tsai-Hill criterion, so that it is possible to identify the layer inside the laminate which fails for the first time. A safety factor is computed with respect to a FPF criterion, and thus the weakness in the strength characteristics are visualized. A direction of improvement in the material is then possible.

The present work is based on preliminary findings by Almanzar & Godoy (1997b) on columns, and the results are compared in Section 3 with experiments. The analysis is extended in Section 4 to study some frame behavior.

FORMULATION OF THE PROBLEM

The investigation of post-buckling and FPF leads to a non-linear problem. Advanced computer models that include geometrically non-linear behavior and non-linear material properties are available to the engineer; however, even for the present day computing facilities this is an expensive computation, and more so if different possibilities need to be considered. A more convenient solution can be obtained by coupling the general theory of elastic stability with a FPF condition of the composite. The basic approach is to evaluate the post-buckling response of the structure using elastic properties for the material, and including the non-linear material behavior as a constraint to the post-critical path. Such approach has been discussed by Hutchinson (1974), Croll (1983) and others. All previous studies have focused on metal structures and the von-Mises criterion, while in the present work the formulation and results are extended to laminated composites. There are several ways to include the material behavior as a constraint, as pointed out by Godoy (1998).

Because of limitations of space, only a description of the formulation is presented here. The first step in the analysis is the computation of equilibrium paths using an elastic constitutive relation. The total potential energy of the system is built using a displacement field in terms of a small number of degrees of freedom. For the analysis of an isolated column, local and global buckling modes can be modeled as in Godoy, Barbero & Raftoyiannis (1995). The displacements are assumed for the web and the flanges, and compatibility conditions are employed to put them together as part of the more complex shape. Classical lamination theory is used to compute the stiffness of web and flanges. Such formulation for simply supported columns has also been used by Almanzar & Godoy (1997a) for sensitivity analysis of the post-buckling path.

Only global buckling within each member is considered for frames, although a buckling mode can have displacements in all members. Each member is assumed to have displacements in the form of cubic polynomials. The constitutive equations are those of the laminated composite for the flanges and for the web, as in the case of the isolated column. The energy contribution of each element of the frame is assembled into the total potential energy V of the structure. Notice that because non-linearity of the membrane strain is included, then V becomes quartic in the degrees of freedom of the system.

The energy V is next used in the context of the general theory of elastic stability to compute the fundamental equilibrium path, the critical state, and the post-critical equilibrium path. Further details of the energy formulation can be seen in Flores & Godoy (1992), and Almanzar (1998). A main difference between the behavior of an isolated column and of a frame is that bifurcation is symmetric in the former, but it can be symmetric or asymmetric in the latter.

The second step in the analysis is the implementation of a FPF criterion that can be used together with the stability and post-buckling formulations. In this work we have used the Tsai-Hill quadratic criterion (see Tsai, 1988) which can be written as

$$(\sigma_1/S_L)^2 - (\sigma_1\sigma_2/S_L^2) + (\sigma_2/S_T)^2 + (\tau_{12}/S_{LT})^2 = 1 \quad (1)$$

where $(\sigma_1, \sigma_2, \tau_{12})$ are the stresses in the ply considered; S_L is the longitudinal compressive strength; S_T is the transverse compressive strength; and S_{LT} is the longitudinal shear strength. Evaluation of the above strengths of a unidirectional or fabric ply is determined from relatively simple tests. In order to avoid FPF the left-hand side of Eq. (1) should be <1 , and failure is predicted if it is ≥ 1 . The failure surface generated by this equation is an ellipsoid in the $(\sigma_1, \sigma_2, \tau_{12})$ space, which is symmetric about the origin if equal strengths are assumed in tension and in compression. In most composites the tensile and the compressive strengths are different.

In the application of the failure criterion the next step is the computation of the stresses in a lamina from the displacements along the equilibrium path. The stresses should also be computed at several locations in the column because one does not know a priori where FPF occurs. These locations are to be searched along the length of each member, with the height of the web, and along the flanges. Only a few points are employed but care should be taken to include the location of more severe stresses. Thus, the stresses in each lamina are computed and compared with the Tsai-Hill criterion.

Because the formulation first constructs the energy and then employs its derivatives, a symbolic manipulator is very convenient. The above formulation has been implemented in a computer code written in the symbolic manipulator MAPLE V.

FIRST-PLY FAILURE OF COLUMNS IN EXPERIMENTS AND IN THE MODEL

Numerical as well as experimental work in composite columns and frames indicate that the material remains elastic until linear buckling occurs. For post-buckling equilibrium states, however, there is evidence of damage associated to the large post-buckling displacements.

To investigate damage, several columns were tested by Barbero and co-workers at West Virginia University, as reported in Dede (1996) and Barbero & Trovillon (1998). Tests were performed on a column with dimensions $b = d = 304.8\text{mm}$, thickness $t = 12.7\text{mm}$ ($12 \times 12 \times 1/2\text{in}$), $A = 112.9\text{mm}^2$, $I = 5998.5\text{mm}^4$, and $L = 1816\text{mm}$. The sections tested contained roving (unidirectional fibers) and continuous strand mat, with axial stiffness $EA = 289\text{MN}$ and bending stiffness $EI = 1.5\text{MNm}^2$.

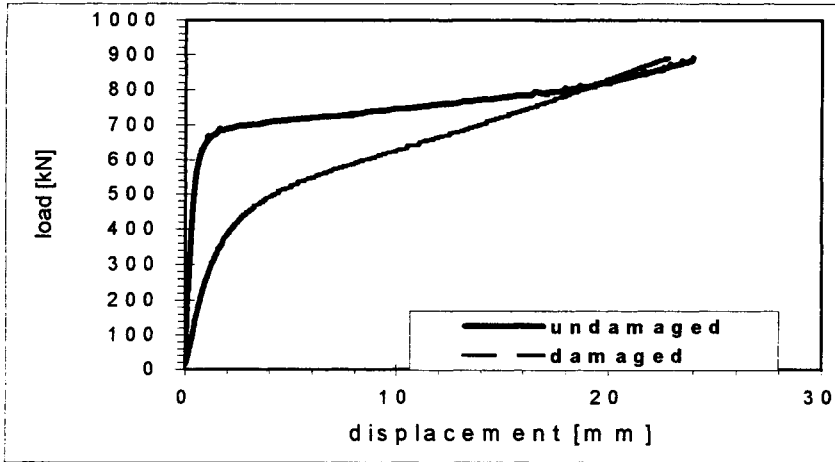


Figure 1

The sample was loaded using an MTS hydraulic machine at a loading rate of $89\text{kN}/\text{min}$. The ends of the column were simple supported. Load and displacements of the flanges were recorded using a data acquisition system. Post-buckling displacements of approximately 20mm were recorded during first loading of the column up to 900kN (approximately 30% higher than the critical load), and are shown as a solid curve in Figure 1. The structure had damage in the material at this stage. This is next observed by unloading and reloading, in which case the equilibrium path is the dotted line in Figure 1. Clearly, the initial stiffness of the structure has now changed, with a decrease due to damage. In the undamaged structure one may observe a bifurcation at a load of approximately 700kN ; the damaged column, on the other hand, is dominated by the non-linear response.

The present global experimental measurements do not allow to detect the occurrence of FPF; however, it gives bounds within which theoretical predictions of FPF should be. The column has been studied using the theoretical and numerical models described in Section 2. Buckling was computed for three half waves in the longitudinal direction, completely in agreement with experimental tests. First-ply failure was detected at a load approximately 15% higher than the critical load, thus within the bounds found experimentally. A difference between the present model and the experiments is the mode shape: there is a mode attenuation in the experiments, while this is not taken into account by the present simplified model.

FIRST-PLY FAILURE IN BUCKLED FRAME STRUCTURES

Next, a simple frame structure is considered, as shown in Figure 2a. This is a four-bar frame, but because sway buckling is prevented, then the analysis can be performed with only two members and conditions of symmetry. Each member of the frame is a thin-walled I -section, with dimensions $6\times 6\times 1/4\text{in}$ and $L=200\text{in}$ (5m), constructed with 7 layers of thickness 0.0357in each one. The internal angles between the vertical and inclined members are 11.25° , and $Ll=5\text{m}$. Fiber volume fraction is 0.3, and for e-glass we employed $E_1=E_2=10.6\times 10^6\text{psi}$ and $\nu=0.22$, while for epoxy the properties are $E_1=E_2=0.5\times 10^6\text{psi}$ and $\nu=0.35$.

For simplicity of the presentation only results for one element for each bar are reported here, with the active degrees of freedom shown in Figure 2b. For this problem, the fundamental equilibrium path has vertical displacements Q_2^F and Q_5^F . The critical state is a linear eigenvalue problem leading to a critical load factor $A^C=30,998.21b$.

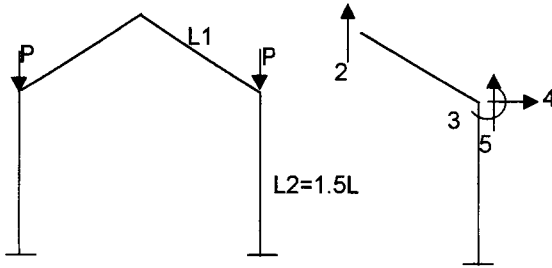


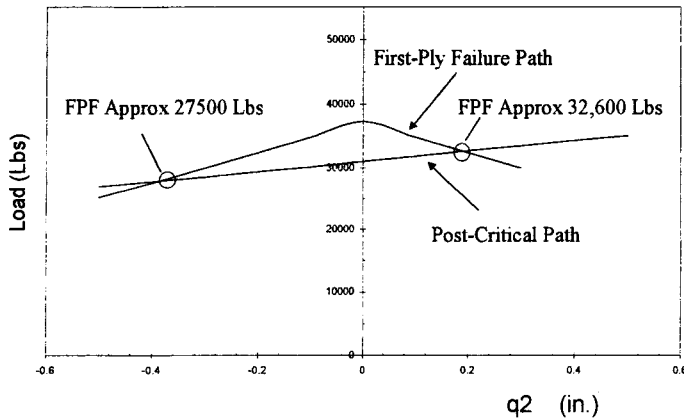
Figure 2

For the post-buckling equilibrium path the perturbation parameter s chosen is the vertical displacement at the apex of the frame, $s=Q_2$. The post-buckling path is written using the regular perturbation expansion

$$A(s) = A^C + s A^{(1)} + s^2 A^{(2)} + \dots \tag{2}$$

For the evaluation of the slope $A^{(1)}$ and curvature $A^{(2)}$ of the post-buckling path we require the coefficients A, B, C (see for example Flores & Godoy, 1992), which in this case result in $C = -395$, $B =$

Figure 3



-0.0245 , $A = -0.152 \times 10^{-5}$. Because $C \neq 0$, then we are in the presence of an asymmetric bifurcation. The slope of the post-buckling path results in $A^{(1)} = 1/2 C/B = 8,064$ and $A^{(2)} = 40,320$. One can now compute the post-buckling path of the structure and this has been plotted in Figure 3.

A FPF path has to be computed next for each location selected in the structure. The Tsai-Hill criterion, Eq. (1), is used with the material parameters already used for the isolated column. From the displacement field we have computed the stresses and the load-path, which is also indicated in Figure 3. On the stable part of the path, FPF occurs at a load which is 5% higher than the critical load, with displacements of 0.2in; while on the unstable branch, FPF is predicted for 88% of the critical load with displacements of 0.4in.

On the unstable branch the influence of imperfections is to reduce the maximum load in the elastic range; however, because the post-buckling path is relatively shallow in most frame structures, then it is expected that the present approximation should be a good estimate of the post-buckling FPF.

CONCLUSIONS

The theoretical approach followed in this work is aimed at the evaluation of FPF in laminated composite for buckled structures. The theme structures considered are thin-walled columns and frames assembled with such members. The specific materials studied are fiber reinforced polymers using e-glass and formed by pultrusion. The elastic post-buckling behavior is computed using the general theory of elastic stability, from which a perturbation expansion of the post-buckling path is obtained. FPF is introduced as a material constraint, and the FPF path is evaluated together with the post-buckling equilibrium path. FPF occurs at the intersection of the two paths.

For isolated columns, the paper considers the local buckling modes, and results are compared with bounds of experimental results. In the experiments it is not possible to identify FPF; however, the results for the columns with damage represent upper bounds to the theoretical results.

The displacements w_{FPF} for FPF normalized with respect to the thickness t of the walls are of $0.5 \geq w_{FPF}/t \geq 2$. This occurs for cases as diverse as column local buckling or frame buckling in global mode. This means that soon after buckling the structure reaches FPF. It is not necessary to advance into too large displacements to have failure in one ply.

In its present form, the model presented can be used as a limit to elastic behavior. Damage of the structure occurs following FPF and this was shown to change the initial stiffness for subsequent unloading and reloading of the structure. Such important changes are undesirable, so that care must be taken that the structure (either column or frame) works below a FPF limit.

ACKNOWLEDGEMENTS

Work at the University of Puerto Rico was supported by a grant from NSF-EPSCoR on "Behavior of structures with damage". The samples tested were provided by Creative Pultrusions Inc.

REFERENCES

- Almanzar, L. (1998), *Design Sensitivity of Composite Material Structures*, Ph. D. Thesis, University of Puerto Rico, Mayaguez, Puerto Rico.
- Almanzar, L. and Godoy, L. (1997a). Design sensitivity of buckled thin-walled composite structural elements, *Applied Mechanics Reviews*, 50:11, 3-10.
- Almanzar, L. and Godoy, L. (1997b). Failure of post-buckled thin-walled composite columns, in *Building to Last* (ed. L. Kempner Jr. and C. B. Brown), ASCE, New York, 2, 889-893.
- Barbero, E. and Trovillon, (1998). Prediction and measurement of post-critical behavior of fiber-reinforced composite columns, *Composite Science and Technology*, in press.
- Croll, J. G. A. (1983). *Metal Shell Buckling*, LNCC, CNPq, Rio de Janeiro, Brazil.

- Dede, E. (1996). *Experimental Validation Of Buckling Mode Interaction In Intermediate Length FRP Columns*, M. S. Thesis, West Virginia University, Morgantown, WV, USA.
- Flores, F. and Godoy, L. (1992). Elastic post-buckling analysis via finite element and perturbation techniques, Part 1: Formulation, *Int. J. Numerical Methods in Engineering*, 33, 1775-1794.
- Godoy, L. A. (1998). Design sensitivity of post-buckling states including material behavior, In: *Computational Mechanics: New Trends and Applications*, Ed. E. Onate and S. Idelsohn, CIMNE, Barcelona, Spain.
- Godoy, L. A., Barbero, E. J., and Raftoyiannis, I. (1995), Interactive buckling analysis of fiber-reinforced thin-walled columns, *J. Composite Materials*, 29:5, 591-613.
- Hutchinson, J. W. (1974). Plastic buckling. In: *Advances in Applied Mechanics*, 14, Ed. C-S Yih, Academic Press, New York, 67-144.
- Tsai, S. W. (1988). *Composites Design*, 4 Ed., Think Composites, Dayton, OH, USA.

This Page Intentionally Left Blank

PROGRESSIVE DAMAGE ANALYSIS OF GRP PANELS UNDER EXTREME TRANSVERSE PRESSURE LOADING

S.S.J.Moy¹, R.A.Shenoi², H.G.Allen¹, Z-N.Feng¹ and G.S.Pahdi^{1,2}

¹ Department of Civil and Environmental Engineering, Southampton University,
Southampton, SO17 1BJ, UK

² Department of Ship Science, Southampton University,
Southampton, SO17 1BJ, UK

ABSTRACT

Glass reinforced plastic panels are subject to various modes of progressive damage under increasing load, which affect the stiffness and integrity of the panel. A unified progressive damage model for composites, reinforced with unidirectional and woven fibres, under transverse pressure loading is presented. The unified method incorporates the results of micro-structural analysis of a woven composite unit into the macro analysis of composite panels. The Hashin criterion is used to predict the initiation of various damage modes in the composite and local appropriate stiffness reduction is employed in the model. The results of analyses of three thin composite panels are presented and compared with test results to demonstrate the accuracy of the method.

KEYWORDS

GRP composites, unidirectional and woven reinforcement, thin panels, transverse pressure, damage criterion, progressive damage analysis

INTRODUCTION

Glass reinforced plastics (GRP) are widely used in the aerospace and ship building industries because of their high strength and stiffness, and low weight. They are now finding applications in construction for remediation and new build. Another advantage of composites is that stiffness and strength can be tailored to specific load requirements by suitable arrangement of the reinforcement. Under increasing load laminated composites suffer various types of localised damage such as cracking of the resin (plastic) matrix, fibre-matrix debonding, fibre breakage and delamination. As damage accumulates there is permanent loss of integrity of the structure and loss of stiffness and strength. The ability to predict the initiation and growth of such damage is necessary for assessing the performance of composite structures and for designing safe and reliable structures which exploit the advantages offered by composite materials.

In the last decade considerable progress has been made in understanding the initiation and evolution of the damage modes in laminated composites. These researches have concentrated on panels subjected to in-plane loading, see typically Shahid & Chang (1995, beams in bending, Kim *et al* (1996), and generally composites consisting of stacks of unidirectional laminae, Tolson & Zabarar (1991). GRP panels subjected to transverse loading are usually thin so that their behaviour is complicated due to both material and geometric non-linearities which occur once damage has been initiated. Material non-linearity results from damage and geometric non-linearity from the large deflections during bending.

There are many different types of fibre reinforcement available. Most of the work reported has been concerned with unidirectional fibres which are straight even when embedded in the composite. However there are various woven fibres which are available in fabric form. The weaving process distorts the fibres and causes stress concentrations in the fibres and resin when the composite is loaded. These stress concentrations can result in premature failure of the fibres, Feng *et al* (1998), and must be considered in any progressive damage model.

The purpose of this paper is to present a methodology for progressive damage analysis of GRP panels subject to transverse pressure loading up to complete failure. The analysis considers unidirectional and woven fibres, the various types of local damage and geometric non-linearity. Results are presented which show the accuracy of the analysis when compared to experimental observations.

GLASS FIBRE REINFORCED LAMINATED COMPOSITES

Glass fibre reinforcement is produced in various forms. For panels the most common are unidirectional fibres and woven fabric. In unidirectional reinforcement approximately 90% of the fibres run in one direction, the remainder are woven at right angles to hold the main fibres together. Details are shown in Figure 1a. In woven fabrics 50% of the fibres run in each direction. Different weaving patterns are used but the most common is the plain weave shown in Figure 1b. The main unidirectional fibres are practically undeformed but the weaving process produces significant deformation of woven fibres.

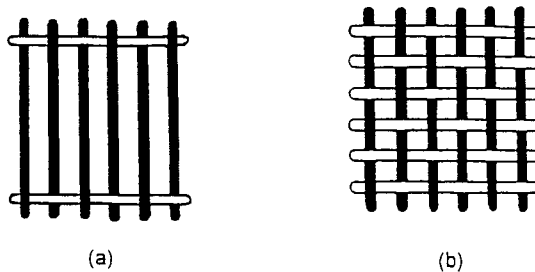


Figure 1: Typical reinforcement weaves

A composite panel will be made up of several layers of reinforcement, which can be placed so that they run in different directions. The arrangement of the layers of reinforcement and their incorporation within the resin matrix is called the lay-up. The resin can be added in various ways. In the simplest, called hand (or wet) lay-up, a layer of reinforcement is placed in the required orientation in a mould and a measured quantity of resin is added and rolled out to thoroughly wet the reinforcement. Subsequent layers are built up in a similar manner until the desired amount of composite at the

required thickness is achieved. More sophisticated techniques involve resin transfer moulding under vacuum. The mechanical properties of the composite can be predicted from the properties of the constituent materials and can be checked by testing coupons cut from the composite.

A micromechanical analysis of a repeating unit element (RUE), see Figure 2, of a woven composite was performed using the finite element method, Feng *et al* (1998), and showed that the interlacing and undulation of the woven fabric induced stress concentrations in the fibres and pure resin regions which would initiate damage earlier in a woven composite than in a composite with the same quantity of unidirectional reinforcement. The analysis showed that the effect of the stress concentrations can be conveniently expressed in terms of a *stress variation factor* (SVF). For example the SVF in the fibres in the direction of the applied stress is more than 1.2, meaning that the maximum longitudinal stress is over 20% higher than the nominal average stress. Using this concept each layer of woven fabric (lamina) can be replaced by two orthogonal unidirectional layers (each called the *nominal unidirectional composite*). The strength of the *nominal unidirectional composite*, called the

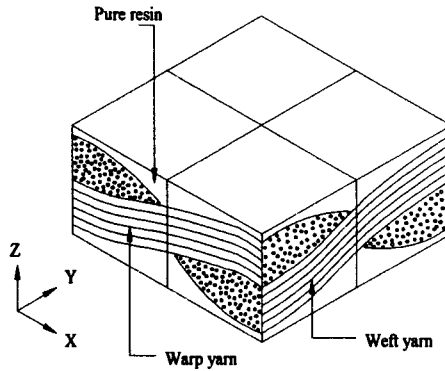


Figure 2: Repeating unit element of a woven lamina

conversion strength, can be found from the properties of the constituent materials and the *stress conversion factor*. The *conversion strength* (X') in the fibre direction is given by

$$X' = X / SVF \quad (1)$$

where X is the strength from the materials alone. The finite element analysis showed that the stress concentrations had little effect on the transverse strength (Y) and the shear strength (S) because the negative effects (stress concentrations) and positive effects (obstacles to damage growth due to fabric interlacing) tended to cancel each other. Hence the corresponding *conversion strengths* are

$$Y' = Y \quad (2)$$

$$S' = S \quad (3)$$

Using this approach the progressive damage modelling of unidirectional and woven fabric reinforced panels can be carried out in the same manner.

DAMAGE CRITERIA

In order to carry out progressive damage analysis it is necessary to be able to predict when damage will occur. Various damage criteria have been proposed but the one developed by Hashin, see Feng *et*

al (1998), is particularly convenient because it predicts the type of damage as well as when it will occur. It has the advantage of being simple to apply and its only drawback is that it neglects the effects of stress interactions. The Hashin criterion has subsets for predicting the three modes of in-plane failure: namely resin matrix cracking, fibre matrix shearing and fibre breakage. It can be expressed as:

$$\begin{aligned}
 \text{matrix cracking} & \quad \left(\frac{\sigma_2}{Y}\right)^2 + \left(\frac{\sigma_6}{S}\right)^2 \geq 1 \\
 \text{fibre - matrix shear} & \quad \left(\frac{\sigma_1}{X}\right)^2 + \left(\frac{\sigma_6}{S}\right)^2 \geq 1 \\
 \text{fibre breakage} & \quad \left(\frac{\sigma_1}{X}\right)^2 + \left(\frac{\sigma_6}{S}\right)^2 \geq 1
 \end{aligned} \tag{4}$$

where σ_1 , σ_2 and σ_6 are respectively the longitudinal, transverse and shear stresses in the composite, and X, Y and S are the longitudinal, transverse and shear strengths of the composite. When the composite has woven reinforcement the conversion strengths, X', Y' and S' are used in place of X, Y and S. Depending on the signs of σ_1 and σ_2 the tension or compression strength values are used for X and Y (or X' and Y').

If the values of the equations in (4) are greater than unity the criterion is indicating that a particular type of damage is occurring in the composite. The progress damage analysis is then instigated.

PROGRESSIVE DAMAGE AND STIFFNESS REDUCTION

The stiffness of a laminated composite will decrease when damage occurs in the laminae. However the implementation of numerical methods in macroscopic damage modelling is complicated by factors such as crack density. The simplest model is to totally discount the stiffness and strength of a lamina in which damage has occurred. However this is too simplistic because it ignores the fact that damage is localised and that the damaged lamina has residual strength and stiffness away from the damage. In the work reported here a simple stiffness reduction model based on experimental observations has been used. The finite element method is the basis and sophisticated, multi-layer shell elements are used to model the laminated composite. Each layer represents a lamina of the composite and contains Gauss integration points. Damage is implemented at an integration point when the stresses at that point satisfy the damage criterion and one of the equations (4) is equal to more than unity. The actual stiffness reduction depends on the damage mode indicated. Elastic modulus or Poisson's ratio values, as shown in Table 1, are reduced to zero at the integration point. As a result of the stiffness reduction the stresses which would have been carried by the damaged region of the material have to be redistributed to surrounding regions. The material non-linear solution procedure re-establishes equilibrium by redistributing stresses until the damage index in equation (4) is within 0.01 of unity (an error of at most 1%). The analysis requires an iterative solution procedure with very small load increments in order to obtain convergence to a correct solution. As damage accumulates the number of iterations to convergence increases considerably. Failure is indicated by a dramatic reduction in slope of the load-deflection graph, indicating an inability to support additional load, or by the solution failing to converge. A typical analysis required 500 load increments.

The solution process is very computer intensive. It was carried out using the ABAQUS finite element package, with various user defined subroutines, mounted on a single node of an IBM SP2 parallel processing computer with a Power2 processor, 256 Mbytes RAM and 32Kb instruction cache. A full analysis used about 50 hours of CPU time.

TABLE 1
STIFFNESS REDUCTION SCHEME

Damage mode	Mechanical Property			
	E_x	E_y	ν_{xy}	G_{xy}
No damage	E_x	E_y	ν_{xy}	G_{xy}
Matrix cracking	E_x	0	0	G_{xy}
Fibre-matrix shear	E_x	E_y	0	0
Fibre breakage	0	0	0	0

NUMERICAL RESULTS

36 panels have been tested in the laboratory as reported by Moy *et al* (1996). Three panels were tested at each lay-up and aspect ratio to check repeatability and obtain averages. The results of progressive damage modelling (PDM) of three panels are presented. The tests were conducted in a rig with nominally fixed edges: although this was true for rotation, it was found that there were small in-plane movements at the edges. These were included in the analysis by means of a series of springs around the edges (PDM – spring model). Details of the panels and the test results are presented in Table 2. Table 3 gives a comparison of test and analysis results. Figures 3 to 5 show load-central deflection curves for the three panels and Figures 6 and 7 show typical load-strain curves.

TABLE 2
DATA CONCERNING THE THREE PANELS ANALYSED

	Panel 1	Panel 2	Panel 3
Overall thickness (mm)	4.15	2.84	3.43
Fibre content by volume	0.365	0.547	0.308
Dimensions (mm)	600x600	600x600	600x1200
Composite type	five woven laminae	Five woven laminae	Unidirectional (0/45/90/-45/0)
Failure pressure (bar)	2.93	4.24	4.5
Failure deflection (mm)	29.2	35.9	59.5
In-plane edge displacement before failure (mm)	0.3	0.8	3.0 (at 3.75 bar)

TABLE 3
COMPARISON OF TEST AND ANALYSIS DAMAGE PRESSURES

Panel	Damage Pressure	Analysis		Test
		PDM	PDM-spring	
Panel 1	Initial Damage	0.50 bar	0.50 bar	1.30 bar
	Failure	3.10 bar	3.15 bar	2.93 bar
Panel 2	Initial Damage	0.20 bar	0.20 bar	-
	Failure	4.00 bar	4.10 bar	4.24 bar
Panel 3	Initial Damage	0.10 bar	0.10 bar	0.40 bar
	Failure	4.60 bar	4.70 bar	4.50 bar

DISCUSSION OF RESULTS

The deflections and failure pressures predicted by the PDM-spring model, (Figures 3 to 5), agree well with the test measurements. This gives some confidence that the progressive damage predictions are accurate. The importance of allowing for the edge displacements is also evident from the results. The panels tested were all thin (span/thickness about 150) so that geometric non-linearity was marked. The results indicate that the panels rapidly changed from plate bending to membrane behaviour except at the edges where there was localised bending. The ratio of failure deflection to thickness was in the range 7 to 16.

Strain gauges were mounted on both faces of the panels and had a gauge length of 10mm. Figure 6 shows that there was good agreement between analysis and test strains in the central membrane region of the panel. However at the edges, Figure 7, there were differences between predicted and test strains. At the edges the strains change very rapidly and since the strain gauges only measure average strain over the gauge length such discrepancies are to be expected.

The progressive damage model predicted matrix cracking at lower pressures than observed in the tests. However audible cracking noise was taken as initiation of damage in the tests but it is likely that microcracking was occurring at lower pressures. In panels 1 and 2, which had woven reinforcement, matrix cracking was the dominant damage mode as load was increased, with extensive cracking at the edges. Final failure was by widespread fibre breakage at the edges. In panel 3, with unidirectional reinforcement, after initial matrix cracking there was shearing in the corners which spread along the edges. Failure was due to extensive de-bonding around the edges. The predicted damage and failure patterns agreed well with the damage observed in the tests.

CONCLUSIONS

1. The accuracy of the method of predicting progressive damage in thin composite panels has been demonstrated by the results presented in the paper.
2. The PDM-spring model reliably predicts the overall load-deflection behaviour of the panel.
3. Strains are predicted well in the membrane region of the panel. Edge strains are not predicted well but this may be a result of not comparing like with like in the analysis and test results.
4. The model predicts damage modes as damage spreads through the material and as the panel fails.
5. The progressive damage model can deal with unidirectional and woven reinforcement in a unified manner. This is a significant advantage of the method.
6. The model is very computer expensive. However fabrication and testing of panels is even more expensive in terms of cost and labour. The progressive damage model provides a means for developing design rules for thin GRP composite panels. No general rules exist at present and there is a need for them so that the potential of this class of composites can be exploited in construction.

REFERENCES

- Shahid I. and Chang F.K. (1995). An Accumulative Damage Model for Tensile and Shear Failure of Laminated Composite Plates. *Journal of Composite Materials* **29**, 926-981
- Kim Y., Davalos J.F. and Barbero E.J. (1996). Progressive Failure Analysis of Laminated Composite Beams. *Journal of Composite Materials* **30**, 536-558
- Tolson S. and Zabarar N. (1991). Finite Element Analysis of Progressive Failure in Laminated Composite Plates. *Computers and Structures* **38**, 361-376

Feng Z, Allen H. and Moy S.S.J. (1998). Study of Stress Concentrations in Woven Composites. *Journal of Reinforced Plastics and Composites*, accepted for publication

Moy S.S.J., Shenoi R.A. and Allen H.G. (1996). Strength and Stiffness of Fibre Reinforced Plastic Plates. *Proceedings of the Institution of Civil Engineers* 116:2, 204-220

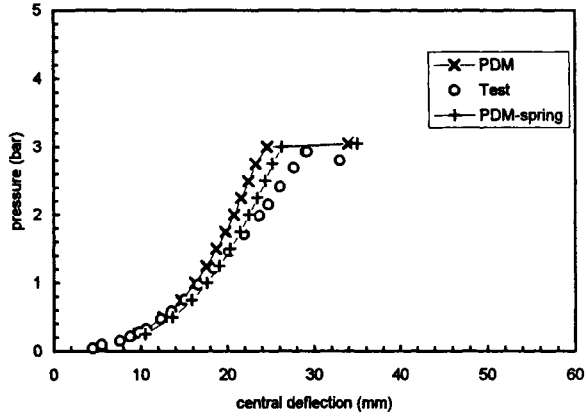


Figure 3: Central deflection vs. pressure, Panel 1 (woven)

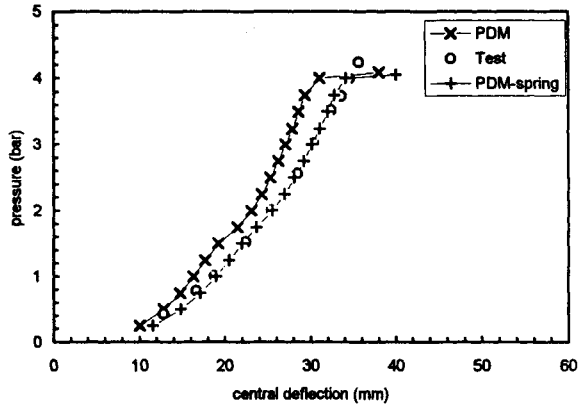


Figure 4: Central deflection vs. pressure, Panel 2 (woven)

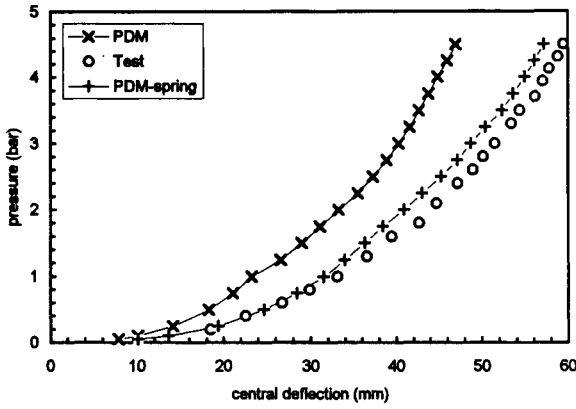


Figure 5: Central deflection vs. pressure, Panel 3 (non-woven)

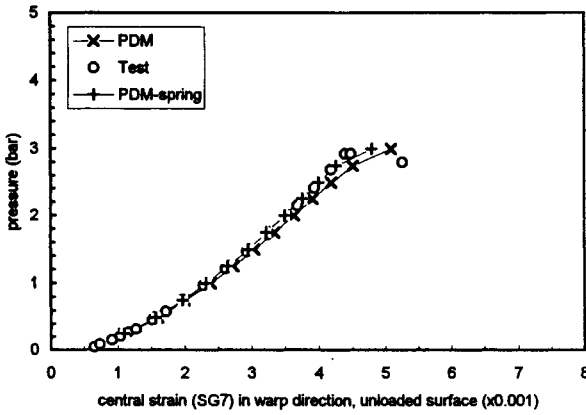


Figure 6: Central strain in warp direction, unloaded surface of Panel 1 (woven)

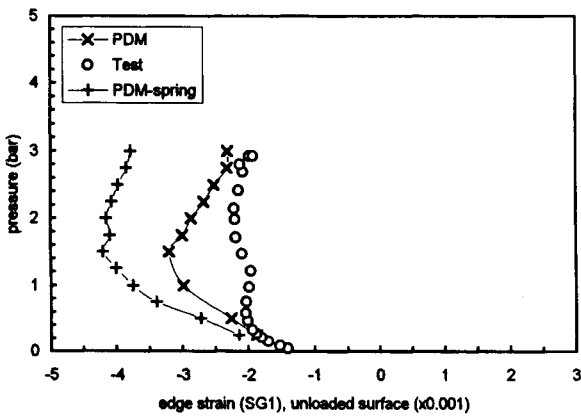


Figure 7: Edge strain (10 mm from edge) in warp direction, unloaded surface of Panel 1 (woven)

SNAP-THROUGH BUCKLING OF PLASTIC-GLASSY SHEETING

S.L. Chan¹, A.K.W. So² and S.W. Yuen²

¹ Department of Civil and Structural Engineering,
Hong Kong Polytechnic University

² Research Engineering Development Facade Consultants Limited

ABSTRACT

Plastic-glassy sheeting is commonly used as covering plates for canopy and skylight requiring the passing through of sunlight and aesthetic out-look. The advantage of the material is on its low -cost and ability to bent to a convenient shape. This paper describes the snap-through type of buckling behaviour for the sheeting using a geometrically non-linear finite element method.

KEYWORDS

Stability, Snap-through buckling, Shells and Plates, Plastic-glassy Sheeting

INTRODUCTION

Plastic-glassy sheeting is a relatively new material in place of glass panels for some applications as sheeting in skylight, dome and canopy allowing the passing through of sun-light. It is much cheaper than curved glass panels and the shape can be easily bent to fit the structural frame. Also, the consequence of failure for this type of

structure is relatively less severe than glass and usually does not cause injury and casualties since it is light and its debris normally adhere to the supporting frame after breakage.

One major architectural disadvantage of the material is on its change of colour under sun-light after a long period. Further its Young's modulus is much lowered than glass. This can be considered as a merit during installation since it is easier to bent manually. On the other hand, from the structural point of view, it is more susceptible to instability and buckling. Snap-through buckling may become a realistic design consideration when under wind pressure. Although the consequence may not lead to casualties, it is undesirable since the replacement of hundreds of plastic-glassy panels will cause much inconvenience and capital loss. Further, cracking of the sheeting will lead to water leakage which is highly undesirable and may lead to court dispute.

This paper describes the snap-through buckling analysis of a plastic-glassy panel used in a canopy. The method of design follows the same concept by Chan and Zhou (1998) for steel buildings and frames. Thus, the stress under a particular set of factored loads is determined and the design load under this set of loads is then computed. During the computational process, the effects due to change of geometry and snap-through instability are allowed for. For the analysis of thin plates of thickness equal to 10mm and overall dimension in the order of 1000mm, the thin-plate element derived on the basis of the Kirchoff's theory ignoring shear strain energy is appropriate and thus adopted here. For engineering and practical analysis, the linear strain triangle with drilling degrees of freedom to model the membrane component and the discrete Kirchoff hypothesis imposed at the corner and mid-side nodes for the bending component is used. When compared to the other two approaches of degenerated element and curved element, this facet element is more reliable, simple and suitable for geometrically non-linear analysis involving a complex change of geometry during the loading stage. Its disadvantage of heavier computational time has been offset by the availability of low-cost and efficient personal computers.

FORMULATION OF A DKT THIN PLATE ELEMENT

In the present application, the thickness of the shell is assumed to be small compared to the other dimensions of the plate element. Thus, the Kirchoff's theory for thin plates is adopted in which the shear deformation is neglected. The membrane strain is then expressed as,

$$[\epsilon] = \begin{bmatrix} \epsilon_x \\ \epsilon_y \\ \epsilon_{xy} \end{bmatrix} = \begin{bmatrix} \frac{\partial u}{\partial x} \\ \frac{\partial v}{\partial y} \\ \frac{\partial u}{\partial y} + \frac{\partial v}{\partial x} \end{bmatrix} = [B_m] [U_m] \quad (1)$$

in which ϵ_x , ϵ_y and ϵ_{xy} are the direct and shear strains, $[B_m]$ is the strain versus displacement matrix and $[U_m]$ is the displacement vector corresponding to the membrane stiffness.

The membrane stiffness matrix $[k_m]$ can then be evaluated as,

$$[k_m] = \int_A [B_m]^T [D_m] [B_m] t dA \quad (2)$$

in which $[D_m]$ is the material matrix for membrane components, t is the thickness of the element and A is the element area.

The bending strain of the present Kirchoff element, κ_b , is given by,

$$[\kappa_b] = \begin{bmatrix} \frac{\partial \beta_x}{\partial x} \\ \frac{\partial \beta_y}{\partial y} \\ \frac{\partial \beta_x}{\partial y} + \frac{\partial \beta_y}{\partial x} \end{bmatrix} = [B_b][u_b] \quad (3)$$

in which β_x and β_y are the rotation of the normal to the undeformed middle surface in the x-z and y-z planes and $[B_b]$ is the strain versus displacement matrix for the bending component. The stiffness for the bending component is then evaluated as,

$$[K_b] = 2A \int_0^1 \int_0^{1-\eta} [B_b]^T [D_b] [B_b] d\xi d\eta \quad (4)$$

in which $[D_b]$ is the bending component of the element matrix. ξ and η are the area coordinates of the element.

Adding the components for the membrane and the bending stiffness, one obtains the element stiffness for the shell element. The curved surface of the sheeting is then modelled by an assemblage of facet elements by the segment approximation. A more detailed description of the formulation of the element and its application to large deflection of glass panels is given by So and Chan (1996).

NUMERICAL PROCEDURE

In tracing the equilibrium path, the geometry changes continuously with the applied loads. Thus, an incremental and/or an iterative method must be adopted for tracing this non-linear path. For design against a specific set of loads, the Newton-Raphson method will be used for checking the stress at the design load level. In tracing the post-buckling response, a modified method such as the arc-length method (Crisfield, 1982) or the minimum residual displacement method (Chan, 1988) should be used. Note that, the load control and limit point traversing techniques cannot be used interchangeably since the load level for the solution may not be the one desired or convergence cannot be achieved.

In the present approach, the equilibrium path beyond the limit point is plotted

and the limit load or a load leading to the attainment of the maximum stress to the breaking stress. The Newton-Raphson type of iterative analysis procedure allowing for a control other than load can be written as (Chan, 1988),

$$[\Delta F] + \Delta\lambda[\Delta\bar{F}] = [K_T] ([\Delta u] + \Delta\lambda[\Delta\bar{u}]) \quad (5)$$

$$\begin{aligned} \Delta\lambda &= \frac{\Delta S}{\sqrt{[\Delta\bar{u}]^T [\Delta\bar{u}]}} \quad \text{for 1st iteration} \\ &= -\frac{[\Delta\bar{u}]^T [\Delta u]}{[\Delta\bar{u}]^T [\Delta\bar{u}]} \quad \text{for 2nd and onward iteration} \end{aligned} \quad (6)$$

in which $[K_T]$ is the tangent stiffness matrix composed of the bending and membrane stiffness, $\Delta\lambda$ is a scalar for modifying the load level, Δu and $\Delta\bar{u}$ are the displacement increments due to unbalanced ΔF and applied force vectors $\Delta\bar{F}$. ΔS is the square of the displacement increment and physically as the arc-distance of displacements.

Based on the element described above and the incremental-iterative procedure, the equilibrium path is plotted and the stresses at various load levels are then computed and compared with the breaking stress for the glassy-plastic sheeting plate.

PROBLEM DESCRIPTION

A number of plastic-glassy sheetings are to be installed on top of a canopy supporting framework of a canopy. The typical module is shown in Figure 1. The dimension of the sheeting is 4160 mm long x 1170 mm wide x 10 mm thick. The Young's modulus of elasticity for the material is 3500 MPa, the Poisson's ratio is 0.35 and the breaking stress is 80 MPa. In the analysis meeting the local building regulation, the pressure based on the objected area is assumed to apply uniformly downward.

A uniform incremental load of 0.1 kPa is applied to the structure vertically and proportionally and the load factor versus at quarter-mid point deflection is then plotted in Figure 1. The complete equilibrium path will then be used to assess the limit load of the structure and the maximum stress at various load level is then

computed.

It can be seen in Figure 2 that the load versus deflection curve exhibits a sharp turn at a pressure about 1.5 kPa. However, the stress at this load intensity is only 3.6 MPa, which is considerably less than the breaking stress of the material. After the snap-through, the sheeting generates a stiffening membrane force which increases with the sheeting deflection. The buckled shape of the sheeting is plotted in Figure 3. This buckling mode for shallow shell with four edges roller-supported appears to have not been reported before. Even in this post-buckling range, the sheeting is not loaded to its breakage stress, showing that the ultimate load of the sheeting is well above the working wind pressure. However, it is believed that, in actual condition, the local stress along the supporting edges may have a stress greater than the breaking stress due to the supporting edges are neither fully frictionless rollers nor built-in clamped edges.

This example illustrates the inadequacy of using stress alone for checking the safety of a practical structure. In pace with the invention and commercialisation of new structural forms and materials, more attention should be paid to the non-linear behaviour of the structure.

CONCLUSION

A self-developed non-linear finite element analysis program, NAF-SHELL, was applied to design a thin-walled plastic-glassy sheeting susceptible to snap-through instability. The stress alone cannot be used to check the strength of the structure owing to the importance of instability. Further, the mode of buckling for the thin shell sheeting is also interesting and appears to have not been reported before. It can be viewed as buckling of a cylindrical plate stiffened by ring beams and under external pressure. The mode is also found to be sensitive to the boundary conditions and the failure, defined as the situation that the structure is unfit for uses, can be controlled by instability rather than by material yielding.

REFERENCES

So, A.K.W. and Chan, S.L. (1996), "Stability and strength analysis of glass wall system stiffened by glass fins", *Finite Element in Analysis and Design*, 23, pp.57-75.

Crisfield, M.A. (1981), "A faster incremental iterative procedure that handles snap-through", *Computers and Structures*, 13, pp.55-62.

Chan, S.L. (1989), "Geometric and material non-linear analysis of beam,-columns and frames using the minimum residual displacement method", *International Journal for Numerical Methods in Engineering*, 11, pp.23-30.

Chan, S.L. and Zhou, Z.H. (1998), "Nonlinear integrated design and analysis of skeletal structures", to appear in *Journal of Engineering Structures*, 1998.

NAF-SHELL - Non-linear analysis of frames and shells, User's Manual, 1995.

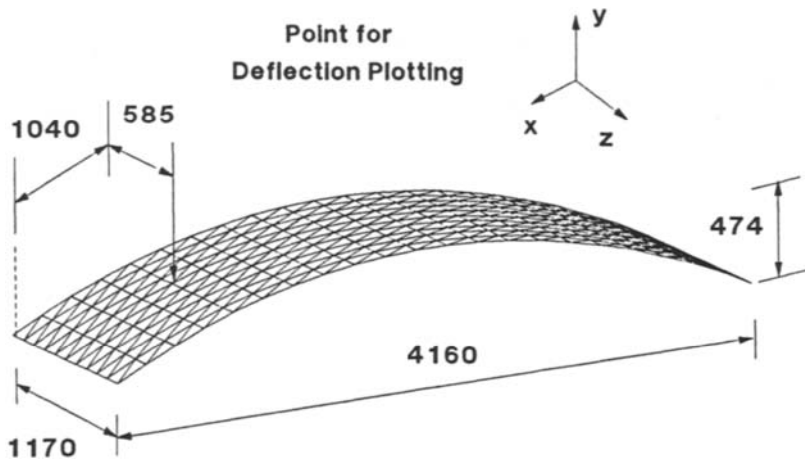


Figure 1 The plastic-glassy sheet before loaded

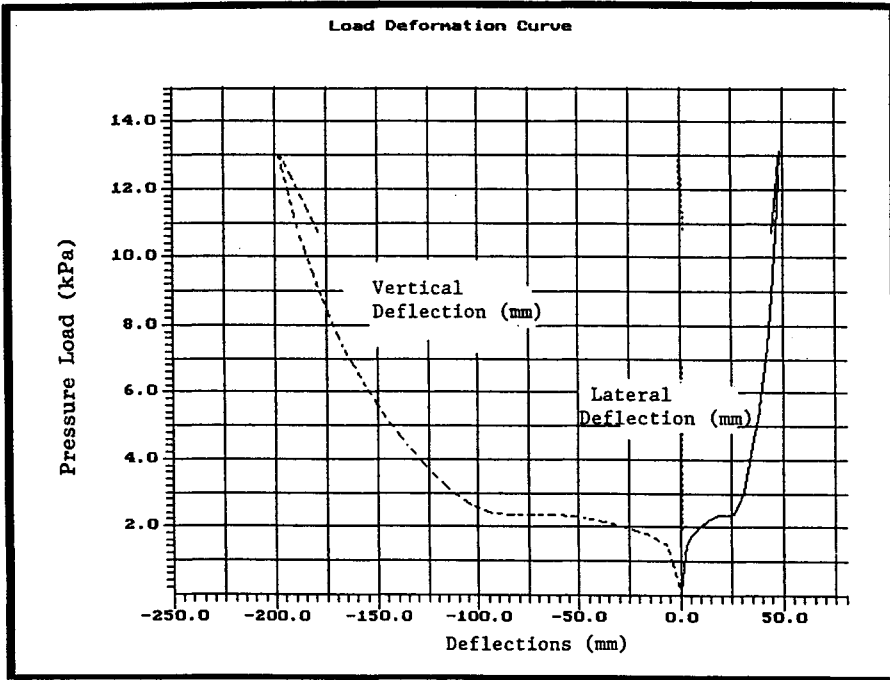


Figure 2 The load vs. deflection of the quarter point

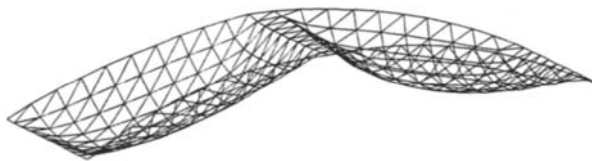


Figure 3 The plastic-glassy sheet after loaded

BEHAVIOUR OF THIN WALLED COMPOSITE BEAMS AND COLUMNS

K.M.A. Hossain ¹ , L. Mol ² and H.D. Wright ³

^{1,2} Department of Civil Engineering, The PNG University of Technology,
Private Mail Bag, Lae, Papua New Guinea

³ Department of Civil Engineering, University of Strathclyde,
107 Rottenrow, Glasgow G4 0NG, UK

ABSTRACT

The behaviour of TWC beams and columns with normal concrete (NC) and light weight volcanic pumice concrete (VPC) as in-fill, is described based upon experimental results. The capacity of the column is found to be enhanced due to the increased strength of confined concrete and increased steel plate buckling capacity resulting from composite action. It is found that the TWC columns of strength comparable to NC, can be manufactured using VPC in-fill. The columns may fail due to tearing of steel plate or local plastic yielding of steel plate due to the formation of local buckles or global buckling, depending on the plate thickness and slenderness of the columns. The strength of the beam is limited by the compression buckling capacity of the steel plate at the top of the open box section. The performance of the beam and enhancement of the strength of the beam can be possible by stiffening the compression steel plates at the open end of box section. The improved performance of the VPC in confined environment demonstrates the potential of using volcanic pumice (VP) as light weight aggregate in this form of construction.

KEYWORDS

Volcanic pumice, columns, beams, thin walled, buckling, slenderness, strength, light weight, composite.

INTRODUCTION

Thin walled composite (TWC) sections is a new idea for beams and columns comprising cold formed steel elements with an infill of concrete that are suitable as replacement for hot-rolled steel or reinforced concrete in small to medium sized building. Typical TWC sections are shown in Figure 1. The inherent advantages of this system are derived from its structural configurations. Open box sections for beams will allow easy casting of in-fill concrete. TWC sections do not require temporary form work for infill concrete as the steel acts as form work in the construction stage and as reinforcement in the service stage.

They are simple to fabricate and construct compared to conventional reinforced concrete where skilled workers are needed to cut and bent complex forms of reinforcement. The infill concrete in TWC sections is less likely to be affected by adverse temperature and winds as experienced in the case of reinforced concrete. The in-fill concrete is generally cured quickly and in any case, the load capacity of the steel alone may be relied upon for most construction loads. In most cases, the geometry (Wright, 1993) of proprietary hot rolled steel tubes has been found to be such that local buckling is avoided. It may, be however desirable for slender hot rolled and cold formed steel sections to be utilised for both columns and beams (Lowe, 1992). These sections can be designed, primarily, for the construction load of wet concrete, workmen and tools.

There are constraints on the amount of reinforcement in a conventional reinforced column which, when combined with specific detailing requirements, ensure sufficient ductility. The ductility (Lowe, 1992) of the filled tubes has been shown to be high. TWC sections are more susceptible to fire, although the thermal mass of the concrete infill provides reasonable protection to most fire loads. The smooth metallic finish of TWC sections is superior to conventional concrete and accepts more paint finish. Concrete filled steel elements as a means of providing aesthetic and economical structural elements attract interests in the construction industry. The new Eurocode (1994) includes detailed rules for the design of such sections.

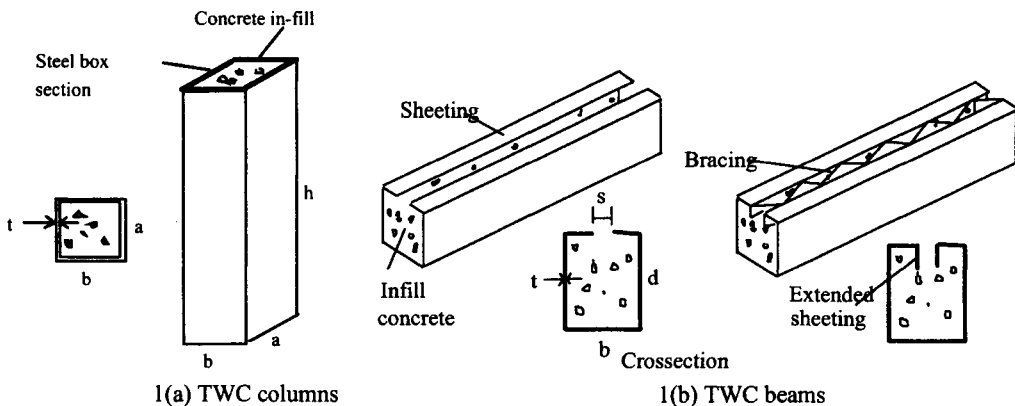


Figure 1: Schematic of thin walled composite sections

Research is now ongoing, to investigate the behaviour and potential use of TWC sections as beams and columns. Emphasis is also provided on the use of locally available material, economy and local structural needs. As a consequence, volcanic pumice which is a natural waste from volcanic activities in Papua New Guinea is used to manufacture infill light weight concrete for TWC sections. This paper will present the results of investigations on the behaviour of TWC beams and columns using both NC and VPC.

EXPERIMENTAL INVESTIGATIONS

Comprehensive series of experimental investigation is now under progress to study the behaviour of TWC sections as beams and columns. The experiments are designed to provide information on the load-deformation response, stress-strain characteristics and failure modes. The experiments are also designed to study the effect of geometric dimensions, type of concrete and steel thickness.

Manufacture, Instrumentation and testing of TWC specimens

The TWC columns are manufactured using hollow steel sections available in the market and also using flat sheet folded to hollow sections in the house with welded seam joint. The thickness of the steel varies from 0.45 mm to 3 mm. The dimensional properties of the typical columns are indicated in Figure 1(a). The 'a' and 'b' represent the cross-sectional dimensions of the columns with 'b' representing minimum dimension, 'h' represents the height and 't' represents the thickness of the steel plate. For beams, 'd' represents depth, 'b' represents width, 't' is thickness of steel and 's' represents the opening at the box sections at the top (Figure 1(b)).

Comprehensive research has been carried out by Hossain (1998) on the properties of lightweight volcanic pumice concrete (VPC). Investigations suggested that, it is possible to obtain a VPC (1:2:4) of 30% lighter than normal concrete and having a strength 30 MPa. The infill concrete for TWC beam-columns either VPC or normal concrete (NC) is made from 10 mm maximum size aggregates. The specimens are cast vertically in a especially fabricated stand and concrete is compacted in layers by air hose. Control specimens in the form of cubes are also cast for each batch of concrete. The TWC specimens are then air cured at room temperature until tested. The behaviour of thin steel sheeting under wet concrete is observed during the casting operation. The hollow section for columns and open box sections for beams behaved perfectly as form work with no sign of outward buckling. The concrete casting is also much simpler than reinforced concrete.

The strain gauges are installed at key locations of the specimens as shown in Figure 2. Axial deformation for column and central deflection for beam are measured by dial gauges. For beams, dial gauges are used at the end, to measure the slip between steel and concrete and the test set-up is shown in Figure 2. The specimens are then tested by applying compression in a hydraulic testing machine. The load is applied in increments and at each load increment strains and axial and central deformations are measured to get complete load-deformation response of both columns and beams.

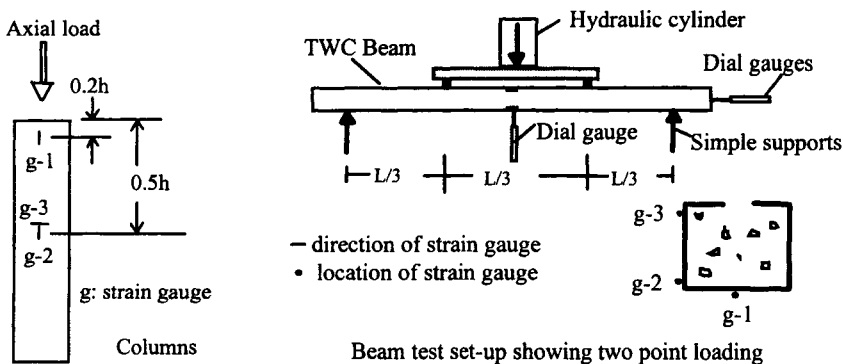
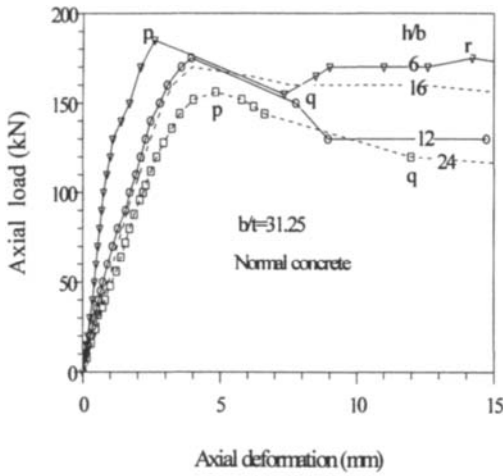


Figure 2: Instrumentation and testing of TWC columns and beams

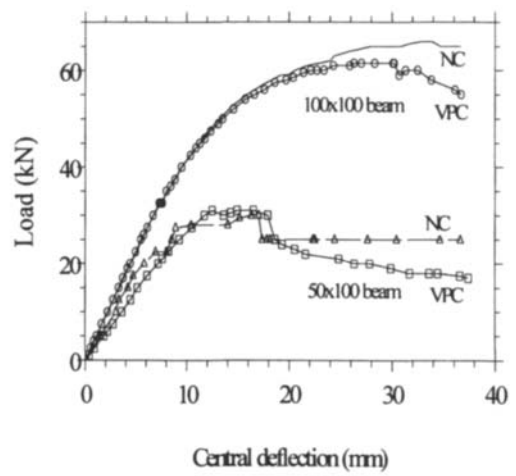
Load-deformation response and failure modes

The typical axial load-deformation responses of the TWC columns having normal concrete in-fill and the effect of slenderness (h/b ratio) is shown in Figure 3(a). At about 25% of load at 'p', the initiation of debonding or cracking of concrete is marked by sound and the first local buckling starts to form at about 90% of load at 'p' which marks the beginning of large axial deformation. In most cases, the first local buckling is formed either near the top or bottom end of the column. Between 'p' and 'q', the load starts to

fall with large axial deformation. In the zone of local buckling, the steel suffers excessive outward buckling and that portion of the steel plate seems to reach yielding. Between 'q' and 'r', the column tries to regain its stable form after the destabilisation process of first local buckling and the load starts to increase again until it reaches the point 'r'. At point 'r', second local buckling is formed close to the first one. The load starts to decrease again with large axial deformation. The column suffers excessive outward deformation in the buckling zone and finally it shows sign of local bending in the region (Figure 4 (a)) due to plastic yielding of the steel plate. The column never regains its stability after the initiation of local bending and finally it fails. The first peak load at 'p' is found to be always higher than subsequent peak load ('r') and can be taken as the ultimate load of the column. For comparatively slender columns ($h/b=24$), the zone 'q-r' is absent (Figure 3(a)). The peak load at 'p' is governed by the global buckling of the columns (Figure 4(a)) and the load-deformation response only constitutes a falling branch 'p-q'. However, in the post buckling stage local buckling is found to develop near the mid-height of the columns.

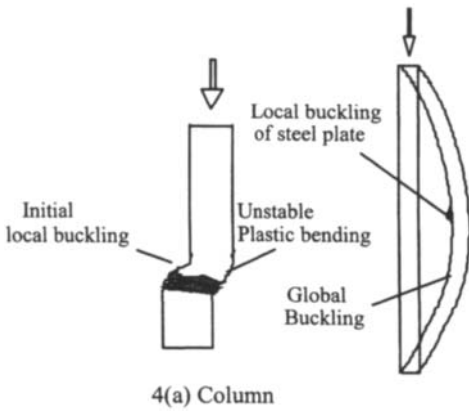


3(a) Columns

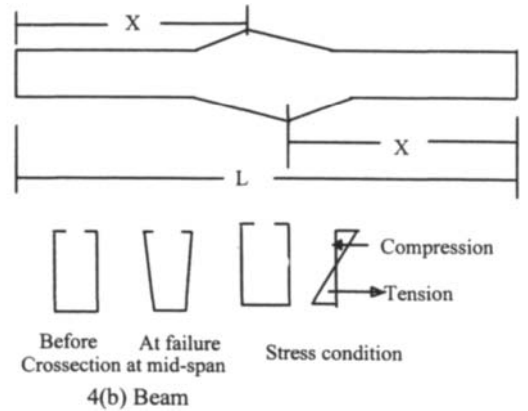


3(b) TWC beams

Figure 3: Typical load-deformation response



4(a) Column



4(b) Beam

Figure 4: Modes of failure

The typical load-central deflection response for TWC beams are shown in Figure 3(b). After initial stages of debonding, the lateral separation between steel and concrete starts due to compression (Figure 4(b)) in the open top flange where the steel plate is free to deform laterally. As load increases, the increased compression force causes the steel plate at the top open flange, to buckle at about 90% of the ultimate load. The load and deflection steadily increase up to the point of buckling and after that, the continuing outward buckling (as shown in Figure 4(b)) of the steel plate causes large deflection and reduce the strength of the beam significantly. The transition between start of buckling and failure is quick and finally the beam fails due to excessive outward buckling and cracking of in-fill concrete. The Figure 4(b) shows failure characteristics of the beam. The distance, X , between the point of buckling and the support lies between 0.44 to 0.48L. To avoid lateral separation between sheeting and concrete at the top open compression flange and to increase the strength, it is necessary to provide connections between sheeting in the form of bracing or to extend the sheeting to concrete in-fill as shown in Figure 4(b). Tests are now on going with different modes of connections to investigate the effect. The interface slip between steel and concrete is found to increase as the outward buckling of the sheeting from concrete increase and the details can be found from Hossain (*).

Strain characteristics

The typical variation of axial strains for both NC and VPC in-fill columns is shown in figures 5. The strains are found to increase steadily with the increase of load. The higher strain at the top end of the column (gauge-1) compared to the centre (gauge 2), confirms the higher stress development in that region for comparatively short column with slenderness, $h/b=6$. This may be due to the fact that the steel plates near the top and bottom end are open and unsupported and much weaker than the plates in the mid height region. As a consequence, in most of the columns, the local buckling is formed near the top and bottom end of the column and the failure is due to plastic yielding of steel resulting from series of local buckle formation. The situation is reversed for comparatively slender column with slenderness, $h/b=24$. The strain in the middle of the column (gauge 2) is found to be higher than that at the top (gauge 1) for both NC and VPC columns. This is due to the global buckling mode of failure in these columns causing higher stress concentration in the middle. The strains in VPC columns are found to be higher than those in NC columns.

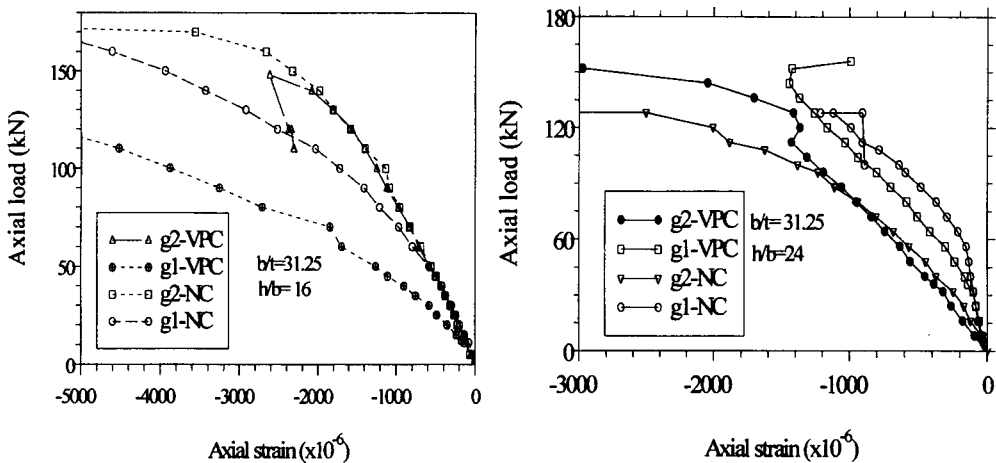


Figure 5: Variation of axial strain in TWC columns

The effect of slenderness (h/b ratio) on the development of strain is illustrated in figure 6 and both NC and VPC columns show similar type of behaviour. The strain at the top (g-1) decrease with the increase of h/b from 6 to 24. On the other hand, the strain at the centre (g-2 and g-3) seems to be not affected up to 50 to 60% of the failure load but eventually increase with the increase of slenderness. The tensile strain in gauge 3 confirmed the development of hoop stress in the columns but the strains do not exceed yield strain. This confirmed no tearing mode of failure in the tested columns (with $b/t= 31.25$) compared to the columns with very thin sheeting (with $b/t = 165$) where tearing mode of failure was observed (Hossain,*).

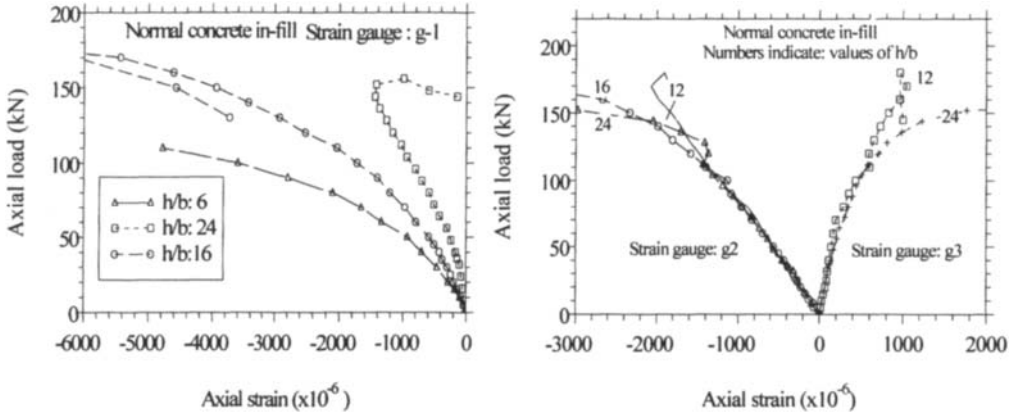


Figure 6: Effect of slenderness on axial strain

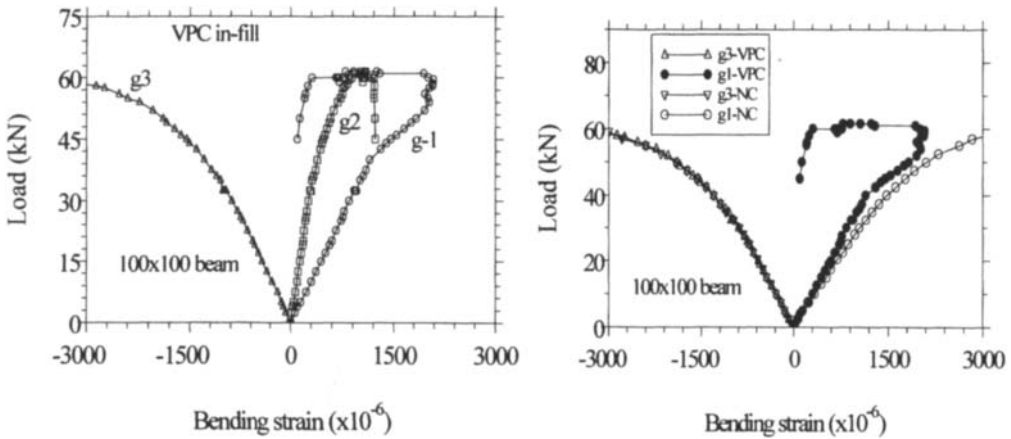


Figure 7: Variation of bending strain in TWC beams

The typical variation of bending strain with load of TWC beams with VPC in-fill is shown in figure 7 and the similar behaviour is also observed with NC in-fill. The strain in gauge 2 is found to be less than that in gauge 1 as expected. The strain in gauge 3 is found to be higher than that in gauge 1, particularly in the final stages due to compression buckling of the steel plates in that region. The strain gauges also show the attainment of yield strain in the steel at the final stages. The bending strains in VPC and NC beams are compared to each other in figure 7(b). The compressive strain in gauge 3 seems to be similar in both type of beams although the tensile strain in gauge 1 shows higher values for VPC beams. But it seems to be that the type of concrete has less influence on the strain than that observed in columns.

COMPARATIVE STUDY

The behaviour of component steel plates in TWC sections is not similar to that of free plates as they are in intimate contact with concrete. This will force any slender compressed plates into a buckled wave-form that may be approximated by a cosine rather than sine function which lies wholly on one side of the plane of the plate. The wavelength of the buckle is much shorter than the free plate and therefore higher buckling capacities are possible. This means that relatively slender TWC sections can resist high axial force when filled with concrete. The buckling stress of plates in these circumstances can be determined using methods described by Timoshenko (1982) and Wright (1993). The full analysis of buckling stress for TWC column specimens and the steel plates in beams with different types connections at the open end can be found from Hossain [*]. Table 1 summarises the results of experimental studies and compares the test results with theoretical analysis. Comparative study shows that VPC columns undergo higher axial deformation than NC columns. This is reasonable as the modulus of elasticity of VPC (Hossain (1998)) is found to be lower than NC. Taking into consideration the effect of different cube strength of concrete (f_{cu}), the VPC columns are found to have similar strength when compared with NC columns. It seems to be that the confinement of concrete in TWC sections improve the performance of VPC and the failure load is dictated by the performance of steel section. It is interesting to note that the VPC columns are more ductile than NC columns of same strength.

TABLE 1
COMPARATIVE STUDY OF TEST AND THEORETICAL RESULTS

Test no.	TWC columns								TWC beams			
	Parameters			Axial capacity, kN				Expt./BS		Type	Failure Load, kN	
	h/b	b/t	a/b	NC	VPC	BS5400		NC	VPC		b x d x t 50x100x3	b x d x t 100x100x3
1	6.0	31.25	1.0	180	150	176	170	1.02	0.88	Expt.		
2	9.0	31.25	1.0	180	--	176	170	1.02	-	NC	30	66
3	12.0	31.25	1.0	170	152	176	170	0.97	0.89	VPC	31	61.5
4	16.0	31.25	1.0	175	150	176	170	0.99	0.88	Analy		
5	18	31.25	1.0	165	129	176	170	0.94	0.76			
6	24	31.25	1.0	156	128	176	170	0.89	0.75			
7	16	16.66	2.0	435	395	458	447	0.95	0.88	RCC	61.71	130.7
8	9	33.33	1.0	680	530	672	648	1.01	0.82			
9	6	75	1.0	760	--	755	--	1.00	--			

$f_{cu}=26\text{Mpa (NC); } 22\text{Mpa(VPC) and } f_y= 445\text{N/mm}^2$; Span , $L = 1.5\text{m}$ for TWC beam

The strength is found to be affected by the slenderness of the columns. The axial strength is found to be not reduced when h/b ratio varies from 6 to 16 as global buckling does not dictate the failure of the columns in this range. However for comparatively slender columns with h/b ratio of 24, the strength is reduced by about 15% compared to columns with h/b ratio of 6 as the failure is dictated by global buckling. The axial capacity of columns are compared with those derived from BS5400 (assuming material partial safety factors to be unity) in table 1. BS 5400 under predicts the axial load of columns with normal concrete in-fill where global buckling mode of failure is prominent and found to be safe for columns with local buckling mode of failure. For columns with VPC in-fill, the BS5400 over predicts the axial loads and found not safe. It can be seen that tested TWC columns appear to be slightly more heavily reinforced (12% to 17%) than conventional bar reinforced concrete (0.5% to 8%).

The load-deflection response for NC and VPC beams are compared in Figure 3(b). Both beams show similar behaviour with strength seems to be not affected by the type of concrete. A comparison has been made by comparing the capacity with an equivalent reinforced concrete beam in table 1. The TWC beams are transformed into an equivalent singly reinforced concrete beam of cross-section 'b x d' and by lumping the cross-sectional steel area at an effective depth of 0.8d (Hossain, *). The capacity of TWC beams are found to be almost 50% of equivalent RCC beams (Table 1). Compared to reinforced concrete of same size and same amount of reinforcement, the steel in TWC beams are found to be only 50% effective due to their geometry, placement and bond in steel-concrete interface.

CONCLUSION

This paper describes the behaviour of TWC sections as columns and beams using both normal and light weight volcanic pumice concrete. TWC columns are found to have high resistance to axial load due to the reduced likelihood of local compression plate bending. The axial load capacity of this elements is based upon the increased strength of the concrete as confined by the steel and the increased steel plate buckling capacity due to composite action. The test on beams revealed that the compression buckling of the steel plates governs the strength of the beam. The performance of VPC in TWC sections is found satisfactory and in future, volcanic pumice can be used as a potential source of alternative aggregate.

ACKNOWLEDGEMENTS

The authors are grateful to the Research Committee of The PNG University of Technology for providing financial support in the form research grant to this project. The effort of the Technicians of the Central workshop, Structure and Concrete laboratories are also gratefully acknowledged.

REFERENCES

- BS 5400 (1979). Steel, concrete and composite bridges: part 5: Code of Practice for design of composite bridges, *British Standard Institution*.
- European Committee for Standardisation (1994). Design of composite steel concrete structures, Part 1.1 general rules and rules for building, *Eurocode 4*, ENV 1994-1-1, Brussels.
- Hossain K.M.A.(*), Behaviour of thin walled composite beams and columns (Under preparation).
- Hossain K.M.A (1998). Properties of volcanic pumice based cement and light weight concrete, Communicated to *Magazine of Concrete Research*, London, UK.
- Lowe P.G. (1992), Externally Reinforced Concrete- A New Steel / Concrete Composite, *Transactions of the Institution of Professional Engineers New Zealand*, Vol. 19, No 1/CE, pp 42-48.
- Timoshenko S.P. and Gere, J.M.(1982). *Theory of elastic stability*, McGraw-Hill International, New York.
- Wright H.D. (1993). Local buckling of Rectangular Hollow sections, *5th International Symposium on Tubular Structures*, Nottingham, 25-27 August.
- Wright H.D. (1993). Buckling of plates in contact with rigid medium, *The Structural Engineer*, London, UK, Vol. 71, No. 12, pp 209-215.

DEVELOPMENT OF THE 'SLIMDEK' SYSTEM USING DEEP COMPOSITE DECKING

R M Lawson and D L Mullett

The Steel Construction Institute
Silwood Park, Ascot SL5 7QN, UK

ABSTRACT

The '*Slimdek*' system comprises a new Asymmetric Slim floor Beam (ASB) and deep decking to create a composite floor structure with span capabilities of 6 to 8m. This paper reviews the design and development of a new deep decking profile, designated as SD225. Load tests were carried out on the decking to represent the construction stage loading, on the composite slab to represent in-service loading, and on the fire resistance of the composite slab. Design guidance has been presented in accordance with Eurocode 3 and 4.

Keywords

Steel, Decking, Composite, Design, Fire, Testing,

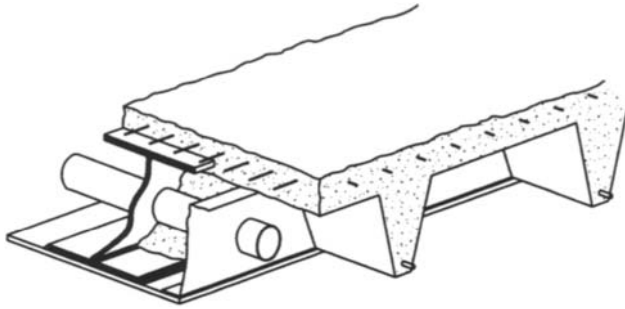
INTRODUCTION

Slim floor construction is the name given to a form of construction where the steel beams are encased in the floor slab so that only the bottom flange or support plate is exposed. The partial encasement means that the beam can achieve 60 minutes fire resistance without further protection, and the structural properties are improved by composite action.

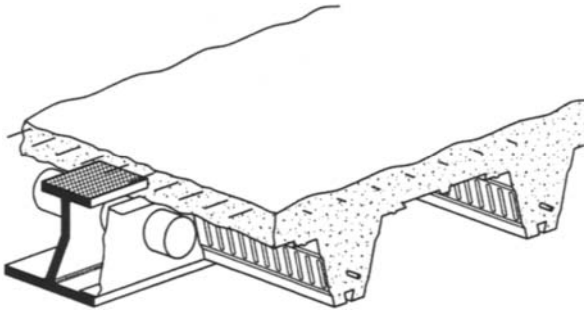
'*Slimflor*' is the registered trade name for a UC or HE or WF section with a welded plate which can support either:

- a precast concrete slab
- deep decking forming a composite slab.

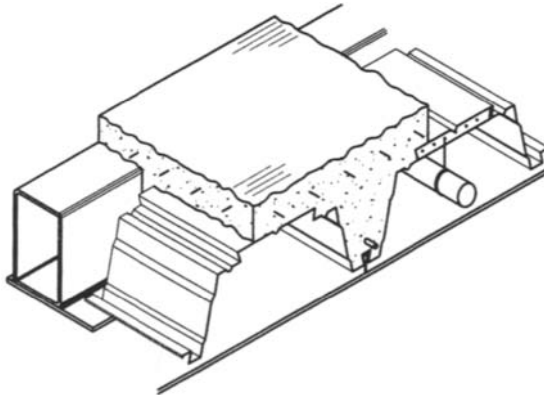
The Asymmetric Slimflor Beam (ASB) has been specifically developed to provide further economy, and is used to support deep decking, as part of the '*Slimdek*' system. RHS beams may also be used as edge beams. These different forms of construction are shown in Figure 1.



(a) *Slimflor* Beam (UC section and welded plate)



(b) Asymmetric *Slimflor* Beam (ASB) in *Slimdek* construction



(c) RHS *Slimflor* as an edge beam

Figure 1 Different forms of *Slimflor* and *Slimdek* construction

The deep decking is designated as SD225, being 225 mm deep. It replaces the former CF210 decking, as it has improved properties and spanning capabilities. However, essentially the behaviour of these decks is similar. The advantages of deep decking are:

- its light weight in comparison to a reinforced concrete slab.
- it can span up to 6m in the construction stage without temporary propping.
- it can span up to 9m as a composite slab (design is limited by serviceability requirements).
- the space between the deck ribs may be used for services and lighting units.
- the floor slab may be perforated by small openings.

The SD225 deck profile is illustrated in Figure 2. It is manufactured in steel thicknesses of 1.1 and 1.25 mm, and in S350 steel to BS EN 10147. End diaphragms attached to the supporting beams prevent loss of concrete during the concreting operation and increase the local shear resistance of the decking.

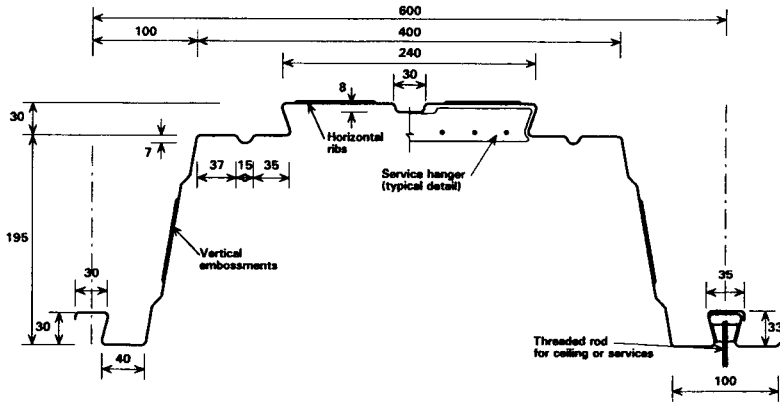


Figure 2 Cross-section of SD 225 decking

TESTING OF DECK PROFILE

Various load tests were carried out to simulate conditions existing during construction. These tests included:

- vacuum tests
- point load tests

These load tests were carried out by British Steel's Welsh Technology Centre. The vacuum tests exerted negative pressure by a plastic membrane placed over the top part of the profile. This form of loading is relatively severe as it accentuates the loading on the compression part of the profile, whereas concrete pressure would be more applied to the ribs. For this reason, direct load tests were also carried out by point loads applied to boards with sand filling the ribs.

The test results for both the SD225 and former CF210 decking are summarized in Table 1. All test loads were reduced according to the ratio of the design strength of steel (350 N/mm^2) divided by the measured yield strength (typically 370 to 400 N/mm^2).

The effective cross-section for bending is illustrated in Figure 3. The design properties of both profiles are presented in Table 2. The design of these complex profiles is not amenable to conventional analysis, and therefore the properties are established from tests.

Table 1 Test results for CF210 and SD225 decking at the construction stage

Deck type/ Steel thickness	Clear Span (m)	Failure load (kN m^2)	Measured steel strength (N/mm^2)	Test regime	
CF210 ($t = 1.25\text{mm}$)	5.5	7.31	373	Vacuum tests	
	6.0	5.64	378		
	2 x 4.0	12.46	366	375	Point load tests
		8.3			
		8.7			
8.0					
SD225	6.0	6.78	392	Vacuum test	
($t = 1.25 \text{ mm}$)	5.6	9.35	393	Point load test	
SD225 $t = 1.1 \text{ mm}$)	6.0	5.64 6.0	390	Vacuum tests	

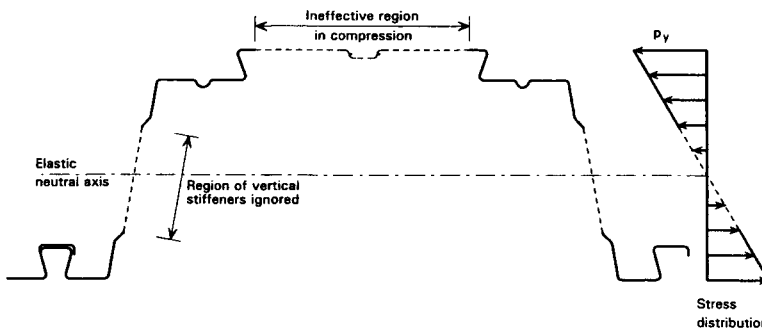


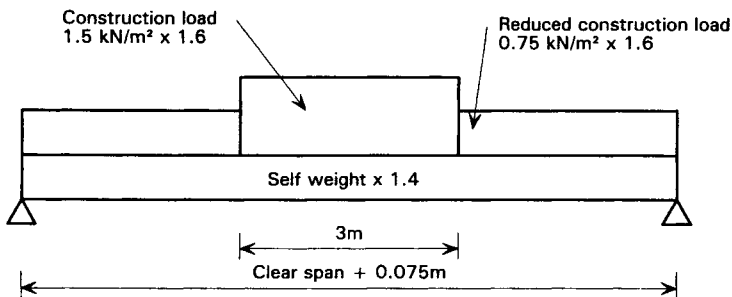
Figure 3 Effective section property of SD 225 decking

Table 2 Section properties of deep decking

Deck profile	Section modulus ($\text{cm}^3/\text{m width}$)	Second moment of area (cm^4/m)
CF 210	66.3	855
SD 225	81.0	960

$$t = 1.25 \text{ mm} \quad p_y = 350 \text{ N/mm}^2$$

The loads acting on long span decking at the construction stage are illustrated in Figure 4. A basic construction load of 1.5 kN/m^2 is considered to act over a 3 m square area, and 0.75 kN/m^2 elsewhere. An allowance for the additional weight of concrete (ponding) is made when the deflection of the decking exceeds either $\text{span}/180$ or slab depth/10.

**Figure 4** Factored loads acting at the construction stage to BS 5950

Based on these factored loads and bending resistances, it may be established that spans of up to 6 m can be achieved without propping for normal weight concrete slabs and 6.5 m for light weight concrete slabs of the minimum depth to satisfy structural and fire resistance requirements. Because of possible distortion at temporary prop positions, it is recommended that props are placed at no more than 3 m apart.

COMPOSITE SLAB TESTS

Composite slab tests were carried out at the University of Kaiserslautern in Germany, and at the University of Salford in the UK. The Kaiserslautern tests were devised in order to establish the parameters required for composite design to Eurocode 4 Part 1.1. The Salford tests were carried out on short and long span tests using light weight concrete in order to extend the range of test data. The reinforcing bars were all placed at 70 mm axis distance from the bottom of the ribs.

Table 3 Test results for composite slab tests using SD 225 decking

Test parameter	3 m span	4 m span	6 m span	8 m span
Slab depth (mm)	300	300	300	300
Average concrete strength (N/mm ²)	35	40	40	40
Reinforcement in rib (mm diameter)	16	16	20	25
Vertical shear resistance in test (kN/rib)	85	1. 99 2. 85 3. 94	1. 74 2. 76 3. 76	36
Longitudinal shear resistance τ_R (N/mm ²)	0.42	0.36	0.23	-

No shear clips were used in these tests.

The vertical shear resistances given in Table 2 include the self weight of the slab and loading equipment, and are expressed per rib (multiply by 1.67 to obtain the resistance per metre width). The similar shear resistances obtained for the 3 m and 4 m slab tests lead to the conclusion that the pure vertical shear resistance of the slab has a magnitude of 85 kN/rib.

The relevant parameters for composite design are ‘m and k’ to BS 5950 Part 4, and τ_{Rd} is the design value of this shear-bond resistance to Eurocode Part 1.1 divided by a partial safety factor of 1.25.

The average value of τ_R back-analysed from these tests is 0.36 N/m² for the 4m span tests and 0.23 N/m² for the 6m span tests. The lower value obtained for the 6m span tests results from the observation that these tests failed in pure bending rather than shear-bond. The effective tensile area of the decking is 1500 mm²/m width (t = 1.25 mm).

The pure bending resistance may be calculated from conventional reinforced concrete action by adding the tensile resistances of the decking and reinforced directly. This action is illustrated in Figure 5. The load resistance is the smaller of the bending or shear-bond resistances.

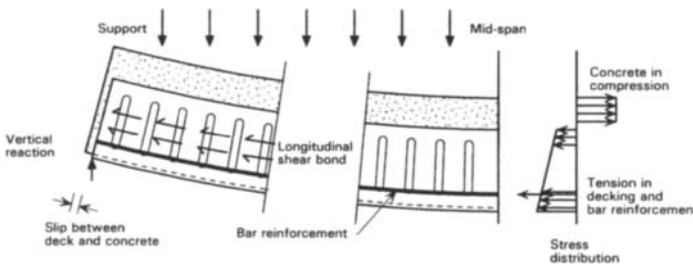


Figure 5 Action of composite slab and its reinforcement

The pure shear resistance of the slab is obtained from the sum of the resistances of the concrete and decking. For design purposes, it is proposed that the shear resistance of the decking is established using a shear strength of $0.3p_y$, to avoid interaction effects with the concrete at failure.

The stiffness of the composite section is calculated from its cracked section property multiplied by a factor of 0.9 to account for the effect of slip. However, where continuity is provided by mesh reinforcement over the support beams, the deflection can be reduced by 10%. Therefore, the above factor increases to unity when calculating the deflection of notional simply supported slabs in *Slimdek* construction.

The design value of modular ratio is taken as 10 for normal weight concrete and 15 for light weight concrete for non-permanent loading (typical of normal conditions). On the basis of these properties, it is established that clear spans of 8 to 9m can be achieved depending on the load intensity, when the slab is propped at one or two points along its length in the construction stage. These spans are limited by serviceability considerations rather than bending resistance.

FIRE RESISTANCE

The fire resistance of the composite slab may be established from conventional principles to Eurocode 4 Part 1.2, knowing:

- the temperature rise in the concrete and bar reinforcement at 60, 90 and 120 minutes.
- the strength properties of the materials at elevated temperatures.

Partial factors are set to unity in fire conditions, and the imposed loading is further reduced (to 0.6 or 0.8 of its normal design value). The strength of the decking is ignored, and the fire resistance relies on the reduced strength of the bar reinforcement in the ribs, and the unaffected strength of the mesh reinforcement over the beams.

Fire tests on slabs comprising the former CF210 decking have shown that 120 minutes fire resistance can be achieved with the reinforcement that is suitable for normal design. The minimum depth of slab is governed by insulation requirements in fire conditions and these depths are presented in Table 4.

Table 4 Minimum slab depths (mm) over the top of the decking for deep deck composite slabs

Fire Resistance (mins)	Concrete Type	
	LWC	NWC
30	50	60
60	60	70
90	70	80
120	80	95

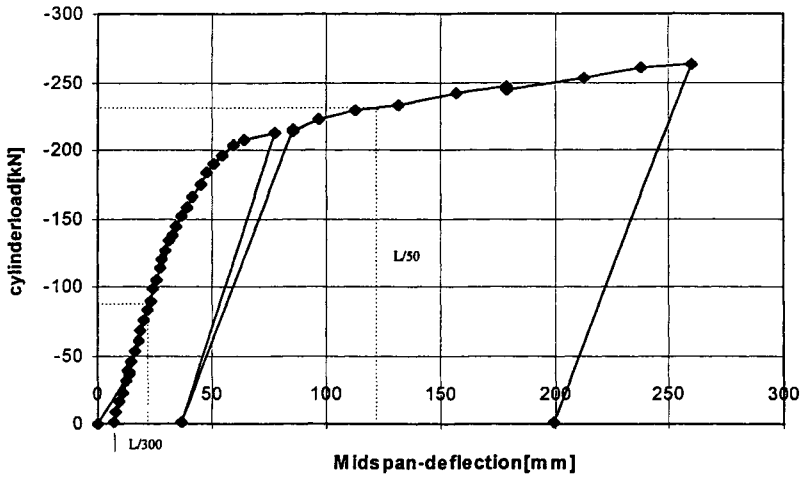


Figure 6 Load-deflection graph for 6m span composite slab

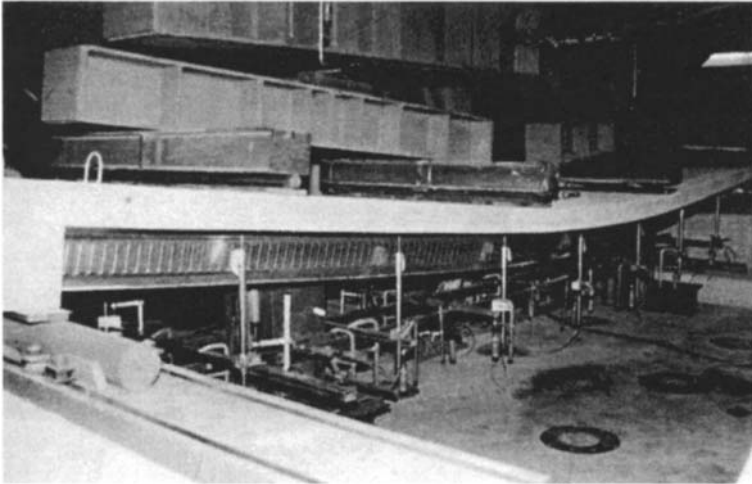


Figure 7 Composite slab during testing

CONCLUSIONS

The *Slimdek* method of construction offers considerable advantages, and the deep decking acts as a highly efficient composite slab with the in-situ concrete. The longitudinal shear-bond strength is 0.25 N/mm^2 for the new SD225 deck profile. Spans of up to 9m can be achieved when the slab is propped during construction.. A fire resistance of 120 minutes can be achieved, depending on the bar size used in the ribs.

REFERENCES

1. MULLETT, D.L. and LAWSON, R.M.
Design of slim floors with deep decking
The Steel Construction Institute publication P-127, 1993, Ascot, UK
2. LAWSON, R.M., MULLETT, D.L. and RACKHAM, J.W.
Design of Asymmetric 'Slimflor' Beams using deep composite decking
The Steel Construction Institute publication P-175, 1997, Ascot, UK
3. British Steel (Sections, Plates & Commercial Steels)
Design in Steel 3: Fast-track 'Slimflor'
British Steel, Teesside, UK
4. ENV 1994-1-1: Eurocode 4: Design of composite steel and concrete structures. Part 1.1
General rules and rules for buildings, 1994.
(Published by the National Standards Organisations in Europe)
5. BS5950 The structural use of steelwork in buildings Part 4. Code of practice for design
of composite slabs with profiled steel sheeting, 1994.

This Page Intentionally Left Blank

GEOMETRIC AND MATERIAL NONLINEAR BEHAVIOUR OF STEEL PLATES IN THIN-WALLED CONCRETE FILLED BOX COLUMNS

Q. Q. Liang¹ and B. Uy²

¹School of the Built Environment, Victoria University of Technology,
Melbourne, VIC 8001, Australia

²Department of Civil, Mining and Environmental Engineering,
University of Wollongong, Wollongong, NSW 2522, Australia

ABSTRACT

This paper is concerned with the geometric and material nonlinear behaviour of steel plates as part of a thin-walled concrete filled box column. A finite element analysis is utilised to investigate the effects of various geometric imperfections, residual stresses and width to thickness ratios on the post-local buckling behaviour and strength of clamped steel plates. A novel method is developed for determining the fictitious critical loads of plates associated with a nonlinear analysis. An effective width model is proposed for the design of clamped steel plates, and is used in the calculation of the ultimate strength of short thin-walled concrete filled box columns. Finally, the proposed design model is compared with existing experiments with a good degree of parity.

KEYWORDS

Composite columns, concrete, critical loads, effective width, finite element analysis, geometric and material nonlinearities, post-local buckling, steel plates.

INTRODUCTION

Thin-walled concrete-filled steel box columns have increased in popularity in tall building construction because they can offer greater structural efficiency and economy than both reinforced concrete and steel columns. There is a tendency to use very thin steel plates in composite steel-concrete columns based on economical considerations. However, thin steel plates in concrete filled box columns may locally buckle away from the concrete core when subjected to axial compression. The local, post-local buckling behaviour and strength of steel plates in composite steel-concrete members have been of increasing concern in recent years by various researchers.

Wright (1993) has used an energy method to derive the maximum width to thickness ratios of steel plates in contact with concrete. Ge and Usami (1994) have undertaken a strength analysis of thin-walled concrete filled box columns. Uy and Bradford (1996) have obtained the elastic local buckling coefficients of steel plates restrained by concrete by using a finite strip approach. Shakir-Khalil and Mouli (1990) and Uy (1998) have conducted tests on concrete-filled steel box columns. However, the post-local buckling characteristics of steel plates in concrete-filled box columns have not been quantified adequately, and there is also a lack of an efficient method for evaluating the true critical loads of plates associated with a theoretical nonlinear analysis.

This paper presents a theoretical study on the geometric and material nonlinear behaviour of steel plates in thin-walled box columns filled with concrete. The finite element model is outlined briefly and then the effects of various parameters on the post-local buckling characteristics of clamped steel plates are investigated. A novel method is developed for evaluating the true critical load of plates with initial imperfections. Two effective width formulas are proposed for the design of clamped steel plates and a design model is also proposed for calculating the ultimate strength of short thin-walled concrete-filled box columns. Finally, the theoretical predictions using the proposed design model are compared with independent test results.

ANALYTICAL MODEL

The finite element analysis program STRAND6.1 (1993) was used to investigate the post-local buckling behaviour of square steel plates in thin-walled concrete-filled box columns. A 10x10 mesh with eight-node quadratic plate elements was employed to discretise the plate and this can adequately quantify the local buckling mode of the plate. The von Mises yield criterion and layer approach were adopted in the analysis to model the plasticity of the material. Steel plates in concrete filled columns were assumed to have four clamped edges due to the restraint of the concrete core.

Geometric imperfections that have the same half-wavelength as the local buckling mode were considered in the analysis. A small lateral pressure applied to the plate was used to represent the initial geometric imperfections in the nonlinear analysis. In order to examine the established model, a clamped elastic square steel plate with an initial geometric imperfection of $w_0=0.1t$ was analysed and the results were compared with the postbuckling solution given by Yamaki (1959) as illustrated in Figure 1. It can be seen that the present model provided a good degree of parity with the classical solution.

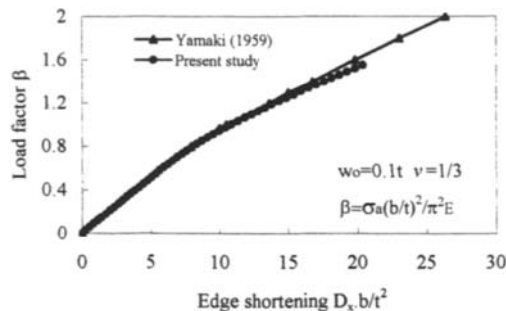


Figure 1: Comparison of present study with Yamaki's results

Residual stresses are usually induced in the plate during the process of welding. Experiments indicated that the tensile residual stresses present in the region of the weld are balanced by the compressive residual stresses locked in the remainder of the plate. An idealised residual stress distribution in a concrete-filled box column

fabricated with welded steel plates as suggested by Dwight (1975) was incorporated in the analysis as illustrated in Figure 2.

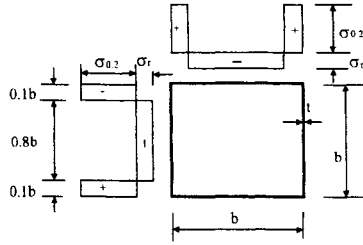


Figure 2: Residual stress pattern for welded concrete-filled steel box columns

The material stress-strain behaviour of a welded steel plate is affected by the residual stresses. Under compression, premature yielding will occur due to the presence of compressive residual stresses locked in the plate. The material stress-strain curve of a steel plate with residual stresses was defined by using the model suggested by Ramberg and Osgood (1943) in this study. The Ramberg-Osgood equation is expressed by

$$\epsilon = \frac{\sigma}{E} \left[1 + \frac{3}{7} \left(\frac{\sigma}{\sigma_{0.7}} \right)^n \right] \tag{1}$$

where ϵ is the strain, σ is the stress, E is the elastic modulus, $\sigma_{0.7}$ is the stress corresponding to $E_{0.7} = 0.7E$ and n is the knee factor. The knee factor $n = 25$ was used for structural mild steel with residual stresses in the present analysis.

PARAMETRIC STUDY

Plates with different geometric imperfections

Clamped square plates ($b/t=100$) with different geometric imperfections and with the compressive residual stresses of $\sigma_r = 0.125\sigma_{0.2}$ were analysed in order to determine the effects of geometric imperfections on the post-local buckling behaviour. The material properties of the plate adopted in the analysis were: proof stress $\sigma_{0.2} = 300\text{ MPa}$, elastic modulus $E = 200,000\text{ MPa}$ and Poisson's ratio $\nu=0.3$. The elastic critical buckling stress σ_{cr} was calculated by using the formula given by Bulson (1970) as

$$\sigma_{cr} = \frac{k\pi^2 E}{12(1-\nu^2) \left(\frac{b}{t} \right)^2} \tag{2}$$

where b and t are the width and thickness of the plate respectively, and k is the elastic local buckling coefficient. This study adopted a minimum elastic local buckling coefficient of 9.81 for plates in concrete filled steel box columns, which was obtained by undertaking a linear elastic finite element buckling analysis of plates based on the bifurcation buckling theory as described in STRAND6.1.

The load-transverse deflection curves of clamped plates obtained from the analysis are shown in Figure 3, from which it can be seen that plates with larger geometric imperfections will undergo more total or net transverse deflections. In addition, the post-local buckling stiffness decreases with an increase in the geometric imperfection. Furthermore, the ultimate strength of plates also decreases with an increase in the level of geometric imperfections.

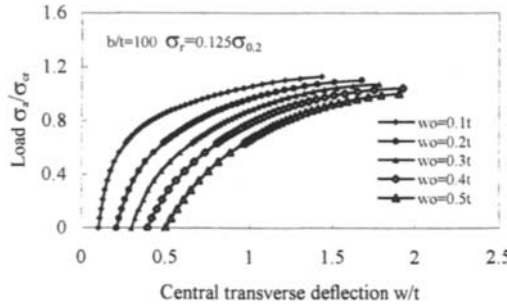


Figure 3: Load-deflection curves of plates with different geometric imperfections

Plates with different residual stresses

The sensitivity of the post-local buckling behaviour of steel plates to residual stresses was investigated. Geometric imperfections of 0.1t were also considered in the analysis. Figure 4 illustrates the effects of different residual stress levels on the post-local buckling characteristics of steel plates in thin-walled concrete-filled box columns. It can be seen from Figure 4 that residual stresses have a more pronounced effect on stocky plates. Moreover, the ultimate strength of plates decreases with an increase in compressive residual stress levels. In comparison with stress relieved plates, the ultimate strength of heavily welded plates ($\sigma_r = 0.25\sigma_{0.2}$) is reduced approximately by 9% for plates with $b/t=40$, by 6% for plates with $b/t=70$ and by 3% for slender plates with $b/t=100$.

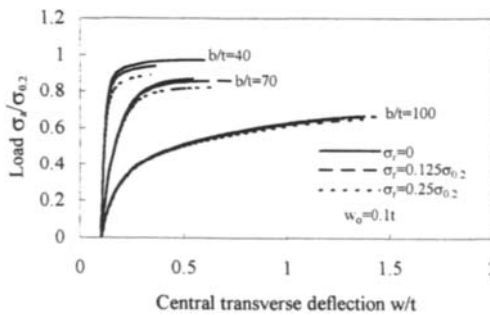


Figure 4: Load-deflection curves of plates with different residual stresses

Plates with different b/t ratios

Plates with different b/t ratios were studied in order to quantify the post-local buckling behaviour and ultimate strength of different sized thin-walled concrete filled columns. The geometric imperfections of 0.1t and compressive residual stresses of $\sigma_r = 0.25\sigma_{0.2}$ were incorporated in the analysis. The load-transverse

deflection behaviour of clamped plates with different b/t ratios obtained from this study is illustrated in Figure 5. It can be seen that plates with larger b/t ratios possess a lower local buckling stress and ultimate strength but have a higher post-local buckling reserve of strength.

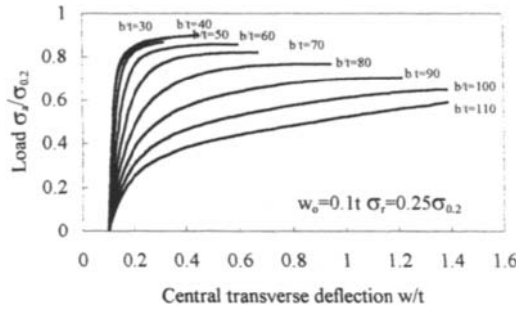


Figure 5: Load-deflection curves of plates with different b/t ratios

NOVEL METHOD FOR DETERMINING CRITICAL LOADS

Due to the presence of initial geometric imperfections, no bifurcation point can be observed in the load-transverse deflection curves of plates as shown in Figure 5, and this leads to difficulty in evaluating the critical loads. Coan (1951) suggested that the critical load of a plate could be evaluated by determining the inflection point on the load-central transverse deflection curve. This method has been found difficult to apply in practice because it is required to determine the minimum slope on the load-deflection curve.

A novel method has been developed by the authors for determining the true critical loads of steel plates with geometric imperfections based on the load-transverse deflection response. By plotting the central transverse deflection versus the ratio of the deflection to the applied load w / σ_a , it has been found that the minimum ratio of w / σ_a corresponds to the inflection point where local buckling occurs. It is noted that the inflection point of stocky plates indicates initial yielding or plastic local buckling since only yielding and plastic local buckling can cause the significant increase in plastic deformations under a small loading increment. Figure 6 illustrates the non-dimensional transverse deflection versus w / σ_a plots for plates with various geometric imperfections. It is shown in Figure 6 that the minimum value of w / σ_a highlights the onset of initial local buckling.

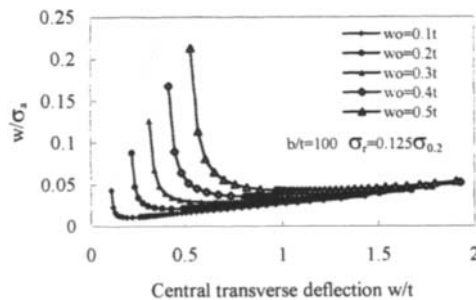


Figure 6: Load-deflection plots for determining critical loads of plates

The post-local buckling reserve of strength of steel plates σ_p can be defined as the difference between the ultimate strength σ_u and the critical local buckling stress σ_c . The critical loads and post-local buckling reserve of strength of clamped plates with $b/t=100$ and $\sigma_r = 0.125\sigma_{0.2}$ are summarized in Table 1. It is evident that the critical buckling loads σ_c for plates with initial imperfections are less than that of a perfect plate. Moreover, the critical buckling stress increases with the increase in the level of geometric imperfections and this is because the stiffness of a plate with geometric imperfections has been reduced by deflecting out of the plane before the load is applied. Furthermore, it can be concluded that the ultimate strength and post-local buckling reserve of strength of plates with larger geometric imperfections is lower than that of plates with smaller ones.

TABLE 1
CRITICAL LOADS AND POST-LOCAL BUCKLING RESERVE OF STRENGTH OF PLATES

w_0 / t	$(w / \sigma_c)_{\min}$ (mm/MPa)	w / t	t (mm)	σ_c (MPa)	σ_p (MPa)	σ_u (MPa)	$\frac{\sigma_p}{\sigma_u}$ (%)
0.1	0.011	0.194	5	88.182	111.818	200	56
0.2	0.021	0.429	5	102.143	92.857	195	48
0.3	0.029	0.653	5	112.586	77.414	190	41
0.4	0.036	0.874	5	121.389	63.611	185	34
0.5	0.042	1.078	5	128.333	49.167	177.5	28

EFFECTIVE WIDTH MODEL

The post-local buckling characteristics of clamped steel plates can be expressed approximately by the effective width, which can be evaluated from the results of a nonlinear finite element analysis as

$$\frac{b_e}{b} = \frac{\sigma_u}{\sigma_{0.2}} \quad (3)$$

in which b_e is the effective width of the plate. Table 2 presents the effective width of clamped steel plates with a geometric imperfection of 0.1t and residual stress of $\sigma_r = 0.25\sigma_{0.2}$ obtained from the finite element analysis. Based on the present finite element results, two effective width formulas were derived for the design of plates in thin-walled concrete-filled steel box columns as

$$\frac{b_e}{b} = 0.6753 \sqrt{\frac{\sigma_{cr}}{\sigma_{0.2}}} \quad (4)$$

when $\sigma_{cr} \leq \sigma_{0.2}$, and

$$\frac{b_e}{b} = 0.9153 \sqrt{\frac{\sigma_{cr}}{\sigma_{cr} + \sigma_{0.2}}} \quad (5)$$

when $\sigma_{cr} > \sigma_{0.2}$.

The effective width of clamped steel plates is expressed by the proof stress $\sigma_{0.2}$ or the yield stress of the plate and the elastic critical local buckling stress σ_{cr} , which is calculated by using Eqn. 2 with a minimum buckling coefficient of 9.81. It can be seen from Table 2 that Eqns. 4 and 5 provide conservative estimates to the finite element result. This is because the proposed formulas have considered that steel plates in real thin-walled concrete-filled box columns may have greater imperfections than the present finite element model.

TABLE 2
EFFECTIVE WIDTH OF STEEL PLATES IN CONCRETE-FILLED BOX COLUMNS

$\frac{b}{t}$	σ_{cr} (MPa)	b_e / b (Finite Element Results)	b_e / b Eqn. 4	b_e / b Eqn. 5
30	1969	0.9	0.872	
40	1108	0.89	0.845	
50	709	0.869	0.814	
60	492	0.859	0.78	
70	361.5	0.822	0.748	
80	276.8	0.768		0.657
90	218.7	0.706		0.607
100	177	0.65		0.566
110	146.4	0.595		0.53

STRENGTH OF CONCRETE-FILLED STEEL BOX COLUMNS

The ultimate strength of a short thin-walled concrete-filled steel box column in compression can be calculated by combining the ultimate strength of the concrete core and the steel plates, which is expressed by

$$N_u = 0.85 f_c A_c + f_y A_{se} \quad (6)$$

in which f_c is the compressive cylinder strength of concrete, A_c is the concrete area of the cross section, f_y is the yield stress of the steel plate and A_{se} is the total effective steel area of the cross section which is determined by using the proposed effective width formulas Eqns. 4 and 5. Because of the uncertainty between the test cylinder strength and in-situ strength, the reduction factor for the cylinder compressive strength of concrete is taken as 0.85.

COMPARISON WITH EXPERIMENTAL RESULTS

The proposed design model for the ultimate strength of short thin-walled concrete filled box columns is examined by comparing with existing experimental results as shown in Table 3. Specimens NS1~NS17 were undertaken by Uy (1998) whilst specimens C1~C9 were conducted by Shakir-Khalil and Mouli (1990). The effective width of specimens C1~C9 in Table 3 is the average value of the adjacent sides of the section since the columns were rectangular. In specimens NS5, NS11 and NS17 the loads were carried by steel plates only. It can be observed from Table 3 that the theoretical determinations of the ultimate strength of concrete-filled box columns using the proposed design model agree very well with the experimental results. The mean theoretical ultimate strength is 94% of that of the experimental results. This illustrates the conservative nature of the model.

CONCLUSIONS

The post-local buckling characteristics of steel plates in concrete-filled box columns have been investigated by using the finite element method. Steel plates with different levels of geometric imperfections, residual stresses and b/t ratios have been analysed in order to determine the post-local buckling strength of clamped steel plates. The critical loads as well as the post-local buckling reserve of strength of plates with initial imperfections can be determined efficiently from a theoretical analysis by using the novel method presented in this study. The proposed effective width formulas can be used in the ultimate strength calculation of short thin-walled concrete filled box columns in compression. The accuracy of the design models has been examined by comparisons with a classical solution as well as experimental results.

TABLE 3
ULTIMATE STRENGTH OF CONCRETE-FILLED STEEL BOX COLUMNS

Specimen	Size $b \times b$	f_y (MPa)	E (10^3 MPa)	f_c (MPa)	b/t	b_e / b Theory	$N_{uTheory}$ (kN)	N_{uTest} (kN)	$\frac{N_{uTheory}}{N_{uTest}}$
NS1	186x186	294	200	33.6	60	0.783	1428.6	1555	0.919
NS5	186x186	281	200	NA	60	0.787	483.5	517	0.935
NS7	246x246	292	200	40.6	80	0.663	2548.8	3095	0.824
NS11	246x246	292	200	NA	80	0.663	561	563	0.996
NS13	306x306	281	200	44	100	0.579	3953.3	4003	0.988
NS14	306x306	281	200	47	100	0.579	4182.8	4253	0.983
NS15	306x306	281	200	47	100	0.579	4182.8	4495	0.931
NS16	306x306	281	200	47	100	0.579	4182.8	4658	0.898
NS17	306x306	281	200	NA	100	0.579	587.3	622.3	0.944
C1	120x80	357.5	205	41.6	24(16)	0.892	848.3	850	0.998
C2	120x80	341	205	42.6	24(16)	0.892	819.3	900	0.91
C3	120x80	341	205	46.2	24(16)	0.892	841.6	920	0.915
C4	120x80	362.5	205	42.4	24(16)	0.891	863.6	950	0.909
C5	120x80	362.5	205	40.8	24(16)	0.891	857.2	955	0.898
C6	150x100	346.7	209.6	46	30(20)	0.881	1158.6	1210	0.958
C7	150x100	346.7	209.6	46.2	30(20)	0.881	1155.1	1200	0.963
C8	150x100	340	208.6	46.6	30(20)	0.882	1155.4	1190	0.971
C9	150x100	340	208.6	47.2	30(20)	0.882	1159.6	1200	0.966
Mean									0.94

REFERENCES

- Bulson, P.S. (1970). *The Stability of Flat Plates*, Chatto and Windus, London.
- Coan, J. M. (1951). Large deflection theory for plates with small initial curvature loaded in edge compression. *Trans. Am. Soc. Mech. Engrs.* **73**, 143-162.
- Dwight, J.B. (1975). Prediction of residual stresses caused by welding. *Steel Construction* **9:1**, 2-9.
- Ge, H.B. and Usami, T. (1994). Strength analysis of concrete-filled thin-walled steel box columns. *Journal of Constructional Steel Research* **30**, 259-281.
- Ramberg, W. and Osgood, W.R. (1943). Description of stress-strain curves by three parameters. *NACA Technical Note*, No. 902.
- Shakir-Khalil, H. and Mouli, M. (1990). Further tests on concrete-filled rectangular hollow-section columns. *The Structural Engineer* **68:20**, 405-413.
- STRAND6.1 (1993). *Reference Manual and User Guide*, G+D Computing Pty Ltd, Sydney.
- Uy, B. (1998). Local and post-local buckling of concrete-filled steel welded box columns. *Journal of Constructional Steel Research* (to appear).
- Uy, B. and Bradford, M.A. (1996). Elastic local buckling of thin steel plates in composite steel-concrete members. *Engineering Structures* **18:3**, 193-200.
- Wright, H.D. (1993). Buckling of plates in contact with a rigid medium. *The Structural Engineer* **71:12**, 209-215.
- Yamaki, N. (1959). Postbuckling behaviour of rectangular plates with small initial curvature loaded in edge compression. *J. Appl. Mech. Am. Soc. Mech. Engrs.* **26**, 407-414.

LATERAL-DISTORTIONAL BUCKLING OF COMPOSITE CANTILEVERS

M.A. Bradford

School of Civil and Environmental Engineering, The University of New South Wales, Sydney, NSW 2052, Australia

ABSTRACT

Composite steel-concrete tee-beams cantilevered from a fixed root and subjected to gravity loading are a form of composite construction in which the entire steel I-section is subjected to a combination of negative bending and compression. Under such loading, the steel component is subjected to lateral-distortional buckling, since the top flange is restrained by the concrete slab. This paper considers the elastic buckling of composite cantilevers, which represents a grey area in design against structural instability. Hitherto, design methods such as the well-known inverted U-frame approach have been applied to this problem, in lieu of the extremely conservative assumption of treating the problem as one of lateral-torsional buckling. A well-publicised finite element method of analysis is applied to the problem, and the behaviour of a specific cross-section cantilever beam is considered. In particular, the buckling mode shapes are considered, as is the positioning of a lateral brace within the span that prevents the transverse and twist buckling displacements of the bottom flange.

KEY WORDS

Bracing, buckling, cantilevers, composite beams, distortion, elasticity, restraint.

INTRODUCTION

Steel-concrete composite beams cantilevered from a support are a form of construction that is occasionally met in practice. It is of particular interest in structural stability, as the top flange of the steel I-section component is fully or close to fully restrained by the concrete slab, rendering the bottom compressive flange free to buckle by translation and twist, with this flange being restrained only by the flexibility of the web. It is thus the extreme case of the more commonly met continuous composite beam in negative bending. The buckling mode of a steel I-section member loaded and restrained in this way is depicted in Figure 1.

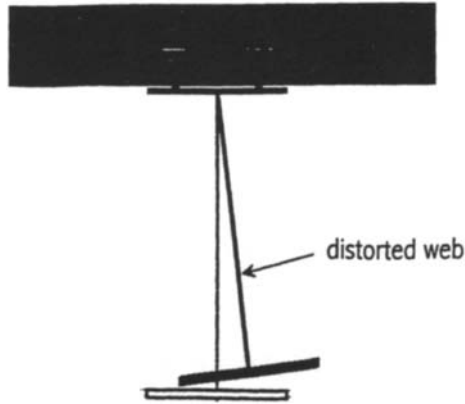


Figure 1: Buckled shape illustrating web distortion

Attempts to treat the problem as a buckling analysis with Vlasov-type assumptions, that is lateral-torsional buckling (Trahair 1993, Trahair and Bradford 1998), fail on two counts. Firstly, if the steel I-section component is treated as a free cantilever under gravity loading, then the restraint provided by the concrete slab is ignored and, as will be demonstrated herein, the buckling load is severely underestimated. Secondly, if the restraint is included in the analysis, the top flange is completely restrained against lateral deflection and completely (or nearly so) restrained against twist during buckling. Invoking the Vlasov assumption of a non-deformable cross-section in this case suggests that the buckling load approaches infinity. Of course, both of these aspects of modelling the instability of the steel component using Vlasov theory are incorrect, and the overall instability must be of a lateral-distortional type (Bradford 1992).

A rational modelling of the lateral-distortional buckling of composite beams in negative bending was made by Hamada and Longworth (1974) using the finite element method, but little progress was made in the rational analysis of the problem for the next decade. Johnson and Bradford (1983) used a specially-developed elastic line-type finite element to model the buckling, and provided a design proposal. This design proposal was later extended by Bradford and Johnson (1987) and another was suggested by Weston and Nethercot (1987). Both of the latter analyses deployed an inelastic finite element method. The inelastic line-type distortional buckling finite element developed by Bradford (1986) was used in a further study (Bradford 1989) to propose a simple design rule based on the Australian AS4100 (1990) steel code, and this rule was calibrated against the sophisticated analyses presented by Weston and Nethercot (1987). Further finite element studies were made of an *encastre* composite tee-beam by Bradford and Gao (1992) and Williams *et al.* (1993), and tapered composite cantilevers were considered by Bradford and Ronagh (1995, 1997).

In lieu of using the aforementioned research-based finite element models, recourse is usually made to the 'inverted U-frame' approach (Oehlers and Bradford 1995) for routine structural design. This method assumes that the bottom (compression) flange of the steel component of a composite tee-beam

in negative bending buckles as a uniformly compressed strut, restrained continuously by the stiffness of the deformable web. This method is an over-simplification, as in practice the steel component is subjected to moment gradient, and consequently the compression in the flange 'strut' is not constant. In order to account for the nonuniform compression in the bottom flange, Svensson (1985) presented a buckling model with a number of loading conditions that cause nonuniform stressing of an elastically-restrained strut, and solved the differential equations to produce design charts. He applied this method to model the buckling of composite tee-beams with a negative moment region, but the example presented was only approximate as it did not account for the increased compression in the flange induced by tension in the slab reinforcement, nor for the propensity of the web itself to buckle. In addition, it has been shown in a number of studies by the author (which are summarised in Bradford 1997) that even the modelling of a uniformly compressed beam flange whose other flange is restrained as a U-frame idealisation is prone to error.

It is therefore clear that the problem of the instability of a composite tee-beam with a negative moment region does not have a simple solution, and represents a grey area in studies of structural instability. This paper deploys a widely described and used line-type finite element method of analysis developed over fifteen years ago by Bradford and Trahair (1981) to study the buckling of a composite cantilever with a tip load. This loading represents an extreme case of negative bending of the composite member, and has been chosen here primarily to demonstrate the lateral-distortional buckling of the steel component. The problem is interesting, in that the bottom flange at the tip of the cantilever is unrestrained and subjected to zero bending moment, while the root of the cantilever is fully restrained against buckling yet subjected to the maximum bending moment along the member. By observing the buckling mode shape, it is shown how the provision of a bottom flange brace (as in conventionally-used cross-bracing) at the position of maximum buckling displacement increases the elastic buckling load substantially.

THEORETICAL MODELLING

General

A cantilever whose cross-section is shown in Figure 2 is loaded by a concentrated load at the tip. An in-plane analysis is undertaken firstly, followed by an out-of-plane analysis to determine the buckling load factor λ . Since an elastic buckling analysis is being undertaken, the effects of yielding are ignored, however the concrete is assumed cracked throughout.

In-Plane Analysis

If the cantilever is of length L and the longitudinal coordinate x is measured from the root, the moment in the section is $P(L-x)$, where P is the tip load. Because all of the stress resultants in the I-section component are increased monotonically until buckling occurs, the reinforcement is assumed to remain elastic. Although in reality the reinforcement would be at yield, being typically 2% of the concrete area, its remaining elastic is necessary for the buckling analysis and is consistent with the elastic in-plane analysis for an elastic buckling analysis.

When the cross-section is subjected to a negative moment M , a tensile force N_s is induced in the reinforcement, and equilibrium requires an equal and opposite compressive force in the steel component of N_s , as shown in Figure 2. The steel component is also subjected to a (negative) moment M_s equal to the difference between the applied moment M and the couple produced by the forces N_s and N_s .

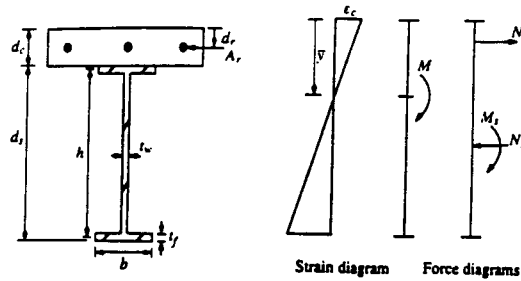


Figure 2: Section and actions

From elementary mechanics, it can be shown that the actions in the steel I-section component are:

$$M_s = M \left(1 - \frac{A_r (\bar{y} - d_r) (d_c + d_s / 2 - d_r)}{I_s + A_s (d_c + d_s / 2 - \bar{y})^2 + A_r (\bar{y} - d_r)^2} \right) \quad (1)$$

$$N_s = M \left(\frac{A_r (\bar{y} - d_r)}{I_s + A_s (d_c + d_s / 2 - \bar{y})^2 + A_r (\bar{y} - d_r)^2} \right) \quad (2)$$

where the dimensions are shown in Figure 2, A_r , A_s and I_s are the area of the reinforcement, area of the steel component and second moment of area of the steel component, and \bar{y} is the depth of the neutral axis from the top of the slab.

Out-of-Plane Analysis

The buckling analysis is carried out using the 'Bradford-Trahair' line element (Bradford and Trahair 1981). This element is well-documented in the aforementioned reference and elsewhere, and will not be described in detail here. It is worth mentioning, however, that during buckling the cross-section of the element permits distortion of the web as a cubic curve, but models the flanges as rigid beam-like elements. The element has six buckling degrees of freedom at each end or node, corresponding to lateral displacement and twist of the top and bottom flanges and minor axis rotation of the top and bottom flanges. For the analysis herein, the top flange buckling degrees of freedom are fixed, and the global stiffness matrix $[K]$ and the global stability matrix $[G]$ are assembled, the latter matrix from the initial actions determined from Eqns. 1 and 2. The buckling condition is represented by the familiar equation

$$([K] - \lambda[G]) \cdot \{Q\} = \{0\} \quad (3)$$

where $\{Q\}$ is the vector of buckling degrees of freedom. Equation 3 may be solved by a routine eigensolver for the buckling load factor or eigenvalue λ and eigenvector or mode shape $\{Q\}$.

ILLUSTRATION

A cantilever with the geometric cross-sectional parameters $h = 1200\text{mm}$, $b = 300\text{mm}$, $t_f = 20\text{mm}$, $t_w = 10\text{mm}$, $d_r = 50\text{mm}$ and $d_c = 30\text{mm}$ was studied. Further, the reinforcement was taken as 3-Y20 bars and the Young's modulus and Poisson's ratio of the steel as 200,000 MPa and 0.3 respectively. In order to maintain practical relevance to the problem, cantilever lengths of $L = 10\text{m}$, 15m and 20m were analysed.

In order to demonstrate the beneficial effects of the slab restraint, the elastic distortional buckling load P_{od} incorporating continuous and full restraint was compared with the lateral buckling load P_{ob} , calculated assuming the I-section is unrestrained, but both under the same loading regime. The results are presented in Figure 3. It can be seen that the buckling load is increased over sixfold for a beam of length 10m down to about threefold for a beam of length 20m. This increase in capacity due to the restraint provided by the slab is substantial, and cannot be ignored in design.

Figure 4 shows the buckled deflection of the bottom flange. The maximum buckling deformations can be seen to occur towards midspan, at which location the balance between moment and restraint permits the bottom flange to deflect most. As x moves towards the origin, the restraint at the root becomes dominant, while as $x \rightarrow L$ the low moment region becomes dominant, so that in both cases the buckling deformations decrease away from midspan. Of course, the eigenvector is indeterminate in magnitude, and so the deformations are normalised with respect to a maximum value of unity.

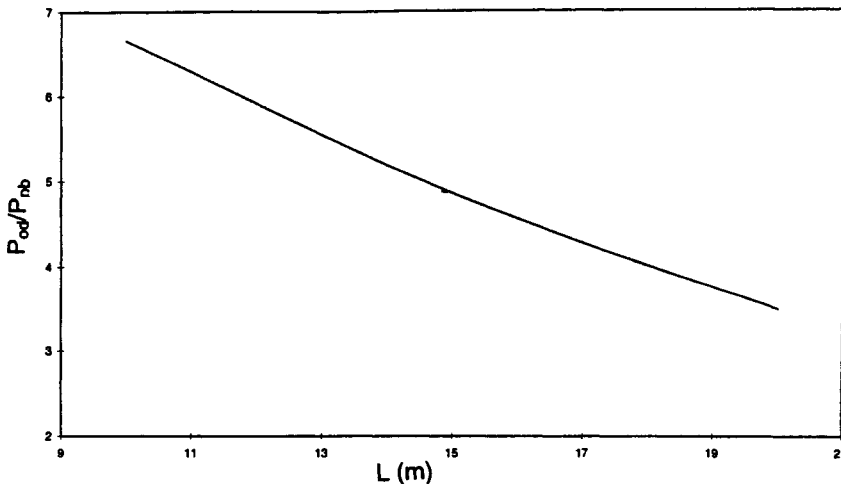


Figure 3: Enhanced elastic buckling loads due to slab restraint

A cantilever of length $L = 15\text{m}$ was considered with its bottom flange braced at a discrete point along the member against lateral deflection and twist, as would be encountered with cross-bracing. Figure 5 shows the ratio of the distortional buckling with a brace $(P_{od})_{brace}$ to that determined without a brace, P_{od} , as the brace position moves along the beam. Not surprisingly, the most advantageous position to position the brace is close to the maximum buckling position near $x/L = 0.4$. The buckling mode with the brace at this position is shown in Figure 6. With a brace at this position, the position of the next largest buckling deformation occurs near $x/L = 0.8$, and bracing this position as well increases the buckling load to $2.31P_{od}$.

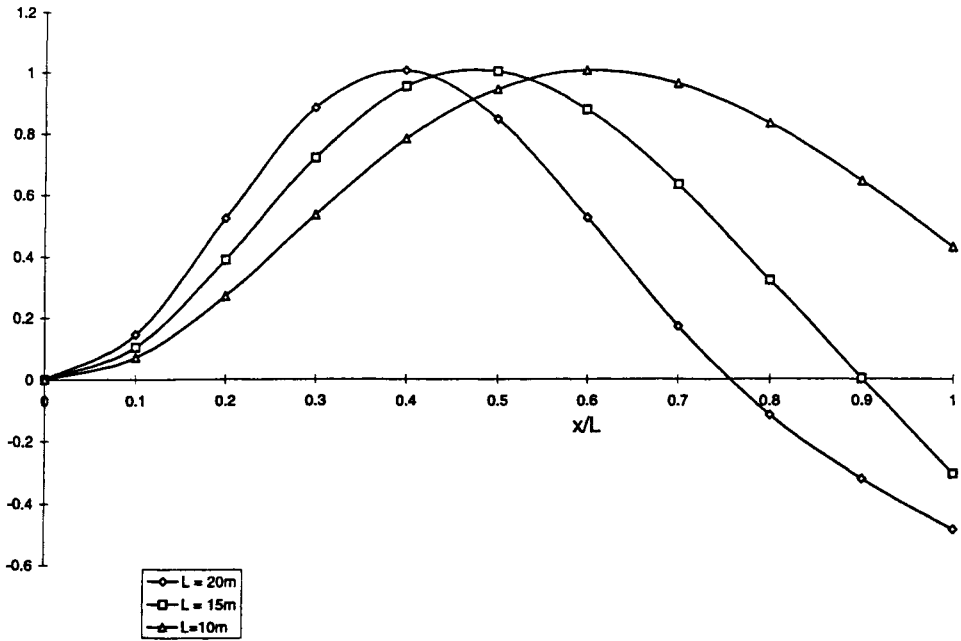


Figure 4: Relative bottom flange translational buckling modes

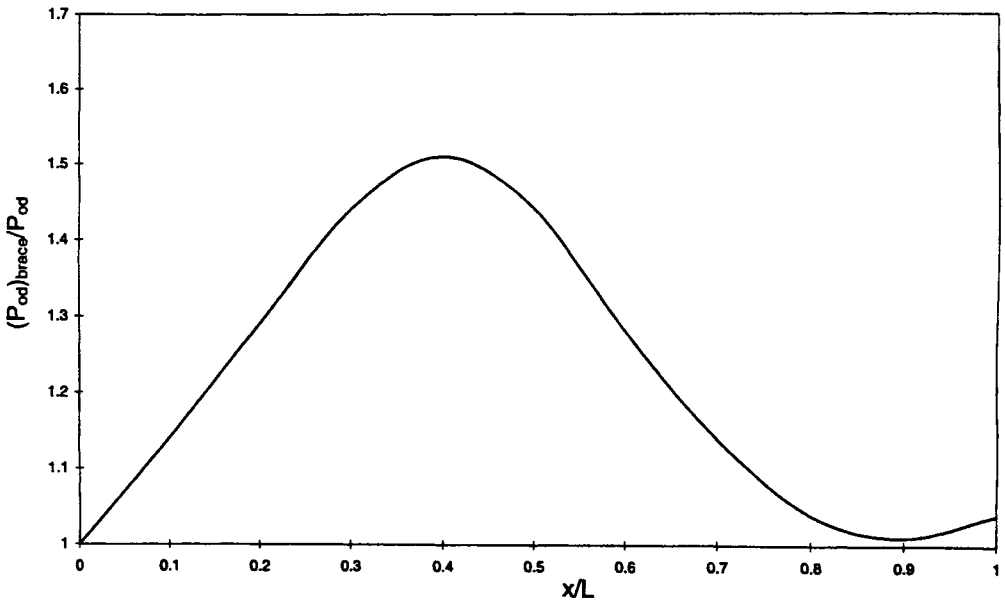


Figure 5: Enhanced buckling loads due to bracing

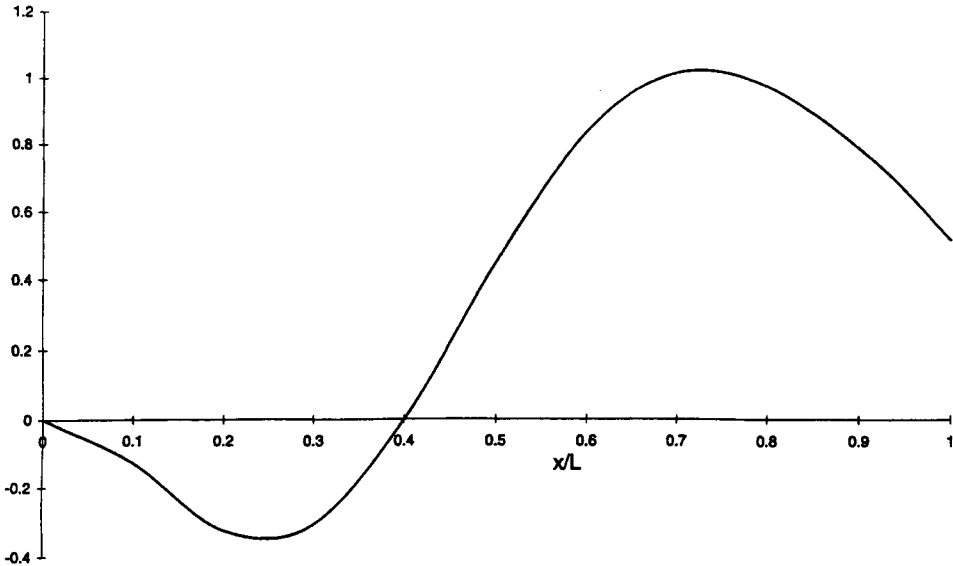


Figure 6: Buckling mode with brace at $x = 0.4L$

CONCLUDING REMARKS

A rational finite element method of analysis has been used to investigate the lateral-distortional buckling of a composite tee-section cantilever with a tip load. The substantial increase in buckling load provided by the restraint of the slab over the lateral-torsional buckling load ignoring this restraint has been demonstrated. Mode shapes have been plotted using the elastic distortional buckling analysis, and the maximum buckling deformation of the bottom flange was found to occur just on the root side of midspan. The effect of cross-bracing was illustrated, and not surprisingly the optimum position for the brace was at the position of the maximum buckling displacement. Bracing at the next most highly deformed position with this near-midspan brace increased the buckling load by 231%.

Lateral-distortional buckling of composite beams that exhibit a negative moment region is a grey area in structural stability research, and this paper was intended to shed some light on the phenomenon when the entire beam was subjected to negative bending.

ACKNOWLEDGEMENT

The work described in this paper was supported by a grant awarded to the author by the Australian Research Council.

REFERENCES

- Bradford, M.A. (1986). Inelastic distortional buckling of I-beams. *Computers and Structures* **24**:6, 923-933.
- Bradford, M.A. (1989). Buckling strength of partially restrained I-beams. *Journal of Structural Engineering*, ASCE **115**:5, 1272-1276.
- Bradford, M.A. (1992). Lateral-distortional buckling of steel I-section members. *Journal of Constructional Steel Research* **23**, 97-116.
- Bradford, M.A. (1997). Lateral-distortional buckling of continuously restrained columns. *Journal of Constructional Steel Research* **42**:2, 121-139.
- Bradford, M.A. and Gao, Z. (1992). Distortional buckling solutions for continuous composite beams. *Journal of Structural Engineering*, ASCE **118**:1, 73-89.
- Bradford, M.A. and Johnson, R.P. (1987). Inelastic buckling of composite bridge girders near internal supports. *Proceedings of the Institution of Civil Engineers*, London, Part 2 **83**, 143-159.
- Bradford, M.A. and Ronagh, H.R. (1995). Lateral-distortional instability of tapered composite beams. *Proceedings, EASEC-5*, Gold Coast, Australia, 2093-2098.
- Bradford, M.A. and Ronagh, H.R. (1997). Elastic distortional buckling of tapered composite beams. *Structural Engineering and Mechanics* **5**:3, 269-282.
- Bradford, M.A. and Trahair, N.S. (1981). Distortional buckling of I-beams. *Journal of Structural Engineering*, ASCE **107**:ST2, 355-370.
- Hamada, S. and Longworth, J. (1974). Buckling of composite beams in negative bending. *Journal of the Structural Division*, ASCE **100**:ST11, 2205-2220.
- Johnson, R.P. and Bradford, M.A. (1983). Distortional lateral buckling of unstiffened composite bridge girders. *Int. Conference on Instability and Plastic Collapse of Steel Structures*, Manchester, UK, 569-580.
- Oehlers, D.J. and Bradford, M.A. (1995). *Composite Steel and Concrete Structural Members: Fundamental Behaviour*, Pergamon, Oxford, UK.
- Standards Australia (1990). *AS4100 Steel Structures*, SA, Sydney, Australia.
- Svensson, S.E. (1985). Lateral buckling of beams analysed as elastically supported columns subjected to varying axial force. *Journal of Constructional Steel Research* **5**, 179-193.
- Trahair, N.S. (1993). *Flexural-Torsional Buckling of Structures*, E&FN Spon, London, UK.
- Trahair, N.S. and Bradford, M.A. (1998). *The Behaviour and Design of Steel Structures*, 3rd edn., E&FN Spon, London, UK.
- Weston, G. and Nethercot, D.A. (1987). Continuous composite bridge beams - stability of the steel compression flange in hogging bending. *Proceedings, Stability of Plates and Shell Structures, ECCS*, Vandepitte, 47-52.
- Williams F.W., Jemah, A.K. and Lam, D.H. (1993). Distortional buckling curves for composite beams. *Journal of Structural Engineering*, ASCE **119**:7, 2134-2149.

LIGHTWEIGHT THIN WALLED PROFILED STEEL SHEETING/DRYBOARD (PSSDB) COMPOSITE FLOOR SYSTEM

W.H. Wan Badaruzzaman¹ and H.D. Wright²

¹ Department of Civil & Structural Engineering, Universiti Kebangsaan
Malaysia, Bangi 43600, Selangor Darul Ehsan, Malaysia

² Department of Civil Engineering, University of Strachlyde, 107
Rottenrow, Glasgow G4 ONG, UK

ABSTRACT

This paper describes an innovative lightweight thin walled composite construction system, known as the "Profiled Steel Sheet Dry Board (PSSDB) System" developed by the authors over several years of research work. The composite panel system consists of dry boarding, such as chip, ply, or cement board, attached to a core of profiled steel sheeting using mechanical screws. Floors in buildings or small bridges are possible applications for the PSSDB system and can now be built within a shorter period of time compared to the traditional methods and materials of construction. Apart from the speed of construction and earlier occupation time of buildings, and no wastage of temporary construction materials, the PSSDB system also appeals to many clients as the panels are lightweight (approximately a quarter of the weight of normal reinforced concrete slabs) with a reduced construction depth, meaning a reduction in the floor to floor height in buildings. The PSSDB system may also be used as load bearing wall panels, and as folded plate roof structure. This paper highlights on the Bondek II/Cemboard Floor Panel (BCCFP), a derivative of the PSSDB system that has won three gold medals, i.e. the best overall invention award by the World Intellectual Property Organisation (WIPO), beating 58 other participants in the Invention & Design Competition (MINDEX/INNOTEX '97), held in Kuala Lumpur in 1997, a gold medal from the Ministry of Science, Technology and Environment, Malaysia in the same exhibition, and another gold medal received during the 26th Geneva International Exhibition on Invention, 1998. The application of the BCCFP system in flooring at the Hyatt Hotel, Sabah, Malaysia and other projects will be described in this paper.

KEYWORDS

Profiled Steel Sheet, Dryboard, Composite, Lightweight

INTRODUCTION

Traditional concepts of construction normally involve reinforced concrete system, timber building system, precast or prefabricated concrete system, load bearing masonry construction etc. Newer concepts include steel building systems, composite slab system, and various modular systems such as the hollow block panels, lightcrete panels, drywall building system, and other similar industrialised system that are increasingly becoming available to the construction industry. The new systems and materials are introduced in view of the need to meet increasing demands for those aspects listed below:-

- Cost effective buildings.
- Innovative design flexibility.
- Reduce construction time.
- Reduce the heavy equipment on site.
- Require fewer specialised trades.
- Simplified utility installation.
- Greater structural integrity.
- Provide for excellent thermal/sound barrier.
- Environmentally intelligent.
- More durable.

In view of the above mentioned need for change, Wright, Burt and Evans (1986, 1989) introduced an innovative construction system known as the profiled steel sheeting dryboard (PSSDB) system. The system has been developed from a SERC (Science and Engineering Research Council of the United Kingdom) sponsored collaborative research carried out by investigators at Cardiff and Strathclyde Universities.

PSSDB SYSTEM – BACKGROUND AND HISTORY

Wright, Burt and Evans (1987a, 1987b, 1987c, 1994a) were involved in testing several types of sheeting used for composite slabs that has dominated floor construction during the eighties in the United Kingdom. They were studying the behaviour of the sheeting under the load of wet concrete during the construction phase and the performance of the slab under service loading once the concrete has hardened. The critical design constraint for many slabs is during the wet concrete stage, where loads of around 4 kN/m^2 , the weight of wet concrete, tools and construction workers, were required to be resisted by the steel sheeting alone. These loads are far in excess of many service loads specified for small offices, domestic accommodation etc. This led to the thought that the sheeting alone could be used as flooring for these situations. The wearing surface would, of course, have to be provided by boarding which, when attached to the sheeting, enhanced the strength and stiffness of the system. Chip boarding has become the most common form of wearing surface for domestic and similar buildings. It is generally available in both large sheets and 600 mm wide flooring panels that have tongue and grooved edges. Preliminary calculations showed that with adequate connection between 100 mm deep steel sheeting and a 19 mm chipboard, spans of over 4 m with an applied loading of well over 1.5 kN/m^2 were possible.

The original research programme concentrated upon the development of the system for use in the construction of flooring units in domestic scale buildings. In such a context, the system carries the out of plane bending and shear. From the research works conducted it was found that the connection between the steel and the chipboard could be formed using proprietary self drill and tap screws. It was possible to achieve approximately 30% increase in stiffness and considerably more increase in strength

(stiffness is likely to be the major design criterion in these situations) by using one screw every 300 mm along each rib of the sheeting. The tests also validated the use of tongue and groove panels and included the development of a special hanger bracket. A complete 4 m square area of floor was constructed and showed that the system provided the strength and stiffness of a traditional timber floor twice its depth (Wright 1986, 1989). The system became known as the PSSDB or the Profiled Steel Sheet Dry Board System. Figure 1 illustrates the PSSDB system which consists of profiled steel sheeting, compositely connected by self tapping screws to ply- or chip-boarding, to form individual panels.

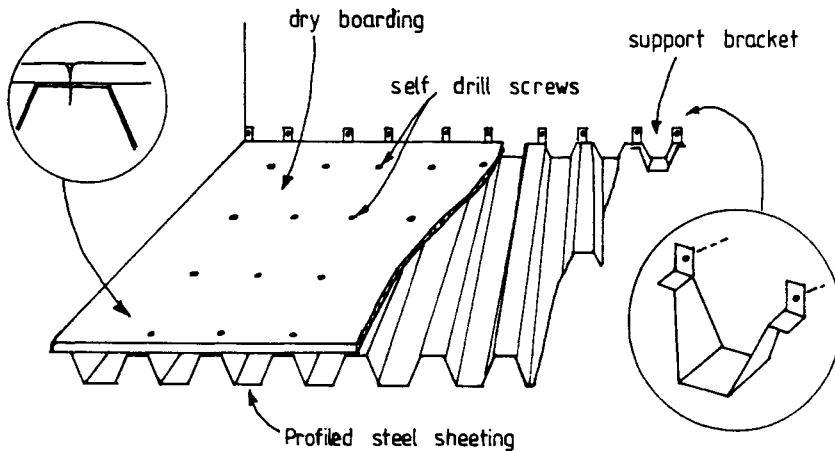


Figure 1: The envisaged profiled steel system/dryboard floor

ADVANTAGES OF PSSDB SYSTEM

Some advantages of the PSSDB system are:-

- (i) PSSDB is relatively very light.
- (ii) The overall span to depth ratio obtained from previous investigation (1989, 1994b) is 30 in comparison to one of approximately 16 for the traditional timber floor. It was shown that the PSSDB system could be designed to be 100 mm less deep than the traditional timber joist flooring system for a 4m span floor carrying domestic loading.
- (iii) The construction procedure is simple. It doesn't require temporary formwork or propping. Therefore, it can be erected quickly by unskilled labour, hence saving cost.
- (iv) The system is easily transportable due to its lightweight. Also, the profiled steel sheeting and boarding can be stacked up on top of each other during transportation.
- (v) Renovation work involving PSSDB panels is much easier to handle.
- (vi) When used as roofing systems, it will possess the significant advantage of doing away with the internal bracing of normal roof truss construction and therefore creating additional living space.

Traditional systems such as the timber joist floor boards system, *in situ* cast concrete system, and precast concrete system do possess many disadvantages (1989). Therefore, PSSDB system will help eliminate problems associated with these traditional systems.

FURTHER DEVELOPMENT ON PSSDB FLOORING

A recent study on the structural behaviour of PSSDB as flooring units has been conducted by Wan Badaruzzaman (1995) and are further reported in other references (Ahmed 1996a, Wan Badaruzzaman *et. al.* 1996b, 1996c, Ahmed *et. al.* 1996d, 1996e). Different steel sheet profiles from those used by Wright *et. al.* (1986, 1989) were used. The objective of the study is to confirm the previous findings mentioned above in order to enable a specific PSSDB derivative product (see Figure 2) known as the BCCFP (Bondek II/Cemboard Composite Floor Panel) to be practically implemented in real commercial projects that will be described later.

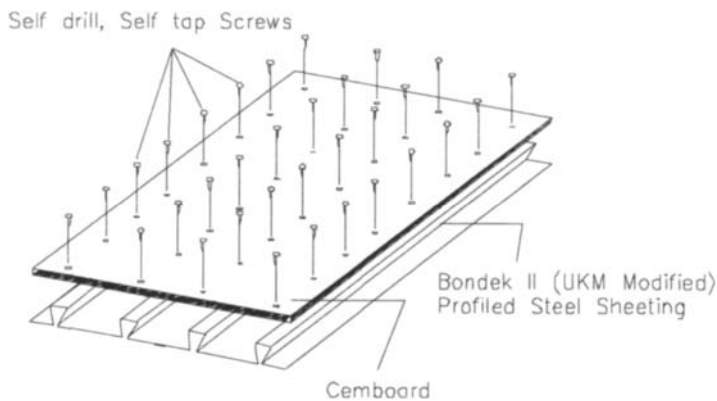


Figure 2: Bondek II/Cemboard Composite Panel (BCCFP)

A series of non-structural tests on various BCCFPs were conducted by Wan Badaruzzaman (1995, 1996f). These tests include fire rating, sound, vibration, and waterproofing tests of the BCCFPs. Various internal infill and external protective materials such as dry sand, rockwool, polyurethane, cellulose product, lightweight clay concrete, lightweight palm shell concrete, protective lower layer of thin cemboard, and cementitious fire spray coatings were explored and they served as additional features to the basic system. The panels fire ratings ranges between 1 ½ to 3 hours, hence able to conform to building regulations imposed by any authorities. Figure 3 shows an example of a panel being lowered onto a furnace for fire rating test. The sound and vibration levels of the panels were found to be acceptable and within tolerance limits of human comfort. A type of water base acrylic coating was found to be the most water resistant material compared with other coatings tried such as water soluble wax and water base silicon coatings. Figure 4 shows a cemboard panel being tested to find its modulus of elasticity and modulus of rupture after being soaked under water for 24 hours.

DESIGN PHILOSOPHY

An exclusive code of practice for the design of PSSDB system is yet to be developed. Research work to develop an integrated design method for the system is in progress. However, at present, the PSSDB system can be designed in line with and to satisfy the various design and serviceability requirements of the British Standard BS 5950: 1995: Structural Use of Steelwork in Building.

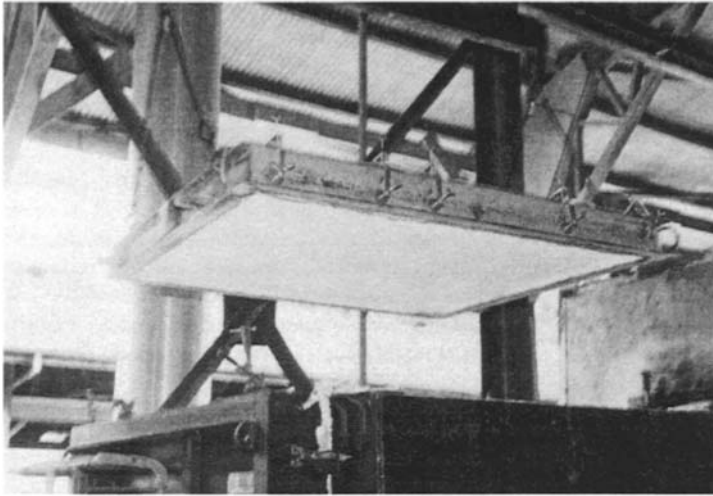


Figure 3: A BCCFP being lowered into a furnace for fire rating test



Figure 4: Cemboard specimen being tested for modulus of elasticity

Various studies show (Wright *et. al.* 1989, Ehsan 1996a) that the behaviour of the PSSDB floor system is mainly linear elastic in the working load range. The design load of the PSSDB floor has been found to be limited by the need to restrict deflection even in relatively shorter span. For this reason, an elastic method of design is more appropriate and has been adopted. To satisfy serviceability requirement, the maximum deflection of the PSSDB floor must not exceed $1/360$ of span. Accurate elastic analysis that includes the flexibility of the connection medium is carried out in predicting the deflections and stresses

of the PSSDB floors. Partial interaction analysis based on simple beam theory (Wright *et al.* 1989) and folded plate method of analysis (Wan Badaruzzaman 1994c) have been successfully used by the authors to design various practical PSSDB floors. Other design requirements such as fire rating, acoustic, water proofing, vibration control, etc. are non-structural which can vary from project to project and can be met by some minor modification of the system.

Although it is unlikely that ultimate moment capacity of the system will be a limiting function in the design, the requirement to ensure safety must be maintained. It was found that moment capacity based on fully composite elastic stress block gives a conservative prediction of ultimate moment compared with experimental results (Wright *et al.* 1989, Ehsan 1996a). It is therefore recommended that, when designing the system, the ultimate moment is based on the fully composite stress block and the tensile stress is limited to an allowable value. The allowable value would be the steel yield stress if limit state, load factor design was used or a permissible steel stress if permissible stress design was being employed.

PRACTICAL APPLICATIONS

It has been mentioned earlier in the paper that an extensive study is being carried out on the BCCFP system to eliminate problems that might occur during real construction and also during occupation of buildings. As the BCCFP system is relatively new in terms of construction techniques and materials, questions pertaining to, for example, fire rating, sound, vibration and waterproofing properties, have to be convincingly answered, before clients would allow any such system to be implemented at their project site.

The first chance to practically apply a BCCFP system was when a Civil & Structural Engineering Consultant company approached BHP Steel Building Products Malaysia. They were looking for a lightweight structural system in order to build raised floor system on top of existing reinforced concrete slab at the lobby and atrium areas in a refurbishment project of the 5-Star Hyatt Hotel in Kota Kinabalu, Sabah, Malaysia. The existing floor level was to be raised by 25 mm to 100 mm. The consultant proposed the use of BCCFP/PSSDB system as one of the alternatives to be considered by the client. When the client agreed, the PSSDB system found its way into a commercial project for the first time ever.

The floor area involved was approximately 5,000 square feet. The BCCFP floor system was designed to cater for a dead load of 2.0 kN/m², and an imposed load of 5.0 kN/m² with a deflection limit of 0.5 mm (or as minimum as possible to avoid cracking of an assortment of marbles, slates, tiles and stones profile finish). An important condition imposed by the owner was that the vibration level should be as minimum as possible to eliminate hollow sound effect while walking on the flooring system. A BCCFP system was recommended using modified Bondek II connected to 16 mm thick Cemboard with self drilling, self tapping screws spaced at 200 mm centre to centre. The BCCFP system was supported on mild steel C-channel spaced at 900 mm centre to centre rested on existing reinforced concrete slab. This gave a very good control on the deflection of the system to prevent cracking of the marbles/tiles. Lightweight concrete with a density of 1000 kg/m³ was used as infill in order to eliminate the hollow sound effect and vibration while walking on the floor. In order to fix the marbles/tiles to the cemboard, a type of adhesive grout was recommended. Figures 5 and 6 show some views during the construction process of the BCCFP floor at the Hyatt Hotel.

The new lobby and atrium floors of the hotel have now been completed (refer to Figure 7) and are adorned with plants, landscapes and dining furniture. The estimated occupancy of the floors is between 150 to 200 people all the time. From the feedback received from the client, despite the heavy traffic and additional loadings onto the floor, the BCCFP system is performing excellently. Also, according to

the client, the system is comparative in cost, easy and fast to implement. All parties involved with the refurbishment work including the client, project manager, consultants (architect, structural engineer, quantity surveyor, etc.) and the contractor were very proud to be associated with the first time implementation of the BCCFP system. The system has also been successfully implemented as floors for new lecturers' rooms at the Institute of MARA, Malaysia and as a floor for a new exhibition gallery at the Faculty of Engineering, Universiti Kebangsaan Malaysia.



Figure 5: A view of the BCCFP floor at the Hyatt Hotel during construction

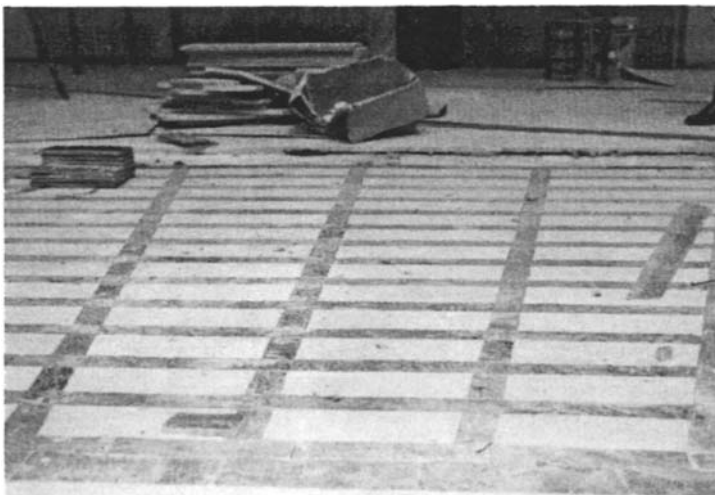


Figure 6: Tiles placed on the BCCFP floor at the Hyatt Hotel

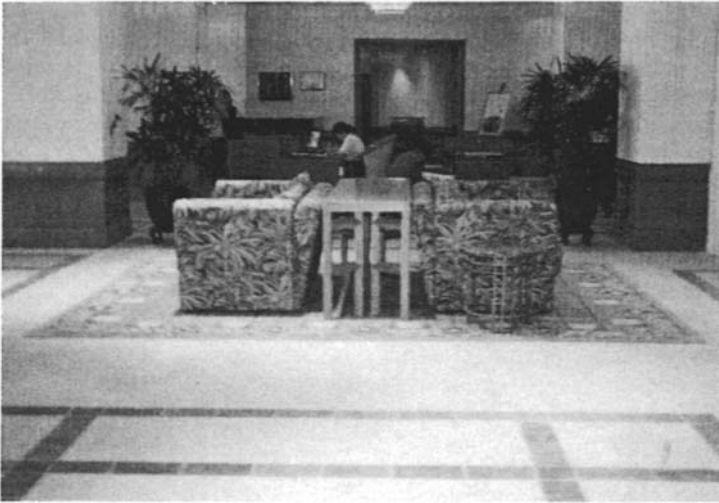


Figure 7: A view of the finished BCCFP floor at the Hyatt Hotel

WIDER POTENTIAL

Moving on from the original research works on PSSDB as flooring units, various researchers were trying to develop the system further and have carried out tests on wall and roof panels using the same system. Wall panels may be considered by using two skins of dry boards screwed either side of the sheeting. The chipboard contributes significantly to the bending stiffness of the panel thus delaying buckling whilst providing little additional strength in compression. Interaction curves which allow designers to accurately size wall panels subject to both axial and bending forces were developed from theoretical and experimental work (Jekale 1992, Benayoune 1998).

Also, the likelihood of significant shear stiffness that can be provided by the board led to its potential use as a provider of racking and shear stability. In roofing systems, the in-plane shear resistance provided by the boarding is of potential value. A theoretical and experimental study into the use of PSSDB panels in folded plate structures have been conducted (Wan Badaruzzaman 1994c) and further work is currently taking place (Ehsan 1996g). It was demonstrated that significant spans are possible with the PSSDB as roofing systems. A full scale roof structure has been erected and serves as a test bed as shown in Figure 8. Computer models developed will allow design of structures that may have application in domestic roofs and emergency shelters (Manesha 1994d, James 1994e, Wood 1994f) have been further validated by experimental models.

The authors are currently looking into the possibility of developing a building system that can be built completely using the PSSDB concept. The main thrust of the work has been in the development of proper jointing system between the floor, wall, and roof panels to form a complete building. This is thought to be the best way to bring the research forward to promote the use of the PSSDB on a bigger scale.

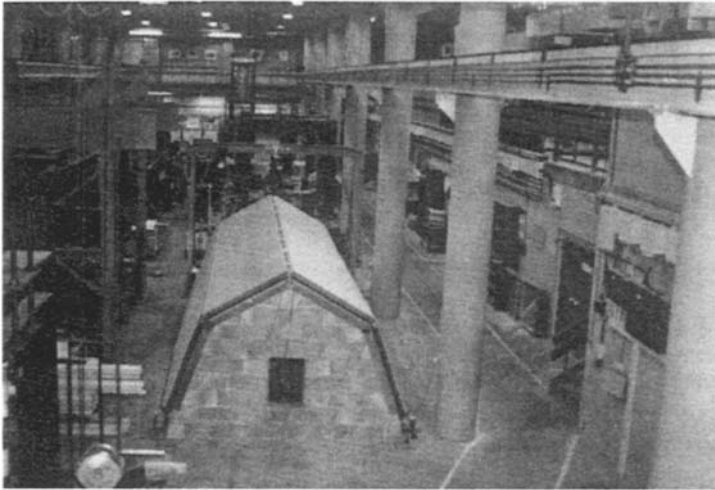


Figure 8: Roof structure under test

CONCLUSIONS

This paper has described an innovative lightweight thin walled composite construction system, known as the “Profiled Steel Sheet Dry Board (PSSDB) System”. Originally, the use of the PSSDB system was envisaged as a replacement to traditional flooring and walling systems in domestic building construction. The potential for use is however much wider. The PSSDB system when assembled into a folded plate configuration has a considerable potential.

The key characteristics of the proposed system are its lightweight, the ease with which it can be transported and the fact that it can be assembled and erected rapidly with unskilled labour. There are many structures in which the characteristics are very beneficial.

As flooring system, it can provide slender sections for mezzanine and domestic floors. In walls, it provides excellent axial, bending and racking resistance. It is quite common for profiled steel sheeting to be used as a support membrane in roofing and for this to be faced with boarding to provide easy fixing of tiled roofs. The advantages associated with treating this membrane as a composite system could be significant in terms of the removal of internal trussing and support for housing and or for use in emergency shelters for disaster relief (1994c, 1994d, 1994e).

This paper has also highlighted on the Bondek II/Cemboard Floor Panel (BCCFP), a derivative of the PSSDB system that has won three gold medals, i.e. the best overall invention award by the World Intellectual Property Organisation (WIPO), beating 58 other participants in the Invention & Design Competition (MINDEX/INNOTEX '97), held in Kuala Lumpur in 1997, a gold medal from the Ministry of Science, Technology and Environment, Malaysia in the same exhibition, and another gold medal received during the 26th Geneva International Exhibition on Invention, 1998. The application of the BCCFP system in flooring at the Hyatt Hotel, Sabah, Malaysia and other projects have been described in this paper.

References

- Wright H.D. and Evans H.R. (1986). Profiled Steel Sheeting for the Replacement of Timber Flooring in Building Renovation. *SERC Grant GR/D/76875*.
- Wright H.D., Evans H.R. and Harding P.W. (1987a). The use of Profiled Steel Sheeting in Floor Construction. *Journal of Constructional Steel Research* 7:4, 279-295.
- Wright, H.D. and Evans, H.R. (1987b). A Folded Plate Method of Analysis for Profiled Steel Sheeting in Composite Floor Construction. *Thin-walled structures* 5:1, 21-37.
- Wright H.D. and Evans H.R. (1987c). Observation on the Design and Testing of Composite Floor Slabs. *Steel Construction Today* 1, 91-99.
- Wright H.D., Evans H.R. and Burt C.A. (1989). Profiled Steel Sheet/Dryboarding Composite Floors. *The Structural Engineer* 67:7, 114-129.
- Jekale W. (1992). The Behaviour of Composite Structures Formed from Profiled Steel Sheeting and Dry Boarding. *MSc Thesis, University of Strathclyde*.
- Wright H.D. and Evans H.R. (1994a). Profiled Steel Sheet Dry Board Construction. *New Steel Construction* 2:6, 20.
- Wan Badaruzzaman W.H. and Evans H.R. (1994b). Profiled Steel Sheeting/Dry Board System as an Alternative to Existing Traditional Systems. *Proceeding of the 1st. International Conference ICAST, Universiti Kebangsaan Malaysia*, 139-145.
- Wan Badaruzzaman W.H. (1994c). The Behaviour of Profiled Steel Sheet/Dryboard System. *Ph.D Thesis. University of Wales, College of Cardiff, U.K.*
- Nepaul M. (1994d). An Experimental Study of a Rapidly Erected Shelter System. *MSc thesis University of Wales, College of Cardiff, U.K.*
- James R. (1994e). Temporary Disaster Relief Housing. *BEng Dissertation. University of Wales, College of Cardiff, U.K.*
- Wood C. (1994f). Temporary Disaster Relief Housing. *BEng Dissertation. University of Wales, College of Cardiff, U.K.*
- Wan Badaruzzaman W.H. and Rashid K. (1995). The Behaviour of Profiled Steel Sheet Dryboard System. *Universiti Kebangsaan Malaysia Research Grant FK/003/95*.
- Ahmed E. (1996a). Behaviour of Profiled Steel Sheet Dryboard Panel. *MSc Thesis, Universiti Kebangsaan Malaysia, Bangi, Selangor Darul Ehsan, Malaysia*.
- Wan Badaruzzaman W.H., Ahmed E. and Rashid K. (1996b). Out-of Plane Bending Stiffness Along the Major Axis of Profiled Steel Sheet Dry Board Composite Panels. *Jurnal Kejuruteraan UKM* 8, 79-95.

Wan Badaruzzaman W.H., Ahmed E. and Rashid K. (1996c). Behaviour of Profiled Steel Sheet Dry Board System. *Proceeding of the CIB International Conference on Construction Modernization and Education, Beijing, China.*

Ahmed E., Wan Badaruzzaman W.H. and Rashid K. (1996d). A Simplified Elastic Composite Floor Section Analysis with Incomplete Interaction. *Jurnal Kejuruteraan UKM* **8**, 67-78.

Ahmed E., Wan Badaruzzaman W.H. and Rashid K. (1996e). Composite Partial Interaction of Profiled Steel Sheeting Dry Board Floor Subject to Transverse Loading. *Proceeding of the CIB International Conference on Construction Modernization and Education, Beijing, China.*

Wan Badaruzzaman W.H. *et. al.* (1996f). Lightweight Composite Wood/Profiled Steel Sheeting System. *Ministry of Science, Technology & the Environment Malaysia Research Grant 09-02-02-0009.*

Ahmed, E. (1996g). Behaviour of Profiled Steel Sheet Dry Board Panels as Folded Plate Units. *PhD thesis in progress, Universiti Kebangsaan Malaysia.*

Benayoune, A.G. (1998). Behaviour of Profiled Steel Sheeting Dry Board Panel as Wall Units. *MSc Thesis, Universiti Kebangsaan Malaysia, Bangi, Selangor Darul Ehsan, Malaysia.*

This Page Intentionally Left Blank

LOCAL BUCKLING OF COLD FORMED STEEL SECTIONS FILLED WITH CONCRETE

B. Uy¹, H.D. Wright² and A.A. Diedricks¹

¹Department of Civil, Mining and Environmental Engineering, University of Wollongong,
Wollongong, NSW 2522, AUSTRALIA

²Department of Civil Engineering, University of Strathclyde,
Glasgow, G4ONG, UK

ABSTRACT

This paper investigates the local buckling behaviour of cold formed steel sections which have been constructed with a concrete infill. The beneficial effect of the restraint offered by the rigid concrete medium is modelled using a semi-analytical finite strip method. The finite strip method employs the use of a nonlinear model to represent the stress-strain characteristics of the cold formed steel. The analysis also considers the effect of residual stresses caused through the cold-working process, in addition to the increased longitudinal yield stress which occurs in the vicinity of the bent regions. A thorough parametric study is undertaken in this paper to consider the effects of yield stress and residual stresses for various boundary conditions. The results of the analyses show that after careful consideration of the regions of increased yield stress coupled with the accurate modelling of the residual stresses, that the effects of these issues can be considered to be negligible. This leads to the ability to design for local buckling of cold formed steel sections filled with concrete using elastic local buckling coefficients. The paper concludes with some design suggestions for local buckling and areas of further research which may be necessary.

KEYWORDS

buckling, cold formed steel, columns, composite construction, local buckling, stability

INTRODUCTION

Cold formed steel has been extensively used in the automotive industry and for industrial storage rack systems as it has a high strength to weight ratio. More recently, depletion of timber stocks and the increasing impact on the environment of deforestation has seen alternative methods for house framing arise. The use of cold formed steel has also found extensive application in the commercial building sector. Cold formed steel in structures have traditionally been used as purlins and girts in roofing and walling systems and it is in these applications that the members are required to exhibit moderate

strengths and stiffnesses. In the application of these members to house framing similar demands are placed on members, however improvements in structural performance could result in increased usage. The thin-walled nature of cold formed steel sections makes them susceptible to local buckling, however it has been shown that both the strength and stiffness can be significantly increased by the application of both lightweight or normal strength concrete as an infill material, (Schmidt et al. 1998). Furthermore, the local buckling capacity is significantly increased by the presence of concrete and this study therefore considers the aspect of local buckling of cold formed steel when concrete infill is used. The analysis incorporates the effects of residual stresses caused by cold bending in addition to the increased yield stress in the edges of the plate members.

LOCAL BUCKLING OF CONCRETE FILLED STEEL SECTIONS

The local buckling behaviour of steel sections filled with concrete was first identified by Matsui (1985) and shown to be substantially larger than that for hollow sections. This study showed empirically that the post-local buckling strength of concrete filled steel sections was 150% of the post-local buckling strength of hollow steel sections. This increase in buckling strength is created by a change in the buckling mode which is illustrated in Figure 1 for concrete filled box columns.

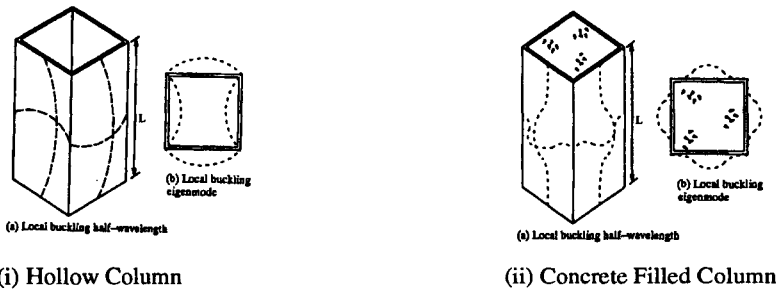


Figure 1: Local buckling modes of columns, (Uy, 1998)

Wright (1993) used the energy method to determine the local buckling behaviour of steel plates restrained by a rigid medium, which was applicable for concrete filled steel sections for a large variety of boundary conditions. The analysis was applicable to plates subjected to uniform compression, without the presence of residual stresses. This study was then further augmented to include the effects of shear stresses by Wright (1995).

Uy and Bradford (1994) developed a finite strip method to consider the local buckling of cold formed steel plates in profiled composite beams. This analysis was applicable to plates in non-uniform compression, however it ignored the effect of residual stresses caused through the bending process associated with cold formed steel sections. Furthermore, it did not include the effects of increased yield stress associated with the manufacture of cold formed steel sections. Uy (1998) modified the finite strip method for fabricated welded box sections, to incorporate the effects of residual stresses associated with the welding process. This study showed the effects of residual stresses to be quite significant to the elastic local buckling behaviour, however it was found to be less significant for the results for inelastic local buckling associated with stocky steel plates.

As it is common practice to design cold formed steel sections as slender plated elements, it is thus important to ascertain the true local buckling behaviour of these sections. The application of the concrete infill and the effects of residual stresses and increased yield stresses associated with cold forming will thus be augmented into the finite strip method developed in previous studies.

FINITE STRIP METHOD

A semi-analytical finite strip method originally developed by Cheung (1976) was modified to consider elastic and inelastic local buckling of plates with clamped loaded edges by Uy and Bradford (1994). This model has been calibrated against benchmark experiments on cold formed profiled steel sheeting restrained by concrete (Uy and Bradford 1995). This finite strip method satisfies zero slope and out-of-plane displacement at the ends of the strip by using a sine squared function and thus adequately models the restraint offered by the concrete. This section outlines the augmentation of this model to incorporate the presence of residual strains and stresses and the clamped boundary conditions existent in a cold formed steel section. The method has been fully outlined by Uy and Bradford (1995) and only pertinent changes required for incorporating the residual stresses and increased yield stresses will be discussed herein.

Residual Strains and Stresses

Residual strains and stresses for cold formed steel are created through the cold-working or bending process. These residual strains have been determined in a very detailed experimental study by Weng and Pekoz (1990). The results of these experiments have been adapted and used in the analyses conducted herein. The results of residual strains from a typical test on a C-channel are illustrated in Figure 2. The analysis herein used the average strain across the width of the plate in the analysis. This resulted in a net compressive strain of $250 \mu\epsilon$ in the plate for the web regions and $150 \mu\epsilon$ in the flange outstand regions which could produce premature local buckling.

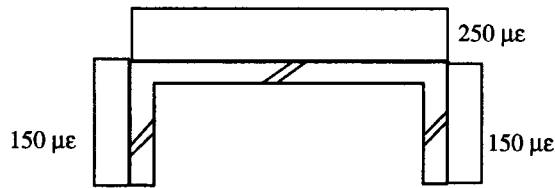


Figure 2: Idealised residual compressive strains of cold formed channel after Weng and Pekoz, (1990).

Increased Yield Stress

The effect of increased yield stress which occurs in the bent regions of cold formed stainless steel members has been determined in a very detailed analysis by Macdonald et al. (1996). The results of this study have been incorporated in the model described herein. The increased yield stresses were typically in the order of 10-20 % as illustrated from a typical distribution shown in Figure 3. For the analysis an increase in yield stress of 15 % was assumed and this was incorporated over 20 % of the width for the flange outstand and over 10 % for the webs of the box sections analysed. The result of this distribution creates a tension stiffening effect at the support which has the effect of reducing the likelihood of local buckling.

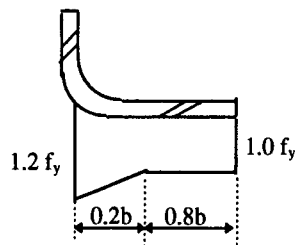


Figure 3: Idealisation of yield stress variation for cold formed section after Macdonald et al. (1996).

PARAMETRIC STUDY

In order to consider the coupled effects of residual stresses and increased yield stress on the local buckling of cold formed steel sections, a parametric study has been completed. The parametric study considers the effects of residual stresses and increased yield stresses. Two boundary conditions were chosen, which represented a box section and a flange outstand as shown in Figure 4. The boundary conditions for these were varied as simple and fixed supports to consider the effects on the local buckling capacity. The value of yield stress considered in the analysis was 300 MPa which represents a typical lower value of yield stress representative of cold formed steel sections used throughout the world.



Figure 4: Cross-sections considered in parametric study

Box Section

Cold formed steel sections which are formed into box sections provide very good structural behaviour as the local buckling capacity is substantially increased over sections with flange outstands. The presence of concrete will significantly increase the strength and stiffness of the section. Furthermore, since the local buckling capacity is significantly increased by the presence of concrete the amount of steel can be reduced and this can result in greater structural economy. Figures 5 and 6 shows the non-dimensionalised local buckling stress versus slenderness limit for both simply supported and fixed unloaded edges. The plastic limit for both the simply supported and fixed cases is shown to be 20. This plastic limit would be sufficient to ensure that the rigid plastic method common for composite beams and columns could be used in strength determination of these members. The yield limit for both cases was chosen as the slenderness limit at which the steel reaches the proof stress which is lower than the yield stress. This was determined as 50 and 60 for each of the simply supported and fixed cases. The proof stress for the steel was approximately 90 % of the yield stress of the nominal yield stress of the steel.

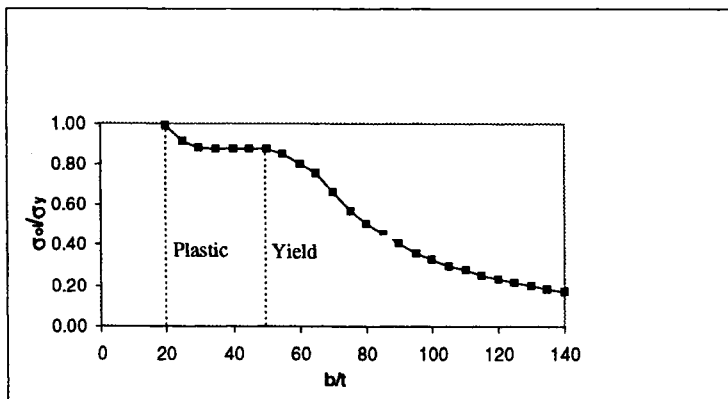


Figure 5: Box Section ($f_y=300$ MPa, Simply Supported)

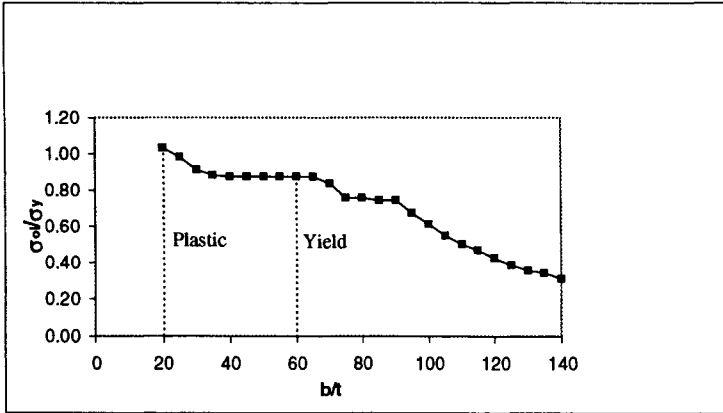


Figure 6: Box Section ($f_y=300$ MPa, Fixed)

Flange Outstand

Cold formed sections produced with flange outstands generally include C or Z sections and these are economical as they only involve bending in their manufacture, with welding being eliminated from the process. The local buckling capacity of these sections is usually increased by providing lipped edges which require significant additional energy to produce. If concrete infill is used the lips may be able to be eliminated as the concrete itself will provide restraint to increase the local buckling capacity of the section. The non-dimensionalised local buckling stress versus slenderness limit for both simply supported and fixed unloaded edges is shown in Figure 7 and 8 respectively. The plastic and yield slenderness limits were selected using the same method as that adopted for the box section. The plastic limit for both the simply supported and fixed cases was determined as 10, whereas the yield limits were determined to be 20 and 30 respectively for the simply supported and fixed cases.

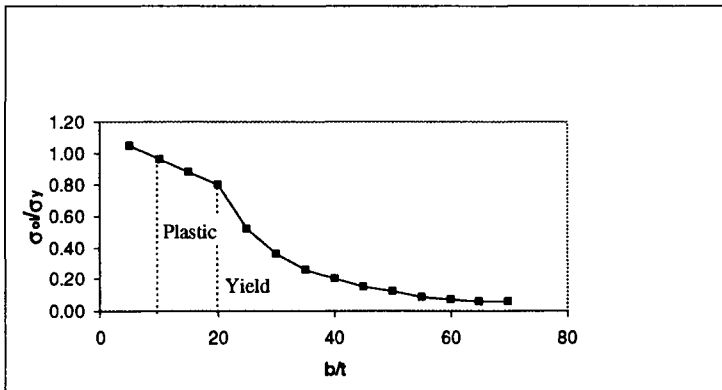


Figure 7: Flange Outstand ($f_y=300$ MPa, Simply Supported)

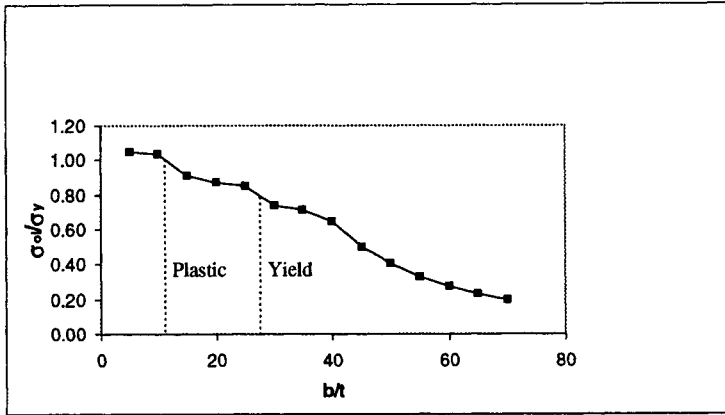


Figure 8: Flange Outstand ($f_y=300$ MPa, Fixed)

CODE COMPARISONS

Current international codes for hot-rolled and cold-formed steel do not consider the beneficial effect of the restraint provided by the concrete when determining the local buckling stress or slenderness limit. When utilising a concrete infill, substantially larger slenderness limits may be achieved which can lead to significant cost reductions in steel. Some comparisons of slenderness limits and buckling coefficients of this study are made here with existing international codes. This should highlight the significant increased slendernesses which can be achieved. The cold formed steel codes generally adopt the use of local buckling coefficients so that local buckling is accepted as occurring in the design. Hot-rolled and structural steel members are generally designed so that local buckling does not occur and thus allowable slenderness limits are adopted.

Table 1 illustrates the comparisons of the clamped finite strip method (FSM) with those of the British and Australian steel codes for the box section. Firstly the local buckling coefficient adopted in the British and Australian cold formed steel codes for the component plates of a box section subjected to uniform compression is 4.0 in BS5950 and AS/NZS4600. The clamped FSM in this analysis has resulted in a local buckling coefficient of 5.5 and 10.3, depending on the degree of restraint assumed for the unloaded edges. Furthermore, the slenderness limits established in the existing British and Australian steel codes BS5950 and AS4100 are compared with the FSM. The comparisons show that a significant increase in the yield limits results although the plastic limits are shown to be fairly similar.

TABLE 1
SLENDERNESS LIMITS AND LOCAL BUCKLING COEFFICIENTS FOR BOX SECTIONS ($F_y=300$ Mpa)

METHOD	B/T		K BUCKLING COEFFICIENT
	YIELD	PLASTIC	
BS5950: PART 1 (1990)	27	22	
BS5950: PART 5 (1987)			4.0
AS4100 (1990)	37	27	
AS/NZS4600 (1996)			4.0
CLAMPED FSM (SS)	50	20	5.5
CLAMPED FSM (FIXED)	60	20	10.3

Table 2 summarises the comparisons of the international steel codes with the clamped finite strip method for a flange outstand. These comparisons further illustrate the benefits of the use of a rational local buckling analysis.

TABLE 2
SLENDERNESS LIMITS AND LOCAL BUCKLING COEFFICIENTS FOR OUTSTANDS ($F_y=300$ MPa)

METHOD	B/T		K BUCKLING COEFFICIENT
	YIELD	PLASTIC	
BS5950: PART 1 (1990)	12	7	
BS5950: PART 5 (1987)			0.425
AS4100 (1990)	14	7	
AS/NZS4600 (1996)			0.43
CLAMPED FSM (SS)	20	10	0.6
CLAMPED FSM (FIXED)	25	10	2.0

CONCLUSIONS

The clamped finite strip method which is a rational local buckling analysis has been found to provide benefits when considering local buckling. Local buckling coefficients have been derived which incorporate the beneficial effect of concrete and these may be used in place of existing local buckling coefficients in international cold formed steel codes when concrete infill is present. Furthermore slenderness limits have been derived and shown to be in excess of those limits established in international structural steel codes. The results of the parametric study have shown that the most significant issue to be considered in the local buckling behaviour of cold formed steel sections filled with concrete is the effect of boundary conditions. The effects of both residual stresses and increased yield stress due the cold forming process were considered but were found to provide no significant detrimental effects. Thus the local buckling coefficients obtained from an elastic local buckling analysis are sufficient when considering cold formed steel sections. Whilst this may seem paradoxical this paper has shown and validated that the increase of residual stress at the corner may be negated by the increase of yield stress in cold formed structural steel members.

FURTHER RESEARCH

The major parameter found to affect the behaviour of the members in this paper was the boundary conditions of the sections. To ascertain the true boundary conditions it is considered necessary to undertake some experiments and to compare the results with the results of the theoretical analysis. Further tests to ascertain the effects of interaction buckling associated with local and global buckling are necessary as it is anticipated that local buckling can have a significant effect on stiffness when it occurs in the elastic range and this can subsequently influence the global buckling load of the column.

ACKNOWLEDGEMENTS

The authors would like to thank the Australian Research Council and the Department of Civil Engineering at the University of Strathclyde for support of the first author whilst conducting the research during a short period of study leave in Glasgow in September, 1997.

REFERENCES

- British Standards Institution, (1990) British Standard, Structural use of steelwork in building, *BS 5950: Part 1, Code of practice for design in simple and continuous construction: hot rolled sections*.
- British Standards Institution, (1987) British Standard, Structural use of steelwork in building, *BS 5950: Part 5, Code of practice for design of cold formed sections*.
- Cheung, Y.K. (1976) *Finite strip method in structural analysis*, Pergamon Press.
- Macdonald, M. Rhodes, J. Crawford, M. and Taylor, G.T. (1996) A study of the effect of cold forming on the yield strength of stainless steel type 304-Hardness test approach, *Thirteenth International Specialty Conference on Cold-formed Steel Structures, Missouri*, 513-521.
- Matsui, C.K (1985) Local buckling of concrete filled steel square tubular columns, *International Association for Bridge and Structural Engineering, ECCS Symposium, Luxembourg*, 269-276.
- Schmidt, L.C., Tsatsas, G. and Uy, B. (1998) Strength and stability of light gauge cold formed steel section filled with concrete, *To appear in the Australasian Structural Engineering Conference, Auckland, New Zealand*.
- Standards Australia, (1990) *Australian Standard -Steel Structures, AS4100*.
- Standards Australia/Standards New Zealand, (1996) *Australian/New Zealand Standard - Cold-formed steel structures, AS/NZS 4600*.
- Uy, B. and Bradford, M.A. (1994) Inelastic local buckling behaviour of thin steel plates in profiled composite beams, *The Structural Engineer*, **72:16**, 259-267.
- Uy, B. and Bradford, M.A. (1995) Local buckling of thin steel plates in composite construction: Experimental and theoretical study, *Proceedings of the Institution of Civil Engineers, London, Structures and Buildings*, **110:4** , 426-440.
- Uy, B. (1998) Local and post-local buckling of concrete filled steel welded box columns. *To appear in Journal of Constructional Steel Research, An International Journal*, (In press).
- Weng, C.C. and Pekoz, T. (1990) Residual stresses in cold-formed steel members, *Journal of Structural Engineering, ASCE*, **116:6**, 1611-1625.
- Wright, H.D. (1993) Buckling of plates in contact with a rigid medium. *The Structural Engineer*, **71:12**, 209-215.
- Wright, H.D. (1995) Local stability of filled and encased steel sections, *Journal of Structural Engineering, ASCE*, **121:10**, 1382-1388.

THE DYNAMIC RESPONSE OF FILLED THIN WALLED STEEL SECTIONS

H D Wright and A W Mohamad

Department of Civil Engineering, University of Strathclyde,
Glasgow, G4 0NG, UK

ABSTRACT

Thin-walled structural steel sections may be particularly susceptible to dynamic excitation. Often this manifests itself in high amplitude vibration at a range of frequencies. This may cause discomfort to users through global movement of the element at low frequencies or noise generation when local plates in the section vibrate at higher frequencies. This paper describes the use of concrete in-filling to provide attenuation of vibrations. An experimental programme is described where top-hat section elements are excited by the application of a vibration source. An additional parameter, the use of improved concrete bond through mechanical connectors, has also been investigated. The tests demonstrate that the addition of the concrete mass influences the natural frequency and reduces the amplitude of natural vibration. Cracking and de-bonding of the concrete steel interface provide significant damping. The practical use of in-filling is then discussed with special reference to the use of composite connection in the provision of earthquake resistance.

INTRODUCTION

Thin-walled steel elements are frequently used in structures to reduce the mass both during construction and in service. Their popularity is increasing, particularly in the medium sized commercial building and domestic house market. However their response to applied dynamic excitation may cause discomfort to occupants.

The response may be noise generation when the exciting frequency is high. This could occur when electrical appliances, such as florescent tubes, are inadequately fixed and respond to the alternating frequency of the supply. In this case it is likely to be the individual plates which make up the section that may vibrate. Plate vibration causes mass air movements thus creating considerable noise.

The whole element may also vibrate in a global manner. This would occur when the exciting frequency is lower and may typically be caused by general occupancy particularly when repetitive actions occur (dancing or aerobic exercise). In this case discomfort comes from a perception of construction movement (the symptoms being a little like sea-sickness). Elements with natural

frequencies less than about 4Hz are known to fall into this category and this is used as a limiting value in Codes of Practice (Structural 1990, 1996)

In many cases both global and individual plate vibrations occur in a coupled reaction to the applied excitation. The excitation may not be well conditioned and could contain numerous frequencies, and not necessarily harmonics of the predominant frequency. Hence the prediction, and therefore avoidance, of natural frequencies that may cause discomfort either through noise or movement is extremely complex and often not attempted at the design stage. Consequently remedial work is often required to correct a problem.

One solution is to fill or attach a secondary composite element to the steel. This has several beneficial effects.

- The mass and stiffness of the element is increased which generally reduces the natural frequency
- The individual component plates of the section are restrained thus preventing plate vibration
- The friction between the steel and composite material causes damping which reduces the amplitude of the vibration

The increase in mass is easily calculated, however the increase in stiffness is more difficult due to the complex nature of composite connection. Plate vibration is directly related to the buckling wave-form of the plate and changes in this may be predicted when the plate is prevented from free movement by a contact surface. The damping characteristics are perhaps the hardest to evaluate, particularly as the composite material used may have a complex stepped behaviour as will have the friction between it and the steel.

In this paper top-hat thin-walled steel sections are used in an experimental programme to evaluate the effect of filling the section with concrete. The concrete increases the mass, provides composite connection to increase the stiffness, restrains the component plates and as the load is increased cracks and de-bonds to provide significant damping.

The results of the tests are in the form of natural frequencies and amplitudes. The damping characteristics occur almost as soon as the concrete cracks and it is thought that this phenomenon could be used to provide damping for structures subject to earthquake loading.

EXPERIMENTAL PROGRAMME

In all 16 tests have been carried out on flexural elements of the cross section shown in figure 1. The specimens were cut and modified from samples of Ward Multideck 60 profiled steel sheeting which is used in composite floor construction. The steel sheeting used in this form of construction normally includes embossments often rolled into the webs to provide shear keys that enable composite connection between the concrete and steel. Certain of these sheets had been purpose rolled without embossments thus providing the means to test both embossed and non-embossed top hat specimens.

The ability of specimens to pivot freely at the support is important when dynamic experiments are being considered. Consequently a special support system was fabricated with nylon bearings. This also had the advantage of providing an easy method of connecting the samples in the loading frame. Each specimen was 1.8m long which when connected to the support system provided a simple span of 2m.

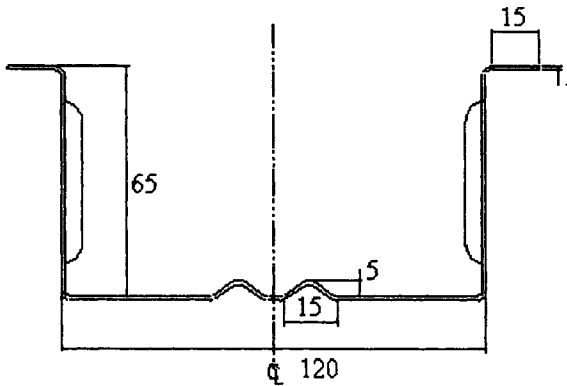


Figure 1. Cross section of top-hat specimen

The test sequence on each specimen involved static and forced vibration tests. Loading in the static test was provided by a single hydraulic jack acting at the mid-span position. The forced vibration tests involved a rotating mass “exciter”. This consisted a small electric motor with an eccentric mass flywheel attached. The motor was positioned at mid-span and could be rotated at increasing frequencies through the variation of the applied electricity supply.

Instrumentation was restricted to electric resistance strain gauges across the mid-span section, linear voltage displacement transducers at mid and quarter points on the span and accelerometers at the mid-span.

In the tests the static load deformation behaviour and forced vibration characteristics were considered to establish behaviour for the following situations;

- Non-embossed and embossed steel section
- Non-embossed and embossed sections filled with concrete that is bonded and de-bonded from the steel.
- Non-embossed and embossed sections filled with cracked concrete that is bonded and de-bonded from the steel.
- Non-embossed and embossed sections filled with cracked concrete that has de-bonded

EXPERIMENTAL RESULTS

Static load tests

Figure 2 shows the static load - central deflection plot for embossed and non-embossed plain sheeting. It can be seen that the embossments tend to reduce the stiffness of the section as has been observed in previous tests by Wright (1998). This is assumed to be due to the embossments acting like cut-outs in the web and reducing their bending and shear stiffness. The tests were stopped well

short of reaching yield strains in the steel so that the same sample could be used for the dynamic and filled section tests.

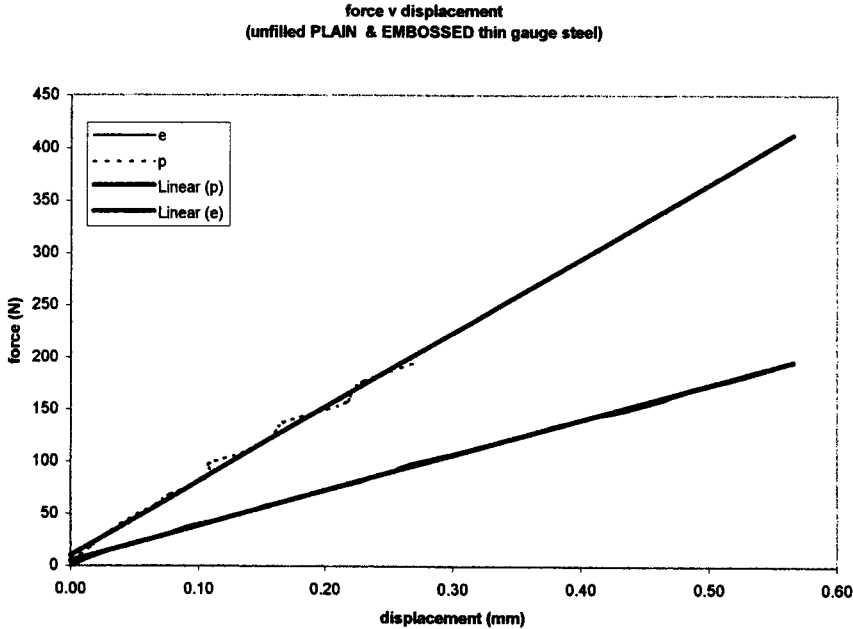


Figure 2 Static load test results

Figure 3 shows the same comparisons for filled sections. Initially the specimens were loaded within the elastic range when the concrete was assumed not to have cracked. The scale at which Figure three is drawn is such that it does not show how the stiffness of both plain and embossed is very similar at this stage. This is most probably due to the fact that the chemical bond between the steel and concrete is maintained at this stage. Both specimens were used to determine the dynamic behaviour at this stage.

The load deformation response for the filled sections when loaded to a level when slip has occurred is also plotted on the graph. It is interesting to note that the plain specimen follows a rather erratic load deflection curve whereas the embossed profile was much smoother. It is possible that the concrete in the plain specimen would crack in a discrete fashion whilst the embossments would lead to a more distributed cracking pattern. Neither specimen was tested to failure at this stage as they were used in the dynamic tests.

The final load deformation response is plotted for the specimens when loaded to failure following the dynamic test. It can be seen that the non-embossed sheet could withstand less than 2kN whilst the embossed profile could be loaded to over 3kN prior to a failure. It is likely that the embossed specimen would have displayed a ductile failure, however the deformation gauge malfunctioned preventing the full recording of the deformation at higher loads. The reduced capacity of these tests when compared to the previous curves is thought to be due to the damage caused by dynamic loading.

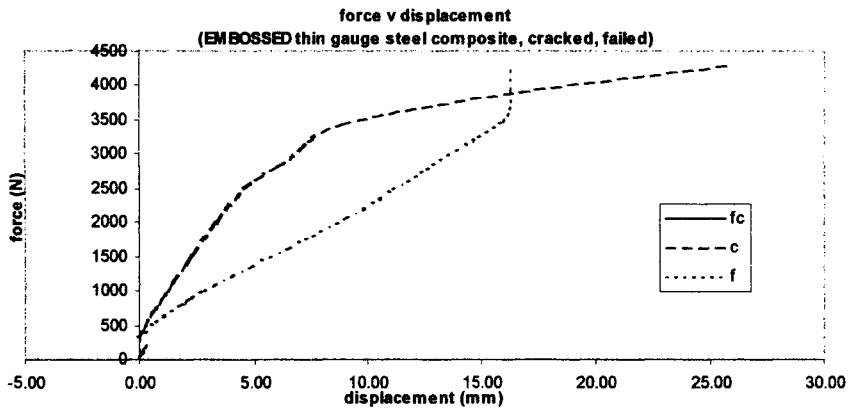
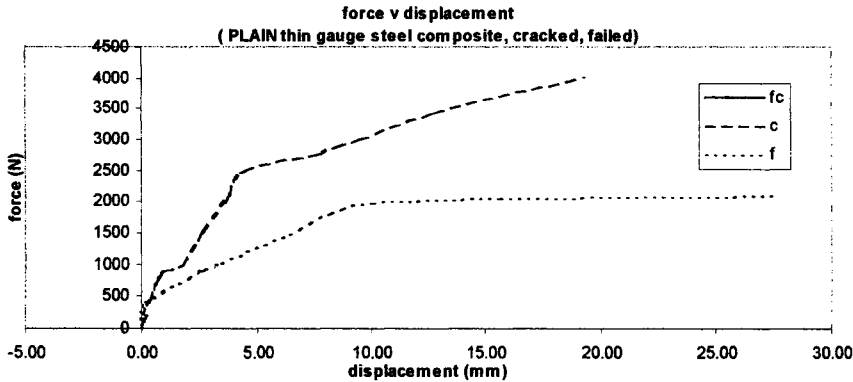


Figure 3 Static load deflection plots for the filled sections subject to various load cases

Forced vibration tests

Figures 4 and 5 shows the dynamic amplitude with excitation frequency for the non-embossed and the embossed specimens. Both demonstrate a very clear natural frequency around the 20 to 25Hz level and a definable response (secondary peak) at between 15 and 18Hz when tested without concrete filling. The embossed profile has a lower natural frequency and secondary peak most probably due to its reduced stiffness. It is possible that the secondary peak is due to either local plate buckling or a torsion or warping mode.

On filling the sections with concrete the secondary peak disappears and the amplitude of the primary natural frequency reduces. It is interesting to note that the increase in mass and stiffness for both specimens largely counteract each other leaving the natural frequencies around the same value. The

concrete clearly restrains the secondary vibration mode as shown by the removal of the secondary peaks in the figures.

Once the specimens had been loaded to a level when the concrete had cracked the dynamic response changed substantially as the amplitude and the natural frequency reduce. This would indicate that not only the stiffness decreases (as confirmed by the static tests) but also that the damping is much greater. In the experiments the noise level was significantly less in these tests than in the unfilled tests.

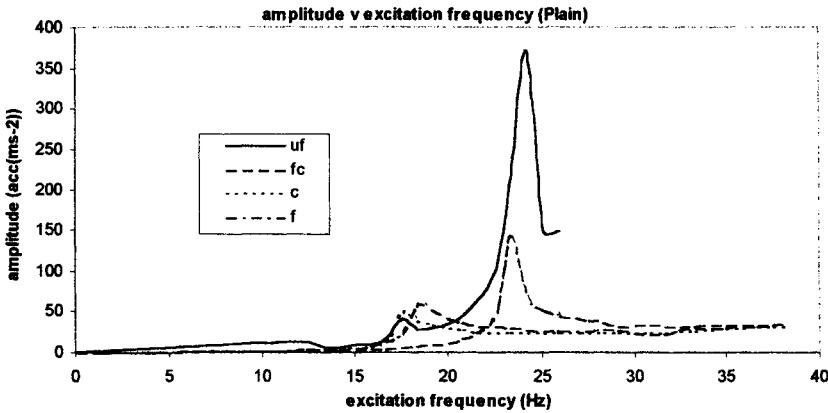


Figure 4 Forced vibration response for the non-embossed profile

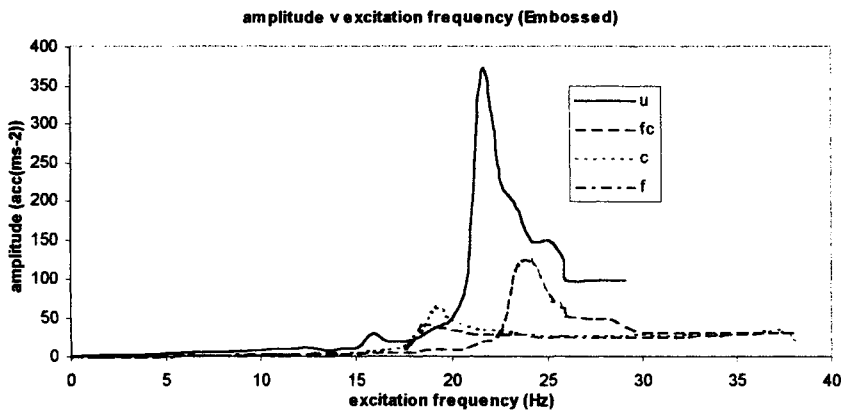


Figure 5 Forced vibration response for the embossed profile

A similar situation occurs when the dynamic tests were carried out after the specimens had been statically loaded to ensure de-bonding and slip. In this case the natural frequency and amplitude was reduced even further. The embossed profile can also be seen to provide slightly more damping. There is an absence of a defined peak in this curve.

IMPLICATIONS FOR PRACTICE

Static loading

The tests on the top-hat sections confirm many of the characteristics associated with composite slab behaviour. Whilst filling the section with concrete increases the stiffness, strength and possibly the ductility the increase in mass is an obvious negative aspect. However it is possible that in-filling with a lighter material could have similar effect.

Dynamic loading

One of the negative aspects of thin gauge steel behaviour is its susceptibility to dynamic excitation. This may be associated with high frequency “noise” or lower frequency “liveliness”. In both cases the in-filling of the section would appear to assist. The reduction in amplitude and elimination of the secondary peaks in the response clearly reduces the likelihood of noise from the section. In the case of the global response the reduction in amplitude will make any structure comprising this form of construction appear less flimsy, however it is the increase in stiffness that is more likely to make the major difference in perception (Murray 1998).

The particular dynamic behaviour of composite structures exhibited by these tests has also been considered in a possible application to earthquake resistance. Consider the following scenario:-

The composite structure is designed to carry the dead and live loads with suitable load factors. This design would assume that the concrete may suffer micro-cracking but this would not be extensive and the steel concrete connection would not exceed a low elastic limit. The dynamic response of the structure would be satisfactory for normal occupation but would not necessarily satisfy the criteria imposed for earthquake resistance.

During an earthquake the load factors are exceeded, the concrete cracks more extensively and the connection deformation increases. It is likely that the static load resistance is still sufficient for the normal service loading on the structure allowing safe evacuation of the premises. The natural frequency of the structure will have changed with the concrete cracking and connector deformation. More critically there will be a natural damping action caused by the cracking and altered connection stiffness. The altered natural frequency and particularly damping may be sufficient for the structure to satisfy the earthquake loads.

Following the earthquake it may be possible that the structure may be refurbished by grouting to achieve its original strength and stiffness.

CONCLUSIONS

This paper has described a series of static and dynamic tests on thin walled steel beams that have been filled with concrete.

It has been shown that:-

- Sections that have been embossed in the web area to provide additional mechanical shear keying with the concrete have a lower stiffness than non-embossed sections before the concrete has been poured. This manifests itself in a lower natural frequency when the sections are subjected to

dynamic excitation. Secondary vibration modes occur as the individual plates vibrate in a possibly coupled mode with the global torsion modes of the beams.

- Once the sections have been filled with concrete that remains un-cracked both embossed and non-embossed profiles behave in a very similar way. The amplitude of the dynamic response for both sections reducing three fold and secondary peaks in the response curve are eliminated.
- On loading beyond the cracking level the natural frequency of both embossed and non-embossed sections reduces and the amplitude again reduces three-fold. This is further reduced once the static load level causes de-bonding between the steel and concrete. The embossed profile providing the most damping.

It is surmised that the behaviour of concrete filled thin-walled sections may provide a structure that reacts well under earthquake loading. The composite structure changes natural frequency and provides significant damping as the concrete cracks and de-bonds from the steel.

REFERENCES

British Standard 5950 Part 3.1 (1990) Structural use of steelwork in building, Code of Practice for Design of Simple and Continuous composite beams.

Eurocode 4, (1996) Design of composite steel concrete structures: Part 1.1 General Rules and Rules for Buildings, DD ENV 1994-1-1, BSI London.

Wright HD and Essawy MI, (1996) Bond in Thin Gauge Steel Concrete Composite Structures Composite Construction in Steel and Concrete III, Proceedings of an Engineering Foundation Conference, ASCE, June 1996 630-643.

Murray TM and Howard JN (1998) Serviceability: Lively Floors - North American and British Design Methods J. Construct. Steel Research Vol 46 Nos 1-3 pp 105 paper 251.

A STUDY OF THIN-WALLED FERROCEMENT ELEMENTS FOR PREFABRICATED HOUSING

M. A. Mansur¹, K.L. Tan¹, A.E. Naaman² and P. Paramasivam¹

¹Department of Civil Engineering, National University of Singapore,

²Department of Civil and Environmental Engineering, University of Michigan at Ann Arbor, USA.

ABSTRACT

An experimental investigation was conducted to study the ultimate load behaviour of ferrocement thin-walled channel beams representing the basic unit for a proposed prefabricated housing system with the aim of developing simple design charts for strength. The study comprises testing under pure bending of a total of six panels, three of these panels were tested in an upright position and three in inverted position. The main parameter considered was the volume fraction of reinforcement. The results of these tests are presented and discussed in this paper. Based on experimental observation of the behaviour at ultimate load and a comparison with the general method of analysis by equilibrium and strain compatibility for a wide range of geometric and material parameters, the familiar 'rigid-plastic' concept has been justified for ultimate strength analysis of ferrocement structural sections. The method is suitable for the development of design charts. Typical charts are presented for rapid assessment of flexural strength or to expedite the design process.

KEYWORDS

Composite materials, design charts, ductility, ferrocement, flexural strength, panels, prefabrication, tests.

INTRODUCTION

Ferrocement, a composite comprising cement mortar as the matrix and uniformly distributed fine wire mesh as the reinforcement, is a material ideally suitable for high-level prefabrication and for the production of light-weight elements for use in the building industry. Many different shapes of such elements have been explored and, among them, channel elements appear to have an enormous

potential in the development of a fully industrialized housing system. This emanates from the versatility in its use. The same element, with or without minor modifications, could be employed as a load bearing wall, partition wall, floor and ceiling or as roofing. Using channel elements as the building block, several industrialized and semi-industrialized housing systems have been proposed by various researchers. Such a housing system is currently being developed at the National University of Singapore in collaboration with the University of Michigan at Ann Arbor, USA.

In order to translate such a concept into practical use, it is necessary to make a thorough investigation into the element response, response of the connections between the elements, and global response of the structure built by assembling these elements. This study is concerned with the element response. Salvaged from an ongoing study on moment connections, a series of tests was carried out to evaluate the flexural strength of channel beams. The main objectives were to check the applicability of the usual strength theory for conventional reinforced concrete to ferrocement and to identify a method suitable for the development of simple design charts. Such charts will be useful for rapid assessment of strength and possible optimization of the section.

TEST PROGRAMME

The panels considered here have the shape of a channel with closed ends as shown in Fig. 1(a). Six such panels were tested, three in the upright position and three in the inverted position. Each panel was 1500 mm-long, 500 mm-wide and contains 150 mm-deep ribs (webs). The thickness of the rib was fixed at 20 mm while the flat surface (flange) was 15-mm thick. All panels were symmetrically reinforced across the thickness with a clear cover of 3 mm on either side. As illustrated in Fig. 1(b), two layers of fine welded wire mesh with 12.5-mm square openings and 1.42-mm wire diameter ($f_y = 364$ MPa; $E_s = 148$ GPa), folded into the webs, and isolated bars, 6mm in diameter, placed near the outer face of each rib provided the basic reinforcement. A layer of welded wire mesh of 2 mm wire diameter ($f_y = 367$ MPa; $E_s = 143$ GPa) was used as skeletal steel. It was placed in between the two layers of fine mesh. The variation in the volume fraction of reinforcement was achieved by varying the opening size of the skeletal mesh in the flange and by changing the number of bars in the web. Two types of bars, high-yield deformed ($f_y = 551$ MPa; $E_s = 200$ MPa) bars designated as T6 and smooth mild steel ($f_y = 343$ MPa; $E_s = 176$ GPa) bars denoted as M6, were used. A small strip of fine wire mesh was wrapped around the bar to prevent it from bulging out of the panel. Table 1 shows details of the test programme.

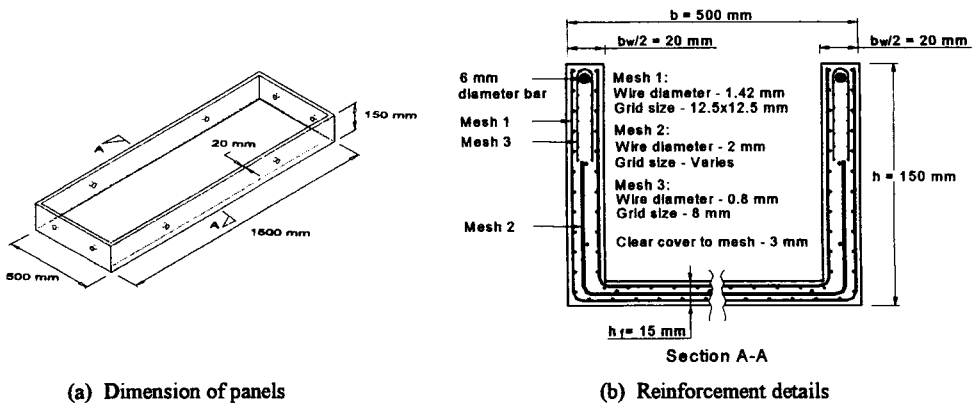
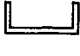



Fig. 1 Details of panels

TABLE 1
TEST PROGRAMME

Panel	Testing mode	Cylinder compressive strength of mortar, f_c (MPa)	Total thickness of longitudinal rib, B_w (mm)	Total vol. fraction of reinforcement in flange $(V_f)_f$ (%)	Rebars in web
U1	Upright 	55.9	43.9	3.38	2-T6
U2		54.5	40.0	3.59	2-T6
U3		45.8	44.3	3.80	2-T6
I1	Inverted 	55.9	41.5	3.38	2-T6
I2		49.3	41.0	3.38	2-T6, 2-M6
I3		54.1	41.9	3.38	4-T6

Ordinary Portland cement and natural sand passing through U.S. sieve No.16 (1.18) were used in the ratio of 1:2 by weight for the mortar. In the mix, 15 percent by weight of cement was replaced by fly-ash. The water-cement ratio used was 0.5 by weight for a target of mortar strength of 50 MPa. Suitable admixtures with dosage conforming to manufactures' recommendations were added to improve workability and accelerate early development of strength.

All panels were cast while on a vibration table and demoulded 24 hour after casting. They were cured under wet condition for 6 days and were then air-dried in the laboratory before testing. The compressive strengths at testing age were obtained from companion 100x200-mm cylinders and are presented in Table 1.

The panel was simply supported over a span of 1.35 m and was tested under two symmetrical point loads spaced at 350 mm. A spreader beam was used at each point to distribute the load across the width of the panel. For testing in the upright position, the ribs were clamped to the spreader beam to prevent any possible buckling of the rib in compression.

Prior to testing, the actual thickness of the two longitudinal ribs was measured. The specimen was instrumented for measuring deflection and curvature at mid-span of the panel. The load was applied to the specimen through a spreader beam via a 20 kN load cell using a servo-hydraulic actuator. The loading rate used was 0.004-mm/s. Prior to the commencement of actual test, a small load (~1000N) was applied to overcome any slack and then removed. All the instruments were then initialized. The applied load and the corresponding deformation readings were recorded in a computer file using a data logger. Tests were continued until a definite mode of failure could be recognized.

TEST RESULTS

The experimental moment-curvature relationships presented in Fig. 2 indicate that the panels behaved in a manner similar to a conventional reinforced concrete beam in flexure: initial elastic response followed by cracked, a near-elastic regime with a reduced slope and finally to a horizontal plateau before collapse. However, due to more uniform dispersion of reinforcing elements, the panels exhibited numerous cracks at a spacing much closer than that commonly observed in conventional reinforced concrete beams (see Fig. 3).

Fig. 2(a) shows the moment-curvature relationships of the panels tested in the upright position where the ribs are subjected to compression. It can be seen that Panel U1 that contained the lowest volume fraction of reinforcement in the flange in the series exhibited a long plateau of constant moment with increasing rotation. Failure of this specimen was caused by crushing of the mortar that eventually led to buckling of the wire mesh and spalling of the mortar cover Fig. 3 (a). The other two panels also failed in a similar manner. It may be seen in Fig. 2(a) that an increase in V_f results in an increase in ultimate strength, but a drop in curvature ductility, as expected and none of the panels show a premature instability failure.

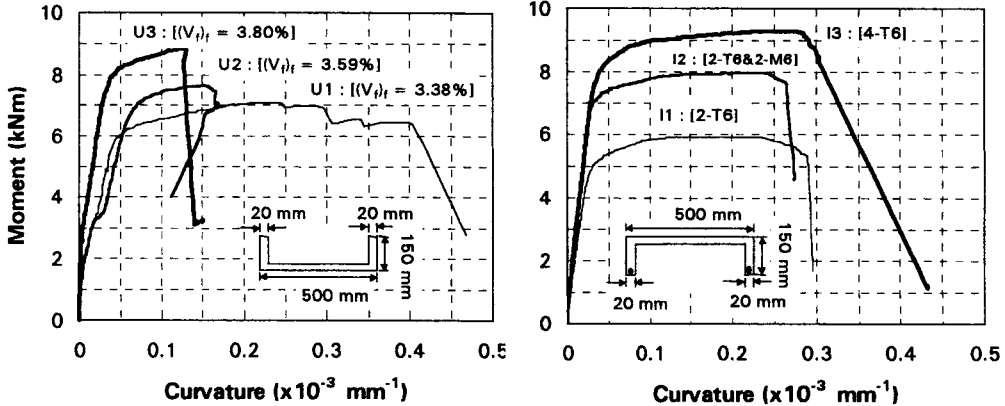
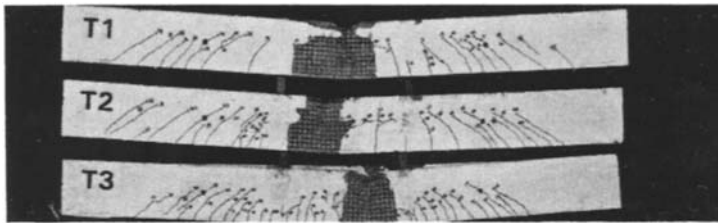
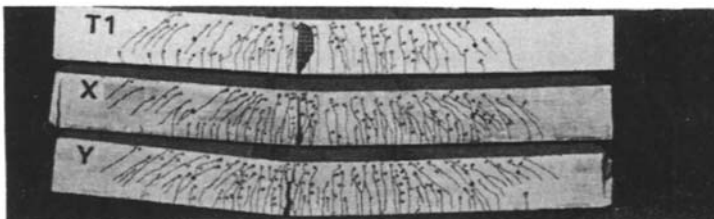


Fig. 2 Moment-curvature relationships of the panles



(a) Bending in upright position



(b) Bending in inverted position

Fig. 3 Test specimens after failure

When the panels are tested in an inverted position, the failure was somewhat different. As can be seen in Fig. 2(b), an increase in the amount of bar reinforcement leads to an increase in ultimate strength but, unlike the panels tested in the upright position, the curvature ductility remains relatively unaffected. All the panels exhibited considerable ductility and failure occurred by rupture of the rebars in the web. At failure, no crushing of the mortar was noted on the compression face.

ANALYSIS

Ferrocement is basically a form of reinforced concrete where reinforcing elements are more uniformly dispersed in the matrix and coarse aggregate in the concrete is replaced by fine aggregate. Therefore an analysis similar to that used for reinforced concrete should equally be applicable to ferrocement. This has been confirmed by many investigators in the past. However, as many reinforcing layers are involved in ferrocement, no closed form solution is possible. Analysis needs a trial and error procedure to satisfy the basic requirements of equilibrium, compatibility and material laws.

An alternative approach, suitable for a direct solution, was proposed by Mansur & Paramasivam (1986). The method is based on the contention that ferrocement transforms into a plastic material, both in tension and compression, at ultimate. This has been justified by the availability of an extraordinary amount of ductility under flexural loading. The method was tested against a large amount of experimental data on ferrocement rectangular sections containing various arrangement of reinforcement, and was used as a basis for developing a series of design charts [Mansur (1988)].

In the present analysis of ferrocement U-sections, the above approaches designated as Method A and Method B, respectively, are considered. The conditions represented by the two methods for upright and inverted position of the panels are shown in Figs. 4(a) and (b), respectively.

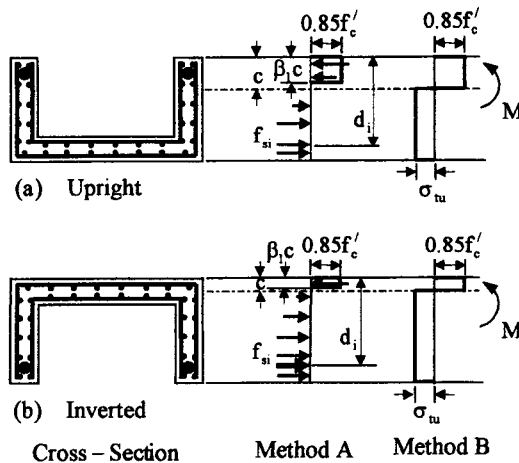


Fig. 4 Conditions at collapse represented by Methods A and B

Method A is based on equilibrium and strain compatibility using the recommendations of the ACI Code (1996). The application of the method is fully illustrated by Naaman and Hormich (1986). Method B is the rigid-plastic analysis proposed by Mansur and Paramasivam (1986) in which the stress levels σ_{cu} and σ_{tu} at which ferrocement transforms into a plastic material in flexural compression

and tension are assumed respectively as $0.85 f'_c$ and $\eta V_f f_{ym}$, where f'_c is the cylinder compressive strength of mortar, V_f , f_{ym} and η are the volume fraction, yield strength and global efficiency factor of mesh reinforcement, respectively [Naaman & Hormich (1986)]. Bar reinforcement in the rib (see Fig. 1) which is necessary to enhance the strength of the section under negative (hogging) moment, is assumed to have yielded in tension with a stress of f_{yb} and is treated in a manner similar to conventional reinforced concrete. Using the force and moment equilibrium, the following equations for the neutral axis depth, x at plastic collapse and the corresponding collapse moment, M_u may be easily derived for the section subjected to positive (sagging) moment [see Fig. 4] as:

$$\frac{x}{h} = \left[2 + \frac{b}{h} - 2 \frac{h_f}{h} \right] / \mu \tag{1}$$

$$\frac{M_u}{f'_c b h^2} = \psi_m \frac{h_f}{h} \left[\left(1 - \frac{1}{2} \frac{h_f}{h} + \zeta \right) - \left(2 + \frac{1}{2} \frac{b}{h} - 2 \frac{h_f}{h} + 2\zeta \right) / \mu \right] \tag{2}$$

where

$$\zeta = \frac{h}{b} - 2 \frac{h_f}{h} \frac{h}{b} + \frac{h_f^2}{h^2} \frac{h}{b}; \quad \mu = 2 + \frac{0.85 b_w}{\psi_m b} \frac{h}{h_f}; \quad \psi_m = \frac{\eta V_f f_{ym}}{f'_c}$$

In order to ensure yielding of steel, ψ_m should be limited to a value such that $x/h \leq 0.5$.

Under negative moment, the neutral axis would generally be located within the flange. Therefore, the reinforcement within the flange will contribute very little to the bending resistance of the section. Ignoring the contribution of reinforcement in the flange, the following equations for x and M_u may be derived

$$\frac{x}{d} = \left(\psi_b + \psi'_m \frac{h}{d} \right) / (0.85 + \psi'_m) \tag{3}$$

$$\frac{M_u}{f'_c b d^2} = \psi_b \left(1 - \frac{1}{2} \frac{x}{d} \right) + \frac{\psi'_m}{2} \left(\frac{h}{d} \right)^2 \tag{4}$$

where

$$\psi_b = \frac{A_{sb} f_{yb}}{f'_c b d}; \quad \psi'_m = \frac{\eta V_f f_{ym} b_w}{f'_c b}$$

For Eqs. (3) and (4) to be valid, x should be less than or equal to h_f , the thickness of the flange.

The predictions of the two methods as outlined above are compared in Table 2 with the present test data. It may be seen that both the methods give equally good predictions of the ultimate moment capacity of the panels in either mode of bending, thus justifying the validity of method B.

DESIGN CHARTS

In order to further check the accuracy of the 'rigid-plastic' analysis in comparison with the universally accepted method of strain compatibility (Method A), a hypothetical U-section was chosen. It has been assumed that the section contains two layers of fine wire mesh with a grid size of 12.5 x 12.5 mm and one rebar in each rib similar to the panels considered in this study. Analyses were carried out by varying the diameter of wires from 0.8 mm to 2.00 mm, and size of rebars from 6 to 12 mm. Also

varied were the width of panel, B (from 300 to 500 mm), total width of ribs, B_w (from 30 to 50 mm), thickness of flange, H_f (from 10 to 20 mm), depth of panel, H (from 100 to 150 mm) and mortar strength, f_c' (from 30 to 60 mm). Using these wide ranges of geometric and material parameters, over 150 panels were analyzed by both the methods A and B. These results are plotted in Fig. 5. It can be seen that the predictions of method B are well within about $\pm 6\%$ of the more sophisticated analysis, method A. Hence, the rigid-plastic analysis may be assumed to provide acceptable results.

TABLE 2
ACCURACY OF PREDICTION METHODS FOR ULTIMATE FLEXURAL STRENGTH

Panel	Testing mode	Ultimate moment, M_u (kNm)			Test/prediction moment ratio	
		Test	Predicted		Method A	Method B
			Method A	Method B		
U1	Upright	7.09	7.00	7.14	1.01	0.99
U2		7.64	8.18	7.73	0.93	0.99
U3		8.87	8.22	8.29	1.08	1.07
I1	Inverted	5.93	5.65	5.81	1.05	1.02
I2		7.98	7.87	8.10	1.01	0.99
I3		9.29	9.21	9.49	1.01	0.98
Average					1.02	1.02
Standard deviation					0.06	0.04

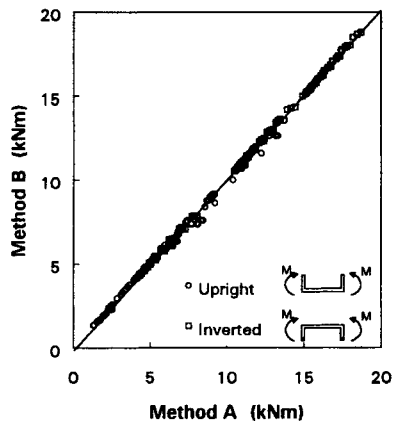


Fig. 5 Comparison between the predictions of Methods A and B

One attraction of the rigid-plastic analysis (Method B) is that it can be readily recast to develop a series of useful design charts. Two such typical charts, one for U-section and the other for inverted U-section are presented in Figs. 6 (a) and (b), respectively. Obviously, these charts are also valid for a T- or inverted T-section. Similar charts can be easily generated for unsymmetrical I-sections or box sections using the same concept.

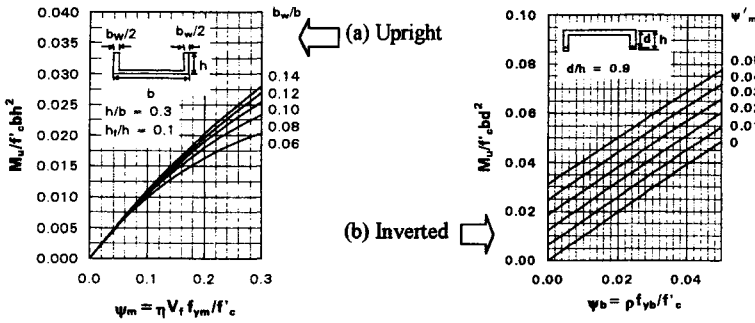


Fig. 6 Typical design charts

CONCLUDING REMARKS

Presented in this paper are the results in pure bending of a total of six thin-wall ferrocement panels having a channel (or U) section that has been proposed for the development of a prefabricated housing system. The existence considerable ductility suggests that a rigid-plastic analysis should be applicable to predict the ultimate moment capacity of these panels. This has been confirmed by generating a large amount of data for a hypothetical panel with a wide range of material and geometric parameters as discussed. It should be noted here that the method is valid only when the panels are under-reinforced, and this can be ensured by restricting the neutral axis depth at collapse as imposed herein. Using the method, design charts have been developed for typical thin-walled panels.

ACKNOWLEDGEMENTS

The research reported in this paper is supported by Research Grant, RP 3960645 with funds given by the National University of Singapore.

REFERENCES

ACI Committee 318 (1995). Building Code Requirements for Reinforced Concrete (ACI 318-95). *American Concrete Institute*.

Mansur, M.A. (1988). Ultimate Strength Design of Ferrocement in Flexure. *Journal of Ferrocement* **18: 4**, 385-395.

Mansur, M.A., and Paramasivam, P. (1986). Cracking Behaviour and Ultimate Strength of Ferrocement in Flexure. *Journal of ferrocement*, **16: 4**, 405-415.

Naaman, A.E. (1989). Ferrocement Housing: Toward Integrated High Technology Solutions. *Journal of Ferrocement* **19: 2**, 141-149.

Naaman, A.E.; and Hammoud, H. (1992). Ferrocement Prefabricated Housing: The Next Generation. *Journal of Ferrocement*, **22: 1**, 35-47.

Naaman, A.E.; and Homrich, J.R. (1986). Flexural Design of Ferrocement: Computerized Evaluation and Design Aids. *Journal of ferrocement* **16:2**, 101-116.

LONG-TERM DEFORMATION ANALYSIS OF THIN-WALLED OPEN-PROFILE RC BEAMS

W. A. M. Alwis

*Department of Civil Engineering, National University of Singapore
10 Kent Ridge Crescent, Singapore 119260*

ABSTRACT

Outlined herein is a procedure for obtaining a description of a time-dependent generalised stress-strain relationship for reinforced concrete beams of thin-walled open-profile sections made up of flat segments. This procedure is derived by extending a bilinear moment-curvature curve derived for beams under no axial load, the validity which has been justified by comparing with experimental and predicted beam deflections. The generalised stress components considered here are those that contribute to longitudinal stresses acting normal to the section, ie. axial force, bending moment and bimoment. The relationship defined herein is meant for a beam length subjected to a loading maintained constant in time as opposed to a section subjected to axial forces and moments that vary with time. The curve would be valid for a specific chosen time instant and therefore referred to as an isochrone. In order to derive this curve, the time-dependent concrete material behaviour subjected to the environmental humidity and temperature conditions is assumed to be characterised by the shrinkage strain and an effective modulus. The beam behaviour is then derived by considering uncracked and fully cracked flat segments of the section. A piecewise-linear relationship is adopted in the post-cracking range, taking into account the tension stiffening effect.

KEYWORDS

Reinforced Concrete; long-term deformation; creep; shrinkage; thin-walled; open-profile

INTRODUCTION

Concrete material behaviour is dependent upon a host of variables such as concrete mix proportions, humidity, temperature, size and load duration. Further technical difficulties arise due to the spatial and temporal variations of concrete properties and the differences in concrete deformation behaviour under tension and compression.

Given the stochastic nature of concrete properties and structural loading, deterministically established deflection estimates would be of limited meaning for a typical concrete structure. To determine parameters useful for design purposes hypothetical loading programmes can be adopted.

Considered in this study is one such simple loading programme where a concrete beam is imagined to undergo a period of drying without any external loading and then subjected to a constant loading for the rest of its existence.

In presently available simplified methods for beam deflection estimation (ACI Committee 431 1966; British Standards Institution 1972; Branson 1977) the deflection contributions of short-term (sometimes referred to as instantaneous), creep and shrinkage effects are normally thought of as separate entities. From a theoretical point of view, this amounts to application of the beam theory for the individual instantaneous, creep and shrinkage strain components separately, ignoring the interactions between them. However, concrete shrinkage strains cannot exist in isolation because of incompatibility with steel strains. Concrete and steel stresses would then develop in response, giving rise to instantaneous and creep strains in concrete. In such a situation, although the resulting deformation is originated by shrinkage and sometimes even referred to as shrinkage deformation, the unavoidable development of other fundamentally distinct strain types in the structure has to be recognized.

In a recent study (Alwis *et al* 1994) deflection analysis was attempted assuming that the total strain profile is linear across the depth of the beam. No condition on the individual distributions of shrinkage, creep or instantaneous strain profiles were imposed. Conformity with the BP2 creep and shrinkage model (Bažant and Panula 1980) was assumed and tensile behaviour comprising uncracked, tensile softening and cracked phases was introduced with a provision for tensile unloading. Predictions of time dependent deflections were made for several sets of available experimental beams on the basis of reported material, geometrical and loading data together with averaged humidity of the test environment. These predictions were found to agree reasonably well with the reported observations. This can be considered as a demonstration of the effectiveness of methodical accounting of factors known to be linked with concrete deformation, such as the loading history, humidity of the environment, concrete mix proportions and the unsymmetric tensile and compressive behaviour.

A particular disadvantage of the aforementioned approach in terms of practical application is the relatively heavy computing effort needed. What is desirable then is an engineering concept or a methodology, or a combination of both, that can effectively remove or reduce the necessity for intensive computing, without sacrificing much of the accuracy. Outlined in this paper is a method which requires less computing effort but takes into account most of the significant aspects of concrete long-term deformation behaviour.

RECTANGULAR SEGMENT UNDER MOMENT AND AXIAL FORCE

The intensity of loading is assumed to remain constant in time, within the service load range. It is assumed that the time dependent deformation behaviour of concrete in this beam under the prevailing environmental humidity and temperature conditions can be characterised by two parameters, namely, the shrinkage strain e_{sh} and the effective modulus E_{ce} . These are defined such that the total compressive strain due to a compressive concrete stress σ_c within the service load range is $e_{sh} + \sigma_c/E_{ce}$.

Apart from the aforementioned two variables, the only other concrete parameter required for the proposed analysis herein is the tensile strength f_t of concrete, which is assumed to be independent of time. The total strain in concrete is assumed to be equal to the algebraic sum of shrinkage, instantaneous and creep strain components. Perfect bonding between steel and concrete is assumed. Steel is assumed to behave linearly elastically throughout the service load range considered herein.

When the total longitudinal strain is e at a generic location at a given time instant, the concrete stress σ_c and steel stress σ_s can be expressed as,

$$\sigma_c = E_{ce}(e - e_{sh}) \tag{1a}$$

$$\sigma_s = E_s e \tag{1b}$$

where E_s is the elastic modulus of steel; compressive stresses and strains taken as positive. Equation (1a) is assumed to be valid for uncracked concrete, in tension and compression. Let the sectional areas of concrete and steel be A_c and A_s respectively. Let $A_g = A_c + \zeta A_s$, denote area of the transformed section constructed by augmenting the steel area using the time-dependent modular ratio defined as

$$\zeta = \frac{E_s}{E_{ce}} \tag{2}$$

The behaviour of the thin-walled open profile beam is derived by considering the straight segments of the section separately and assembling them in a manner that ensures that the total strain profile is agreeable with the deformation conditions assumed in Vlasov's thin-walled member theory. Each flat segment of the member is treated as a rectangular section that is subjected to an axial force N and a bending moment M acting in the middle plane. Member section is assumed to undergo no distortion.

Assuming that the total strain profile is linear across the depth of the considered rectangular section and no concrete cracking occurs, by considering equilibrium it can be shown that

$$N = E_{ce}A_g(e_a - e_o) \tag{3}$$

$$M = E_{ce}I_g(\kappa - \kappa_o) \tag{4}$$

where e_a = total strain (compression positive) at the centroid of the transformed section which is chosen as the origin of the y axis (pointing downwards), κ = curvature (sagging positive), I_g is the moment of inertia of the transformed section about the horizontal axis through the centroid, and

$$e_o = \frac{A_c}{A_g} e_{sh} \tag{5}$$

$$\kappa_o = \frac{A_c d_c}{I_g} e_{sh} \tag{6}$$

in which d_c is the distance to the centroid of concrete area from G measured upwards. It follows from equations (5) and (6) that e_o and κ_o denote the time dependent centroidal strain under zero axial force and curvature under zero moment, respectively.

At the cracking point let the sectional moment be $M = M_{cr}$. The concrete stress would then be at the tensile capacity $\sigma_c = -f_t$ at the extreme tensile edge of the section located at $y = D_2$. Equation (1a) leads to,

$$-f_t = E_{ce}(e_{cr} + e_o - e_{sh} - \kappa_{cr}D_2) \tag{7}$$

where e_{cr} and κ_{cr} denote the centroidal strain and curvature at the cracking point. It follows that

$$\kappa_{cr}D_2 - e_{cr} = \frac{f_t}{E_{ce}} - \frac{\zeta A_s}{A_g} e_{sh} \tag{8}$$

It is evident from equations (5) and (6) that,

$$N = E_{ce}A_g(e_{cr} - e_o) \tag{9}$$

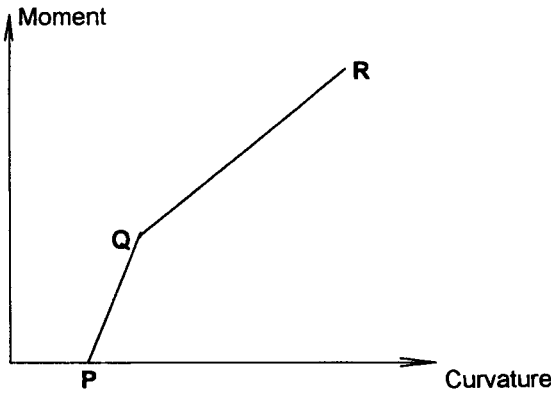


Figure 1. Moment-curvature isochrone

$$M = M_{cr} = E_{ce} I_g (\kappa_{cr} - \kappa_o) \quad (10)$$

The point P in the moment-curvature space of Figure 1 denotes the zero-moment curvature given by κ_o which is independent of axial force. The point Q denotes the cracking point (M_{cr}, κ_{cr}) which varies with the magnitude of the axial force. The point P as well as the slope of PQ are nevertheless independent of axial force.

The linear segment QR of the moment curvature curve depicts an assumed linear post-cracking behaviour, denoting a tension stiffening phase. This segment is proposed to be established by determining the point $R = (M', \kappa')$ associated with a certain 'fully-cracked' section defined herein by the following features. The tensile steel is at an assigned limit strain e'_s for steel, associated with the upper limit of the service load; concrete is uncracked wherever the total strain is compressive; the constitutive relation of equation (1a) is applicable within this uncracked domain; and concrete carries no stress where the total strain is tensile. Note that this model contains a limited region of tensile concrete wherein the maximum tensile stress is $E_{ce} e_{sh}$.

Let d_n be the depth of the uncracked segment, d_s be the depth of the centroid of all steel in the section and d' be the depth of the centroid of tensile steel, measured from the compressive (top) edge. The curvature of the fully-cracked section defined herein would then be given by,

$$\kappa' = \frac{e'_s}{d' - d_n} \quad (11)$$

For the case of a rectangular section of width t considered herein, the equilibrium of axial force leads to,

$$t(0.5 + \beta)d_n^2 + (\zeta A_s - \beta t d' + \alpha)d_n - \zeta A_s d_s - \alpha d' = 0 \quad (12)$$

where d_s denotes the depth of the centroid of steel area from the top edge,

$$\alpha = \frac{N}{E_{ce} e'_s} \quad (13)$$

$$\beta = \frac{e_{sh}}{e'_s} \quad (14)$$

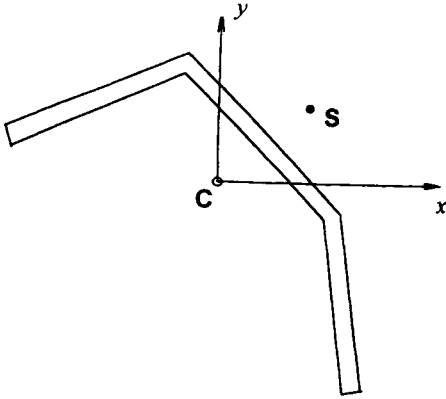


Figure 2. Member section

Equation (12) can be solved to determine d_n and thereafter using (11) the corresponding value of κ' can be established. By taking the first moment of stress over the sectional area, the corresponding moment can be expressed as,

$$M' = E_{cc}(I'_g \kappa' - \frac{1}{2} b d_n^2 e_{sh}) \tag{15}$$

where I'_g is the second moment of area of the transformed cracked section (ie. the section in which the concrete area below the depth d_n had been removed) about the axis at the depth d_n . The slope of the moment-curvature curve for a cracked beam segment is given by,

$$EI_* = \frac{M' - M_{cr}}{\kappa' - \kappa_{cr}} \tag{16}$$

THIN-WALLED OPEN-PROFILE SECTION

Let the axes C_x and C_y shown in Figure 2 denote the principal Cartesian axes of the section passing through the centroid C . In the following ω denotes the double sectorial area coordinate of a point in the middle plane of the section profile with respect to the pole located at the shear centre S . Adopting Vlasov's theory for thin-walled open-profile members, the total strain distribution in the section is expressed as

$$e = \delta + x\kappa_y + y\kappa_x + \omega\phi \tag{17}$$

where δ , κ_x , κ_y and ϕ are the generalised strains of the complete section that denote the axial strain, curvature about x - axis, curvature about y - axis and angle of twist, respectively.

In a generic flat segment of the section the strain profile is linear along its length. (This length of the flat segment in section is interpreted as the depth D in the derivation in the previous section for a segment taken in isolation and treated as a rectangular section of breadth t .)

The generalised stresses acting on the section are the axial force N , the bending moments about the x - and y - axes M_x and M_y , and the bimoment B . If the magnitudes of these stresses are

sufficiently small so that the section is uncracked, the behaviour of the section according to the present model will be linear and can be analysed as follows.

Consider the flat segment k joining the end nodes i and j in the member section. Then the axial force and bending moment in the section would be given by (3) and (4). The sectional properties A_{gk} , I_{gk} and the position of the centroid are to be determined taking into account the steel area and locations. The required values of e_a and κ can be expressed by

$$e_a = e_i(1 - \gamma_{ki}) + e_j\gamma_{ki} \quad (18)$$

$$\kappa = \frac{e_j - e_i}{D_k} \quad (19)$$

where D_k is the depth of the segment k and $\gamma = d_{ki}/D_k$ in which d_{ki} = the distance to the centroid from the node i . It follows that the axial force and the bending moment of each flat segment can be expressed as a linear function of the generalised strain components of the section.

$$N_k = n_0 + n_1\delta + n_2\kappa_x + n_3\kappa_y + n_4\phi \quad (20)$$

$$M_k = m_1\delta + m_2\kappa_x + m_3\kappa_y + m_4\phi \quad (21)$$

where

$$n_0 = -E_{ce}A_{gk}e_{ok} \quad (22a)$$

$$n_1 = E_{ce}A_{gk} \quad (22b)$$

$$n_2 = E_{ce}A_{gk}[(1 - \gamma_{ki})y_i + \gamma_{ki}y_j] \quad (22c)$$

$$n_3 = E_{ce}A_{gk}[(1 - \gamma_{ki})x_i + \gamma_{ki}x_j] \quad (22d)$$

$$n_4 = E_{ce}A_{gk}[(1 - \gamma_{ki})\omega_i + \gamma_{ki}\omega_j] \quad (22e)$$

$$m_0 = -E_{ce}I_{gk}\kappa_{ok} \quad (23a)$$

$$m_1 = 0 \quad (23b)$$

$$m_2 = E_{ce}I_{gk}[(y_j - y_i)/D_k] \quad (23c)$$

$$m_3 = E_{ce}I_{gk}[(x_j - x_i)/D_k] \quad (23d)$$

$$m_4 = E_{ce}I_{gk}[(\omega_j - \omega_i)/D_k] \quad (23e)$$

By considering the whole section and algebraically combining the effects of the axial force and moment in each flat segment the generalised stresses N , M_x , M_y and B can be expressed as linear functions of the generalised strains δ , κ_x , κ_y and ϕ . Using the known values of stresses the unknown strains can thus be determined using the resulting system of 4 equations with 4 unknowns.

Procedurally it will be advantageous to determine the initial linear behaviour first in order to establish whether any further analysis of cracked behaviour is needed and if so the node which will crack first. Some other nodes also may crack at different levels and combinations of generalized stress values and it will be simpler to follow the sequence in which the nodes crack as the stress levels are increased proportionally. This approach is similar to that conventionally adopted for elasto-plastic analysis of structures under proportional loading. In the present model the load-deformation behaviour is assumed to be linear in-between two levels of applied loading at which cracking is initiated sequentially at two nodes of the section profile. Therefore the analysis can be carried out in a manner similar to that outlined for the initial linear behaviour.

CONCLUDING REMARKS

The multi-linear load-deformation outlined herein is meant for a beam length subjected to a load maintained constant over time as opposed to a section subjected to a varying load. The time-dependent concrete material behaviour is assumed to be characterised by the shrinkage strain and an effective modulus. The beam behaviour is then derived by considering the uncracked and a fully cracked section. A linearised load-deformation relationship is adopted for the cracked beam segments, in order to represent the tension stiffening effect.

The proposed load-deformation description formally links the load-dependent deformation to shrinkage which is fundamentally a stress-independent deformation measure. Similarly, the stress-dependent deformation of the concrete elements due to instantaneous and creep effects, is formally linked to the beam deformation under zero loading. This is a departure from the current approaches of calculating separate deflection terms based on shrinkage and effective stiffness, where the fundamental stress-independent and stress-dependent deformation measures are considered separately when calculating deflections.

The moment-curvature relationships implied by the conventional effective stiffness approaches that accommodate tension stiffening, are usually nonlinear. In comparison, the multi-linear curve proposed herein for the complex problem of thin-walled sections has certain advantages. However, due to the involvement of solution of a 4×4 system of equations and further repetitive calculations for progressive cracking of the section, the proposed approach practically requires the use of a computer for its implementation.

References

- ACI Committee 431. (1966). Deflections of reinforced concrete flexural members, *ACI J* **63:6**, 637–674.
- Alwis, W. A. M., Olorunniwo, A. and Ang, K. K. (1994). Long-term deflection of RC Beams, *ASCE J. Struct. Engrg.*, 1994, **120:7**, 2220–2226.
- Bazant, Z. P. and Panula, L. (1980). Creep and shrinkage characterization for analysing prestressed concrete structures, *J. Prestressed Concrete Inst.*, USA, 1980, **25:3**, 86–122.
- Branson, D. E. (1977). *Deformation of concrete structures*, McGraw-Hill, New York.
- British Standards Institution. (1972). *The structural use of concrete, Part 1; Design, materials, workmanship*, London, CP110:Part 1: 1972.

This Page Intentionally Left Blank

Section IV

COMPRESSION MEMBERS

This Page Intentionally Left Blank

DESIGN PROCEDURES FOR STUB COLUMNS

K. Y. Teo and S. M. Chou

School of Mechanical and Production Engineering, Nanyang Technological University,
Nanyang Avenue, Singapore 639798

ABSTRACT

This paper presents a finite element analysis on the post-buckling behaviour of thin-walled cold-formed lipped channel and hat-section stub columns under axial compression. The specimens were modelled exactly as that used in the carefully controlled stub column tests conducted by Zaras and Rhodes. Numerical predictions on the load versus end-shortening characteristics and ultimate load capacity of the structures were obtained using a non-linear finite element analysis. The effect of the input parameters such as the degree of prescribed initial imperfection and the size of the element mesh, on the convergence of the solution is examined. The initial imperfection for post-buckling analysis is achieved by making use of the exact linear buckling wave form. Standard design procedures are developed of post-buckling analysis for thin-walled stub columns using finite element method. Results from the design procedure correlate well with experimental data and BS5950 predictions.

KEYWORDS

Thin-walled structures, stub-columns, post-buckling, finite element analysis, ultimate load.

1 INTRODUCTION

The wider use of thin-walled cold-formed structural components in many areas of application has promoted considerable interest in the local instability of these members. A problem of particular interest is to investigate their post buckling behaviour and ultimate load capacity. Most industrialised countries have issued their own design codes of practice for cold-formed steel structures. The ultimate strength derived from these codes are largely empirical and can sometimes be tedious.

In this study, the finite element analysis is proposed as an alternative and complementary method to the design of cold formed steel structures. A design procedure using finite element method which was earlier developed by Chou and Chai (1997) is modified to improve the robustness and efficiency of the procedure for determining the ultimate load capacity. Four specimens were modelled exactly as that used in the carefully controlled stub column tests conducted by Zaras and Rhodes (1987) as well as two specimens from Lim (1985). This design procedure only applies to stub columns with simply

supported boundary conditions at the ends. The thin-walled stub-columns are subjected to an uniaxial uniform compression loading.

The design procedure is applied to fourteen stub columns; three specimens were selected from Chilver (1953), six from Lim (1985) and five from Weng and Pekoz (1988) which is documented in Chou and Rhodes (1997).

2 FINITE ELEMENT ANALYSIS

A commercial finite element software ANSYS Revision 5.3 was used in this numerical study. A linear buckling analysis is first performed on the specimens to obtain its buckling mode shape, followed by the non-linear post-buckling analysis to predict the load versus end-shortening characteristics curves and ultimate load capacity. The design considerations for the finite element analysis (FEA) is illustrated in the following sections and have been proven suitable when used in conjunction with the finite element software computer code in Chou and Chai (1997).

2.1 *Type of Elements*

The element type used is a 4-noded 3-dimensional linear quadrilateral shell element with 6 degrees-of-freedom at each node. Elastic shell elements are used in the finite element model for linear buckling analysis, whereas, plastic shell elements are used in the modelling for non-linear post-buckling analysis.

2.2 *Element Mesh Size*

Two types of element size are used in the modelling of specimens. Mesh A uses an element size equal to the respective specimen's lip width, whereas, mesh B uses an element size equal to half of the lip width. A typical finite element model is shown in Figure 1.

2.3 *Boundary Condition*

Aluminium end plates were glued to both ends of each specimen during the experiment in order to prevent the loaded ends of the specimens from moving laterally, while offering little resistance to out-of-plane rotation of the plate elements.. This type of end support so achieved was regarded as a close approximation to simple support condition. The end plates were modelled in the finite element model as shown in Figure 1. At the immovable end, nodes on all edges are constrained in the x-direction except for the two corner nodes as shown, where additional constraints are imposed. At the moveable end, only the two corner nodes are constrained in the direction as shown. The boundary conditions are similar for both lipped channel and hat-section stub columns.

2.4 *Geometric Imperfection*

The linear buckling mode shape is used to provide an initial geometric imperfection for the non-linear post-buckling analysis. This is the main difference from the the design procedure developed by Chou and Chai (1997) which uses small perturbation forces to impose the initial imperfection in the finite element model for the non-linear buckling analysis.

The degree of initial imperfection is the maximum amplitude of the buckling mode shape and is prescribed as a percentage of the structure's thickness. In order to determine the effect of the prescribed degree of imperfection on the convergence of the results, four sets of values were used for the study. They are 0.10t, 0.50t, 1.00t where t is the thickness of structure and Walker's suggested expression for

degree of imperfection: $0.3(P_y/P_{cr})^{1/2}t$ where P_y is the yield load and P_{cr} is the critical buckling load. Table 1a shows the five different cases with varying magnitude of degree of imperfection and mesh density applied to all the specimens. Table 1b shows the calculated degree of imperfection using the Walker's expression.

3 NUMERICAL RESULTS

3.1 *Ultimate load prediction*

The ultimate loads obtained from this study are tabulated in Table 2 and 3. The effect of the degree of imperfection prescribed on the finite element models and mesh density on the ultimate load predictions is illustrated to determine the most suitable condition to be used for the development of design procedure. All the ultimate loads predicted overestimate (non-conservative) the experimental and prediction using BS5950. From Table 2, the predictions using Walker's degree of imperfection produced the most consistent result with a standard deviation of 1.99 and 1.70 for mesh A and B respectively. The FEA predictions show better agreement when compared with the experimental results as shown in Table 3.

Although the ultimate loads predicted using higher degree of imperfection are in generally closer to the experimental results and theoretical predictions, the improvement of about 2% is insignificant. At this point, it is still not conclusive which degree of imperfection is suitable to be used for the development of the design procedure. Therefore, addition tests were performed on two other stub column specimens (labelled as specimen no. 5 and 6 in Table 3) selected from Lim (1985) using only two degree of imperfection values: using Walker's expression and 1.0t. The ultimate loads predicted are generally higher than the experimental results except for specimen no. 5 using 1.0t degree of imperfection. This shows that the 1.0t degree of imperfection is not suitable since it produces inconsistent results. It is concluded that the degree of imperfection suggested by Walker be used in the design procedure. A safety factor of 1.25 is recommended based on the largest percentage difference of 23.66% for specimen 4 using mesh A and a safety factor of 1.18 is suggested based on the largest percentage difference of 17.18% for specimen 1 using mesh B, both as shown in Table 2.

Table 4 shows the comparison of ultimate load predictions for the specimens after considering the safety factors; 1.25 is used for Mesh A and 1.18 is used for Mesh B. From the tabulated results, the corrected ultimate load predictions underestimate (conservative) the analytical predictions and experimental results. It can be concluded that the ultimate load predictions obtained from the finite element analysis were found to be in good agreement with the analytical predictions using BS5950 and the experimental results.

3.2 *Load versus End-shortening Characteristic Curves*

The load versus end shortening characteristic curves for one of the specimen obtained from the FEA is shown in Figure 3. Also shown in the figures, are the curves obtained by experimental results and analytical predictions using BS5950:Part 5. The finite element model consisting of shell elements demonstrate a similar load versus end-shortening characteristic to the experimental and design code results. These curves are quite consistently close to the experimental and theoretical curves, although they in general indicate smaller degree of end-shortening than obtained in the experiments and theoretical predictions. In the experiment, the aluminium end plates were found to be indented at the end of each test. If this had been avoided it is likely that the experimental end-shortening would have been somewhat nearer to that estimated by BS5950 and FEA predictions.

During the initial stages of loading, all the curves show linear relationship between the load and the end-shortening. As the end-shortening increases and exceed the critical buckling loading, the columns enters the post-buckling range where non-linear behaviour dominates. In the post-buckling range, the load increases progressively at a slower rate as the end-shortening increases. This can be noticed as the gradient of the curves is slightly more gentle than that at the initial stage. At the ultimate load, the stub columns failed and lost its ability to carry further load. Therefore, the load curve decreases with the end-shortening beyond the ultimate load.

3.3 Stress Distribution and Deflected Waveform

The stress distribution and deflected wave form at collapse load step is shown in Figure 2. The deflected wave form at failure was not restricted to any one component plate of the section, but occurred in all the component plates as illustrated in the figure. It can be noticed that all the failed specimens have highest stress concentration at the curvature near the edges of the corners. These are in agreement with the 'effective width' concept. All the specimens failed due to local buckling. The length of buckles is of the same order to the dimensions of the cross-section rather than the length of the structure as is normally the case with other types of buckling. This is distinct from overall buckling (either of a strut or beam) in which the wavelength of buckle is of the same order as the length of the structure.

4 DESIGN PROCEDURE

The results of this study is used to develop a design procedure using finite element analysis. The design procedure is proposed as follows:

- a. Perform linear buckling and non-linear buckling analysis on the model using lip width as the element size. Note the mesh density (number of elements used in the model) and buckling mode shape after linear buckling. Standard input data listing for lipped channel and hat-section stub columns can be found in Teo (1998).
- b. For stub columns without reinforced lip, perform linear buckling and non-linear buckling analysis on the model using Eqn. 1 and 2 below to calculate the recommended element size for a coarse mesh or fine mesh respectively. Note the mesh density and buckling mode shape after linear buckling.
 - Element size for a coarse mesh = $0.049 \times (\text{overall surface area of column})^{1/2}$ (1)
 - Element size for a fine mesh = $0.0245 \times (\text{overall surface area of column})^{1/2}$ (2)
- c. Determine the preliminary estimated ultimate load, P_{fea} at the end of the non-linear post-buckling analysis to extract the results. The load-displacement path could be plotted using the results.
- d. The final design ultimate load, P_{max} can then be predicted using the expression $P_{max} = P_{fea} / 1.25$ or $P_{max} = P_{fea} / 1.18$ for mesh density less than 1500 elements and more than 1500 elements respectively for all types of stub columns.

5 DESIGN PROCEDURE EVALUATION

The design procedure is applied to fourteen stub column specimens (eight lipped channel and six hat-section) selected from Chilver (1953), Lim (1985) and Weng and Pekoz (1988). The details of the specimens such as the geometry, material properties can be found in the above references.

From the tabulated results shown in Table 5, it can be seen that all the P_{max} predictions are consistent and conservative as compared to the experimentally obtained ultimate loads. The ultimate load

predictions using the design procedure underestimate by 1.91% to 19.11% when compared to the experimental results. These predictions give conservative estimates and are therefore suitable in the design of stub columns. The number of elements used in all the finite element models were less than 1500 elements, thus a safety factor of 1.25 is used.

A correlation curve shown in Figure 4 is plotted based on the results obtained from Table 5 (P_{\max}) and compared to that suggested by Chilver (1953). From the results, a relationship $\sigma_{\max}/\sigma_y = 0.6535 (\sigma_{cr}/\sigma_y)^{0.2912}$ can be determined using regression analysis which show good agreement to that suggested by Chilver. Using the author's suggested expression would yield more conservative results when compared to that suggested by Chilver. This again proved the suitability and reliability of the design procedure for the design of stub columns.

6 CONCLUSION

A commercially available finite element computer software, ANSYS Rev. 5.3 was used to determine the post-buckling behaviour of thin-walled stub columns and develop a standard design procedure to predict the ultimate load capacity of these structures. The ultimate load obtained using the design procedure consistently underestimates the experimental results and analytical predictions using BS5950. These conservative predictions are suitable for the design of stub columns. FEA can therefore be used as an alternative and complementary method to the design of cold-formed steel structure to predict the ultimate load with reasonable accuracy.

REFERENCES

- Chilver A.H. (1953). The stability and Strength of Thin-Walled Steel Struts. *The Engineer*, **196** (5086), 180-3.
- Chou S.M. and Chai G.B. (1997). Ultimate Design Load of Thin-Walled Stub-Columns. *International Journal of Computer Applications in Technology, UK*. **V10, N1/2**, 27-33.
- Chou S.M. and Rhodes J. (1997). Review and Compilation of Experimental Results on Thin-Walled Structures. *Computers & Structures* **Vol. 65: No. 1**, 47-67.
- Guo Y.L. (1992). Ultimate Load Behaviour of Welded Thin-Walled Stub Columns Under Combined Loading of Axial Compression and Bending. *Computers & Structures* **Vol. 42, No. 4**, 591-597.
- Lim B.S. (1985). *Buckling Behaviour of Asymmetric Edge Stiffened Plates*. PhD thesis, University of Strathclyde, Glasgow.
- Teo K.Y. (1998). *Finite Element Analysis on Post-Buckling of Thin-Walled Structures using ANSYS*, Final Year Project Report TKY/98, School of Mechanical and Production Engineering, Nanyang Technological University, Singapore.
- Walker A.C. (1975). *Design and Analysis of Cold-formed Sections*, International Textbook Company Ltd.
- Weng C.C. and Pekoz T. (1988). Compression Tests of Cold-Formed Steel Columns. *9th International Specialty Conference on Cold-formed Steel Structures*, edited by Yu, W.W. and Senne, J.H.
- Zaras J. and Rhodes J. (1987). Carefully Controlled Compression Tests on Thin-Walled Cold-Formed Sections. *Applied Solid Mechanics-2*, edited by A.S. Tooth and J. Spence, 519-551.

TABLE 1
DEGREE OF IMPERFECTION USED FOR NON-LINEAR POST-BUCKLING ANALYSIS

(a)			(b)	
Case No.	Mesh Density	Degree of Imperfection	Spec. No	Degree of imperfection calculated for case 3 and 5
Case 1	Mesh A	0.1t	1	0.765t
Case 2		0.5t	2	0.775t
Case 3		$0.3(P_y/P_{cr})^{0.5} t$	3	0.790t
Case 4		1.0t	4	0.823t
Case 5	Mesh B	$0.3(P_y/P_{cr})^{0.5} t$		

TABLE 2
COMPARISON OF ULTIMATE LOAD FOR FE AND BS5950 PREDICTIONS

Spec. No.	Ultimate Load (kN)						Comparison - Percentage Differences (%)				
	BS5950	0.10t,A	0.50t,A	wal,A	1.00t,A	wal, B	1 vs 2	1 vs3	1 vs 4	1 vs5	1 vs 6
	1	2	3	4	5	6					
1	41.399	50.389	49.970	49.669	49.375	48.511	-21.72	-20.70	-19.98	-19.27	-17.18
2	41.719	50.464	50.129	49.872	49.626	47.059	-20.96	-20.16	-19.54	-18.95	-12.80
3	41.122	49.363	48.932	48.652	48.425	46.737	-20.04	-18.99	-18.31	-17.76	-13.65
4	40.327	50.556	50.211	49.867	49.672	46.597	-25.37	-24.51	-23.66	-23.17	-15.55
Average error							-22.02	-21.09	-20.37	-19.79	-14.80
Standard deviation							2.02	2.07	1.99	2.03	1.70

% diff for 1vs 2 =((BS5950 - 0.10t, A) / BS5950 * 100%
 '+' - conservative
 '-' - non-conservative

TABLE 3
COMPARISON OF ULTIMATE LOAD FOR FE PREDICTIONS AND EXPERIMENTAL RESULTS

Spec. No.	Ultimate Load (kN)						Comparison - Percentage Differences (%)				
	Exp	0.10t,A	0.50t,A	wal,A	1.00t,A	wal, B	1 vs 2	1 vs 3	1 vs 4	1 vs 5	1 vs 6
	1	2	3	4	5	6					
1	43.993	50.389	49.970	49.669	49.375	48.511	-14.54	-13.59	-12.90	-12.23	-10.27
2	41.880	50.464	50.129	49.872	49.626	47.059	-20.50	-19.70	-19.08	-18.50	-12.37
3	42.925	49.363	48.932	48.652	48.425	46.737	-15.00	-13.99	-13.34	-12.81	-8.88
4	44.082	50.556	50.211	49.867	49.672	46.597	-14.69	-13.90	-13.12	-12.68	-5.71
5	19.570	-	-	20.529	19.354	-	-	-	-4.90*	+1.10*	-
6	33.080	-	-	37.574	36.540	-	-	-	-13.59*	-10.46*	-
Average error							-16.18	-15.30	-14.61	-14.06	-9.31
Standard deviation							2.50	2.55	2.59	2.57	2.42

% diff for 1vs 2 =((Exp - 0.10t, A) / Exp * 100%
 '+' - conservative
 '**' - not included in the computation of average error and standard deviation
 '-' - non-conservative

TABLE 4
COMPARISON OF CORRECTED ULTIMATE LOAD WITH ANALYTICAL PREDICTIONS

Spec. No.	Ultimate Load (kN)				Comparison - Percentage Differences (%)			
	BS5950	Exp	A	B	1 vs 3	1 vs 4	2 vs 3	2 vs 4
	1	2	3	4				
1	41.399	43.993	39.735	41.111	+4.02	+0.70	+9.68	+6.55
2	41.719	41.880	39.898	39.881	+4.37	+4.41	+4.73	+4.77
3	41.122	42.925	38.922	39.608	+5.35	+3.68	+9.33	+7.73
4	40.327	44.082	39.894	39.489	+1.07	+2.08	+9.50	+10.42
Average error					+3.70	+2.72	+8.31	+7.37
Standard deviation					2.02	2.07	2.07	2.05

A - Obtained using safety factor of 1.25

B - Obtained using safety factor of 1.18

% diff for 1vs 2 = ((BS5950 - A) / BS5950)*100%

'+' - conservative

'-' - non-conservative

TABLE 5
COMPARISON OF ULTIMATE LOADS

Spec. No.	Ultimate Load (kN)			Comparison - Percentage Differences (%)
	P _{exp}	P _{tea}	P _{max}	
	1	2	3	
p24rfc11	158.700	166.110	132.888	+16.26
p24rfc13	155.700	166.650	133.320	+14.37
p24rfc14	130.800	135.970	108.776	+16.84
p24pbc13	104.530	108.270	86.616	+17.14
p24pbc14	78.730	86.400	69.120	+12.21
p5lip1	43.040	47.658	38.126	+11.42
p5lip4	69.840	71.995	57.596	+17.53
p5lip6	46.310	56.533	45.226	+2.34
p17a5	19.570	23.996	19.197	+1.91
p17b5	68.960	69.723	55.778	+19.11
p17b6	66.070	70.197	56.158	+15.00
p17c3	33.080	37.574	30.059	+9.13
p17c4	37.820	40.199	32.159	+14.97
p17c6	40.950	43.027	34.422	+15.94
Average error				+13.16
Standard deviation				5.36

% diff for 1vs 3 = ((P_{exp} - P_{max}) / P_{exp})*100%

'+' - conservative

'-' - non-conservative

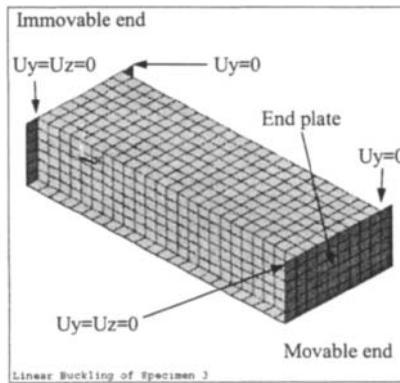


Figure 1 : Typical finite element model (Specimen 3)

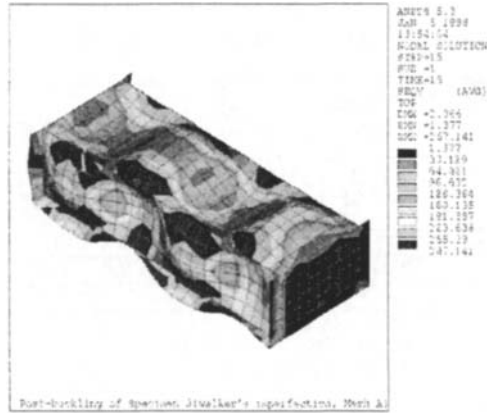


Figure 2 : Stress distribution and deflected wave form of specimen 3 at collapse load

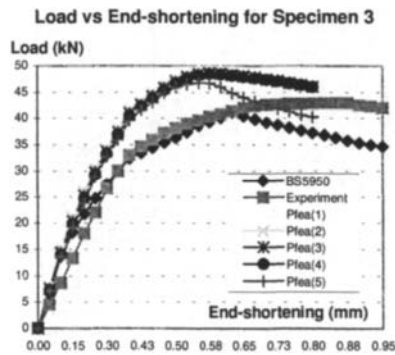


Figure 3 : Load versus end-shortening curves for specimen 3

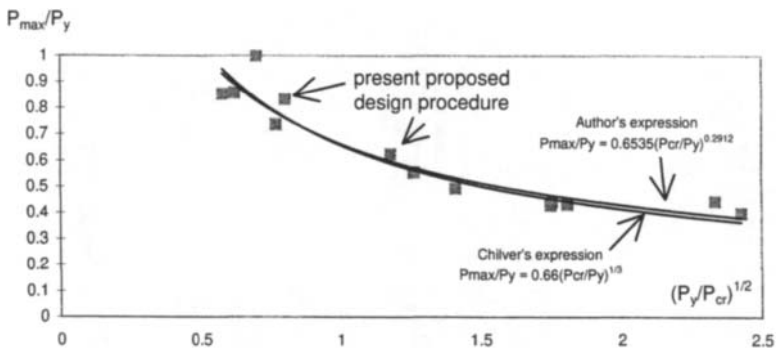


Figure 4 : Graph of (P_{max}/P_y) versus $(P_y/P_{cr})^{1/2}$

INELASTIC BIFURCATION ANALYSIS OF LOCALLY BUCKLED CHANNEL COLUMNS

B. Young and K. J. R. Rasmussen

Department of Civil Engineering, University of Sydney,
Sydney, NSW, 2006, Australia

ABSTRACT

The paper describes an inelastic bifurcation analysis of locally buckled columns. The members are assumed to be geometrically perfect in the overall sense but could include geometric imperfections and yielding in the local mode. The method of analysis uses an inelastic geometric non-linear finite strip local buckling analysis to determine the tangent rigidities of the locally buckled section. These tangent rigidities are substituted into the flexural and flexural-torsional equations to calculate the inelastic overall bifurcation loads. The bifurcation analysis is applied in the present paper to plain channel columns and compared with tests on fixed-ended cold-formed columns. The bifurcation loads are in good agreement with the test strengths. In addition, the effect of yielding is highlighted in this paper.

KEYWORDS

Buckling, Channel column, Fixed-ended, Inelastic bifurcation analysis, Tangent rigidities, Yielding.

INTRODUCTION

The primary effect of local buckling is to reduce the member stiffnesses against overall flexure and torsion. Consequently, bifurcation in an overall mode can be calculated by using the stiffness of the locally buckled cross-section rather than the stiffness of the undistorted cross-section. This result has been used widely (Bijlaard and Fisher 1953, Hancock 1981) to determine the flexural buckling load of locally buckled doubly symmetric columns. In this case, the buckling load can be obtained simply by replacing the flexural rigidity (EI) of the unbuckled section by the flexural rigidity of the locally buckled section in the Euler formula. Flexural-torsional buckling can be analysed using a similar approach, in which case the stiffnesses of the locally buckled member against flexure and torsion are required. Bradford and Hancock (1984) analysed the bifurcation of locally buckled beams by employing a non-linear finite strip method to determine the flexural rigidity of the section in minor axis bending. The minor axis rigidity was also used for determining the warping rigidity of the locally buckled section. The method was applied to doubly symmetric I-sections in uniform bending.

The bifurcation analysis of locally buckled members was formally described (Rasmussen 1997, Young and Rasmussen 1997) by deriving the governing equations for the fundamental and bifurcated states. The analysis was applicable to members of arbitrary cross-section shapes subjected to arbitrary types of loading. The members were assumed to be geometrically perfect in the overall sense but could include imperfections in the local mode. The bifurcation analysis described in Young and Rasmussen (1997) is applied in the present paper to fixed-ended singly symmetric columns, for which the tangent rigidities of a locally buckled section are obtained by using inelastic non-linear finite strip methods. The tangent rigidities are substituted into the flexural and flexural-torsional equations for the overall bifurcation loads.

The purpose of this paper is to compare bifurcation loads with tests on fixed-ended plain channel columns, and to study the effect of yielding on the overall bifurcation loads of channel columns.

BIFURCATION ANALYSIS

Model of Locally Buckled Member

The bifurcation analysis of locally buckled singly symmetric columns described in this paper applies to cross-sections composed of thin plates. A model is used which assumes that the locally buckled cross-section consists of an assembly of narrow strips, the tangential axial stiffnesses (E_t) of which vary around the cross-section as functions of the extent of local buckling. The model allows the effect of local buckling, which is to cause a *geometrical* loss of stiffness to be considered as a *material* effect in the overall bifurcation analysis. Consequently, the theory for the bifurcation of thin-walled members with *undistorted* cross-sections can be used by changing only the stress-strain relations, as detailed in Rasmussen (1997).

Bifurcation Equations for Fixed-ended Singly Symmetric Column

The critical load factors for flexural buckling (λ_{c_x}) and flexural-torsional buckling ($\lambda_{c_{*}}$) of a locally buckled fixed-ended singly symmetric column are obtained from, (Young and Rasmussen 1997)

$$\lambda_{c_x} = \frac{\left(\frac{2\pi}{L}\right)^2 \left((EI_y)_t - \frac{(ES_y)_t^2}{(EA)_t} \right)}{\bar{N}} \quad (1)$$

$$\lambda_{c_{*}} = \frac{-B \pm \sqrt{B^2 - 4AC}}{2A} \quad (2)$$

where

$$A = \frac{\bar{N}\bar{W}}{r_o^2 + x_s^2} \quad (3)$$

$$B = -\bar{N} \left(P_x \frac{\frac{\bar{W}}{\bar{N}} + x_s^2}{r_o^2 + x_s^2} + P_z + 2 \left(\frac{2\pi}{L} \right)^2 \frac{x_s}{r_o^2 + x_s^2} (EI_{x\theta})_t \right) \quad (4)$$

$$C = P_x P_z - \left(\frac{2\pi}{L}\right)^4 \frac{(EI_{x\omega})_i^2}{r_o^2 + x_s^2} \quad (5)$$

$$P_x = \left(\frac{2\pi}{L}\right)^2 (EI_x)_i \quad (6)$$

$$P_z = \frac{\left(\frac{2\pi}{L}\right)^2 (EI_\omega)_i + (GJ)_i}{r_o^2 + x_s^2} \quad (7)$$

$$r_o^2 = \frac{I_p}{A} = \frac{I_x + I_y}{A} = \frac{\int (x^2 + y^2) dA}{A} \quad (8)$$

In Eqns (3-5), A , B and C are the constants of the quadratic equation (2), \bar{N} and \bar{W} are the applied axial force and Wagner stress resultant respectively, r_o is the polar radius of gyration, x_s is the x -coordinate of the shear centre, and L is the specimen length. In Eqns (6-7), P_x and P_z are the loads for pure flexural buckling about x -axis and torsional buckling respectively, G is the shear modulus, and J is the torsion constant. In Eqn. (8), I_p is the polar moment of area, I_x and I_y are the second moments of area for bending about x and y axes respectively, and A is the full cross-section area.

Tangent Rigidities

The tangent rigidities of the locally buckled member may be determined from a non-linear post-buckling analysis of a length of section equal to the local buckle half-wavelength (l), as described in Rasmussen (1997). The analysis produces rigidities that are average values for this length of section. In this paper, the tangent rigidities $((EA)_i, (ES_y)_i, (EI_y)_i, (EI_x)_i, (EI_\omega)_i, (EI_{x\omega})_i)$ are determined using both elastic and inelastic non-linear finite strip buckling analyses, as described in Hancock (1985) and Key and Hancock (1993) respectively. In the analyses, a locally buckled cell of length equal to the local buckle half-wavelength (l) was subjected to increasing values of axial compression and at each load level, small increments of generalised strain were applied. This allowed the tangent rigidities to be obtained at each load level, as described in Rasmussen (1997). Subsequently, the bifurcation curves were obtained by expressing Eqns (1-8) in terms of the lengths (L) to cause flexural and flexural-torsional buckling at a given load. This procedure allowed the bifurcation curves to be obtained without iteration.

EXPERIMENTAL INVESTIGATION

The test program described in Young and Rasmussen (1998) provided experimental ultimate loads and failure modes for cold-formed channel columns. The tests were performed on plain channels brake-pressed from high strength zinc-coated Grade G450 steel sheets with nominal yield stress of 450MPa. Both pin-ended and fixed-ended columns were tested, although only the fixed-ended test results are used in the present paper. Of the two series tested with two different cross-sections, only the results of the plain channel Series P36 tests are used in this paper. The average values of measured cross-section dimensions of the test specimens are shown in Table 1 using the nomenclature defined in Fig. 1. Table 1 also contains the full cross-section area (A), the second moments of area (I_x) and (I_y) for bending about the x and y axes respectively, the warping constant (I_ω), and the torsion constant (J). The specimens were tested between fixed ends at various column lengths.

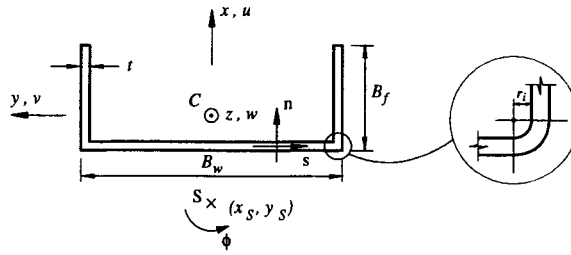


Figure 1: Nomenclature for plain channel section

TABLE 1
CROSS-SECTION DIMENSIONS

Series	B_f	B_w	t^*	r_i	A	I_x	I_y	I_w	J
	(mm)	(mm)	(mm)	(mm)	(mm ²)	(mm ⁴)	(mm ⁴)	(mm ⁶)	(mm ⁴)
P36	36.8	96.9	1.47	0.85	247	3.47×10^5	3.10×10^4	4.99×10^7	1.77×10^2

* Base metal thickness

The base metal properties determined from the coupon tests are summarised in Table 2. The table contains the measured static 0.01% ($\sigma_{0.01}$) and 0.2% ($\sigma_{0.2}$) tensile proof stresses, and the initial Young's modulus (E_o). The measured stress-strain curves obtained from the coupon tests are detailed in Young and Rasmussen (1998).

TABLE 2
LOCAL BUCKLING DETAILS AND MEASURED MATERIAL PROPERTIES

Series	Local Buckling			Material Properties			
	E	σ_l	l	E_o	$\sigma_{0.01}$	$\sigma_{0.2}$	n
	(MPa)	(MPa)	(mm)	(MPa)	(MPa)	(MPa)	
P36	2.10×10^5	177	110	2.10×10^5	380	550	8

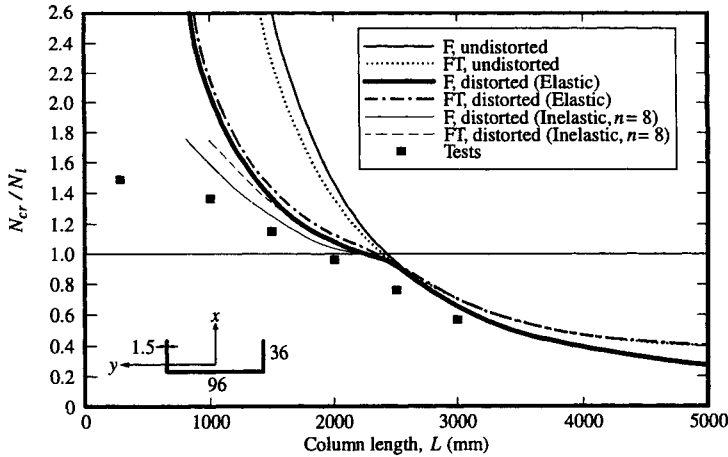
Local and overall geometric imperfections were measured prior to testing. The measured maximum local imperfections were found to be of the order of the plate thickness at the tip of the flanges for all specimens. The maximum overall minor axis flexural imperfections at mid-length were 1/1400 of the specimen length. The measured local and overall geometric imperfection profiles are detailed in Young and Rasmussen (1995).

A 250kN servo-controlled hydraulic actuator was used to apply a compressive axial force to the specimen. The fixed-ended bearings were designed to restrain both minor and major axis rotations as well as twist rotations and warping. Details of the test rig and the fixed-ended bearings are given in Young and Rasmussen (1995).

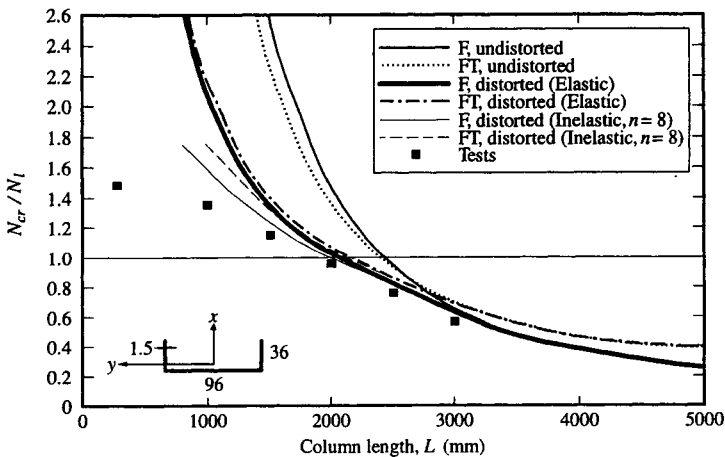
COMPARISON OF BIFURCATION ANALYSIS AND EXPERIMENTAL RESULTS

The elastic and inelastic bifurcation loads ($\lambda_{c_e} \bar{N}, \lambda_{c_i} \bar{N}$) obtained from Eqns (1) and (2) for flexural and flexural-torsional buckling are compared with tests on fixed-ended plain channel columns (Young and Rasmussen 1998) in Fig. 2. Because the test specimens were produced by brake-pressing, the corner radii and residual stresses were small and could be ignored in the numerical analysis. Prior to the overall bifurcation analysis, the cross-section was analysed using a finite strip buckling analysis

(Hancock 1978) to determine the elastic local buckling stress. The results are given in Table 2, in which E is the measured value of Young's modulus, σ_l is the local buckling stress and l is the corresponding local buckle half-wavelength.



(a) $w_o/t = 0.02$



(b) $w_o/t = 0.2$

Figure 2: Non-dimensionalised load (N_{cr}/N_l) vs column length (L) for fixed-ended channel section

In Figs 2a and 2b, the bifurcation loads ($\lambda_{c_x} \bar{N}$, $\lambda_{c_w} \bar{N}$) are shown as N_{cr} on the vertical axis, non-dimensionalised with respect to the elastic local buckling load ($N_l = A\sigma_l$). The figures include the flexural (F) and flexural-torsional (FT) bifurcation curves of both the locally buckled and undistorted cross-sections. The curves are shown in Fig. 2a for a magnitude (w_o) of the local geometric imperfection (in the shape of the local buckling mode) of $w_o = 0.02t$ and in Fig. 2b for a magnitude of the local geometric imperfection of $w_o = 0.2t$. The ultimate loads are plotted against the column length (L). The specimens failed in combined local and flexural buckling modes at short and intermediate lengths ($L \leq 1500\text{mm}$), and in a pure flexural buckling mode at long lengths.

As mentioned in the Introduction, the purpose of this paper is to compare the inelastic bifurcation analysis with the test results. For the inelastic bifurcation analysis, the measured stress-strain curve was modelled using the Ramberg-Osgood expression (Ramberg and Osgood 1943),

$$\epsilon = \frac{\sigma}{E_o} + 0.002 \left(\frac{\sigma}{\sigma_{0.2}} \right)^n \tag{9}$$

where ϵ is the strain, σ is the stress, $\sigma_{0.2}$ is 0.2% proof stress, E_o is the initial modulus of elasticity and n is a parameter that describes the shape of the curve. In the limit, $n \rightarrow \infty$, the Ramberg-Osgood expression represents elastic-perfectly plastic materials. The measured stress-strain curve (Young and Rasmussen 1998) was used to determine E_o and the proof stresses ($\sigma_{0.01}$, $\sigma_{0.2}$), as shown in Table 2. The parameter n could be obtained from $\sigma_{0.01}$ and $\sigma_{0.2}$ using $n = \ln(0.01/0.2) / \ln(\sigma_{0.01}/\sigma_{0.2})$. This expression provided the value of $n = 8$ for the test Series P36.

The test results shown in Figs 2a and 2b for local imperfection magnitudes of $w_o = 0.02t$ and $w_o = 0.2t$ respectively are lower than the inelastic bifurcation curves. The discrepancy is attributed to overall geometric imperfections. However, at short to intermediate lengths, the inelastic bifurcation curves follow much more closely the test strengths than the elastic bifurcation curves. The flexural buckling mode observed in the tests was accurately predicted at all lengths.

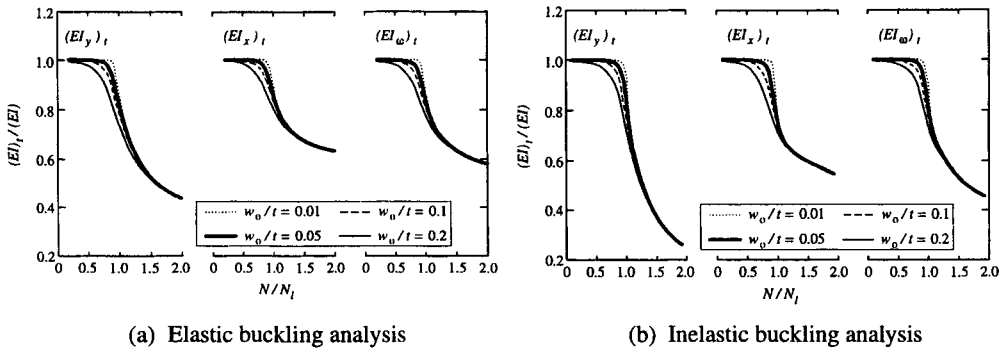


Figure 3: Tangent rigidity curves for channel section ($w_o/t = 0.01, 0.05, 0.1$ and 0.2)

Figures 3a and 3b show the elastic and inelastic tangent rigidities ($(EI_y)_t$, $(EI_x)_t$, $(EI_\omega)_t$) as functions of the load (N / N_t). The inelastic tangent rigidities were obtained using $n = 8$. The rigidity curves are shown for four values of local geometric imperfection, $w_o / t = 0.01, 0.05, 0.1$ and 0.2 . It follows that both the elastic and inelastic stiffness against minor axis flexure ($(EI_y)_t$) drops more rapidly than the stiffnesses against major axis flexure ($(EI_x)_t$) and warping torsion ($(EI_\omega)_t$) for this section, and that yielding accentuates the drop. This causes flexural buckling to be more critical than flexural-torsional buckling at short and intermediate lengths. It also explains why the flexural curves for the locally buckled section are lower than the flexural-torsional curves in Figs 2a and 2b, despite the fact that the lowest curves are the flexural-torsional curves for the undistorted cross-section.

For the purpose of demonstrating the effect of yielding on the bifurcation curves, three different material stress-strain curves, defined by $n = 5$, $n = 25$ and $n \rightarrow \infty$, were used to produce bifurcation curves, as shown in Fig. 4 for a local imperfection magnitude of $w_o = 0.02t$. The flexural bifurcation loads are shown as N_{cr} on the vertical axis, non-dimensionalised with respect to the elastic local buckling load (N_t). The figure shows the flexural bifurcation curves of the undistorted, elastic distorted

and inelastic distorted cross-section. For the locally buckled section ($N_{cr} / N_I \geq 1$), the flexural bifurcation curve for $n = 5$ lies well below that for $n \rightarrow \infty$ at intermediate column lengths. The flexural bifurcation curve for $n = 25$ lies between those for $n = 5$ and $n \rightarrow \infty$ at intermediate column lengths. The flexural bifurcation curve for $n = 5$ follows most closely that of the test strengths, as should be expected since the value $n = 8$ deduced from the measured stress-strain curve is closest to $n = 5$. For $n = 25$ and $n \rightarrow \infty$, the bifurcation load approaches a limiting value of $N_{cr} / N_I \cong 1.7$ at $L \cong 1000\text{mm}$, but this is not the case for $n = 5$. This apparent limiting load is simply a statement of the fact that an ultimate load was reached in the inelastic finite strip analysis for $n = 25$ and $n \rightarrow \infty$ but not for $n = 5$. For $n = 25$ and $n \rightarrow \infty$, the bifurcation loads corresponding to $L < 1000\text{mm}$ were obtained from the tangent rigidities determined in the post-ultimate range of the finite strip analysis. These loads do not have physical relevance, since for $L < 1000\text{mm}$ the strength is simply the limiting load $N_{cr} / N_I \cong 1.7$ (the stub column strength) which is not a bifurcation load.

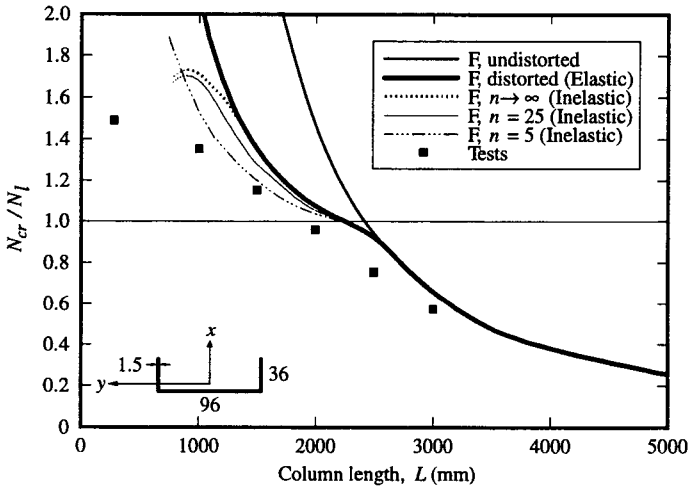


Figure 4: Flexural inelastic bifurcation curves for channel section ($n = 5, 25$ and ∞)

The tangent rigidities ($(EI_y)_t$, $(EI_x)_t$, $(EI_\omega)_t$) are shown in Fig. 5 for $n = 5$, $n = 25$ and $n \rightarrow \infty$. It appears that the initial drops in the minor axis flexural and warping-torsion tangent rigidities are steeper the smaller the value of n , leading to lower bifurcation curves as evidenced in Fig. 4. The attainment of an ultimate load in the inelastic finite strip analysis for $n = 25$ and $n \rightarrow \infty$ is also apparent from Fig. 5.

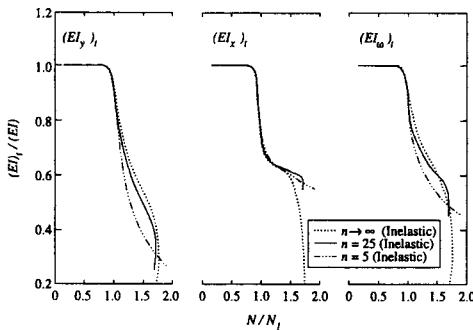


Figure 5: Inelastic tangent rigidity curves for channel section ($n = 5, 25$ and ∞)

CONCLUSIONS

The overall flexural and flexural-torsional bifurcation loads of locally buckled singly-symmetric columns have been presented and applied to a fixed-ended plain channel section. The analysis uses an inelastic non-linear finite strip buckling analysis to determine the tangent rigidities of the locally buckled section. The tangent rigidities are substituted into the overall flexural and flexural-torsional bifurcation equations.

The inelastic bifurcation loads of plain channel section columns are compared with test results. Good agreement is found between the test strengths and the bifurcation loads obtained using the inelastic buckling analysis. The test strengths were generally lower than the bifurcation loads as a result of overall geometric imperfections.

The inelastic bifurcation loads for different material stress-strain curves were presented using different values of the parameter n of the Ramberg-Osgood expression. The bifurcation curves for small values of n were generally lower than those for high values of n , although the stub column strengths, and hence the bifurcation curves, were higher for small values of n at short column lengths.

REFERENCES

- Bijlaard P.P. and Fisher G.P. (1953). Column Strength of H-Sections and Square Tubes in Post-buckling range of Component Plates. *National Advisory Committee for Aeronautics*, TN 2994.
- Bradford M.A. and Hancock G.J. (1984). Elastic Interaction of Local and Lateral Buckling in Beams. *Thin-walled Structures* **2**, 1-25.
- Hancock G.J. (1978). Local, Distortional and Lateral Buckling of I-Beams. *Journal of the Structural Division*, ASCE **104**:11, 1787-1798.
- Hancock G.J. (1981). Interaction Buckling in I-Section Columns. *Journal of the Structural Division*, ASCE **107**:1, 165-179.
- Hancock G.J. (1985). Non-linear Analysis of Thin-walled I-Sections in Bending. *Aspects of Analysis of Plate Structures*, eds D.J. Dawe, R.W. Horsington, A.G. Kamtekar & G.H. Little, 251-268.
- Key P.W. and Hancock G.J. (1993). A Finite Strip Method for the Elastic-Plastic Large Displacement Analysis of Thin-Walled and Cold-Formed Steel Sections. *Thin-walled Structures* **16**, 3-29.
- Ramberg W. and Osgood W.R. (1943). Description of Stress-Strain curves by Three Parameters. *Technical Note No. 902*, National Advisory Committee for Aeronautics, Washington, D.C.
- Rasmussen K.J.R. (1997). Bifurcation of Locally Buckled Members. *Thin-Walled Structures* **28**:2, 117-154.
- Young B. and Rasmussen K.J.R. (1995). Compression Tests of Fixed-ended and Pin-ended Cold-Formed Plain Channels. *Research Report R714*, School of Civil and Mining Engineering, University of Sydney, Australia.
- Young B. and Rasmussen K.J.R. (1997). Bifurcation of Singly Symmetric Columns. *Thin-Walled Structures* **28**:2, 155-177.
- Young B. and Rasmussen K.J.R. (1998). Tests of Fixed-ended Plain Channel Columns. *Journal of Structural Engineering*, ASCE **124**:2, 131-139.

STABILITY AND BRACING OF THIN-WALLED COLUMNS

Pratyoosh Gupta¹, S.T. Wang² and George E. Blandford²

¹ Consultant, Deloitte & Touche Consulting Group, Ste. 825,
1225 North Loop West, Houston, TX 77008.

² Professor, Department of Civil Engineering, University of Kentucky
Lexington, KY 40506-0281.

ABSTRACT

A three-dimensional second-order analysis is used to study the effects of lateral and torsional brace stiffness on the elastic stability of doubly and singly symmetric thin-walled columns. The finite element formulation uses an iterative updated Lagrangian scheme to include the second-order geometric-nonlinear effects in the space frame element as well as the connection element, which is used to model the lateral and torsional braces of a column. A parametric study has been performed to investigate the effects of various lateral and torsional brace stiffness on the buckling strength of columns with singly and doubly symmetric sections. Results on interaction among initial imperfections, the lateral and torsional brace stiffness and the corresponding buckling strength of columns are presented. It has been found that columns with singly symmetric sections are very sensitive to the magnitude and direction of initial imperfections and brace stiffness.

KEYWORDS

Bracing, Buckling, C-Section, Finite-Element, Geometric-Nonlinear, Initial Imperfection, Second-Order, Singly Symmetric, Thin-Walled, Torsional-Flexural, Three-Dimensional.

INTRODUCTION

Thin-walled structures are becoming increasingly popular resulting in lightweight and slender structural members. In order to more effectively utilize thin-walled columns, it is essential to provide lateral and/or torsional bracing to increase the buckling capacity of the column and to make sure that the provided braces are adequate and the deflections of the column are within permissible tolerances. Full bracing is defined as equivalent in effectiveness to an immovable lateral or torsional support. The effect of lateral bracing on the buckling strength of columns has been studied extensively by various researchers over the years. Winter (1960) presented a simple method that permits the lower limits of strength and rigidity of lateral support in order to provide full bracing. Wang *et al.* (1980) presented a bifurcation analysis on the bracing requirements for locally buckled thin-walled columns with both doubly and singly symmetric

sections. Wang and Nethercot (1989) investigated the brace stiffness requirements using a three-dimensional analysis and included the effects of initial imperfections and plasticity on the braced I-beams. Plaut and Yang (1993, 1995) performed extensive parametric studies to determine the lateral brace stiffness requirements for multi-span columns with two or three spans, which based all their findings on two-dimensional analyses, i.e., pure flexural analysis about the weak axis for hot-rolled sections. Most of the authors mentioned above presented two-dimensional analyses for pure flexural buckling or bifurcation analysis for torsional-flexural buckling for hot-rolled steel sections. Recently, Gupta et al. (1996a, 1996b) presented a study on lateral and torsion bracing stiffness requirements for hot rolled and cold-formed columns based on two-dimensional and three-dimensional analyses with the inclusion of second-order geometric nonlinear effects. In this paper, some results from a recent study, which is a part of an on-going research program on bracing requirements and column buckling, are presented. Various lateral and torsional brace stiffness and initial imperfections are considered. A connection element is used to model the brace stiffness at the column mid-height based on a second-order analysis including geometric nonlinear effects.

FINITE ELEMENT FORMULATION AND NUMERICAL ANALYSIS

The finite element formulation used for the large-deformation analysis of space frame structures is based on second-order geometric-nonlinear theory and Vlasov's theory for thin-walled beams (i.e., large displacement of members with small strains, and includes the warping deformation influence). Rodriguez's modified rotation vector is used to represent angular deformations, which avoids rotational discontinuities at the joints of deformed space frame structures. Two local coordinate systems are used in the finite element development: complete (fixed local) reference, which is used to locate the initial beam position, and a cantilever bound reference. A displacement field defined on the cantilever bound reference experiences no displacement or rotation at end a (Figure 1) except for the warping deformation. Details of the finite element formulation and numerical analysis procedures are given in Chen (1990), and Chen and Blandford (1991a, b; 1993; 1995).

There are eight deformation degrees of freedom for the space frame finite element, $u_{sx}^b, u_{sy}^b, u_{sz}^b, \theta_x^b, \theta_y^b, \theta_z^b, \chi_x^a, \chi_x^b$ where subscript 's' refers to the displacements at the section shear center; superscripts 'a' and 'b' refer to beginning and end nodes of the finite element, respectively; transnational displacements are represented by u ; Euler rotations by θ ; and warping deformation by χ . An element stiffness matrix is developed using the usual finite element procedures based on a cubic interpolation for torsion and bending about each axis with a linear interpolation of the axial deformation. For the usual finite element development, the rotational displacement components $\theta_x (= \phi_x)$, θ_y , and θ_z are chosen, but components θ_y and θ_z do not equal the modified rotation vector components ϕ_y and ϕ_z . A geometric discontinuity results at a corner node where an axial rotation component ϕ_x of one member is assembled to a bending rotation component θ_y or θ_z of another member. Components of the modified rotation vector are chosen as the rotational displacement field and the eight deformation degrees of freedom for the cantilever bound reference are $u_{sx}^b, u_{sy}^b, u_{sz}^b, \phi_x^b, \phi_y^b, \phi_z^b, \chi_x^a, \chi_x^b$ (Figures 1, and 2). The flexible connection element has the same number degree of freedom and nonlinear capability as frame element and its development follows the same steps as that for the frame element. An iterative updated Lagrangian scheme is used to include second-order geometric-nonlinear effects, i.e., the structure geometry is updated for each iteration within the load step based on the iterative change in displacements. Work-increment-control and modified Newton Raphson methods are used for the solution of the nonlinear global stiffness equations.

NUMERICAL RESULTS

Lateral Brace Stiffness Requirement for Two-Dimensional Doubly Symmetric I-Section Column

The effect of lateral bracing provided at mid-height on the buckling strength of a doubly symmetric I-section column is studied (Gupta *et al.* (1996a)), which consists of two channel sections back to back. Geometrical and material properties for this section are: $A_x = 3.28 \text{ cm}^2$; $I_y = 2.39 \text{ cm}^4$; $I_z = 26.47 \text{ cm}^4$; $J = 0.078 \text{ cm}^4$; $C_w = 23.44 \text{ cm}^6$; and L (length of column) = 64 cm; $E=20000 \text{ kN/cm}^2$; and $G=7590 \text{ kN/cm}^2$. The boundary conditions for the column are such that the column is forced to act as a two-dimensional column. Only rotations about weak axis and displacement along column length are allowed. An asymmetric initial geometric imperfection Δ_x is specified. The initial deflection (imperfection) is provided by adding together a half sine wave Δ_{x1} with amplitude d_{01} and a full sine wave Δ_{x2} with amplitude d_{02} . These deflections are expressed as

$$\Delta_{x1} = d_{01} \sin\left(\frac{\pi x}{L}\right); \quad \Delta_{x2} = d_{02} \sin\left(\frac{2\pi x}{L}\right); \quad \Delta_x = \Delta_{x1} + \Delta_{x2} \quad (1)$$

An initial asymmetric imperfection is used so that the second buckling mode will be clearly identifiable. The stability or the buckling load P_{cr} for braced columns is defined as the load corresponding to a mid-height lateral deflection of twice the initial imperfection ($2d_{01}$), as for practical design purposes it is undesirable to have deflections greater than $2d_{01}$ at mid-height of the column (Winter 1960).

For the column considered, an initial geometric imperfection (Δ_x) is given about the weak axis in accordance with Eqn. 1 to initiate bending. An amplitude of $d_{01}=L/1000$ for the half sine wave and an amplitude of $d_{02}=L/10000$ for the full sine wave are used in Eqn. 1. A concentrated force is applied on the top of the column. The lateral brace (with stiffness K_{bx}) at mid-height is modeled using a flexible connection element and the non-dimensionalized brace stiffness is defined as

$$S_x = \frac{K_{bx} L}{P_y} \quad (2)$$

Geometric non-linearity in the connection element is also considered. The lateral brace stiffness is adjusted by varying the translational stiffness of the connection element (K_{bx}). All the degrees of freedom of the connection element except the translational degree of freedom are slaved to the mid-height node of the column.

Figure 3 shows the stability load ratios, i.e., P_{cr}/P_y , with varying lateral brace stiffness for the two-dimensional column. It should be noted that the stability load P_{cr} for braced columns is defined as the load corresponding to a mid-height lateral deflection of twice the initial imperfection ($2d_{01}$), as discussed above. It is because of this reason that even with no lateral brace, the value P_{cr} is not equal to P_y . It is seen that $S_x = 27.33$ yields a stability load of $4P_y$, i.e., buckling load for the second mode. Hence, full bracing is achieved for this column. Deflected shapes of the column about the weak axis for different values of lateral brace stiffness are shown in Figure 4. It is observed that the second flexural buckling mode occurs at a lateral brace stiffness of $S_x = 27.33$. In no case, the lateral deflection at mid-height of the column exceeds twice the initial imperfection. It is seen that with full lateral brace the deflection is slightly less than $2d_{01}$ and with a very stiff brace of $S_x=35$, the lateral deflection is way below $2d_{01}$.

Torsional Brace Stiffness Requirement for Three-Dimensional Singly Symmetric C-Section Column

A thin-walled channel section originally analyzed by Wang *et al.* (1980) with the same material properties as above is considered. The flange dimensions are 6.35 cm x 0.2032 cm. and web dimensions are 12.29 cm x 0.2032 cm. The length of the column is 213.36 cm. The boundary conditions for this column at the bottom support are: restrained against translation in all three directions, free to rotate about weak and strong axes, restrained against torsion but free to warp and the boundary conditions at the top support of the column are similar to that at the bottom support, except that it is free to translate in the longitudinal direction or along the column length (i.e., roller support). None of the displacement degrees of freedom at intermediate nodes (seven at each node) are restrained.

In order to study the effect of initial imperfections, no braces are provided in this column at first. Asymmetrical initial imperfections are provided about either the strong or the weak axis or both in accordance with Eqn.1 with amplitudes of $d_{01}=L/1000$ and $d_{02}=L/10000$. Figure 5 shows the load-deflection curves for this column with various initial imperfections. It is seen that the C-section column is very sensitive to the direction of initial imperfections. If an initial moment perturbation is provided (0.0001P), the stability load is very close to the theoretical torsional-flexural buckling load. The positive initial imperfection in strong axes towards the centroid of the cross-section leads to a very low stability load as shown in Figure 5. The direction of initial imperfection in weak direction does not impact the carrying capacity of the column.

Subsequently, a symmetrical initial imperfection with a full sine wave is provided for the C-section column with $d_{01}=L/1000$ and $d_{01}=L/10,000$ and a full lateral brace is provided at the mid-height of the column ($S_x=28$). The stability or the buckling load P_{cr} for this column is defined as the load corresponding to a mid-height lateral deflection of twice the initial imperfection ($2d_{01}$) in either direction as defined in case of I-section column. For practical design purposes, it is undesirable to have deflections greater than $2d_{01}$ at mid-height of the column (Winter 1960). A flexible connection element is used to model the torsional stiffness of the brace ($K_{b\theta y}$) to the column at mid-height. The non-dimensionalized torsional brace stiffness ($S_{\theta y}$) is expressed as

$$S_{\theta y} = \frac{K_{b\theta y} L}{GJ} \quad (3)$$

in which J is the torsion constant of the column. Figure 6 shows the non-dimensionalized stability loads of the column with increasing torsional stiffness of the brace at mid-height. It is observed even with $S_{\theta y} = 0$, i.e., with no torsional brace, stability loads are not the same for the two cases with different magnitudes of initial imperfection. It is also seen that in case of initial imperfection of lesser magnitude, higher stability loads are obtained than the stability loads for columns with larger initial imperfections as expected. In both cases, the stability load never reaches $4P_y$ due to initial imperfection and torsional-flexural behavior, even with large value of torsional brace stiffness.

SUMMARY AND CONCLUSIONS

A finite element formulation for large-deformation analysis of space frame structures based on second-order geometric nonlinear theory and iterative updated Lagrangian geometry corrections has been used to perform analyses of columns with a mid-height lateral and torsional brace. A flexible connection element included in the program is used to model the lateral and torsional brace of each column. The lateral brace stiffness required in order to provide an effective brace for the column to buckle into the second mode has been evaluated when the column is restricted to pure flexural bending about the weak axis. A parametric study has been performed on a singly symmetric column to show the effect of direction of initial imperfections. The analytical results show that initial imperfections in positive strong direction, i.e., towards the centroid of the section can lead to severe drop in the carrying capacity of the C-section

column. A study has also been carried out in order to determine the effect of initial imperfection on the requirement of torsional stiffness of brace at mid-height of the column. It is observed that the stability load of the column never reaches the flexural stability load of $4P_y$, due to initial imperfections and torsional-flexural behavior, even with very large torsional stiffness of the brace. It must be pointed out that the magnitude of initial imperfections considered in this study is within the allowable tolerances.

REFERENCES

- Blandford, G.E. (1994). Stability Analysis of Flexibly Connected Thin-Walled Space Frames. *Computers & Structures* **39**:5, 609-617.
- Chen, H. (1990). *Nonlinear Space Frame Analysis Including Flexible Connection and Bifurcation Behavior*, Dissertation submitted to the University of Kentucky, Lexington, KY, in partial fulfillment for the degree of Doctor of Philosophy.
- Chen, H. and G.E. Blandford (1991a). Thin-Walled Space Frames. I: Large-Deformation Analysis Theory. *Journal of Structural Engineering*, ASCE **117**:8, 2499-2520.
- Chen, H. and G.E. Blandford (1991b). Thin-Walled Space Frames. II: Algorithmic Details and Applications. *Journal of Structural Engineering*, ASCE, **117**:8, 2521-2539.
- Chen, H. and G.E. Blandford (1995). FE Model for Thin-Walled Space Frame Flexible Connection Behavior. *Journal of Structural Engineering*, ASCE, **121**:10, 1514-1521.
- Gupta, P., S.T. Wang, and G.E. Blandford (1996a). Effect of Bracing Stiffness on Elastic Stability of Cold-Formed Steel Columns. *Proceedings of the Thirteenth International Specialty Conference on Cold-Formed Steel Structures*, October 17-18, 1996, St. Louis, MO.
- Gupta, P. and G. E. Blandford (1996). Space Frame Stability Including Flexible Translational, Bending and Warping Connection Behavior. *Proceedings of the 5th International Colloquium on Stability of Metal Structures (SSRC)*, April 15-18, 1996, Chicago, IL, 279-288.
- Gupta, P., S.T. Wang, and G.E. Blandford (1996b). Effect of Bracing Stiffness on Flexural-Torsional Strength of Columns. *Proceedings of the 5th International Colloquium on Stability of Metal Structures (SSRC)*, April 15-18, 1996, Chicago, IL, 333-342.
- Plaut, R.H. and J.G. Yang (1995). Behavior of Three-Span Braced Columns With Equal or Unequal Spans. *Journal of Structural Engineering*, ASCE, **121**:6, 986-994.
- Plaut, R.H. and J.G. Yang (1993). Lateral Bracing Forces in Columns with Two Unequal Spans. *Journal of Structural Engineering*, ASCE, **119**:10, 2896-2912.
- Timoshenko, S.P. and J.M. Gere (1961). *Theory of Elastic Stability*, McGraw-Hill, New York, 2nd Edition.
- Wang, S.T., H.Y. Pao, and R. Ekambaram (1980). Lateral Bracing of Locally Buckled Columns. *Proc. 5th Int. Specialty Conference of Cold-Formed Steel Structures*. St. Louis, Missouri, 263-274.
- Wang, Y.C. and D.A. Nethercot (1989). Ultimate Strength Analysis of Three-Dimensional Braced I-Beams. *Proceedings of Institution of Civil Engineers, Britain*. Part 2, **87**, 87-112.
- Winter, G. (1960). Lateral Bracing of Columns and Beams. *ASCE Trans.*, **125**, 807-845.

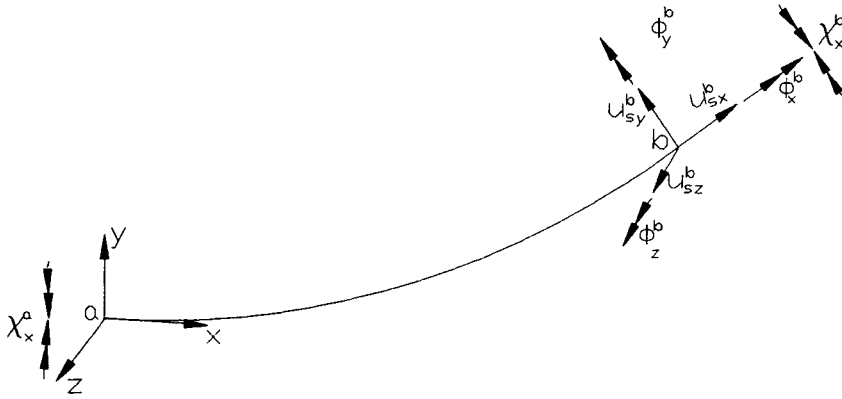


Figure 1: Cantilever Bound Deformation Degrees of Freedom for the Frame Element

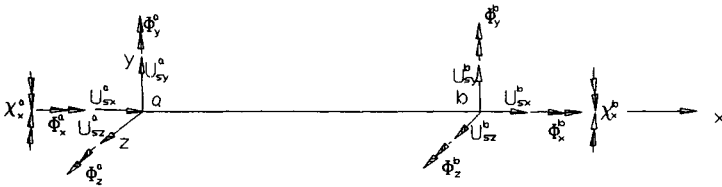


Figure 2: Complete Reference Displacement Degrees of Freedom for the Frame Element

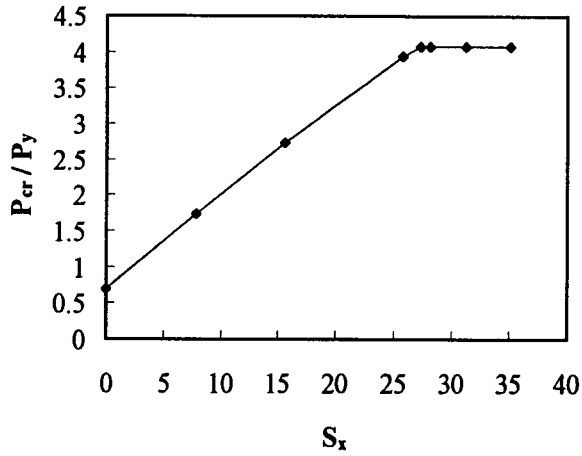


Figure 3: Variation of Buckling Load with Increasing Lateral Brace Stiffness for Two-Dimensional I-Section Column

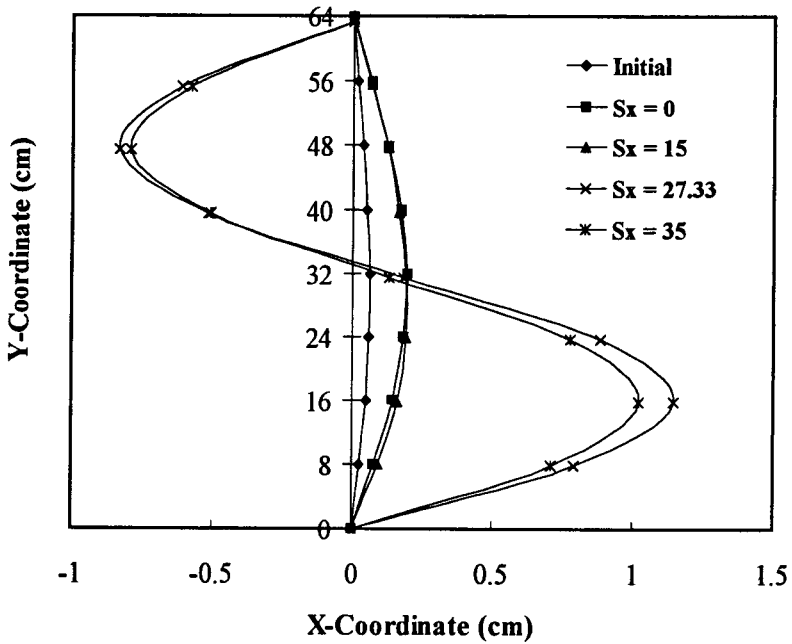


Figure 4: Buckling Modes of Two-Dimensional I-Section Column about the Weak Axis with Various Lateral Brace Stiffness

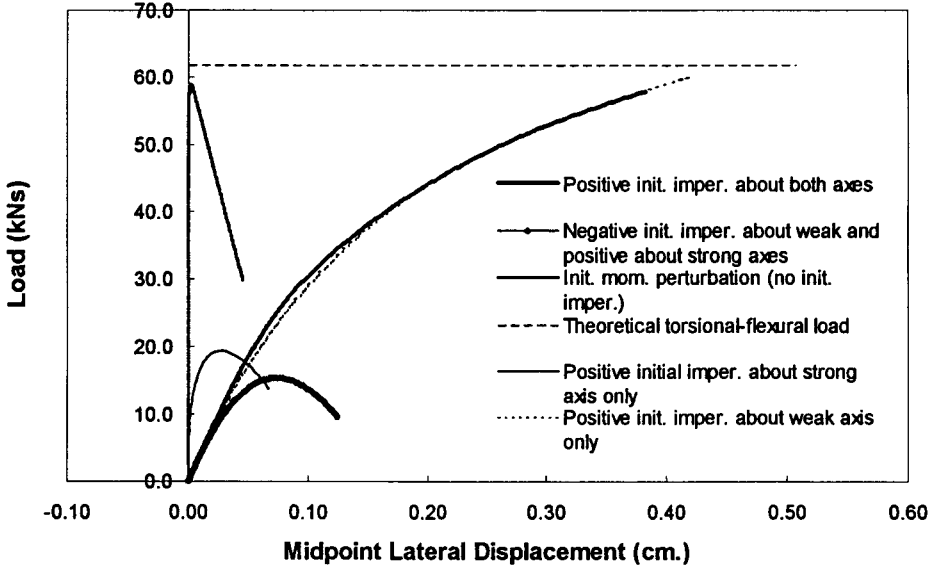


Figure 5: Load-Deflection Curves for Various Initial Imperfections for C-Section Column

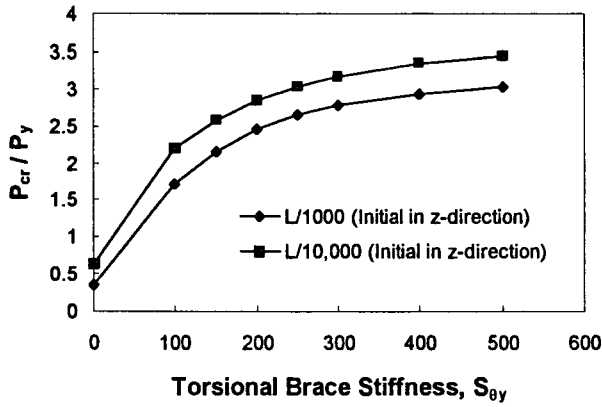


Figure 6: Variation of Buckling Load for Increasing Torsional Brace Stiffness for Three-Dimensional C-Section Column with Full Lateral Brace Stiffness Provided ($S_x = 28$)

Influences of Welding Imperfections on Buckling/Ultimate Strength of Ship Bottom Plating Subjected to Combined Bi-axial Thrust and Lateral Pressure

Tetsuya Yao¹, Masahiko Fujikubo¹, Daisuke Yanagihara¹, Balu Varghese¹ and Osamu Niho²

¹Department of Naval Architecture and Ocean Engineering, Faculty of Engineering, Hiroshima University, 1-4-1, Kagamiyama, Higashi-Hiroshima 739-8527, Japan

²Basic Design Department, Ship & Ocean Project Headquarters, Mitsui Engineering & Shipbuilding Co. Ltd., 1, Yawatakaigan-Dori, Ichihara, Chiba 290-8601, Japan

ABSTRACT

Characteristics of initial imperfections in panels and stiffeners due to welding are discussed based on the measured results. Then the buckling/ultimate strength of ship bottom plating as a stiffened plate subjected to combined bi-axial thrust and lateral pressure is investigated based on the results of new and recent analyses considering the influences of initial deflection and welding residual stresses. It has been concluded that: (1) buckling strength of a local panel between stiffeners is increased owing to the influences of lateral pressure and stiffeners; (2) welding residual stresses reduce both buckling strength and ultimate strength; (3) mode of initial deflection affects the ultimate strength a little, but the capacity in the post-ultimate strength range considerably under the longitudinal thrust.

KEYWORDS

Buckling Strength, Ultimate Strength, Combined Bi-axial Thrust and Lateral Pressure Loads, Initial Deflection, Welding Residual Stresses

INTRODUCTION

A ship structure is constructed by welding, and its structural members are accompanied by welding distortions and residual stresses. These initial imperfections due to welding affect the buckling and ultimate strength of structural members and systems. Because of this, plenty of research works have been performed up to now on buckling/ultimate strength of structural members and systems considering the influences of initial imperfections due to welding.

In the present paper, ship bottom plating as a stiffened plate is considered, which is subjected to combined bi-axial thrust and lateral pressure. At the beginning, initial deflections in panels and

longitudinal stiffeners are measured on an existing ship and the characteristics of initial deflection are discussed. Then, the method how to evaluate the welding residual stresses is presented based on simple empirical formulae in terms of welding heat input or leg length of fillet weld.

After the discussion on initial imperfections, it is shown how the analytical solution of elastic local buckling strength of a stiffened plate is derived considering the influences of longitudinal stiffeners and welding residual stress as well as lateral pressure. The calculated results are compared with those by the FEM eigenvalue analyses, and the accuracy of the analytical solution is examined.

Influence of the shape of initial deflection as well as welding residual stresses on collapse behaviour and ultimate strength of continuous stiffened plating are investigated based on the results of elastoplastic large deflection analyses by the FEM. At the end, the ultimate strength interaction relationships of ship bottom plating subjected to combined bi-axial thrust and lateral pressure are presented and are compared with the buckling strength by design rules.

INITIAL IMPERFECTIONS IN STIFFENED PLATING DUE TO WELDING

In a continuous stiffened plate, initial deflection is produced both in panel and stiffeners due to fillet welding. This is because the stiffener deflects as illustrated in Figure 1 (a) due to the thermal shrinkage of weld metal. At the same time, the panel also deflects of which deflection mode is decomposed into three modes indicated in Figure 1 (b).

The initial deflection in a panel in the vertical direction can be expressed as:

$$w_0 = w_{0P} + w_{0T} + w_{0L} \tag{1}$$

where

$$w_{0P} = \sum_{i=1}^{m_p} \sum_{j=1}^{n_p} A_{ij} \sin \frac{i\pi x}{a} \sin \frac{j\pi y}{b} \tag{2}$$

$$w_{0T} = \sum_{k=1}^{n_s} \left(\frac{x}{a} B_k + \frac{a-x}{a} C_k \right) \sin \frac{k\pi y}{b} \tag{3}$$

$$w_{0L} = \sum_{\ell=1}^{m_s} \left(\frac{y}{b} D_\ell + \frac{b-y}{b} E_\ell \right) \sin \frac{\ell\pi x}{a} \tag{4}$$

The deflections, w_{0P} , w_{0T} and w_{0L} correspond to Modes I, II and III in Figure 1 (b), respectively.

In stiffeners, initial deflection in the vertical direction, w_{0L} , and that in the horizontal direction, v_{0L} , are produced. The horizontal initial deflection can be expressed as:

$$v_{0L} = \frac{z}{h} \sum_{m=1}^{m_h} F_m \sin \frac{m\pi x}{a} \tag{5}$$

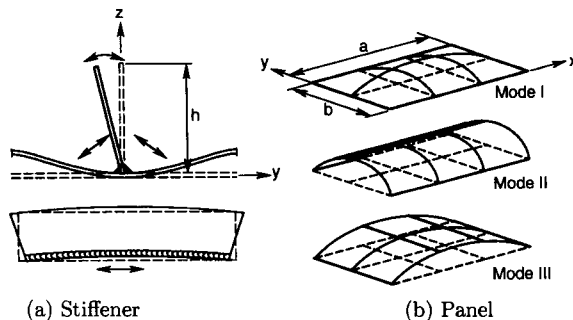


Figure 1: Initial deflection in stiffened plate

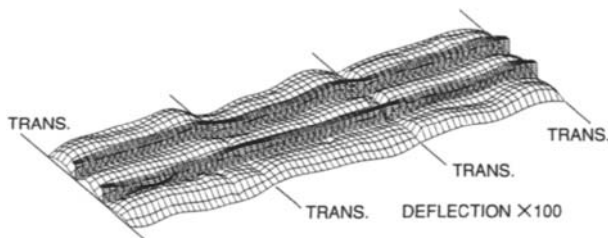


Figure 2: Measured mode of initial deflection in stiffened plate

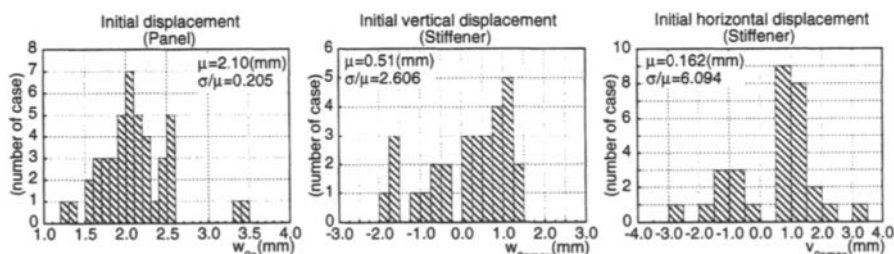


Figure 3: Distribution of maximum initial deflection in stiffened plate

A series of measurements of initial deflection was conducted on inner bottom plates of an existing Handy-sized Bulk Carrier (Ship A in Table 1). On panels bounded by longitudinal stiffeners and floors (transverse girders), initial deflection of $w_{0P} + w_{0T}$ was measured, and on stiffeners both w_{0L} and v_{0L} . For the measurements, electric transducers were used fixed on a rigid frame.

The measurements were carried out on 45 panels and 30 spans. A part of the measured results is illustrated in Figure 2. It is known that initial deflection in a panel is of a hungry horse mode. The distribution of the maximum values of initial deflections are shown in Figures 3 (a), (b) and (c) together with the mean values and the standard deviations.

Applying the Method of Least Squares, the coefficients in Eqns. 2 and 3 are evaluated. Some of the results are plotted in Figure 4. It can be seen that the odd components are larger than the even ones, and that the first component is the largest. These features result in a hungry-horse mode of initial deflection.

The welding residual stresses are produced also by the thermal shrinkage of weld metal. In a continuous stiffened plating with angle-bar or tee-bar stiffeners, the distribution of welding residual stresses can be approximated by a rectangular shape as indicated in Figure 5.

Based on the results of thermal elastoplastic analysis, the breadth where tensile residual stress is produced can be evaluated as (Yao 1985):

$$b_1 = t_w/2 + 0.26\Delta Q_{max}/(2t_p + t_w), \quad h_1 = (t_w/t_p) \times 0.26\Delta Q_{max}/(2t_p + t_w) \quad (6)$$

where t_p (mm) and t_w (mm) are the thicknesses of panel and stiffener web, respectively, and ΔQ_{max} (Cal/cm) is the maximum welding heat input in multi-pass welding, and is given as follows based on the measured results (Matsuoka & Yoshii, 1997):

$$\Delta Q_{max} = 78.8 \times f^2 \quad (7)$$

f (mm) in Eqn. 7 represents the leg length of fillet weld, and is taken as 70% of the web thickness, but not more than 7 mm in ship structures.

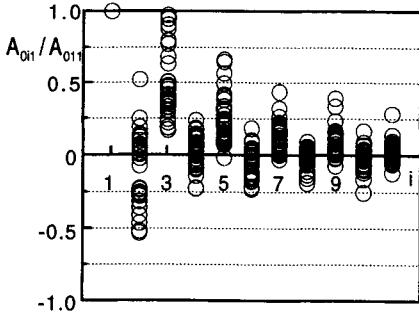


Figure 4: Components of initial deflection

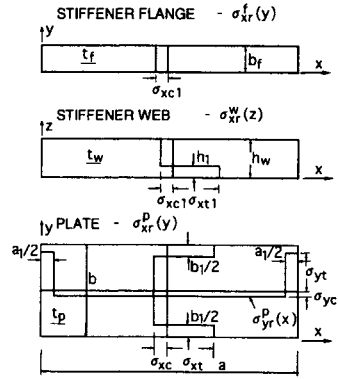


Figure 5: Welding residual stresses

The tensile residual stress is taken equal to the yielding stress of the material. Considering the self-equilibrating conditions of forces in a panel and a stiffener independently, the compressive residual stresses are derived as:

$$\sigma_{xc} = (b_1/b) / \{1 - (b_1/b)\} \cdot \sigma_{YP}, \quad \sigma_{yc} = (a_1/a) / \{1 - (a_1/a)\} \cdot \sigma_{YP} \tag{8}$$

$$\sigma_{xc1} = h_1 t_w / \{(h_w - h_1)t_w + b_f t_f\} \cdot \sigma_{YS} \tag{9}$$

LOCAL BUCKLING STRENGTH OF STIFFENED PLATING

When local buckling takes place in a continuous stiffened plate, the transverse cross-section deforms as illustrated in Figure 6, and the bending/torsional moments are produced along the panel/web and the web/flange intersection lines as indicated in Figure 6. Then, the local buckling mode in the panel can be approximated as:

$$w = W_1 \sin \frac{m\pi x}{a} \sin \frac{\pi y}{b} + \frac{1}{2} W_2 \sin \frac{m\pi x}{a} \left(1 - \cos \frac{2\pi y}{b}\right) \tag{10}$$

and that in a stiffener as:

$$v = V_1 \frac{z}{h_w} \sin \frac{m\pi x}{a} + V_2 \sin \frac{m\pi x}{a} \left(1 - \cos \frac{\pi z}{2h_w}\right) + V_3 \sin \frac{m\pi x}{a} \sin \frac{\pi z}{2h_w} \tag{11}$$

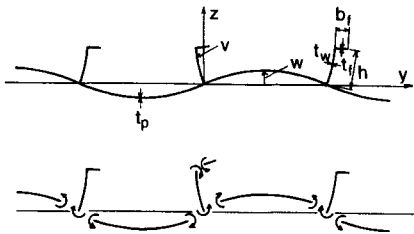


Figure 6: Deformation and sectional bending/torsional moments at transverse cross-section

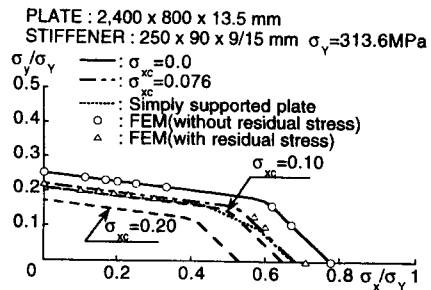


Fig. 7: Local buckling strength of stiffened plate under bi-axial thrust

TABLE 1
DIMENSIONS OF PANELS AND STIFFENERS FOR ANALYSES

Ship	Type	Panel (in mm)	Stiffener (in mm)	σ_Y (MPa)
A	Bulk Carrier	2,400 × 800 × 13.5	250 × 90 × 9/15 (Angle-bar)	313.6
B	Bulk Carrier	2,400 × 780 × 15	250 × 90 × 9/15 (Angle-bar)	313.6
C	VLCC	4,200 × 840 × 19	625 × 14 + 200 × 30 (Tee-bar)	352.8

Here, the following three boundary conditions are considered.

- a) Continuity condition of rotation angle along the panel/web intersection
- b) Equilibrium conditions of moments along the panel/web intersection
- c) Equilibrium condition of moments along the web/flange intersection

Applying the Principle of Minimum Potential Energy, the local buckling strength of a continuous stiffened plate is obtained in the form:

$$\kappa_1 \sigma_{xcr}^2 + \kappa_2 \sigma_{xcr} \sigma_{ycr} + \kappa_3 \sigma_{ycr}^2 - \kappa_4 \sigma_{xcr} - \kappa_5 \sigma_{ycr} + \kappa_6 = 0 \tag{12}$$

The parameters, $\kappa_1 - \kappa_6$ are given by Fujikubo *et al.* (1998).

For the bottom plate of an existing bulk carrier (Ship A in TABLE 1), bi-axial buckling strength is calculated applying Eqn. 12, and the results are plotted in Fig. 7. The dotted line and the solid lines are the buckling strength without and with considering the influence of longitudinal stiffeners. For these two cases, welding residual stresses are not considered. It is known that the buckling strength is increased owing to the influence of stiffeners. The results of FEM analysis for the stiffened plate is plotted by \circ , which shows good agreements with the predicted values.

The dashed lines in Figure 7 are the case with welding residual stresses of different magnitudes. The compressive residual stress, σ_{xc} , in the plate is taken as 10% and 20% of the yielding stress.

On the other hand, the chain line represents the result for the case with residual stresses calculated by Eqns. 8 and 9. For this case, the FEM analysis is also performed, and the results are plotted by \triangle in Figure 7. It is known that the predicted and the calculated values show good agreements each other.

Comparing the dashed and the chain lines, it can be said that the increase in buckling strength owing to the stiffener is compensated by the decrease due to the welding residual stress in this case.

The influence of lateral pressure is also considered for longitudinal thrust and transverse thrust, respectively. The buckling strength under the action of lateral pressure, q , is given as (Fujikubo *et al.* 1998):

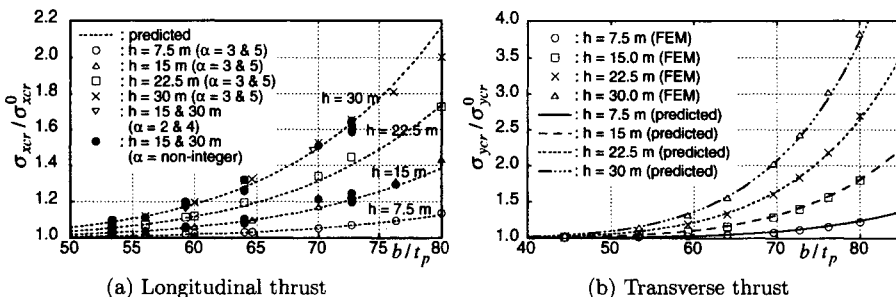


Figure 8: Influence of lateral pressure on buckling strength of continuous plates

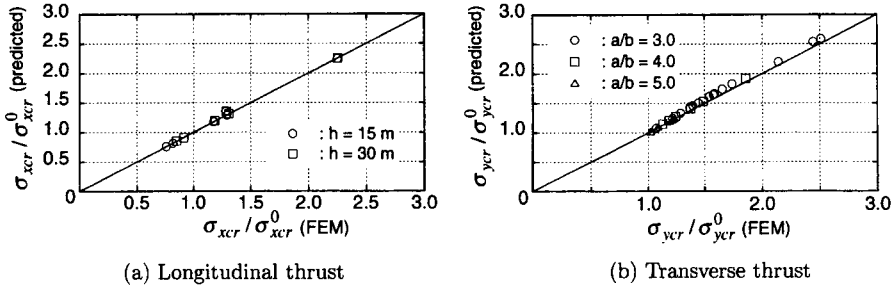


Figure 9: Accuracy of predicted buckling strength of continuous stiffened plate

$$\sigma_{xcr}^p = \{1 + (qb^4/Et_p^4)^{1.6}/576\} \cdot \sigma_{xcr} \quad (\text{for longitudinal thrust; } a/b \geq 2.0) \quad (13)$$

$$\sigma_{ycr}^p = [1 + (qb^4/Et_p^4)^{1.75}/\{160(a/b)^{0.95}\}] \cdot \sigma_{ycr} \quad (\text{for transverse thrust; } a/b \geq 2.0) \quad (14)$$

σ_{xcr} and σ_{ycr} are the buckling strength obtained by Eqn. 12.

The evaluated buckling strength by Eqns. 13 and 14 are compared with those by the FEM analyses in Figures 8 and 9 for the cases of continuous unstiffened and stiffened plates, respectively. It is known that the buckling strength is predicted very accurately by Eqns. 13 and 14.

ULTIMATE STRENGTH OF STIFFENED PLATING

For the bottom plate of an existing Bulk Carrier (Ship B in TABLE 1), elastoplastic large deflection analyses are performed. For this case, uni-axial load is applied in the longitudinal and the transverse directions, respectively. For the longitudinal thrust, triple-bay/triple-span model is used, and for the transverse compression double-span/triple-bay model introducing periodically continuous condition along the boundaries of the model. The floor (transverse girder) is not modelled.

Initial deflection in the panel is represented by Eqn. 1, and that in stiffeners by Eqns. 3 and 4. Only the first term is considered as for the deflection components in the transverse direction. The measured coefficients of initial deflection are used for panels. Regarding the stiffeners, four cases are considered changing the magnitude and mode of initial deflection as shown in Figure 10.

Regarding the welding residual stresses, two cases are considered with and without them. The welding residual stresses both in the longitudinal and the transverse directions are given of which magnitude is calculated by Eqns. 8 and 9.

The average stress-average strain relationships under longitudinal and transverse thrust are plotted in Figure 11. When the stiffened plate is subjected to longitudinal thrust, the ultimate strength is almost the same regardless of the mode of vertical initial deflection in stiffeners, but the capacity



Figure 10: Assumed modes of initial deflection in stiffeners

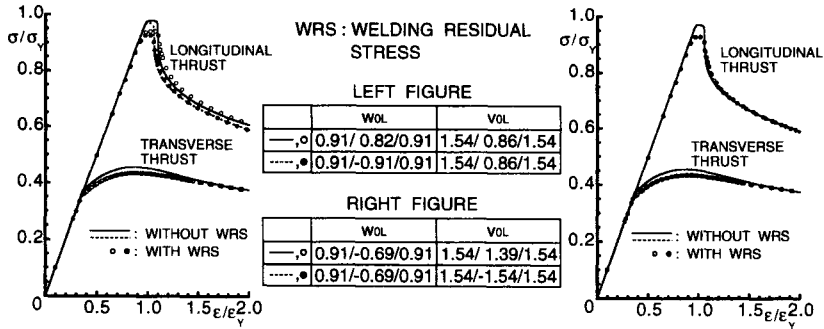


Figure 11: Influences of initial imperfections on collapse behaviour of stiffened plate

after the ultimate strength is affected under the longitudinal thrust. It is known that the capacity is lower when the initial deflection is in a buckling mode (unsymmetrical mode).

The welding residual stresses reduce the ultimate strength. The reduction is more significant under the longitudinal thrust, because the welding residual stress in the longitudinal direction is higher than that in the transverse direction.

The ultimate strength interaction relationships for bottom plating of Bulk Carrier and VLCC (Ships A and C in TABLE 1) are shown by dashed lines in Figures 12 (a) and (b), respectively (Yao *et al.* 1997). In these cases, the welding residual stresses are not considered, but the lateral pressure is varied as indicated in the figure.

Owing to the lateral pressure, the elastic buckling strength increases, but the yielding starts earlier because of the bending deformation produced by lateral pressure. So, lateral pressure has opposite effects on the ultimate strength. This is the reason why the ultimate strength with lateral pressure in case of Bulk Carrier is in some cases higher than that without lateral pressure in certain ranges of the bi-axial stress ratio.

The buckling strength interaction relationships calculated by the rule formulae of the Classification Societies are also plotted in Figure 12. The chain line with a dot represents the relationship by DNV (1995), the broken line by LRS (1978) and the solid line by ABS (1996).

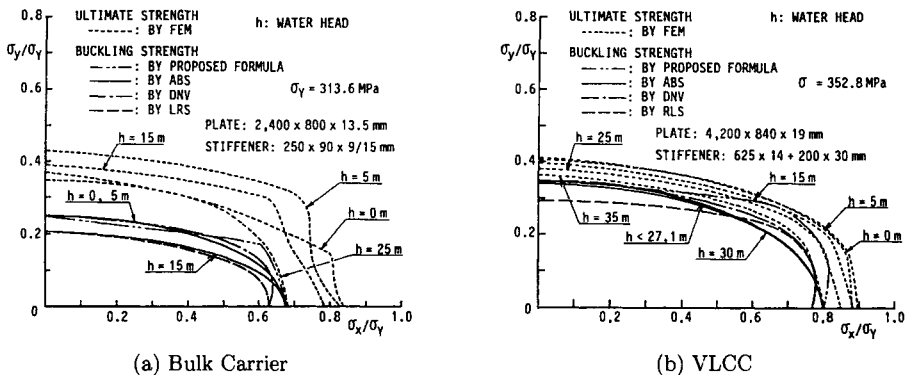


Figure 12: Comparison between actual ultimate strength and buckling strength specified by rules

The buckling strength by LRS rule is derived assuming that the plate is simply supported. In DNV rule, the buckling strength under transverse thrust is increased introducing the magnification factor of $c = 1.21$. This may be the result that the constraint by longitudinal stiffeners is considered. In the ABS rule, the buckling strength under longitudinal thrust is also increased. The magnification factors for the longitudinal and transverse thrust are taken as $C_1 = 1.1$ and $C_2 = 1.2$, respectively. In addition to this, in the ABS rule, the influence of lateral pressure is also considered.

The buckling strength interaction relationships by Eqn. 12 are also plotted in Figure 12 by chain lines with two dots performing Johnson's plasticity correction when it is necessary. Influence of lateral pressure is not considered. It is known from Figure 12 that the buckling strength by the rule formulae is on a safe side in most cases.

The ultimate strength is higher than any of the buckling strength by rule formulae even when the highest lateral pressure is acting. However, as is known from the case of VLCC, the elastoplastic buckling strength simply calculated by the Johnson's plasticity correction gives unsafe assessment of compressive strength when lateral pressure becomes large even if the elastic buckling strength is accurately calculated. However, the rationality of such elastoplastic buckling strength with simple correction should be examined.

CONCLUSIONS

In the present paper, the characteristics of initial deflection are discussed based on the measured results, and simple formulae are presented to calculate the welding residual stresses. Then, derivation of very accurate formulae are presented to evaluate elastic bi-axial buckling strength considering the influences of stiffener, welding residual stresses and lateral pressure. At the end, the ultimate strength of ship bottom plating as a continuous stiffened plate is discussed considering the influences of initial deflections and welding residual stresses.

It has been found that:

- (1) Elastic local buckling strength of a continuous stiffened plate is increased owing to the influences of lateral pressure and stiffeners.
- (2) Welding residual stresses reduce both buckling strength and ultimate strength.
- (3) Mode of initial deflection in stiffeners slightly affects the ultimate strength, but considerably affects the capacity in the post-ultimate strength range under the longitudinal thrust.

References

- American Bureau of Shipping (1996). Rules for Building and Classing Steel Vessels, Pt.5, Sec.2, 46.
- Det Norske Veritas (1995). Rules for Classification of Ships, Pt.3, Ch.1, Sec.14, 104.
- Fujikubo, M, Yao, T, Varghese, B, Zha, Y, and Yamamura, K (1998). "Elastic Local Buckling Strength of Stiffened Plates Considering Plate/Stiffener Interaction and Lateral Pressure," *Proc. 8th Int. Offshore and Polar Engineering Conference*, (to be presented).
- Lloyd's Register of Shipping (1978). Direct Calculation Procedural Document, Ch.4.
- Matsuoka, K, and Yoshii, T (1997). "Weld Residual Stress in Corner Boxing Joints," *J Soc. Naval Arch. Japan*, **180**, 753-761 (in Japanese).
- Yao, T, Niho, O, Fujikubo, M, Varghese, V, and Mizutani, K (1997). "Buckling/Ultimate Strength of Ship Bottom Plating," *Proc. Int. Conf. Advances in Marine Structures*, 2.
- Yao, T (1980). Compressive Ultimate Strength of Ship Structural Members, *Doctoral Thesis*, Osaka University.

POST-ULTIMATE BEHAVIOUR OF STIFFENED PANELS SUBJECTED TO AXIAL COMPRESSION

S.-R. Cho, B.-W. Choi, and I.-C. Song

Division of Naval Architecture and Ocean Engineering
School of Transportation Systems Engineering, University of Ulsan
Nam-Ulsan P.O. Box 18, Ulsan, Korea

ABSTRACT

Experimental and theoretical study on the ultimate and post-ultimate behaviour of stiffened panels is reported herein. Test results of stiffened panels which undergo far beyond their ultimate state show the interaction of the column buckling of the stiffener together with associated plate and the torsional buckling(tripping) of the stiffener. A robust design formulation is proposed to predict the ultimate strength of multi-bay stiffened plates under combined axial compression, lateral pressure and end bending moment. A simple equation is also derived to represent the average strain and stress relation of stiffened plates up to far beyond the ultimate state.

KEYWORDS

Stiffened Panel, Axial Compression, Column Buckling, Torsional-Lateral Buckling, Experiment, Design Formulation, Ultimate Strength, Ultimate Strain, Post-Ultimate State

INTRODUCTION

Stiffened panels are extensively adopted as major structural elements of various onshore and offshore structures and many kinds of their strength formulations have been proposed and some of them are adopted in design codes. Code recommendations for offshore structures were reviewed by Ellinas et al.(1984) and those for onshore structures were by Brosowski and Ghavami(1996). In any of the strength formulation reviewed by them the torsional buckling of stiffeners and overall buckling of stiffened plates are not treated explicitly, which are necessary for optimum design. However, in DNV classification notes(1992) the torsional buckling is considered for the stiffeners whose web slenderness ratios cannot satisfy the limit values.

For redundant structural systems composed of stiffened plates like the ship's hull girder or bridge's box girder, some of local elements may show post-ultimate behaviour before reaching the ultimate state of the whole systems. However, most of the theoretical and experimental investigations on stiffened panels reported in the open literature so far are mainly concerning the responses up to their ultimate states.

In this paper the results of axial compression tests are reported on thirteen stiffened panels which underwent far beyond their ultimate state and showed the interaction of the column buckling of the stiffener together with associated plate and the torsional buckling(tripping) of the stiffener. A robust strength formulation is proposed to predict the ultimate strength of stiffened plates under combined axial compression, lateral pressure and end bending moment. In the formulation all kinds of buckling modes are retained including column buckling of stiffener and plate, torsional buckling of stiffener and overall buckling of stiffened plates. A simple equation is derived for the average strain-stress relation of stiffened plates, by which their post-ultimate behaviour can also be traced.

AXIAL COMPRESSION TESTS

Axial compression tests were performed on thirteen single-bay stiffened plates. The main purpose of the tests is to provide the experimental informations beyond ultimate state. All the models were fully welded by CO₂ gas welder and the end boundary conditions were expected to be of simply supported. The geometries, material properties, initial shape imperfections and eccentricity of applied load are summarised

in Table 1. The length and stiffener spacing of all the models were 600mm and 100mm respectively. The initial shape imperfections in the table are those of maximum values and the material properties are those of the average values of five tensile testing coupons from each parent sheet. The values of Young's modulus are a bit high than the range of the standard mild steel, say 205000 N/mm² - 210000 N/mm². The eccentricity of applied load was measured from the outer surface of plating.

TABLE 1
GEOMETRY AND MATERIAL PROPERTIES OF TEST MODELS

Model	Dimension				Initial imperfection			σ_y <E> (N/mm ²)	e (mm)
	B (mm)	t (mm)	Stiffener size (mm)	No. of Stiff	Plate (ω_o/b)	Stiffener			
						Trans (w_o/l)	Lateral (w_l/l)		
S3-F-A1(1)	400	2.13	50x2.13 F.B	3	-0.0085	-0.00158	-0.00158	332.4 <248000>	13.05
S3-F-A1(2)	400	2.13	50x2.13 F.B	3	0.0056	0.00225	-0.00342	332.4 <248000>	13.26
S3-F-A2	300	2.13	50x2.13 F.B	3	-0.0065	0.00167	-0.00308	332.4 <248000>	12.51
S3-F-A3	250	2.13	50x2.13 F.B	3	-0.0060	-0.00092	-0.00225	332.4 <248000>	12.81
S5-F-A1	600	2.13	50x2.13 F.B	5	-0.0050	0.00333	-0.00208	332.4 <248000>	13.22
S5-F-A2	500	2.13	50x2.13 F.B	5	-0.0040	-0.00208	-0.00308	332.4 <248000>	13.72
S5-F-A3	450	2.13	50x2.13 F.B	5	-0.0060	-0.00208	-0.00475	332.4 <248000>	12.55
S3-I-A1	400	2.13	40x15x2.13 I.A	3	-0.0040	0.00125	-0.00125	329.7 <235000>	12.75
S3-I-A2(1)	300	2.13	40x15x2.13 I.A	3	-0.0055	0.00042	-0.00292	329.7 <235000>	12.52
S3-I-A3	250	2.13	40x15x2.13 I.A	3	-0.0045	-0.00083	-0.00217	329.7 <235000>	12.69
S5-I-A1	600	2.13	40x15x2.13 I.A	5	-0.0055	-0.00250	0.00300	329.7 <235000>	12.49
S5-I-A2	500	2.13	40x15x2.13 I.A	5	-0.0065	0.00125	0.00333	329.7 <235000>	12.48
S5-I-A3	450	2.13	40x15x2.13 I.A	5	0.0080	-0.00125	-0.00208	329.7 <235000>	12.41

Notes :

- B is the overall breadth , - b is the stiffener spacing(100mm),
- l is the model length(600mm), - e is the load eccentricity measured from the plate.
- the initial lateral imperfection of plate and stiffener ;
- (+) toward plate, (-) toward stiffener,
- the initial transverse imperfection of stiffener ; (+) toward left, (-) toward right.

TABLE 2
TEST RESULTS

Model	Parameters			Max. Load (tons)	σ_u (N/mm ²)	$\frac{\sigma_u}{\sigma_y}$		
	β	λ_c	λ_t			test	pred.	Xm
S3-F-A1(1)	1.72	0.53	0.91	17.5	155.6	0.468	0.641	0.73
S3-F-A1(2)	1.72	0.53	0.91	20.2	180.0	0.542	0.571	0.95
S3-F-A2	1.72	0.53	0.91	18.7	203.6	0.613	0.573	1.07
S3-F-A3	1.72	0.53	0.91	20.0	245.5	0.739	0.528	1.40
S5-F-A1	1.72	0.53	0.91	26.4	152.2	0.458	0.573	0.80
S5-F-A2	1.72	0.53	0.91	24.3	158.6	0.477	0.575	0.83
S5-F-A3	1.72	0.53	0.91	32.3	136.8	0.681	0.625	1.09
S3-I-A1	1.76	0.53	0.33	25.2	218.2	0.662	0.736	0.90
S3-I-A2	1.76	0.53	0.33	24.6	224.5	0.786	0.721	1.09
S3-I-A3	1.76	0.53	0.33	23.5	277.5	0.842	0.752	1.12
S5-I-A1	1.76	0.53	0.33	41.7	233.5	0.708	0.753	0.94
S5-I-A2	1.76	0.53	0.33	35.4	224.0	0.679	0.754	0.90
S5-I-A3	1.76	0.53	0.33	33.8	228.4	0.693	0.762	0.91

- Notes : - the predicted ultimate strengths were obtained using eqn (1)
- Xm is the ratio of actual to predicted ultimate strength

The results of the axial compression tests are given in Table 2 together with slenderness parameters, β , λ_c and λ_t whose definitions are given as follows :

β is the plate slenderness, $(b/t)\sqrt{\sigma_y/E}$

λ_c is the slenderness of the stiffener for column buckling, $\sqrt{\sigma_y/\sigma_{ec}}$

λ_t is the slenderness of the stiffener for torsional buckling, $\sqrt{\sigma_y/\sigma_{et}}$

where

σ_{ec} is the Euler column buckling stress of stiffener including the associate plating

σ_{et} is the elastic torsional buckling stress of stiffener, $\frac{1}{I_o}(GJ + \frac{4\pi^2}{L^2}EC_w)$

The ratios of actual to predicted strengths are also provided in the table. The predicted strengths were obtained using the proposed formulation, eqn (1). The mean and COV of the ratios are 0.978 and 17.9% respectively. This will be discussed later. The photographs of collapsed models, models S3-I-A3 and S5-I-A2, are presented in Fig. 1, which are showing that model S3-I-A3 was failed by plate buckling but model S5-I-A2 was failed by the coupling mode of column and torsional bucklings.

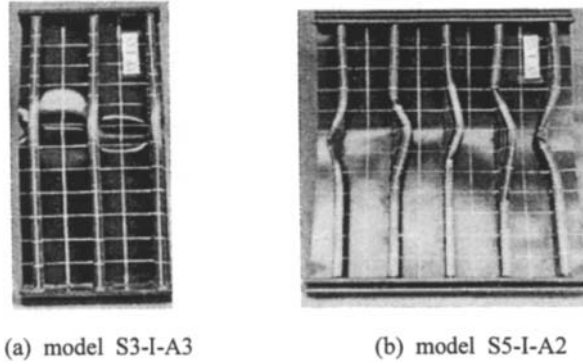


Figure 1: Collapsed models after axial compression test

ULTIMATE STRENGTH FORMULATION

For the prediction of the ultimate strength of multi-bay stiffened plates under combined axial compression, lateral pressure and end bending moment, a robust formulation, eqn (1), has been derived. In the derivation the generalised Merchant-Rankine formula was adopted as its basis in hoping to consider all possible failure modes and their interactions. The knock-down factors in the equation were obtained from the regression analysis of test results. Test data of forty-five multi-bay stiffened plates were utilised in the regression analysis. The detail procedures to derived this design equation can be found else where(Cho et al. 1998).

$$\left(\frac{\sigma_{xao}}{\rho_c \sigma_{ec}} + \frac{\sigma_{xao} + \sigma_{xbs}}{\rho_t \sigma_{et}} + \frac{\sigma_{xao}}{\rho_{oa} \sigma_{eoa}} \right)^2 + \left(\frac{\sigma_{xa} + \sigma_{xb}}{\sigma_Y} \right)^2 = 1 \tag{1}$$

where

σ_{xa} is applied axial compression stress

σ_{xbs} is bending stress at stiffener flange due to M_{eq}

$\sigma_{xao} = \sigma_{xa}$ for $\sigma_{xa} < 0$, = 0 for $\sigma_{xa} > 0$

$\sigma_{xbs} = \sigma_{xbs}$ for $\sigma_{xbs} < 0$, = 0 for $\sigma_{xbs} > 0$

$\sigma_{xb} = \sigma_Y \times \frac{M_{eq}}{M_P}$, equivalent bending stress due to end bending moment and lateral pressure

$$M_{eq} = M_e + \frac{\rho b l^2}{16}$$

$$\sigma_{e\max} = \frac{n^2 \pi^2 D_y}{a_x B^2} \left[\frac{D_x B^2}{D_y L^2} + \frac{2m^2 D_{xy}}{n^2 D_y} + \frac{m^4 L^2}{n^4 B^2} \right] \quad , \text{ overall grillage buckling stress}$$

$$\rho_c = 2.49 \beta^{-0.7} \lambda_c^{1.2} \lambda_t^{0.1} \quad , \text{ knock-down factor for column buckling}$$

$$\rho_t = 2.69 \beta^{-0.3} \lambda_c^{0.8} \lambda_t^{1.1} \quad , \text{ knock-down factor for torsional buckling of stiffener}$$

$$\rho_{\alpha} = 1.0 \quad , \text{ knock-down factor for overall grillage buckling}$$

POST-ULTIMATE BEHAVIOUR

As mentioned earlier the predictions of the post-ultimate behaviour of stiffened plates are necessary for the ultimate strength analysis of redundant structures. An attempt has been made herein to provide an approximation of the average strain - average stress relation for stiffened plates. The relation is assumed to be linear until the average stress is less than or equals to two third of the ultimate value and to be sinusoidal shape up to the ultimate value. In the post-ultimate regime a plastic hinge is assumed to be formed at the mid-length of the stiffener. This relation can be expressed as follows:

$$\frac{\sigma}{\sigma_Y} = \frac{\epsilon}{\epsilon_Y} \quad \text{for} \quad \frac{\epsilon}{\epsilon_Y} \leq \frac{\epsilon_1}{\epsilon_Y} \quad (2a)$$

$$\frac{\sigma}{\sigma_Y} = \frac{1}{3} \frac{\sigma_u}{\sigma_Y} \left[2 + \sin \left(\frac{\pi}{2} \frac{\epsilon/\epsilon_Y - \epsilon_1/\epsilon_Y}{\epsilon_u/\epsilon_Y - \epsilon_1/\epsilon_Y} \right) \right] \quad \text{for} \quad \frac{\epsilon_1}{\epsilon_Y} < \frac{\epsilon}{\epsilon_Y} \leq \frac{\epsilon_u}{\epsilon_Y} \quad (2b)$$

$$\frac{\sigma}{\sigma_Y} = \frac{\sigma_u}{\sigma_Y} \frac{\sqrt{\epsilon_u/\epsilon_Y (2/\epsilon_Y - \epsilon_u/\epsilon_Y)} + 2 \delta_i/\epsilon_Y}{\sqrt{\epsilon/\epsilon_Y (2/\epsilon_Y - \epsilon/\epsilon_Y)} + 2 \delta_i/\epsilon_Y} \quad \text{for} \quad \frac{\epsilon}{\epsilon_Y} > \frac{\epsilon_u}{\epsilon_Y} \quad (2c)$$

where

$$\frac{\epsilon_1}{\epsilon_Y} = \frac{2}{3} \frac{\sigma_u}{\sigma_Y}$$

$$\frac{\epsilon_u}{\epsilon_Y} = 0.12 \lambda_c^{-2.2} \lambda_t^{-0.4} \beta^{0.5} \left(\frac{\sigma_u}{\sigma_Y} \right)^{-1.3} + 0.43$$

δ_i is the non-dimensionalised initial lateral imperfection of the stiffener

DISCUSSION

The ultimate strength formulation for multi-bay stiffened plates proposed in this paper has been substantiated using the forty-five multi-bay stiffened plates test data. The results are summarised in Table 3. As can be seen in the table the mean and COV of X_m are 1.000 and 13.7% respectively. The COV of X_m is a bit larger than those

of other good formulations for single reference loadings, say 13%. But considering the complexity of loadings and variety of failure modes of multi-bay stiffened plates the proposed formulation seems to be of sufficient accuracy. As can be seen in eqn (1) only the torsional buckling is considered as the local failure of the stiffener. It seems necessary to include the lateral buckling of the stiffener in the formulation in order to improve the accuracy of its prediction.

TABLE 3
ACCURACY OF THE PROPOSED FORMULATION

Loading type	No. of test data	Range of Parameters			X_m	
		β	λ_c	λ_t	Mean	COV
Axial Comp.	41	0.53~3.67	0.06~1.89	0.11~1.09	0.990	14.0%
A. C. + L. P.	4	1.42~2.74	0.24~0.72	0.27~0.54	1.105	6.2%
Total	45	0.53~3.67	0.06~1.89	0.11~1.09	1.000	13.7%

For the thirteen single-bay test models reported in this paper the predicted ultimate strengths using the proposed formulation are given in Table 2 . The COV of the predictions is 17.9%. Cho et al.(1998) discussed the effects of boundary conditions on the ultimate strength of stiffened plates. It was concluded that the boundary conditions for a single panel of multi-bay stiffened plates are different from those of isolated panels with either simply supports or fixed ends. This conclusion is supported by the numerical investigation of Smith(1975). Therefore, the uncertainty of the results of single-bay model tests cannot be properly identified using any strength formulations for multi-bay stiffened plates.

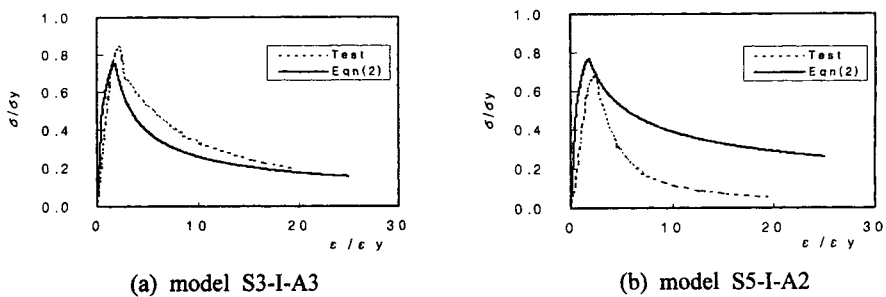


Figure 3: Comparison of the predicted average strain-stress relation for stiffened plates with test results

The proposed average strain - average stress relation, eqns(5a-5c), has been compared with those of the test results of models S3-I-A3 and S5-I-A2. In Fig. 3 the relations are visualised. For model S3-I-A3, which failed by the plate buckling, the two curves show reasonable agreement. But the curves for model S5-I-A2, which failed by the coupling modes of column and torsional buckling of the stiffeners, show a big deviation. It seems likely that the further developments of torsional deformation of the stiffeners can be attributable to that. Therefore, to improve the predictions the further stiffener deformation in the post-ultimate regime is necessary to be considered.

CONCLUSIONS

The results of thirteen axial compression tests on single-bay models have been reported herein, which were compressed up to far beyond their ultimate states. A robust ultimate strength formulation for multi-bay stiffened plates has been proposed. Equations to trace the average strain - average stress for stiffened plates have been derived, which can be utilised in the ultimate strength analysis of redundant structures composed of stiffened plates. In order to improve the predictions of ultimate strengths and post-ultimate behaviors the inclusion of lateral buckling of stiffeners and consideration of further stiffener deformations in post-ultimate regime seems necessary respectively.

REFERENCES

- Brosowski, B. and Ghavami, K. (1996). Multi-criteria optimal design of stiffened plates. Part 1. choice of the formula for the buckling load. *Thin-Walled Structures* **24**, 353-369.
- Cho, S-R, Choi, B-W and Frieze, P.A. (1998). Ultimate strength formulation for ship's grillages under combined loadings. to be presented at PRADS'98, Hague, Netherlands.
- Det Norske Veritas (1992). Buckling Strength Analysis, Classification Notes, No. 30.1, Hovik, Norway.
- Ellinas, C.P., Supple, W.J. and Walker, A.C. (1984). *Buckling of Offshore Structures*, Granada, London, U.K.
- Smith C.S. (1975). Compressive strength of welded steel grillages. *Trans. RINA* **117**, 325-359.

STRENGTH AND DUCTILITY OF STEEL STIFFENED PLATES UNDER CYCLIC LOADING

H. B. GE, T. Usami and T. Watanabe

Department of Civil Engineering, Nagoya University, Nagoya 464-8603, JAPAN

ABSTRACT

In this paper, numerical results of ductility of steel stiffened plates subjected to cyclic loading are presented. The width-thickness ratio parameter, aspect ratio and stiffener's slenderness ratio parameter are taken to be main parameters of the plates. To account for material nonlinearity, a modified two-surface model is employed to trace accurately the inelastic cyclic behavior of steel. In the analysis, two kinds of cyclic loading sequences are considered. For a comparison, monotonic analysis of the stiffened plate is also carried out. As a result, a modification factor considering the effect of aspect ratio is introduced to the previously proposed ductility formula for stiffened plates.

KEYWORDS

Cyclic loading, Ductility, Elasto-plastic analysis, Local buckling, Stiffened plate, Strength.

INTRODUCTION

Ductility of steel plated structures with thin-walled sections is controlled mainly by local buckling of its cross-section or component plates. Therefore, the deformation capacity of the section or component plate can be adopted for the definition of ultimate state in the analysis of such structures.

In the past, a great number of researches related to stiffened plates are available, but most of them were aimed at studying the ultimate strength under monotonic loading condition. Furthermore, little research on the quantitative evaluation of ductility of such plates under either monotonic loading or cyclic loading has been reported so far. In a previous paper (Usami et al., 1995), a ductility formula was proposed for stiffened plates, but it was obtained from a pure compression analysis of monotonic loading and the scope of parameters such as width-thickness ratio and aspect ratio are not sufficiently wide for practical use. For this reason, strength and ductility of steel stiffened plates subjected to cyclic loading are numerically investigated in this study. The plates with small width-thickness ratios, where local buckling does not occur or develop significantly before the occurrence of strain hardening, are accentuated. Besides the width-thickness ratio parameter, other two main parameters considered are aspect ratio and stiffener's slenderness ratio parameter. In order to trace accurately the inelastic cyclic behavior of steel, a modified two-surface model is employed to account for material nonlinearity. In the analysis, two kinds of

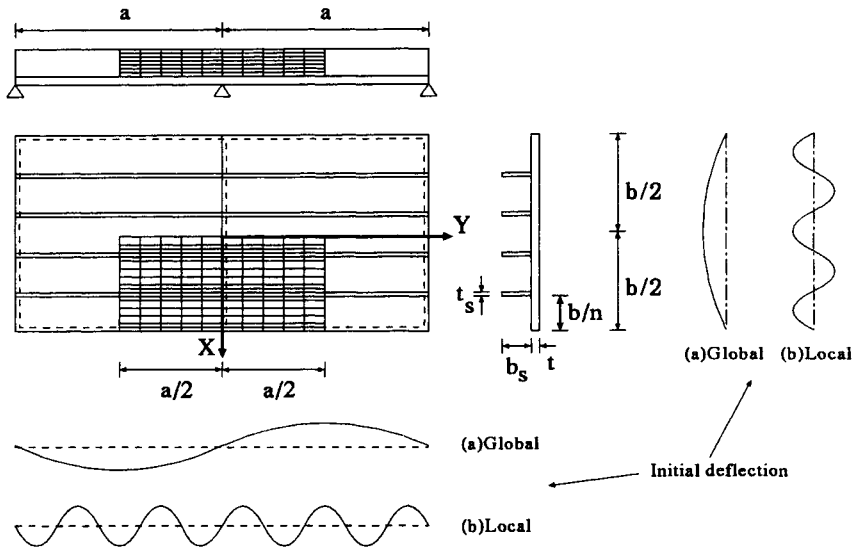


Figure 1: Analytical model

cyclic loading sequences are considered. For a comparison, monotonic analysis of the stiffened plate is also carried out. As a result, a modification factor considering the effect of aspect ratio is introduced to the previously proposed ductility formula for stiffened plates.

NUMERICAL METHOD

A continuous stiffened plate model is shown in Figure 1. It has been pointed out in a literature (*Guideline*, 1987) that ultimate strength of such a multi-stiffener plate can be obtained with good accuracy from the analysis of a T-shaped sectional column composed of one stiffener and its adjacent subpanels. However, post-buckling behavior predicted by the two models is not clear. For this reason, the global model is adopted here. Figure 1 shows a simply supported plate with four longitudinal stiffeners. The distance between two diaphragms (or adjacent transverse stiffeners with sufficient rigidity) is a , and b is the width of plate. Owing to the symmetry of both geometry and loading, a quarter of the plate is analyzed. This plate is divided into 16 segments along y direction, and 15 segments along x direction. The mesh division of stiffeners along y direction is just the same as that of the panel, and along the width direction, it is divided into 7 segments. Simply supported boundary condition is assumed in the position where a diaphragm exists. Shell element S4R included in the ABAQUS software (1995) is employed in this analysis. Five integration points are assumed along the plate thickness. A two-surface model (2SM) recently developed at Nagoya University (Shen et al., 1995) is adopted to model material nonlinearity. The accuracy of the 2SM has been verified by the experimental data, and its validity in predicting the cyclic behavior of steel structures has been established in previous researches (e.g., Gao et al., 1998). The following initial deflection equations including both the global and local distortions of the stiffened plate are assumed (see Figure 1):

$$\delta = \delta_G + \delta_L \tag{1}$$

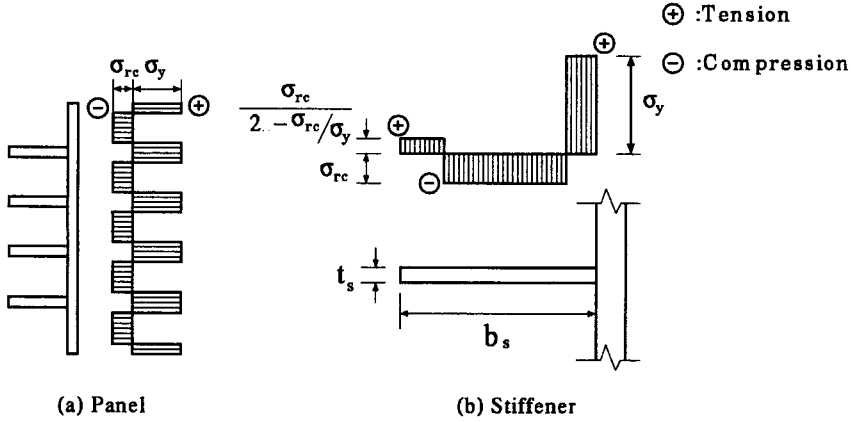


Figure 2: Residual stresses

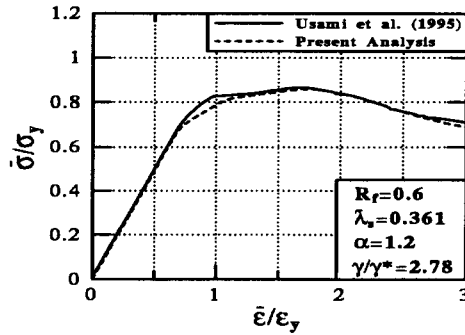


Figure 3: Comparison with existing numerical results

$$\delta_G = a/1000 \cdot \sin\left(\frac{\pi}{a}y\right) \cdot \cos\left(\frac{\pi}{b}x\right) \tag{2}$$

$$\delta_L = b/150 \cdot \sin\left(5\frac{\pi}{a}y\right) \cdot \cos\left(\frac{\pi}{b/n}x\right) \tag{3}$$

where n = number of subpanels.

In this analysis, an idealized pattern of residual stresses due to welding is employed, as shown in Figure 2. The maximum residual stress is assumed to be σ_y in tension side and $0.3\sigma_y$ in compression side.

COMPARISON WITH EXISTING NUMERICAL RESULTS

To verify the validity of the present analytical model, a compressed stiffened plate analyzed by Usami et al. (1995) is re-analyzed. The geometrical parameters of this plate are: $R_f = 0.60$, $\lambda_w = 0.361$; $\alpha = a/b = 1.2$; and $\gamma/\gamma^* = 2.78$. Here, R_f denotes the width-thickness ratio parameter, and it is defined as follows:

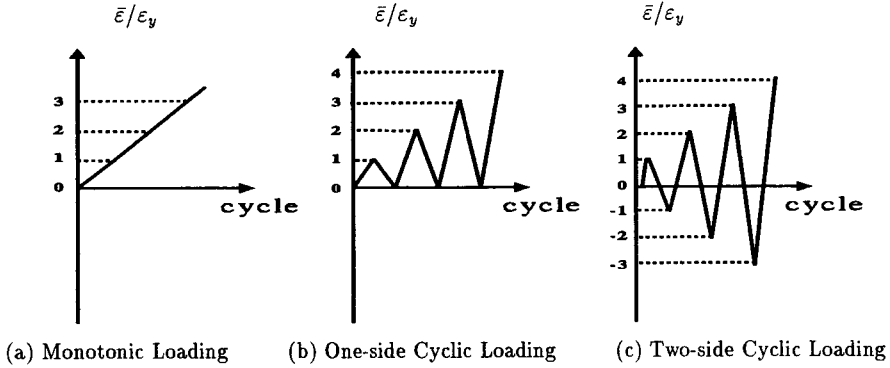


Figure 4: Loading pattern

$$R_f = \frac{b}{nt} \sqrt{\frac{12(1-\nu^2)}{4\pi}} \sqrt{\frac{\sigma_y}{E}} \tag{4}$$

$\bar{\lambda}_s$ is the stiffener’s equivalent slenderness ratio parameter defined by

$$\bar{\lambda}_s = \frac{1}{\sqrt{Q}} \frac{a}{r_s} \frac{1}{\pi} \sqrt{\frac{\sigma_y}{E}} \tag{5}$$

where

$$Q = \frac{1}{2R_f} [\beta - \sqrt{\beta^2 - 4 R_f}] \tag{6}$$

$$\beta = 1.33R_f + 0.868 \tag{7}$$

in which σ_y = yield stress; E = Young’s modulus; ν = Poisson’s ratio; t = plate thickness; r_s = radius of gyration of the T-shape cross section which consists of one longitudinal stiffener and the adjacent subpanels. Moreover, γ = relative flexural rigidity of stiffener, γ^* = optimum value of γ obtained from linear buckling theory (*DIN4114*, 1953). The plate is made of JIS steel grade SS400 with $\sigma_y = 235$ MPa, $E = 206$ GPa, $\varepsilon_{st} = 10\varepsilon_y$, and $E_{st} = E/40$. With respect to model parameters of the 2SM, detailed descriptions can be found in the literature (Shen et al., 1995).

Comparison of the current analytical result with the result by Usami et al. (1995) is illustrated in Figure 3. It is observed that the two curves coincide well at both the peak and postbuckling stages, which indicates that the present model is quite convincing.

PARAMETRIC STUDY

To propose a failure strain equation of stiffened plates under cyclic loading, a extensive parametric study is carried out. The main parameters considered are R_f , α , and $\bar{\lambda}_s$. The geometrical parameters are listed in Table 1. Specimen designations starting with a “SP” refer to stiffened plates. In each specimen, three ordered numerals are related to values of $\bar{\lambda}_s$, α , and R_f , respectively. In the table, b_s and t_s are the width and thickness of stiffener, respectively. The material used is JIS steel grade SS400 with the same properties as given previously.

To investigate the effect of loading history on the peak load and postbuckling behavior, three loading patterns are employed, as shown in Figure 4. Figure 4(a) shows the monotonic loading

TABLE 1
GEOMETRICAL PARAMETERS OF STIFFENED PLATES

Specimen	λ_s	α	R_f	γ/γ^*	b (mm)	b/n (mm)	t (mm)	b_s (mm)	t_s (mm)
[1] SP-205-10-30	0.205	1.0	0.30	3.82	1461	292	20	225	40
[2] SP-205-05-35	0.205	0.5	0.35	3.90	1705	341	20	149	40
[3] SP-205-05-40	0.205	0.5	0.40	5.22	1948	390	20	172	40
[4] SP-225-10-30	0.225	1.0	0.30	3.05	1461	292	20	232	40
[5] SP-225-05-35	0.225	0.5	0.35	3.10	1705	341	20	136	40
[6] SP-225-05-40	0.225	0.5	0.40	4.15	1948	390	20	157	40
[7] SP-250-10-35	0.250	1.0	0.35	3.24	1705	341	20	244	40
[8] SP-250-05-40	0.250	0.5	0.40	3.21	1948	390	20	142	40
[9] SP-300-10-42	0.300	1.0	0.425	3.20	2070	414	20	251	40
[10] SP-400-10-55	0.400	1.0	0.55	3.06	2679	536	20	259	40
[11] SP-550-10-72	0.550	1.0	0.725	3.03	3531	706	20	273	40
[12] SP-600-10-55	0.600	1.0	0.55	1.16	2679	536	20	177	40
[13] SP-200-05-55	0.200	0.5	0.55	12.5	2679	536	20	259	40
[14] SP-275-05-72	0.275	0.5	0.725	12.3	3531	706	20	273	40
[15] SP-300-05-55	0.300	0.5	0.55	4.75	2679	536	20	177	40

case, while Figures 4(b) and 4(c) illustrate cyclic loading cases. Here, we stipulate that the compressive displacement is positive. One-side cyclic loading program means that upon unloading, the applied displacement will only be reduced to zero and no negative displacement is applied to the plate. In contrast, two-side cyclic loading program indicates that the plate is applied with alternative compression and tension loads. It is worthy to note that the two-side cyclic loading program is also simply referred to as cyclic loading in the following description.

Average Stress and Average Strain Curves: Hysteretic and Envelope Curves

Computed hysteretic curves of three specimens subjected to one-side cyclic loading and two-side cyclic loading are respectively illustrated in Figure 5. The computed results under monotonic loading are also plotted in the figure. Comparison of envelope curves in the compression side as well as the monotonic results are shown in Figure 6. It is observed that the computed results with one-side and two-side cyclic loading are always larger than monotonic results before the occurrence of local buckling mainly due to the effect of cyclic strain hardening. Moreover, strength hardening of the plate with two-side cyclic loading begins earlier than that of the plate with one-side cyclic loading. The possible reason lies in that the cyclic strain hardening phenomenon behaves significantly for the plate with two-side loading. As a consequence, the local buckling occurs earlier for the latter case. Therefore, it can be concluded that the ductility capacity obtained from the analysis with two-side cyclic loading is the most severe case.

Comparison of Ductility Capacities

Ductility of the plate is defined with the failure strain, which is at a point corresponding to 95% of maximum strength after the peak load. Figure 7(a) shows the effect of α on the failure strain of stiffened plates. The real curve refers to the failure strain equation proposed by Usami et al. (1995), and defined by

$$\frac{\epsilon_s}{\epsilon_y} = \frac{0.145}{\lambda_s - 0.2} + 0.119 \quad (8)$$

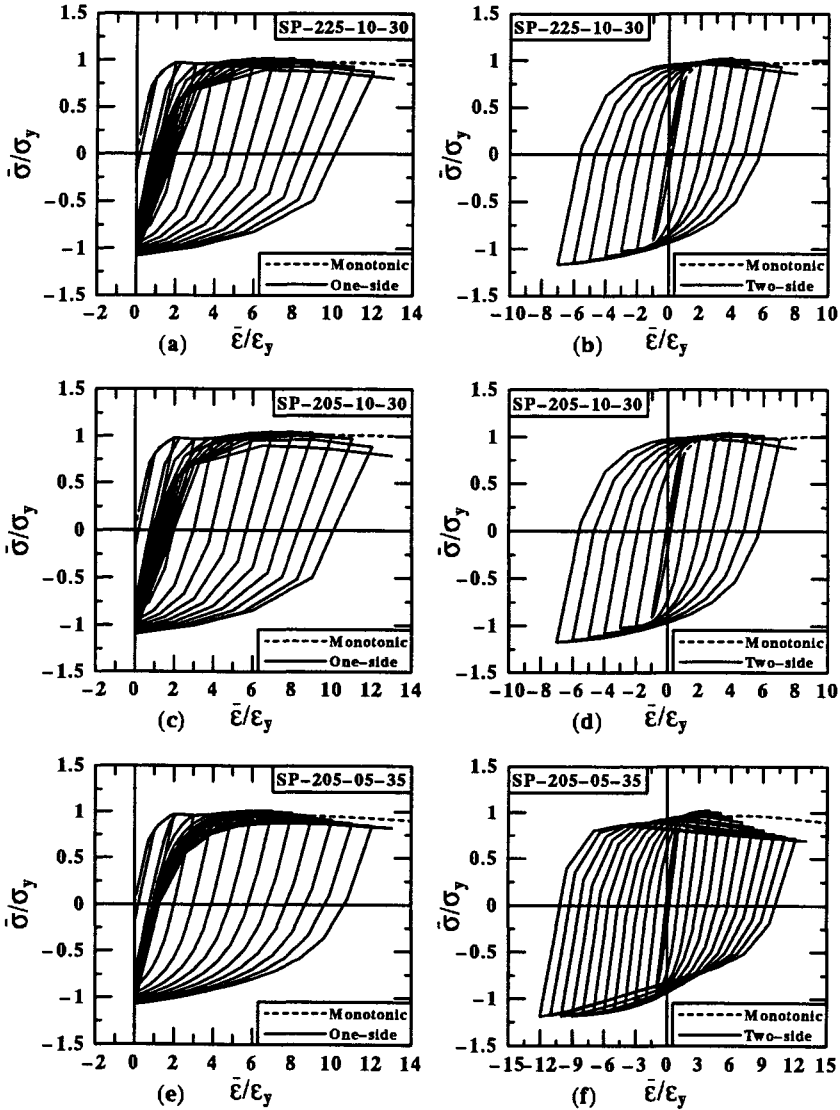


Figure 5: Computed hysteretic curves of stiffened plates

It is found that the computed results in the case of $\alpha = 1.0$ well fit the curve, while those in the case of $\alpha = 0.5$ are quite lower. That is to say, $\bar{\lambda}_s$ can not properly be employed to evaluate the failure strains of the stiffened plates with small values of α . Comparison of the computed results with the proposed curve is illustrated in Fig. 8(a). It is observed that: (1) The current computed results under monotonic loading generally match the proposed curve. However, a large discrepancy is observed for the small values of $\bar{\lambda}_s$. The possible reason lies in that in the literature (Usami et al., 1995), only two plates with $R_f = 0.20$ were analyzed in the cases of $\bar{\lambda}_s \leq 0.21$. In present analysis, three plates with R_f varying from 0.30 to 0.40 and α varying from 1.0 to 0.5

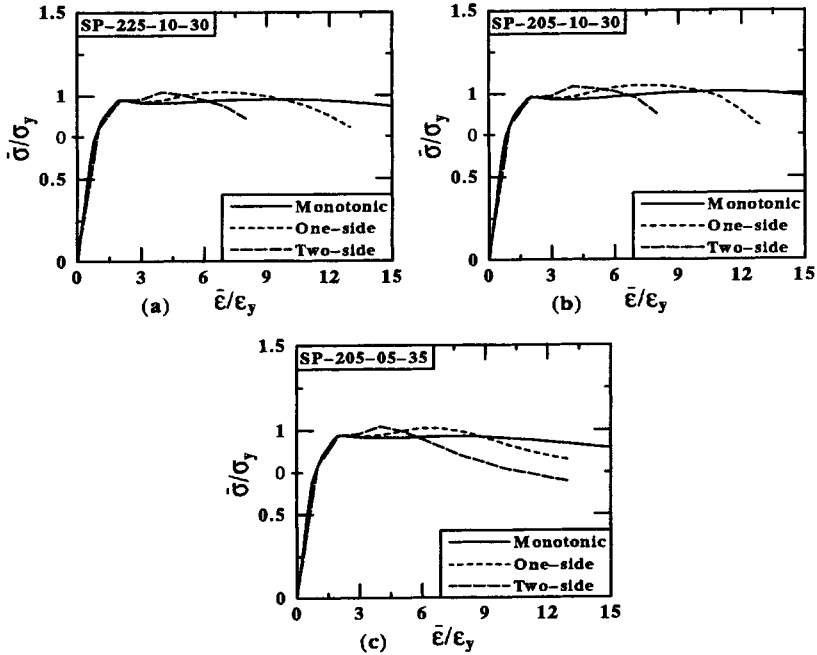


Figure 6: Comparison of envelope curves of stiffened plates

are analyzed in the case of $\bar{\lambda}_s = 0.205$. It is found that the computed failure strain with $R_f = 0.30$ and $\alpha = 1.0$ approaches the curve, while the other two results are quite small due to the effect of α and R_f . (2) Compared with monotonic results, the computed results under two-side cyclic loading are quite different from the proposed curve. It is mainly due to the earlier strength deterioration under cyclic loading.

To accurately account for the effect of α on the failure strains of stiffened plates, a modification factor $1/\sqrt[3]{\alpha}$ is introduced into the expression of $\bar{\lambda}_s$ as given in Eq.(5). That is to say, a modified stiffener's equivalent slenderness ratio $\bar{\lambda}'_s$ is now defined as follows:

$$\bar{\lambda}'_s = \frac{1}{\sqrt{Q}} \frac{1}{\sqrt[3]{\alpha}} \frac{a}{r_s} \frac{1}{\pi} \sqrt{\frac{\sigma_y}{E}} \tag{9}$$

The computed failure strains against $\bar{\lambda}'_s$ are plotted in Figures 7(b) and 8(b), respectively. The following equation is also plotted in the figures.

$$\frac{\epsilon_s}{\epsilon_y} = \frac{0.145}{\bar{\lambda}'_s - 0.2} + 0.119 \tag{10}$$

The above equation is the same as Eq.(8), but $\bar{\lambda}_s$ is replaced with $\bar{\lambda}'_s$. It is observed that the computed results in the case of $\alpha = 0.5$ also approach the curve. Moreover, the curve will always give a safe-side prediction to the ductility capacity of the stiffened plate under a monotonic loading [see Figure 8(b)]. Although two data lie below the curve, the computed results in the case of two-side cyclic loading also match the present curve. Hence, it can be concluded that $\bar{\lambda}'_s$ is a valid parameter in evaluating the ductility capacity of the stiffened plates.

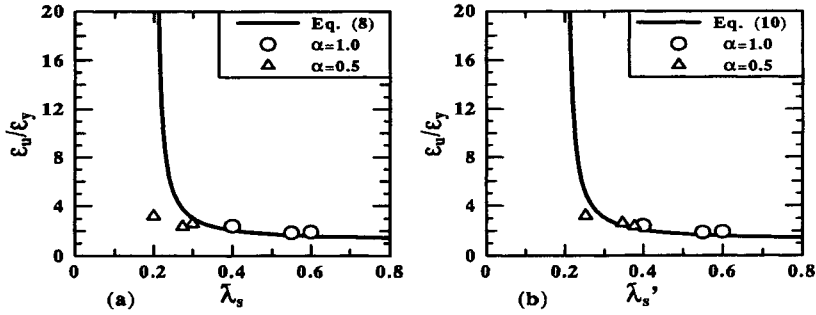


Figure 7: Effect of α on failure strains

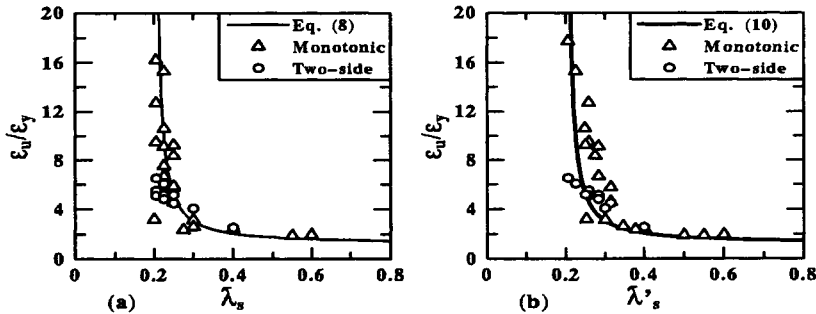


Figure 8: Comparison between failure strains and proposed formula

CONCLUSIONS

This paper was concerned with the ductility evaluation of stiffened plates under cyclic loading. From the numerical results, the following main conclusions can be obtained: (1) Comparisons showed that the loading history has a large influence on ductility of the stiffened plate, and the two-side cyclic loading analysis is the most severe case. (2) The ductility of the stiffened plate can be obtained from a previously proposed ductility formula by introducing a modification factor into the stiffener's equivalent slenderness ratio parameter.

REFERENCES

ABAQUS/Standard User's Manual. (1995). Hibbitt, Karlson & Sorenson, Inc., Ver. 5.5, Vol. I & II.

DIN 4114, Blatt2. (1953). *Stahlbau, Stabilitatsfalle (Knickung, Kippung, Beulung), Berechnungsgrundlagen*, Richtlinien, Berlin, Germany.

Gao, S. B., Usami, T. and Ge, H. B. (1998). Ductility evaluation of steel bridge piers with pipe-sections. *J. Engrg. Mech.*, ASCE, **124**:3, 260-267.

Guideline for stability design of steel structures. (1987). Fukumoto, Y., ed., JSCE, Japan.

Shen, C., Mamaghani, I. H. P., Mizuno, E., and Usami, T. (1995). Cyclic behavior of structural steels. II: Theory. *J. Engrg. Mech.*, ASCE, **121**:11, 1165-1172.

Usami, T., Suzuki, M., Mamaghani, I. H. P., and Ge, H. B. (1995). A proposal for check of ultimate earthquake resistance of partially concrete-filled steel bridge piers. *Struct. Mech. / Earthquake Engrg., Proc. of JSCE*, **508**/I-31, 1-14.

THIN PLATES SUBJECTED TO UNIFORMLY VARYING EDGE-DISPLACEMENTS

N. E. Shanmugam¹ and R. Narayanan²

¹ National University of Singapore, Singapore

² Duke University, Durham, North Carolina, USA

ABSTRACT

This paper is concerned with plates subjected to linearly varying load. Energy method based on effective width concept is applied to study the post buckling behaviour of plates with initial imperfection and clamped along loaded edges and simply supported on unloaded edges. Expressions for effective width are obtained for two cases in which the unloaded edges may be held straight or allowed free to pull-in. Results are given to illustrate the variation of effective width.

KEYWORDS

Plates, uniformly varying load, clamped edge, effective width, energy method, load carrying capacity.

INTRODUCTION

Timoshenko (1961) investigated the buckling behavior of a simply supported rectangular plate subjected to a uniformly varying axial force, acting in the middle plane of the plate and given by

$$N_x = N_0 \left(1 - \alpha \frac{y}{b} \right) \quad (1)$$

In the above equation, setting $\alpha = 0$ and 2 , will correspond to uniform compression and pure bending load, respectively. $\alpha > 2$ corresponds to a combination of bending and tension and $\alpha < 2$ to a similar combination of bending and compression.

Methods of evaluating post buckled behavior of plates using large deflection theory have been developed but these are not popular with designers on account of the complexity of the available solution procedures. This has opened the way for the development of simplified approximate methods. Plates under linearly varying loads have been investigated by Walker (1967), Rhodes and Harvey (1971), Rhodes et al. (1975), Kalyanaraman and Ramakrishna (1984) and Narayanan and Chan (1985). This paper is a continuation of

studies by Narayanan and Chan (1985) who assumed the plates to be simply supported and with two types of unloaded support conditions, viz, the unloaded edges were free to pull-in or held straight. The loading condition considered is the one that would be obtained from a linearly varying edge displacement, the ratio of strains at the two edges being kept constant. In this paper, a similar plate is considered, with its loaded edges clamped and unloaded edges simply supported. Practical plates have support conditions which lie between ideally simply supported and ideally fixed conditions, hence the effective widths can be expected to be between these two theoretical cases.

ASSUMPTIONS

In carrying out the analysis, it is assumed that (i) the material of the plate is homogeneous, isotropic, elastic and then perfectly-plastic. The effect of strain hardening is negligible; (ii) all edges are free from applied or restraining moments; (iii) the finite buckled shape in the post-buckling shape is identical with the shape of infinitely small buckles during incipient buckling; (iv) the values of displacements in the *x* and *y* directions are extremely small in comparison with the transverse displacement in the *z* direction; (v) the second order membrane strains are assumed to be entirely dependent upon out-of-plane displacements; (vi) for the purpose of analysis, only a single wave of buckling is considered (i.e., the plate is an approximately square one). The buckled shape is in the same form as the assumed initial imperfection surface.

CRITICAL LOAD OF A PLATE UNDER A TRAPEZOIDALLY VARYING LOAD

The analytical treatment described below pertains to an initially imperfect plate which has its unloaded edges simply supported and the loaded edges clamped (Fig. 1). As no law governs the general pattern of plate imperfections, it is usual to assume a suitable shape for the sake of simplicity of analysis, which takes

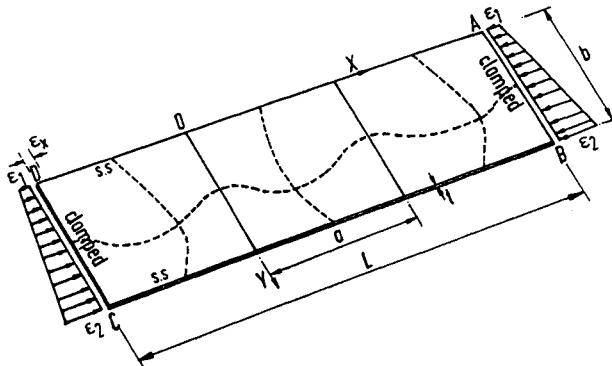


Figure 1: Plate Subjected to Uniformly Varying Edge Displacement

the same form as the final buckled shape. When σ_x reaches the elastic critical stress σ_{cr} , the plate will be assumed to buckle in a series of half wavelengths the deflected form being given by:

$$w = \left(1 - \cos \frac{2\pi x}{a} \right) \left(a_1 \sin \frac{\pi y}{b} + a_2 \sin \frac{2\pi y}{b} \right) \tag{2}$$

in which *w* is the out-of-plane deflection of the plate and *a*₁, *a*₂ refer to amplitudes of the buckling wave. The initial surface of the plate before any loads are applied can be expressed by an expression similar to

Eqn. (2), i.e.,:

$$w_0 = \left(1 - \cos \frac{2\pi x}{a}\right) \left(A_1^0 \sin \frac{\pi y}{b} + A_2^0 \sin \frac{2\pi y}{b}\right) \quad (3)$$

in which A_1^0, A_2^0 = amplitudes of the wave of initial imperfections. The final buckled shape will be given by Eqn. (3).

The total strain energy (U) of a plate is given by

$$U = \frac{D}{2} \int_0^b \int_0^a \left(\frac{d^2 w}{dx^2} + \frac{d^2 w}{dy^2} \right)^2 dx dy$$

Substituting for w one obtains

$$U = \frac{\pi^4 D ab}{2} \left[a_1^2 \left(\frac{4}{a^4} + \frac{2}{a^2 b^2} + \frac{3}{4b^4} \right) + a_2^2 \left(\frac{4}{a^4} + \frac{8}{a^2 b^2} + \frac{12}{b^4} \right) \right] \quad (4)$$

The external work done is given by:

$$T = \frac{1}{2} \int_0^b \int_0^a t \sigma_x \left(\frac{dw}{dx} \right)^2 dx dy$$

$$\sigma_x = \sigma_{cr1} \left(1 + \frac{\phi-1}{b} y \right) \quad \text{where } \phi = \frac{\varepsilon_2}{\varepsilon_1}$$

$$T = \frac{1}{2} t \frac{4\pi^2}{a^2} \sigma_{cr1} \int_0^b \int_0^a \sin^2 \frac{2\pi x}{a} \left(1 + \frac{\phi-1}{b} y \right) R \cdot dx dy$$

$$\text{where } R = \left(a_1 \sin \frac{\pi y}{b} + a_2 \sin \frac{2\pi y}{b} \right)^2$$

$$T = \frac{\pi^2 \sigma_{cr1} t}{a} \int_0^b \left(1 + \frac{\phi-1}{b} y \right) R dy$$

$$\text{or } T = \frac{\pi^2 \sigma_{cr1} t}{a} \left[a_1^2 \frac{b}{2} + a_2^2 \frac{b}{2} + \frac{\phi-1}{b} \left(a_1^2 \frac{b^2}{4} - \frac{16a_1 a_2}{9\pi^2} b^2 + a_2^2 \frac{b^2}{4} \right) \right]$$

Equating the internal energy to the external work, we get

$$\frac{\pi^4 D ab}{2} \left[a_1^2 \left(\frac{4}{a^4} + \frac{2}{a^2 b^2} + \frac{3}{4 b^4} \right) + a_2^2 \left(\frac{4}{a^4} + \frac{8}{a^2 b^2} + \frac{12}{b^4} \right) \right]$$

$$= \frac{\pi^2 \sigma_{cr1} t}{a} \left[a_1^2 \frac{b}{2} + a_2^2 \frac{b}{2} + \frac{\phi-1}{b} \left(a_1^2 \frac{b^2}{4} - \frac{16 a_1 a_2}{9 \pi^2} b^2 + a_2^2 \frac{b^2}{4} \right) \right] \tag{5}$$

Putting:

$$K_1 = \frac{4}{a^4} + \frac{2}{a^2 b^2} + \frac{3}{4 b^4} \quad \text{and} \quad K_2 = \frac{4}{a^4} + \frac{8}{a^2 b^2} + \frac{12}{b^4} \quad \text{and} \quad A' = \frac{\pi^2 D a^2 b^2}{2 t \cdot \sigma_{cr1}}$$

equation (5) becomes

$$\left(A' K_1 - \frac{\phi+1}{4} b^2 \right) a_1^2 + (\phi-1) \frac{16}{9 \pi^2} b^2 a_1 a_2 + \left(A' K_2 - \frac{\phi+1}{4} b^2 \right) a_2^2 = 0 \tag{6}$$

Differentiating equation (6) and noting that at buckling, the determinant is zero, we get

$$K_1 K_2 A'^2 - \frac{\phi+1}{4} (K_1 + K_2) b^2 A' + \frac{(\phi+1)^2}{16} b^4 - \frac{64}{81 \pi^4} (\phi-1)^2 b^4 = 0 \tag{7}$$

Solving Equation (7), an expression for A' can be obtained and with $K = \frac{b^4 a^2}{2 A'}$, the expression

for buckling coefficient K ($= \sigma_{cr} \frac{b^2 t}{\pi^2 D}$) is given as

$$K = \frac{4 K_1 K_2 b^2 a^2}{(\phi+1) \left[(K_1 + K_2) + \sqrt{(K_1 + K_2)^2 - 4 K_1 K_2 \left[1 - 0.13 \left(\frac{\phi-1}{\phi+1} \right)^2 \right]} \right]} \tag{8}$$

ULTIMATE STRENGTH OF A PLATE FIXED ALONG LOADED EDGES WITH SIMPLY SUPPORTED EDGES FREE TO PULL-IN

The function describing the initial imperfections will be assumed to have the same form as the final buckled shape:

$$w_0 = \left(1 - \cos \frac{2\pi x}{a} \right) \left(A_1^0 \sin \frac{\pi y}{b} + A_2^0 \sin \frac{2\pi y}{b} \right) \tag{9}$$

The strain energy due to bending stored in a half wavelength is given by:

$$U_b = \frac{t}{2} \int_0^a \int_0^b \sigma_{cr1} \left(1 + \frac{\phi-1}{b} y \right) \left(\frac{dw}{dx} \right)^2 dx dy \tag{10}$$

In the expression for strain energy the actual deflection (i.e., the final minus the initial deflection) may be replaced by:

$$w = (a_2 - A_2^\circ) \left(1 - \cos \frac{2\pi x}{a} \right) \left(\beta \sin \frac{\pi y}{b} + \sin \frac{2\pi y}{b} \right) \quad (11)$$

$$\text{where } \beta = \frac{a_1}{a_2} = \frac{A_1^\circ}{A_2^\circ}$$

It is assumed that the buckled shape remains the same as at incipient buckling. Therefore, the ratio β remains constant although the actual values increase with the increase of loading. The expression for strain energy due to bending is therefore obtained by the following expression

$$U_b = \frac{\pi^2 \sigma_{cr} t}{a} \int_0^b \left(1 + \frac{\phi-1}{b} y \right) (a_2 - A_2^\circ)^2 R \, dy \quad (12)$$

$$R = \beta^2 \sin^2 \frac{\pi y}{b} + 2\beta \sin \frac{\pi y}{b} \sin \frac{2\pi y}{b} + \sin^2 \frac{2\pi y}{b}$$

The strain energy due to mid-plane strain is given by:

$$U_s = \frac{1}{2E} \int_0^b \int_0^a (\sigma_x^2 + \sigma_y^2 - 2\nu \sigma_x \sigma_y) t \, dx dy \quad (13)$$

Since the edges are free to pull-in, $\sigma_y = 0$ along AD and BC and we have, therefore,

$$U_s = \frac{t}{2E} \int_0^b \int_0^a \sigma_x^2 \, dx dy$$

The total strain energy is given by:

$$U_{int} = U_b + U_s$$

$$U_{int} = \frac{\pi^2 \sigma_{cr} t}{a} \int_0^b \left(1 + \frac{\phi-1}{b} y \right) (a_2 - A_2^\circ)^2 R \, dy + \frac{t}{2E} \int_0^b \int_0^a \sigma_x^2 \, dx dy \quad (14)$$

The incremental change of the total energy (dU_{int}) due to incremental change of amplitude (from a_2 to $(a_2 + da_2)$), is equated to the corresponding incremental change of external work done (i.e., stress multiplied by the change in volume) as was done by Narayanan and Chan. We obtain the relation between the applied edge strain and the corresponding stress at any section.

$$\epsilon_1^c = \frac{3\pi^2 A_2^{\circ 2} (m^2 - 1)(\beta^4 + 4\beta^2 + 1)}{8a^2 \left[\frac{\beta^2 + 1}{2} + (\phi - 1) \left(\frac{\beta^2}{4} - \frac{16\beta}{9\pi^2} + \frac{1}{4} \right) \right]} + \frac{\sigma_{cr1} (m - 1)}{Em} \tag{15}$$

$$\sigma_x = E \left[\epsilon_x \frac{\pi^2}{a^2} (a_2^2 - A_2^{\circ 2}) R \right]$$

or

$$\sigma_x = E \left[\left[\frac{3\pi^2 A_2^{\circ 2} (m^2 - 1)(\beta^4 + 4\beta^2 + 1)}{8a^2 \left[\frac{\beta^2 + 1}{2} + (\phi - 1) \left(\frac{\beta^2}{4} - \frac{16\beta}{9\pi^2} + \frac{1}{4} \right) \right]} + \frac{\sigma_{cr1} (m - 1)}{Em} \right] \left(1 + \frac{\phi - 1}{b} y \right) - \frac{\pi^2}{a^2} (a_2^2 - A_2^{\circ 2}) R \right] \tag{16}$$

The mean stress σ_m is given by:

$$\sigma_m = \frac{1}{b} \int_0^b \sigma_x dy$$

$$\sigma_m = E \left[\left[\frac{3\pi^2 A_2^{\circ 2} (m^2 - 1)(\beta^4 + 4\beta^2 + 1)}{8a^2 \left[\frac{\beta^2 + 1}{2} + (\phi - 1) \left(\frac{\beta^2}{4} - \frac{16\beta}{9\pi^2} + \frac{1}{4} \right) \right]} + \frac{\sigma_{cr1} (m - 1)}{Em} \right] \frac{\phi + 1}{2} - \frac{\pi^2}{2a^2} A_2^{\circ 2} (m^2 - 1)(\beta^2 + 1) \right] \tag{17}$$

Application to Design Problems

Based on the theory proposed above, an approximate method of estimating the ultimate capacity of plates subjected to uniformly varying edge displacement is developed. It is postulated that when the longitudinal stress at any section has just reached the yield stress (σ_{ys}), the plate is no longer able to sustain any load increment. This would be particularly true of wide plates, where the loss of stiffness beyond the onset of first yield is rapid. The effective width of the plate will therefore be computed as the ratio of the mean stress at first yield σ_m' to the yield stress σ_{ys} . The ultimate strength of a plate can, therefore, be determined as the product of effective width, thickness and the yield stress.

By using the above criterion, the effective width of plates with unloaded longitudinal edges free to pull-in is obtained from Eqn. (17) as

$$K_{bs} = \frac{E}{\sigma_{ys}} \left[\left\{ \frac{3\pi^2 A_2^2 (m^2 - 1) (\beta^4 + 4\beta^2 + 1)}{8a^2 \left[\frac{\beta^2 + 1}{2} (\phi - 1) \left(\frac{\beta^2}{4} - \frac{16}{9\pi^2} \beta + \frac{1}{4} \right) \right]} + \frac{\sigma_{cr1} (m - 1)}{Em} \right\} \left(\frac{\phi + 1}{2} \right) - \frac{\pi^2}{2a^2} A_2^2 (m^2 - 1) (\beta^2 + 1) \right] \quad (18)$$

In the same way as explained above, the case of plates with unloaded longitudinal edges held straight can be considered and the corresponding expression for effective width is obtained as

$$K_{bs} = \frac{E}{\sigma_{ys}} \left[\left\{ \frac{3\pi^2 A_2^2 (m^2 - 1) (\beta^4 + 4\beta^2 + 1)}{8a^2 \left[\frac{\beta^2 + 1}{2} + (\phi - 1) \left(\frac{\beta^2}{4} - \frac{16}{9\pi^2} + \frac{1}{4} \right) \right]} + \frac{\sigma_{cr1} (m - 1)}{Em} \right. \right. \\ \left. \left. + \frac{17\pi^2 a^2 A_2^2 (\beta^2 + 4)^2 (m^2 - 1)}{128b^4 \left[\frac{\beta^2 + 1}{2} + (\phi - 1) \left(\frac{\beta^2}{4} - \frac{16}{9\pi^2} + \frac{1}{4} \right) \right]} \right\} \left(\frac{\phi + 1}{2} \right) - \frac{\pi^2}{2a^2} A_2^2 (m^2 - 1) (\beta^2 + 1) \right] \quad (19)$$

For any chosen value of initial imperfection, effective width curves can be obtained simply from Eqns (18) and (19) for a number of parameters such as plate slenderness, edge strain ratio etc. Variations of K_{bs} for two different edge conditions viz. one in which the unloaded edges are free to pull-in and the other in which the edges are kept straight are given in Figs 2 and 3, respectively for a number of varying edge displacements using $\nu = 0.3$, $E = 200,000 \text{ N/mm}^2$ and $\sigma_{ys} = 250 \text{ N/mm}^2$.

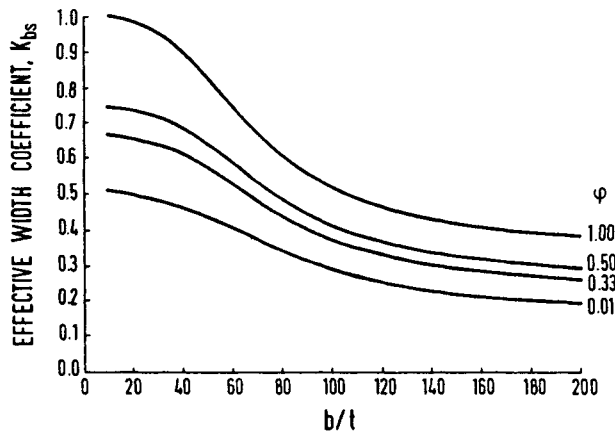


Figure 2 Variation of Effective Width Factors - Plate with unloaded edges free to pull-in

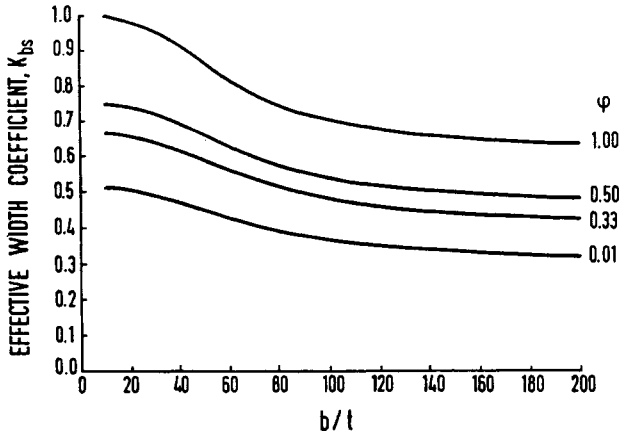


Figure 3 Variation of Effective Width Factors - Plate with unloaded edges kept straight

Values of effective width factors K_{bs} were calculated for square plates with edge conditions considered in the present study and compared with the corresponding values obtained by the equations given by Narayanan and Chan (1985) for plates with all edges simply supported as shown in Table 1. Plate slenderness (b/t) values ranging from 30 to 120 have been considered for comparison. It can be seen from the table that the effect of edge conditions on effective width factors is significant for plates having large plate slenderness i.e thin plates. For example in the case of plates with b/t of 100 and having all sides simply supported, there is an increase of 17 percent in K_{bs} value for edges kept straight compared to the case in which edges are allowed free to pull-in. The corresponding increase of K_{bs} values in the case of plates with two loaded edges clamped and the remaining edges simply supported is 14 percent. There is a marked increase in the values of K_{bs} corresponding to plates with clamped – simply supported edges compared to simply supported plate. Such increases are 30 percent and 26 percent, respectively, for edges free to pull-in and edges kept straight. For plates having b/t ratios less than 70 the change in K_{bs} values for different boundary conditions is practically nil.

TABLE 1
COMPARISON OF K_{bs} VALUES FOR DIFFERENT BOUNDARY CONDITIONS

b/t	Loaded edges clamped – unloaded edges simply supported		All edges simply supported	
	Edges free to pull-in	Edges held straight	Edges free to pull-in	Edges held straight
30	0.745	0.746	0.745	0.749
40	0.745	0.744	0.745	0.745
50	0.744	0.744	0.744	0.744
60	0.744	0.744	0.744	0.744
70	0.744	0.744	0.638	0.664
80	0.742	0.742	0.547	0.596
90	0.643	0.684	0.484	0.549
100	0.568	0.646	0.438	0.515
120	0.469	0.574	0.380	0.471

CONCLUSIONS

An effective width method based on the energy method has been proposed for assessing the strength of an approximately square plate subjected to a linearly varying edge displacement. The loaded edges were assumed to be clamped while the unloaded edges were taken to be simply supported. Two different cases were considered for the simply supported edges. They were either held straight or allowed to pull-in. The method is simple since there are no tedious calculations present and it is easily programmable. The method, however, gives an upper bound to the load predicted. It is observed that there is significant change in K_{bs} values for plates with clamped edges compared to those with simply supported edges. This increase becomes more significant when the edges are held straight.

REFERENCES

- Timoshenko S. (1961). *Theory of Elastic Stability*, McGraw-Hill Book Company, Inc, New York.
- Walker A.C. (1967). Flat Rectangular Plates Subjected to a Linearly Varying Edge Compressive Loading, *Thin Walled Structures*, Chatto and Windus, London
- Rhodes J. and Harvey J.M. (1971). Effect of Eccentricity of Load or Compression on the Buckling and Post-Buckling Behaviour of Flat Plates, *International Journal of Mechanical Sciences*, Vol. 13, 867-879.
- Rhodes J., Harvey J.M. and Fok C. (1975). The Load-Carrying Capacity of Initially Imperfect Eccentrically Loaded Plates, *International Journal of Mechanical Sciences*, Vol. 17, 161-175.
- Kalyanaraman V and Ramakrishna P. (1984) Non-Uniform Compressed Stiffened Elements, *University of Missouri-Rolla*, 75-92.
- Narayanan R. and Chan S.L. (1985) Ultimate Capacity of Plates Containing Holes under Linearly Varying Edge Displacements, *Computers and Structures*, 21:4, 841-849.

This Page Intentionally Left Blank

Section V

ANALYSIS AND DESIGN

This Page Intentionally Left Blank

GEOMETRIC NONLINEAR ANALYSIS OF DIAPHRAGM-BRACED C-PURLINS

Y.J.Zhu¹ Y.C.Zhang² X.L.Liu¹

¹Department of Civil Engineering, Tianjin University, China

²Department of Building Engineering, Harbin University of
Architecture & Engineering, China

ABSTRACT

The method for geometric nonlinear analysis of diaphragm-braced C-purlins under gravity and wind uplift loading was presented. An updated Lagrangian formulation was adopted to establish the structural nonlinear equilibrium equation. Variable cylindrical arc length method had been used together with the modified Newton-Raphson method as the iteration strategy, to trace the equilibrium paths. Using this method, the behavior of C-purlins with diaphragm bracing at one flange only under gravity and wind uplift loading was investigated. The research results indicate that the diaphragm bracing can improve the behavior of C-purlins obviously and increase their load carrying capacity. Finally, based on theoretical and experimental results, pertinent conclusions are obtained.

KEYWORDS

geometric nonlinearity, diaphragm bracing, C-purlin, finite element method

INTRODUCTION

Corrugated metal sheets are widely used as wall cladding, roof decking or floor panels in building structures. Diaphragms formed by interconnecting such panels and the supporting members can resist shear deformation in their own plane. Because of their shear rigidities, diaphragm can be very effective in bracing purlins against lateral buckling and increase their load carrying capacity, if proper connections are made between diaphragm and purlins. In addition to shear rigidity, the diaphragm has a cross bending stiffness along its corrugation. This can also provide rotational bracing to the purlins. Especially for the channel and Z-section purlins, because they are weak against torsion and bending in the lateral direction, diaphragms can brace them to use their bending capacity in their strong direction and very economical design can be obtained.

The behavior of diaphragm braced steel beams and columns has been investigated by many researchers and the previous work was reviewed in detail by Zhu and Zhang(1995). The research approaches include experimental method, simplified analytical method and finite element method. Generally, the results provided by the experimental method are only applicable for the special situations. Simplified analytical method is suitable for treating the problems with simple boundary condition and simple load distribution, and can not be extended easily to include the effects of initial sweep and twist of members on the overall behavior.

The research reported herein was conducted at Harbin University of Architecture and Engineering , sponsored by the Natural Science Foundation of China. Firstly, on the basis of reviewing existing research results, the finite element model of diaphragm braced steel member is established. Then, in accordance with the basic theory of nonlinear finite element method, the formulation for large deflection, large rotation and small strain problem of diaphragm braced member was founded by use of the Updated Lagrangian description. A finite element program was developed in which variable arc length method was used for each increment, together with the modified Newton-Raphson method as the iteration strategy. The program was tested and verified by several numerical examples and some experimental data by Zhu(1996). Finally, the behavior of C-purlins with diaphragm bracing on one flange only under gravity and wind uplift loading was investigated. The effect of diaphragm shear rigidity and rotation restraint on purlin behavior were taken into account.

GENERAL THEORY

Finite Element Model of Steel Purlin

The steel purlin is treated as general thin-walled open sectional beam and with the assumptions:

- (i) The shear strain in the middle surface is neglected.
- (ii) Cross sections do not distort.

- (iii) The material remains elastic.
- (iv) Local bulking is not considered.

Assume the axial displacement varies linearly along the member and lateral deflection curve is cubic, the incremental form of the element tangential stiffness equation can be obtained as:

$$([K_L]_b^e + [K_G]_b^e) \{\Delta\delta\}_b^e = \{\Delta F\}_b^e \quad (1)$$

where $[K_L]_b^e$ and $[K_G]_b^e$ are the linear and geometric stiffness matrices respectively. Their detail expressions were given by Zhu(1996).

The Finite Element Model of Panel

In general, the material constituting panel is isotropic. Because of cross section geometric, panel will respond to loading orthotropically. In this paper, an equivalent orthotropic flat sheet is defined which has the planar dimensions of the panel and behaviors in the same manner. The material constants of the equivalent flat sheet can be obtained according to the equivalent conditions. Then the equivalent flat sheet is divided into a number of small 8-node degenerated solid shell elements.

Experience with actual diaphragms has indicated that excessive bearing deformation or tearing of the sheet material around the connector as well as the inclination of screws constitutes the very important part of diaphragm nonlinear behavior. In present study, only connector nonlinearity is considered and shell elements are assumed elastic throughout the loading range.

Using the Updated Lagrangian formulation and the stress-strain equation, the incremental equilibrium equation of the shell element can be derived from the standard steps of finite element method as:

$$([K_L]^e + [K_G]^e) \{\Delta\delta\}^e = \{\Delta F\}^e \quad (2)$$

in which, $[K_L]^e$ and $[K_G]^e$ are the element linear and geometric stiffness matrices, respectively. The detail definition of $[K_L]^e$, $[K_G]^e$, $\{\Delta\delta\}^e$ and $\{\Delta F\}^e$ was given by Zhu(1996).

The Connectors

In an actual structure, panels are connected to each other and to steel members using connectors such as screws or welds at discrete points. Experimental information has shown that slight relative slipping motions between panels and members will occur when load is applied. As a result, the behavior of diaphragm-braced C-purlins will be nonlinear at rather lower load level.

A nonlinear connection is established here to model the behavior of the connector and the panel material in the immediate vicinity of the connector. The connection is an initial nondimensional element that concludes a group of nonlinear springs and links diaphragm and C-purlins at nodes.

In general, the spring stiffnesses are obtained by connection tests. In this paper, the spring stiffness is different in several load ranges in order to consider the connection nonlinearity. The connector has a 12×12 stiffness matrix and the stiffness values can be obtained by experimental results.

Structural Stiffness Matrix and Solution Techniques of Nonlinear Equilibrium Equation

With the all element stiffness matrices established, the stiffness matrix for the complete structure can be obtained by superimposing element stiffness of all C-purlins, shells and connectors. For C-purlins and shell elements, the element stiffness can be assembled directly into structural stiffness matrix after transformed from their local coordinate system to global coordinate system. In general, panel is fixed at the purlin flange instead of the element nodes, so one of connector ends does not coincide with the element node. It's necessary to transform connector stiffness matrix to the stiffness matrix respect to beam nodes before added into global structural stiffness matrix. The incremental equilibrium equation for the whole structure may be written as:

$$[K_T] \{\Delta\delta\} = \{\Delta F\} \quad (3)$$

in which, $[K_T]$ is the global structural stiffness matrix; $\{\Delta\delta\}$ and $\{\Delta F\}$ are the incremental structural nodal displacement and force vectors, respectively.

The nonlinear equilibrium equations(3) are solved by an incremental iterative approach. For each load increment, the variable arc length method has been employed. The modified Newton-Raphson(mNR) procedure is used as the iteration strategy because it is computationally more efficient since the stiffness matrix is reformed and refactorized only at the beginning of each increment and remains unchanged at each iteration. An energy-based convergence criterion is adopted for the iteration.

C-PURLIN EXAMPLE

A series of tests on simply-supported channel purlins screw-fastened to steel sheeting under uplift loading has been performed at Harbin University of Architecture & Engineering(Yang 1993). The one of test specimens,LT2, was 5.7 meter long and the two lines of purlins were spaced at 1.7 meter as shown in Figure 1. The measured dimensions of the channel are detailed in Figure 2. All purlins were constructed from the steel of yield point 270Mpa.V-125 trapezoidal profiled steel sheeting with thickness of 0.8mm made in China was used in each test. No.6 self-drilling screws were used to fasten the purlins to the sheeting at every trough and located at purlin mid-flanges. Uplift loading is simulated by applying load blocks on sheeting

along purlins. Four displacement transducers were used to measure the twist rotation ϕ of each purlin in the midspan section and the lateral and vertical deflections of the unbraced flange-web junction of the purlin after each loading increment.

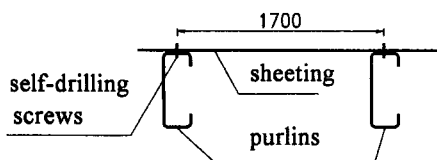


Figure 1: Test specimen LT2 of Yang(1993)

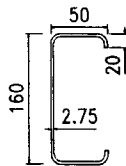
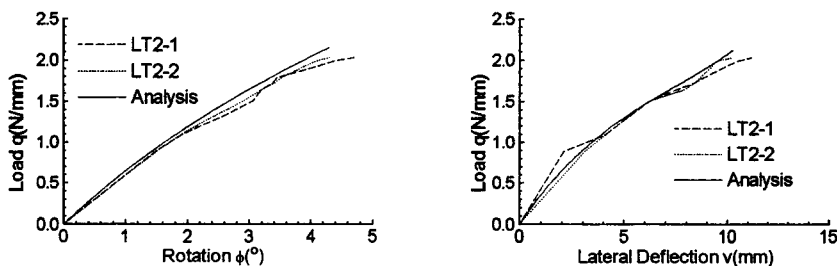


Figure 2: Channel geometry
(all dimensions in mm)

Loading was increased from zero until failure of one of the purlins obtained. The failure occurred when a line load of 2.759N/mm was applied. The rotations and deflections until failure was reached are shown in Figure 3. Nonlinearity can be observed in these figures. Nonlinear analysis of the purlins was performed by using the finite element method presented in this paper. The deflection and rotation results are compared with test results on Figure 3 and they are in close agreement.



(a)Midspan rotation ϕ versus line load q (b)Lateral deflection u versus line load q

Figure 3: Load-deflection paths for purlins

BEHAVIOR OF C-PURLIN

Using the nonlinear finite element method, behavior of C-purlins is investigated. The analyze model is based on the test specimens of Yang(1993). Yield criterion is adopted as the failure criterion, that is, if the calculated stress at any given point in the purlin flange reaches the yield stress of the steel, the purlin is considered failed. The corresponding load will represent the yield load capacity of the purlins.

Firstly, the concept of full-bracing is introduced. Full-bracing is defined as bracing such that the beam will deflect only in vertical direction and no twist and lateral deflection under vertical

loading. Let F_L and Q_L denote the sheeting rotation restraint to the purlins and the sheeting shear rigidity of the test specimen LT2 of Yang(1993). When Q_L remains unchanged, the computative lateral deflections of the shear center and rotation of the purlin LT2-1 midspan section under gravity loading can be obtained as shown in Figure 4 and Figure 5, assuming the rotation restraint to be F_L and θ respectively. It is shown that the rotation restraint has a great effect on the purlin behavior. Because of the existing of rotation restraint, the rotation θ of the midspan section decrease to a great degree, therefore the lateral deflections of shear center decrease.

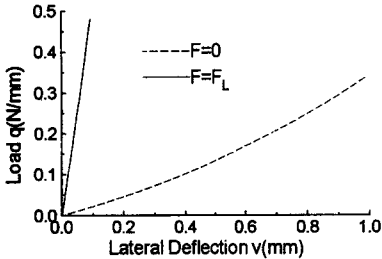


Figure 4: Shear center lateral deflection for various value of rotation restraint F

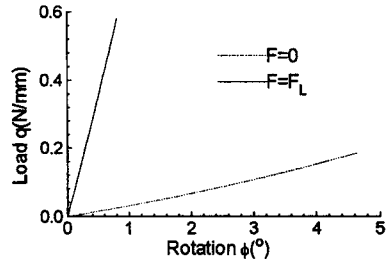


Figure 5: Mid-span rotation versus Line load for various value of rotation restraint F

Because diaphragm braces the purlin compressive flange laterally and restrains the rotation of section under gravity loading, the purlin stability will increase. With the increasing of rotation restraint F and diaphragm shear rigidity, the purlin yield load will also increase.

Figure 6 gives the plots of the ratio of purlin yield load to full bracing beam yield load, i.e., q_r/q_y , versus rotation restraint F for various values of shear rigidity Q. It indicates that with the F increasing, q_r/q_y will become large. The larger diaphragm shear rigidity is, the higher the value of q_r/q_y will be, if rotation restraint F remains unchanged. Figure 7 gives plots of the purlin midspan rotation ϕ versus rotation restraint F at yield load. When F is equal to zero, the values of ϕ are very large. With F increasing, the values ϕ decrease sharply. Once the values of ϕ reduce to some extent, the change of ϕ will become more smooth. The phenomenon will be very similar for $Q=0, Q=Q_L$ and $Q=\infty$. ϕ is large at $Q=0$ than at $Q=Q_L$ and $Q=\infty$ at the same rotation restraint F.

Under wind uplift loading, the tension flange of purlin is attached to diaphragm. In general, the channel section will rotation under uplift loading. The tension flange has small lateral deflection because of diaphragm bracing. Diaphragm rotation restraint to purlins can reduce their twist, therefore increase their load carrying capacity. Figure 8 and 9 show the plots of purlin midspan rotation and shear center lateral deflection versus line load, respectively under wind uplift loading. They indicate that the rotation restraint F has important effect on purlin deformation. Existing of rotation restraint reduces purlin twist greatly, thereby decrease lateral deflection of the purlin unconnected flange. As a result, the purlin yield load increases.

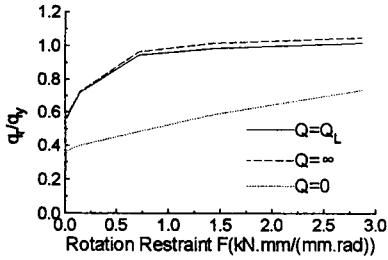


Figure 6: The ratio q_r/q_y versus rotation restraint F for various values of shear rigidity Q

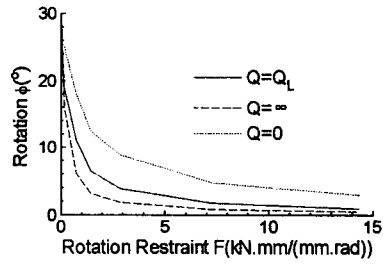


Figure 7: Rotation ϕ versus rotation restraint F for various values of shear rigidity Q

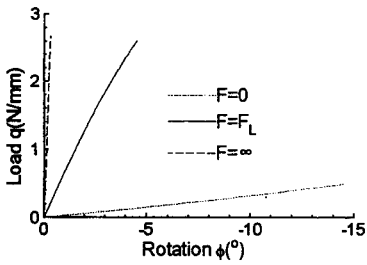


Figure 8: Midspan rotation ϕ versus line load for various values of rotation restraint F under uplift loading

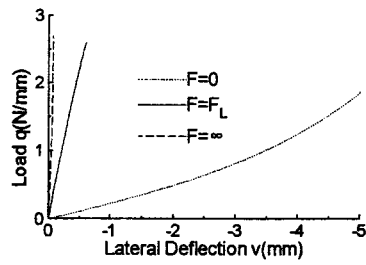


Figure 9: Lateral deflections versus line load for various values of rotation restraint F under uplift loading

Figure 10 shows the plots of the ratio of purlin yield q_r to full bracing beam yield load q_y , i.e., q_r/q_y versus rotation restraint F . It can be observed that in the initial stage of the curve, varying of F can cause a rapid change in q_r/q_y . When rotation restraint F has gone up to some extent, however, the change in yield load is quite small. Figure 11 gives plots of the angle of rotation at

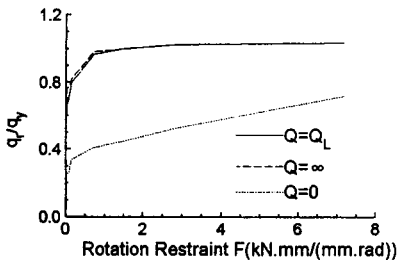


Figure 10: Ratio q_r/q_y versus rotation restraint F for various values of shear rigidity Q under uplift loading

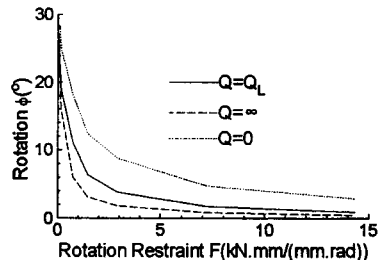


Figure 11: Rotation restraint F versus angle of rotation ϕ for various values of shear rigidity Q under uplift loading

purlin midspan versus rotation restraint F at yield load. It can be seen that there is a rapid decrease in the angle of rotation with F increasing for the initial range of the curve. As F increases further, the change in the angle of rotation is very small. Obviously, to provide a large rotation restraint F would be no significant effect on purlin behavior but uneconomical in practical design.

CONCLUSION

A nonlinear finite element method has been developed for analyzing the behavior of diaphragm braced C-purlins under gravity and wind uplift loading. The results obtained are in good agreement with that determined from the C-purlin tests. The research results indicate that the effect of lateral bracing and rotation restraint offered by sheeting on purlins can improve the behavior greatly. The magnitude of rotation restraint F has significant effect on purlin deflections. Rotation restraint reduces the rotation ϕ of purlin, this, in turn causes a reduction in the lateral deflection of C-purlins and increases the yield load capacity.

When the magnitude of rotation restraint F is small, with its increasing, the rotation ϕ reduces sharply and the yield load capacity increases rapidly. But if F reaches a certain extent, the further increase of F would cause a very small change on the rotation ϕ and yield load capacity. In this case, the further increase of F has little effect on purlin behavior but uneconomical in practical design.

REFERENCES

- Zhu, Y.J. and Zhang, Y.C.(1995). Review of Research on the Static Behavior of Diaphragm Braced Steel Components. *Journal of Harbin University of Architecture & Engineering(in Chinese)* **28:4**, 121-127.
- Zhu, Y.J.(1996). *Static Behavior of Diaphragm Braced Steel Members*. Ph.D. Dissertation, Harbin University of Architecture & Engineering .
- Yang, B.(1993). *Experimental Study of Diaphragm Braced C-purlins Subjected to Wind Uplift Loading*, Dissertation for Master Degree of Engineering, Harbin University of Architecture & Engineering .

“A RECTANGULAR PLATE ELEMENT” FOR ULTIMATE STRENGTH ANALYSIS

Koji Masaoka¹, Hiroo Okada¹ and Yukio Ueda²

¹Department of Marine System Engineering, College of Engineering,
Osaka Prefecture University, Sakai, Osaka, Japan

²Department of Mechanical Engineering, School of Biology-oriented Science & Technology,
Kinki University, Uchita-cho, Wakayama, Japan

ABSTRACT

In order to increase the safety of plated structures such as ships, strength analysis to the ultimate strength state should be performed taking into account of local failures of buckling and yielding of component plate elements. Direct application of the finite element method still needs enormous computation time and is not economical to use at the design stage, even most advanced computers are provided. In order to achieve this purpose, one of the authors proposed the “Idealized Structural Unit Method (ISUM)” and proved its usefulness by many applications developing many ISUM elements such as rectangular plate, stiffened plate, tabular beam-column and so on.

In this paper, a new rectangular plate element is developed, which can analyze all stages of behaviors to ultimate strength such as elasto-plastic, buckling and post-buckling, taking into account initial deflection and residual stress. The deflection function is composed of selective eigen-functions with some parameters. Partial yielding of the element is dealt with a through-thickness plasticity condition. The stiffness of the element is calculated by numerical integration. Necessary computation time is very short for any aspect ratios and the accuracy is very high in comparison with FEM. This element is not only a new efficient rectangular ISUM element but also can be used for general purposes.

KEYWORDS

Idealized Structural Unit Method (ISUM), Rectangular plate, Buckling, Ultimate strength, Selective eigen-function, Sectional yielding condition, Initial imperfection

1 Introduction

Thin walled structures such as ships and offshore structures are composed of many stiffened plate panels. To analyze these structures efficiently, “Idealized Structural Unit Method (ISUM)” was proposed by one of the authors [1], [2], [3]. In this study, to analyze large deflection elasto-plastic behaviour of a rectangular plate, a new rectangular element is developed as one of the ISUM element using selective eigen-functions for large deflection[4] and sectional yielding condition of the numerical integration points for plasticity. Ultimate strength of a rectangular plate with initial imperfection such as initial deflection and welding residual stress can be analyzed efficiently and accurately using this element.

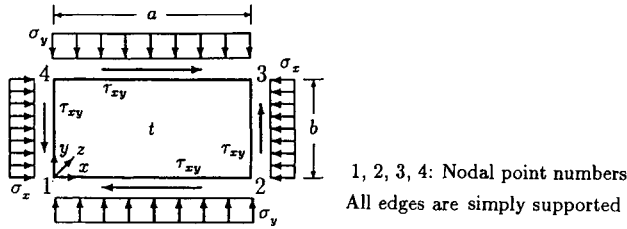


Figure 1: Rectangular plate subjected to compression and shear

2 Theory

A model is a simply supported rectangular plate subjected to axial and shear forces shown in Fig. 1. A rectangular plate element in Fig. 1 has only 4 nodal points at the corners and shape functions are expressed by selective eigen-functions. Stiffness of the plate is calculated using numerical integration method and sectional yielding condition is applied at each integration point to treat plasticity. Nonlinear behaviour of the loaded plate are solved by Newton-Raphson method at each incremental step.

2.1 Shape functions

Deflection w and initial deflection w_0 of the rectangular plate are expressed in Eq. (1).

$$\begin{aligned}
 w &= \sum_{i=1}^m \sum_{j=1}^n W_{ij} \sin \frac{i\pi x}{a} \sin \frac{j\pi y}{b}, \\
 w_0 &= \sum_{i=1}^m \sum_{j=1}^n W_{0ij} \sin \frac{i\pi x}{a} \sin \frac{j\pi y}{b}.
 \end{aligned}
 \tag{1}$$

where, W_{ij} is the coefficient of deflection functions and W_{0ij} is that of initial deflection ones.

Equilibrium equations of the rectangular plate are derived for x , y and z directions based on the large deformation theory. Being substituted Eq. (1) into two inplane equilibrium equations in x and y directions, inplane displacements u and v are expressed by nodal displacements $U_1, U_2, U_3, U_4, V_1, V_2, V_3, V_4$, and deflection parameters W_{ij}, W_{0ij} [5].

$$\begin{aligned}
 u &= \left(1 - \frac{x}{a}\right)\left(1 - \frac{y}{b}\right)U_1 + \frac{x}{a}\left(1 - \frac{y}{b}\right)U_2 + \frac{x}{a}\frac{y}{b}U_3 + \left(1 - \frac{x}{a}\right)\frac{y}{b}U_4 \\
 &\quad + \sum_{i=1}^m \sum_{j=1}^n \left\{A_1 \sin \frac{2i\pi x}{a} + A_2 \sin \frac{2i\pi x}{a} \sin \frac{2j\pi y}{b}\right\}, \\
 v &= \left(1 - \frac{x}{a}\right)\left(1 - \frac{y}{b}\right)V_1 + \frac{x}{a}\left(1 - \frac{y}{b}\right)V_2 + \frac{x}{a}\frac{y}{b}V_3 + \left(1 - \frac{x}{a}\right)\frac{y}{b}V_4 \\
 &\quad + \sum_{i=1}^m \sum_{j=1}^n \left\{B_1 \sin \frac{2i\pi y}{b} + B_2 \sin \frac{2i\pi y}{b} \sin \frac{2j\pi x}{a}\right\}.
 \end{aligned}
 \tag{2}$$

where,

$$\begin{aligned}
 A_1 &= \frac{a\pi}{16i} \left(\frac{j^2\nu}{b^2} - \frac{i^2}{a^2}\right)(W_{ij}^2 - W_{0ij}^2), \quad A_2 = \frac{i\pi}{16a} (W_{ij}^2 - W_{0ij}^2), \\
 B_1 &= \frac{b\pi}{16j} \left(\frac{i^2\nu}{a^2} - \frac{j^2}{b^2}\right)(W_{ij}^2 - W_{0ij}^2), \quad B_2 = \frac{j\pi}{16b} (W_{ij}^2 - W_{0ij}^2).
 \end{aligned}$$

$U_1, U_2, U_3, U_4, V_1, V_2, V_3,$ and V_4 are the nodal displacements and their subscripts mean the nodal numbers.

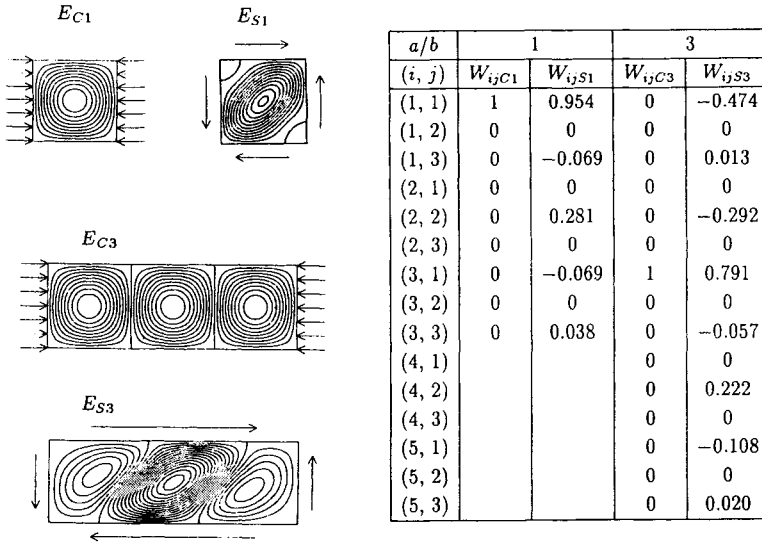


Figure 2: The shapes of eigen functions and buckling deflection coefficient ratios of rectangular plates subjected to compression or shear

2.2 Selective eigen-function for deflections

In this section, a rectangular plate with aspect ratio (a/b) equal to 3 subjected to compression and shear is taken as an example to explain selective eigen-functions. Assuming that the post-buckling deflected shape subjected to compression and shear is expressed by Eq. (3).

$$w(x, y) = W_{C3}E_{C3}(x, y) + W_{S3}E_{S3}(x, y). \tag{3}$$

where, E_{C3} is a buckling deflected shape under pure compression and E_{S3} is a buckling deflected shape under pure shear. W_{C3} and W_{S3} are weight parameters of respective buckling deflections. E_{C3} and E_{S3} are selective eigen-functions shown in Eq. (4).

$$E_{C3} = \sum_{i=1}^m \sum_{j=1}^n W_{ijC3} \sin \frac{i\pi x}{a} \sin \frac{j\pi y}{b},$$

$$E_{S3} = \sum_{i=1}^m \sum_{j=1}^n W_{ijS3} \sin \frac{i\pi x}{a} \sin \frac{j\pi y}{b}. \tag{4}$$

W_{ijC3} and W_{ijS3} of Eq. (4) are coefficients of Fourier series of the respective buckling deflected shapes. The buckling deflected shapes and the components of the Fourier series are shown in Fig. 2 in the case of the plate aspect ratios are 1 and 3. Figure 2 shows a compressive buckling deflected shape E_{C1} and a shearing buckling deflected shape E_{S1} of a square plate and similarly E_{C3} and E_{S3} of a rectangular plate whose aspect ratio a/b equals to 3. Buckling shape is obtained by solving the eigen-value problem so that the coefficients of eigen-functions are determined[6]. Only W_{C3} and W_{S3} are parameters to determine deflection of a plate because that weight parameters of Eq. (1) are expressed by the selective eigen-functions instead of W_{ij} . The relation between W_{C3} , W_{S3} and W_{ij} is Eq. (5).

$$\{W_{ij}\} = [Tw] \left\{ \begin{matrix} W_{C3} \\ W_{S3} \end{matrix} \right\}. \tag{5}$$

where,

$$\{W_{ij}\} = \{ W_{11} \ \dots \ W_{mn} \}^T,$$

$[TW]$ is the coefficient matrix obtained from Fig. 2.

Displacements u and v of Eq. (2) can be expressed by WC_3 and WS_3 using Eq. (5). That is,

$$\begin{aligned} u &= u(U_1, U_2, U_3, U_4, WC_3, WS_3), \\ v &= v(V_1, V_2, V_3, V_4, WC_3, WS_3). \end{aligned} \quad (6)$$

2.3 Strain

With large deflection effect, the relation between strains and displacements is Eq. (7).

$$\begin{aligned} \varepsilon_x &= \frac{\partial u}{\partial x} + \frac{1}{2} \left(\frac{\partial w}{\partial x} \right)^2 - \frac{1}{2} \left(\frac{\partial w_0}{\partial x} \right)^2, \quad \varepsilon_y = \frac{\partial v}{\partial y} + \frac{1}{2} \left(\frac{\partial w}{\partial y} \right)^2 - \frac{1}{2} \left(\frac{\partial w_0}{\partial y} \right)^2, \\ \gamma_{xy} &= \frac{\partial v}{\partial x} + \frac{\partial u}{\partial y} + \frac{\partial w}{\partial x} \frac{\partial w}{\partial y} - \frac{\partial w_0}{\partial x} \frac{\partial w_0}{\partial y}, \\ \kappa_x &= -\frac{\partial^2(w-w_0)}{\partial x^2}, \quad \kappa_y = -\frac{\partial^2(w-w_0)}{\partial y^2}, \quad \kappa_{xy} = -2\frac{\partial^2(w-w_0)}{\partial x \partial y}. \end{aligned} \quad (7)$$

Equations (3) and (6) being substituted into Eq. (7), strains are expressed by the nodal displacements $U_1, U_2, U_3, U_4, V_1, V_2, V_3, V_4$ and coefficients of eigen-functions WC_3, WS_3 .

2.4 Plasticity

Sectional yielding condition at each numerical integration point is expressed by Eq. (8)[7]. If $\Gamma < 0$ at an integration point, the point is elastic and if $\Gamma = 0$, it is plastic.

$$\Gamma = Q_n + 0.5Q_m + \sqrt{0.25Q_m^2 + Q_{nm}^2} - 1. \quad (8)$$

where,

$$\begin{aligned} Q_n &= \bar{N}_x^2 - \bar{N}_x \bar{N}_y + \bar{N}_y^2 + 3\bar{N}_{xy}^2, \quad Q_m = \bar{M}_x^2 - \bar{M}_x \bar{M}_y + \bar{M}_y^2 + 3\bar{M}_{xy}^2, \\ Q_{nm} &= \bar{N}_x \bar{M}_x - 0.5(\bar{N}_x \bar{M}_y + \bar{N}_y \bar{M}_x) + \bar{N}_y \bar{M}_y + 3\bar{N}_{xy} \bar{M}_{xy}. \end{aligned}$$

$\bar{N}_x, \bar{N}_y, \bar{N}_{xy}, \bar{M}_x, \bar{M}_y, \bar{M}_{xy}$ are non-dimensional values.

$$\bar{N}_x = N_x/N_Y, \quad \bar{N}_y = N_y/N_Y, \quad \bar{N}_{xy} = N_{xy}/N_Y,$$

$$\bar{M}_x = M_x/M_Y, \quad \bar{M}_y = M_y/M_Y, \quad \bar{M}_{xy} = M_{xy}/M_Y.$$

N_x, N_y, N_{xy} are section forces and M_x, M_y, M_{xy} are section moments. $N_Y (= \sigma_Y t)$ is the fully plastic section force and $M_Y (= \sigma_Y t^2/4)$ is the fully plastic section moment. t is thickness of a plate.

2.5 Incremental equilibrium equations

2.5.1 $[B]$ matrix and $[G]$ matrix

The relation between incremental strain and incremental nodal displacement Eq. (9) is derived as incremental form of Eq. (7).

$$\{\Delta \varepsilon\} = [B]\{\Delta U\}. \quad (9)$$

where $\{\varepsilon\}$ is strain vector and Δ indicates an increment.

$$\{\varepsilon\} = \left\{ \varepsilon_x \quad \varepsilon_y \quad \gamma_{xy} \quad \kappa_x \quad \kappa_y \quad \kappa_{xy} \right\}^T.$$

$\varepsilon_x, \varepsilon_y, \gamma_{xy}$ are strains and $\kappa_x, \kappa_y, \kappa_{xy}$ are curvatures.

$\{U\}$ is the nodal displacement vector.

$$\{U\} = \left\{ U_1 \quad U_2 \quad U_3 \quad U_4 \quad V_1 \quad V_2 \quad V_3 \quad V_4 \quad WC_3 \quad WS_3 \right\}^T.$$

Deformation gradient matrix $[G]$ is defined as follows.

$$\left\{ \begin{array}{l} \partial \Delta w / \partial x \\ \partial \Delta w / \partial y \end{array} \right\} = [G]\{\Delta U\}$$

2.5.2 [D] matrix

The relation between section force and strain is expressed by Eq. (10).

$$\{\Delta N\} = [D]\{\Delta \epsilon\}. \tag{10}$$

where, $\{N\}$ is section force vector.

$$\{N\} = \left\{ N_x \quad N_y \quad N_{xy} \quad M_x \quad M_y \quad M_{xy} \right\}^T.$$

[D] in Eq. (10) is $[D^e]$ when elastic and $[D^p]$ when plastic. That is,

$$[D^e] = \begin{bmatrix} C & C\nu & 0 & 0 & 0 & 0 \\ C\nu & C & 0 & 0 & 0 & 0 \\ 0 & 0 & C(1-\nu)/2 & 0 & 0 & 0 \\ 0 & 0 & 0 & D & D\nu & 0 \\ 0 & 0 & 0 & D\nu & D & 0 \\ 0 & 0 & 0 & 0 & 0 & D(1-\nu)/2 \end{bmatrix}.$$

where, $C(= Et/(1-\nu^2))$ is the in-plane stiffness of a plate and $D(= Et^3/12(1-\nu^2))$ is the bending stiffness. E is Young's modulus and ν is Poisson's ratio.

$[D^p]$ is derived from plastic flow theory and expressed by Eq. (11).

$$[D^p] = [D^e] - [D^e]\{\Phi\}\{\Phi\}^T/[D^e]\{\Phi\}\{\Phi\}^T. \tag{11}$$

$\{\Phi\}$ is obtained by Eq. (8) as follows.

$$\{\Phi\} = \left\{ \partial\Gamma/\partial N_x \quad \partial\Gamma/\partial N_y \quad \partial\Gamma/\partial N_{xy} \quad \partial\Gamma/\partial M_x \quad \partial\Gamma/\partial M_y \quad \partial\Gamma/\partial M_{xy} \right\}^T.$$

2.5.3 Incremental equilibrium equation

Equilibrium between internal force $\{f\}$ and external force $\{X\}$ is considered at the n -th step by incremental analysis. Unbalanced forces $\{\Psi\}$ of the nodal points are expressed by Eq. (12).

$$\{\Psi\} = \{f\} - \{X\} \rightarrow \{0\}. \tag{12}$$

where,

$$\{f\} = \int_0^a \int_0^b [B]^T \{N\} dy dx,$$

$$\{X\} = \left\{ X_1 \quad X_2 \quad X_3 \quad X_4 \quad Y_1 \quad Y_2 \quad Y_3 \quad Y_4 \quad Z_{C3} \quad Z_{S3} \right\}^T.$$

$X_1 \sim Y_4$ are the nodal forces, Z_{C3} and Z_{S3} are the corresponding forces for W_{C3} and W_{S3} .

In order to solve nonlinear equation Eq. (12) so as to diminish unbalanced forces $\{\Psi\}$, incremental form of Eq. (12) is derived below. When increments of the external forces are assumed constant at each incremental step, increments of the nodal displacements $\{\Delta U\}$ shall be obtained from Eq. (13).

$$\{\Delta \Psi\} = \int_0^a \int_0^b [B]^T \{\Delta N\} dy dx + \int_0^a \int_0^b [\Delta B]^T \{N\} dy dx = ([K_L] + [K_G])\{\Delta U\}. \tag{13}$$

where $[K_L]$ is initial displacement matrix and $[K_G]$ is initial stress matrix, which are shown as,

$$[K_L] = \int_0^a \int_0^b [B]^T [D] [B] dy dx,$$

$$[K_G] = \int_0^a \int_0^b [G]^T [S] [G] dy dx.$$

$[S]$ is stress matrix defined by the following equation.

$$[S] = \begin{bmatrix} N_x & N_{xy} \\ N_{xy} & N_y \end{bmatrix}.$$

Being solved nonlinear equation Eq. (12) by Newton-Raphson method, the equilibrium state at a considered incremental step can be achieved[8].

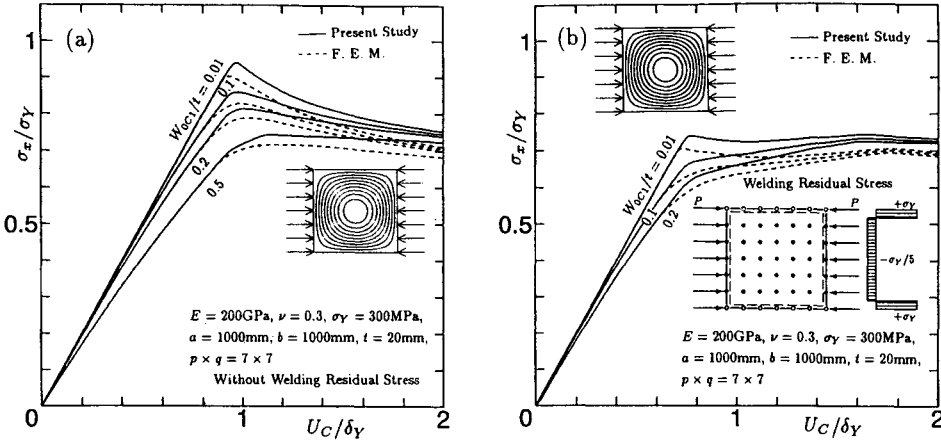


Figure 3: Load-displacement curves of square plates subjected to compression. (a) With initial deflection. (b) With initial deflection and welding residual stress.

3 Examples of this method

To demonstrate applicability of the present method, some examples will be analyzed, which are rectangular plates shown in Fig. 1. The material properties of the plates are Young's modulus $E = 200$ [GPa], Poisson's ratio $\nu = 0.3$, yielding stress $\sigma_Y = 300$ [MPa] and of no strain hardening. The examples analyzed by this method are compared with those by FEM. The proposed method is required less than 1/100 of necessary computation time by using FEM. And it is found that consuming time by this method is mainly for numerical integration.

3.1 Compressive strength of a square plate with initial imperfections

First, the accuracy of this method is examined by analyzing compressive strength of square plates with initial deflection $W_{0C_1}/t = 0.01, 0.1, 0.2,$ and 0.5 . Numerical integration is performed by the trapezoidal integration method for both x and y directions and the number of integration points of the plate is $7 \times 7 = 49$ points. Only E_{C_1} is necessary to consider for a selective eigen-function. Figure 3 (a) shows load-displacement curves, which are compared with those of FEM for various initial deflections. The results indicate good accuracy even in elasto-plastic region

Compressive behaviour of square plates with various initial deflections and welding residual stresses are analyzed for the second example. Residual stresses are uniform along the longitudinal direction and keep equilibrium in tension and compression. The points indicated by \circ and \bullet in Fig. 3 (b) are the integration points. The magnitude of welding residual stress is assumed tensile yield stress $+\sigma_Y$ at points indicated by \circ along the upper and lower edges and $-\sigma_Y/5$ at points \bullet in the middle part of the plate. It is found from Figs. 3 (a) and (b) that ultimate loads decrease with welding residual stress, but when compressive displacement becomes larger post ultimate strength is almost same in both cases regardless the existance of welding residual stresses.

It is clear from these examples that the ultimate strength and the post ultimate strength with initial imperfections can be obtained with good accuracy by the present method.

3.2 Elasto-plastic strength of a rectangular plate subjected to compression and shear

Elasto-plastic analysis is performed on rectangular plates of aspect ratio being 3 subjected to compression and shear. Selective eigen-functions are E_{C_3} and E_{S_3} and the deflection of the plate is given by Eq. (14).

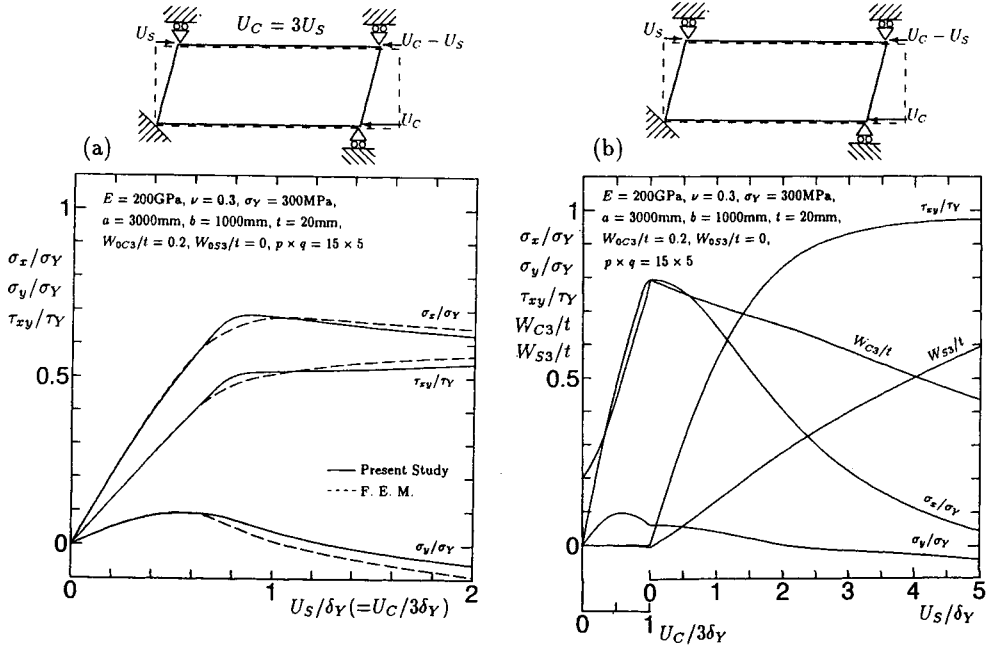


Figure 4: Rectangular plate subjected to compression and shear ($a/b = 3$).

$$w = W_{C3}E_{C3} + W_{S3}E_{S3} \tag{14}$$

Coefficients of the selective eigen-functions E_{C3} and E_{S3} in Eq. (14) are shown in Fig. 2. Initial deflections for eigen-functions are $W_{0C3}/t = 0.2$ and $W_{0S3}/t = 0$. Figure 4 (a) shows the case under compression and shearing. The present element can express large deflection elasto-plastic behavior of a rectangular plate only one element having 4 nodes.

Figure 4 (b) is a case where the plate is subjected to compressive displacement at the first stage, and shear displacement at the second stage being kept the compressive displacement constant. At the second stage the average shear stress τ_{xy} increases with the increasing shear displacement, but the average axial stress σ_x decreases. It is also found that eigen-function W_{C3} for compression decreases with holding the same compressive displacement and increasing the shear displacement.

It is found from these examples that by this element elasto-plastic behavior of a rectangular plate with large deflection can be analyzed efficiently and accurately under various combination of inplane axial force and shearing force.

4 Conclusion

The following conclusions are obtained by proposing the new method for analysis of nonlinear behaviour of thin plates and showing some examples.

1. A new element is developed by using appropriate selective eigen-functions and sectional yielding condition for integration points. By this method elastic-plastic buckling behavior of a rectangular plate element with large deflection can be analyzed efficiently and accurately under various combined loading of compressive and shearing forces.

2. Initial imperfections such as initial deflection and welding residual stress are taken into account easily in this method.
3. For analysis, this method needs a very short time and it takes less than 1/100 of necessary computation time by using FEM.
4. The element developed by this method can be used as a very efficient rectangular plate element of the Idealized Structural Unit Method.

References

- [1] Ueda, Y. and Rashed, S.M.H.: The Idealized Structural Unit Method and its applications on deep girder structures, *Computer and Structures*, Vol. 18, (1984).
- [2] Ueda, Y., Rashed, S.M.H., Nakacho, K. and Sasaki, H.: Ultimate Strength Analysis of Offshore Structures — Application of Idealized Structural Unit Method —, *J. Kansai Soc. N.A.*, Japan, No. 190, (1983), (in Japanese).
- [3] Ueda, Y., Rashed, S.M.H. and Abdel-Nasser, Y.: An improved ISUM rectangular plate element: Taking account of post-ultimate strength behavior, *Journal of Soc. of Naval Architecture of Japan*, Vol. 171, (1992).
- [4] Masaoka, K., Okada, H. and Ueda, Y.: Estimating Method of Buckling Strength of Rectangular Plates Using Selected Eigen-functions, *Proc., ISOPE'96, IV*, 341–346, (1996)
- [5] Ueda, Y., Umemoto, K. and Masaoka, K.: Elasto-plastic Large deflection analysis of beam-columns and rectangular plates by using plastic node method, *Journal of SNAJ*, Vol.171, (1992).
- [6] Masaoka, K., Rashed, S.M.H. and Ueda, Y.: An efficient method of buckling analysis of rectangular plates, *Journal of SNAJ*, Vol. 172, (1992), (in Japanese).
- [7] Robinson, M.: A comparison of yield surfaces for thin shells, *Int. J. Mech. Sci.*, Vol. 13, 1971.
- [8] Zienkiewicz and Taylor: *The finite element method*, 4th edition, Vol.2, McGraw-Hill, 1989.

GENERAL SOLUTION FOR C-SHAPED BELLOWS OVERALL-BENDING PROBLEMS

W. P. Zhu, Q. Huang, P. Guo and W. Z. Chien

Shanghai Institute of Applied Mathematics and Mechanics, Shanghai University
149 Yanchang Road, Shanghai, 200072, P. R. CHINA

ABSTRACT

Equations for overall-bending problems of slender ring shells are presented based on E. L. Axelrad's equations of shells of revolution with small deflection under asymmetrical loading. It turns out that the equations are analogous to that of simplified Novzhilov's equations of symmetrical ring shells, where general solutions have been given by W. Z. Chien. Hence, by analogy with Chien's solution, the authors put forward a general solution for the equations and use it to calculate the angular displacements and stresses for C-shaped bellows under bending moments.

KEYWORDS

shells of revolution, circular ring shells, slender ring shells, bellows

INTRODUCTION

Bellows, with profiles such as toroidal, C-shaped and U-shaped, are composed of sections of circular ring shells and ring plates, and their solutions can be attributed to the solutions of ring shells. The research for symmetrical circular ring shells began early in this century. The general solutions for slender shells (shells with ratio $\alpha = b / R_m \ll 1$, where b is the radius of ring shell section and R_m is the radius of the whole shell) and for circular ring shells based on Novzhilov's equations of complex variables were given by W. Z. Chien^[2,3] in 1979 and 1980, which are continuity and convergence at every point within the full range as well as cope with the boundary conditions of ring shells. By means of the solutions, Chien^[4,5] also successfully solved the related bellows problems in 1981. After that, in 1986, Q. Huang^[6,7] presented a system of first-order differential equations and a numerical method for shells of revolution with large axial deflections to tackle the nonlinear problems of

axisymmetrically loaded ring shells and bellows. Concerning the asymmetrical problems, E. L. Axelrad^[1] in 1976 systematically introduced the equations and calculations for shells of revolution and bellows. To dispose the equations, Axelrad used the theory of flexible shells, which simplifies the equations and accords with the formation of shells like bellows. To solve the equations, under the condition of small deflection, Axelrad presented perturbation method and trigonometric-series method etc. Based on Axelrad's equations with small deflection, Ref. [8] (1992) calculated the overall-bending rigidity for S-shaped bellows by using shooting method. In engineering, the calculation of bellows, such as adopted by EJMA^[9] (1993), uses the principle of equivalent axial rigidity to appraise the angular and lateral rigidities.

In this paper, firstly the equations for overall-bending problems of slender ring shells are presented based on Axelrad's equations of shells of revolution with small deflection under asymmetrical loading. As it happens, the equations are analogous to that of simplified Novzhilov's equations of symmetrical ring shells, where the general solutions have been given by W. Z. Chien. Then following Chien's approach, the authors put forward a general solution for the equations, naturally, which satisfies the full range and boundaries of the problem. Finally, by using the solution, we calculate the angular displacements and stresses for C-shaped bellows under bending moments.

COMPLEX EQUATIONS OF SLENDER RING SHELLS OVERALL-BENDING IN A MERIDIAN PLANE

The geometry of an opened slender circular ring shell with constant thickness and its coordinates and loading are shown in Figure 1. We assume that the shell is flexible and its deflection is small. The loading on the shell given by the equivalent bending moment L_y and transverse force P_x , are symmetric with respect to the plane $\theta = 0$, that is to say, the shell undergoes overall-bending in the meridian plane $\theta = 0$. Comparing the geometry of this shell with that of shells of revolution described by Axelrad^[1], we can let b in Axelrad's formation to be the radius of ring shell section and R_m to be the radius of the whole shell; then $d(\)/d\eta = d(\)/d\psi$ and

$$R = R_m + b \cos \psi . \tag{1}$$

Besides, according to Love-Kirchhoff hypothesis and for the slender ring shells, the terms

$$\frac{h}{b}, \frac{h}{R}, \frac{hR_m}{bR}, \alpha = \frac{b}{R_m} \tag{2}$$

can be neglected as being small when compared to 1. Therefore, the equations for overall-bending problems of slender ring shells can be expressed by complex variables as follows:

$$\frac{d^2V}{d\psi^2} + 2i \mu \cos \psi V = P_x^0 \cos \psi - L_y^0 \sin \psi , \tag{3}$$

where $V = \chi + iT$ is the auxiliary complex function. Its real part χ and imaginary part T are respectively displacement and force functions which are defined by

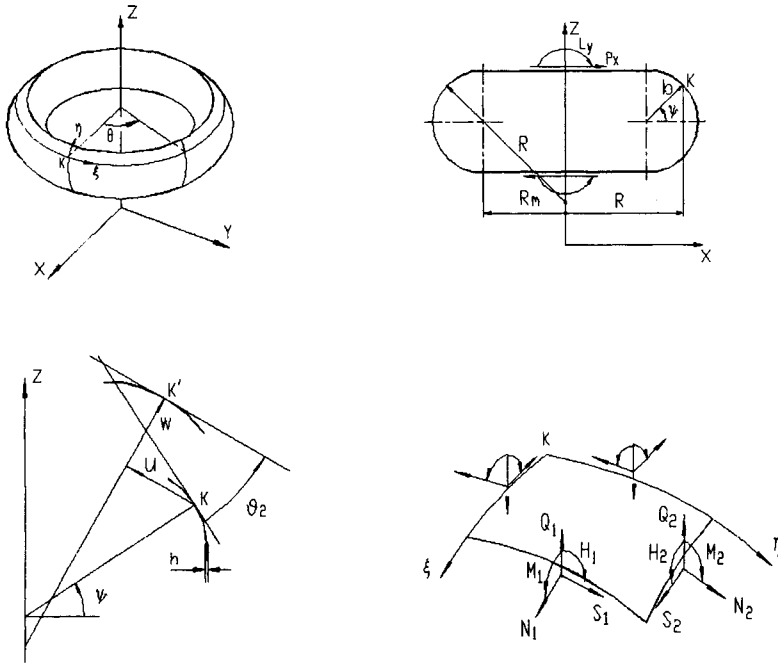


Figure 1: Circular ring shell overall bending in a meridian plane

$$\chi = \vartheta_2^1 - \frac{u_z^1}{R} \tag{4}$$

and

$$T = V_1^1 \sqrt{12(1-\nu^2)} \frac{1}{E h^2}, \quad \frac{d}{bd\psi} (RV_1^1) = RN_1^1 + M_1^1 \cos \psi, \tag{5}$$

in which $\vartheta_2^1, u_z^1, N_1^1$ and M_1^1 are that of ϑ_2, u_z (the resultant of u and w on axis z), N_1 and M_1 in Fig. 1 when $\theta = 0$.

And the expressions for μ, P_x^0 and L_y^0 are

$$2\mu = \sqrt{12(1-\nu^2)} \frac{b^2}{hR_m}, \tag{6}$$

$$P_x^0 = \frac{b^2}{\pi DR_m} P_x, \quad L_y^0 = \frac{b^2}{\pi DR_m^2} L_z, \quad (D = \frac{E h^3}{12(1-\nu^2)}). \tag{7}$$

The related internal forces may be expressed as

$$\begin{aligned}
 [N_1 \quad N_2 \quad M_1 \quad M_2 \quad Q_2] &= [N_1^1 \quad N_2^1 \quad M_1^1 \quad M_2^1 \quad Q_2^1] \cos \theta, \\
 [S_1 \quad S_2 \quad H_1 \quad H_2 \quad Q_1] &= [S_1^1 \quad S_2^1 \quad H_1^1 \quad H_2^1 \quad Q_1^1] \sin \theta,
 \end{aligned}
 \tag{8}$$

where

$$\begin{aligned}
 \frac{bM_1^1}{D} &= \nu \frac{d \operatorname{Re} V}{d\psi}, & \frac{bM_2^1}{D} &= \frac{d \operatorname{Re} V}{d\psi}, & \frac{bH^1}{D} &= -\alpha(1-\nu) \operatorname{Re} V, \\
 \frac{bN_1^1}{K} &= \frac{d \operatorname{Im} V}{d\psi}, & \frac{bN_2^1}{K} &= -\alpha \operatorname{Im} V \sin \psi - \frac{\alpha L_y^0}{2\mu} \cos \psi, \\
 \frac{bS_1^1}{K} &= \alpha \operatorname{Im} V, & \frac{bQ_2^1}{K} &= \alpha \operatorname{Im} V \cos \psi - \frac{\alpha L_y^0}{2\mu} \sin \psi,
 \end{aligned}
 \tag{9}$$

$$(H = \frac{H_1 + H_2}{2}, \quad S = S_1 - \frac{H_2}{R_2} = S_2 - \frac{H_1}{R_1}),$$

$$(K = \frac{E h^2}{\sqrt{12(1-\nu^2)}}).$$

The stresses on outside (inside) surface of shells may be written as

$$[\sigma_1, \sigma_2] = [\sigma_1^1, \sigma_2^1] \cos \theta, \quad [\sigma_{12}, \sigma_{21}] = [\sigma_{12}^1, \sigma_{21}^1] \sin \theta,
 \tag{10}$$

where

$$\sigma_1^1 = \frac{N_1^1}{h} \pm \frac{6M_1^1}{h^2}, \quad \sigma_2^1 = \frac{N_2^1}{h} \pm \frac{6M_2^1}{h^2}, \quad \sigma_{12}^1 = \sigma_{21}^1 = \frac{S_1^1}{h} \pm \frac{6H_1^1}{h^2}.
 \tag{11}$$

And the displacements may be described as

$$[\vartheta_2, u_z] = [\vartheta_2^1, u_z^1] \cos \theta,
 \tag{12}$$

where

$$\vartheta_2^1 = \operatorname{Re} V|_{\psi_1}^{\psi} - \alpha \int_{\psi_1}^{\psi} \operatorname{Re} V \sin \psi d\psi + \vartheta_2^1(\psi_1), \quad \frac{u_z^1}{R} = -\alpha \int_{\psi_1}^{\psi} \operatorname{Re} V \sin \psi d\psi.
 \tag{13}$$

In practice, such shells as curved-tubes and bellows can be treated as the slender ring shells. Eqs. (3) and (8) to (13) may be used to calculate the overall bending of slender ring shells in a meridian plane

under pure bending moments and transverse forces. There are some other forms of equation for slender ring shells, for examples, Meissner-type equations^[1] which can be solved by the perturbation or trigonometric-series methods and a set of first-order differential equations^[8] which are suitable for numerical methods. The advantage of equation (2) is that it is analogous to simplified Novzhilov's complex equation for axisymmetrical ring shells and the general solutions given by Chien^[2] not only continue and converge in the full range of ring shells but also satisfy with the boundary conditions. So, it is convenient to present a general solution equation (2) to solve the bellows problem.

GENERAL SOLUTION FOR SLENDER RING SHELLS OVERALL BENDING UNDER PURE BENDING MOMENTS

In this case, we have $P_x = 0$ in Fig. 1 and Eq. (3). The simplified Novzhilov's equation of axisymmetrical slender ring shells tackled by Chien^[2] is

$$\frac{d^2V}{d\varphi^2} + 2i \mu \sin \varphi V = 2\mu P_0 \cos \varphi. \tag{14}$$

In order to compare with Chien's solutions, we let $\psi = \pi/2 - \varphi$. As a result, $L_y^0(\varphi) = -L_y^0(\psi)$; and Eq. (3) becomes

$$\frac{d^2V}{d\varphi^2} + 2i \mu \sin \varphi V = L_y^0 \cos \varphi; \tag{15}$$

It is obvious that Eqs. (14) and (15) are of the identical type and share the same solutions if only substituting the constant coefficient L_y^0 for $2\mu P_0$. Hence, according to Chien's results, we have the non-homogeneous solution of Eq. (15) as follows:

$$V^* = -\frac{L_y^0}{\mu} \{A_1 \cos \varphi + A_2 \sin 2\varphi - A_3 \cos 3\varphi - A_4 \sin 4\varphi + A_5 \cos 5\varphi + A_6 \sin 6\varphi - A_7 \cos 7\varphi - A_8 \sin 8\varphi + \dots\}. \tag{16}$$

And the homogeneous equation and its solution related to Eq. (15) or (14) can be expressed as

$$\frac{d^2V}{d\varphi^2} + \mu(e^{i\varphi} - e^{-i\varphi})V = 0. \tag{17}$$

$$V^0 = [C_0' + i\bar{C}_0']e^{-\lambda(\varphi_2 - \varphi)}[f_1(\varphi) + i f_2(\varphi)] + [B_0' + i\bar{B}_0']e^{-\lambda(\varphi - \varphi_1)}[g_1(\varphi) + i g_2(\varphi)]. \tag{18}$$

In Eq. (16), the coefficients A_1, A_2, A_3, \dots are functions dependent upon μ (defined by Eqs. 6) and determined by a set of recursion formulae with limit of zero, so the solution V^* converges absolutely. The formation of the homogeneous solution in Eq. (18) is convenient for boundary problems, in which λ is a real index dependent upon μ ; $f_1(\varphi), f_2(\varphi), g_1(\varphi)$ and $g_2(\varphi)$ are real functions in the form of

trigonometric series, (A detailed discussion is given in Ref. 2); C_0' , \bar{C}_0' , B_0' and \bar{B}_0' are real constants to be determined by boundary conditions; $\varphi = \varphi_1$ and $\varphi = \varphi_2$ are two boundaries of the shell. Finally, combining Eqs. (16) with (18), we obtain the general solution for the problem of slender ring shells in a meridian under pure moments as follows:

$$V = V^* + V^0 . \tag{19}$$

CALCULATION FOR C-SHAPED BELLOWS OVERALL BENDING IN A MERIDIAN PLANE

By means of the general solution presented above, we can calculate the angular displacements and stresses for C-shaped bellows under pure bending moments. As shown in Fig. 2, C-shaped bellows are composed of semi-circular ring shells with positive and negative curvatures, in which $\alpha = b / R_m$ is small (about 0.1, or still less) as usual, so it is practical to deal with the bellows as slender ring shells in calculation.

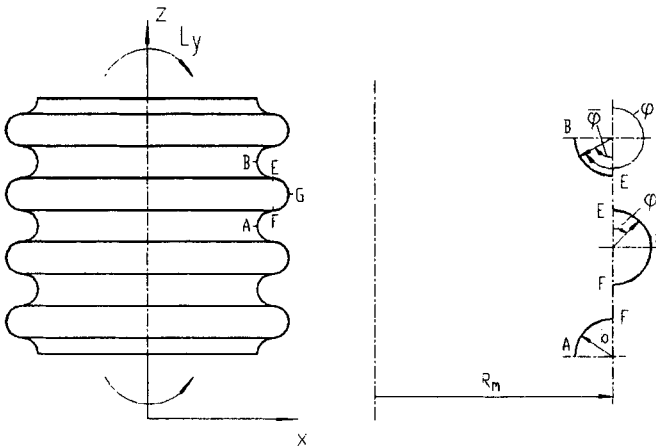


Figure 2. Overall bending C-shaped bellows under pure moments

We now take a convolution AFGBE from the bellows to investigate. Because the convolution is symmetrical with respect to point G, we can take half of it, say, the upper segment BEG into consideration. Divide BEG into two segments BE and EG (called part I and part II); and set up two angular coordinates φ and $\bar{\varphi}$ ($\bar{\varphi} = \varphi - \pi$), shown in Fig. 2, for each part. Eqs. (15), (16), (18) and (19) take the responsibility for each part. The solution for each part, denoted by V_I and V_{II} , contains four integral constants (see Eq. 18), so there are altogether eight undetermined constants. Using the conditions of symmetry with respect to point G, the number of undetermined constants will be reduced to four, and they can be calculated properly by the continuity condition of N_1^I , N_2^I , M_2^I and u_2^I / R at point G ($\varphi = \bar{\varphi} = 0$).

Now, we calculate the rotation angle of cross sections A relative to cross section B i. e., the rotation angle of a convolution. This angle equals two times the angle of cross section B rotates with respect to G. Hence, by using Eq. (13) to segments BE and EG (part I and part II) respectively and then putting them together, we get the rotation angle of a convolution as follows:

$$\Omega_y = -2\alpha \left[\int_0^{\frac{\pi}{2}} \operatorname{Re} V_I \cos \varphi d\varphi + \int_0^{\frac{\pi}{2}} \operatorname{Re} V_{II} \cos \bar{\varphi} d\bar{\varphi} \right]. \tag{20}$$

EXAMPLE

Suppose a C-shaped bellows has following sizes, material properties and loading:

$$R_m = 176.0\text{mm} , \quad b = 43.5\text{mm} , \quad h = 1.40\text{mm} ; \quad E = 200 \times 10^3 \text{MPa} , \quad \nu = 0.3 , \quad L_y = 855\text{N.m.}$$

Using the method presented in this paper, we have the results: The character parameters are $\alpha = 0.247$, $\mu = 12.689$. The rotation angle of a convolution is $\Omega_y = 0.45^\circ$. The stresses distribution on outside surface of bellows are shown in Fig. 3.

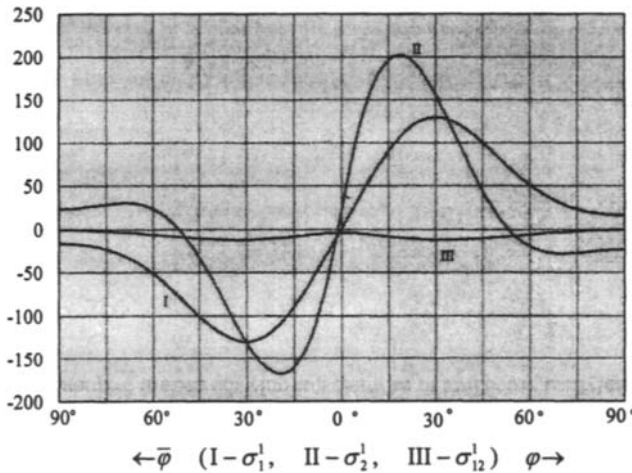


Fig. 3. Stresses distribution on outside surface of the bellows (stress unit: MPa)

Evidently, in the problem, the stresses are symmetrical with respect to the meridian plane of $\theta = 0^\circ$ and in the symmetrical plane the stresses ($\sigma_{12} = \sigma_{21} = 0$) are analogous to that of axial symmetry problems. Thus, as it should be, σ_1^I , σ_2^I in Fig. 3 have the same patterns as that of axial symmetry problems in Ref. 5. But, the essential distinction of our problem is that in-plane shearing stresses σ_{12} (or σ_{21}) exist and vary with circumferential angle θ in sine curve; whereas normal stresses vary with θ in cosine curve; besides, transverse shearing stresses in direction of radius of ring sections exist and can be calculated, however, their effects are comparatively small and will not be considered here.

CONCLUSION

In this paper, a proper equation and its solution are found for the problem of bellows overall-bending under small elastic deflection by enlarging the application of Chien's slender ring shells theory.

The accuracy of the general solution for slender ring shells has been discussed in Ref. 4, which has indicated that the solution is accurate enough to calculate the ring shells with α so large as to reach about 0.25. Thus, a lot of concerned practical problems may be solved by the method presented in this paper.

Using this method, the authors have also calculated the overall-bending problems of bellows with other profiles such as Ω -shaped and U-shaped. The results will be presented in other papers.

REFERENCES

1. Axelrad E. L. (1976). *Flexible Shells*, Izdatielstvo Nauka, Moscow (in Russian)
2. Chien W. Z. (1979). Equations of Axisymmetrical Shells in Complex Quantities and Their General for Slender Ring Shells. *J. of Qing Hua University* **19**: 1, 27-47. (in Chinese)
3. Chien W. Z. (1980). General Solution for Axisymmetrical Circular Ring Shells. *Applied Mathematics and Mechanics* **3**: 3, 287-299 (in Chinese)
4. Chien W. Z. (1980). Non-homogeneous Solutions of Slender Ring Shell Equation and Their Applications in Instrumental Design. *J. of Instruments and Meters* **1**, 89-112 (in Chinese)
5. Chien W. Z. (1981). Calculations for C-shaped Bellows — an Application of the General Solution for Ring Shells. *Applied Mathematics and Mechanics* **2**: 1, 97-111 (in Chinese)
6. Huang Q. (1986). On the Problem of Axisymmetrically Loaded Shells of Revolution with Small Strains and Arbitrarily Large Axial Deflections. *Applied Mathematics and Mechanics* **7**: 2, 115-125 (in Chinese)
7. Huang Q. (1986) Perturbation Initial Parameter Method for Solving the Geometrical Nonlinear Problem of Axisymmetrical Shells. *Applied Mathematics and Mechanics*. **7**: 6, 533-543 (in Chinese)
8. Skoczen B. and Skrzypek J. (1992). Application of the Equivalent Column Concept to the Stability of Axially Compressed Bellows. *int. J. Mech. Sci.* **34**: 11, 901-916
9. Standards of the Expansion Joint Manufacturers Association (EJMA) Inc. (6 edn). EJMA, New York, 1993

Advanced Inelastic Analysis of Thin-Walled Core-Braced Frames

J Y Richard Liew, H Chen, C H Yu and N E Shanmugam

Department of Civil Engineering, National University of Singapore,
10 Kent Ridge Crescent, Singapore 119260

ABSTRACT

This paper presents the advanced inelastic analysis theory for nonlinear analysis of thin-walled core-braced frames. It focuses on a second-order plastic hinge method for studying the nonlinear behaviour of space steel frames comprising of internal core walls. The steel frameworks surrounding the building core walls are modelled by using the inelastic frame element. The core walls are modelled as thin-walled frame elements. An Updated Lagrangian approach is used to describe the motion of elements. Nonlinear solution methods and numerical strategies for computer implementation are presented. Numerical examples are provided to verify the proposed nonlinear analysis theory and the computer package. Finally, a 24-storey thin-walled core-braced frame is analysed using the advanced inelastic analysis program, and the inelastic behaviours of the core-braced frame are studied.

KEYWORDS

Advanced inelastic analysis, buckling, instability, second-order, geometrical and material nonlinearities, plastic hinge, frame element, thin-walled frame element.

1. INTRODUCTION

The past few decades have witnessed intensive research efforts towards the development of advanced inelastic analysis tools which are capable of predicting the nonlinear responses of steel framework. Although theory and computational methods for advanced inelastic analysis of plane frames have been well developed (Liew et al., 1993 and 1994; Chen et al., 1994 and 1996), additional research works are still required for inelastic analysis of space frames (Orbison, 1982; Ziemian et al., 1992; and Liew, 1997). Moreover, "exact" methods for analysing steel-concrete composite building system (Liew, 1995), which is a more efficient and economical structural system compared to pure steel frame system, are not yet well established. Analytical models to evaluate the nonlinear system responses of composite structures are generally not available. Many of the nonlinear analysis tools previously developed for analysing pure steel frame system are not directly applicable to the composite system.

Composite building system can be broadly categorised into two forms (Liew, 1995): one utilises the core-braced system by means of interior shear walls, and the other utilises exterior framing to form a tube for lateral load resistance. Taller buildings can be constructed by combining the two structural forms together. Conventional methods to analyse and design the core-braced frame rely on elastic analysis and member capacity check based on semi-empirical equations, considering approximately the stability and inelastic interaction between member and frame behaviour by using a column effective length procedure. However, the method will not be adequate in estimating the strength and stability of individual members in the framework with interaction effects from core walls. Extensive research (Liew et al., 1997; Chen et al., 1997) is currently underway to develop advanced inelastic analysis tools for capturing the nonlinear behaviour of core-braced frames.

Core-braced frames mainly consist of five types of structural components: beam, column, core wall, joint and slab. In the proposed approach, steel beams and columns are modelled as inelastic frame elements. Core walls provide a major part of the bending and torsional resistance in a building structure; they are modelled by using thin-walled frame elements for their proportional similarity to Vlasov's thin-walled beams (Liew et al., 1997; Chen et al., 1997). The centre line of the core wall is located on the shear centre axis. Any significant twisting action should be analysed to include both warping and torsional effects. Semi-rigid beam-to-column connections can be modelled as rotational spring elements. For normal building frameworks, floor slab can be modelled as rigid diaphragm, which is assumed to provide infinite in-plane stiffness and without any out-of-plane stiffness. The detailed formulation that incorporates the diaphragm action is given in Liew et al. (1997). The analytical methods described in this paper can be used to analyse 3-D frameworks with or without rigid floor diaphragm. However, it is important to model the flexibility of the floor slab for building frames with complex floor geometry or with lateral braces. Currently only a limited number of frame modelling packages allow the definition of flexible floor slab.

Geometrical nonlinearities (second-order effects) are modelled through the use of a geometric stiffness matrix and an Updated Lagrangian approach. Material nonlinearities (inelastic effects) of frame elements are modelled by using a concentrated elastic-plastic hinge formulation (Orbison, 1982; Liew et al., 1993 and 1997; Chen et al., 1994 and 1996). Material nonlinearities of core walls are considered approximately. Updating of element forces is based on the natural displacement approach which is consistent with the Updated Lagrangian approach and the plastic hinge formulation. Arc-length method combined with adaptive load increment controlling strategies is used as the solution method. Non-proportional loading sequences can be performed. The methodology presented in this paper and the computer implementation are verified using a number of examples. The nonlinear behaviour of a 24-storey core-braced frame is investigated using the proposed analysis theory and computer program.

2. FINITE ELEMENT FORMULATION

The frame element has twelve degrees-of-freedom. The thin-walled frame element has an additional warping degree-of-freedom at each element end. The development of the stiffness matrices of both elements starts from a fundamental virtual work equation based on the Updated Lagrangian approach, adopts basic assumptions of engineering beam theory and Vlasov's thin-walled beam theory respectively, uses standard finite element procedures, and considers the coupling effects between axial, flexural and torsional deformations. The detailed derivations for the elastic and geometric stiffness matrices ($[k_e]$ and $[k_g]$) of both elements are given by Liew et al. (1997). Transverse shear deformation effects are included by modifying the moments of inertia in the elastic stiffness matrices. The geometric stiffness matrix of thin-walled frame element is composed of two parts. The first part is for the doubly symmetric thin-walled sections. The second part is for generic sections that the shear centre and the centroid may not be at the same point, or the principal axes are inclined to the section axes.

Material nonlinearities are modelled by using the elastic-plastic hinge formulation (Orbison, 1982; Liew et al., 1993; Liew, 1997; Chen et al., 1994 and 1996). The element is assumed to remain elastic except at places where zero-length plastic hinges are allowed to form. A three-parameter plastic strength surface proposed by Orbison (1982) is used to model the plastic behaviour of steel beam-columns with wide flange section. Special algorithms (Liew et al., 1997) have been developed to deal with the numerical problems associated with elastic unloading at plastic hinges, pure axial plasticity, plastic hinges at common node adjoining two elements, and internal plastic hinge forming between element ends. It is recognised that the accuracy is reasonable only for the cases where spread of plasticity is not significant and where material stress-strain law is essentially elastic-perfectly-plastic without strain-hardening. Otherwise, the spread-of-plasticity approach must be used. Alternatively, an approximate method based on the refined plastic hinge approach (Liew et al., 1993; Liew, 1997; Chen et al., 1994 and 1996) or a force compensation method by the notional load approach (Liew et al., 1994; Chen et al., 1994 and 1996) may be used in lieu of the spread-of-plasticity analysis to capture member strength and stability.

Because the height-to-width ratio of core walls is large and the axial force respective to the sectional area is small in practical building frames, material nonlinearities of core walls are considered approximately, assuming that the plastic strength is controlled by bending action only. The locations of the shear centre and the centroid of cross-section are assumed not to change due to the inelastic effects.

In the Updated Lagrangian procedure, the incremental equilibrium equation of frame and thin-walled frame elements can be expressed as

$$\left([k_e] + [k_g] + [k_p] \right) \{du\} = [k_t] \{du\} = \{df\} \quad (1)$$

in which $\{du\}$ is the incremental displacement vector; $\{df\}$ is the incremental force vector; and $[k_e]$, $[k_g]$, $[k_p]$, and $[k_t]$ are the elastic, geometric, plastic reduction and tangent stiffness matrices respectively. Depending on the analysis type (e.g. first-order or second-order, elastic or inelastic), $[k_e]$ and $[k_p]$ may or may not be included in the analysis.

The structure incremental equilibrium equation is written as

$$[K_t] \{dU\} = \{dP\} \quad (2)$$

in which $\{dU\}$ is the structure incremental displacement vector, $\{dP\}$ is the incremental load vector applied on the structure, and $[K_t]$ is the structure tangent stiffness matrix obtained by assembling all the transformed element tangent stiffness matrices together. The kinematic relations between core walls, floor diaphragm and the adjoining beams and columns are derived in order to establish the transformation matrices for the assembly of element tangent stiffness matrices in the global coordinate system (Liew et al., 1997)

3. SOLUTION METHODS

Arc length method (Crisfield, 1981) combined with adaptive load increment controlling strategies (Liew et al., 1997; Chen et al., 1997) is implemented to perform the nonlinear analysis. In the solution method, loads can be applied either proportionally or non-proportionally. The incremental loading is described by a series of different and subsequent load vectors. Each load vector is formed by one basic load case or a combination of several basic load cases, and a load ratio that defines the relative size of the load increment. Each load vector is repeated for a given number of load steps, or until a specified

relative load level is reached. The load increment is added on to the previous loads. The total series of load vectors then form the loading history of the analysis.

The sign of load increment is governed by the determinant of structure tangent stiffness matrix and the current stiffness parameter S_p (Bergan, 1978). The current stiffness parameter is a normalised parameter that represents the stiffness of structure during deformation. It has an initial value of unity. The value increases as structure gets stiffer, and decreases as structure becomes softer. A global instability point or a bifurcation point is signified by zero current stiffness parameter or zero determinant of structure tangent stiffness matrix. Load increment increases as long as S_p is positive and the structure stiffness matrix has no negative pivot element, and decreases if S_p is negative and the structure stiffness matrix has one or more negative pivot elements. The size of load increment is determined by arc-length method together with the load increment control using the following criteria (Liew et al., 1997; Chen et al., 1997): a) constraint on the maximum incremental displacement; b) load increment control due to the formation of plastic hinges; c) constraint of force point movement on the plastic strength surface.

4. NUMERICAL EXAMPLES

The advanced inelastic analysis theory and computer program have been verified in terms of robustness, accuracy and efficiency by using a number of examples (Liew et al., 1997; Chen et al., 1997) including both geometric and material nonlinear effects. In this section, the lateral-torsional instabilities of columns and beams with thin-walled sections are studied by using the proposed thin-walled frame element.

Buckling of column with channel-shaped sections

Fig. 1a shows the channel-shaped section which is symmetric about z-axis. Section and material properties are: sectional area $A = 6.0E3 \text{ mm}^2$; torsional constant $J = 2.0E5 \text{ mm}^4$; moments of inertia about the principal z and y axes, $I_z = 9.0E7 \text{ mm}^4$ and $I_y = 1.406E7 \text{ mm}^4$, respectively; warping constant $C_\omega = 2.215E11 \text{ mm}^6$; the distance between the shear centre and centroid is $z_0 = 93.75 \text{ mm}$; modulus of elasticity $E = 200.0 \text{ kN/mm}^2$; and shear modulus $G = 80.0 \text{ kN/mm}^2$. The buckling load of simply supported columns with monosymmetric section under axial compression load can be determined by the lowest of the following three loads (Trahair, 1993)

$$P_1 = P_y, \quad P_{2,3} = \frac{(P_x + P_z) \pm \sqrt{(P_x + P_z)^2 - 4P_x P_z r_0^2 / (r_0^2 + z_0^2)}}{2r_0^2 / (r_0^2 + z_0^2)} \quad (3, 4)$$

in which L = length of column, $r_0^2 = (I_y + I_z) / A$, $P_x = (GJ + \pi^2 EC_\omega / L^2) / (r_0^2 + z_0^2)$, $P_y = \pi^2 EI_y / L^2$, and $P_z = \pi^2 EI_z / L^2$.

Fig. 1b shows that the buckling loads predicted by modelling the column as one thin-walled frame element are consistent with the theoretical values obtained by Eqns. 3 & 4. It can be seen from Fig. 1b that the column buckles in a flexural mode about y-axis at P_y if the column length is long, or in a flexural-torsional mode by flexure about z-axis and torsion about x-axis at the lower of P_2 and P_3 if the column length is short. The mode changes at $L = 4565 \text{ mm}$.

Lateral-torsional buckling of cantilever beam with I-section

A cantilever beam with I-section shown in Fig. 2a is subjected to a load P at its tip. All degrees-of-freedom including warping are restrained at the support. Section and material properties are: $A = 1.962E4 \text{ mm}^2$, $J = 3.403E6 \text{ mm}^4$, $I_z = 8.660E8 \text{ mm}^4$, $I_y = 1.563E7 \text{ mm}^4$, $C_\omega = 1.338E12 \text{ mm}^6$, $E = 206.0$

kN/mm², and $G = 79.23$ kN/mm². The theoretical elastic lateral-torsional buckling load is given by (Trahair, 1993)

$$P_{cr} = \frac{\sqrt{EI_y GJ}}{L^2} \left(3.95 + 3.52 \sqrt{\frac{\pi^2 EC_w}{GJL^2}} \right) = 47.22 \text{ kN} \quad (5)$$

To study the lateral-torsional buckling behaviour, an imperfection load $0.01P$ is applied at the free end in the Y-direction. The cantilever beam is modelled using two, four and eight thin-walled frame elements respectively. It is found that lateral torsional instability can be predicted if the beam is modelled as two elements, however, the buckling load is overestimated by four percent. Although the lateral-torsional buckling load can be predicted accurately by using four elements, some discrepancy in the post-buckling region can be observed compared to that based on eight element modelling.

5. ANALYSIS OF THIN-WALLED CORE-BRACED FRAME

Fig. 3 shows the plan view of a 24-storey thin-walled core-braced frame (Liew et al., 1997) with storey height 3.658m (12 ft). The total height of the structure is $H = 87.792$ m. Column section sizes are shown in Table 1. A36 steel are used for all sections. Height of concrete lintel beam is 1.219 m. Thickness of concrete core walls is 0.254 m. Concrete properties are: modulus of elasticity $E = 24,822$ MPa (3,600 ksi) and compressive strength $f_c = 27.6$ MPa (4 ksi). In this example, the height-to-width ratio of core walls is 24:1. It is assumed that the plastic resistance of core walls is dominated by the plastic bending capacity about the major axis, M_{z} , only. The major axis of the core wall section is parallel to the global X-axis and the corresponding plastic section modulus is $Z = 2.549$ m³ (155,520 in³). Second-order inelastic analysis are performed for assumed plastic bending capacity of core wall as $M_{z} = (4/5) Zf_c$ ($Zf_c = 70,282$ kNm). The plastic bending capacity is reduced to account approximately the effects of tensile cracking and axial force interaction. Refined models to capture material nonlinearities of core walls will be developed in the future research.

The structure is analysed for the most critical load combination of gravity loads and wind loads that act in the Y-direction. The gravity loads, which are equivalent to a uniform floor load of 4.8 kN/m² (100 psf), are applied as concentrated loads at the beam quarter points and at core walls of every storey. The wind loads are simulated by applying the horizontal forces in the Y-direction at every beam-column joints of the front elevation, and are equivalent to a uniform pressure of 0.96 kN/m². All floors are assumed to be rigid in plane to account for the diaphragm action of concrete slabs. Beam-to-column and core wall connections are assumed to be rigid. The core-braced frame is modelled by 48 thin-walled frame elements and 3,792 frame elements. The total number of degrees of freedom is 9,048.

The loads are proportionally applied until the frame collapses. First plastic hinge occurs in the beam at the tenth storey at a load ratio of 1.178. With further increase of loads, plastic hinges mainly spread in the beams between axes B and C and the beams located on axes 3 and 4. At load ratio of 1.662, plastic hinges occur at the base of core walls. When the loads increase further, more plastic hinges occur in the beams and columns; and additional plastic hinges form in the core walls at the bottom of the second storey at load ratio of 1.799. The frame can still resist more loads by inelastic redistribution of forces and hence leads to the formation of additional plastic hinges in beams and columns. Finally, at load ratio of 1.857, the core-braced frame reaches its limit of resistance. The load versus top storey deflection curves are shown in Fig. 4. The overall frame resistance can be enhanced by increasing the sectional area, reinforcement ratio and ductility of concrete core walls at the lower storeys.

The above analysis assumes that all beams are rigidly connected to columns and core walls. For comparison purpose, the subsequent analysis is carried out by assuming that the joints between beams

and columns and core walls are pin-connected, i.e., the relative rotation between beam end and the node to which it is connected is allowed to rotate freely about the major-axis of beam section. The loads are proportionally applied, and plastic hinges form at the base and at the bottom of the second storey of core walls. Then the frame collapses at load ratio of 0.680. As shown in Fig. 4, the load resistance capacity of the frame with pin connection is about thirty seven percent of the resistance capacity of the frame with rigid connection, and the stiffness of the frame with pin connection is much lower than that of the frame with rigid connection. This is because the core-braced pin-connected frame relies on core walls to provide the overall lateral resistance. To achieve the same capacity as the rigid frame, the dimension and thickness of core walls of the pin-connected frame have to be increased to enhance the lateral stiffness.

6. CONCLUSIONS

The advanced inelastic analysis theory and computer package have been developed and tested against problems known to be sensitive to the element models. The methods are accurate and efficient for analysing large-scale steel structures including the coupling effects between frameworks, core walls and floor diaphragms. A direct second-order inelastic analysis provides better insight into the structural behaviour up to failure by observing the load-displacement characteristic of the structure and the sequence of hinge formation in the frame. The design will in general turn out to be more economical as it allows for inelastic force redistribution. With the advancement of computational power coupling with graphics software for pre- and post-processing, the advanced inelastic method will allow a greater freedom in structural analysis and design, and certainly provide both efficient and cost-effective design solutions. This is particularly true for designing complex structures, in which the conventional design methods based on member capacity check may not be sufficient for the assessment of the overall strength and stability.

7. ACKNOWLEDGEMENT

The investigation presented in this paper is part of the research program on 'Advanced Analysis and Design of Space Frames' being carried out in the Department of Civil Engineering, National University of Singapore. The work is funded by the research grants (RP 940661 & RP 960648) made available by the National University of Singapore.

8. REFERENCES

- Bergan, P. G. (1978). Solution technique for nonlinear finite element problems. *Int. J. Numer. Meth. Eng.*, 12, 1677-1696.
- Chen, H., Liew, J. Y. R., Yu, C. H., and Shanmugam, N. E. (1997). Nonlinear analysis of three-dimensional core-braced frames. *Proceedings of the IASS International Symposium '97 on Shell & Spatial Structures*, vol. 1, Nov. 10-14, 1997, Singapore, 217-225.
- Chen, W. F., and Toma, S. ed. (1994). *Advanced Analysis of Steel Frames: Theory, Software, and Applications*. Boca Raton, FL: CRC Press.
- Chen, W. F., Goto, Y., and Liew, J. Y. R. (1996). *Stability Design of Semi-Rigid Frames*. John Wiley & Sons Inc., New York.
- Crisfield, M. A. (1981). A fast incremental/iterative solution procedure that handles snap-through. *Comp. Struct.*, 13, 55-62.
- Liew, J. Y. R., White, D. W., and Chen, W. F. (1993). Second-order refined plastic hinge analysis of frame design: Parts I and II. *J. Struct. Eng.*, ASCE, 119(11), 3196-3237.

Liew, J. Y. R., White, D. W., and Chen, W. F. (1994). Notional load plastic hinge method for frame design. *J. Struct. Eng.*, ASCE, **120**(5), 1434-1454.

Liew, J. Y. R. (1995). Design concepts and structural schemes for multi-storey building frames. *J. Singapore Struct. Steel Soc., Steel Struct.*, **6**(1), 45-59.

Liew, J. Y. R., Chen, H., Yu, C. H., Shanmugam, N. E., and Tang, L. K. (1997). *Second-order inelastic analysis of three-dimensional core-braced frames*. Research Report No. CE024/97, Department of Civil Engineering, National University of Singapore.

Liew, J. Y. R. (1997). Limit load analysis of spatial frames subjected to local and global instability. *Proceedings of the 5th International Colloquium on Stability and Ductility of Steel Structures*, vol. 2, July 29-31 1997, Nagoya, Japan, Edited by Usami, 739-746.

Orbison, J. G. (1982). *Nonlinear static analysis of three-dimensional steel frames*. Report No. 82-6, Department of Structural Engineering, Cornell University, Ithaca, New York.

Trahair, N. S. (1993). *Flexural-torsional buckling of structures*. Boca Raton, FL: CRC Press, 97 & 174 pp.

Ziemian, R. D., McGuire, W., and Deierlein, G. G. (1992). Inelastic limit states design: Parts I and II. *J. Struct. Eng.*, **118**(9), 2532-2567.

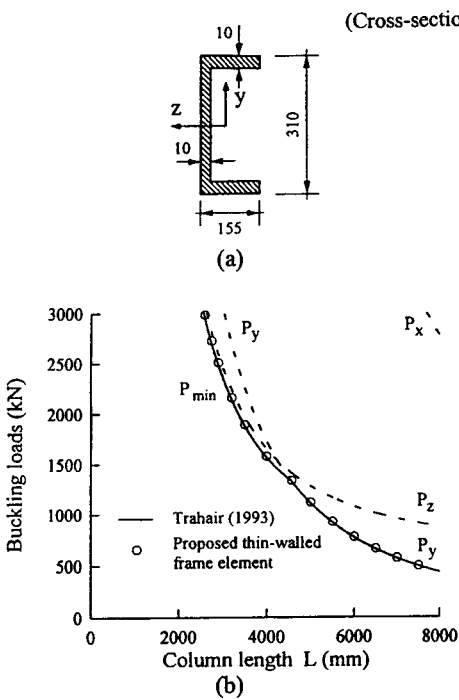


Fig. 1 Column with channel-shaped section
(a) Section dimensions
(b) Buckling loads

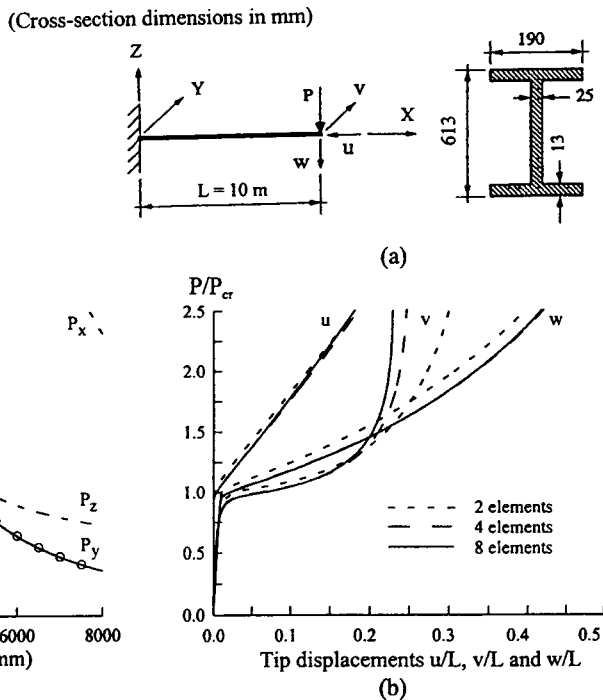


Fig. 2 Cantilever beam with I-section
(a) Geometry and section dimensions
(b) Load - tip displacement curves

TABLE 1
COLUMN SECTION SIZES OF THIN-WALLED CORE-BRACED FRAME

Storey No.	Columns of axes A & B	Columns of axes C & D	Storey No.	Columns of axes A & B	Columns of axes C & D
1 ~ 2	W14 x 398	W14 x 311	13 ~ 14	W14 x 193	W14 x 145
3 ~ 4	W14 x 370	W14 x 283	15 ~ 16	W14 x 159	W14 x 132
5 ~ 6	W14 x 311	W14 x 257	17 ~ 18	W14 x 132	W14 x 109
7 ~ 8	W14 x 283	W14 x 233	19 ~ 20	W14 x 109	W14 x 82
9 ~ 10	W14 x 257	W14 x 211	21 ~ 22	W12 x 79	W12 x 58
11 ~ 12	W14 x 211	W14 x 176	23 ~ 24	W12 x 58	W12 x 40

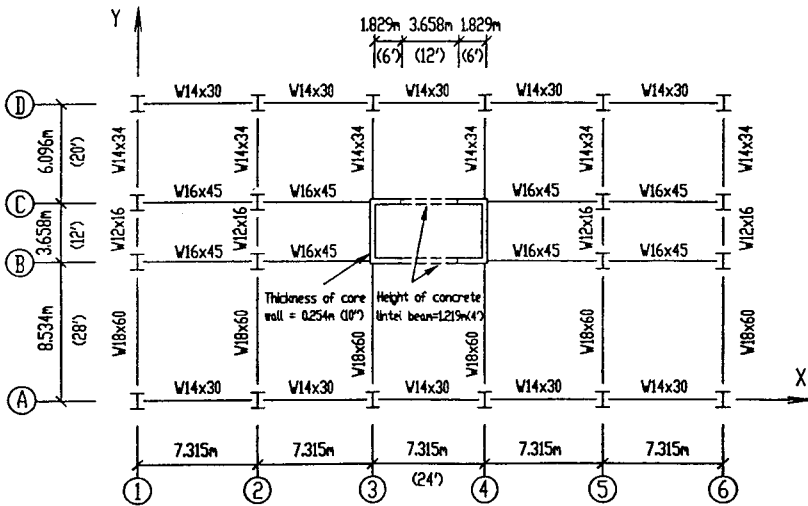


Fig. 3 Plan view of 24-storey thin-walled core-braced frame

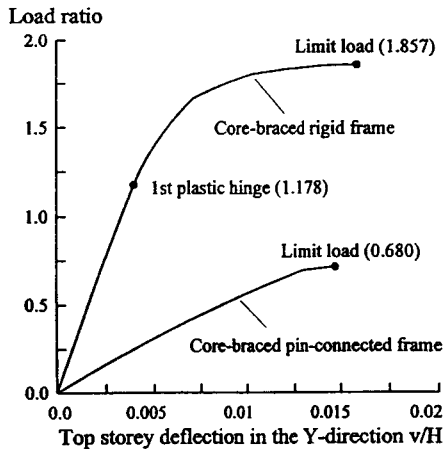


Fig. 4 Top storey load - deflection curves
(H = total height of core-braced frame)

INVESTIGATION OF COLLAPSED RACK STORAGE SYSTEMS

R.H.R. Tide and F.A. Calabrese

WISS, JANNEY, ELSTNER ASSOCIATES, INC.
Northbrook, Illinois, 60062-2095, USA

ABSTRACT

Several recent rack collapses suggest that the stability of the systems have not been fully understood by their respective designers because the designs do not fully comply with the sideways buckling provisions inherent in design specifications. The designers assumed the beam-to-column connections to be rigid and effective in developing moment frame stiffness. Similarly, the designers assumed the down-aisle bracing to have sufficient strength and stiffness to justify designing the rack as a braced frame. Collapses have occurred in rack systems fabricated with hot rolled steel shapes and in racks with thin gage steel sheet members that are cold formed into structural shapes. The investigations included testing of the connections to develop moment-rotation curves. Similarly, strength and stiffness parameters for the diagonal bracing were developed. The connection test data and bracing parameters were then incorporated in both traditional as well as finite element method analyses of the racks. Data from computer inventory systems precisely described the loading conditions at the time of the collapse. Although several collapses have been investigated, the emphasis of this paper will be placed on one project.

KEYWORDS

Racks, steel, braced, moment frames, lateral buckling, sideways, partially restrained connections.

INTRODUCTION

Rack storage systems are often designed on a modular basis. Standard components are used to construct the rack allowing both horizontal and vertical growth based on the design of a basic unit. Storage capacity can be added by extending the rows or by placing additional rows in adjacent empty space. Warehouse space usage is optimized by placing storage racks back-to-back with the aisle sized to permit efficient placement and retrieval of products. The horizontal load support beams are connected to the vertical columns by means of proprietary moment connections that are easily assembled or disassembled. Down-aisle supplemental bracing between back-to-back rows of racks provides additional lateral bracing for the system. Representative collapses are shown in Figures 1 and 2 for racks constructed of hot rolled channels and cold formed members, respectively.



Figure 1 - Collapse of hot rolled steel shape rack



Figure 2 - Collapse of cold formed steel shape rack

The design of rack structures has evolved into a very efficient system to optimize storage space within a building envelope. Typically, the rack's dimensions are governed by ASME Pallet Sizes (1996), which dictates the pallet sizes and capacity. The rack frame design is governed by the Rack Manufacturers Institute (RMI 1990) specification, which in turn is fundamentally based on the American Institute of Steel Construction, Inc. (AISC, 1989) and the American Iron and Steel Institute (AISI, 1986) criteria for hot rolled and cold formed members, respectively. Rack frames are typically designed to consist of vertical trusses in one direction (cross-aisle) and a braced frame or moment frame in the other direction (down-aisle). In many cases the down-aisle direction frame stability is accomplished by mobilizing both systems. Down-aisle vertical bracing is optimized by placing the diagonal members in the space between two back-to-back racks. The space between racks also accommodates pallet placement tolerances and, if necessary, sprinkler piping. Some additional frame redundancy is obtained by connecting the racks above the top level of the system. Generally, the racks are not attached to the warehouse structural framing system.

The client specified loads are typically limited to pallet weights of 18 kN. The pallet widths are nominally 1220 mm. Rack framing is optimized by placing vertical approximately 1070 mm wide rack trusses every two pallets at approximately 2650 mm. Support beams occur approximately every 1830 mm vertically. The optimized warehouse storage volume is then dictated by the number of back-to-back racks, the aisle widths between each pair of racks, the down-aisle length of the racks and the height of the building. In addition, a service area is usually required at one end of the rack rows to facilitate loading/unloading of the delivery trucks and rack retrieval equipment. The particular rack truss framing under consideration consisted of C102x8.0 channel chords and angles of various sizes as shown in Figure 1. The bases of the columns were welded to steel plates, which were bolted to the concrete floor. The down-aisle beams were C102x6.7 channels. The beam-to-truss connections consisted of angles welded to the end of the beams and then bolted to the truss chords using 13 mm ASTM A325 (SAE Gr5) bolts. A typical connection is shown in Figure 3. One level of down-aisle vertical bracing consisted of a 16 mm diameter, 3250 mm long steel rods with threaded ends as shown in Figure 4. The bracing was anchored to the back-to-back racks by L89x89x6.4 angles welded to steel plates, which in turn were bolted to the truss chords.

The particular rack system under consideration consisted of five back-to-back rows plus two single rows against the warehouse walls. In the down-aisle direction there were 26 two-pallet bays. Each bay had ten support beams resulting in a rack height of 19,200 mm. Because of a computer monitored rack loading, unloading and inventory control system, an accurate distribution and loading record was created at the collapse time. On the day of the collapse, the load on the relatively new rack system was greater than it had ever been before. The individual rack row loads varied from 23.9 percent to 67.4 percent with an overall average of 47.7 percent of maximum design capacity.

COLLAPSE MECHANISMS

The orientation of any collapsed structure and its contents typically is an indication of how a collapse occurred. The location of the debris of collapsed racks usually indicates a sideways down-aisle movement of the racks and their contents. In contrast, if an individual column anywhere in the system buckled, there would be a tendency for all rack frames to collapse towards that one column or to implode. Once the racks and its contents begin to move, it is highly unlikely that they will substantially change direction in mid-collapse, though some deflection of movement may occur if the collapsing contents strike a relatively rigid object.

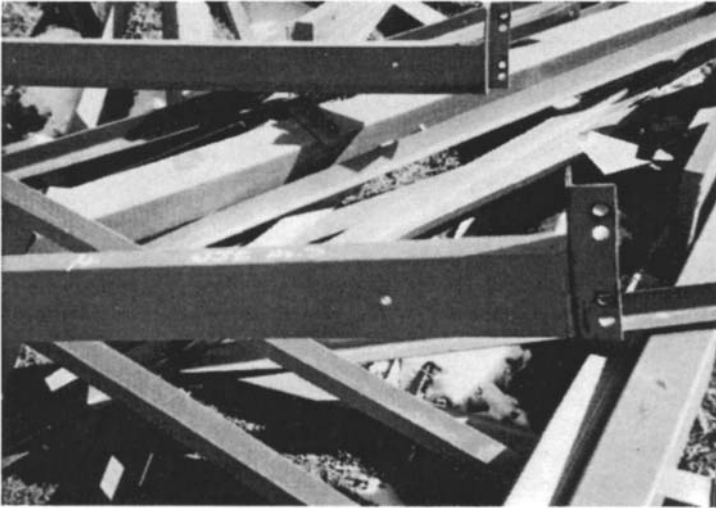


Figure 3 - Beam-end connectors - hot rolled channels

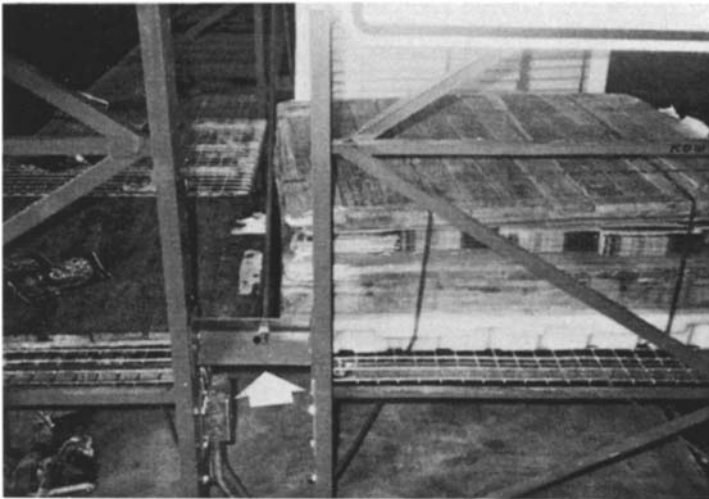


Figure 4 - Rack spacer angle and down-aisle bracing rod

TESTING PROGRAM

The beam-to-truss chord connection test data were made available for the investigation. Because of their proprietary nature, only a summary of the test results is shown in Figure 5. The moment-rotation ($M-\phi$) curve "A" in Figure 5, represents the upper bound for the test results. Curve "B" represents an average of the test data. Both curves clearly indicate that the connections are flexible and can be classified as partially restrained. The beam line describing the moment-rotation characteristics for a C4x4.5 (C102x6.7) channel is also shown as well as the theoretical 80 percent $M-\phi$ curve. Any connection rotational stiffness greater than 80 percent is normally considered a rigid connection.

Although no tests were performed on the vertical bracing system for this investigation, tests have been conducted on similar bracing systems. The results indicate that the effective bracing system stiffness is considerably less than the theoretical value because of the twisting of the rack spacer connection angles. The spacer connection angles are shown in Figure 4. Originally, it was assumed for the analysis of this investigation that the rack spacer angles were rigidly attached to the rack truss chords. In a subsequent analysis, the bracing flexibility was accounted for by a 55 percent reduction in modulus of elasticity for steel from 200,000 MPa to 90,300 MPa, which includes the effect of spacer angle twisting but not the effect of spacer angle end connection flexibility. Furthermore, the bracing effectiveness on the truss chord farthest from the bracing should realistically be additionally reduced.

Samples of truss chords, diagonal members and horizontal angles, load beams and vertical bracing rods were recovered and tested. The tests indicate that the floor beam and truss chord channel steel had a minimum yield stress of 365 MPa. The minimum yield stress for the truss angles and bracing rods was 310 MPa and 380 MPa, respectively.

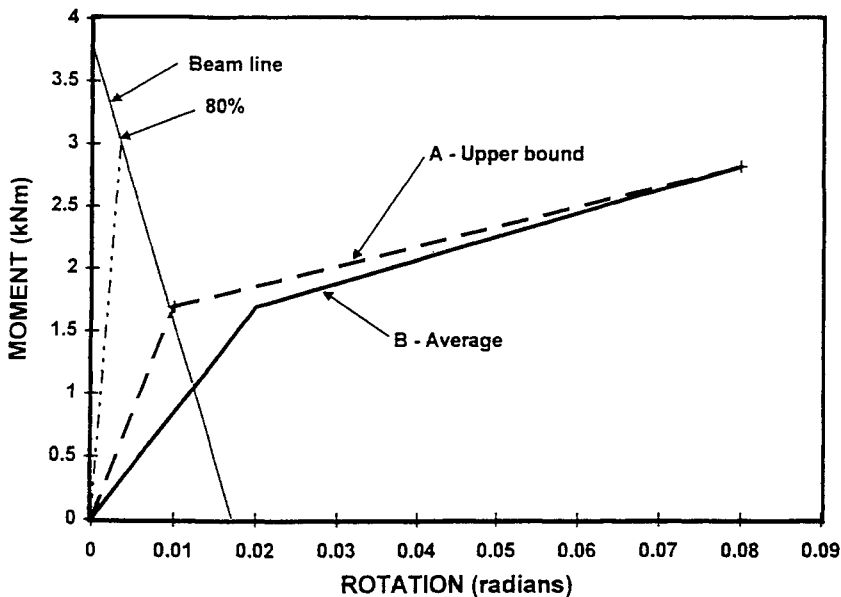


Figure 5 - Connection test moment-rotation curves

RACK ANALYSIS AND DESIGN

Preliminary Analysis

Initially, hand calculations were performed to identify design adequacy or potential problems. These hand computations indicated that if vertical loads alone are considered and if a nearly rigid connection exists between the beams and columns, the frame design incorporates the normal safety factors inherent in steel design based on AISC (1989) and RMI (1990) criteria. However, two anomalies were identified that suggested the need for a more detailed analysis.

The first anomaly concerns the stress and local stability when one of the lower level shelves is empty and when all the shelves above are fully loaded (checkerboard). In this case, stress levels above those permitted by the specifications occur. However, in spite of a reduced safety factor, a collapse condition is not indicated.

The second anomaly concerns the omission of minimum lateral loads as required by the RMI (1990) Specification Section 7.3.1. The computed ratio of axial load to allowable load (f_a/F_a) for a fully loaded rack slightly exceeds 1.0, with no consideration given to lateral loads and to down-aisle bending in the columns due to unbalanced loading, wind, impact or seismic loading. The designer considered this adequate because an effective column length factor (K) equal to 1.7 was used as required by RMI (1990) Section 5.3.1.1. The validity of this assumption was not verified by the designer even though the connection test results ($M-\phi$ plots) were available and suggested otherwise.

Computer Analysis

A more detailed computer analysis was performed to substantiate the design issues identified by the hand computations. The FEM analysis indicated that as long as the frame was essentially vertical with insignificant misalignment ($L/3000$), the second order P-delta effects would also be insignificant and the beam-to-column moments would be on the lower segment of the bi-linear $M-\phi$ curve shown in Figure 5. As a result, the stress in the column would be below the critical buckling level. At full design load, a lateral displacement of only 18 mm occurred as shown in Figure 6. In subsequent analysis, a lateral load of 1.5 percent of the vertical load was applied to the structure to represent misalignment and unbalanced loading per RMI (1990) Section 7.3.1. The vertical load was incremented in 10 percent of full load steps, and then in reduced step size as the second slope of the bi-linear $M-\phi$ was reached.

Two load cases were considered that incorporated the RMI lateral load. The first case considered the specified design load and the upper bound to the connection stiffness test data ($M-\phi$ curve) shown in Figure 5. The second case considered the actual loads on the most heavily loaded rack and the most probable connection stiffness or the lower curve shown in Figure 5. Lateral displacements at the top of the rack of 250 mm and 235 mm were computed, respectively, as shown in Figure 6.

The FEM analysis indicated that the first level down-aisle bracing was ineffective because axial shortening of the columns resulted in almost no force in the bracing rods until significant lateral movement of the racks frames had occurred.

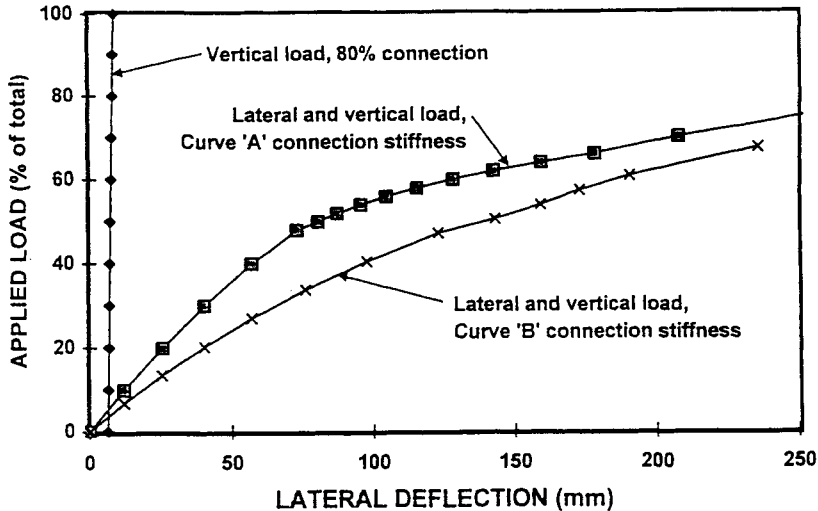


Figure 6 - Frame deflection when subjected to lateral load

Sideways Collapse

The $M-\phi$ curves shown in Figure 5 indicate that the frame's stiffness is considerably less than an idealized frame with rigid beam-to-column connections. The effect of the reduced stiffness can be predicted using classical column buckling concepts inherent in the AISC LRFD Specification (1993) with the column equation developed by Tide (1985). The stiffness coefficient for the upper curve in Figure 5 is 170 kNm per radian. In comparison, the slope of the 80 percent connection capacity intercept of the beam line is 881 kNm per radian. The effective connection stiffness, is therefore approximately 20 percent of an idealized case. Using this effective connection stiffness, a column effective length factor (K) of 2.8 is computed, which results in a predicted column buckling stress of 103 MPa. The column area of 1025 mm² and a nominal yield stress of 365 MPa were used to compute a column capacity of 106 kN. The most heavily loaded rack-row had an average column load of 96 kN per column. Considering an effective connection stiffness less than 170 kNm and closer to the average stiffness shown in Figure 5 would reduce the column capacity below 96 kN confirming that when one rack-row load of approximately 67.4 percent of capacity was reached down-aisle sideways buckling would occur.

The rack frame load displacement behavior under lateral and vertical loads, shown in Figure 6, indicates that the frame does not possess adequate stiffness to restrain any lateral movement. Once the frame begins to move laterally, the frame stiffness deteriorates and lateral movement progresses into a completely unstable frame.

SUMMARY AND CONCLUSIONS

An investigation into the cause of a rack collapse was conducted and included material testing, basic stability computations and finite element method (FEM) analyses. The connection tests performed by others indicated that the beam-to-column connections were flexible, and could not be considered as fully rigid moment connections. Their ability to support the column behavior as a rigid frame was at best 20 percent effective. Similarly, the partial height vertical down-aisle bracing was not fully effective because of its significantly reduced stiffness due to a flexible anchoring system.

The FEM analyses showed that when the rack frame was subjected to the specification-mandated lateral load, the P-delta deformation indicated inadequate rack frame stiffness. Although rack frame design using flexible connections is an acceptable concept, the designer must ensure that adequate rack frame strength and stiffness are provided to resist minimum lateral loads and buckling conditions.

The investigation indicated that the design of the rack frame was inadequate. Furthermore, the Rack Manufacturer's Institute (RMI) provision concerning column effective length factor (K) equal to 1.7 for unbraced frames is inadequate where flexible or partially restrained connections occur in the system.

REFERENCES

- AISC (1989), "Specification for Structural Steel Buildings", American Institute of Steel Construction, Inc, June 1, 1989, Chicago, Illinois
- AISC (1993), "Load and Resistance Factor Design Specification for Structural Steel Buildings", American Institute of Steel Construction, Inc., December 1, 1993, Chicago, Illinois.
- AISI (1986), "Specification for the Design of Cold-Formed Steel Structural Members", American Iron and Steel Institute, August 19, 1986, Washington, D.C.
- ASME (1996), "Pallet Sizes – MH1.2.2M-1989", The American Society of Mechanical Engineers, Reaffirmed 1996, New York, New York.
- RMI (1990), "Specifications for the Design, Testing and Utilization of Industrial Steel Storage Racks", Rack Manufacturers Institute, June 1990, Charlotte, North Carolina.
- Tide, R.H.R. (1985), "Reasonable Column Design Equations", Proceedings, Annual Technical Session of Structural Stability Research Council, April 16-17, 1985, Cleveland, Ohio, Lehigh University, Bethlehem, Pennsylvania.

NATURAL FREQUENCIES AND MODE SHAPES OF THIN-WALLED MEMBERS UNDER IN-PLANE FORCES

M.Ohga¹, K.Nishimoto², T.Shigematsu³ and T.Hara³

¹ Department of Civil and Environmental Engineering, Ehime University, Matsuyama 790, Japan

² Chodai Ltd., Takamatsu 760, Japan

³ Tokuyama Technical College, Tokuyama 745, Japan

ABSTRACT

In this paper, an analytical procedure to estimate not only the natural frequencies but also vibration mode shapes of the thin-walled members under in-plane forces, by the transfer matrix method, is presented. The transfer matrix is derived from the differential equations for the vibration problems of the plates under in-plane forces. Therefore, the interactions between the panels of the cross section can be considered exactly. The natural frequencies and mode shapes of the box and I-section members under axial forces and bending moments are presented for various aspect ratios of the members and the effects of in-plane forces to the natural frequencies and mode shapes of the members are examined.

KEYWORDS

Thin-walled member, transfer matrix method, natural frequency, mode shape, in-plane force, box-section member, I-section member

INTRODUCTION

Thin-walled members are widely used in a broad range of structural applications to reduce the material cost as well as the dead weight of a structure. To clarify the natural frequencies and vibration mode shapes of the members is very important for the earthquake, wind and noise problems. In practical use, the thin-walled members are subjected to the in-plane loads depend on the dead weight and various active loads. Therefore, it is very important that the effect of these loads to the vibration property of the thin-walled members. The considerable amount of research has been done on vibration analysis of thin-walled members, but in most of them, the effects of the in-plane loads to the natural frequencies and mode shapes of the thin-walled members are not considered.

In this paper, an analytical procedure to estimate not only the natural frequencies but also vibration mode shapes of the thin-walled members under in-plane forces by the transfer matrix method is presented. The transfer matrix is derived from the differential equations for the vibration problems of the plates under in-plane forces. Therefore, the interactions between the panels of the cross section can be considered exactly.

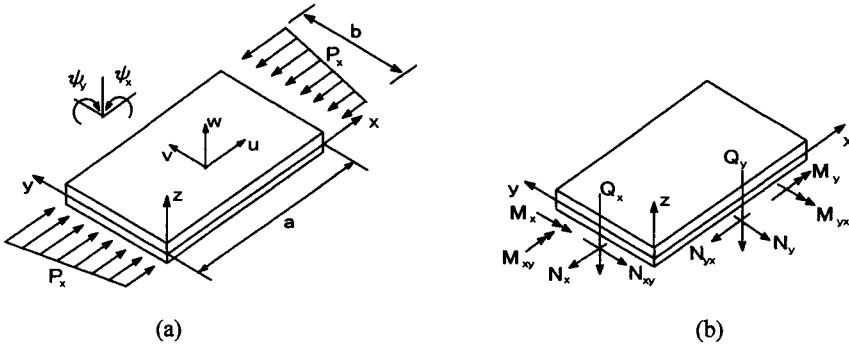


Figure 1 Plate panel

Although the transfer matrix method is naturally a solution procedure for one-dimensional problems, this method is applied to thin-walled members by introducing the trigonometric series into the governing equations of the problems [Ohga (1995a,b); Ohga(1996)].

The natural frequencies and mode shapes of the box and I-section members under the axial forces and bending moments are presented for various aspect ratios of the members and the effects of in-plane forces to the natural frequencies and mode shapes of the members are examined.

ANALYTICAL PROCEDURES

Transfer matrix for plate panels under in-plane forces

From the equilibrium equations of forces in vibration problems and the relations between the strains and deflections for the plate panels, the partial differential equations for the state variables, $Z = \{w, \varphi_y, M_y, V_y, v, u, N_y, N_{yx}\}^T$, are obtained as follows (Figure 1):

$$\frac{\partial}{\partial y} Z = Z' = A(y)Z \tag{1}$$

When the sides $x = 0$ and $x = a$ of the plate panel are simply supported, the state variables can be assumed in the form:

$$w(x, y) = \bar{w}(y) \sin \alpha x \tag{2}$$

where, $\alpha \equiv \frac{m\pi}{a}$, a : plate length, m : vibration mode in x direction.

Substituting Eq.(2) into (1), the following ordinary differential equation referred to the variable y only are obtained:

$$\frac{d}{dy} Z = Z' = A(y)Z \tag{3}$$

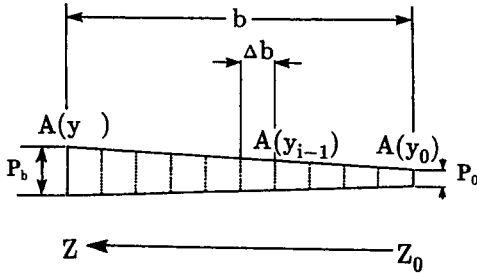


Figure 2 Romberg integration method

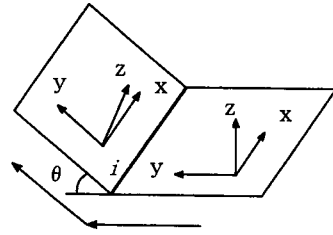


Figure 3 Relation between consecutive panels

Eq.(3) is a differential equation with variable coefficient, $A(y)$, therefore, the equation is integrated numerically. In this paper, the Romberg integration method is used for this integration. In this integration method, the plate panel is divided into m subsections as shown in Figure 2 ($m=2M$, M being the subdividing parameter), and the transfer matrix for the subdividing parameter M is obtained as

$$Z = \frac{1}{2}(C_{m-1} + C_m + \Delta b \cdot A(\psi_m) \cdot C_m)Z_0 = F \cdot Z_0 \tag{4}$$

$$C_0 = I, C_1 = I + \Delta b A(\psi_0), C_i = C_{i-2} + 2\Delta b A(\psi_{i-1})C_{i-1}, m \geq i \geq 2, I : \text{Unit matrix} \tag{5}$$

For a plate panel under uniform in-plane load, the transfer matrix is obtained as follows:

$$Z = \exp(Ay)Z_0 = FZ_0 \tag{6}$$

$$\exp(Ay) = I + (Ay) + \frac{1}{2!}(Ay)^2 + \frac{1}{3!}(Ay)^3 + \dots \tag{7}$$

where Z_0 is the initial state vector and F is the transfer matrix.

Point matrix

As the state vectors for each panel are referred to the local coordinate system, the relations between the state vectors of consecutive two panels are required, in order to allow the transfer procedures of the state vectors over the cross section of the members. Considering the relation between the state vectors at the left and right hand sides of section i (Figure 3), the point matrix, P , is obtained as follows:

$$Z_i^L = P_i Z_i^R \tag{8}$$

where superscripts L and R indicate left and right hand sides at section i .

Natural frequency equations

Box-section member : Applying the aforementioned transfer and point matrices, F and P , to the box-section members, the transfer procedures are described as follows (Figure 4(a)):

$$Z_0 = P_4 Z_4 = P_4 F_4 P_3 F_3 P_2 F_2 P_1 F_1 Z_0 = UZ_0 \tag{9}$$

From Eq.(9), the natural frequency equations for the box-section members are obtained as follows:

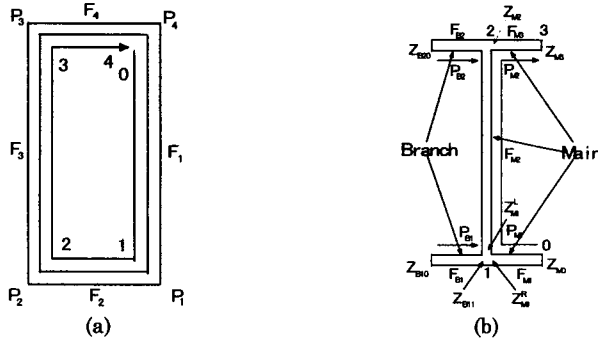


Figure 4 Transfer procedures of state vector

$$[U - I]Z_0 = 0 \tag{10}$$

I-section member : Considering the compatibility and equilibrium conditions between the state vectors of the main panel and those of the branched panel of I-section members at sections 1 and 2, the relation between the initial state vectors of the main and branched panels, Z_{M0}, Z_{B10}, Z_{B20} and that at section 3 Z_{M3} is described as follows (Figure 4(b)):

$$\begin{bmatrix} Z \\ 0 \\ 0 \end{bmatrix}_{M3}^L = \begin{bmatrix} F_{M3}P_{M2}F_{M2}P_{M1}F_{M1} & F_{M3}P_{M2}F_{M2}P_{B1}F_{B2}^F & F_{M3}P_{B2}F_{B2}^F \\ [P_{M1}F_{M1}]^\delta & -[P_{B1}F_{B1}]^\delta & 0 \\ [P_{M2}F_{M2}P_{M1}F_{M1}]^\delta & [P_{M2}F_{M2}P_{B1}F_{B1}^F]^\delta & -[P_{B2}F_{B2}]^\delta \end{bmatrix} \begin{bmatrix} Z_{M1} \\ Z_{B1} \\ Z_{B2} \end{bmatrix} \tag{11}$$

where superscripts δ and F indicate the displacement and force components of the state vector, respectively; superscripts L and R indicate the left and right side of the sections, and subscripts M and B indicate the variables of the main and branched panels.

Considering the boundary conditions of the members, the natural frequency equations for the I-section members are obtained as follows:

$$U'Z'_0 = 0 \tag{12}$$

It is required that the determinants of the matrices of Eqs (10) and (12) to be zero. Substituting the natural frequency, ω obtained above, and setting the first unknown variable of the initial state vector, $\bar{w}_0 \equiv 1$, unknown initial state variables can be obtained. The state vector at any point of the cross section is obtained by further transfer procedure and then the mode shape corresponding to the natural frequency can be simply obtained.

NUMERICAL EXAMPLES

In Table 1, first five natural frequency parameters ($\Omega = (b^2\omega / \pi^2)\sqrt{\rho / D}$, D : bending stiffness, a : width of plate) of the simply supported square plate under uniform axial loads ($P/P_{cr}=0, 0.2, 0.4, 0.6, 0.8, 1.0$, P : axial load, P_{cr} : buckling load), obtained by the proposed method (TMM) are compared with the exact solutions [Leissa (1969)]. The numbers in the parentheses are the modes in the x- and y-directions). As shown in Table 1, the complete agreement exists between the both results.

TABLE 1
NATURAL FREQUENCIES OF SIMPLY SUPPORTED SQUARE PLATE

Modes (m,n)	Methods	P/P _{cr}					
		0.0	0.2	0.4	0.6	0.8	1.0
1st (1,1)	TMM	2.0000	1.7889	1.5492	1.2649	0.89943	0.0000
	Exact	2.0000	1.7889	1.5492	1.2649	0.89943	0.0000
2nd (2,1)	TMM	5.0000	4.6690	4.3128	3.9243	3.4928	3.0000
	Exact	5.0000	4.6690	4.3128	3.9243	3.4928	3.0000
3rd (3,1)	TMM	5.0000	4.9193	4.8374	4.7539	4.6690	4.5826
	Exact	5.0000	4.9193	4.8374	4.7539	4.6690	4.5826
4th (4,1)	TMM	8.0000	7.7974	7.5895	7.3756	7.1554	6.9298
	Exact	8.0000	7.7974	7.5895	7.3756	7.1554	6.9298
5th (5,1)	TMM	10.000	9.9599	9.9197	9.8793	9.8387	9.7980
	Exact	10.000	9.9599	9.9197	9.8793	9.8387	9.7980

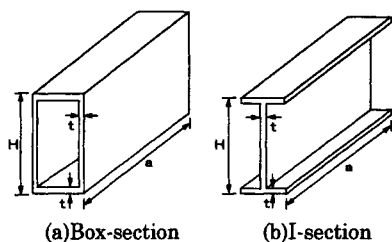


Figure 5 Analytical models

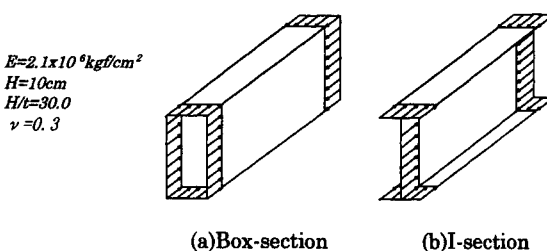


Figure 6 Thin-walled members under in-plane loads

Figure 7 shows the fundamental frequency parameters ($\Omega = (H^2 \omega / \pi^2) \sqrt{\rho / D}$) of the box-section members under the compression axial load $P=0.3P_{cr}$ (Figures 5(a),6(a)). In Figure 8, the mode shapes corresponding to the fundamental frequencies are shown for the members of $a/H=2.0, 4.0$ and 10.0 . As shown in Figure 8, the mode shape for $a/H=2.0$ exhibits the local deformation of the panels composing the cross section of the members. In the case of $a/H=4.0$, the mode shape shows the distortional deformation (combination of local and global deformations). The mode shape for $a/H=10.0$ exhibits the lateral flexural deformation (without distortional deformation of cross section). As shown in Figure 7, the fundamental frequency parameter decreases when the length of the member increases.

The fundamental frequency parameters of the members obtained by the beam theory, and those for the web panel, in which the boundary conditions at upper and lower edges are assumed to be simply supported (s-s) and fixed (c-c), are also shown in Figure 7. In the large aspect ratio range (lateral flexural deformation range), the results obtained by TMM agree well with those by beam theory. On the other hand, in the small aspect ratio (local deformation range), the frequency parameter obtained by TMM lies the values between the results for the web with simply supported and fixed boundary conditions.

Figures 9 and 10 show the fundamental frequency parameters and mode shapes of the I-section members (Figures 5(b),6(b)) under the axial load ($P=0.3P_{cr}$). As shown in Figures 9 and 10, the similar results to those of the box-section members are obtained. In the small aspect ratio, while the frequency parameters obtained by the TMM lie between the results for the web with simply supported and fixed as the case of the box-section members, those are close to the results for simply supported condition.

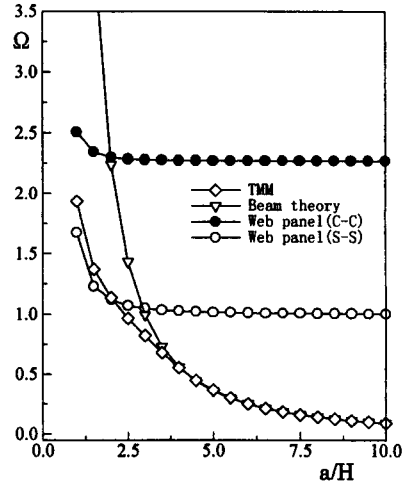
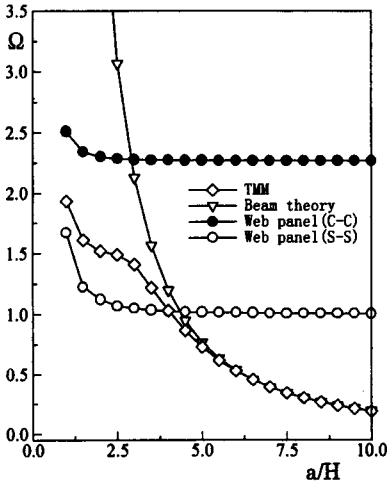


Figure 7 Fundamental natural frequencies (box-section ; $P=0.3P_{cr}$)

Figure 9 Fundamental natural frequencies (I-section ; $P=0.3P_{cr}$)

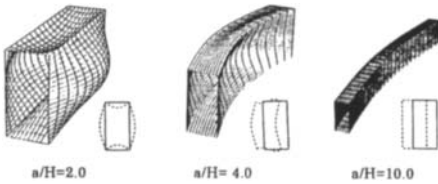


Figure 8 Mode shapes (box-section ; $P=0.3P_{cr}$)

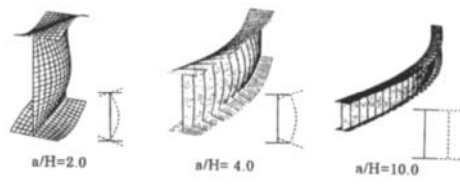


Figure 10 Mode shapes (I-section ; $P=0.3P_{cr}$)

Figure 11 shows the variation of the first five natural frequency parameters of the box-section members ($a/H=5.0$) under the bending moments, when the bending moment changes from $P/P_{cr}=0.0$ to 1.0 . The numbers in the parentheses are the modes in the axial and lateral directions, respectively. In this figure, the natural frequency parameter, of which the mode shape coincides with the buckling mode shape (6,1) is also shown. As shown in Figure 11, while the 1st, 3rd, 5th and natural frequency of buckling mode decrease, the 2nd and 4th increase when the bending moment increases. In Figure 12, the mode shapes corresponding to the first five natural frequencies and to that of buckling mode are shown for bending moments $P/P_{cr}=0.0, 0.5$ and 1.0 . As shown in Figure 12, some changes in the mode shapes can be seen when the bending moment increases.

In Figure 13, the variation of the first five natural frequency parameters of the I-section members under bending moments are shown, and Figure 14 shows the mode shapes corresponding to the first five natural frequencies and that of buckling mode, for bending moments $P/P_{cr}=0.0, 0.5$ and 1.0 . As shown in Figures 13 and 14, the similar results to those of the box-section members are obtained, and some changes in the mode shapes can be seen when the bending moment increases.

CONCLUSIONS

In this paper, an analytical procedure to estimate not only the natural frequencies but also vibration

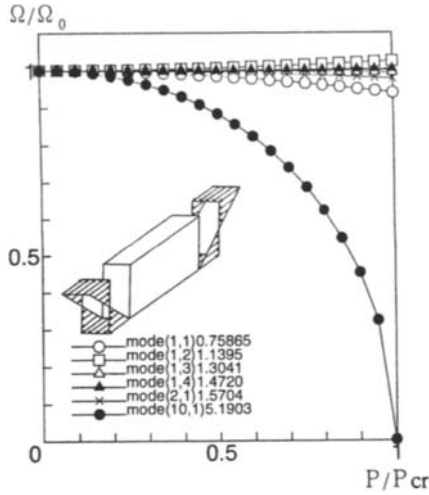


Figure 11 Variation of natural frequencies of box-section members

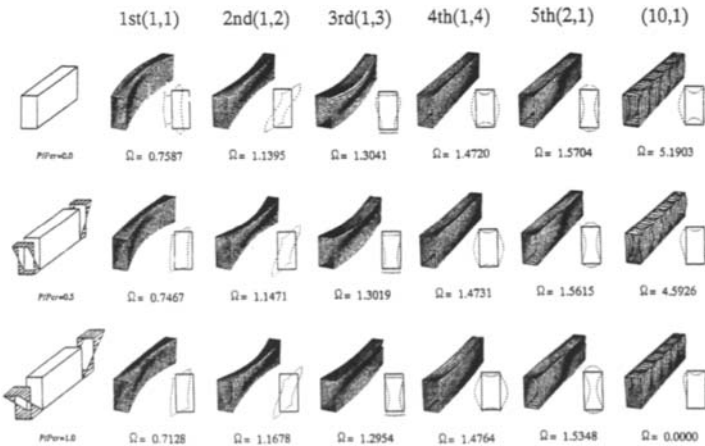


Figure 12 Mode shapes of box-section members

mode shapes of the thin-walled members under in-plane forces by the transfer matrix method is presented. From the numerical examples presented in this paper, the following conclusions are obtained.

1. The exact natural frequencies and mode shapes of the thin-walled members under in-plane forces are obtained with very small computational efforts.
2. Some mode shapes corresponding to the natural frequencies of the thin-walled members under in-plane bending moments are changed as these forces are increased.
3. The mode shapes obtained by the transfer matrix method are very effective to clarify the complicated vibration phenomenon of the thin-walled members under in-plane forces.

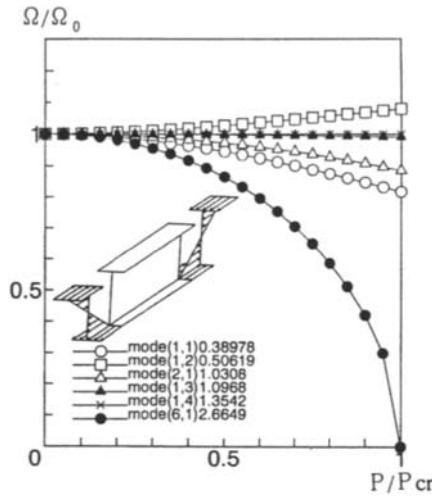


Figure 13 Variation of natural frequencies of I-section members

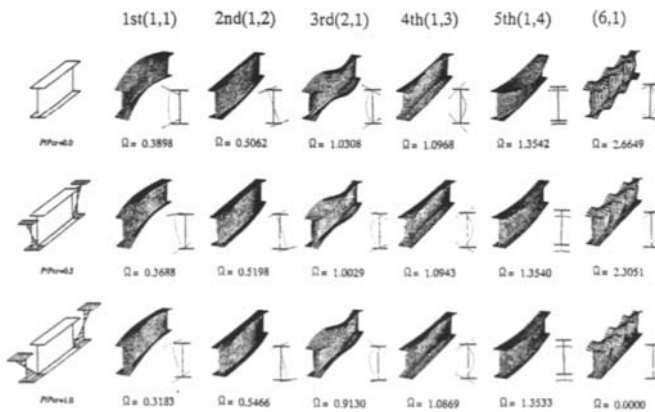


Figure 14 Mode shapes of I-section members

REFERENCES

Leissa A W (1969). *Vibration of Plates*. NASA, Washington, D.C..

Ohga M, Takao H and Hara T (1995a). Natural Frequencies and Mode Shapes of Thin-Walled Members. *Computers & Structures* 55:6, 971-978.

Ohga M, Takao T and Shigematsu T (1995b). Natural Frequencies and Modes of Open Cylindrical Shells with a Circumferential Thickness Taper. *J. Sound & Vibration* 183:1, 143-156.

Ohga M, Takao M and Shigematsu T (1996). Vibration Analysis of Curved Panels with Variable Thickness. *Int. J. Computer-Aided Engineering and Software* 13:2/3/4, 226-239.

NON – LINEAR DYNAMIC ANALYSIS OF THIN – WALLED TAPERED TOWERS WITH CONCENTRATED MASSES

G. T. Michaltsos¹ and T. G. Konstandakopoulos²

^{1,2} Department of Civil Engineering, National Technical University of Athens
42, Patission Str., ATHENS, 106 82, GREECE

ABSTRACT

The present paper, deals with the non-linear dynamic analysis of a thin-walled tower with varying gross-section and concentrated masses. It, especially, deals with the effect of the rotary inertias of those masses, which have been neglected up to now. Using the Galerkin's method, we can find the spectrum of the eigenfrequencies and, also, the shape functions. Finally, we can solve the equations of the problem of the forced vibrations, by using the Carson-Laplace's transformation. Applying this method on a tall mast with 2 concentrated masses, we can examine the effect of the inertias rotary of the above masses, because of seismic loads and, also, harmonic loads, caused by wind forces.

KEYWORDS

non-linear dynamic; concentrated masses; variable thin-walled member; tall masts

INTRODUCTION

In all the world, power-transmission towers, or wind-generator towers or, even, telecommunication towers, are often made from a conical cantilever, whose tip is cut out and has a circular or polygonal thin-walled cross-section, which is varied along the axis of the cantilever. Additionally, very often, there are significant concentrated masses, because of floors, observatories or look-out restaurants. Not only these masses, but also the varying gross-section make the problem a strong non-linear dynamic problem, with serious mathematical difficulties. There are many papers on this field. Rohde (1953) gave a power series solution to this problem. Wang and Lee (1973) extended Rohde's method and Gaines and Voltera (1976) investigated the eigenfrequencies of those constructions. Prathap and Varadan (1976) presented a finite deflection of such cantilever. Bouchet and Biswas (1977) presented a non-linear analysis by means F.E.M. and a vibration analysis, in 1979. Takabatake and others (1990,1993 and1995) proposed a solution using Dirac's functions. We are, also, obliged to refer to the Kounadis's study (1976) on the dynamic response of a cantilever beam-column, with attached masses, but with unchanged sections along its length. In the present paper, assuming linear strain-displacement

relations and using Heaviside's and Dirac's functions, we can write the equations of coupled dynamic motion of the cantilever. At first, we investigate the free vibrations and with the help of Galerkin's method and that of the shape modes of the simple cantilever with constant cross-section and without concentrated masses, we determine the equation, which gives the spectrum of the eigenfrequencies and, further more, the shape functions. Therefore, we attempt to solve the problem of the forced vibrations, also by using the Galerkin's method and solving the resulting system with Carson-Laplace's transformation.

ANALYSIS

We consider the model of figure 1. This is made from isotropic homogeneous material, having modulus of elasticity E . The relation between length ℓ , diameter of the basis and thickness is the suitable for a thin-walled construction. The transverse gross section has geometrical inertias and rigidity parameters varying along the length ℓ . Each of the above parameters can be expressed by the equation:

$$R(x) = R_0 r_R(x) + R_i \delta(x - \alpha_i) = R_0 \left[r_R(x) + \frac{R_i}{R_0} \delta(x - \alpha_i) \right] = R_0 \rho_R(x) \tag{1}$$

where: $R(x)$ is any of the above parameters, R_0 is its value for $x=0$, R_i is the corresponding parameter of rigidity of the i concentrated mass, $r(x)$ is a given function of x depended on the law of the variation R of the cantilever and $\delta(x-\alpha_i)$ the Dirac function. Neglecting the longitudinal and torsional inertia forces, associated with warping, the equations of the problem are:

$$\left. \begin{aligned} [EI_y(x)w''(x,t)]'' + m(x)\ddot{w}(x,t) + c_w\dot{w}(x,t) + \sum_{i=0}^k J_y \ddot{w}'(x,t) \cdot \delta'(x - \alpha_i) &= p_z(x,t) - m'_y(x,t) \\ [EC_T(x)\phi''(x,t)]'' - (GI_D(x)\phi')' + c_\phi\dot{\phi}(x,t) + \Theta(x)\ddot{\phi}(x,t) &= m_x(x,t) \end{aligned} \right\} \tag{2}$$

Where $w(x,t)$, $\phi(x,t)$ the displacement and torsional components of the axial line, I_y the moment inertia, J_y the polar moment inertia round the y axis, I_D the St. Venant torsional moment of inertia, Θ the polar moment of inertia round the x axis, c_w , c_ϕ the damping coefficients for the transverse and torsional vibrations, $m(x)$ the mass per unit length, p_z , m_x , m_y the external loads and $C_T(x)$ the warping rigidity. We, also, note that is neglected the effect of the diaphragm influence of the concentrated masses. Finally, is noticeable that the part of the load due to the torsional vibration in Eqn. 2a is obtained from the corresponding moment: $m_{y_o} = J_y \ddot{w}'(x,t) \cdot H(x - \alpha_i)$ after double differentiation.

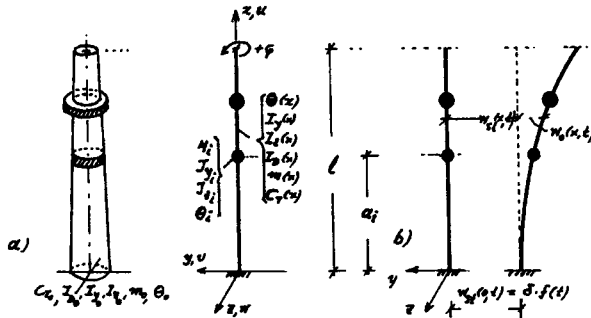


Figure 1

The Free Vibration

Free flexural vibration

The equation of the free flexural vibration if the damping $c_w=0$, is:

$$[EI_y(x)w''(x,t)]'' + m(x)\ddot{w}(x,t) = 0 \tag{3}$$

which, taking $w(x,t) = X(x) \cdot T(t)$ gives:

$$[EI_y(x) \cdot X(x)]'' - \omega_w^2 \cdot m(x) \cdot X(x) = 0 \tag{4}$$

The Eqn. 4, because of Eqn. 1, is written:

$$\rho_{I_y}(x) \cdot X''''(x) + 2\rho_{I_y}'(x) \cdot X'''(x) + \rho_{I_y}''(x) \cdot X''(x) - \lambda \cdot \rho_m(x) \cdot X(x) = 0 \quad \text{with: } \lambda = \frac{\omega_w^2 m_0}{EI_{y_0}} \tag{5}$$

In order to apply the Galerkin's method, we put:

$$X(x) = c_1\Psi_1(x) + c_2\Psi_2(x) + \dots + c_n\Psi_n(x) \tag{6}$$

where: c_i are unknown coefficients, which will be determined and $\Psi_i(x)$ are arbitrarily chosen functions of x , but satisfying the boundary conditions. As such functions, we choose the shape functions of the simple cantilever (without varying gross-section) given by Eqns. (a) of appendix. Introducing Eqn. 6 into 5, multiplying the coming successively by $\Psi_1, \Psi_2, \dots, \Psi_n$ and intergrating the results from 0 to ℓ , we obtain the following homogeneous, linear system without second member of n equations, with unknowns c_1, c_2, \dots, c_n .

$$c_1(A_{i_1} - \lambda \cdot B_{i_1}) + c_2(A_{i_2} - \lambda \cdot B_{i_2}) + \dots + c_n(A_{i_n} - \lambda \cdot B_{i_n}) = 0 \quad (i = 1,2,\dots,n) \tag{7}$$

where:

$$\left. \begin{aligned} A_{ij} &= \int_0^\ell [\rho_{I_y}(x) \cdot \Psi_j'''(x) + 2\rho_{I_y}'(x) \cdot \Psi_j''(x) + \rho_{I_y}''(x) \cdot \Psi_j'(x)] \Psi_i(x) dx \\ B_{ij} &= \int_0^\ell \rho_m(x) \cdot \Psi_i(x) \cdot \Psi_j(x) dx \end{aligned} \right\} \tag{8}$$

In order to have the system non-trivial solutions, the determinant of the coefficients must be zero:

$$|\Gamma_{ij}| = 0 \quad \text{with: } i, j = 1,2,\dots,n \quad \text{and} \quad \Gamma_{ij} = A_{ij} - \lambda B_{ij} \tag{9}$$

From Eqn. 9 we determine n values for λ and, therefore from Eqn. 5b the spectrum of eigenfrequencies ω_{wi} . From the first $(n-1)$ equation of Eqn. 9, we can finally find:

$$\left. \begin{aligned} \frac{c_j}{c_1} &= \frac{\left| \begin{array}{cccc} \Gamma_{12} & \dots & \Gamma_{11} & \dots & \Gamma_{1n} \\ \dots & \dots & \dots & \dots & \dots \\ \Gamma_{(n-1)2} & \dots & \Gamma_{(n-1)1} & \dots & \Gamma_{(n-1)n} \end{array} \right|}{|\Gamma_y|} & \text{with : } i = 1, 2, \dots, (n-1) \quad j = 2, 3, \dots, (n) \\ \text{and therefore: } X_n(x) &= c_1 \sum_{j=2}^n \left(\Psi_1 + \frac{c_j}{c_1} \Psi_j \right) \end{aligned} \right\} \quad (10)$$

Free torsional vibration

The equation of the free torsional vibration if the damping $c_\varphi=0$, is:

$$[EC_\tau(x) \cdot \varphi''(x,t)]'' - [GI_D(x) \cdot \varphi'(x,t)]' + \Theta(x) \cdot \ddot{\varphi}(x,t) = 0 \quad (11)$$

Following the same way as in *Free flexural vibration* , we obtain:

$$[EC_\tau(x) \cdot \varphi''(x,t)]'' - [GI_D(x) \cdot \varphi'(x,t)]' - \omega_\varphi^2 \cdot \Theta(x) \cdot \varphi(x) = 0 \quad (12)$$

The Eqn. 12, because of Eqn. 1, gives:

$$\left. \begin{aligned} &[\rho_c(x)\varphi'''(x) + 2\rho'_c(x)\varphi''(x) + \rho''_c(x)\varphi'(x)] - \mu_0[\rho_{I_D}(x)\varphi''(x) + \rho'_{I_D}(x)\varphi'(x)] - \nu_0\rho_\theta(x)\varphi(x) = 0 \\ \text{with: } \mu_0 &= \frac{GI_{D_0}}{EC_{T_0}} \quad , \quad \nu_0 = \frac{\omega_\varphi^2 \Theta_0}{EC_{T_0}} \end{aligned} \right\} \quad (13)$$

Applying the Galerkin's method, we finally find:

$$|\Delta_{ij}| = 0 \quad , \quad \varphi_n(x) = d_1 \sum_{j=2}^n \left(\Phi_1 + \frac{d_j}{d_1} \Phi_j \right) \quad (14)$$

which, give the spectrum of eigenfrequencies ω_φ and the shape functions. Where:

$$\left. \begin{aligned} \Delta_{ij} &= Z_{ij} - \mu_0 \cdot H_{ij} - \nu_0 \cdot \Lambda_{ij} \quad , \quad Z_{ij} = \int_0^l [\rho_c(x)\Phi_j'''(x) + 2\rho'_c(x)\Phi_j''(x) + \rho''_c(x)\Phi_j'(x)]\Phi_i(x)dx \\ H_{ij} &= \int_0^l [\rho_{I_D}(x)\Phi_j''(x) + \rho'_{I_D}(x)\Phi_j'(x)]\Phi_i(x)dx \quad , \quad \Lambda_{ij} = \int_0^l \rho_\theta(x) \cdot \Phi_i(x) \cdot \Phi_j(x)dx \end{aligned} \right\} \quad (15)$$

The coefficients $\frac{d_j}{d_1}$ are found by solving the (n-1) first equations of the above system.

The Forced Vibration

Flexural forced vibration

The equation of motion for the flexural forced vibration, is given by Eqn. 2a, which, because of Eqn. 1, becomes:

$$EI_{y_0} \left[\rho_{by}(x)w'''(x,t) + 2\rho'_{by}(x)w''(x,t) + \rho''_{by}(x)w'(x,t) \right] + c_w \cdot \dot{w}(x,t) + m_0\rho_m(x) \cdot \ddot{w}(x,t) + \left. \begin{aligned} &+ \sum_{i=1}^k J_{y_i} \ddot{w}(x,t) \delta'(x - \alpha_i) = p_z(x,t) - m'_y(x,t) \end{aligned} \right\} \quad (16)$$

We search for a solution with the form: $w(x,t) = \sum_n X_n(x) \cdot P_{w_n}(t)$ where: $P_{w_n}(t)$ are unknown functions of the time, which will be determined and $X_n(x)$ are functions of x , arbitrary chosen, but satisfying the boundary conditions. As such functions, we choose these of Eqn. 10, which still satisfy the Eqn. 6. The above Eqn. 16, because of Eqn. 4, after multiplication with X_σ and integrating the coming for 0 to ℓ , becomes:

$$\left. \begin{aligned} &m_0 \sum_n \omega_{w_n}^2 D_{\sigma,n}^1 \cdot P_{w_n} + c_w \sum_n D_{\sigma,n}^2 \cdot \dot{P}_{w_n} + m_0 \sum_n D_{\sigma,n}^1 \cdot \ddot{P}_{w_n} - \sum_{i=1}^k \left[J_{y_i} \cdot \sum_n D_{\sigma,n}^3 \cdot \ddot{P}_{w_n} \right] = D_\sigma^4 \\ &\text{and: } D_{\sigma,n}^1 = \int_0^\ell \rho_m(x) X_n X_\sigma dx \quad D_{\sigma,n}^2 = \int_0^\ell X_n X_\sigma dx \\ &D_{\sigma,n}^3 = X_n''(\alpha_i) X_\sigma(\alpha_i) + X_n'(\alpha_i) X_\sigma'(\alpha_i) \quad D_\sigma^4 = \int_0^\ell [p_z(x,t) - m'_y(x,t)] X_\sigma dx \end{aligned} \right\} \quad (17)$$

The above system of Eqn. 17a, is a differential system with unknowns the $P_{w_1}, P_{w_2}, \dots, P_{w_n}$.

Torsional forced vibration

The equation of motion for the torsional forced vibration is given by Eqn. 2b. Following the same methodology as in *Flexural forced vibration*, we reach to the system:

$$\left. \begin{aligned} &\Theta_0 \sum_n \omega_{\varphi_n}^2 \Xi_{\sigma,n}^1 P_{\varphi_n} + c_\varphi \sum_n \Xi_{\sigma,n}^2 \dot{P}_{\varphi_n} + \Theta_0 \sum_n \Xi_{\sigma,n}^1 \ddot{P}_{\varphi_n} = \Xi_\sigma^3 \quad \text{where:} \\ &\Xi_{\sigma,n}^1 = \int_0^\ell \rho_\theta(x) \varphi_n \varphi_\sigma dx \quad \Xi_{\sigma,n}^2 = \int_0^\ell \varphi_n \varphi_\sigma dx \quad \Xi_\sigma^3 = \int_0^\ell m_x(x,t) \varphi_\sigma dx \quad \text{and: } \sigma = 1,2,\dots,n \end{aligned} \right\} \quad (18)$$

The above system of Eqn. 18a is a differential system, with unknowns the $P_{\varphi_1}, P_{\varphi_2}, \dots, P_{\varphi_n}$.

Solution of the systems 17a and 18a

The systems 17a and 18a, with use of the Carlson-Laplace's transformation, come under the form:

$$\alpha_{i1}g_1(p) + \alpha_{i2}g_2(p) + \dots + \alpha_{in}g_n(p) = \beta_i \cdot F(p) \quad (19)$$

where:

$$\left. \begin{aligned}
 g_{\kappa}(p) &= LP_{\kappa}(t) \quad F(p) = L \cdot f(t) \quad p_z(x,t) = \bar{p}_z(x) \cdot f(t) \quad m_y(x,t) = \bar{m}_y(x) \cdot f(t) \\
 \text{For the flexural vibration :} \\
 \alpha_{ij} &= m_0 \omega_{wi}^2 D_{ij}^1 + c_w D_{ij}^2 \cdot p + \left[m_0 D_{ij}^1 + \left(\sum_{\lambda=1}^{\kappa} J_{y_{\lambda}} \right) D_{ij}^3 \right] p^2 = A_{ij} + p \cdot B_{ij} + p^2 \cdot \Gamma_{ij} \\
 \beta_i &= \int_0^{\ell} [\bar{p}_z(x) - \bar{m}'_y(x)] X_i dx \\
 \text{and for the torsional vibration :} \\
 \alpha_{ij} &= \Theta_0 \omega_{\varphi i}^2 \Xi_{ij}^1 + c_w \Xi_{ij}^2 \cdot p + \Theta_0 \Xi_{ij}^1 \cdot p^2 = A_{ij} + p \cdot B_{ij} + p^2 \cdot \Gamma_{ij} , \quad \beta_i = \int_0^{\ell} \bar{m}_x(x) \cdot \Phi_i \cdot dx
 \end{aligned} \right\} \quad (20)$$

The usual forms of functions $f(t)$, $F(p)$ are rational functions of p . Then g_{κ} comes in the form:

$$g_{\kappa}(p) = \frac{N_{\kappa}(p)}{M_{\kappa}(p)} \quad u = 1, 2, \dots, n \quad (21)$$

where N_{κ} , M_{κ} are polygonials with respect to p with $M_{\kappa}(p)$ of higher order than $N_{\kappa}(p)$. The Heaviside rule can thus be applied, leading finally:

$$P_{\kappa}(t) = L^{-1} g_{\kappa}(p) = L^{-1} \frac{N_{\kappa}(p)}{M_{\kappa}(p)} = \frac{N_{\kappa}(0)}{M_{\kappa}(0)} + \sum_{i=1}^n \frac{N_i(p_i) \cdot e^{p_i t}}{p_i \cdot M'_{\kappa}(p_i)} \quad (22)$$

in which p_i , are the roots of polynomial $M_{\kappa}(p)$.

The special case of the earthquake

The forced motion due to earthquake can be represented by the ground motion and introduces in equations as a support motion under the form: $w_{gs}(0,t) = \delta \cdot f(t)$ where δ is a constant, with length units. With the help of figure 1b, we reach finally to:

$$[EI_y(x)w_0''(x,t)]'' + m(x)\ddot{w}(x,t) + c_w \dot{w}_0(x,t) + \sum_{i=1}^{\kappa} J_{y_i} \dot{w}'(x,t) \delta'(x - \alpha_i) = -\delta m(x)\ddot{f}(t) - \delta c_w \dot{f}(t) \quad (23)$$

The above is solved as Eqn. 16 with: $D_{\sigma,n}^1, D_{\sigma,n}^2, D_{\sigma,n}^3$ given by Eqn. 17, while system (19) becomes:

$$\alpha_{n1}g_1 + \alpha_{n2}g_2 + \dots + \alpha_{ng_n} = -\zeta_{n1}L\ddot{f}(t) - \zeta_{n2}L\dot{f}(t) , \text{ with : } \zeta_{n1} = \delta m_0 \int_0^{\ell} \rho_m(x) X_n dx , \zeta_{n2} = \delta c_w \int_0^{\ell} X_n dx \quad (24)$$

NUMERICAL RESULTS AND CONCLUSIONS

We consider two towers which have the same: length $\ell=40m$, circular gross-section with $R_0=0,625m$, $t_0=0,012m$, $c_{w_d}=0,02$ and two concentrated masses, the first at $\alpha_1=34m$ (with $M_1=3, I_1=0,40, J_1=8$) and the second at $\alpha_2=37m$ (with $M_2=6, I_2=0,80, J_2=9$), but different $R_e=0,50m$ and $R_e=0,25m$. They are named (in table 1) as case 1 and case 2.

For the free vibrations we calculate, through the present method, the three first eigenfrequencies for the above two towers, with and without concentrated masses, as well as for the two equivalent towers without masses, with $R = \frac{0,625 + 0,5}{2} = 0,5625m$, for the first case and $R = \frac{0,625 + 0,25}{2} = 0,4375m$, for the second one.

These results are compared with them of the two last cases but with calculation of its eigenfrequencies by using the classical well-known equations. This last comparison (table 1, columns 9 and 10) shows the very well validity of the proposed solving method.

Table 1

	1	2	3	4	5	6	7	8	9	10
	case1	case 2	case 1 without M	case 2 without M	Equiv. to case 1	Equiv. to case 2	Classic. solving 1	Classic. solving 2	Comp. 5 to 7	Comp. 6 to 8
ω_1	3,86797	3,57829	5,44868	7,09296	4,46281	3,4723	4,47712	3,48221	0,32%	0,28%
ω_2	26,9428	22,7565	29,8196	27,2596	27,9231	21,7810	28,0118	21,7870	0,31%	0,02%
ω_3	78,3527	71,0705	81,4683	75,5169	78,9920	61,5001	79,0766	61,5042	0,11%	0,007%

For the forced vibrations are being studied the above two towers, with the concentrated masses taking, at first, into account the influence of the inertias rotary ($J_i \neq 0$) but, after, without that influence ($J_i=0$).

The external loads were: the wind pressure given by the form: $p(x,t) = p\left(\frac{x}{10}\right)^{0,17} (1 + 0,1 \sin \Omega t)$

($p=1, \Omega=5$) and as a second loadcase the earthquake under the form: $f(t) = \delta \cdot e^{-\alpha t} \sin \Omega t$ (with: $\alpha=0,07, \Omega=0,8, \delta=0,10$ and $0,20$).

For the case of the wind load: The influence of the inertias rotary is amounted for the towercase 1 about 5% for the period of the windshock (at time 0 to 5sec) and 1% for the period after the shock, while for the towercase 2 exists the same influence for the first time period, but that becomes 2%, for the second period.

In figure 2 is being shown the deformation of the top (at $x=\ell$) for $t=0$ to 150sec.

For the case of the earthquake load: The influence of the inertias rotary is amounted for the towercase 1, about 1,5 to 4%, for the usual move ($\delta=0,10$) and the same for a large move ($\delta=0,20$).

For the towercase 2, the influence is about 1 to 8%, either for a usual move ($\delta=0,10$), or for a large move ($\delta=0,20$).

In figure 3 is being shown the deformation of the top, for $t=0$ to 200sec.

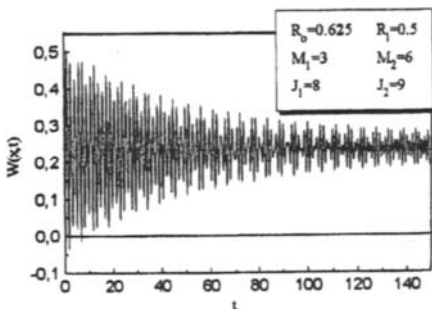


Figure 2

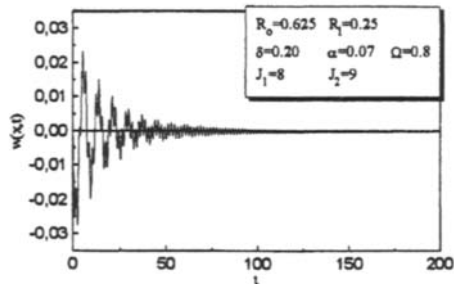


Figure 3

REFERENCES

- Bouchet A.V. and Biswas (1977). Non-linear Analysis of Towers and Stacks. *Journal of Structures Div. ASCE* **103:8**, 1631-1641.
- Gaines J.H. and Voltera E. (1976). Upper and Lower Frequencies of Tapered Beams. *Journal of Engineering Mech Div ASCE* **94:2**, 465-488.
- Kounadis A. (1976). Dynamic Response of Cantilever Beam-columns with Attached Masses Supported on a Flexible Foundation. *Proceedings of International Symposium on Earthquake Structure Engineering*, St. Louis Missouri, U.S.A., 473-482.
- Prathap G. and Varadan T.K. (1976). Finite Deflection of Tapered Cantilevers. *Journal of Engineering Mech Div ASCE* **102:3**, 549-552.
- Rohde F.V. (1953). Large Deflections of Cantilever Beam with Uniformly Distributed Load. *Quarnt Appl Math* **11**, 337.
- Takabatake H. (1990). Cantilever and Linearly Tapered Thin-walled Members. *Journal of Engineering Mech ASCE* **116:4**, 733-750.
- Takabatake H., Mukai H. and Hirano T. (1993). Doubly Symmetric Tube Structures I: Static Analysis. *Journal of Structure Engineering ASCE* **119:7**, 1981-2001.
- Takabatake H., Mukai H. and Hirano T. (1993). Doubly Symmetric Tube Structures II: Dynamic Analysis. *Journal of Structure Engineering ASCE* **119:7**, 2002-2006.
- Takabatake H. and Mizuki A. (1995). Simplified Dynamic Analysis of Slender Tapered Thin-walled Towers with Additional Mass and Rigidity. *Structures Engineering and Mechanics* **3:1**, 61-74.
- Wang T.M. and Lee C.H. (1973). Tapered Cantilevers with Varying Distributed Loads. *Journal of Engineering Mechanics Div ASCE* **99:4**, 919-925.

APPENDIX

1. The shape functions of the free flexural vibrating cantilever (without varying gross-section) are:

$$\Psi_n(x) = c_{2n} \left[\frac{c_{1n}}{c_{2n}} (\sin \lambda_n x - \sinh \lambda_n x) - (\cos \lambda_n x - \cosh \lambda_n x) \right], \text{ with: } \frac{c_{1n}}{c_{2n}} = \frac{\cos \lambda_n \ell + \cosh \lambda_n \ell}{\sin \lambda_n \ell + \sinh \lambda_n \ell} \quad (\text{a})$$

2. The shape functions of the free torsional vibrating simple cantilever (without varying gross-section) are:

$$\left. \begin{aligned} \Phi_n(x) &= c_{1n} \left[\sin k_{1n} x - \frac{k_{1n}}{k_{2n}} \cdot \sinh k_{2n} x - \frac{c_{4n}}{c_{1n}} (\cos k_{1n} x - \cos k_{2n} x) \right], \text{ with:} \\ k_{1n}, k_{2n} &= \sqrt{\mp \frac{\mu}{2} + \sqrt{\left(\frac{\mu}{2}\right)^2 + \frac{\omega_{n\sigma}^2 \cdot \Theta}{EC_T}}}, \mu = \frac{GI_D}{EC_T}, \frac{c_{4n}}{c_{1n}} = \frac{k_{1n}^2 \sin k_{1n} \ell + k_{1n} k_{2n} \sinh k_{2n} \ell}{k_{1n}^2 \cos k_{1n} \ell + k_{2n}^2 \cosh k_{2n} \ell} \end{aligned} \right\} \quad (\text{b})$$

OPTIMAL DESIGN OF PIECEWISE-CONSTANT THICKNESS CIRCULAR PLATES FOR MINIMAX AXISYMMETRIC DEFLECTION

C.M. Wang and K.K. Ang

*Department of Civil Engineering, The National University of Singapore
Kent Ridge, Singapore 119260*

ABSTRACT

A canonical exact deflection expression for piecewise constant circular plates under any rotationally symmetric transverse loading is presented. The circular plates may be simply supported or clamped at the edges. Based on the analytical deflection expression, we derive the optimality conditions for the optimum values of segmental thickness and boundaries that minimise the maximum (central) deflection of piecewise-constant thickness circular plates of a given volume. As certain portions of the optimal plate design may become rather thick, the effect of transverse shear deformation has been taken into consideration in accordance to the Mindlin plate theory for a more accurate calculation of the deflection.

KEYWORDS

Circular plate; piecewise constant thickness; optimal design; Mindlin plate theory; minimax deflection

INTRODUCTION

A substantial increase in the stiffness, buckling and vibration capacities of plates over their uniform thickness counterpart may be realised by appropriately varying the thickness distribution. The optimisation problem of non-uniform thickness plates with deflection constraints has attracted many researchers. Hegemier and Tang 1975 considered the optimisation plate problem with bounds on the transverse deflection at several prescribed locations. They used a variational method to derive the optimality criterion and employed the finite element method to obtain numerical solutions for sandwich plates. Armand and Lodier 1978 used a finite element formulation for optimising rectangular plates with a single deflection constraint. Interestingly, their optimal designs developed ribs that enhance the stiffness. Banichuk and his associates 1975, 1977, 1978, 1981 proposed a theory and computational method for the minimum weight design of plates with a deflection constraint over the entire plate. Owing to the general treatment of arbitrary shaped plates, the method used by Banichuk is rather complicated.

This study considers the class of non-uniform thickness, circular plates in which the thickness distribution takes the form of annular piecewise constant. The segmental thickness and boundaries are to be optimally selected so as to minimise the maximum deflection of the circular plate under a rotationally symmetric, transverse loading. In the optimal design, the effect of transverse shear deformation on the deflection is also taken into consideration as certain portions of the optimal plate may become rather thick and this effect can become significant. A canonical exact deflection expression for such loaded plates with edges either simply supported or clamped has been derived.

PROBLEM DEFINITION

Consider an axisymmetric circular plate of radius R , volume V and consisting of n piecewise-constant annular segments as shown in Figure 1. The piecewise-constant i -th segment has a thickness of h_i and its end radial coordinates measured from the plate centre are $r = a_{i-1}$ and $r = a_i$. The plate material has a modulus of elasticity E , Poisson's ratio ν , and shear modulus $G = E / [2(1 + \nu)]$. The plate is subjected to a rotationally symmetric, transverse loading $q(r)$. The problem at hand is to optimise the material distribution of such a plate for minimax deflection with respect to the segmental thickness and boundaries.

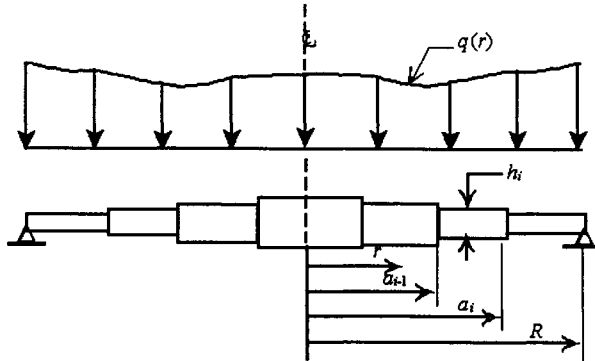


Figure 1. Piecewise-constant circular plate under rotationally symmetric loading

CANONICAL EXACT DEFLECTION EXPRESSION

As the optimal design of the plate may involve somewhat thick segmental portions, the effect of transverse shear deformation may become significant and thus should not be neglected. This effect may be included by using the first order shear deformation plate theory proposed by Mindlin 1951. Recently, Wang 1997 derived an exact relationship between the deflections of the Kirchhoff (or classical thin) plate theory and the Mindlin plate theory for statically determinate, axisymmetric tapered plates under rotationally symmetric loading. This relationship is given by

$$w^M(r) = w^K(r) - \int_r^R \frac{Q_r^K}{\kappa^2 Gh} dr \tag{1}$$

where w is the transverse deflection, κ^2 the Mindlin shear correction factor, and the superscripts M and K denote quantities belonging to the Mindlin plate theory and Kirchhoff plate theory, respectively. Q_r^K is the Kirchhoff transverse shear force given by

$$Q_r^K = -\frac{d}{dr} \left[D \left(\frac{d^2 w^K}{dr^2} + \frac{1}{r} \frac{dw^K}{dr} \right) \right] \tag{2}$$

in which $D(r) = Eh^3(r) / [12(1 - \nu^2)]$ is the flexural rigidity. The relationship given by (1) allows one to bypass solving the more complicated shear deformation plate equations since only the Kirchhoff plate solutions are needed. Below, we derive the exact deflection expression for a piecewise constant thickness, circular Kirchhoff plate.

For the considered axisymmetric plate bending problem, the equilibrium equation for vertical forces is given by

$$\frac{d}{dr}(rQ_r^K) = -qr \Rightarrow Q_r^K = -\frac{1}{r} \int_0^r qr \, dr \quad (3a,b)$$

Note that the integrating constant in (3b) is zero as $Q_r^K = 0$ at $r = 0$. Upon substitution of (2) into (3b) and after integration yields

$$\frac{d}{dr} \left(r \frac{dw^K}{dr} \right) = \frac{r}{D} [f(r) - C_1] \quad (4)$$

where C_1 is a constant of integration and the function $f(r)$ is given by

$$f(r) = \int_0^r \left\{ \frac{1}{r} \int_0^r qr \, dr \right\} dr \quad (5)$$

By integrating (4) with respect to r and noting that $dw^K / dr = 0$ at $r = 0$, we have

$$r \frac{dw^K}{dr} = g_1(r) - C_1 g_2(r) \quad (6)$$

where

$$g_1(r) = \int_0^r \frac{rf}{D} \, dr \quad (7)$$

$$g_2(r) = \int_0^r \frac{r}{D} \, dr \quad (8)$$

Finally, integrating (6) we obtain

$$w^K(r) = e_1(r) - C_1 e_2(r) + C_2 \quad (9)$$

where

$$e_1(r) = \int_0^r \frac{g_1(r)}{r} \, dr \quad (10)$$

$$e_2(r) = \int_0^r \frac{g_2(r)}{r} \, dr \quad (11)$$

The constants C_1 and C_2 may be evaluated using the following boundary conditions at $r = R$:

for a simply supported edge

$$w^K(R) = 0, \quad M_r^K = -D_n \left(\frac{d^2 w^K(R)}{dr^2} + \frac{\nu}{R} \frac{dw^K(R)}{dr} \right) = 0 \quad (11a)$$

for a clamped edge

$$w^K(R) = 0, \quad \frac{dw^K(R)}{dr} = 0 \quad (11b)$$

In view of the foregoing boundary conditions, (4), (6), and (9), the integrating constants are found to be

$$C_2 = C_1 e_2(R) - e_1(R) \quad (12)$$

and

$$C_1 = \frac{g_1(R) - s_0 \frac{R^2 f(R)}{D_n(1-\nu)}}{g_2(R) - s_0 \frac{R^2}{D_n(1-\nu)}}, \quad (13)$$

where the scalar indicator $s_0 = 1$ for simply supported plates and $s_0 = 0$ for clamped plates.

Thus the deflection expression for a piecewise constant plate according to Mindlin plate theory is given by

$$\begin{aligned} w^M(r) &= C_1 [e_2(R) - e_2(r)] - [e_1(R) - e_1(r)] - \int_r^R \frac{Q_r^K}{\kappa^2 Gh} dr \\ &= C_1 \int_r^R \frac{g_2}{r} dr - \int_r^R \frac{g_1}{r} dr - \int_r^R \frac{Q_r^K}{\kappa^2 Gh} dr \end{aligned} \quad (14)$$

OPTIMISATION PROBLEM AND OPTIMALITY CONDITIONS

The optimisation problem at hand is to optimally design the plate segmental thickness $h_i, i = 1, 2, \dots, n$ and segmental boundaries $a_j, j = 1, 2, \dots, n-1$ that will minimise the maximum deflection of the circular plate of a given volume $V = \pi R^2 h_0$, where h_0 is the uniform thickness of a reference plate. For such axisymmetric bending problems of circular plates under a vertical, rotationally symmetric loading, the maximum deflection is at the plate centre. Thus, the optimisation problem may be written as

$$\begin{aligned} \text{Min}_{h_i, a_j} w^M(0) &= \int_0^R \left\{ C_1 \frac{g_2}{r} - \frac{g_1}{r} - \frac{Q_r^K}{\kappa^2 Gh} \right\} dr + \Lambda \left[R^2 h_0 - \sum_{k=1}^n (a_k^2 - a_{k-1}^2) h_k \right], \\ & \quad i = 1, 2, \dots, n \text{ and } j = 1, 2, \dots, n-1 \end{aligned} \quad (15)$$

where $a_0 = 0, a_n = R$, and Λ is a Lagrangian multiplier which is used to impose the volume constraint.

First consider the optimisation problem of a circular plate with prescribed segmental boundaries while the segmental thickness are to be optimally selected. By taking the stationarity conditions of the central deflection with respect to h_i , one obtains the following optimality condition

$$\begin{aligned} \frac{\partial w^M(0)}{\partial h_i} &= \frac{\partial C_1}{\partial h_i} \int_0^R \frac{g_2}{r} dr - C_1 \frac{\partial}{\partial h_i} \left(\int_0^R \frac{g_2}{r} dr \right) - \frac{\partial}{\partial h_i} \left(\int_0^R \frac{g_1}{r} dr \right) \\ &+ \frac{1}{\kappa^2 G h_i^2} \int_{a_{i-1}}^{a_i} Q_r^K dr - \Lambda (a_i^2 - a_{i-1}^2) = 0, \quad i = 1, 2, \dots, n \end{aligned} \quad (16)$$

The stationarity condition of (15) with respect to Λ gives the volume constraint, *i.e.*

$$R^2 h_0 - \sum_{k=1}^n (a_k^2 - a_{k-1}^2) h_k = 0 \quad (17)$$

So the optimal segmental thickness are determined by solving (16) and (17).

For the more general optimisation problem in which the segmental boundaries are to be optimised as well, the additional optimality condition is obtained by taking the stationarity condition of (15) with respect to a_j , i.e.

$$\begin{aligned} \frac{\partial w^M(0)}{\partial a_j} &= \frac{\partial \mathcal{C}_1}{\partial a_j} \left[\int_0^R \frac{g_2}{r} dr \right] - C_1 \frac{\partial}{\partial a_j} \left(\int_0^R \frac{g_2}{r} dr \right) - \frac{\partial}{\partial a_j} \left(\int_0^R \frac{g_1}{r} dr \right) \\ &+ \frac{\partial}{\partial a_j} \left(\int_0^R \frac{Q_r^K}{\kappa^2 Gh} dr \right) - 2\Lambda a_j h_j = 0, \quad j = 1, 2, \dots, n-1 \end{aligned} \tag{18}$$

Thus, by solving (16), (17) and (18), one obtains the optimum values of h_i and a_j . The set of nonlinear equations may be solved using the Newton method or any standard iterative search technique.

AN ILLUSTRATIVE EXAMPLE

Consider the case of a circular plate under a uniform load p . Under this loading condition, we have

$$q = p \Rightarrow Q_r^K = -\frac{pr}{2}, \quad f = \frac{pr^2}{4} \tag{18}$$

$$C_1 = \frac{\frac{p}{16} \left(\sum_{k=1}^n \frac{a_k^4 - a_{k-1}^4}{D_k} \right) - s_0 \frac{pR^4}{4D_n(1-\nu)}}{\frac{1}{2} \left(\sum_{k=1}^n \frac{a_k^2 - a_{k-1}^2}{D_k} \right) - s_0 \frac{R^2}{D_n(1-\nu)}} \tag{19}$$

As a result of (14), the maximum deflection at the plate centre is given by

$$\begin{aligned} w^M(0) &= C_1 \left[\frac{1}{4} \left\{ \sum_{k=1}^n \frac{a_k^2 - a_{k-1}^2}{D_k} \right\} - \frac{1}{2} \left\{ \sum_{k=1}^n \frac{a_{k-1}^2 \ln(a_k/a_{k-1})}{D_k} \right\} \right] \\ &- \frac{p}{64} \left\{ \sum_{k=1}^n \frac{a_k^4 - a_{k-1}^4}{D_k} \right\} + \frac{p}{16} \left\{ \sum_{k=1}^n \frac{a_{k-1}^4 \ln(a_k/a_{k-1})}{D_k} \right\} + \frac{p}{4\kappa^2 G} \left\{ \sum_{k=1}^n \frac{a_k^2 - a_{k-1}^2}{h_k} \right\} \end{aligned} \tag{20}$$

For optimum segmental thickness, the optimality condition of (16) yields

$$\begin{aligned} \frac{\partial \mathcal{C}_1}{\partial h_i} \left[\frac{1}{4} \left\{ \sum_{k=1}^n \frac{a_k^2 - a_{k-1}^2}{D_k} \right\} - \frac{1}{2} \left\{ \sum_{k=1}^n \frac{a_{k-1}^2 \ln(a_k/a_{k-1})}{D_k} \right\} \right] &+ C_1 \left[\frac{-3(a_i^2 - a_{i-1}^2)}{4h_i D_i} + \frac{3a_{i-1}^2 \ln(a_i/a_{i-1})}{2h_i D_i} \right] \\ &+ \frac{3p(a_i^4 - a_{i-1}^4)}{64h_i D_i} - \frac{3pa_{i-1}^4 \ln(a_i/a_{i-1})}{16h_i D_i} - \frac{p(a_i^2 - a_{i-1}^2)}{4\kappa^2 Gh_i^2} - \Lambda(a_i^2 - a_{i-1}^2) = 0 \end{aligned} \tag{21}$$

where

$$\frac{\partial \alpha_1}{\partial h_i} = \frac{\left[-\frac{3p(a_i^4 - a_{i-1}^4)}{16h_i D_i} + s_1 \frac{3pR^4}{4h_n D_n (1-\nu)} \right] \left[\frac{1}{2} \left(\sum_{k=1}^n \frac{a_k^2 - a_{k-1}^2}{D_k} \right) - s_0 \frac{R^2}{D_n (1-\nu)} \right] - \left[-\frac{3(a_i^2 - a_{i-1}^2)}{2h_i D_i} + s_1 \frac{3R^2}{h_n D_n (1-\nu)} \right] \left[\frac{p}{16} \left(\sum_{k=1}^n \frac{a_k^4 - a_{k-1}^4}{D_k} \right) - s_0 \frac{pR^4}{4D_n (1-\nu)} \right]}{\left[\frac{1}{2} \left(\sum_{k=1}^n \frac{a_k^2 - a_{k-1}^2}{D_k} \right) - s_0 \frac{R^2}{D_n (1-\nu)} \right]^2}$$

$i = 1, 2, \dots, n$ (22)

with $s_1 = 0$ for $i \neq n$ and $s_1 = 1$ for $i = n$.

For segmental boundaries, the optimality condition of (18) yields

$$\frac{\partial \alpha_1}{\partial a_j} \left[\frac{1}{4} \left\{ \sum_{k=1}^n \frac{a_k^2 - a_{k-1}^2}{D_k} \right\} - \frac{1}{2} \left\{ \sum_{k=1}^n \frac{a_{k-1}^2 \ln(a_k / a_{k-1})}{D_k} \right\} \right] + C_1 \left[\frac{a_j}{2D_j} - \frac{a_{j-1}^2}{2a_j D_j} \right] - \frac{pa_j^3}{16D_j} + \frac{pa_{j-1}^4}{16a_j D_j} + \frac{pa_j}{2\kappa^2 Gh_j} - 2\Lambda a_j h_j = 0$$

(23)

where

$$\frac{\partial \alpha_1}{\partial a_j} = \frac{\frac{pa_j^3}{4D_j} \left[\frac{1}{2} \left(\sum_{k=1}^n \frac{a_k^2 - a_{k-1}^2}{D_k} \right) - s_0 \frac{R^2}{D_n (1-\nu)} \right] - \frac{a_j}{D_j} \left[\frac{p}{16} \left(\sum_{k=1}^n \frac{a_k^4 - a_{k-1}^4}{D_k} \right) - s_0 \frac{pR^4}{4D_n (1-\nu)} \right]}{\left[\frac{1}{2} \left(\sum_{k=1}^n \frac{a_k^2 - a_{k-1}^2}{D_k} \right) - s_0 \frac{R^2}{D_n (1-\nu)} \right]^2}$$

(24)

Owing to length limitation, only some sample results will be presented for piecewise-constant, circular plates under a uniform load. Figures 2 and 3 give the optimal solutions for equally segmented thin ($h_0 / R = 0$) plates with simply supported and clamped edges, respectively, taking $\nu = 0.3$ and $\kappa^2 = 5/6$. These solutions involve optimising only the segmental thickness with the segmental lengths kept equal. The effect of transverse shear deformation on the optimal central deflections may be observed from Figure 4 for the clamped case which shows a substantial increase in the deflection values with thicker plates (as the parameter h_0 / R increases). It can also be noted that the deflection can be significantly reduced by increasing the number of segments. This reduction, however, tapers off after about 5 segments.

Figure 5 compares the optimal designs between equally segmented and optimal segmented lengths for simply supported plates with $n = 2$ and $n = 5$. It is evident from the results that by also optimising the segmental lengths, one may obtain a more effective distribution of plate material and obtain a further reduction in the maximum central deflection.

CONCLUDING REMARKS

A canonical exact deflection expression for piecewise constant thickness, circular plates under rotationally symmetric loadings has been derived. The effect of transverse shear deformation is accounted for so that the solutions may still be accurate when dealing with thick plates. Based on this analytical expression, we have derived the optimality conditions for the segmental thickness and boundaries that minimise the maximum deflection of the circular plate of a given volume. The optimal

design of such plates not only show the engineer the significant economical distribution of the material but it also serves as a reference to measure the efficiency of other nonuniform thickness plates.

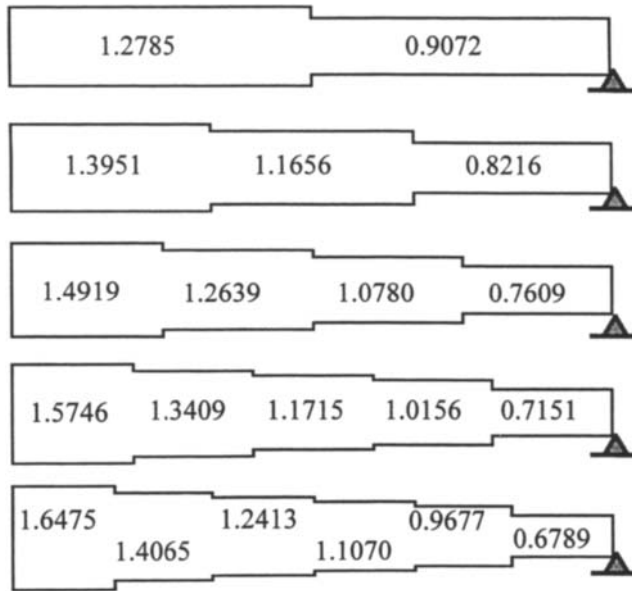


Figure 2. Optimal thickness for equally segmented simply-supported thin plates

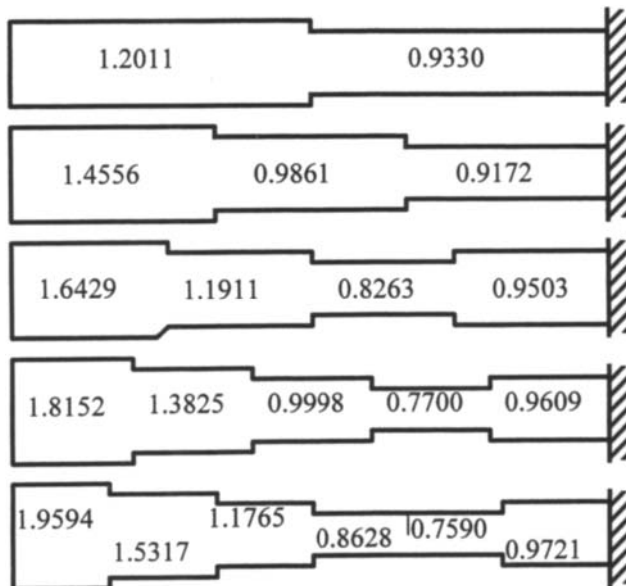


Figure 3. Optimal thickness for equally segmented clamped thin plates

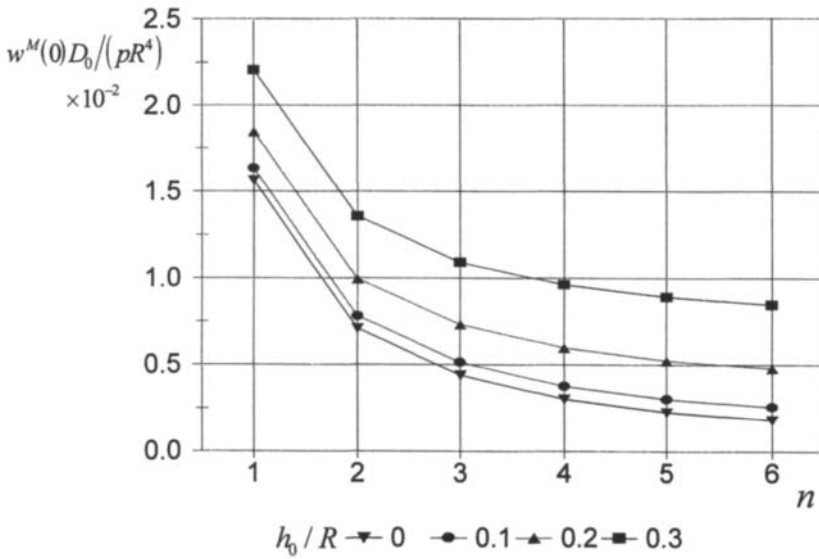


Figure 4. Maximum deflections for equally segmented clamped plates

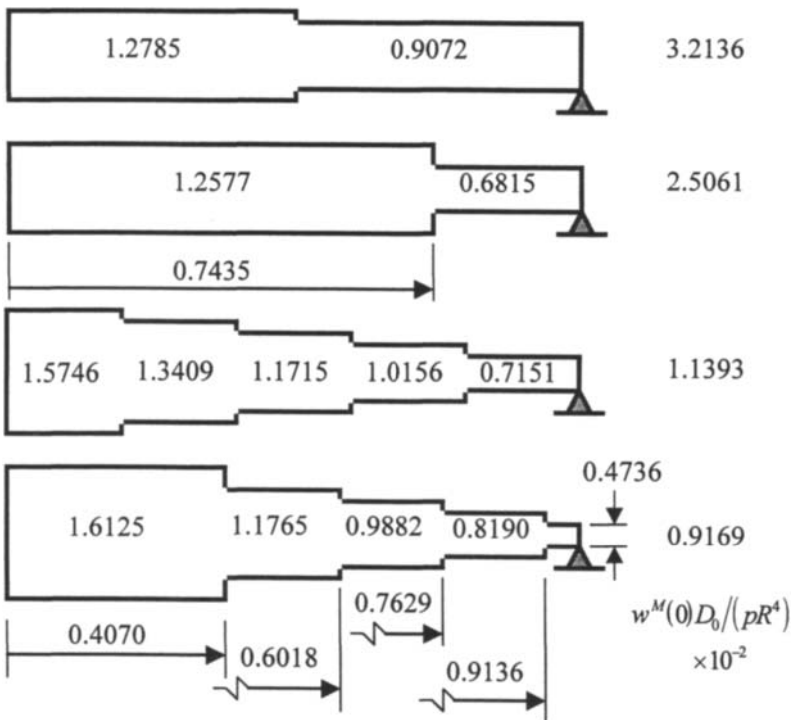


Figure 5. Maximum deflections for equally segmented clamped plates

REFERENCES

- Armand, J.L. and Lodier, B. (1978). Optimal design of bending elements, *International Journal of Numerical Methods in Engineering*, **13**, 373-384.
- Banichuk, N.V. (1975). Optimal elastic plate shapes in bending problems, *MTT*, **10:5**, 151-158.
- Banichuk, N.V., Karelshvili, V.M. and Mironov, A.A. (1977). Numerical solution of two-dimensional optimisation problems for elastic plates, *MTT*, **12:1**, 65-74.
- Banichuk, N.V., Karelshvili, V.M. and Mironov, A.A. (1978). Optimisation problems with local performance criteria in the theory of plate bending, *MTT*, **13:1**, 116-122.
- Banichuk, N.V. (1981). Design of plate for minimum stress and deflection, *Optimisation of Distributed Parameter Structures, Iowa, 1980*, 333-361.
- Hegemier, G.A. and Tang, H.T. (1975), A variational principle, the finite element methods, and optimal design for given deflection, *Optimisation in Structural Design* (Ed. Sawczuk and Mroz), Springer-Verlag, New York, 464-483.
- Mindlin, R.D. (1951). Influence of rotatory inertia and shear in flexural motion of isotropic, elastic plates, *Trans. ASME, Journal of Applied Mechanics*, **18**, 1031-1036.
- Wang, C.M. (1997). Relationships between Mindlin and Kirchhoff bending solutions for tapered circular and annular plates, *Engineering Structures*, **19:3**, 255-258.

This Page Intentionally Left Blank

ANALYSIS WITH NON-ORTHOGONAL FUNCTIONS FOR ANISOTROPIC SHELLS

Kai-yu Xu, Zhe-wei Zhou and Wei-zang Chien

Shanghai Institute of Applied Mathematics and Mechanics, Shanghai University
149 Yanchang Road, Shanghai 200072, P. R. CHINA

ABSTRACT

This paper investigates the dynamic nonlinear behavior of a laminated anisotropic circular cylindrical shell under a harmonic excitation applied on its both ends. For this, the modified Flugge partial differential equations of motion for displacements are reduced to a finite degree of freedom system using the Galerkin method. Three displacements are described by a series of non-orthogonal basis that satisfy the relevant boundary and continuity conditions. The resulting differential equations of motion are solved by Liapunov-Schmidt reduction and the center manifold theorem. To study $1/2$ and $1/4$ subharmonic parametric resonance of the circular cylindrical shell, transition sets in parameter plane and bifurcation diagrams are plotted for a number of situations. Results indicates that, for some fixed static load levels, the shell may display jumps due to the presence of dynamic periodic load with small amplitude. Additionally, different physical situations are identified in which periodic oscillating phenomena can be observed, and especially, the type of $1/4$ subharmonic parametric resonance is a representative Hopf bifurcation.

KEYWORDS

Non-orthogonal functions, nonlinear dynamics, anisotropy, laminated cylindrical shell, nonlinear oscillation, parametric resonance, subharmonic bifurcation

INTRODUCTION

In structural mechanics, dynamic stability or instability has received considerable attention in the past 40 years. Several studies have been conducted by various investigations on structural system which are dynamically loaded (sudden loads and periodic or nonperiodic time-dependent loads). One of the best

defined of dynamic stability problems are those falling in the category of parameter resonance. So far, in describing the phenomenon of parametric resonance, the forcing functions have been assumed to be parametric also. According to Bolotin [1], the first analysis of parametric resonance of a structural configuration was presented by Beliaev [2]. For the more comprehensive and expanded treatment see References [3]. Some studies and reviews have appeared in the literature on this subject. Most of these deal with a single particular structural configuration Examples for which the phenomenon of parametric resonance is due to pulsating forces including columns, shallow arches and shells[4-6].

Laminated composites have been more and more extensively used in many different branches of engineering as most efficient structural members and thus have received special attention. Most papers were concerned with laminated plates under periodic forces while few deal with shells. Birman [7] published a study on the dynamic stability of unsymmetrically laminated rectangular plates subjected to in-plane harmonic forces using a single-model approach of transverse displacement. The Liapunov direct method has been applied to nonlinear cross-ply laminated plates [8]. The intent of the present paper is the investigation of parametric resonance problem for a laminated anisotropic circular cylindrical shell obeying modified Flugge equations, where the mechanical coupling is taken into account. The non-orthogonal series are adopted in Galerkin method to obtain finite dimensional approximations in analysis of dynamics. Using the singularity theory method [9], sufficient conditions for dynamic stability, transition sets in parameter plane as well as bifurcation diagrams for parametric resonance are derived. A significant advantage is offered by the method that the equations of motion do not have to be solved in order to examine the dynamic buckling.

FORMULATION AND BIFURCATION EQUATIONS

Let us consider a thin, laminated anisotropic circular cylindrical shell of constant thickness h , radius R and length L . The Kirchhoff-Love hypothesis and Flugge-type geometric non-linearity are taken into account. Neglecting coupling inertial, the governing partial differential equations are given as [10]

$$\begin{aligned} & \left[N_{\alpha\beta} \left(\delta_{1\beta} + u_{1,\beta} \right) \right]_{,\alpha} - P u_{1,11} - \rho h u_{1,tt} = 0 \\ & \left[N_{\alpha\beta} \left(\delta_{2\beta} \left(1 + \frac{u_3}{R} \right) u_{2,\beta} \right) \right]_{,\alpha} - \frac{N_{2\beta}}{R} \left(u_{3,\beta} - \delta_{2\beta} \frac{u_2}{R} \right) + \frac{M_{\alpha 2, \alpha}}{R} - P u_{2,11} - \rho h u_{2,tt} = 0 \\ & \left[N_{\alpha\beta} \left(u_{3,\beta} - \delta_{2\beta} \frac{u_2}{R} \right) \right]_{,\alpha} - \frac{N_{2\beta}}{R} \left(u_{2,\beta} + \delta_{2\beta} \left(1 + \frac{u_3}{R} \right) \right) + M_{\alpha\beta, \alpha\beta} - P u_{3,11} - \rho h u_{3,tt} = 0 \end{aligned} \quad (1)$$

where u_i ($i = 1, 2, 3$) denote axial, circumferential and radial displacements of the middle surface respectively, $N_{\alpha\beta}$ and $M_{\alpha\beta}$ ($\alpha, \beta = 1, 2$) are respectively the components of the internal forces and bending moments applied per unit length, $P = p_0 + \varepsilon p(t)$ is external axial time-dependent pressure, p_0 and ε are positive numbers, $p(t)$ is a periodic function, namely $p(t + 2\pi) = p(t)$, ρ is the density of shell material, and δ_{ij} is Kroneck delta. In these equations the repeated index in a term indicates summation with respect to this index.

Equation (1) is the mathematical model of the dynamic buckling problem of laminated anisotropic circular cylindrical shell. Energy approaches like Galerkin method can be used to solve this problem. We

assume an expansion for the displacement modes as

$$(u_1, u_2, u_3) = \left(\sum_{i=1}^n f_i^{(1)}(t) \psi_i^{(1)}, \sum_{i=1}^n f_i^{(2)}(t) \psi_i^{(2)}, \sum_{i=1}^n f_i^{(3)}(t) \psi_i^{(3)} \right) \quad (2)$$

in which $(\psi_1^{(k)}, \psi_2^{(k)}, \dots, \psi_n^{(k)}) (k = 1, 2, 3)$ are non-orthogonal series satisfying the boundary conditions and capable of representing the mode of deformation, $f_i^{(k)}(t)$ are underdetermined variable coefficients of time. By the principle of virtual work a first order ordinary differential equation obtained

$$\frac{dy}{dt} = \begin{bmatrix} \mathbf{0}_{3n \times 3n} & \mathbf{I}_{3n \times 3n} \\ -p_0 \mathbf{G}_M - \mathbf{K}_M & \mathbf{0}_{3n \times 3n} \end{bmatrix} y - \begin{bmatrix} \mathbf{0}_{3n \times 1} \\ \epsilon p \mathbf{G}_M y^{(0)} + \mathbf{Q}_M(y^{(0)}) + \mathbf{C}_M(y^{(0)}) \end{bmatrix} \quad (3)$$

in which

$$y_i = f_i^{(1)}, y_{i+n} = f_i^{(2)}, y_{i+2n} = f_i^{(3)}, y_{i+3n} = \frac{dy_i}{dt} \quad (i = 1, 2, \dots, 3n) \quad (4)$$

$$y^{(0)} = (y_1, y_2, \dots, y_{3n})^T, y^{(1)} = (y_{3n+1}, y_{3n+2}, \dots, y_{6n})^T, y = (y^{(0)}, y^{(1)})^T$$

where $\mathbf{G}_M = \mathbf{M}^{-1} \mathbf{G}, \mathbf{K}_M = \mathbf{M}^{-1} \mathbf{K}, \mathbf{Q}_M = \mathbf{M}^{-1} \mathbf{Q}, \mathbf{C}_M = \mathbf{M}^{-1} \mathbf{C}, \mathbf{M}, \mathbf{G},$ and \mathbf{K} are mass matrixes, geometric rigidity matrix with regard to external load, and rigidity of the shell respectively. The quadratic and cubic nonlinear mappings \mathbf{Q} and \mathbf{C} satisfy

$$\mathbf{Q}: \mathbb{R}^{2n} \rightarrow \mathbb{R}^n, \mathbf{Q}(\sigma \mathbf{F}(t)) = \sigma^2 \mathbf{Q}(\mathbf{F}(t)), \quad \mathbf{C}: \mathbb{R}^{2n} \rightarrow \mathbb{R}^n, \mathbf{C}(\sigma \mathbf{F}(t)) = \sigma^3 \mathbf{C}(\mathbf{F}(t)) \quad (5)$$

in which σ is an arbitrary real number. Equation (3) constitutes a system of equations for the motion of the shell.

In order to discuss various types of dynamic buckling problems of equation (3), we will use center manifold theorem for the periodic case and indicate non-hyperbolic structure of the flow on the center manifold. Denote the rigidity matrix

$$\mathbf{A} = \begin{bmatrix} \mathbf{0}_{3n \times 3n} & \mathbf{I}_{3n \times 3n} \\ -p_0 \mathbf{G}_M - \mathbf{K}_M & \mathbf{0}_{3n \times 3n} \end{bmatrix} \quad (6)$$

More specifically, we consider the case that the submatrix $\mathbf{A}_0 = (-p_0 \mathbf{G}_M - \mathbf{K}_M)$ of \mathbf{A} only has one eigenvalue with zero real part. Take a similarity transformation

$$y = \mathbf{T}x, \quad \mathbf{T} = \begin{bmatrix} \mathbf{S} & \mathbf{0} \\ \mathbf{0} & \mathbf{S} \end{bmatrix}, \quad \mathbf{S}^{-1}(-p_0 \mathbf{G}_M - \mathbf{K}_M)\mathbf{S} = \begin{bmatrix} \mathbf{C} & \mathbf{0} \\ \mathbf{0} & \mathbf{B} \end{bmatrix} \quad (7)$$

in which $\mathbf{C} = 0$ if \mathbf{A} has a zero eigenvalue, and $\mathbf{C} = -\omega^2$ if \mathbf{A} has a pair of purely conjugate imaginary eigenvalues. Using the transformation (7), the equation (3) leads to

$$\begin{aligned} \frac{du}{dt} &= \mathbf{C}u - \epsilon p(t) \mathbf{G}_T^{(u)} u - \mathbf{N}_1(u, v) \\ \frac{dv}{dt} &= \mathbf{B}v - \epsilon p(t) \mathbf{G}_T^{(v)} v - \mathbf{N}_2(u, v) \end{aligned} \quad (8)$$

From (5), one obtains $N_1(0,0) = 0, DN_1(0,0) = 0, N_2(0,0) = 0, DN_1(0,0) = 0$, in which “D” denotes the partial derivative. It is clear that there are no coupling terms in the periodic system (8). Now we need to recall results on center manifold. According to Chow [11], the center manifold for an autonomous system are easily extended to the periodic case. Suppose that $h(t, u, \epsilon)$ is a center manifold of (8), then the function h satisfied $h(t,0,0) = 0, Dh(t,0,0) = 0$. So the first equation in (8) yields

$$\frac{du}{dt} = Cu - \epsilon p(t)G_T^{(u)}u - N_1(u, h(t, u, \epsilon)) \tag{9}$$

The flow on center manifold is given by the scalar differential equation (9). From the center manifold theory, the dynamic properties of the periodic solutions of (8) can be determined directly from the bifurcation equation (9). This, in turn, means that the dynamic properties of the periodic solutions of equation (3) are determined from the bifurcation equation.

SUBHARMONIC BIFURCATONS

Suppose the state matrix A has a pair of purely conjugate eigenvalues $\pm i\omega$ ($\omega > 0$) besides the others with non-zero real parts. The problem is to determine the bifurcation solution of the equation based on equations (8). Without loss generality, we may assume the external periodic load to be $p(t) = -2 \cos kt$ and the harmonious parameter $\lambda = \omega^2 - m^2$ can be regarded as a bifurcation parameter. The flow on the center manifold is given by a 2-order ordinary differential equation (8) replacing u_1 by u , that is

$$\frac{d^2u}{dt^2} + (m^2 + \lambda)u(t) + \alpha u^2(t) + \beta u^3(t) - 2\epsilon \cos(kt)u(t) = 0 \tag{10}$$

This is a nonlinear Mathieu equation. We next apply the singularity theory to study the subharmonic parametric resonance of equation (16). Applying the Liapunov-Schmidt reduction to equation (16), we may obtain a equation which can be written in the complex function as follows

$$\lambda z + \alpha(a_{20}z^2 + a_{11}z\bar{z} + a_{02}\bar{z}^2) + 3\beta z^2\bar{z} + \epsilon(a_{10}z + a_{01}\bar{z} + a_{12}z\bar{z}^2 + a_{30}z^3 + a_{03}\bar{z}^3) = 0 \tag{11}$$

Now, let us consider tow kinds of subharmonic bifurcations of the shell.

1/2 Subharmonic Parametric Resonance

In this case, $m/k = 1/2$, letting $z = e^{i\theta}$, substituting it into (17), and neglecting trivial solution of equation, while the non-trivial bifurcation solutions satisfy the equation

$$Dr^4 - \epsilon^2 \frac{\xi}{6m^2} \left(\frac{\alpha^2}{m^2} + \frac{3\beta}{2} \right) r^2 + 6\lambda\beta r^2 + \lambda^2 - \epsilon^2 = 0 \tag{12}$$

where

$$\xi = \cos 4\theta, \quad D = 9\beta^2 - \frac{\epsilon^2}{144m^4} \left(\frac{\alpha^2}{m^2} + \frac{3\beta}{2} \right)^2 \tag{13}$$

We assume that $D \neq 0$, introducing a nonlinear transformation $\phi R^4 = |D|r^4, \phi = \text{sgn}(D)$, the bifurcation

equation (12) can be written as follows

$$\phi R^4 + 2\eta\lambda R^2 + \lambda^2 - \alpha_1 R^2 - \varepsilon^2 = 0 \tag{14}$$

in which

$$\eta = \frac{3\beta}{\sqrt{|D|}}, \quad \alpha_1 = \frac{1}{\sqrt{|D|}} \frac{\varepsilon^2 \xi}{6m^2} \left(\frac{\alpha^2}{m^2} + \frac{3\beta}{2} \right) \tag{15}$$

The various components of the transition set $\Sigma = H_0 \cup B_0 \cup B_1$ are described by the following equations

$$H_0: \eta^2 \varepsilon^2 = \left(\frac{\alpha_1}{2} \right)^2, \quad B_0: \varepsilon = 0, \quad B_1: \varepsilon^2 = (\alpha_1/2)^2 / (\eta^2 - \phi), \quad \text{sgn}(-\alpha_1) = \text{sgn}(\eta^2 - \phi) \tag{16}$$

We show this transition set and bifurcation diagrams associated to equation (14), see Figure 1.

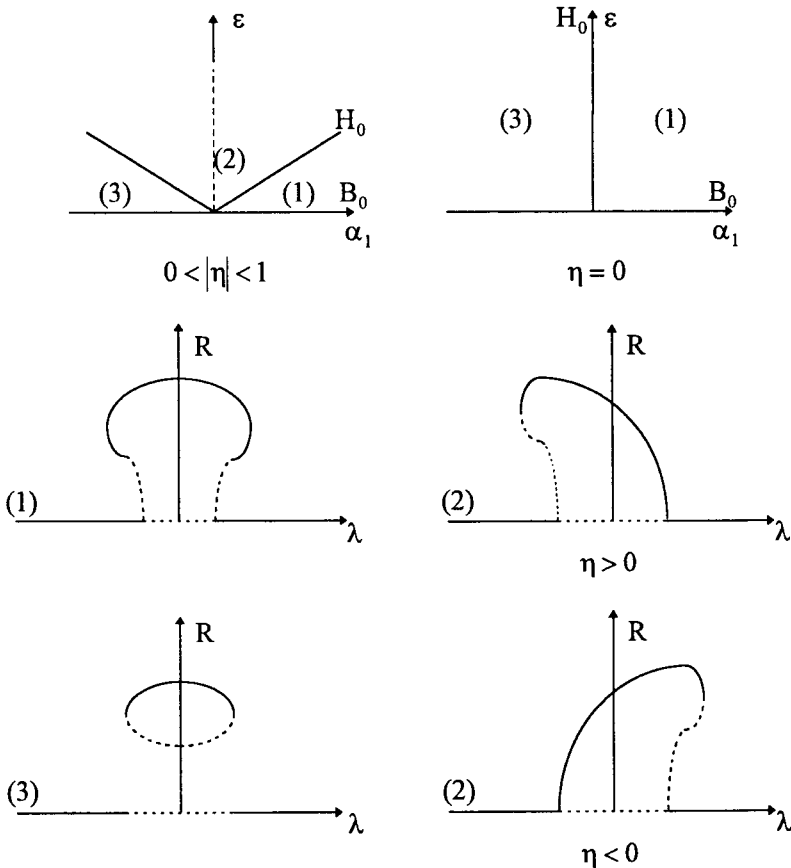


Figure 1: Transition sets in the parameter plane and bifurcation diagrams for $\phi = 1, 0 \leq |\eta| < 1$. Full lines designate stable solutions and dashed lines unstable ones.

In this figure, the horizontal axes are represented by the bifurcation parameter λ , the vertical axes are denoted by the amplitude of periodic solution, respectively, and the dotted lines are unstable solution curves. One can see that there are nine dynamic buckling patterns in the 1/2 subharmonic parametric resonance, and all of the curves on the transition set are straight lines.

The figure also show that the coefficient of the second order nonlinear term α changes the bifurcation diagram shapes, whereas the coefficient of the third order nonlinear term β not only changes the bifurcation diagram shapes, but also the transition set. In summary, the influence due to the third order nonlinear term in the 1/2 parametric resonance on the transition set and bifurcation diagrams is very pronounced. Further, if $\beta = 0$, the amplitude of periodic solution is approximately equal to a constant corresponding to a small change of the bifurcation parameter λ .

In the light of Figure 1, if the amplitude of the external periodic load is small, i.e., $D > 0$, it was found that the zero solution is stable under these cases, and if $D < 0$, then the 1/2 parametric resonance will occur.

1/4 Subharmonic Parametric Resonance

In this case, $m/k = 1/4$, the bifurcation equation can be written as

$$9\beta^2 u^2 + \lambda^2 + 6\lambda\beta u - \alpha_1 u^2 = 0 \tag{17}$$

where

$$u = r^2, \quad \alpha_1 = \frac{\epsilon^2}{144m^2} \left(\frac{\alpha^2}{m^2} + \frac{3\beta}{2} \right)^2 \tag{18}$$

Since there is only one parameter in equation (17), the transition set degenerate into a point

$$H_0 = H_1; \epsilon = \frac{36m^2|\beta|}{\left| (\alpha/m)^2 + (3\beta/2) \right|} \equiv \epsilon_0 \tag{19}$$

The transition set and the bifurcation curves are plotted in Figure 2.

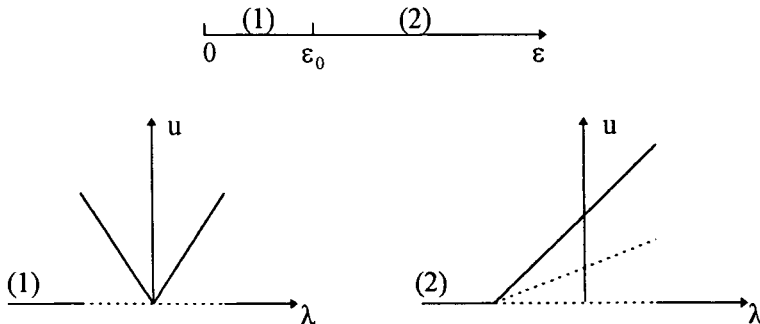


Figure 2: Transition set in the parameter plane and bifurcation diagrams for $\beta > 0$. Full lines designate stable solutions and dashed lines unstable ones.

Note that the bifurcation curves in Figure 2 are determined by straight lines, one obtains, for a laminated anisotropic circular cylindrical shell loaded axially by a periodic force $P = p_0 + 2\epsilon \cos kt$, if the rigidity matrix A has a pair of pure imaginary eigenvalues $\pm i\omega$ ($\omega > 0$), such that $\omega / k = 1/4$, then the 1/4 parametric resonance will arise. There are only two bifurcation branch curves in the diagrams, in addition, the linear relation between the amplitude of periodic solution and the bifurcation parameter λ can be found.

From the above results follows that for some fixed static load levels, the circular cylindrical shell may display mode jumps due to the presence of dynamic periodic load with small amplitude, i.e., bifurcation from a periodic solution or a steady solution. The phenomenon of 1/4 subharmonic parametric resonance is more simple than the 1/2 one. Because of the linear relation between the amplitude and the bifurcation parameter, the phenomenon of Hopf bifurcation can be observed in the 1/4 subharmonic parametric resonance.

DISCUSSION

To show how the non-orthogonal series adopted in energy method play an important role, we take an expansion (2) for the displacement modes in which $(\Psi_1^{(k)}, \Psi_2^{(k)}, \dots, \Psi_n^{(k)})$ ($k = 1, 2, 3$) are orthogonal each other. The ordinary differential equations (3) can be rewritten as

$$M \frac{d^2 F(t)}{dt^2} + (p_0 + \epsilon p(t)) H F(t) + S^{-1} K S F(t) + S^{-1} Q(S F(t)) + S^{-1} C(S F(t)) = 0 \tag{20}$$

where M is a diagonal positive definite matrix, and H a diagonal matrix which is similar to the matrix G in equation (3), namely $H = S^{-1} G S$.

The flow on center manifold given by equation (9) now becomes

$$\frac{du}{dt} = Cu - \epsilon p(t) Gu - N_1(u, h(t, u, \epsilon)) \tag{21}$$

We consider the subharmonic resonance again. In this case the differential equation on the center manifold is in the form

$$\frac{d^2 u}{dt^2} + (m^2 + \lambda)u(t) + \alpha u^2(t) + \beta u^3(t) - 2\epsilon(m^2 + \lambda)\cos(kt)u(t) = 0 \tag{22}$$

The fact is that the bifurcation parameter is coupled on the amplitude of external excitation in equation (22), which leads to it is impossible for us to investigate this problem using the singularity theory. The selection of pertinent trial functions in taking the mechanical coupling into account is very important, and the strong coupling effect in general anisotropic cylindrical shell may be the reason that the nonorthogonal series can obtain some significance results in this paper.

CONCLUSION

The main results in this paper are as follows:

1. If the rigidity matrix A has a pair of pure imaginary eigenvalues, the subharmonic parametric resonance will occur.
2. For some fixed external static load levels, the shell may jump due to the presence of dynamic periodic load with small amplitude, i.e., bifurcation of a periodic solution from another periodic solution or from a steady solution.
3. There are four dynamic buckling states in the $1/2$ subharmonic parametric resonance. The transition sets and the bifurcation diagrams are highly sensitive to the cubic nonlinear term in the differential equation.
4. The $1/4$ subharmonic parametric resonance has only two bifurcation diagrams. The linear relation between the amplitude and the bifurcation parameter are identified. This result shows that Hopf bifurcation can be observed.

REFERENCES

1. Bolotin V. V. (1964). *The Dynamic Stability of Elastic Systems*, Holden Day, San Francisco.
2. Beliaev N. M. (1924). Stability of Prismatic Rods Subject to Variable Longitudinal Forces, in *Engineering Constructions and Structural Mechanics*, Put, Leningrad, 149-167.
3. Simitsev G. J. (1987). Instability of Dynamically-Loaded Structures. *Applied Mechanics Reviews* **40:10**, 1403-1408.
4. Gurgoze M. (1985). On the Dynamic Stability of a Pre-Twisted Beam Subjected to a Pulsating Axial Load. *Journal of Sound Vibration* **102:3**, 415-422.
5. Huang K. Y. and Plaut R. H. (1982). Snap-Through of a Shallow Arch under Pulsating Load. in *Stability in the Mechanics of Continua*, F. H. Schroeder (ed.), Springer-Verlag, Berlin, 215-223.
6. Yao J. C. (1965). Nonlinear Elastic Buckling and Parametric Excitation of a Cylinder under Axial Loads. *Journal of Applied Mechanics* **32**, 109-115.
7. Birman V. (1985). Dynamic Stability of Unsymmetrically Laminated Rectangular Plates. *Mechanics Research Comm.* **12**, 81-86.
8. Tylikowski A. (1993). Dynamic Stability of Nonlinear Antisymmetrically Laminated Angle-Ply Plates. *Int. Journal Non-Linear Mechanics* **28**, 291-300.
9. Golubisky M. and Schaeffer D. (1985). *Singularities and Groups in Bifurcation Theory*, Vol. I, Springer-Verlag, New York.
10. Yamaki N. (1984). *Elastic Stability of Circular Cylindrical Shells*, Noth-Holland.
11. Chow S. N. and Hale J. K. (1982). *Methods for Bifurcation Theory*, Springer-Verlag, New York.

TRANSFORMATIONS OF DISPLACEMENT AND FORCE QUANTITIES BETWEEN SYSTEMS OF AXES AND GENERIC POINTS OF RIGID OPEN CROSS-SECTIONS

Risto Koivula

Department of Mechanical Engineering, Lappeenranta University of
Technology, P.O.B FIN-53851 Lappeenranta, Finland

ABSTRACT

The displacement and force quantities of Vlasov-beams with a rigid in plane open cross-section are defined in a system of axes and generic points, depending on six system parameters, expressed in an "absolute" system of axes: two coordinates of the origin, two coordinates of the sectorial pole, the direction angle of the axes, and the constant term (or zero point) of the sectorial area.

For a non-guided Vlasov beam the stiffness matrix is formed in the fundamental system characteristic of each cross section, in which the origin is placed at the centroid and the pole at the shear center, the direction of axes is that of the principle axes, and the sectorial area is an equilibrium system. The force quantities, defined in this system, are mutually orthogonal in the sense that they do not do virtual work in one another's reference deformations.

For a guided beam the deformations are restricted by longitudinally continuous restraints preventing one or several lateral or axial degrees of freedom. Then the active, the effective degrees of freedom are often mutually orthogonal in some other, transformed, non-fundamental system of axes and special points, here called the solving system, in which the stiffness (sub)matrix for effective degrees of freedom is now formed. (Special points have physical meaning, generic points are arbitrary.)

In order that the force quantities from elements with different cross-sections can be added and the displacement quantities connected like vectors at nodes to form the basic equations of FEM of Vlasov beams, the force and displacement quantities from elements with different cross-sections must be transformed to one (nodal) system of axes and generic points.

The state of deformation of a Vlasov beam can be regarded as a mathematically objective, tensor-like quantity, able to be expressed in the form of displacement and force "quantity vectors" in arbitrary systems of axes and generic points. The transformation matrices from one system of axes and generic points to any other within one prismatic Vlasov element are derived in this article.

KEYWORDS

Vlasov beam, Vlasov element, off-set element, guided beam, sectorial area, system of axes and special points, system of axes and generic points, torsional axis, extensional axis

INTRODUCTION

The deformations of a non-guided Vlasov beam with a rigid open cross-section can be expressed comprehensively by means of four displacement functions: the axial extension $u(x)$, the deflections in the principle directions $v(x)$ and $w(x)$ of the torsional axis which for a non-guided beam coincides with the shear axis, and the angle of twist $\theta_t(x)$ around the torsional axis. These displacements with their associate deformations and force quantities embody, in terms of the generalized beam theory /4/, the fundamental modes of a Vlasov beam. The fundamental modes are mutually orthogonal in the sense that axial stresses due to force quantities associated to one mode do not do virtual work in deformations associated to any other mode.

When the deformations of the beam are restrained by continuous rigid supports, which eliminate one or several axial or transversal degrees of freedom of any longitudinal axis, the state of deformations of the beam is often able to be divided in mutually orthogonal modes in a quite different, transformed solving system of axes and special points. In this case the torsional axis, in other words the axis of deflections, often does not coincide with the shear axis, the extensional axis may differ from the centroid axis, and the sectorial coordinate $\omega(s)$ is not necessarily an equilibrium system /2/. In this case the beam is called guided.

Due to the orthogonality, the displacement functions in the solving system can be applied to an element without giving rise to displacements or distributed support forces associated to any other mode. This is a necessary prerequisite for constructing a stiffness matrix in a system of axes and special points. Each row of the basic group of equations of the finite element method

$$[K]\{U\} - \{F\} = \{0\} \quad (1)$$

is a sum of virtual works of nodal and equivalent loads and local force quantities, acting at one node, in one node displacement. In equilibrium conditions this sum equals zero. The admissible node displacements for a joint of Vlasov elements are six rigid body motions and one node deformation, depending on the joint construction and embodying the transmission of the rate of twist $d\theta_t(x)/dx$ at the node, for instance the rate of deplanation of a transversal joint plate. The transformations of quantities from the solving systems of axes to the nodal systems are analogical to those between the local systems: the transformation matrices have the same form, but different physical meaning.

It is typical of beams with open cross-section, that their shear axes do not coincide with their centroid axes, whereupon it is mostly impossible to construct centric joints between elements with different profile lines. In a centric joint the deformations are continuous and forces addible as vectors in the solving system. Eccentric joints are the rule and centric joints the exception. Angled joints may be eccentric even for identic profile lines if the centroid and shear axes of the cross-section do not coincide. As a rule, Vlasov-elements are off-set elements. This article deals with the transformations from fundamental to solving systems.

This research was done in the Department of Mechanical Engineering at Lappeenranta University of Technology under Professor of Steel Constructions Erkki Niemi.

TRANSFORMATION MATRICES OF DISPLACEMENT AND FORCE QUANTITIES

Definition of fundamental notions

The study is based on deformations of a prismatic thin-walled beam with an open rigid in plane cross-section. The shear stresses are supposed to be sufficiently parallel with the profile line. Then the beam can be regarded to be strengthened with transverse rigid in plane diaphragms. Outside the profile lines an axis now denotes the locus of the intersectional points of a straight axial line with the diaphragms in the case of a non-deformed beam, and the deflection of the axis denotes the locus taken by these points in the case of a deformed beam. The shear deformation at the profile line is negligible:

$$\gamma_{xz}(x,s) = \frac{\partial u(x,s)}{\partial s} + \frac{\partial v_x(x,s)}{\partial x} = 0 \tag{2}$$

Without restricting the generality, any lateral motion of a cross-section can be expressed by means of two perpendicular deflections $v(x, a_{y_i}, a_{z_i})$ and $w(x, a_{y_i}, a_{z_i})$ of an arbitrary pole axis $A_i = (a_{y_i}, a_{z_i})$ and an angle of twist $\theta_{ui}(x)$ around this axis. The displacements of an arbitrary point $P(s) = (y(s), z(s))$ of the profile line are now obtained in systems of axes and special points of figure 1 in the following way:

$$v(x, y(s), z(s)) = v(x, a_{y_i}, a_{z_i}) - \theta_{ui}(x)[z(s) - a_{z_i}] \tag{3}$$

$$w(x, y(s), z(s)) = w(x, a_{y_i}, a_{z_i}) - \theta_{ui}(x)[y(s) - a_{y_i}] \tag{4}$$

The tangential displacement $v_t(x, s)$ of this point in the notations used in figure 1 is now

$$\begin{aligned} v_t(x, s) &= -v(x, y(s), z(s))\cos\alpha(s) + w(x, y(s), z(s))\sin\alpha(s) \\ &= -v(x, a_{y_i}, a_{z_i})\cos\alpha(s) + w(x, a_{y_i}, a_{z_i})\sin\alpha(s) - \theta_{ui}(x)h(s), \text{ in which} \end{aligned} \tag{5}$$

$$h(s) = \vec{r}_i \cdot \vec{i}_t = -\vec{r}_i \cdot \vec{i}_x \times \vec{i}_s = -\vec{i}_x \cdot [\vec{p}(s) - \vec{a}_i] \times \vec{i}_s = -[z(s) - a_{z_i}]\cos\alpha(s) + [y(s) - a_{y_i}]\sin\alpha(s) \tag{6}$$

Based on assumption (2) the axial displacement distribution is obtained by

$$u(x, s) = \int [v'(x, a_{y_i}, a_{z_i})\cos\alpha(s) - w'(x, a_{y_i}, a_{z_i})\sin\alpha(s) + \theta_{ui}'(x)h(s)] ds \tag{7}$$

$$= \int [v'(x, a_{y_i}, a_{z_i})dy(s) - w'(x, a_{y_i}, a_{z_i})dz(s) + \theta_{ui}'(x)d\omega(s)] \tag{8}$$

$$= u(x) + v'(x, a_{y_i}, a_{z_i})[y(s) - y_{0i}] - w'(x, a_{y_i}, a_{z_i})[z(s) - z_{0i}] + \theta_{ui}'(x)[\omega(s) - \omega_{0i}] \tag{9}$$

$$= u(x) + \theta_{ui}(x, a_{y_i}, a_{z_i})[y(s) - y_{0i}] + \theta_{wi}(x, a_{y_i}, a_{z_i})[z(s) - z_{0i}] + \theta_{ui}'(x)[\omega(s) - \omega_{0i}] \tag{10}$$

$$\omega(s) = \int_{s_0}^s h_i(s) ds = -\vec{i}_x \cdot \int_{s_0}^s \vec{r}_i \times \vec{i}_s ds = -\vec{i}_x \cdot \int_{s_0}^s \vec{r}_i \times d\vec{s} = -\vec{i}_x \cdot \int_{s_0}^s [\vec{p}(s) - \vec{a}_i] \times d\vec{s} \tag{11}$$

The parameters y_{0i} and z_{0i} now define in an "absolute system of axes" a new generic point called here the origin, because it serves this function in expressions of unit deformations $y - y_{0i}$ and $z - z_{0i}$. A prime (') denotes derivation with respect to x .

The difference between sectorial areas, calculated according to two different poles $A_1 = (a_{y_1}, a_{z_1})$ and $A_2 = (a_{y_2}, a_{z_2})$, starting from one sectorial origin, s_0 , is obtained from

$$\begin{aligned} \omega_2(s) - \omega_1(s) &= -\vec{i}_x \cdot \int_{s_0}^s (-\vec{a}_2 + \vec{a}_1) \times d\vec{s} = \vec{i}_x \cdot \int_{s_0}^s (\vec{a}_2 - \vec{a}_1) \times \vec{p}(s) \\ &= -(a_{y_2} - a_{y_1})[z(s) - z(s_0)] + (a_{z_2} - a_{z_1})[y(s) - y(s_0)] \end{aligned} \tag{12}$$

Without restricting the generality, the sectorial origins s_0 can be selected so that for each $\omega_i(s)$ is valid

$$\int_A \omega_i(s) dA = 0 \tag{13}$$

Both $\omega_i(s)$ can be now associated with a separate arbitrary ω_{0i} .

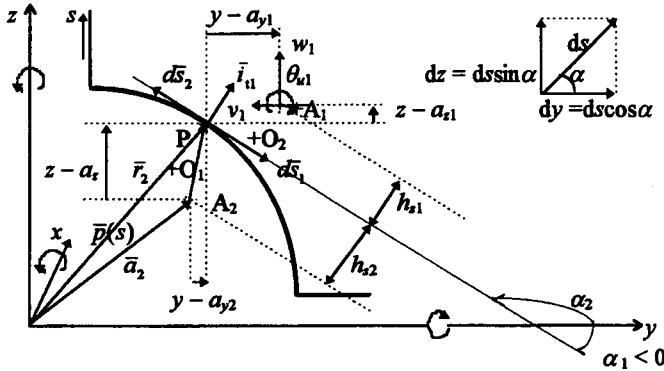


Figure 1. The introduced notations in two separate systems of axes and generic points O_1A_1xyz and O_2A_2xyz . The displacements $u(x)$, $v(x)$ and $w(x)$, the rotations $\theta_w(x) = -w'(x)$ and $\theta_u(x) = v'(x)$, the angle of twist $\theta_w(x)$, the rate of twist $\theta_w'(x)$ and the force quantities F_{ui} , F_{vi} , F_{wi} , M_{ui} , M_{vi} , M_{wi} and B_i are expressed in a right-handed system of axes uvw , but the geometric quantities of the cross-section in a left-handed system xyz . Then the system is in accordance with the FEM-program AGI-FAP /6/, developed in Lappeenranta University of Technology. The aim of this exceptional choice of systems of axes is to eliminate unnecessary negative signs from the equations between force and displacement quantities.

The axial strains are obtained by derivating the axial displacements (8) with respect to x :

$$\varepsilon(x,s) = u'(x,s) \tag{14}$$

The axial normal stresses are obtained now according to Hooke's law, E is the Young's modulus:

$$\sigma(x,s) = E\varepsilon(x,s) \tag{15}$$

The force quantities in an arbitrary system of axes and generic points $A_iO_ixyzs_{0i}$ is obtained by multiplying the stresses from (19) with the unit deformation functions ("warpings" in terms of /4/) $1, y - y_{0i}, z - z_{0i}$ and $\omega_i(s) - \omega_{0i}$ of the system, and integrating over the cross-section area:

$$F_{ui} = \iint_A \sigma_x dA = E \iint_A \varepsilon_x dA = E [u_i' \iint_A dA + \theta_w' \iint_A (z - z_{0i}) dA + \theta_w'' \iint_A (y - y_{0i}) dA + \theta_{ui}'' \iint_A (\omega_i - \omega_{0i}) dA = E(u_i' A + \theta_{vi}' S_{wi} + \theta_{wi}' S_{vi} + \theta_{ui}'' S_{\omega i}) \tag{16.1}$$

$$M_{vi} = E \iint_A \varepsilon_x (z - z_{0i}) dA = E [u_i' \iint_A (z - z_{0i}) dA - w'' \iint_A (z - z_{0i})^2 dA + v'' \iint_A (z - z_{0i})(y - y_{0i}) dA + \theta_{vi}'' \iint_A (\omega_i - \omega_{0i})(z - z_{0i}) dA = E(u_i' S_{vi} + \theta_{vi}' I_{vi} - \theta_{wi}' I_{vwi} + \theta_{ui}'' I_{\omega vi}) \tag{16.2}$$

$$M_{wi} = E \iint_A \varepsilon_x (y - y_{0i}) dA = E [u_i' \iint_A (y - y_{0i}) dA - w_i'' \iint_A (z - z_{0i})(y - y_{0i}) dA + v_i'' \iint_A (y - y_{0i})^2 + \theta_i'' \iint_A (\omega_i - \omega_{0i})(y - y_{0i}) dA = E(u_i' S_{wi} - \theta_{vi} I_{vwi} + \theta_{wi} I_{wi} + \theta_{ui}'' I_{awi}) \quad (16.3)$$

$$B_i = E \iint_A \sigma_x (\omega_i - \omega_{0i}) dA = E [u_i' \iint_A (\omega_i - \omega_{0i}) dA - w_i'' \iint_A (z - z_{0i})(\omega_i - \omega_{0i}) dA + v_i'' \iint_A (\omega_j - \omega_{0i})(y - y_{0i}) dA + \theta_{ui}'' \iint_A (\omega - \omega_{0i})^2 dA = E(u_i' S_{oi} + \theta_{vi} I_{awi} + \theta_{wi} I_{awi} + \theta_{ui}'' I_{wi}) \quad (16.4)$$

The relation between force and displacement quantities in matrix form:

$$\{F\}_i = \begin{Bmatrix} F_u \\ M_v \\ M_w \\ B \end{Bmatrix}_i = E \begin{bmatrix} A & S_v & S_w & S_\omega \\ S_v & I_v & -I_{vw} & I_{v\omega} \\ S_w & -I_{vw} & I_w & I_{w\omega} \\ S_\omega & I_{v\omega} & I_{w\omega} & I_\omega \end{bmatrix}_i \begin{Bmatrix} u' \\ \theta_v' \\ \theta_w' \\ \theta_u'' \end{Bmatrix}_i = E[D]_i \{u\}_i \quad (17)$$

The cross-section integrals, the elements of the matrix of equation (17), are given in a right-handed system, as the indexation shows. By placing the origin at the centroid $O_1 = (y_0, z_0)$, the pole at the shear center $A_1 = (a_{y0}, a_{z0})$, and assuming that $\omega_{0i} = 0$, the following form is obtained:

$$\{F\} = \begin{Bmatrix} F_u \\ M_v \\ M_w \\ B \end{Bmatrix} = E \begin{bmatrix} A & 0 & 0 & 0 \\ 0 & I_{v0} & -I_{vw0} & 0 \\ 0 & -I_{vw0} & I_{w0} & 0 \\ 0 & 0 & 0 & I_{\omega0} \end{bmatrix} \begin{Bmatrix} u' \\ \theta_v' \\ \theta_w' \\ \theta_u'' \end{Bmatrix} = E[D_0] \{u\} = E[\Phi(\phi)] [\tilde{D}] [\Phi(\phi)]^T \{u\} \quad (18)$$

$$= E \begin{bmatrix} 1 & 0 & 0 & 0 \\ 0 & \cos \phi & \sin \phi & 0 \\ 0 & -\sin \phi & \cos \phi & 0 \\ 0 & 0 & 0 & 1 \end{bmatrix} \begin{bmatrix} A & 0 & 0 & 0 \\ 0 & \tilde{I}_{v0} & 0 & 0 \\ 0 & 0 & \tilde{I}_{w0} & 0 \\ 0 & 0 & 0 & \tilde{I}_{\omega0} \end{bmatrix} \begin{bmatrix} 1 & 0 & 0 & 0 \\ 0 & \cos \phi & -\sin \phi & 0 \\ 0 & \sin \phi & \cos \phi & 0 \\ 0 & 0 & 0 & 1 \end{bmatrix} \begin{Bmatrix} u' \\ \theta_v' \\ \theta_w' \\ \theta_u'' \end{Bmatrix} \quad (19)$$

$$\phi = -\frac{1}{2} \arctan \frac{2I_{vw0}}{I_{w0} - I_{v0}} \quad (20)$$

A circumflex (\sim) over a symbol, mostly a matrix or vector, denotes quantities given in the fundamental system, a subscript zero (0) denotes quantities in a centric (but non-principle) system with the origin at the centroid and pole at the shear center. The force and displacement symbols of the quantities of the fundamental system are written without subscripts.

Transformation matrices of displacement quantities

In this chapter the directions of the "absolute axes" are those of the (centric) principle axes. A number subscript, for instance (1), denotes a quantity given in a non-fundamental, transformed system.

Due to the orthogonality $u(x)$, $v(x)$, $w(x)$ and $\theta_u(x)$ in the fundamental system AOxyz are independent. Then a following distribution of axial displacements can be applied at an end of an element:

$$u(x, y, z) = u(x) + v'(x)(y - y_0) - w'(x)(z - z_0) + \theta_u'(x)\omega \quad (21)$$

$$= u(x) + \theta_w(x)(y - y_0) + \theta_u(x)(z - z_0) + \theta'_u(x)\omega \quad (22)$$

According to (3) and (4) the deflections of an arbitrary axis $A_1 = (a_{y1}, a_{z1})$ are

$$v_1(x) = v(x) - (a_{x1} - a_{x0})\theta_w(x) \tag{23}$$

$$w_1(x) = w(x) - (a_{y1} - a_{y0})\theta_u(x) \tag{24}$$

$$v_1'(x) = v'(x) - (a_{x1} - a_{x0})\theta_w'(x) = \theta_w(x) - (a_{x1} - a_{x0})\theta_w'(x) = \theta_{w1}(x) \tag{25}$$

$$w_1'(x) = w'(x) - (a_{y1} - a_{y0})\theta_u'(x) = -\theta_u(x) - (a_{y1} - a_{y0})\theta_u'(x) = -\theta_{v1}(x) \tag{26}$$

When equation (13) is valid both for fundamental ω and transformed ω_1 and (y_0, z_0) is the centroid

$$\omega_1 - \omega = -(a_{y1} - a_{y0})(z - z_0) + (a_{x1} - a_{x0})(y - y_0) \tag{27}$$

$$= (a_{y1} - a_{y0})(z - z_{01}) - (a_{x1} - a_{x0})(y - y_{01}) + (a_{y1} - a_{y0})(z_{01} - z_0) - (a_{x1} - a_{x0})(y_{01} - y_0) \tag{28}$$

We now place the origin at an arbitrary point (y_{01}, z_{01}) and add a constant $-\omega_{01}$ to the sectorial area. The physical meaning of the extension $u_1(x)$ is now turned from a constant distribution with respect to s of axial displacement to a same kind of quantity, not explained by the other terms of the axial displacement distribution (8). Based on equations (25), (26) and (28) the axial displacement (22) is

$$\begin{aligned} u(x, y, z) &= [u(x) + \theta_w(x)(y_{01} - y_0) + \theta_u(x)(z_{01} - z_0) - \theta_w(x)(a_{x1} - a_{x0})(y_{01} - y_0) \\ &+ \theta_u(x)(a_{y1} - a_{y0})(z_{01} - z_0) + \theta_w(x)\omega_{01}] + [\theta_u(x) - \theta_w(x)(a_{x1} - a_{x0})](y - y_{01}) \\ &+ [\theta_w(x) + \theta_u(x)(a_{y1} - a_{y0})](z - z_{01}) + \theta_w(x)(\omega_1 - \omega_{01}) \end{aligned} \tag{29}$$

$$= u_1(x) + \theta_{v1}(x)(z - z_{01}) + \theta_{w1}(x)(y - y_{01}) + \theta_w(x)(\omega_1 - \omega_{01}) \tag{30}$$

So here one and the same axial displacement distribution is expressed in separate systems of axes and generic points. Based on (29) and (30) this relation is in matrix form:

$$\begin{Bmatrix} u_1 \\ \theta_{v1} \\ \theta_{w1} \\ \theta'_u \end{Bmatrix} = \begin{bmatrix} 1 & z_{01} - z_0 & y_{01} - y_0 & (a_{y1} - a_{y0})(z_{01} - z_0) - (a_{x1} - a_{x0})(y_{01} - y_0) + \omega_{01} \\ 0 & 1 & 0 & a_{y1} - a_{y0} \\ 0 & 0 & 1 & -(a_{x1} - a_{x0}) \\ 0 & 0 & 0 & 1 \end{bmatrix} \begin{Bmatrix} u \\ \theta_v \\ \theta_w \\ \theta'_u \end{Bmatrix}, \text{ or (31)}$$

$$\{u\}_1 = [T]_{1,0}^T \{\bar{u}\} \tag{32}$$

By inverting the matrix of equation (33) is obtained matrix $[T]_{0,1}^T$, which transforms from a non-fundamental, transformed system with axes in principle directions to the fundamental system:

$$\{\bar{u}\} = \begin{Bmatrix} u \\ \theta_v \\ \theta_w \\ \theta'_u \end{Bmatrix} = [T]_{1,0}^{-T} \{u\}_1 = [T]_{0,1}^T \{u\}_1 = \begin{bmatrix} 1 & -(z_{01} - z_0) & -(y_{01} - y_0) & -\omega_{01} \\ 0 & 1 & 0 & -(a_{y1} - a_{y0}) \\ 0 & 0 & 1 & a_{x1} - a_{x0} \\ 0 & 0 & 0 & 1 \end{bmatrix} \begin{Bmatrix} u_1 \\ \theta_{v1} \\ \theta_{w1} \\ \theta'_{u1} \end{Bmatrix} \tag{35}$$

A transformation matrix of displacements from a system O_1A_1xyz to another non-fundamental system O_2A_2xyz in the principle direction is obtained by changing the arbitrary subscript 1 to 2 in the matrix of equation (33) and multiplying the matrix of equation (35) by this matrix:

$$\begin{Bmatrix} u_2 \\ \theta_{v2} \\ \theta_{w2} \\ \theta'_{u2} \end{Bmatrix} = \begin{bmatrix} 1 & z_{02} - z_{01} & y_{02} - y_{01} & (a_{y2} - a_{y1})(z_{02} - z_0) - (a_{x2} - a_{x1})(y_{02} - y_0) + \omega_{02} - \omega_{01} \\ 0 & 1 & 0 & a_{y2} - a_{y1} \\ 0 & 0 & 1 & -(a_{x2} - a_{x1}) \\ 0 & 0 & 0 & 1 \end{bmatrix} \begin{Bmatrix} u_1 \\ \theta_{v1} \\ \theta_{w1} \\ \theta'_{u1} \end{Bmatrix}, \text{ eli (36)}$$

$$\{u\}_2 = [T]_{2,1}^T \{u\}_1 = [T]_{1,2}^{-T} \{u\}_1 = [T]_{2,0}^T [T]_{0,1}^T = [T]_{2,0}^T [T]_{1,0}^{-T} = [T]_{2,0}^T \{\bar{u}\} \tag{37}$$

For matrices $[T]$ within one cross-section the following relationship is valid

$$[T]_{ij}^T [T]_{jk}^T = [T]_{ik}^T \tag{38}$$

Transformation matrices of force quantities

If we examine the force quantities defined by the integrals (16.1-4) in the fundamental system $AOxyz$ and in a transformed system $A_1O_1xyz_{01}$ in the principal direction:

$$F_{u1} = \iint_A \sigma_x dA = \tilde{F}_u \tag{39.1}$$

$$M_{v1} = \iint_A \sigma_x (z - z_{01}) dA = \iint_A \sigma_x (z - z_0) dA - (z_{01} - z_0) \iint_A \sigma_x dA = \tilde{M}_v - (z_{01} - z_0) \tilde{F}_u \tag{39.2}$$

$$M_{w1} = \iint_A \sigma_x (y - y_{01}) dA = \iint_A \sigma_x (y - y_0) dA - (y_{01} - y_0) \iint_A \sigma_x dA = \tilde{M}_w - (y_{01} - y_0) \tilde{F}_u \tag{39.3}$$

$$\begin{aligned} B_1 &= \iint_A \sigma_x (\omega_1 - \omega_{01}) dA = \iint_A \sigma_x [\omega - (a_{y1} - a_{y0})(z - z_0) + (a_{x1} - a_{x0})(y - y_0) - \omega_{01}] dA \\ &= \iint_A \sigma_x \omega dA - (a_{y1} - a_{y0}) \iint_A \sigma_x (z - z_0) dA + (a_{x1} - a_{x0}) \iint_A \sigma_x (y - y_0) dA - \omega_{01} \iint_A \sigma_x dA \\ &= \tilde{B} - (a_{y1} - a_{y0}) \tilde{M}_v + (a_{x1} - a_{x0}) \tilde{M}_w - \omega_{01} \tilde{F}_u \end{aligned} \tag{39.4}$$

$$\{F\}_1 = \begin{Bmatrix} F_{u1} \\ M_{v1} \\ M_{w1} \\ B_1 \end{Bmatrix} = \begin{bmatrix} 1 & 0 & 0 & 0 \\ -(z_{01} - z_0) & 1 & 0 & 0 \\ -(y_{01} - y_0) & 0 & 1 & 0 \\ -\omega_{01} & -(a_{y1} - a_{y0}) & (a_{x1} - a_{x0}) & 1 \end{bmatrix} \begin{Bmatrix} \tilde{F}_u \\ \tilde{M}_v \\ \tilde{M}_w \\ \tilde{B} \end{Bmatrix} = [T]_{0,1} \{\tilde{F}\} \tag{40}$$

The transformation matrix $[T]_{0,1}$ of eq. (40) is a transpose to the matrix of eq. (35). A transformation matrix from a transformed system in the principle directions to the fundamental system, a transpose of the matrix of (31), is obtained by inverting this matrix. In the same way as in the previous chapter a "universal" transformation matrix is obtained between arbitrary systems in principle directions:

$$\begin{Bmatrix} F_{u2} \\ M_{v2} \\ M_{w2} \\ B_2 \end{Bmatrix} = \begin{bmatrix} 1 & 0 & 0 & 0 \\ -(z_{02} - z_{01}) & 1 & 0 & 0 \\ -(y_{02} - y_{01}) & 0 & 1 & 0 \\ -(a_{y2} - a_{y1})(z_{01} - z_0) + (a_{x2} - a_{x1})(y_{01} - y_0) - (\omega_{02} - \omega_{01}) & -(a_{y1} - a_{y0}) & (a_{x2} - a_{x1}) & 1 \end{bmatrix} \begin{Bmatrix} F_{u1} \\ M_{v1} \\ M_{w1} \\ B_1 \end{Bmatrix} = [T]_{1,2} \{F\}_1 \tag{41}$$

Generally $[T]_{i,k} [T]_{j,l} = [T]_{j,k}$ (42)

By expressing $\{F\}$ and $\{u\}$ in a transformed system $A_1O_1xyz_{01}$ is obtained

$$\{F\} = [T]_{0,1}^{-T} \{F\}_1 = E[D_0][T]_{0,1}^T \{u\}_1, \text{ based on which} \tag{43}$$

$$\{F\}_1 = E[T]_{0,1}[D_0][T]_{0,1}^T \{u\}_1 = E[D_1]\{u\}_1 \tag{44}$$

By rotating $\{F\}_1$ and $\{u\}_1$ by angle ϕ into a system in non-principle directions is obtained

$$\begin{aligned} \{F\}_2 &= E\left([\Phi(\phi)]_{2,0}[T]_{0,1}[\Phi(\phi)]_{2,0}^T\right)\left([\Phi(\phi)]_{2,0}[\bar{D}_0][\Phi(\phi)]_{2,0}^T\right)\left([\Phi(\phi)]_{2,0}[T]_{0,1}^T[\Phi(\phi)]_{2,0}^T\right)\{u\}_2 \\ &= E[T]_{0,2}[D_0]_2[T]_{0,2}^T\{u\}_2 \end{aligned} \tag{45}$$

The bracketed expressions denote tensor rotations of angle ϕ of the matrices $[T]$ and $[D]$. So the transformation matrices $[T]$ are formed in the same way regardless of the angle ϕ of the systems. The generalized Steiner's rule gives (for instance) the elements of matrix $[D]_i$ in an eccentric system as functions of the elements of the centric, but usually non-principle matrix $[D_0]$:

$$\begin{bmatrix} A & S_v & S_w & S_w \\ S_v & I_v & -I_{vw} & I_{vw} \\ S_w & -I_{vw} & I_w & I_{wo} \\ S_w & I_{vw} & I_{wo} & I_w \end{bmatrix}_1 = [D_1] = \tag{46}$$

$$\begin{bmatrix} 1 & 0 & 0 & 0 \\ -(z_{01}-z_0) & 1 & 0 & 0 \\ -(y_{01}-y_0) & 0 & 1 & 0 \\ -\omega_{01} & -(a_{y1}-a_{y0}) & a_{x1}-a_{x0} & 1 \end{bmatrix} \begin{bmatrix} A & 0 & 0 & 0 \\ 0 & I_{v0} & -I_{wv0} & 0 \\ 0 & -I_{wv0} & I_{w0} & 0 \\ 0 & 0 & 0 & I_{w0} \end{bmatrix} \begin{bmatrix} 1 & -(z_1-z_0) & -(y_1-y_0) & -\omega_{01} \\ 0 & 1 & 0 & -(a_{y1}-a_{y0}) \\ 0 & 0 & 1 & a_{x1}-a_{x0} \\ 0 & 0 & 0 & 1 \end{bmatrix}$$

CONCLUSIONS

The force and displacement quantity vectors $\{u\}$ and $\{F\}$ are tensor-like mathematically objective quantities, able to be expressed in arbitrary cross-sectional systems of axes and generic points. Adding of forces and connecting of displacements at nodes prerequisites expressing these quantities in one system.

Based on the transformations between the systems of axes and generic points, it is possible to construct a FEM of Vlasov-beams /2/, /5/. For many types of joints of Vlasov beams as "exact" as the traditional FEM of beam constructions for solid beams. In place of the traditional global and local types of systems of axes, FEM of Vlasov beams includes four types: the global, the nodal, the solving and the local types of systems.

REFERENCES

/1/ Koivula Risto: Avoprofilisen sauvan ohjattu vääntö (Guided beams with open cross-sections), Journal of structural mechanics Rakenteiden mekaniikka, Vol. 18 No 4 1985, pages 57 - 94 (in Finnish)
 /2/ Koivula Risto: Siirtymä-ja voimasuureiden välityminen keskenään erilaisten avoprofiilien jatkuvassa päittäisliitoksessa (Transmission of displacement and force quantities in continuous joints between different two-flange cross-sections) Rakenteiden mekaniikka Vol. 30 No 1 1997, pages 25 - 46 (in Finnish)
 /3/ Schardt, Richardt: Verallgemeinerte Technische Biegetheorie (1989), Springer Verlag
 /4/ Vlasov V. Z.: Tonkostennye uprugie sterzhni, Moskva 1959
 /5/ Yang Y-B. Linear and non-linear analysis of space frames with non-uniform torsion using iterative computer graphics. Cornell university, Thesis 1984
 /6/ AGIFAP, User Guide, version 5.51, Lappeenranta University of Technology, Department of Mechanical Engineering, 1985

Numerical Modelling of Extended Endplate and Composite Flush Endplate Connections

S Troup, R Y Xiao and S S J Moy

Department of Civil & Environmental Engineering,
University of Southampton, Southampton, SO17 1BJ, UK

ABSTRACT

The results of a number of finite element analyses are reported to highlight methods of modelling steel endplate and composite connections. The ANSYS finite element package has been used to develop models using both solid and shell elements for the beam, column and endplates. Test results have been used to calibrate an extended endplate model, and assess the performance of the shell and solid elements. A discussion of the bolt model is included, with details of the moment-rotation curves and the stresses in the endplate. The extended endplate model is developed further to include the strength contribution of the slab in a composite connection. Methods of providing the stiffness and strength of the reinforcement and shear connection are discussed. The complicated force transfer through the connection is identified using the finite element model. Based on the contact elements the prying forces between the plates are determined. The model is shown to be accurate and numerically stable and suitable for assessing engineering design standards such as EC3 and EC4.

KEYWORDS

Steel Connections, Composite Connections, Extended Endplate, Finite Element Model, Yield Line, Moment-Rotation, Stress, Shear Connection.

INTRODUCTION

Structural frames are normally designed with either rigid or pinned joints using elastic or plastic frame analysis techniques. It has long been recognised that pinned connections possess some rotational stiffness that could be included for semi-rigid design. Some frame analysis programs can include rotational springs for connections, therefore the standard pinned or rigid assumption need no longer apply. Reliable stiffness and strength data is needed if frames can be analysed with confidence. This paper will describe the finite element analysis of typical connections used in multi-storey construction. Both composite and bare steel connections are studied with results compared to experimental data. Bolted endplate connections are the most common semi-rigid connection in steel frames. The endplate may be flush or extended beyond the tension flange. Extended endplate connections provide greater rotational stiffness because of the additional bolt row and greater lever arm. By making use of the strength of the concrete slab further gains in the rotational stiffness can be made. By including the rotational stiffness of the connection in design

savings can be made in the weight of the beams, and mid-span deflections are reduced. Figure 1 indicates a typical endplate composite connection.

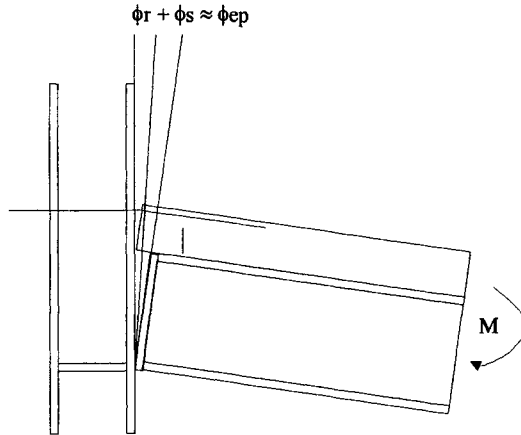


Figure 1: Typical composite semi-rigid connection

FINITE ELEMENT MODELLING OF EXTENDED ENDPLATE CONNECTIONS

Through the study of basic components of the joint conclusions can be drawn regarding the element type and mesh density for the model. Troup, Xiao and Moy (1998) previously reported numerical modelling work on tee-stub connections. Tee-stub connections are a useful method of testing numerical modelling techniques. If connections are to be modelled accurately suitable bolt models need to be found. The principle components of a bolt are the head and shank. Much of the previous work has used a combination of plate or brick elements representing the head, and bar or beam elements for the shank. This method is preferred to a full discretisation which requires a large number of nodes. Provided the load-deformation relationship in the bolt is correct a simplified model can be justified. Nethercot and Ahmed (1997) used a thick plate element for the bolt head with 3-D spring elements for the shanks. Nodes on the bolt head plates were tied to the corresponding points on the endplate or column flange. The model was too simple to model the bolt accurately. The bolt head is modelled as a square preventing an even transfer of forces from the bolt head to the endplate with stress concentrations occurring in the plate. Where possible the bolt head should have at least 6 sides or more if the washer is to be modelled accurately. Sherbourne and Bahaari (1994) also used a combination of solid and beam elements to describe the bolt. The bolt head was made from solid elements and the shank from bar elements. The modelling is more advanced than Ahmed's because of the hexagonal shape of the bolt head, allowing the force to be applied evenly over the surfaces of the column flange or endplate. Owing to the greater thickness of the bolt head there will be an improved stress transfer between the two surfaces. Comparison between the tests and the model were encouraging, however the loading of the model was simplified as pure bending, ignoring the effects of shear. It is inadequate to model a beam-column connection without shearing effects. If shear is introduced into the model bolt loads become more complicated with the shank to head connection detail becoming more critical. Bursi and Jaspart (1997) provided a detailed analysis of bolts in the tee-stub connection producing a very fine discretisation for the shank and head. The finite element analysis was later calibrated against bolt test results. Rather than using a solid head and a beam shank, a "spin" bolt using beam elements was used. Unlike the spin element previous models could only describe bolt shank loads with little attention paid to forces in the head.

The chosen bolt models are shown in Figure 2 (a) and (b). In the shell model the head is made from four shell elements forming an octagon maintaining simplicity in the model. Inaccuracies associated with stress concentrations at corners of the head are also reduced. The bolt shank was formed from a combin39 non-

linear spring element. Care should be taken when using shell elements where the thickness of the plate is included in the formulation of the element rather than the geometry of the mesh. If a bar or beam element is used the tensile stiffness will be inaccurate because it will be dependent on the length (EA/L). A non-linear force-deflection relationship is used in the shell model, which was derived from the stress-strain curves for the bolt. For plates of differing thickness the relationship will vary because the length of the bolt shank will change. Figure 2 indicates the close proximity of the bolt head. For the shell model bending in the bolt shank was ignored. Nine elements in total were used for the shell bolt model.

The 3-D bolt model comprises of 28 solid element forming both the head and shank of the bolt. Bending in the bolt shank was included in the solid model. It is assumed that there is negligible slip and permanent contact between the bolt head and endplate or column flange. It is therefore reasonable to tie the lower face of the bolt head to the surface of the plate. The bolt models used are intended to have the same characteristics as the actual bolt, whilst adding the minimum number of additional elements and nodes to the model.



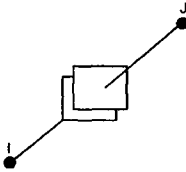
Figure 2: 2-D and 3-D model of bolt

The area of contact between the endplate and column flange will change during loading. Krishnamurthy and Graddy (1976) used no tension boundary conditions to represent the contact between the endplate and column flange successfully. However this cannot represent the influence of the column on prying forces. Sherbourne and Bahaari (1994) used contact52 elements from ANSYS to satisfy the contact condition between plate and flange. The contact52 element is the most suitable element offered by the ANSYS finite element program, Figure 3. The finite element results include the normal forces applied to the contact elements by the plates. The contact forces can be used to assess the effects of prying between the plates in the tension region. The contact elements are based on a spring with finite stiffness to control the contact of two nodes. It is important to achieve a high value for the contact stiffness in order to minimise the penetration into the target surface. The contact elements are extremely important as they provide continuity through the connection. They also have an important effect on the rate of convergence for the solution, particularly during early time steps where the correct configuration has not been achieved.

The choice of using solid or shell elements in a finite element analysis will have a great effect on the solution accuracy and efficiency. Solid elements have been used successfully to model connections, but the efficiency of the solution remains questionable. According to Bursi and Jaspart (1997) at least three elements through the thickness should be used in problems dominated by bending. If three elements are used there will be four nodes through the thickness, quadrupling the number used in a shell analysis. Such an increase in the node number is likely to increase the solution time considerably. For specific problems the cost of the analysis might be justified, but generally this is not the case. The models described in this paper are being used for parametric studies to enable improvements in design. For parametric studies the

efficiency of the model is fundamental to its overall performance. Figure 4 indicates the elements used in the analysis and in Figure 5 the meshes of the extended endplate connection are shown.

Contac52: Point to Point Contact Element



The contac52 element is used to describe areas in the model requiring a no tension condition.

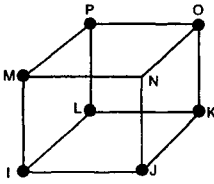
Combin39: Non-linear Spring



The combin39 element is used for the force-deflection relationship in the bolts at coincident nodes.

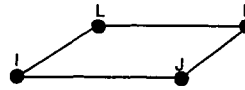
Figure 3: Contac52 and Combin39 Elements

Solid45 - 3-D Structural Solid



3-D eight noded structural solid with 3 translational degrees of freedom at each node. Eight integration points

Shell43 - Plastic Large Strain Shell



3-D four noded quadrilateral shell with 3 translational and 3 rotational degrees of freedom at each node. 4 integration points. Shear deflection included.

Figure 4: Shell43 and Solid45 elements

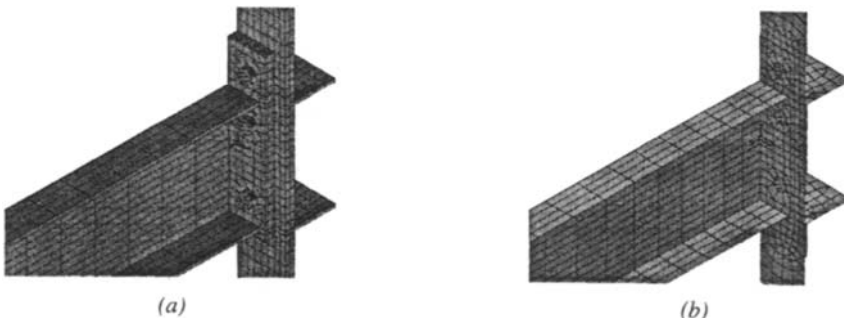


Figure 5: Solid45 and Shell43 connection meshes

CALIBRATION OF THE EXTENDED ENDPLATE FINITE ELEMENT MODEL

Extended endplate connections were modelled and compared to test results reported by Jenkins, Tong and Prescott (1986). Two approaches to modelling were investigated using solid45 and shell43 elements from ANSYS for the steel connection components. The bolt shanks were modelled using either solid45 elements for the solid model or combi39 elements for the shell model. Contact52 elements were also used between the endplate and column flange. Solid elements provide a more complete reflection of the stress distribution but place greater demands on processing time and on disk and memory requirements. Shell elements, owing to the reduced number of degrees of freedom run more efficiently, but cannot reflect localised stresses as effectively. Jenkins tested 18 bare steel endplate connections to investigate their moment-rotation characteristics. Generally the finite element analysis results for the shell model were encouraging, including the correct initial stiffness and ductility. Connection ductility stemmed from yielding of the endplate and deformation of the bolts, with the proportion of each dependant on the endplate thickness. The rotational stiffness reduction is due to the change in bending stiffness of the endplate. The moment-rotation curve from the solid element analysis was not so accurate. Figure 6 (a) and (b) indicate the curves for both shell and solid element meshes respectively, compared with the test curves for thick and thin endplates.

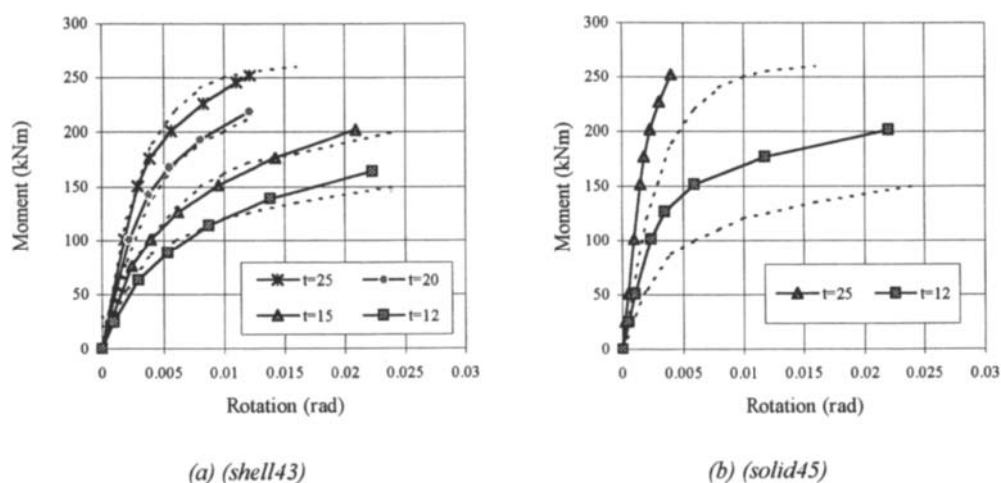


Figure 6: Comparison of solid and shell moment-rotation curves with the test

The shell element model was by far the superior model when compared with the test results. Both the stiffness and ductility of the connection were reflected in the moment-rotation curves. The point of yielding in the endplate that initiates the softening of the curve occurred at the correct load. Yielding in the bolts was observed for the thicker endplate connections. For thin endplates the endplate yielded before the bolt capacity was reached. There was a considerable increase in the prying forces after the endplate had yielded. The solid element model was not as accurate as the shell model and was unable to reflect the correct softening behaviour. The rotational stiffness of the connection was considerably greater than in the test. In addition the failure load was overestimated. Solid element meshes are stiffer than shell because their formulation does not allow as much distortion of the element under high loads. This is particularly important for areas of significant bending deformation. The ductility of thin endplate connections is derived from bending in the endplate and column flange. This could not be simulated in the solid element model. Stresses in the solid model were reasonable and were similar to those from the shell model. Shell elements were chosen for continuing finite element analysis of bare steel and composite connections. Figure 7 shows the variation of a number of parameters in the endplate for a connection with a thickness of 12 mm. Figures 7 (a) and (b) show the distribution of bending stresses in the x and y directions. The plot of deflection in the z direction (Figure 7 (c)) clearly demonstrates the flexible shell model leading to the

yield lines shown in Figure 7 (d). The shell element model was able to produce high quality load deflection and stress results at considerably lower cost than the solid model.

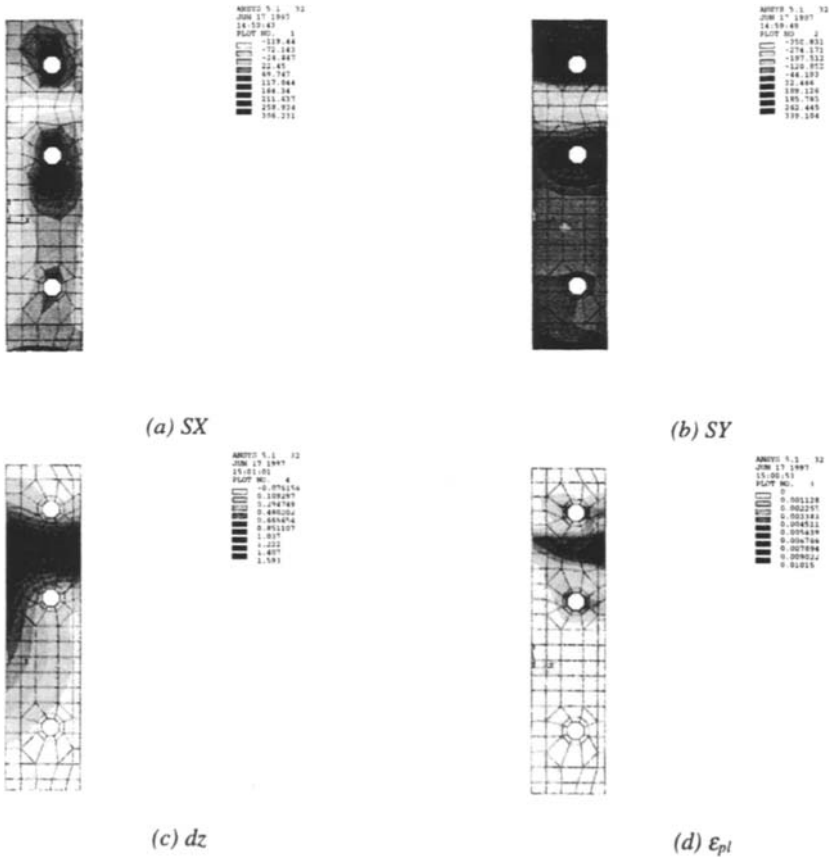


Figure 7: Stress and deformation in the thin endplate

FINITE ELEMENT MODELLING OF COMPOSITE ENDPLATE CONNECTIONS

Slab Modelling

The shell element model was shown to be reliable at predicting the moment-rotation characteristics of extended endplate connections. The ductility of the connections and the strength was modelled correctly. A composite connection model requires the contribution from the slab and reinforcement to be included. Two approaches can be made to this problem, including and excluding the contribution of the concrete slab. In both cases the influence of the reinforcement will be included. After cracking the tensile contribution from the concrete will be small. A simple model is presented here which excludes the contribution of the concrete, and uses non-linear spring elements (combin39) to provide the shear connection.

Two methods of shear connection between the rebar and beam flange were investigated. Firstly a "beam" model was proposed using beam4 elements to represent shear connectors, that were attached to the rebar, Figure 8 (a). An advantage of this arrangement is that the shear connectors are actually modelled. However, the deflection of the beam elements, and the slip elements themselves are combined with the

overall relationship being unclear. Further study indicated that the beam elements were deflecting significantly adding to the slip and transferring additional load to the bolts. It was concluded that a model with a single load-slip relationship would be more appropriate allowing more control of the shear interaction in the beam. For the truss model the shear connection was supplied by *conbin39* elements and the uplift connection by *conbin40* elements. In order for the slip to be from the slip elements along the diagonal members of the truss had large cross sectional areas, giving negligible displacements. To be concise only the truss model is reported here. Further models including the effect of the metal decking and slab are being developed.

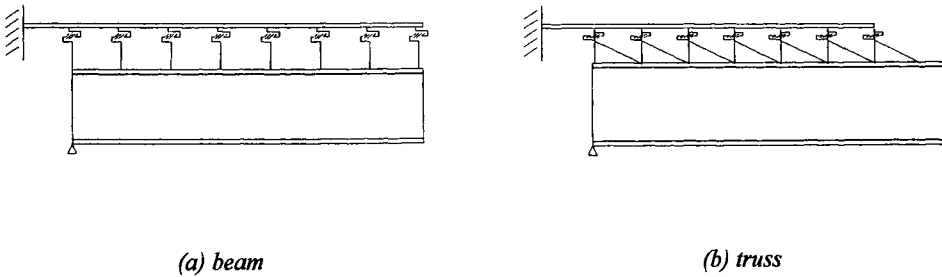


Figure 8: Shear connection model

In the composite slab the load transfer from beam to reinforcement is provided primarily by the surrounding concrete. Testing of composite connections has generally not considered the shear lag effect to be fundamental to their characteristics and there is little data available. Shear lag should be included in the numerical model if the correct moment-rotation curve is to be achieved. To allow for the distribution of tensile force across the width of the slab each reinforcing bar was provided with an individual connecting element. Each connecting element has a different load-slip relationship; as a consequence the load in each bar varies across the width of the slab as indicated in Figure 9 (a). The relationship was chosen because progressive yielding across the width of the slab is demonstrated, with the yielding of all rebars attained. Figure 9 (b) indicates the moment-rotation relationship for the model. At the point of yielding there is a smoother reduction of stiffness, corresponding to test data. Previously the redistribution of force to the bolts after rebar yielding had been very angular, but the new model allows a gradual increase in load. A lumped area model cannot demonstrate the smooth yielding in the connection.

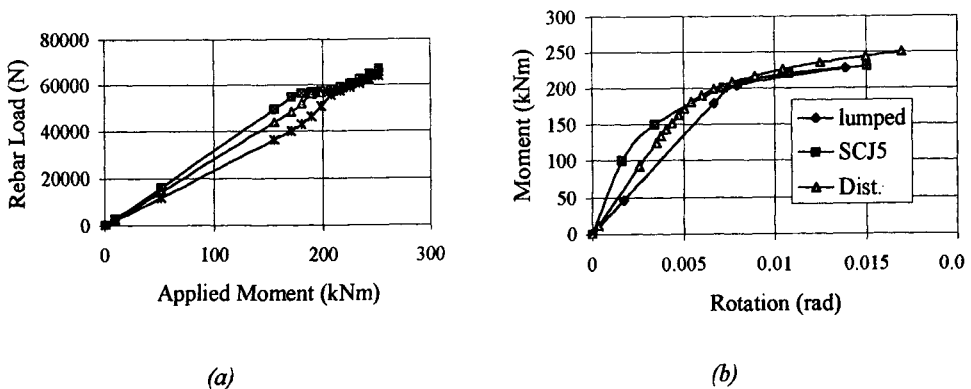


Figure 9: Moment-rebar force relationships and moment-rotation curves

Xiao, Choo and Nethercot (1994) performed a number of tests on composite connections to investigate their behaviour with different levels of reinforcement. Cleated, finplate and flush endplate connections were all tested with moment-rotation curves recorded accordingly. SCJ5 represents a flush endplate connection with 10 T12 rebars forming the reinforcement. The members used in the specimen were a 305x165x40 UB and a 203x203x52 UC in grade 43 steel. Compression web stiffeners were provided in the column to limit the failure to the tension region. Moment-rotation curves are presented demonstrating an accurate prediction of connection strength, Figure 9 (b). The initial rotational stiffness of the numerical model is lower than that from the test because there is no provision for the pre-cracking strength of the concrete. The strength comparison remains correct because at that stage there is negligible tensile strength in the concrete remaining. The numerical model has been assessed against moment-rotation data, and the local stresses should now be checked.

Compression Zone and Beam Web Stress

The stiffness and strength of a connection is derived from the stiffness and strength of its components. The tensile and compressive forces, including prying effects, from these components should be in equilibrium at all times during loading. By examination of the individual components in the joint a system of load transfer can be identified. Figure 10 indicates the stress distribution through the depth of the web for a series of applied moments. The stress in the compression flange increases as the required compressive force increases. From Figure 10 it can be seen that there is a compressive stress zone in the web that rises after yielding of the compression flange has occurred. There is also a redistribution of load to the web after the compression stiffener in the column has yielded.

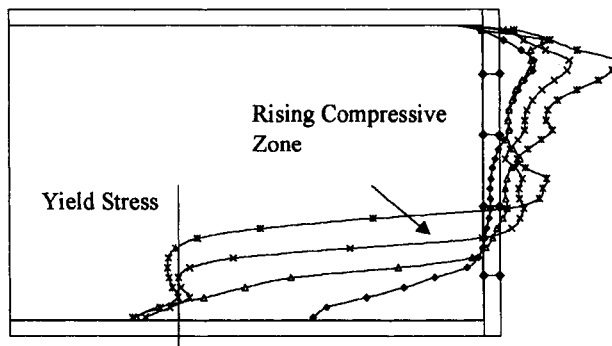
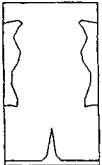


Figure 10: Stress in the beam compression flange and beam web

Tension Zone and Column Web Stress

The contact elements between the endplate and column flange can be used to assess the transfer of force from the compression flange of the beam and its web to the column web and stiffener. The elements can also monitor the progress of prying forces around the bolts. Prying forces form a considerable proportion of the total tensile force from the bolts as indicated in Table 1. Prying forces for a relatively thin endplate are high, particularly after endplate or column flange yielding. Figure 11 indicates the relationship between the force in the rebar and bolt elements and the applied moment. There is a clear increase in the bolt loads after the rebar yield load has been reached. This is because the loss of stiffness in the rebar causes a transfer of tensile load to the bolts. The top two bolt rows are the most heavily loaded. Figure 12 shows how the stresses in the beam web diminish rapidly with distance away from the connection justifying the vertical dimension of the column model. An increase of stresses in the tension zone is observed after the rebar has yielded because of the increased bolt load.

TABLE 1
COMPARISON OF PRYING FORCE AT DIFFERENT LOAD LEVELS

Endplate Contact Footprint	Moment	Tensile Bolt Force	Prying Force	Percentage
	71 kNm	119 kN	19.1 kN	16%
	165 kNm	273 kN	45.1 kN	17%
	194 kNm	320 kN	53.2 kN	17%
	221 kNm	408 kN	84.4 kN	21%
	249 kNm	501 kN	121.5 kN	24%

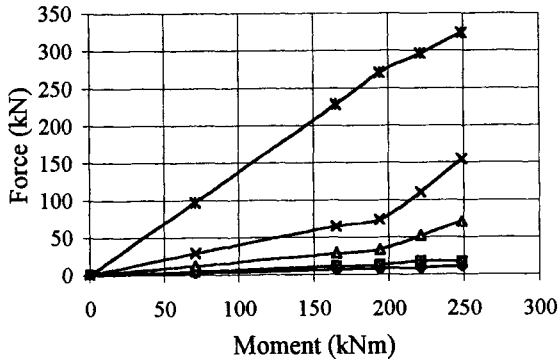


Figure 11: Development of bolt and rebar Load

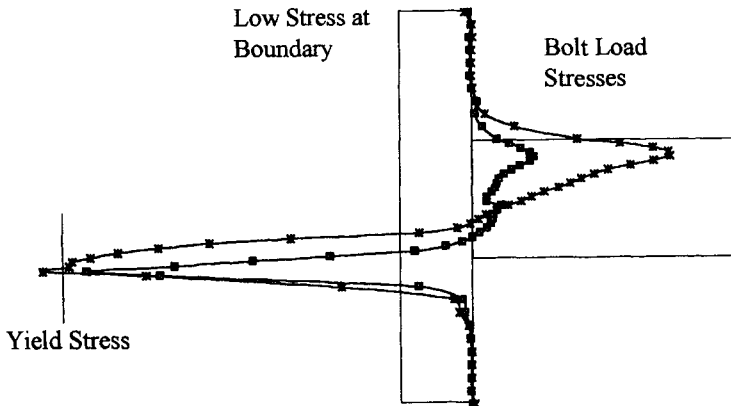


Figure 12: Column web and stiffener stresses

CONCLUSIONS

- The choice of element used in a connection is important, and dependent on the task required and the computing resources available. Shell elements are preferred because of the significant saving in run time for an analysis. Some special considerations should be made when using shell elements.
- Plates in endplate connections can have high curvatures due to bending in the tension region. Solid elements are not suitable for large deflection analyses with geometrical non-linearities. Shell elements are more appropriate for large deflection problems.
- Finite element models should be checked for global characteristics such as the moment-rotation curve, and for local effects such as the stresses in the beam, endplate and column.
- The same model strategy for bare connections can be transferred to composite connections, but with a facility for the transfer of the rebar forces to the beam.
- The method of modelling the shear connection is the most important part of a composite connection model. The concrete will generally be ignored to enable a stable model to be developed. This does however remove a number of important aspects of the connection such the metal decking. Shear lag across the slab should be included if the correct moment-rotation curve is to be simulated.
- The forces in the connection can be identified using the finite element model. This includes the effect of prying forces and yielding in the tension and compression zones.
- The models described here are being used for parametric study to improve design procedures such as EC3 and EC4.

REFERENCES

- Troup S., Xiao R.Y., Moy S.S.J., Numerical Modelling of Bolted Steel Connections, *Second World Conference on Steel Construction*, (1998), Number 362.
- Bursi O.S., Jaspart J.P., Benchmarks for Finite Element Modelling of Bolted Steel Connections, *Journal of Construction Steel Research*, Vol. 43 No. 1-3, (1997), 17-42.
- Nethercot D.A., Ahmed B, Numerical Modelling of Composite Connections and Composite Frames, *Proceedings of the Engineering Foundation Conference*, (1997), 809-822
- Sherbourne A.N., Bahaari M.R., 3-D Simulation of End-plate Bolted Connections, *ASCE Journal of Structural Engineering*, Vol. 120 No. 11, (1994), 3122-3136.
- Bursi O.S., Jaspart J.P., Calibration of a Finite Element Model for Bolted Endplate Steel Connections, *Journal of Construction Steel Research*, Vol. 44 No. 3, (1997), 225-262.
- Krishnamurthy N., Graddy D., Correlation Between 2 and 3-Dimensional Finite Element Analysis of Steel Bolted End-plate Connections, *Computers and Structures*, Vol. 6, (1976), 381-389.
- Jenkins W.M., Tong C.S., Prescott A.T., Moment-transmitting Endplate Connections in Steel Construction, and a Proposed Basis for Flush Endplate Design, *The Structural Engineer*, Vol. 64A, (1986), 121-132
- Xiao Y., Choo B.S., Nethercot D.A., Composite Connections in Steel and Concrete. I. Experimental Behaviour of Composite Beam-Column Connections, *Journal of Constructional Steel Research*, Vol. 31, (1994), 3-30

A SIMPLE NONLINEAR FRAME ELEMENT AND ITS APPLICATION TO POSTBUCKLING ANALYSIS

Y. B. Yang¹, S. R. Kuo², and S. C. Yang³

¹Department of Civil Engineering, National Taiwan University, Taipei, Taiwan, R.O.C.

²Department of Harbor and River Engineering, National Taiwan Ocean University,
Keelung, Taiwan, R.O.C.

³Department of Civil Engineering, Chung Cheng Institute of Technology,
Taoyuan, Taiwan, R.O.C.

ABSTRACT

Based on the assumption of small strains, small rotations, and small displacements, the elastic stiffness matrix and geometric stiffness matrix are derived for a two-dimensional frame element using the force-displacement relations well known in mechanics of materials. This approach is referred to as a direct approach, which differs from the conventional ones in that there is no need to deal with terms such as variations, potential energy, nonlinear strains, etc. Through consideration of the rigid body properties of initially stressed elements, the proposed element matrices have been successfully employed in the postbuckling analysis of structural frames. The advantage of the present approach is its simplicity and clear physical meanings involved.

KEYWORDS

Buckling, elastic stiffness matrix, force recovery, geometric stiffness matrix, nonlinear analysis, postbuckling analysis, rigid body motion

INTRODUCTION

Historically, the elastic stiffness matrices of the truss and the two-dimensional beam elements have been of theoretical importance, simply because they can be directly derived from force-displacement relations well known in mechanics of materials or theory of structures. They therefore serve as a bridge for linking the fundamental mechanics theories to the finite element method, which is good from the point of instruction. However, as we move from linear to nonlinear analysis, we find ourselves relying much more on advanced theories including the variational principles, hybrid element method, etc., which may or may not be covered by advanced courses such as elasticity, continuum mechanics, and nonlinear mechanics, etc., not to mention that most of these courses were not taken by our

graduates. It is under this situation that nonlinear analysis remains essentially as a black box, that is, in the form of a software package. What is available to the structural analysts is the several examples offered in the User's Manual for checking the input data format.

In this paper, a physically intuitive approach will be employed to derive the elastic stiffness matrix and geometric stiffness matrix for a two-dimensional beam element using the force-displacement relations commonly encountered in mechanics of materials. There is no need to deal with terms such as variations, potential energy, nonlinear strains, and so on. The geometric stiffness matrix derived is simpler than the conventional ones, but it contains the most essential properties that must be possessed by such a matrix. The present approach is tutorially attractive, since it is consistent with the understanding that nothing can be more practical than a simple theory (Chen 1998).

FORMULATION OF THE THEORY

For illustration, consider a cantilever subject to loadings of increasing magnitude in Figure 1. Three configurations can be identified for the cantilever, i.e., the initial (unloaded) C_0 configuration, the last (known) configuration C_1 , and the current (unknown) configuration C_2 . In this study, the updated Lagrangian formulation will be adopted, in that all the equations established for C_2 will be expressed with reference to C_1 . For the present purpose, let us consider a typical element AB of length L_1 used to represent part of the cantilever at C_1 . In response to increase in loadings, this element will be deformed into an element AB of length L_2 at C_2 .

Kinematics and Displacements

As shown in Figure 2(a), let us denote the longitudinal and transverse axes of the element at C_1 by x and y , respectively. Also, let us denote the displacements of the two nodes A and B of the element from C_1 to C_2 by (u_A, u_A) and (v_B, v_B) , respectively. The length L_2 of the element at C_2 is

$$L_2^2 = (L_1 + u_B - u_A)^2 + (v_B - v_A)^2 \quad \text{or} \quad L_2 \approx L_1 + u_B - u_A \quad (1)$$

assuming the displacements to be small compared with the length of the beam. The rigid displacements u_r and v_r of the element at C_2 are

$$u_r(x) = \frac{1}{2}(u_A + u_B) \quad v_r(x) = \frac{1}{2}(v_A + v_B) + \frac{x}{L_1}(v_B - v_A) \quad (2)$$

and the rigid rotation θ is

$$\theta \approx \frac{1}{L_1}(v_B - v_A) \quad (3)$$

In Figure 2(b), $\hat{A}\hat{B}$ denote the position of the element after rigid rotation, but with no stretching. The axes x and y have translated by an amount equal to the rigid translations. The axis \bar{x} connecting the two nodes \hat{A} and \hat{B} of the element at C_2 can be related to the axis x as $\bar{x} = (L_2/L_1)x$. The angle between the \bar{x} and x axes is θ . By deducting the rigid body displacements, the displacements of the element with respect to the (x, y) axes can be written as

$$\hat{u}(x) = u(x) - u_r(x) \quad \hat{v}(x) = v(x) - v_r(x) \quad (4)$$

and those with respect to the (\bar{x}, \bar{y}) axes as

$$\bar{u}(x) = \hat{u}(x)\cos\theta + \hat{v}(x)\sin\theta \quad \bar{v}(x) = -\hat{u}(x)\sin\theta + \hat{v}(x)\cos\theta \quad (5)$$

or

$$\bar{u}(x) = \hat{u}(x) + \frac{1}{L_1}(v_B - v_A)\hat{v}(x) = \hat{u}(x) \quad \bar{v}(x) = -\frac{1}{L_1}(v_B - v_A)\hat{u}(x) + \hat{v}(x) = \hat{v}(x) \quad (6)$$

based on the assumption of small rotations and neglecting the higher-order terms.

Hooke's Law and Statics

Figure 3 shows the initial forces acting on the element at C_1 , which are in equilibrium and known. In response to the increase in external loads, some force increments will occur on the beam. Figure 4 shows the resulting forces acting on the beam, expressed as the sum of initial forces and force increments. Based on the assumption of small strains, the axial force increment ΔV and moment increment ΔM in Figure 4 can be computed as

$$\begin{aligned} \Delta N &= EA \frac{d\bar{u}}{dz} = EA \frac{d\bar{u}}{dx} \frac{dx}{d\bar{x}} = EA \frac{d\hat{u}}{dx} = EA \frac{du}{dx} \\ \Delta M &= EI \frac{d^2\bar{v}}{d\bar{x}^2} = EI \frac{L_1^2}{L_2^2} \frac{d^2\bar{v}}{dx^2} = EI \frac{d^2\hat{v}}{dx^2} = EI \frac{d^2v}{dx^2} \end{aligned} \quad (7)$$

where E is Young's modulus, A the cross-sectional area, and I moment of inertia of the beam. The shear force increment ΔV should be obtained from the condition of equilibrium (see Figure 4), i.e.,

$$(V_B + \Delta V_B)L_2 = -(M_B + \Delta M_B) + (M_A + \Delta M_A) \quad (8)$$

which leads to

$$\Delta V_B = \frac{-1}{L_2}(M_B - M_A) - V_B - \frac{1}{L_2}(\Delta M_B - \Delta M_A) \quad (9)$$

By the condition of equilibrium at C_1 ,

$$V_B = -\frac{1}{L_1}(M_B - M_A) \quad (10)$$

the following can be derived,

$$\begin{aligned} \Delta V_B &= -\frac{1}{L_2}(\Delta M_B - \Delta M_A) + \left(\frac{1}{L_1} - \frac{1}{L_2}\right)(M_B - M_A) \\ &= -\frac{1}{L_1}(\Delta M_B - \Delta M_A) + \frac{1}{L_1}(M_B - M_A) \frac{u_B - u_A}{L_1} = -\frac{1}{L_1}(\Delta M_B - \Delta M_A) - V_B \frac{u_B - u_A}{L_1} \end{aligned} \quad (11)$$

The force increments derived in this section with reference to the C_2 axes have been expressed in terms of the notation commonly used in mechanics of materials.

Finite Element Nodal Forces

The force increments derived in the preceding section can be transformed to the C_1 axes and expressed in terms of the finite element notation, i.e., a quantity is taken as positive when directed rightward, upward, or counterclockwise. Figure 5 and 6 respectively show the finite element nodal forces existing at C_1 and C_2 , both with reference to C_1 , in which the left superscripts are used to indicate the configuration of occurrence. By comparing Figure 5 with Figure 3, one can show that ${}^1M_{zB} \equiv M_B$, ${}^1F_{xB} \equiv N_B$, ${}^1F_{yB} \equiv V_B$, etc. Also, by comparing Figure 6 with Figure 4, the following can be derived,

$${}^2M_{zB} = \Delta M_B + M_B \quad (12)$$

$${}^2F_{xB} = (N_B + \Delta N_B)\cos\theta - (V_B + \Delta V_B)\sin\theta \approx (N_B + \Delta N_B) - V_B \frac{v_B - v_A}{L} \quad (13)$$

$${}^2F_{yB} = (N_B + \Delta N_B)\sin\theta + (V_B + \Delta V_B)\cos\theta \approx N_B \frac{v_B - v_A}{L} + (V_B + \Delta V_B) \quad (14)$$

where small rigid rotations are assumed and $L \equiv L_1$ should be recognized. By the relations ${}^2F_{xB} = {}^1F_{xB} + \Delta F_{xB}$, ${}^2F_{yB} = {}^1F_{yB} + \Delta F_{yB}$, etc., the force increments can be computed from Eqns. (12)-(14),

$$\Delta M_{zB} = \Delta M_B \quad (15)$$

$$\Delta F_{xB} \approx \Delta N_B - \frac{{}^1F_{yB}}{L}(v_B - v_A) \quad (16)$$

$$\Delta F_{yB} \approx \Delta V_B + {}^1F_{xB} \frac{v_B - v_A}{L} = -{}^1F_{yB} \frac{u_B - u_A}{L} + {}^1F_{xB} \frac{v_B - v_A}{L} - \frac{1}{L}(\Delta M_B - \Delta M_A) \quad (17)$$

Governing Equations and Boundary Conditions

The differential equations of equilibrium for the element at C_2 can be written as

$$\begin{aligned} EA \frac{d^2 \bar{u}}{d\bar{x}^2} &= EA \left(\frac{L}{L_2} \right)^2 \frac{d^2 \bar{u}}{d\bar{x}^2} = EA \frac{d^2 \bar{u}}{d\bar{x}^2} = EA \frac{d^2 \hat{u}}{d\bar{x}^2} = EA \frac{d^2 u}{d\bar{x}^2} = 0 \\ EI \frac{d^4 \bar{v}}{d\bar{x}^4} &= EI \left(\frac{L}{L_2} \right)^4 \frac{d^4 \bar{v}}{d\bar{x}^4} = EI \frac{d^4 \bar{v}}{d\bar{x}^4} = EI \frac{d^4 \hat{v}}{d\bar{x}^4} = EI \frac{d^4 v}{d\bar{x}^4} = 0 \end{aligned} \quad (18)$$

Correspondingly, the boundary conditions are

$$\Delta M_{zB} = EI v''(L) \quad (19)$$

$$\Delta M_{zA} = -EI v''(0) \quad (20)$$

$$\Delta F_{xB} = EA u'(L) - \frac{{}^1F_{yB}}{L}(v_B - v_A) \approx EA u'(L) + \frac{{}^1M_{zA} + {}^1M_{zB}}{L^2} [v(L) - v(0)] \quad (21)$$

$$\Delta F_{xA} = -EA u'(0) - \frac{{}^1M_{zA} + {}^1M_{zB}}{L^2} [v(L) - v(0)] \quad (22)$$

$$\begin{aligned} \Delta F_{yB} &= -\frac{1}{L}(\Delta M_B - \Delta M_A) + {}^1F_{xB} \frac{v_B - v_A}{L} - {}^1F_{yB} \frac{u_B - u_A}{L} \\ &= -\frac{EI}{L} [v''(L) - v''(0)] + \frac{{}^1F_{zB}}{L} [v(L) - v(0)] + \frac{{}^1M_{zA} + {}^1M_{zB}}{L^2} [u(L) - u(0)] \end{aligned} \quad (23)$$

$$\Delta F_{yA} = -\frac{EI}{L} [v''(L) - v''(0)] - \frac{{}^1F_{zB}}{L} [v(L) - v(0)] - \frac{{}^1M_{zA} + {}^1M_{zB}}{L^2} [u(L) - u(0)] \quad (24)$$

Derivation of Stiffness Matrices

From the governing equations (18), the displacements u and v can be solved as linear and cubic

polynomials, respectively, which can be further related to the nodal displacements as

$$u = \left(1 - \frac{x}{L}\right) \frac{x}{L} \{u_x\} \tag{25}$$

$$v = \left\{1 - 3\left(\frac{x}{L}\right)^2 + 2\left(\frac{x}{L}\right)^3, 3\left(\frac{x}{L}\right)^2 - 2\left(\frac{x}{L}\right)^3, x\left(1 - \frac{x}{L}\right)^2, \frac{x^2}{L}\left(\frac{x}{L} - 1\right)\right\} \{u_y\} \tag{26}$$

where $\{u_x\}$ and $\{u_y\}$ respectively denote the column vector containing the axial and transverse degrees of freedom (DOFs), i.e.,

$$\{u_x\}^T = \{u_A \ u_B\} \quad \{u_y\}^T = \{v_A \ v_B \ \theta_A \ \theta_B\} \tag{27}$$

By the substitution of Eqns. (25) and (26), the force increments given in Eqns. (19)-(24) can be expressed as

$$\Delta M_{zA} = EI \left\{ \frac{6}{L^2} \quad -\frac{6}{L^2} \quad \frac{4}{L} \quad \frac{2}{L} \right\} \{u_y\} \tag{28}$$

$$\Delta M_{zB} = EI \left\{ \frac{6}{L^2} \quad -\frac{6}{L^2} \quad \frac{2}{L} \quad \frac{4}{L} \right\} \{u_y\} \tag{29}$$

$$\Delta F_{xA} = EA \left\{ \frac{1}{L} \quad -\frac{1}{L} \right\} \{u_x\} + \frac{{}^1M_{zA} + {}^1M_{zB}}{L^2} \{1 \ -1 \ 0 \ 0\} \{u_y\} \tag{30}$$

$$\Delta F_{xB} = EA \left\{ -\frac{1}{L} \quad \frac{1}{L} \right\} \{u_x\} + \frac{{}^1M_{zA} + {}^1M_{zB}}{L^2} \{-1 \ 1 \ 0 \ 0\} \{u_y\} \tag{31}$$

$$\Delta F_{yA} = \frac{{}^1M_{zA} + {}^1M_{zB}}{L^2} \{1 \ -1\} \{u_x\} + \frac{{}^1F_{xB}}{L} \{1 \ -1 \ 0 \ 0\} \{u_y\} + \frac{EI}{L} \left\{ \frac{12}{L^2} \quad -\frac{12}{L^2} \quad \frac{6}{L} \quad \frac{6}{L} \right\} \{u_y\} \tag{32}$$

$$\Delta F_{yB} = \frac{{}^1M_{zA} + {}^1M_{zB}}{L^2} \{-1 \ 1\} \{u_x\} + \frac{{}^1F_{xB}}{L} \{-1 \ 1 \ 0 \ 0\} \{u_y\} + \frac{EI}{L} \left\{ -\frac{12}{L^2} \quad \frac{12}{L^2} \quad -\frac{6}{L} \quad -\frac{6}{L} \right\} \{u_y\} \tag{33}$$

The preceding six equations can be recast in the following form:

$$([k_e] + [k_g])\{u\} = \{\Delta f\} \tag{34}$$

where the force increment vector $\{\Delta f\}$ has been moved to the right-hand side for convenience, $\{u\}$ is the displacement increment vector, $[k_e]$ the elastic stiffness matrix, and $[k_g]$ the geometric stiffness matrix, all given as follows:

$$\{\Delta f\} = \{\Delta F_{xA} \ \Delta F_{yA} \ \Delta M_{zA} \ \Delta F_{xB} \ \Delta F_{yB} \ \Delta M_{zB}\}^T \tag{35}$$

$$\{u\} = \{u_A \ v_A \ \theta_A \ u_B \ v_B \ \theta_B\}^T \tag{36}$$

$$[k_e] = \begin{bmatrix} EA/L & 0 & 0 & -EA/L & 0 & 0 \\ 12EI/L^3 & 6EI/L^2 & 0 & -12EI/L^3 & 6EI/L^2 & 0 \\ & 4EI/L & 0 & -6EI/L^2 & 2EI/L & 0 \\ & & EA/L & 0 & 0 & 0 \\ & & & 12EI/L^3 & -6EI/L^2 & 0 \\ \text{Symm.} & & & & & 4EI/L \end{bmatrix} \tag{37}$$

$$[k_g] = \begin{bmatrix} 0 & ({}^1M_{zA} + {}^1M_{zB})/L^2 & 0 & 0 & -({}^1M_{zA} + {}^1M_{zB})/L^2 & 0 \\ & {}^1F_{xB}/L & 0 & -({}^1M_{zA} + {}^1M_{zB})/L^2 & -{}^1F_{xB}/L & 0 \\ & & 0 & 0 & 0 & 0 \\ & & & 0 & ({}^1M_{zA} + {}^1M_{zB})/L^2 & 0 \\ & & & & {}^1F_{xB}/L & 0 \\ \text{Symm.} & & & & & 0 \end{bmatrix} \quad (38)$$

The elastic stiffness matrix $[k_e]$ is exactly the one conventionally used for the six-DOF beam element (Yang and Kuo 1994). The geometric stiffness matrix $[k_g]$ is identical to the one derived by considering only the rigid body effects of the initial forces acting on the beam, but neglecting the natural deformations (Yang et al. 1997). It has been demonstrated that the $[k_g]$ matrix of the form derived herein can be successfully used along with the $[k_e]$ matrix in the eigenvalue buckling analysis of planar frames, if a practically fine mesh has been used.

The merit with the present $[k_g]$ matrix is its simplicity and clear physical meanings involved, which is approximate due to the assumption of small strains, small rotations, and small displacements. However, the present procedure is attractive for tutorial reasons, because the $[k_g]$ matrix has been directly derived from the force-displacement relations well known in mechanics of materials, serving as a link for connecting the fundamental mechanics to nonlinear finite element analysis.

INCREMENTAL-ITERATIVE NONLINEAR ANALYSIS

By the conditions of equilibrium and compatibility at nodal points, the element equations (34) can be assembled to form the equations of equilibrium for the structure, also in incremental form:

$$[K]\{U\} = \{\Delta P\} \quad (39)$$

where $[K]$ is the stiffness matrix, $\{U\}$ the displacements of the structure with the restrained DOFs removed, and $\{\Delta P\}$ the applied load increments from C_1 to C_2 . At a typical step of an incremental-iterative analysis, the load increments $\{\Delta P\}$ are first applied and the structure displacement increments $\{\Delta U\}$ solved. The displacement increments $\{u\}$ for each element can then be computed, from which the force increments $\{\Delta f\}$ are determined, using the simplest form in this study, as given below:

$$\{\Delta f\} = [k_e]\{u\} \quad (40)$$

The total element forces existing at the end of the incremental step are computed as

$$\{{}^2f\} = \{{}^1f\} + \{\Delta f\} \quad (41)$$

where the subscript has been inserted to indicate the axes of reference. The first term in Eqn. (41) represents the rigid body displacement effect and the second term the natural deformation effect. According to the rigid body rule (Yang and Chiou 1987), the forces $\{f\}$ that were initially acting on the element should be interpreted as if they were acting along the rotated axes after rigid rotation. By summing the element forces $\{{}^2f\}$ over all the structure nodal points and checking against the total loads $\{{}^2P\}$ ($= \{{}^1P\} + \{\Delta P\}$), the balanced forces can be computed. If they are greater than a preset tolerance, then another iteration is required.

The method for determining the load step size at each incremental step and for guiding the direction of iteration is the generalized displacement control (GDC) method proposed by Yang and Shieh (1990). This method has been demonstrated to be effective and reliable for tracing the postbuckling paths of structures involving multi looping curves.

NUMERICAL EXAMPLES

A great number of examples have been solved using the proposed element and the GDC method by Yang (1996). For the purpose of illustration, only two examples will be given here.

The shallow arch shown in Figure 7 is hinged at both ends with the following data: $L = 100$ in. (254 cm), $h = 5$ in. (12.7 cm), $E = 200$ psi (1,378 kPa), $I = 1$ in.⁴ (41.62 cm⁴), and $A = 1$ in.² (6.45 cm²). In analysis, the arch was first represented by 25 elements. The portion of the arch covered by the central element was then divided into two elements, in order to provide a nodal point at the apex for application of the vertical load. For the symmetrical or perfect loading case, a vertical load was applied at the central load. To represent the effect of imperfection, this load was dislocated to the nearest node. The result obtained for both loading cases have been plotted in Figure 9, along with those obtained by the conventional approach (Yang and Kuo 1994), using the geometric stiffness matrix derived from the variational principle considering all the nonlinear effects. It is interest to note that the present solutions agree excellently with those obtained based on the sophisticated theory.

The second example studied herein is the beam shown in Figure 9, used to simulate the symmetric buckling of a simple under uniform bending. The beam is fixed against rotation about the y -axis at end A , and about the y and z axes at end B , assuming $L = 10$ cm, $I_z = 0.135$ cm⁴, $I_y = 5.4 \times 10^{-5}$ cm⁴, $J = 2.16 \times 10^{-4}$ cm⁴, $A = 0.18$ cm², $E = 7.124 \times 10^6$ N/cm², and $G = 2.719 \times 10^6$ N/cm². Ten elements were used. The axial displacement of end A and the vertical displacement of end B vs. the moment load have been plotted in Figures 10 and 11, respectively, along with the results computed using the conventional approach. From the figures, the ultimate load is found to be ± 148.6602 N-cm, in good agreement with the critical load of ± 149.945 N-cm solved by the eigenvalue approach. For this example, no distinction can be made between the present solutions and those obtained by the conventional approach.

CONCLUSIONS

Based on the assumption of small strains, small rotations, and small displacements, a two-dimensional beam element has been derived from the force-displacement relations well known in fundamental mechanics. It should be noted that if a practically fine mesh is used and if the loadings are applied in an incremental sense, such an element can be used as well to simulate various large-displacement problems. The present approach is attractive, because of its simplicity and clear physical meanings involved. The derived element has been demonstrated to be effective for tracing the postbuckling analysis. The research reported herein is partly sponsored by the National Science Council of the Republic of China through Grant No. NSC87-2211-E-002-031.

REFERENCES

- Chen W. F. (1998). From Theory to Practice: A Structural Engineer's Own Reflection, *Lecture* given at Department of Civil Engineering, National Taiwan University, Taipei, R.O.C. (April 14).
- Yang S. C. (1996). Nonlinear Analysis of Framed Structures—Simplified Finite Element Method, Department of Civil Engineering, National Taiwan University, Taipei, R.O.C.
- Yang Y. B. and Chiou H. T. (1987). Rigid Body Motion Test for Nonlinear Analysis with Beam Elements, *Journal of Engineering Mechanics*, ASCE, **113**:9, 1404-1419.
- Yang Y. B. and Kuo S. R. (1994). *Theory and Analysis of Nonlinear Framed Structures*, Prentice-Hall, Singapore.
- Yang Y. B. and Shieh M. S. (1990). Solution Method for Nonlinear Problems with Multiple Critical Points, *AIAA Journal*, **28**:12, 2110-2116.

Yang Y. B., Yang S. C. and Yau J. D. (1997). Simplified Procedure for Derivation of Geometric Stiffness Matrix for Planar Frame Element, *Journal of the Chinese Institute of Civil and Hydraulic Engineering*, 9:2, 249-261 (in Chinese).

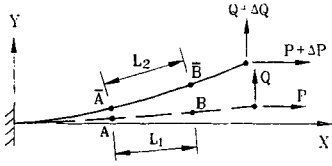


Figure 1 Cantilever subjected to increasing loads

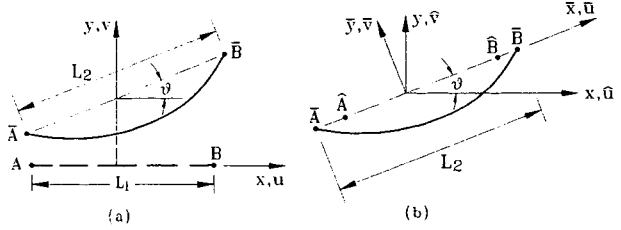


Figure 2 Element AB: (a) rigid displacements; (b) coordinates



Figure 3 Initial forces at C₁

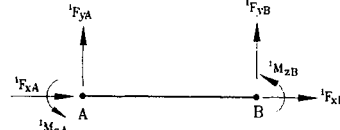


Figure 5 Nodal forces at C₁

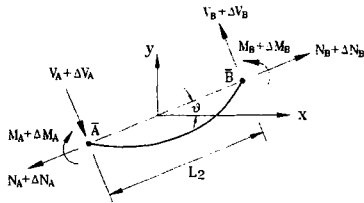


Figure 4 Resulting forces at C₂

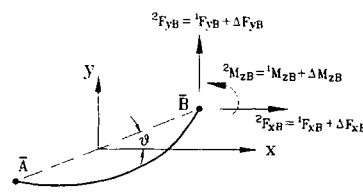


Figure 6 Nodal forces at C₂

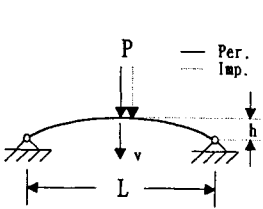


Figure 7 Shallow arch

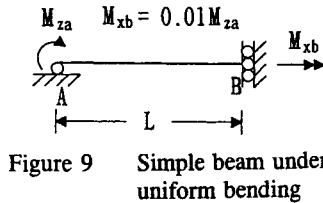


Figure 9 Simple beam under uniform bending

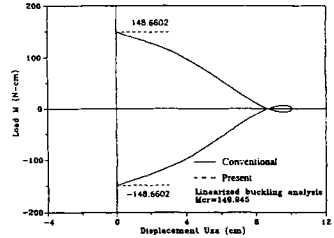


Figure 10 Axial displacement of end A vs. moment

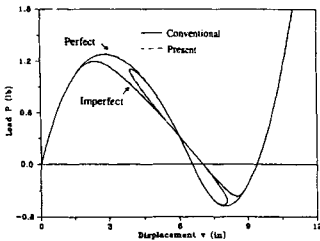


Figure 8 Load deflection curve for shallow arch

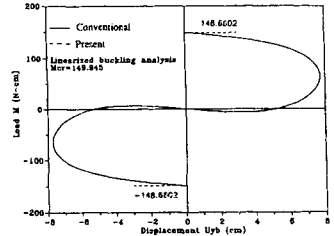


Figure 11 Vertical displacement of end B vs. moment

Section VI

PERFORATED MEMBERS

This Page Intentionally Left Blank

DESIGN OF PERFORATED PLATES UNDER IN-PLANE COMPRESSION

V Thevendran, N E Shanmugam and Y H Tan

Department of Civil Engineering, National University of Singapore
10 Kent Ridge Crescent, Singapore 119260

ABSTRACT

Post-buckling behaviour and ultimate load capacity of centrally perforated plates with different boundary conditions and subjected to uniaxial or biaxial compression are considered herein. Finite element analysis has been used to carry out extensive studies covering parameters such as plate slenderness, opening size, boundary conditions and nature of loading. A design formula, based on a best-fit regression analysis using the results from the finite element analyses, is proposed for determining the ultimate load carrying capacity. The accuracy of the proposed formula is established by comparing with experimental values of ultimate capacity and also with similar finite element analysis results.

KEYWORDS

Finite element method, centrally perforated plates, uniaxial and biaxial compression, ultimate load, design formula.

INTRODUCTION

The main structural components of the deck and the bottom of ship structures, platforms on oil rigs, dock gates, and plate girder and box girder bridges consist of steel plate elements. It is not uncommon to find such plate elements have openings to provide access for inspection and maintenance. The presence of openings in plate elements will result in changes in stress distribution within the member, besides a reduction of strength and variations in the buckling characteristics of the plate elements. The elastic and ultimate load behaviour of such members will also be affected significantly. The performance of such plate elements is influenced by the type of applied stress as well as by the shape, size, location and number of openings.

Extensive studies have been carried out by many researchers on the post buckling and ultimate behaviour of solid plate elements subjected to various types of loading. However, it appears that not much of work has been carried out on the ultimate load characteristics of steel plate elements containing openings. The exact analysis and design of such elements are complex particularly when the shape of openings and their arrangement are unusual. Approximate design methods for evaluating

the ultimate capacity of plate elements containing openings and subjected to in-plane axial or shear loading have been proposed by several researchers. The effective width concept can be extended with certain modifications or the elasto-plastic analysis can be applied to obtain the complete load history until the failure. Yu and Davies [1] proposed that the effective width concept can be extended to perforated plates with slight modifications to the formula. Finite element method has been successfully applied to predict the elastic buckling of perforated plates with various boundary conditions and subjected to different types of loading [2]-[3]. The finite element formulation based on variational principles could predict the non-linear behaviour of perforated plates, right up to collapse [4]-[5]. Narayanan and Chow suggested an approximate design method for evaluating the ultimate capacity of plates containing openings and subjected to uniaxial or biaxial compression [6]-[8]. All these methods require proper understanding of the plate behaviour and the effective-width concept. A simple design formula is proposed for predicting the ultimate capacity of thin-plates containing openings and subject to in-plane compressive loading. A single formula covers different shapes of openings, different types of axial loading and different combinations of boundary conditions and no rigorous mathematical computations are required.

In the present study, finite element analyses have been carried out on square plates containing centrally located circular or square openings, in order to obtain data on the buckling and post-buckling behaviour of these plates. The parameters considered are the shape and size of the openings, plate slenderness, boundary conditions along the edges of the plate and in-plane loading. As openings larger than half the size of the plate are unlikely to be used in practice, the studies have been confined to cutouts having a maximum diameter or side, equal to half the width of the plate. However, the ratio of diameter of circular openings or the side of square openings to the width of plates has been varied in the analysis up to 0.7 in order to cover a wider range. Plates having various width/thickness ratios ranging from 20 to 70 has been examined. The boundary conditions considered are (i) all edges simply supported, (ii) all edges clamped, (iii) two opposite edges simply supported whilst the remaining two edges clamped, and (iv) three edges simply supported whilst the fourth edge which is unloaded is free. The boundary conditions provided are in the direction normal to the plane of the plate and it has been assumed that the edges are not free to pull-in. Plates have been assumed to be subjected to either uniaxial loading or biaxial loading.

The simplifying assumptions that have been made so as to reduce the complexities in the solution process are (a) the material is homogenous, isotropic, elastic and perfectly plastic and that the effect of strain hardening is neglected; (b) plane sections initially normal to the mid-surface remain plane and normal to that surface after bending; (c) only a single wave of buckling is considered, i.e. the plate is approximately square and that the buckling shape is in the same form as the assumed initial imperfection; (d) the finite buckled shape in the post-buckling phase is identified as the shape of infinitely small buckles during incipient buckling; and, (e) the in-plane displacement in the x and y directions are considered to be very small as compared with the transverse deflection in the z direction.

FINITE ELEMENT ANALYSIS

A finite element package, ABAQUS, which is capable of dealing with both material and large-displacement geometric nonlinear effects has been used for the analysis. Material non-linearity is modelled using an incremental plasticity theory assuming the material to be elastic-plastic without strain hardening. Material yielding is defined by the von Mises yield function with isotropic material behaviour. The yield function only depends on deviatoric stress, so that plastic part of the response is incompressible. The volumetric strain is only calculated at the centroid of the element. The non-linear response of the plate in the loading path is solved by using the Newton iterative technique. The

response in the unloading path is traced using the arc-length control method [8]. The Newton method iterates at a constant load while the arc-length method iterates for an unknown load increment factor.

A typical finite element mesh used in the present analysis is shown in Fig. 1. This mesh was chosen after performing an extensive convergence study in which the values of axial compression and lateral displacement were considered. A denser or graded mesh was adopted in the highly stressed regions. The quadrilateral element is a four-noded, reduced integration, doubly curved shell element with hourglass control. This element allows for transverse shear and can be used as thick shells or thin shells. Each node of the quadrilateral element has six active degrees of freedom – three displacement and three in-surface rotation components. The boundary conditions are so chosen that the nodes along the edges of the plate are restrained in the direction normal to the plane of the plate in the case of simply supported edge conditions and these nodes were, in addition, restrained from rotation corresponding to the plane of bending for clamped edge conditions. Uniaxial and biaxial loading conditions were modeled by applying uniform nodal displacement along the loaded edges assuming that the St Venant principle is valid. Quarter of the plate was analyzed taking advantage of symmetry in boundary and loading conditions wherever possible and full plate was analyzed otherwise. Appropriate boundary conditions were imposed along the line of symmetry whenever the advantage is taken of the symmetrical boundary and loading conditions of the problem.

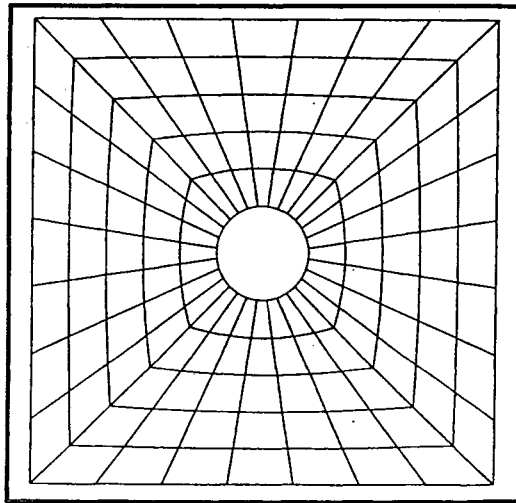


Figure 1: Typical Mesh of a Perforated Plate

In order to establish the accuracy of the analytical method by using ABAQUS, the method was first applied to analyse a number of perforated square plates tested by Narayanan and Chow [6], who carried out tests for investigating the effects of plate slenderness, size and shape of holes and the eccentricity of cut outs on the ultimate load behaviour of perforated plates and also to establish the accuracy of the analytical method proposed by them. Each square plate is of side, b , of 125 mm and thickness, t , of 1.615 mm ($b/t = 77.4$) while the yield stress is taken as 323.3 kN/mm^2 . The other details of the test specimens, along with the experimental failure loads along with the corresponding values obtained by from ABAQUS analysis are summarized in Table 1. The comparison between the two sets of values is also given in the table.

Comparison of the experimental results for ultimate load carrying capacity of perforated plates with the corresponding values obtained from the ABAQUS analysis, given in Table 1, shows that there is good agreement between the two sets of results. Underestimation or overestimation by the analytical method is within an acceptable level, the maximum deviation being around 7%. Judging from the accuracy obtained it was decided to use the finite element package to carry out a parametric study on plates containing circular or square openings and simply supported or clamped along the edges.

TABLE 1: DETAILS OF SPECIMENS STUDIED IN REFERENCE [6] AND COMPARISON OF RESULTS

Specimen	d (mm)	d/b	δ_o (mm)	δ_o/t	P_{Abaq} (kN)	P_{Expt} (kN)	$P_{\text{Abaq}}/P_{\text{Expt}}$
PL1a	0.0	0.0	0.229	0.141	40.45	39.32	1.03
CIR2a	25.0	0.2	0.229	0.142	36.49	37.46	0.97
CIR3a	37.5	0.3	0.136	0.084	34.97	33.94	1.03
CIR4a	50.0	0.4	0.304	0.188	30.93	29.57	1.05
CIR5a	62.5	0.5	0.279	0.173	29.41	27.35	1.08
SQ2	25.0	0.2	0.097	0.060	32.46	33.48	0.97
SQ3	37.5	0.3	0.141	0.087	27.49	28.85	0.95
SQ4	50.0	0.4	0.113	0.070	26.18	25.52	1.03
SQ5	62.5	0.5	0.209	0.129	23.46	21.86	1.07

PARAMETRIC STUDIES

In the derivation of a design formula, consideration has been given to the parameters that should be included in the expression while keeping it simple and reliable. Since simplicity and accuracy are often conflicting requirements for design, one must ensure that a reasonable degree of accuracy is attained without necessarily sacrificing the simplicity. This objective can be achieved if the design equations include only the most important parameters.

In an analysis of perforated plates, the parameters which need to be considered are extensive. The single most important parameter that governs the plate strength is the plate slenderness b/t in which b is the plate width and t the thickness. In calculating the ultimate load of perforated plate, the opening size in relation to the size of the plate is another parameter to be considered. In order to make it common for square or circular opening, the ratio of opening area to the surface area of the plate (A_o/A_p) was chosen as a parameter to represent hole size. Initial imperfection was taken to be a nominal design value equal to $b/1000$ that is recommended usually in practice. The ultimate load capacity is represented as the ratio of the load to the squash load of the plate i.e $P_{\text{ult}}/P_{\text{sq}}$. Another important parameter is the support condition and, four different combinations were considered in the analyses. They are: (i) all four edges simply supported, (ii) all four edges clamped, (iii) two parallel edges clamped while the remaining parallel edges simply supported and (iv) three edges simply supported with the fourth edge is left free. Two different loading conditions viz. uniaxial or biaxial were considered in the analyses.

Extensive finite element analysis was carried out on plates varying a particular parameter while keeping the other parameters constant. Thus each of the parameters was varied and in each case the ultimate load carrying capacity was determined. Plate slenderness b/t was varied from 10 to 70 while the d/b ratio in which d refers to the size of openings and b the plate width was varied from 0.0 to 0.7. These analyses were carried out for the selected boundary conditions referred earlier and subjected to uniaxial or biaxial loading.

DESIGN FORMULA

For given boundary and loading conditions, the ratio of ultimate load to squash load (P_{ult}/P_{sq}) of perforated plates is assumed to be a function of plate slenderness (b/t) and opening size (d/b) ratios. The investigations on the results have shown that if the ratio A_h/A_p , where A_h is the area of the (square or circular) opening and A_p is the surface area of the plate, is adopted instead of d/b ratio, then one single approximate expression can be derived for predicting P_{ult}/P_{sq} . Using the results obtained from the finite element analyses, best fit regression analyses have been carried out on the values of P_{ult}/P_{sq} for different b/t and A_h/A_p values. The analyses considered quadratic and cubic polynomial fits which combine the effects of the two parameters stated above. As the cubic fit was not found to increase the accuracy significantly, the quadratic fit was adopted and the corresponding expression can be given by

$$\frac{P_{ult}}{P_{sq}} = C_1 \left(\frac{A_h}{A_p} \right) + C_2 \left(\frac{A_h}{A_p} \right)^{\frac{1}{2}} + C_3 \quad \text{where } C_i = f_i \left(\frac{b}{100t} = S \right)$$

The values of coefficients C_i are listed for different loading and support conditions in Tables 2 and 3.

An interesting observation has been made in the case of uniaxially compressed clamped plate in which the ultimate load calculated for a given size of a hole remained the same irrespective of the shape of the opening. It was found to be true over a wide range of the size of openings and a straight line relation was observed between the ratio of ultimate load to squash load and ratio of hole size to the plate width. Also, it was observed that the ultimate load is independent of plate slenderness ratio for a wide range of d/b ratio viz from d/b equal to 0.3 to 0.7. A separate equation as shown in Table 4 is proposed for this case. If it is required to find the ultimate capacity of a given perforated plate the steps involved are very simple now. Expressions for coefficients C_1 , C_2 and C_3 are chosen from the Tables for the given loading and support conditions and substituted in the formula for ultimate capacity. One has to calculate only the plate slenderness ratio, area ratio or hole size ratio and the squash load of the plate in order to obtain the ultimate load.

TABLE 2: LIST OF COEFFICIENTS C_1 , C_2 AND C_3

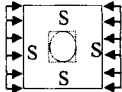
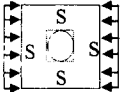
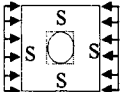
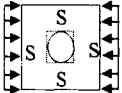
Boundary Conditions	C_1	C_2	C_3
	$-0.1S^2 - 0.39S - 0.061$	$0.6S^2 + 0.61S - 1.0671$	$-0.59S + 1.1$
 Unloaded edges free to pull in	$-0.4S^2 - 0.51S + 0.1125$	$1.59S - 1.3522$	$-0.7S + 1.1633$
	$-10S^3 - 14S^2 + 5.8S + 0.66$	$-0.1S^2 + 1.44S - 1.14$	$0.6S^2 - 1.57S + 1.2$
	$10S^3 - 12S^2 + 3.74S - 0.28$	$-0.6S^2 + 2.13S - 1.2913$	$-1.14S + 1.1$

TABLE 3 LIST OF COEFFICIENTS C_1 , C_2 AND C_3

Boundary Conditions	C_1	C_2	C_3	Note
	$-2S^2 + 2.2S + 0.94$	$3S^2 - 2.2S - 0.062$	$-S^2 + 0.48S + 0.76$	$0 < d/b < 0.4$
	0	-0.89	0.89	$0.4 < d/b < 0.7$
	$-4S^2 + 1.58S - 0.1286$	$3S^2 - 1.52S - 0.8674$	$-S^2 + 0.49S + 0.9585$	$0 < d/b < 0.4$
	0	-0.96	0.973	$0.4 < d/b < 0.7$
	$3.0S^2 - 3.25S + 0.404$	$-2.0S^2 + 3.58S - 1.51$	$-0.1S^2 - 0.95S + 1.14$	$0 < d/b < 0.7$

TABLE 4: LIST OF COEFFICIENTS C_1 , C_2 AND C_3

Boundary Conditions	C_1	C_2	C_3	Note
	$-5S^3 + 5S^2 - 1.29S + 0.0891$	$2S^2 - 1.37S - 0.8465$	$-0.6S^2 + 0.4S + 0.9549$	$0 < d/b < 0.4$
	0	-0.97	0.981	$0.4 < d/b < 0.7$
$\frac{P_{ult}}{P_{sq}} = C_1 \left(\frac{d}{b}\right)^2 + C_2 \left(\frac{d}{b}\right) + C_3 \quad \left(0 < \frac{d}{b} < 0.7\right) \quad S = \frac{b/t}{100} \quad (20 < b/t < 70)$				

VERIFICATION OF THE PROPOSED FORMULA

The parameters included in a design formula must be such that the predictions are always within a narrow scatter band independent of the values of parameters not included in the equation. This means that when applying the formula to predict the value of a specific response, one cannot expect it to be the exact but instead to be within an acceptable error limits. The prediction of the exact value of the response can only be achieved by methods of rigorous analysis (experimental or numerical), in which all the characteristics of the component and of the loading are represented and properly accounted for.

Narayanan and Chow [6] tested plates with large b/t ratios, simply supported along all four edges kept straight and containing circular openings. Their values for ultimate loads are compared with the ones obtained using the proposed formula. Table 5 shows the details of the test specimens along with the experimentally observed (P_{expt}) and analytically predicted (P_{des}) ultimate loads expressed as the respective ratio of the corresponding squash loads (P_{sq}). Comparison between the two sets of values are shown in the Table. There is good agreement between the two values, maximum deviation being 11% and in this case the formula overestimates the failure load. The equation is found to be reasonably accurate in predicting the ultimate capacity in all cases.

TABLE 5: COMPARISON OF PROPOSED DESIGN FORMULA WITH EXPERIMENTAL VALUES FROM REFERENCE [6]

Specimen	b/t	d/b	P_{des}/P_{sq}	P_{expt}/P_{sq}	P_{des}/P_{expt}
CIR2a	77.4	0.200	0.610	0.574	1.06
CIR3a	77.4	0.300	0.561	0.520	1.08
CIR4a	77.4	0.400	0.501	0.453	1.11
CIR5a	77.4	0.500	0.430	0.419	1.03
CIR6	42.3	0.291	0.702	0.721	0.97
CIR10	42.3	0.465	0.549	0.575	0.95
CIR11	53.3	0.465	0.519	0.493	1.05
CIR12	88.5	0.465	0.428	0.410	1.04

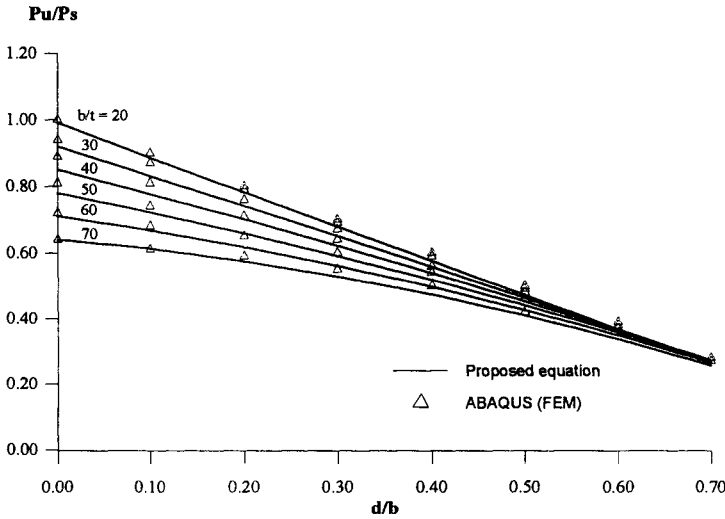


Figure 2: Uniaxially Compressed Plates with Square Opening: Four Edges Simply Supported

In order to establish the accuracy of the proposed design formula for a wider range of problems, a number of plates with b/t ratios ranging from 20 to 70, different loading and support conditions and different sizes (d/b ratios ranging from 0.0 to 0.7) and shapes (circular or square) of openings were analysed by using the formula and the finite element package, ABAQUS. The proposed formula is found to give good approximation for all cases compared with the FEM results. Figure 2 shows typical comparison of the results corresponding to uniaxially compressed plates with square opening and with all four edges simply supported. In most cases, it is found that the formula is conservative in predicting the ultimate capacity of the perforated plates.

It has been observed from the results that the ultimate load carrying capacity of the perforated plates decreases with increasing hole size and the extent by which the load carrying capacity drops is influenced by the nature of loading and boundary conditions. This drop in strength with increasing opening size corresponds to the loss of stiffness of the plate due to the presence of holes. It is found in most cases that the ultimate load tends to converge regardless of the slenderness ratio as the hole size

becomes larger. This shows that the influence of hole is more significant on the strength or stiffness of the plate when the opening size ratio exceeds 0.4 to 0.5 irrespective of the plate slenderness.

It has been observed that ultimate load of perforated plates with small slenderness ratio (thick plates) tends to vary linearly with opening size ratio. However, for thin plates they are non-linear, close to parabolic behaviour.

Generally, for simply supported plates with the same hole size, the ultimate loads are higher when the unloaded edges are constrained to remain straight in plane as compared to those with unloaded edges free to pull-in. Plates clamped at four edges yield higher ultimate loads with little effect by the slenderness ratio or hole size or hole type.

CONCLUSIONS

A simplified design formula to predict the ultimate load capacity of centrally perforated plates with different boundary conditions and subjected to compressive load is proposed. Two different types of loading conditions, uniaxial or biaxial compression, have been investigated. Square or circular openings have been considered and their sizes have been varied to cover those that are used in practice. Plates of varying slenderness have been studied. Best fit regression analysis has been employed for developing the design formula. The formula expresses the ultimate load in terms of opening area ratio and plate slenderness. The proposed formula has been verified using ABAQUS results. It is found that the proposed equation gives a slightly conservative prediction with an error of less than 10% for most cases and this is acceptable in design.

REFERENCES

1. Yu, W. W., and Davis, C. S., "Buckling behavior and post-buckling strength of perforated stiffened compression elements", *Proc. First Specialty Conference on Cold-Formed Steel Structures*, (August 1971), University of Missouri-Rolla, Missouri, 1973, pp.59-64.
2. Shanmugam, N. E. and Narayanan, R., "Elastic buckling of perforated square plates for various loading and edge conditions", *Int. Conf. Finite Element Methods*, Shanghai, 1982.
3. Sabir, A. B. and Chow, F. Y., "Elastic buckling of flat panels containing circular and square holes", *Int. Conf. Instability and Plastic Collapse of Structures*, Manchester, 1983.
4. Azizan, Z. G. and Roberts, T. M., " Buckling and elasto-plastic collapse of perforated plates", *Proc. of the the Michael R. Horne Conference on Instability and Plastic Collapse of Steel Structures*, Manchester, 1983, pp.322-328.
5. Roberts, T. M. and Azizan, Z. G., "Strength of perforated plates subjected to in-plane loading", *Thin Walled Structures* (1984), pp.153-164.
6. Narayanan, R. and Chow, F. Y., "Ultimate capacity of uniaxially compressed perforated plates", *Thin Walled Structures*, 2, (1984) pp.241-264.
7. Narayanan, R. and Chow, F. Y., "Strength of biaxially compressed perforated plates", *Seventh Int. Specialty Conf. on Cold-Formed Steel Structures* St. Louis, U.S.A., Nov. 13-14, 1980, pp.55-73.
8. Narayanan, R., A Simplified Procedures for the Strength Assessment of Axially Compressed Plates with or without Openings, *Proceedings, Int. Conf. on Steel and Aluminium Structures*, Cardiff, 1987, pp. 592-606.

STUDY ON THE EFFECT OF SYMMETRICAL OPENINGS ON THE ULTIMATE CAPACITY OF LIPPED CHANNELS

Y. Pu¹, M.H.R. Godley¹, R.G. Beale¹ and J. Wallace²

¹School of Construction & Earth Sciences, Oxford Brookes University
Oxford OX3 0BP, UK

²Department of Physics, Astronomy and Mathematics
University of Central Lancashire, UK

ABSTRACT

The paper reports the results of an investigation into the load-carrying capacity of symmetrically perforated lipped channels. 21 tests of lipped channels have been carried out to investigate the effects of the size, position and aspect ratio of rectangular holes on the ultimate compressive strength of perforated columns. A formulation is proposed to predict the ultimate load-carrying capacity of such channels. The proposed formulation is shown to predict the ultimate strength of perforated columns accurately. The size of holes is the most influential factor determining the weakening effect. The positions and the aspect ratio of the rectangular holes have only marginal effects for lipped columns.

KEYWORDS

Perforation, Cold-formed structures, Ultimate strength, Openings, Columns, Perforated channels.

INTRODUCTION

Symmetrically perforated lipped channels are common components in pallet racking systems. A considerable amount of research has been carried out to investigate the effect of a single hole on the buckling load and ultimate compression capacity of web plates or columns (Yu and Davis, 1973, Ritchie and Rhodes, 1975, Loov, 1984, Narayanan and Chow, 1984, Sivakumaran, 1987, Miller and Pekoz, 1994, Shanmugam, 1996), but only few papers have been dedicated to the effects of multiple holes. Rhodes and Schneider (1994) have studied the effect of different patterns of multiple circular holes on the compressive capacity of plain channels, and various modified methods to the design codes have been derived to take perforations into account. The effect of perforation length was further investigated by Rhodes and Macdonald (1996). Leach, et al (1996) used a finite element method and generalised beam theory to predict the failure load of perforated light gauge steel columns and the results were compared with tests. Current knowledge on the effects of multiple perforation is so limited that when such members are designed their behaviour must be assessed by experiment.

The objective of this paper is to systematically investigate the effect of the size, position and aspect ratio, which is defined as the ratio of length to width, of rectangular holes on the ultimate compressive strength of perforated columns. A total of 21 tests of lipped channels was first carried out. A formulation was then derived to predict the ultimate load-carrying capacity of such channels. This formulation was based on an unstiffened strip approach, which was first introduced by Yu and Davis (1973) for a single hole and further extended by Miller and Pekoz (1994), and also incorporated Perry-Robertson approach.

EXPERIMENT

A total of 21 tests of lipped channels was carried out. The dimensions of the lipped channels in the experiment were 370 mm long, the widths of the web, flanges and lips were 88, 40 and 10 mm respectively, as shown in Fig. 1. The thickness of the columns was 2 mm. The inner radius of the corners was 4 mm.

The tests were carried out on a testing machine with a maximum capacity of 2000 kN in accordance with AISI Specification (1996) as shown in Fig. 2. Both upper and lower loading heads of the testing machine could be adjusted for rotation about two horizontal axes and could be fixed by four screws. The upper loading head assembly could be raised or lowered to accommodate the different sizes of specimens. The tests were carried out by the following procedure. The endplates were firstly connected to each end of the column by screws and then the assembled column was put on a load cell, which was sitting on the fixed lower loading head. The upper loading head, which was free to rotate, was then lowered down. To eliminate possible gaps between components of the column assembly and to ensure fine contact in bearing between the endplates and the loading machine platens a pre-load of 70 kN was applied briefly and removed. The upper loading head was then fixed to prevent any rotation. The load was applied by raising the lower loading head through a hydraulic piston at a speed of 0.15 mm per minute. Details of the experimental procedure are given in Pu et al (1997, 1998).

The failure loads and yield stresses of the columns are shown in Table 1, in which L_h and W_h are length and width of the rectangular holes respectively, P_u^e and P_u^p are the experimental and predicted failure load of the column respectively, P_y is squash load of the column (equal to $A_g \times \sigma_y$), A_g is the gross cross-sectional area, σ_y is yield stress of the material. The 'Test No.' in Table 1 consists of four parts separated by hyphens. The first part represents the positions of the holes, 'U' refers to unperforated columns, 'M' means that the holes are a quarter of the web width away from the edge in each side, as shown in Fig. 1(a) (called quarter holes), 'C' for the hole in the centre of the web (called a central hole, as shown in Fig. 1(b)), 'E' indicates that the holes are in the edges of the web, as shown in Fig. 1(c) (called edge holes). The second part represents the aspect ratio of the rectangular holes. The third part represents the width of the holes. The number is the percentage of the ratio of the width of a hole to the web width. For each layout of perforation there were three identical specimens, which were designated by the fourth part of code.

From the table it is seen that the yield stresses varied from 231.6 to 306.1 N/mm², this caused difficulty in judging the consistency of the observed maximum compressive loads. To reduce the effect of yield stress, the non-dimensional maximum load, which was defined as the ratio of the maximum load to the product of yield stress and cross-sectional area, was used. It was found that this made the results fairly consistent. The difference in the non-dimensional maximum loads of three identical columns in each group was within ten percent for all the cases except for columns 'U-0-0-2 and M-2-15-1'. It is

believed that the results of these two columns are not correct because they are far away from the values in their groups. Therefore they were not included in the later analysis and discussions.

TABLE 1
EXPERIMENTAL AND PREDICTED FAILURE LOADS OF COLUMNS

Test No.	L_h (mm)	W_h (mm)	σ_y (N/mm ²)	P_u^* (kN)	P_u^p (kN)	P_u^p/P_u^*	P_y (kN)	P_u^*/P_y	mean of P_u^*/P_y
U-0-0-1	0.00	0.00	286.0	114.1			125.5	0.909	
U-0-0-2	0.00	0.00	268.9	88.5			118.0	0.750	0.897
U-0-0-3	0.00	0.00	234.9	91.2			103.1	0.885	
M-2-10-1	18.43	9.71	292.0	103.7	105.3	0.985	128.1	0.809	
M-2-10-2	18.40	9.46	287.4	104.4	103.9	1.005	126.1	0.828	0.822
M-2-10-3	18.45	9.81	283.2	103.2	101.9	1.013	124.3	0.830	
M-2-15-1	26.00	13.69	260.1	101.1			114.1	0.886	
M-2-15-2	25.95	13.55	297.2	101.7	102.9	0.988	130.4	0.780	0.766
M-2-15-3	26.05	13.57	304.3	100.4	105.4	0.953	133.5	0.752	
M-2-20-1	32.44	19.05	280.3	91.1	91.3	0.998	123.0	0.741	
M-2-20-2	32.20	18.56	288.2	87.4	94.4	0.926	126.5	0.691	0.711
M-2-20-3	32.50	18.68	239.3	73.6	77.9	0.945	105.0	0.701	
M-1-15-1	13.91	13.50	280.9	99.3	97.4	1.020	123.3	0.806	
M-1-15-2	13.87	14.05	284.4	99.1	98.1	1.010	124.8	0.794	0.795
M-1-15-3	13.73	13.63	287.4	98.9	99.6	0.993	126.1	0.784	
C-1-30-1	26.90	26.90	306.1	104.9	101.4	1.035	134.3	0.781	
C-1-30-2	26.55	26.78	231.6	81.2	76.8	1.057	101.6	0.799	0.787
C-1-30-3	26.60	26.65	237.6	81.3	78.9	1.030	104.3	0.780	
E-2-15-1	26.04	13.10	290.3	95.6	98.4	0.972	127.4	0.750	
E-2-15-2	25.85	13.29	305.4	104.7	103.7	1.010	134.0	0.781	0.776
E-2-15-3	26.43	13.32	286.8	100.3	97.0	1.034	125.9	0.797	

Based on the results, the effect of the size, positions and aspect ratio of the rectangular holes can be investigated. The mean values of the non-dimensional ultimate strength of each group was used. The effect of the size of the holes is shown in Table 2, in which W is width of the web plate, A_n is the net cross-sectional area of the column, $\phi_m = P_u^*/P_y$ is the ratio of experimental failure load to the squash load of the column. It was observed that the reduction in cross-sectional area is close to the reduction in the strength when the perforation of a single hole is less than 10% of web width. However, the reduction in strength is greater than the reduction in cross-sectional area when the holes are large.

TABLE 2
THE EFFECT OF THE SIZE OF THE HOLE

W_h/W	0%	10%	15%	20%
A_n/A_g	1	0.92	0.88	0.84
Values of ϕ_m	0.897	0.823	0.766	0.711
Reduction in ϕ_m (%)	-	-8.3	-14.6	-20.7

The effect of the positions of the holes is shown in Table 3. The central hole has the least weakening effect on the strength of the columns. The difference in the maximum load caused by the positions of the holes is marginal. It is interesting to note that quarter holes have the largest weakening effect. A similar phenomenon was observed by Rhodes and Schneider (1994) and Pu et al (1996) for stocky

columns and plates respectively. The effect of the aspect ratio of the rectangular holes is shown in Table 4. The difference in maximum load caused by aspect ratio of the holes is insignificant.

TABLE 3
THE EFFECT OF THE POSITIONS OF THE HOLES

Position of holes	Edge holes	A quarter of web width	Central hole
Values of ϕ_m	0.776	0.766	0.787
Difference in ϕ_m (%)	-1.4	-2.7	-

TABLE 4
THE EFFECT OF THE ASPECT RATIO OF THE HOLES

Aspect ratio of the holes	2	1
Values of ϕ_m	0.766	0.795
Difference in ϕ_m (%)	-3.6	-

THE PROPOSED FORMULATION

Yu and Davis (1973) used an unstiffened strip approach to predict the compressive capacity of stiffened plates with a single central hole. This approach was further extended by Miller and Pekoz (1994) for plates with a single central rectangular hole. The accuracy of this method is reasonably good. Therefore this method is adapted for plates with two rectangular holes.

In the proposed method, the regions between the edges of the web and the holes were treated as unstiffened elements. The formulae for unstiffened elements in codes, such as AISI (1996) and FEM (1994), could be used to calculate the effective width of these regions. The area between the two holes is treated as a column (this area is referred to as central column later). A modified Perry-Robertson's approach is used to evaluate the effective width of this area. The formulae of the modified Perry-Robertson's approach are expressed as follows:

$$\frac{\sigma_a}{\sigma_y} = \frac{1}{2} \left[1 + (1 + \eta) \frac{\sigma_E}{\sigma_y} \right] - \sqrt{\frac{1}{4} \left[1 + (1 + \eta) \frac{\sigma_E}{\sigma_y} \right]^2 - \frac{\sigma_E}{\sigma_y}} \quad (1)$$

where σ_a is the average ultimate stress of a column, σ_y is yield stress, σ_E is the Euler stress of a wide column, which is:

$$\frac{\sigma_E}{\sigma_y} = \frac{\pi^2 E t^2}{12 L_h^2 \sigma_y (1 - \nu^2)} \quad (2)$$

in which L_h is the length of the openings, t is thickness of the column, E is Young's modulus, ν is poisson's ratio.

The value of η was determined by a regression analysis on the experimental results. For a given lipped channel the loads (P_r) carried by lips, flanges, corners and regions between the edges of the web and the holes were first evaluated. The difference between the ultimate load, which was obtained from the

experiment, of the channel and P_r was the load which was supposed to be carried by the central column. The Newton-Raphson's method was then used to calculate the value of η in Eq(1). Finally a regression analysis was carried out to find out the relation between the η and the slenderness β of the central column, where $\beta = \frac{X_h}{t} \sqrt{\frac{\sigma_y}{E}}$, X_h is the width of the central column. In this study the AISI code (1996) was used to estimate the effective width of flanges, lips and regions between the edges of the web and the holes. The lips were treated as unstiffened elements while the flanges were treated as elements with an edge stiffener. The regressed relation between η and β is expressed as:

$$\eta = 0.186 + \frac{0.45}{\beta^2} \quad (3)$$

A few of interesting points about the proposed formulation are worth mentioning.

1. In Eq.(2) the formula for a wide column, which differs from the original Euler stress equation by a factor of $(1-\nu^2)$, was chosen because in most of cases the ratio of width to thickness of plating between the two holes is quite large, especially for edge holes.
2. The parameter η is no longer the initial imperfection as in the original Perry-Robertson's method. It was adjusted according to experimental data. Hence the possible errors in estimating the unstiffened elements by using formulae in codes were also compensated in this parameter.
3. The channels studied in this paper were stocky (with small ratio of width to thickness). With the increasing availability of experimental data for slender channels Eq.(3) can be easily updated to cover the full range of channels in practice. An ongoing research project in the School is aimed at this.
4. The effective widths of unstiffened and stiffened elements were evaluated by AISI code (1996). Eq.(3) is associated with the AISI code in this study. The idea can be applied to other codes such as FEM (1994) and EURO code (1996).

APPLICATION OF THE PROPOSED FORMULATION

The proposed approach was applied to the perforated channels. The results are shown in Table 1. It is seen that the predicted results are in very good agreement with experiment. The minimum and maximum values of the ratio of experimental to predicted results (X_m) are 0.926 and 1.057 respectively. The mean value and coefficient of variation of X_m are 0.998 and 3.5% respectively. The X_m of channels with a central hole (see samples C-1-30-1, -2 and -3), which were similar to the cases studied by Miller and Pekoz (1994), suggested again that the unstiffened strip approach are applicable to single perforation with reasonable accuracy.

Bearing in mind that the holes were in the webs of the columns, the proposed formulation is only applicable to stiffened elements with two symmetrical rectangular holes. In addition, the columns in the present study are stocky. To generalise the proposed formulation more experimental evidence for slender columns is required. Nevertheless the methodology presented here can be used for slender columns.

CONCLUSIONS

It may be concluded that the proposed formulation predicts the ultimate strength of perforated columns with good accuracy. The size of holes is the most influential factor determining the weakening effect.

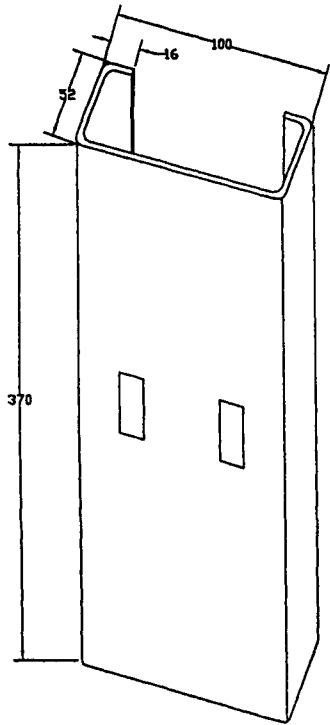
The positions and the aspect ratio of the rectangular holes have only marginal effect for this type of columns. This marginal effect may become larger if the columns are more slender than those in this experiment.

ACKNOWLEDGEMENT

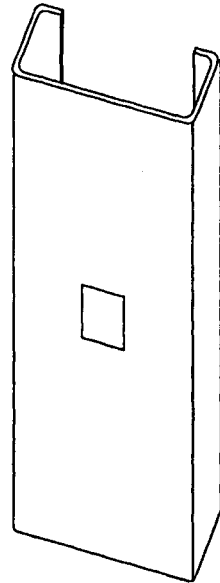
The authors would like to express their gratitude to Professor J. Rhodes for supplying his published papers which inspire the current research.

REFERENCES

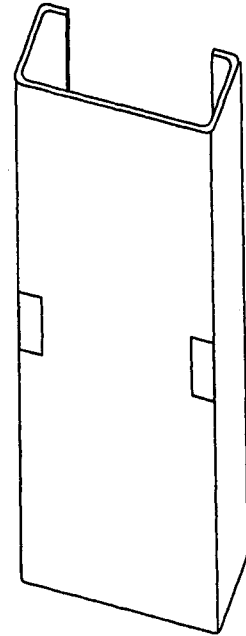
- American Iron and Steel Institute (AISI) (1996). *Cold-Formed Steel Design Manual*, 50th Commemorative Issue, 1996 Edition.
- Eurocode 3, Part 1.3 (1996). *General Rules, Supplementary Rules for Cold Formed Thin Gauge Members and Sheeting*, ENV 1993-1-3, European Committee for Standardisation.
- Federation Europeenne De La Manutention (FEM), Section X (1994). *Recommendations for the Design of Steel Static Pallet Racking and Shelving*, March 1994.
- Leach, P., Taylor, A. and Davies, J.M. (1996). The Behaviour of Light Gauge Steel Perforated Sections Subject to Combined Axial Loading Plus Bending. *Proceeding of Bicentenary Conference on Thin-Walled Structures*, 2nd - 4th December, Glasgow.
- Loov, R.(1984). Local Buckling Capacity of C-Shaped Cold-Formed Steel Sections with Punched Webs. *Canadian Journal of Civil Engineering*, **11**: 1, 1-7.
- Miller, T.H. and Pekoz, T.(1994). Unstiffened Strip Approach for Perforated Wall Studs. *Journal of Structural Engineering*, **120**: 2, 410-421.
- Narayanan, R. and Chow, F.Y.(1984). Ultimate Capacity of Uniaxially Compressed Perforated Plates. *Thin-Walled Structures*, **2**, 241-264.
- Pu, Y., Beale, R.G. and Godley, M.H.R.:(1996). Nonlinear Analysis of Symmetrically Perforated Plates. Submitted to *Thin-Walled Structures*.
- Pu, Y., Godley, M.H.R. and Beale, R.G. (1997). Experimental Investigation of the Effect of Symmetrical Openings on the Ultimate Capacity of Stub Columns. submitted to *Experimental Mechanics*.
- Pu, Y., Godley, M.H.R. and Beale, R.G. (1998). Effect of Experimental Procedures on Failure Load. *14th International Specialty Conference on Cold-Formed Steel Structures*, St. Louis, MO, USA, October 15-16, 1998.
- Rhodes, J. and Schneider, F.D.(1994). The Compressional Behaviour of Perforated Elements. *Proceeding of Twelfth International Specialty Conference on Cold-Formed Steel Structures*, St. Louis, Missouri, USA, October 18-19, 1994, pp. 11-28.
- Rhodes, J. and Macdonald, M.(1996). The Effect of Perforation Length on the Behaviour of Perforated Elements in Compression. *Proceeding of 13th International Specialty Conference on Cold-Formed Steel Structures*, St. Louis, Missouri, USA, October 1996.
- Ritchie, D. and Rhodes, J.(1975). Buckling and Post-Buckling Behaviour of Plates with Holes. *Aeronautical Quarterly*, **26**, 281-296.
- Shanmugam, N.E.(1996). Openings in Thin-Walled Steel Structures. *Bicentenary Conference on Thin-Walled Structures*, Glasgow, Scotland, 2nd-4th December.
- Sivakumaran, K.S.(1987). Load Capacity of Uniformly Compressed Cold-Formed Steel Section with Punched Web. *Canadian Journal of Civil Engineering*, **14**: 4, 550-558.
- Yu, W.W. and Davis, C.S.(1973). Cold-Formed Steel Members with Perforated Elements. *Journal of the Structural Division, ASCE*, **99**, No. ST10, October, 2061-2077.



(a) Quarter Holes



(b) Central Hole



(c) Edge Holes

Fig. 1 Dimensions of the specimens and the layout of the holes

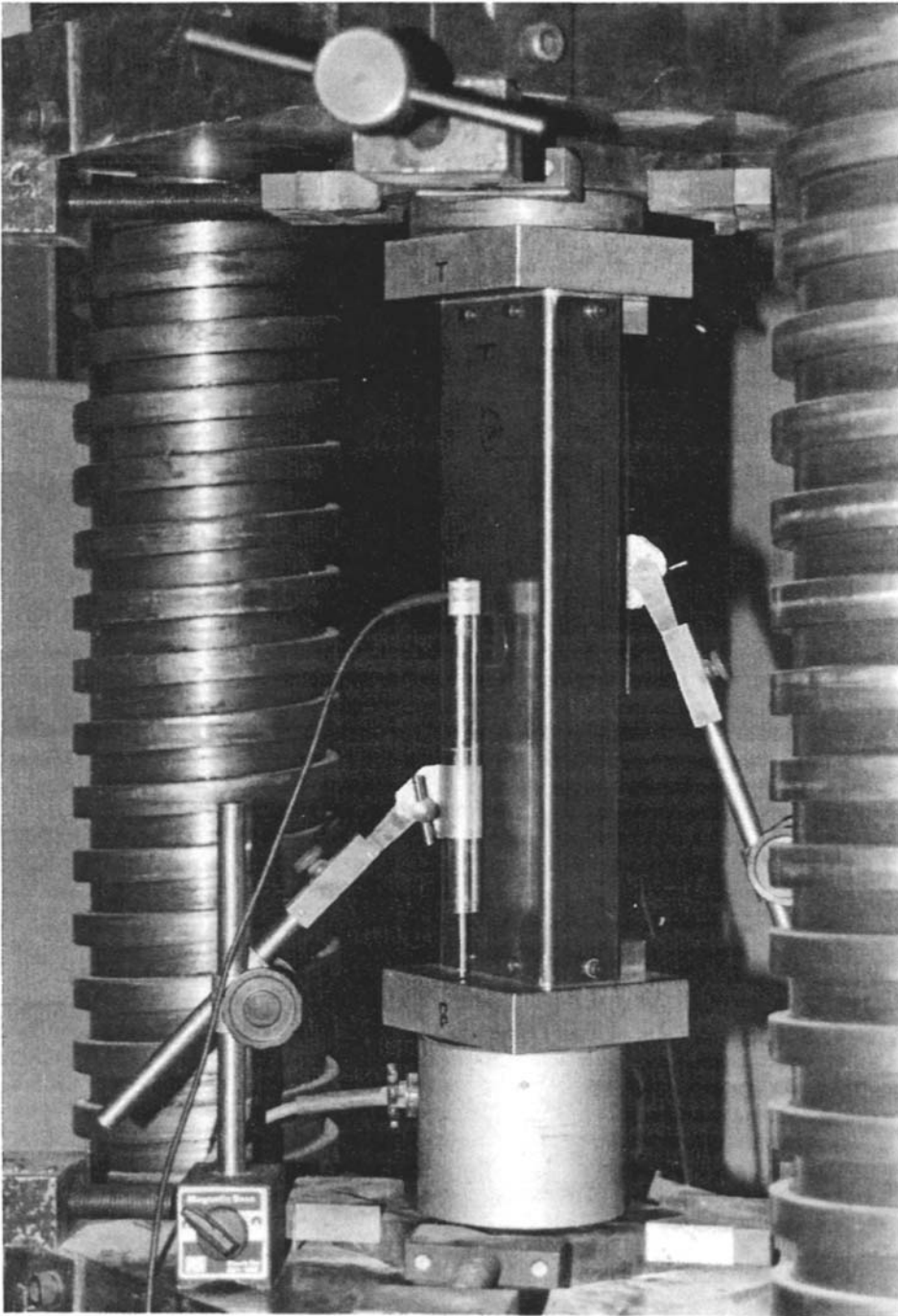


Fig. 2 The Arrangement of the Test

TENSION BUCKLING OF PLATES HAVING A HOLE UNDER COMBINED LOADINGS

S.SHIMIZU¹ and H.NISHIMURA²

¹ Department of Civil Engineering, Shinshu University,
500 Wakasato, Nagano, NAGANO 380-8553 JAPAN

² Chuo Fukken Consultants Co. Ltd.,
5-26 Higashi-Mikuni 3 Chome, Yodogawa-Ku, Osaka 532-0002 JAPAN

ABSTRACT

In this paper, following to the author's study on the tension buckling, the buckling behaviour of plates having a hole subjected to the tensile loading combined with the compression, bending or shear is dealt with. An elasto-plastic large deflection FEM is used as a numerical method. Ratio of the magnitude of the tension against the another loadings is adopted as a parameter, and the results are compared with those of plates subjected to the pure tension. Through this study, followings are found; When the compression or shear is applying together with the tension, the larger compressive stress is appeared near the hole, and in the result, the critical load of the plate becomes smaller than that of a plate subjected to only tension. On the other hand, when a plate is subjected to tension together with the in-plane bending, the compressive stress becomes smaller, and the plate has larger critical load.

KEYWORDS

tension buckling, plate, hole, combined load, FEM, box girder

INTRODUCTION

This paper represents numerical results on the buckling behaviour of plates which have a hole and are subjected to the tensile loading combined with the bending, compression or shear.

When a plate has a hole and is subjected to tension, the compressive stress is locally appeared near the hole. For example, when a plate has a rectangular hole and is subjected a set of tensile loading vertically as illustrated in Fig.1, horizontal compression shall be appeared in the upper and lower parts of the hole. This compressive stress may cause the local buckling of the plate near the hole. On this phenomenon, named as the tension buckling in this paper, some studies has been made. Bamberger (1987) gave an analytical results on the tension buckling of a plate with a circular hole. Fujimoto (1987) made a numerical study on the elastic or the elasto-plastic buckling of plates having a crack under tension.

One of the author(1991) made a parametric study on the tension buckling of plates of rectangular hole as a bifurcation problem. The author(1991, 1992) also made a series of elasto-plastic large deflection analysis on the tension buckling, and by these studies the post buckling behaviour is traced.

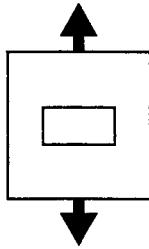


Fig.1 A plate having a hole subjected to tension

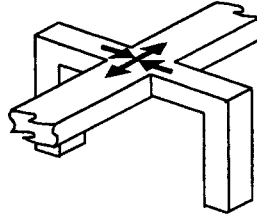


Fig.2 A box girder connected to the pier

Recently, especially in the highways in the urban areas, a box girder supported by a steel portal frame is often used. When the box girder is connected directory to the pier as a portal frame as shown in Fig.2, the stress acting the flange panel is more complicated. If, within the complicated stress, the tensile stress is dominant, little attention has been paid to the buckling in the practical bridge design procedure. However, if a manhole is arranged at the flange plate of such a girder, tension buckling may occur near the manhole.

In this paper, following to the author's studies on the tension buckling, the buckling behaviour of a plate having a hole subjected to tensile loading combined with the compression, bending or shear is dealt with. An elasto-plastic large deflection FEM is used as a numerical method. Ratio of the magnitude of the tension against the another loadings is adopted as a parameter, and the results are compared with the results on the "pure" tension buckling (buckling of plates subjected to the pure tension).

MODELS AND PARAMETERS

A 800mm×800mm square plate having a 400mm×200mm rectangular hole with its plate thickness of 6mm shown in Fig.3 is analyzed. In the analysis, grade SM490 steel, which has its material properties of the yield stress $\sigma_y=314\text{MPa}$, Young's modulus $E=206\text{GPa}$ and Poisson's ratio $\nu=0.3$, is used. This plate is considered to have an initial out-of-plane deflection of the sine shaped half wave with its maximum amplitude of 1/50 of the plate thickness.

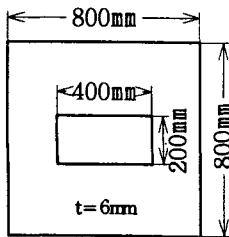


Fig.3 A plate with a hole

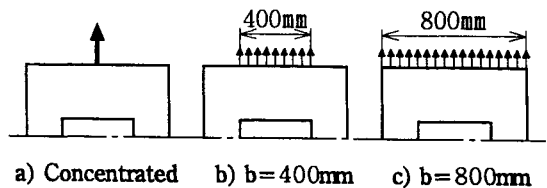


Fig.4 Tensile loadings

In this study, to verify the basic characteristics of the "pure" tension buckling, a plate subjected to only uni-axis tension is dealt with together with a plate subjected to the combined loading. The loading

conditions are considered as parameters. For the "pure" tension buckling analysis, the width of the load is adopted as a parameter as shown in Fig.4, here the names of T0, T4 and T8 are the loading type names.

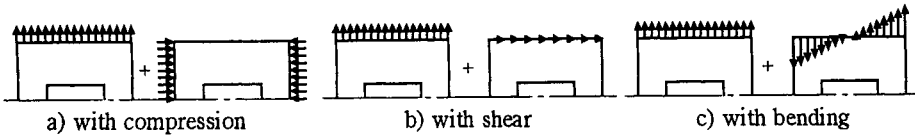


Fig.5 Combined Loadings

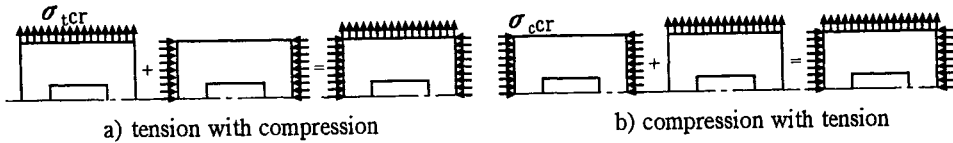


Fig.6 Two Points of View on Combined Loadings

For the analyses of the combined loading shown in Fig.5, the model T8 is considered with the additional compression, shear or in-plane bending. In these cases, the ratios of the lateral compression σ_c , shear τ or the bending σ_b to the tension σ_t (i.e. σ_c/σ_t , τ/σ_t or σ_b/σ_t) are adopted as parameters. The values of these ratios are 1/4, 1/2(2/4), 3/4, 1(4/4), 2(8/4), 4(16/4) and 1/0. Here, the ratio of 1/0 means that the plate is subjected to only the pure compression, shear or the tension, and subjected to no tension. These loading ratios are denominated as "14", "12", "34", "11", "21", "41" and "10" respectively, and model names are defined that a character "C", "S" or "B" followed by the ratios. For example, the model "S14" is subjected to the shear of $\tau/\sigma_t=1/4$ together with the tension, and the model "B10" is subjected to only the bending and to no tension. These models for the combined loadings are summarized in the Table 1.

TABLE 1
MODELS FOR COMBINED LOADINGS

$\sigma_t / \sigma_c, \tau$ or σ_b	1/4	1/2	3/4	1	2	4	1/0
lateral compression	C14	C12	C34	C11	C21	C41	C10
shear	S14	S12	S34	S11	S21	S41	S10
in-plane bending	B14	B12	B34	B11	B21	B41	B10

It should be noted that there are two points of view to discuss the buckling strength of the combined loadings as shown in Fig.6. One is that the plate is subjected to the tension with, for example, compression. In this point of view (Fig.6 a), the buckling strength is expressed with the tensile stress σ_{tcr} , and it is considered that "the tension buckling strength is influenced by the compression". The alternate point of view is that the plate is considered to be subjected mainly compression with the tension (Fig.6 b), and the buckling strength is expressed with the compression buckling stress σ_{cr} .

In this view, it is considered that "the compression buckling stress is influenced by the tension". The buckling stress as the tension buckling, σ_{tcr} , is used for the discussion to comparing the strength under the combined loading to the strength of the pure tension, and the strength as the compression buckling, σ_{ccr} , is used to compare the results to the pure compression. The same manner is adopted for the combined loadings of the tension–shear and tension–bending. In this paper, for the combined loadings, the buckling stresses expressed with both the two points of view are shown.

PURE TENSION BUCKLING BEHAVIOUR

In Fig.7, contours of the horizontal stress of models T0, T4 and T8 under the pure tensile load of 10kN are illustrated. It is clear in this figure that the horizontal compression stresses of 10–4MPa are found just above the hole. If the tensile load is increased, it is easily expected that the local buckling shall be occurred by the compression.

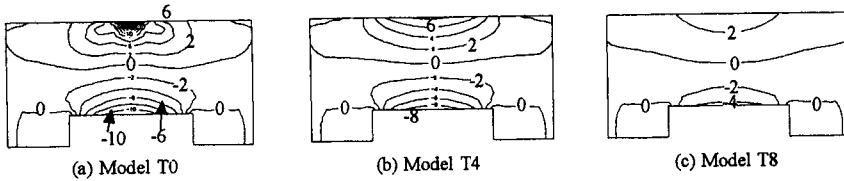


Fig.7 Stress Contours (MPa)

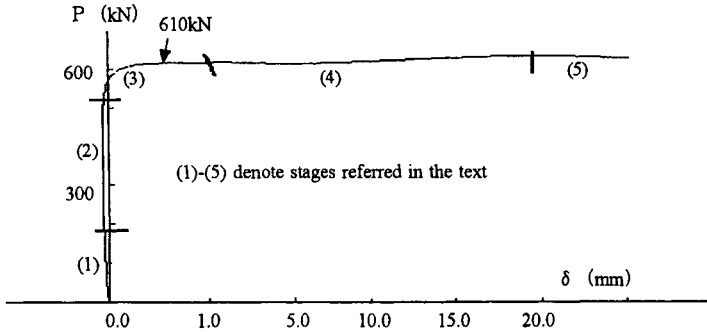


Fig.8 Load–Deflection Curve under Pure Tension

Fig.8 is a figure showing the load–deflection curve of the model of T8. The horizontal axis of this figure denotes the additional out-of-plane deflection (deflection from the initial deflection). Please note on the horizontal scale of this figure because, in this figure, the curve is enlarged horizontally only near the vertical axis. In the earlier stage (stages (1)–(2) in the figure), the deflection curve shown in this figure lies at the negative area. This means that the initial deflection is being vanished by the tensile load. However, when the load is reached to about 600kN (stage (3)), the curve becomes almost horizontal and lie for the positive direction. That is, at this stage, the out-of-plane deflection is increased very rapidly. This phenomenon is obviously considered to be the buckling. From the curve, the buckling load of this model is about 610 kN. This figure also indicates that the maximum load of this model is 632kN. In the Table 2, the buckling loads (P_{cr}) and the maximum loads (P_{max}) of models

T0, T4 and T8 are summarized. In this table the ratios of these buckling or the maximum loads to the yield load of the plate are also shown in the parentheses.

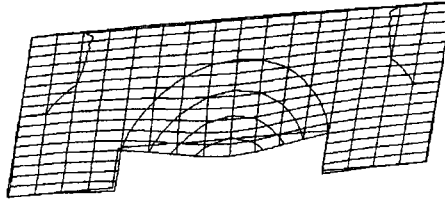


Fig.9 Out-of-plane Deformation Layout of Model T8

In the practical design procedure on a plate subjected to the tension, generally, not the buckling but the yield of the materials is referred as the strength of the plate. However, this table clearly indicates that the tension buckling strength is considerably smaller than the yield loads. For the example, the model T0 has its buckling load of 255kN and the maximum load of 297kN, and these values are smaller by 66–61% than the yield load. Even the model T8 has its P_{cr} and P_{max} smaller by 19–16% smaller than the yield load. This fact suggests that the tension buckling cannot be ignored when the plate has a hole.

TABLE 2
 P_{cr} AND P_{max} OF PLATES UNDER PURE TENSION

models	T0	T4	T8	
P_{cr}	255(34)	350(46)	610(81)	
P_{max}	297(39)	386(51)	632(84)	kN (%)

The deformation of the model T8 caused by the tension buckling is illustrated in the Fig.9. This deformation is of the stage (4) in the load deflection curve shown in Fig.8. This figure shows that out-of-plane deformation of the plate is generally small except the zone adjacent to the hole. At the upper zone of the hole, the out-of-plane deflection is found as a half wave with its length of almost the width of the hole.

PLATES SUBJECTED TO THE COMBINED LOADINGS

Tension with Lateral Compression

As described in the previous section, the tension buckling is occurred by the lateral compression stress caused by the tension. If a plate having a hole is subjected to the lateral compression together with the tension, the compression shall be much larger than that of the plate with only pure tension, and in the result it may be much severer for the tension buckling. In the Table 3, the buckling loads and the buckling stresses of models subjected to tension and the lateral compression are summarized. In this table, the "buckling load P_{cr} " or the "buckling stress σ_{cr} " means that the magnitude of the tensile load or the tensile stress on the stage at which the buckling is occurred, and the "buckling stress σ_{cr} " is the magnitude of the corresponding compression stress at the buckling. Here, the buckling stress σ_{cr} is obtainable by dividing P_{cr} with the section area of the plate A , 80cm \times 0.6cm, i.e. $\sigma_{cr}=P_{cr}/A$. In this table, the buckling load of the model T8 which is subjected to only pure tension is also shown and the

model C10 is subjected to only the compression. The values in the parentheses are ratios of the buckling stresses against the model T8 or the model C10.

TABLE 3
BUCKLING UNDER TENSION AND LATERAL COMPRESSION

models	T8	C14	C12	C34	C11	C21	C41	C10	
Pcr	610	420	275	160	120	45	20	—	(kN)
σ_{cr}	127	88	57	33	25	9	4	—	(MPa)
	(100)	(69)	(45)	(26)	(20)	(7)	(3)	—	(% for T8)
σ_{ccr}	—	22	29	25	25	19	17	21	(MPa)
	—	(105)	(138)	(119)	(119)	(90)	(81)	(100)	(% for C10)

This table shows that the lateral compression reduces the buckling load. The model C14 which is subjected to the slight lateral compression (25% of the tension) has Pcr of 420kN, and this is smaller by 31% than one of the model T8. This suggests that, when a plate with a hole is subjected to the bi-axial loading of tension and compression, the plate shall easily buckled even if the tension is dominant. On the other hand, the compression buckling stress σ_{ccr} of the model C10 being subjected to pure compression is 21 MPa and σ_{ccr} of model C41 is 17MPa. Model C41 is also subjected to the tensile stress of 4MPa at the buckling. This means that, in this case (the case that a plate is subjected to a slight tension, i.e.25% of the compression), the tension reduces the buckling stress σ_{ccr} from 21MPa to 17MPa. The buckling stress σ_{ccr} of the model C21 is also reduced by about 2MPa by the tension, although the another models have larger σ_{ccr} than the model C41.

Although the figure is not shown in this paper, the out-of-plane deflection of these models are similar to one of the model T8. However, the magnitude of the deflection is larger in these models, and especially in the models with larger lateral compression, the length of the half wave is larger than that of the model T8. That is, if the magnitude of the lateral compression is larger, the "normal buckling" like deformation is observed.

Tension and Shear

The buckling loads and the buckling stresses of models with shear and tension are shown in the Table 4 with the same manner to the Table 3. That is, values in the lines of Pcr and σ_{cr} are the tensile loads and tensile stresses at which buckling is occurred, and τ_{cr} the corresponding shear stresses.

TABLE 4
BUCKLING UNDER TENSION AND SHEAR

models	T8	S14	S12	S34	S11	S21	S41	S10	
Pcr	610	595	440	330	250	100	40	—	(kN)
σ_{cr}	127	124	92	69	52	21	8	—	(MPa)
	(100)	(98)	(72)	(54)	(41)	(16)	(7)	—	(% for T8)
τ_{cr}	—	31	46	52	52	42	33	52	(MPa)
	—	(60)	(88)	(100)	(100)	(81)	(63)	(100)	(% for S10)

The model S14, which is subjected to the shear of 25% of the tension, the buckling load is 595kN and this is 2% smaller than model T8. That is, shear stress is not so severer to reduce the buckling load. However, if the shear is increased, the buckling load is reduced, and in the model S12, the buckling load is 28% smaller than T8. Observing the buckling shear stress τ_{cr} , the models S34 and S11 have almost same buckling stress to the model S10 with pure shear. The remaining models have smaller strength than that of the models S10. Models S14 has its buckling shear stress τ_{cr} smaller by 40 % than S10, and S41 smaller by 37%. That is, on the view of the shear buckling of a plate having a hole, it can be said that the tension acts often badly.

Tension and In-plane Bending

The buckling loads and buckling stresses of plates subjected to the tension and in-plane bending are summarized in the Table 5. The all models except B41 in this table has the tension buckling load or the tension buckling stress larger than the model T8, and the tension buckling is seemed to be restricted by the in-plane bending except the model B41. Observing the bending buckling stress σ_{bc} , all models except B14 have larger buckling stress than B10. Therefore, it is found that the combined loading of tension and shear is generally advantageous in the buckling. However, if the plate is subjected to the tension with the large bending or the bending with large tension, the buckling may be occurred with the relatively small loading.

TABLE 5
BUCKLING UNDER TENSION AND IN-PLANE BENDING

models	T8	B14	B12	B34	B11	B21	B41	B10
P_{cr}	610	845	980	1195	1250	1140	395	— (kN)
σ_{cr}	127	176	204	249	260	237	82	— (MPa)
	(100)	(139)	(161)	(196)	(205)	(187)	(65)	— (% for T8)
σ_{bc}	—	44	102	187	260	475	329	84 (MPa)
	—	(52)	(121)	(223)	(310)	(565)	(392)	(100) (% for B10)

REMARKS ON THE RESULTS

At first, behaviour under the pure tension is discussed. Under the pure tension, the smaller loading width brings the smaller buckling load. However, within the current study, when a plate is subjected to the tensile load applying the full width of the plate, the buckling load is still smaller than the yield load. In the practical design procedure, if a plate is subjected to a tensile load, the buckling behaviour is generally not considered in its design. This result indicates that the tension buckling cannot be ignored when the plate has a hole.

If a plate having a hole is subjected to the lateral compression together with the tension, the buckling load (or the buckling stress) becomes smaller and the tension buckling may be occurred very easily rather than the plate with pure tension. The buckling behaviour on the combined loadings of compression-shear or compression-bending and so on have been studied by many researchers. On the other hand, buckling behaviour under the combined load of tension-compression has not been considered because that the tension is believed not to cause the buckling. However, with the view of the "normal" buckling (buckling under the compression), the buckling load may be reduced due to the tensile load.

Therefore, a designer should take notice that the tension sometimes reduces the buckling stress when the plate has a hole.

Above facts are generally true for also the combined loading of the shear and the tension. That is, the buckling load of the tension buckling is reduced by the additional shear. Considering this combined loading as "shear with additional tension", the tension generally reduces the buckling stress. When shear is larger by 4-times than the tension or the tension is larger by 4-times than the shear, the buckling stress is reduced by about 40% by the combined loading.

On the combined loading of the tension and the bending, the models have generally larger bending buckling stress than the pure bending. Therefore, in this case, it seems to be safe when the plate is designed against the in-plane bending buckling. However, when the plate is subjected to the larger tension with the bending, the tension buckling should be considered.

The combined loadings dealt with in this paper are often appeared in the complex structures such as shown in Fig.2. In designing the plates in such a structure, attention should be paid to the buckling behaviour under the combined load including the tension.

CONCLUSION

In this paper, numerical analyses are made on the tension buckling of a plates having a hole under combined loadings. On the tension buckling problem, very few studies have been made, and therefore very few information is provided for the practical design procedure. Although the very limited conditions are considered in this study, results presented in this paper shall be effective for the design of a plate having a hole, although the authors feel that the further study is required in this problem.

The authors wish to thank Mr.M.Kameko, graduate school student of Shinshu University, for his help in providing figures in this paper.

REFERENCES

- Bamberger, Y. and Voidoire, F. (1987). Stabilité en Traction D'une Plaque Trouée, *Proc. of ECCS Colloquium on Stability of Plate and Shell Structures*, ed. P. Dubas and D. Vandepitte, Ghent, Belgium, 241-246.
- Fujimoto, T. and Sumi, S. (1987). Buckling Deformation Behaviour of Center Cracked Plates under Tension, *J. JSME Part A* **53**, 593-600. (in Japanese)
- Shimizu, S., Yoshida, S. and Enomoto, N. (1991). Buckling of plates with a Hole under Tension, *Thin Walled Structures* **12**, 35-49
- Shimizu, S. and Yoshida, S. (1991). Strength of Plates with a Hole under Tensile Loading, *Proc. of International Conference on Steel and Aluminum Structures (ICSAS 91)*, ed. S. L. Lee and N. E. Shanmugam, Singapore, 501-510
- Shimizu, S. and Yoshida, S. (1992). A Large Deflection Analysis of Plates with a Hole having Initial Out-of-Plane Deflection, *Journal of Structural Engineering, JSCE*, **38A**, 203-212 (in Japanese)

ULTIMATE STRENGTH OF CYLINDRICAL TUBULAR COLUMNS WITH CIRCULAR PERFORATION

S Murakami¹, N Nishimura², S Takeuchi³, H Inoguchi⁴ and K Jikuya⁴

¹Department of Civil Engineering, Gifu University, Yangido 1-1, Gifu, Gifu, Japan

²Department of Civil Engineering, Osaka University, Yamadaoka 2-1, Suita, Osaka, Japan

³Division of Engineering, Sakai Iron Works Co Ltd, Dejima-Nishimachi, Sakai, Osaka, Japan

⁴Transmission Line Section, Wakayama Branch, The Kansai Electric Power Company Inc, Okayama 40, Wakayama, Wakayama, Japan

ABSTRACT

Maintenance work for civil structures is essential to sustain their long lives. Some damage to steel member, such as thickness decreasing or perforating, brings deterioration of their ultimate strengths and shortening of their lifetime. However, a damage criterion for the steel member is still indistinct. Therefore, it becomes important how to evaluate residual strength of damaged members.

This paper presents a buckling test and finite element analysis of perforated cylindrical tubular members, which are looked on as a damaged member, and characteristics of their ultimate strengths. Results of numerical analysis made influences of the perforation on the ultimate strength deterioration clear quantitatively.

KEYWORDS

electric resistance welded (ERW) pipe, damaged pipe, tubular column, circular perforation, buckling behavior, stress concentration

INTRODUCTION

Because of the symmetry, cylindrical shape is an effectual section under uni-axial compression or internal/external uniform pressure. Cylindrical tubular members are, therefore, widely used for constructing a column and a pressure vessel. Some exterior damage to the members, such as perforation, does not only take from the mechanical advantages but also deteriorate their ultimate strengths.

Buckling behavior of cylindrical panels with a circular or rectangular cutout is quite different from that of the virgin panels. As the ground for the differences is mainly caused by stress concentration around

the cutout, it seems that a perforation in the tubular member gives certain influence on its ultimate strength and buckling behavior.

TEST SPECIMENS

Test specimens are made of an electric resistance welded (ERW) pipe. Steel grade of the ERW pipe is STK400 regulated by the Japanese Industrial Standards (JIS). Structural properties of the test specimens are listed in Table 1 and a sample of them is illustrated in Fig. 1. All of specimens have the same diameter of 89.1 mm and wall thickness of 3.2 mm. In order to examine the influence of the perforation, the specimen has a manmade circular perforation whose diameter is sized 14, 40 or 62 mm into the wall. The diameter of 14, 40 and 62mm bring 5%, 15% and 25% decrease of cross-sectional area of specimen, respectively. The cross-view of perforated sections are illustrated in Figs. 2. All of test specimens can be classified as NS-Series or NL-Series by column length. Column length of NS-Series and NL-Series are 1500 mm and 3100 mm, respectively. Parameter "a" is the distance from edge of column to the center of perforation. Parameter η is the ratio of parameter "a" to column length and means the position of perforation in longitudinal. Parameter ξ is the ratio of the residual area to non-damaged area and named the sectional-decreasing ratio. These parameters are given as follows,

$$\xi = (\text{disappearance of wall in circumference}) / (\text{non-damaged area}), \tag{1}$$

$$\eta = (\text{distance from edge to perforation}) / (\text{column length}) = a / L, \tag{2}$$

TABLE 1
PARAMETERS OF TEST SPECIMENS

Series	Structural Properties	Model Name	Diameter of Perforation	Position of Perforation
NS	Diameter of cross section 89.1 mm	NS-00	none	none
	Thickness of wall 3.2 mm	NS-05-A,B,C,D	14 mm (5 %)	L/2,3L/8, L/4,L/8
	Column length 1500 mm	NS-15-A,B,C,D	40 mm (15 %)	
		NS-25-A,B,C,D	62 mm (25%)	
NL	Diameter of cross section 89.1 mm	NL-00	none	none
	Thickness of wall 3.2 mm	NL-05-A,B,C,D,E	14 mm (5 %)	L/2,3L/8,L/4, L/8,150mm
	Column length 3100 mm	NL-15-A,B,C,D,E	40 mm (15 %)	
		NL-25-A,B,C,D,E	62 mm (25%)	

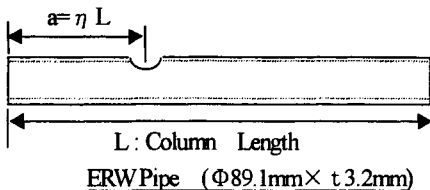
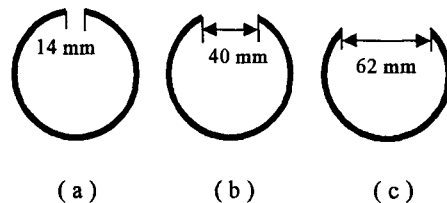


Figure 1: Parameter of test specimen



Figures 2: Cross-view of perforated section

where L is the column length.

The first section of model-name means the column length classification, the second section means the sectional-decreasing ratio and the third section means the position of perforation. The models of which second section are given like "00" mean non-damaged member.

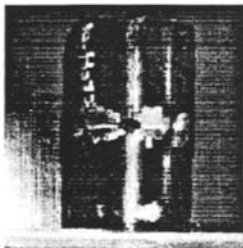
MATERIAL TEST

Material properties are obtained by tensile tests and compression tests of stub column. The material properties, which consist of tensile yield stress(σ_y), Young's modulus(E), Poisson's ratio, compressive strength of stub column and so on, are listed in Table 2. Tensile yield stress of STK400 is much higher than the nominal value 235 MPa. This high yield stress owes mainly to the plastic work in manufacturing processes of the ERW pipe. The ratio of compressive strength of the perforated stub column to that of non-damaged one are 92.0%, 79.4% and 65.9%, respectively. These deteriorating ratios of the ultimate strength are over the sectional-decreasing ratios, respectively.

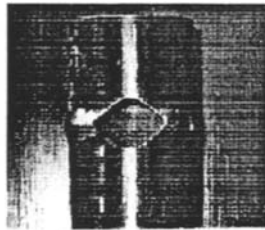
Deformations of stub columns are shown in Photos. 1(a)-(c). Specimens with 15% and 25% sectional-decreasing perforation show large outward deformations at both transversal edges of the perforation. In the case of 5% sectional-decreasing perforation, on the other hand, the deformation in longitudinal direction are larger than that in transversal direction. These different ultimate strength deterioration and deformations are caused by the eccentricity of cross section. The eccentricity of cross section derives

TABLE 2
MATERIAL PROPERTIES OF TEST SPECIMENS

Tensile Yield Stress (σ_y)		365.0 MPa
Compressive Yield Stress		346.9 MPa
Young's Modulus (E)		206.0 GPa
Poisson's Ratio		0.29
Tensile Strength		425.7 MPa
Compressive Strength of Stub column	non-damaged	400.6 MPa
	5% sectional-decreasing	368.5 MPa
	15% sectional-decreasing	318.0 MPa
	25% sectional-decreasing	263.8 MPa



(a)5% sectional-decreasing



(b)15% sectional-decreasing



(c)25% sectional-decreasing

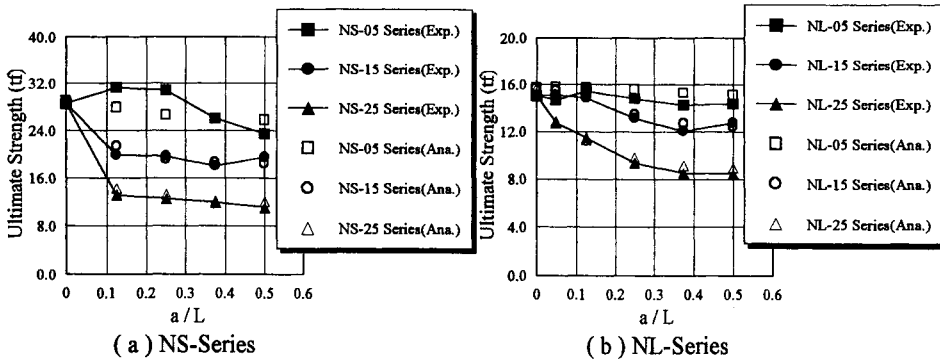
Photographs 1: Deformations of the perforated stub columns

both of the stress concentration and the increase of plate bending moments around the perforation.

BUCKLING TEST

Figures 3(a) and 3(b) show variations of ultimate strength caused by the position of perforation. The vertical and horizontal axes mean the actual load and the position of perforation, respectively. In the case of NS-05-Series, ultimate strength of columns slightly decreases as a/L increases. On the other hand, in the other case of NS-Series, decreases of ultimate strength are only under the influence of the sectional-decreasing ratio. These cases show that the position of perforation do not dominate the ultimate strength. All of specimens for NS-Series show the local deformation around the perforation and collapse. The deformation behaviors around the perforation are same as those of the perforated stub columns. In the case of the specimens for NL-05-Series, membrane buckling occurs before collapse. In these series, it is able to say that the perforation gives no influence on buckling behavior. In the other series, NL-15 and NL-25-Series, ultimate strength become lower under the influence of the position of perforation than the membrane buckling strength of non-damaged column. In these series, specimens are collapsed with interactive behavior between membrane buckling and local deformation.

Ultimate strength of numerical models same as test specimens are analyzed by a finite displacement analysis program, named NASHIEL, which has been developed by authors using 8-nodes isoparametric shell element. Figure 4 shows a sample of element arrangement for perforated column. In Figs. 3(a) and 3(b), analytical results plotted as white symbols are compared with test results plotted as black symbols



Figures 3: Variations of ultimate strength caused by the position of perforation.

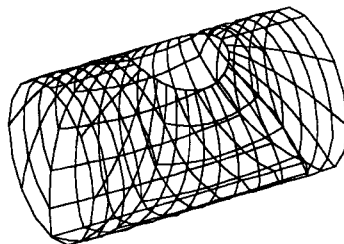
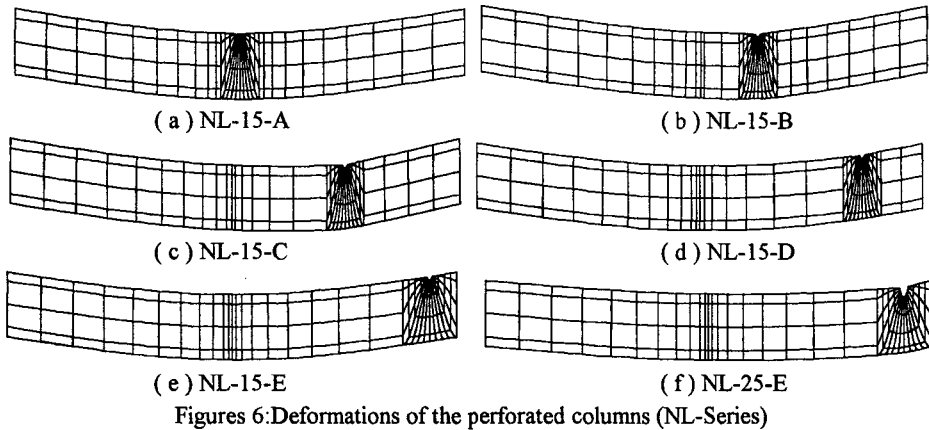
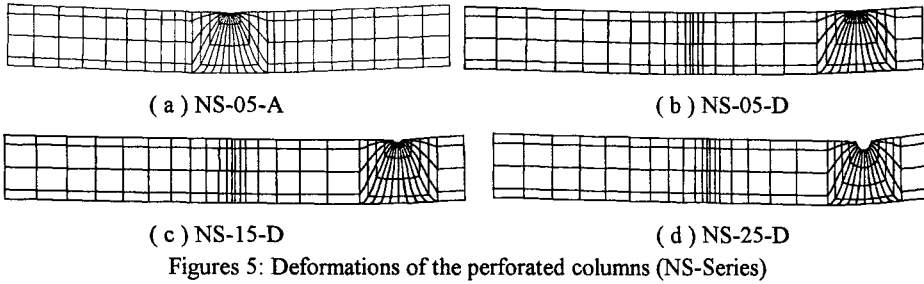


Figure 4: A sample of element arrangement.



with solid line. White symbols conform to solid lines well. The deformations of column are shown in Figs. 5 and 6. The tendency for deformation obtained by analyses well agrees with that of buckling tests. From above results, it seems properly that the various buckling behaviors of test specimens and analytical conditions, example for boundary conditions and element arrangement, are reappeared well in finite displacement analyses.

ULTIMATE STRENGTH OF PERFORATED COLUMN

Using perforated column models, a parametric study is carried out. Structural properties of which are listed in Table 3. Results of material tests are used for the material properties.

Figures 7(a)-(d) show relationship between the ultimate strength changes and the position of perforation. The horizontal axes of them are the position of perforation. The vertical axes are the ultimate strength ratios. These ratios are the percentage of ultimate strength of the perforated column to that of non-damaged one. In the case of stocky columns, the sectional-decreasing ratio gives much influence on ultimate strength than the position of perforation. Most of them collapse owing mainly to local deformation. On the other hand, in the case of slender columns, the position of perforation gives more influence on the ultimate strength than the sectional-decreasing ratio. These columns collapse owing to membrane buckling or interactive behavior between membrane buckling and local deformation.

Figures 8(a) and 8(b) show column strengths in the case of $a=L/2$ and in the case of $a=L/8$, respectively. The horizontal axes are the slenderness parameter of column ($\bar{\lambda}$) given as follows,

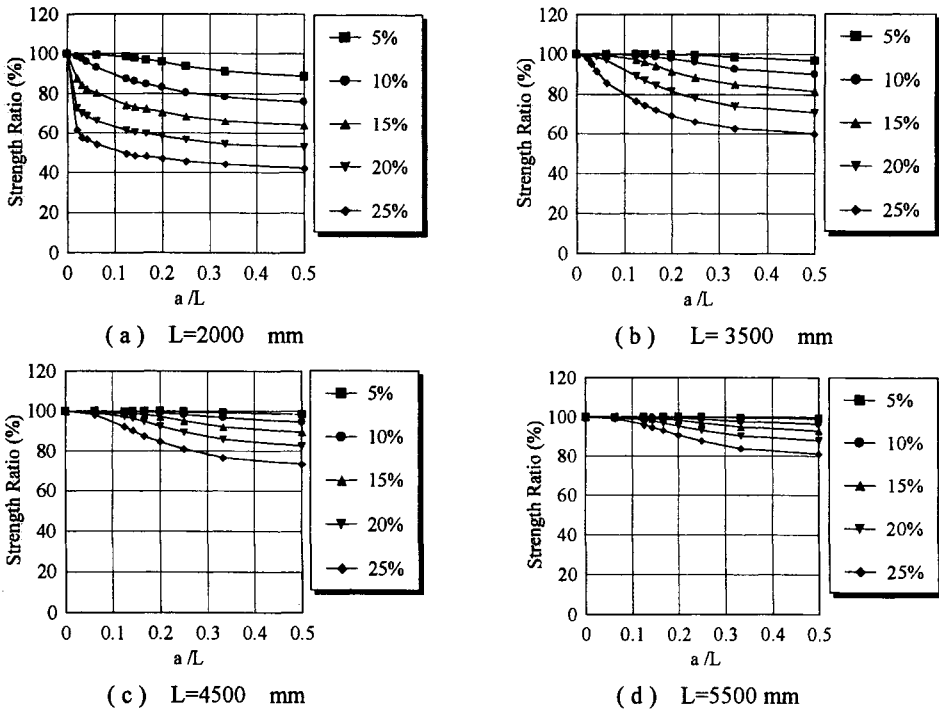
$$\bar{\lambda} = \frac{1}{\pi} \frac{L}{r} \sqrt{\frac{\sigma_Y}{E}} \tag{3}$$

where r is the radius of gyration of the cross section.

The vertical axis is the non-dimensional strength that is given as the ratio of ultimate strength of perforated column to yield strength in non-damaged section. In these figures, the ECCS-a0 curve which

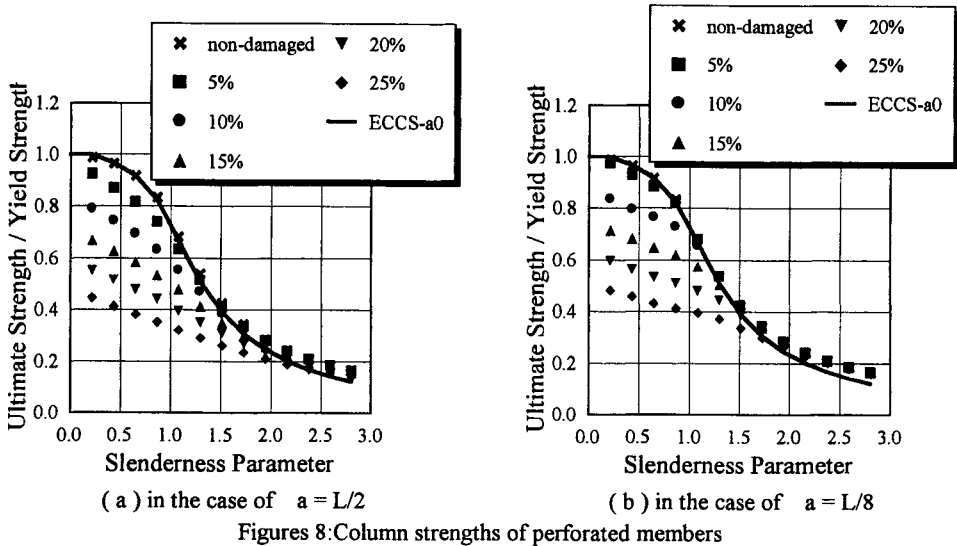
TABLE 3
STRUCTURAL PROPERTIES OF NUMERICAL MODELS

Yield Stress	365 (MPa)
Young's Modulus	206 (GPa)
Poisson's Ratio	0.3
Column Length	500, 1000, 1500, 2000, 2500, 3000, 3500, 4000, 4500, 5000, 5500, 6000, 6500 mm
Diameter of Perforation	none, 14, 28, 40, 52, 62 mm
Position of Perforation	L/2, L/8

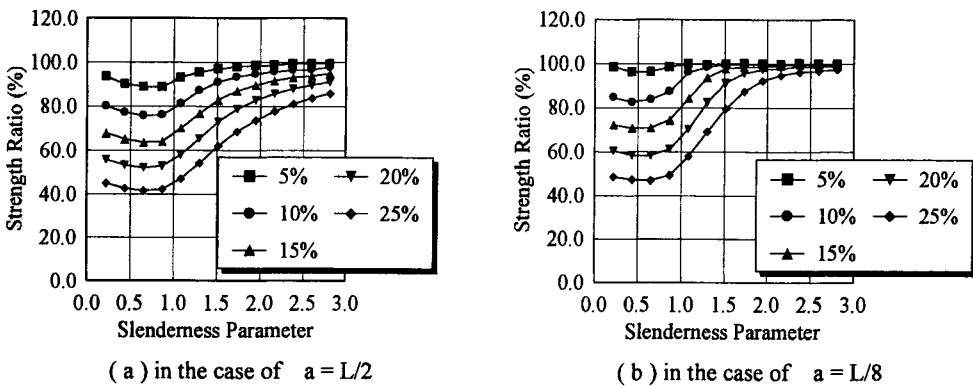


Figures 7: Relationship between the ultimate strength changes and the position of perforation.

is proposed as the column strength curve for tubular members are drawn with a thick solid line. In the region of slender columns, ultimate strengths of the perforated columns are well fitted to the ECCS-curve. On the other hand, in the region of stocky columns, ultimate strengths are below the curve. Figures 9(a) and 9(b) show the ultimate strengths varying with the slenderness parameters of the columns. The vertical axis is the strength ratio of the ultimate strength of the perforated column to that of non-damaged ones. In the region of stocky columns, the ratios of strength deterioration are over the sectional-decreasing ratios in most cases. On the other hand, in the region of slender columns, ratios of strength deterioration are less than the sectional-decreasing ratios. Such tendencies are not related to the position of the perforation. However, the values of the strength deterioration in the case of $a=L/2$ are larger than those in the case of $a=L/8$. The ground of this difference is caused by the magnitude of the eccentric moment occurred by deflection of column. Both of the stress concentration around perforation



Figures 8: Column strengths of perforated members



Figures 9: The ultimate strengths varying with the slenderness parameters of the columns.

and the eccentric moment bring large deformation of perforation and ultimate strength deterioration with interacting each other. Lower limiting of ultimate strength ratios are given in the case that slenderness parameter is given about 0.6.

CONCLUSIONS

From the analytical and experimental results, the buckling behavior of the perforated cylindrical tubular column and the influences of the perforation on the ultimate strength decreasing are investigated. The concluding remarks given in this study can be summarized as follows.

- (1) In order to the stress concentration around the perforation, the strength deteriorating ratios of perforated stub columns are higher than the sectional-decreasing ratios.
- (2) Buckling behavior which dominate ultimate strength deterioration of perforated column can be described as the interactive behavior between membrane buckling and local deformation around perforation. This interactive behavior gives the strength deterioration to the perforated column member.
- (3) In the region of slenderness parameter about 0.6, above interactive behavior gives maximum deterioration on the ultimate strength.

ACKNOWLEDGEMENT

We would record here our acknowledgement to Mr. N. Tabuchi and Mr. Y. Fushimi for their assistance in experiments and numerical analyses.

REFERENCES

- Murthu M. V. V.(1969). Stress Around an Elliptic Hole in a Cylindrical Shell, *Journal of Applied Mechanics*, 39-46.
- Madenci E. and Baurt A.(1994). Pre- and Post-buckling Response of Curved, Thin, Composite Panels with Cutouts under the Compression, *International Journal for Numerical Method in Engineering* 37, 1499-1510.
- Nishimura N., Murakami S. and Takeuchi S. (1995). Elasto-Plastic Finite Displacement Analysis of Thin-Walled Shells. *Technology Reports of the Osaka University* 45:2331, 213-220.
- Zienkiewicz O. C. (1977). *The Finite Element Method*, McGraw-Hill Book Co., New York, USA
- Commission of the European Communities (1990). Common Unified Code of Practice for Steel Structures, *Eurocode 3*.

Section VII

**SHELLS AND
PRESSURE VESSELS**

This Page Intentionally Left Blank

THE BUCKLING BEHAVIOUR OF HORIZONTAL STORAGE VESSELS – EXPERIMENTS AND CODES

A.S Tooth¹, J Spence¹ and G.C.M. Chan²

¹Department of Mechanical Engineering, University of Strathclyde,
Glasgow, G1 1XJ, UK

²CAD-IT Consultants (Asia) Ltd., Singapore 575625
(formally at University of Strathclyde, Glasgow, UK)

ABSTRACT

When horizontal cylindrical vessels are used for liquid storage and the internal pressure surcharge is relatively small, gravity loading becomes the primary design condition. This invariably results in a 'thin walled' vessel with a high value of the radius to thickness (R/t) ratio. Experimental work, by the authors, has indicated that such vessels failed by buckling when the R/t ratio was greater than 200. It was noted that the stresses that cause buckling behaviour are the longitudinal and circumferential membrane compressive stresses at the vessel mid-span and the saddle centre profiles. Allowable buckling stress values, based on simple loading patterns, are obtained based on present British Standard rules, and on ECCS and European recommendations. These values are compared with the experimental results for a range of thin-walled vessels, in an effort to provide corroborative evidence for the approach used by the Code.

KEYWORDS

Horizontal storage vessels, thin walled, buckling, allowable stress, experimental work, Code comparisons.

INTRODUCTION

Cylindrical vessels are employed extensively in the chemical and process plant industry. When the contents are stored under internal pressure, the cylindrical vessels employed are provided with a dished end closure. In general such vessels are supported horizontally by twin saddles which are either loosely fitted or welded to the vessel. The arrangement of the vessel, its contents and support, induce compressive membrane and shear stresses in the vessel, either close to the support or at the vessel mid-span. When the vessel is thin-walled these may cause either elastic or plastic buckling, depending on the yield stress of the material. The failure is generally caused by the compressive longitudinal membrane stresses reaching a critical value. However, when loose saddles are employed, the

compressive circumferential stress at the nadir (the bottom region of the vessel) in the support region predominates. In other cases shear buckling has been observed close to a ring and leg support, where this arrangement is used as an alternative to a saddle support.

Such failure modes are addressed, and appropriate proposals introduced, by most national Standards and Codes, for example BS 5500 (1997) and the ECCS rules (1988). The approach is to limit the allowable stresses by using "knock-down" factors on the critical stress obtained from the 'classical' analysis of the axially loaded cylinder. These take into account the fact that the vessels used inevitably contain geometric imperfections, which will influence the onset of buckling.

The aim of this paper is to compare the allowable stress values derived from the existing and draft codes with those of the collapsed vessels in order to provide corroborative evidence of the predictions made by the Code. The paper extends the earlier work of the authors, Chan, Tooth & Spence (1996 & 1998a) in comparing the experimental results with the proposals made in the Draft of the new European Code, EC 3(1997), Part 1.6

EXPERIMENTAL INVESTIGATIONS

It has been found that high values of longitudinal membrane compressive stress occur at the mid-span and saddle centre profiles, at the zenith (the highest) and nadir (the lowest) locations, for both welded and loose saddles. If they reach a critical value they could cause a longitudinal buckling failure of the vessel at any one of these four positions. However, when loose saddles are used to support the vessels, a plastic failure mode occurs causing a 'foot-print' indentation in the vessel/saddle region over riding the likelihood of a longitudinal stress buckling failure. In addition, in the case of the loose saddle, a high value of circumferential compressive membrane stress is noted in this region with a maximum value at the nadir. These high compressive stresses cause corrugations in the 'foot-print' region. This latter mode of failure is not examined here, but will be considered in a later paper.

Investigations of the various failure modes of these types of vessels have been carried out by Krupka, (1994) and more recently by the authors, reported by Chan et. al (1998b), where the models were manufactured from thin steel sheet. This enabled the phenomenon of plastic collapse (both plastic buckling and plastic limit load behaviour) to be examined.

Type of model employed

The experimental tests reported in this paper have concentrated on the buckling behaviour of the vessel in the region of the support. The present tests were carried out on end supported cylinders loaded through a central saddle. The value of the force on the saddle was equal to one half of the total of the fluid and self-weights. It is considered that the work done by the fluid and self-weight is small compared with that done by the force at the saddle because the deformations only occur in the immediate region of the saddle. For these investigations therefore, the fluid can be omitted and the force applied to the centrally located saddle of the end supported inverted cylinder. This experimental set-up provided a convenient means of progressively increasing the saddle load to detect the onset of buckling.

The portion of vessel isolated was equal to $2R$ from either side of the saddle, that is a vessel of length $4R$. A total of 40 model cylindrical vessels were fabricated with R/t ratios varying from 62 to 455 and supported with loose and welded saddles of 120° and 150° embracing angles. These experiments are reported in detail by the authors 1998b.

Longitudinal Stress Induced Buckles

It was noted that ‘longitudinal membrane compressive stress induced buckles’ occurred in 10 of the 40 vessels (20 loose and 20 welded) tested, and in only those where the saddles were welded to the vessels. This type of buckling did not occur when the vessels were placed loosely on the saddles, where failure was generally dominated by plastic limit load behaviour. Because of their relevance to this study only these 10 cases will be discussed here, the other failures are reported in detail by Chan et.al (1998b). Two kinds of longitudinal stress induced buckle were recorded in these cases.

The first kind was similar to those observed by Křupka, (1994), that is a symmetric diamond shaped buckle in the vicinity of the nadir of the side of the welded saddle. A typical buckle of this type is shown in Figure 1. These occurred when the R/t ratio was between 213 and 328 for vessels whose yield stress varied from 153 to 276 N/mm^2 . The other type of buckle, shown in Figure 2, occurred for higher R/t ratios 295 to 455, and when the yield stress of the vessel material was slightly higher (332 N/mm^2). In this latter buckle configuration the shell deforms dramatically into random large amplitude diamond like patterns, producing a “crumpled” shape, again in the general region of the nadir of the welded saddle. The geometric details, collapse loads and mode for these 10 vessels, numbered 1 to 10 are given in Table 1.

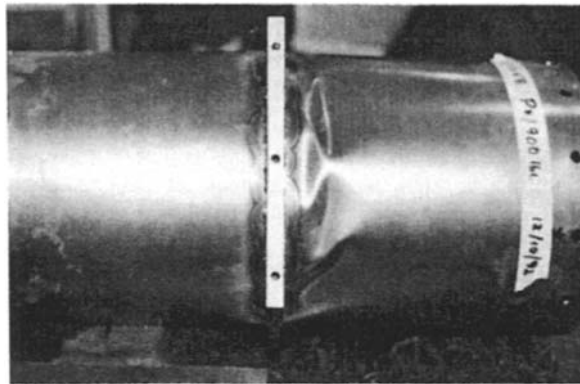


Figure 1: “Diamond” shaped buckle collapse of vessel with welded saddle (Vessel 2, $R/t = 217$)

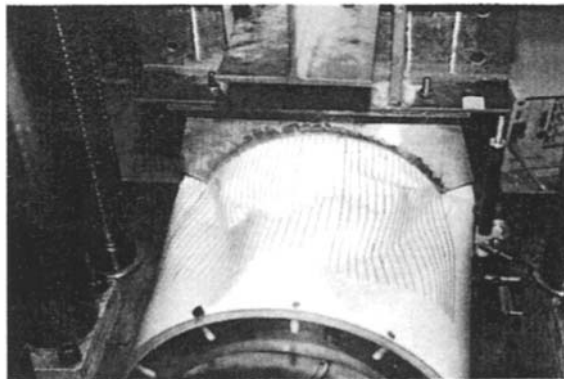


Figure 2: “Crumpled” buckle collapse of vessel with welded saddle (Vessel 7, $R/t = 455$)

TABLE 1
VESSELS WITH WELDED SADDLES: LONGITUDINAL STRESS INDUCED BUCKLES
(saddle width $b_1 = 10$ mm)

Vessel No.	Radius R (mm)	Thickness t (mm)	Length L (mm)	R/t	Saddle angle 2α (°)	Yield stress σ_y (N/mm ²)	Collapse Load P (kN)	Collapse Mode
1	130	0.44	555	295	120	332	7.20	Crumpled buckle
2	130	0.60	555	217	120	153	8.45	Diamond buckle
3	130	0.75	555	173	120	176	13.79	Plastic action then buckling
4	130	0.44	555	295	150	332	10.35	Crumpled buckle
5	130	0.61	555	213	150	276	18.00	Diamond buckle
6	130	0.79	555	165	150	187	22.95	Plastic action then buckling
7	200	0.44	835	455	120	332	5.85	Crumpled buckle
8	200	0.61	835	328	120	276	12.15	Diamond buckle
9	200	0.79	835	253	120	187	16.52	Diamond buckle
10	200	0.97	835	206	120	160	18.22	Plastic action then buckling

CODE RULES

In a design situation the stresses obtained for the four critical areas, referred to above, must be compared with an allowable buckling stress to examine the likelihood of buckling. The existing formulae for the allowable buckling stress are mostly based on variations of "knock-down" factors of the classical buckling stress of an axially loaded cylinder. This approach is used in the European recommendations, ECCS (1988) and the new Eurocode 3 (1997). An alternative based on the collapse behaviour of an externally pressurised equivalent sphere is used as in the B.S. Standard (1997). These methods will now be discussed.

"Knock-Down" Factors

The classical critical buckling stress for an axially loaded cylinder is given as:

$$\sigma_{cr} = \frac{E}{\sqrt{3(1-\nu^2)}} \frac{t}{R}$$

When $\nu = 0.3$, the classical critical stress is:

$$\sigma_{cr} = 0.605 \frac{Et}{R} \quad (1)$$

The actual collapse stress is usually much smaller due to the imperfections in the cylinder. It is suggested, from the scatter of experimental results, that an allowable buckling stress, $\sigma_{c(allowable)}$, should be 1/10 of the classical stress, i.e.:

$$\sigma_{c(allowable)} = 0.06 \frac{Et}{R} \quad (2)$$

This value is similar to that contained in BS 1500 (an early pressure vessel standard, 1958), where,

$$\sigma_{c(allowable)} = 0.0625 \frac{Et}{R}$$

British Standard - BS 5500 (1997) - Limits to the longitudinal membrane compressive stress.

For cylinders which are not externally pressurised, the present British Pressure Vessel Standard BS 5500 (1997) Annex A.3.5, limits the longitudinal compressive stress, σ_z , to:

$$\sigma_{c(allowable)} < \Delta s f \tag{3}$$

where

Δ = the ratio of the allowable external design pressure (p) to the pressure at which membrane stresses in the spherical shell reaches the yield point of the material (p_{yss}), where $p_{yss} = 2sf/R$. The value Δ is obtained from figure A.2 BS 5500 (1997) in terms of K , which in this context is defined as $K = p_e/p_{yss} = (0.605Et)/(sR)$ [since the elastic instability pressure in a perfect sphere is $p_e = 1.21Et^2/R^2$].

f = the design stress of the material

s = a factor relating f to the yield point of the material

It is worth noting that an alternative method is proposed in BS 5500 as an Enquiry Case (EC 5500/105) for the derivation of the allowable compressive stress based on the ECCS (1988) rules.

European Recommendations for longitudinal membrane compressive stress, ECCS (1988)

The philosophy of the European recommendations for the buckling of steel structures, ECCS (1988) is to apply a reduction factor (or “knock-down factor”) α , to the classical buckling stress. This is based on the lower bound curve of experimental results of well-manufactured cylindrical shells (with an $R/t < 1500$) which are subjected to axial compression. It is modified slightly for the shell subjected to overall pure bending. This form is considered more appropriate for the horizontal vessel filled with fluid than the case of pure axial compression and is, therefore, presented in this paper. It is given by:

$$\alpha = 0.1887 + 0.8113 \alpha_0$$

where $\alpha_0 = \frac{0.83}{\sqrt{1 + 0.01(R/t)}}$ for $R/t < 212$

or $\alpha_0 = \frac{0.7}{\sqrt{0.1 + 0.01(R/t)}}$ for $R/t > 212$

The rules differentiate between elastic and elastic-plastic buckling on the basis of whether, $\alpha \sigma_{cr} \leq 0.5 \sigma_y$ or $\alpha \sigma_{cr} \geq 0.5 \sigma_y$, where σ_y is the yield stress of the shell.

If $\alpha \sigma_{cr} \leq 0.5 \sigma_y$, then elastic buckling is more likely to take place and the buckling stress, σ_u , is given by:

$$\sigma_u = 0.75 \alpha \sigma_{cr} \tag{4}$$

For vessels which fail by elastic-plastic buckling where, $\alpha \sigma_{cr} \geq 0.5 \sigma_y$, the buckling stress, σ_u is given by:

$$\sigma_u = \sigma_y \left[1 - 0.4123 \left(\frac{\sigma_y}{\alpha \sigma_{cr}} \right)^{0.6} \right] \tag{5}$$

An additional load factor of 1.5 is applied to the buckling stress, σ_u as a design factor of safety, so that the allowable stress, or the ‘design stress’ in the compressive region is given by: -

$$\sigma_{c(allowable)} = \sigma_u / 1.5 \tag{6}$$

These rules are applicable to well-manufactured cylinders where the ratio of the largest measured inward imperfection amplitude, \bar{w} , to the corresponding template length, l_r ($l_r = 4\sqrt{Rt}$), does not exceed 0.01. When the ratio is 0.02, the reduction factor, α , is halved. Linear interpolation between the limits is allowed.

Eurocode 3: Part 1-6: General Rules: Supplementary Rules for the Strength and Stability of Shell Structures (August 1997)

The critical meridional (axial) classical buckling stress, eqn (1), referred to in the Eurocode 3 as σ_{xRc} , can be modified by a factor C_x , to allow for the length of the vessel and the end boundary conditions. In the case of the 10 vessels tested, $C_x = 1$, so that

$$\sigma_{xRc} = 0.605 C_x E t / R = 0.605 E t / R \tag{7}$$

The “knock-down” (or imperfection) factor is given as: -

$$\alpha_x = \frac{0.62}{1 + 1.91(w_k/t)^{1.44}} \tag{8}$$

where w_k is the characteristic imperfection amplitude: $w_k = \frac{t}{Q} \sqrt{\frac{R}{t}}$

in which Q is the meridional (axial) compression quality parameter.

The quality parameter Q is taken from Table D.2 for the specified quality class.

TABLE 2 (Table D.2 of code)
VALUES OF QUALITY PARAMETER Q

Quality Class	Description	Q
Class A	Excellent	40
Class B	High	25
Class C	Normal	16

The non-dimensional shell slenderness parameter for the axial stress is determined from: -

$$\bar{\lambda}_x = \sqrt{f_{y,k} / \sigma_{xRc}} \text{ where } f_{y,k} \text{ is the characteristic yield point and } \sigma_{xRc} \text{ is given by eqn. (7).}$$

The meridional (axial) squash limit slenderness value is taken as: $\bar{\lambda}_{x0} = 0.20$ and $\bar{\lambda}_p = (2.5\alpha)^{0.5}$

The meridional (axial) stability reduction factor χ_x is determined as a function of the factor $\bar{\lambda}_x$ from: the general relationships for λ and χ :-

$$\begin{aligned} \chi &= 1 && \text{when } \bar{\lambda} \leq \bar{\lambda}_0 \\ \chi &= 1 - 0.6 \frac{\bar{\lambda} - \bar{\lambda}_0}{\bar{\lambda}_p - \bar{\lambda}_0} && \text{when } \bar{\lambda}_0 < \bar{\lambda} < \bar{\lambda}_p \\ \chi &= \alpha / \bar{\lambda}^2 && \text{when } \bar{\lambda}_p \leq \bar{\lambda} \end{aligned}$$

The characteristic axial buckling stress (which accounts for the geometric and structural imperfection and the inelastic material behaviour) is given by :- $\sigma_{xRk} = \chi_x \cdot f_{yk}$ (9)

and the design axial buckling stress is obtained from :- $\sigma_{xRd} = \sigma_{xRk} / \gamma_M$ (10)

where γ_M is the partial safety factor for resistance, taken as 1.1 for these cases.

The partial safety factor for liquid induced loads during operation is $\gamma_F = 1.20$ and during test $\gamma_F = 1.00$.

COMPARISONS WITH EXPERIMENTAL RESULTS

The experiments give results for the buckling loads directly, whereas the codes give allowable stresses. In order to make a comparison between the two it is necessary to derive the membrane longitudinal stresses at the nadir in the experimental vessels. This has been done using linear elastic shell analysis developed for the twin saddle supported cylinder, Duthie et. al (1982), supplemented by finite element analysis. The derived stress values are referred to as “experimental” stress and given with the Code allowable stresses in Table 3.

The ECCS allowable stress values are based on the pure bending condition and provide values for imperfection amplitudes of $\bar{w}/l_r = 0.01$ and 0.02 , with the safety factor of 1.5 as given in eqn (6). The Eurocode 3 values for the partial safety factor for load is assumed to be, $\gamma_F = 1.00$, appropriate for test conditions. Two values of quality parameter Q for Class B and C (Table 2) are considered.

TABLE 3
ALLOWABLE (DESIGN) BUCKLING STRESS AND “EXPERIMENTAL” VALUES (N/mm²)

Vessel No.	Classical (eqn. 1)	BS5500 (eqn. 3)	ECCS (based on pure bending)		ENV 1993-1-6 (August 1997)		“experimental” stress
	σ_{cr}	$\sigma_{c(allow)}$	$\sigma_{c(allow)}^A$	$\sigma_{c(allow)}^B$	$\sigma_{xRd} (Class B)$	$\sigma_{xRd} (Class C)$	σ_x
1	410	47	101	53	109	74	124
2	558	53	75	61	101	91	100
3	699	64	88	74	121	111	125
4	410	47	101	53	109	74	117
5	568	61	115	79	145	117	139
6	733	67	94	78	128	119	131
7	266	31	60	30	59	38	70
8	369	42	87	46	94	63	99
9	478	49	82	60	106	88	99
10	567	55	78	64	106	96	85

^A Imperfection amplitude $\bar{w}/l_r = 0.01$, using a the factor of safety of 1.5

^B Imperfection amplitude $\bar{w}/l_r = 0.02$, using a the factor of safety of 1.5

CONCLUDING COMMENTS

In the main the allowable (design) stress are less than the “experimental” values. The exception to this occurs in the design values obtained from the Eurocode 3. To determine a factor of safety for all the

cases given in Table 3 the ratio of the “experimental”/allowable (design) has been derived. An overall impression of these values has been obtained by averaging the above ratio for the 10 vessels. The results are as follows: -

BS 5500 average ratio = 2.13;

ECCS ($\bar{w}/l_r = 0.01$) average ratio = 1.23; ECCS ($\bar{w}/l_r = 0.02$) average ratio = 1.88;

ENV 1993-1-6 Class B, average ratio = 1.02 and for Class C, average ratio = 1.31.

The safety factor for the BS 5500 and the ECCS should not be less than 1.5 and on this basis the BS 5500 and ECCS ($\bar{w}/l_r = 0.02$) may be deemed to be satisfactory. The safety factor for the Eurocode 3 ENV 1993-1-6 should not be less than 1.1 and thus only the Class C values are satisfactory. In comparing the ECCS and Eurocode 3 proposals, it is worth noting that the ECCS provides an advantageous “knock-down” factor specifically for the bending case, whereas the Eurocode 3 considers the bending case to be part of the constant axial load case, which is more onerous. However, the use of the ‘quality parameter’ given in Table 2 is considered an advantage at the design stage compared to the ‘amplitude imperfection’ values given in ECCS (1988) which can only be obtained with certainty after manufacture.

Acknowledgements

The authors would like to thank the UK Government ORS Award Scheme and the University of Strathclyde for financial support given to Dr Moses Chan during the course of his post graduate study.

References

Chan, G C M, Tooth, A S and Spence J. (1996 & 1998a) A Study of the Buckling Behaviour of Horizontal Saddle Supported Vessels. *The Bi-Centenary Conf. on thin-Walled Structures, Univ. Strathclyde, Glasgow, Dec. 2-4, 1996*. To be published in *The Intern. Journal of Thin-Walled Structures, 1998*.

Chan, G C M, Tooth, A S and Spence, J.(1998b) An Experimental Study of the Collapse of Horizontal Saddle Supported Storage Vessels, To be published in *Proc. Inst. Mech. Eng. Part E, Journal of Process Mechanical Engineering; Special Commemorative Issue 1998*.

British Standard BS 5500:1997. Specification for Unfired Fusion Pressure Vessels. *British Standards Institution, London, 1997*.

European Recommendation, ECCS, (1988) Buckling of Steel Shells, 4th edition, No.56, 1988.

Eurocode 3: Design of Steel Structures, Part 1.6 (1997), General Rules: Supplementary Rules for the Strength and Stability of Shell Structures. European Prestandard ENV 1993-1-6 (August 1997), CEN/TC 250/SC3/PT4.

Křupka, V (1994) Saddle and Lug Supported Tanks and Vessels, *Proc. Of the Inst. Mech. Eng. Journal of Process Mech. Eng. Vol. 208 (E1), 17-22, 1994*.

Duthie, G, White, G C and Tooth A S.(1982), Stresses in horizontal vessels under local loading – application to saddle vessel problems, *Jn Strain Analysis, Vol17, No 3, pp 157-167, 1982*

BUCKLING STRENGTH OF T-SECTION TRANSITION RINGBEAMS IN ELEVATED STEEL SILOS AND TANKS

J. G. Teng and F. Chan

Department of Civil and Structural Engineering
Hong Kong Polytechnic University
Hung Hom, Kowloon, Hong Kong, China

ABSTRACT

A ring is generally provided at the intersection between the cylinder and the cone of an elevated storage silo or tank to resist a large circumferential compressive force at the intersection (the transition junction). This ring is a main structural member and is often referred to as a ringbeam (in contrast to relatively light rings as stiffeners on shell walls). The ringbeam may be an annular plate, but an annular plate is weak in torsion and is thus susceptible to failure by out-of-plane buckling. A common way to increase the out-of-plane stiffness of an annular plate ringbeam is to attach a vertical stiffener to the outer edge of the annular plate, resulting in a T-section ringbeam. This paper describes a simple approximate method developed in recent studies for assessing the out-of-plane buckling strength of these ringbeams. The method may be used in practical design directly and is suitable for future inclusion in relevant design codes.

KEYWORDS

Buckling, T-Sections, Ringbeams, Rings, Silos, Tanks, Shells, Stability, Design

INTRODUCTION

A ring is generally provided at the intersection between the cylinder and the cone of an elevated storage silo or tank to resist a large circumferential compressive force at the intersection (the transition junction) (Figure 1). This compressive force arises from the radial inward component of the meridional tension in the conical hopper. This ring is a main structural member and is often referred to as a ringbeam (in contrast to relatively light rings as stiffeners on shell walls). The ringbeam may be an annular plate, but an annular plate is weak in torsion and is thus susceptible to failure by out-of-plane buckling. A common way to increase the out-of-plane stiffness of an annular plate ringbeam is to attach a vertical stiffener to the outer edge of the annular plate, resulting in a T-section ringbeam. Figure 2 shows the geometry of a typical transition junction with a T-section ringbeam.

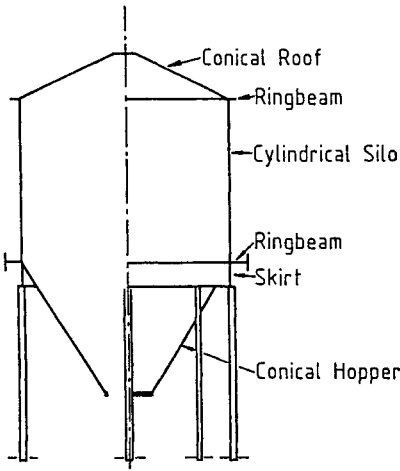


Figure 1: Typical Elevated Steel Silo

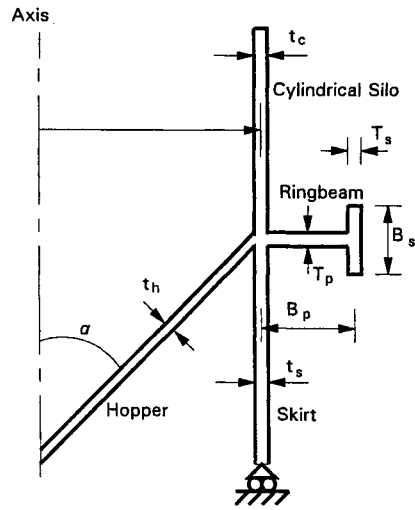


Figure 2: Geometry of Typical Transition Junction

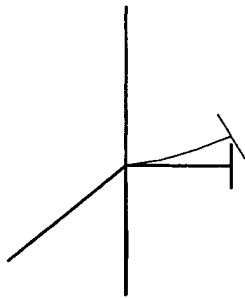


Figure 3: Out-of-Plane Buckling Mode

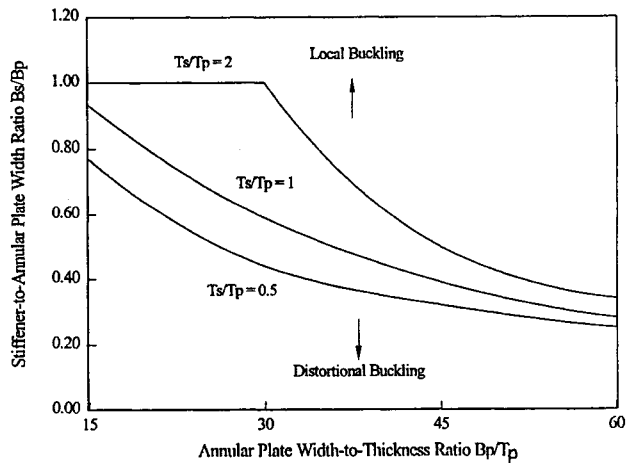


Figure 4: Geometric Limits for Distortional Buckling

Under this circumferential compressive force, buckling may become the critical failure mode. Theoretically speaking, both in-plane buckling and out-of-plane buckling are possible. The out-of-plane buckling mode (Figure 3) is usually more critical than the in-plane buckling mode as in-plane buckling deformations are generally prevented by the membrane stiffness of the cone (Jumikis and Rotter, 1983). The out-of-plane buckling mode generally involves significant cross-sectional distortion and is similar to the buckling mode of continuously restrained columns (Bradford, 1996). Another possible buckling mode is local buckling. The local buckling mode can be prevented by ensuring that the ringbeam geometry satisfies the geometric limits for distortional buckling as given in the chart of

Figure 4 developed by Teng and Chan (1998a). The present paper is concerned only with the out-of-plane distortional buckling strength of T-section transition ringbeams.

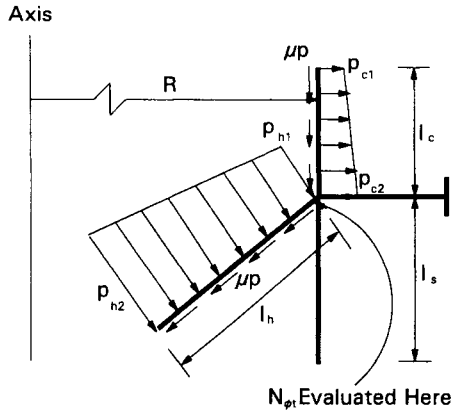


Figure 5: Effective Section and Local Pressures

The out-of-plane buckling of T-section rings has been the subject of a number of previous studies (Rotter and Jumikis, 1985; Teng and Rotter, 1988; Teng and Rotter, 1991a), but these studies did not produce a rational stability design method for the ringbeam. This paper describes such a method developed in recent studies (Teng and Chan, 1998a; 1998b; 1998c; 1998d), based on existing information on elastic buckling and plastic collapse, and extensive finite element numerical studies using NEPAS (Teng and Rotter, 1989). The paper begins by defining the equivalent circumferential compressive force at the transition junction, followed by a description of a simple method to relate this force to the inner edge circumferential compressive stress in a T-section ringbeam. The elastic buckling strength and plastic collapse strength, in terms of the equivalent circumferential compressive force, are then given. Finally, the plastic buckling strength is formulated by considering interaction between elastic buckling and plastic collapse. The stability design method described here may be used directly in practice and is suitable for future inclusion in relevant design codes.

CIRCUMFERENTIAL COMPRESSION AT THE JUNCTION

A steel silo transition junction is generally subjected to non-uniform internal pressures and corresponding downward frictional tractions (Figure 5). For the development of strength rules for the transition junction, some simple way of characterising this complex loading has to be used. As far as junction failures are concerned, the controlling force is the circumferential compressive force at the transition junction derived chiefly from the radial component of the meridional tension at the top of the hopper. This force is resisted by the ringbeam together with a short effective length of each participating shell segment (Rotter, 1985). Denoting the meridional tensile force at the top of hopper as N_{ϕ} (Figure 5), the equivalent circumferential compressive force F taking into account the effect of pressures on the effective ringbeam of Figure 5 is given by (Rotter, 1985)

$$F = N_{\phi} R \sin \alpha - 0.5(p_{c1} + p_{c2})l_c R - 0.5(p_{h1} + p_{h2})(\cos \alpha - \mu \sin \alpha)l_h R \quad (1)$$

in which R is the radius of the cylinder, α is the apex half angle of the hopper, l_c and l_h are the effective lengths of the cylinder and the hopper respectively, and the pressure values p_{c1} , p_{c2} , p_{h1} and p_{h2} are as defined in Figure 5. Although the variation of pressure p is generally non-linear, a linear approximation over the effective lengths can be used without much loss of accuracy as the effective lengths are generally small compared to the total lengths of the shell walls. The circumferential compressive force F is an

important parameter, as for a given geometry, the failure strength in terms of F is largely independent of the specific load distributions on the silo walls (Rotter, 1987; Greiner, 1991; Teng and Rotter, 1991a; 1991b; 1991c; Teng, 1997). As pointed out by Teng (1997), the effective lengths l_e and l_h are different for elastic stress analysis and plastic collapse analysis, which leads to two values of the circumferential compressive force F which differ from each other very slightly. To avoid confusion and inconvenience, it has been recommended (Teng, 1997) that in finding the equivalent circumferential compressive force F from Eqn. 1, the effective lengths under elastic conditions should always be used, regardless of whether elastic buckling or plastic collapse is being investigated. This recommendation is adopted here.

EFFECTIVE SECTION ANALYSIS FOR THE INNER EDGE COMPRESSIVE STRESS

The most direct way to characterise the elastic buckling strength of transition ringbeams is probably to use the inner edge circumferential compressive stress as has been done in a number of previous studies (eg Jumikis and Rotter, 1983; Rotter and Jumikis, 1985). In an annular plate transition ringbeam, the circumferential compressive stress varies over the annular plate and reaches the maximum value at its inner edge. For a T-section transition ringbeam, the maximum circumferential compressive stress may not occur at the inner edge (Teng and Chan, 1998c), but the inner edge stress is still used here to define the elastic buckling stress in the first instance. In order for the buckling strength of a T-section ringbeam at a transition junction under a general pattern of loading to be defined using the equivalent circumferential compressive force F given by Eqn. 1, a link needs to be established between the inner edge circumferential stress and the equivalent force. This link can be achieved using a modified version of the effective section method proposed by Rotter (1985) for junctions with an annular plate ringbeam. The modifications involve the omission of terms of the order of B_p/R in comparison to 1. With such modifications, the inner edge circumferential compressive stress in a T-section transition ringbeam may be found as

$$\sigma_\theta = \frac{F}{A_e} \quad (2)$$

where the total effective area A_e for elastic stress analysis is defined by

$$A_e = A_r + \sum_{i=1}^{NS} l_{ei} t_i \quad (3)$$

where NS = number of shell segments forming the junction, A_r is the cross-sectional area of the T-section ringbeam ($=B_p T_p + B_s T_s$), and l_{ei} and t_i are the elastic effective length and thickness of the i th shell segment. To determine the effective length l_{ei} for each shell segment, it is necessary to first separate the shell segments into two groups, those above and those below the annular plate of the ringbeam. For each group with n shell segments, the equivalent thickness of the group is defined as

$$t_{eq} = \sqrt{\sum_{i=1}^n t_i^2} \quad (4)$$

Denoting the thinner group as group A (the group with a smaller equivalent thickness) and the thicker one group B, the equivalent thickness ratio ξ is then found as

$$\zeta = t_{eqA} / t_{eqB} \quad (5)$$

The effective length of each shell segment is given by

$$l_{ei} = 0.778 \gamma_{ei} \sqrt{R t_i / \cos \phi} \quad (6)$$

where $\phi = 0$ for a cylindrical component and $\phi = \alpha$ for the hopper. The appropriate value of γ_{ei} for the i th shell segment is

$$\gamma_{ei} = 1 \quad \text{for the thinner group} \quad (7)$$

$$\gamma_{ei} = \gamma_e = 0.5(1 + 3\zeta^2 - 2\zeta^3) \quad \text{for the thicker group} \quad (8)$$

The simple method described above predicts the inner edge circumferential stress in a T-section transition ringbeam accurately (Teng and Chan, 1998c). If the variation of the circumferential membrane stress over the ringbeam cross-section is required, the more sophisticated method recently developed by Chen and Rotter (1997) should be used.

ELASTIC BUCKLING STRENGTH

Transition Ringbeams

In terms of the equivalent circumferential compressive force, the elastic buckling strength of a T-section transition ringbeam is given by (Teng and Chan, 1998c)

$$F_e = \sigma_{\theta cr} A_e \tag{9}$$

where A_e is the effective section area defined by Eqn. 3 and $\sigma_{\theta cr}$ is the inner edge circumferential stress at buckling, referred to as the buckling stress hereafter. Following the approach of Jumikis and Rotter (1983), the buckling stress of a T-section transition ringbeam is interpolated from the buckling stresses of the ringbeam with the two idealised inner edge conditions: σ_s for a simply supported inner edge and σ_c for a clamped inner edge. This interpolation is given by

$$\sigma_{\theta cr} = \frac{\eta_s \sigma_s + \eta_c \sigma_c}{\eta_s + \eta_c} \tag{10}$$

where η_s and η_c are interpolation parameters which may be functions of all or some of the following eight dimensionless geometric parameters: t_c/T_p , t_h/T_p , t_s/T_p , B_p/R , B_p/T_p , B_s/B_p , T_s/T_p and α for a T-section consisting of an annular plate of $B_p \times T_p$ and a stiffener of $B_s \times T_s$ (Figure 2) on a silo with a hopper apex half angle of α . The expressions for η_s and η_c used by Jumikis and Rotter (1983) for annular plate ringbeams were found by Teng and Chan (1998c) to be also appropriate for T-section ringbeams. These expressions are

$$\eta_s = 0.43 + \frac{(R / B_p)^2}{4000} \tag{11}$$

$$\eta_c = \frac{1}{2} \left[\left(\frac{t_c}{T_p} \right)^{2.5} + \left(\frac{t_h}{T_p} \right)^{2.5} + \left(\frac{t_s}{T_p} \right)^{2.5} \right] \tag{12}$$

Ringbeams with a Simply Supported Inner Edge

The buckling stress of T-section ringbeams simply-supported at the inner edge can be closely approximated by the following equation which is a modified form of Teng and Rotter's (1988) simplified solution for such ringbeams (Teng and Chan, 1998b)

$$\sigma_s = \frac{EI_x}{A_r r_o^2} [c_1 + 2.3\sqrt{c_1} \sqrt{\beta}] \tag{13}$$

$$r_o^2 = \frac{I_x + I_y + A_r x_c^2}{A_r} \tag{14}$$

$$c_1 = \frac{GJ}{EI_x}, \text{ and } \beta = \frac{B_p}{R} \tag{15}$$

where E and G are the elastic modulus and the shear modulus respectively; I_x and I_y are the second moments of area about the radial and vertical axes of the section, respectively; J is the torsional constant; and x_c is the distance between the centroid and the inner edge of the T-section ringbeam.

Ringbeams with a Clamped Inner Edge

The buckling stress of inner edge clamped ringbeams can be closely approximated by (Teng and Chan, 1998a)

$$\frac{\sigma_c}{E} = \psi \left(\frac{T}{B_p} \right)^{1.1} \quad (16)$$

with

$$\psi = \lambda [0.016 + 0.5\rho - 0.25\rho^2] \quad (17)$$

$$\rho = \frac{B_s}{B_p} \sqrt{\frac{T_s}{T_p}} \quad (18)$$

$$\lambda = \frac{1 + 5\rho}{1 + 5B_s T_s / (B_p T_p)} \quad (19)$$

It may be noted that for a uniform thickness ringbeam, the above approximation reduces to

$$\frac{\sigma_s}{E} = \left[0.016 + 0.5 \left(\frac{B_s}{B_p} \right) - 0.25 \left(\frac{B_s}{B_p} \right)^2 \right] \left(\frac{T}{B_p} \right)^{1.1} \quad (20)$$

PLASTIC COLLAPSE STRENGTH

The plastic collapse strength, in terms of the equivalent circumferential compressive force, can be closely approximated by the following equation developed by Teng and Rotter (1991b; 1991c):

$$F_p = \sigma_y A_p = \sigma_y (A_r + A_{ps}) = \sigma_y \left(A_r + \sum_{i=1}^{NS} l_{pi} t_i \right) \quad (21)$$

where A_{ps} is the effective area of the shell segments in resisting the circumferential compression at an equivalent stress of the yield stress σ_y at plastic collapse and NS is the number of shell segments forming the transition junction. The plastic effective length l_{pi} for the i th shell segment is given by

$$l_{pi} = 0.975 \gamma_{pi} \sqrt{R t_i} \cos \phi \quad (22)$$

where γ_{pi} assumes different values for the two groups of segments above and below the annular plate of the ringbeam respectively and is given by

$$\gamma_{pi} = 1 \quad \text{for the thinner group} \quad (23)$$

$$\gamma_{pi} = \gamma_p = 0.7 + 0.6\zeta^2 - 0.3\zeta^3 \quad \text{for the thicker group} \quad (24)$$

with the equivalent thickness ratio ζ being the same as that defined in Eqn. 5. The above method was developed from an earlier simpler proposal by Rotter (1987) for junctions of uniform shell wall thickness. Although it was initially developed for transition junctions with an annular plate ringbeam (Teng and Rotter, 1991b; 1991c), its predictions have also been shown to be accurate for transition junctions with a T-section ringbeam (Teng and Chan, 1998d).

PLASTIC BUCKLING STRENGTH

Elastic buckling only governs the strength of junctions with a slender ringbeam or with a high yield stress, while the plastic collapse strength of Eqn. 21 generally overestimates the ultimate strength as plastic buckling is likely to precede plastic collapse (Teng and Chan, 1998d). For most transition ringbeams, failure is by plastic buckling. As plastic buckling results from interaction between elastic buckling and plastic collapse, the plastic buckling strength was formulated in terms of the elastic buckling strength and the plastic collapse strength (Teng and Chan, 1998d) and is given by

$$\frac{F_f}{F_p} = 1 - 0.383\lambda, \quad 0 < \lambda \leq 1.62 \quad (25)$$

where the slenderness parameter λ is defined as

$$\lambda = \sqrt{\frac{F_p}{F_e}} \quad (26)$$

Using Eqn. 26, the elastic buckling strength approximation may be recast into

$$\frac{F_f}{F_p} = \frac{1}{\lambda^2}, \quad 1.62 < \lambda \quad (27)$$

In Eqns. 25 and 27, F_f denotes the ultimate failure strength due to either elastic buckling, plastic buckling or plastic collapse. Teng and Chan (1998d) found that non-symmetric plastic buckling occurs before axisymmetric plastic collapse for all the cases analysed by them.

Eqns. 25 and 27 constitute the final design proposal for the buckling strength of T-section transition ringbeams. The division between elastic buckling and plastic buckling is based on the strength behaviour, so the elastic buckling region covers purely elastic buckling failures as well as nearly elastic buckling failures occurring after limited yielding. The above equations give the same value at the transition point of $\lambda = 1.62$. The value of λ for separating the elastic buckling region from the plastic buckling region adopted here is the same as that used by Teng (1997) for junctions with an annular plate ringbeam. This consistency is certainly a desirable feature. Eqns. 25 and 27 are thus satisfactory as a design proposal. Appropriate load and resistance factors should be used with Eqns. 25 and 27 in a limit state design formulation.

CONCLUSIONS

This paper has presented the first ever rigorous design proposal for the buckling strength of T-section transition ringbeams in elevated steel silos and tanks. The elastic buckling strength approximation is based on a suitable interpolation of the elastic buckling strengths of the two idealized cases: inner edge simply supported ringbeams and inner edge clamped ringbeams. The plastic buckling strength is formulated by considering interaction between elastic buckling and plastic collapse. The design proposal may be used directly in practice, and is suitable for future inclusion in relevant design codes.

ACKNOWLEDGEMENT

The work described in this paper forms part of the project Buckling and Collapse of Rings at Shell Intersections. The authors wish to thank The Hong Kong Polytechnic University for its financial support.

REFERENCES

- Bradford, M.A. (1996) "Lateral-Distortional Buckling of Continuously Restrained Columns", *UNICIV Report No. R-351*, School of Civil Engineering, The University of New South Wales.
- Chen, J.F. and Rotter, J.M. (1997) "Stresses in Asymmetric Ring Stiffeners for Cylindrical Shells", *Proc., International Conference on Carrying Capacity of Steel Shell Structures*, 1-3 Oct., Brno, Czech Republic, pp 340-346.
- Greiner, R. (1991) "Elastic Plastic Buckling at Cone Cylinder Junctions of Silos", in *Buckling of Shell Structures on Land, in the Sea and in the Air*, Ed. J.F. Jullien, Elsevier, London, pp 304-312.
- Jumikis, P.T. and Rotter, J.M. (1983) "Buckling of Simple Ringbeams for Bins and Tanks", *Proceedings, International Conference on Bulk Materials Storage, Handling and Transportation*, IEAust, Newcastle, August, pp. 323-328.
- Rotter, J.M. (1985) "Analysis and Design of Ringbeams", *Design of Steel Bins for the Storage of Bulk Solids*, School of Civil and Mining Engineering, University of Sydney, Australia, March, pp 164-183.
- Rotter, J.M. (1987) "The Buckling and Plastic Collapse of Ring Stiffeners at Cone/Cylinder Junctions", *Proc., International Colloquium on Stability of Plate and Shell Structures*, Gent, Belgium, April, pp 449-456.
- Rotter, J.M. and Jumikis, P.T. (1985) "Elastic Buckling of Stiffened Ringbeams for Large Elevated Bins", *Proc., Metal Structures Conference*, IEAust, Melbourne, May, pp. 104-111.
- Teng, J.G. (1997) "Plastic Buckling Approximation for Transition Ringbeams in Steel Silos", *Journal of Structural Engineering*, ASCE, Vol. 123, No. 12, December, pp 1622-1630.
- Teng, J.G. and Chan, F. (1998a) "New Buckling Approximations for T-Section Ringbeams Simply-Supported at Inner Edge", *Engineering Structures*, Accepted for Publication.
- Teng, J.G. and Chan, F. (1998b) "Out-of-Plane Distortional Buckling of T-Section Ringbeams Clamped at Inner Edge", *Engineering Structures*, Vol. 20.
- Teng, J. G. and Chan, F. (1998c) "T-Section Transition Ringbeams in Steel Silos and Tanks: Part I- Elastic Buckling", To be published.
- Teng, J. G. and Chan, F. (1998d) "T-Section Transition Ringbeams in Steel Silos and Tanks: Part II- Plastic Buckling", To be published.
- Teng, J.G. and Rotter, J.M. (1988) "Buckling of Restrained Monosymmetric Rings", *Journal of Engineering Mechanics*, ASCE, Vol. 114, No. 10, October, pp. 1651-1671.
- Teng, J.G. and Rotter, J.M. (1989) "Non-Symmetric Bifurcation of Geometrically Non-Linear Elastic-Plastic Axisymmetric Shells subject to Combined Loads including Torsion", *Computers and Structures*, Vol. 32, No. 2, pp 453-477.
- Teng, J.G. and Rotter, J.M. (1991a) "Plastic Buckling of Rings at Steel Silo Transition Junctions", *Journal of Constructional Steel Research*, Vol. 19, pp 1-18.
- Teng, J.G. and Rotter, J.M. (1991b) "The Collapse Behaviour and Strength of Steel Silo Junctions-Part I: Collapse Mechanics", *Journal of Structural Engineering*, ASCE, Vol. 117, No. 12, pp 3587-3604.
- Teng, J.G. and Rotter, J.M. (1991c) "The Collapse Behaviour and Strength of Steel Silo Junctions-Part II: Parametric Study", *Journal of Structural Engineering*, ASCE, Vol. 117, No. 12, pp 3605-3622.

CYLINDRICAL SHELLS SUBJECTED TO VERTICAL EDGE DEFORMATION AND INTERNAL PRESSURE

M. Jonaidi, M. Chaaya and P. Ansourian

Department of Civil Engineering, The University of Sydney, Sydney 2006, Australia

ABSTRACT

The problem of cylindrical shells under vertical edge deformation is considered in this paper. The deformation shape is assumed in the form of a saddle, represented by cosine curve at $n = 2$. This reflects the practical problem of settlement of storage tanks and bins. The radial and tangential movements are restrained at both ends, while the vertical displacements is imposed at the base. Initially a simple solution based on membrane theory is given in terms of meridional stresses at the base. The solution is compared with finite element analysis results. Linear buckling analysis is also presented and simplified expressions given for critical stress; the associated eigenmode is one of shear. Under combined internal pressure and vertical harmonic settlement, non-linear analysis shows that the eigenmode is not evident but failure occurs at the base as an 'elephant foot' phenomenon.

KEYWORDS

Bin, tank, shell, buckling, non-linear, settlement, pressure

INTRODUCTION

Foundations of large steel cylindrical tanks for bulk and fluid storage tend to be shallow and may consequently suffer differential settlement under load. These tanks are ductile and are able to tolerate limited settlement without distress. The differential component is the principal potential source of overstress and distortion. The measured settlement values when plotted relative to the tilt plane have an irregular shape that can be expressed as a Fourier series in n harmonics (Malik et al, 1977, Kamyab and Palmer, 1989). The most frequently experienced deformation shape is in the form of a saddle (Figure 1), represented by cosine curve with $n = 2$ (De Beer, 1969, Marr et al, 1982 and D'Orazio et al, 1989). In order to evaluate the shell behaviour under harmonic edge settlement several shell theories ranging from modified Donnell theory to inextensional theory have been applied by researchers. These have been based on linear elastic analysis of a uniform thickness shell. FEA has been applied to evaluate the linear behaviour of storage tanks with stepped thickness under the effect of differential settlement. (Jonaidi and Ansourian, 1997 - 1998).

Shell overstressing due to differential settlement is of special concern in closed-top cylinders (open-top cylinders at $n = 2$ are not significantly stressed at the base (Jonaidi and Ansourian, 1998b)). The

significant stressing occurs at the base as meridional membrane compression, and at the top as circumferential membrane stresses. The former is particularly important due to the potential for buckling near the base. In this paper, linear analysis based on membrane theory is firstly presented, and leads to a simple expression for evaluating meridional stress at the base. Most previous theoretical research in this area has centred on linear analysis and no buckling or non-linear investigation have been presented.

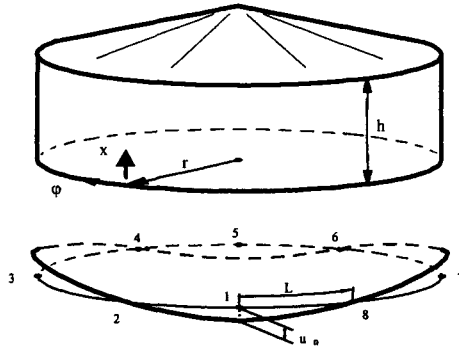


Figure 1: Tank under saddle settlement ($n = 2$)

Results of experiments (Jonaidi and Ansourian (1998a), provided insight into large deformation behaviour. One of the principal effects was the occurrence of shear buckling, and this effect is studied numerically in this paper. In practice, maximum settlement of the base occurs when the tank is full. As failure under settlement occurs by buckling and yielding, it is important to study the effect of internal pressure due to the tank content. This paper finally considers a tank under combined internal pressure and vertical harmonic settlement up to large displacements and failure.

LINEAR ANALYSIS BY MEMBRANE THEORY

This theory is based on the neglect of flexure which is a valid assumption in the present context, at $n = 2$; comparisons with full shell theory prove this. Flexure becomes significant when n increases (Kamyab and Palmer, 1989). We consider a cylinder of wall thickness t , proportions of Figure 1, sustaining radial deflection w , meridional and circumferential displacements u and v respectively. Following Vinson (1974), the governing equations are as follows for a circular cylindrical shell subjected to in-plane loads:

$$\frac{\partial N_x}{\partial x} + \frac{1}{r} \frac{\partial N_{x\phi}}{\partial \phi} = 0 \tag{1}$$

$$\frac{\partial N_{x\phi}}{\partial x} + \frac{1}{r} \frac{\partial N_\phi}{\partial \phi} = 0 \tag{2}$$

$$N_x = K \left[\frac{\partial u}{\partial x} + \frac{v}{r} \frac{\partial v}{\partial \phi} + \frac{v}{r} w \right] \tag{3}$$

$$N_\phi = K \left[\frac{1}{r} \frac{\partial v}{\partial \phi} + \frac{w}{r} + v \frac{\partial u}{\partial x} \right] \tag{4}$$

$$N_{x\varphi} = N_{\varphi x} = \frac{1-\nu}{2} K \left[\frac{1}{r} \frac{\partial u}{\partial \varphi} + \frac{\partial v}{\partial x} \right] \quad 5$$

where $K = Et/(1-\nu^2)$ is the extensional stiffness. The meridional and shear stress resultants N_x and $N_{x\varphi}$ at the base ($x = 0$) are :

$$N_x(0) = N_n \cos(n\varphi) \quad 6$$

$$N_{x\varphi}(0) = N_n^s \sin(n\varphi) \quad 7$$

where N_n and N_n^s are the modal in-plane meridional and shear stress resultants respectively. Due to axisymmetric loading and in the absence of any internal pressure we have $N_\varphi = 0$. Integration of Eqn. 2 results in

$$N_{x\varphi} = f_1(\varphi) \quad 8$$

which implies that shear stresses are constant along the height of the shell (Eqn. 7):

$$N_{x\varphi} = N_n^s \sin(n\varphi) \quad 9$$

Likewise Eqn. 1 can be integrated to yield:

$$N_x = -\frac{1}{r} \int \frac{\partial N_{x\varphi}}{\partial \varphi} dx + f_2(\varphi) = -\frac{n}{r} N_n^s x \cos(n\varphi) + f_2(\varphi) \quad 10$$

where $f_2(\varphi)$ is determined as $f_2(\varphi) = N_n \cos(n\varphi)$, using Eqn. 6 as a boundary condition at the base. Therefore:

$$N_x = N_n \left[1 - \frac{n}{r} \left(\frac{N_n^s}{N_n} \right) x \right] \cos(n\varphi) \quad 11$$

It is assumed that at the top of the shell ($x = h$), $N_x = 0$. Hence

$$N_n^s = \left(\frac{r}{nh} \right) N_n \quad 12$$

and the remaining stress resultants are:

$$N_x = N_n \left(1 - \frac{x}{h} \right) \cos(n\varphi) \quad 13$$

$$N_{x\varphi} = N_n \left(\frac{r}{nh} \right) \sin(n\varphi) \quad 14$$

Further, the stress resultants are related to the displacements by manipulation of Eqn. 3 through Eqn. 5:

$$\begin{aligned}\frac{\partial u}{\partial x} &= \frac{1}{Et} (N_x - \nu N_\varphi) \\ \frac{1}{r} \frac{\partial v}{\partial \varphi} + \frac{w}{r} &= \frac{1}{Et} (N_\varphi - \nu N_x) \\ \frac{1}{r} \frac{\partial u}{\partial \varphi} + \frac{\partial v}{\partial x} &= \frac{2(1+\nu)}{Et} N_{x\varphi}\end{aligned}\quad 15$$

By integrating these and setting $N_\varphi = 0$, expressions for deflection become:

$$u = \frac{1}{Et} \int N_x dx + f_3(\varphi) \quad 16$$

$$v = \frac{2(1+\nu)}{Et} \int N_{x\varphi} dx - \frac{1}{r} \int \frac{\partial u}{\partial \varphi} dx + f_4(\varphi) \quad 17$$

$$w = \frac{\nu r}{Et} N_x - \frac{\partial v}{\partial \varphi} \quad 18$$

$f_3(\varphi)$ and $f_4(\varphi)$ are functions to be determined by the other boundary conditions. At $x = 0$, $u_x = u_n \cos(n\varphi)$, so $f_3(\varphi) = u_n \cos(n\varphi)$. Placing $\frac{\partial u}{\partial \varphi}$ into Eqn. 17 results in $f_4(\varphi) = 0$, using $v(0) = 0$. Then,

$\frac{\partial v}{\partial \varphi}$ is extracted from 17 and substituted into 18:

$$w = - \left[\frac{\nu r}{Et} N_n \left(1 - \frac{x}{h}\right) + \frac{2(1+\nu)r}{Eth} N_n x + \frac{n^2}{r} u_n x + \frac{n^2}{Etr} N_n \left(\frac{x^2}{2} - \frac{x^3}{6h}\right) \right] \cos(n\varphi) \quad 19$$

Since $w = 0$ at $x = h$ (closed top), the following expression for relating settlement u to the maximum stress resultant at the base is obtained as:

$$N_n = \frac{\frac{n^2 h}{r} u_n}{\frac{2(1+\nu)r}{Et} + \frac{n^2 h^2}{3Etr}} \quad 20$$

Eqn. 20 can be expressed in dimensionless form (S_n) which contains the maximum meridional stress at the base (σ_x) at harmonic $n = 2$:

$$S_{n=2} = \frac{\sigma_x / E}{u_2 / h} = \frac{1}{\frac{(1+\nu)}{2} \left(\frac{r}{h}\right)^2 + \frac{1}{3}} \quad 21$$

In this latter equation, only the $v = 0$ boundary condition at the base was used, and gave results indistinguishable from the 'rigorous' FEA solution (Figure 2). In a different approach (Jonaidi and Ansourian, 1997b) $v = w = 0$ was used at the base and resulted in the slightly different equation:

$$S_{n=2} = \frac{1}{\frac{(2+\nu)}{4} \left(\frac{r}{h}\right)^2 + \frac{1}{3}} \quad 22$$

It is again stressed that, while the above equations are derived for a general n , membrane theory is only valid in the low to medium range of n , when flexural actions are small.

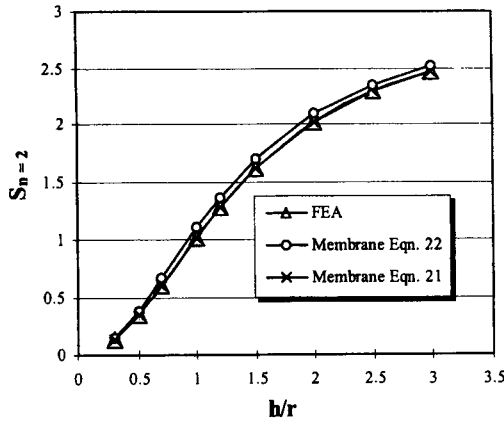


Figure 2: Comparison of membrane solutions with FEA

BUCKLING ANALYSIS

Definition of the Model

The FE model consists of one half wave ($n = 2$) of a cylindrical shell, supported along two generators and along two circular edges normal to the axis (Figure 3). The boundary conditions of the panel are shown in Figure 3. In this reduced but accurate model, refined meshes were possible and adopted.

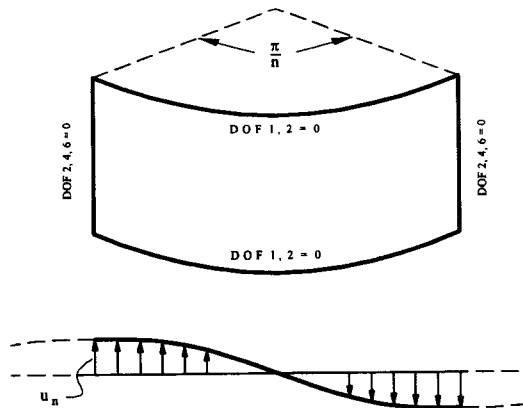


Figure 3 Loading and geometry of the panel

Results of Parametric Study

Linear buckling analyses using highly refined meshes were made for tank structures of wall slenderness $r/t = 300, 500, 700, 1000, 1500$ and 2000 , and geometry $h/r = 0.3, 0.5, 0.7, 1.0, 1.5, 2$ and 3 . Radial and circumferential movement were restrained at the base and top, modeling closed top-tanks. Differential settlements at harmonic n from 2 up to 24 were imposed at the base and the first eigenvalue was extracted for each case. Results for the saddle deformation are given here. Following an analysis of the results and consideration of buckling modes, it was found that the maximum meridional stresses (σ_x) at the base at the critical settlement level depend on both r/t and h/r ; and the buckling mode is one of shear. This mode is shown in Figure 4(a) for uniform thickness and 4(b) for tapered shell ($T_{\text{ratio}} = 3$). For $n = 2$, the best fit is given by:

$$\sigma_x = \frac{1.267E}{\sqrt{(1-\nu^2)}} \left(\frac{h}{r}\right)^{0.438} \left(\frac{t}{r}\right)^{1.198} \quad 23$$

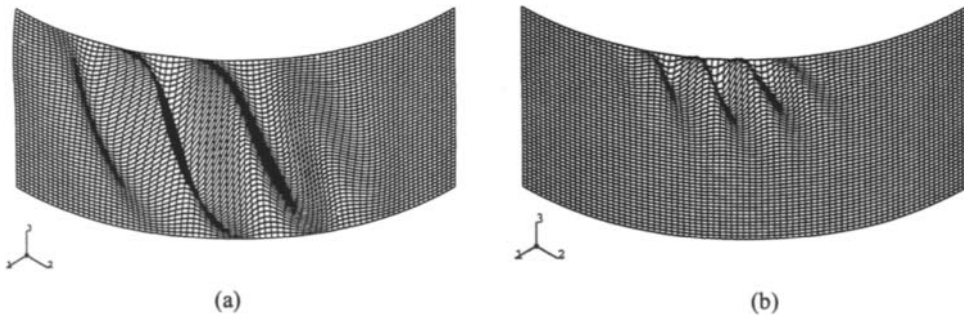


Figure 4: Shear buckling mode for (a) uniform and (b) tapered shell of $h/r = 0.7, r/t = 1000$

NON-LINEAR ANALYSIS WITH INTERNAL PRESSURE

A uniform thickness tank under uniform internal pressure p is considered here, subjected to settlement $n = 2$. The ratio pressure/settlement is significant. A range of pressures was considered, creating final nominal hoop tensile stresses between 20 and 110 MPa at the ultimate state of the shell ($f_y = 250$ MPa); the target ratios for nominal hoop stress were 50 MPa to 150 MPa for $u/t = 1$. Pressures and settlements were raised proportionally in the non-linear analysis (ABAQUS, 1996). Geometrical ratios were considered in the range $h/r = 0.5 - 2.0$ and $r/t = 500 - 1500$; the initial surface of the cylinder was assumed perfect.

Results are summarised in Figure 5 where the ultimate membrane stress is plotted against r/t for a range of h/r and pressure/settlement ratio. The stress is compared with the perfect shell buckling stress under uniform compression. The failure points are gathered in the band shown in the Figure. The effect of p on the ultimate behaviour is similar to an initial imperfection in the lower part of the shell. The short-wave deformation near the base creates a symmetrical imperfection and additional stresses that reduce the ultimate strength. The limiting state is reached when the stresses in the outer layers of the shell reach yield under combined stresses, and occurs at the upward settlement zone (Figure 6). The deformation at the ultimate state is in the form of an elephant's foot failure, as shown in Figure 7. The average reduction in maximum meridional stress below the perfect uniform compression value has a range from 40% ($r/t = 500$) to 18% ($r/t = 1500$).

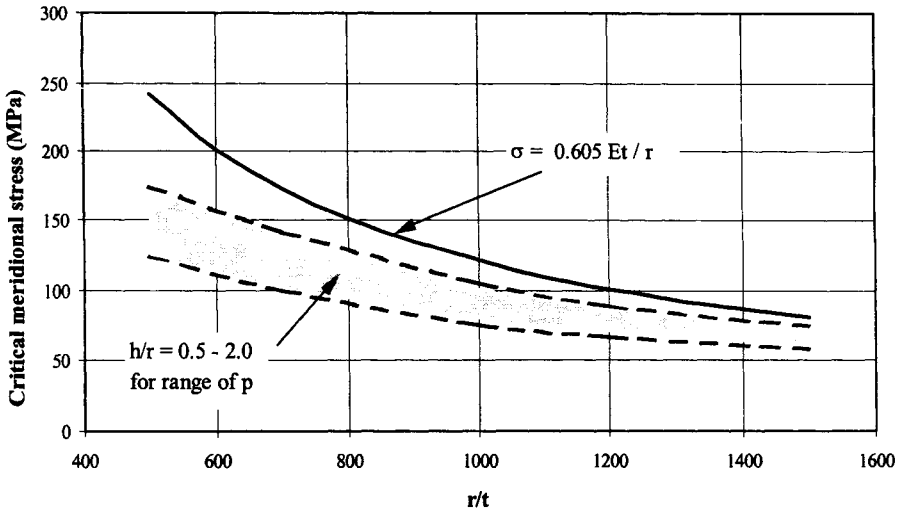


Figure 5: Ultimate meridional stress from non-linear analysis

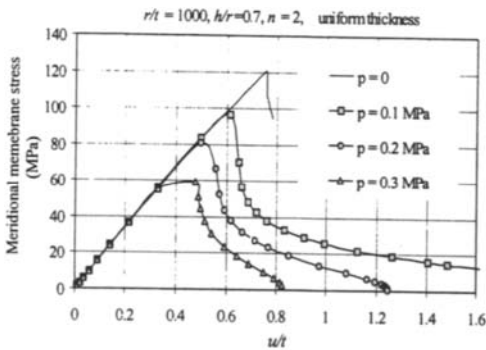


Figure 6: Base stress vs settlement for proportional pressure (e.g. $p = 0.1$ MPa for $u/t = 1$)

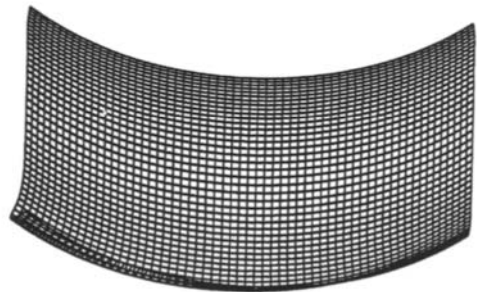


Figure 7: Elephant's foot failure for $n = 2$ and internal pressure

CONCLUSIONS

Cylindrical shells under vertical edge deformation were analysed in this paper. The deformation shape was assumed in the form of a saddle ($n = 2$). A simple solution based on membrane theory was given for the meridional stresses at the base. The solution was almost indistinguishable from 'rigorous' finite element results. Linear buckling solutions were used to derive simplified expressions for critical meridional stress at the base; the associated eigenmode was one of shear.

Under combined internal pressure and vertical harmonic settlement, non-linear analysis showed that the eigenmode was not evident, but that failure occurred at the base as an 'elephant foot' phenomenon under combined stresses. The short-wave deformation near the base created a symmetrical imperfection and additional stresses that reduced the ultimate strength. The limiting state was reached when the combined stresses in the outer layers of the shell reached yield, and occurred at the peak upward settlement zone.

ACKNOWLEDGMENT

The first author is supported by a Scholarship of the Ministry of Culture and Higher Education of Iran. The second author is supported by a Grant from the Australian Research Council. The authors gratefully acknowledge this support.

REFERENCES

- ABAQUS (1996). Abaqus Users Manual 5.6, Habbit, Karlsson & Sorensen Inc., USA.
- De Beer, E., (1969). Foundation problems of petroleum tanks, *Annales de l'Institut Belge de Petrole*, **6**, 25-40.
- D'Orazio, T.B., Duncan, J.M., and Bell, R.A. (1989). Distortion of steel tanks due to settlement of their walls, *Journal of Geotechnical Eng.*, ASCE **115:6**, 871-890.
- Jonaidi, M. and Ansourian, P. (1997a). Non-linear behaviour of storage tank shells under harmonic edge settlement, Intl Conf on carrying capacity of steel shell structures, Brno, Czech Republic, Oct., (Ed.: Krupka V, and Schneider, P.), 164- 170.
- Joraidi, M. and Ansourian, P. (1997b). 'Base Settlement Effects on Fixed Roof Storage Tank Shells', *Proc. 15th Australasian Conference on the Mechanics of Structures and Materials*, Ed. Grzebieta, Al-Mahaidi & Wilson (Eds), Balkeema, Rotterdam, 505-510.
- Jonaidi, M. and Ansourian, P. (1998a). 'Behaviour of Storage Bins under Harmonic Edge Settlement, (in print) *Proc. 6th Intl. Conf. on Bulk Materials Storage, Handling and Transportation*, Wollongong.
- Jonaidi, M. and Ansourian, P. (1998b in Print). 'Harmonic Settlement Effects on Uniform and Tapered Tank Shells', *Thin-walled Structures*, Vol. , No. , - (In Print, Paper No. TWST2405).
- Kamyab, H., and Palmer, S. C., (1989). Analysis of displacements and stresses in oil storage tanks caused by differential settlement. *Proc. Instn Mech. Engrs*, **Part C203:C1**,60-70.
- Malik, Z., Morton, J. and Ruiz, C. (1977). Ovalization of cylindrical tanks as a result of foundation settlement. *Journal of Strain Analysis*. **12(4)**: 339-348.
- Marr, W.A., Ramos, J.A., and Lambe, T.W. (1982). Criteria for settlement of tanks, *J. Geotech. Eng. Div.*, Proc. ASCE, **18:GT8**, 1017-1039.
- Vinson, J.R., (1974). *Structural mechanics: The behaviour of plates and shells*, John Wiley & Sons, New York.

INELASTIC BUCKLING OF A LAYERED CONICAL SHELL

J. Zielnica¹

¹ Applied Mechanics Institute, Poznan University of Technology,
Piotrowo 3, 60-965 Poznan, Poland

ABSTRACT

The purpose of the study is investigation of large displacement stability loss of a bilayered conical shell loaded by longitudinal forces and uniformly distributed external pressure. The shell under consideration is made of a material with exponential work-hardening.

The physical relations used in the elastic-plastic analysis are those of the incremental Prandtl-Reuss plastic flow theory with the Huber-Mises yield condition. The virtual work principle is the basis to derive the strain energy expression. The analysis is based on the energy minimization, where the total strain ϵ in the shell can be expressed in terms of reference surface strains and changes in curvature and these reference surface quantities can then be expressed in terms of displacement vector components. The Ritz method is accepted in order to derive the stability equations for the considered shell. The final form of stability equation, being a function of deflection function parameter, makes possible to trace the equilibrium paths for the shell under consideration. An iterative computer algorithm was elaborated which makes it possible to analyze the shells in elastic, elastic-plastic or in totally plastic prebuckling state of stress. The numerical examples show the influence of principal geometrical and physical parameters of the shell on the stability loss at large deflections.

KEYWORDS

Stability, critical load, strain energy, large displacements, plastic flow theory, yield condition.

INTRODUCTION AND GEOMETRICAL RELATIONS

The subject of the stability analysis is a free-supported bilayered conical panel (see Fig.1) loaded by longitudinal and transversal forces. It is assumed that the shell is bilayered; each layer can be made of the material with different physical properties, and with different stress-hardening parameters. The analysis is made with the assumptions of geometrical and physical nonlinearities, with taking into account the physical relations of the J_2 Prandtl-Reuss plastic flow theory. It is assumed that the material of the shell is compressible with exponential stress-hardening. The $K-L$ hypotheses are accepted and the active deformation processes (Shanley concept) are considered. The following assumptions usually considered in the theories of thin shells are also made: (a) the displacements are small compared to length or mean diameter of the shell, but may be of a magnitude comparable to the thickness, and (b)

there are no normal stresses in the radial direction, and lines originally normal to the middle surface, which is the contact surface between the two layers, remains so after loading. The virtual work principle is the basis to develop the strain energy expression; the minimization of this results in the stability equation from which we get the load-deformation relationships and the critical buckling loads. The numerical calculations are performed by an iterative procedure.

The review of the most important works on stability of elastic plastic shells are presented by Bushnell (1982); the review is focused mostly on numerical methods. Introduction of geometrical nonlinearity considerably complicates the governing equations. Even the introduction of simplifications following from the Kármán's theory enables calculation of large elastic-plastic deflections of shells only by approximate methods, see Bushnell (1982). The problems of linear and nonlinear stability of elastic-plastic conical shells; problem formulation, solution methods and numerical analyses are discussed in paper written by Zielnica (1987). In that paper the expressions for strains and changes in curvature are derived for a conical shell, on the basis of tensor analysis. Once a transition is made from tensor to physical space we get the following variations of strains $\delta\varepsilon_{\alpha\beta}$ and changes in curvature $\delta\kappa_{\alpha\beta}$

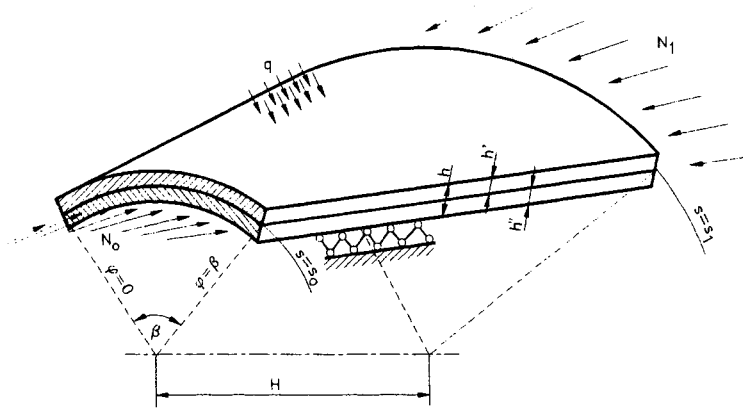


Figure 1. Considered bilayered conical shell

$$\delta\varepsilon_{11} = u_{,s} + \frac{1}{2}(u_{,s}^2 + v_{,s}^2 + w_{,s}^2),$$

$$\delta\varepsilon_{22} = \frac{v_{,\phi}}{s \sin \alpha} + \frac{u}{s} - \frac{w}{s} \cot \alpha + \frac{1}{2s^2 \sin^2 \alpha} \left[(u_{,\phi} - v \sin \alpha)^2 + (v_{,\phi} + u \sin \alpha - w \cos \alpha)^2 + (w_{,\phi} + v \cos \alpha)^2 \right] \quad (1)$$

$$\delta\gamma_{12} = 2\delta\varepsilon_{12} = v_{,s} + \frac{u_{,\phi}}{s \sin \alpha} - \frac{v}{s} + \frac{1}{s \sin \alpha} \left[u_{,s} (u_{,\phi} - v \sin \alpha) + v_{,s} (v_{,\phi} + u \sin \alpha - w \cos \alpha) + w_{,s} (w_{,\phi} + v \cos \alpha) \right]$$

$$\delta\kappa_1 = w_{,ss} + w_{,ss} u_{,s} + \frac{v_{,s}}{s \sin \alpha} \left[w_{,s\phi} + v_{,s} \cos \alpha - \frac{1}{s} (w_{,\phi} + v \cos \alpha) \right],$$

$$\delta\kappa_2 = \frac{w_{,s}}{s} + \frac{w_{,\phi\phi}}{s^2 \sin^2 \alpha} + \frac{w_{,\phi} \cos \alpha}{s^2 \sin^2 \alpha} + \frac{1}{s^2 \sin^2 \alpha} \left\{ \left[w_{,s\phi} - \frac{1}{s} (w_{,\phi} + v \cos \alpha) \right] (u_{,\phi} - v \sin \alpha) + \frac{1}{s \sin \alpha} (v_{,\phi} + u \sin \alpha) (w_{,\phi\phi} + v_{,\phi} \cos \alpha + (w_{,s} s \sin^2 \alpha)) - \frac{w}{s \tan \alpha} (w_{,\phi\phi} + v_{,\phi} \cos \alpha + w_{,s} s \sin^2 \alpha) \right\} \quad (2)$$

$$\delta\kappa_{12} = \frac{w_{,s\phi}}{s \sin \alpha} - \frac{w_{,\phi}}{s^2 \sin \alpha} + \frac{v_{,s}}{2s \tan \alpha} - \frac{v}{s^2 \tan \alpha} + \frac{1}{2s \sin \alpha} \left\{ u_{,s} \left[w_{,s\phi} - \frac{1}{s} (w_{,\phi} + v \cos \alpha) \right] + w_{,ss} (u_{,\phi} - v \sin \alpha) - \frac{v_{,s}}{s \sin \alpha} (w_{,\phi\phi} + v_{,\phi} \cos \alpha + w_{,ss} s \sin^2 \alpha) + \frac{1}{s \sin \alpha} \left[w_{,s\phi} + v_{,s} \cos \alpha - \frac{1}{s} (w_{,\phi} + v \cos \alpha) \right] (v_{,\phi} + u \sin \alpha - w \cos \alpha) \right\}$$

We assume that the considered shell have a perfect geometry (no imperfections); we also accept that there is a membrane prebuckling stress state in the shell and that the effective stress in the shell can exceed the yield stress of the material.

CONSTITUTIVE RELATIONS OF THE PLASTIC FLOW THEORY

The basic difference between the theory of elasticity and the discussed plastic low theory is determined by the fact that the stresses and the stress increments in the plastic flow theory are connected with the strain increments, or strain rates, by a nonholonomic physical plastic flow rule, which is the plastic flow rule accompanied by H-M-H (Huber-Mises-Hencky) yield condition, which is generalized on the case of stress-hardening in the plastic range. It has been shown that the finite Lagrangian strain tensor can be expressed as the sum of elastic ϵ_{ij}^e and plastic ϵ_{ij}^p parts. Consider an isothermal plastic state at which the loading (yield) function vanishes

$$f(S_{ij}, \epsilon_{ij}^p, \lambda) = 0 \tag{3}$$

where λ is the strain-hardening parameter that depends on the states of stress and strain and their histories. Drucker postulate establishes two requirements: 1) the loading surface is convex and 2) at a smooth point of $f=0$, the plastic strain-rate vector is always directed along the normal to the loading surface or

$$\dot{\epsilon}_{ij}^p = \begin{cases} G \frac{\partial f}{\partial S_{ij}} \frac{\partial f}{\partial S_{kl}} \dot{S}_{kl} & \text{for } f = 0 \text{ and } \frac{\partial f}{\partial S_{kl}} \dot{S}_{kl} \geq 0 \\ 0 & \text{for } f < 0 \text{ and } \frac{\partial f}{\partial S_{kl}} \dot{S}_{kl} \leq 0 \end{cases} \tag{4}$$

where G is a scalar function of the state of the material. If the recoverable elastic strains are infinitesimal, the isothermal relations between the stress rates and elastic strains rates may be taken to be homogeneous and linear, or

$$\dot{S}_{ij} = C_{ijkl} \dot{\epsilon}_{kl}^e = C_{ijkl} (\dot{\epsilon}_{ij} - \dot{\epsilon}_{ij}^p) \tag{5}$$

where the coefficients C_{ijkl} may be functions of the current state of stress and the orientation of the axes of anisotropy or constants. The physical relations of the plastic flow theory can be expressed in a deviatoric form

$$D_{\dot{\epsilon}} = \lambda D_{\dot{\sigma}} + \frac{1}{2G} D_{\dot{\sigma}}, \quad \dot{\epsilon}_{ij} = \lambda s_{ij} + \frac{1}{2G} \dot{s}_{ij} \tag{6}$$

Here $D_{\dot{\epsilon}}$ and $D_{\dot{\sigma}}$ are deviators of strain rates and stress rates, λ is strain-hardening parameter that has to be determined from the yield condition. The increments of plastic strains can be expressed as

$$d\varepsilon_{ij} = \frac{1}{2G} \left(d\sigma_{ij} - \delta_{ij} \frac{3\nu}{1+\nu} d\sigma_m \right) + 3d\lambda (\sigma_{ij} - \delta_{ij} \sigma_m),$$

$$\sigma_m = \frac{1}{3} \sigma_{kk}, \quad d\lambda = \frac{1}{2} \frac{d\bar{\varepsilon}_i^p}{\sigma_i} \quad (7)$$

If we take an exponential stress-strain curve $\sigma_i = E^{(o)} \varepsilon_i^\xi$, generalized on the effective stress and strains, we can determine the secant and tangent moduli, respectively.

$$E_s = \begin{cases} k_1 \left[p s \sqrt{k_s (k_s - 2) + 4} \right]^\zeta, & \sigma_i \geq \sigma_{pl} = \left[E^{(o)} / E^\xi \right]^{1-\xi} \\ E, & \sigma_i < \sigma_{pl} \end{cases}$$

$$E_t = \begin{cases} \xi E_s, & \sigma_i \geq \sigma_{pl} \\ E, & \sigma_i < \sigma_{pl} \end{cases} \quad (8)$$

where E is Young's modulus, ξ is a shape factor, and

$$k_1 = \left[E^{(o)} \right]^{1/\xi} \left(\frac{\tan \alpha}{2h} \right)^\zeta, \quad k_s = 1 - \left(\frac{s_o}{s} \right)^2 \left(1 - \frac{2N_o}{p s_o \tan \alpha} \right), \quad \zeta = \frac{\xi - 1}{\xi}$$

We assume that all the quantities related with the outer (external) layer are denoted by an accent ('), and all ones related with the inner (internal) layer are denoted by a double-accent (''). If we accept that the main surface, which all the internal quantities are related with, is the contact surface of the both layers, we can calculate the forces and moments developed by the stability loss in the shell by the following relations

$$\begin{aligned} \delta N_1 &= \int_0^{h'} \delta \sigma'_s dx_3 + \int_{-h''}^0 \delta \sigma''_s dx_3, & \delta N_2 &= \int_0^{h'} \delta \sigma'_\varphi dx_3 + \int_{-h''}^0 \delta \sigma''_\varphi dx_3, \\ \delta T &= \int_0^{h'} \delta \tau'_{s\varphi} dx_3 + \int_{-h''}^0 \delta \tau''_{s\varphi} dx_3, & \delta M_1 &= \int_0^{h'} \delta \sigma'_s x_3 dx_3 + \int_{-h''}^0 \delta \sigma''_s x_3 dx_3, \\ \delta M_2 &= \int_0^{h'} \delta \sigma'_\varphi x_3 dx_3 + \int_{-h''}^0 \delta \sigma''_\varphi x_3 dx_3, & \delta H &= \int_0^{h'} \delta \tau'_{s\varphi} x_3 dx_3 + \int_{-h''}^0 \delta \tau''_{s\varphi} x_3 dx_3 \end{aligned} \quad (9)$$

Here $\delta \sigma_s, \delta \sigma_\varphi, \delta \tau_{s\varphi}$ are the variations of stress in the shell developed by stability loss, x_3 is the distance from the main surface to arbitrary point across the shell thickness. Zielnica (1987) derives the stress variations for a conical shell with the assumption of Kirchhoff-Love hypotheses. These are as follows

$$\begin{aligned} \delta \sigma'_s &= \frac{1}{h'} \left[b_{11} \delta \varepsilon_1 + b_{12} \delta \varepsilon_2 - b_{13} \delta \gamma_{12} - x_3 (b_{11} \delta \kappa_1 + b_{12} \delta \kappa_2 - 2b_{13} \delta \kappa_{12}) \right], \\ \delta \sigma'_\varphi &= \frac{1}{h'} \left[b_{21} \delta \varepsilon_1 + b_{22} \delta \varepsilon_2 - b_{23} \delta \gamma_{12} - x_3 (b_{21} \delta \kappa_1 + b_{22} \delta \kappa_2 - 2b_{23} \delta \kappa_{12}) \right], \\ \delta \tau'_{s\varphi} &= \frac{1}{h'} \left[-b_{31} \delta \varepsilon_1 - b_{32} \delta \varepsilon_2 + b_{33} \delta \gamma_{12} - x_3 (b_{31} \delta \kappa_1 + b_{32} \delta \kappa_2 - 2b_{33} \delta \kappa_{12}) \right] \end{aligned} \quad (10)$$

Here $\delta \varepsilon_1, \delta \varepsilon_2, \delta \gamma_{12}$ are strain variations in the main surface and $\delta \kappa_1, \delta \kappa_2, \delta \kappa_{12}$ are the changes in curvature of the main surface at the moment of stability loss. The similar relations are valid for the inner

($\prime\prime$) layer. The coefficients of local stiffness matrix in the above expressions are as follows

$$\begin{aligned}
 b_{11} &= \psi_o \left\{ 2(1 + \nu) + \psi_t \left[\frac{1 + \nu}{2} (2\bar{\sigma}_\varphi - \bar{\sigma}_s)^2 + 9\bar{\tau}_{s\varphi}^2 \right] \right\}, \\
 b_{12} = b_{21} &= \psi_o \left\{ 2\nu(1 + \nu) - \psi_t \left[\frac{1 + \nu}{2} (2\bar{\sigma}_s - \bar{\sigma}_\varphi)(2\bar{\sigma}_\varphi - \bar{\sigma}_s) + 9\bar{\tau}_{s\varphi}^2 \right] \right\} \\
 b_{13} = b_{31} &= 3\psi_o \psi_t \bar{\tau}_{s\varphi} [(2 - \nu)\bar{\sigma}_s - (1 - 2\nu)\bar{\sigma}_\varphi], \\
 b_{22} &= \psi_o \left\{ 2(1 + \nu) + \psi_t \left[\frac{1 + \nu}{2} (2\bar{\sigma}_s - \bar{\sigma}_\varphi)^2 + 9\bar{\tau}_{s\varphi}^2 \right] \right\}, \\
 b_{23} = b_{32} &= 3\psi_o \psi_t \bar{\tau}_{s\varphi} [(2 - \nu)\bar{\sigma}_\varphi - (1 - 2\nu)\bar{\sigma}_s], \\
 b_{33} &= \psi_o \left\{ (1 - \nu^2) + \frac{1}{4} \psi_t [(5 - 4\nu)(\bar{\sigma}_s^2 + \bar{\sigma}_\varphi^2) - 2(4 - 5\nu)\bar{\sigma}_s\bar{\sigma}_\varphi] \right\}
 \end{aligned} \tag{11}$$

Here

$$\psi_o = \frac{Eh}{1 + \nu} \left\{ 2(1 - \nu^2) + \frac{1}{2} \psi_t [(5 - 4\nu)(\bar{\sigma}_s^2 - \bar{\sigma}_\varphi^2) - 2(4 - 5\nu)\bar{\sigma}_s\bar{\sigma}_\varphi + 18(1 - \nu)\bar{\tau}_{s\varphi}^2] \right\}^{-1}, \quad \psi_t = \frac{E}{E_t} - 1$$

The barred quantities in (11) are the relative stresses of the prebuckling state of stress related with effective stress σ_i . As one may see, the constitutive relations of the Prandtl-Reuss plastic flow theory are expressed in terms of tangent stiffness modulus E_t . For the accepted external load acting the shell we have $\bar{\tau}_{s\varphi} = \tau_{s\varphi} / \sigma_t = 0$, since $b_{\alpha 3} = b_{3\alpha} = 0$, then relations (10) take a more simple form.

If we substitute Eqs. (11) and (10) into (9) and perform prescribed integration, we get

$$\begin{aligned}
 \delta N_1 &= C_{11} \delta \varepsilon_1 + C_{12} \delta \varepsilon_2 - C_{13} \delta \gamma_{12} - C_{14} \delta \kappa_1 - C_{15} \delta \kappa_2 + C_{16} \delta \kappa_{12}, \\
 \delta N_2 &= C_{21} \delta \varepsilon_1 + C_{22} \delta \varepsilon_2 - C_{23} \delta \gamma_{12} - C_{24} \delta \kappa_1 - C_{25} \delta \kappa_2 + C_{26} \delta \kappa_{12}, \\
 \delta T &= -C_{31} \delta \varepsilon_1 - C_{32} \delta \varepsilon_2 + C_{33} \delta \gamma_{12} + C_{34} \delta \kappa_1 + C_{35} \delta \kappa_2 - C_{36} \delta \kappa_{12}, \\
 \delta M_1 &= C_{41} \delta \varepsilon_1 + C_{42} \delta \varepsilon_2 - C_{43} \delta \gamma_{12} - C_{44} \delta \kappa_1 - C_{45} \delta \kappa_2 + C_{46} \delta \kappa_{12}, \\
 \delta M_2 &= C_{51} \delta \varepsilon_1 + C_{52} \delta \varepsilon_2 - C_{53} \delta \gamma_{12} - C_{54} \delta \kappa_1 - C_{55} \delta \kappa_2 + C_{56} \delta \kappa_{12}, \\
 \delta H &= C_{61} \delta \varepsilon_1 + C_{62} \delta \varepsilon_2 - C_{63} \delta \gamma_{12} - C_{64} \delta \kappa_1 - C_{65} \delta \kappa_2 + C_{66} \delta \kappa_{12}
 \end{aligned} \tag{12}$$

The following notation is introduced in Eqs. (12)

$$\begin{aligned}
 C_{11} &= b'_{11} + b''_{11}, \quad C_{12} = C_{21} = b'_{12} + b''_{12}, \quad C_{13} = C_{31} = b'_{13} + b''_{13}, \quad C_{14} = C_{41} = \frac{1}{2}(h' b'_{11} - h'' b''_{11}), \\
 C_{15} &= C_{51} = \frac{1}{2}(h' b'_{21} - h'' b''_{21}), \quad C_{16} = 2C_{61} = h' b'_{13} - h'' b''_{13}, \quad C_{22} = b'_{22} + b''_{22}, \\
 C_{23} &= C_{32} = b'_{23} + b''_{23}, \quad C_{24} = C_{42} = \frac{1}{2}(h' b'_{21} - h'' b''_{21}), \quad C_{25} = C_{52} = \frac{1}{2}(h' b'_{22} - h'' b''_{22}), \\
 C_{26} &= 2C_{62} = h' b'_{32} - h'' b''_{32}, \quad C_{33} = b'_{33} + b''_{33}, \quad C_{34} = C_{43} = \frac{1}{2} C_{16} = \frac{1}{2}(h' b'_{13} - h'' b''_{13}), \\
 C_{35} &= C_{53} = \frac{1}{2}(h' b'_{23} - h'' b''_{23}), \quad C_{36} = 2C_{63} = h' b'_{33} - h'' b''_{33}, \quad C_{44} = \frac{1}{3}(h'^2 b'_{11} - h''^2 b''_{11}), \\
 C_{45} &= C_{54} = \frac{1}{3}(h'^2 b'_{12} - h''^2 b''_{12}), \quad C_{46} = 2C_{64} = \frac{2}{3}(h'^2 b'_{13} + h''^2 b''_{13}), \quad C_{55} = \frac{1}{3}(h'^2 b'_{22} - h''^2 b''_{22}), \\
 C_{56} &= 2C_{65} = \frac{2}{3}(h'^2 b'_{23} + h''^2 b''_{23}), \quad C_{66} = \frac{2}{3}(h'^2 b'_{33} - h''^2 b''_{33})
 \end{aligned} \tag{13}$$

DEVELOPMENT OF THE POTENTIAL ENERGY AND STABILITY EQUATIONS

The system of stability equations expressed by the displacements does not have an exact solution. Any approximate solution, e.g. by an orthogonalization method is complicated because the appropriate calculations are time consuming. The necessity to satisfy the kinematic and static boundary conditions, leads to the assumption of approximate functions in a very complicated form. In order to avoid the above mentioned difficulties the Ritz method is applied. The conditions of equilibrium for classical buckling problem can be obtained from the variation of the total potential energy Π_T . In order to obtain the stability conditions from the variation relations, the principle of stationary potential energy will be invoked, with the bilayered conical shell considered to be in a state of neutral equilibrium. Since the principle of stationary potential energy states that a necessary condition of the equilibrium of any given state is that the variation of the total potential energy vanishes, it follows that

$$\delta \Pi_T = \delta(W + L) = 0 \tag{14}$$

where W is the change in strain energy stored in the shell. The second term L represents the potential energy of the external loads. Equation (14) with its nature has a form of equilibrium equations in variational sense, and it is correct both for pre- and postcritical deformation state.

Instead of exact expressions for the displacements u_i we introduce the approximate functions with coefficients A_i . These coefficients must be chosen in such a way that they fit as far as possible to real displacements. The equation

$$\delta \Pi_T = \sum_{i=1}^k \Pi_{T,A_i} \delta A_i = 0 \tag{15}$$

is satisfied for arbitrary value of variation of parameters δA_i where $i=1,2,3,\dots,k$. Thus we have

$$\Pi_{T,A_i} = 0 \tag{16}$$

The total potential energy in the shell is obtained by summing up the particular terms related with both layers: W_T^+ (outer layer), W_T^- (inner layer), and with the potential energy of the external loads L , i.e.

$$\Pi_T = W_T + L = W_T^+ + W_T^- + L \tag{17}$$

The terms in Eqn. (17) related with strains energy are as follows

$$W_T^\pm = \frac{1}{2} \int \int_{s_0}^{\beta} \left(\delta N_1^\pm \delta \epsilon_{11}^\pm + \delta N_2^\pm \delta \epsilon_{22}^\pm + \delta T^\pm \delta \gamma_{12}^\pm + \delta M_1^\pm \delta \kappa_1^\pm + \delta M_2^\pm \delta \kappa_2^\pm + \delta H^\pm \delta \kappa_{12}^\pm \right) r d\varphi ds, \tag{18}$$

If we use Eqs. (12) and perform the integration over the whole surface of the considered conical shell, we get the following expression for the strain energy

$$\begin{aligned} W = \int \int_A \overline{W} ds r d\varphi = \frac{1}{2} \int \int_{s_0}^{\beta} [& C_{11} \delta \epsilon_{11}^2 + C_{22} \delta \epsilon_{22}^2 + (C_{12} + C_{21}) \delta \epsilon_{11} \delta \epsilon_{22} - (C_{14} \delta \kappa_1 + C_{15} \delta \kappa_1) \delta \epsilon_{11} + \\ & -(C_{14} \delta \kappa_1 + C_{15} \delta \kappa_2) \delta \epsilon_{22} + (C_{33} \delta \gamma_{12} - C_{36} \delta \kappa_{12}) \delta \gamma_{12} + (C_{41} \delta \epsilon_{11} + C_{42} \delta \epsilon_{22}) \delta \kappa_1 + \\ & -C_{44} \delta \kappa_1^2 - C_{55} \delta \kappa_{22}^2 - (C_{45} + C_{54}) \delta \kappa_1 \delta \kappa_2 + (C_{51} \delta \epsilon_{11} + C_{52} \delta \epsilon_{22}) \delta \kappa_2 + \\ & -(C_{63} \delta \gamma_{12} - C_{66} \delta \kappa_{12}) \delta \kappa_{12}] ds r d\varphi \end{aligned} \tag{19}$$

The term L is the potential energy of the external loads and is given by :

$$L = - \iint_A q w ds r d\varphi - \frac{1}{2} \iint_A N_o \frac{s_o}{s} w_s^2 ds r d\varphi = -q \sin \alpha \int_{s_o}^{s_1} \int_0^\beta w s d\varphi ds - \frac{1}{2} N_o s_o \sin \alpha \int_{s_o}^{s_1} \int_0^\beta w_s^2 d\varphi ds \quad (20)$$

Now, we substitute the local stiffness matrix coefficients b_{ij} (11) into Eqs. (13), then we substitute expressions (1) and (13) into (19). Thus, we get a general form of the total potential energy Π_T for the deformed shell expressed in terms of the displacements u , v , and w .

Once the geometry, material constants, and load conditions are specified, we chose the displacement functions w , u , and v in the following form

$$u_i(s, \varphi) = A_i r^2 (s) \sin m_i (s - s_o) \sin n_i \varphi, \quad i = 1, 2, 3 \quad (21)$$

where $[u_1, u_2, u_3] = [w, u, v]$, $m_l = \frac{m\pi}{l}$, $n_l = \frac{n\pi}{\beta}$, $l = s_1 - s_o$

Here m and n are parameters. The approximate functions (21) satisfy the kinematic boundary conditions of simply supported shell edges.

$$w|_{\substack{s=s_o \\ s=s_1}} = 0, \quad w|_{\substack{\varphi=0 \\ \varphi=\beta}} = 0, \quad u|_{\varphi=0} = 0, \quad v|_{\substack{s=s_o \\ s=s_1}} = 0 \quad (22)$$

We substitute approximate functions (21) into Eqs. (1) and (19). Then we substitute Eqn. (19) and Eqn. (20) into the total potential energy expression (17); then following relations (16) we differentiate the total potential energy Π_T with respect to coefficients A_i , i.e.

$$\Pi_{T, A_i} = 0, \quad i = 1, 2, 3 \quad (23)$$

Thus, we get a system of nonlinear algebraic equations written in the following general form

$$\begin{aligned} & -\frac{1}{2} \left(N_o E_4 + \frac{h^2}{12} \bar{D}_4 \right) \sin^2 \alpha A_1 - \frac{1}{4} \sin^2 2\alpha \bar{D}_1 A_2 + \frac{h^2}{24} \cos \alpha \bar{D}_2 A_3 = \\ & = \frac{1 - (-1)^n}{n_1} \left(\frac{3}{2} \cos \alpha \bar{D}_7 A_1^2 - \sin \alpha \bar{D}_7 A_1 A_2 + \bar{D}_8 A_1 A_3 \right) \sin^3 \alpha - \frac{1}{2} p E_5 + \frac{1}{16} \sin^6 \alpha \bar{D}_{10} A_1^3 \\ & \cos \alpha \bar{D}_1 A_1 - \sin \alpha \bar{D}_3 A_2 + \bar{D}_3 A_3 = \frac{1 - (-1)^n}{3n_1 \beta} \sin^3 \alpha \bar{D}_7 A_1^2 \\ & \frac{(h' + h^n)^2}{12} \frac{p \cot \alpha}{\sin \alpha} \bar{D}_2 A_1 - \frac{p}{\sin \alpha} \bar{D}_3 A_2 + \bar{D}_6 A_3 = \frac{[1 - (-1)^n] \sin^2 \alpha}{3\beta} \bar{D}_8 A_1^2 \end{aligned} \quad (24)$$

Here \bar{D}_i are integral expressions where, among all, the stiffness matrix elements b_{ij} are included, which depend on material constants and on the prebuckling stress state. Thus, we determine \bar{D}_i using Simpson's rule of numerical integration.

We have, for example

$$\bar{D}_1 = \int_{s_o}^{s_1} s \left\{ [(2 \cos k \psi - ks \sin k \psi) b_{12} + \cos k \psi b_{22}] s^2 \sin k \psi + \right.$$

$$+ \frac{(h' + h'')^2}{12} \frac{p^2}{\sin^2 \alpha} (\sin k \psi + ks \cos k \psi) \cos k \psi b_{33} \Big\} ds \quad (25)$$

$$\begin{aligned} \bar{D}_2 = & \int_{s_0}^s \left\{ \sin k \psi \left[(2 - k^2 s^2) \sin k \psi + 4ks \cos k \psi \right] b_{12} + \right. \\ & \left. + \left[\frac{12s^2 \sin k \psi}{(h' + h'')^2} + \left(2 - \frac{p^2}{\sin^2 \alpha} \right) \sin k \psi + ks \cos k \psi \right] b_{22} - (k^2 s^2 \cos^2 k \psi - \sin^2 k \psi) b_{33} \right\} ds \end{aligned}$$

When we solve the set of nonlinear algebraic equations (24) with respect to deflection function parameter A_1 , we obtain the stability equation in the form of

$$-\frac{\sin^4 \alpha \bar{E}_1 A_1^3 + \sin^2 \alpha \bar{E}_2 A_1^2 + \bar{E}_3 A_1}{\frac{\bar{E}_5}{\sin^2 \alpha} q + N_o \bar{E}_4 A_1} = 1 \quad (26)$$

If we solve Eqn. (26) with respect to the parameter of lateral pressure q , we get a relation more suitable to use in numerical analysis and to trace the different equilibrium paths of the considered elastic-plastic bilayered conical shell. An iterative algorithm of calculation was elaborated, which analyses the shells in elastic, elastic-plastic or in totally plastic prebuckling state of stress.

DETERMINATION OF EQUILIBRIUM PATHS

The objective of the numerical calculation is the analysis of postcritical equilibrium paths for arbitrary combination of lateral to longitudinal loads, and also the study of the influence of geometrical and physical parameters on the value of critical load and the form of stability loss. From the analysis of stability equation (26) the following procedure results, aiming to determine the "upper" (q_+^* ; N_{o+}^*) and the "lower" (q_-^* ; N_{o-}^*) critical load: (a) we assume geometrical and material data for the shell and the fixed ratio of lateral to longitudinal loads $\kappa = qs_o/N_o$; (b) we adopt a series of values for parameters m and n (number of half-waves in longitudinal and circumferential directions); (c) for a sequence of increasing values A_1 we calculate the respective maximal deflection w and load q (or N_o); (d) in the system of coordinates (w, q) or (w, N_o) we obtain two-parameter family of curves $q(w; m, n)$ or $N_o(w; m, n)$; (e) from the family of curves we chose the points of the less values of q (or N_o) with specified values of variable w and we obtain a curve which constitute the solution; (f) local maximum and minimum of the curve determine the "upper" (q_+^* ; N_{o+}^*) and the "lower" (q_-^* ; N_{o-}^*) critical loads, respectively.

Because of the complex character of the resulting relations and the complicated process of the determination of the critical loads within the elastic-plastic region, a computer algorithm was elaborated. The algorithm reflects a specific feature of elastic-plastic shell stability problem, where the stability equation (26) is a transcendental function; the coefficients of this functions depend on the load acting the shell.

References

- Bushnell D. (1982). Plastic Buckling of Various Shells, *Trans. ASME, Journ. of Pressure Vessel Technology* **104**:5, 51-72.
- Maciejewski J. and Zielnica J. (1984). Nonlinear stability problem of an elastic-plastic open conical shell. *Engineering Transactions*, **32**:3, 361-380 (in Polish).
- Zielnica J. (1987). Stability of elastic-plastic conical shells. *PUT Transactions*. **182**, p.271 (in Polish).

MODELLING METHODOLOGIES WITH BEAM FINITE ELEMENTS FOR COLLAPSE ANALYSIS OF TUBULAR MEMBERS/CYLINDRICAL SHELLS

B.Skallerud¹ and J.Amdahl²

¹ Div. Applied Mechanics, Norwegian Univ. Science and Techn.

² Div. Marine Structures, Norwegian Univ. Science and Techn.
N-7034 Trondheim, Norway

ABSTRACT

The present study addresses how local inelastic buckling of tubular members may be accounted for in beam finite element models. This gives very efficient computation of large structural systems loaded into the nonlinear regime. Criteria for onset of local buckling are presented and compared to test results for D/t-ratios ranging from 21 to 80. The importance and utilisation of stub-column data is pointed out. The beam elements are either based on integration of (uniaxial) stresses over cross section or plastic hinge models. Accounting for local buckling, both ways of modelling simulate collapse load, combined global and local buckling, and post-local buckling very well for the D/t-ratios investigated.

KEYWORDS

Beam finite elements, nonlinear geometry, plasticity, local buckling, stub-column stress-strain curve.

INTRODUCTION

Offshore steel jacket structures are built up of tubular members of varying diameter to thickness ratios (D/t). During overloading situations some critical members may be subjected to buckling. Depending upon the degree of redundancy first buckling of a member may not represent ultimate collapse of the platform. Whether the structure can take more load or not depends also on the post-collapse behaviour of the component. If the member still can carry significant load in the post-collapse range, the platform is more likely to possess additional strength reserves. The post-collapse strength is to some extent influenced by the member slenderness, but the most important factor is the ability of the cross-section to maintain shape. For low D/t-ratios (<25) the cross section maintains its circular shape even for deflections far into the post-collapse region for the member. However, for higher D/t-ratios local buckling occurs shortly after, or even before, member buckling. Also for structures with little redundancy, the post-buckling behaviour is of importance, because slender cross-sections are vulnerable to imperfections or small, local damages. With recent progress in computers and algorithms, the trend is to take all strength reserves into account in ultimate strength calculation, particularly in

conjunction with reassessment of existing structures. For this purpose progressive collapse or pushover analysis is often carried out using non-linear Finite Element Methods. The structure is conveniently modelled as a space frame using beam finite elements. However, if conventional beam elements are used, local buckling is not taken into account implicitly and has to be given explicit consideration. An alternative is to use shell element modelling at critical sections, but this is not always feasible due to excessive demand for computational resources. If several wave directions are analysed, a relatively large number of members will need modelling with shell elements and also the modelling work may increase unduly. It would therefore be of great value if the effect of local buckling could be accounted for within the framework of beam finite element modelling. A key to this is the approach used for modelling of plasticity. Several modelling methods are available, with different levels of accuracy and sophistication. One approach employs integration over the cross section in order to capture the elastic-plastic material behaviour. It does not account for local geometrical non-linearities such as local buckling. Hence, criteria for onset of local buckling should be supplemented. If local buckling is detected the member behaviour should be modified accordingly in the post-local buckling regime. Another beam finite element approach uses a stress resultant based plasticity modelling, i.e. the integration over cross section in order to account for plasticity is circumvented. The input to such models is parameters describing the elastic-plastic response of the cross section. Usually simple tensile stress-strain test data is utilised on cross sectional level. Residual stresses disturb this idealised behaviour, and are accounted for herein by means of stub-column test data.

The present study addresses the predictive capabilities of proposed design oriented models with material behaviour accounting for residual stresses, and models for initiation of local buckling. An important aspect is to put the various response effects in the proper part of the model. E.g. often a calibrated initial out-of-straightness is employed in order to account for residual stresses. The present investigation shows that if the residual stresses are accounted for in the plastic hinge modelling, the *actual*, as opposed to *equivalent*, *imperfection* may be used. Furthermore, using a modified stress-strain curve accounting for local buckling when integrating over the cross section, the simple fibre based beam element models yields good predictions.

LOCAL BUCKLING CRITERIA

A test program was carried out with the objective to study the cyclic plastic capacity of tubular members of different D/t -ratios (Skallerud et al, 1996). However, as the members exhibited local buckling in the first excursion, and the extreme fibre strain was monitored, important data on critical strains was obtained. The D/t -ratios were 35, 45, 60, and 80. Thicknesses of magnitude 4mm and 6mm were employed. For thickness 4mm, the member length was 3380mm for the two lowest D/t -ratios and 5936mm for the two highest ratios. For thickness 6mm the length was 5936mm. The axial load was applied with an eccentricity of 4mm (for $D/t=35-60$) and 8mm (for $D/t=80$) in order to introduce a small 1.order bending moment in the tubular and a preferred direction for global buckling. The imperfections of the tubes in terms of out-of-straightness were very small, less than 2 mm.

The steel was of type ST52-3N, i.e. a normalised CMn structural steel typically applied in the offshore industry. The tensile yield stress obtained from coupon tests on the actual material was approximately 410MPa. The tensile strength and fracture strain was approximately 490MPa and 36%, respectively. Some stub-column tests were also carried out for the tube with $D/t=45$. Figure 1 illustrates the stress-strain behaviour from a tensile (coupon) test and a stub column test. In addition, a Ramberg-Osgood fit to the stub-column curve is plotted. The early yielding due to residual stresses is observed in this curve contrary to the coupon tensile test.

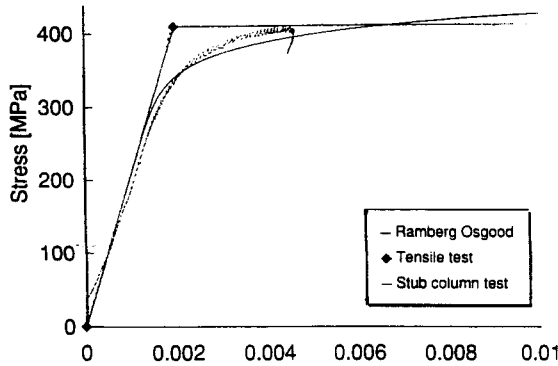


Figure 1: Coupon, stub-column, and Ramberg-Osgood fit stress-strain curves.

Typically, design codes classify the cross section of tubular members according to the wall slenderness; e.g. the following classes are specified by API (1983) using actual material parameters:

$$(I) \quad \frac{D}{t} \leq 0.056 \frac{E}{\sigma_y} = 29, \quad (II) \quad \frac{D}{t} \leq 0.078 \frac{E}{\sigma_y} = 40, \quad (III) \quad \frac{D}{t} \leq 0.112 \frac{E}{\sigma_y} = 57$$

Class I members may be subjected to significant plasticity before local buckling. For class III members, local buckling occurs when the yield stress is attained, i.e. elastic shell buckling. Thus, with reference to the present investigation, the members with the two largest D/t-ratios should buckle elastically, whereas the specimen with the smallest D/t-ratios should only buckle locally after having undergone significant plastic deformation. It should be borne in mind that the above classification is developed for design purposes, and therefore may be considered conservative, representing a lower limit. In the present context, a quantitative local buckling criterion is more feasible. In (Nomota and Enosawa, 1985) an inelastic strain criterion based on the tangent and secant modulus for the material is proposed. This criterion is derived by Gerard (1962), and reads

$$\epsilon_{cr} = 1.32 \sqrt{\frac{E_t}{E_s}} \frac{t}{D}$$

The criterion was initially intended for use in analysis of cylindrical aluminium members, where the stress-strain curve may be well modelled by means of the Ramberg-Osgood curve:

$$\epsilon = \frac{\sigma}{E} + \alpha \left(\frac{\sigma}{\sigma_y} \right)^n$$

For welded, hot rolled steel components like a tubular member, stress-strain relationships obtained in stub column tests are also modelled fairly well by this curve. This was utilised by Nomota and Enosawa(1985) with success. The inelastic strain at buckling is a function of strain, as $E_t = E_t(\epsilon)$ and $E_s = E_s(\epsilon)$. Hence, ϵ_{cr} can be obtained by iterations. Figure 2 shows the result for this criterion along with some simple critical strain criteria based on D/t-ratios only (Sohal and Chen, 1987, Zimmermann et al, 1995, DNV, 1996). Test results of critical strain for D/t-ratios ranging from 21 to 80 are depicted in the figure. The results for D/t<35 are given in (Nomota and Enosawa, 1985). The other D/t ratios are investigated by the authors. Here, the open symbols represent thickness 4mm and the filled symbols represent t=6mm. The criteria based only on D/t give conservative buckling strains (except for the curve denoted Sohal, which is a fit not valid for D/t<30).

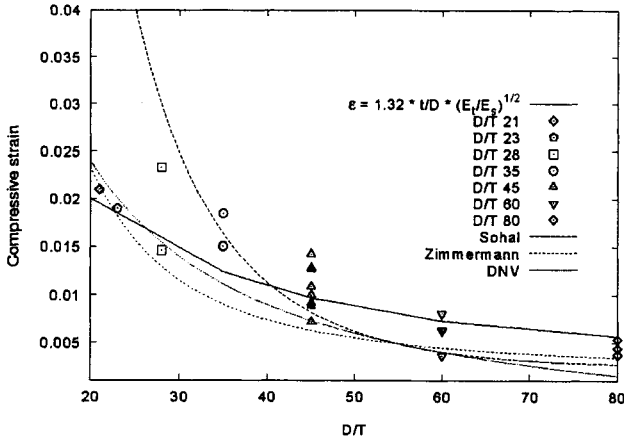


Figure 2: Local buckling criteria.

BEAM FINITE ELEMENT MODELLING

Two approaches are investigated in the present study as alternatives to detailed shell element modelling. One is the simple and usual way with discretisation in length, and integration over the cross section using a uniaxial stress-strain curve to describe the material response. The other utilises a plastic hinge with properties describing the initial cross section yield, transition to fully plastic, and an asymptotic cross section hardening. Both approaches account for large out-of-plane displacements, hence capturing the global instability of the members. Local buckling is simulated differently in the two models. The first approach is obtained within a Timoshenko based beam element, using ABAQUS (Hibbitt et al, 1997) with linear interpolation of nodal degrees of freedom (DOF). Eight integration points over the cross-section are employed to determine cross section response. The important point here is that the initial part of the stress-strain curve used is based on the stub-column curve, and after fulfilling the elastic/inelastic local buckling criterion a negative slope is used to simulate effects of local buckling, see Figure 5a. Six elements were used for the member length, with the smallest length (approximately equal to member diameter) at member mid length, where the plastic hinge is developing. The second beam element modelling, using the program USFOS (SINTEF, 1997), is somewhat special and is described briefly. With this approach the tubular members were modelled with 2 beam elements, with a node at mid length.

Stress resultants based modelling

The basic entity of USFOS is the beam-column. The program employs a coarse element mesh, only one finite element is initially required per physical member of the structure. It operates on element stress resultants, i.e. cross-sectional forces and moments. Yield hinges are used to model material nonlinearities. Element subdivision is performed automatically if a hinge is detected at midspan. The USFOS beam element is valid for large displacements, but restricted to moderate strains. A co-rotational formulation is used based on Green strains. For moderate element deflection, the von Karman approximation applies, and is used herein. The elastic stiffness can be derived from potential

energy consideration. Total and incremental equilibrium equations are established by taking the first and second variation of the strain energy and the potential of the external forces. The shape functions used in the derivation of the elastic stiffnesses and consistent loads are based on the exact solution to the 4th order differential equation of a beam-column. Integration of the element stiffness expressions can be carried out analytically. The "quality" of the shape functions allows for a very simple modelling; one element between each joint is normally sufficient to simulate the elastic nonlinear column behaviour with satisfactory accuracy. Because exact element displacement functions are used, elastic buckling is predicted at the exact Euler buckling load for single beam-columns with different end conditions.

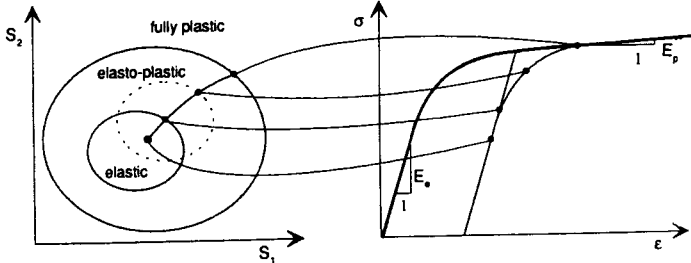


Figure 3: Plasticity model.

The plasticity model implemented in USFOS is formulated in the stress resultant force space and is based on the bounding surface concept. This approach allows for an explicit formulation of the beam element tangential stiffness matrix, including both the geometric nonlinearities as well as nonlinear plastic behaviour characterised by gradual plastification of the cross section including material hardening. Two interaction surfaces are used; a yield surface and a bounding surface. The bounding surface represents full plastic utilisation of the cross section. When the cross section is loaded, the force point travels through the elastic region and intersects with the yield surface. This represents first fibre yields in the cross section. At this stage a yield hinge is introduced. When further loading takes place the yield surface translates such that the force state remains on the yield surface. The bounding surface translates also, but at much smaller rate. This is used to model strain hardening, according to a kinematic hardening model. The translation of the yield surface which approaches the bounding surface during the loading process, provides for a smooth transition from initial yield to full plastification. The yield surface is written as a function of the cross sectional stress resultants on the following form, see Fig. 3;

$$F_y = f\left(\frac{\mathbf{S} - \boldsymbol{\beta}}{Z_y \mathbf{S}_p}\right) = \cos\left(\frac{\pi N - \beta_1}{2 Z_y N_p}\right) - \frac{\sqrt{(M_y - \beta_5)^2 + (M_z - \beta_6)^2}}{Z_y M_p} = 0$$

where $\mathbf{S}^T = (N, Q_y, Q_z, M_x, M_y, M_z)$ and $\mathbf{S}_p^T = (N_p, Q_{yp}, Q_{zp}, M_{xp}, M_{yp}, M_{zp})$ are the cross sectional stress resultants and corresponding plastic capacities, $\boldsymbol{\beta}^T = (\beta_1, \beta_2, \dots, \beta_6)$ and $Z_y < 1$ are the yield surface offsets and yield surface size, respectively. The right hand side of the equation corresponds to a tubular cross-section subjected to axial force and bi-axial bending.

The yield surface size depends upon the stress strain curve for the material and the cross-sectional shape. Strictly it should be different for each stress resultant, but for practical reasons it is assumed constant. For a linear-elastic, perfectly plastic material and pure bending the size will be equal to the inverse of the shape factor. In the general case, with a non-linear stress-strain curve the size is determined by calibration. This is discussed in a later section.

LOCAL BUCKLING MODELS

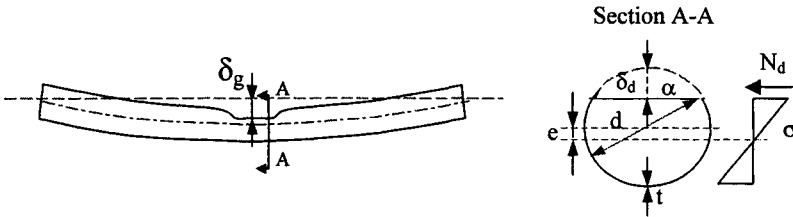


Figure 4: Dented tube model.

Stress resultant based model

A calculation model for a dented tube has been developed by Taby and Moan (1985), and is shown in Figure 4. The cross-sectional shape in the dented region is idealised by subdividing into an undamaged part and a dented flat section. Assuming the dented section ineffective, reduced cross-sectional relationships are obtained. The capacity of beam-columns is typically expressed by means of a Perry-Robertson type formula v.i.z. a first yield criterion. For the damaged tube the following relationship is proposed (Taby and Moan, 1985):

$$\frac{N - N_d}{\sigma_y A_r} + \left\{ \frac{Na_0}{1 - \frac{N}{N_E}} + Ne - N_d \left\{ e + \frac{d}{2} - \delta \right\} \right\} \frac{1}{\sigma_y w_r} = 1$$

The total force acting through the member is N. The fraction of the total load acting through the flat section is N_d. The first term represents the mean axial compression in the undamaged section. The parenthesis contains the bending contribution. The first term is the conventional magnification due to initial imperfection a₀. The second term accounts for the shift of neutral axis. The associated bending moment is only local and is not magnified significantly by axial force. The same holds true for the third term, which is due to the bending contribution from the forces transferred through the flat section. This component has been derived semi-empirically:

$$N_d = 80 \sigma_y d t \alpha \left\{ \sqrt{\left(\frac{2\eta}{d}\right)^2 + \left(\frac{t}{d}\right)^2} - \frac{2\eta}{d} \right\}$$

$$\frac{\eta}{d} = \frac{1}{2} \{ \sin \alpha - \cos \alpha \}, \alpha = \arccos \left\{ 1 - \frac{2\delta_d}{d} \right\}, N_E = \frac{\pi^2 EI}{l_k^2}$$

It should be noted that slender structures can be very sensitive to small imperfections exhibiting steep unloading beyond the critical load. In such cases bifurcation point analysis as outlined above may be nonconservative.

Stress-strain based modelling

A constructed stress-strain curve is employed as illustrated in Figure 5a. The first part is fitted to the stub-column data and is valid up to the critical strain for onset of local buckling (ε_{cr}).

The second part is the post-local buckling "softening" curve (simulating the reduced ability to carry longitudinal membrane stress due to local buckling). The drop in stress beyond local buckling is estimated by means of simple plastic theory. It is assumed that each fibre deforms as a three-hinge mechanism after buckling as shown in Figure 5b. The post-buckling stress-strain relationship depends upon the wave length for the buckle. Based on elastic theory the wave length varies from $l/t = 8-11$, the smaller values associated with the smaller diameter to thickness ratios.

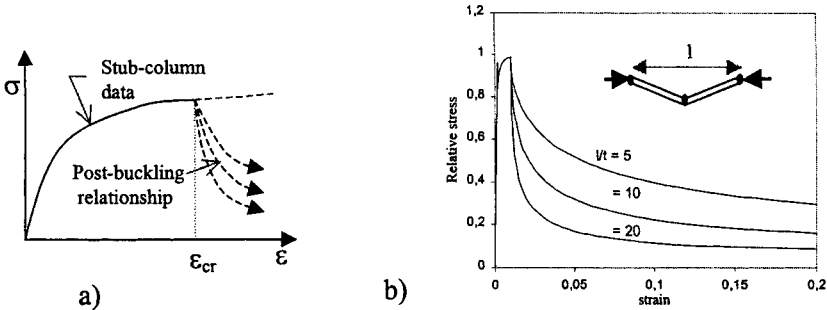


Figure 5: Stress-strain curve modified for local buckling - a) Principle sketch b) Model

In the elasto-plastic range the wave length is smaller. Using tangent modulus theory the wave lengths quoted above should be multiplied with the factor $\sqrt{E_t/E}$ where E_t is tangent modulus at initiation of buckling (Timoshenko and Gere, 1955). The actual stress-strain relationships used in numerical simulations with ABAQUS are shown in Figure 6.

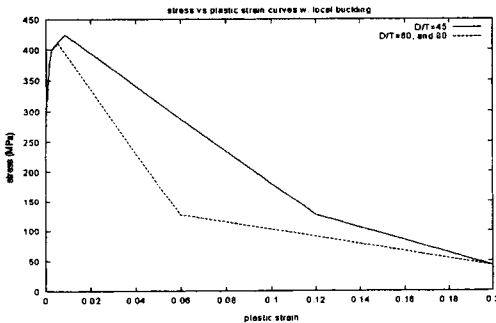


Figure 6 Stress-strain relationships used in numerical simulations.

NUMERICAL SIMULATIONS

In the following, results obtained with the two different finite element models are distinguished by a U or A (referring to the corresponding software USFOS or ABAQUS), followed by the D/t-ratio. The actual global imperfection of the specimens was used in the models. For all specimens this was about 1.5 mm. In addition, the first order bending moment due to the eccentrically applied axial load gives a deterministic global buckling direction. Both models employ full Newton-Raphson equilibrium iterations combined with arc-length control to pass limit points. It should be noted that no bifurcation

analysis needs to be carried out to find local buckling modes, as this is automatically accounted for in the respective phenomenological local buckling models.

D/t=45

For the plastic hinge model, an initial calibration of parameters was carried out in order to make the model comply with the stub-column behaviour. Although the plasticity model has several parameters, only one seems important: the size of the initial yield surface. The remaining parameters are kept as default. The default size of the yield surface relative to the bounding (fully) plastic surface is 0.79. The calibration yields, however, a value of 0.65. It should be noted that the tensile coupon test yield stress is used as model yield stress, and the plasticity parameters accounts for initial yielding and transition to fully plastic behaviour. Another point is that the usual value of Young's modulus for steel is somewhat too high when compared to the stub-column behaviour. Hence, a value of 188000 MPa is used in the calibration. Figure 7a shows the U45-simulation with or without local buckling accounted for. It is observed that the peak load is well predicted as well as the onset of local buckling. If local buckling is not accounted for, the post-collapse behaviour is overpredicted significantly. When local buckling is included the response is simulated quite well. Figure 7b shows the corresponding A45-simulation. It is noted that the peak load is underpredicted somewhat. The onset of local buckling is well predicted. Several post-local buckling slopes in the stress-strain curve were checked (Figure 6), two results are plotted in the Figure 7b. The one denoted gentle corresponds to the one plotted in Figure 6. It is seen that for this stress-strain curve the post-collapse response is accurately computed.

D/t=60

Figure 7c depicts the U60 simulations and corresponding test result. Here Young's modulus had to be reduced further to 170000 MPa in order to have a correct elastic member stiffness. Furthermore, the size of the initial yield surface had to be reduced from 0.65 to 0.45, or else the peak load would be overpredicted. With the above calibration a reasonable prediction of collapse load is obtained. After global collapse the beam element model does not capture the load reduction very well, but accounting for local buckling the post-local buckling simulation is quite good. It should be pointed out that a stub-column test for this *D/t*-ratio probably would lead to earlier nonlinearity in stress-strain curve than for the curve corresponding to *D/t*=45. Unfortunately, these tests were not successful (premature shell buckling due to boundary inaccuracies). It should also be noted that detailed shell element analyses of the member also show overprediction in peak load when the stub-column curve in Figure 3 is used. The local buckling and post-local buckling behaviour is, however, well predicted with the shell element model (Skallerud et al, 1996). The results for the A60 beam model using cross section integration is plotted in Figure 7d. The correspondence with the test result is good in all parts of the curve. The reduced elastic modulus is used here also. The stress-strain curve with the steeper reduction in stress shown in Figure 6 is employed for this *D/t*. Using the stress-strain curve for *D/t*=45 leads to a post-local buckling response with too high load carrying capacity. The deviation from nonlinearity in the test results prior to global buckling indicates that the stress-strain curve used as input to the beam model should have a "yield stress" lower than that obtained from the *D/t*=45 stub column test. Still, a rather impressive simulation is obtained considering the simplistic modelling.

D/t=80

With this *D/t*-ratio, the cross-section buckles elastically according to the API cross section classification. In the test, the member shows a combined global and local buckling behaviour, indicating that there is interaction between the two collapse modes. From the test result plotted in Figure 7e, the post-collapse behaviour is very nonlinear, with a large (dynamic) load reduction. Now the U80 simulation has more problems with a correct prediction. The size of the yield surface has to be reduced further to 0.35. Accounting for local buckling one sees that the simulation follows the test nicely up to test collapse load, then some overprediction in peak load is predicted. The post-peak load behaviour is quite well computed, although the final load carrying capacity is overpredicted. But, still one should keep in mind that this severe nonlinear (shell) behaviour is calculated with a uniaxial beam element model (6 DOF in contrast to a shell element model that would have 2-3 orders of magnitude

more DOF). Figure 7f shows the A80 fibre based element model result. Also here the stress-strain curve employed is based on the $D/t=45$ stub-column test up to onset of local buckling, followed by the stress reduction shown in Figure 6. The accuracy of the simulation is quite impressive. The post-collapse behaviour is predicted accurately.

CONCLUDING REMARKS

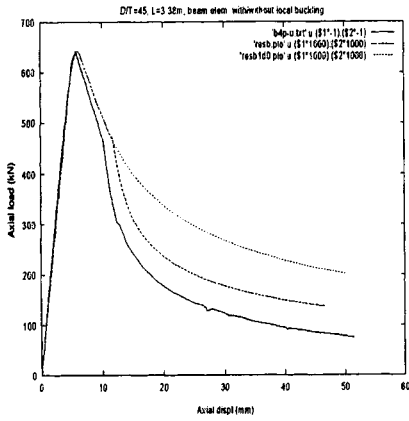
Ultimate strength assessment of offshore jackets requires that ultimate capacity as well as post-collapse behaviour of each individual member be calculated high accuracy. This is affected significantly by residual stresses from fabrication and local buckling of tube wall. The effect of residual stresses is not measured in conventional strain gauge tests, but is captured in stub column tests. One limitation with this method is, however, that local buckling will proceed yielding for thin-walled sections. Local buckling has a significant effect on the post-collapse resistance for diameter to thickness ratios exceeding 45. For diameter to thickness ratios exceeding 60 even the ultimate capacity becomes increasingly affected by local buckling. Rigorously, local buckling requires shell element modelling in order to be accounted for in numerical analysis. Neither the modelling nor the analysis is, however, straightforward.

The present study shows that both the effects of residual stresses and local buckling may be taken into account in conventional beam finite element modelling by using a phenomenological approach. In a stress-strain based analysis, nonlinear stress strain relationships derived from stub column tests are used to describe the material up to the onset of local buckling. The effect of local buckling is modelled by a reduction in the stress level, derived from a simple plastic hinge mechanism for a fibre of the cross-section. In the stress-resultants based model, local buckling is described by a simple geometric model. Non-linear material behaviour is taken into account by calibration of parameters describing the yield - and bounding surfaces.

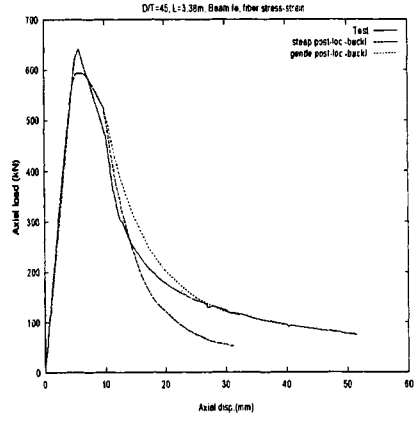
The numerical analyses of the tests with tubular beam-columns demonstrate that both approaches are capable of simulating the load-end shortening relationship including local buckling with high accuracy. This is very satisfactory as the need for costly and demanding shell finite element modelling for ultimate strength assessment of jackets is eliminated.

REFERENCES

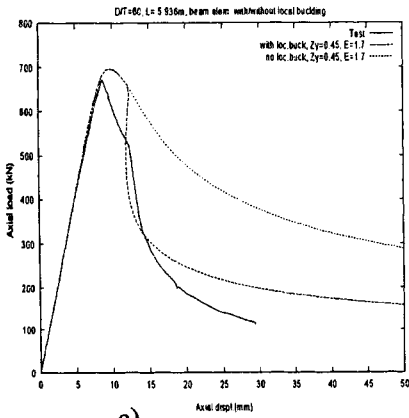
- American Petroleum Institute: *Recommended Practice for Planning, Designing and Constructing Fixed offshore Platforms*. API RP 2A, 1983.
- Chen W.F., and Han, D.J. (1985). *Tubular members in offshore structures*. Pitman advanced publishing program.
- DNV (1996). *Rules for submarine pipeline systems*.
- Hibbitt, Karlson and Sorensen: *ABAQUS Manuals, Version 5.5*, 1997
- Gerard G. (1962), *Introduction to structural stability theory*. McGraw-Hill.
- Nomoto, T. and Enosawa, M. (1986): On the Cyclic Inelastic Buckling of Tubular Columns. Proc. Safety Criteria in Design of Tubular Structures, Tokyo
- Skallerud B., Amdahl J., Johansen A., and Eide O.I. (1996), Cyclic capacity of tubular beam-columns with local buckling: Numerical and experimental studies. Proc. OMAE Florence.
- Sohal I.S., and Chen W.F. (1987). Local buckling and sectional behaviour of fabricated tubes. J.Struct. Engng, vol.113,no.3.
- Timoshenko, and Gere (1961). *Theory of elastic stability*. McGraw-Hill.
- Zimmermann T.J.E., Stephens M.J., DeGeer D.D., and Chen Q. (1995). Compressive strain limits for buried pipelines. OMAE-95, vol.5.



a)

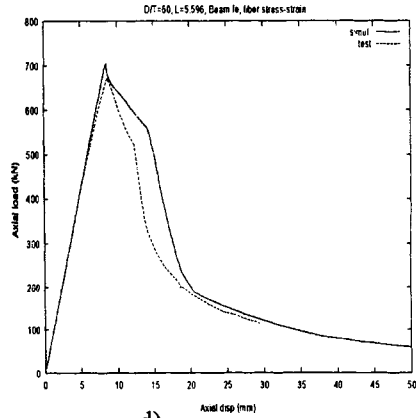


b)

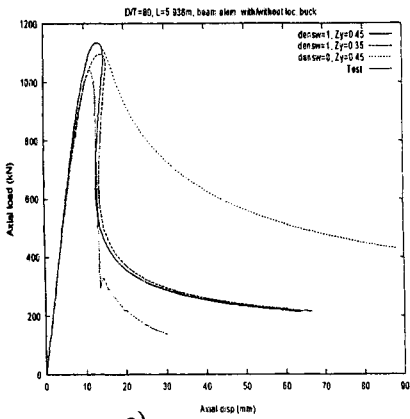


c)

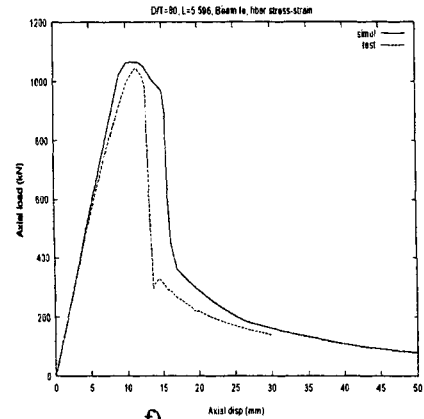
1



d)



e)



f)

Figure 7 Load-end shortening relationships for tubular columns

NONLINEAR VIBRATION AND DYNAMIC INSTABILITY OF THIN SHALLOW CONICAL SHELL

Y.E. Zhiming

Department of Civil Engineering, Shanghai University
Shanghai Institute of Applied Math. & Mech.
149 Yan Chang Road
Shanghai, 200072, P. R. China

ABSTRACT

Based on the dynamic version of Marguerre's equations, the nonlinear vibration and dynamic instability of thin shallow conical shells subjected to periodic transverse and in-plane loads are studied under two different boundary conditions. Applying Galerkin's method, the basic equations are reduced to a system of Duffing and Mathieu equations, from which various kinds of nonlinear vibration and dynamic instability are determined using numerical methods. For illustration, nonlinear vibration frequencies and dynamic instability regions for a particular conical shell are determined. The effects of static load as well as static snap-buckling on the instability regions are also examined.

KEY WORDS

Nonlinear vibration, dynamic instability, thin shallow conical shell

INTRODUCTION

To clarify the nonlinear vibration and dynamic instability of shallow shells is of great importance for design of aerospace structures. However, only a few studies have been derived in this subject. Recently, the writer analyzed the nonlinear vibration problems of thin shallow shells using an iterative approach and Galerkin's method. The results were satisfactory for a large number of particular cases.

In this paper, the nonlinear vibration and dynamic instability of thin shallow conical shells subjected to periodic transverse and in-plane loads are investigated. The Marguerre's type dynamic equations used for the analysis of shallow shells are solved by Galerkin's method resulting a system of total differential equations in the time functions, Duffing and Mathieu equations, from which the various kinds of nonlinear vibration and dynamic instability are determined by using numerical methods. Numerical results are presented for axisymmetric vibrations and dynamic instabilities of shallow conical shells with (a) clamped and (b) supported edge conditions. As numerical examples, nonlinear

vibration frequencies and instability regions for shell are determined. The effects of static load as well as static snap-buckling on the instability are also investigated.

BASIC EQUATIONS AND BOUNDARY CONDITIONS

We will consider a shallow conical shell with thickness h , base circle radius a and height of arch f , subjected to the uniformly distributed edge forces N and normal pressure q as shown in Fig.1. The Marguerre's dynamic equations may be given by following equation form:

$$\frac{1}{r} \frac{\partial}{\partial r} \{ r [D \frac{\partial}{\partial r} (\frac{\partial^2 w}{\partial r^2} + \frac{\nu}{r} \frac{\partial w}{\partial r})] \} + \frac{1}{r} \frac{\partial}{\partial r} [D(1-\nu) (\frac{\partial^2 w}{\partial r^2} - \frac{1}{r} \frac{\partial w}{\partial r})] + \rho h \frac{\partial^2 w}{\partial t^2} = q(t) + \frac{1}{r} \frac{\partial}{\partial r} [r N_r \{ \frac{\partial (w+z_0)}{\partial r} \}], \tag{1a}$$

$$\frac{\partial}{\partial r} \{ r (\frac{\partial (r N_r)}{\partial r} - \nu N_r) \} - N_r + \nu \frac{\partial (r N_r)}{\partial r} = - \frac{Eh}{2} \{ (\frac{\partial w}{\partial r})^2 + 2 \frac{\partial w}{\partial r} \frac{\partial z_0}{\partial r} \} \tag{1b}$$

In these expressions, $D = Eh^3 / 12(1 - \nu^2)$ is the flexural rigidity of the shell, E, ν and ρ are Young's modulus, Poisson's ratio and mass density, respectively. The incremental strain-deflection relationship is given by

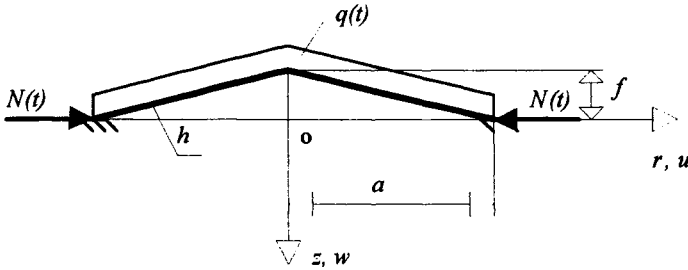


Fig. 1 Geometric relations of shallow conical shell

$$\frac{\partial (r \epsilon_r)}{\partial r} - \epsilon_r + \frac{1}{2} (\frac{\partial w}{\partial r})^2 = 0 \tag{2}$$

while the relations between the incremental displacements and bending moments are given by

$$M_r = -D (\frac{\partial^2 w}{\partial r^2} + \frac{\nu}{r} \frac{\partial w}{\partial r}), \quad M_\theta = -D (\frac{1}{r} \frac{\partial w}{\partial r} + \nu \frac{\partial^2 w}{\partial r^2}) \tag{3a,b}$$

The nonlinear incremental strains in the radial and tangential directions are given by

$$\epsilon_r = \frac{\partial u}{\partial r} + \frac{1}{2} (\frac{\partial w}{\partial r})^2, \quad \epsilon_\theta = \frac{u}{r} \tag{4}$$

In the following equations nondimensional notation is introduced. We definite

$$\left. \begin{aligned} x = \frac{r}{a}, \quad W = \sqrt{12(1-\nu^2)} \frac{w}{h}, \quad p = [12(1-\nu^2)]^{\frac{3}{2}} \frac{qa^4}{Eh}, \\ S = 12(1-\nu^2) \frac{N_r a^2}{Eh^3} x, \quad \tau = \frac{h}{a^2 \sqrt{12(1-\nu^2)}} \sqrt{\frac{E}{\rho}} t \quad \text{and} \quad K = \sqrt{12(1-\nu^2)} \frac{f}{h} \end{aligned} \right\} \tag{5}$$

The governing equations are given in a form via:

$$\left(\frac{\partial^2}{\partial x^2} + \frac{1}{x} \frac{\partial}{\partial x}\right)\left(\frac{\partial^2 W}{\partial x^2} + \frac{1}{x} \frac{\partial W}{\partial x}\right) + \frac{\partial^2 W}{\partial \tau^2} = p(\tau) + \frac{1}{x} \left\{S \frac{\partial^2 W}{\partial x^2} + \frac{\partial S}{\partial x} \left(\frac{\partial W}{\partial x} + K\right)\right\} \quad (6a)$$

$$\frac{\partial^2 S}{\partial x^2} + \frac{1}{x} \frac{\partial S}{\partial x} - \frac{S}{x^2} = -\frac{1}{2x} \left(\frac{\partial^2 W}{\partial x^2} + 2 \frac{\partial W}{\partial x} K\right) \quad (6b)$$

Concerning the boundary conditions for the problems, the following two cases will be considered at $x = 0$ and 1 .

S: $W|_{x=1} = \left(\frac{\partial^2 W}{\partial x^2} + \frac{\nu}{x} \frac{\partial W}{\partial x}\right)|_{x=1} = 0, \quad S|_{x=1} = S_s, \quad S|_{x=0} - \text{finite} \quad (7)$

C: $W|_{x=1} = \frac{\partial W}{\partial x}|_{x=1} = 0, S|_{x=1} = S_s, S|_{x=0} - \text{finite} \quad (8)$

In these expressions, S and C correspond to the simply supported and clamped cases, respectively. The problem consists in the finding limiting values of nonlinear natural frequencies, the forced vibration response and dynamic instability behavior for which the basic equations have some solutions under the given loading and boundary conditions.

METHODS OF SOLUTION

An approximate solution is obtained by assuming the nonlinear vibrations to have the same spatial shape, i.e.,

$$W(x, \tau) = T(\tau)Y(x) \quad (9)$$

or $W(x, \tau) = T(\tau)(1 - a_1 x^2 + a_2 x^4) \quad (10)$

and boundary conditions (7, 8) then yield

C: $a_1 = 2, \quad a_2 = 1 \quad (11)$

and S: $a_1 = \frac{6 + 2\nu}{5 + \nu}, \quad a_2 = \frac{1 + \nu}{5 + \nu} \quad (12)$

Substituting expression (9) or (10) in equation (8b), integrating the resulting equation and making use of boundary conditions (6) or (7) yields

$$S(x) = -\frac{1}{180x} (30T^2 a_2^2 x^8 - 60T^2 a_1 a_2 x^6 + 42T^2 a_1^2 x^4 + 48TKa_2 x^3 - 120TKa_1 x^3 + 3T^2 a_1^2 x^3) + x(S_s + \frac{1}{6}T^2 a_2^2 - \frac{1}{3}T^2 a_1 a_2 + \frac{1}{4}T^2 a_1^2 + \frac{4}{15}TKa_2 - \frac{2}{3}TKa_1) \quad (13)$$

Substituting $W(x, \tau)$ and $S(x)$ from equations (10) and (13) into the equation of motion (8a) and applying the Galerkin's procedure (multiplying both sides by $xW(x, \tau)$ and integrating from $x=0$ to 1), one obtains the following equation

$$A_1 \frac{d^2 T}{d\tau^2} + \{A_2 + A_3 S_s(\tau) + A_4 K^2\} T + A_5 K T^2 + A_6 T^3 = A_7 p(\tau) + A_8 S_s(\tau) K \quad (14)$$

where, $A_1, A_2, A_3, A_4, A_5, A_6, A_7$ and A_8 are the functions of a_1 and a_2 . Some numerical results for these are listed in Table 1.

TABLE 1
Value of functions A_1-A_8 ($\nu = 0.3$)

	A_1	A_2	A_3	A_4	A_5	A_6	A_7	A_8
C	0.1000	10.667	-3.333	0.1689	-0.3278	0.1429	0.1667	0.5333
S	0.1472	3.6037	-3.144	0.1228	-0.2162	0.0867	0.2296	0.6340

NUMERICAL RESULTS

The responses for different static and dynamic cases are obtained as follows.

1. **Static snap-through buckling:** When $S_s = 0$, the snap-buckling response is obtained from equation (14) by setting $\ddot{T} = S_s = 0$, to yield

$$P = \frac{1}{A_7} \{ (A_2 + A_4 K^2) T + A_5 K T^2 + A_6 T^3 \} \tag{15}$$

The snap-through buckling load p_{cr} is given by

$$K_{cr} = \sqrt{\frac{3A_2 A_6}{A_5^2 - 3A_4 A_6}}, \quad T_{p_{cr}} = -\frac{A_5 K_{cr}}{3A_6}, \tag{16}$$

$$p_{cr} = \frac{1}{A_7} \{ (A_2 + A_4 K_{cr}^2) T_{p_{cr}}^2 + A_5 K_{cr} T_{p_{cr}}^2 + A_6 T_{p_{cr}}^3 \}$$

and the numerical results are listed in Table 2.

TABLE 2
The snap-through buckling loads

	K_{cr}	$T_{p_{cr}}$	p_{cr}
Clamped edge	11.41238498	8.728997049	570.2533343
Supported edge	9.230984567	6.485637082	427.6700267

These results are the same as one of author's in reference.

2. **Free non-linear vibration :** The free nonlinear vibrations are governed by

$$\ddot{T} + \omega_0^2 \left\{ \left(1 + \frac{A_4}{A_2} K^2 \right) T + \frac{A_5}{A_2} K T^2 + \frac{A_6}{A_2} T^3 \right\} = 0 \tag{17}$$

where ω_0 is the dimensionless linear frequency, which is $\omega_0 = \sqrt{A_2 / A_1}$. The ratio of nonlinear frequency ω_N and linear ω_0 is given by

$$\frac{\omega_N}{\omega_0} = \lim_{T_1 \rightarrow T_0} \frac{2\pi}{4 \int_0^{T_1} \frac{dT}{\sqrt{\left(1 + \frac{A_4}{A_2} K^2 \right) (T_0^2 - T^2) + \frac{2A_5}{3A_2} K (T_0^3 - T^3) + \frac{A_6}{4A_2} (T_0^4 - T^4)}}} \tag{18}$$

and the nonlinear period f_N is given by $f_N = \frac{1}{2\pi} \omega_N$ or

$$f_N = \lim_{T_1 \rightarrow T_0} \frac{\omega_0}{4 \int_0^{T_1} \sqrt{\left(1 + \frac{A_4}{A_2} K^2\right) (T_0^2 - T^2) + \frac{2A_3}{3A_2} K (T_0^3 - T^3) + \frac{A_6}{2A_2} (T_0^4 - T^4)}} dT} \tag{19}$$

The formulas (18) and (19) could be expressed in terms of the elliptic integral of the first kind. The numerical results of nonlinear frequencies and periods are listed in Table 3 and Table 4.

TABLE 3

$\frac{\omega_N}{\omega_0}$ ($\nu = 0.3, S_s = 0$) for conical shells

T_0	0.5	1.0	2.0	3.0
C: K = 0	1.00253	1.00788	1.02190	1.04577
K = 5	1.16954	1.16265	1.10642	1.06384
K = 10	1.58724	1.54114	1.45873	1.38150
S: K = 0	1.00630	1.01811	1.04192	1.08320
K = 5	1.32030	1.28252	1.19672	1.12318
K = 10	2.04734	1.99708	1.87193	1.75179

TABLE 4

$f_N = () \omega_0$ for conical shells

T_0	0.5	1.0	2.0	3.0
C: K = 0	0.159558	0.160408	0.162641	0.166439
K = 5	0.186139	0.185042	0.176092	0.169316
K = 10	0.252618	0.245279	0.232164	0.219873
S: K = 0	0.160158	0.162038	0.165826	0.172397
K = 5	0.210133	0.204120	0.190464	0.178759
K = 10	0.325845	0.317846	0.297927	0.278806

The free nonlinear vibrating solution of equation (17) is shown in Fig.2 and Fig.3. From equation (18), we have the following statement of conservation of energy:

$$\frac{1}{2} \dot{T}^2 = H - F(T) \tag{20}$$

and
$$F(T) = \omega_0^2 \left\{ \left(1 + \frac{A_4}{A_2} K^2\right) \frac{T^2}{2} + \frac{A_3}{3A_2} K T^3 + \frac{A_6}{4A_2} T^4 \right\} \tag{21}$$

where, H is the constant determined from the initial conditions and is the energy level. When $K \leq K_0$ (C: $K_0 = 22.52$, S: $K_0 = 18.58$), the case of $F(T)$ has the stable equilibrium state as indicated in Fig. 4.

3. Forced non-linear vibration: We now consider the conical shell are contiguously excited. In this paper, two types of excitations are considered: (a) $p(\tau) \neq 0, S_s = 0$ and (b) $p(\tau) \neq 0, S_s = S_s(\tau)$. (a) The excitation appears as an inhomogeneous term in the equation governing the motion of the shell. The basic equation reduces a kind of Duffing equation:

$$\ddot{T} + \omega_0^2 \left\{ \left(1 + \frac{A_4}{A_2} K^2\right) T + \frac{A_3}{A_2} K T^2 + \frac{A_6}{A_2} T^3 \right\} = p_0 \cos \Omega \tau \tag{22}$$

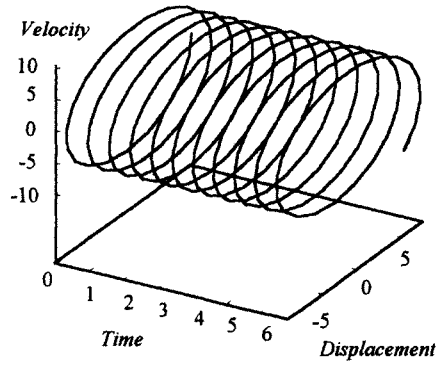


Fig. 2 Free vibration of conical shell ($K = 5, S_s = 0$)

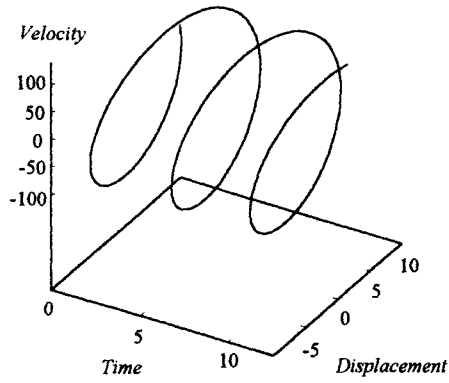


Fig.3 Free vibration of conical shell ($C, S_s = S_0$)

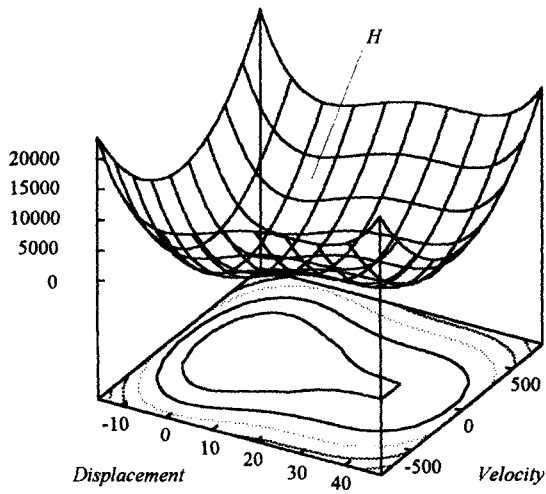


Fig.4 The energy level H of stable equilibrium state ($K_0 = 22.52$)

The equation (22) could be rewritten as follows:

$$\begin{aligned} \dot{T}_1 &= \omega_0 T_2, \\ \dot{T}_2 &= -\omega_0 \left\{ \left(1 + \frac{A_4}{A_2} K^2\right) T_1 + \frac{A_5}{A_2} K T_1^2 + \frac{A_6}{A_2} T_1^3 \right\} + \frac{P_0}{\omega_0} \cos \Omega \tau \end{aligned} \quad (23)$$

The initial conditions are as follows:

$$T|_{\tau=0} = T_0, \quad \dot{T}|_{\tau=0} = 0 \quad (24)$$

or
$$T_1|_{\tau=0} = T_0, \quad T_2|_{\tau=0} = 0 \quad (25)$$

We use a kind of *Longe-Kutta Method* to solve above Duffing equation. When $\Omega = \frac{1}{3} \omega_0$, the result is shown in Fig. 5.

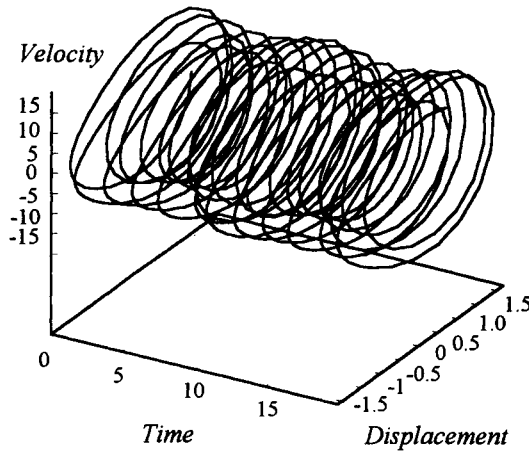


Fig.5 Forced vibration of conical shell ($\Omega = \frac{1}{3} \omega_0$)

(b) The excitations appear as coefficients in the governing differential equation. We use Mettlet's result to analyze problem. When $\omega_0 = \varpi$ (main resonance), there is a kinetic snap-through. Otherwise, $\omega_0 = m\varpi$ (m is integer), these are parametrically excited vibrations and there are some instability regions.

$$\ddot{T} + \omega_0^2 \left\{ \left(1 + \frac{A_4}{A_2} K^2 + \frac{A_3}{A_2} S^* \cos \varpi \tau\right) T + \frac{A_5}{A_2} K T^2 + \frac{A_6}{A_2} T^3 \right\} = 0 \quad (26)$$

The equation (25) can be rewritten as follows:

$$\ddot{T} + \omega_0^2 \left[\left(1 + \frac{A_4}{A_2} K^2\right) T + \frac{A_5}{A_2} T^2 \right] + \frac{A_6}{A_1} T^3 + \frac{A_3}{A_1} T S^* \cos \varpi \tau = 0 \quad (27)$$

Since here the resonance coefficient A_3 / A_1 is non-zero, the general theory predicts that a main resonance must occur if $\varpi = \omega_0$ and a subharmonic resonance of order 2 with $\varpi = 2\omega_0$, and they yield the following relation

$$\frac{\omega}{\omega_0} = 1 + \frac{A_4}{A_2} K^2 + \frac{3A_6}{8A_1} \frac{1}{\omega_0^2} Q^2 \mp \frac{A_3 S^*}{2A_1} \frac{1}{\omega_0^2} \quad (28)$$

Eq. (28) indicates that an increasing load S^* causes an increment of the amplitude Q , until a point with a horizontal tangent line is reached. Then with further increment of S^* the Q jumps to a higher value. This is an analogy to the static snap-through, therefore one calls it kinetic snap-through. By analogy with theory of static stability, the two points where the solution $Q \neq 0$ branch off from the solution $Q = 0$ are called bifurcation points and kinetic bifurcations. The bifurcation points are listed in Tables 6a,b and 7a,b. But as it has been shown, the forced vibrations and parametrically excited vibrations show no clear distinction if one excludes main resonance.

CONCLUSION

This paper has presented a brief look at the nonlinear vibration and dynamic stability problems of shallow conical shell. The results are also given for the static snap-through buckling, free nonlinear vibration and forced nonlinear vibration which includes two types of excitations.

ACKNOWLEDGMENT: *This project was supported by Shanghai Science Fund for Returning Scholars.*

REFERENCES

- Chang, W. P. and Wan, S. M., (1986), Thermomechanically coupled nonlinear vibration of plates, *International Journal of Nonlinear Mechanics*, **21**, 1986, 375-389.
- Chia, C. Y. and Chia, D. S., (1992), Nonlinear vibration of moderately thick anti-symmetric angle-ply shallow spherical shell, *Computers and Structures*, **44**, 797-805.
- Chia, C. Y., (1985), Nonlinear vibration of anisotropic rectangular plates with nonuniform edge constraints, *Journal of Sound and Vibration*, **101**, 1985, 539-550.
- Denisov, V. N. and Zhinzher, N. I., (1985), Asymptotic method in the problem of nonlinear vibrations of rectangular isotropic shells, *Mechanics of Solids*, **20**, 142-148.
- Dumir, P.C., (1986), Nonlinear vibration and post-buckling of isotropic thin circular plates on elastic foundations, *Journal of Sound and Vibration*, **107**, 1986, 253-263.
- Evansen, D. A., (1967), Nonlinear flexural vibrations of thin-walled circular cylinders, *NASA TND-4090*.
- Goncalves, P. B. and Batista, R. C., (1988), Nonlinear vibration analysis of fluid-filled cylindrical shells, *Journal of Sound and Vibration*, **127**, 133-143.
- Herrmann, G., (1965), *Dynamic stability of structures*, Proc. of IC., Oct. 1965, Pergamon Press.
- Kornecki, A. (1966), Dynamic stability of truncated conical shells under pulsating pressure. *Israel J. Techn.* **4**, 1966, 110.
- Ramachandran, J. (1976), Large amplitude vibrations of shallow spherical shell with concentrated mass, *Journal of Applied Mechanics*, **43**, 2, 363-365.
- Tani, J. (1976), Influence of deformations prior to instability on the dynamic instability of conical shells under periodic axial load, *Journal of Applied Mechanics*, **43**, 1, 87-91.
- Tsai, C. T. and Palazotto, A. N., (1989), On the finite element analysis of nonlinear vibration for cylindrical shells with high-order shear deformation theory, *International Journal of Non-linear Mechanics*, **24**, 1989, 127-137.
- Ye, Z. M. (1997), The nonlinear vibration and dynamic instability of thin shallow shells, *Journal of Sound & Vibration*, **202**, 3, 303-311.

EVALUATION OF THE PRINCIPAL STRESSES IN A DEAERATOR VESSEL OF A THERMOELECTRIC POWER PLANT

N. S. Maia¹; E. B. Medeiros² and T. R. Mansur¹

¹Comissão Nacional de Energia Nuclear (CNEN)/Centro de Desenvolvimento da Tecnologia Nuclear (CDTN)/Supervisão de Ensaios e Metrologia (AT1), Belo Horizonte, Brasil

²Departamento de Engenharia Mecânica da Universidade Federal de Minas Gerais (UFMG), Belo Horizonte, Brasil

ABSTRACT

This paper addresses the problem of stress evaluation in a typical deaerator operating in a thermoelectric power plant. The stress analysis problem was initially numerically evaluated, and then monitored by means of a strain gauge set-up. The main results presented clearly indicate the need for constant monitoring, since this experience has shown that deaerator vessels can sometimes operate outside the original design condition.

KEYWORDS

Deaerator, Experimental Stress Analysis, Numerical Simulation, Strain Gauge, Structural Integrity, Thermoelectric Power Plant.

INTRODUCTION

Deaerator vessels operate in conditions which vary between extremes of temperature, pressure, and simultaneously with water and steam. As a consequence, cyclic stresses develop in the vessel structure and can also be affected by weather exposure. Additionally, a power plant cannot normally be stopped for inspection of one of its pressure vessels, since energy "blackouts" or even more serious consequences would certainly take place. The resulting engineering problem is complex, requiring considerable skill and good judgement.

Among the several pressure vessels used in a thermoelectric power plant, the deaerator vessel can be mentioned as one of the components that introduces some of the biggest problems of variation in the operation conditions, mainly during the start up of the system.

The function of the deaerator vessel in the cycle of a steam plant is to reduce oxygen and other dissolved gases in the feedwater to acceptable levels.

Severe oxygen contamination can occur in a boiler feedwater as a consequence of mechanical problems in deaerators, feedwater pumps, turbine gland seals and systems operating under vacuum. Incomplete deaeration can be caused by many factors, including improper venting, operational changes that cause an influx of cold makeup water, improperly aligned trays, plugged or broken water spray nozzles and operation in a temperature gradient different from specifications.

The deaerator vessel of the thermoelectric power plant of CEMIG in Juatuba/Minas Gerais/Brazil has a length of about 16,400 mm and external diameter of 3,200 mm. The temperature of the deaerator vessel varies between 125 and 152°C, depending on the operation pressure that varies between 1.8 and 4.0 atm.

Good performance of deaerators year after year has causing sometimes monitoring and inspection programs to be forgotten. However, several problems can result from misoperation and lack of inspection of such equipment. The January 1983 catastrophic failure of a deaerator in southeastern United States has called attention to this point. The subsequent detection of cracks in numerous deaerators throughout the United States and Canada and the identification of corrosion fatigue as the likely cause of the cracking highlighted the need to take this problem into account and to identify the operating and water chemistry parameters that may influence deaerator deterioration [1].

To avoid this type of failure to occur it is necessary to know the behavior of the deaerator vessel during the operation.

The stress analysis problem was initially numerically evaluated, being used the computational code ANSYS, and than monitored by means of a strain gauge set-up.

EXPERIMENTAL STRESS ANALYSIS TECHNIQUES

The experimental stress analysis can be used for evaluating the results obtained by the employment of experimental techniques to measure strain, displacements or stresses present in equipment subject to several types of loads, static or dynamic [2]. These techniques can be divided into two groups:

1. "Global field": it allows measuring (generally with smaller resolution) the distribution of deformations and stresses in a great area of the structure. Photoelasticity, Fragile Varnish, and Moiré are examples of such techniques.
2. "Punctual": it is used to study specific points of the structure. Strain gauge techniques use strain gauges of electric resistance to measure deformations. The strain gauge techniques are based on the variation of a wire electric resistance when strained. During the experiments, the strain gauge has to be perfectly bonded to the surface of the sample, so that the deformations can be transmitted without attenuations.

Besides of the cost, a great advantage of the electric resistance strain gauge is that it could be installed in equipment working under real operational conditions. Therefore the measured strains are the true strains present during the operation of the structure [3].

To identify the areas of larger solicitations and, therefore, of larger interest for bonding strain gauges, a numerical simulation was made at room temperature. The computational code ANSYS, that uses finite

elements was the tool used for numerical simulation of the vessel. Ten points for monitoring were selected. In this simulation it was assumed that the structural integrity of the deaerator is guaranteed, without the presence of cracks, corrosion or residual stresses [4]. In Figure 1 a drawing of the deaerator vessel is shown, as well as the location of the monitored points.

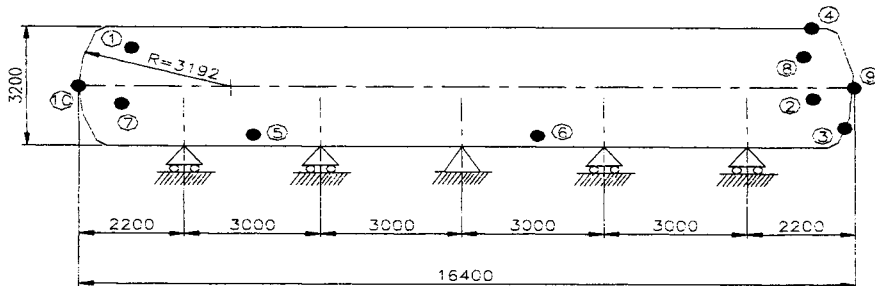


Figure 1 - Drawing of the deaerator vessel and the location of the monitored points in "mm".

To determine the stress state at these points of the deaerator it was necessary to measure strains in three directions, using rectangular rosetts, once the prior directions of the principal stresses were not known. Figure 2 exhibits the disposition of the strain gauges in each monitored point.

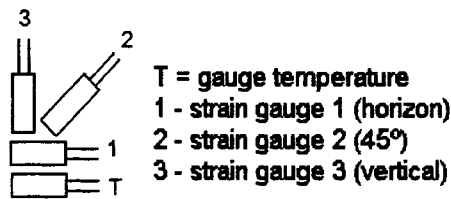


Figure 2 - The disposition of the strain gauges in each monitored point.

Each monitored point has a rectangular roset and a gage of temperature. The temperatures were measured using gages of temperature, manufactured with the same technique for manufacturing the strain gage. The difference is in the fact that the alloy of which the gage of temperature is manufactured is insensitive to mechanical deformation. They are only sensitive to temperature variation.

EXPERIMENTAL PROCEDURE

In the monitored points, the thermal protection that involves the deaerator was removed and initiated the preparation of the surface for bonding of the strain gauges following procedures [5, 6] and manufacturer recommendations.

The excitement of the Wheatstone bridges was obtained through a source of conventional continuous voltage and the correspondent read unbalance was sent to the multiplex through a transmitter of 4 to 20 mA. The collection and storage of the read unbalances were obtained through specific software for data acquisition, developed in CDTN (Center of Development of the Nuclear Technology).

The monitoring of each point can be visualized in the diagram block presented in Figure 3.

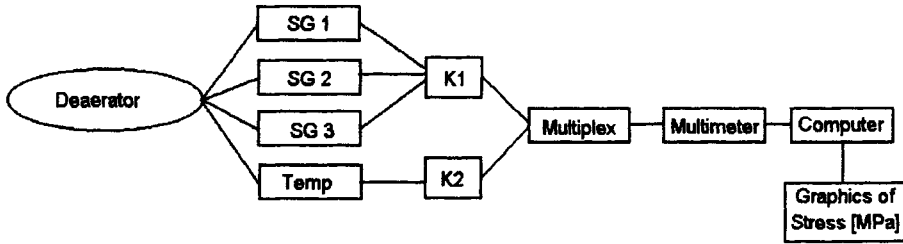


Figure 3 - Block diagram for each monitored point.

The deaerator strains were initially measured at room temperature and calculated the principal stresses to aid the refinement of the mesh used in the numerical simulation.

Parallel to the tests a new simulation of the deaerator behavior will be made at a temperature of 152°C, in order to compare with the obtained results and to supply good feedback for the numerical simulation.

RESULTS

Using specific procedure for strain gauge technique [7, 8], the values of the principal stresses in each monitored point were determined. The results obtained at room temperature through the numeric simulation by ANSYS are presented in Figures 4, 5 and 6.

Figure 4 shows the global stress field in the deaerator submitted to a water height of 2.4 m and a pressure of 4 atm; in Figure 5 the values of principal stresses are presented for a water height of 2.4 m and 2 atm of pressure; in Figure 7 the values of the principal stress are presented for a water height of 2.4 m and 4 atm of pressure for the points to be monitored.

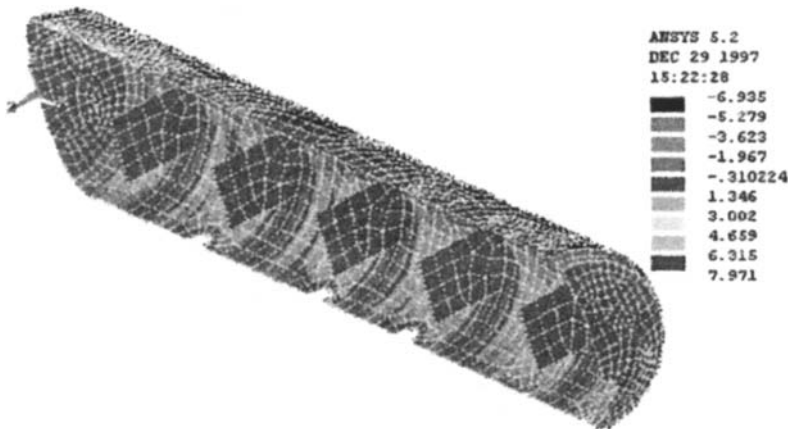


Figure 4 – Global stress field numerically evaluated through ANSYS, data referred to the axis X, showing the internal constrains, for 2.4 m of height of water and 4 atm of pressure.

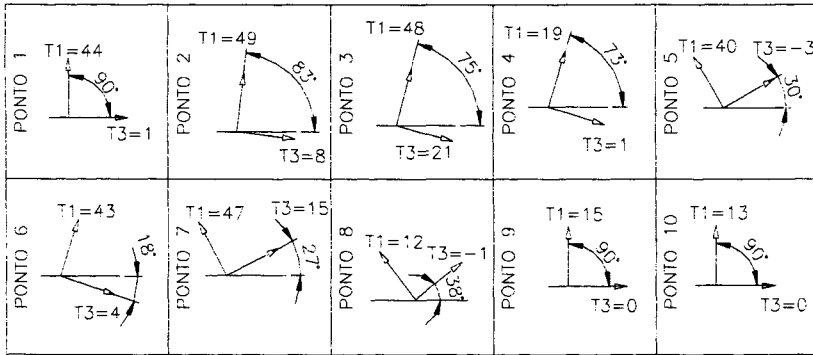


Figure 5 - Behavior of the principal stress in MPa for points 1 to 10 of the deaerator for 2.4 m of height of water and 2 atm of pressure, at room temperature, numerically evaluated by ANSYS ($T_i = \sigma_i$).

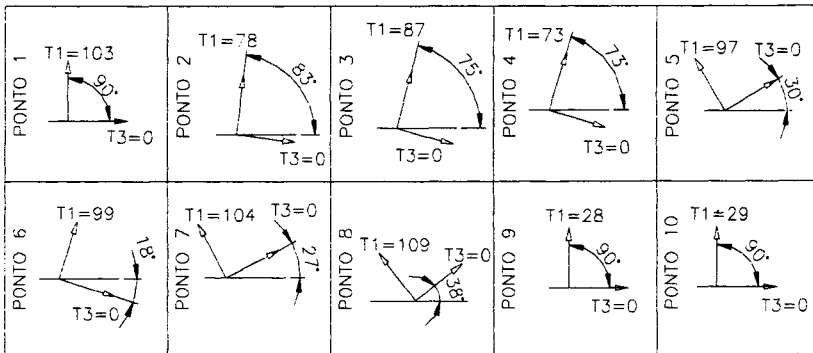


Figure 6 - Behavior of the principal stresses in MPa for points 1 to 10 of the deaerator for 2.4 m of height of water and 4 atm of pressure, at room temperature, numerically evaluated by ANSYS ($T_i = \sigma_i$).

The results obtained at room temperature, using strain gauge are presented in Figures 7 and 8 and the data obtained during in service operation of the thermoelectric plant are presented in Figure 9.

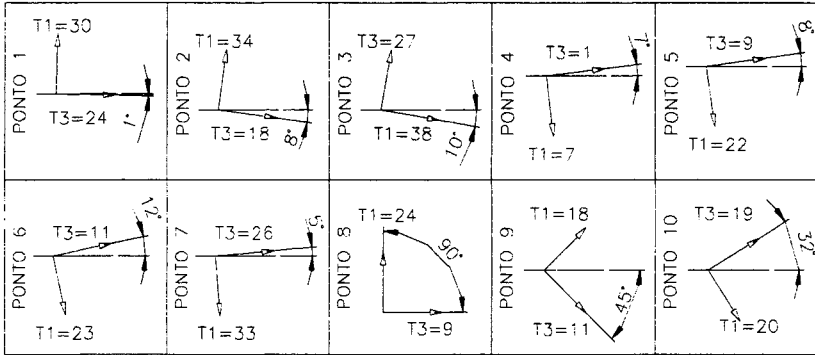


Figure 7 - Behavior of the experimental principal stress in MPa for points 1 to 10 of the deaerator for 2.4 m of height of water and 2 atm of pressure obtained through compressed air at room temperature ($T_i = \sigma_i$).

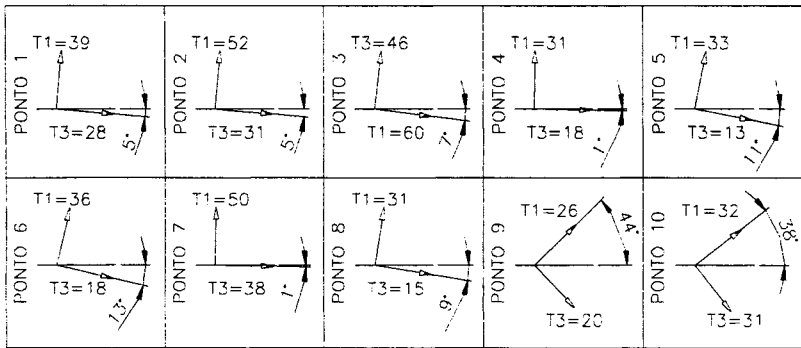


Figure 8 - Behavior of the experimental principal stresses in MPa for points 1 to 10 of the deaerator for 2.4 m of height of water and 3 atm of pressure obtained through compressed air at room temperature ($T_i = \sigma_i$).

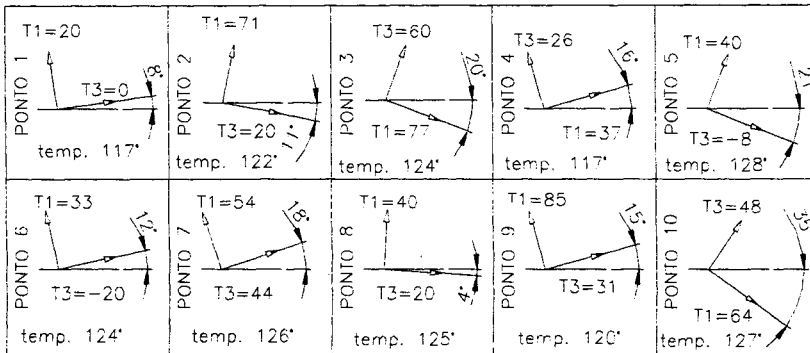


Figure 9 - Behavior of the experimental principal stresses in MPa for points 1 to 10 of the deaerator in service conditions with the power plant supplying 125 MW, for a pressure of approximately 4 atm ($T_i = \sigma_i$).

CONCLUSIONS

From the analysis of Figures 5 and 6, it can be verified that in the numerical simulation, a change in the behavior of the minimum principal stresses, for the pressure of 4 atm, is observed in all points where the minimum principal stresses is zero, what suggests a uniaxial stress state, differently from the biaxial stress state suggested by the simulation whit 2 atm. No alteration of the position of the principal stresses could be verified, although the pressure has been duplicated.

From the analysis of Figures 5 and 7 a variation of the results obtained by the numerical simulation and the experimental ones can be observed. This variation suggests a more detailed verification of the boundary conditions imposed to the model and a refinement of the used mesh.

From the analysis of Figures 7 and 8 is was observed that the behavior of the pressure increment is not linear whit the principal stresses increment, besides the variation of the direction of the angles of the principal stresses, demonstrating the existence of restrictions that are not evident in the drawing of the deaerator.

The experimental stress analysis using strain gauge has shown perfectly adapted for acquisition of the deformations/stresses present in the deaerator vessel and it does not interfere in thermoelectric's operation.

The deaerator vessel continues to be monitored for verification of the principal stresses in more severe conditions of operation, giving continuity to the work of Structural Integrity Evaluation.

It can be observed in Figure 9 that during the in service operation of thermoelectric power plant the values of the temperatures have the same magnitude in the monitored points.

It can be verified through Figures 6, 8 and 9 a change of the point of maximum solicitation. For the simulation using 4 atm of pressure and at room temperature, maximum solicitation is found in point 8. In the experimental measurements at room temperature using 3 atm of pressure, the point of maximum solicitation is point 2 and for the in service operation condition the point 9 is the one of maximum solicitation.

REFERENCES

- [1] NACE - National Association of Corrosion Engineers (1990): *Recommended Practice for Prevention, Detection and Correction of Deaerator Cracking*.
- [2] Araújo, N. B. M.; Castro, S. T. (1996) *Garantia da Integridade Estrutural do Rotor da Turbina da Usina Hidrelétrica de São Simão para funcionamento em Potências Superiores à Nominal, 11º Congresso Brasileiro de Manutenção, 456-467, Belo Horizonte.*
- [3] Maia, N. S.; Lourenço, R.; Gomes, P. T. V.; Mansur, T. R. (1996): High temperature strain measurements, *Proceedings SPIE (The International Society for Optical Engineering) International Conference on Experimental Mechanics: Advances & Applications, 244-249, vol 2921, Singapore.*
- [4] Mourão, R. P.; Terra, J. L. (1995): Verificação Estrutural do Tanque Desaerador da Usina Termoeletrica de Igarapé, *Relatório de Progresso / CNEN.*
- [5] Avril J. (1974): *Encyclopedie Vishay D'Analyse Des Contraintes, Vishay-Micromesures.*
- [6] Mansur, T. R.; Di Lorenzo, R. F. (1995): Medição de Tensões em Tubulação submetida a Transientes de Pressão Interna e Temperatura, *X ENFIR, 389-392, Águas de Lindóia, São Paulo.*
- [7] Mansur, T. R.; Di Lorenzo, R. F.; Moraes, J. R. G. (1985): Correção de Medidas Extensométricas e Avaliação dos Erros nos Resultados Experimentais, *Nota Técnica / NUCLEBRÁS.*
- [8] Beer, F. P. (1982), *Resistência dos Materiais, McGraw-Hill.*
- [9] Maia, N. S.; Mansur, T. R. (1997): *.. Análise de tensões de um vaso desaerador em operação em usina termelétrica, III Congresso Ibero Americano de Engenharia Mecânica, 5-131, Cuba.*

GRATEFULNESS:

To the Supervision of Tests and Metrology and its *TEAM* for the support rendered in the installation of the strain gauges in field and in the interpretation / discussion of the obtained data as well as the made numerical simulation.

To CEMIG for giving us easy access to its physical facilities and the cooperation of its employees.

STRENGTH OF RETICULATED SHELLS DESIGNED BY SECOND-ORDER ELASTIC ANALYSIS

S. Kato¹, I. Mutoh² and Y. Matsunaga¹

¹Department of Architecture and Civil Engineering, Toyohashi University of Technology,
Tempaku, Toyohashi, Aichi, JAPAN

²Department of Architecture and Civil Engineering, Gifu National College of Technology,
Shinsei, Motosu, Gifu 501-0495, JAPAN

ABSTRACT

The paper is concerned with development of design procedure against buckling of reticulated shells, on the basis of numerical analysis and with evaluation of ultimate strength of the designed structures. For design of reticulated shells are presented two topics : (1) a second-order elastic analysis(SOA) to estimate additional bending moment effects on overall strength, (2) a second-order plastic hinge analysis(SOPHA), to evaluate overall load capacity of designed structures with a specific geometric imperfection and discuss reduction of ultimate strength from it for perfect geometries.

KEYWORDS

reticulated shells, buckling design procedure, second-order elastic analysis, second-order plastic hinge analysis, initial geometric imperfections, overall load capacity, ultimate strength

INTRODUCTION

Many studies have employed a second-order plastic hinge analysis(SOPHA) to develop prediction methods for ultimate strength of axially compressed members in frame structures by adopting a concept of an "equivalent" column slenderness, e.g. Galambos(1989). Authors have also adopted the

column slenderness concept to evaluate the ultimate strength of reticulated domes, Kato et al(1992) and cylindrical shell roofs, Kato et al(1995), by considering both of the shell-like buckling and material plasticity.

The present paper is concerned with evaluation of overall strength of reticulated shells designed by a second-order elastic analysis(SOA). The procedure, see Kato et al(1998), presented here for dimensioning member cross sections includes geometric nonlinearities, second-order effects to stresses and stiffness and shell-like buckling instability, by performing : (1) a linear static analysis to obtain fundamental stresses, (2)SOA but once, to estimate the P- Δ effects on the bending moment amplification due to pre-buckling deformations and the equivalent buckling slenderness ratio of reticulated shells, and (3)estimation of strength reduction for shell buckling due to geometric imperfections. In contrast to the procedure for beam-columns in frame buildings, e.g. Al-Mashary and Chen(1990), the effect of shell-like buckling on member strength reductions is needed to appropriately consider a “knock-down” factor as found in design recommendations for shell, e.g. by IASS(1979). Then the strength reduction due to a specific geometric imperfection is discussed in view of its influence of member section arrangements on the overall load capacity and collapse behavior.

PROCEDURE FOR DIMENSIONING MEMBERS

The approach for the procedure is illustrated, see Kato et al(1998) in detail, as follows. The parameters α_0 and γ in the Steps (6) and (7) for the procedure are adopted directly from the results in Kato et al(1998).

(1)Selection of a structural system with particular boundary condition; the member slenderness ratio with a reference member length, the nominal design load intensity and the load factor which leads to the ultimate design load P_{ult} .

(2)Preliminary selection of member size; the initial wall thickness t_0 for each member.

(3)Calculation of the structural characteristics of all the members based on the wall thickness and the member slenderness ratio λ_0 with the yield stress σ_f .

(4)Execution of a first-order elastic analysis to estimate axial forces N_d and the bending moments M_{dy} and M_{dz} about each axis of rotations, under the ultimate design load P_{ult} which is discussed later. Here a first-order elastic analysis means as follows, with the linear stiffness matrix $[K_L]$, displacements $\{d\}$ and forces $\{P_{ult}\}$:

$$[K_L] \{d\} = \{P_{ult}\} \quad (1)$$

(5)Execution of SOA, but once, to estimate the P- Δ effects of the nonlinear deformations on the reticulated shells under P_{ult} . The axial forces N_d^* and the bending moments M_{dy}^* and M_{dz}^* can be evaluated. Here, SOA means as follows, with the secant stiffness $[K_S]=[[K_L]+[K_G(N_d^*)]]$ in which $[K_G(N_d^*)]$ stands for the geometric stiffness under axial force N_d^* , and $\{d\}$, $\{P_{ult}\}$:

$$[[K_L] + [K_G(N_d^*)]] \{d\} = \{P_{ult}\} \quad (2)$$

The secant stiffness matrix is formulated through an exact solution to buckling equations for the three

dimensional beam-columns with the aid of stability functions and bowing effects.

(6) Estimation of the appropriate effective length factors, $K=(N_d/N_{cr}^{lin})^{1/2}$, or the “generalized slenderness” parameter for member design as follows, Kato et al(1992,1998).

$$N_{cr}^{lin}=N_d \{ |M_d^*-M_d| + |M_d| \} / |M_d^* - M_d| \tag{3}$$

$$M_d^*=(M_{dy}^2 + M_{dz}^2)^{1/2}, \quad M_d=(M_{dy}^2 + M_{dz}^2)^{1/2} \tag{4}$$

If N_{cr}^{lin} is greater than the Euler buckling load N_e for a member with a buckling length or $K=1$,

$$N_e=\pi^2 EI_p / l_0^2 =\pi^2 EA_p / \lambda_0^2 \tag{5}$$

where EI_p is the bending stiffness and EA_p is the axial stiffness, then N_{cr}^{lin} is replaced by N_e for the i -th member. The “generalized slenderness” parameter of the i -th member is given as below,

$$\Lambda=(N_p / N_{cr}^{lin})^{1/2} \tag{6}$$

which is used for estimation of the elastic plastic axial buckling strength ratio N_{cr}^{pl} / N_p of the member. In this study, an evaluation of N_{cr}^{pl} , with $N_p=A_p \times \sigma_f$, is based on the modified Dunkerley strength interaction formula as follows.

$$\Lambda^2 \times N_{cr}^{pl} / (\alpha_0 \times N_p) + (N_{cr}^{pl} / N_p)^2 = 1 \tag{7}$$

where α_0 is a knockdown factor to approximately represent the influence of shell-like nonlinearity and imperfection sensitivity. In this study, the magnitude of the factor α_0 is assumed 0.7 for cylindrical shell roofs and 0.6 for dome roofs, on the basis of the previous researches, Kato et al(1992,1996,1998).

(7) Modification of the wall thickness t based on both the strength interaction between the axial force and the bending moments, strength check Eqn(8), and the buckling strength, stability check Eqn(9).

$$\{ N_d / N_p \}^2 + \{ M_d^* / M_p \} = 1 \tag{8}$$

$$N_d / N_{cr}^{pl} \leq 1 \tag{9}$$

A note should be given here that Eqn(8) is applied to both of the tensioned and compressed members, however, Eqn(9) is applied to compressed members. For the members under so small stresses, the following design stresses as shown below are assumed based on a factor γ .

$$N_{d(min)} = \gamma \times N_{d(max)} \quad \text{where } N_{d(max)} = \text{Max}(|N_d|) \tag{10}$$

$$M_{d(min)} = \gamma \times M_{d(max)} \quad \text{where } M_{d(max)} = \text{Max}(|M_d|) \tag{11}$$

$$M_{d(min)}^* = \gamma \times M_{d(max)}^* \quad \text{where } M_{d(max)}^* = \text{Max}(|M_d^*|) \tag{12}$$

When the maximum values for stresses are detected at the tension-ring, the values are excluded in the case of the dome roofs with roller supports.

(8) If the wall thickness t is very close to the one in the previous calculation, the numerical procedure is stopped. Otherwise, calculations are repeated from Step(3) on the basis of the revised thickness until an enough convergence is reached.

ASSUMPTIONS

Geometric imperfection

In the previous studies, e.g. Kato et al(1992,1995,1996), an influence of geometric imperfections on the ultimate strength (buckling or collapse) has been discussed on the basis of certain modes and

maximum amplitude for initial imperfections, and summarized as the imperfection sensitivity as a function of magnitude parameters. The sensitivity is not so significant in case of reticulated shells constructed in geometric configurations to be designed in practice.

The mode of geometric imperfection is assumed for analytical model; particular eigenmode corresponding to minimum eigenvalue due to linear eigenvalue analysis applied to the overall structures. The maximum downward amplitude of imperfections is assumed : the magnitude parameter ε_g equals to 20% of an “equivalent” shell’s thickness t_e , which is defined: $t_e=2\sqrt{3}r_g$ with r_g of radius of gyration of pipe member.

The investigation of influences of geometric imperfections into collapse/buckling behaviors and strength evaluations will be followed, in cases of reticulated shells designed as (1)various cross sections by a second-order analysis(SOA), (2)average wall thickness of uniform size distribution to be modified to (1), (AVT) and (3)uniform wall thickness modified cross sections for SOA under the same self-weight as for SOA(CSW).

Ultimate design load

The loading is assumed in the present study to be proportional to gravity load and to have uniform distribution vertically downward, for simplicity, although it can be of other type; non-uniform or a combination of several loadings. The ultimate design load intensity w_{ultd} per unit area over reticulated shells, might be defined on the basis of the nominal design load w_d with the static safety (load) factor v_s . The magnitude v_s can be determined based on some recommendation or code, e.g. IASS(1979) , however, further discussion will be needed. The concentrated load for one node, corresponding to the tributary area over the length l_0 is given as below.

$$P_{ultd} = w_{ultd} \times \sqrt{3} l_0^2 / 2 \quad \text{where } w_{ultd} = v_s \times w_d \quad (13)$$

In the present study, an assumption of $w_{ultd}=3.92\text{kN/m}^2$, in case of cylindrical roofs and dome roofs, leads to $P_{ultd}=41.6\text{kN}$ and 400kN per each node, respectively.

Geometries of analytical models

We investigate the behavior of two types of reticulated shells: the cylindrical roof(braced barrel vault, BBV) with simply supports as shown in Fig.1, and the dome roof(braced dome, BD) with roller supports as shown in Fig.2. The grids are of the three-way, and the constituent members are assumed of tubular sections jointed rigidly at nodes with almost same length in their respective structures. The diameter d_0 and thickness t of pipe are defined as shown in Fig.3. The member slenderness ratio is defined as $\lambda_0=2\sqrt{2} l_0/d_0$, the reference member length being assumed by l_0 as mentioned before. The diameter is assumed constant for every member except the tension ring in case of dome roofs, although the diameter may change in the present procedure depending on stress distributions. The section parameters for the i -th member in the shells are calculated approximately as follows.

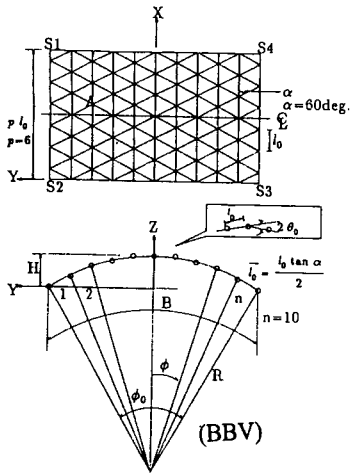


Fig.1 Geometry of cylindrical roof

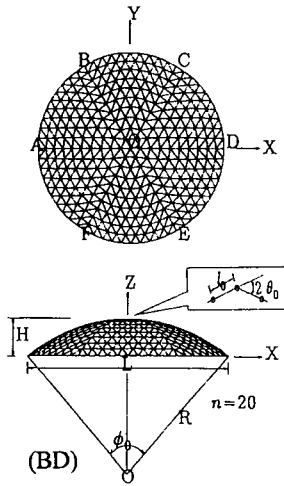


Fig.2 Geometry of dome roof

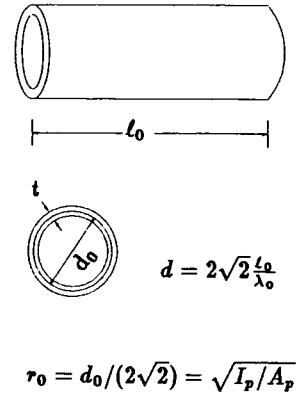


Fig.3 Cross section of pipe member

Table1 Geometry of analyzed cylindrical roofs

θ_0	B(cm)	H(cm)	R(cm)
3deg.	3031.1	387.96	2894.5
5deg.	3031.1	621.15	1736.7

Table2 Diameter of member cross section in cylindrical roofs

λ_0	20	40	60	80
d_0 (cm)	49.497	24.749	16.499	12.374

Table3 Geometry of analyzed dome roofs

θ_0	L(cm)	H(cm)	R(cm)
2deg.	20000.00	3639.70	1557.2

Table4 Diameter of member cross section in dome roofs

λ_0	60	80	100
d_0 (cm)	51.189	38.392	30.713

$$A_p = \pi d_0 t, \quad I_p = \pi d_0^3 t / 8; \quad N_p = \sigma_r A_p, \quad M_p = \sigma_r d_0^2 t \quad (14)$$

in which A_p, I_p, N_p and M_p are the section area, second moment of inertia, plastic axial resistant force, and plastic moment, respectively. In the present analysis a value σ_r of 23.52kN/cm² is adopted. The thickness of each member as a starting value t_0 is to be preliminary determined through the first-order elastic analyses.

The geometric parameters are p, n, ϕ_0 and θ_0 , meaning the panel number in the x-direction as shown in Fig.1, the number of subdivision in the circumferential direction, the open angle and the divided angle for the circular edge given by $\phi_0 = 2n\theta_0$, respectively. The values in the study are $p=6, n=10$ and θ_0, λ_0 with geometric parameters are listed in Tabs. 1 and 2.

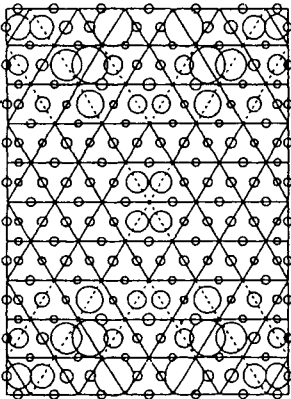
For BD as shown in Fig.2, the number of members along the meridian AOD is $n=20$ and the open angle ϕ_0 is 80degs., leading to $\theta_0=2$ degs. The geomtric parameters and λ_0 are listed as in Tabs.3 and 4. All the members have a constant diameter d_0 as same as those of the meridional members, except the tension ring. The diameter of the tension ring is assumed twice d_0 of the internal members.

NUMERICAL RESULTS

Distribution of wall thickness and strength checks by second-order plastic hinge analysis

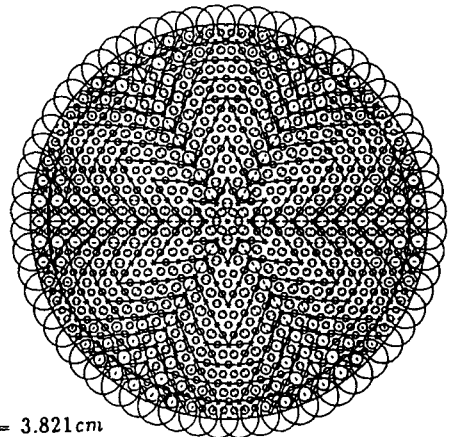
In this analysis, $\gamma=0.2$ and $\alpha_0=0.7$ in case of BBV, and $\gamma=0.5$ and $\alpha_0=0.6$ in case of BD are assumed, according to IASS(1979) for a knockdown factor. Examples of how the wall thicknesses of the members are determined based on the above procedure for SOA of perfect geometries are illustrated as in Figs. 4 and 5. The members denoted by solid lines are dimensioned by strength check, Eqn(8), on the other hand, the broken lines by stability check, Eqn(9), respectively. The circles on each member are normalized to the diameters by the member with the maximum wall thickness t_{max} .

The ultimate strength P_{cro}^{pl} at one node for BBV, which is determined as a limit point just after initial yieldings of member ends of specific member, is 42.33kN. The initial yielding load P_y is 39.88kN. As mentioned $P_{ult}=41.6$ kN, the designed BBV shows almost the same ultimate strength, but 1.75% higher. The P_{cro}^{pl} at one node for BD, which is determined as a limit point in a similar manner for BBV is 463.15kN. The designed BD shows a little higher strength by 15.7% than $P_{ult}=400$ kN. Such a difference in the ultimate strength will come out due to a particular combinations between γ and α_0 .



$\theta_0 = 5^\circ, \lambda_0 = 60, \gamma = 0.3$
 $t_{max} = 0.770\text{ cm}, t_{min} = 0.157\text{ cm}$

Fig.4 Wall thickness distribution(BBV)



$t_{ring} = 3.821\text{ cm}$
 $\theta_0 = 2^\circ, \lambda_0 = 60, \gamma = 0.5$
 $t_{max} = 1.376\text{ cm}, t_{min} = 0.691\text{ cm}$

Fig.5 Wall thickness distribution(BD)

Effect of geometric imperfection on overall load carrying capacity

The linear buckling modes for BBV and BD designed by SOA, are shown as in Figs.6 and 7, respectively. The linear buckling loads are summarized in Tab.5. The maximum amplitudes w_0 of geometric imperfection for BBV and BD are 40.4mm and 125.4mm, respectively. Both the value w_0

Table5 Linear buckling loads P_{cr}^{lin} (kN/node), and $(\cdot) = q$ (kN/m²)

	SOA	AVT	CSW
BBV	65.4 (6.17)	66.2 (6.25)	63.9 (6.03)
BD	909.0 (8.91)	943.5 (9.25)	1028.0 (10.08)

Note: BBV=Braced barrel vault, BD=Braced dome

Table6 Elastic plastic collapse load(kN) for BBV

	SOA	AVT	CSW
P_{cr0}^{pl}	42.3	30.5	29.4
P_{cr}^{pl}	36.5	28.6	27.5
$1 - \rho_{pl}$	13.70	6.05	5.92

Note: $\rho_{pl} = P_{cr}^{pl} / P_{cr0}^{pl}$ reduction ratio(%)

Table7 Elastic plastic collapse load(kN) for BD

	SOA	AVT	CSW
P_{cr0}^{pl}	463.2	329.0	420.7
P_{cr}^{pl}	376.1	364.6	397.3
$1 - \rho_{pl}$	18.8	6.95	5.56

Note: $\rho_{pl} = P_{cr}^{pl} / P_{cr0}^{pl}$ reduction ratio(%)

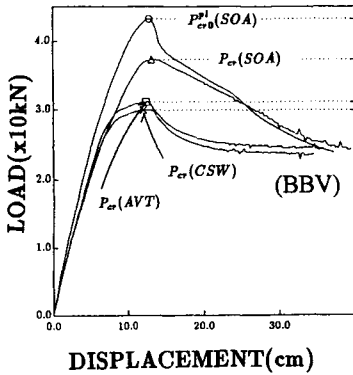


Fig. 8 Load-displacement curves

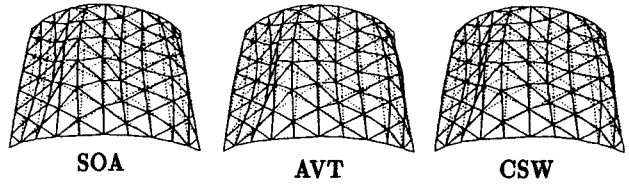


Fig.6 Linear buckling mode(BBV)

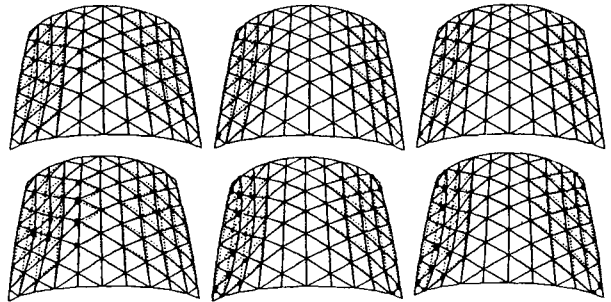


Fig.10 Plastic hinges development(BBV), top(P_{top}),bottom(P_{max})



Fig.7 Linear buckling mode(BD)

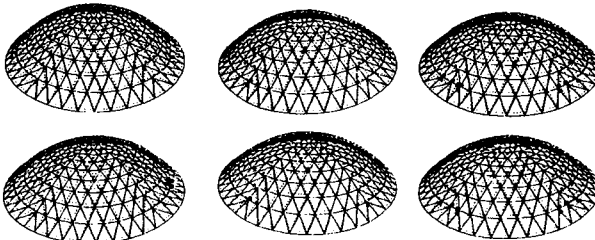


Fig.11 Plastic hinges development(BD), top(P_{top}),bottom(P_{max})

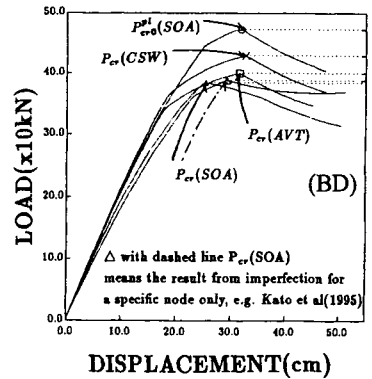


Fig.9 Load-displacement curves

correspond to 0.012 against the member length as well as to an “equivalent buckling half-wavelength”, Kato et al(1992,1995,1996). The linear buckling loads per node P_{cr}^{lin} for BBV and BV are 65.37kN and 909kN, respectively. And in Tabs.5 and 7 the results from a second-order plastic hinge analysis for the models of (1)SOA, (2)AVT and (3)CSW are summarized with reduction factors $(1 - \rho_{pl})$.

In Figs.8 and 9, the relationships between load and displacement for BBV and BD are depicted, respectively. From the corresponding collapse behaviors, which illustrate the development of plastic hinges and deformation modes as shown in Figs.9 and 10, characteristic differences in the ultimate strengths for each BBV and BD due to the difference of distribution of thickness can be observed. Almost the same reduction of 6 to 7% can be found in case of AVT and CSW for BBV and BD. However the results for SOA, show the reduction of 19% in case of BD, and of 14% in case of BBV. Insofar as the amount of reduction for both BBV and BD may be accounted, the knock-down factor α_0 tends to 0.5 by multiplying the reduction factor to the factor assumed in the procedure.

CONCLUSIONS

The paper is described that the effect of geometric imperfection on the overall load capacity of reticulated shells, BBV and BD, which are designed by SOA. There is a little sensitivity for shells with the member section arrangement: (1)SOA, (2)AVT and (3)CSW under a limit to the parameters, γ and α_0 , which may influence fundamental behaviors of reticulated shells including second-order bending displacements. In case of the maximum amplitude $w_0=0.2t_c$ of imperfection which has the mode of least eigenvalue, the shells designed by SOA show the imperfection sensitivity among others, AVT and CSW, but lesser strength reduction of 14% or 19% for BBV and BD, respectively.

References

- Al-Mashary,F. and Chen,W.F.(1990). Elastic Second-Order Analysis for Frame Design. *Journal of Constructional Steel Research* 1:5, 303-322.
- Galambos,T.V.(1988). *Guide to Stability Design Criteria for Metal Structures*. John Wiley & Sons.,NY.
- IASS(1979). *Recommendations for Reinforced Concrete Shells and Folded Plates*. IASS,Madrid.
- Kato,S. and Iida,M.(1995). Buckling Strength Estimation of Reticulated Cylindrical Shell Roofs with Rigid Joint under Uniform Loading. *Proc. Of IASS International Symposium*, Milano, 1, 587-594.
- Kato,S. and Mutoh,I.(1996). Influence of Local Imperfections on Buckling Strength of Reticulated Shells. *Journal of Structural Engineering*, JSCE, 42A, 147-158.
- Kato,S., Shomura,M.,Shibata,R. and Ueki,T.(1992). Estimation of Elasto-Plastic Buckling Loads for Reticular Domes on a Circular Plan. *Journal of Structure and Constructional Engineering*, AIJ, 439, 111-119(in Japanese).
- Kato,S., Matunaga,S. and Mutoh,I.(1998). Towards Design-by-Analysis for Reticulated Shells, *Proc. Of Structural Engineers World Congress*, San Francisco, CA (to be presented).

STRESSES IN ELASTIC CYLINDRICAL SHELLS UNDER WIND LOAD

Martin Pircher¹, Werner Guggenberger², Richard Greiner², Russell Bridge¹

¹School of Civic Engineering and Environment
University of Western Sydney, Nepean
PO Box 10, Kingswood, NSW 2747, Australia
²Institute of Steel, Timber and Shell Structures
Technical University Graz, Austria

ABSTRACT

Thin-walled shell structures of a circular cylindrical shape are widely used in structural engineering to serve in applications such as silos, tanks or chimneys. The design of such structures poses some considerable challenges to structural engineers, especially for non-axisymmetric load cases. Very often a comprehensive numerical analysis results in considerable expense and the vast amount of data which is typically generated makes it hard to understand the underlying load-carrying behaviour of the structure. The introduction of an engineering method to handle wind load on circular cylindrical thin-walled shell structures is the objective of this paper. Using the semi-membrane-concept, a series of diagrams was prepared to facilitate this task. The proposed method offers a quick way to generate critical section forces independently of the wind design code being used.

KEYWORDS

Cylinder, thin-walled, wind load, semi-membrane-concept, silo, tank, chimney

INTRODUCTION

Many aspects of the load carrying behaviour of cylindrical thin-walled shell structures are well understood and a vast theoretical background is available to describe their structural performance. Asymmetric loading conditions like wind loading are not an exception. Sophisticated computer programs, often based on the Finite Element Method, are readily available for the analysis of highly complicated load patterns on such shells. Even though these programs provide detailed results, one significant disadvantage of their usage cannot be denied. The results typically generated represent a number of influences but the principles underlying the load carrying behaviour are not clearly visible any more. An understanding of these principles is a prerequisite when improvements to the design of shell structures become necessary. Even basic verification checks of the achieved results prove impossible without this knowledge. As an alternative to the computer analyses which are often expensive,

approximate methods based on the simple membrane theory are available to the design engineer. These membrane solutions tend to neglect important features of the behaviour of the shell and therefore often produce unsatisfactory results. The method presented in this paper positions itself between these two extremes of complexity and simplicity. It is well suited as a tool in its own right to derive governing stress resultants. If a computer analysis is carried out, the presented diagrams serve as a quick means to check some of the derived results. All major contributing factors in connection with wind load cases are accounted for by the semi-membrane-concept (SMC) on which this paper is based. Analogies to beam theory exist, which facilitate a deeper understanding of the load-carrying behaviour of the cylindrical thin-walled shell. Improvements on cylindrical structures can therefore be made using the familiar concept of beam structures.

THE SEMI MEMBRANE CONCEPT

Linear elastic shell theory, using a full set of section forces to establish equilibrium, leads to a system of three-fourth order partial differential equations for the cylindrical shell. The nature of the considered load case allows the following simplifications in the initial equilibrium equations:

- (i) Circumferential strain is set to zero ($\varepsilon_\varphi = 0$).
- (ii) Axial and torsional bending stiffness are set to zero ($D_x = 0, D_{x\varphi} = 0$).

The resulting state of equilibrium therefore consists of all membrane forces plus circumferential bending (Figure 1). Forces, displacements and loading in the circumferential direction is then developed into a Fourier-analysis, reducing the original two-dimensional problem to a one-dimensional one. This results in the following system of two homogenous fourth order differential equations

$$\left[\frac{\partial^4}{\partial \xi^4} - k \frac{D_x}{D_{x\varphi}} m^2 (m^2 - 1)^2 \frac{\partial^2}{\partial \xi^2} + k \cdot m^4 (m^2 - 1)^2 \right] \begin{bmatrix} U_m \\ V_m \end{bmatrix} = \begin{bmatrix} 0 \\ 0 \end{bmatrix} \quad (1)$$

in which ξ is the normalised axial coordinate, D_x is the stiffness in axial direction and $D_{x\varphi}$ is the shear stiffness, m is the wavenumber of the Fourier-wave and k is given by

$$k = \frac{K_\varphi}{R^2 D_x} \quad (2)$$

in which K_φ is the circumferential bending stiffness. U and V are the displacements in the axial and tangential directions. Displacements in the radial direction W are coupled with V and can be computed by

$$W_m = -m \cdot V_m \quad (3)$$

A detailed discussion of the basic assumptions, the derivation and solution of the differential equations and a report of their usage in a computer program based on the deformation method can be found in the paper by Guggenberger & Pircher (1998).

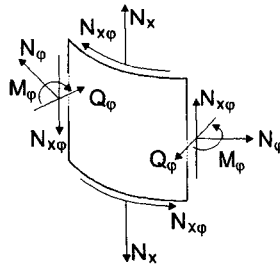


Figure 1 Reduced set of section forces used in the SMC

Similar approximations have been used in the investigation of the buckling of cylindrical shells by Biezeno, Koch (1938), Ebner (1952) and Wlassow (1958). Their usage in stress analyses can be traced back to Schnell (1955) who evaluated a series of simplifications. Wind load is only one of many applications for which SMC can be used. Greiner (1980) applied the same principles to investigate stress distributions in elevated silos, the effects of ring stiffeners and support settlement among other problems. Mostly used as a hand method, SMC lost popularity with the advance of computer methods, incorrectly as the authors believe, for the abovementioned reasons.

The two differential equations describing the SMC-shell are of the same mathematical structure as the equations modelling a beam on elastic foundation, taking into account the shear deformation. This similarity allows the engineer to think of any shell design problem in the more familiar terms of elastically supported beams. Among others, the following analogies can be listed to facilitate this approach:

<u>Beam on elastic foundation</u>		<u>SMC – shell</u>
bending stiffness	(EJ)	$E \frac{tR^2}{m^4}$
shear stiffness	(GA _s)	$G \frac{t}{m^2}$
bending moment	M(x)	$N(x) \frac{R}{m^2}$
rotational displacement	φ(x)	$U(x) \frac{m^2}{R}$
distributed load	q	p _r

ANALYSIS MODEL

Cylindrical Shell

The diagrams given in Figure 4 to Figure 7 refer to any cylindrical shell with fixed bottom support and a ring diaphragm or roof at the top, restricting movement in the tangential and radial direction. Tanks, silos or chimneys are commonly constructed in this manner. Figure 2 shows the properties of the described structural system and its analogue of the elastically supported beam model.

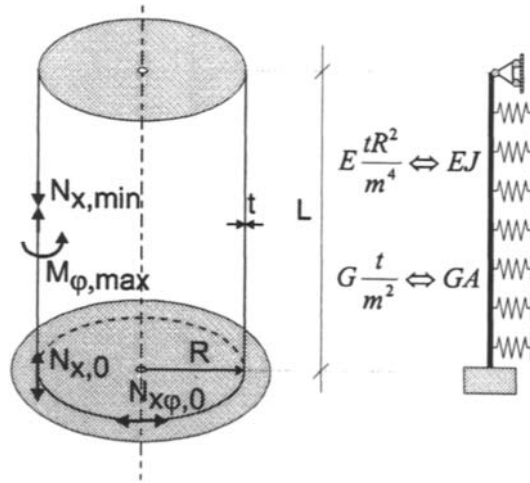


Figure 2 Structural system - SMC-shell and beam analogy

The section forces outlined in Figure 2 can be used as a guideline when dimensioning a structure of the considered type. The axial membrane force and the shear force at the bottom cross section will generally govern the design of the support cross section of the cylinder. The maximum compression force in combination with the maximum circumferential bending moment elsewhere in the cylinder will give an indication of the possible need to design against buckling.

Wind Loading

Extensive experimental data on wind pressures around circular structures is available. Many parameters influence the load exerted on cylinders - a thorough discussion of many of the factors involved can be found in Kwok (1985). Radial wind pressure varies around the circumference and also up the height of the cylinder. One very common way to describe the pressure distribution around the circumference is by approximating experimental results with a Fourier-analysis leading to the following formula for the wind pressure coefficient

$$p_{wind}(\varphi) = \sum_{m=1}^n p_m \cos(m\varphi) = p_r \cdot \sum_{m=1}^n c_m \cos(m\varphi) \tag{4}$$

where p_r is the actual wind load, c_m are the amplitudes of the load waves, m is the number of the load wave and $p_{wind}(\varphi)$ is the resulting windload. Figure 3 illustrates the structural significance of the various load waves: Wave $m = 0$ describes the axisymmetric component of the load and can be handled by simple formulas based on the membrane theory. Wave $m = 1$ stands for the loading effect of the wind force on the cylinder as a whole, which in the considered case, acts as a cantilever. Finally, all waves $m > 1$ combine to form the cross-section-deforming portions of the wind load and are incorporated in the SMC. Different wind specifications give different values for the individual wave-dependent coefficients c_m . The diagrams developed for this paper take this fact into account and allow for any combination of these factors. Wind pressure up the height of the cylinder was assumed to be constant and the roof was not loaded.

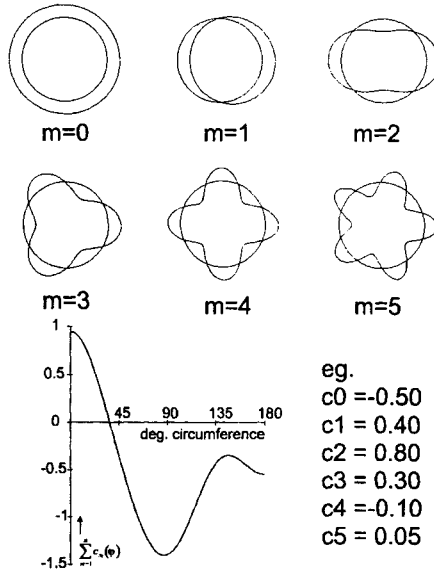


Figure 3 Fourier-analysis of wind loading

GENERAL RESULTS FOR UNIT LOAD CASES

The diagrams in Figure 4 to Figure 7 are provided to gain results for waves $m > 1$ for unit wind pressure $p_r=1 \text{ kN/m}^2$. After reading values from these diagrams, they need to be multiplied by the wave-dependent factors c_m provided by the specific wind code in use and the actual value of wind pressure applicable for the analysed structure.

Distributed Radial Pressure Loading

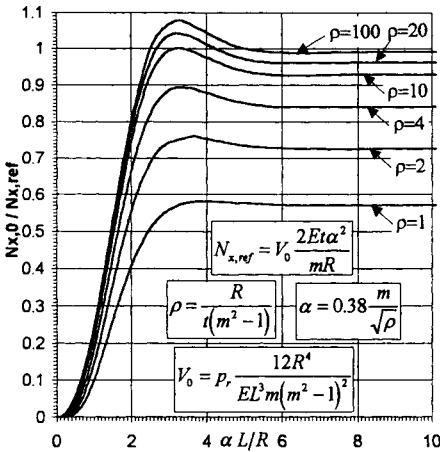


Figure 4 $N_{x,0}$ - unit wind load

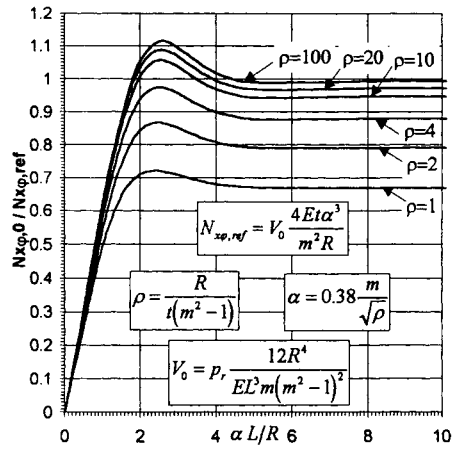


Figure 5 $N_{x,\phi,0}$ - unit wind load

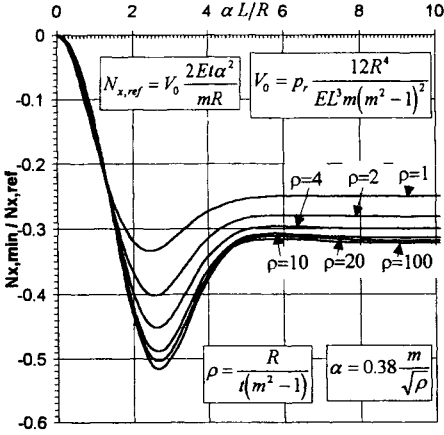


Figure 6 $N_{x,min}$ - unit wind load

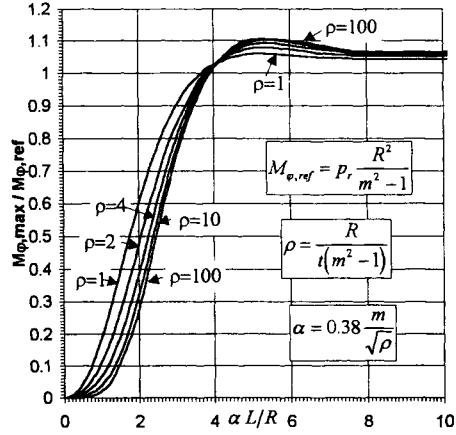


Figure 7 $M_{\phi,max}$ - unit wind load

PRACTICAL APPLICATION

Consider an unstiffened cylinder made from steel ($E = 2.1E8 \text{ kN/m}^2$, $\nu = 0.3$) under wind loading of 1kN/m^2 with the following geometric properties: $R = 10\text{m}$, $L = 50\text{m}$ and $t = 2.5\text{cm}$. Wave factors as suggested in Figure 3 will be used. The section forces outlined in Figure 2 will be computed. Table 1 lists the system parameters which are necessary to use the diagrams in Figure 4 to Figure 7:

Table 1: System parameters for the worked example

m	C_m	ρ	α	α^*L/R	V_0	$N_{x,ref}$	$N_{xp,ref}$	$M_{\phi,ref}$
2	0.8	133.3	0.07	0.33	2.0317	4620.8	304.1	33.3
3	0.3	50.0	0.16	0.81	0.1905	1732.8	186.2	12.5
4	-0.1	26.7	0.29	1.47	0.0406	924.2	136.0	6.7
5	0.05	16.7	0.47	2.33	0.0127	577.6	107.5	4.2

As wave $m = 0$ does not contribute to the section forces listed above, only wave $m = 1$ is of interest in addition to the results listed in Table 2.

$$\begin{aligned}
 m = 1: N_{x,0} &= p_r \cdot c_1 \frac{L^2}{2R} = 50.0 \text{ kN/m} \\
 N_{xp,0} &= p_r \cdot c_1 \cdot L = 20.0 \text{ kN/m}
 \end{aligned}
 \tag{5}$$

Table 2 lists the results for the individual loading waves and the accumulated end result. These values compare to within 10% of values gained from a comparison with a computer program (Guggenberger & Pircher (1998)) and also with the results given by Greiner (1980).

Table 2: Diagram readings and results for the worked example

$N_{x,o}/N_{x,ref}$ (Figure 4)	$N_{xp,o}/N_{xp,ref}$ (Figure 5)	$N_{x,min}/N_{x,ref}$ (Figure 6)	$M_{p,max}/M_{p,ref}$ (Figure 7)	$N_{x,o}$ [kN/m]	$N_{xp,o}$ [kN/m]	$N_{x,min}$ [kN/m]	$M_{p,max}$ [kN/m]
0.03	0.17	-0.03	0.005	110.9	41.4	-110.9	0.1333
0.13	0.48	-0.14	0.01	67.6	26.8	-72.8	0.0375
0.52	0.82	-0.32	0.12	-48.1	-11.2	29.6	-0.0800
0.9	1.06	-0.475	0.44	26.0	5.7	-13.7	0.0917
Wave m=1:				50.0	20.0	-	-
Σ				206.4	82.7	167.8	0.1825

CONCLUSION

The semi-membrane-concept (SMC) has been used to develop a tool to provide governing section forces for the design of thin-walled circular cylindrical shell structures under wind load. Four diagrams are given for the considered asymmetric load case to facilitate the computation of these section forces. The system can be used with any combination of shape factors for the individual Fourier-waves and is therefore independent of the wind code in use. The elegant semi-membrane-concept, as presented in the diagrams in this paper, provides a simple means of determining the wind sensitivity of cylindrical shells initially designed for other loading conditions.

REFERENCES

- Biezeno C.B., Koch J.J. (1938). The Buckling of a Cylindrical Tank of Variable Thickness under External Pressure. *Proc. 5. Intern. Congr. Appl. Mech.*, Cambridge, Mass.
- Ebner H. (1952). Theoretische und experimentelle Untersuchungen über das Einbeulen zylindrischer Tanks durch Unterdruck. *Stahlbau*, v21, 153-159
- Greiner R. (1980). Ingenieurmassige Berechnung dünnwandiger Kreiszyklinderschalen. *Research Report*, Institute of Steel, Timber and Shell Structures, Technical University Graz, Austria, Heft 1
- Greiner R., Derler P. (1995). Effect of Imperfections on Wind-Loaded Cylindrical Shells. *Thin-Walled Structures*, v23, 271-281
- Guggenberger W., Pircher M. (1998). Computerized Stress Analysis of Circular Cylindrical Shells Based on the Semi-Membrane Concept. *submitted to Advances in Structural Engineering J.*
- Kwok K.C.S. (1985). Wind Loads on Circular Storage Bins. *Proc. Joint U.S.-Australian Workshop on Loading, Analysis and Stability of Thin Shell Bins, Tanks and Silos*, Univ. of Sydney, 49-54
- Schnell W. (1955). Krafteinleitung in versteifte Zylinderschalen. *Z. Flugwiss.*, 3:12, 385
- Wlassow W.S. (1958). *Allgemeine Schalentheorie und ihre Anwendung in der Technik*. Technik. Akademie Verlag Berlin

This Page Intentionally Left Blank

THE INFLUENCE OF WELD-INDUCED RESIDUAL STRESSES ON THE BUCKLING OF CYLINDRICAL THIN-WALLED SHELLS

Martin Pircher, Martin O'Shea and Russell Bridge

School of Civic Engineering and Environment
University of Western Sydney, Nepean
PO Box 10, Kingswood, NSW 2747, Australia

ABSTRACT

The load carrying behaviour of cylindrical thin-walled shell structures under axial load is strongly dependent on imperfections invariably caused by manufacturing processes. Axisymmetric imperfections have been known to result in particularly severe reductions in strength. Imperfections in the vicinity of circumferential welds in steel silos and tanks fall into this category and therefore deserve special attention. Finite element models were used to analyse imperfect cylindrical shells and special care was taken to model the weld-induced imperfection. The geometry was calibrated against data gained from measuring such imperfections on existing silos, and residual stresses were taken into account. Interaction with global imperfections in the cylindrical shape was investigated. A number of parameters were evaluated in respect to their influence on the buckling behaviour of the modelled cylinders. The load carrying behaviour of the investigated models was found to be strongly dependent on the depth of the local imperfection. Residual stresses were found to have only a small influence on the buckling load. Shape of the weld depression and properties of the welding material also contributed to small variations in the buckling behaviour.

KEYWORDS

Cylindrical thin-walled shell, residual stress, axial load, stability, buckling, imperfection, weld

INTRODUCTION

In the 1930s, external surfaces of aircraft started to be manufactured from thin sheet metal and were made load-bearing. Experiments led to the discovery that buckling failure loads of circular cylindrical thin-walled shells were often far less than their predictions based on classical buckling theory. Early research by Karman et al (1941) demonstrated the detrimental effect that imperfections can have on the buckling strength of cylindrical thin walled shell structures. As axisymmetric imperfections do not generally occur in aircraft structures, their influence on buckling was not investigated in depth until the

1970s (Koiter (1945, 1963), Arbocz(1974)). However, for circular cylindrical steel shell structures such as silos or tanks, axisymmetric imperfections do occur during construction when rolled steel plates are formed into a series of individual strakes and joined together by circumferential welds (Figure 1). Circumferential deformations at each joint are partly caused by the rolling process and from welding shrinkage of the heated zone.

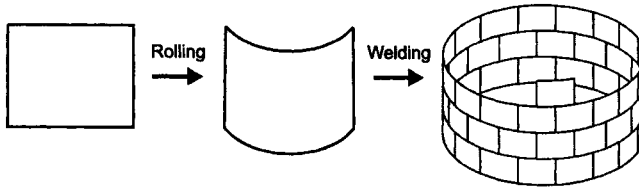


Figure 1: Erection of a Circular Silo or Tank

A close look at the area in the immediate vicinity of this axisymmetric imperfection shows that the geometric imperfection is accompanied by various other interacting influences (Figure 2). Residual stresses result mainly from weld shrinkage and reach yield in the tension zone close to the weld. For equilibrium reasons, these tension stresses have to be accompanied by compression stresses further away from the weld. The material properties of the filler material of the weld and also the heat affected zone may have different properties than the material used for the actual shell structure. Overall deviations from the cylindrical shape also play a role in reducing the buckling strength of the structure even further. Moreover, each individual strake is typically not high enough to isolate the effects of one weld imperfection from its neighbours.

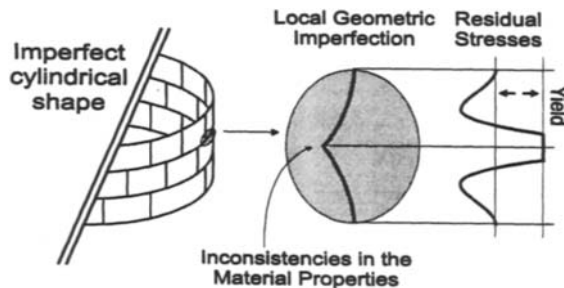


Figure 2: Circumferential weld imperfection

Two papers are known to have looked at circumferential welds in circular cylindrical shell structures including the effects of residual stresses (Bornscheuer et al (1983), Rotter (1996)). These two papers reach different conclusions. Bornscheuer et al (1983) report a decrease of the buckling strength of their model by up to 10% while Rotter (1996) concludes that "Circumferential residual stresses in the welded joint, developed by shrinkage of the weld, appear to increase the buckling strength...". The motivation behind this paper was to clarify the role of circumferential weld induced depressions in combination with the effects of the accompanying residual stresses for axially compressed cylinders.

MODELLING THE IMPERFECT CYLINDER

Cylinder geometry

The case study performed in this paper was based on the geometric properties of a silo in Port Kembla (Australia) on which weld imperfections have been carefully measured (Clarke, Rotter (1988)). Therefore, the steel silo for the study in this paper was represented by a cylinder of a radius R of 12m. The wall thickness t was taken to be 12mm. A single strake height H of 3m was modelled and axial load was taken to be constant along this limited partition of the structure. This approach led to a computer model of one circumferential joint with half a strake height on each side of the joint (Figure 3).

Depression Shape

The shape of these depressions has been the subject of some research. Rotter proposed two different shape functions based on theoretical arguments (Rotter 'a', Rotter 'b') and used them in some of his work (Rotter & Teng (1989), Teng & Rotter (1992)). These shape functions were revised later on the basis of data gathered at the reference silo in Port Kembla using empirical techniques by Rotter (1996). Of the several alternative shapes suggested, the two functions 'closed' and 'final' are included in Figure 4. For compatibility reasons with Rotter's paper, the shape function 'closed' was chosen for the investigations in this paper.

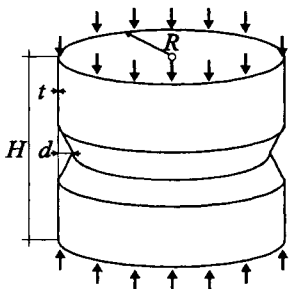


Figure 3: Analysed system

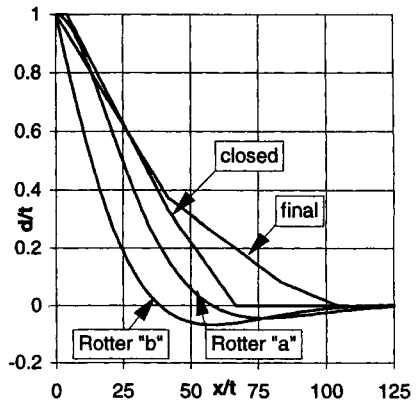


Figure 4: Shape functions representing weld imperfection geometries

Adjacent Joints

The strake height typically used in silos or tanks is small enough to ensure interaction between adjacent weld imperfections. The behaviour of adjacent strakes was taken to be symmetrically identical to that of the studied strake. This is only one of several different ways of modelling this problem (Figure 5) and more work lies ahead to investigate other possible interaction patterns.

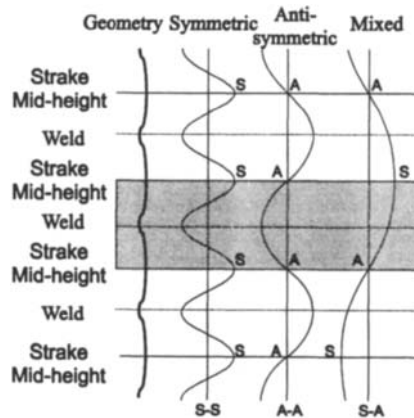


Figure 5: Strake midheight boundary conditions and buckling modes

Residual stresses

All analyses in this paper were based on a bi-linear material law with ultimate stress reached at a plastic strain of 0.2%. Steel with a yield stress of 200 MPa was chosen. A preliminary analysis looked at different ways of modelling the shrinkage of the weld which is the primary source of the residual stresses found in the vicinity of the depression. In a first step, material properties of the cylinder were modelled in a detailed way, including temperature dependencies. The cooling process of the weld was then analysed. This was compared to an alternate method of modelling the shrinkage problem which follows a procedure described by Rotter (1996). A length of the shell of 50mm above and below the weld was subjected to a shrinkage strain equal to the yield strain (0.00125). These strains led to stresses (Figure 6) which the system attempted to relieve by deforming. Therefore the geometry of the weld depression was changed by the application of residual strains. As a result of this, the depth of the geometric imperfection was scaled to an amplitude of 9.48mm after which the residual strains were applied, resulting in the desired imperfection of a magnitude of one wall thickness (Figure 7). Imperfection shape 'closed' was chosen for the initial imperfection to allow comparison with Rotter's results. The two methods of achieving residual stress patterns and geometric imperfections gave similar results and compared well to measured results. The second method was used for all ensuing analyses.

Overall Imperfection

It will be shown that overall imperfections of the cylindrical shape in combination with the local weld imperfection can have an influence on the buckling behaviour of the investigated cylinders. Assumptions for the shape of these overall imperfections needed to be made as no measured data was available. An obviously conservative approach was taken in superimposing an overall imperfection in the shape of the first buckling eigenmode.

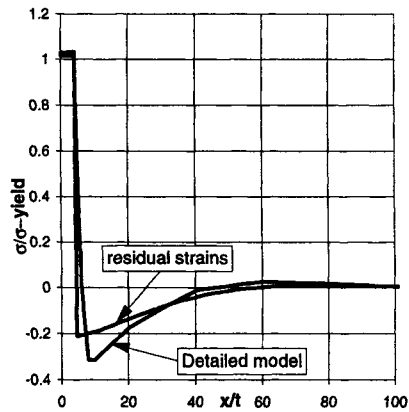


Figure 6: Circumferential residual stresses after weld shrinkage

FE-Model

Boundary conditions of the computer model were set in a way that one single buckling wave was described. Several different buckling modes needed to be investigated to determine the mode with the smallest load that leads to failure and to account for the fact, that many possible modes lie within a very small difference in load.

To determine the effects that residual stresses have on the buckling behaviour two sets of models were investigated:

- (1) The first set included stresses and deformations induced by weld shrinkage followed by the application of axial load.
- (2) The second set used the same induced weld deformations ignoring the residual stresses followed by the application of axial load.

Finite Element code ABAQUS was used for all computer investigations for this paper.

RESULTS

Weld Shrinkage

On the basis of empirical studies, Faulkner (1977) has suggested using a tension zone of a magnitude of 3 to 6 wall thicknesses on each side of the weld with tensile stresses close to yield. A value of 0.2 to 0.4 is suggested for the ratio of tension stress at the weld to compression stress away from the weld. Both methods of generating residual stresses around the weld depression used in this paper resulted in stress fields that fell well within these suggested limits (Figure 6). In addition to these circumferential membrane forces, all other section forces contribute to achieve equilibrium. Starting the analysis with a local circumferential imperfection of the shape 'closed' with a depth of 9.48mm resulted in a groove with an amplitude of 12.11mm. The geometry of this groove was recorded and used as an initial stress-free imperfection for the second set of cylinders modelled for this investigation (Figure 7).

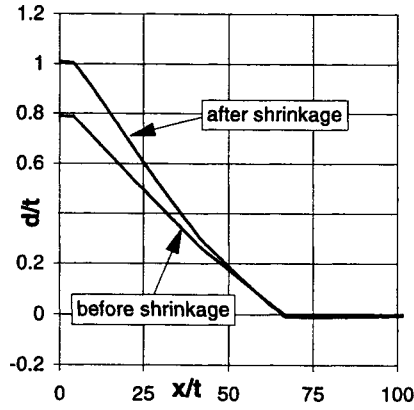


Figure 7: Imperfection shape before and after weld shrinkage

Buckling Modes

A significant aspect of the buckling behaviour of cylindrical thin walled systems under axial load is the close proximity of bifurcation points along the load deflection curve. Each bifurcation point corresponds to a different buckling mode. Obviously, the bifurcation point which requires the smallest load is the one of most interest. The buckling strength of an imperfect cylinder is commonly related to the classical elastic critical stress σ_{cl} which is given by

$$\sigma_{cl} = \frac{E}{\sqrt{3(1-\nu^2)}} \frac{t}{R} \approx 0.605 \frac{Et}{R} \quad (1)$$

in which E stands for the elastic modulus and ν for Poisson's ratio. In a first analysis several buckling modes were investigated for the stress-free model as well as for the model which included residual stresses. The results for some of the buckling modes investigated can be seen in Figure 8. These results compared well with results gained by Rotter (1996) and contradict the results of Bornscheuer et al (1983). When residual stresses are considered in the buckling analysis, the critical load is slightly higher than in the stress-free systems of the same geometry. Also, a different buckling mode applies for the two systems. This has been explained by the partially alleviating stress patterns of the two load conditions. The stress-free system is under meridional and circumferential compression at the point of buckling whereas the residual circumferential tension stresses in the other system have a stabilising effect up until the bifurcation point is reached. The parts of the shell a small distance away from the weld are under circumferential compression due to weld shrinkage which are gradually relieved as the axial load increases (Figure 9).

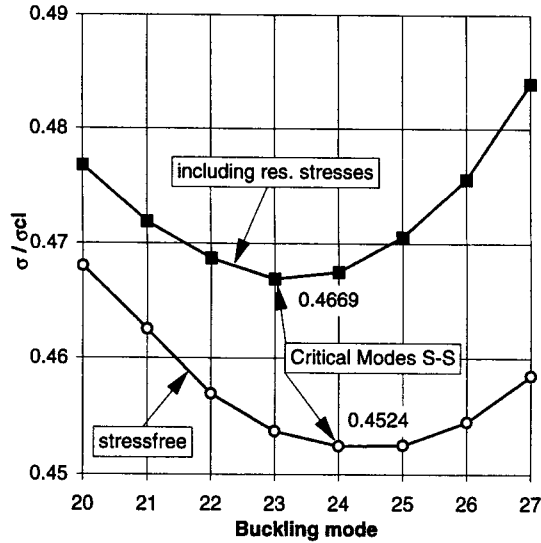


Figure 8: Buckling modes and corresponding critical loads

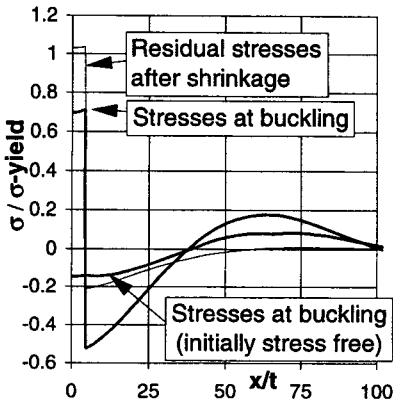


Figure 9: Circumferential stresses at buckling

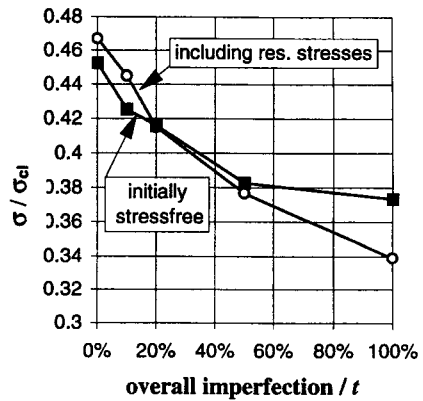


Figure 10: Interaction between local weld imperfection and overall imperfection

Overall Imperfection

In order to investigate the interaction of the local weld imperfection with global deviations from the overall cylindrical shape, an overall imperfection was superimposed onto the two critical buckling modes. This overall imperfection was scaled to various amplitudes of up to one wall thickness and was assumed to be of the shape of the first eigenmodes. As can be seen in Figure 10, the buckling strength of the model which includes residual stresses decreases at a greater rate than the buckling strength of the stress free model. An explanation for this behaviour can be found in the increase of

bending moments which goes hand in hand with the increase of the overall imperfection. This can be explained by considering the offset from the perfectly cylindrical shape in combination with the circumferential stresses.

CONCLUSION

The paper studies the influence of weld induced residual stresses in the vicinity of circumferential joints in cylindrical thin-walled structures under axial load. A case study was undertaken that used the geometric properties of an existing silo in Port Kembla (Australia). It was found that on an axisymmetric model for local weld imperfection, residual stresses increased the buckling strength of the studied cylinder by a small amount. However, when deviations from the perfect axisymmetric shape were introduced, the buckling strength of the models which consider residual stresses dropped below the models which did not take these residual stresses into account. More scope for work lies in the variation of geometric parameters, the variation of the imperfection depth and the investigation of different interaction forms between the individual strakes.

REFERENCES

- Bornscheuer F.W., Hafner L., Ramm E. (1983). Zur Stabilität eines Kreiszylinders mit einer Rundschweißnaht unter Axialbelastung. *Der Stahlbau* **52:10**, 313-318
- Clarke, M.J. & Rotter, J.M. (1988). A Technique for the Measurement of Imperfections in Prototype Silos and Tanks. *Research Report R565*, School of Civil and Mining Engineering, University of Sydney, Australia
- Faulkner, D. (1977). Effects of residual stresses on the ductile strength of plane welded grillages and of ring stiffened cylinders. *J. Strain Analysis for Engng Design*, **v12**, 130-139
- Karman T. v., Dunn L. G., Tsien H. S. (1941). The Buckling of Thin Cylindrical Shells under Axial Compression. *J. Aeronaut. Sci* **v8**, 303-312
- Koiter W. T. (1945). *The Stability of Elastic Equilibrium*, Dissertation at the Technische Hooge School, Delft.. English translation by E. Riks: Technical Report AFFDL-TR-70-25, Air Force Flight Dynamics Laboratory, Air Force Systems Command, Wright-Patterson Air Force Base, Ohio, 1970
- Koiter W. T. (1963). The Effect of Axisymmetric Imperfections on the Buckling of Cylindrical Shells under Axial Compression. *Proc. Koninklijke Nederlandse Akademie van Wetenschappen*, 265-279
- Arbocz, J. (1974). The Effect of Initial Imperfections on Shell Stability., *Thin Shell Structures*, 205-246
- Rotter, J.M. (1996). Buckling and Collapse in Internally Pressurised Axially Compressed Silo Cylinders with Measured Axisymmetric Imperfections: Imperfections, Residual Stresses and Local Collapse. *Imperfections in Metal Silos Workshop, Lyon, France*, 119-139
- Rotter J.M. & Teng J.G. (1989). Elastic Stability of Cylindrical Shells with Weld Depressions. *Journal of Structural Engineering, ASCE*, **116:8**, 1244-1263
- Teng, J.G. & Rotter J.M. (1992). Buckling of Pressurized Axisymmetrically Imperfect Cylinders under Axial Loads. *Int. of Engineering Mechanics*, **118: 2**, 229-247

BENDING EFFECTS ON INSTABILITIES OF INTERNALLY PRESSURISED TUBES MODELLED BY A NONLOCAL MEMBRANE THEORY

Lars Pilgaard Mikkelsen¹ and Viggo Tvergaard²

¹Cambridge University Engineering Department,
Trumpington Street, Cambridge CB2 1PZ, UK

²Department of Solid Mechanics,
Technical University of Denmark, 2800–Lyngby, Denmark

ABSTRACT

For a closed–end elastic–plastic tube under internal pressure the development of tensile instabilities in the tube wall is analysed numerically. A nonlocal enhanced membrane analysis is used to account for 3D effects in the context of a 2D analysis. The first instability is seen as the development of an axisymmetric bulge on the tube, and a secondary instability involves the development of necking on one side of the bulge. The effect of realistic end conditions on the development of the instabilities is studied.

KEYWORDS

nonlocal plasticity, tensile instabilities, finite strain, pressurised tubes, membrane analyses.

INTRODUCTION

Experimental studies of the instabilities and final failure modes in pressurized tubes made of aluminium or copper have been presented by Larsson *et al.* (1982), who used closed–end tubes with the internal pressure applied by means of a hydraulic loading device. Some features of these experimental results were explained in terms of results for plane strain conditions (Larsson *et al.*, 1982), as had also been studied by Storåkers (1971), Strifors and Storåkers (1973), and Chu (1979), but plane strain analyses could not explain the experimentally observed formation of a localized bulge on one side of the tube. In a study without restrictions to planar deformations Tvergaard (1990) found that the first critical bifurcation corresponds to an axisymmetric non–cylindrical mode of deformation, which subsequently develops into an axisymmetric bulge on the tube, and well into the

post-bifurcation range the formation of a neck on one side of the bulge occurs as a secondary bifurcation.

In a recent paper Mikkelsen and Tvergaard (1997) used an enhanced membrane analysis of a pressurized tube to analyse the full tube problem without simplifying assumptions of plane strain or axisymmetric behaviour. This study made use of a nonlocal plane stress model recently developed by Mikkelsen (1997), in which a dependence on the gradient of the effective plastic strain is used to introduce a material length that accounts for thickness effects. The model is similar to a 3D finite strain model used by Benallal and Tvergaard (1995), and belongs to a group of 3D strain gradient plasticity models (Aifantis, 1984; Zbib and Aifantis, 1989; de Borst and Mühlhaus, 1992; Fleck *et al.*, 1993, 1994).

The studies of Tvergaard (1990) and Mikkelsen and Tvergaard (1997) considered a tube with periodicity conditions at the ends, so that in fact a very long tube with uniform spacings between bulges was analysed. In the present investigation the actual closed-end tube boundary conditions are prescribed, which allow for transverse deflections of the tube end during bulging. The effect of the real boundary conditions is studied to check how much the development of instabilities is affected by the edge effects.

PROBLEM FORMULATION

A closed end tube under internal pressure is analysed. The initial geometry of the tube is specified by the length $2L_0$, the middle surface radius R_0 and the wall thickness H_0 . An undeformed cylindrical coordinate system is chosen as the reference system with the coordinates x^1 and x^2 in the axial and the circumferential directions, respectively. The coordinate along the outward surface normal is denoted x^3 . The corresponding displacement components on the reference base vectors are denoted by u^i . Latin indices range from 1 to 3 while Greek indices range from 1 to 2. The continuum description is based on a finite strain theory written in a standard Lagrangian convected convected coordinate formulation, see e.g. Hutchinson (1973). General tensor notation is used where upper and lower indices denote contravariant and covariant components, respectively, and repeated indices denote summation.

Due to symmetry, only one half of the tube in the circumferential direction is analyzed with symmetry boundary conditions at $x^2 = 0$ and $x^2 = \pi R$. Contrary to Mikkelsen and Tvergaard (1997) the present work does not assume a constant tube length throughout the deformation. Instead, the boundary $x^1 = -L_0$ is simply supported while the boundary $x^1 = L_0$ is prescribed to follow the displacements and the rotation of a stiff end plate. Here, this is done by introducing three additional unknowns, U , V and Ψ for the axial displacement, the vertical displacement and the rotation of the end plate, respectively. The total displacements at all nodes along the boundary $x^1 = L_0$ are then given by

$$\begin{aligned} u^1 &= U + R_0 \cos \alpha \sin \Psi \\ u^2 &= \sin \alpha [V + R_0 \cos \alpha (1 - \cos \Psi)] \\ u^3 &= -\cos \alpha [V + R_0 \cos \alpha (1 - \cos \Psi)] \end{aligned} \quad (1)$$

where $\alpha = x^2/R$. The three equilibrium equation for the end plate subject to the hydrostatic pressure p on the area $A_s = \pi R_0^2$ and the traction components T^i along the boundary $x^1 = L_0$ are given by

$$\begin{aligned} pA_s \cos \Psi + \int_0^{2\pi} (-T^1 R_0) d\alpha &= 0 \\ pA_s \sin \Psi + \int_0^{2\pi} (-T^2 \sin \alpha + T^3 \cos \alpha) R_0 d\alpha &= 0 \\ \int_0^{2\pi} [-T^1 \cos \Psi + (-T^2 \sin \alpha + T^3 \cos \alpha) \sin \Psi] R_0 R_0 \cos \alpha d\alpha &= 0 \end{aligned} \tag{2}$$

The necking behaviour on one side of the tube is initiated by a non-axisymmetric imperfection in the wall thickness of the form

$$\bar{H}_0 = H_0 \left[1 - \bar{\xi}_H \cos \frac{x^2}{R_0} \right] \tag{3}$$

(Larsson *et al.*, 1982) where $\bar{\xi}_H$ is the non-dimensional imperfection amplitude. Contrary to the analyses of Tvergaard (1990) and Mikkelsen and Tvergaard (1997), the edge effects in the present work represent in reality an axisymmetric imperfection. Therefore, no additional imperfection is necessary in order to initiate the first critical instability mode; an axisymmetric non-cylindrical mode of deformation.

The analysis of the instability behaviour is performed by a 2D membrane finite element model. The third dimension, the thickness effect, is taken into account by introducing an internal length scale. A good agreement with the accurate 3D finite element analysis is found, Mikkelsen (1997), if the length scale $\ell = 0.29H$ is used. Here, H is the current thickness of the tube wall. The length scale is incorporated into the von Mises yield surface, f , by taking

$$f = \sigma_e(\sigma^{ij}) - \bar{\sigma}_y(\lambda, \nabla^2 \lambda) \leq 0, \quad \bar{\sigma}_y(\lambda, \nabla^2 \lambda) = \sigma_y(\lambda) - \ell^2 \nabla^2 \lambda \sigma_y(\lambda) \tag{4}$$

where $\sigma_e = (3s^{ij}s_{ij}/2)^{1/2}$ is the von Mises stress given by the stress deviator $s^{ij} = \sigma^{ij} - G^{ij}G_{kl}\sigma^{kl}/3$. The tensor components G^{ij} specify the metric of the deformed configuration and σ^{ij} are the Cauchy stresses. The Laplacian of the plastic multiplier, $\nabla^2 \lambda$, is taken with respect to the current deformed state

$$\nabla^2 \lambda = \frac{\partial}{\partial x^\alpha} \left(G^{\alpha\beta} \frac{\partial \lambda}{\partial x^\beta} \right) \tag{5}$$

Mikkelsen (1997, 1998), where $\partial(\cdot)/\partial x^\alpha$ denotes the partial derivative. The hardening material behaviour is modelled by a power law variation of the local yield stress, $\sigma_y(\lambda)$, as in Mikkelsen and Tvergaard (1997).

The numerical solution is obtained by an incremental finite element method based on the virtual work on incremental form and the consistency condition, $\dot{f} = 0$, written on a weak form, see Mikkelsen and Tvergaard (1997). In the present analysis the virtual work is used with the additional term

$\int_S T^i \delta u_i dS$, to represent the boundary conditions (2). The boundary conditions (1) are prescribed in a combined Rayleigh–Ritz/finite element method (Tvergaard, 1976), by adding the unknowns U , V and Ψ (see Fleck *et al.*, 1989) to the unknowns already used by Mikkelsen and Tvergaard (1997), and by requiring that these extra unknowns satisfy the equilibrium equations (2). Further details on the numerical procedure can be found in Mikkelsen (1997) and Mikkelsen and Tvergaard (1997).

RESULTS

As in Mikkelsen and Tvergaard (1997) the material properties are taken to be $\sigma_0/E = 0.004$, $n = 10$ and $\nu = 1/3$. Furthermore, in all cases studied here the additional material parameter ℓ , the material length, is taken to be $\ell = 0.29H$. Fig. 1 illustrates the problem analysed, where the fastening of the tube at the left end is represented by simple support boundary conditions, the closed right end is represented by the end–plate boundary conditions, and the well developed bulge with necking on one side has formed on the middle of the tube, due to the edge effects. Note that the same location of the bulge, in the middle, is also predicted by a uniform mesh. The stretching of the mesh in Fig. 1 is only used in order to be able to continue the computation further into the post–necking range.

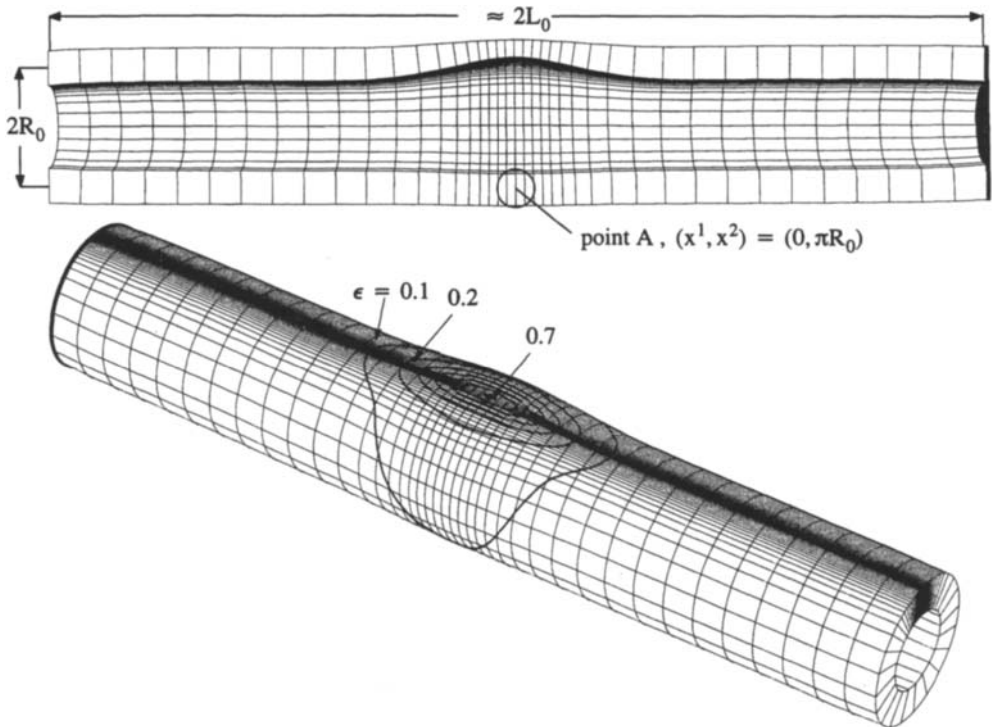


Fig. 1. Two views of the deformed nonlocal membrane elements at $H_{min} = H_0/2$ ($V/V_0 = 1.140$) for a closed end tube with $L_0/R_0 = 8.0$, $H_0/R_0 = 0.6$, $\xi_H = 0.005$, $\sigma_0/E = 0.004$, $n = 10$, $\nu = 1/3$ and $\ell = 0.29H$. The lowest figure includes the contours of the maximum principal logarithmic strain.

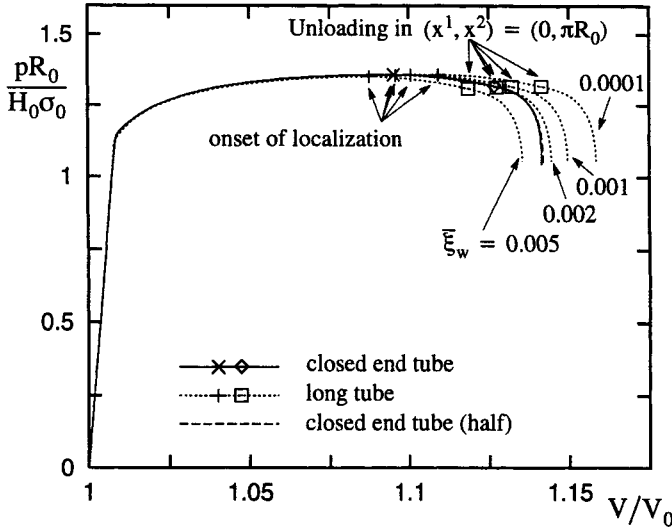


Fig. 2. Pressure versus enclosed volume for tubes with $L_0/R_0 = 8.0$, $H_0/R_0 = 0.6$, $\xi_H = 0.005$, $\sigma_0/E = 0.004$, $n = 10$, $\nu = 1/3$ and $\ell = 0.29H$.

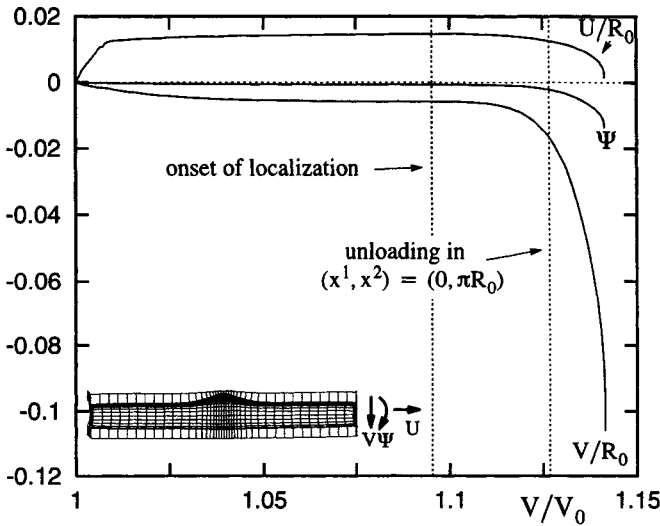


Fig. 3. Displacements U and V , and angle of rotation Ψ (rad.), of the rigid end plate versus enclosed volume for the closed end tube with $L_0/R_0 = 8.0$, $H_0/R_0 = 0.6$, $\xi_H = 0.005$, $\sigma_0/E = 0.004$, $n = 10$, $\nu = 1/3$ and $\ell = 0.29H$.

The solid curve in Fig. 2 represents the pressure vs. enclosed volume development for the closed end tube illustrated in Fig. 1. The dashed curve is computed by analysing only the right half of the tube, assuming symmetry boundary conditions at $x^1 = 0$, and it is seen that this curve nearly coincides with that for the full tube. The remaining dotted curves are predictions for a long tube with uniform spacings between bulges, as analysed by Mikkelsen and Tvergaard (1997), where a localised axisymmetric imperfection with amplitude ξ_w was necessary to try to represent the edge effects in the real closed end tube. In fact, the predicted tube instabilities are not dramatically changed by accounting

for the finite length. But it is seen in Fig. 2 that the long tube results are quite sensitive to the arbitrary choice of the value of $\bar{\epsilon}_w$, and that rather good agreement with the closed end tube is obtained for $\bar{\epsilon}_w = 0.003$.

The development of the displacements and rotation of the end plate are illustrated in Fig. 3 for the case also considered in Fig. 1. It is noted that the transverse displacement V grows negative, so that the end displacement is upwards, in the direction of the bulge. The corresponding rotation of the end plate is negative, as expected. The stage of deformation illustrated in Fig. 1 is near the end of the curves in Fig. 3.

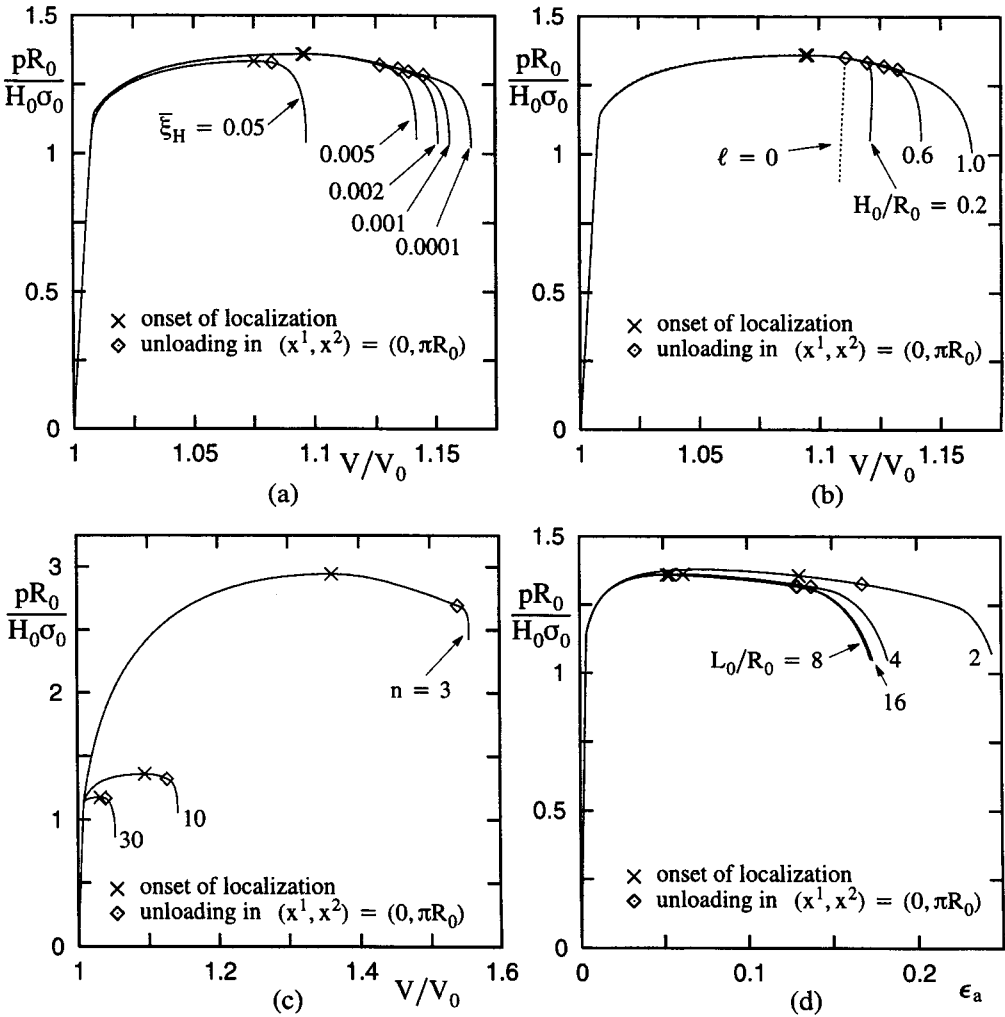


Fig. 4. Pressure versus enclosed volume (a-c) or average hoop strain along the symmetry line $x^1 = 0$ (d), found by an enhanced membrane theory with $\sigma_0/E = 0.004$, $\nu = 1/3$ and $\ell = 0.29H$: (a) $L_0/R_0 = 8.0$, $H_0/R_0 = 0.6$ and $n = 10$; (b) $L_0/R_0 = 8.0$, $\bar{\epsilon}_H = 0.005$ and $n = 10$; (c) $L_0/R_0 = 8.0$, $H_0/R_0 = 0.6$ and $\bar{\epsilon}_H = 0.005$; (d) $H_0/R_0 = 0.6$, $\bar{\epsilon}_H = 0.005$ and $n = 10$.

Parametric studies of the effect of different parameters are shown in Fig. 4. These computations are carried out for the half closed end tube, but the comparison of the solid and dashed curves in Fig. 2 shows that this gives practically no difference from predictions for the full closed end tube. There is a strong sensitivity to the amplitude of the non-axisymmetric imperfection (Fig. 4a), so that for $\bar{\xi}_H = 0.05$ there is only a small delay between the onset of axisymmetric bulge formation at the maximum pressure point and the onset of necking on one side of the bulge. Fig. 4b shows that increasing tube thickness tends to delay the onset of necking on one side of the bulge, while the expected strong effect of the level of material strain hardening is illustrated in Fig. 4c. It is noted that the curve for $\ell = 0$ in Fig. 4b coincides with that for $H_0/R_0 \rightarrow 0$, since $\ell/H = 0.29$ is used in all the present calculations. Finally, in Fig. 4d the effect of the length to radius ratio of the tube is considered in a plot of p vs. the average logarithmic hoop strain at $x^1 = 0$, ϵ_a . For the shortest tube, $L_0/R_0 = 2$, both axisymmetric and non-axisymmetric localizations are noticeably delayed by end effects. The three larger lengths considered show rather similar behaviour, but it is noted that for $L_0/R_0 = 16$ there is again a slight delay towards that expected for an infinitely long tube with no axisymmetric imperfection (see also Fig. 2).

CONCLUDING REMARKS

The interest in studying the actual closed end boundary conditions, rather than the idealised long tube conditions analysed by Mikkelsen and Tvergaard (1997), is related to the fact that the final necking mode has one wave around the circumference, and so does the mode of tube bending as a beam. Therefore, the freedom of the closed end tube to bend freely could interact significantly with the tensile instabilities. Fig. 2 shows that there is an effect, but it is not very strong.

It should be emphasised that the nonlocal membrane analysis applied here is an important tool, which accounts for the ability to analyse the full closed end tube behaviour without simplifications to axisymmetry or planar deformations. The alternative would be a full 3D numerical analysis, which would require much larger computational effort, and could be hardly feasible at all in cases of extreme tube dimensions.

ACKNOWLEDGEMENT

Financial support by the MUP2 research programme Materials Processing, Properties and Modelling, financed by the Danish Agency for Development of Trade and Industry, the Danish Natural Science Research Council, and the Danish Technical Research Council is gratefully acknowledged.

REFERENCES

- Aifantis, E.C. (1984). On the microstructural origin of certain inelastic models. *J. Engng. Mater. Tech.* **106**, 326–334.
- Benallal, A. and Tvergaard, V. (1995). Nonlocal continuum effects on bifurcation in the plane strain tension–compression test. *J. Mech. Phys. Solids* **43**, 741–770.
- de Borst, R. and Mühlhaus, H.–B. (1992). Gradient–dependent plasticity: Formulation and algorithmic aspects. *Int. J. for Num. Meth. in Engn.* **35**, 521–539.

- Chu, C.-C. (1979). Bifurcation of elastic-plastic circular cylindrical shells under internal pressure. *J. Appl. Mech.* **46**, 889-894.
- Fleck, N.A., Hutchinson, J.W. and Tvergaard, V. (1989). Softening by void nucleation and growth in tension and shear. *J. Mech. Phys. Solids* **37**, 515-540.
- Fleck, N.A. and Hutchinson, J.W. (1993). A phenomenological theory of strain gradient plasticity. *J. Mech. Phys. Solids* **41**, 1825-1857.
- Fleck, N.A., Muller, G.M., Ashby, F. and Hutchinson, J.W. (1994). Strain gradient plasticity: theory and experiment. *Acta Metall. Mater.* **42**, 475-487.
- Hutchinson, J.W. (1973). Finite strain analysis of elastic-plastic solids and structures. in *Numerical Solution of Nonlinear Structural Problems* (eds. R.F. Hartung), p. 17, ASME, New York.
- Larsson, M., Needleman, A., Tvergaard, V. and Storåkers, B. (1982). Instability and failure of internally pressurized ductile metal cylinders. *J. Mech. Phys. Solids* **30**, 121-154.
- Mikkelsen, L.P. (1997). Post-necking behaviour modelled by a gradient dependent plasticity theory. *Int. J. Solids Structures* **34**, 4531-4546.
- Mikkelsen, L.P. (1998). Necking in rectangular tensile bars approximated by a 2-D gradient dependent plasticity model. *Manuscript in preparation*.
- Mikkelsen, L.P. and Tvergaard, V. (1997). A nonlocal two-dimensional analysis of instabilities in tubes under internal pressure. DCAMM-report 560, Technical University of Denmark, Lyngby, Denmark (to appear in *J. Mech. Phys. Solids*).
- Mikkelsen, L.P. and Tvergaard, V. (1998). A 2-D Non-local Analysis of Hydroforming for Thin Sheets. In *Proc from 2nd Euromech-Mecamat Conf. on Mech. of Materials with Intrinsic Length Scale* (eds. A. Bertram, S. Forest and F. Sidoroff) 242-249, Magdeburg, Germany, 1998 (to appear in *Journal de Physique*).
- Storåkers, B. (1971). Bifurcation and instability modes in thick-walled rigid-plastic cylinders under pressure. *J. Mech. Phys. Solids* **19**, 339-351.
- Strifors, H. and Storåkers, B. (1973) Uniqueness and stability at finite-deformation of rigid plastic thick-walled cylinders under hydrostatic pressure. In *Foundations of Plasticity*, **1** (ed. A. Sawczuk), 327. Nordhoff, Leiden.
- Tvergaard, V. (1976) Effect of thickness inhomogeneities in internally pressurized elastic-plastic spherical shells. *J. Mech. Phys. Solids* **24**, 291-304.
- Tvergaard, V. (1990) Bifurcation in elastic-plastic tubes under internal pressure. *Eur. J. Mech., A/Solids* **9**, 21-35.
- Zbib, H.M. and Aifantis, E.C. (1989) A gradient-dependent flow theory of plasticity: Application to metal and solid instabilities. *Appl. Mech. Rev.* **42**, S295-S304.

Section VIII

SHEAR AND BENDING

This Page Intentionally Left Blank

AN EXPERIMENTAL STUDY OF VISCOPLASTICITY-CREEP INTERACTION OF THIN-WALLED TUBES UNDER PURE BENDING

W. F. Pan¹ and C. M. Hsu²

¹Department of Engineering Science National Cheng Kung University,
Tainan, Taiwan

²Department of Arts-Craft Tung Fung Junior College of Technology,
Kao Hsiung County, Taiwan

ABSTRACT

Pure bending with a constant curvature-rate followed by creep (hold constant moment for a period of time) tests were conducted to investigate the effect of prior curvature-rate at preloading stage on the subsequent creep behavior (viscoplasticity-creep interaction). Thin-walled tubes of 304 stainless steel were used in this investigation. The curvature-ovalization measurement apparatus, designed by Pan et al.⁽¹⁾, was used for conducting the present experiments. It has been found that the curvature-rate at the preloading stage has a strong influence on the subsequent creep deformation under pure bending.

KEYWORDS

Thin-Walled Tube, Pure Bending, Curvature-Rate, Viscoplasticity, Creep, Tube Ovalization

INTRODUCTION

Industrial thin-walled tubular components such as offshore pipelines, platforms in offshore deep water, nuclear reactors, etc., are generally subjected to bending loads. Most of the loads exceed the

elastic limit that causes plastic deformation. Nonlinear moment-curvature curve and ovalization of tube cross-section (Brazier effect) can be observed. The magnitude of tube ovalization increases when the magnitude of the bending moment increases. Such increase in ovalization of tube cross-section causes a progressive reduction in its bending rigidity (accumulation of damage) which can ultimately result in buckling of the tube⁽²⁻⁶⁾. Therefore, the study of the response of thin-walled tubes subjected to bending is very important for many industrial applications.

It has been known that engineering alloys, such as 304 and 316 stainless steel as well as high-strength titanium alloys, exhibit viscoplastic behavior. If the constant loading-rate (strain-rate or stress-rate) straining followed by creep is considered, the strain or stress amplitude and the loading-rate are found to have strong influence on the subsequent creep deformation⁽⁷⁻⁸⁾. Therefore, if a thin-walled tube is bent by a constant loading-rate (curvature-rate or moment-rate) followed by creep (hold constant moment for a period of time) deformation, the curvature or moment amplitude and the loading-rate should have strong influence on the subsequent creep deformation. Based on this recognition, an experimental investigation on the effect of curvature-rate at preloading stage on creep behaviors of thin-walled tubes under pure bending was carried out in this study.

In the present study, a four-point bending machine (similar to the facilities reported in previous studies⁽⁴⁻⁶⁾) was used for conducting the pure bending tests. The material of the thin-walled tube chosen for this study was AISI 304 stainless steel. The curvature-ovalization measurement apparatus (COMA), designed by Pan et al.⁽¹⁾, was used. Based on the capability of the bending machine, different curvature-rates were employed at the preloading stage of the tube. The subsequent creep deformation was controlled by the load cell. It was observed from the experimental result that due to the hardening of the metal tube under higher curvature-rates, a larger magnitude of moment is required to bend the specimen at the preloading stage. However, the ovalization of tube cross-section increases when the applied curvature-rate increases. For the subsequent creep deformation, it is found that the creep curvature is larger with a higher constant curvature-rate at the preloading stage than that with a lower one. A similar result has been found in the tube ovalization curves.

EXPERIMENTAL FACILITY

A bending test facility was developed and used to carry out a number of experiments on thin-walled tubes. The facility consists of a pure bending device and a curvature-ovalization measurement apparatus (COMA). Further description of the test facility is made in the following.

Bending Device

Figure 1(a) shows a schematic drawing of the bending device, and Figure 1(b) shows a picture of the bending device. It was designed as a four-point bending machine, capable of applying bending.

Similar devices were reported by Kyriakides and coworkers⁽⁴⁻⁶⁾. The device consists of two rotating sprockets, about 30 cm in diameter, symmetrically resting on two support beams of 1.25 m apart. The maximum length of the test specimen allowed is 1 m. The sprockets support two rollers which apply point loads in the form of a couple at each end of the test specimen. Heavy chains run around these sprockets and are connected to two hydraulic cylinders and load cells forming a closed loop. Once either the top or bottom cylinder contracts, the sprockets rotate, and pure bending of the test specimen is achieved. The contact between the tube and the rollers is free to move along axial direction during bending. The load transfer to the test specimen is in the form of a couple formed by concentrated loads from the two rollers. Detailed description of such a bending device can be found in literature⁽⁴⁻⁶⁾.

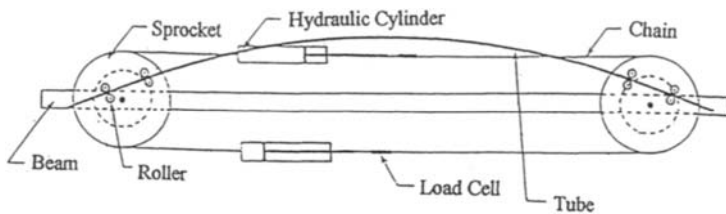


Figure 1(a) Schematic drawing of the bending device

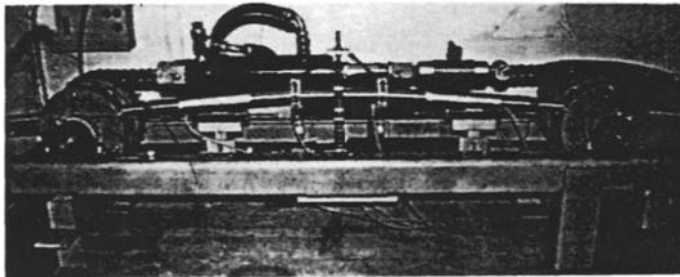


Figure 1(b) A picture of the bending device

Curvature-Ovalization Measurement Apparatus (COMA)

The curvature-ovalization measurement apparatus (COMA), as shown in Figure 2(a), is a lightweight instrument, mounted close to the tube's mid-span. A picture of the COMA used in this study is shown in Figure 2(b). Using a magnetic detector (middle part of the COMA), it can monitor the changes in the major and minor diameters of the tube cross-section (the ovalization of tube cross-section). Simultaneously, it can measure variations in the tube curvature close to the mid-span from the signals of inclinometers. There are three inclinometers (side-inclinometer 1, side-inclinometer 2 and center-inclinometer) in this COMA (see Figure 2(a)). Based on the fixed distance between the two side-inclinometers and the angle changes detected by the two side-inclinometers, the tube curvature can be obtained. Detail description of the COMA is shown in the work by Pan et al.⁽¹⁾.

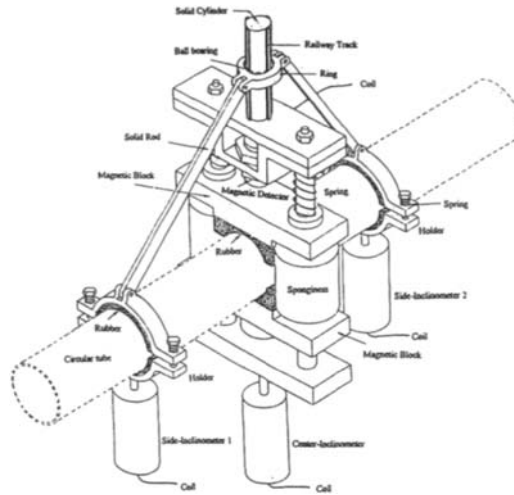


Figure 2(a) Schematic drawing of the COMA

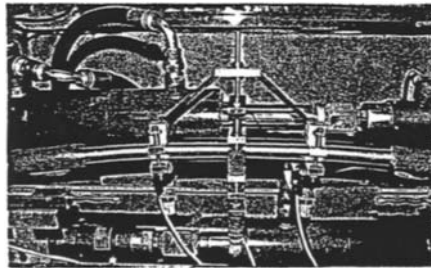


Figure 2(b) A picture of the COMA

EXPERIMENTAL INVESTIGATION

Material and Specimens

The material used in this study was AISI 304 stainless steel, with chemical composition: Cr 18.36, Ni 8.43, Mn 1.81, Si 0.39, C 0.05, P 0.28, S 0.004 and Fe remainder. To obtain the desired ratio of outer diameter D to wall thickness t (D/t), the tubes originally with $D = 31.8$ mm and $t = 1.5$ mm ($D/t = 21.2$) were slightly machined on the outer surface. Figure 3 shows the dimensions of the test specimen. The outer diameter, wall thickness and gage length are 30.33, 0.76 and 388 mm, respectively, i.e. D/t is approximately equal to 40.

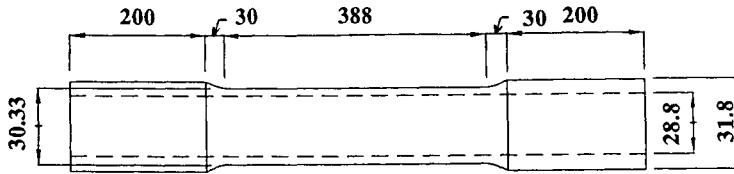


Figure 3 Geometry of thin-walled tubular specimen (all dimensions in mm)

Test Procedures

The bending test was conducted by using the bending device described in Section 2.1. The magnitudes of the curvature and curvature-rate were controlled and measured by the COMA which also measured the ovalization of tube cross-section. The bending moment can be calculated from the signals detected by the two load cells, mounted in the bending device. Based on the capability of the bending machine, three different curvature-rates, viz. 3×10^{-1} , 3×10^{-2} and 3×10^{-3} m^{-1}/sec , were employed at the preloading stage.

In the subsequent creep test, the specimen was bent in the curvature-controlled mode (controlled by the COMA) at the preloading stage while the computer monitored the magnitude of the moment. As soon as the moment magnitude reached the preset creep holding moment, the loading process stopped. The test system was programmed to switch to the moment-controlled mode (controlled by the load cells) instantaneously and the moment was kept at this constant magnitude, while the creep curvature and ovalization were being recorded.

RESULTS AND DISCUSSION

Figure 4 presents the moment (M) - curvature (κ) curves of the thin-walled tubular specimen under three different curvature-rates at preloading stage. It can be seen that the moment-curvature curves are sensitive to the magnitude of curvature-rate. The higher the applied curvature-rate, the greater the degree of hardening for tubular specimen is. Figure 5 shows the corresponding ovalization of tube cross-section as a function of the applied curvature. The ovalization of tube cross-section is defined by $\Delta D/D$ where D is the outer diameter and ΔD is the change in outer diameter. It can be noted that the ovalization of tube cross-section increases when the applied curvature increases. The higher degree of the ovalization of tube cross-section can be observed under higher curvature-rates.

Creep Stage

Figure 6 depicts the curvature (κ) - time (t) profiles of the whole creep process under pure bending (the loading stage and the creep stage). The starting and buckling points of the creep stage are marked by

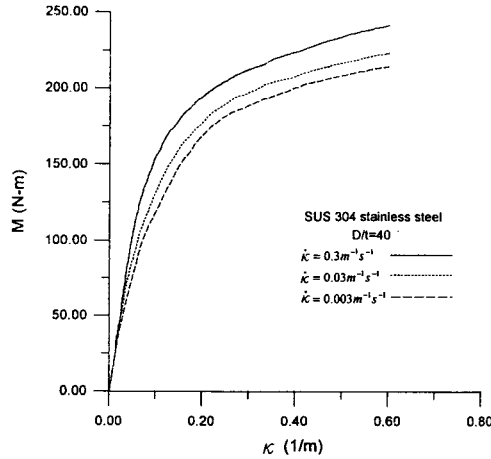


Figure 4 Moment-curvature curves under three different curvature-rates.

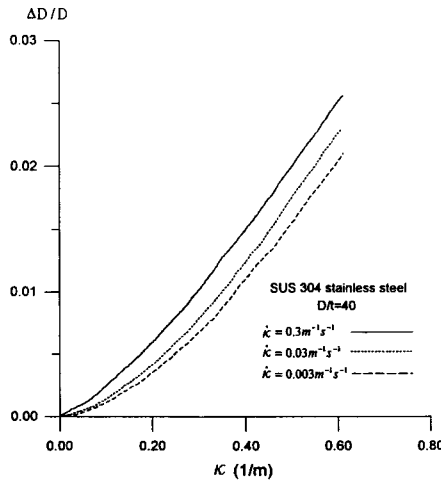


Figure 5 Ovalization-curvature curves under three different curvature-rates

"*" and "x", respectively. The profiles confirm the constant curvature-rate control of each curve prior to reaching the hold moment. Although the magnitude of the moment just prior to creep stage are almost the same (170 N-m), the creep curves for three curvature-rates at preloading stage are quite different. It could be seen that as soon as the creep is started the magnitude of the tube curvature quickly increases. The initial creep-rate of the creep test with fast curvature-rate preloading is large, and the corresponding creep curvature is larger than that of the creep test with a slower curvature-rate preloading. Owing to the continuously increasing curvature at the creep stage, the tube specimen buckles eventually. Figure 7 demonstrates the ovalization-time profiles of the whole creep process under pure bending at same holding moment of 170 N-m (the loading stage and the creep stage). The

starting and buckling points of the creep stage are also marked by "*" and "x", respectively. It is shown that the ovalization curves are also strongly influenced by the curvature-rate at the preloading stage and the ovalization of the tube cross-section increases faster with a higher constant curvature-rate preloading than that with a lower one.

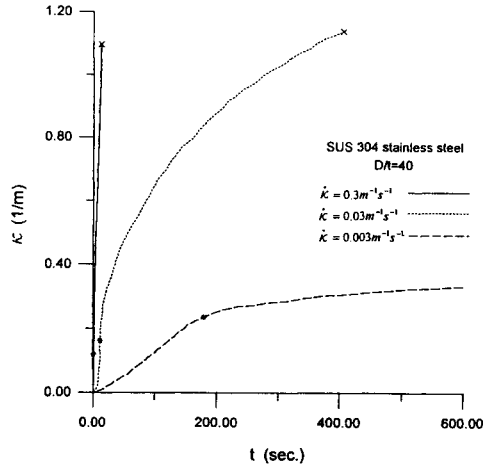


Figure 6 Curvature-time profiles with curvature-rate controlled preloading ("*" and "x" denote the starting and buckling points of the creep stage, respectively).

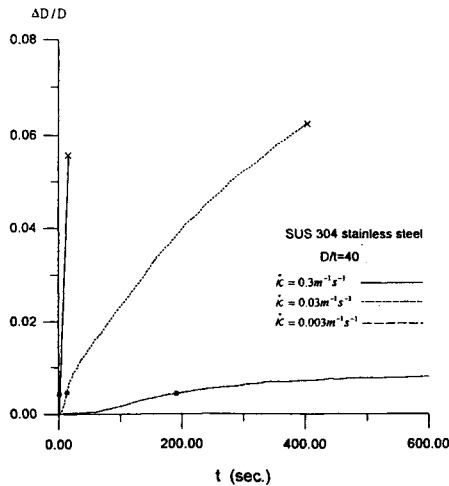


Figure 7 Ovalization-time profiles with curvature-rate controlled preloading ("*" and "x" denote the starting and buckling points of the creep stage, respectively).

CONCLUSION

The effect of curvature-rate at preloading stage on creep behaviors for thin-walled tubes under pure bending is investigated in this study. A bending machine and a curvature-ovalization measurement apparatus (COMA) were used for conducting the present experimental tests on thin-walled tubular specimens of 304 stainless steel. The thin-walled tube hardens when curvature-rate increases. The higher the applied curvature-rate, the greater the degree of hardening of the tube is. The ovalization of tube cross-section increases when the curvature-rate increases. The higher the applied curvature-rate, the greater the degree of ovalization of tube cross-section is. For the subsequent creep stage, the creep curvature is larger with a higher constant curvature-rate at the preloading stage than that with a lower one. The creep ovalization of tube cross section increases faster with a higher constant curvature-rate at the preloading stage than that with a lower one.

ACKNOWLEDGEMENT

The work presented was carried out with the support of National Science Council under grant NSC 87-TPC-E-006-025. Its support is gratefully acknowledged.

REFERENCES

- (1) Pan, W.F., Wang, T.R. and Hsu, C.M. (1998), A Curvature-Ovalization Measurement Apparatus for Circular Tubes under Cyclic Bending. *Int. J. Experimental Mechanics*, **38**:2, p. 99.
- (2) Reddy, B.D. (1979), An Experimental Study of the Plastic Buckling of Circular Cylinders in Pure Bending. *Int. J. Solids Struct.*, **15**, p. 669.
- (3) Gellin, S. (1980), The Plastic Buckling of Long Cylindrical Shell under Pure Bending. *Int. J. Solids Struct.*, **16**, p. 397.
- (4) Kyriakides, S. and Shaw, P.K. (1987), Inelastic Buckling of Tubes under Cyclic Loads. *ASME J. Press. Vessel Technol.*, **109**, p. 169.
- (5) Corona, E. and Kyriakides, S. (1991), An Experimental Investigation of the Degradation and Buckling of Circular Tubes under Cyclic Bending and External Pressure. *Thin-Walled Struct.*, **12**, p. 229.
- (6) Kyriakides, S. and Ju, G.T. (1992), Bifurcation and Localization Instabilities in Cylindrical Shells under Bending - I. Experiments. *Int. J. Solids Struct.*, **29**:9, p. 1117.
- (7) Xia, Z. and Ellyin, F. (1993), An Experimental Study on the Effect of prior Plastic Straining on Creep Behavior of 403 Stainless Steel. *ASME J. Engng. Mat. Tech.*, **115**, p. 200.
- (8) Wu, H.C. and Ho, C.C. (1995), An Investigation of Transient Creep by Means of Endochronic Viscoplasticity and Experiment. *ASME J. Engng. Mat. Tech.*, **117**, p. 260.

DYNAMIC EQUILIBRIUMS OF NONPRISMATIC THIN-WALLED BEAMS CONSIDERING THE EFFECTS OF TRANSVERSE SHEAR DEFORMATIONS DEFINED ON AN ARBITRARY COORDINATE SYSTEM

C.N. Chen

Department of Naval Architecture and Marine Engineering
National Cheng Kung University, Tainan, Taiwan

ABSTRACT

In this paper, Hamilton's principle is used to derive the dynamic equilibrium equations of nonprismatic composite beams of generic section considering the effects of transverse shear deformations. The displacements are defined on an arbitrarily selected coordinate system. The obtained dynamic equilibrium equations and natural boundary conditions are highly coupled.

KEYWORDS

Hamilton's principle, anisotropic material, orthotropic material, isotropic material, warping function, reduced stiffness, effective stiffness, shear deformation.

INTRODUCTION

The solution of nonprismatic thin-walled beam problems is important since a lot of engineering structures are formed by nonprismatic thin-walled beam members. The response behavior of generic thin-walled beams is very complex. Hence, the commonly used methods for describing the dynamic equilibrium of generic thin-walled beams always involve the selection of a specific reference coordinate system. Classical approaches which locate the origin of the reference coordinate system at the centroid or shear center of the cross section and orienting the two axes on the cross section to the principal directions lead to obtain a lowly coupled or uncoupled equation system. The application of the resulting equation systems obtained by these approaches to the analysis of structural problems is generally limited.

The dynamic equilibrium equations of nonprismatic beams neglecting the effects of transverse shear deformations defined on an arbitrary coordinate system have been derived by the author (Chen, 1996). In this paper the equations including the effects of shear deformations are derived.

CONSTITUTIVE RELATIONS FOR ANISOTROPIC MATERIALS

Consider the rectangular Cartesian coordinate system with coordinate axes (x_1, x_2, x_3) , the generalized Hooke's law for anisotropic materials can be expressed by the following equation

$$\sigma_i = C_{ij}\epsilon_j \tag{1}$$

where $\sigma_i \equiv \{\sigma_1 \ \sigma_2 \ \sigma_3 \ \tau_{23} \ \tau_{31} \ \tau_{12}\}^t$ are stresses, $\epsilon_j \equiv \{\epsilon_1 \ \epsilon_2 \ \epsilon_3 \ \gamma_{23} \ \gamma_{31} \ \gamma_{12}\}^t$ strains and C_{ij} elastic stiffnesses. The constitutive law defined by the rectangular Cartesian coordinate system with coordinate axes (x, y, z) which will be used to define the dynamic nonprismatic beam problems can similarly be expressed as follows:

$$\sigma_i = \bar{C}_{ij}\epsilon_j \tag{2}$$

Consider that the coordinate axis z is aligned along the axis of the beam. The constitutive relations can be represented by the following matrix equation

$$\begin{Bmatrix} \sigma_z \\ \tau_{xy} \\ \tau_{xz} \end{Bmatrix} = \begin{bmatrix} \bar{Q}_{33} & \bar{Q}_{34} & \bar{Q}_{35} \\ \bar{Q}_{34} & \bar{Q}_{44} & \bar{Q}_{45} \\ \bar{Q}_{35} & \bar{Q}_{45} & \bar{Q}_{55} \end{bmatrix} \begin{Bmatrix} \epsilon_z \\ \gamma_{xy} \\ \gamma_{xz} \end{Bmatrix} \tag{3}$$

where \bar{Q}_{ij} are the reduced stiffnesses which can be expressed as functions of the stiffnesses \bar{C}_{ij} . If the $x - y$ plane is one of elastic symmetry, the material is called monoclinic material and \bar{Q}_{34} and \bar{Q}_{35} vanish. Then stiffnesses are not altered by the reflection in the plane $x - y$ or the coordinate transformation $x' = x, y' = y, z' = z$. This is called monoclinic symmetry. It means that the material properties are identical along any two rays symmetric with respect to the $x - y$ plane. If the material possesses three mutually perpendicular planes of elastic symmetry and the principal material symmetry axes are aligned along the coordinate directions (x, y, z) , the material is called orthotropic material and \bar{Q}_{45} also vanishes. If the material is isotropic, \bar{Q}_{33} is the Young's modulus E and \bar{Q}_{44} and \bar{Q}_{55} represent the shear modulus G . If the coordinate directions (x, y) are not aligned along the principal material symmetry directions (x_1, y_1) of an orthotropic material but rotated about z_1 to make an angle θ with (x_1, y_1) , the reduced elastic stiffnesses \bar{Q}_{ij} can be expressed by Q_{ij} which are the elastic stiffnesses defining the stress-strain relations in the principal material symmetry coordinate system. Let $l = \cos\theta$ and $m = \sin\theta$, the transformation relations are expressed by the following matrix equation

$$\begin{Bmatrix} x \\ y \\ z \end{Bmatrix} = \begin{bmatrix} l & m & 0 \\ -m & l & 0 \\ 0 & 0 & 1 \end{bmatrix} \begin{Bmatrix} x_1 \\ y_1 \\ z_1 \end{Bmatrix} \tag{4}$$

Using the transformation matrix in the above equation into the transformation relations for stresses and strains, \bar{Q}_{ij} can be related to Q_{ij} by the following transformation equation

$$\begin{Bmatrix} \bar{Q}_{33} \\ \bar{Q}_{44} \\ \bar{Q}_{55} \\ \bar{Q}_{45} \end{Bmatrix} = \begin{bmatrix} 1 & 0 & 0 \\ 0 & l^2 & m^2 \\ 0 & m^2 & l^2 \\ 0 & lm & -lm \end{bmatrix} \begin{Bmatrix} Q_{33} \\ Q_{44} \\ Q_{55} \end{Bmatrix} \tag{5}$$

TORSION THEORY OF BARS MADE BY ANISOTROPIC MATERIALS

Figure 1 shows the definition of the coordinate system. The coordinate system fixed on the cross section has the origin O . A is a varying arbitrary point. The theory of pure torsion is a potential problem. In developing this theory, the cross section is assumed to be rigid in its own plane. Thus the displacements of A in x and y directions caused by twisting can be expressed as:

$$\bar{U}(x, y, z, t) = -y\theta(z, t), \quad \bar{V}(x, y, z, t) = x\theta(z, t) \tag{6}$$

Let $\bar{w}(x, y, z, t)$ denote the displacement in z direction due to torsion. Consider a composite bar made of multiple bars which have their own materials and are firmly bonded together to act as a single member. Then the whole domain of a cross-section is composed of many subdomains. In a specific subdomain, the two shear strains are

$$\bar{\gamma}_{xz} = \frac{\partial \bar{w}}{\partial x} - y \frac{\partial \theta}{\partial z}, \quad \bar{\gamma}_{xy} = \frac{\partial \bar{w}}{\partial y} + x \frac{\partial \theta}{\partial z} \tag{7}$$

Considering that the axial strain $\tilde{\epsilon}_z$ does not exist and using Eqn. 3, the two shear stresses can be expressed by

$$\tilde{\tau}_{zx} = \bar{Q}_{55}\tilde{\gamma}_{zx} + \bar{Q}_{45}\tilde{\gamma}_{zy}, \quad \tilde{\tau}_{zy} = \bar{Q}_{44}\tilde{\gamma}_{zy} + \bar{Q}_{45}\tilde{\gamma}_{zx} \quad (8)$$

From the equilibrium in z direction, the following equation can be obtained

$$\bar{Q}_{55} \frac{\partial^2 \tilde{w}}{\partial x^2} + 2\bar{Q}_{45} \frac{\partial^2 \tilde{w}}{\partial x \partial y} + \bar{Q}_{44} \frac{\partial^2 \tilde{w}}{\partial y^2} = 0 \quad (9)$$

Consider a point on the boundary of the cross section and define a coordinate system with the origin located at that point, one coordinate axis oriented in z direction and the other two coordinate axes (n, s) are aligned along the outward unit normal vector and the unit tangential vector. This coordinate system is also right-handed. Assuming that the coordinate axes (n, s) are oriented to make an angle θ with (x, y) , the direction cosines are $l = \cos(n, x)$ $m = \sin(n, y)$. The condition that the shear stress in n direction must vanish leads to the following boundary condition

$$(l\bar{Q}_{55} + m\bar{Q}_{45})\left(\frac{\partial \tilde{w}}{\partial x} - y\frac{\partial \theta}{\partial z}\right) + (l\bar{Q}_{45} + m\bar{Q}_{44})\left(\frac{\partial \tilde{w}}{\partial y} + x\frac{\partial \theta}{\partial z}\right) = 0 \quad (10)$$

Referring to the above equation, the axial displacement $\tilde{w}(x, y, z, t)$ is assumed as

$$\tilde{w}(x, y, z, t) = \frac{\partial \theta(z, t)}{\partial z} \omega(x, y) \quad (11)$$

where $\omega(x, y)$ is the warping function. The condition that the normal stress in z direction does not exist leads to the following equation

$$\frac{\partial \tilde{w}(x, y, z, t)}{\partial z} = 0 \quad (12)$$

Consequently, the twisting rate $\frac{\partial \theta(z, t)}{\partial z}$ is constant. Then Eqn. 9 leads to the following potential equation

$$\bar{Q}_{55} \frac{\partial^2 \omega}{\partial x^2} + 2\bar{Q}_{45} \frac{\partial^2 \omega}{\partial x \partial y} + \bar{Q}_{44} \frac{\partial^2 \omega}{\partial y^2} = 0 \quad (13)$$

And Eqn. 10 leads to the following equation

$$(l\bar{Q}_{55} + m\bar{Q}_{45})\left(\frac{\partial \omega}{\partial x} - y\right) + (l\bar{Q}_{45} + m\bar{Q}_{44})\left(\frac{\partial \omega}{\partial y} + x\right) = 0 \quad (14)$$

On the inter-subdomain boundary of two adjacent subdomains r and s , the axial displacements must be the same. Let $\omega^{(r)}$ and $\omega^{(s)}$ denote the warping functions in subdomain r and subdomain s , respectively. The following relation can be obtained by referring Eqn. 11

$$\omega^{(r)}(x, y) = \omega^{(s)}(x, y) \quad (15)$$

In addition, the shear strains in the tangential direction on inter-subdomain boundary must satisfy the compatibility condition. This results in the following equation

$$m^{(r)}\left(\frac{\partial \omega^{(r)}}{\partial x} - \frac{\partial \omega^{(s)}}{\partial x}\right) - l^{(r)}\left(\frac{\partial \omega^{(r)}}{\partial y} - \frac{\partial \omega^{(s)}}{\partial y}\right) = 0 \quad (16)$$

Equation 13 defined in all subdomains, Eqn. 14 defined on subdomain boundaries which compose the domain boundary and Eqns. 15 and 16 defined on all inter-subdomain boundaries form a partial differential equation system which governs the pure torsion of a composite anisotropic bar made of multiple bars. If the material in the specific subdomain is orthotropic with the principal material symmetry directions (x, y, z) , \bar{Q}_{45} vanishes and Eqns. 13 and 14 can be simplified. This will result in an elliptic-type equation problem. If the material in the specific subdomain is isotropic, the problem can further be simplified. This will result in the Laplace equation problem.

The above general formulation is good for generic nonprismatic beams which can be solid or thin-walled. If the nonprismatic composite anisotropic beam is thin-walled, simplified approach of assuming that the distribution of warping function is uniform across the thickness of the wall can also be adopted to determine the warping function. Define the local coordinate system with

the origin located on the centerline of the cross section. Then the shear strains in the tangential direction s and the outward unit normal direction n can be expressed by

$$\begin{aligned}\tilde{\gamma}_{zs}(s, t) &= -m\tilde{\gamma}_{zx}(s, t) + l\tilde{\gamma}_{zy}(s, t) = \left[lx + my + \frac{\partial\omega(s)}{\partial s} \right] \frac{\partial\theta}{\partial z}, \\ \tilde{\gamma}_{zn}(s, t) &= l\tilde{\gamma}_{zx}(s, t) + m\tilde{\gamma}_{zy}(s, t) = -(mx + ly) \frac{\partial\theta}{\partial z}\end{aligned}\quad (17)$$

By adopting the averaging stiffness approach, the effective constitutive relations can be constructed. Consider that a specific thin-walled segment in the cross section has the effective reduced stiffnesses \hat{Q}_{44} , \hat{Q}_{55} and \hat{Q}_{45} which are coefficients in the constitutive relations of shears defined by the coordinate system with coordinate axes (n, s) . The constitutive relations are expressed as:

$$\tilde{\tau}_{zs} = \hat{Q}_{44}\tilde{\gamma}_{zs} + \hat{Q}_{45}\tilde{\gamma}_{zn}, \quad \tilde{\tau}_{zn} = \hat{Q}_{45}\tilde{\gamma}_{zs} + \hat{Q}_{55}\tilde{\gamma}_{zn}\quad (18)$$

The introduction of Eqn. 17 into Eqn. 18 leads to

$$\begin{aligned}\tilde{\tau}_{zs} &= \left[\hat{Q}_{44} \left(lx + my + \frac{\partial\omega(s)}{\partial s} \right) - \hat{Q}_{45}(mx + ly) \right] \frac{\partial\theta}{\partial z}, \\ \tilde{\tau}_{zn} &= \left[\hat{Q}_{45} \left(lx + my + \frac{\partial\omega(s)}{\partial s} \right) - \hat{Q}_{55}(mx + ly) \right] \frac{\partial\theta}{\partial z}\end{aligned}\quad (19)$$

For an open section, the tangential shear stress on the center line is approximately equal to zero. Thus, by referring Eqn. 19 the following equation can be obtained

$$lx + my + \frac{\partial\omega(s)}{\partial s} = 0\quad (20)$$

Equation (20) can be integrated to obtain the warping function which is expressed by the following equation

$$\omega(s) = - \int_0^s (lx + my) ds + \omega_B\quad (21)$$

where ω_B is the value of warping function at the point B . Let $\vec{r} = x\vec{i} + y\vec{j}$ be the position vector of a point in the section. In Eqn. 21, $-(lx + my)ds$ equals the component of the vector product $\vec{r} \times d\vec{s}$ in the direction of axis z . On the other hand, for a closed section τ_{zs} is uniform across the wall thickness. Since the shear stress in the outward unit normal direction is approximately equal to zero, the following relation can be obtained

$$mx + ly = \frac{\hat{Q}_{45}}{\hat{Q}_{55}} \left(lx + my + \frac{\partial\omega(s)}{\partial s} \right)\quad (22)$$

Using Eqn. (22), τ_{zs} can be rewritten as

$$\tau_{zs} = \frac{\hat{Q}_{44}\hat{Q}_{55} - \hat{Q}_{45}^2}{\hat{Q}_{55}} \left(lx + my + \frac{\partial\omega(s)}{\partial s} \right) \frac{\partial\theta}{\partial z}\quad (23)$$

Multiplying both sides of Eqn. (23) by ds and integrating around the total periphery S of the section, the following relation can be obtained:

$$\oint d\omega = \oint \frac{\hat{Q}_{55}\tilde{\tau}_{zs} ds}{\hat{Q}_{44}\hat{Q}_{55} - \hat{Q}_{45}^2} - \frac{\partial\theta}{\partial z} \oint (lx + my) ds\quad (24)$$

The integral on the left side of this equation vanishes because it equals the difference in ω at $s = 0$ and $s = S$ which are identical. In addition, $-\oint (lx + my) ds = \oint |\vec{r} \times d\vec{s}| ds = 2\Omega$, $M_t = 2\Omega\tilde{\tau}_{zs}\delta(s)$, where Ω is the area enclosed by the center line, M_t the twisting moment and $\delta(s)$ the wall thickness. Thus, the following relation is obtained

$$\frac{\partial\theta}{\partial z} = \frac{1}{2\Omega} \oint \frac{\hat{Q}_{55}\tilde{\tau}_{zs} ds}{\hat{Q}_{44}\hat{Q}_{55} - \hat{Q}_{45}^2} = \frac{M_t}{4\Omega^2} \oint \frac{\hat{Q}_{55} ds}{(\hat{Q}_{44}\hat{Q}_{55} - \hat{Q}_{45}^2)\delta(s)}\quad (25)$$

Using the relation $\bar{\tau}_{zs} = M_t/2\Omega\delta(s)$ and Eqn. 25 in Eqn. 23 and integrating it, the formula defining the distribution of warping function can be obtained

$$\omega(s) = \frac{2\Omega}{\oint \frac{\bar{Q}_{33}ds}{(\bar{Q}_{44}\bar{Q}_{55} - \bar{Q}_{45}^2)\delta(s)}} \int_0^s \frac{\bar{Q}_{55}ds}{(\bar{Q}_{44}\bar{Q}_{55} - \bar{Q}_{45}^2)\delta(s)} - \int_0^s (lx + my)ds + \omega_B \tag{26}$$

The above equation can be used to define the distribution of warping function of a generic closed section which might be composed of many segments having different material properties.

DERIVATION OF THE DYNAMIC EQUILIBRIUM EQUATIONS

The cross section is rigid in its own plane. And the displacements are small. Figure 1 shows the definition of coordinate system. The fixed reference coordinate system on a cross section is xyz with O as the origin. A is a varying arbitrary point. Since the cross section is rigid in its own plane, the displacements of A can be expressed as:

$$\begin{aligned} U(x, y, z, t) &= u(z, t) - y\theta(z, t), & V(x, y, z, t) &= v(z, t) + x\theta(z, t), \\ W(x, y, z, t) &= w(z, t) - x\phi(z, t) + y\psi(z, t) + \omega(x, y)\gamma(z, t) \end{aligned} \tag{27}$$

Displacement components U and V consist of lateral displacements on axis z and the relative lateral displacements due to the rotation of the beam. The axial displacement W is composed of the average axial displacement, axial displacements due to flexural deformation and the warping displacement due to the warping of the beam. Using Eqn. 27, the strain components can be obtained:

$$\begin{aligned} \epsilon_x &= \frac{\partial w}{\partial z} - x \frac{\partial \phi}{\partial z} + y \frac{\partial \psi}{\partial z} + \omega \frac{\partial \gamma}{\partial z}, & \gamma_{zx} &= \frac{\partial u}{\partial z} - \phi + \frac{\partial \omega}{\partial x} \gamma - y \frac{\partial \theta}{\partial z}, \\ \gamma_{zy} &= \frac{\partial v}{\partial z} + \psi + \frac{\partial \omega}{\partial y} \gamma + x \frac{\partial \theta}{\partial z}, & \epsilon_x &= \epsilon_y = \gamma_{xy} = 0 \end{aligned} \tag{28}$$

Then the stress components are

$$\begin{aligned} \sigma_x &= \bar{Q}_{33} \left(\frac{\partial w}{\partial z} - x \frac{\partial \phi}{\partial z} + y \frac{\partial \psi}{\partial z} + \omega \frac{\partial \gamma}{\partial z} \right) + \bar{Q}_{34} k_{zy} \left(\frac{\partial v}{\partial z} + \psi \right) + \bar{Q}_{34} \left(\frac{\partial \omega}{\partial y} \gamma + x \frac{\partial \theta}{\partial z} \right) + \bar{Q}_{35} k_{zx} \left(\frac{\partial u}{\partial z} - \phi \right) + \bar{Q}_{35} \left(\frac{\partial \omega}{\partial x} \gamma - y \frac{\partial \theta}{\partial z} \right), \\ \tau_{zx} &= \bar{Q}_{55} k_x \left(\frac{\partial u}{\partial z} - \phi \right) + \bar{Q}_{55} \left(\frac{\partial \omega}{\partial x} \gamma - y \frac{\partial \theta}{\partial z} \right) + \bar{Q}_{45} k_{xy} \left(\frac{\partial v}{\partial z} + \psi \right) + \bar{Q}_{45} \left(\frac{\partial \omega}{\partial y} \gamma + x \frac{\partial \theta}{\partial z} \right), \\ \tau_{zy} &= \bar{Q}_{44} k_y \left(\frac{\partial v}{\partial z} + \psi \right) + \bar{Q}_{44} \left(\frac{\partial \omega}{\partial y} \gamma + x \frac{\partial \theta}{\partial z} \right) + \bar{Q}_{45} k_{yx} \left(\frac{\partial u}{\partial z} - \phi \right) + \bar{Q}_{45} \left(\frac{\partial \omega}{\partial z} \gamma - y \frac{\partial \theta}{\partial z} \right), & \sigma_x &= \sigma_y = \tau_{xy} = 0 \end{aligned} \tag{29}$$

where $k_x, k_y, k_{xy}, k_{yx}, k_{zx}$ and k_{zy} are shear coefficients. Using Eqns. 28 and 29, the strain energy of a generic beam of length l can be defined:

$$U = \frac{1}{2} \iiint_V (\sigma_x \epsilon_x + \tau_{zx} \gamma_{zx} + \tau_{zy} \gamma_{zy}) dx dy dz \tag{30}$$

Let ρ denote the mass density. The kinetic energy is written as:

$$T = \frac{1}{2} \iiint_V \rho \left[\left(\frac{\partial U}{\partial t} \right)^2 + \left(\frac{\partial V}{\partial t} \right)^2 + \left(\frac{\partial W}{\partial t} \right)^2 \right] dx dy dz \tag{31}$$

Let $b_x(x, y, z, t), b_y(x, y, z, t)$ and $b_z(x, y, z, t)$ denote the distributed forces in the structural domain in x, y and z directions, respectively. Also let $\bar{i}_x(x, y, t), \bar{i}_y(x, y, t)$ and $\bar{i}_z(x, y, t)$ denote the boundary traction forces on the two boundary sections $z = 0$ and $z = l$. Then the work of external forces can be written as:

$$\begin{aligned} W &= \iiint_V (b_x U + b_y V + b_z W) dx dy dz - \iint_A (\bar{i}_x U + \bar{i}_y V + \bar{i}_z W) |_{z=0} dx dy \\ &+ \iint_A (\bar{i}_x U + \bar{i}_y V + \bar{i}_z W) |_{z=l} dx dy \end{aligned} \tag{32}$$

Hamilton used the kinetic energy and potential energy to construct a stationary principle. Consider that the nonprismatic beam has the initial conditions $u(z, t_0)$, $\frac{\partial u(z, t_0)}{\partial t}$, $v(z, t_0)$, $\frac{\partial v(z, t_0)}{\partial t}$, $w(z, t_0)$, $\frac{\partial w(z, t_0)}{\partial t}$, $\psi(z, t_0)$, $\frac{\partial \psi(z, t_0)}{\partial t}$, $\theta(z, t_0)$, $\frac{\partial \theta(z, t_0)}{\partial t}$, $\gamma(z, t_0)$ and $\frac{\partial \gamma(z, t_0)}{\partial t}$ at the instant $t_0 = 0$, then Hamilton's principle between two time stages t_1 and t_2 can mathematically be expressed as:

$$\delta \int_{t_1}^{t_2} (U - W - T) dt = 0 \quad (33)$$

Substituting Eqns. 30, 31 and 32 into Eqn. 33 and carrying out the integration by parts for some mathematical terms, then from the admissibilities of ϕ , u , ψ , v , w , γ and θ in domain $0 < z < l$; the dynamic equilibrium equations and the related boundary conditions can be obtained. They are highly coupled. The degree of coupling will decrease following the increase of planes of elastic symmetry. For monoclinic beams, there exist one plane of elastic symmetry. The orthotropic beams possess three mutually perpendicular planes of elastic symmetry. And the isotropic beams which are elastically equivalent in all directions possess complete symmetry. The dynamic equilibrium equations of the nonprismatic orthotropic beams with the principal material symmetry axes aligned along the coordinate directions (x, y, z) are listed below:

$$G_{55} \left(\frac{\partial u}{\partial z} - \phi \right) + \frac{\partial}{\partial z} (D_{33xz} \frac{\partial \phi}{\partial z}) - \frac{\partial}{\partial z} (D_{33xy} \frac{\partial \psi}{\partial z}) - \frac{\partial}{\partial z} (B_{33x} \frac{\partial w}{\partial z}) - G_{55y} \left(\frac{\partial \theta}{\partial z} - \gamma \right) - \frac{\partial}{\partial z} (D_{33wx} \frac{\partial \gamma}{\partial z}) - \rho I_{xx} \frac{\partial^2 \phi}{\partial t^2} + \rho I_{xy} \frac{\partial^2 \psi}{\partial t^2} + \rho I_x \frac{\partial^2 w}{\partial t^2} + \rho I_{wx} \frac{\partial^2 \gamma}{\partial t^2} = -m_y \quad (34-1)$$

$$- \frac{\partial}{\partial z} \left[G_{55} \left(\frac{\partial u}{\partial z} - \phi \right) \right] + \frac{\partial}{\partial z} \left[G_{55y} \left(\frac{\partial \theta}{\partial z} - \gamma \right) \right] + \rho A \frac{\partial^2 u}{\partial t^2} - \rho I_y \frac{\partial^2 \theta}{\partial t^2} = q_x \quad (34-2)$$

$$\frac{\partial}{\partial z} (D_{33yz} \frac{\partial \phi}{\partial z}) + G_{44} \left(\frac{\partial v}{\partial z} + \psi \right) - \frac{\partial}{\partial z} (D_{33yy} \frac{\partial \psi}{\partial z}) - \frac{\partial}{\partial z} (B_{33y} \frac{\partial w}{\partial z}) + G_{44x} \left(\frac{\partial \theta}{\partial z} - \gamma \right) - \frac{\partial}{\partial z} (D_{33wy} \frac{\partial \gamma}{\partial z}) - \rho I_{yy} \frac{\partial^2 \phi}{\partial t^2} + \rho I_{yy} \frac{\partial^2 \psi}{\partial t^2} + \rho I_y \frac{\partial^2 w}{\partial t^2} + \rho I_{wy} \frac{\partial^2 \gamma}{\partial t^2} = m_x \quad (34-3)$$

$$- \frac{\partial}{\partial z} \left[G_{44} \left(\frac{\partial v}{\partial z} + \psi \right) \right] - \frac{\partial}{\partial z} \left[G_{44x} \left(\frac{\partial \theta}{\partial z} - \gamma \right) \right] + \rho A \frac{\partial^2 v}{\partial t^2} + \rho I_x \frac{\partial^2 \theta}{\partial t^2} = q_y \quad (34-4)$$

$$\frac{\partial}{\partial z} (B_{33z} \frac{\partial \phi}{\partial z}) - \frac{\partial}{\partial z} (B_{33y} \frac{\partial \psi}{\partial z}) - \frac{\partial}{\partial z} (A_{33} \frac{\partial w}{\partial z}) - \frac{\partial}{\partial z} (B_{33w} \frac{\partial \gamma}{\partial z}) - \rho I_x \frac{\partial^2 \phi}{\partial t^2} + \rho I_y \frac{\partial^2 \psi}{\partial t^2} + \rho A \frac{\partial^2 w}{\partial t^2} + \rho I_w \frac{\partial^2 \gamma}{\partial t^2} = p \quad (34-5)$$

$$G_{55y} \left(\frac{\partial u}{\partial z} - \phi \right) + \frac{\partial}{\partial z} (D_{33wx} \frac{\partial \phi}{\partial z}) - G_{44x} \left(\frac{\partial v}{\partial z} + \psi \right) - \frac{\partial}{\partial z} (D_{33wy} \frac{\partial \psi}{\partial z}) - \frac{\partial}{\partial z} (B_{33w} \frac{\partial w}{\partial z}) - G_K \left(\frac{\partial \theta}{\partial z} - \gamma \right) - \frac{\partial}{\partial z} (D_{33wz} \frac{\partial \gamma}{\partial z}) - \rho I_{wx} \frac{\partial^2 \phi}{\partial t^2} + \rho I_{wy} \frac{\partial^2 \psi}{\partial t^2} + \rho I_w \frac{\partial^2 w}{\partial t^2} + \rho I_{wz} \frac{\partial^2 \gamma}{\partial t^2} = m_w \quad (34-6)$$

$$\frac{\partial}{\partial z} \left[G_{55y} \left(\frac{\partial u}{\partial z} - \phi \right) \right] - \frac{\partial}{\partial z} \left[G_{44x} \left(\frac{\partial v}{\partial z} + \psi \right) \right] - \frac{\partial}{\partial z} \left[G_p \left(\frac{\partial \theta}{\partial z} - \gamma \right) \right] - \frac{\partial}{\partial z} (G_J \gamma) - \rho I_y \frac{\partial^2 u}{\partial t^2} + \rho I_x \frac{\partial^2 v}{\partial t^2} + \rho I_p \frac{\partial^2 \theta}{\partial t^2} = m_z \quad (34-7)$$

And the boundary conditions on boundaries $z = 0$ and $z = l$ are:

$$D_{33zx} \frac{\partial \phi}{\partial z} - D_{33xy} \frac{\partial \psi}{\partial z} - B_{33x} \frac{\partial w}{\partial z} - D_{33wx} \frac{\partial \gamma}{\partial z} = \bar{M}_y \quad \text{or} \quad \delta \phi = 0 \quad (35-1)$$

$$G_{55} \left(\frac{\partial u}{\partial z} - \phi \right) - G_{55y} \left(\frac{\partial \theta}{\partial z} - \gamma \right) = \bar{V}_x \quad \text{or} \quad \delta u = 0 \quad (35-2)$$

$$D_{33zy} \frac{\partial \phi}{\partial z} - D_{33yy} \frac{\partial \psi}{\partial z} - B_{33y} \frac{\partial w}{\partial z} - D_{33wy} \frac{\partial \gamma}{\partial z} = -\bar{M}_x \quad \text{or} \quad \delta \psi = 0 \quad (35-3)$$

$$G_{44} \left(\frac{\partial v}{\partial z} + \psi \right) + G_{44x} \left(\frac{\partial \theta}{\partial z} - \gamma \right) = \bar{V}_y \quad \text{or} \quad \delta v = 0 \quad (35-4)$$

$$- B_{33x} \frac{\partial \phi}{\partial z} + B_{33y} \frac{\partial \psi}{\partial z} + A_{33} \frac{\partial w}{\partial z} + B_{33w} \frac{\partial \gamma}{\partial z} = \bar{P} \quad \text{or} \quad \delta w = 0 \quad (35-5)$$

$$- D_{33zx} \frac{\partial \phi}{\partial z} + D_{33xy} \frac{\partial \psi}{\partial z} + B_{33w} \frac{\partial w}{\partial z} + D_{33wx} \frac{\partial \gamma}{\partial z} = \bar{M}_w \quad \text{or} \quad \delta \gamma = 0 \quad (35-6)$$

$$- G_{55y} \left(\frac{\partial u}{\partial z} - \phi \right) + G_{44x} \left(\frac{\partial v}{\partial z} + \psi \right) + G_p \left(\frac{\partial \theta}{\partial z} - \gamma \right) + G_J \gamma = \bar{M}_z \quad \text{or} \quad \delta \theta = 0 \quad (35-7)$$

where the elastic restoring forces related constants are defined by

$$\begin{aligned}
 A_{33} &= \iint_A \bar{Q}_{33} dx dy, & B_{33x} &= \iint_A \bar{Q}_{33x} dx dy, & B_{33y} &= \iint_A \bar{Q}_{33y} dx dy, & B_{33\omega} &= \iint_A \bar{Q}_{33\omega} dx dy, \\
 D_{33xx} &= \iint_A \bar{Q}_{33x^2} dx dy, & D_{33yy} &= \iint_A \bar{Q}_{33y^2} dx dy, & D_{33\omega\omega} &= \iint_A \bar{Q}_{33\omega^2} dx dy, & D_{33x\omega} &= \iint_A \bar{Q}_{33x\omega} dx dy, \\
 D_{33\omega y} &= \iint_A \bar{Q}_{33y\omega} dx dy, & D_{33xy} &= \iint_A \bar{Q}_{33xy} dx dy, & G_p &= \iint_A (\bar{Q}_{44x^2} + \bar{Q}_{55y^2}) dx dy, & G_{44x} &= \iint_A \bar{Q}_{44x} dx dy, \\
 G_{55y} &= \iint_A \bar{Q}_{55y} dx dy, & G_J &= \iint_A \left[\bar{Q}_{55} \left(\frac{\partial \omega}{\partial x} - y \right)^2 + \bar{Q}_{44} \left(\frac{\partial \omega}{\partial y} + x \right)^2 \right] dx dy, & G_K &= G_p - G_J & & (36)
 \end{aligned}$$

the inertia forces related constants are defined by

$$\begin{aligned}
 A &= \iint_A dx dy, & I_x &= \iint_A x dx dy, & I_y &= \iint_A y dx dy, & I_\omega &= \iint_A \omega dx dy, & I_{xx} &= \iint_A x^2 dx dy, \\
 I_{yy} &= \iint_A y^2 dx dy, & I_p &= I_{xx} + I_{yy}, & I_{\omega\omega} &= \iint_A \omega^2 dx dy, & I_{\omega x} &= \iint_A x\omega dx dy, & I_{\omega y} &= \iint_A y\omega dx dy, \\
 I_{xy} &= \iint_A xy dx dy, & J &= \iint_A \left[\left(\frac{\partial \omega}{\partial x} - y \right)^2 + \left(\frac{\partial \omega}{\partial y} + x \right)^2 \right] dx dy, & K &= I_p - J & & (37)
 \end{aligned}$$

and the loads are defined by

$$\begin{aligned}
 q_x(z, t) &= \iint_A b_x dx dy, & q_y(z, t) &= \iint_A b_y dx dy, & p(z, t) &= \iint_A b_z dx dy, & m_x(z, t) &= \iint_A y b_x dx dy, \\
 m_y(z, t) &= - \iint_A x b_x dx dy, & m_z(z, t) &= \iint_A (x b_y - y b_x) dx dy, & m_\omega(z, t) &= \iint_A \omega b_z dx dy, & \bar{V}_z(t) &= \iint_A \bar{i}_z dx dy, \\
 \bar{V}_y(t) &= \iint_A \bar{i}_y dx dy, & \bar{P}(t) &= \iint_A \bar{i}_z dx dy, & \bar{M}_x(t) &= \iint_A y \bar{i}_z dx dy, & \bar{M}_y(t) &= - \iint_A x \bar{i}_z dx dy, \\
 \bar{M}_z(t) &= \iint_A (x \bar{i}_y - y \bar{i}_x) dx dy, & \bar{M}_\omega(t) &= \iint_A \omega \bar{i}_z dx dy & & & & (38)
 \end{aligned}$$

A dynamic generic nonprismatic composite beam problem can be solved by using Eqns. 34-1 to 34-7 and Eqns. 35-1 to 35-7. If the beam structure is thin-walled, the simplified approach for defining the warping function can be adopted. Then the integrations for calculating various constants and loads in defining the dynamic equilibrium equations and the related boundary conditions can be taken along the tangential direction of all thin-walled segments in the composite thin-walled section.

In addition, if the averaging stiffness approach is adopted, the effective constitutive relations can be constructed and the effective stiffnesses can be obtained. Let \bar{Q}_{33} , \bar{Q}_{44} and \bar{Q}_{55} denote the effective stiffnesses. Also adopt the normalized warping function denoted by $\bar{\omega}$ and defined by $\bar{\omega} = \omega - I_\omega/A$ for the torsion formulation, the dynamic equilibrium equations of which the longitudinal and torsional vibrations are not coupled can be obtained:

$$\begin{aligned}
 \bar{Q}_{55} k_x A \left(\frac{\partial u}{\partial z} - \phi \right) + \frac{\partial}{\partial z} (\bar{Q}_{33} I_{xx} \frac{\partial \phi}{\partial z}) - \frac{\partial}{\partial z} (\bar{Q}_{33} I_{xy} \frac{\partial \psi}{\partial z}) - \frac{\partial}{\partial z} (\bar{Q}_{33} I_x \frac{\partial \omega}{\partial z}) - \bar{Q}_{55} k_x I_y \left(\frac{\partial \theta}{\partial z} - \gamma \right) \\
 - \frac{\partial}{\partial z} (\bar{Q}_{33} I_{\omega x} \frac{\partial \gamma}{\partial z}) - \rho I_{xx} \frac{\partial^2 \phi}{\partial t^2} + \rho I_{xy} \frac{\partial^2 \psi}{\partial t^2} + \rho I_x \frac{\partial^2 \omega}{\partial t^2} + \rho I_{\omega x} \frac{\partial^2 \gamma}{\partial t^2} = -m_y & (39-1)
 \end{aligned}$$

$$\begin{aligned}
 - \frac{\partial}{\partial z} \left[\bar{Q}_{55} k_x A \left(\frac{\partial u}{\partial z} - \phi \right) \right] + \frac{\partial}{\partial z} \left[\bar{Q}_{55} k_x I_y \left(\frac{\partial \theta}{\partial z} - \gamma \right) \right] + \rho A \frac{\partial^2 u}{\partial t^2} - \rho I_y \frac{\partial^2 \theta}{\partial t^2} = q_x & (39-2)
 \end{aligned}$$

$$\begin{aligned}
 \frac{\partial}{\partial z} (\bar{Q}_{33} I_{xy} \frac{\partial \phi}{\partial z}) + \bar{Q}_{44} A \left(\frac{\partial v}{\partial z} + \psi \right) - \frac{\partial}{\partial z} (\bar{Q}_{33} I_{yy} \frac{\partial \psi}{\partial z}) - \frac{\partial}{\partial z} (\bar{Q}_{33} I_y \frac{\partial \omega}{\partial z}) + \bar{Q}_{44} I_x \left(\frac{\partial \theta}{\partial z} - \gamma \right) \\
 - \frac{\partial}{\partial z} (\bar{Q}_{33} I_{\omega y} \frac{\partial \gamma}{\partial z}) - \rho I_{xy} \frac{\partial^2 \phi}{\partial t^2} + \rho I_{yy} \frac{\partial^2 \psi}{\partial t^2} + \rho I_y \frac{\partial^2 \omega}{\partial t^2} + \rho I_{\omega y} \frac{\partial^2 \gamma}{\partial t^2} = m_x & (39-3)
 \end{aligned}$$

$$-\frac{\partial}{\partial z} \left[\bar{Q}_{44} A \left(\frac{\partial v}{\partial z} + \psi \right) \right] - \frac{\partial}{\partial z} \left[\bar{Q}_{44} I_x \left(\frac{\partial \theta}{\partial z} - \gamma \right) \right] + \rho A \frac{\partial^2 v}{\partial t^2} + \rho I_x \frac{\partial^2 \theta}{\partial t^2} = q_y \tag{39-4}$$

$$\frac{\partial}{\partial z} \left(\bar{Q}_{33} I_x \frac{\partial \phi}{\partial z} \right) - \frac{\partial}{\partial z} \left(\bar{Q}_{33} I_y \frac{\partial \psi}{\partial z} \right) - \frac{\partial}{\partial z} \left(\bar{Q}_{33} A \frac{\partial w}{\partial z} \right) - \rho I_x \frac{\partial^2 \phi}{\partial t^2} + \rho I_y \frac{\partial^2 \psi}{\partial t^2} + \rho A \frac{\partial^2 w}{\partial t^2} = p \tag{39-5}$$

$$\begin{aligned} & \bar{Q}_{55} k_x I_y \left(\frac{\partial u}{\partial z} - \phi \right) + \frac{\partial}{\partial z} \left(\bar{Q}_{33} I_{\omega x} \frac{\partial \phi}{\partial z} \right) - \bar{Q}_{44} I_x \left(\frac{\partial v}{\partial z} + \psi \right) - \frac{\partial}{\partial z} \left(\bar{Q}_{33} I_{\omega y} \frac{\partial \psi}{\partial z} \right) \\ & - G_k \left(\frac{\partial \theta}{\partial z} - \gamma \right) - \frac{\partial}{\partial z} \left(\bar{Q}_{33} I_{\omega \omega} \frac{\partial \gamma}{\partial z} \right) - \rho I_{\omega x} \frac{\partial^2 \phi}{\partial t^2} + \rho I_{\omega y} \frac{\partial^2 \psi}{\partial t^2} + \rho I_{\omega \omega} \frac{\partial^2 \gamma}{\partial t^2} = m_{\omega} \end{aligned} \tag{39-6}$$

$$\begin{aligned} & \frac{\partial}{\partial z} \left[\bar{Q}_{55} k_x I_y \left(\frac{\partial u}{\partial z} - \phi \right) \right] - \frac{\partial}{\partial z} \left[\bar{Q}_{44} I_x \left(\frac{\partial v}{\partial z} + \psi \right) \right] - \frac{\partial}{\partial z} \left[G_p \left(\frac{\partial \theta}{\partial z} - \gamma \right) \right] - \frac{\partial}{\partial z} (G_J \gamma) \\ & - \rho I_y \frac{\partial^2 u}{\partial t^2} + \rho I_x \frac{\partial^2 v}{\partial t^2} + \rho I_p \frac{\partial^2 \theta}{\partial t^2} = m_x \end{aligned} \tag{39-7}$$

And the boundary conditions are:

$$\bar{Q}_{33} I_{xx} \frac{\partial \phi}{\partial z} - \bar{Q}_{33} I_{xy} \frac{\partial \psi}{\partial z} - \bar{Q}_{33} I_x \frac{\partial w}{\partial z} - \bar{Q}_{33} I_{\omega x} \frac{\partial \gamma}{\partial z} = \bar{M}_y \quad \text{or} \quad \delta \phi = 0 \tag{40-1}$$

$$\bar{Q}_{55} k_x A \left(\frac{\partial u}{\partial z} - \phi \right) - \bar{Q}_{55} k_x I_y \left(\frac{\partial \theta}{\partial z} - \gamma \right) = \bar{V}_x \quad \text{or} \quad \delta u = 0 \tag{40-2}$$

$$\bar{Q}_{33} I_{xy} \frac{\partial \phi}{\partial z} - \bar{Q}_{33} I_{yy} \frac{\partial \psi}{\partial z} - \bar{Q}_{33} I_y \frac{\partial w}{\partial z} - \bar{Q}_{33} I_{\omega y} \frac{\partial \gamma}{\partial z} = -\bar{M}_x \quad \text{or} \quad \delta \psi = 0 \tag{40-3}$$

$$\bar{Q}_{44} A \left(\frac{\partial v}{\partial z} + \psi \right) + \bar{Q}_{44} I_x \left(\frac{\partial \theta}{\partial z} - \gamma \right) = \bar{V}_y \quad \text{or} \quad \delta v = 0 \tag{40-4}$$

$$-\bar{Q}_{33} I_x \frac{\partial \phi}{\partial z} + \bar{Q}_{33} I_y \frac{\partial \psi}{\partial z} + \bar{Q}_{33} A \frac{\partial w}{\partial z} = \bar{P} \quad \text{or} \quad \delta w = 0 \tag{40-5}$$

$$-\bar{Q}_{33} I_{\omega x} \frac{\partial \phi}{\partial z} + \bar{Q}_{33} I_{\omega y} \frac{\partial \psi}{\partial z} + \bar{Q}_{33} I_{\omega \omega} \frac{\partial \gamma}{\partial z} = \bar{M}_{\omega} \quad \text{or} \quad \delta \gamma = 0 \tag{40-6}$$

$$-\bar{Q}_{55} k_x I_y \left(\frac{\partial u}{\partial z} - \phi \right) + \bar{Q}_{44} I_x \left(\frac{\partial v}{\partial z} + \psi \right) + G_p \left(\frac{\partial \theta}{\partial z} - \gamma \right) + G_J \gamma = \bar{M}_x \quad \text{or} \quad \delta \theta = 0 \tag{40-7}$$

REFERENCES

Chen C.N. (1996). Variational Derivation of the Dynamic Equilibrium Equations of Nonprismatic Thin-walled Beams Defined on an Arbitrary Coordinate System. *ASME, Proc. 15th Intl. Conf. Offshore Mechanics and Arctic Engineering*, Florence, ITALY, Vol. 1, 319-326.

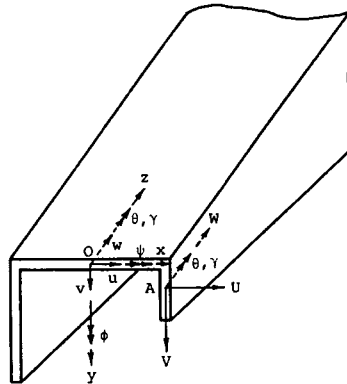


Figure 1: Coordinate system of the nonprismatic beam

LATERAL BUCKLING CAPACITIES OF THIN-WALLED MONOSYMMETRIC I-BEAMS

M. Kubo¹ and H. Kitahori²

¹Department of Civil Engineering, Meijo University,
Tenpaku-ku, Nagoya 468-8502, Japan

²Bridge Design Division, Tokyo Engineering Co., Ltd.,
Nakamura-ku, Nagoya 453-0801, Japan

ABSTRACT

This paper presents test results on lateral-torsional buckling of welded monosymmetric I-beams with various flange plate sizes. Ten different sections including doubly symmetric ones are tested under a concentrated load at the midspan of simply supported beams. Four span lengths ranging from 1.5 m to 3.75 m are chosen for each section. The influences of the monosymmetry and slenderness of sections on the rotation capacity and the ultimate strength are investigated, and the test results are compared with a proposed method to take account of the coupled behavior between lateral-torsional and local buckling.

KEYWORDS

welded steel beam, monosymmetric I-beam, non-compact section, lateral-torsional buckling, local buckling, ultimate strength, rotation capacity, experiment

INTRODUCTION

Studies on lateral-torsional buckling of steel beams have been made actively for doubly symmetric I-sections, and their results have been reflected on design codes (Fukumoto 1997). However, in order to cope with various sectional shapes and fabrication conditions even in the strength design for steel beams, Trahair (1994) suggested that multiple strength curves should be introduced as in the case of the column design method, and requested to develop the study on inelastic buckling

concerning other sectional beams such as monosymmetric I-shapes, channel and box shapes. Taking this into consideration, Kubo and Kitahori (1997) clarified the influences of monosymmetric sections on the lateral-torsional buckling strength and deformation capacity for compact welded I-beams. Against the lateral-torsional buckling, it was shown that the monosymmetric sections with enlarged compression flange are more effective than doubly symmetric sections.

In thin-walled beams having large width-thickness ratio, the influences of the web distortion and the coupled behavior between lateral-torsional and local buckling become important subjects (Rondal et al. 1996). Kubo and Fukumoto (1988) conducted buckling tests using four types of welded light-weight I-beams. As a result, it was found that beams having intermediate slenderness ratio failed in coupled buckling mode, thus lowering the load-carrying capacity considerably. They also proposed that the coupled buckling strength could be evaluated by using the Q -factor method based on the concept of effective width in the same manner as column design. Available test results on the coupled buckling of welded steel I-beams were reported by Yoda et al. (1989) and Lindner and Gregull (1992). However, these researches dealt with doubly symmetric I-beams.

This paper experimentally studies on non-compact welded I-beams having relatively large web depth and flange width. Buckling tests for simply supported beam subjected to a concentrated load at the midspan are conducted for 40 specimens in total using ten types of sectional shapes in order to investigate the influences of the monosymmetry and slenderness of sections on the failure mode and load-carrying capacities.

TEST SPECIMENS AND LOADING CONDITIONS

Ten welded I-sections were fabricated from SS400 steel of a nominal yield stress, $F_y = 245$ MPa. Only a hybrid section had SM490 steel of $F_y = 314$ MPa in tension flange. Figure 1 illustrates the beam specimen and the loading system.

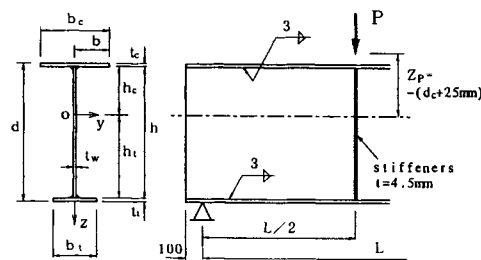


Figure 1: Beam specimen and loading system

The nominal cross-sectional dimensions are constant values of overall depth, $d = 300$ mm and web thickness, $t_w = 3.2$ mm with exception of flange sizes. The measured cross-sectional dimensions are listed in Table 1. Numeral in the specimen label indicates the width-thickness ratio for the compression flange. A parameter ρ indicates the degree of monosymmetry for I-sections, and is defined by

$$\rho = \frac{I_c}{I_c + I_t} = \frac{1}{1 + (b_t/b_c)^3(t_t/t_c)} \quad (1)$$

TABLE 1
MEASURED DIMENSIONS OF BEAM SPECIMENS

Specimen	Lot	ρ	d (mm)	b_c (mm)	b_t (mm)	t_w (mm)	t_c (mm)	t_t (mm)	b/t_c	$2h_c/t_w$
DS11	(A)	0.50	300.2	100.0	99.9	3.19	4.31	4.35	11.60	91.53
MS11		0.29	300.9	100.0	134.9	3.20	4.31	4.30	11.60	98.60
MS11T		0.26	300.3	99.9	100.2	3.19	4.31	12.04	11.59	117.95
ML04T		0.74	300.5	100.1	99.9	3.20	12.05	4.32	4.15	60.32
DS15	(B)	0.50	300.4	135.0	135.1	3.07	4.25	4.27	15.88	95.39
MS15		0.31	301.1	134.9	160.6	3.06	4.26	5.68	15.83	108.97
ML15		0.71	299.9	135.1	100.2	3.06	4.26	4.25	15.86	87.66
ML18		0.80	300.3	158.1	100.1	3.05	4.25	4.25	18.60	83.60
ML20		0.85	299.8	180.2	100.2	3.05	4.25	4.25	21.20	79.83
MH15		0.71	301.2	134.8	90.1	3.06	4.25	5.69	15.86	92.47

Note: Lot= lot number of material in Table 2; h_c = depth of the web in compression. Span length $L=1.5, 2.0, 2.5$ and 3.0 m for the sections DS11, MS11, MS11T, ML04T, DS15, MS15 and MH15, while $L=1.5, 2.25, 3.0$ and 3.75 m for other sections.

in which I_c , I_t = the second moments of area about weak axis (z-axis) of the compression and tension flanges, respectively. The width-thickness ratios of b/t_c for the compression flange ranged from 4 to 21. Using the depth of web in compression, h_c at elastic bending, the ratios of $2h_c/t_w$ ranged from 60 to 118. The test specimens except for the section ML04T are not satisfied the conditions of compact section in the AISC LRFD Specification (AISC 1986). Four different span lengths ranging from 1.5 m to 3.75 m were chosen in each of the sections.

Test arrangement is the same that described in previous papers (Kubo and Fukumoto 1988; Kubo and Kitahori 1997). The beams are simply supported against lateral-torsional deformation at their ends, and are subjected to a vertical concentrated load at the midspan as shown in Figure 1. The height of load application is at the position 25 mm above the top flange. Vertical and horizontal deflections, and normal strains during loading are measured at the midspan section. In order to obtain rotation angles due to in-plane bending, the slopes at both ends are also measured.

MATERIAL PROPERTIES AND INITIAL IMPERFECTIONS

Steel materials used in test beams consist of two kinds of manufacturing lot. The material properties were obtained from the tensile coupon tests and the average values are summarized for each of the nominal thickness in Table 2.

The initial crookedness of flanges and the out-of-plane deflections of web plates were measured, and the mean values m (with coefficient of variation ω) obtained from the maximum value in each beam can be expressed in the form of ratio to the span length L and the web depth h as follows. The crookedness of the compression flange are $v_0 = L/3490$ ($\omega = 0.57$) about the strong axis and $u_0 = L/2467$ ($\omega = 0.45$) about the weak axis. The deflection of the web plate is $w_0 = h/634$ ($\omega = 0.62$).

Residual stress measurements were performed on three specimens, the doubly symmetric section

TABLE 2
MATERIAL PROPERTIES OF STEEL PLATES

Steel plate		Lot	Yield stress, F_y (MPa)	Ultimate stress, F_u (MPa)	Young's modulus, E (GPa)	Poisson's ratio, ν	Elongation, Δl (%)
Nominal thickness, t (mm)	Number						
3.2 for web	4	(A)	331	469	227	0.275	30
4.5 for flange	4		270	425	225	0.290	31
12.0 for flange	4		263	427	217	0.281	34
3.2 for web	9	(B)	292	379	212	0.287	32
4.5 for flange	5		286	375	209	0.291	32
6.0 for flange	4		282	381	204	0.290	30
6.0 for flange ^a	4		399	557	208	0.277	27

^a This plate is SM490 and other plates are SS400 in standard JIS.

DS15 ($\rho = 0.5$) and the monosymmetric sections ML15 ($\rho = 0.71$) and ML18 ($\rho = 0.80$) as shown in Figure 2. The longitudinal residual stress resulting from welding are measured by the sectioning method at mid-section of the 1 m long specimen, using electric strain gauges on the measuring points. The compressive residual stress, about $0.5F_y$ was observed at the flange tips because the shear cut plates are used for the sections. For the monosymmetric sections ML15 and ML18, the values on both surfaces of the web considerably differ due to the existing of out-of-plane bending stresses, and the distributions in the webs have larger compressive values at the side of smaller flange.

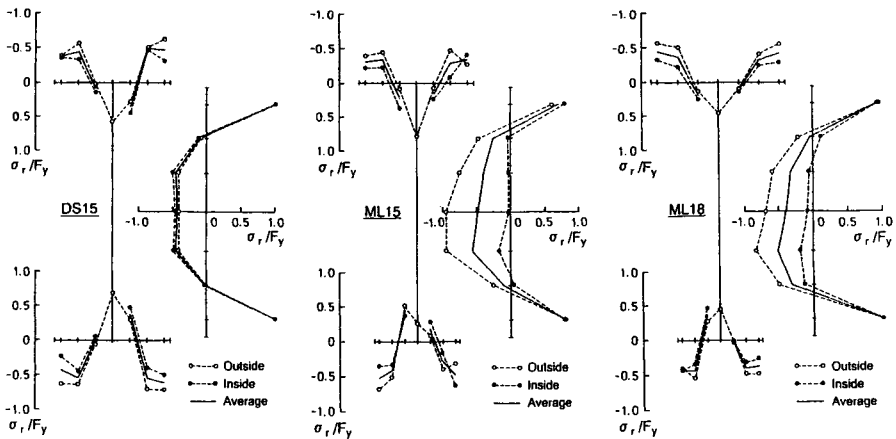


Figure 2: Residual stress distributions

MOMENT-ROTATION CURVES

Figure 3 shows the moment-rotation curves for the test beams ($L = 1.5$ m) in which have the variation of flange width or thickness. The ordinate is the ratio M/M_p of bending moment ($M = PL/4$) to full plastic moment M_p , while the abscissa is the ratio θ/θ_p of measured rotation to the value of $\theta_p = M_p L / (2EI_y)$, where EI_y = the flexural rigidity about strong axis. The rotation θ is expressed as the sum of the deflection angles at both end supports. The loading stages for local buckling

observed in the compression flange are marked in the figure, and these correspond to the load when the strains on the flange tip reversed due to plate bending (Kubo and Fukumoto 1988). In comparison with the doubly symmetric beam DS11-1, the monosymmetric beam ML04T-1 with larger flange thickness in compression has slower reduction in the unloading region and so it is superior in the rotation capacity. Though the monosymmetric beam ML15-1 with larger width in compression has high ultimate strength, the rotation capacity in the unloading region reduce due to the local buckling before the maximum load. For the doubly symmetric beam DS11-1, the monosymmetric beams MS11-1 and MS11T-1 with larger flange in tension, the plastic rotation capacity could not be obtained.

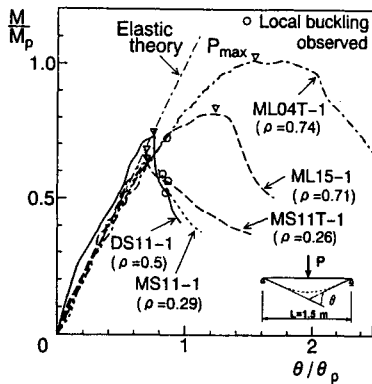


Figure 3: Moment-rotation curves of beams with various flange widths and thicknesses

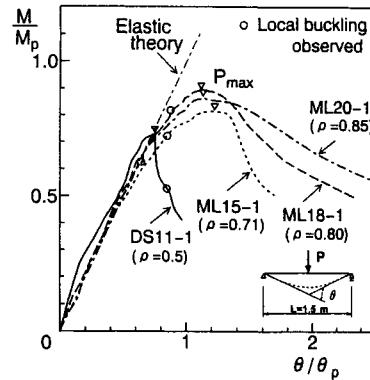


Figure 4: Moment-rotation curves of beams with wider flange in compression

In the case of beams having constant tension flange and various width-thickness ratios in compression flange, the relation of $M - \theta$ curves are shown in Figure 4. All the beams behave elastically until approximately $M/M_p = 0.65$ and then inelastic rotation curves differ with their cross-sectional shape. Though local buckling occurred before the maximum load in the wider flange beams, the curves in unloading region do not drop rapidly. It can be seen that if the width-thickness ratio is taken excessively large, the ultimate strength of thus short beam is reduced.

ULTIMATE STRENGTH AND FAILURE MODE

In Figure 5, the ultimate strength M_u/M_p are plotted against the slenderness ratio, L/r_z about weak axis. The monosymmetric sections ($\rho > 0.5$) with enlarged compression flange have higher strength. However, in short beam length of $L/r_z < 60$ the reduction of strength can be observed due to local flange buckling. On the other hand, the monosymmetric sections ($\rho < 0.5$) with enlarged tension flange have lower strength than the doubly symmetric sections ($\rho = 0.5$).

In test beams having large width-thickness ratio of $b/t_c = 16, 19$ and 21 , local flange buckling occurred before the maximum load at the corresponding span length of $L/b_c \leq 11, 14$ and 17 , respectively. The coupled buckling failure mode of the beam ML20-3 ($L/b_c=17$; $b/t_c=21$) is shown in the photograph of Figure 6. The local buckling failure occurred only at one side of the compression flange which is about $0.5b_c$ apart from the midspan, and the half wavelength was about $0.8b_c$.

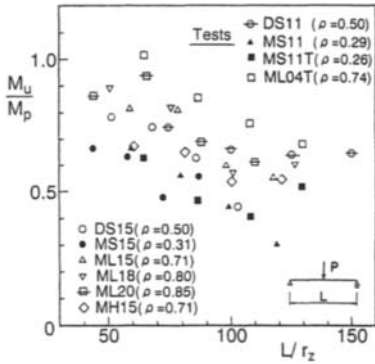


Figure 5: Ultimate moment of test beams

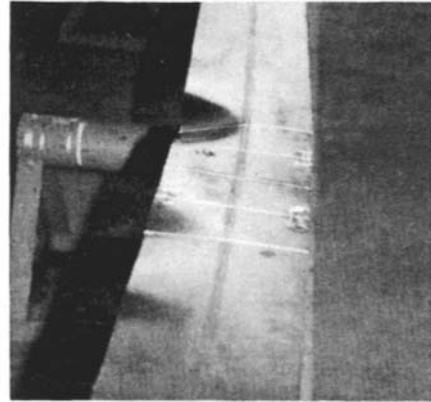


Figure 6: Coupled buckling mode in ML20-3

EVALUATION OF TEST RESULTS

Reduction Factor for Local Buckling

The load-carrying capacity of thin-walled beams must reflect the influence of local buckling. The in-plane bending strength is commonly obtained from the yield moment for a reduced cross-section based on the effective width concept. This method can not account for partial plastic bending and interactive effects between two adjacent plates at their junction. In this paper the simple method proposed by Kubo and Ogawa (1991) is applied to the bending strength M_s of I-sections. The reduction factor Q_s regarding to full plastic moment M_p is directly expressed as following equation (Fukumoto 1997).

$$Q_s = M_s/M_p = 0.88/(\lambda_s + 0.2) \leq 1.0 \tag{2}$$

where

$$\lambda_s = \sqrt{\lambda_{pf}\lambda_{pw}} \tag{3}$$

in which λ_s is defined as the equivalent slenderness parameter of the section by using the geometric mean of the width-thickness ratio parameters of flange and web in plate buckling. Considering the buckling coefficients of $k = 0.43$ for the flange and $k = 23.9$ for the web, respectively:

$$\lambda_{pf} = 1.604(b/t_c)\sqrt{F_{yf}/E} \tag{4}$$

$$\lambda_{pw} = 0.215(2h_c/t_w)\sqrt{F_{yw}/E} \tag{5}$$

Ultimate Strength Curves

In previous paper (Kubo and Kitahori 1997) the Perry-Robertson formula was examined to the test data of monosymmetric beams with compact section. In order to consider for the interaction between lateral-torsional and local buckling, the basic formula is modified based on the Q-factor method that is commonly used in column design. Using the reduction factor Q_s , and the full

plastic moment M_p replace by effective moment capacity $M_s = Q_s M_p$, ultimate strength equation on coupled buckling of beams is expressed as follows:

$$\frac{M_u}{Q_s M_p} = \frac{1}{Y + \sqrt{Y^2 - \bar{\lambda}_{bq}^2}} \leq 1 \tag{6}$$

in which

$$Y = 0.5[1 + \alpha(\bar{\lambda}_{bq} - \bar{\lambda}_{b0}) + \bar{\lambda}_{bq}^2] \tag{7}$$

and modified slenderness ratio $\bar{\lambda}_{bq}$ of a beam is defined by

$$\bar{\lambda}_{bq} = \sqrt{Q_s M_p / M_e} \tag{8}$$

where M_e = elastic lateral-torsional buckling moment; $\bar{\lambda}_{b0}$ = the limiting slenderness to reach the section capacity M_s ; α = an imperfection factor. These values are recommended for based on the test of welded doubly symmetric I-beams as follows:

for mean strength curve

$$\bar{\lambda}_{b0} = 0.4 ; \quad \alpha = 0.25 \tag{9}$$

and for lower bound strength curve

$$\bar{\lambda}_{b0} = 0.2 ; \quad \alpha = 0.50 \tag{10}$$

The comparison between the proposed curves and the present test results are shown in Figure 7. The test points are non-dimensionalized by the measured yield stresses and cross-sectional dimensions of each beam, and also the elastic buckling moment M_e is calculated based on the actual loading conditions. The reduction factor Q_s of the test sections except for the section ML04T ($Q_s = 1$) varies from 0.952 to 0.764. It can be seen that the data of ten different sections including two doubly symmetric ones are plotted almost along the mean strength curve and that higher than the lower bound curve. Thus the proposed method can be applied to the evaluation of ultimate strength in thin-walled beams.

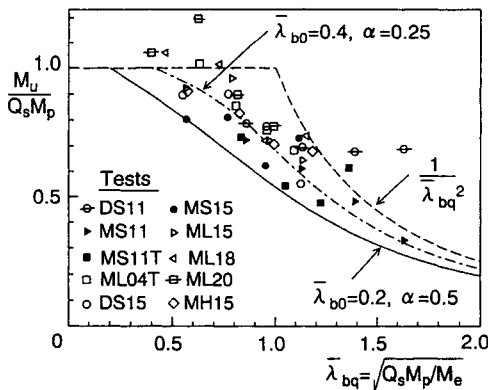


Figure 7: Ultimate strength curves

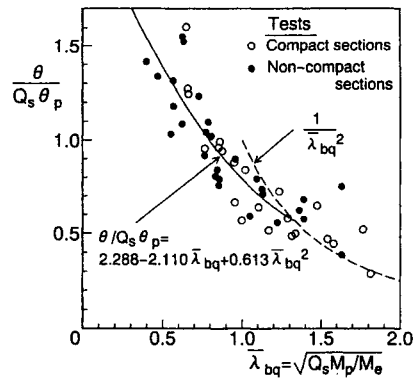


Figure 8: Rotation capacity curve

Rotation Capacity Curve

As shown in Figures 3 and 4, the rotation capacities of non-compact beams are affected by local buckling, therefore it need to modify by the same method as the case of ultimate strength

mentioned above. Figure 8 shows the rotation capacity $\theta/(Q_s\theta_p)$ at the ultimate moment for the compact and non-compact beams plotted all together against the modified slenderness ratio, $\bar{\lambda}_{bq}$. It can be seen to summarize the test results without any regard to the sectional shapes. Though there is small scatter in this figure, the mean curve of rotation capacity in the inelastic range is given by

$$\theta/(Q_s\theta_p) = 2.288 - 2.110\bar{\lambda}_{bq} + 0.613\bar{\lambda}_{bq}^2 \geq 0.566 \quad (11)$$

From Eqn. 11, the plastic rotation capacity, $\theta/(Q_s\theta_p) = 1$ may be kept by the limit slenderness ratio of $\bar{\lambda}_{bq} = 0.79$.

CONCLUSIONS

Lateral-torsional buckling tests were performed on thin-walled I-beams with various flange sizes. The residual stress in the welded I-sections of unequal flanges has an uneven distribution pattern within the section on the small flange side. The influence of the monosymmetry and slenderness of sections on the ultimate strength and the rotation capacity were clarified. As in the case of compact beams, the buckling capacities are high with the monosymmetric sections of $\rho > 0.5$, and are low with the monosymmetric sections of $\rho < 0.5$ on the contrary. When, however, the width-thickness ratio of compression flange is made excessively large, its effect decreases because of combined failure with the local buckling. The coupled buckling capacities could be evaluated by using the Q-factor method, and the proposed formulas give a satisfactory representation for it.

REFERENCES

- American Institute of Steel Construction (AISC 1986). *Load and Resistance Factor Design Specification for Structural Steel Buildings*, Chicago.
- Fukumoto, Y.(1997). *Structural Stability Design, Steel and Composite Structures*, Pergamon, Oxford, U.K.
- Kubo, M. and Fukumoto, Y.(1988). Lateral-Torsional Buckling of Thin-Walled I-Beams, *Journal of Structural Engineering, ASCE, Vol.114, No.4*, 841-855.
- Kubo, M. and Ogawa, H. (1991). A Simple Method for Evaluating Ultimate Strength of Thin-Walled Steel Beams, *Journal of Structural Engineering, JSCE, Vol.37A*, 145-154 (in Japanese).
- Kubo, M. and Kitahori H.(1997). Buckling Strength and Rotation Capacity of Monosymmetric I-beams, *Proc. of the 5th International Colloquium on Stability and Ductility of Steel Structures, JSSC, Vol.1*, 523-530.
- Lindner, J. und Gregull, T.(1992). Zur Traglast von Biegeträgern, die durch gleichzeitiges Auftreten von örtlichem Beulen und Biegedrillknicken versagen, *Stahlbau 61, Heft 1*, 9-15 (in German).
- Rondal, J., Dubina, D. and Gioncu, V.(1996). *Coupled Instabilities in Metal Structures; CIMS'96*, Imperial College Press, London.
- Trahair, N. S. (1994). Laterally Unsupported Beams, *Proc. of 1994 SSRC 50th Anniversary Conference, SSRC*, Lehigh University, Pennsylvania, 79-95.
- Yoda, K., Imai, K., Kurobane, Y. and Ogawa, K. (1989). Tests on Moment-Rotation Behavior of Thin-Walled H-section Portals, *Journal of Structural and Construction Engineering, AIJ, No.402*, 89-99.(in Japanese).

POST BUCKLING DEFORMATIONS OF RECTANGULAR HOLLOW SECTIONS IN BENDING

Frode Paulsen¹ and Torgeir Welo²

¹Department of Machine Design and Materials Technology, Norwegian University of Science and Technology, N-7034 Trondheim, Norway

²Hydro Raufoss Automotive Holland Inc., 365 West 24th Street, Holland, MI 49423, USA

ABSTRACT

Local deformation of individual cross-sectional members is of great interest in bending of aluminium alloy extrusions for automotive applications. The primary concern is the impact of such distortions on the manufacturability of components as well as the dimensional tolerances of the final build. This paper presents analytical models for the determination of local post buckling and suck-in deformations in bending. The models are based on the deformation theory of plasticity combined with an energy method using appropriate shape functions. The analytical predictions are being verified with experimental results. Based on the present findings, an approximate design method for evaluation of the bendability of sections in industrial forming operations is being proposed. The results show that the slenderness (b/t) and the width of the flange are the main parameters related to the bending radius at the onset of plastic buckling and the magnitude of local deformations, respectively. Material parameters have proven to be relatively more important to buckling radius than to deformation of individual cross-sectional members. Although there is some discrepancy between the experimental and theoretical results at tight nominal bend radii, the overall correlation is surprisingly good. It is therefore concluded that the present approach provides an efficient method to the evaluation of bendability of rectangular hollow sections.

KEYWORDS

Industrial forming operations, dimensional tolerances, bending of sections, local deformations, onset of buckling, post-buckling deformations, suck-in.

1. INTRODUCTION

The behaviour of thin-walled sections in bending has frequently been examined for structural purposes, focusing entirely on load carrying capacity. In today's applications of formed thin-walled parts, however, new challenges have arisen including prediction of dimensional tolerances. One example from the automotive industry is the aluminium space frame concept, which consists of bent aluminium

extrusions connected into a framework aimed to reduce the vehicle weight. Here distortions of cross-sectional members in the form of pre- and post buckling deformations during manufacturing of individual parts have a major impact on the tolerance of the final build. Local distortions also greatly influence the robustness of the manufacturing process and hence the overall costs.

Over the years, numerous authors have examined the bending behaviour of thin-walled sections from different perspectives. Examples are: Ades (1957), Lay (1965), Reddy (1979), Gellin (1980), Shaw and Kyriakides (1985), Kyriakides and Shaw (1987), Ju and Kyriakides (1992), Reid, Yu and Yang (1994), Welo (1996), Paulsen and Welo (1996) and Corona and Vaze (1996). However, very few attempts have been made in trying to develop relatively simple analytical models for prediction of local deformations in industrial forming operations. From this point of view, the present work aims to identify the most essential material and geometry parameters affecting local deformations of cross sectional members, and incorporate these in user-friendly design models. An experimental program has been conducted to verify the applicability of the models.

2. THEORETICAL MODELS

2.1 Constitutive description

According to deformation theory of plasticity, the relation between stress and plastic strain in a state of plane stress is¹

$$\sigma_{\alpha\beta} = C_{\alpha\beta\gamma\delta} \varepsilon_{\gamma\delta}, \quad C_{\alpha\beta\gamma\delta} = \frac{1}{3} E_s (\delta_{\alpha\gamma} \delta_{\beta\delta} + \delta_{\alpha\delta} \delta_{\beta\gamma}) + \frac{2}{3} E_s \delta_{\alpha\beta} \delta_{\gamma\delta} \quad (1)$$

where $E_s = \sigma_e / \varepsilon_e$ is the secant modulus, σ_e and ε_e are the effective stress and strain, respectively.

Consider a long plate subjected to gradually increasing compressive stresses applied at the two shorter edges. At the onset of buckling, a slight distortion of the plate gives rise to a variation of the strain components $\varepsilon_{\alpha\beta}$. Assume further that these bending strain components vary linearly across the plate's thickness, and that they are unaffected by the membrane strain at the median plane of the plate. According to the variation theory of Stowell (1948), integration of Eqn. 1 across the thickness gives the following relation between the individual bending moment and curvature components:

$$\delta M_{\alpha\beta} = -D (L_{\alpha\beta\gamma\delta} \delta \kappa_{\gamma\delta}), \quad L_{\alpha\beta\gamma\delta} = \frac{1}{E_s} C_{\alpha\beta\gamma\delta} - \left(1 - \frac{E_t}{E_s} \right) \frac{\sigma_{\alpha\beta} \sigma_{\gamma\delta}}{\sigma_e^2} \quad (2)$$

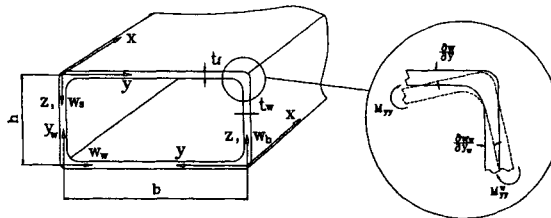


Figure 1: Co-ordinate system for local deformations in bending

¹ Greek indices range from 1 to 2 and the co-ordinate directions 1 equals x and 2 equals y .

in which $D = E_s t^3 / 12$ is the flexural rigidity, E_t is the tangent modulus, t is the member's thickness and $\kappa_{\alpha\beta}$ is the local curvature ($\delta\kappa_{\alpha\beta} = \partial^2 w / \partial x_{\alpha\beta}^2$).

2.2 Shape function for an inelastically built-in flange

Considering local deformations, the mechanics of a bent profile's flange resembles that of a long plate discussed above as long as the global deformations are reasonably small. A main challenge, however, is to establish a shape function that satisfies appropriate boundary conditions along the edges such that restraining effects from adjacent members can be taken into consideration. A suitable shape function to describe the deflections of an inelastically built-in flange is proposed as follows:

$$w = w_0 \sin\left(\frac{m\pi x}{l}\right) \left(c \sin\left(\frac{\pi y}{b}\right) + \frac{1}{2}(c-1) \left(\cos\left(\frac{2\pi y}{b}\right) - 1 \right) \right) \tag{3}$$

where b is the width of the flange, and m is the number of half-waves developing over the length l . The constraint factor c may be written on the form

$$c = \frac{\pi_f^3}{\pi_f^3 + \frac{(2-n)t_w^3 b}{h}} \tag{4}$$

Here t_f and t_w are the flange and web thicknesses, respectively, h is the depth of the cross section and n is the strain-hardening coefficient of the material. It is noticed that $c = 0$ in case of completely fixed edges ($(t_w^3 b) / (t_f^3 h) \rightarrow \infty$), and $c = 1$ in case of simply supported edges ($(t_w^3 b) / (t_f^3 h) \rightarrow 0$). A more detailed discussion on the fundamentals associated with Eqn. 4 is presented in Paulsen and Welo (1998).

2.3 Suck-in type deformations

For a constantly curved, thin-walled flange loaded with a constant circumferential tensile stress across its thickness, equilibrium gives an inward stress component

$$\sigma_{zz} = \frac{\sigma_{\theta\theta} t_f}{R^*} \tag{5}$$

where $R^* = R + h/2 + w_s$ is the instantaneous bending radius at a given position of the flange, R is the nominal bending radius and w_s is the local inward deformation of the flange, as defined in Eqn. 3 with $m = 1$. Notice that w_s is of minor importance to R^* and is therefore only included in calculating the bending stress $\sigma_{\theta\theta}$.

Consider now the stress component σ_{zz} as an external load under the assumption that the only internal action is local bending. The total potential energy of an element of the flange is

$$\delta I = \frac{\sigma_{\theta\theta} t_f}{R^*} w_s R^* d\theta dy - M_{yy} \kappa_{yy} R^* d\theta dy \tag{6}$$

By adopting a power law to represent the uniaxial stress-strain curve, i.e. $E_t / E_s = n$, the global bending stress may be expanded in terms of a truncated Taylor series if w_s is much smaller than the depth of the cross section. By minimising the potential energy with respect to the maximum deflection w_{0s} , a third

order equation is obtained. At large radii, higher order terms of w_{0s} can be neglected such that a reasonably close approximation to the solution of w_{0s} is

$$w_{0s} = \frac{3 b^4 h}{2 t_f^2 \pi} \frac{\Gamma_1}{(10\pi^4 R(2R+h)\Gamma_2 + 3nb^4 \Gamma_3 / t_f^2)}, \quad \begin{cases} \Gamma_1 = (360\pi - 1440)c - 360\pi \\ \Gamma_2 = (15\pi - 16)c^2 + (16 - 24\pi)c + 12\pi \\ \Gamma_3 = (315\pi - 960)c^2 + (960 - 270\pi)c + 135\pi \end{cases} \quad (7)$$

2.4 Onset of local buckling

Summarising the assumptions to be made in the analysis to follow, there are no external loads acting in the width direction of the flange such that uniaxial stress conditions prevail in the median plane of the flange plate prior to buckling. The deflection is assumed to follow Eqn. 3 for any arbitrary (integer) value of m , and the restraining coefficient c is given in Eqn. 4. The local bending moments are calculated in state of plane stress. Referring to the co-ordinate system in Figure 1, the potential energy of an element may be calculated from:

$$\delta l = \left(\sigma_{\theta\theta} t_f \left(\frac{\partial w_b}{\partial x} \right)^2 - \delta M_{\alpha\beta} \delta \kappa_{\alpha\beta} \right) R d\theta dy \quad (8)$$

where w_b is the buckling depth and $\sigma_{\theta\theta} = K(h/2R)^n$. By integrating over the flange area, and minimising the potential energy with respect to the buckling radius R_c , the global bend radius at the onset of buckling is after some manipulation found as

$$R_c = \frac{18hb^4 m^2 l^2 \Psi_1}{\pi^2 t_f^2 (16l^4 \Psi_3 + 32\Psi_2 m^2 l^2 b^2 + (3n+1)b^4 m^4 \Psi_1)}, \quad \begin{cases} \Psi_1 = c^2(21\pi - 64) + c(64 - 18\pi) + 9\pi \\ \Psi_2 = c^2(6\pi - 16) + c(16 - 6\pi) + 3\pi \\ \Psi_3 = c^2(15\pi - 16) + c(16 - 24\pi) + 12\pi \end{cases} \quad (9)$$

where the number of half-waves that maximises the radius is $m = [(2l)/b] \Psi_3 / [\Psi_1(3n+1)]^{1/4}$.

2.5 Post Buckling Deformations

Upon further bending after buckling, the post-deformations will continue to increase until the section collapses. In the further analysis, it is assumed that no localised deformation takes place, i.e. the buckling waves are regularly shaped along the length, and the number of half-waves m remains constant during further bending. For simplicity, the strain in the median plane of the flange is being used in the constitutive equations, meaning that local bending moments do not affect the instantaneous stiffness of the flange. As for the two other models presented above, the global bending stress ($\sigma_{\theta\theta}$) used in the constitutive equation is assumed to be uniaxial.

In order to include large deformations, the increased length of a buckled flange during folding has to be included. This involves that,

$$\sigma_{\theta\theta} = K \left(\frac{h}{2R} - \frac{1}{2} \left(\frac{\partial w_s}{\partial x} \right)^2 \right)^n \quad (10)$$

Expanding this equation in terms of a truncated Taylor series, and integrating over the area of the flange and finally minimising the potential energy with respect to the buckling wave depth w_{ob} , a third order equation is obtained. One of the solutions represents further uniform contraction of the flange plate, whereas the two other solutions represent the searched folding of the flange,

$$w_{ob} = \pm \sqrt{1120 \frac{\left(\frac{\pi^2(3n+1)m^4b}{72l^3} - \frac{m^2bh}{4lt_f^2R} \right) \Psi_1 + \frac{4\pi^2m^2}{9lb} \Psi_2 + \frac{2\pi^2l}{9b^3} \Psi_3}{\left(\frac{\pi^4(3n+1)(n-1)m^6bR}{72l^3h} - \frac{3\pi^2nm^4b}{4l^3t_f^2} \right) \Psi_4 + \frac{4\pi^4(n-1)m^4R}{l^3bh} \Psi_5 + \frac{4\pi^4(n-1)m^2R}{9lb^3h} \Psi_6}} \quad (11)$$

where the constraint constants Ψ_4 to Ψ_6 are quoted as follows:

$$\begin{aligned} \Psi_4 &= (33915\pi - 106496)c^4 + (204800 - 65100\pi)c^3 + (47250\pi - 147456)c^2 + (49152 - 14700\pi)c + 3675\pi \\ \Psi_5 &= (1225\pi - 3840)c^4 + (7936 - 2520\pi)c^3 + (1960\pi - 6144)c^2 + (2048 - 700\pi)c + 175\pi \\ \Psi_6 &= (7665\pi - 23808)c^4 + (53504 - 17010\pi)c^3 + (14385\pi - 44544)c^2 + (14848 - 5880\pi)c + 1470\pi \end{aligned} \quad (12)$$

3. EXPERIMENTAL SET-UP

Experiments were performed in the bending set-up shown in Figure 2. The set-up is designed to provide a constant moment along the beam with minimum effects of axial forces and clamping at the ends. An angle sensor is used to register the end rotation (global curvature) during bending. A three-point curvature sensor is placed in the profile's centre to determine the local curvature in the corner of the section. A scanner is being developed to measure the deformation of the flanges at different stages of bending, moving the profile against a small wheel connected to a plate that follows the flange's contour. A position sensor (LVDT) is mounted on the plate to register the vertical movement while an incremental pulse transmitter is connected to one of the rollers to record the longitudinal position. Strain gauges are used to detect the onset of buckling as deduced from any change of strain relative to that in the profile's corner.

In the test program, single (SC) and double chamber (DC) aluminium alloy AA6060-T4 sections were used. These two section types provide different constraint conditions along the edge of the flange plate upon bending. The profiles were 600 mm long, of which a 120 mm portion at each side was clamped, leaving a length of 360 mm subjected to a constant bending moment.

4. RESULTS

The buckling radius (R_c) normalised with the radius R_{ss}^e predicted by assuming the flange as a simply supported elastic plate is shown for different constraint conditions in Figure 3. Since the normalised buckling radius is relatively independent of the flange slenderness, the conventional factor $(bt_f)^2$ is the major factor even for buckling in the inelastic range. As expected, the present model predicts a

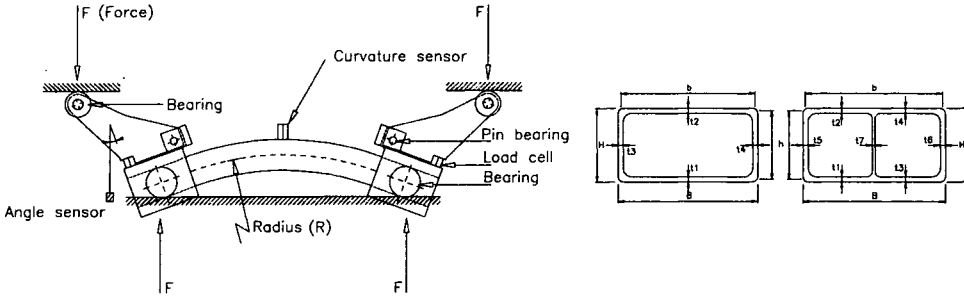


Figure 2: (left) Bending set-up; (right) single and double chamber cross sections

buckling radius that lies between those found for respectively simply supported and clamped edges using the so-called effective modulus theory presented in Bleich (1952). Predicting a constraint factor of $c = 0.63$ for the sections used by Corona and Vaze (1996), the present analytical model is in excellent agreement with their much more involved numerical model as well as their experiments shown as filled circles. The analytical results are also in reasonably good agreement with the experimental results obtained herein ($c = 0.44$). It is concluded that the factor $(b/t_f)^2$ is as important for buckling beyond the elastic limit as it is for elastic buckling.

Figure 4 shows the maximum suck-in of the external flange for single (SC) and double chamber (DC) sections. Notice that neither of the curves uses material parameters as variables as these are found to be of less importance to local deformations of tensile members. It appears that the curve for a SC section increases more rapidly with the parameter $b^4/(t_f^2 R^2)$ due to a relatively smaller restraint coefficient c provided by the two inelastically built-in edges, as compared to one fixed and one inelastically built-in. For each section type, the predicted curves for three different flange thicknesses (2.0, 2.5 and 3.0 mm) merge perfectly together, indicating that the parameter $b^4/(t_f^2 R^2)$ is the main parameter with respect to distortions of the tensile flange. It is further observed that the predictions coincide quite well with the experimental results, especially if the relative local deformation w_0/h is less than 0.1 where the considered relationship is almost linear. The sagging depth of the DC section tends to deviate somewhat for large values of w/h , most likely as a result of strong non-linear effects provided by localised post buckling deformations of the internal flange.

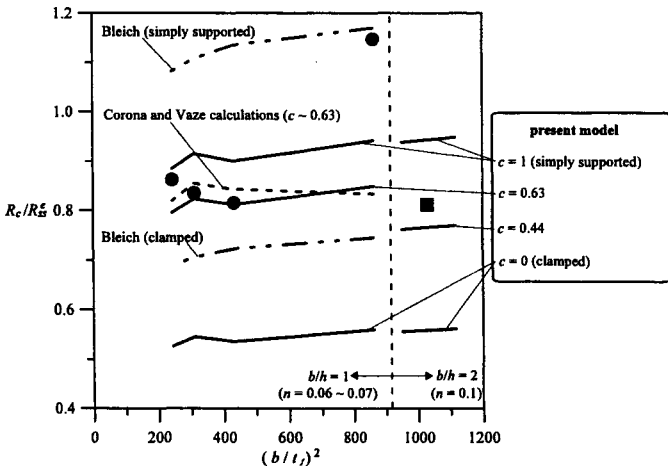


Figure 3: (left) Normalised buckling radius versus the flange slenderness factor $(b/t_f)^2$

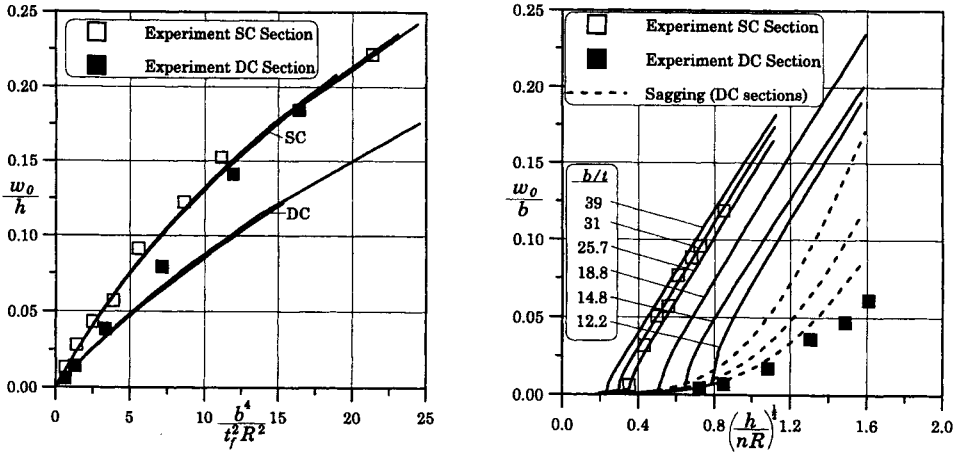


Figure 4: (left) Suck-in of tensile of tensile flange; (right) buckling wave depth of compressive flange for six width-to-thickness ratios and suck-in of tensile flange for three width-to-thickness ratios (DC)

The right-hand graph in Figure 4 shows the maximum wave depth (w_b/b) along the compressive flange plotted as full lines versus the parameter $\sqrt{h/(nR)}$ for different width-to-thickness ratios. Noticing that the predicted curves for the internal flange follow those of the external flange in the beginning, continuing relatively linear after the onset of local buckling, it is suggested that the parameter $\sqrt{h/(nR)}$ has been identified as the main influential parameter with respect to post-buckling wave depth. Comparing the predicted curves with the experimental results for a SC section with b/t ratio

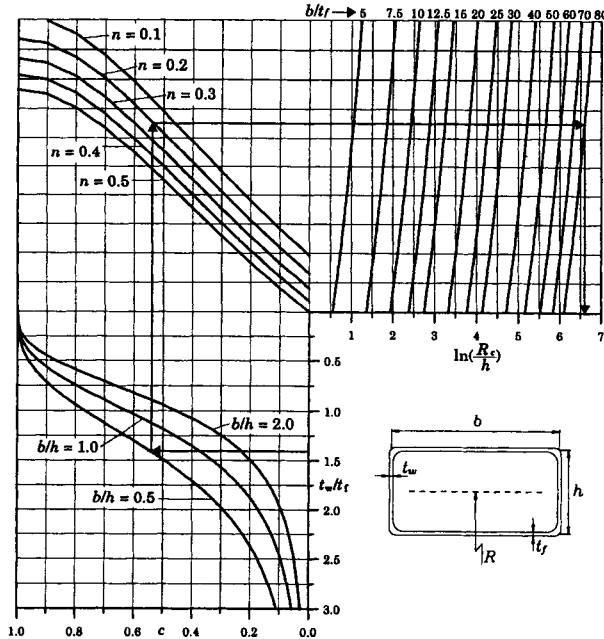


Figure 5: Diagram illustrating a method for determination of the radius at the onset of buckling

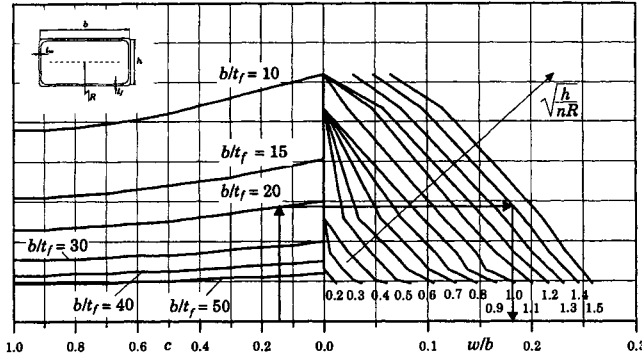


Figure 6: Diagram illustrating a method for determination of post buckling wave depth

of 31 (open square markers), the agreement is remarkably good. The experimental post buckling plots for a DC section ($b/t = 18.8$), however, are found to resemble the predicted uniform sagging mode of the external flange rather than the wavy appearance predicted for the internal flange. The reason for the discrepancy between theoretical and experimental results is not exactly known.

5. A PRACTICAL DESIGN METHOD FOR EVALUATION OF BENDABILITY

The theoretical predictions have been converted into a practical method for design of rectangular hollow sections. Although rectangular hollow sections have been used to exemplify the method, the model is general in the sense that it can easily be modified to other types of cross sections by modifying the shape function and boundary conditions in Eqns. 3 and 4.

According to Figure 5, the bending radius at the onset of buckling can be determined by entering the diagram with the parameter t_w/t_f and the constraint factor c for a given b/h ratio. Following the sequence indicated in the diagram, the critical radius is uniquely determined through the parameters n , b/t_f and h . In case the specified bending radius is smaller than the buckling radius, the depth of the post buckling waves (w) can be found from Figure 6 which is based on the parameters b/t_f , $\sqrt{h/(nR)}$ and h using the constraint factor c found in Figure 5 as input. The suck-in of tensile flange of the cross section can also be determined in relatively simple way using the diagram shown in Figure 7. The present procedure follows the sequence of entering the diagram with the parameter t_w/t_f and then determine the constraint factor c , which leads to the overall suck-in (w) based on b/h , $b^4/(t_f^2 R^2)$ and h .

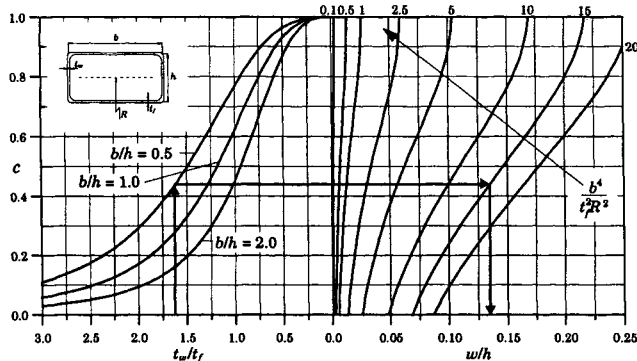


Figure 7: Diagram illustrating a method for determination of suck-in of the tensile flange

5. CONCLUSIONS

The present investigation aims to predict local deformations and buckling of rectangular hollow sections in order to better understand factors affecting dimensional tolerances in industrial bending operations. Using the deformation theory of plasticity and the energy method, analytical models that provide simple closed-form solutions for various shapes and materials are being developed. The results revealed a very strong influence of flange width on local deformations at both faces of the profile. The instantaneous bending stiffness (constraint condition) of the web also seriously affects the local deflection of connected flange members. Unlike local buckling, the such-in of the external flange is almost independent of strain hardening and initial yield stress of the material. The models developed have proven to provide results that are in good agreement with experimental findings. Their validity is found to cover most practical cases; though shortcomings are revealed at large local deformations owing to localisation of post buckling deformations in the experiments. It is therefore concluded that the developed models provide to be an efficient, simple tool to the evaluation of bendability of thin-walled sections.

5. REFERENCES

- Ades C.S. (1957). Bending Strength of Tubing in the Plastic Range. *J. Aero. Sci.* **24**, 605-620.
- Bleich H.H. (1952). *Buckling Strength of Metal Structures*. McGraw-Hill Book Company, Inc., US.
- Corona E. and Vaze S.P. (1996). Buckling of Elastic-Plastic Square Tubes under Bending. *Int. J. Mech. Sci.* **38:7**, 753-775.
- Gellin S. (1980). The Plastic Buckling of Long Tubes under Combined Bending and Pressure Loads. *Int. J. Solids Struct.* **10**, 397-407.
- Ju G.T and Kyriakides S. (1992) Bifurcation and Localization Instabilities in Cylindrical Shells under Bending—II. Predictions. *Int. J. Solids Structures* **29:9**, 1143-1171.
- Kyriakides S. and Shaw P.K. (1987). Inelastic Buckling of Tubes under Cyclic Bending. *ASME J. Press. Vessel Techn.* **109**, 169-178.
- Lay G. (1965). Flange Local Buckling in Wide-Flange Shapes. *J. Structural Divison* **6**, 95.
- Paulsen F. and Welo T. (1996). Application of Numerical Simulation in the Bending of Aluminium-Alloy Profiles. *J. Mat. Proc. Tech.* **58**, 274-285.
- Paulsen F. and Welo T. (1998). The Bendability of Thin-Walled Hollow Extrusions. To be published.
- Reddy B.D. (1979). An Experimental Study of the Plastic Buckling of Circular Cylinders in Pure Bending. *Int. J. Solids Struct.* **15**, 669-685.
- Reid S.R., Yu T.X. and Yang J.L. (1994). Hardening-Softening Behaviour of Circular Pipes under Bending and Tension. *Int. J. Mech. Sci.* **36:12**, 1073-1085.
- Shaw P.K. and Kyriakides S. (1985). Inelastic Analysis of Thin-Walled Tubes under Cyclic Bending. *Int. J. Solids Struct.* **21**, 1073-1100.
- Stowell E.Z. (1948). A Unified Theory of Plastic Buckling of Columns and Plates. *NACA Tech. Note*, 1556.
- Welo T. (1996). Bending of Aluminium Extrusions for Automotive Application: A Commentary on Theoretical and Practical Aspects. In Proc. *6th. Int. Aluminium Extrusion Techn. Sem.*, 271-282 (Edited by Werner R.I.), Chicago, Illinois.

This Page Intentionally Left Blank

A UNIFIED METHOD FOR CALCULATING SHEAR STRESSES IN THIN-WALLED SECTIONS

Ali H. Khan and Mark J. Sharrock

SPN-Khan & Associates, Engineering & Management Consultants, Winchester, UK

ABSTRACT

A unified method for calculating shear stresses in thin-walled sections due to both flexure and torsion, is presented. The distribution of shear stress in many commonly used thin-walled structures, is complex and it is usually difficult to assess such stresses manually. Although the available computer-based numerical methods of analysis can predict accurate stress distribution in these structures, the relative importance of the individual action-effects is not apparent from the results, because they usually provide spot values or contours of the combined effects. The analytical method presented enables a designer to calculate the shear stress distribution in all types of thin-walled cross-sections due to each individual action of flexure and torsion, one at a time.

KEYWORDS

Flexure, Torsion, Twist, Shearflow, Multi-cell sections, Principal axes, Shear centre, Sectorial coordinates, Warping, Warp-restrained torsion, , Bimoment, Warping torque.

INTRODUCTION

This paper presents a simple unified approach to the calculation of shear stresses in members with thin-walled cross-sections. The method is widely applicable and enables a designer to calculate shear stresses arising from both flexure and torsion in open, closed, mixed open and closed and multi-cell sections.

At present, in most of the design offices, a simple unified procedure such as here described, is not available for common use. When the case of calculating shear stresses in complex sections arises, designers usually resort to either a crude manual analysis of an over-simplified section, or an advanced computer-based method of numerical analysis. The disadvantage of either of these approaches is that, the behaviour of the section due to the individual actions of flexure and torsion, is seldom apparent from the results. Whilst the former approach is likely to underestimate certain action-effects and overestimate the others, the latter usually provides spot-values of the combined action-effects. Therefore, the designers are not able to gain an insight into their relative importance.

The calculation method being described herein, evaluates the effects of both flexure and torsion by treating them separately. It also provides a manual method of analysis of thin-walled structures, for preliminary design and to confirm the reasonableness of the results of a complex numerical analysis, for example, finite element analysis⁶.

ASSUMPTIONS AND FORMULATION

In formulating the analytical method, the usual assumptions of elastic, small-deflection theory are implied. It is also assumed that the shape of the cross-section remains constant or undistorted in its plane under all loading conditions. The assumption of undeformed cross-section is satisfied in members which have sufficient support of diaphragms or floor connections at right angles to the walls or segments or, where the applied forces are well distributed over the cross-section rather than acting in concentrated form. The assumption of thin-walled behaviour is generally acceptable if, L/d and d/t ratios for the member are about 8 or greater.

When a structural member with thin-walled sections is subjected to lateral loading, in general there will be a flexural response as well as a torsional response. However, if the resultant of the lateral forces passes through the shear centre of the cross-section, there will, by definition, be no torsional displacements. For analytical purposes it is convenient to treat the flexural and torsional actions separately, and this is appropriate also for an appreciation of the relative importance of the two actions. The applied lateral forces are therefore, considered to be replaced by equivalent forces acting at the shear centre, together with couples corresponding to the actual point of action. This enables a relatively straightforward calculation of the shear stresses in each principal axis direction separately, and added together to obtain the final result.

The right hand Cartesian coordinate axes, x , y and z are used in the formulation. It is found more convenient to use the curvilinear z - s axes for thin-walled sections which are usually represented by their middle surfaces. In this system, z is directed along the longitudinal axis of the member and $s = f(x,y)$, is directed along the profile line of the member cross-section. The origin of z is usually taken at a terminal transverse plane; any convenient generator line on the middle surface can be taken as the origin of s , see Figure 1.

DISTRIBUTION OF FLEXURAL SHEAR STRESS

Let us consider a thin-walled member with an arbitrary cross-sectional shape subjected to lateral forces, F_x and F_y , in the directions of the principal x and y axes respectively. These shear forces will give rise to a shearflow, $q = \tau.t$, at any point on the profile line. The formulation in terms of q , i.e. shearflow, rather than the shear stress, τ , is more convenient as this automatically allows for thickness variation around the profile line. The value of the shearflow at some arbitrary datum point in the section, where $s = 0$, is denoted as q_0 and the shearflow at any point where $s = s$, is denoted by q .

From simple beam theory,

$$\sigma_z = -M_x \cdot y/I_x + M_y \cdot x/I_y$$

Hence,

$$\begin{aligned} q &= q_0 - \int (-dM_x/dz \cdot y/I_x + dM_y/dz \cdot x/I_y) dA \\ &= q_0 - (F_y/I_x) S_x - (F_x/I_y) S_y \end{aligned} \quad (1)$$

where $S_x = \int y \cdot dA$ and $S_y = \int x \cdot dA$, are the 'first moments of area' of the cross-sectional element about the principal x and y axis respectively. These quantities are also commonly represented by Q or, $A\bar{y}$ and $A\bar{x}$.

Open and Single Cell Sections

Eqn. 1 defines the shear stress distribution completely in a thin-walled section. This for a section subject to a shear force, F_y in the principal y-axis direction only, can be written as,

$$\begin{aligned} q &= - (F_y/I_x). S_x \quad \text{for an open section,} \\ q &= q_o - (F_y/I_x).S_x \quad \text{for a single cell closed section} \end{aligned} \tag{1a}$$

There are two conditions available to determine the unknown shearflow, q . These are: i) the line of action of resultant of the shearflow, q , around the complete section must coincide with that of F_y i.e. must pass through the shear centre and, ii) the rate of twist of the section is equal to zero, since F_y has been assumed to pass through the shear centre, i.e., there is no torsion.

The first condition involves taking moments of all forces about an axis parallel to y and passing through the shear centre and equating to zero, which will give an equation to evaluate q . The location of the shear centre can also be found from this condition as the eccentricity of the resultant forces. This method is simple in concept and is more suitable for open and simpler sections; but the second condition is more generally applicable to sections with closed parts and all types of complex sections. In the following all derivations of equations and formulas will be based on the second condition, i.e., the condition of zero rate of twist. However, in order to formulate the general condition of zero rate of twist, first of all we need to consider the rotational behaviour of the section under pure (i.e., unrestrained) torsion.

In a thin-walled section subject to pure or St. Venant torsion, the section is undeformed in its plane and there is no longitudinal stresses or any transverse stress-resultants. If $\theta(z)$ is the angle of rotation of any section, $z = \text{const.}$, the shear strain at any point, s , on the middle surface is given by,

$$\gamma = (\delta u / \delta s) + h. (\delta \theta / \delta z) = (q/ Gt) \tag{2}$$

where h is the perpendicular distance of the tangent at s to the centre of rotation, O (see Figure 1b).

Integration of Eqn. 2 gives the following expression for $u(z)$,

$$u(z) = \int (q/Gt).ds - d\theta/dz \int hds + u_0 \tag{2a}$$

where u_0 is the displacement of the point taken as $s = 0$, i.e. the start point. If the integration is carried around the complete loop of the cell, u must return to its starting value, u_0 . Hence,

$$\begin{aligned} u_0 &= \oint (q/Gt).ds - d\theta/dz \oint hds + u_0 \\ \text{or,} \quad (d\theta/dz) \Omega &= \oint (q/Gt).ds \end{aligned} \tag{2b}$$

where, $\Omega = \oint h.ds$, twice the area enclosed by the profile line and the symbol \oint denotes integration around a complete closed loop.

If we consider flexure of the section only, there is no torsional effect and the rate of twist, $\theta'(z) = (d\theta / dz)$, of the section is zero, i.e.,

$$\theta'(z) = \oint (q/ \Omega Gt).ds = 0 \tag{3}$$

For the purpose of analysis, we assume that the shearflow, q in Eqn. 3 consists of two parts, viz.

- i) A shearflow, $q_o = - F_y \cdot (S_x^o/I_x)$, that would develop if the section is made singly-connected or open, by introducing a 'cut' in the profile, and $S_x^o = \int y \cdot dA$, for this open section, and,
- ii) A circulating shearflow, $q_c = - F_y \cdot (R_x/I_x)$, which would restore compatibility at the 'cut'. The quantity, R_x , is the correction necessary to define an 'effective first moment of area' of a closed section, as described below.

Figure 2 illustrates the above condition. In other words, if S_x^* is defined as the 'effective first moment of area' of a closed section, the unknown shearflow, q , is given by,

$$q = - F_y \cdot (S_x^*/I_x) \tag{4}$$

where, $S_x^* = S_x^o + R_x$ (5)

From Eqns. 3 and 4, $\oint (S_x^*/t) \cdot ds = 0$ (6)

or, $\oint (S_x^o/t) \cdot ds + (R_x/t) \cdot ds = 0$ (6a)

which gives, $R_x = - (\oint S_x^o \cdot ds/t) / (\oint ds/t)$ (7)

An alternative formulation is given by Oden¹ using the virtual work principles, but the above expression in terms of equivalent geometrical properties of the cross-section, is more familiar to an engineer in the design office.

Multi-cell and Mixed Open and Closed Sections

For sections with more than one closed cell, the procedure for evaluating the 'effective first moment of area' about the principal x (or, y) axis, S_x^* (or, S_y^*) is similar to that of a single cell closed section given above. If there are $i = 1, 2, 3, \dots, n$ cells in the section, we introduce n number of 'cuts' or origin points to make it singly-connected or open. To restore compatibility at the 'cuts', n circulating shearflows, q_{ej} ($j = 1, 2, 3, \dots, n$) giving as many R_x will be required. In other words, the required shearflow, q , at any point is given by the same form of Eqn. 4, i.e.,

where, $q = - F_y \cdot (S_x^*/I_x)$
 $S_x^* = S_x^o + \sum c_i \cdot R_{xi}$ (8)

in which S_x^o is the value of $\int y \cdot dA$ obtained after introducing n 'cuts' and taking $S_x^o = 0$ at each 'cut' and any free end, c_i defines the sign of R_x as explained in Eqn. (11) below. The summation $\sum c_i \cdot R_{xi}$ is taken over all of the n circuits in the section. Applying the conditions of zero twist, as in Eqn. 3, we get,

$$\oint (S_x^*/t) \cdot ds = 0 = \oint (S_x^o/t) \cdot ds + \oint (\sum c_i \cdot R_{xi}/t) \cdot ds \tag{9}$$

Eqn. 9 gives n simultaneous equations which can be expressed in matrix form as

$$\underline{S} + \underline{A} \underline{R} = 0 \tag{10}$$

where

$$S_i = \oint c_i (S_x^o/t) \cdot ds$$

$$A_{ij} = \oint c_j \cdot c_i \cdot (ds/t) \tag{11}$$

In the above,

$i = 1, 2, \dots, n$, the number of the closed loop,

$j = 1, 2, \dots, n$, the number of the shearflow, q_{ej}

and

$c_j = 1$, if q_{ej} is in the direction of increasing s in circuit i ,

$= 0$, if q_{ej} is absent at point s ,

$= -1$, if q_{ej} is in opposite direction to increasing s in circuit i (11a)

The solution of Eqn. 10 can be written as, $\underline{R} = -\underline{A}^{-1} \cdot \underline{S}$ (12)

Having determined the values of R_{xi} , the value of S_x^* at any point can be found from Eqn. 8 and hence the shearflow corresponding to the shear force, F_y , from Eqn. 4.

DISTRIBUTION OF TORSIONAL SHEAR STRESS

Let us consider a thin-walled member with an arbitrary cross-sectional shape and with one end restrained against warping displacement, and subjected to a torque, T , at the free end as shown in Figure 3a .

The applied torque, T , produces shearing stresses at points on the section which consists of two St. Venant components, τ_b and τ_f and a warping component, τ_ω (see Figure 3b). τ_b is the Bredt-Batho shear stress which circulates uniformly around each cell, τ_f varies linearly across the wall thickness and has a zero value at the middle line and τ_ω is a non-circulating uniform stress across the wall thickness which changes direction from one part of the section to another. τ_ω is distributed over the whole section including any open parts with zero values at the free edges.

For convenience, equations for torsional shear stresses may also be written in terms of shearflow, q defined as,

$$q = \int \tau \cdot dt \tag{13}$$

$$\text{or, } q = \tau \cdot t = (\tau_b + \tau_\omega) \cdot t \tag{13a}$$

It should be noted that because of the reversal of sense of τ_f across the thickness, it is eliminated in the integration of Eqn. 13.

In a state of St. Venant torsion, the shearflow around a section is proportional to the rate of twist, $\theta^1(z)$ and the longitudinal strains are zero. When there is a warping restraint, the shearflow is no longer uniform, nor proportional to $\theta^1(z)$ and longitudinal strains exist. It is convenient to consider the shearflow in the latter case as the sum of two shearflows, one that corresponds to the actual rate of twist $\theta^1(z)$ and zero longitudinal strains, and another that corresponds to a zero rate of twist and the actual longitudinal strains. The two are called St. Venant and warp-restrained torsional shearflows and are identified by suffices v and ω i.e., q_v and q_ω . The torques corresponding to the two shearflows are T_v and T_ω respectively giving the following equilibrium equation,

$$T = T_v + T_\omega \tag{14}$$

St. Venant Torsional Shear Stress

For an open section or for open parts of a mixed open and closed section thin-walled beam, as shown in Fig. 4, the circulating part of St. Venant shear stress, τ_b , and hence the shearflow, $q_b (= \tau_b \cdot t)$ is zero. In these open segments, shear stress component τ_f only will be present. The calculation of τ_f , based on membrane analogy, is well familiar and therefore, will not be discussed here. For single or multi-cell closed sections and closed parts of mixed sections, both τ_f and τ_b components of the shear stress are present, the circulating component τ_b providing the major part of the resisting torque.

Let q be the unknown shearflow in a multi-cell section due to an applied torque. If the cells of the section are identified as $i = 1, 2, 3 \dots n$ closed circuits, then q_i is the shearflow circulating each circuit. Eqn. 2b for the multi-cell section may be re-written as,

$$\oint (q_i/G.t).ds = \Omega_i \cdot \theta^t \tag{15}$$

In a section with n cells, there are n circulating shearflows and Eqn. 15 gives n simultaneous equations. These can be expressed in matrix form as ²,

where,
$$\underline{A} \cdot \underline{q} = \underline{\Omega} \cdot G \theta^t \tag{16}$$

$$A_{ij} = \oint c_j (ds/t), \text{ as explained in Eqn. 11a.}$$

On solving Eqn. 16, we get,
$$\underline{q} = (\underline{A}^{-1} \underline{\Omega}) G \theta^t = \underline{b}_i G \theta^t \tag{17}$$

in which,
$$\underline{b}_i = \underline{A}^{-1} \cdot \underline{\Omega} \tag{17a}$$

Hence, from Eqn. 17, the shearflow, q_i in cell i is,

$$q_i = b_i \cdot G \theta^t \tag{18}$$

The total torque, T_v, which corresponds to the St. Venant shear stress, is given by,

$$T_v = T_b + T_f = G (I_c + J) \theta^t = G I_d \theta^t \tag{19}$$

where,
$$I_d = I_c + J, \text{ the combined St. Venant torsion constant,}$$

$$I_c = \sum b_i \Omega_i \text{ and } J = \alpha/3 \cdot \int t^3 ds, \alpha \text{ being a constant close to unity.} \tag{20}$$

Distribution of Shear Stress in Warp-restrained Torsion

The warping or longitudinal displacement, u, in St. Venant torsion, is given by Eqn. 2a as ^{3,4},

$$u = u_0 + \int (q/G.t).ds - \theta^t \int h.ds = u_0 - \omega \theta^t \tag{21}$$

where
$$\omega = \omega(s) - \int \sum b_i (ds/t), \text{ the 'reduced sectorial coordinate' for closed sections } ^2,$$

 and
$$\omega(s) = \int_0^s h.ds, \text{ the sectorial coordinate of a point on the profile line } ^3.$$

The above longitudinal displacement is the same for every section of the thin-walled member. In warp-restrained torsion, however, the longitudinal displacement varies from section to section being zero at the section where it is completely restrained against warping. It may be assumed that the effect of the restraint is equivalent to superposing equal and opposite displacements to those in the section when unrestrained. Therefore, for all sections of the member, the resulting warping displacement may be assumed to vary as $\bar{\omega}$. but the magnitude of the distribution varies along the length of the member. This can be expressed ² as,

$$u = u_0 - \omega \cdot \beta^t \tag{22}$$

The relation between $\beta^t(z)$ and $\theta^t(z)$ can be established from the basic differential equation of warp-restrained torsion and is given by ^{4,2},

$$\beta^t(z) = 1/\mu \cdot \theta^t - [T(z)/G(I_p - I_c)] \tag{23}$$

where,
$$\mu = 1 - (I_c + J)/(I_p + J), \text{ is the 'warpability factor' } ^2 \tag{23a}$$

Considering the equilibrium conditions of an elemental segment, ds x dz of the middle surface of the thin-walled member, Figure 5, the relation between the axial stress, σ_ω and shearflow, q_ω can be expressed as,

$$(\delta\sigma_\omega/\delta z).t + (\delta q_\omega/\delta s) = 0 \tag{24}$$

On substituting $\sigma_\omega = - [B(z). \varpi / I_\omega]$, in Eqn. 24, we have, on integration,

$$q_\omega = q_{\omega 0} - (T_\omega(z) / I_\omega) . S_\omega \tag{25}$$

where, $S_\omega = \int \varpi . dA$, (25a)
 and, $T_\omega = dB/dz$, the warping torque.

S_ω is the ‘first sectorial moment of area’ or sectorial static moment, for the part of the section between the selected origin, O, and the point of consideration, s.

Eqn. 25 defines completely the distribution of shearflow due to warp-restrained torsion in an open section since at the free ends $q_{\omega 0}$ is zero and also, the origin of s in the summation can be taken at a free end. For closed and mixed open and closed sections, the method given for evaluating the flexural shearflow is adopted as follows.

We define S_ω^* as the ‘effective first sectorial moment of area’ as,

$$S_\omega^* = S_\omega^\circ + \sum c_i . R_{\omega i} \tag{26}$$

So that the unknown shearflow, q_ω , can be given by, $q_\omega = - T_\omega . (S_\omega^* / I_\omega)$ (27)

In the above, S_ω° is the value of $\int \omega . dA$ (or $\int \omega . t . ds$), obtained after introducing n ‘cuts’ or origin points in an n-celled section and taking $S_\omega^\circ = 0$, at each origin and at any free end. $R_{\omega i}$ is the correction required for defining an ‘effective first sectorial moment of area’ of a section with closed parts and corresponds to a circulating shearflow around each cell.

Applying the condition of zero rate of twist, since the forces are referred to the shear centre, we get,

$$\oint (S_\omega^*/t) . ds = 0 = \oint (S_\omega^\circ/t) . ds + \oint (\sum c_i . R_{\omega i} / t) . ds \tag{28}$$

Eqn. 28 may be rewritten in matrix notation as,

On solving, $\underline{S} + \underline{A} \underline{R} = 0$ (29)

$$\underline{R} = - \underline{A}^{-1} . \underline{S} \tag{30}$$

where, $S_i = \oint (S_\omega^\circ/t) . ds$,
 and as before, $A_{ij} = \oint c_j (ds/t)$ (31)

Having determined $R_{\omega i}$, the value of S_ω^* at any point can be found from Eqn. 26 and hence the shearflow corresponding to warp-restrained torsion, from Eqn. 27.

Total Shear Stress at a Point

The total shear stress at any point on a member with thin-walled cross-section due to both flexural and torsional actions can be written as,

$$\tau(s,z) = F_x(S_y^*/I_y.t) + F_y(S_x^*/I_x.t) + T_b(\sum b_i/I_c.t) + T_t(t/J) + T_\omega . (S_\omega^* / I_\omega.t) \tag{32}$$

References

1. Oden, J.T. (1967). *Mechanics of Elastic Structures*, McGraw-Hill Book Company, New York, USA.
2. Khan, A.H., Tottenham, H. and Stafford-Smith, B. (1979) The General Theory of Torsion of Thin-walled Structures with Undeformed Cross-sections, *Structural Mechanics Series No. 79-2*, McGill University, Montreal, Canada.
3. Khan, A.H. (1974). Analysis of Tall Shear Wall-frame and Tube Structures, *Ph.D. Thesis, University of Southampton*, Southampton, UK.
4. Urban, I.V. (1955). *Theory of Design of Thin-wall Beam Structures (in Russian)*, Transzheldorizdat, Moscow, USSR.
5. Vlasov, V.S. (1961). *Thin-walled Elastic Beams, (English Translation)*, Israel Program for Scientific Transactions, Jerusalem, Israel.
6. Irons, B. and Ahmad, S.(1980). *Techniques of Finite Elements*, Ellis Harwood Ltd., Chicester, UK.

Notation

A	Cross-sectional area
B	Bimoment (or, stress-resultant for warping axial stress)
b	Shearflow co-efficient
d	Depth or width of a section
G	Shear Modulus
I_c	St. Venant torsion constant for closed parts
I_d	Combined St. Venant torsion constant for the section
I_p	Tangential polar moment of inertia, $\int h^2.dA$
I_x, I_y, I_{xy}	Second moments of area about x and y axes respectively
I_ω	Sectorial second moment of area
J	St. Venant torsion constant for thin segments
L	Total length
M_x, M_y	Bending moments about x and y axes respectively
q	Shearflow
R_x, R_y, R_ω	Geometrical constants used in calculating S_x^*, S_y^*, S_ω^*
s	Distance along the profile line
S_ω^*	First sectorial moment of area
S_x^*, S_y^*	Effective first moments of area of a closed section
S_ω^*	Effective first sectorial moment of area of a closed section
t	Thickness of the thin-walled segment
u	Longitudinal displacement
v	Tangential displacement
$\beta^t = (d\beta/dz)$	Warping parameter
μ	Warpability factor
$\theta(z)$	Angle of rotation
$\theta'(z)$	$(d\theta/dz)$
τ	Shear stress
σ_z	Axial stress in flexure
σ_ω	Axial stress in warp-restrained torsion
ω	Sectorial coordinate or, sectorial area
$\bar{\omega}$	Effective Sectorial coordinate of the closed section

All other notations are given in the text.

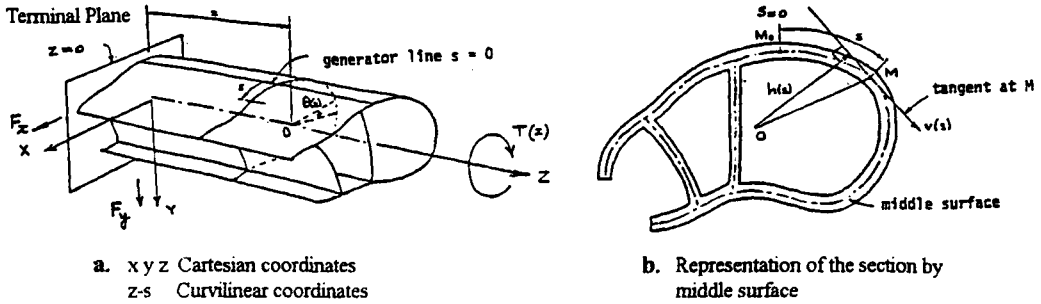


Figure 1. Idealization of a Thin-walled Section

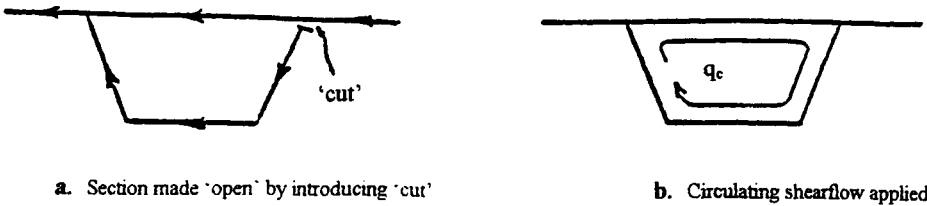


Figure 2. Evaluation of Shearflow in Open and Closed Sections

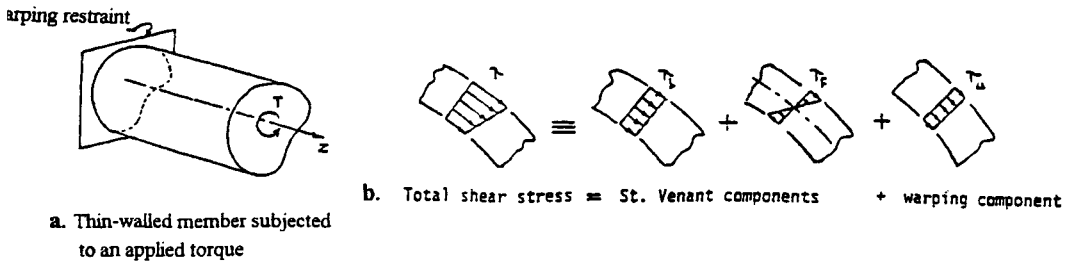


Figure 3. Shear Stresses due to an Applied Torque

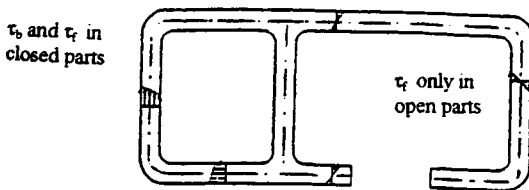


Figure 4. Shear Stresses in St. Venant Torsion

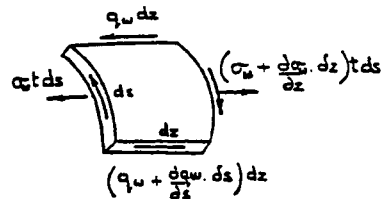


Figure 5. Equilibrium Condition in Warp-restrained Torsion

This Page Intentionally Left Blank

INFLUENCE OF SHEAR BUCKLING ON THE DUCTILITY OF STEEL MEMBERS

Ioannis Vayas

Faculty of Civil Engineering, National Technical University of Athens, Greece

ABSTRACT

It is widely known that the stability of steel members is adversely influenced by stability loss. In dependence on the geometrical and loading conditions, there exist several possible instability modes which may appear individually or in combination. The present paper aims at numerically investigating the coupled instability between local and shear buckling, both prior and after the attainment of the ultimate load. This is done by controlling the normal and shear strain applied to the member. Local buckling due to normal strain is taken into account by introduction of effective widths for the individual plated elements of the member cross section. Geometrical imperfections and residual stresses may be allowed for explicitly or implicitly through selection of an appropriate buckling curve. Shear buckling is accounted for by application of the simple post-critical method as proposed by Eurocode 3. The response of individual steel plated elements for various slenderness levels and strain ratios is studied. Subsequently I-beam sections for various web and flange slenderness are investigated. It is shown that the response of steel beams in terms of strength and ductility is a function of the geometrical conditions of their subpanels and the relation between the applied shear to the normal strain.

KEYWORDS

Steel members, strength, ductility, local buckling, shear buckling, interaction.

INTRODUCTION

The introduction of plastic design methods in modern codes of practice and the necessity for an economic design of steel structures in seismic regions, require an evaluation of the strength and ductility properties of steel members and subassemblages. The response of such members is governed by the ductility of the material and various instability modes that may appear during loading. The advantages of the high ductility of steel may be lost if stability failures occur. For steel members several stability modes, like local buckling, torsional buckling, shear buckling, lateral buckling etc. are possible. Depending on the geometrical and loading conditions, these modes may appear individually or in combination, leading to coupled instability problems. The appearance of coupled instabilities is the normal situation in steel members, unless special measures to prevent one or another mode are taken

into account. This is i.e. the case when beams are braced laterally in order to prevent lateral torsional buckling.

This paper presents a method for the evaluation of the coupled instability between direct and shear stresses to steel members. The response is studied both prior and after the attainment of the ultimate load. This allows for the determination of the strength and ductility of the member. The method is applied to plate panels, shear links of eccentric truss bracing systems and transversely loaded plate girders.

RESPONSE TO DIRECT STRESSES

In order to numerically study the panel response, its loading must be applied strain-controlled, as it is the case in experimental investigations. The panel response to direct loading will be studied according to a strain oriented formulation for stability problems proposed by Vayas (1997). Considering a plate panel subjected to direct strain ε as in Figure 1, two regions may be distinguished as following:

- For $\varepsilon \leq \varepsilon_y$:

$$\text{Stress:} \quad \sigma_0 = \varepsilon E \quad (1a)$$

$$\text{Slenderness:} \quad \bar{\lambda} = \sqrt{\frac{\sigma_0}{\sigma_{cr}}} = \sqrt{\frac{\varepsilon E}{\sigma_{cr}}} \quad (2a)$$

- For $\varepsilon > \varepsilon_y$:

$$\text{Stress:} \quad \sigma_0 = [\varepsilon_y + (\varepsilon - \varepsilon_y)h]E \quad (1b)$$

$$\text{Slenderness:} \quad \bar{\lambda} = \sqrt{\frac{[\zeta_1 \varepsilon_y + \eta_1 (\varepsilon - \varepsilon_y)]E}{\sigma_{cr}}} \quad (2b)$$

$$\text{where } h = E_T / E = \text{strain hardening ratio,} \quad (3)$$

$$\sigma_{cr} = \kappa_\sigma \frac{\pi^2 E}{12(1-\nu^2)} \left(\frac{t}{b}\right)^2 = \text{critical buckling stress} \quad (4)$$

and the values of the parameters ζ_1 and η_1 as proposed by Wittemann (1993) from results of yield line analyses are equal to:

$$\text{For } \varepsilon_y < \varepsilon \leq 6\varepsilon_y: \quad \zeta_1 = 1.0, \quad \eta_1 = 0.5 \quad (5a)$$

$$\text{For } 6\varepsilon_y < \varepsilon \leq 20\varepsilon_y: \quad \zeta_1 = 3.5, \quad \eta_1 = 0.2 \quad (5b)$$

$$\text{For } 20\varepsilon_y < \varepsilon: \quad \zeta_1 = 6.3, \quad \eta_1 = 0.1 \quad (5c)$$

The value of the buckling factor κ_σ is a function of the supporting and strain conditions of the plate panel.

For a given slenderness, which according to eqs. (2a and b) is a function of the loading level, a reduction factor χ according to a plate buckling curve as given by eq. (6) and shown in Figure 2 may be determined.

$$\chi = \frac{1}{\bar{\lambda}} - \frac{0.22}{\bar{\lambda}^2} \leq 1 \quad (6)$$

The panel response is then given by eq. (7)

$$\sigma = \chi \sigma_0 \quad (7)$$

or is alternatively expressed in terms of an effective plate width, according to eq. (8):

$$b_e = \frac{\sigma}{\sigma_0} b = \chi b \quad (8)$$

More details on the application of the method, as well as the possibility to explicitly consider of geometrical imperfections and residual stresses may be found in the above referred publication and in Vayas/Psycharis (1992) and (1993).

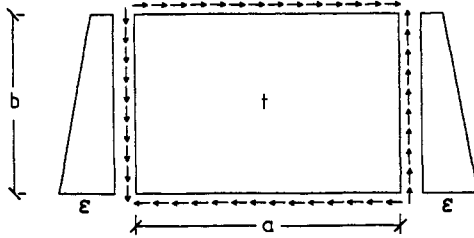


Figure 1. Plate panel under consideration

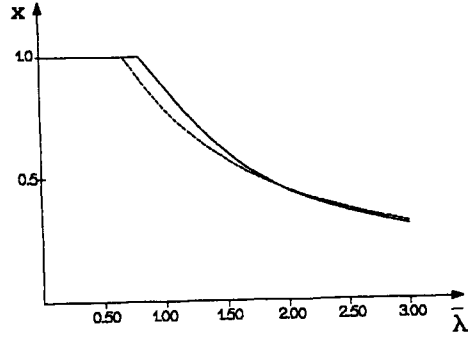


Figure 2 Plate buckling curves

RESPONSE TO SHEAR

In order to determine a panel response according to Figure 1 to shear over the entire strain range, a strain oriented formulation has to be applied. Similarly as for direct stresses, following expressions may be introduced:

- For $\gamma \leq \gamma_y$:

Shear stress: $\tau_0 = \gamma G$ (9a)

Slenderness: $\bar{\lambda}_w = \sqrt{\frac{\tau_0}{\tau_{cr}}} = \sqrt{\frac{\gamma G}{\tau_{cr}}}$ (10a)

- For $\gamma > \gamma_y$:

Shear stress: $\tau_0 = [\gamma_y + (\gamma - \gamma_y)h]G$ (9b)

Slenderness: $\bar{\lambda}_w = \sqrt{\frac{[\zeta_2 \gamma_y + \eta_2 (\gamma - \gamma_y)]G}{\tau_{cr}}}$ (10b)

where $\tau_{cr} = \kappa_r \frac{\pi^2 E}{12(1-\nu^2)} \left(\frac{t}{b}\right)^2 = \text{critical buckling shear stress}$ (11)

The parameters ζ_2 and η_2 may be determined by comparison of the results with rigid plastic methods. Since the influence of imperfections for shear loading is small compared to direct loading, it is expected that their values are generally smaller compared to the corresponding ones of eq. (2b). In the present work the values 1 and 0.3 for ζ_2 and η_2 were adopted.

The buckling factor for shear κ_r in eq. (11) takes following values in dependence on the aspect ratio $\alpha = a/b$ of the panel:

For $\alpha < 1$: $\kappa_r = 4 + \frac{5.34}{\alpha^2}$ (12a)

For $\alpha \geq 1$: $\kappa_r = 5.34 + \frac{4}{\alpha^2}$ (12b)

For a given slenderness, which according to eqs. (10a and b) is a function of the loading level, a reduction factor χ_v according to a plate buckling curve for shear may be determined. In the present work the buckling curve according to the simple post-critical method as proposed in Eurocode 3 (1993) will be adopted. The analytical expressions for this curve is given by eq. (13), the curve is shown in Figure 2.

For $\lambda_w \leq 0.8$: $\chi_v = 1$ (13a)

$$\text{For } 0.8 < \lambda_w \leq 1.2: \quad \chi_v = 1 - 0.625(\lambda_w - 0.8) \quad (13b)$$

$$\text{For } \lambda_w > 1.2: \quad \chi_v = 0.9 / \lambda_w \quad (13c)$$

The panel response is then given by eq. (14)

$$\tau = \chi_v \tau_0 \quad (14)$$

INTERACTION OF DIRECT STRESSES WITH SHEAR

When direct stresses and shear are simultaneously present, their interaction, in dependence on the level of the acting shear, has to be considered. If the acting shear is smaller than a certain percentage of the shear buckling resistance no interaction exists, otherwise an interaction has to be taken into account. Accordingly, the ratio between acting shear force and shear buckling resistance as expressed by eq. (15) is formed

$$v = \frac{V_s}{V_R} = \frac{\tau}{\tau_u}, \quad (15)$$

where τ is the acting shear according to eq. (14) and τ_u the ultimate shear resistance, which is determined by the procedure outlined in the previous section when $\gamma = \gamma_y$.

The interaction relations proposed by Eurocode 3 are the following:

If $v \leq 0.5$ no interaction direct stress - shear interaction exists.

If $v > 0.5$ the interaction has to be considered. The relevant expression is written as

$$\rho_r = 1 - (2v - 1)^2 \quad (16)$$

In the present work this reduction factor is applied to the yield stress of the panel, so that all other expressions given in the previous sections remain unchanged. This corresponds to uniformly distributing the effects of shear yielding or buckling over the panel width. This assumption has been verified experimentally and numerically by other investigations.

PLATE PANELS

In the following, results of analyses on plate panels subjected to direct stresses and shear will be presented. The panels are simply supported at their edges. The parameters considered are the b/t-ratio,

the aspect ratio α , the applied strain ratio $\frac{\gamma / \gamma_y}{\varepsilon / \varepsilon_y}$ or its inverse value if no direct stresses are present,

and the distribution of direct stresses along the panel width, i.e. pure compression or bending. The yield stress in all cases is equal to 235 Mpa.

Figure 3a shows the influence of the b/t-ratio of plate panels subjected to pure shear. For stocky panels that reach the yield shear strength, unloading occurs at various strain levels in dependence on the stockiness. The rate of unloading is the same, independent on the slenderness of the panel. According to Eurocode 3, shear buckling has to be considered in cases where b/t exceeds the value of 69. This is confirmed here, although a slightly higher figure could be applied.

Figure 3b shows the influence of the aspect ratio of a panel with b/t=69 subjected to pure shear. As may be seen from this curve only the ductility, but not the strength are influenced by the aspect ratio. This indicates that transverse stiffeners may enhance the ductility of a girder.

Figure 4 shows the response of a panel with b/t=69 and $\alpha=2$, subjected to compression and shear. Five ratios of applied strain are considered and each ratio, with the exception of the shear-only case, have two corresponding shear and direct stress-strain response curves. Similarly as the results of Harding, direct stresses and shear are interacting what strength is concerned, the ductility remaining more or less unaffected.

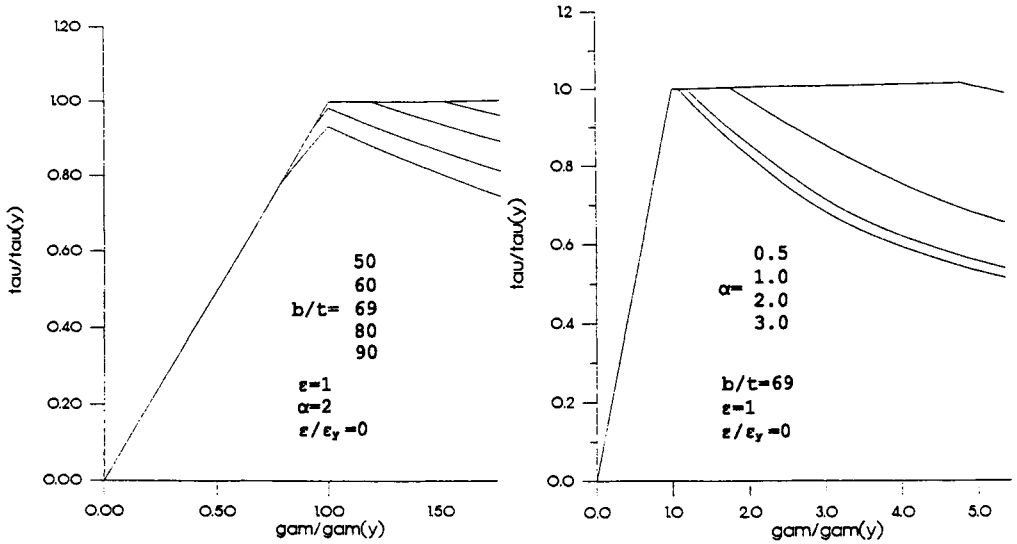


Figure 3: Stress-strain response for plates under pure shear. Influence of a) the b/t-ratio and b) the aspect ratio

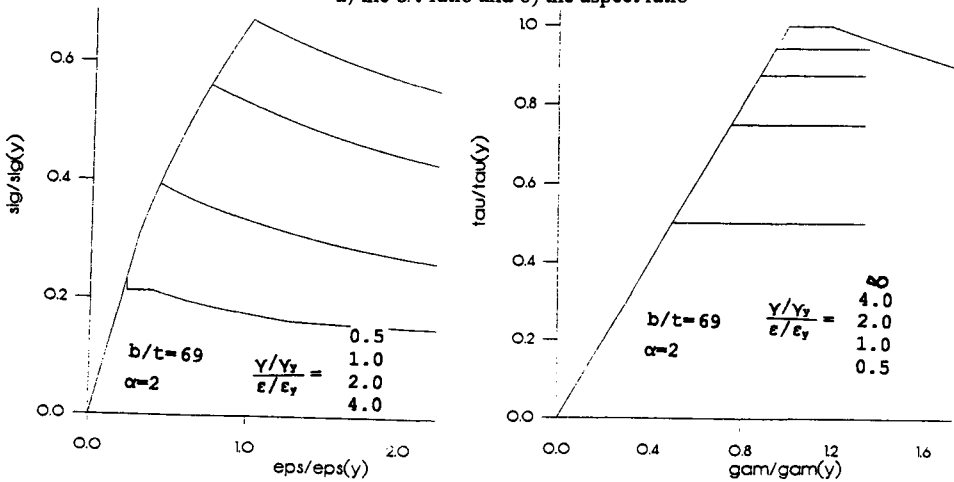


Figure 4: Stress-strain response for plates under compression and shear. a) direct stresses, b) shear stresses

Figure 5 shows the response of plates with various slendernesses subjected to bending and shear, for applied strain ratios 0 (no shear), 1 and 2. According to Eurocode 3, plate panels are classified in respect to their b/t-ratio into 4 categories. For the supporting conditions and the yield strength considered here, the relevant b/t limits between categories are 72, 83 and 124 if the panels are subjected to bending only. Accordingly, panels with b/t=60, 75, 90 and 120, as in Figure 5a, 5b, 5c and 5d, belong to categories 1, 2, 3 and 4 respectively. The response of the panels for an applied strain ratio equal to 0 as shown in Figure 5, confirms this. Having in mind that the shape coefficient for a plate is 1,5, Fig. 5a shows that a panel with b/t=60 has a bending capacity exceeding the plastic moment and a curvature ductility ratio of approximate $7/1.5=4.7$. For b/t=75 the plastic moment is reached but the

curvature ductility ratio is limited to $4/1.5=2.7$. When $b/t=90$ the ultimate moment exceed the yield moment but is below the plastic moment. A panel with $b/t=120$ just exceeds the yield moment. The results with higher strain ratios indicate, that due to the presence of shear the strength of the panels decreases but their ductility increases. This shows that shear buckling is a ductile failure mode, so that that if shear prevails the response may be ductile.

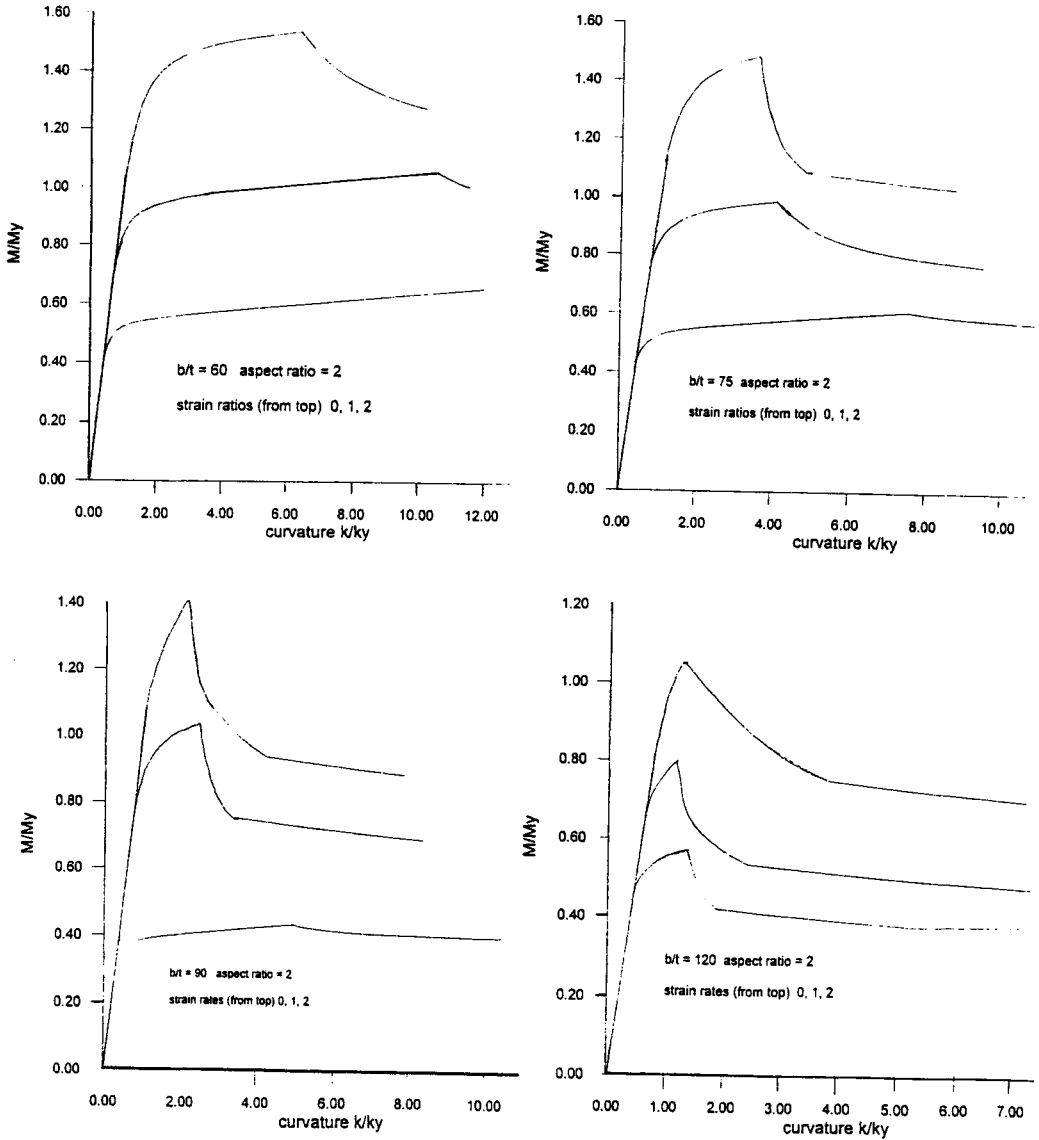


Figure 5: Moment-curvature response for plates under bending and shear for strain-ratios $\frac{\gamma/\gamma_y}{\epsilon/\epsilon_y} = 0$ (no shear), 1 and 2. Moments and curvatures are normalized to the corresponding yield values.

SHEAR LINKS

Shear links as shown in Figure 6 are supposed to represent ductile elements in eccentric truss braced frames, subjected to high shear. Having in mind that the shear and direct strains are given from eqs. (17) and (18):

$$\gamma = \frac{V / A_v}{G} \tag{17}$$

$$\varepsilon = \frac{M / W}{E} \tag{18}$$

where A_v = shear area and W =section modulus of the beam, the strain ratio is determined from eq. (19):

$$\frac{\gamma / \gamma_y}{\varepsilon / \varepsilon_y} = \frac{V \sqrt{3W}}{M A_v} \tag{19}$$

For the critical length of the link l_{cr} that corresponds to the situation where the plastic moment and the plastic shear force are simultaneously developed at the end of the beam it is (with W_p =plastic section modulus):

$$V/M = V_p/M_p = 1: (A_v / \sqrt{3W_p}) \tag{20}$$

so that the strain ratio is equal to one over the shape factor of the cross section.

Results of shear links consisting of equally high IPE- and HEA-sections for three cases (no shear, length equal to critical length and half of it), are shown in Figure 6. The selected sections are class-1 sections, so that shear yielding and not shear buckling occurs. The IPE-sections have very compact flanges and no local buckling even at high ductility ratios occurs. For the wide flange HEA-sections, local buckling occurs at a ductility ratio of approximate 2.3. The presence of shear doesn't influence the moment capacity of the HEA-section like that of the IPE-section, due to the fact that in the former the ratio between the web to the flange area is smaller. Due to the low web slenderness, the ductilities of the sections are not strongly influenced by the presence of shear.

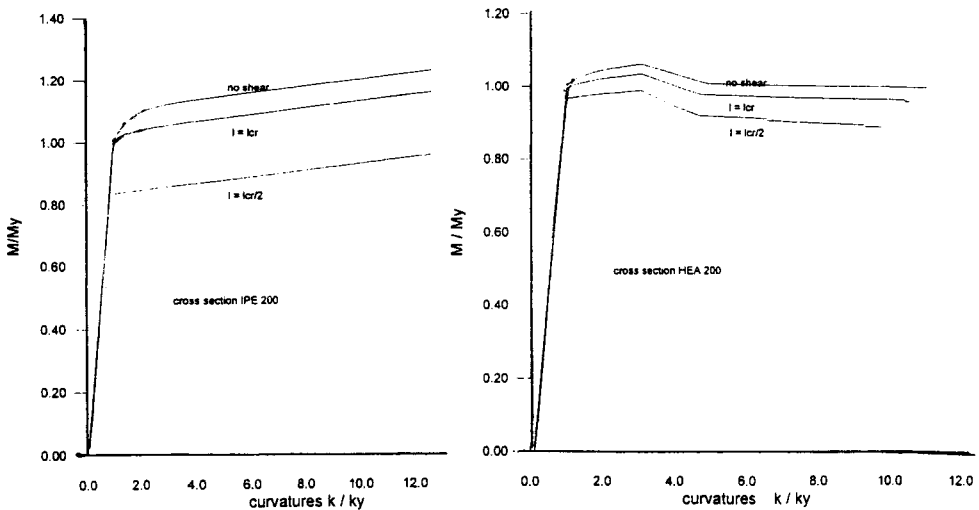


Figure 6: Response of shear links consisting of a) an IPE-section and b) a HEA-section

PLATE GIRDERS

Plate girders have usually compact flanges and slender webs. Due to their slenderness, the webs are prone to local and/or shear buckling. These buckling modes, individually and in combination, highly influence the response of the girders in respect to strength and ductility. Figure 7 shows the response of the plate girder T3, tested by Pasternak (1997). The flange slenderness is equal to $80/1.85=43$ and the web slenderness equal to $350/1.85=190$, the aspect ratio of the panel between transverse stiffeners is equal to $875/350=2.5$. Both the flange and the web are classified into class 4 according to Eurocode 3. This is confirmed by the numerical results. The occurrence of shear buckling and subsequently local flange buckling lead to a maximal moment capacity equal to 80% of the yield moment.

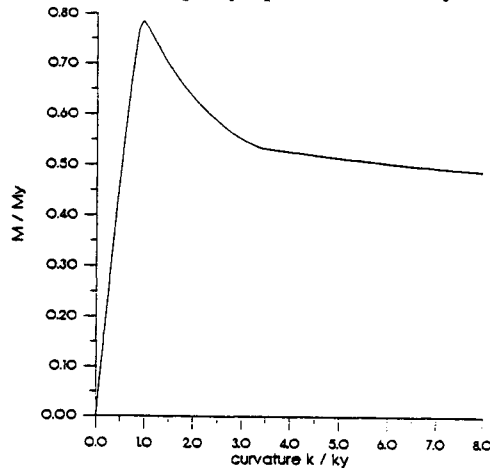


Figure 7: Response of a plate girder section

CONCLUSIONS

An effective method for the evaluation of the coupled instability between local and buckling stresses to steel members has been presented. By increasing the strains rather than the stresses, the response both prior and after the attainment of the ultimate load may be studied. Applications to various types of members are presented. It was shown that the presence of shear is many times enhancing the member ductility, while strength is always reduced.

REFERENCES

- Vayas, I. (1997). Stability and Ductility of Steel Elements, *J. of Constructional Steel Research* Vol. 44, No 1-2, 23-50
- Vayas, I., Psycharis, I. (1992). Dehnungsorientierte Formulierung der Methode der wirksamen Breite, *Stahlbau* 61, 275-283.
- Vayas, I., Psycharis, I. (1993). Ein dehnungsorientiertes Verfahren zur Ermittlung der Duktilität bzw. Rotationskapazität von Trägern aus I-Profilen, *Stahlbau* 62, 333-341
- Eurocode 3. Design of steel structures, CEN, European Committee for Standardization, ENV 1993-1-1
- Wittemann, K. (1993). Traglastermittlung für Kaltprofile, PhD-Thesis TU Karlsruhe, Germany
- Harding, J. Interaction of direct and shear stresses on plate panels, in R. Narayanan (ed). *Plated Structures: Stability and Strength*, Applied Science Publishers, UK
- Pasternak, H., Branka, P. (1997). Durchlaufträger ohne Durchlaufwirkung?-Untersuchung an Stahlträgern mit schlanken Stegen, *Bauingenieur*, Vo 72, 9, 385-391

QUALITIES AND USE OF BEAMS WITH EXPANDED METAL.

M. Hellsten

**BALCUS AB
Lyckevagen 3
S-311 92 Falkenberg
Sweden**

ABSTRACT

The rotary expander technique can be used for integrating expanded metal with solid sheet in long cold-formed metal profiles. This technique will distribute the material to where it's best needed.

Valuable qualities possible are:

- low weight and optimal strength
- low energy transmission (noise and heat)
- soft deformation and favorable energy absorbing properties
- good fatigue resistance
- high flexibility in design and product qualities

These qualities are useful in applications like:

- light and strong steel framing systems for buildings
- energy absorbing support structures in road equipment
- light vehicles
- construction pipes and profiles

Manufacturing of expanded metal implies a strain hardening of the mesh. This effect is more obvious in rotary expander manufacturing, due to a forced extension to match the solid metal strips. The use of strain hardened material to make light profiles with high stiffness. In combination with plaiting, it is possible to produce rigid C- and Z-studs.

KEYWORDS

Hollow sections, profiles, expanded metal, energy absorption, energy transmission, flexible design, plaiting, steel framing, studs, Latticework, construction, building.

MANUFACTURING

Hollow sections and open profiles of Expanded Metal with solid corners can be manufactured from strip metal in the same way as conventional profiles. Depending on profile geometry and desirable qualities, the location of the expanded metal sections and their geometry are fixed.

A metal strip is expanded in a rotary expander, before roll forming to make a latticework in one piece, exhibiting expanded metal sections integrated in solid sheet. In the roll-forming process, the profile is shaped and then sealed with welding or by a folding seam.

It is possible first forming a tube and after the welding transform the tubular section into other hollow section profiles.

The rotary expander machine technique was developed to make it possible to manufacture steel products with integrated longitudinal areas of expanded metal from a sheet metal coil. This development has contributed to light products with low energy transmission and soft deformation.

QUALITIES

Manufacturing of expanded metal implies a strain hardening of the mesh. This effect is more obvious in rotary expander manufacturing, due to a forced extension to match the solid metal strips. In a profile with expanded metal and solid sheet, the width and location of the solid sheet sections and the expanded metal sections can be chosen freely as well as the geometry (mesh) of the expanded metal. This is a way of locating the material where it is needed and using strain hardened material can be expected to make light profiles with high stiffness.

Expanded metal sections can be expected to have a relative low transmission of energy (heat, sound etc.), due to the sparse material and the lengthened energy transport. In combination with plaiting, it is possible to increase rigidity in construction C- and Z-profiles.

Expanded metal sections can be expected to have a soft deformation quality, possibly useful in traffic environment etc. A light column for example, will be flattened, retarding a hitting vehicle.

The fatigue properties have been subject for different opinions. Some fatigue specialists have characterized expanded metal as consisting of crack fronts only. Others have predicted that the meshes would act as plate springs.

USAGE

Road equipment like light columns and similar structures can be designed for energy absorption. The BALCUS concept, with solid corners and expanded metal sections is suitable for production of energy absorption road structures. A BALCUS beam (for example a light column or a safety fence) hit by a vehicle will be flattened out while retarding the hitting vehicle. By adapting the design of the parameters such as mesh size, corner width, plate thickness and tensile strength to the product, it is possible to achieve the energy absorption properties desired.

Framing structures in buildings can be designed with a minimum of material for low transmission of energy (noise and heat). BALCUS concepts permit a 50% reduction of material in the framing system compared to regular steel framing and will reduce energy transmission with 50 % compared to wood framing. Increased fire resistance and reduced cost for additional surface structures.

The SPINE system, light, rigid C- and Z- studs for steel framing are made with a plaited expanded metal web to guarantee rigidity, and contain 2/3 of the material in comparable solid stud.

The SCIROCCO truss system will reduce steel frame weight with approximately 50%. Vehicle parts can be made lighter with increased ability to absorb energy, by soft deformation. Beams and profiles in vehicle construction, fenders, seat framing and interior support structures are examples of details where weight, energy absorption and deformation qualities is crucial.

Filter framing in industrial applications, vehicle silencers and filters are commonly made from expanded metal or perforated sheet metal, screwed, welded, clinched or riveted to solid metal strip. The BALCUS concept allows simpler, tidier and cheaper production methods.

Perforated tube, are common in many industrial applications. Perforation implies scrap metal, take time and energy. Rotary expanded BALCUS tubes can be made cheaper and often with increased quality.

TEST PROJECT

Balcus designed a research project together with Dr.ing. A. Aalberg and B. Haugen at the Department of Structural Engineering at the Norwegian University of Science and Technology in Trondheim. The aim was to obtain knowledge providing development of metal profiles with low weight and energy transmission, soft deformation, and favorable energy absorption and fatigue qualities.

In the autumn of 1996 a project called "Experimental Investigation of a Hollow Steel Section with Solid Corners and Expanded Metal Sections" was carried out. This project investigated the following qualities, and models for calculation were developed.

TEST SPECIMENS, MATERIAL AND MATERIAL TESTS

A quadratic cross section with overall dimensions 80 mm * 80 mm and plate thickness 1.5 & 3.0 mm was chosen. Expanded metal was used for the four sidewalls of the profiles and solid sheet for the corner sections. A specimen length of 1200 mm were chosen for the beams and 360 mm length for the axial (stub) tests.

At this time, only open profiles with micromesh were regularly manufactured. The specimens were spot welded and showed out-of-straightness imperfections and twists, although of general good quality. The expanded metal sections in the sidewalls of the specimens were spot-welded to the corners using TIG-welding. Standard expanded metal of different mesh sizes and weight (kg/m²) were chosen from a manufacturer catalogue, ranging from a fine-meshed expanded metal to a relatively coarse-meshed material.

TEST PROGRAM

The test program investigated the following qualities:

- elastic and inelastic bending
- axial loading, static and dynamic
- fatigue
- heat transfer

ELASTIC BENDING

Laboratory measurements bending tests were performed for Beams in order to find the behavior of the beams in the elastic range. The beams were supported with a concentrated load at the midpoint. The load was applied by adding hanging weights to the beams by hand. In order to obtain a proper contact (support) on the rough surface of the BALCUS beams, the support points and loading point were smoothed with plastic padding. The beams had internal stiffeners at the supports and loading point. Deflections were measured at the supports and at the loading point. An analytical model has predicted the measured deformations. The total deflection of the beam is viewed as the sum of two contributions; bending-deformation and shear-deformation.

The grid of the expanded metal is viewed as a pure truss structure since the axial stiffness of the grid is very low when the loading is not parallel to any of the grid-"fibers". The bending stiffness of the beam thus only includes the corners.

For the BALCUS beam the moment of inertia is computed from the solid plate corner sections.

The expression for the bending deformation will give higher- values then the actual contribution from bending since one has neglected that part of the moment is also carried by the expanded metal section in the top and bottom of the beam.

The truss model of the expanded metal grid gives that the shear force is carried by the sidewalls as a force. That is tensile for one grid direction and compression for the other, thus giving no net axial force along the beam axis.

This is analogous to a model commonly used for I-shaped wood sections where the web is made by crossed boards.

This shear model has neglected the bending stiffness of the grid points of the expanded metal. Finite element analysis has shown that the axial stiffness of such a zigzag truss is approximately half of the stiffness of the similar straight truss. Including this reduced axial stiffness in the analytical model will thus approximately double the shear deformation numbers.

The deflection from the analytical model has been compared with the lab results. The analytical deformations are based on elastic modulus of $E = 210000 \text{ N/mm}$.

For all the BALCUS beams the error is within this range of error up to about 20% as for the solid-walled beams. The analytical model does however consistently underestimate the actual deformation. This underestimation is assumed to be caused by neglecting the centerline jumps in the grid model when calculating the shear deformations. Again, with the reduced axial stiffness of the expanded metal trusses in the shear deformation model, one will get increased (doubled) shear deformation numbers. This will bring the total deflection in the analytical model up to numbers with mean value around 100% of the measured deflection, and not consistently lower as is the case now.

INELASTIC BENDING

Tests were carried out for a total of 13 beam specimens. 10 of these were Balcus Beams, with large variety to geometry and density of expanded metal sections. Two different loading situations were considered. Concentrated load and distributed load applied over the central 440 mm. of the span. The response curves for the Balcus-beams show a behavior almost as for the solid plate beams. The inelastic behavior is caused by a combination of gradual plastification of the corner steel and deformations of the compressed corner sections down into the beam or sideways. The efficiency of the Balcus Beams with respect to maximum load ($P_{max}/Weight$, in kg/m) can be greater or smaller compared to solid beams. The test show which geometry is most efficient in the tested specimens. The effect of corner width show that an increase of corner width give a rather small increase of the maximum loads carried. The mesh geometry effects the maximum load ratio. The contribution of the expanded metal sections to the capacity of the Balcus-beams were found from testing a pure expanded metal beam.

A model for the bending capacity of Balcus-beams was designed. In this model only the solid corners of the Balcus-beam were considered. This model gives a predicted capacity quite far below maximum load in 90% of the tests.

AXIAL LOADING

Static tests were carried out with compressive axial loading of short columns. The specimens were compressed at a low deformation rate. Response curves for axial load versus displacement was recorded. The deformation mode is much similar to that of the reference stub, with folding of the sidewalls in a quite symmetric buckling pattern.

It seems as the fine meshed expanded metal is better fitted to prevent cross sectional distortions. Flat rolled expanded metal raises the deformation resistance. Filling with aluminum foam raises the absorbed energy of the Balcus stub apparently. The ratio between the peak load and the mean load is an important criterion for crashworthiness. Aluminum foam equalizes the peak-mean load ratio.

Dynamic tests were performed for a total of 6 stubs. Test specimens were mounted in a test rig and subjected to a 56 kg projectile at impact velocities from 8.5 to 14.5 m/s. An increase in peak-load between 90-110% was observed. For the reference stub the peak load increased with almost 200%. A ratio between the total energy in the dynamic tests and the absorbed energy in the corresponding static tests of 2:1 was found.

FATIGUE

Fatigue tests were carried out with two beams of Balcus type. Both beams with identical geometry. Important to the fatigue issue is remembering that the expanded metal in the sidewalls of the beams is spot-welded to the steel plate corners in the beams. Welding on a component in most cases governs its fatigue capacity, and the final Balcus product is to be produced without welding. Different load levels were chosen for the two beams, corresponding to a maximum normal stress slightly above the basic yield stress of the steel for the first test and about 50% of the basic yield stress for the other. The heavily loaded beam failed suddenly at 165.000 load cycles, from a crack starting at a spot weld in one of the edges at the tension side of the beam. The testing of the other beam was stopped when 500 000 load cycles was reached without any signs of failure. The test result implies that the Balcus beams, and particularly the expanded metal in the beams, show signs of distinctly favorable effects with respect to fatigue.

THERMO TECHNICAL

Introduction

The Norwegian Building Research Institute (NBI) has, after commission to The Department of Structural Engineering at The Norwegian University of Science and Technology, investigated the thermal conductivity of BALCUS profiles used as cross beams in thermal insulated wall constructions.

Method

This investigation is based on a simplified calculation of heat transmission by conductivity in expanded metal. We have designed an expression, which under certain given geometric conditions will give equivalent heat conductivity with good accuracy for expanded metal.

The expression is valid for expanded metal with near right angular meshes. In the BALCUS beams we borrowed, the meshes fulfil this request.

The expression utilizes the relationship that the cross section is reduced and the length is increased for the meshes due to plastic dimensional change when the expanded metal is stretched (when the mesh width is increased). These calculations, are made in a simplified way, shows that it is possible to make a BALCUS-profile which by means of insulation is equally good compared to massive wood or to other slotted thin plate profiles. Earlier calculations of thin plate profiles shows a profile with 6 rows of slots in the waist and 0.7mm plate thickness is equivalent to a profile of massive wood. In these rough calculations the effect of flanges and facing material is neglected. For profiles used in isolated constructions, it's useful to make a qualified calculation with the help of a program for 2-dimensional heat transmission.

REFERENCE

Aalberg, A. and Haugen, B. 1997. BALCUS, An experimental investigation of a rectangular hollow steel section with solid corners and expanded metal sections. MHAB, ISBN 91-973094-0-0.

STEEL FRAMING DEVELOPMENT

In the construction industry, open sheet metal profiles C-, Z- or hat- shaped are commonly used.

Weak webs specially in slotted profiles (studs) need stiffening, and web-stiffeners are common.

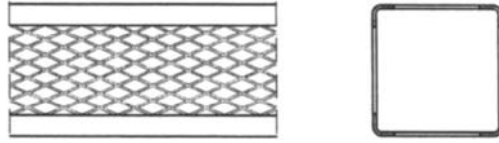
In profiles (studs) with expanded metal, or pre-spaced metal the web needs stiffening.

To make it possible to save raw material, and to use simple studs in construction it is necessary to stiffen the web or flange in such profiles. Plaiting the expanded metal web will make it rigid.

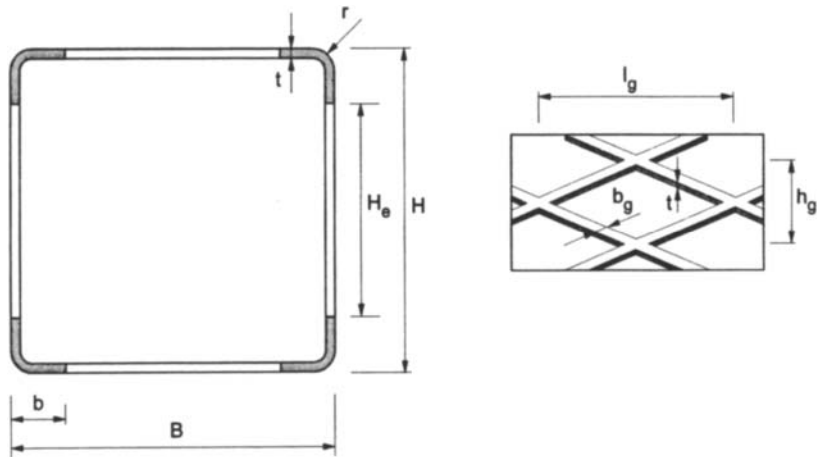
Maximum rigidity will appear perpendicular to the direction of the plaiting.

In construction expanded metal can add several valuable qualities. Reduced weight, facilitate easier handling and increased rate of production in the construction site, reduced cost of material and transportation. Healthy buildings due to full aeration of walls and trusses.

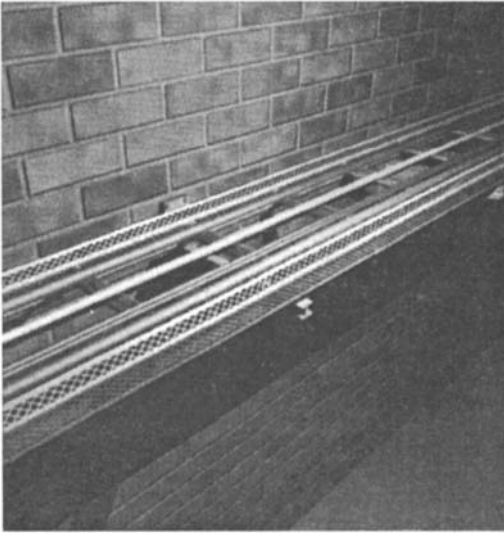
To optimize the effect in studs with expanded metal, the mesh size is decreased in connection to elongated sections of solid sheet. A plaiting of the web is preferably arranged in two angular parts for maximum overall rigidity.



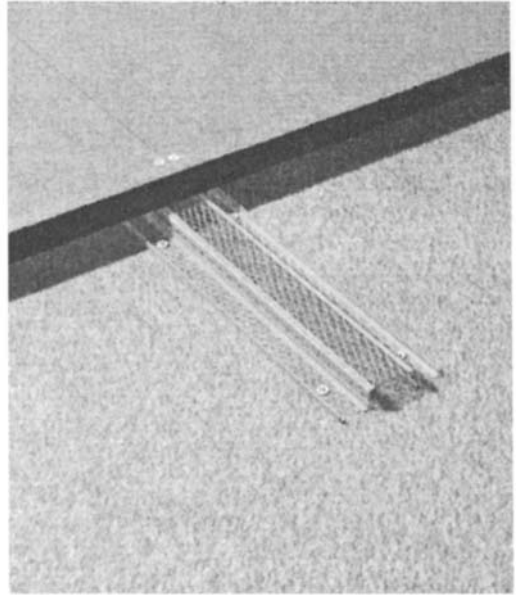
Side view and cross section of BALCUS* profile.
*** Patent Pending**



BALCUS*, cross section and geometry of expanded metal.



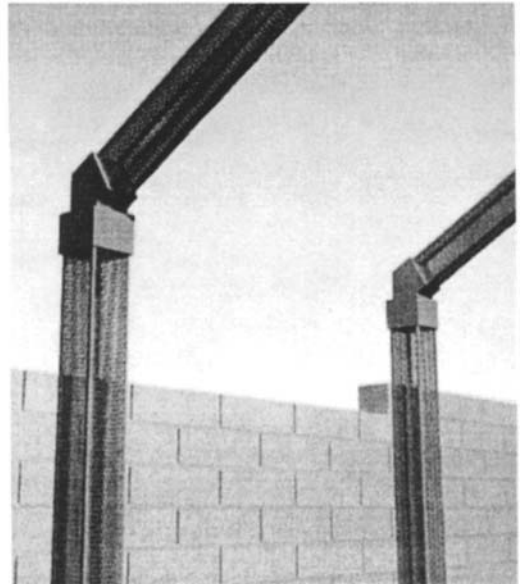
Cable shelf



Scirocco* truss aeration



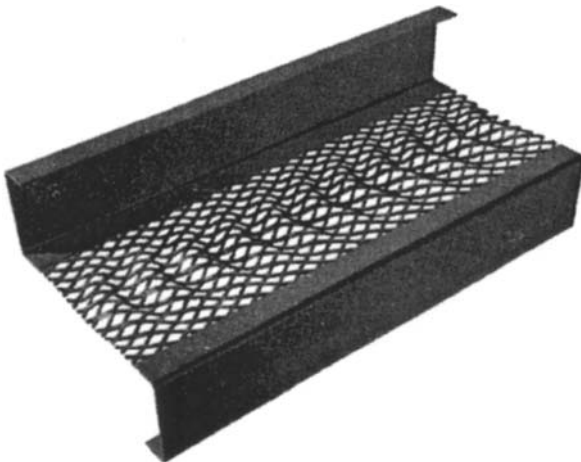
Energy absorbing road equipment



Construction beams



SPINE* C-stud, with plaited expanded metal web for optimal rigidity, low weight and energy transmission. * Patent Pending.



SPINE* Z-stud, with plaited expanded metal web for optimal rigidity, low weight and energy transmission. * Patent Pending.

This Page Intentionally Left Blank

Section IX

**TUBULAR MEMBERS
AND BRIDGE PIERS**

This Page Intentionally Left Blank

BLAST LOADING OF OFFSHORE STRUCTURAL MEMBERS USING NOVEL EXPERIMENTAL TECHNIQUES

S S Hsu, M D White and G K Schleyer

Impact Research Centre, Department of Engineering
The University of Liverpool
Liverpool, L69 3GH, UK

ABSTRACT

Results from the first tests carried out on 0.5 m square, 1 mm thick mild steel plates using a new pulse pressure loading test facility are reported. The test facility is capable of generating uniform pressure pulses of different forms to simulate characteristic blast loading in a controlled manner. Static and dynamic pulse pressure tests were carried out on clamped plates which produced large inelastic deformations. The effect of in-plane restraint and edge displacements was investigated. The plates without in-plane restraint and consequently with the least membrane resistance exhibited distinct diagonal yield lines, half way from the corner to the centre of the plate, as well as yield lines along the edges. Further test results will be reported later.

KEYWORDS

Pulse pressure loading, transient response, plates, large inelastic deformation, experimental techniques.

INTRODUCTION

The main drawback with experimental work on blast loading of structures is being able to produce repeatable uniform loading. A new test facility has been developed for studying the blast loading of structures which uses novel experimental techniques to simulate transient pulse pressure loading on a given structural member. The pulse pressure loading produced by this new test facility is repeatable, uniform and controllable.

Limited experimental data on blast loading has been reported in the literature since this data is often classified information. Moreover, the available data lacks information regarding failure and scaling effects. Jones et al. (1970), Nurick et al. (1986), and more recently, Nurick et al. (1995) and Teeling-Smith and Nurick (1991) carried out experiments on the dynamic plastic behaviour of circular and rectangular plates using sheet explosives. Houlston et al. (1991) conducted full scale air blast loading tests on fixed steel panels by detonating high explosives. Previous experimental and theoretical work

has focused more on impact and impulsive type loads, such as the work by Nurick et al. (1995). However, Schubak et al. (1989) and Yu and Chen (1992) have shown that the rise time of a pulse load has considerable effect on the transient response of a structure. The work reported here using the new test facility seeks to address the area of dynamic loading particularly with regard to scaling and failure of pulse loaded structures which has received less attention in the past due to the difficulties with carrying out meaningful experimental work.

The test facility is being used to study the pulse pressure loading of stiffened and unstiffened plates as used on offshore topsides to construct various levels and partitions. These structural components contribute little if any to the main load bearing capacity of the platform under normal operating conditions yet they have to be capable of resisting extreme transient loading in the event of a gas explosion. Their main function from a safety viewpoint is to contain the overpressure in an explosion and prevent fire from spreading to other areas and causing further escalation of the incident. The structural integrity of these members is therefore critical in such an event and the understanding of their response to blast loading is essential to predicting possible damage or failure.

The work described in this paper on the blast loading of 1 mm thick, 0.5 m square plates is a continuation of the work begun on 2 mm thick, 1 m square plates, reported by Schleyer et al. (1998). The 1 m square and 0.5 m square plates are approximately one third and one sixth respectively of full size plates typically used on offshore platforms. The aim in these studies is to produce well defined loading and response data which can be used to validate different methods of analysis and for the further development of numerical design methods as well as for bench marking of finite element numerical design codes. An important aspect of this work is to evaluate scaling effects and the effect of in-plane restraint and edge displacement on the overall response of the plates.

Some static and dynamic pulse test results on unstiffened, 1 mm thick, 0.5 m square mild steel plates are presented in the paper. At the time of writing, the material properties of the 1 mm thick plates were not available. However, the material properties of the 2 mm thick plates which have a similar specification to the 1 mm thick plates are reported in the paper.

This paper is concerned with the application of novel experimental techniques to the investigation of pulse loaded offshore structural members which are required to withstand extremely high levels of transient loading arising from an explosion.

EXPERIMENTAL FACILITY

The new test rig, shown in Figure 1, has been designed initially to simulate dynamic overpressure loading conditions typically produced in a confined hydrocarbon explosion on structural components up to 1 m square. The rig takes the form of a split horizontal pressure vessel constructed in two halves with a dividing plate for fixing the test specimens. The two halves of the pressure vessel clamp together over a support plate to make a bolted joint as shown schematically in Figure 2. The support plate, which has a central 1 m square hole, divides the vessel into two pressure loading chambers and supports the test plate and clamp frame. Each chamber is capable of being pressurised independently or simultaneously and has a rapid pressure release system consisting of a large 0.5 m diameter flanged nozzle to which is attached a burstable diaphragm. The support plate can also accommodate other fixing arrangements and structures. In the tests described in this paper, a substantial reduction plate was used to accommodate the 0.5 m square test plates. The whole assembly is suspended from a lifting frame. Geared trolleys with hoist attachments on the lifting frame enable the two chambers to be separated easily for access to the support plate. Additional items on the rig are observation windows for high speed photography and cable entries on the support plate for the various instrumentation lines.

EXPERIMENTAL PROCEDURE

The purpose of the pulse pressure loading rig is to apply controlled and repeatable uniform pressure pulses to a given structural member. This is achieved by means of the timed blow-down of back-to-back pressure loading chambers. The structural member is fixed and sealed to the support plate and a thin diaphragm material is placed over the nozzle area making the two chambers air-tight. The diaphragm material used in these tests was 75 μm thick Melinex which is capable of containing a pressure of about 0.7 bar in the vessel as a single sheet. For greater pressures, multiple layers are used. A loop of fuse wire is attached to the diaphragm about 25 mm from the edge. The diaphragm is burst by energising the fuse wire with a strong electric current.

The air pressure in the chambers is increased equally at the same time to the test pressure, P_1 , so as not to impart a resultant load on the structural member. With reference to Figure 3, at time $t = 0$ the pressure in one side of the vessel is suddenly released by bursting one of the diaphragms causing a difference in pressure across the member. At a pre-defined time later, $t = a$, the second diaphragm is burst, releasing the pressure in the other side of the vessel. The loading on the member is over by time $t = b$. The characteristic resultant pulse loading applied to the structural member is representative of overpressure loading on a boundary wall in a partially confined hydrocarbon explosion, for example. The load duration can be altered by changing the internal volume and the nozzle area. The tests presented in this paper were carried out with full nozzle area and approximately 70% volume reduction. The test rig has also been used successfully to simulate transient pressure and blast wind loading imparted to an object such as equipment or plant arising from a confined vented explosion by locating the object just in front of the nozzle area inside or outside the vessel. The procedure for static loading is much simpler and consists of securing substantial end plates to the nozzles and gradually increasing the pressure in one of the chambers. In this case, the opposite chamber is vented to atmosphere. Instrumentation for both the static and dynamic tests consisted of pressure and displacement transducers.

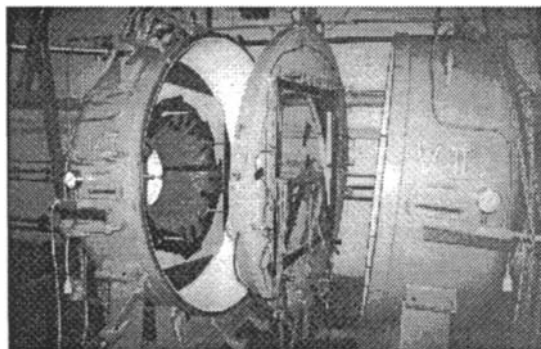


Figure 1. Pulse pressure loading test facility

Two boundary conditions were investigated, namely clamped with assumed full in-plane restraint and clamped without in-plane restraint. The 1.2 m square reduction plate is bolted to the support plate using 60 studs. Some 36 studs on the reduction plate are used to secure the 0.5 m square test plate and 0.66 m square clamp frame. In the unrestrained tests, the corners of the test specimens were removed and 2 mm thick spacers were inserted at the corners between the clamp frame and the reduction plate leaving a gap of 2 mm between the test plate and the reduction plate. Only the corner studs were utilized in the unrestrained tests allowing in-plane edge displacement of the test plates.

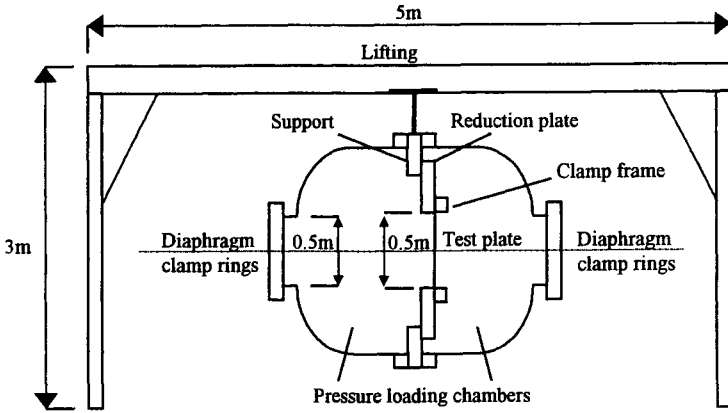


Figure 2. Schematic of test facility

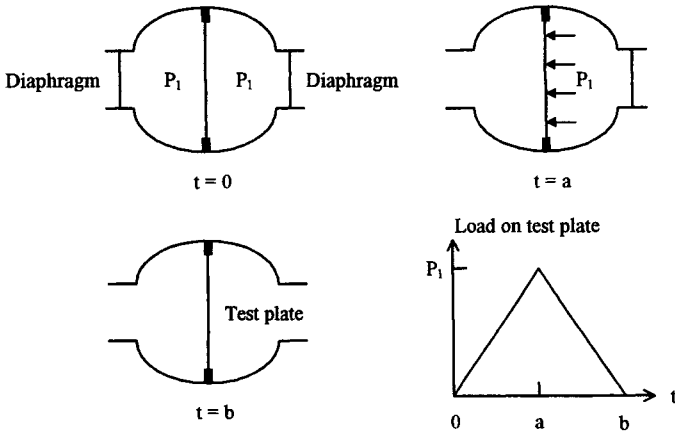


Figure 3. Principle of operation of the rapid pressure release system

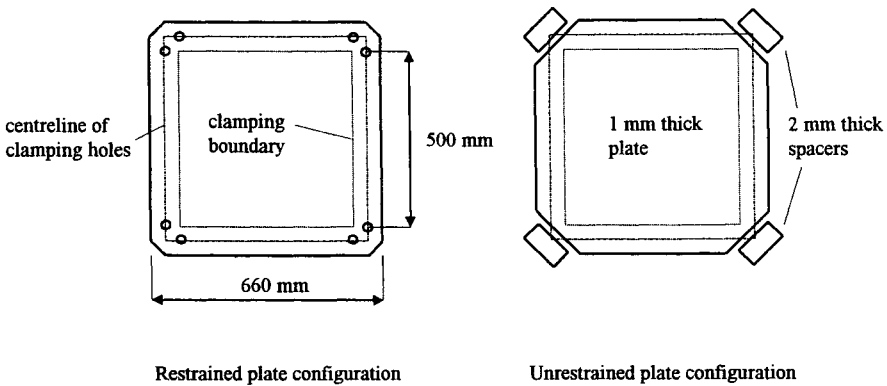


Figure 4. Fixing arrangements of the test plates

Normally in a static test, the clamp frame will seal around the plate and prevent the leakage of air between the two chambers when the plate is clamped all round. A bellows arrangement made from tape was used to seal around the test plate in the static tests when the gap was introduced. This bellows arrangement was not necessary in the dynamic tests since the air escapes more rapidly through the nozzles than it does from one chamber to the other. The two clamping arrangements are shown schematically in Figure 4.

RESULTS

The tests plates are 1 mm thick and measure 660 mm square (0.5 m square loading area when clamped) and have 36 punched holes for locating and clamping of the plate onto the support plate. The material used to manufacture the plates is hot rolled mild steel (43A grade) having a yield stress of 185 MPa, an ultimate tensile strength of 299 MPa and the rupture strain of 0.45. The average Cowper-Symonds coefficients D and q at yield are 44.71 s^{-1} and 4.7 respectively. These material properties were obtained from 2 mm thick uniaxial tensile test specimens with a similar specification to the 1 mm thick sheet material used for the 0.5 m square test plates.

The results presented here are for 4 test plates, 2 plates statically tested and 2 dynamically tested. In both the static and dynamic pulse tests, two boundary conditions were investigated, namely clamped with in-plane restraint and clamped without in-plane restraint. Miniature piezoresistive pressure transducers were attached to the support frame at three positions and linear voltage displacement transducers were attached at the half span and quarter span positions. The pressure and displacement transducer signals were recorded on a TRA800 transient recorder at a 25MHz sampling frequency. The deflection-time histories of the plates at quarter span and half span positions are presented in Figures 5 with the corresponding pulse pressure-time histories in Figure 6. The static load-deflection results are presented in Figure 7.

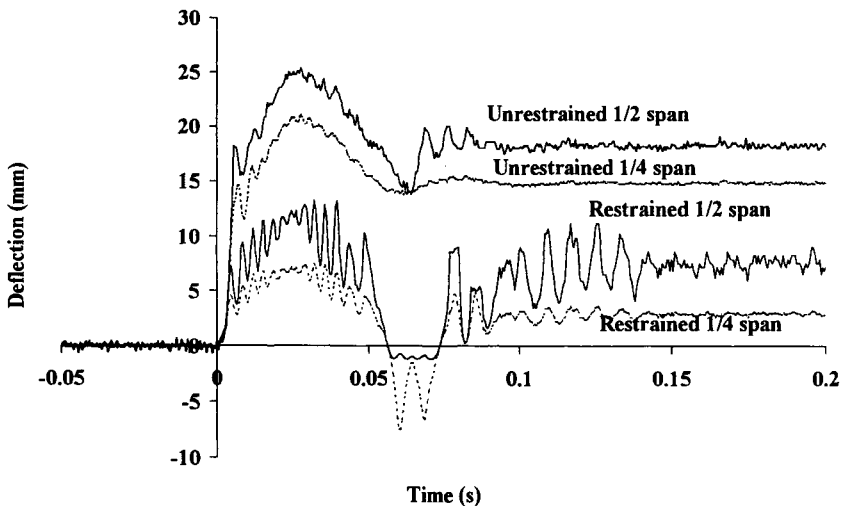


Figure 5. Deflection-time histories for dynamic tests

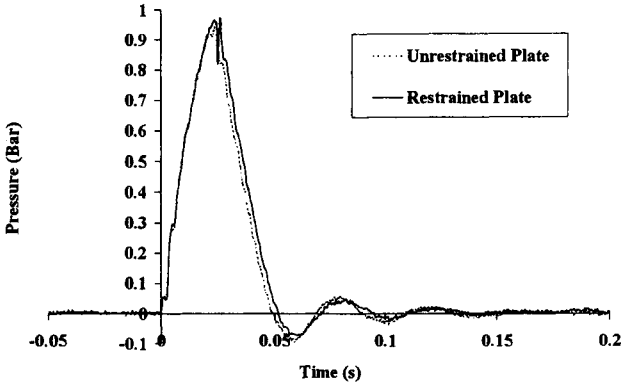


Figure 6. Pulse loading for dynamic tests

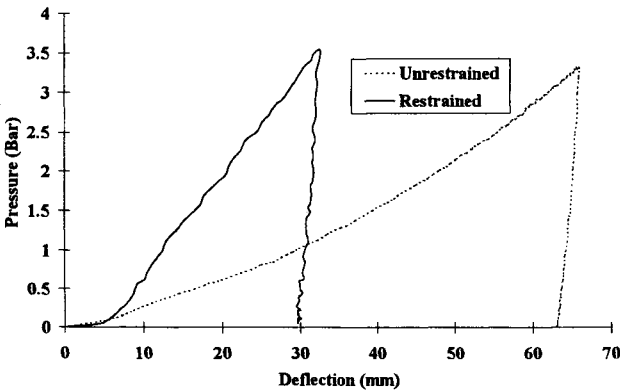


Figure 7. Load-deflection curves for static tests

Dynamic Tests

The test rig was configured with 70% volume reduction and full nozzle area in both chambers. The test pressure was almost 1 bar giving a load duration of around 50 msec. The blow down time for each chamber was around 25 msec. The pulse pressure-time histories for the two dynamic test are given in Figure 6. The equivalent 2 mm thick, 1 m square plate tests were carried out at a similar load level and load durations of around 65 msec. Greater volume reduction in the chambers will therefore be necessary in future tests in order to further reduce the loading times by the appropriate scaling factor with respect to the larger 1 m square plate tests according to the laws of geometrically similar scaling. The plates failed by large permanent deformation with deflection-thickness ratios of up to 25. Both plates deformed like a shallow shell as shown from the surface profile measurements in Figure 8. No distinct diagonal hinge lines were formed, although faint hinge lines were apparent at the clamped

boundary. The maximum edge movement for the unrestrained plate was 2 mm whereas none was observed for the restrained plate. It is interesting to note that both the maximum and permanent deflections of the unrestrained plate at both the quarter span and half span positions were approximately twice that of the restrained plate. The pressure loading in both cases was nearly identical, each pulse having a peak pressure of almost 1 bar.

Static Tests

The test pressure in the static tests of 3.5 bar was much higher than the pulse pressure dynamic tests and consequently produced larger permanent deformations. The final deflection of the unrestrained plate at both mid span and quarter span positions were both twice that of the restrained plate, a similar result to that of the dynamic tests. The load-displacement curves for the two tests are given in Figure 7. Distinctive diagonal yield lines, half way from the corners to the centre of the plate, were observed for the unrestrained plate caused by the larger deformations of the plate and reduction in membrane resistance. The unrestrained plate also exhibited obvious lateral buckling behaviour at the edges due to the space between the clamp frame and the test plate. The edge slippage was significant at a maximum of 18 mm. No slippage was detected however for the restrained plate, only plastic hinge lines at the clamping boundary were pronounced, as with the unrestrained plate.

CONCLUDING COMMENTS

Novel experimental techniques have been used successfully to simulate blast loading on scaled offshore structural members. The new rig is capable of producing repeatable and consistent uniform dynamic pressure loading in a controlled manner. The pulse shape can easily be altered to simulate different characteristics of blast loading by configuring the test rig parameters such as internal volume, nozzle area and timing. The results are being used to improve understanding of the failure and scaling of pulse loaded structures and to evaluate different methods of analysis on account of the well defined nature of the loading and response data produced by the test rig.

At the time of writing, further tests are being conducted on 0.5 m square plates with shorter pulse durations to compare with the same tests on twice size 1 m square, 2 mm thick mild steel plates. These results will be reported later.

REFERENCES

- Jones, N., Uran, T. and Tekin, S. A. (1970), 'The dynamic plastic behaviour of fully clamped rectangular plates'. *Int. J. Solid Struct.*, **6**, pp.1499-1512.
- Nurick, G. N., Pearce, H. T. and Martin, J. B. (1986), 'The deformation of thin plates subjected to impulsive loading'. *Inelastic Behaviour of Plates and Shells*, ed. L. Bevilacqua, Springer, New York.
- Schubak, R. B., Anderson, D. L. and Olson, M. D. (1989), 'Simplified dynamic analysis of rigid-plastic beams'. *Int. J. Impact Engng*, **8/1**, pp. 27-42.
- Houlston, R., Slater, J. E., and Ritzel, D. V. (1991), 'Damage assessment of naval steel panels subjected to free-field and enhanced air-blast loading'. *Int. Conf. Advances in Marine Structures*, ed. C. S. Smith and R. S. Dow, Elsevier Applied Science, London.

Teeling-Smith, R. G., and Nurick, G. N. (1991), 'The deformation and tearing of thin circular plates subjected to impulsive loads'. *Int. J. Impact Engng*, **11/1**, pp. 77-91.

Yu, T. X. and Chen, F. L. (1992), 'The large deflection dynamic plastic response of rectangular plates'. *Int. J. Impact Engng*, **12/4**, pp. 603-616.

Nurick, G. N., Olson, M. D., Fagnan, J. R. and Levin, A. (1995), 'Deformation and tearing of blast-loaded stiffened square plates'. *Int. J. Impact Engng*, **16/2**, pp. 273-291.

Schleyer, G. K., Hsu, S. S. and White, M. D., 'Blast loading of stiffened plates: experimental, analytical and numerical investigations'. To be presented at ASME PVP Conf., 26-30 July 1998, San Diego.

ACKNOWLEDGEMENTS

The authors gratefully acknowledge the EPSRC (grant reference GR/K80976), Shell Expro, BP Exploration, BG plc, Mobil North Sea Limited and the HSE Offshore Safety Division for supporting this work. The technical assistance of Mr J Curran in this work is also appreciated.

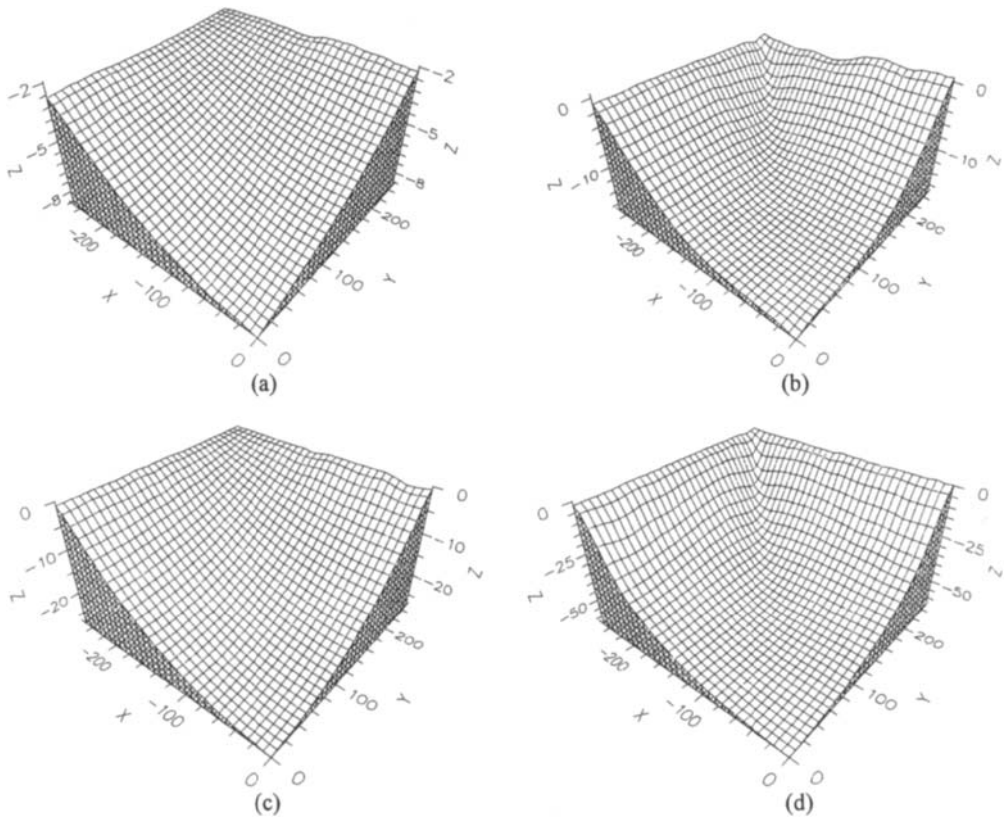


Figure 8. Post test deformed shape of plates (quarter plate shown). (a) Restrained, dynamic, (b) unrestrained, dynamic, (c) restrained, static and (d) unrestrained, static.

LATERAL (DIAMETRAL) CRUSHING OF STEEL CIRCULAR CYLINDRICAL TUBES, WELDED TO THE PLATENS

S.V. Khonsari and S.M.H. Parvinnia

Department of Civil Engineering, Sharif University of Technology,
P.O.Box 11365-9313, Tehran, Iran

ABSTRACT

As parts of a more elaborate system, liable to receive energy and expected to absorb it in a smooth manner, a series of steel circular cylindrical tubes were crushed in lateral (diametral) quasi-static compression. Due to the condition of placement of the tubes in the system which must be welded to the supporting top and bottom plates, the individual single tubes, the subject of this paper, were initially tested under the same condition. That is, welded to the supporting plates, and diametrically crushed under compression. As expected, the results were totally different from those of the tubes simply crushed laterally between parallel platens without being welded to them, available in the literature, also obtained in this work. These include the mode of collapse, the total and specific energy, and the rest of collapse parameters. In order to study the adverse consequences of welding on various collapse characteristics of the tubes, similar specimens were tested after being subjected to a stress relieving (annealing) process. These adverse effects, which are mainly the brittleness of the material and developed cracks at the welded areas and their vicinity, and also the residual stresses developed in the same areas, are more pronounced for tubes of smaller diameters. Such phenomenon may be attributed to the less exposure to the air and hence the lower rate of cooling of such tubes. In addition to removing these effects, annealing reduces the average crushing load experienced by the welded tubes, leading to more tolerable decelerations, in those circumstances where welded tubes are used as energy absorbers.

KEYWORDS

Annealing, Circular Tubes, Diametral Crushing, Energy Absorption, Lateral Crushing, Quasi-Static Loading, Steel Tubes, Stress Relieving, Welding.

INTRODUCTION

Cylindrical tubes of various cross sections and materials have long been used as energy absorbers [see Andrews *et al.* (1983), Jones (1989) & Khonsari (1992) for detailed discussions and references on crushed tubes]. The common types of cross sections are circular, square, rectangular, etc. Also, the materials have been of quite wide diversity including metallic and non-metallic materials. Such tubes have been exploited as energy absorbers while crushed in either direction, namely longitudinal and lateral, or even in a combined manner, say in an oblique impact loading. Investigations made on tubes as “deforming material energy absorbers,” as opposed to other types of energy absorbers, “frictional,” etc., has been under various types of loading including “quasi-static” and “dynamic.” Despite the fact that it should be acknowledged that in general, it is in an “impact loading context” that the need for absorbing a certain amount of energy, released in a short period of time, becomes necessary, and makes sense, however, due to many reasons, the potential of absorbing energy of many devices has been studied under quasi-static loading. The major reason is that to carry out quasi-static tests is much simpler, cheaper and less difficult to interpret. The other reason may be that the condition and the type of loading to which the device used as an energy absorber will be subjected, may indeed have a quasi-static nature. Or, it may be a non-impact dynamic loading such as earthquake. However, quasi-static loading has proven to give a reasonable indication of the energy absorption capacity of a system, unless due to such phenomena as rate-sensitivity of the material, this capacity and/or the mode of collapse is changed.

Circular tubes crushed diametrically, has been the subject of extensive research during the last four decades [see DeRuntz & Hodge (1963), Redwood (1964), Reid & Yella Reddy (1978), Reid (1983)]. Such tubes, known as ‘flattening tubes,’ have the highest stroke to length ratio (crush efficiency), i.e. a figure close to unity. Though while used in arrays, this figure reduces to 70%. The specific energy absorption of such tubes (the energy absorbed by the unit mass of the tube while it is completely crushed) is in the range of 4500-15000 N.m/kg [Jones (1989)]. Reid (1983) carried out a comprehensive experimental as well as theoretical study on the behaviour of single circular and arrays of both circular and square metallic tubes under quasi-static and dynamic lateral loading. In all of the above-mentioned work, the tube(s) were laid between crushing plates, in contact with them, without being somehow connected to them, e.g. by welding or using bolts or rivets.

During designing an elaborate system which was expected to receive a certain amount of energy and dissipate it, need arose to know the behaviour of metallic circular cylindrical tubes, welded to two parallel plates and crushed laterally between them. Despite the abundance of test results on laterally crushed circular tubes, nothing was found in this regard (tubes welded to the platens) in the literature. Therefore, it was decided to carry out some tests on such tubes and obtain some insight into their behaviour.

EXPERIMENTAL WORK

As mentioned above, in order to investigate the crushing characteristics of metallic circular cylindrical tubes welded to parallel platens which were also parallel to the longitudinal axis of the tubes, a series of tests were carried out. These include quasi-static tests in which the specimens were totally crushed laterally (diametrically). Altogether, tubes of three sizes were studied. That is, of three different diameters and thicknesses, called C-1 to C-3 series. The length of the specimens were kept almost the same (8 cm.). In order to have a measure for comparison, for each case (each tube size), a similar specimen but without being welded to the platens was tested as well. Also, to investigate the ‘conceived adverse effects of welding’ on the behaviour of the welded tubes, similar welded specimens

were also tested after being subjected to an annealing process. Figure 1 depicts a drawing of one of the welded specimens of the C1 series (the tube with the smallest diameter) and the condition of its loading.

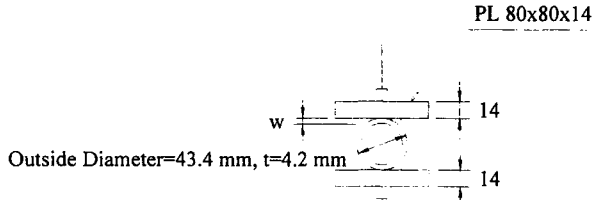


Figure 1: The welded C1 series of tubes.

Table 1 contains the dimensions of the specimens together with their status with regard to their type of interface with the platens as well as their heat treatment condition. It should be emphasized that due to welding operations, carried out on Cx-2 and Cx-3 specimens, some degree of ovality was observed in them.

TABLE 1
DIMENSIONS AND THE CONDITIONS OF THE TESTED TUBES.

Specimen		Outside Diameter (mm)	Thickness (mm)	Length (mm)	Welded?	Annealed?	Confined to Vertical Movement?
C1 Series	C1-1	43.4	4.2	80.5	No	N/A	N/A
	C1-2	43.4	4.2	84.8	Yes	No	No
	C1-3	43.4	4.2	82.5	Yes	Yes	No
C2 Series	C2-1	60.7	3.9	80.0	No	N/A	N/A
	C2-2	60.7	3.9	81.5	Yes	No	Yes
	C2-3	60.7	3.9	83.5	Yes	Yes	Yes
C3 Series	C3-1	88.0	3.0	84.0	No	N/A	N/A
	C3-2	88.0	3.0	85.7	Yes	No	Yes
	C3-3	88.0	3.0	83.0	Yes	Yes	Yes

As can be noted in this table, unwelded specimens were simply crushed between the platens of the universal testing machine. However, during crushing of the welded specimens of the C1 series (C1-2 & C1-3 specimens), it was observed that the two supporting plates, to which the tubes were welded, gradually slipped on the platens of the machine, disturbing the symmetry of deformation and leading to a tilting mode of collapse (see Figures 2 & 3). In particular this phenomenon was severely pronounced with regard to the unrelieved specimen (C1-2) due to the paint applied to the surfaces of the two supporting plates. In order to prevent further welded specimens from undergoing such unsymmetrical deformation patterns, a device was designed and used by the authors to restrain the two platens (welded supporting plates) to move just in the direction perpendicular to them without allowing any lateral displacement (parallel to the platens). Therefore, the welded C2 and C3 specimens were in fact tested under somewhat different conditions. It was done to create a condition similar to that such tubes would have in the above-mentioned elaborate energy absorber. This device, together with Specimen C2-3 positioned in it, is shown in Figure 4.

The material of the tubes was believed to be mild steel, though no attempt was made by the authors to substantiate this, either through test or any other means. The main objective is to have a comparison between the results of unwelded tubes with their similar welded counterparts, both, annealed and

unannealed. In other words, the main objective is to investigate the effects of welding on various characteristics of circular tubes crushed laterally. It should also be emphasized that the authors are not confident as to whether the three series were all of the same material. Bearing in mind that mild steel is highly rate-sensitive [see Jones (1989) and Khonsari (1992)], during all of the tests reported here, the speed of loading was kept very low to reduce the effects of strain rate on the behaviour of tubes hence on the tests results. The ductility of the material of the tubes was, to some extent, confirmed by the observations made on tests carried out on their unwelded specimens (Cx-1 specimens). In all of such tests, the flattening of the tubes took place without developing any cracks in them, producing load-deflection curves very similar to those reported by DeRuntz & Hodge (1963) and Redwood (1964).

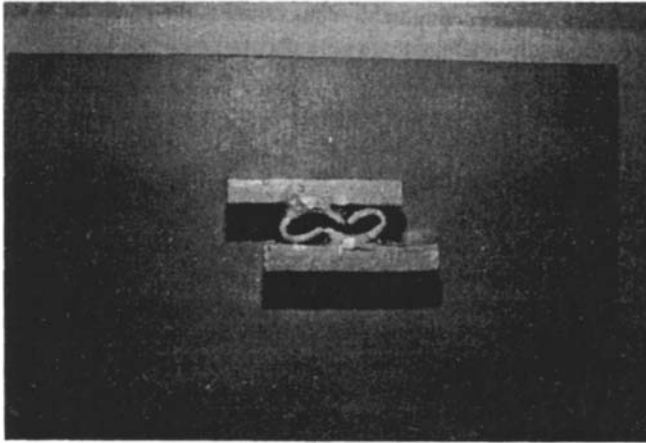


Figure 2: C1-2 after the test.

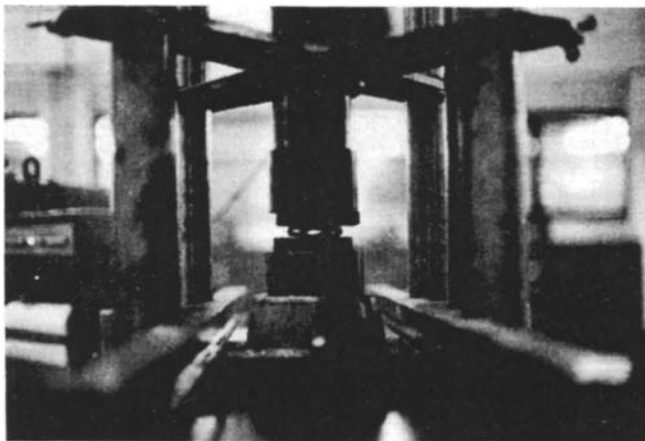


Figure 3: C1-3 at the end of the test, before removing from the universal testing machine.

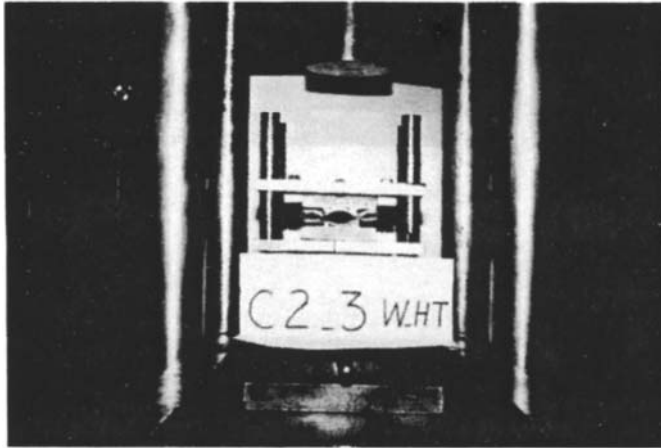


Figure 4: C2-3 positioned inside the vertical-guiding device.

The annealing process of the welded specimens was carried out by putting them in an annealing furnace and gradually raising the temperature to 650 degrees Celsius, keeping them at this temperature for 2 hours and then leaving them to gradually cool down in the furnace overnight.

RESULTS AND DISCUSSION

Since the tubes were mainly studied in an energy absorption context, it was their energy absorption capacity which was the main concern of the authors in this study. Obviously, one of the main features of the test results, which is quite indicative in this respect, is the mode of collapse. While unwelded tubes, all followed the well-known 'flattening' fashion, all of the welded specimens, collapsed in a totally different mode. This new mode, as may be noted in Figure 3, comprises 3 double-crescents which seems to have six fixed plastic hinge lines. C1-2, however, was an exception in that 2 double-crescents were developed during its collapse. The flattening mode, on the other hand, comprises 4 hinges (yield lines) which depending on the behaviour of the material may extend to six; two of the hinges remain stationary and each of the remaining two, gradually convert to two moving hinges [see Reid & Yella Reddy (1978), Yella Reddy & Reid (1980) and Reid (1983)]. Here, the nearly 2 double-crescents mode, developed by C1-2, as a result of severe sliding of the welded plates on the machine platens, is considered as a rare incident. The modes of collapse of the tested tubes are given in Table 2. The severe cracks observed in C1-2, at the two hinges which developed in the vicinity of welding material (Figure 2), are clear indications of the brittleness of the tube material, induced by welding operations. Such severe cracks were not detected in the unrelieved welded specimens of the other two series. The reason for this phenomenon seems to be the better exposure to the air of tubes with larger diameters, hence their higher rate of cooling, which leads to less brittleness of the base material.

As it is seen in Figures 1 & 3, the crush (geometric, stroke) efficiency of the 3 double-crescents mode is dependent on the distance w , the height of the weld, as well as the D_0/t ratio. Therefore, theoretically, we have,

$$e_{\text{theo.}} = \frac{D_O - 2t - 2w}{D_O} \quad (1)$$

In the above, D_O is the outside diameter of the tube, and t is its thickness. If the term $2w$ is eliminated from this formula, the crush efficiency of the flattening mode will be recovered which as the ratio D_O/t increases, tends towards unity. The experimental (real) value for the geometric efficiency, however, is worked out as

$$e_{\text{expt.}} = \frac{S}{D_O}, \quad (2)$$

where S is the stroke. This characteristic of the tested tubes together with their strokes are also given in Table 2.

TABLE 2
TESTS RESULTS. DCs: DOUBLE-CRESCENTS, T: TILTING, ST: SLIGHT TILTING.

Specimen		$\frac{D_O}{t}$	Mode of Collapse	Total Absorbed Energy (N.m)	Specific Energy (N.m/kg)	Stroke (S) (mm)	$e_{\text{expt.}}$
C1 Series	C1-1	10.33	Flattening	1261.81	3857.54	33.02	0.76
	C1-2	10.33	2 DCs + T	1404.77	4076.82	23.12	0.53
	C1-3	10.33	3 DCs + ST	2328.00	6944.51	29.00	0.67
C2 Series	C2-1	15.56	Flattening	1061.94	2427.98	50.50	0.83
	C2-2	15.56	3 DCs	1173.17	2632.92	39.00	0.64
	C2-3	15.56	3 DCs	0891.89	1953.71	41.60	0.68
C3 Series	C3-1	29.33	Flattening	0986.32	1865.72	78.00	0.89
	C3-2	29.33	3 DCs	0928.93	1722.30	65.90	0.75
	C3-3	29.33	3 DCs	0715.99	1370.68	67.80	0.77

Figure 5 depicts the load-deflection characteristics of the three series of tubes, comparing the results of the tubes of each series in a single graph. The total and the specific energy of the tubes, as the principal outcomes of this study, are worked out and given in Table 2. The former is the area under the load-deflection curve of the tube under consideration, whereas the latter is the result of dividing this area by the mass of the tube. Here, it has been assumed that the welding material, due to its brittleness, and the supporting platens do not have any contribution towards the energy absorption process. While the specific energy of C1-1 is almost consistent with the lower limit of the range given above for tubes crushed in flattening mode (4500-15000 N.m/kg), the values obtained for C2-1 and C3-1 are both totally out of this range. This necessitates a reconsideration in the lower limit of this range, apparently after carrying out more tests. The specific energy of all of the specimens are compared in Figure 6. This bar chart indicates that, at least for the tested specimens, a unique trend between the specific absorbed energy of the three specimens of each series does not exist. While for the first series, an upward trend is observed, for the other two, different trends, even different with one another, are followed. This inconclusiveness of the results, with regard to the relation between the specific absorbed energy of similar unwelded (UW), unrelieved welded (W-UR), and stress-relieved welded (W-SR) specimens, also shows the need for a more comprehensive study on this subject. In particular, the distinct differences between the D_O/t ratios for the three series of tubes, noted in Table 2, gives this idea that, as categorized by Andrews *et al.* (1983) for 'folding' circular tubes, it is likely that the trend of variation of specific energy for the three conditions (UW, W-UR & W-SR) of similar tubes is a function of D_O/t or $D_{\text{avr.}}/t$ ratios. This may have its roots in the following two facts. First, the yield stress of steel is dependent on the thickness of the tested specimens. Second, as D_O/t increases, the moment arms for the side hinge lines increase as well, whereas the plastic resisting moment of the cross section (through the thickness) of the tube remains constant.

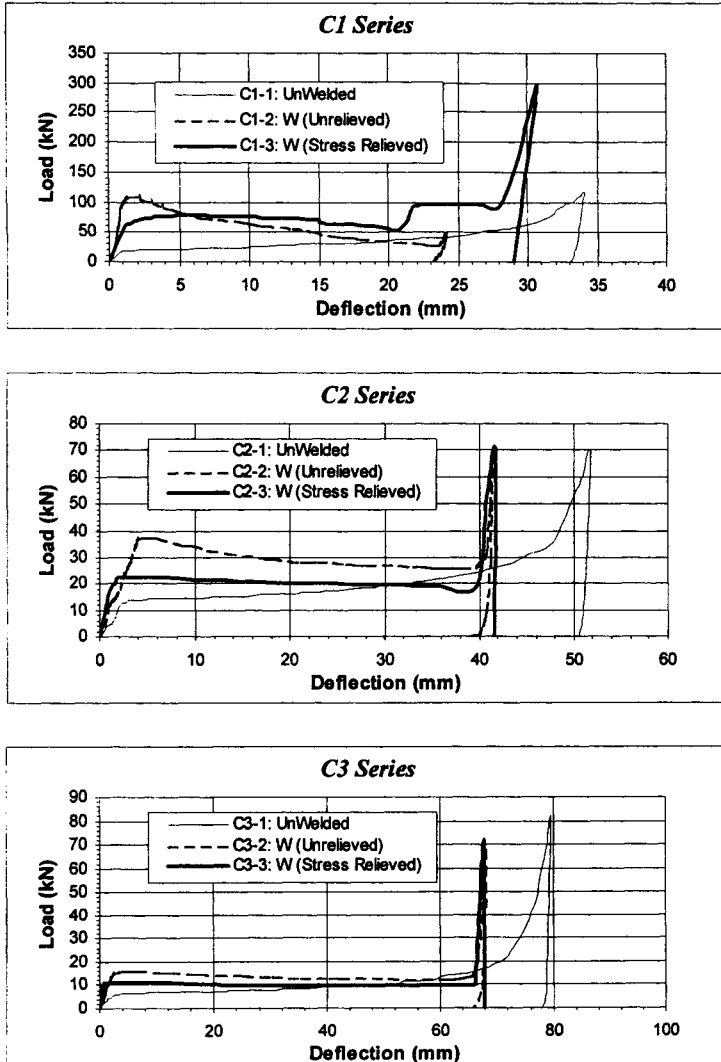


Figure 5: Load-Deflection characteristics of the three series of specimens.

CONCLUSIONS

Before making any conclusions, the authors would like to express that they acknowledge that their study has been limited to a few cases, and in order to draw clear conclusions, a more comprehensive research programme has to be conducted. Therefore, the following conclusions are based on this limited experimental work.

1-The range already given for the specific energy absorption of circular tubes, collapsed in flattening mode, needs to be reconsidered; in particular, its lower limit and with regard to tubes with higher D/t ratios.

2-Diametral crushing of circular cylindrical tubes, welded to parallel platens and confined to displace in the direction of loading, leads to a 3 double-crescents mode of collapse. It seems that for tubes with

D_0/t less than 15, this mode has a higher specific energy than the flattening mode. This takes place despite the fact that flattening mode has a higher crush efficiency.

3- Stress relieving reduces the average load, hence leading to a more tolerable deceleration in such circumstances where welded tubes are used as energy absorbers. This point should also be confirmed by impact tests during which, in particular, the rate sensitivity of mild steel is strongly present and may even change the mode of collapse. It is likely that the annealing process has also removed the residual stresses developed in the tubes during their manufacture, as a result of rolling.

4- Stress relieving is capable of removing the brittleness, induced in the base material, in the vicinity of the welded area, as a result of welding.

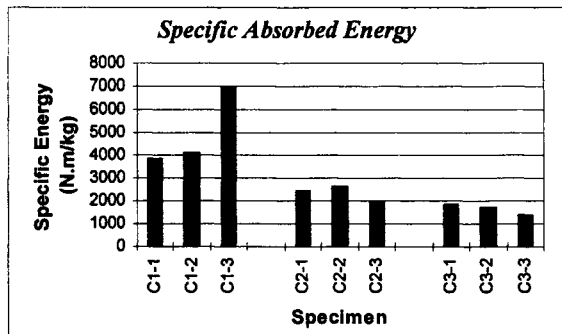


Figure 6: Comparison between the specific absorbed energy of the tubes.

ACKNOWLEDGEMENT

The full financial support of this project, provided by Sharif University of Technology is gratefully acknowledged.

REFERENCES

- Andrews, K.R.F., England, G.L. and Ghani, E. (1983). Classification of the Axial Collapse of Cylindrical Tubes Under Quasi-Static Loading. *Int. J. Mech. Sci.* **25:9-10**, 687-696.
- DeRuntz, J.A. and Hodge, P.G. (1963). Crushing of a Tube Between Rigid Plates. *J. Appl. Mech.*, ASME, **30**, 391-395.
- Jones, N. (1989). *Structural Impact*, Cambridge University Press, Cambridge, U.K.
- Khonsari (1992). *Numerical Modelling of Dynamic Progressive Collapse of Rate Sensitive Circular Cylindrical Tubes*, PhD Thesis, University of London, London, U.K.
- Redwood, R.G. (1964). Discussion on Crushing of a Tube Between Rigid Plates. *J. Appl. Mech.*, ASME, **31**, 357-358.
- Reid, S.R. (1983). Laterally Compressed Metal Tubes as Impact Energy Absorbers. *Structural Crashworthiness*, Jones, N. and Wierzbicki, T. (Eds.), 1-43, Butterworths, London, U.K.
- Reid, S.R. and Yella Reddy, T. (1978). Effect of Strain Hardening on the Lateral Compression of Tubes Between Rigid Plates. *Int. J. Solids Structures* **14**, 213-225.
- Yella Reddy, T. and Reid, S.R. (1980). Phenomena Associated with the Crushing of Metal Tubes Between Rigid Plates. *Int. J. Solids Structures* **16**, 545-562.

This Page Intentionally Left Blank

QUASI-STATIC AXIAL COMPRESSION OF THIN-WALLED CIRCULAR METAL TUBES INCLUDING EFFECTS OF FOAM FILLING

S.R. Guillow and G. Lu

School of Engineering and Science, Swinburne University of Technology,
Hawthorn, VIC. 3122, AUSTRALIA.

ABSTRACT

In this paper we present some preliminary findings from a series of 33 experiments that were conducted to investigate the axial compression behaviour of very thin-walled ($D/t \geq 50$) 6060 - T5 aluminium alloy tubes both with and without a filling of polyurethane foam. The aluminium tubes were tested quasi-statically at a constant velocity of 5 mm / min.. A range of tube dimensions were examined with D/t ratios varying from 50 to 200 and L/D ratios varying from 2 to 4. A variety of foam densities from 35 kg / m³ to 140 kg / m³ were considered for the case where $D/t = 98$ and $L/D = 2$. It was found for empty tubes that at large values of D/t the ratio of $F_{max.} / F_{av.}$ became very large and also the variability of this force ratio increased. For foam-filled tubes it was found that the foam density had to be reduced to the low value of 35 kg / m³ for there to be a negligible effect on the collapse mode of the aluminium tube. At higher foam densities a change in collapse mode from asymmetric to at least partially symmetric was observed.

KEYWORDS

Axial Compression, Foam, Thin-Walled, Circular Tube, Aluminium, Collapse Modes

INTRODUCTION

The behaviour of thin-walled metal tubes in axial compression has been studied for many years. This behaviour has been found to be very complex and somewhat intractable to study. It is dependent on certain geometrical parameters (diameter - D , wall thickness - t , and length - L) and material parameters (yield stress - σ_y , and ultimate stress - σ_{ult}). Collapse of metal tubes in quasi-static axial compression may occur by symmetric concertina bellowing, asymmetric progressive buckling, Euler buckling or simple compression (or a combination of these modes).

Early work on the axial compression behaviour of thin-walled tubes was carried out by Johnson, Soden & England (1977), who considered rigid P.V.C. tubes. Andrews, England & Ghani (1983) introduced a classification chart to determine collapse mode based on tests of annealed aluminium alloy tubes. Mamlis and Johnson (1983) tested thin-walled annealed 6061 aluminium cylinders and frustra and developed some useful equations for determining the forces involved. Abramowicz & Jones (1984) considered dynamic effects when crushing thin-walled steel cylinders.

More recent research reflecting the current state of knowledge has been carried out by the following researchers: Abramowicz & Jones (1997) considered the transition between collapse modes for both quasi-static and dynamic loading of mild steel tubes. Grzebieta (1996) presented an overview of his research into axial plastic collapse of ductile steel tubes. N.K. & S.K. Gupta (1993) tested both aluminium and mild steel circular tubes in the as recieved and annealed conditions. Gupta & Gupta considered relatively thick tubes with a $D/t < 33$. Reid (1993) reviewed various modes of plastic deformation which included axial progressive buckling, splitting and inversion for the case of steel tubes.

The above studies generally considered tubes with a D/t ratio < 50 .

Specific research into the effects of in-filling metal tubes with foam has been carried out by Reddy & Wall (1988). This particular research involved testing of very thin-walled ($D/t = 600$) deep drawn aluminium alloy drink cans which had been filled with polyurethane foam.

The aim of our present study is to extend the current level of knowledge particularly with regard to relatively thin-walled aluminium tubes (with a D/t ratio ≥ 50) and also to the effects of filling these metal tubes with polyurethane foam. We tested tubes whose dimensions varied so that the ratio D/t was between 50 and 200 and the length, L , was between 2 and 4 times the diameter. We were particularly interested in the critical value of foam density (and hence its mechanical properties such as elastic modulus and yield stress) corresponding to a *change* of collapse mode - this was identified experimentally.

TEST SPECIMENS AND MATERIAL CHARACTERISTICS

The metal tubes tested were all made from extruded commercial quality 6060 aluminium alloy in the T5 condition (i.e. as recieved). This aluminium alloy had a 0.2 % proof stress of 180 MPa, an ultimate stress (σ_{ult}) of 212 MPa and a Vickers hardness V.H.(5) of 80. Figure 1 below shows a typical stress-strain curve obtained from a standard tensile testpiece cut from a tube and then tested in tension. All of the aluminium tubes tested had the same internal diameter of 96 mm. Stock wall thickness (2 mm) was reduced where necessary by machining the outer surface to achieve the required wall thickness (t) and a consequently reduced outside diameter. Then the ends were cut off square - all testpieces having open ends. Finally dimensions and mechanical properties were measured for later analysis.

Most of the testing involved empty aluminium alloy tubes. However some testing was carried out on aluminium alloy tubes which had been filled with polyurethane foam.

Three different densities of polyurethane foam (35, 60 and 140 kg/m³) were used in testing. Figure 2 below shows typical stress-strain curves for these three different density foams (these curves were obtained from compression tests on 96 mm diameter cylindrical foam blanks).

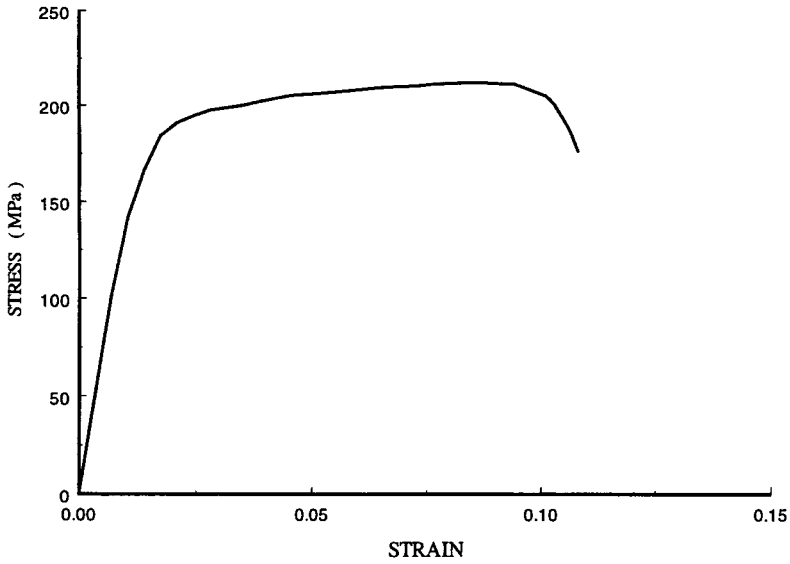


Figure 1 : Typical stress - strain curve for 6060 - T5 aluminium alloy

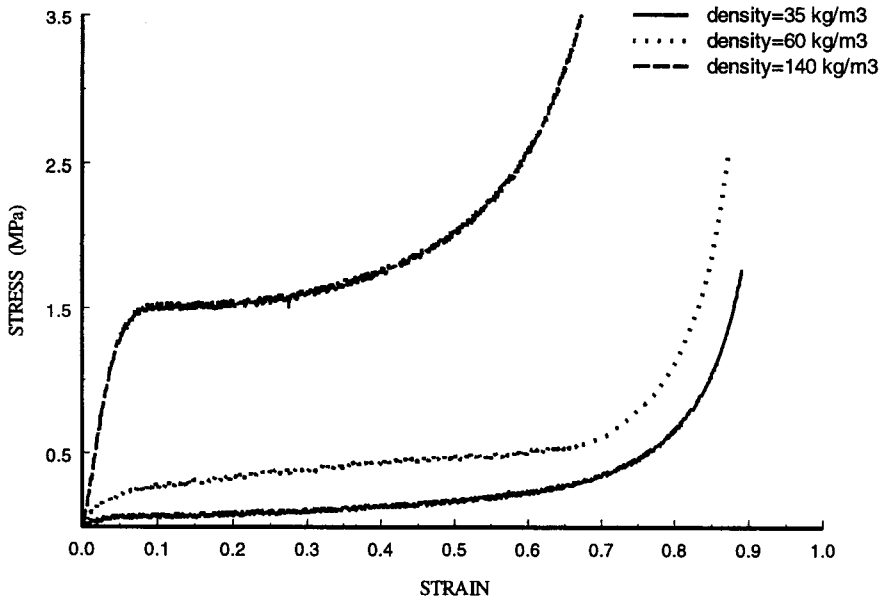


Figure 2 : Stress - strain curves for polyurethane foams of different densities

TEST RIG AND TEST PROCEDURE

All testpieces (except metal tensile ones) were tested in compression using a SHIMADZU 'Autograph' universal testing machine of 250 kN capacity. This machine was connected to a LABTECH data - logger which recorded the load on the SHIMADZU digitally for later analysis. This equipment can be seen in Figure 3 below.

Compression testpieces were placed between two rigid flat metal plates and load applied using the SHIMADZU at a constant velocity of 5 mm / min.. Testing was continued until 'end effects' were observed or the testpiece had clearly collapsed. Basically three types of compression tests were carried out : (i) empty aluminium tubes ; (ii) polyurethane foam cylinder blanks with a diameter of 96 mm and (iii) aluminium tubes which had been filled with polyurethane foam.



Figure 3 : SHIMADZU universal testing machine

TEST RESULTS

A typical force versus displacement curve for an empty aluminium alloy tube tested in compression is shown below in Figure 4. Figure 5 shows the effect of varying the density of the polyurethane foam filling in the aluminium tube. Note that all the aluminium tubes whose test results are shown in Figures 4 and 5 have nominally identical geometric parameters - viz. : O.D. = 98 mm, $t = 1.0$ mm, $L = 2 \times \text{O.D.} = 196$ mm.

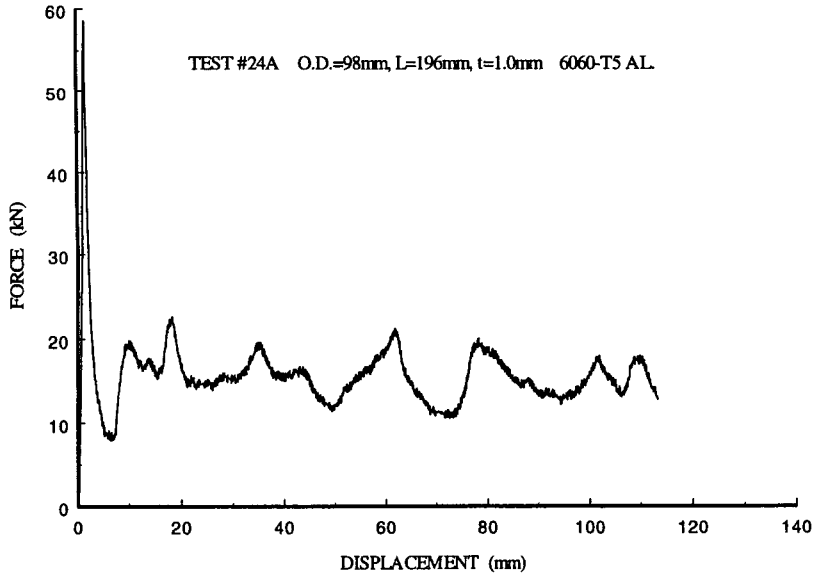


Figure 4 : Force versus displacement for a typical empty aluminium tube

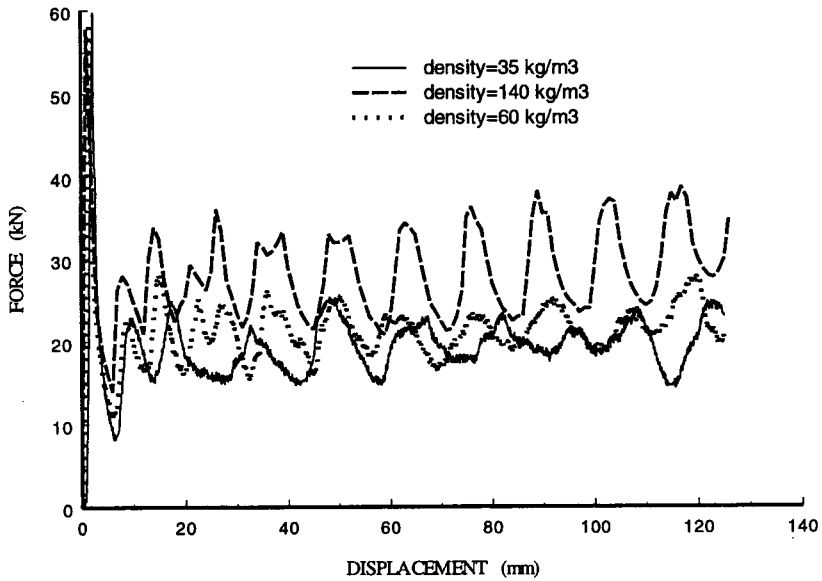


Figure 5 : Effect of varying density of foam filling in aluminium tubes. All tubes are of 6060-T5 aluminium alloy of length 196 mm, outside diameter 98 mm and thickness 1.0 mm.

OBSERVATIONS

After consideration it was found that the most significant result obtained for empty aluminium tubes was the ratio of maximum force, F_{max} , (for the first fold), to average force, F_{av} , - obtained over the stroke. This can be seen in Figure 6. The increase in the F_{max} / F_{av} ratio with increasing D / t is quite pronounced. This increase in F_{max} / F_{av} with increasing D / t has been noted by other researchers - but not we believe for T5 condition aluminium alloys at such high D / t ratios. Also of interest, as the D / t ratio increases it appears that the variability in the F_{max} / F_{av} ratio also increases.

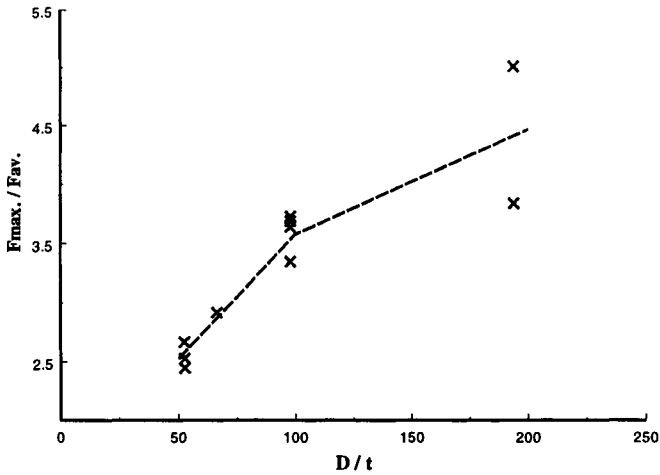


Figure 6 : Variation of F_{max} / F_{av} versus D / t for empty aluminium tubes

Almost all the empty aluminium tubes tested collapsed asymmetrically (typically with 3 or 4 corners or lobes). Only the thickest empty tubes tested ($t = 2.0$ mm), in very short lengths ($L = 196$ mm or $2 \times D$) collapsed entirely by the symmetric concertina mode.

However, the effect of in-filling the aluminium tube with polyurethane foam (of sufficient density) was to force the filled tube to collapse via the symmetric concertina mode. Figure 7 (a) and (b) below show typical specimens for aluminium alloy tubes with and without foam filling.



Figure 7 (a) Typical failed empty aluminium alloy tube



Figure 7 (b) Typical failed aluminium alloy tube with foam filling

We conducted a study to determine the minimum density foam that was required to enforce the symmetric concertina mode on a particular 6060-T5 aluminium alloy tube. In this case we considered a tube of nominal dimensions : outside diameter, O.D. = 98 mm, $t = 1.0$ mm, $L = 196$ mm (ie. $2 \times$ O.D.). The results of this series of tests can be seen in Figure 5. It was found that the foam density had to be reduced to the surprisingly low value of 35 kg/m^3 before the collapse mode became completely asymmetric - i.e. the *same* as for an identical empty aluminium tube . This minimum polyurethane foam density of 35 kg/m^3 corresponded to an elastic modulus (E) of 1.8 MPa and a yield stress (σ_y) of 75 kPa .

We expected to observe an increase in the average crushing load ($F_{av.}$) for aluminium alloy tubes which had been filled with foam as compared with identical empty aluminium tubes. In fact, there is a complex interaction between the metal tubes and their foam filling. The foam tends to provide support for the thin walls of the aluminium tube, obviously increasing the overall crushing load. Less obvious is the stiffening effect provided by the aluminium tube to the foam , primarily by preventing lateral expansion of the foam when compressed. Table 1 below illustrates the point that the average crushing load for a foam filled aluminium tube is *greater* than the sum of the average crushing loads for the identical aluminium tube and foam cylinder blank tested separately.

TABLE 1

COMPARISON OF AVERAGE FORCE FOR FOAM ONLY, EMPTY ALUMINIUM TUBES AND FOAM FILLED ALUMINIUM TUBES

Foam density (kg / m^3)	$F_{AV.}$ for Foam only (kN)	$F_{AV.}$ for empty Aluminium tube (kN)	Sum of two columns at left (kN)	$F_{AV.}$ for Foam filled Al. tubes (kN)
35	0.908	15.53	16.44	19.32
60	2.685	15.53	18.22	21.10
140	12.43	15.53	27.96	28.45

(Note that the average force was calculated over 126 mm stroke under identical conditions for 6060 - T5 aluminium alloy tubes of length 196 mm, outside diameter 98 mm and thickness 1.0 mm)

CONCLUSIONS

From our quasi-static compression testing of 6060 - T5 aluminium alloy tubes both with and without foam filling we draw the following conclusions.

In the case of empty tubes, the very large increase in the ratio of $F_{max.} / F_{av.}$ with increasing D / t , ie. for very thin-walled, tubes of 6060 - T5 aluminium alloy - is of some interest. It seems worthy of further study to determine if there is an upper limit to this force ratio as the D / t ratio increases. Also it would seem worthwhile to consider a larger range of lengths (beyond the range $L = 2$ to $4 \times D$ that we have considered here) to see what effect, if any, length of the test specimen has on the large observed variability in the $F_{max.} / F_{av.}$ ratio at high values of D / t .

The effects on the compression behaviour of filling 6060 - T5 aluminium alloy tubes with polyurethane foam of various densities is perhaps of even greater interest. It would be instructive to investigate what minimum foam density is required to *enforce* a collapse mode change (from for example - asymmetric to symmetric) in aluminium alloy tubes for a wider range of conditions than we have considered here. (The case that we considered was for an aluminium tube with the following dimensions : O.D. = 98 mm, t = 1.0 mm and L = 196 mm.) Complementary theoretical work to explain the effect of foam filling on the collapse mode of thin-walled circular metal tubes is currently underway.

REFERENCES

- Abramowicz W. and Jones N. (1984). Dynamic Axial Crushing of Circular Tubes. *International Journal of Impact Engineering* **2:3**, 263-281.
- Abramowicz W. and Jones N. (1997). Transition from Initial Global Bending to Progressive Buckling of Tubes Loaded Statically and Dynamically. *International Journal of Impact Engineering* **19:5/6**, 415-437.
- Andrews K. R. F., England G. L. and Ghani E. (1983). Classification of the Axial Collapse of Circular Tubes under Quasi-Static Loading. *International Journal of Mechanical Sciences* **25:9/10**, 687-696.
- Grzebieta R. H. (1996). Research into Failure Mechanisms of Some Thin-Walled Round Tubes. *Plasticity and Impact Mechanics - Proceedings of IMPLAST96*, N. K. Gupta ed., New Age International Publishers, 309-324.
- Gupta N. K. and Gupta S. K. (1993). Effect of Annealing, Size and Cutouts on Axial Collapse Behaviour of Circular Tubes. *International Journal of Mechanical Sciences* **35:7**, 597-613.
- Mamalis A. G. and Johnson W. (1983). The Quasi-Static Crumpling of Thin-Walled Circular Cylinders and Frustra. *International Journal of Mechanical Sciences* **25:9/10**, 713-732.
- Johnson W., Soden P. D. and Al-Hassani S. T.S. (1977). Inextensional Collapse of Thin-Walled Tubes Under Axial Compression. *International Journal of Strain Analysis* **12:4**, 317-330.
- Reddy T. Y. and Wall R. J. (1988). Axial Compression of Foam-Filled Thin-Walled Circular Tubes. *International Journal of Impact Engineering* **7:2**, 151-166.
- Reid S. R. (1993). Plastic Deformation Mechanisms in Axially Compressed Metal Tubes Used as Impact Energy Absorbers. *International Journal of Mechanical Sciences* **35:12**, 1035-1052.

CYCLIC LOADING TEST OF STEEL OCTAGONAL SECTION PIER MODELS

M.Suzuki¹ and T.Aoki²

^{1,2} Department of Civil Engineering, Aichi Institute of Technology,
Yakusa-cho Toyota-shi 470-0392, Japan

ABSTRACT

Highway structures in an urban area need to function effectively immediately after an earthquake occurs in order to allow relief operations in the damaged zones. The seismic design philosophy adopted here is that safety coefficients should be based on a minimum total cost of loss occurring in the social system. Simple and quick repair of partially damaged structure is therefore an important consideration in functional design. In the tests reported below, octagonal section steel bridge pier models that had previously been subjected to seismic loading were simply repaired and then retested under cyclic loading. Test results showed good recovery in the load-deflection hysteresis curves.

KEYWORDS

Seismic Design Concept, Repair, Steel Pier, Octagonal Section, Earthquake Resistance Test

INTRODUCTION

Seismic reinforcements of highway and railroad bridges have been undertaken in Japan following the Southern Hyogo Prefecture ("Kobe") Earthquake. Especially for reinforced concrete single column type piers which have suffered shear fracturing, one solution is to clad the structure concerned with steel plates or carbon fibers. For steel piers, the inside can be filled with concrete. But almost all repairs or reinforcements of this kind are performed on structures, either in place or

under construction, which have not yet been subjected to an actual earthquake. Very few studies have been done on methods of retrofit for damaged structures, or on the strength and ductility capacity of such structures after retrofit. In this study, we adopt a basic concept of seismic design from a function and performance point of view, and describe the retrofitting of damaged steel bridge piers and a cyclic loading test performed on them.

REPAIR AND CYCLIC LOADING TEST OF THE OCTAGONAL SECTION STEEL BRIDGE PIER MODELS DAMAGED BY CYCLIC LOADING TEST

In octagonal section steel bridge piers, local buckling is unlikely to occur, and there is a gain in strength thanks to the small width thickness ratio, if the thickness of the plate and the cross sectional area is the same. The seismic resistance performance of octagonal section steel bridge piers therefore lies between that of rectangular and that of cylindrical sections. Cylindrical sections have advantages such as high material strength as a result of bending in the production process, and are resistant to local buckling as a shell effect. But they are prone to suffer “Elephant foot bulge” in case of large width thickness ratios, and, once local buckling has occurred, satisfactory strength cannot be expected of them. In addition, repairs are difficult to perform following an earthquake.

An octagonal section also gives attractive plays of light and shade on the surface of a bridge pier. The optical effect creates an impression of slender elegance. In Italy and elsewhere, reinforced concrete piers of this shape are used on valley crossings to provide a very pleasing appearance. In Japan, too, it would be possible to combine visual attractiveness with a good seismic resistance if an octagonal section pier shape were selected for the planning of future highway bridges.

This study describes the performance and results of seismic resistance tests undertaken to clarify the seismic resistance and strength of octagonal section steel bridge pier models after retrofitting subsequent to earthquake damage.

Planning of tests

In general, steel bridge piers are built up from many sections transported separately from the factory and welded or bolted together at the construction site. To simulate this construction procedure, the test specimens are prepared as follows. First, a pair of half-octagonal sections are made by bending plates of 100R steel. The two halves are then joined using high-tension bolts. The outside width of the section is 900mm, and the height of specimens from the bottom to the loading point is 3500mm. Three stiffeners are set at each side of the octagonal section, and diaphragms are fitted every 450mm from bottom to top. All the specimens are of SS400, of 6mm thickness. The dimensions and shapes of the various parts are shown in Figure 1 and Table 1.

The testing purpose is to clarify the seismic resistance capacity of damaged piers after retrofitting. In previous tests by the same authors, cyclic loads were applied at the top of brand new specimen

columns. In this second test series, cyclic loads were applied in a similar way at the top of damaged specimens. The load was sequentially raised by displacement increments of $1\delta y$ from $1\delta y$ to $7\delta y$, and testing was performed three times at each displacement. We call this procedure “3-cycle testing.”

In the previous tests, testing ended at 6 or $7\delta y$ with either a sharp decrease in strength or the propagation of cracking to approximately half the cross section at the lower end of the column. Photo 1 shows cracking in specimen Type-2. In the present test series, damaged specimens were retrofitted externally through the welding on of stiffened plates, and then subjected to lateral loading at the top of the column, as before.

Testing procedure

Retrofitting

The method of retrofitting was very simple. The convexly buckled areas on the lower parts of the columns were flattened by hammering from the outside after heating. Then, as shown in figure 1, stiffened rib plates of 6mm SS400 steel were welded on to the flattened flange sides and corners. Finally, the edges of these stiffened plates were welded to the flange plates and base plate.

Loading

The loading sequence was the same as for the previous 3-cycle test series; that is to say, a lateral load only was applied at the top of the columns, without any application of an axial load. The yield displacement increment δy was obtained from the specimens before retrofitting, and an increase of $1\delta y$ was applied at each cycle.

Measurement of displacement and strain

Strain was measured by strain gauges set on the stiffened plates. And at the tops of the columns 5 dial gauges were set in the longitudinal direction to measure lateral displacement, and another 4 were set on the base plate to measure rotation.

Test results

Hysteresis curve relation between lateral load and lateral displacement

Relationships between lateral load and lateral displacement, obtained from the cyclic loading tests, are shown in Figures 2 and 3. Figures 2(a) and 3(a) give the results of the previous test series (before retrofit), while Figures 2(b) and 3(b) give the results of the present tests (after retrofit). Both vertical and horizontal axes are normalized by lateral yield strength $H_y (=42.1\text{tf})$ and yield displacement $\delta y (=19.36\text{mm})$, corresponding to H_y . Figure 4 shows the envelope curves of these

tests.

As seen in Figures 2(a), 3(b) and 4, the lateral load – lateral displacement relationships after retrofit are almost the same as those before. However, the deformation capacity decreases from around 6 or 7 δy before retrofit to around 5 or 6 δy after. The maximum load shows an increase of 30% (specimen Type-1) or 16% (specimen Type-2) after retrofit, as compared with before. Photo 2 illustrates the local buckling state found in a specimen Type-1. Binding first began to occur in the outside ribs at loading cycle 3 δy , and by 4 δy local buckling could be observed at between 5 and 25 cm above the retrofit portion in both specimen Type-1 and specimen Type-2. In specimen Type-2, cracking also occurred in the welded connection between the base plate and the stiffened plate.

The maximum load for the specimen Type-1 was about 15% lower than for the specimen Type-2. The reason for this is because of the large crack that occurred in the end plate at the last cycle of loading in specimen Type-2, as a result of which whole load had to be supported by the stiffened plate only. In contrast, specimen Type-1 suffered little damage as the whole load was supported by both the original and the stiffened plates. In actual structures fracturing occurs in a wide variety of forms, so that in practice it is better to achieve small strength increases by retrofitting while simultaneously redistributing the load, for example by cutting away fractured parts.

The likelihood of a structure being subjected twice in its service life to massive earthquakes of the kind which generally hit the same district only once in a millenium is extremely low. Nonetheless, it is wise to obtain small increases in strength through retrofitting in order to guard against damage to substructures such as the main piles in the event of a second quake. Another possible retrofit method might be to eliminate the ribs and use thicker plates, thus combining a small strength increase with higher ductility.

Energy absorption capacity

The areas of the hysteresis loops for the horizontal load —horizontal displacement relations at each cycle in Figures 2 and 3 correspond to energy absorption. Figure 5 shows the relation between cumulative absorbed energy and the displacement at each loading cycle up to failure displacement, the vertical axis being normalized by $H\delta y$. The cumulative absorbed energy up to 6 δy is larger after retrofit than before for both Specimen Type-1 and Specimen Type-2.

CONCLUSIONS

In the event of a severe earthquake such as in Southern Hyogo Prefecture (“Kobe”), urban highways play a vital part in rescue activities and in the free movement of emergency vehicles. Even where structures have been damaged, if the damage is small retrofitting can enable the structure to be used again very soon after the earthquake, thus reducing the overall loss sustained by the social systems. Accordingly, ease of retrofit and speed of reconstruction are factors that need to be considered within the general concept of safety assessment.

This study has shown examples of one retrofit method and its effect on seismic resistance capacity in the case of octagonal section steel bridge pier models subjected to cyclic loading. The method in question, the welding on of stiffened plates, while simple to carry out, results in seismic resistance capacities no worse than in original undamaged specimens. More tests of this kind are necessary in the future.

References

K.Hayashi, M.Nishizawa, T.Aoki, M.Yamada: SEISMIC RESISRANCE TEST OF STEEL OCTAGONAL SECTION PIER MODELS UNDER CYCLIC LOADING, Proceedings of JSCE Annual Meeting, No.51 Vol.1-B pp.566-577, 1996.

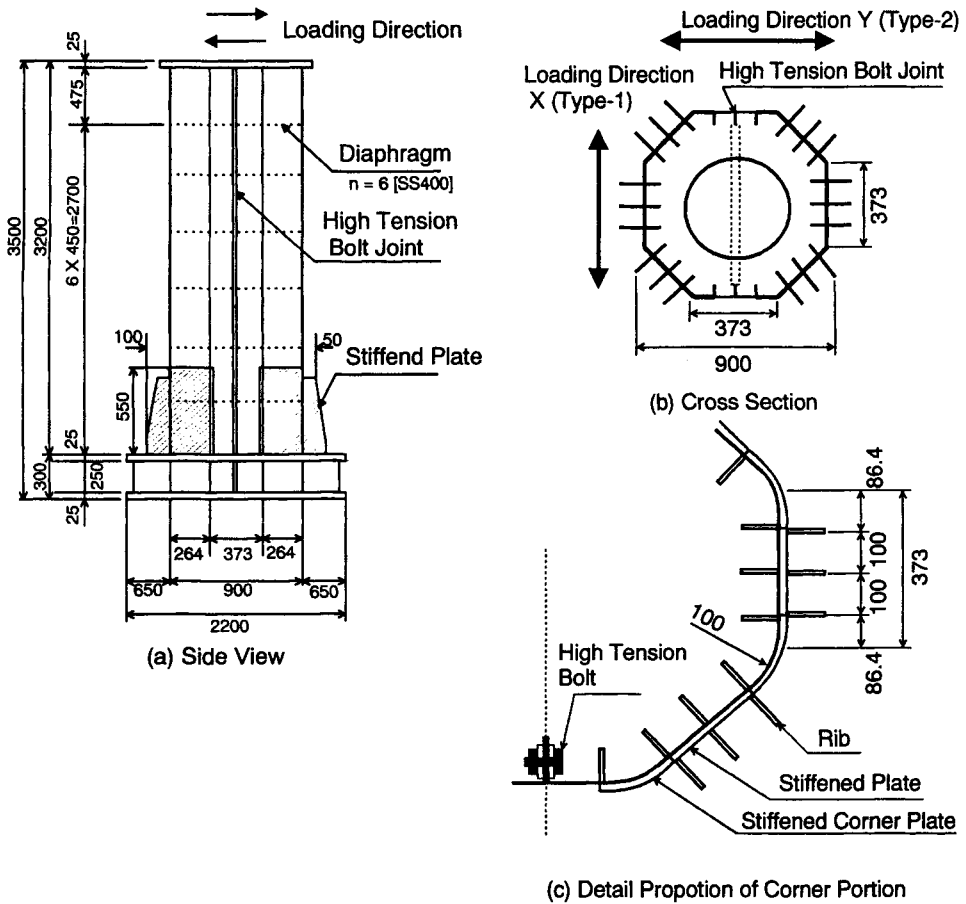


Figure 1 Dimensions of Specimen

Table 1 Specifications of Specimens

		Type-1	Type-2
Cross Sectional Area	A(cm ²)	272.6	
Moment of Inertia	I(cm ⁴)	274600	
Section Modulus	W(cm ³)	6136	
Yield Moment	My(tf·m)	147.3	
Yield Lateral Load	Hy(tf)	42.1	
Yield Lateral Displacement	δy(mm)	19.36	
Loading Direction		Direction X	Direction Y

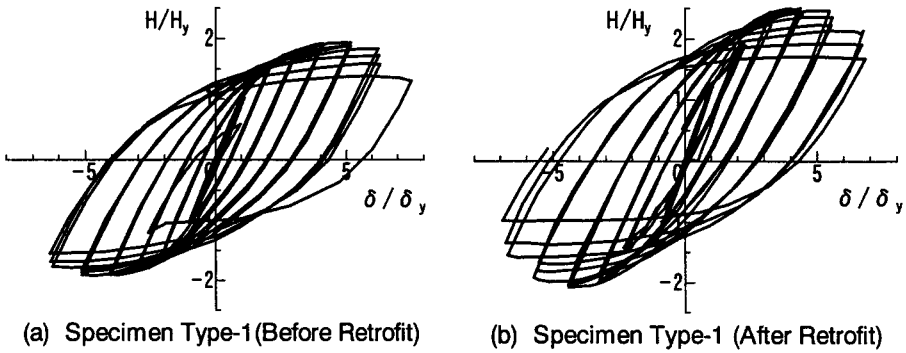


Figure 2 Horizontal load and Displacement Relationship of Specimen Type-1

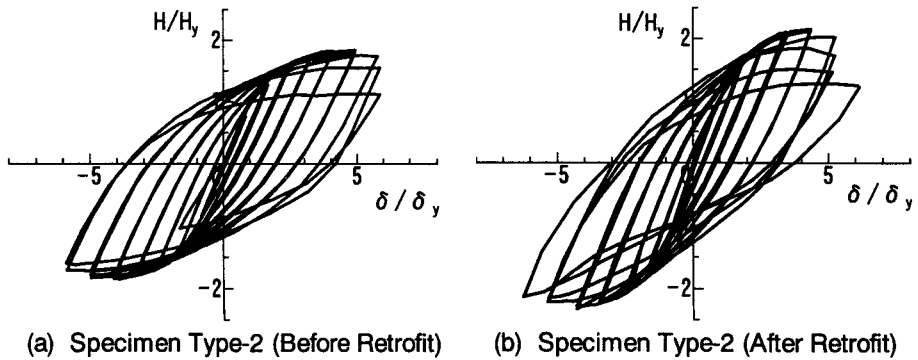


Figure 3 Horizontal load and Displacement Relationship of Specimen Type-2

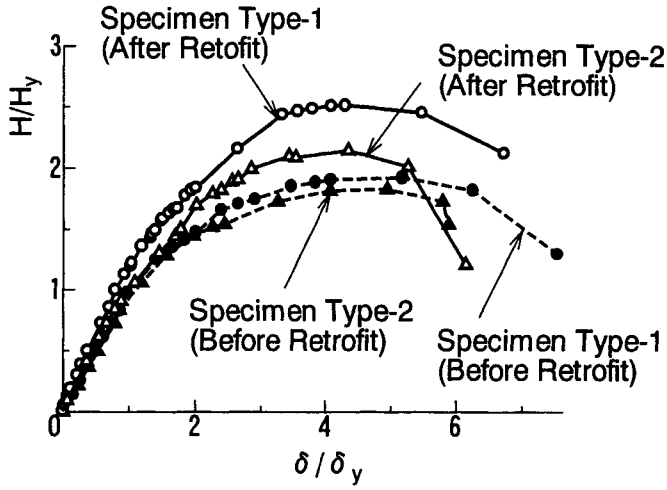


Figure 4 Envelope Curves

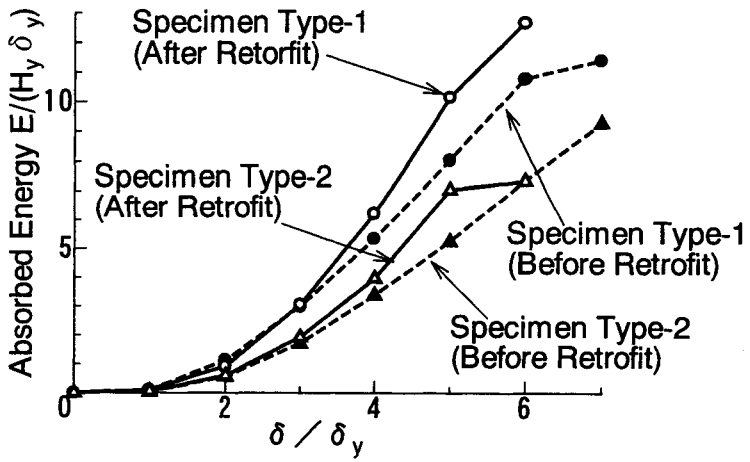


Figure 5 Energy Absorption Curves



**Photo 1 Local Buckling and Crack on the Base Plate Connection
(Specimen Type-2 Before Retrofit)**



**Photo 2 Local Buckling and Crack above the Retrofit Portion
(Specimen Type-1 After Retrofit)**

ELASTO-PLASTIC BEHAVIOR OF STEEL-PIPE PIER MODELS UNDER LATERAL CYCLIC LOADING

H. Koeda¹, S. Ono¹, N. Kishi² and Y. Goto³

¹ Research Laboratory, The Japan Steel Works, Ltd.,
Muroran, Chatsu, 051-8505 Japan

² Civil Engineering, Muroran Institute of Technology,
Muroran, Mizumoto, 050-8585 Japan

³ Civil Engineering, Nagoya Institute of Technology,
Nagoya, Showa, 466-8555 Japan

ABSTRACT

In order to investigate the effect of radius-thickness ratio and an axial force on the maximum lateral loading capacity and ductility of steel-pipe bridge piers, lateral cyclic loading tests under a compressive axial load for steel-pipe pier models are carried out. And also, in order to establish a rational analysis method for the pipe piers under lateral cyclic loading, numerical analyses by means of an elasto-plastic large displacement finite element method (FEM) following three types of constitutive rules are carried out and compared with the experimental results. These rules are isotropic hardening rule, kinematic hardening rule, and three-surface model. From this study, following results are obtained: 1) the effects of radius-thickness ratio and an axial load on the maximum lateral loading capacity are small; 2) ductility can be increased by decreasing radius-thickness ratio and the axial load; and 3) the local buckling mode developed near the basement of pier model can be more rationally estimated by the FEM analysis following three-surface model than the other two rules.

KEYWORDS

Steel-pipe piers, Cyclic loading, Local buckling, Ductility, Elasto-plastic analysis, Three-surface model

INTRODUCTION

In the great Hanshin-Awaji earthquake, occurred in January 1995, many highway bridges and steel bridge piers suffered damages. Those severe damages may be caused by combined action of the dead load of superstructure and laterally exciting due to earthquake. In order to improve the earthquake resistance of steel piers against such type of a great quake, experimental (for example, Nishikawa et al. 1996) and numerical studies (for example, Goto et al. 1998) on cyclic elasto-plastic behavior of steel piers have been conducted by many Japanese researchers.

In those studies, the piers with rectangular cross section are mainly studied. However, a study on the piers with circular cross section (hereafter, called as pipe piers) which possess a higher strength per weight than the rectangular section has probably drawn less attention. The pipe piers may be more economically used than the other cross section piers because of their better ductility and no stiffener requirement.

In these points of views, in this study, in order to investigate the effect of radius-thickness ratio and an axial compressive load on lateral loading capacity and ductility of pipe piers, lateral cyclic loading tests with a constant compressive axial load are performed by using pipe pier models. And also, in order to establish a rational analysis method for the pipe piers, numerical analysis by means of an elasto-plastic large displacement finite element method (FEM) is conducted. Here, an applicability of three constitutive rules (isotropic hardening rule, kinematic hardening rule and three-surface model) is discussed comparing with the experimental results.

EXPERIMENTAL OVERVIEW

Six pipe pier models used in this study are summarized in Table 1. In this table, notation for each pier model is represented by chaining pipe thickness and axial force parameter, in which tm means $m/10$ mm thick pipe and Nn means $n\%$ of the yielding axial force of pipe being axially loaded. Variables on the height from fixed point to lateral loading point, radius and thickness are taken as L , R and t , respectively. Four pier models taking various thickness under an axial compressive loading (t10, t15, t20, t25-N15) and two pier models taking different axial compressive loading with the same thick pipe (t15-N0, -N8) are prepared. The radius-thickness ratio R/t is ranged from 19.4 to 47.8 by varying pipe thickness. All pier

TABLE 1
DIMENSIONS AND PARAMETERS OF TEST SPECIMENS

Specimen	L (mm)	R (mm)	t (mm)	L/R	R/t
t10-N15	631.5	47.75	1.0	13.2	47.8
t15-N15		48.00	1.5		32.0
t20-N15		48.25	2.0		24.1
t25-N15		48.50	2.5		19.4
t15-N0		48.00	1.5		32.0
t15-N8		48.00	1.5		32.0

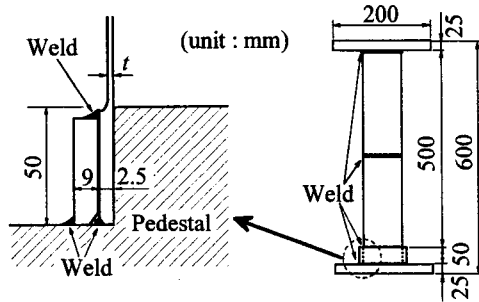


Figure 1: A steel-pipe pier model

TABLE 2
MECHANICAL PROPERTIES ON AXIAL DIRECTION OF STEEL PIPE

Yield stress σ_y (MPa)	Tensile stress σ_u (MPa)	Elongation (%)	Young's modulus E (GPa)
336	452	44.0	206

models are machined in prescribed dimensions using a carbon-steel seamless and hot-formed pressure pipe (JIS G3454 STPG370 90A) with 5.7 mm thickness. The nominal cutting error for prescribed thickness and radius is ± 0.05 mm.

General configuration and dimensions of a pier model are shown in Fig. 1. The model is made by welding two pipe pieces. In order to prevent the rigid body displacement as much as possible, the basement rigidity is increased by making the basement of model plugged into the 50 mm high pedestal and covered with 9 mm thick pipe, and furthermore, both the bottom edge of pier model and covered pipe are welded to pedestal, and the top edge of covered pipe is also welded to pier model.

Mechanical properties of the pier model are obtained by tensile testing according to JIS no.6 test specimens are listed in Table 2.

Figure 2 shows the experimental setup used in this study, in which two loading systems are applied as: 1) lateral cyclic loading under a 1.2 ton lead block set onto the top of pier model (Fig. 2a); and 2) lateral cyclic loading under axial compressive loading using hydraulic actuator (Fig. 2b). The former loading system is taken to really mock up the loading condition of superstructure of bridges. The lateral load is alternatively surcharged following the displacement control way which is loaded following the prescribed lateral displacement. Here, the displacement for each cycle is prescribed referred to δ_y as shown in Fig. 3, which is the lateral displacement when the fiber stress of the bottom of pier model reaches a yielding point, and is estimated using a simple equation:

$$\delta_y = \frac{H_y L^3}{3EI} \tag{1}$$

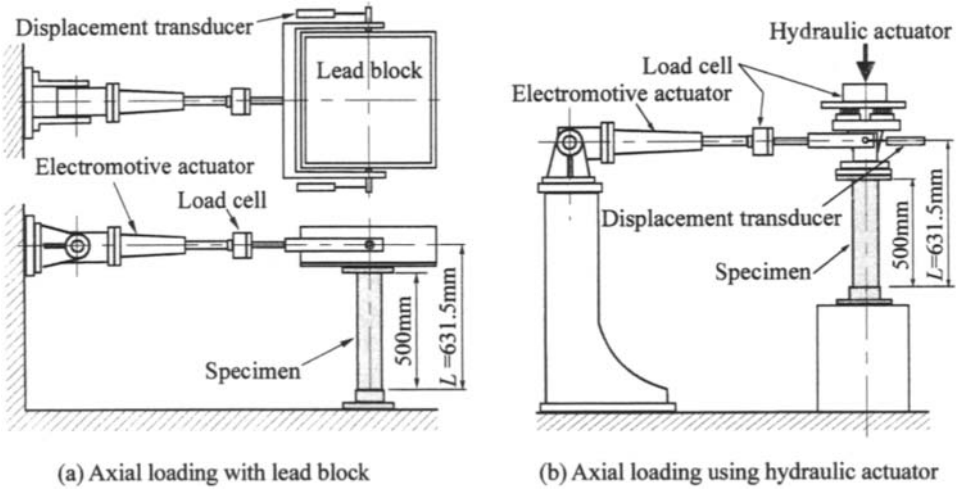


Figure 2: General view of experimental setup

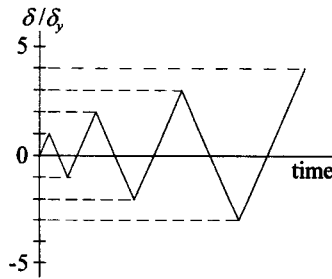


Figure 3: Cyclic loading method

The H_y is the lateral load when $\delta = \delta_y$ and is represented as:

$$H_y = \frac{(\sigma_y - P/A)I}{RL} \tag{2}$$

where, δ_y : yielding stress ; P : axial compressive load;
 A : cross section area; I : moment inertia of cross section.

The lateral load H is the force corresponding to the prescribed lateral displacement δ and increases to the maximum value ($H=H_m$) which is greater than H_y , and then gradually decreases. The load is continuously and alternatively surcharged by using an electromotive actuator with 0.4 mm/s loading speed until the H goes down to the H_y .

EXPERIMENTAL RESULTS AND DISCUSSIONS

In all pipe pier models considered here, two types of the local buckling mode are developed around near the basement corresponding to the radius-thickness ratio R/t as shown in Photo 1, which are: 1) an elephant foot bulge buckling mode for the models with $R/t \leq 32$ ($t \geq 1.5$ mm); and 2) a diamond shaped buckling mode for the model with $R/t = 47.8$ ($t = 1$ mm). The elephant foot bulge buckling mode is developed at the almost same height from the bottom among three pier models and then the height may not be affected by the parameter R/t .

The measured lateral displacement δ may include not only a real lateral displacement due to the model stiffness but a displacement due to rigid body rotation. However, it may be difficult to perfectly remove the rigid body component from δ . Here, the experimental lateral displacement is evaluated by normalizing the measured displacement δ referred to the experimentally obtained lateral displacement δ_{yE} corresponding to the lateral load H_y . The experimental results for the maximum lateral loading capacity H_m , the normalized value H_m/H_y , the displacement δ_u corresponding to the H_y , and a ductility ratio $\mu = \delta_u/\delta_{yE}$ are summarized in Table 3. From this table, it is seen that the pier model with radius-thickness ratio $R/t = 19.4$ ($t = 2.5$ mm) has the biggest lateral loading capacity and ductility among four pier models with the R/t varied. Comparing the results among three pier models with the axial load varied (t15-N0, -N8, -N15), the maximum lateral load H_m is seen not to be much affected by the axial load but the ductility may be decreased with the increasing axial load.

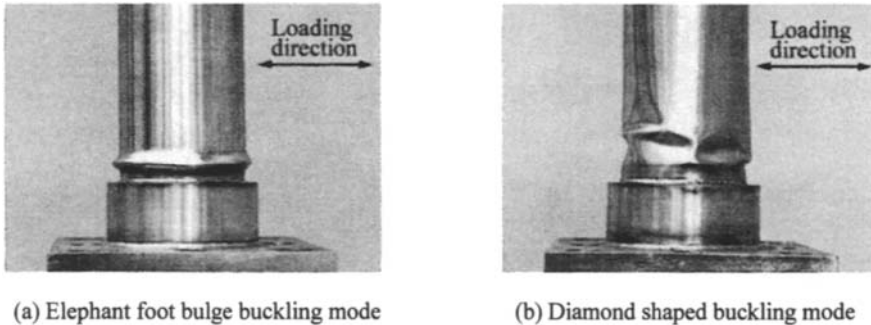


Photo 1: Local buckling modes

TABLE 3
MAXIMUM LOADING CAPACITY AND DUCTILITY

Specimen	R/t	δ_{yE} (mm)	H_m (kN)	H_m/H_y	δ_u (mm)	$\mu = \delta_u/\delta_{yE}$
t10-N15	47.8	4.69	4.97	1.55	14.48	3.09
t15-N15	32.0	4.67	7.26	1.50	17.69	3.79
t20-N15	24.1	4.95	9.36	1.44	23.07	4.66
t25-N15	19.4	4.97	12.06	1.48	26.81	5.40
t15-N0	32.0	5.40	7.61	1.34	23.31	4.31
t15-N8	32.0	4.99	7.18	1.37	19.93	4.00

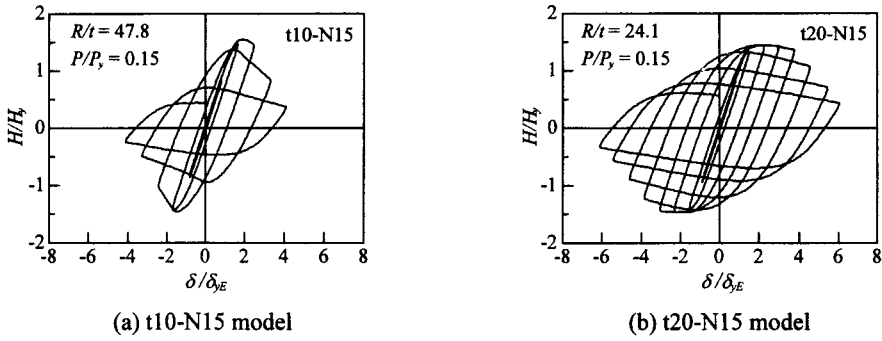


Figure 4: Relationships between non-dimensional lateral load H/H_y , and lateral displacement δ/δ_{yE}

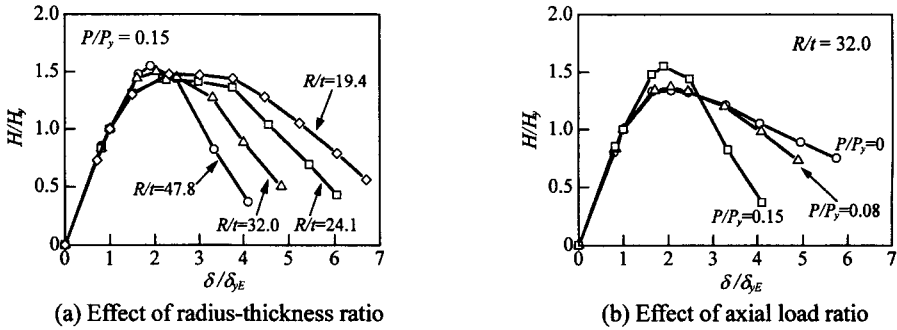


Figure 5: Envelopes of hysteresis loop

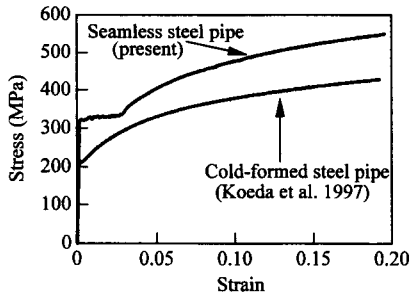


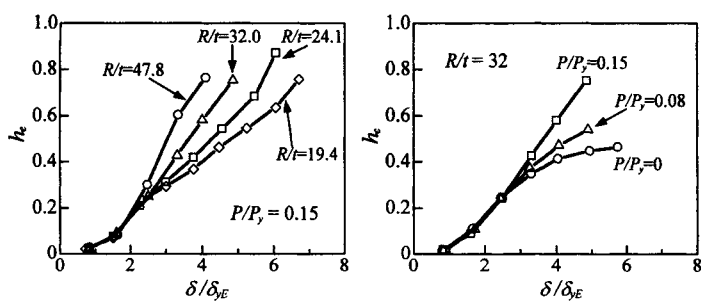
Figure 6: Comparison of stress-strain relations between seamless and cold-formed steel pipes

Figure 4 shows two hysteresis loop examples obtained from the experiments for t10-N15 and t20-N15 models, taking δ/δ_{yE} and H/H_y as abscissa and ordinate, respectively. The envelopes of hysteresis loops with respect to two parameters are drawn in Fig. 5, which are: 1) the case under a constant axial loading $P/P_y = 0.15$; and 2) the case for the pier models with a radius-thickness ratio $R/t = 32$. From these envelope curves, it is confirmed that: 1) a radius-thickness ratio R/t and an axial load ratio P/P_y do not much affect the maximum lateral loading capacity ratio H_m/H_y , and 2) the greater the R/t and P/P_y , the smaller the ductility ratio is. It was reported that the H_m/H_y of pier models machined using a cold-formed steel pipe increases with the decreasing R/t (Koeda et al. 1997). The contradiction of the present study may be

caused from the material properties of the pipe. Because their stress-strain relationships are different each other as shown in Fig. 6. That is to say, the relationship for a cold-formed steel-pipe shows no yield plateau and a prominent strain hardening characteristic.

Figure 7 shows the distribution of an equivalent damping coefficient h_e corresponding to non-dimensional lateral displacement δ/δ_{yE} , in which Figs 7a and 7b are the results for cases of radius-thickness ratio varying with an axial compressive load $P/P_y = 0.15$ and axial load varying for $R/t = 32$ pier model, respectively. From these results, it is seen that, 1) when $\delta/\delta_{yE} = 2$, the h_e is obtained as about 0.2 for all pier models considered here; 2) when $\delta/\delta_{yE} \geq 2$ in Fig. 7a, the bigger the R/t , the bigger the h_e is; and 3) when $\delta/\delta_{yE} < 3$ in Fig. 7b, the h_e is not much affected by the P/P_y ; however, $\delta/\delta_{yE} \geq 3$, the h_e has a tendency to increase with the increment of P/P_y .

Elasto-plastic large displacement FEM analysis for lateral cyclic loading test is conducted by using ABAQUS code (1996). In this study, an applicability of three constitutive rules on the tested pier models is considered, which are isotropic hardening rule, kinematic hardening rule, and three-surface model proposed by Goto et al. (1998). Figure 8 shows the general view of the analysis model for a tested pier model (t15-N8), in which a thick shell element (S4R) is mainly used to analyze.



(a) Effect of radius-thickness ratio (b) Effect of axial load ratio

Figure 7: Relationships between equivalent damping coefficient h_e and lateral displacement δ/δ_{yE}

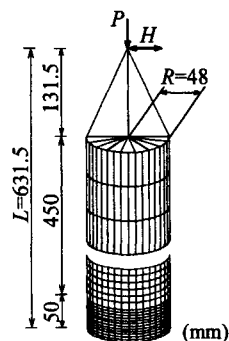
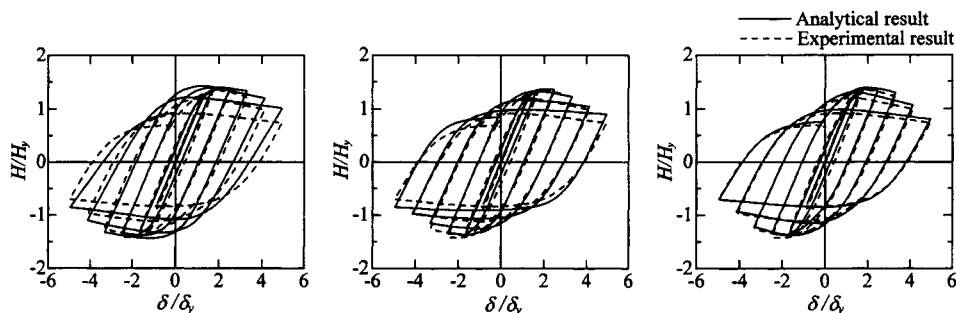


Figure 8: Analysis model



(a) Isotropic hardening rule (b) kinematic hardening rule (c) three-surface model

Figure 9: Comparison of hysteresis loops between numerical and experimental results

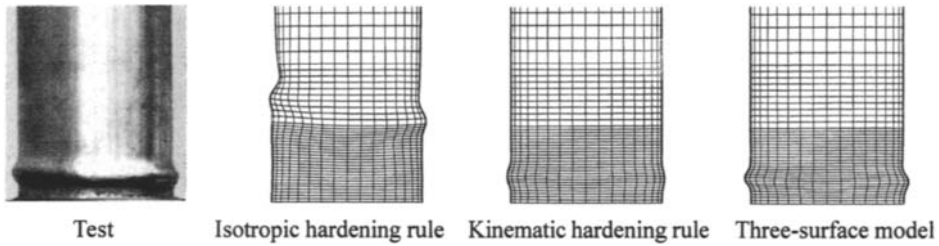


Figure 10: Buckling deformation on cyclic loading test and FEM analysis (t15-N8 model)

Figure 9 shows the hysteresis loop obtained followed each constitutive rule are drawn comparing with the experimental result. From this result, it is seen that, 1) the analysis followed an isotropic hardening rule can not estimate both the maximum lateral loading capacity H_m/H_y , and the hysteresis loop with good accuracy comparing with the experimental ones; 2) on the other hand, following kinematic hardening rule and/or three-surface model, the H_m/H_y can be estimated very well; and 3) three-surface model can give the best results on the H_m/H_y , and the loop among three constitutive rules considered here.

Figure 10 shows a comparison of general configuration of the buckling mode after loading between analytical and experimental results for t15-N8 pier model. From this figure, it can be confirmed that the elasto-plastic behavior of pipe piers under lateral cyclic loading can be predicted very well by using FEM analysis following three-surface model.

CONCLUSIONS

The results obtained from this study are as follows:

- 1) two types of local buckling mode: elephant foot bulge mode and diamond shaped buckling mode, are developed around near the basement corresponding to the radius-thickness ratio;
- 2) the effects of radius-thickness ratio and an axial load on the maximum lateral loading capacity are small; and ductility is increased by both radius-thickness ratio and the axial load decreasing, and that time, an equivalent damping coefficient becomes a big; and
- 3) three-surface model gives better results for elasto-plastic behavior of pipe piers than isotropic hardening rule and kinematic hardening rule.

REFERENCES

- ABAQUS/Standard User's Manual (1996). Hibbitt, Karlsson & Sorensen, Inc., Version 5.6, Vol. I-III.
- Goto Y., Wang Q., Takahashi N. and Obata M. (1998). Three surface Cyclic Plasticity Model for FEM Analysis of Steel Bridge Piers Subjected to Seismic Loading. *Journal of Structural Mechanics and Earthquake Engineering*, JSCE, **591**:I-43, 189-206 (in Japanese).
- Koeda H., Atsumi A., Sato M. and Kishi N. (1997). Cyclic Lateral Loading Tests and FEM Analysis of Steel Pipe Pier Models. *Proceedings of Nonlinear Numerical Analysis and Seismic Design of Steel Bridge Piers*, JSCE, 161-168 (in Japanese).

EXPERIMENTAL STUDY ON ELASTO-PLASTIC DYNAMIC BEHAVIOR OF STEEL-PIPE PIER MODELS

N. Kishi¹, H.Koeda², M.Komuro¹ and K.G.Matsuoka¹

¹ Department of Civil Engineering, Muroran Institute of Technology,
Muroran, 050-8585, Japan

² Muroran Research Laboratory, The Japan Steel Works, Ltd.
Muroran, 051-8505, Japan

ABSTRACT

In order to study dynamic behavior of steel-pipe pier models, shaking test is conducted in which a simple harmonic exciting method is applied. The dimensions of the steel-pipe pier models are diameter: 96 mm, height: 500 mm and thickness: 1.5 mm. A lead block with 1.2 ton mass is set on the top of pier model to mock up mass of the superstructure. In order to investigate the effects of filled concrete on strength and ductility of piers at earthquake, each three pier models with/without filled concrete are used. The results obtained from this study are as follows: 1) in case of no concrete filled pier models, increasing an amplitude of input acceleration, local buckling with elephant foot bulge mode is developed near the bottom on one side of shaking direction and the mode is grown up; finally, the model is totally collapsed; 2) in case of concrete filling pier models, the elephant foot bulge buckling mode is generated around near the bottom with increasing acceleration amplitude; then the cracks are developed in both sides of buckled area in shaking direction, but the models do not collapse and still vibrate with low amplitude against high acceleration input; and 3) it is seen that the ductility of steel-pipe piers can effectively be increased by filling concrete.

KEYWORDS

steel pier, pipe, dynamic behavior, elasto-plastic, shaking table, local buckling, elephant foot bulge buckling mode

INTRODUCTION

In the great Hanshin-Awaji earthquake, occurred in January 1995, more than five thousand lives were lost and many infrastructures suffered damages. In steel bridges, a few bridge piers

were totally collapsed. And many stiffened plates and pipes were locally buckled, were plastically deformed and were cracked. After the quake, it was recommended by Public Works Research Institute (PWRI) of Japan that steel bridge piers should be filled with concrete to increase the ductility against a great quake and their ductility check should be performed by numerical analysis considering both material and geometrical non-linear characteristics (JRA 1996). In order to establish a rational ductility design method for steel bridge piers, many experimental (for example, Nishikawa et al. 1996) and theoretical studies (for examples, Gao et al. 1998; Goto et al. 1998) on the dynamic and static problems have been conducted in Japan.

As an experimental research, performing horizontal monotonic and cyclic loading tests on big pier models, it has been tried to rationally evaluate their restoring capacity and ductility. And pseudo-dynamic tests were also conducted to investigate the dynamic behavior of real steel bridge piers under severe quakes (Usami and Kumar 1996).

In this study, in order to accumulate the fundamental data to establish a rational ductility design procedure of bridge pipe piers with circular cross section, shaking tests on small-sized pipe pier models between elastic and plastic regions are conducted. A shaking table is stationally excited with a constant acceleration amplitude and a constant frequency. Shaking test is iteratively conducted with stepped increment of acceleration amplitude until the pier model is collapsed and/or cracks are developed in the local buckling area near the basement of model. Finally, the effects of filled concrete on the strength and ductility of pier model are experimentally discussed.

EXPERIMENTAL OVERVIEW

Since the main objective of this study is to experimentally discuss the effects of the filled concrete on strength and ductility of steel-pipe pier model, height of filled concrete, input acceleration amplitude and frequency are taken as experimental variables. General configuration and dimensions of pier model are shown in Fig. 1 and listed in Table 1. In this Table, slenderness parameter $\bar{\lambda}$ and radius thickness parameter R_t are defined as:

$$\bar{\lambda} = \frac{2L'}{\pi r} \sqrt{\frac{\sigma_{ys}}{E}} \quad (1)$$

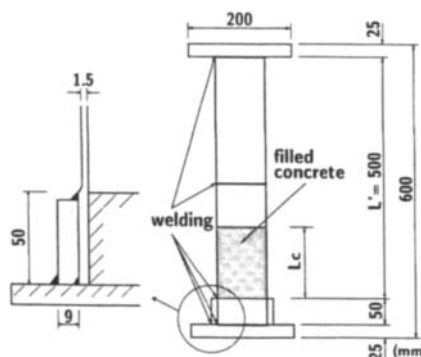


Figure 1: General information and dimensions of pier model

TABLE 1
DIMENSIONS OF SPECIMENS

Specimen	L (mm)	L' (mm)	Height of concrete		Radius R (mm)	Thickness t (mm)	$\bar{\lambda}$	R_t
			L_c (mm)	L_c/L'				
f0-d1 f0-d2 f0-d3	631.5	500.0	0	0.00	48.0	1.5	0.379	0.086
f1-d			125	0.25				
f2-d			285	0.57				
f4-d			500	1.00				

$$R_t = \frac{R}{t} \frac{\sigma_{ys}}{E} \sqrt{3(1-\nu^2)} \quad (2)$$

in which

- R : mean radius of pipe pier model; r : radius of gyration;
 L' : height of pier model; t : thickness;
 E : Young's modulus (= 206 GPa); ν : Poisson's ratio (= 0.3);
 σ_{ys} : yielding stress (= 336 MPa).

Using carbon-steel seamless pressure-pipe (JIS G3454 STPG370 90A) with 5.7 mm thickness, pier models are cut in the prescribed dimensions. In order to prevent the rigid body deformation as much as possible, the basement rigidity of pier model is increased by making that the basement of model is plugged into the 50 mm high pedestal and is covered with 9 mm thick pipe, and furthermore, both the bottom edge of pier model and covered pipe are welded to pedestal and the top of covered pipe is also welded to the model. A 1.2 ton lead block is set onto the top of pier model to mock up the weight of superstructure. The height of filled concrete L_c is taken as four cases of experiment as: $L_c/L' = 0.0, 0.25, 0.57$ and 1.0 and their cases are referred to as f0, f1, f2 and f4, respectively, as shown in Table 1.

Material properties of the pipe pier model used here obtained by tensile testing with JIS 6 test specimens are: yielding stress $\sigma_{ys} = 336$ MPa; nominal tensile strength $\sigma_u = 452$ MPa; Young's modulus $E = 206$ GPa; and Poisson's ratio $\nu = 0.3$. At commencement of experiment, material properties of filled concrete are: compressive strength $f'_c = 19.2$ MPa; Young's modulus $E_c = 16.7$ GPa; and Poisson's ratio $\nu_c = 0.21$.

Figure 2 shows the experimental setup of simplified shaking table used in this study. In this figure, the shaking table is set on two linear-way guides. Dynamic responses of pier model are measured by using three accelerometers mounted on shaking table and at the gravity center of lead block, and five laser-type displacement meters set at shaking table, pier model and lead block. All recorded in analog-type data-recorders are converted into digital ones and are processed into various type figures by using engineering work stations.

Here, two experimental methods are applied as: 1) an experiment for getting the fundamental natural frequency and its logarithmic decrement by letting the actuator suddenly shut down; and 2) an experiment for investigating elasto-plastic dynamic behaviors of the pipe

pier model by exciting with predetermined acceleration amplitude and frequency. Shaking table is excited with a simple harmonic vibration. However, since an actuator takes a few seconds to reach the stage of stationary excitation, the actuator is worked for 8 seconds and then is shut down for each experiment. Each pier model is iteratively excited with a 125 gal stepped increment until the pier model is collapsed and/or cracks is developed near the basement except the test for case of f0-d1. If the pier model is not collapsed and/or crack is not developed under excitement corresponding to the full power of actuator, the test is iteratively conducted with the same amplitude for the pier model to reach the ultimate condition mentioned above.

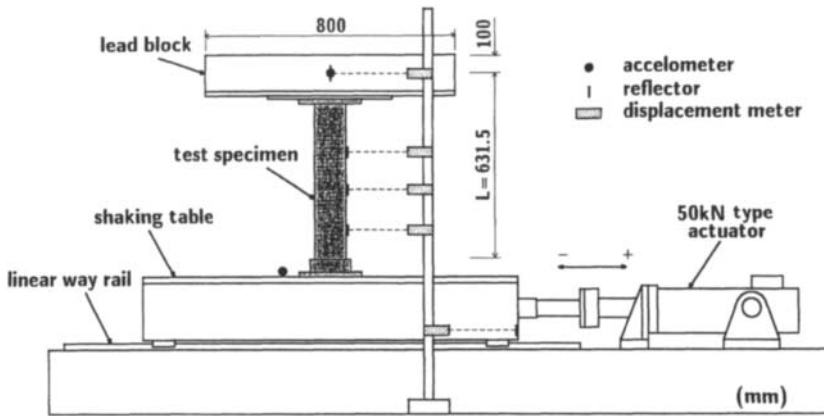


Figure 2: General view of experimental setup

EXPERIMENTAL RESULTS

Fundamental Natural Frequency Test

The fundamental natural frequency and logarithmic decrement obtained from the experiment are listed in Table 2. From this table, it is shown that the values for no concrete filled pier

TABLE 2
LIST OF TEST RESULTS

Specimen	Natural frequency (Hz)	Logarithmic decrement (%)	Input frequency (Hz)	Input acceleration (gal)	Failure mode
f0-d1	4.08	2.7	2.5	125,250,375	Residual strain at near basement
f0-d2	4.23	2.2	3.0	125,250,375	EFB is occurred near basement of actuator side
f0-d3	4.09	2.8	5.0	125,250,375,500,625,750	Pier model is collapsed toward actuator side
f1-d	4.38	4.7	3.0	125,250,375,375,375	EFB is occurred around near basement
f2-d	4.76	8.7		125,250,375,500,500	Cracks are developed along convex of EFB in both excited sides
f4-d	5.56	13.6		125,250,375,500,500	

EFB: Elephant Foot Bulge

model (f0-d) distributes in the area of 4.1 ~ 4.2 Hz and 2.2 ~ 2.7 %, respectively. When concrete is filled in pier model, both natural frequency and logarithm decrement have a tendency to increase. In case of the concrete fully filled pier model (f4-d), these values reach to 5.6 Hz and 14 %, respectively.

Dynamic Responses

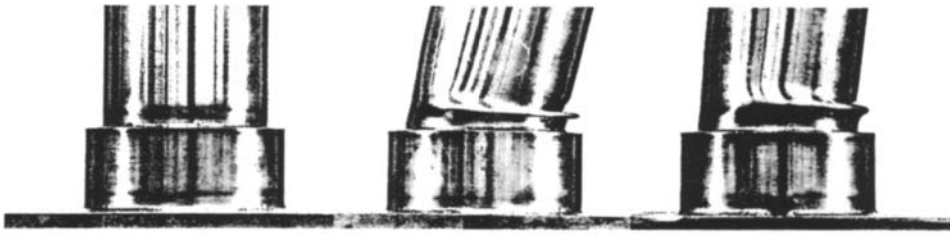
Figures 3 and 4 show the experimental results for general configuration of the local buckling and/or cracks being developed near the basement, and hysteresis loop with respect to displacement and acceleration at the center of lead block.

In the case of no concrete filled pier models (f0-d1, -d2, -d3), since the test for f0-d1 specimen with input frequency $f_i = 2.5$ Hz is terminated by the fiber stress of basement being reached to a yielding point, the hysteresis loop is not remarkably changed except the increment of acceleration amplitude. On the other hand, in case of f0-d2 ($f_i = 3$ Hz), the experiment is terminated at the input acceleration amplitude $\alpha_i = 375$ gal because the pier model is linearly collapsed from the basement by the local buckling being occurred in the actuator side near the basement and that area being crushed. The hysteresis loop in the case shows that the lead block is vibrating with the center gradually shifting in the same direction and the acceleration amplitude is decreasing irrespective of the model alternatively and stationally being excited.

The case of f0-d3 with $\alpha_i = 625$ gal and $f_i = 5$ Hz shows similar results to those in case of f0-d2 at $\alpha_i = 375$ gal. And the acceleration of a lead block does not increase corresponding to the input acceleration increasing from $\alpha_i = 375$ to 750 gal. This implies that plasticization and softening near the basement are progressed.

Figure 4 shows the results for the cases of concrete filled pier models (f1-d, f2-d and f4-d). All these cases are excited with the frequency $f_i = 3$ Hz. In each case, the restoring stiffness is changed as the shaking table being excited with $\alpha_i = 375, 500$ and 500 gal, respectively. At this time, the local buckling may be occurred near the basement. After that, the response acceleration and displacement of the pier models f1-d and f2-d are decreased despite the shaking table is excited with the same acceleration amplitude. From the photos in Fig. 4 taken after experiment, it is seen that an elephant foot bulge (EFB) type local buckling mode is formed around near the basement similarly to the results obtained from the static cyclic loading test and cracks are developed along the convex of local buckling mode in the both excited direction sides. The decreased responses after softening may imply that the energy input by being excited is absorbed by cracking and softening and is not transferred to the upper part of pier model. It can be said that the cracks may be working as a function of aseismatic base isolation system. Both pier models still do not collapse differing from the results for cases of f0-d1 and -d2.

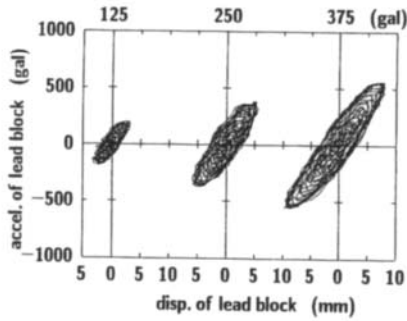
The results for case of f4-d shows that the softening are gradually progressed during first and second excitation at the $\alpha_i = 500$ gal. The cracks are also developed along the local buckling mode in both excited sides similarly to the results of cases f1 and f2. However, this model still has more absorption capacity comparing with the cases f1 and f2 because of the area of hysteresis loop for the model is bigger than those of two cases. Then, these results suggest that the earthquake resistance of concrete filled piers may be increased by increasing the height of filled concrete.



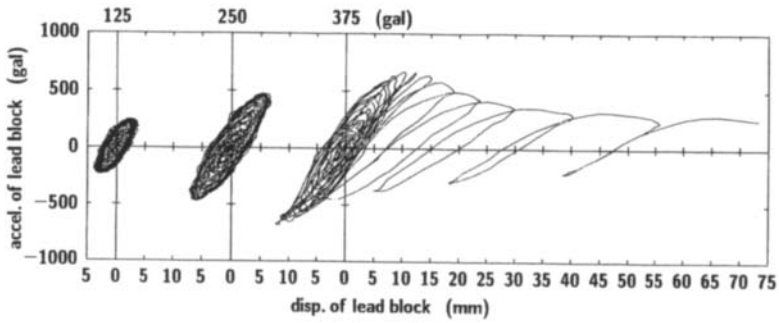
(a) f0-d1

(b) f0-d2

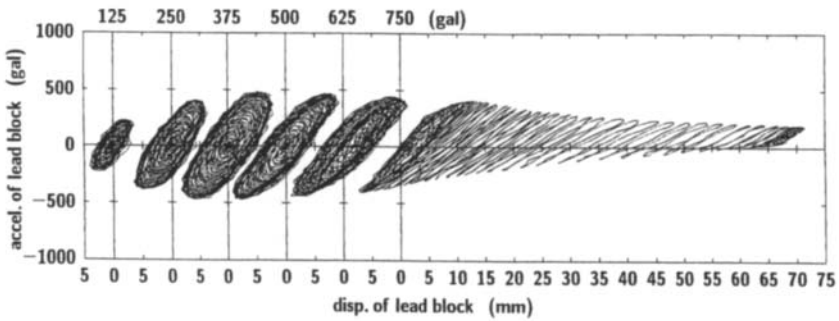
(c) f0-d3



(d) f0-d1, $f_i = 2.5$ Hz

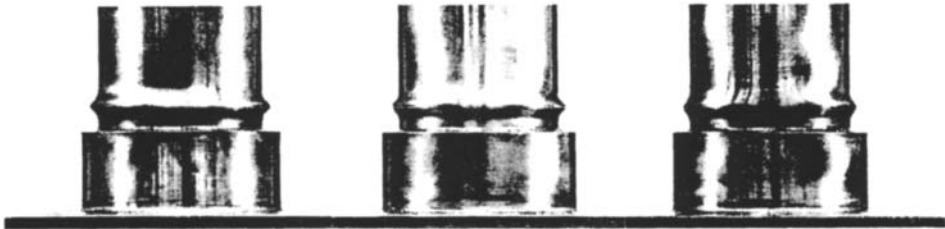


(e) f0-d2, $f_i = 3$ Hz



(f) f0-d3, $f_i = 5$ Hz

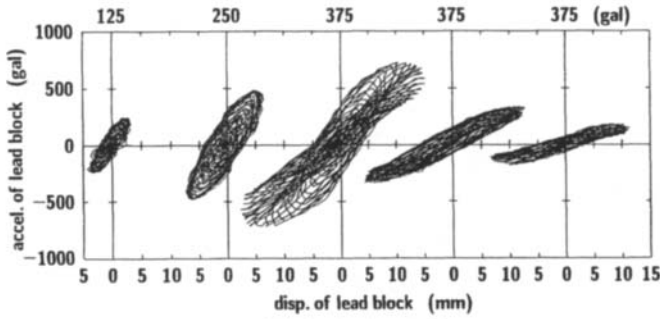
Figure 3: Local buckling at near basement and hysteresis loops (no filled concrete)



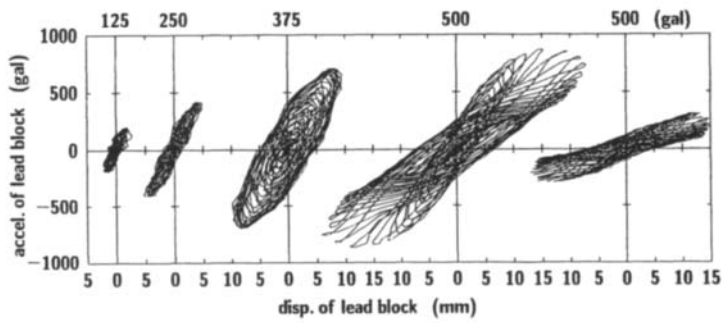
(a) f1-d

(b) f2-d

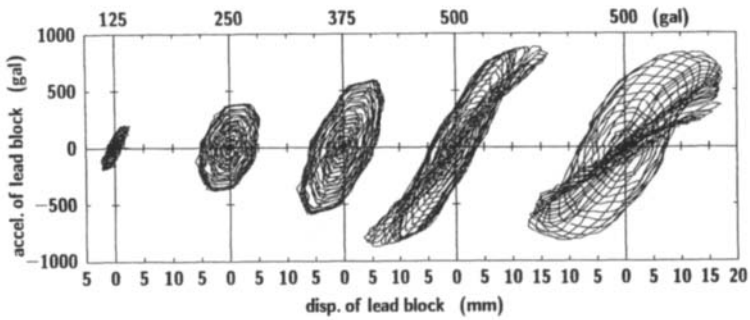
(c) f4-d



(d) f1-d, $f_i = 3$ Hz



(e) f2-d, $f_i = 3$ Hz



(f) f4-d, $f_i = 3$ Hz

Figure 4: Local buckling at near basement and hysteresis loops (filled concrete)

CONCLUSIONS

In order to accumulate the fundamental data on the elasto-plastic dynamic behavior of steel-pipe piers to establish a rational ductility design procedure of bridge pipe piers, a stationary shaking tests using small-sized steel-pipe pier models is performed. A lead block with 1.2 ton mass is set onto the top of model to mock up the weight of superstructure. In this paper, the effects of filled concrete on strength and ductility of piers are also investigated. The results obtained from this experiment are as follows:

- 1) when concrete is filled in piers, a fundamental natural frequency and its logarithmic decrement have a tendency to be high and to be big, respectively;
- 2) The pier models without filled concrete are collapsed with an elephant foot bulge (EFB) buckling mode being developed near the basement in one of the excited direction sides, and forming a big break angle near the basement;
- 3) The concrete filled pier models are not collapsed despite EFB type local buckling mode is formed and cracks are developed along the convex of the EFB buckling mode in both sides of the excited direction; and
- 4) It is seen that the ductility of steel-pipe piers can effectively be increased by filling concrete.

REFERENCE

- Usami T. and Kumar S. (1996). Damage Evaluation in Steel Box Columns by Pseudo-dynamic Tests. *Journal of Structural Engineering*, ASCE, **122:6**, 635-642.
- Gao S., Usami T. and Ge H. (1998). Ductility Evaluation of Steel Bridge Piers with Pipe Sections. *Journal of Engineering Mechanics*, ASCE, **124:3**, 260-267
- Goto Y., Wang Q., Takahashi N. and Obata M. (1998). Three Surface Cyclic Plasticity Model for FEM Analysis of Steel Bridge Piers Subjected to Seismic Loading. *Journal of Structural Mechanics and Earthquake Engineering*, JSCE, **591:I-43**, 189-206 (in Japanese).
- Japan Road Association (JRA). (1996). *Specifications for Highway Bridges—Part V: Seismic Design*. Maruzen, Tokyo, Japan.
- Nishikawa K., Murakoshi J., Josen Y. and Takahashi M. (1996). An Experimental Study on Seismic Retrofit of Steel Bridge Piers. *Proceedings of the 3rd U.S.—Japan Workshop on Seismic Retrofit of Bridges*, PWRI, Japan, 269-288.

ON PLASTICITY MODELS FOR ANALYSIS OF BRIDGE BOX PIER WITH ROUND CORNERS UNDER CYCLIC LOADING

E. Yamaguchi¹, Y. Goto², N. Kishi³, M. Komuro³ and K. Abe¹

¹Department of Civil Engineering, Kyushu Institute of Technology,
Kitakyushu 804, JAPAN

²Department of Civil Engineering, Nagoya Institute of Technology,
Nagoya 466, JAPAN

³Department of Civil Engineering, Muroran Institute of Technology,
Muroran 050, JAPAN

ABSTRACT

After the 1995 Hyogo-ken Nanbu Earthquake, much research was conducted in Japan to improve the seismic performance of bridge piers. The new seismic design specifications for highway bridges are now available. However, although the current specifications require nonlinear dynamic analysis for the seismic design of steel bridge piers, the mechanical behavior of many types of bridge pier under cyclic loading is yet to be well-understood. Therefore, the research is still actively performed. In the present study, we deal with a steel bridge box pier with round corners, which is often employed in a densely populated district from an aesthetic viewpoint. Nonlinear finite element analysis, using shell and beam elements, is carried out. Particular attention is paid to plasticity models: the three-surface model as well as conventional plasticity models are employed. In comparison with experimental data, the study reveals the superiority of the three-surface model for analyzing this type of bridge pier.

KEYWORDS

steel bridge pier; cyclic loading; box section with round corners; plasticity model; three-surface model; finite element analysis; hysteresis loop; local buckling.

INTRODUCTION

Extensive damage of steel bridge piers was observed in the aftermath of the 1995 Hyogo-ken Nanbu Earthquake, Japan. Since then, much research effort has been made to improve behaviors of steel bridge piers during a severe earthquake (Kensetsu 1996). Since the damage was found attributable to cyclic horizontal load due to the earthquake coupled with the weight of a superstructure, many specimens of steel bridge piers have been tested under such loading condition.

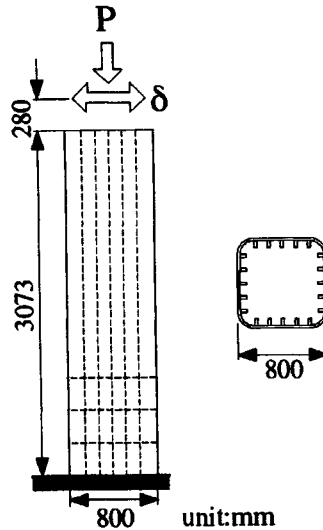


Figure 1: Steel bridge pier specimen

From an aesthetic point of view, steel bridge box piers with round corners are often employed in a densely populated district in Japan. The structural characteristics of a box beam-column with round corners have been investigated in the past (Watanabe et al. 1992). However, the performance of this type of bridge pier under cyclic loading does not seem to be known adequately, although such a knowledge is essential to perform nonlinear dynamic analysis required for the seismic design of steel bridge piers (Japan 1996).

The experimental data are undoubtedly valuable. Nevertheless, it is not practical to conduct many tests since experiments are costly: the number of experiments is inevitably limited, which implies that we cannot depend solely on experiment for seismic design. Therefore, the numerical simulation of steel bridge piers by the finite element method has been also explored so as to make the best use of limited experimental data (Structural 1997). However, such numerical study of a steel bridge pier has been so far confined to a circular section and a box section.

Against the background of the above information, in the present study we carry out the numerical analysis of a bridge box pier with round corners subjected to constant vertical load and cyclic horizontal load. The study employs the finite element method with shell and beam elements, and takes into account the effects of large deformation and material nonlinearity. Particular attention is paid to plasticity models. The results thus obtained are compared with experimental data (Yoshizaki et al. 1997), and the effectiveness of the numerical approach is discussed.

EXPERIMENT

We briefly describe the experiment of a bridge box pier with round corners (Yoshizaki et al. 1997), the results of which will be referred to later. Figure 1 illustrates the experimental specimen. This is basically a cantilever which is fixed at the bottom and free at the top. The corners of the cross section are rounded with a radius of 142 mm. The plate thicknesses of a flange and a web are both 7 mm,

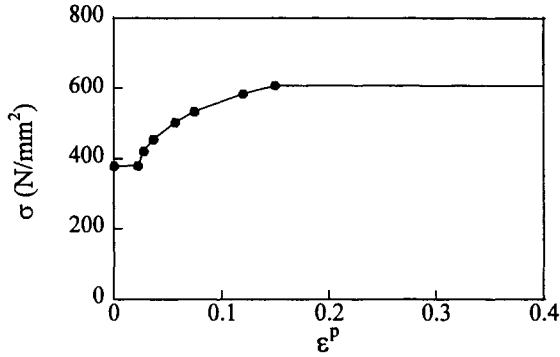


Figure 2: Uniaxial stress-strain relationship

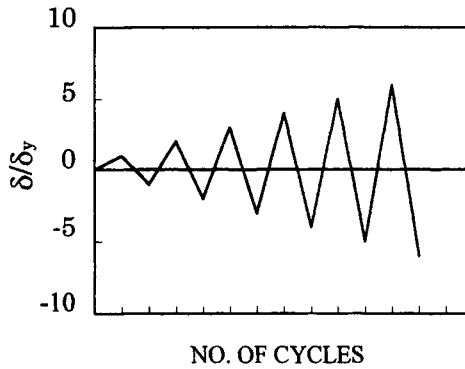


Figure 3: Predetermined displacement path

and the thickness of a stiffener is 8 mm. The uniaxial material test was performed separately: the stress-strain relationship in terms of true stress σ and logarithmic plastic strain ϵ^p is shown in Fig. 2.

The axial compressive force P is 15% of the nominal squash load of the cross section P_y , and the horizontal load H is applied to trace the predetermined path of the horizontal displacement δ at the loading point (Fig. 3). δ_y is the displacement at the initial yielding due to the horizontal force and given by

$$\delta_y = \frac{H_y(h_1 + h_2)^3}{3EI} \tag{1}$$

where h_1 = specimen height (3173 mm); h_2 = distance between the top of the specimen and the loading point (250 mm); and EI = bending rigidity, while H_y is defined by

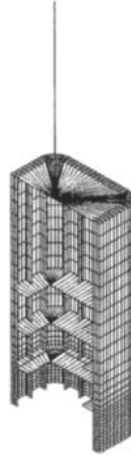


Figure 4: Finite element mesh

$$H_y = \left(\sigma_y - \frac{P}{A} \right) \frac{Z}{h_1 + h_2} \quad (2)$$

where σ_y = nominal yield stress; A = cross-sectional area; and Z = section modulus.

MODELING FOR ANALYSIS

Due to symmetry, only a half of the structure is analyzed. The finite element mesh is given in Fig. 4: 2966 shell elements and 33 beam elements are utilized. The lower portion of the pier specimen where local buckling is to take place is modeled with finer mesh.

The material behavior is assumed to be described by the plasticity theory of von Mises type. We consider three plasticity models in this study: the isotropic-hardening model, the kinematic-hardening model and the three-surface model. They are different from each other in terms of a hardening rule. Except the third model, the plasticity models employed herein are nothing but conventional and the explanation is available in many books (e.g. Chen 1994).

The three-surface model has been proposed by Goto et al. (1998). The model is an extension of the two-surface model (Dafalias and Popov 1976) and embodies the nonlinear features of structural steel such as the yield plateau and the reduction of elastic region. It consists of the bounding surface, the yield surface and the discontinuous surface. The yield surface changes its size as it moves within the region defined by the bounding surface. The discontinuous surface lies between the bounding and yield surfaces, controlling the hardening modulus. Multi-surface plasticity models usually require many material parameters. The three-surface model is not an exception. However, by performing various structural analyses and comparing the numerical results with experimental data, the values of some material parameters have been fixed, so that in practice all the material parameters can be determined only by the result of a uniaxial material test. In the present study, the parameters are obtained by the experimental data shown in Fig. 2

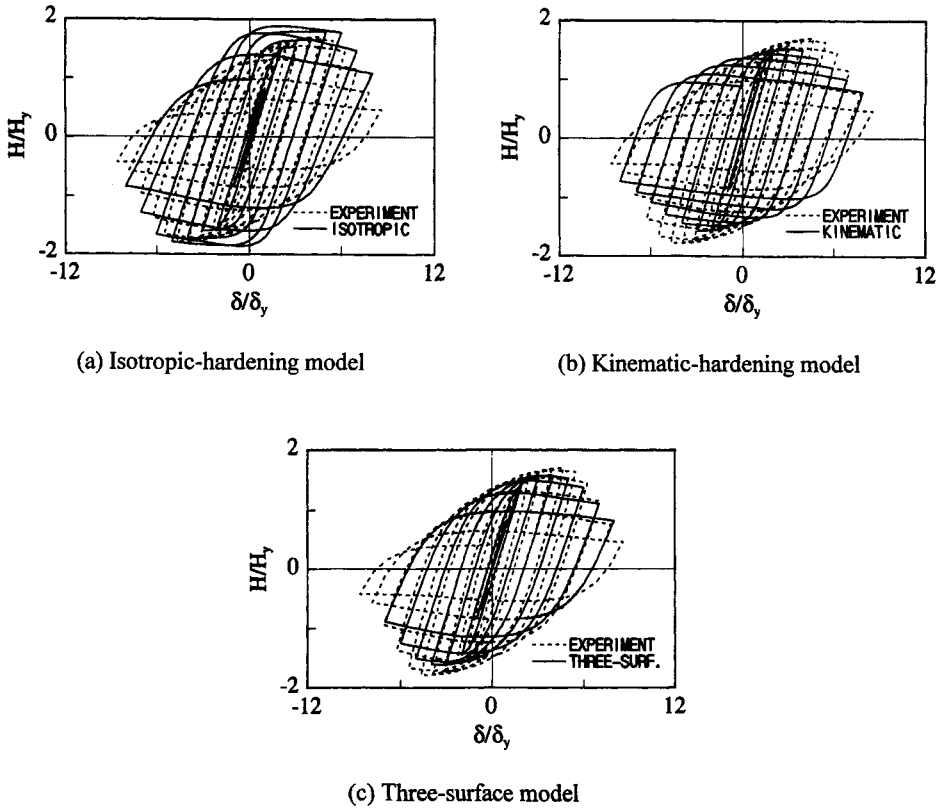


Figure 5: Horizontal load-displacement curves

NUMERICAL RESULTS

The numerical results in the form of hysteresis loop of the load-displacement relationship at the loading point are presented together with the experimental data in Fig. 5. The figure suggests that the isotropic-hardening model yields a hysteresis loop and a point of the ultimate strength quite different from those of the experiment. The kinematic-hardening model produces a better result. However, the effect of the constant elastic region is clearly observed, overestimating the structural stiffness in the reversed loading paths. By the three-surface model, we obtain the best hysteresis loops: the shape of each loop is very similar to that of the experiment and the discrepancy of the ultimate strength is only about 7% whereas the kinematic-hardening model underestimates the strength by 11%.

In the numerical simulation with the three-surface model, local buckling starts taking place when the displacement at the loading point reaches around $+4\delta_y$. The out-of-plane deformation spread across the stiffened plates of the lower portion of the specimen at around $+7\delta_y$. These deformation states coincide with the experimental observations well. Figure 6 shows the deformed configuration of the specimen at the end of the computation ($+8\delta_y$).

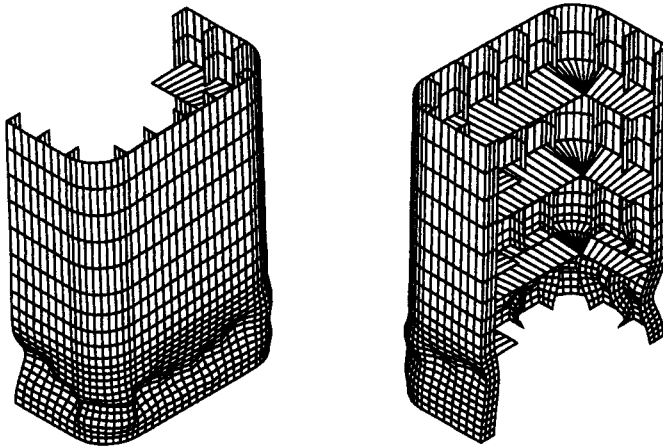


Figure 6: Deformed configuration ($\delta / \delta_y = +8$)

CONCLUDING REMARKS

Using the three plasticity models, we have conducted the finite element analysis of a bridge box pier with round corners under cyclic horizontal load. Different plasticity models yielded very different structural responses, confirming the importance of the constitutive model. The numerical results have clearly showed the superiority of the three-surface model over the other two conventional plasticity models for analyzing this bridge pier: the hysteresis loops of the load-displacement relationship at the loading point are very close to those of the experiment and the discrepancy of the ultimate strength from the experimental value is merely 7%. Therefore, we may conclude that the finite element analysis with the three-surface model can take the place of experiment to some extent for evaluating the structural behavior of a bridge box pier with round corners under seismic loading.

REFERENCES

- Chen, W.F. (1994). *Constitutive Equations for Engineering Materials*, Vol.2, Elsevier, Amsterdam, Netherlands.
- Dafalias, Y.E. and Popov, E.P. (1976). Plastic Internal Variables Formalism of Cyclic Plasticity. *J. Applied Mechanics*, **43**, 645-651.
- Goto, Y, Wang, Q., Takahashi, N. and Obata, M. (1998). Three Surface Cyclic Plasticity Model for FEM Analysis of Steel Bridge Piers Subjected to Seismic Loading. *J. Structural Mechanics and Earthquake Engineering*, JSCE, **591/I-43**, 189-206.
- Japan Road Association (1996). *Design Specifications of Highway Bridges: Part V Seismic Design*, Maruzen, Tokyo, Japan.
- Kensetsu Tosho (1996). *Bridge and Foundation Engineering*, **30:8**, Tokyo, Japan.
- Structural Engineering Committee (1997). *Proceedings of Nonlinear Numerical Analysis and Seismic Design of Steel Bridge Piers*, JSCE, Tokyo, Japan.
- Watanabe, E., Sugiura, K., Mori, T. and Suzuki, I. (1992). Strength and Ductility of Short Stiffened Box Beam-Column with Round Corners. *J. Structural Engineering*, JSCE, **38A**, 143-154.
- Yoshizaki, N., Murayama, T., Yasunami, H., Natori, T. and Tsuji, H. (1997). An Experimental Study on the Cyclic Elasto-plastic Behavior of Steel Box Column with Round Corners. *Proceedings of Nonlinear Numerical Analysis and Seismic Design of Steel Bridge Piers*, JSCE, 339-346.

ELASTO-PLASTIC INSTABILITY OF STEEL COMPRESSION TUBULAR MEMBERS SUBJECTED TO CYCLICALLY APPLIED BI-DIRECTIONAL HORIZONTAL LOADS

Eiichi Watanabe¹, Kunitomo Sugiura², Walter O. Oyawa¹

¹Department of Civil Engineering, Kyoto University, Kyoto 606-8501, JAPAN

²Department of Civil Engineering Systems, Kyoto University, Kyoto 606-8501, JAPAN

ABSTRACT

The unprecedented damage to steel structures during the 1995 Hyogoken-Nanbu Earthquake not only prompted the revision of the Japanese seismic code but also emphasized the need for a comprehensive understanding of buckling damage as well as seismic response, which in reality is complex and multi-directional, as opposed to the conventionally assumed uni-directional approach. Thus, this study investigated the effects of bi-directional load histories on the coupled instability of each plate elements of tubular columns widely used in the construction of elevated highways and building structures. Test results indicate that, in comparison with uniaxial displacement paths, biaxial displacement patterns lead to significant degradation of stiffness, strength and ductility of tubular columns, namely the buckling wave can transmit rapidly in the circumferential direction under the biaxial loading, particularly the non-proportional loading.

KEYWORDS

Tubular member, Cantilever column, Elasto-plastic behavior, Compression, Cyclic loads, Biaxial loading, Non-proportional loading, Earthquake loading, Strength, Ductility

INTRODUCTION

Owing to the unique advantages of steel over concrete, viz strength, weight and speed of construction, bridge piers and building columns in Japan have predominantly been constructed of steel, mostly thin-walled box columns of the cantilever type (Kumar, et al. 1996; Usami, et al. 1992). Although these steel structures have performed adequately during the past moderate earthquakes, their vulnerability to severe seismic loads was sadly exposed during the 1995 Hyogoken-Nanbu Earthquake. The high intensity of this earthquake, one of the largest ever experienced in the world in terms of response spectral value at natural periods of 0.7-2 seconds, resulted in extensive damage to major infrastructure including, most shockingly, steel bridge structures (Watanabe, et al. 1996). The earthquake brought to light the complexity of earthquake excitation and response of structures, prompting the immediate revision of the Japanese seismic design provisions. Accordingly, the seismic codes for road and

railway bridges have been revised, most recent being that of highway bridges in December 1996 which has adopted a limit state design approach which considers elasto-plastic ultimate state of structures in designing for seismic intensity level similar to that of the Hyogoken-Nanbu Earthquake (Japan Road Association 1996). However, these code revisions only stipulate requirements for new construction, reconstruction and repair, hence need to be validated or supported by in-depth research findings in order to assure the safety of structures.

During the Hyogoken-Nanbu Earthquake, rectangular hollow steel piers designed according to 1973 or 1980 specification (Japan Road Association 1973; 1980) with usually high width to thickness ratio, developed local buckling at web and flange plates even though they were stiffened by longitudinal stiffeners and diaphragms (Watanabe, et al. 1996). The buckling of the constituent plates may have caused sudden decrease of bearing capacity in lateral direction after the peak strength resulting in reduced energy dissipation, and also deterioration of the bearing capacity in the vertical direction. Further still, the increase in out-of-plane deformations of the stiffened plates resulted in the corners of the cross-section losing their straightness, finally causing cracks and rupture (Kawashima, et al. 1997). Inevitably, the 1995 Hyogoken-Nanbu Earthquake has focussed attention on the inelastic response of steel structures to severe seismic excitations whose nature may be more complex than originally idealized in design.

Present seismic design codes assume independent action of the uni-directional design seismic motion, which for structures with a regular structural layout, coincide with the principal axes of the structure plan. The design problem thus reduces to one of uniaxial flexure with varying axial force. However in reality, earthquake ground motion is random in nature, and has at least two simultaneous horizontal components causing response in oblique directions and biaxial bending in the columns (Bousias, et al. 1995; Mamaghani, et al. 1995; Zahn, et al. 1989). Moreover, some structures may not have a regular layout and have a tendency to develop torsional response and biaxial bending in the columns, even under uni-directional seismic motions (Watanabe, et al. 1997). As a matter of fact, structural response observed during recent earthquakes has linked some failures to bi-directional load effects, with the most memorable failure being that of the columns of the Imperial County Services building damaged during the 1979 Imperial Valley Earthquake (Saatcioglu, et al. 1989). Hence, in-depth understanding of the inelastic buckling behaviour of rectangular hollow steel columns under cyclic multi-directional load paths is obviously important in seeking enhanced resistance of highway and building structures to severe seismic excitation.

EXPERIMENTATION

Outline of Experimental Program

Studies were conducted on five identical hollow steel box columns modeling bridge piers, tested as cantilever columns under constant axial load and each subjected to a different lateral load history. The lateral load histories investigated included cyclic loading in a designated X-direction parallel to the longer side of the box section, a Y-direction parallel to the shorter side of the box section, a linear XY-direction inclined in the Cartesian axes, and a rectangular XY-direction. Each column specimen was subjected to a constant axial load to simulate the weight of superstructure of magnitude $P=0.125P_y$, where P_y is the axial yield load, and lateral cyclic loads in the desired direction, of incremental displacement amplitudes namely multiples of the predicted yield displacement δ_{y0} due to lateral load in the respective directions. For each displacement amplitude three cycle tests i.e. three cycles of gradual loading and unloading were conducted. Table 1 gives details of the test program. The biaxial displacement amplitudes (points of maximum displacement i.e. tips of the linear XY line and corners of the rectangular XY direction) were multiples of what is referred to here as resultant yield

displacement δ_{Ry0} . The resultant yield displacement, δ_{Ry0} , is the resultant of the yield displacements in the X and Y directions, expressed as $\delta_{Ry0} = \sqrt{(\delta_{y0})_{x-axis}^2 + (\delta_{y0})_{y-axis}^2}$.

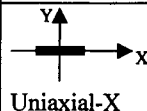
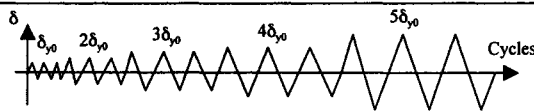
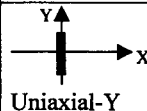
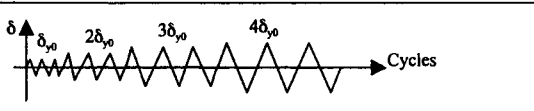
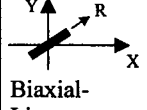

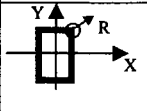
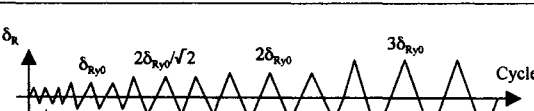
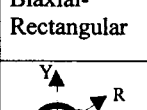

The yield lateral load (H_{y0}) and displacement at yield (δ_{y0}) in X, Y directions were predicted from equations below, for the case of zero axial load.

$$H_{y0} = M_{y0}/h = \sigma_{sy}I/(Z_t h) \tag{1}$$

$$\delta_{y0} = H_{y0}h^3/3EI \tag{2}$$

where M_{y0} = yield moment due to lateral load, I = sectional moment of inertia, Z_t = distance to extreme fibre from the centre of gravity, h = effective height of specimen, σ_{sy} = yield strength of steel, and E_s = modulus of elasticity of steel.

TABLE 1
LOADING AND CYCLING HISTORIES

Specimen	Load path	Cycling history
Sbc-UX	 Uniaxial-X	
Sbc-UY	 Uniaxial-Y	
Sbc-BL	 Biaxial-Linear	
Sbc-BR	 Biaxial-Rectangular	
Sbc-CR	 Biaxial-Circular	

Note: O marks the amplitude (point of maximum displacement at any cycle) for the rectangular loading history, whereupon the second cycling amplitude (δ_{Ry0}) is given as

$$\delta_{Ry0} = \sqrt{(\delta_{y0})_{x-axis}^2 + (\delta_{y0})_{y-axis}^2}$$

The test specimens were fabricated as thin-walled rectangular hollow steel box columns of size B=150mm, D=100mm, t=4.22, length L=881mm and effective length (h)=846mm as shown in Fig. 1. In fabricating each of the specimens, steel plate of grade SS400 was bent to the desired box size with rounded corners and welded at the connecting line or seam to ensure continuity of the box. Plates of size 380x380x24.6mm for bolting on to the testing machine were welded at the ends, and to prevent cross-sectional distortion during tests, diaphragms of about 6.38mm thickness were welded at three spaced locations along the length of the specimens. The base portion of the specimens was stiffened by 6.32 mm thick ribs so as to ensure a rigid base. Accordingly, the test section was the length above the ribs. The plate slenderness parameter (R) is 0.53 for the narrower plates and 0.79 for the wider plates, where R is obtained from plate sectional dimensions and material properties as;

$$R = \frac{b}{t} \sqrt{\frac{\sigma_{sy}}{E_s} \cdot \frac{12(1-\nu^2)}{4\pi^2}} \tag{3}$$

Material properties for the steel, determined from tensile tests on strips cut from the plates of steel box, are illustrated in Table 2, where σ_{su} , ϵ_{sy} and ν_s stand for ultimate strength, yield strain and Poisson's ratio of steel, respectively.

TABLE 2
STEEL MATERIAL PROPERTIES

σ_{su} (N/mm ²)	σ_{sy} (N/mm ²)	ϵ_{sy} (%)	E_s (KN/mm ²)	ν_s	Elongation (%)
446	373	0.177	211	0.272	41.0

Test Setup and Loading

A newly developed multi-directional structure testing system with servo-controlled hydraulic actuators, jointly developed by Kyoto University and Shimadzu Corporation of Japan, was employed in testing the specimens (see Fig. 2). This new six-degree-of-freedom testing system has nine hydraulic actuators (only some are shown in Fig. 2 for clarity), fitted with in-built load cells and LVDTs, with the ability to apply linear or coupling loads in six directions, viz, linear loads along the X-Y-Z axes as well as rotational moments about the X-Y-Z axes. All the actuators have a capacity of 10 tonnes with a stroke of 200mm, with the exception of the axial actuator in the Z direction, which has a capacity of 50 tonnes in compression and 20 tonnes in tension; in addition, all the axial actuators in the X-Y-Z directions, which have a stroke of 100mm.

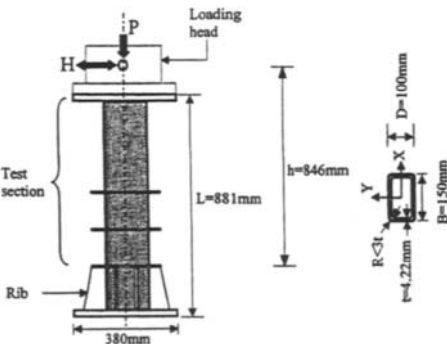


Figure 1: Typical test specimen

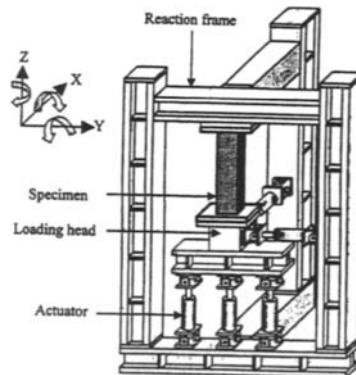


Figure 2: Multi-directional testing system

A specimen for test was securely clamped within the loading head and reaction frame by bolting on to the end plates. Desired lateral cyclic loads with incremental amplitudes, under constant axial force, were then applied quasi-statically through the control of a computer program. In each cycle, the load was applied gradually until the desired maximum displacement and then unloaded, followed by a similar process in the opposite direction. Load and displacement readings were intermittently recorded using a computer as testing progressed. Testing ended when load resistance of the specimen deteriorated to a level near zero, as indicated by on-line computer monitoring, and further confirmed by the observed damage on the specimen.

RESULTS AND DISCUSSIONS

Hysteretic Response

The normalized load-displacement curves of the tested columns, normalized with lateral yield load and displacement at yield, are presented in Figs. 3-7. The arrow mark pinpoints the ultimate normalized horizontal load, and thus gives the ductility when extended to intersect the horizontal axis. A glance at Figs. 3 and 4 show that specimen Sbc-UX has higher ultimate strength (which attains more than the yield stress) and ductility than Sbc-UY as would be expected since the X-direction has the higher sectional moment of inertia (I).

The effects of biaxial load histories are clearly illustrated by comparing Figs. 3, 5(a), 6(a) and 7(a) or Figs. 4, 5(b), 6(b) and 7(b). A reduction in strength and ductility of columns due to biaxial loading, when compared to uniaxial loading is promptly recognized. In the case of uniaxial loading where only two opposite plates are directly loaded, maximum stress is attained in these plates which are perpendicular to the loaded direction, followed by redistribution of stress to the nominally stressed orthogonal plates. These orthogonal plates continue to resist load until their maximum stress level is attained. On the other hand, biaxial loading induces stresses simultaneously in all the four plates forming the box section. When the maximum stress is attained in two opposite plates, it would seem that plastic flow occurs whereby additional stress is redistributed to the orthogonal plates, which also degrade rapidly due to previously accrued stress. A further effect of biaxial loading is the more rapid reduction of column stiffness at each subsequent cycling amplitude, attributable to the simultaneously applied load in all the plates.

The effects of biaxial loading are further illustrated in Fig. 8, which gives the envelope curves of the hysteretic curves for the points of maximum normalized lateral load at each cycling amplitude. In addition to envelope curves for individual uniaxial load histories in the X (Sbc-UY) and Y (Sbc-UX) directions, Fig. 8 also gives the envelope curves of the calculated resultant normalized lateral load versus the resultant displacement normalized by the resultant yield displacement $\delta_{R,y0}$, for the cases of biaxial load histories (Sbc-BL and Sbc-BR) and uniaxial histories (Sbc-UX/UY). The resultant normalized lateral load is given by;

$$\frac{H}{H_{y0}} = \sqrt{\left(\frac{H}{H_{y0}}\right)_{x\text{-component}}^2 + \left(\frac{H}{H_{y0}}\right)_{y\text{-component}}^2} \quad (4)$$

while (in order to facilitate comparison of uniaxial and resultant envelopes) the resultant lateral displacement normalized by resultant yield displacement is given by;

$$\frac{\delta_R}{\delta_{R,y0}} = \frac{\sqrt{\delta_{x\text{-component}}^2 + \delta_{y\text{-component}}^2}}{\sqrt{\delta_{y0\text{-component}}^2 + \delta_{y0\text{-component}}^2}} \quad (5)$$

It is observed that of the three types of biaxial loading histories, biaxial-rectangular loading and biaxial-circular loading are the most damaging as indicated by the sudden drop of its envelope curve in the softening region. Perhaps this is because the rectangular and circular direction has the longer path. Moreover, there exists a state of uniform compressive stress in all the four plates once in any cycle.

A comparison of resultant biaxial envelopes and resultant envelope of combined uniaxial histories confirms that the degrading biaxial effects or interactions are most prominent in the inelastic range. Within the elastic range the biaxial resultants are close to the resultant of the superposed uniaxial load histories suggesting independent action of the plates. However, in the inelastic range, biaxial response is very different from the superposed resultant of the uniaxial load histories. Hence the principal of superposition of uniaxial effects normally employed in design manipulations may not be valid in the inelastic range since the plates are no longer acting independently, but are dependent on each other for load resistance as plastic hinges form. This leads to rapid propagation of buckling deformations in the circumferential direction. Saatcioglu, et al. (1989) have found that for columns subjected to simultaneously varying bi-directional load reversals the level of damage in one direction adversely affects the column in the other direction. They particularly noted that if the deformation in one direction is less than the yield deformation, bi-directional effects on response in the orthogonal direction are small. However, if post-yield deformations are experienced in both directions, severe strength and stiffness degradation is observed.

Local Buckling Deformations

As loading on column specimens progressed, it was observed that the two columns subjected to uniaxial displacement patterns (Sbc-UX and Sbc-UY) first incurred outward buckling on the two opposite plates perpendicular to the direction of loading. Inward buckling in the remaining orthogonal plates occurred in the subsequent cycling amplitude. On the other hand, specimens subjected to biaxial displacement patterns had initial outward buckling in the two wider width plates parallel to the minor axis, soon followed by inward buckling of the short width plates, within the same displacement amplitude. Typical buckling deformation is shown in Photo 1.

The column loaded in biaxial-rectangular and biaxial-circular directions (Sbc-BR, Sbc-CR) had the earliest buckling at $2\delta_{Ry0}$, followed by specimen Sbc-BL of biaxial-linear direction at $3\delta_{Ry0}$, specimen Sbc-UY of uniaxial Y-direction at $3\delta_{y0}$ and finally specimen Sbc-UX at $4\delta_{y0}$. As previously noted, biaxial loading induces stresses simultaneously in all the four plates forming the steel box in a similar mode i.e. they are all flange plates, hence resulting in early occurrence and rapid propagation of buckling deformations in the circumferential direction.

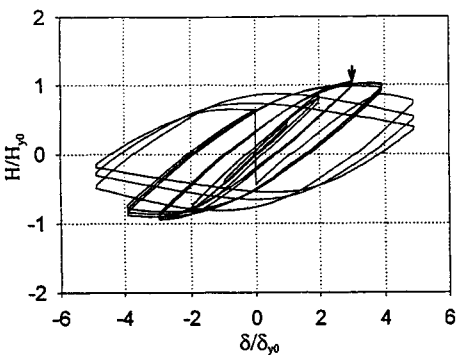


Figure 3: Normalized lateral load-displacement response in uniaxial-X direction

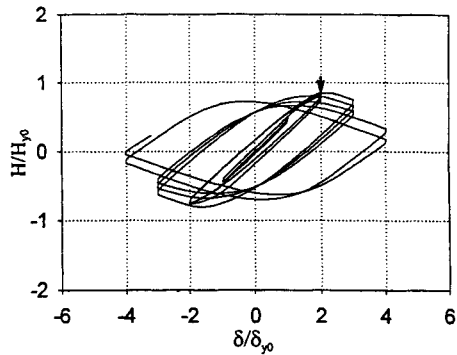


Figure 4: Normalized lateral load-displacement response in uniaxial-Y direction

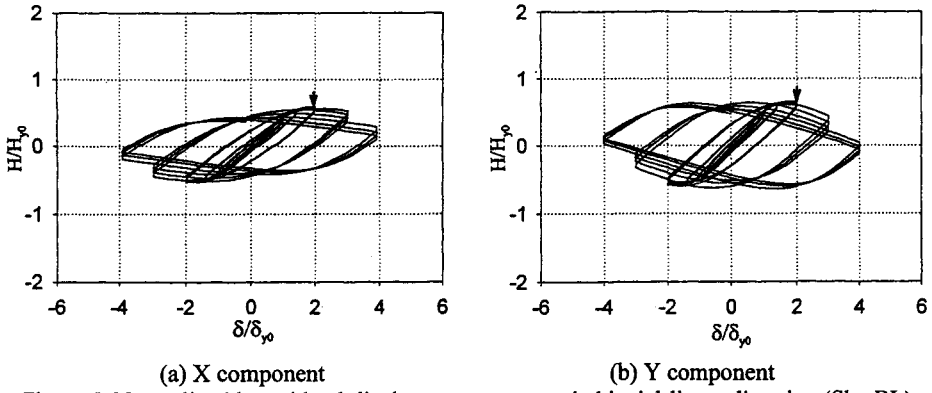


Figure 5: Normalized lateral load-displacement response in biaxial-linear direction (Sbc-BL)

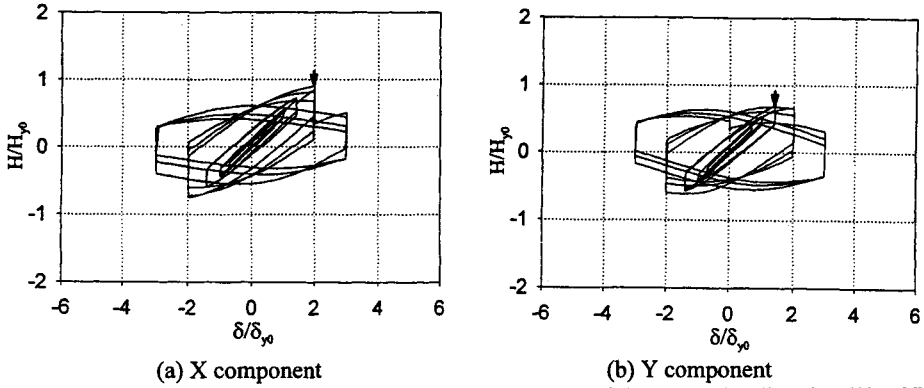


Figure 6: Normalized lateral load-displacement response in biaxial-rectangular direction (Sbc-BR)

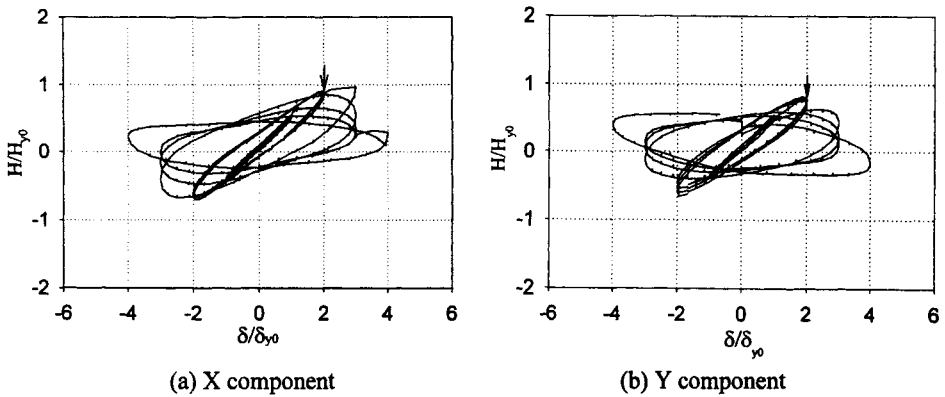


Figure 7: Normalized lateral load-displacement response in biaxial-circular direction (Sbc-CR)

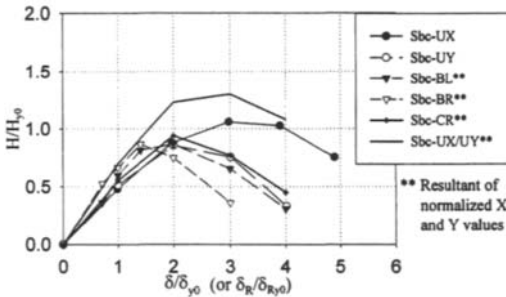


Figure 8: Envelope curves for load vs. displ. relations Photo 1: Typical buckling deformation

CONCLUSIONS

The main conclusion drawn from this experimental study is that, in comparison with uniaxial displacement paths, biaxial displacement paths cause more extensive degradation of column stiffness, strength and ductility, in each of the two transverse directions considered separately. The most damaging such path is that of biaxial-rectangular and biaxial-circular directions. It is particularly noted that biaxial effects are more prominent in the inelastic range. In light of these experimental observations, adequate inclusion of the effects of biaxial loading in structural design would seem most appropriate, in order to satisfy two basic criteria of seismic design; namely high stiffness at working loads and high ductility and energy dissipation in the inelastic range. Considering the randomness of earthquake motion, further study is necessary to quantify the effects of biaxial loading.

REFERENCES

- Kumar, S. and Usami, T. (1996). "Damage evaluation in steel box columns by cyclic loading tests", *J. Struct. Engrg.*, ASCE, **122**(6), 626-634.
- Usami, T., Mizutani, S., Aoki, T., and Itoh, Y. (1992). "Steel and concrete-filled steel compression members under cyclic loading", stability and ductility of steel structures under cyclic loading, edited by Fukumoto, Y. and Lee, G.C., CRC Press, London, 123-138.
- Watanabe, E. and Oyawa, W.O. (1996). "Lessons from the 1995 Great Hanshin-Awaji Earthquake: Performance of concrete and steel bridge structures", *J. Civil Engrg.*, JKUAT, Nairobi, **2**, 40-64.
- Japan Road Association (1997, 1980, 1996), *Specification for highway bridges: II Steel Bridges, & V Earthquake-resistant design* (in Japanese).
- Kawashima, K. and Unjoh, S. (1997). "Impact of Hanshin/Awaji earthquake on seismic design and seismic strengthening of highway bridges", *J. Struct. Engrg./Earthquake Engrg.*, JSCE, **I-38**, 1-30.
- Bousias, S.N., Verzeletti, G., Fardis, N. and Gutierrez, E. (1995). "Load-Path effects in column biaxial bending with axial force", *J. Engrg. Mech.*, ASCE, **121**(5), 596-605.
- Mamaghani, I.H.P., Shen, C., Mizuno, E., and Usami, T. (1995). "Cyclic behaviour of structural steels: Experiments", *J. Engrg. Mech.*, ASCE, **121**(11), 1158-1164.
- Zahn, F.A., Park, R., and Priestley, M.J.N. (1989). "Strength and ductility of square reinforced concrete column section subjected to biaxial bending", *ACI Struct. J.*, **56**(2), 123-131.
- Watanabe, E., Sugiura, K., and Kitane, Y. (1997). "Three Dimensional Response of Bridge Systems Subjected to Strong Ground Motions", *J. Struct. Engrg.*, JSCE, **43A**, 897-906.
- Saatcioglu, M. and Ozcebe, G. (1989). "Response of Reinforced Concrete columns to simulated seismic loading", *ACI Struct. J.*, **86**(1), 3-12.
- Park, R. (1992). "Capacity design of ductile RC building structures for earthquake resistance", *Struct. Engrg.*, **70**(16), 279-289.

AUTHOR INDEX

- Aalberg A 93
Abe K 803
Allen H G 305
Almanzar L I 297
Alwis W A M 391
Amdahl J 629
Ang K K 517
Ansourian P 613
Aoki T 779
Au F T K 53
- Barbero E J 297
Beale R G 197, 571
Bhogal A 77
Blandford G E 417
Bradford M A 347
Bridge R 663, 671
- Calabrese F A 493
Chaaya M 613
Chan F 605
Chan G C M 597
Chan S L 313
Chen C N 697
Chen H 485
Chen Y Y 213
Cheng Q H 289
Cheung Y K 53
Chien W-Z 477, 527
Cho S R 433
Choi B-W 433
Chong K P 3
Chou S M 401
Chung K F 245
- Darr M H 271
Davies A W 77
Davies J M 17
Diedricks A A 367
- Enjily V 197
- Feng Z-N 305
Fujikubo M 425
Ge H B 441
- Godley M H R 197, 571
Godoy L A 297
Goto Y 787, 803
Greiner R 663
Guggenberger W 663
Guillow S G 771
Guo P 477
Gupta N K 263
Gupta P 417
- Hancock G J 145
Hanssen L 67
Hara T 501
Hellsten M 741
Höglund T 129
Hopperstad O S 67, 85, 93
Hossain K M A 321
Hsu C M 689
Hsu S S 753
Huang Q 477
- Inoguchi H 587
- Jikuya K 587
Jonaidi M 613
Jones N 237
- Kabir M Z 189
Kandasamy S 229
Kato S 655
Khan A H 723
Khonsari S V 761
Kishi N 787, 795, 803
Kitahori H 705
Knight G M S 229
Koeda H 787, 795
Koivula R 535
Komuro M 795, 803
Konstandakopoulos T G 509
Kubo M 705
Kuo S R 553
- LaBoube R A 181
Langseth M 53, 85, 93
Lawson R M 329
Lehmkuhl H 253

- Liang Q Q 339
 Liew J Y R 485
 Liu X L 461
 Lok T S 289
 Lu G 771
- Macdonald M 153
 Mahendran M 111, 221
 Maia N S 647
 Malo K A 93
 Mansur M A 383
 Mansur T R 647
 Masaoka K 469
 Matsunaga Y 655
 Matsuoka K G 795
 Medeiros E B 647
 Michaltsos G T 509
 Mikkelsen L P 679
 Moen L 85
 Mohamed A W 375
 Mol L 321
 Moore D B 103
 Moy S S J 305, 543
 Mullett D L 329
 Murakami S 587
 Mutoh I 655
- Naaman A E 383
 Narayanan R 449
 Niho O 425
 Nishimoto K 501
 Nishimura H 579
 Nishimura N 587
- Ohga M 501
 Okada H 469
 Ono S 787
 O'Shea M 671
 Osterrieder P 253
 Oyawa W O 809
- Pahdi G S 305
 Pan S J 213
 Pan W F 689
 Panzeri N 279
 Papangelis J P 41
 Paramasivam P 29, 383
 Parvinnia S M H 761
 Paulsen F 713
 Peköz T 137
 Pi Y-L 41, 121
 Pi Yong-Lin 205
- Pircher M 663, 671
 Poggi C 279
 Pu Y 571
 Put B M 121, 205
- Rao N 229
 Rasmussen K J R 409
 Rhodes J 153, 173
 Rogers C A 145
- Schafer B W 137
 Schleyer G K 753
 Shanmugam N E 449, 485, 563
 Sharrock M J 723
 Shen Z Y 213
 Sheno R A 305
 Shi Y J 245
 Shigematsu T 501
 Shimizu S 579
 Skallerud B 629
 So A K W 313
 Song I-C 433
 Spence J 597
 Sugiura K 809
 Suzuki M 779
- Takeuchi S 587
 Tan K L 383
 Tan Y H 563
 Tang R B 221
 Tang Y 213
 Taylor G T 153
 Telue Y 111
 Teng J G 605
 Teo K Y 401
 Thevendran V 563
 Tide R H R 271, 493
 Tooth A S 597
 Trahair N S 41, 121, 205
 Troup S 543
 Tvergaard V 679
- Ueda Y 469
 Ujihashi S 173
 Usami T 441
 Uy B 339, 367
- van den Berg G J 161
 Varghese B 425
 Vayas I 733
 Velmurugan R 263

- Wada B K 3
Wallace J 571
Wan Badaruzzaman W H 355
Wang C M 517
Wang G Y 213
Wang S T 417
Wang Y C 103
Watanabe E 809
Watanabe T 441
Welo T 713
Werner F 253
White M D 237, 753
Wong H F 173
Wright H D 321, 355, 367, 375
Wu S 181

Xiao R Y 543
Xu K-Y 527

Yamaguchi E 803
Yanagihara D 425
Yang S C 553
Yang Y B 553
Yao T 425
Young B 409
Yu C H 485
Yu W-W 181
Yuen S W 313

Zaras J 173
Zhang Y C 461
Zheng D Y 53
Zhiming Y E 639
Zhou Z-W 527
Zhu W P 477
Zhu Y J 461
Zielnica J 621

This Page Intentionally Left Blank

KEYWORD INDEX

- adaptive structures 3
- advanced inelastic analysis 485
- AISI 137
- allowable stress 597
- aluminium 67, 93, 771
- aluminium alloys 85
- analysis 41
- angles 229
- anisotropy 527
- annealing 761
- arches 41
- average crush load 263
- axial compression 263, 433, 771
- axial load 671
- axial loading 93

- beam 205
- beam finite elements 629
- beam vibration modes 53
- beams 321
- bearing 145
- bellows 477
- bending 197
- bending of sections 713
- bending strength 85
- biaxial bending 121
- biaxial loading 809
- bimoment 723
- bin 613
- bolt 145
- bolted moment connections 245
- box girder 579
- box section with round corners 803
- box-section member 501
- braced 493
- bracing 347, 417
- British standards 103
- buckling 41, 121, 205, 271, 279, 297, 321, 347, 367, 409, 417, 469, 485, 553, 597, 605, 613, 671
- buckling behavior 587
- buckling design procedure 655
- buckling of studs 111
- buckling strength 425
- building 741

- calculus of variation 697
- cantilever column 809
- cantilevers 347
- carbon steel 153
- cassette 17
- centrally perforated plates 563
- channel beams 121
- channel column 409
- channel section 205
- channels 153, 197
- chimney 271, 663
- circular perforation 587
- circular plate 517
- circular ring shells 477
- circular tube 771
- circular tubes 761
- clamped edge 449
- closed hat section 173
- closed-form solution 697
- code calibration 103
- code comparisons 597
- codes of practice and standards 77
- cold formed steel 173, 367
- cold forming 153
- cold-formed 121, 129, 197, 205
- cold-formed members 213
- cold-formed steel 17, 137, 181, 229
- cold-formed steel members 245
- cold-formed steel wall frames 111
- cold-formed structures 571
- collapse modes 771
- column buckling 433
- columns 173, 321, 367, 571
- combined bi-axial thrust and lateral pressure loads 425
- combined load 579
- composite 189, 321, 329, 355
- composite beams 347
- composite columns 339
- composite connections 543
- composite construction 367
- composite cylinders 279
- composite laminated plate 289
- composite materials 383
- composites 3, 263
- composites materials 297

- compression 153, 809
 compressive strength 85
 concentrated masses 509
 concrete 339
 conical shells 263
 connection 145
 construction 741
 corner radii 153
 C-purlin 461
 crack propagation 229
 creep 391, 689
 crest-fixed 221
 critical load 621
 critical loads 339
 crush length 263
 crushing 173, 237
 C-section 417
 curvature-rate 689
 cyclic loading 441, 787, 803
 cyclic loads 809
 cylinder 663
 cylindrical thin-walled shell 671
- damage criterion 305
 damaged pipe 587
 deaerator 647
 debonding 271
 decking 329
 decks 181
 deep beam 53
 deformability 213
 design 41, 129, 329, 605
 design charts 383
 design code 93
 design codes 67
 design formula 563
 design formulae 221
 design formulation 433
 design methods and aids 77
 diametral crushing 761
 diaphragm bracing 461
 dimensional tolerances 713
 direct strength 137
 distortional 205
 distortion 347
 distortional buckling 161
 double-hat sections 237
 dryboard 355
 ductility 145, 383, 441, 733, 787, 809
 dynamic behavior 795
 dynamic instability 639
- earthquake loading 809
 earthquake resistance test 779
 effective width 339, 449
 effective widths 253
 elastic buckling 137
 elastic stiffness matrix 553
 elasticity 347
 elasto-plastic 795
 elasto-plastic analysis 441, 787
 elasto-plastic behavior 809
 electric resistance welded (ERW) pipe 587
 elephant foot bulge buckling mode 795
 empirical 237
 energy absorption 173, 263, 741, 761
 energy method 449
 energy transmission 741
 Eurocode 103
 expanding metal 741
 experiment 433, 705
 experimental investigation 245
 experimental stress analysis 647
 experimental techniques 753
 experimental work 597
 experiments 85, 237
 extended endplate 543
 extensional axis 536
 extrusions 85
- fatigue 229
 FEM 579
 ferrocement 383
 ferrocement cementitious thin wall structures 29
 finite beam elements 253
 finite element analysis 221, 339, 401, 803
 finite element method 289, 461, 563
 finite element model 543
 finite element modelling 245
 finite strain 679
 finite strip 53, 137
 finite-element 417
 fire 329
 fixed-ended 409
 flexible design 741
 flexural 189
 flexural strength 181, 383
 flexure 723
 foam 771
 foams 263
 force recovery 553
 fracture 229, 271
 frame element 485

- frames 297
- full scale wall frame tests 111
- fusion bond 271

- G550 145
- geometric and material nonlinearities 339
- geometric imperfections 279
- geometric nonlinearity 461
- geometric stiffness matrix 553
- geometrical and material nonlinearities 485
- geometric-nonlinear 417
- GRP composites 305
- guided beam 536

- Hamilton's principle 697
- harmonics 53
- high-strength low-ductility steel 181
- hole 579
- hollow flange beams 121
- hollow sections 741
- horizontal storage vessels 597
- house 17
- hysteresis loop 803

- idealized structural unit method (ISUM) 469
- impact resistance 29
- imperfection 671
- imperfections 93
- industrial forming operations 713
- inelastic 197, 205
- inelastic bifurcation analysis 409
- inflatable structures 3
- initial deflection 425
- initial geometric imperfections 655
- initial imperfection 417, 469
- in-plane force 501
- in-plane strength 41
- instability 485
- interaction 733
- I-section member 501

- laminated cylindrical shell 527
- lamination defects 279
- large displacements 621
- large inelastic deformation 753
- lateral 205
- lateral buckling 41, 493
- lateral crushing 761
- lateral-torsional buckling 705
- latticework 741

- lightweight 321, 355
- liner 271
- lipped channel 161
- load capacity 153
- load carrying capacity 449
- loading test 213
- local buckling 161, 213, 367, 441, 629, 705, 733, 787, 795, 803
- local deformations 713
- long-term deformation 391

- membrane analyses 679
- mindlin plate theory 517
- minimax deflection 517
- mode shape 501
- moment frames 493
- moment-rotation 543
- monosymmetric I-beam 705
- monosymmetry 205
- multi-cell sections 723

- National Application Document 103
- natural frequency 501
- net section fracture 145
- non-compact section 705
- non-linear 613
- nonlinear analysis 553
- non-linear dynamic 509
- nonlinear dynamics 527
- non-linear flexural behaviour 289
- nonlinear geometry 629
- nonlinear oscillation 527
- nonlinear vibration 639
- nonlocal plasticity 679
- non-orthogonal functions 527
- non-proportional loading 809
- numerical analyses 67
- numerical simulation 647
- numerical simulations 93

- octagonal section 779
- off-set element 536
- onset of buckling 713
- openings 571
- open-profile 391
- optimal design 517
- out-of-plane strength 41
- overall load capacity 655

- panels 181, 383
- parametric resonance 527
- partially restrained connections 493

- partially stiffened 161
- perforated channels 571
- perforation 571
- perturbation method 289
- perturbation techniques 279
- piecewise constant thickness 517
- pipe 795
- plaiting 741
- plasterboard lining 111
- plastic anisotropy 85
- plastic flow theory 621
- plastic hinge 485
- plastic-glassy sheeting 313
- plasticity 629
- plasticity model 803
- plate 579
- plate buckling 67
- plates 173, 449, 753
- ply-failure 297
- point symmetry 205
- post-buckling 197, 279, 297, 401
- post-buckling analysis 553
- post-buckling deformations 713
- post-local buckling 339
- post-ultimate state 433
- prefabrication 383
- pressure 613
- pressurised tubes 679
- principal axes 723
- profiled steel roof claddings 221
- profiled steel sheet 355
- profiles 741
- progressive buckling 237
- progressive crushing 263
- progressive damage analysis 305
- pull-through/dimpling failures 221
- pulse pressure loading 753
- pultruded 189
- pure bending 689
- purlins 253

- quasi-static loading 761

- racks 493
- rectangular hollow beams 121
- rectangular hollow section 213
- rectangular plate 469
- reinforced concrete 391
- repair 779
- residual stress 671
- resistance 129
- restraint 347

- reticulated shells 655
- rigid body motion 553
- rigorous solution 697
- ringbeams 605
- rings 605
- rotation capacity 705

- S- N curves 229
- Saint Venant's torsion theory 697
- screw 145
- secant modulus 161
- second order analysis 253
- secondary roofing slabs 29
- second-order 417, 485
- second-order elastic analysis 655
- second-order plastic hinge analysis 655
- section strength 41
- sectional yielding condition 469
- sectorial area 536
- sectorial coordinates 723
- seismic design concept 779
- selective eigen-function 469
- semi-membrane-concept 663
- settlement 613
- shaking table 795
- shear buckling 733
- shear centre 723
- shear connection 543
- shear deformation 129, 697
- shear resistance 129
- shear strength 77
- shear wall 53
- shearflow 723
- sheet steel 145
- shell 613
- shells 605
- shells and plates 313
- shells of revolution 477
- shrinkage 391
- sideways 493
- silos 663
- silos 605
- singly symmetric 417
- slender ring shells 477
- slenderness 321
- slots 129
- small scale cladding tests 221
- smart materials 3
- smart structures 3
- snap-through buckling 313
- solid mechanics 3
- space structures 3

- spot welds 173
- stability 189, 313, 367, 605, 621, 671
- stainless steel 153, 161
- static 237
- steel 129, 271, 329, 493
- steel beams 121
- steel bridge pier 803
- steel connections 543
- steel ductility 221
- steel frame 17
- steel framing 741
- steel members 733
- steel pier 779, 795
- steel plates 339
- steel structures 41
- steel tubes 761
- steel-pipe piers 787
- stiffened panel 433
- stiffened plate 441
- stiffened plates 93
- strain energy 621
- strain gauge 647
- strength 321, 441, 733, 809
- stress 543
- stress concentration 587
- stress concentrations 271
- stress relieving 761
- stressed skin 17
- structural control 3
- structural crashworthiness 237
- structural engineering 41, 121
- structural integrity 647
- stub-column stress-strain curve 629
- stub-columns 401
- stud 129
- studs 741
- subharmonic bifurcation 527
- suck-in 713
- sunscreens 29
- system of axes and special points 536

- tall masts 509
- tangent modulus 161
- tangent rigidities 409
- tank 613, 663
- tanks 605
- tensile instabilities 679
- tension buckling 579
- testing 329
- tests 383
- theory 237
- thermoelectric power plant 647

- thin panels 305
- thin plate 53
- thin shallow conical shell 639
- thin walled 129, 321, 391, 417, 663, 597, 771
- thin-walled columns 297
- thin-walled frame element 485
- thin-walled member 501
- thin-walled structures 3, 253, 401
- thin-walled tube 689
- thin-walled tubes 237
- three-dimensional 417
- three-surface model 787, 803
- tilting 145
- titanium 271
- top-hat sections 237
- torsion 121, 723
- torsional 189
- torsional axis 536
- torsional-flexural 417
- torsional-lateral buckling 433
- transfer matrix method 501
- transient response 753
- transverse pressure 305
- transverse shear deformation 289
- T-sections 605
- tube ovalization 689
- tubular column 587
- tubular member 809
- twist 723
- two-span cladding tests 221

- ultimate load 213, 401, 563
- ultimate strain 433
- ultimate strength 425, 433, 469, 571, 655, 705
- uniaxial and biaxial compression 563
- unidirectional and woven reinforcement 305
- uniformly varying load 449

- variable thin-walled member 509
- viscoplasticity 689
- vlasov beam 536
- vlasov element 536
- volcanic pumice 321

- wall stud 17
- warping 723
- warping function 697
- warping torque 723
- warp-restrained torsion 723
- water tanks 29
- weld 671

- welded aluminium girders 77
- welded steel beam 705
- welding 761
- welding residual stresses 425
- wind load 663
- wind uplift 221
- yield condition 621
- yield line 197, 543
- yield strength reduction factors 181
- yielding 409
- zed beams 121
- Z-section 205